Get Full Access and More at ExpertConsult.com

COMPARATIVE ANATOMY AND HISTOLOGY

A MOUSE, RAT, AND HUMAN ATLAS

SECOND EDITION

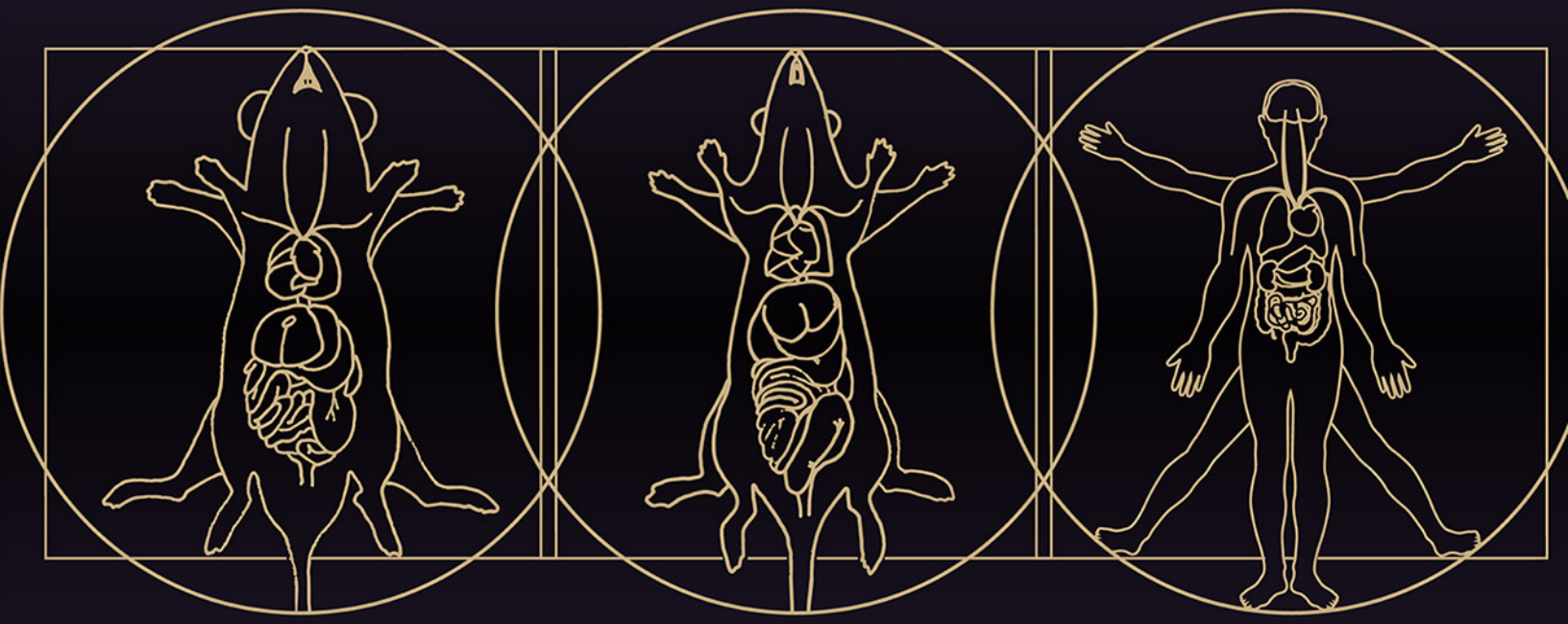

EDITED BY
PIPER M. TREUTING
SUZANNE M. DINTZIS
KATHLEEN S. MONTINE

Expert CONSULT Built with inkling | E books

Any screen. Any time. Anywhere.

Activate the eBook version
of this title at no additional charge.

Expert Consult eBooks give you the power to browse and find content, view enhanced images, share notes and highlights—both online and offline.

Unlock your eBook today.

1. Visit **expertconsult.inkling.com/redeem**
2. Scratch off your code
3. Type code into "Enter Code" box
4. Click "Redeem"
5. Log in or Sign up
6. Go to "My Library"

It's that easy!

Scan this QR code to redeem your eBook through your mobile device:

Place Peel Off Sticker Here

For technical assistance:
email expertconsult.help@elsevier.com
call 1-800-401-9962 (inside the US)
call +1-314-447-8200 (outside the US)

ELSEVIER

Use of the current edition of the electronic version of this book (eBook) is subject to the terms of the nontransferable, limited license granted on expertconsult.inkling.com. Access to the eBook is limited to the first individual who redeems the PIN, located on the inside cover of this book, at expertconsult.inkling.com and may not be transferred to another party by resale, lending, or other means.

2015v1.0

COMPARATIVE ANATOMY AND HISTOLOGY

A MOUSE, RAT, AND HUMAN ATLAS

Second Edition

This page intentionally left blank

Comparative Anatomy and Histology

A Mouse, Rat, and Human Atlas

Second Edition

EDITED BY

Piper M. Treuting, DVM, MS, Diplomate, ACVP
Associate Professor, Chief of Comparative Pathology
Department of Comparative Medicine
Adjunct Associate Professor, Department of Pathology
University of Washington School of Medicine, Seattle, WA, United States

Suzanne M. Dintzis, MD, PhD
Associate Professor, Department of Anatomic Pathology
University of Washington School of Medicine, Seattle, WA, United States

Kathleen S. Montine, PhD, ELS
Senior Principal Research Scientist, Department of Pathology
University of Washington School of Medicine, Seattle, WA, United States

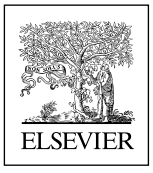

ACADEMIC PRESS
An imprint of Elsevier

Academic Press is an imprint of Elsevier
125 London Wall, London EC2Y 5AS, United Kingdom
525 B Street, Suite 1800, San Diego, CA 92101-4495, United States
50 Hampshire Street, 5th Floor, Cambridge, MA 02139, United States
The Boulevard, Langford Lane, Kidlington, Oxford OX5 1GB, United Kingdom

Copyright © 2018 Elsevier Inc. All rights reserved.

No part of this publication may be reproduced or transmitted in any form or by any means, electronic or mechanical, including photocopying, recording, or any information storage and retrieval system, without permission in writing from the publisher. Details on how to seek permission, further information about the Publisher's permissions policies and our arrangements with organizations such as the Copyright Clearance Center and the Copyright Licensing Agency, can be found at our website: www.elsevier.com/permissions.

This book and the individual contributions contained in it are protected under copyright by the Publisher (other than as may be noted herein).

Notices
Knowledge and best practice in this field are constantly changing. As new research and experience broaden our understanding, changes in research methods, professional practices, or medical treatment may become necessary.

Practitioners and researchers must always rely on their own experience and knowledge in evaluating and using any information, methods, compounds, or experiments described herein. In using such information or methods they should be mindful of their own safety and the safety of others, including parties for whom they have a professional responsibility.

To the fullest extent of the law, neither the Publisher nor the authors, contributors, or editors, assume any liability for any injury and/or damage to persons or property as a matter of products liability, negligence or otherwise, or from any use or operation of any methods, products, instructions, or ideas contained in the material herein.

British Library Cataloguing-in-Publication Data
A catalogue record for this book is available from the British Library

Library of Congress Cataloging-in-Publication Data
A catalog record for this book is available from the Library of Congress

ISBN: 978-0-12-802900-8

For Information on all Academic Press publications
visit our website at https://www.elsevier.com/books-and-journals

Publisher: Mica Haley
Acquisition Editor: Tari Broderick
Editorial Project Manager: Pat Gonzalez
Production Project Manager: Lucía Pérez
Designer: Matthew Limbert

Typeset by MPS Limited, Chennai, India

CONTENTS

List of Contributors xi

Preface to the Second Edition xv

Acknowledgments from the First Edition xvii

CHAPTER 1 INTRODUCTION

Piper M. Treuting, Suzanne M. Dintzis and Kathleen S. Montine

Overview and Introduction to the Second Edition 1
Comparative Pathology: Closing a Gap 1
C57BL/6 Mice as Index Strain 5
Sprague-Dawley Rats as Index Strain 5
Atlas Scope and Design 5
Further Reading and Relevant Websites 6

CHAPTER 2 PHENOTYPING

Cory F. Brayton and Piper M. Treuting

Introduction 9
Phenotyping Study Design 10
- Strategies 10
- Materials and Methods 10

Reporting 16
Conclusion 20
Further Reading and Relevant Websites 20

CHAPTER 3 NECROPSY AND HISTOLOGY

Sue E. Knoblaugh and Julie Randolph-Habecker

Introduction 23
Fixation Considerations Prior to Necropsy 24
- Major Groups of Fixatives 24
- Tissue Fixation Variables to Consider 25
- Decalcification of Bone Samples 26
- Frozen Tissue for Histologic Evaluation 27

Necropsy 27
- Recommended Materials 28
- External Examination 29
- First Incision 30
- Internal Examination 32
- Next Steps 45

Histology 45
- Processing 47
- Embedding 49
- Sectioning 49
- Staining 49

Further Reading and Relevant Websites 51

CHAPTER 4 MICROSCOPY, IMMUNOHISTOCHEMISTRY, DIGITAL IMAGING, AND QUANTITATIVE MICROSCOPY

Paul C. Goodwin, Brian Johnson and Charles W. Frevert

Introduction 53
Key Elements of Microscopy 53
- Magnification 53
- Resolution 54
- Contrast 54

Key Elements of IHC 56
- Background 56
- Tissue Processing 56
- Validation of Antibody Specificity 56
- Protocol Optimization 58
- Antibody Controls 60
- Tissue Controls 60

Key Elements of Digital Imaging 61
Key Elements of Quantitative Microscopy 62
- Background 62
- Stereology 63
- Image Analysis 64

IHC and Imaging Reproducibility 64
Acknowledgments 65
Further Reading 65

CHAPTER 5 SKELETAL SYSTEM

Christopher Jerome, Benjamin Hoch and Cathy S. Carlson

Introduction 67
Skeleton 68
- Gross Anatomy 68
- Histology 69

Long Bones 73
- Gross Anatomy 73
- Histology 75

Spine 82
- Gross Anatomy 82
- Histology 83

Joints 83
- Gross Anatomy 83
- Histology 83

Soft Tissues 85
Further Reading 87

CHAPTER 6 NOSE, SINUS, PHARYNX, AND LARYNX

Jack R. Harkema, Stephan A. Carey, James G. Wagner, Suzanne M. Dintzis and Denny Liggitt

INTRODUCTION 89
Nose and Sinus 90
Gross Anatomy 90
Preparation of Nasal Tissues for Microscopic Exam 92
Histology 94
Other Nasal Cavity Features 103
Pharynx and Larynx 105
Gross Anatomy 105
Preparation of Rodent Pharynx and Larynx for Microscopic Exam 106
Histology 106
Further Reading 112

CHAPTER 7 ORAL CAVITY AND TEETH

Piper M. Treuting, Thomas H. Morton Jr. and Peter Vogel

INTRODUCTION 115
Oral Cavity 115
Gross Anatomy 115
Histology 117
Teeth 121
Gross Anatomy 121
Histology 125
Further Reading 133

CHAPTER 8 SALIVARY GLANDS

Renee R. Hukkanen, Suzanne M. Dintzis and Piper M. Treuting

INTRODUCTION 135
Salivary Gland Features 135
Gross Anatomy 135
General Histology 135
Submandibular Gland 139
Gross Anatomy 139
Histology 142
Parotid Gland 142
Gross Anatomy 142
Histology 142
Sublingual Gland 143
Gross Anatomy 143
Histology 144
Further Reading 144

CHAPTER 9 RESPIRATORY SYSTEM

David K. Meyerholz, Carlos J. Suarez, Suzanne M. Dintzis and Charles W. Frevert

INTRODUCTION 147
Trachea 147
Gross Anatomy 147
Histology 148
Lung 151
Gross Anatomy 151
Bronchi to Terminal Bronchioles 151
Gross Anatomy 151
Histology 152
Respiratory Zone 156
Gross Anatomy 156
Histology 156
Lung Circulatory System 159
Gross Anatomy 159
Histology 159
Pleura 159
Gross Anatomy 159
Histology 160
Further Reading 162

CHAPTER 10 CARDIOVASCULAR

Bernard S. Buetow and Michael A. Laflamme

INTRODUCTION 163
Heart 167
Gross Anatomy 167
Relative Size Considerations 170
Histology 172
Cardiac Valves 178
Gross Anatomy 178
Histology 178
Conduction System 181
Great Vessels and Coronary Vasculature 181
Gross Anatomy 181
Histology 184
Common Incidental Findings in Rodents 187
Further Reading 188

CHAPTER 11 UPPER GASTROINTESTINAL TRACT

Piper M. Treuting, Mark J. Arends and Suzanne M. Dintzis

INTRODUCTION 191
Esophagus 191
Gross Anatomy 191
Histology 192
Stomach 194
Gross Anatomy 194
Histology 195
Small Intestine 201
Gross Anatomy 201
Histology 202
Methods 211
Further Reading 211

CHAPTER 12 LOWER GASTROINTESTINAL TRACT

Piper M. Treuting, Mark J. Arends and Suzanne M. Dintzis

INTRODUCTION 213
Cecum 213
Gross Anatomy 213
Histology 216
Appendix 216
Gross Anatomy 216
Histology 218

Colon 220
Gross Anatomy 220
Histology 223
Gut-Associated Lymphoid Tissue 228
Gross Anatomy 228
Histology 228
Further Reading 228

CHAPTER 13 HEPATOBILIARY SYSTEM

Arlin B. Rogers and Renee Z. Dintzis

INTRODUCTION 229
Liver 230
Gross Anatomy 230
Histology 233
Gallbladder 238
Further Reading 239

CHAPTER 14 PANCREAS

Denny Liggitt and Suzanne M. Dintzis

INTRODUCTION 241
Pancreas 241
Gross Anatomy 241
Histology 243
Further Reading 249

CHAPTER 15 ENDOCRINE SYSTEM

Krista Marie DuBray La Perle and Suzanne M. Dintzis

INTRODUCTION 251
Thyroid Gland 251
Gross Anatomy 251
Histology 253
Parathyroid Gland 255
Gross Anatomy 255
Histology 256
Adrenal Gland 256
Gross Anatomy 256
Histology 258
Pituitary Gland 262
Gross Anatomy 262
Histology 262
Pineal Gland 268
Gross Anatomy 268
Histology 269
Paraganglia 270
Gross Anatomy 270
Histology 271
Further Reading 272

CHAPTER 16 URINARY SYSTEM

Martha A. Delaney, Jolanta Kowalewska and Piper M. Treuting

INTRODUCTION 275
Kidney 275
Gross Anatomy 275
Histology 282
Ureters, Urinary Bladder, and Urethra 291
Gross Anatomy 291
Histology 296
Further Reading 301

CHAPTER 17 FEMALE REPRODUCTIVE SYSTEM

Kelli L. Boyd, Atis Muehlenbachs, Mara H. Rendi, Rochelle L. Garcia and Katherine N. Gibson-Corley

INTRODUCTION 303
Ovary 303
Gross Anatomy 303
Histology 307
Oviduct (Uterine Tube) 310
Gross Anatomy 310
Histology 312
Uterus and Cervix 315
Gross Anatomy 315
Histology 315
Vagina and Clitoris 320
Gross Anatomy 320
Histology 321
Placenta 321
Gross Anatomy 321
Histology 324
Further Reading 334

CHAPTER 18 MALE REPRODUCTIVE SYSTEM

Sue E. Knoblaugh, Lawrence True, Maria Tretiakova and Renee R. Hukkanen

INTRODUCTION 335
Testes 336
Gross Anatomy 336
Histology 338
Efferent Ducts 341
Gross Anatomy 341
Histology 342
Epididymis 342
Gross Anatomy 342
Histology 343
Vas Deferens 343
Gross Anatomy 343
Histology 345
Seminal Vesicles (Vesicular Glands) 346
Gross Anatomy 346
Histology 346
Prostate Gland 348
Gross Anatomy 348
Histology 349
Ampullary Glands 354
Gross Anatomy 354
Histology 354
Bulbourethral Glands 355
Gross Anatomy 355
Histology 355

Preputial Glands 355
Gross Anatomy 355
Histology 355
Urethra 357
Gross Anatomy 357
Histology 360
Penis 360
Gross anatomy 360
Histology 360
Further Reading 362

CHAPTER 19 HEMATOPOIETIC AND LYMPHOID TISSUES

Jerrold M. Ward, Sindhu Cherian and Michael A. Linden

Introduction 365
Bone Marrow 365
Methods 366
Histology and Cytology 369
Peripheral Blood 370
Methods 371
Histology and Cytology 372
Thymus 375
Gross Anatomy 376
Histology 376
Lymph Nodes 381
Regional Anatomy 381
Histology 385
Spleen 390
Gross Anatomy 391
Histology 391
Mucosa-Associated Lymphoid Tissue 397
Milky Spots 400
Acknowledgments 400
Further Reading 400

CHAPTER 20 NERVOUS SYSTEM

Jessica M. Snyder, Catherine E. Hagan, Brad Bolon and C. Dirk Keene

Introduction 403
Brain 405
Gross Anatomy 405
Histology 424
Related Structures 432
Spinal Cord 433
Gross Anatomy 433
Histology 434
Nerves and Ganglia 435
Regional Anatomy 435
Histology 439
Other Considerations 440
Conventions for Neuroanatomic Terminology 440
Special Methods in Neurohistologic Preparation 441
Acknowledgments 443
Further Reading and Relevant Websites 443

CHAPTER 21 SPECIAL SENSES: EYE

Caroline J. Zeiss, Daniel C. Tu, Isabella Phan, Rachel Wong and Piper M. Treuting

Introduction 445
The Eye 445
Gross Anatomy 445
Cornea and Sclera 446
Gross Anatomy 446
Histology 446
Uvea 448
Gross Anatomy 448
Histology 451
Retina 455
Gross Anatomy 455
Histology 456
Vitreous Chamber and Lens 460
Gross Anatomy 460
Histology 460
Optic Nerve 461
Gross Anatomy 461
Histology 463
Extraocular Muscles 463
Gross Anatomy 463
Histology 463
Conjunctiva 463
Gross Anatomy 463
Histology 464
Eyelids 464
Gross Anatomy 464
Histology 464
Lacrimal Gland and Drainage System 467
Gross Anatomy 467
Histology 467
The Developing Eye 467
Further Reading 470

CHAPTER 22 SPECIAL SENSES: EAR

Piper M. Treuting, Suzanne M. Dintzis and Rani Sellers

Introduction 471
External Ear 471
Gross Anatomy 471
Histology 471
Middle Ear 473
Gross Anatomy 473
Histology 478
Inner Ear 479
Gross Anatomy 479
Histology 479
Further Reading 485

CHAPTER 23 MAMMARY GLAND

Robert D. Cardiff, Sonali Jindal, Piper M. Treuting, James J. Going, Barry Gusterson and Henry J. Thompson

Introduction 487
Mammary Gland 487
Gross Anatomy 487
Subgross Anatomy and Histology 490
Mammary Gland Natural History and Reproductive Cycles 499
Early Development 499
Ovarian (Estrous and Menstrual) Cycle 502
Pregnancy and Lactation 502
Postpartum Involution 503
Senescence 506
Further Reading 508

CHAPTER 24 SKIN AND ADNEXA

John P. Sundberg, Carmen J. Booth, Lillian B. Nanney, Philip Fleckman and Lloyd E. King Jr.

Introduction 511
Skin 512
Histology 513
Adnexa 523
Histology 523
Further Reading 540

Index 543

This page intentionally left blank

LIST OF CONTRIBUTORS

Mark J. Arends
University of Edinburgh, Edinburgh, Scotland, United Kingdom

Brad Bolon
GEMpath, Inc., Longmont, CO, United States

Carmen J. Booth
Yale University School of Medicine, New Haven, CT, United States

Kelli L. Boyd
Vanderbilt University Medical Center, Nashville, TN, United States

Cory F. Brayton
Johns Hopkins University School of Medicine, Baltimore, MD, United States

Bernard S. Buetow
Pfizer, Inc., San Diego, CA, United States

Robert D. Cardiff
University of California at Davis, Davis, CA, United States

Stephan A. Carey
Michigan State University College of Veterinary Medicine, East Lansing, MI, United States

Cathy S. Carlson
University of Minnesota College of Veterinary Medicine, St. Paul, MN, United States

Sindhu Cherian
University of Washington School of Medicine, Seattle, WA, United States

Martha A. Delaney
University of Washington School of Medicine, Seattle, WA, United States

Suzanne M. Dintzis
University of Washington School of Medicine, Seattle, WA, United States

Renee Z. Dintzis
Johns Hopkins School of Medicine, Baltimore, MD, United States

Philip Fleckman
University of Washington School of Medicine, Seattle, WA, United States

Charles W. Frevert
University of Washington School of Medicine, Seattle, WA, United States

Rochelle L. Garcia
University of Washington School of Medicine, Seattle, WA, United States

Katherine N. Gibson-Corley
University of Iowa Carver College of Medicine, Iowa City, IA, United States

James J. Going
University of Glasgow, Glasgow, Scotland, United Kingdom

Paul C. Goodwin
GE Healthcare, Issaquah, WA, United States

Barry Gusterson
University of Glasgow, Glasgow, Scotland, United Kingdom

Catherine E. Hagan
The Jackson Laboratory, Sacramento, CA, United States

Jack R. Harkema
Michigan State University College of Veterinary Medicine, East Lansing, MI, United States

Benjamin Hoch
University of Washington School of Medicine, Seattle, WA, United States

Renee R. Hukkanen
Eisai US, Andover, MA, United States

Christopher Jerome
Wake Forest Innovations, Winston-Salem, NC, United States

Sonali Jindal
Oregon Health & Science University, Portland, OR, United States

Brian Johnson
University of Washington School of Medicine, Seattle, WA, United States

C. Dirk Keene
University of Washington School of Medicine, Seattle, WA, United States

Lloyd E. King Jr.
Vanderbilt University Medical Center, Nashville, TN, United States

Sue E. Knoblaugh
The Ohio State University College of Veterinary Medicine, Columbus, OH, United States

Jolanta Kowalewska
Eastern Virginia Medical School, Norfolk, VA, United States

Krista Marie DuBray La Perle
The Ohio State University College of Veterinary Medicine, Columbus, OH, United States

Michael A. Laflamme
University Health Network, Toronto, ON, Canada

Denny Liggitt
University of Washington School of Medicine, Seattle, WA, United States

Michael A. Linden
University of Minnesota, Minneapolis, MN, United States

David K. Meyerholz
University of Iowa Carver College of Medicine, Iowa City, IA, United States

Kathleen S. Montine
University of Washington School of Medicine, Seattle, WA, United States

Thomas H. Morton Jr.
University of Washington School of Dentistry, Seattle, WA, United States

Atis Muehlenbachs
Centers for Disease Control and Prevention, Atlanta, GA, United States

Lillian B. Nanney
Vanderbilt University Medical Center, Nashville, TN, United States

Isabella Phan
Kaiser Permanente, San Francisco, CA, United States

Julie Randolph-Habecker
Fred Hutchinson Cancer Research Center, Seattle, WA, United States

Mara H. Rendi
University of Washington School of Medicine, Seattle, WA, United States

Arlin B. Rogers
Tufts University, North Grafton, MA, United States

Rani Sellers
Pfizer Drug Safety Research and Development, New York, NY, United States

Jessica M. Snyder
University of Washington School of Medicine, Seattle, WA, United States

Carlos J. Suarez
Stanford University School of Medicine, Palo Alto, CA, United States

John P. Sundberg
The Jackson Laboratory, Bar Harbor, ME, United States

Henry J. Thompson
Colorado State University, Fort Collins, CO, United States

Maria Tretiakova
University of Washington School of Medicine, Seattle, WA, United States

Piper M. Treuting
University of Washington School of Medicine, Seattle, WA, United States

Lawrence True
University of Washington School of Medicine, Seattle, WA, United States

Daniel C. Tu
Oregon Health & Science University, Casey Eye Institute, Portland, OR, United States

Peter Vogel
St Jude Children's Research Hospital, Memphis, TN, United States

James G. Wagner
Michigan State University College of Veterinary Medicine, East Lansing, MI, United States

Jerrold M. Ward
Global VetPathology, Montgomery Village, MD, United States

Rachel Wong
University of Washington School of Medicine, Seattle, WA, United States

Caroline J. Zeiss
Yale University School of Medicine, New Haven, CT, United States

INTERNATIONAL ADVISORY PANEL

Mark J. Arends
University of Edinburgh, Edinburgh, Scotland, United Kingdom

Alexander "Sandy" D. Borowsky
University of California at Davis, Davis, CA, United States

Donna M. Bouley
Stanford University Medical Center, Stanford, CA, United States

Virginia L. Godfrey
University of North Carolina Medical Center, Chapel Hill, NC, United States

Harm HogenEsch
Purdue University College of Veterinary Medicine, West Lafayette, IN, United States

Michael Leach
Pfizer, Boston, MA, United States

Dave Malarkey
National Institute of Environmental Health Sciences, Research Triangle Park, NC, United States

Elisabeth McInnes
Cerberus Sciences Ltd., Adelaide, SA, Australia

David Meyerholz
University of Iowa Carver College of Medicine, Iowa City, IA, United States

Alessandra Piersigilli
Weill Cornell Medicine, New York City, NY, United States

Cheryl Scudamore
Mary Lyon Centre, MRC Harwell Institute, Harwell Campus, Oxford, United Kingdom

This page intentionally left blank

PREFACE TO THE SECOND EDITION

For the second edition of this atlas, we are honored to continue to work with our talented group of first edition contributors and to welcome a few new individuals to enrich the scope of expertise. We thank our contributors for their willingness to participate in the revision and enthusiasm for the addition of the rat. While we learned much about the writing, editing, and publishing process with the first edition, there were new challenges with the second edition. We appreciate the patience and tenacity of our contributors, editors, and colleagues as we met challenges and created this new edition.

In addition to the contributors, there were many individuals who assisted in the successful navigation of the revision process. We hope that they find the second edition worthy of their efforts. We enlisted a group of international expert end-users to critique the first edition chapters and provide us with detailed feedback to improve our atlas. The members of this International Advisory Panel are listed after the contributors in the Front Matter. They are our comparative pathology colleagues who volunteered to perform this critical task in order to strengthen the atlas. Their input and encouragement made writing and editing the second edition an efficient process and rendered a second edition that we feel is improved in content and layout. We thank our editors at Elsevier, Jeffery Rossetti and Pat Gonzalez, for their guidance. As with the first edition mouse anatomic illustrations, we are delighted to have the rat rendered in the style of medical illustrator Frank H. Netter, MD. We thank the Netter family and Dragonfly Media Group, especially Rob Duckwall, for their contributions to the new rat images. The cover art for both editions was conceptualized and drafted by Dr. Scout Chou, whose assistance allowed for rapid evolution of the designs with minimal revisions. We thank the members of our departments, especially Denny Liggitt, who served as support systems, contributors, and champions of this academic pursuit.

To our families, we owe a significant debt as the time needed for a reference text of this scope is hewn from weeknights, weekends, and holidays. We greatly appreciate their understanding and support even in the face of knowing its impact on family life, having lived through the process during the first edition. Their sacrifice enabled this work.

In closing, we would like this atlas to serve as a tribute to all rodents used in biomedical research. We hope to honor these critical animals by improving the first edition and expanding it to include rat. In doing so, the overall goal remains the same: supporting a greater understanding of the comparative anatomy of laboratory rodents and humans. This understanding, ultimately, will inform refined models of human disease and strategies for prevention and treatment.

This page intentionally left blank

ACKNOWLEDGMENTS FROM THE FIRST EDITION

PIPER M. TREUTING AND SUZANNE M. DINTZIS
University of Washington School of Medicine, Seattle, WA, United States

An atlas of this scope does not come together without the committed talents of many people. In addition to thanking the expert authors and assistant editors, we (the co-editors in chief) wish to thank the many people whose time, effort, and encouragement helped us to complete this work. We humbly recognize that we may inadvertently miss some that are deserving of a personal thank-you. To all who participated in this work, we are thankful for you and your contributions. We hope that the final product serves as a proper thank-you for a job well done.

Gross and microscopic images are the mainstay of this text, and obtaining publication quality images to compare mouse and human tissues was a formidable challenge. Production of the mouse anatomic images began with skilled and detailed anatomic dissections performed in part by Sue Knoblaugh. Expert macro photography was provided by Gavin W. Sisk. We wish to warmly thank Sue and Gavin for their efforts and good-natured understanding of the need to get "The Perfect Dissection and Shot" and tolerance of our "assistance" with their efforts. We are pleased to present the mouse anatomical preparations rendered, by Dragonfly Media Group, in the style of medical illustrator Frank H. Netter, MD. We thank the Netter family and Elsevier for providing access to Netterimages.com the Netter color palette, and for great patience when working with one of us (PT) in editing the final mouse images.

To obtain mouse microscopic images, harvested mouse tissues were processed by Histology Consultation Services (HCS) of Everson, WA (http://histocs.com/index.html) and we thank LeRoy Brown, CEO, for his assistance. Tissue and slide organization, virtual slide scanning, and database management were performed by the expert technical staff of the University of Washington (UW) Histology and Imaging Core—Kerrie Allen and Brian Johnson—along with student helpers Cara Appel and Kelsie Ovenell. We wish to acknowledge and thank S. Chou who provided encouragement for and gave form to the cover art concept. She also provided a portion of the final cover drawing and the Chapter 1 figures. Sara Samuelson, S. S. Illustrations (sarasamuelson.com), provided the drawings for Chapter 20, including the unique rendition of the sensory and motor musculi.

The successful completion of this work would not have been possible without the collegial support of our Department Chairs: Denny Liggitt, Nelson Fausto, and Tom Montine. Major contributions were also provided by faculty, residents, and students in the UW Departments of Comparative Medicine and Pathology, and by our patient editors at Elsevier, Mara Conner and Megan Wickline. Special recognition is reserved for Kathy Montine, our UW technical editor, who organized the chapters and coordinated the submissions. Her contribution is immeasurable both for the timely completion of this work and for our collective mental health.

Throughout this process, we have learned to float with the ebb and flow of the writing and editing process, pulling authors along with us and occasionally even stalking them in order to make

their unpaid labor a top priority—only to then edit their carefully chosen words.

We suspect that most of our critical readers will be pathologists and will be vociferously opinionated. We welcome their opining along with suggestions for improvement. We recognize that there will be errors in this Atlas for which we take full responsibility.

To our families and the Montine family, we owe many thanks. Your understanding and support of our academic pursuits enabled this work. We recognize the burden this placed on you, and we are grateful for your willingness to cheerfully step in during our absences.

Finally, we wish to thank the mice. It is our hope that this Atlas will allow for greater understanding of the comparative anatomy of the mouse and, ultimately, refined models of human disease.

1 INTRODUCTION

PIPER M. TREUTING, SUZANNE M. DINTZIS AND KATHLEEN S. MONTINE
University of Washington School of Medicine, Seattle, WA, United States

Overview and Introduction to the Second Edition

Comparative Anatomy and Histology is written both for the new rodent investigator and for students, histologists, and pathologists who wish to expand their knowledge of comparative anatomy and histology. It guides the reader through normal mouse and rat anatomy and histology with direct comparisons to human. The side-by-side comparison of rodent and human tissues also highlights the unique biology of the mouse and rat. Such differences have a great impact on the investigation and validation of rodent models of human disease. As the silos of basic academic and preclinical research breakdown, comparative pathologists must be well versed in mouse and rat anatomy and histology as it compares to human.

This atlas was created with the goal of being an easy to use, practical reference for neophytes, as well as experts who may be embarking on the study of a new species, organ system, or tissue. Thus it uses the preferred clinical anatomic terminology used in everyday practice and most familiar to biomedical researchers. The formal Latinized nomenclature recommended by the Nomia Anatomica Veterinaria (NAV) and Terminologia Anatomica (TA) is included in Further Reading and Relevant Websites.

In the second edition we have revised and refined the first edition material based on reviews and comments from readers, our solicited advisory panel of international experts, and the chapter contributors. This group effort has helped improve the original material, especially the figures and offers a more pragmatic organization. In addition to revising the original mouse and human material, the second edition adds the rat. The rat is currently the primary rodent used in toxicologic and industrial research. Increased use of genetically modified rats in basic research is anticipated due to the advent of CRISPR/Cas9 system for genetic modification. We note that in this atlas, the term "rodents" is defined as only *Mus musculus* and *Rattus norvegicus*, the most common laboratory mouse and rat species. Thus the term "rodents" herein does not include all *Rodentia*.

Comparative Pathology: Closing a Gap

Biomedical research institutions worldwide are literally overrun with mice and, increasingly, rats. More than 60% of extramural National Institutes

Comparative Anatomy and Histology. DOI: http://dx.doi.org/10.1016/B978-0-12-802900-8.00001-4
© 2018 Elsevier Inc. All rights reserved.

of Health (NIH)–funded grants use animals; most of these are mouse models of human disease, many of which involve genetically engineered mice. Rats are used in both toxicologic and industrial research and genetically modified rats are poised to compete with mice in their use as genetically modified models. The perceived value of mice and rats is to model the human condition and to support hypothesis-generating and hypothesis-testing research. Rodent models of human disease have proven valuable to biomedical research, but only with appropriate validation and careful translation of rodent data to human systems. Validation of rodent models as defined by Cardiff and colleagues involves determining to what extent the attributes of the experimental system (in this case, the rodent phenotype) match the attributes of human disease. As the phenotype of the human disease or condition being modeled becomes more complex, the validity of the rodent model becomes more important. A rodent model that is not appropriately validated does not value the use of those animals, wastes research dollars, and can even result in risks to humans if preclinical data are incorrectly translated to human patients.

Validation of rodent models through phenotyping (discussed in Chapter 2: Phenotyping) in order to translate of experimental findings in mice and rats to human disease is best done by a comparative pathologist and requires a broad and unique skill set covering rodent and human anatomy, histology, and pathobiology. Formally trained comparative pathologists understand how a research question may be impacted by the interplay of the rodent's background strain, genetic manipulations, breeding schema, sex, housing, diet, age, and intercurrent pathogenic or commensal organisms. Unfortunately the population of formally trained comparative pathologists is not increasing as rapidly as that of rodents. Instead, in our experiences at the University of Washington, we recognize that medical pathologists are increasingly asked to interpret rodent pathologic lesions. Likewise, veterinary pathologists need to know more about human disease, because the bulk of the animals they care for and work with arise from funded research on human disease. In addition, many new rodent investigators are eager to acquire training in comparative pathology that will assist them in planning experiments and interpreting results. Because formal training in rodent pathology to support translational research is limited, the research community looks to novel solutions such as online training academies or annual intensive laboratory animal pathology workshops to bring together geographically and culturally dispersed comparative pathology experts. There are numerous online resources and journal articles, rodent pathology atlases, laboratory animal pathology mini courses, and ever-expanding virtual communities of comparative pathologists that in concert serve to train individuals interested in expanding their comparative pathology skills.

To this growing body of knowledge, our modest contribution is a side-by-side comparison of normal mouse, rat, and human tissue that highlights the unique morphophysiology of the rodent, which has great impact on its histopathology. Although most tissues at the level of the light microscope are similar among *Mus musculus, Rattus norvegicus,* and *Homo sapiens*, there are critical differences (Table 1.1); in order to understand differences arising from various models, normal must be recognized. Recognition of these differences begins with anatomic directional terms and planes of section, which vary between the quadruped rodent and biped human (Fig. 1.1 and Tables 1.2 and 1.3). Use of appropriate directional rodent terms and their human analogs is important in effective communication about rodent models of human disease. This atlas strives to establish a reliable baseline in order to fill a gap in rodent phenotypic evaluation in translational research settings. To observe and measure deviants, normal

TABLE 1.1 Representative Features and Major Differences

General Features	Mouse	Rat	Human
Class	Mammalia	Mammalia	Mammalia
Order	Rodentia	Rodentia	Primata
Family	Muridae	Muridae	Hominidae
Genus and species	*Mus musculus*	*Rattus norvegicus*	*Homo sapiens*
Chromosome numbers (2*n*)	40	42	46
Sexual maturity	4–6 weeks	4–7 weeks	10–15 years
Average adult body weight (female)	18–35 g	250–300 g	75 kg
Average adult body weight (male)	20–40 g	300–400 g	87 kg
Life span	1–3 years	2.5–3 years	Average 71 years
Maximum life span reported	4 years	4 years	122 years
No. of offspring	5–11, strain dependent	8–14, strain dependent	1–2
Gestation	18.5–21 days	21–24 days	Average 40 weeks (or full term: 39–40 weeks)
Young	Altricial	Similar to mouse	Similar to rodent
Legs	4	Similar to mouse	2
Arms	0	Similar to mouse	2
Digits	5 Forefeet and hind feet	Similar to mouse	5 Fingers; 5 toes
Nails	Present	Similar to mouse	Similar to rodent
Tail	Present	Similar to mouse	None or poorly developed
Vertebral formula	C7 T13 L6 S4 Cd28	C7 T13 L6 S4 Cd27-30	C7 T12 L5 S5 Cd4
Integument	Haired skin predominates	Similar to mouse	Glabrous skin predominates
Sweat glands	Eccrine only, restricted to feet	Similar to mouse	Apocrine and eccrine
Vibrissae	Present	Similar to mouse	Absent
Mammary glands	10 (5 pairs), females only	12 (6 pairs)	2 discrete, pectoral
Male nipples	Absent	Absent	Present
Exorbital lacrimal glands	Present	Similar to mouse	Absent
Harderian glands	Present	Similar to mouse	Absent
Lung lobes	4 Right, 1 left	Similar to mouse	3 Right, 2 left
Cerebral gyri and sulci	Absent	Similar to mouse	Present
Liver lobes	4: Right, left, medial, caudate	Similar to mouse	4: Right, left, caudate, quadrate
Nonglandular forestomach	Present	Similar to mouse	Absent
Pancreas	Relatively diffuse in mesentery, indistinct lobation	Similar to mouse	Well-demarcated, left and right lobes, connected by body
Seminal vesicles	Present, very prominent	Similar to mouse	Present, not as prominent as rodents
Prostate	6 Lobes	3 Lobes	Not lobulated, has 3 zones
Bulbourethral gland	Present	Similar to mouse	Similar to rodent
Coagulating gland	Present	Similar to mouse	Absent
Preputial gland	Present	Similar to mouse	Absent
Clitoral gland	Present	Similar to mouse	Absent
Uterus	Bicornate	Duplex, Bicornate	Simplex
Placenta	Discoid, labyrinth, hemotrichorial	Similar to mouse	Discoid, villous, hemochorial
Tonsils	Absent	Similar to mouse	Present
Gut-associated lymphoid tissue	Present	Similar to mouse	Similar to rodent
Nasal-associated lymphoid tissue	Present	Similar to mouse	Absent
Bronchus-associated lymphoid tissue	Variable	Similar to mouse	Present
Zymbal gland	Present	Similar to mouse	Absent, smaller sebaceous glands in external acoustic meatus
Os clitoris	Present	Similar to mouse	Absent
Os penis	Present	Similar to mouse	Absent
Vomerulonasal organ	Present	Similar to mouse	Controversial

must be well understood. Only then can phenotypic differences in the vast array of human disease models be understood and appreciated. We hope this reference helps improve communication between veterinary and medical pathologists, and among rodent investigators, regarding normative structures. Pathology of disease, in which the debate regarding terminology is even more complex, is not within the scope of this atlas. Together with the educational resources noted previously, this atlas provides practical information to improve technical proficiency in basic comparative rodent and human anatomy and histology. Perhaps just as importantly, we hope this atlas will provide insight into when it is prudent to enlist the aid of an expert.

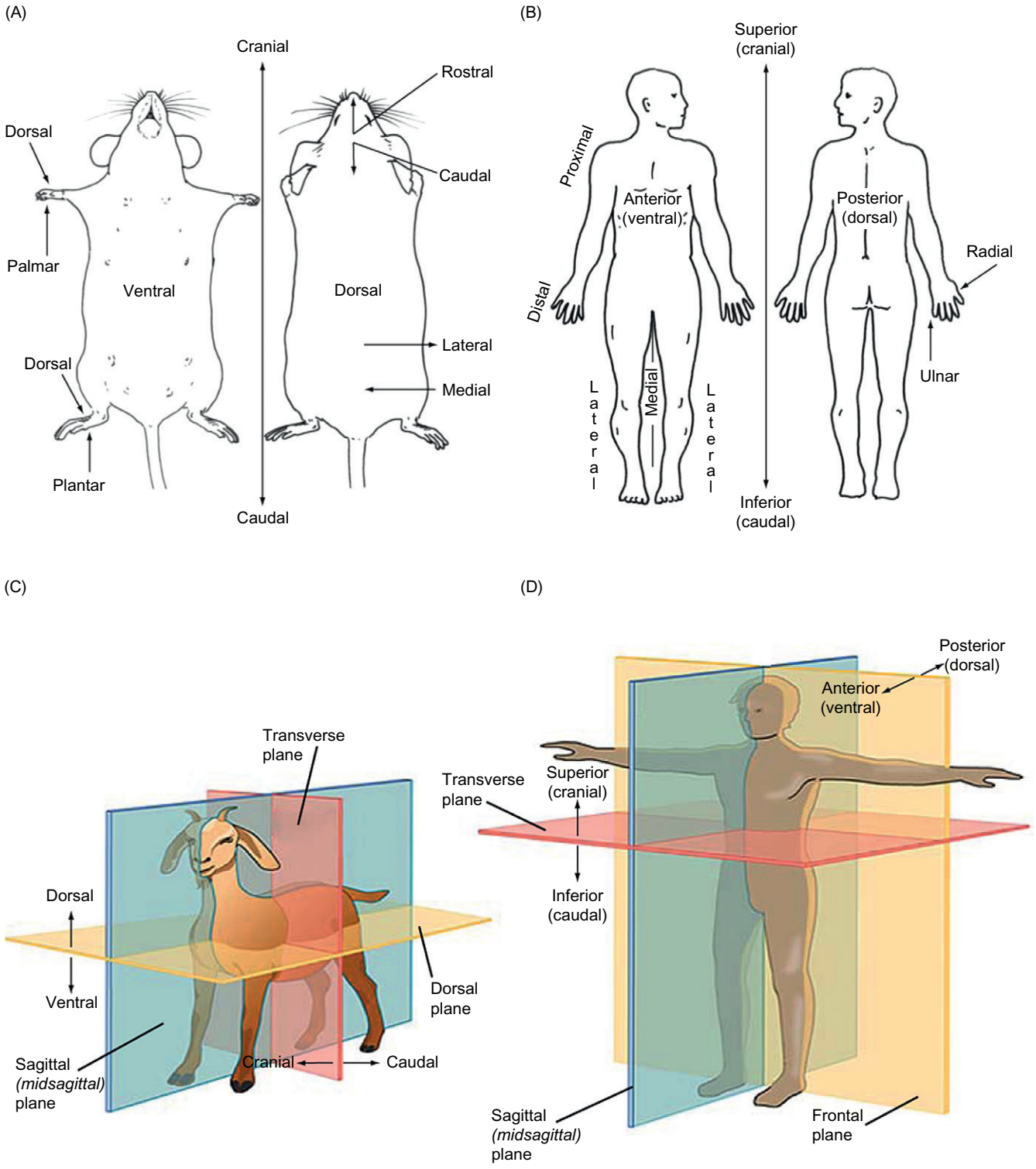

FIGURE 1.1 Anatomic Directional Terms and Planes of Section. (A) Rodent (mouse). (B) Human. Directional terminology in quadrupeds include ventral and dorsal, whereas for bipeds the favored terms are anterior and posterior. Cranial and caudal are the quadruped synonyms for bipedal superior and anterior. In all three species, proximal and distal are used on the appendicular regions, medial and lateral used to refer to relative positions to the center of the body, dorsal/palmar and dorsal/plantar are used on forefeet/hands and feet, respectively. (C) Quadruped (Goat). (D) Biped (Human). Shown are the planes of a quadruped goat and a bipedal human. The midsagittal plane divides the body exactly in half, into right and left portions. The frontal plane divides the front and back, and the transverse plane divides the body into upper and lower portions. Source: (A and B) Drawing by Dr. S. Chou, Charles River, with permission; (C and D) Modified after: OpenStax, Animal Form and Function. OpenStax CNX. June 26, 2013 http://cnx.org/contents/44503b54-9a4c-40c4-ae59-369526d2f9ef@8.

TABLE 1.2 Directional Anatomy Terms

Direction	Quadruped (Rodent)	Biped (Human)[a]
Toward the head	Cranial, craniad	Cranial (axial skeleton)
Toward the nose	Rostral (on head), cranial (on rest of body)	Anterior
Toward the tail	Caudal, caudad	Caudal (axial skeleton)
Toward the abdomen	Ventral, ventrad	Anterior
Toward the feet	Distal	Distal (appendicular skeleton)
Toward the trunk	Proximal	Similar to rodent
Toward the spine	Dorsal, dorsad	Posterior
Toward the palms or soles	Palmar (front), plantar (rear)	Similar to rodent
Away from the palms or soles	Dorsal	Similar to rodent

[a]Human anatomy differs if one is speaking of the axial or appendicular skeleton.

TABLE 1.3 Anatomic Sectional Planes

Anatomic Sectional Planes	Definition	Synonym(s)
Sagittal	Divides the body or structure vertically into even right and left halves	Midsagittal, median
Parasagittal	Divides the body or structure vertically into uneven right and left halves	Lateral
Transverse (Quadrupeds)	Divides the body or structure vertically into even front (cranial) and back (caudal) halves	Cross-sectional, axial
Transverse (Bipeds)	Divides the body or structure horizontally into upper and lower portions	Cross-sectional, axial
Dorsal (Quadrupeds)	Divides the body or structure horizontally into upper and lower portions	Frontal
Frontal (Bipeds)	Divides the body or structure vertically into even front (anterior) and back (inferior) halves	Coronal

C57BL/6 Mice as Index Strain

There are many mouse background strains used in biomedical research, and each has peculiarities in physiology and occasionally anatomic structures. The C57BL/6 mouse is the most commonly used mouse strain in academic institutions. This is likely due to the use of C57BL/6 blastocysts for targeted mutant or knockout mice. Other strains used with some frequency in genetically-engineered model production are FVB and strain 129. Because of the predominant use of C57BL/6 mice, we have chosen to focus the atlas on this inbred strain using representative female and male, 3- or 4-month-old C57BL/6J (Jackson Laboratories, Bar Harbor, ME) to contrast with the human equivalents at the age of 20–30 years. We recognize that there are many different mouse background strains used in biomedical research. Where appropriate, we highlight important strain-specific differences from the C57BL/6J standard within each organ system chapter. Numerous references and resources are provided at the end of each chapter for expanded details on mouse pathobiology, background strains, and specific models.

Sprague-Dawley Rats as Index Strain

The Sprague-Dawley (SD) rat serves as the most commonly used strain in the United States and Japan for pharmaceutical research. For this reason, and the ease of availability for our contributors, we chose this strain as index. Compared to the laboratory mouse, there are fewer rat strains commonly available and used in biomedical research. Other frequently utilized strains include the inbred Fischer 344 and the outbred Wistar. As with the mouse, numerous references and resources are provided at the end of each chapter for expanded information on rat pathobiology, background strains, and specific models.

Atlas Scope and Design

The subsequent chapters will introduce readers to many of the unique differences among mouse, rat, and human gross and histologic anatomy. This atlas is not meant to be a comprehensive review of all histologic, biologic, and physiologic differences

between rodents and humans or between rodents of different background strains. Nor is it a comprehensive histology atlas detailing cellular structure to the level of the election microscope or immunologic identification of subsets of cells or tissues. We focus on differences between mouse, rat, and human tissues encountered in routinely processed sections fixed by immersion in 10% neutral buffered formalin and visualized with hematoxylin and eosin (H&E) staining. Unless otherwise noted, all histologic images are stained with H&E.

The chapters follow a similar format, describing gross anatomical structure first followed by histologic descriptions. In most instances, the order of discussion is rodent then human, with any differences between mice and rats covered. We designed this atlas to be an easy and practical reference for the busy investigator. Key differences are illustrated in the figures and within a summary table, and they are described in more detail in the text. Critical information can be gleaned from the figures and the bulleted Need to Knows. At the end of each chapter, authors offer resources for additional or specialized study. Figures include gross anatomy of organ systems and photomicrographs of histologic images and thanks to Elsevier; we are delighted to present mouse and rat gross anatomy illustrations as a companion to the classic Netter medical images. Many of the histologic images were from contributors' collections and from rodent tissues processed specifically for this atlas. Whenever possible, we have presented similar gross and histologic images from rodents and human adjacently, either on the same page or on the facing pages, for ease of comparison. Where mice and rats do not differ, one or the other species is presented to represent rodents and the species illustrated in the particular figure is noted in parenthesis. In some of the human examples, there are histopathologic lesions present or aging changes. This was necessary when normal tissues are not biopsied in young adults or when presenting the the entire tissue (e.g., the eye). The difference in sizes between mouse, rat, and human bodies, organs and tissues makes it challenging to capture subgross and histologic images at the same magnification, because this would result in poorly oriented and minuscule rodent images. Instead, we have optimized magnifications for ease of visualization, most often capturing mouse images at a higher magnification than rat or human. There are notable exceptions where we have noted original magnifications or commented on the sizing differences. Micrometer bars are not included on the majority of images.

FURTHER READING AND RELEVANT WEBSITES

Barthold SW: "Muromics": genomics from the perspective of the laboratory mouse. *Comp Med* 52:206–223, 2002.

Barthold SW, Borowsky AD, Brayton C, et al: From whence will they come? A perspective on the acute shortage of pathologists in biomedical research. *J Vet Diagn Invest* 19:455–456, 2007.

Bolon B, Couto S, Fiette L, et al: Internet and print resources to facilitate pathology analysis when phenotyping genetically engineered rodents. *Vet Pathol* 49(1):224–235, 2012.

Cardiff RD, Rosner A, Hogarth MA, et al: Validation: the new challenge for pathology. *Toxicol Pathol* 32(Suppl 1):31–39, 2004.

Cardiff RD, Ward JM, Barthold SW: "One medicine–One pathology": are veterinary and human pathology prepared? *Lab Invest* 88:18–26, 2008.

Clemente C: *Anatomy: a regional atlas of the human body*, ed 6, , 2010, Lippincott Williams and Wilkins.

Federative International Programme on Anatomical Terminologies Terminologia Anatomica: http://www.unifr.ch/ifaa/Public/EntryPage/ViewTAOnLine.html. 2011.

Greaves P: *Histopathology of preclinical toxicity studies: interpretation and relevance in drug safety evaluation*, ed 4, New York, NY, 2011, Academic Press.

Greene EC: Anatomy of the rat, Braintree, MA, 1935, Braintree Scientific, Inc.

Ince TA, Ward JM, Valli VE, et al: Do-it-yourself (DIY) pathology. *Nat Biotechnol* 26:978–979, 2008.

INHAND: *International harmonization of nomenclature and diagnostic criteria for lesions in rats and mice.* http://www.toxpath. org/inhand.asp.

Jackson Laboratories: *Festing's inbred strains of mice and rats and their characteristics*. http://www.informatics.jax.org/external/festing/mouse/INTRO.shtml.

Jackson Laboratory. *Mouse nomenclature*. http://www.informatics.jax.org/mgihome/nomen/index.shtml. 2010.

Kittel B, Ruehl-Fehlert C, Morawietz G, et al: Revised guides for organ sampling and trimming in rats and mice: part 2. *Exp Toxicol Pathol* 55:413–431, 2004. http://reni.item.fraunhofer.de/reni/trimming/index.php.

Mendlowitz L. *Diseases of research animals*. Columbia, MO: University of Missouri, Research Animal Diagnostic Laboratory. http://www.radil.missouri.edu/info/dora/Dora.htm.

Mescher A: *Junqueira's basic histology: text and atlas*, ed 14, 2016, McGraw Hill.

Moore KL, Dalley AR, Agur AMR: *Clinically oriented anatomy*, ed 6, Baltimore, 2012, Wolters Kluwer and Lippincott Williams and Wilkins.

Morawietz G, Ruehl-Fehlert C, Kittel B, et al: Revised guides for organ sampling and trimming in rats and mice: part 3. *Exp Toxicol Pathol* 55:433–449, 2004. http://reni.item.fraunhofer.de/reni/trimming/index.php.

Netter FH: *Atlas of human anatomy*, ed 6, New York, 2014, Elsevier.

OpenStax: *Animal form and function. OpenStax CNX. Jun 26, 2013*. http://cnx.org/contents/44503b54-9a4c-40c4-ae59-369526d2f9ef@8.

Ovalle WK, Nahimey PC: *Netter's essential histology*, 2007, Saunders.

Popesko P, Rajtova V, Horak J: *Colour atlas of anatomy of small laboratory animals*, London, UK, 2003, WB Saunders.

Rohen JW, Yokochi C, Lutjen-Drecoll E: *Anatomy: a photographic atlas*, ed 8, Philadelphia, 2016, Wolters Kluwer.

Ross MK, Pawlina W: *Histology: a text and atlas*, ed 7, Philadelphia, 2015, Lippincott Williams and Wilkins.

Ruehl-Fehlert C, Kittel B, Morawietz G, et al: Revised guides for organ sampling and trimming in rats and mice: part 1. *Exp Toxicol Pathol* 55:91–106, 2003. http://reni.item.fraunhofer.de/reni/trimming/index.php.

Scudamore CL: *A practical guide to the histology of the mouse*, 2013, John Wiley & Sons.

Society of Toxicologic Pathology: *Standardized system of nomenclature and diagnostic criteria (SSNDC) guides*. http://www.toxpath.org/ssndc.asp.

Suckow MA, Weisbroth SH, Franklin CL: *The laboratory rat*, 2015, Elsevier Science.

Suttie AW, Leininger JR, Bradley AE: *Boorman's pathology of the rat: reference and atlas*, ed 2, New York, 2017, Academic Press.

Valli T, Barthold SW, Ward JE, et al: Over 60% of NIH extramural funding involves animal-related research. *Vet Pathol* 44:962–964, 2007.

Walker WFJ, Homberger DG: *Anatomy and dissection of the rat*, New York, NY, 1998, WH Freeman & Co.

World Association of Veterinary Anatomists: *Nomina Anatomica Veterinaria*, ed 5, http://www.wava-amav.org/Downloads/nav_2012.pdf.

Young B, Woodford P, O'Dowd G: *Wheater's functional histology: a text and colour atlas*, ed 6, 2013, Churchill Livingstone.

This page intentionally left blank

PHENOTYPING 2

CORY F. BRAYTON
Johns Hopkins University School of Medicine, Baltimore, MD, United States

PIPER M. TREUTING
University of Washington School of Medicine, Seattle, WA, United States

Introduction

In order to identify and assess deviant phenotypes, and to optimize and validate phenotypically relevant rodent models of human disease, it is essential to establish a useful baseline and lexicon for "normal" anatomy and expected phenotype variations. This chapter introduces some basic phenotyping concepts and broadly relevant resources, and discusses the implementation of anatomic, histology, and pathology phenotyping evaluations to optimize and validate rodent models of human disease and gene function.

Phenotyping refers to assessing observable or measurable characteristics (normal features, traits, and possible abnormalities). In genetically engineered animals, phenotyping usually is done to gain insight about gene function. A major goal in much of basic biomedical research is to understand the action of a gene product or pathway in vivo. This is pursued in functional genomics approaches that involve manipulating genomes in diverse species, including yeast, worms, fruit flies, fish, and rodents. As gene targeting and transgenic technologies developed, the mouse—and more recently the rat—emerged as champions of genetically modified animals. Rodents are relatively inexpensive to maintain, the genomes are mapped and amenable to manipulation, and rodent physiology is similar to human. These features have led to the development of thousands of potential genetically relevant mouse and rat models of human diseases. The use of genetically modified (GM) mice and GM rats to elucidate roles of genes, gene products, and pathways in a complex mammalian system continues to increase.

Coordinated international efforts in the International Knockout Mouse Consortium (IKMC), and the International Mouse Phenotyping Consortium (IMPC), are near completion. IKMC aims to develop GM mice on a single (C57BL/6N) background with mutations in every protein coding gene. IMPC is phenotyping mice from IKMC. IKMC and IMPC make the embryonic stem (ES) cells, protocol detail, and curated data accessible to the research community. Additional mouse genome and phenome information is accessible through Mouse Genome Informatics (MGI), Mouse Phenome Database (MPD), and other efforts. IMPC, MGI, MPD, and related resources enhance the value of mice as highly characterized genetic tools for translational research applications. Rats have been widely used in experimental medicine, especially in behavioral research and drug development. Genomics, bioinformatics, and phenotyping tools for rats are

Comparative Anatomy and Histology. DOI: http://dx.doi.org/10.1016/B978-0-12-802900-8.00002-6
© 2018 Elsevier Inc. All rights reserved.

progressing as well, with increasing information accessible through the rat genome database (RGD) and related initiatives. The advent of CRISPR Cas9 technologies is expected to facilitate the development and use of GM rats.

Observed and measured phenotypes in any organism reflect the combined effects of nature (genetics) and nurture (environment). Thus, phenotypes of genetically modified (GM) animals should be expected to reflect influences beyond an intended genetic manipulation. Genetic variables include genetic background(s), variable site integration, copy number, transgenic mosaicism, flanking regions carried over from the original ES cell line, and may include epigenetic effects on gene expression. Environmental variables include diet, housing, autochthonous, or commensal microbial flora (microbiome), as well as exposures to known or potential pathogens such as mouse hepatitis virus or *Helicobacter* species, and to unknown infectious agents which have not been eliminated with regular health monitoring. When developing a phenotyping plan and interpreting phenotype data, such variables should be considered. When reporting phenotyping or other research results, genetic and environmental information can be highly relevant and should be included to maximize the comparative and translational value of the results. Reporting adequate detail in materials and methods to allow others to reproduce and validate the findings, and to enable systematic analyses and reviews, is widely recommended, e.g., in the ARRIVE guidelines, ILAR guidance for reporting animal research (NRC, NAS), and NIH Principles and Guidelines for Reporting Preclinical Research, and increasingly is scrutinized in peer review of manuscripts and grants.

Phenotyping approaches vary with the overall aims of a study, or more broadly of a research program. Phenotyping in an academic research setting usually is hypothesis driven, aiming to answer specific questions about gene function. Phenotyping in an -omics-based approach, such as the IMPC, which aims to be more "hypothesis generating," and the testing should be systematic, broad-based, unbiased. "Big data," -omics approaches generate large and accessible data sets with the potential to inform and support many areas of research. Testing in a pharmaceutical or toxicology setting can be considered purpose-driven phenotyping. It is also systematic and broad-based, with the purpose (aim) of assessing efficacy or safety of a compound, device, or procedure.

Phenotyping Study Design

STRATEGIES

Specific phenotyping strategies at different institutions reflect local logistic and economic resources, interests, and expertise. Hypothesis-driven, hypothesis-generating, and purpose-driven approaches have quite different aims, but share critical elements of study design, including, but not limited to, experimental and control animal selection and determination of appropriate age, sex, strains and genotypes; diet and other husbandry issues; microbial status; equipment and procedures; statistical analyses (and determination of *n*); data formats, integrity and preservation; ethical concerns and ethical review; and adequate reporting and communication. Table 2.1 uses a flowchart format to illustrate broadly relevant elements of study design, to be considered before initiation of the study. Table 2.2 lists some specific study design options relevant to phenotyping, and emphasizing issues in pathology testing, along with some of their advantages or disadvantages.

MATERIALS AND METHODS

Animals

Animal selection and numbers (*n*) are influenced by the aims of the study as well as by local resources and animal availability.

TABLE 2.1 Study Design. Considerations for the Materials and Methods Section Before Initiating the Study

Approach, aims, and budget	**a.** Hypothesis driven/hypothesis testing **b.** Hypothesis generating (omics approach) **c.** Purpose driven (e.g., safety or efficacy testing) **d.** Budget influences many of subsequent considerations and options
1 Animals	**a.** Check/confirm nomenclature and animals in previous publications **b.** Consider options for species, genotypes, mutations, background strain, source, microbial status, age, sex, parity **c.** Consider testing in more than one genotype or strain **d.** What are the appropriate control animals?
2 Husbandry	**a.** Check/confirm husbandry in previous publications **b.** Consider options for caging, diet, bedding, water, light cycles, temperature, enrichments, group vs single housing, single vs mixed sex housing
3 Tests, procedures	**a.** Check/confirm equipment and protocols in previous publications, and resources such as IMPC, MPD, RGD **b.** Consider options for equipment, protocols, order of testing **c.** Consider options for administration of compounds: oral (diet, gavage), parenteral routes, doses, volume, vehicles
4 Pathology	**a.** Plan to assess unexpected morbidity, mortality, subviability of offspring **b.** Plan for pathology assessments at experimental endpoints **c.** Plan for archiving specimens **d.** Plan for characterization and validation of a disease model (if applicable) **e.** See Tables 2.2–2.4 for specific considerations
5 Statistics and determination of *n*	**a.** Check/confirm statistical methods in previous publications **b.** Consider additional options **c.** Use relevant data (e.g., from IMPC, MGI, RGD) for power analyses
6 Data format, reporting	**a.** Consider data formats, nomenclature, and diagnostic criteria for pathology and other outcomes, e.g., from IMPC, MPD, Pathbase, INHAND, MMHCC **b.** Consider preservation, integrity and sharing of primary data **c.** Consider compatibility with relevant publications, databases **d.** Consider reporting guidance, e.g., ARRIVE guidelines, ILAR (NRC) guidance, etc.
7 Institutional Review	**a.** Most institutions or research programs require review of projects by an institutional animal care and use committee (IACUC), ethical review committee, or other animal care committee prior to initiating the study
Perform study	**a.** Publish robust, relevant, reproducible, and predictive translational research results **b.** Use reporting guidance, e.g., ARRIVE guidelines, ILAR (NRC) guidance, etc.

Genetic backgrounds, back-cross and inbreeding generations, age, sex, and source environment, appropriate numbers (n), and relevant concurrent controls are important considerations. Especially in hypothesis-driven research settings, animal availability and budget play important roles.

Exceptionally robust phenotypes, such as extra or missing body parts, or *situs inversus*, can be identified at any age in all of the test animals, and in no control animals, so that selection of optimal controls is not a great concern. Subtle phenotypes may require substantially more test animals, as

TABLE 2.2 Examples of Issues and Options to Consider in Planning for Phenotyping or Other Research

Issue	Mice / Rats	Options	Benefits/Advantages	Concerns/Disadvantages
Animal and Gene Nomenclature				
Nomenclature genes	M R	MGI, http://www.informatics.jax.org/	Search confirm gene name, information	
Nomenclature genes	M R	NCBI GENE, http://www.ncbi.nlm.nih.gov/gene/	Search confirm gene name, information	
Nomenclature	M R	http://www.informatics.jax.org/mgihome/nomen/strains.shtml	Guidelines for nomenclature	
Nomenclature and sources	M	http://www.findmice.org/index.jsp	Search for mice, ES cell lines, and ES cell line origin; submit mouse and ES cell line information	
Nomenclature and sources	R	http://rgd.mcw.edu/	Search for and register rat strains	
Specimen Collection, Pathology Procedures, and Reporting				
Blood collection		Collection sites: anatomic sites for blood collection		Complete blood count (CBC) or clinical chemistry results may vary with site; anticoagulant must be used and mixed thoroughly to avoid platelet clumping
Blood collection	M R	Collection site: cardiac	Largest blood volume	Terminal (under anesthesia, or immediately post euthanasia)
Blood collection	M	Collection site: facial, saphenous, tail	Smaller blood volumes; repeat bleeding	Small blood volumes; stress, trauma depending on operator
Blood collection	R	Collection site: jugular	Larger volume	Requires two operators for restrain and collection; stress
Blood collection	M R	Collection site: retro-orbital		Control of bleeding, trauma
Blood collection	M R	Fasting (precollection)	Recommended for some tests, such as glucose tolerance, insulin response	Possible dehydration; not recommended or necessary for many tests; rats may be fasted overnight; fasting mice for 5 hours is adequate for most metabolic studies
Blood collection	M R	Needle/syringe size		Potential for hemolysis from larger syringe (more pressure), smaller needle (cell trauma)
Blood collection	M R	Procedure site: cage side	Less transport stress	Access to instrument
Blood collection	M R	Time of day: morning	Soon after nocturnal activity and feeding	
Blood collection	M R	Time of day: afternoon	Normally longer period of less activity, eating, and drinking	
Blood collection	M R	Tubes and anticoagulant: ethylenediamine tetraacetic acid (EDTA)	Less platelet clumping; possibly better cell morphology than with heparin	EDTA interferes with some plasma chemistry tests
Blood collection	M R	Tubes and anticoagulant: heparin (lithium heparin, sodium heparin)	Plasma chemistry from same specimen	Sodium heparin interferes with electrolyte assessment
Blood collection	M R	Tubes and anticoagulant: dry anticoagulant	No dilution effect (compared to wet anticoagulant)	Possible adverse effect of dry anticoagulant on inadequate specimen volume
Blood collection	M R	Tubes and anticoagulant: wet anticoagulant		Dilution from wet anticoagulant with inadequate specimen volume
Blood collection	M R	Tubes: gel separator	Cleaner separation of serum, plasma	
Demineralization of bone (decalcification)	M R	Bouin's solution	Fixes and decalcifies Some prefer it for embryos, fetus, reproductive tissues, hematopoietic tissues; may be satisfactory for some immunohistochemistry (IHC)	Rapid but low penetration so specimens should be small or perfused; prolonged exposure shrinks tissues; hazard concern
Demineralization of bone (decalcification)	M R	EDTA	Preferred for some IHC or other tests	Requires previous fixation; slow

(*Continued*)

TABLE 2.2 Examples of Issues and Options to Consider in Planning for Phenotyping or Other Research (Continued)

Issue	Mice / Rats	Options	Benefits/Advantages	Concerns/Disadvantages
Demineralization of bone (decalcification)	M R	Formic acid/formalin-based fixing and demineralizing agents	Simple, simultaneous fix and demineralize small bone specimens; usually permits trimming within 24 h; may be satisfactory for some IHC	Can over decalcify, under decalcify
Demineralization of bone (decalcification)	M R	Nitric acid or other acids	Preferred for some IHC or other tests	Requires previous fixation; can over decalcify quickly
Dissection/ collection	M R	Complete necropsy	Excellent if sufficient time resources	Time; expense; must complete quickly to minimize autolysis
Dissection/ collection	M R	Partial necropsy	Better than no data; save, fixed specimens for later evaluation, ensure airtight (sealed) storage containers	Incomplete data
Fixation: fixative	M R	10% neutral buffered formalin	Generally good histology, even after months, years; excellent IHC with optimal fixation	Aldehyde fixatives cross-link proteins; autofluorescence
Fixation: fixative	M R	Acid alcohol fixatives	Some prefer for eyes and general histology	
Fixation: fixative	M R	Bouin's solution	Fixes and decalcifies; some prefer for embryos, fetus, reproductive tissues, hematopoietic tissues, some IHC	Does not penetrate far, so specimens should be small, or perfused; prolonged exposure shrinks tissues; hazard concern
Fixation: freezing	M R	Freezing	IHC, ISH	Often poor histology
Fixation: method	M R	Perfusion fixation	Convenient preservation; good fixation	May compromise microbiology, gross images
Fixation: method	M R	Immersion fixation	Good fixation with good dissection, sufficient fixative (1:10 V:V)	Compromised by delay to immersion; large specimen size results in poor fixation
Fixation: period	M R	Depends on fixatives; 24–48 h before paraffin processing is frequently recommended for 10% neutral buffered formalin (10%NBF); once fixed, tissues stored for many years in formalin can yield useful histology		Underfixing or overfixing can impact immunohistochemistry (IHC) or other tests depending on fixative type
Fixation: volume		At least 1:10 V:V specimen: fixative is recommended Mixing/rocking may improve fixation; once fixed, tissues can be stored in smaller volumes in sealed containers		
Histology: processing	M R	Professional processing; QA/QC	Good comparable results	Expense
Histology: processing	M R	Coverslips glass	Less scratchable than plastic; can be replaced without losing tissue	
Histology: processing	M R	Coverslips plastic	Cheaper	Scratch, fade, fall off with tissue; compromise photography, scanning, polarization compared to glass
Identification: animals	M R	One number for all tests and information, as in medical record number	Data sharing	Most relevant to centralized laboratory information management systems (LIMS)
Identification: animal/ specimen	M R	Bar codes	Accelerate/facilitate tracking, reduce reporting time, transposition error; facilitate blinded evaluations	Expense of system; probably most valuable with LIMS
Identification: specimens	M R	Preserve any identification on the individual animal, e.g., pelt, tattoos, tags; keep a label or labeled cassettes in container with wet tissues	Redundant (backup) identification may save a study	Time and storage capacity
Storage archiving	M R	Blood: Serum or plasma at −40 or −80	Adequate depending on parameters, analytes	Freeze-thaw can alter some parameters, enzyme activities
Storage archiving	M R	Blood: smears, films, or cytology	Fixed specimens can be stored in protective containers	Stains fade, but restaining or additional tests may be possible

(*Continued*)

TABLE 2.2 Examples of Issues and Options to Consider in Planning for Phenotyping or Other Research (Continued)

Issue	Mice / Rats	Options	Benefits/Advantages	Concerns/Disadvantages
Storage archiving	M R	Blood: whole blood	Perform CBC, smear with fresh blood	Does not store practically
Storage archiving	M R	Digital slides	Accessibility for slide-to-slide comparison, quantification, consulting, and peer review of remote distant specimens	Expense, initial and, maintenance; legacy issues with storage media, software
Storage archiving	M R	Fixed tissues	Neutral buffered formalin can preserve tissue for years in sealed packaging	Picric acid in Bouin's is hazardous (explosive) when dried
Storage archiving	M R	Glass slides	Can be stored usefully for years under good storage conditions	Damage, storage expense, time, and expense to retrieve
Storage archiving	M R	Paraffin blocks	Can be stored usefully for years under good storage conditions	Expense, space; damage from temperature, handling, vermin
Terminology and diagnostic criteria	M R	INHAND, RENI terminology	Relevance to spontaneous and induced lesions; toxicology, safety, efficacy studies	Not always relevant to GM lesions
Terminology and diagnostic criteria	M	MMHCC	Relevance to GM mice	Not all systems; proliferative lesions only
Terminology and diagnostic criteria	M	Pathbase	Relevance to GM mice	
Weighing: animals	M R	Instrument in animal room (cageside)	Comparison throughout in life study	
Weighing: animals	M R	Instrument in laboratory	Accuracy of tissue:body weight ratios	Comparability of different instruments
Weighing: animals	M R	When: before terminal bleed	Relevance to previous weights	
Weighing: animals	M R	When: before perfusion	Relevance to previous weights	Relevance to postperfusion animal and tissue weights
Weighing Specimens/ tissues	M R	When: before fixation	Usually convenient, accurate for large tissues (spleen, liver, heart, kidneys)	Smaller tissues (ovaries adrenals, lymph nodes) may dry out
Weighing specimens/ tissues	M R	When: after fixation	May be easier to standardize dissections and compare specimen weights (especially for small tissues)	Relevance to unfixed weights should be assessed

well as genetically and environmentally relevant control animals (e.g., littermates) in order to detect significant differences. Relevant control animals can be difficult to obtain, especially when genetic backgrounds of test animals are mixed or unclear, and when wild-type littermates are not available. Many GM mice were developed on mixed genetic backgrounds, then bred for homozygosity of a desired genotype, or bred to GM mice carrying other mutations, without consideration of genetic effects of multiple background strains involved. Commercially available genotyping can be used to assess mice to determine the most closely related inbred strain(s), and to select mice for breeding to achieve a congenic strain. Purchased controls or historical control data can be problematic because of genetic differences, as well as differences in environment, diet, and microbial status. Sex-related phenotype differences are common, so both sexes (when available) should be tested, and data usually should be analyzed separately.

Ideally, sample sizes (n) are determined by statistical power analyses. When animals and resources are limited, obtaining and testing only a few age-matched, sex-matched animals of each genotype can be challenging. While data sets from animals of a specific age may suggest an age for animal testing, known or expected

phenotypes may be important considerations regarding the age at which certain tests should be done. Known or expected phenotypes, as well as viability, can direct the zygosity of GM animals to be phenotyped. In some cases, quantitative phenotypes (dose effect) can be demonstrated by phenotyping heterozygotes plus homozygotes. The IMPC selected n=7 for their primary phenotyping pipeline, based on data from earlier EUMorphia and Europhenome phenotyping initiatives.

Tests, Equipment, Procedures, and Analyses

Test selection is influenced by the aims of the study, as well as by local resources and expertise. Targeted, hypothesis-driven phenotyping may involve only a few tests that are specifically relevant to a single system or research question. More comprehensive phenotyping can combine diverse in vivo testing, imaging, molecular phenotyping, challenge tests, clinical laboratory tests, and pathology evaluations to characterize and validate multisystem phenotypes. Mouse phenotyping tests have been referred to as primary, secondary, or tertiary (tier 1, 2, or 3, respectively). In general, tier 1 phenotyping tests are less specific and higher throughput. Higher level (tier 2 or 3) phenotyping tests tend to be more specialized, more expensive, more invasive, and lower throughput. A phenotyping pipeline refers to a test schedule usually involving weekly testing in a specific order to minimize interference between tests. Organized rat phenotyping efforts, coordinated through the RGD, have included quite specialized and interventional assessments of cardiovascular, respiratory, and metabolic phenotypes.

Useful phenotype data can be obtained with no special equipment, and can be included in colony record keeping. Examples include (1) breeding records, (2) growth curves (body weights), and (3) visual in cage observations, with photo or image documentation. Depending on local resources and interests, tier 1 or 2 phenotyping can include some combination of (1) neurobehavioral testing such as open field/automated activity monitoring; grip strength, rotarod, auditory brain stem response (ABR), or prepulse inhibition (PPI); (2) cardiovascular assessment by minimally invasive electrocardiography (ECG) or blood pressure; (3) metabolic assessment by clinical chemistry, calorimetry; (4) immunology assessments by hematology and/or flow cytometry; (5) multisystem assessments by pathology and tissue repository/archiving, basic necropsy/organ weights/tissue blocks. Some pathology data can be obtained from properly collected and preserved tissue or fluid specimens, or entire perfused animals, well after the death of the animal. The IMPC primary phenotyping pipeline tests mice from 5 to 16 weeks old, in a specific test sequence, aiming to minimize interference of each test on subsequent tests, with specific testing done at the same age, at the different sites or Mouse Disease Clinics (MODICs), using similar and well-described protocols (available through IMPC, IMPRESS websites). In the MODIC and IMPC primary phenotyping pipelines, there are approximately 20 tests applied over 10 weeks. This generates more than 600 data parameters that are subjected to rigorous scrutiny and quality assurance (QA) before inclusion in the IMPC phenome database.

Secondary or tier 2 phenotyping usually is more specific to an area of research interest. It may include dietary challenge to further characterize metabolic phenotypes, or infectious challenges to further characterize immune phenotypes, or longer-term studies to assess for cancer and other age-related phenotypes. Tertiary or tier 3 phenotyping is likely to involve highly specialized, invasive, or expensive tests that interfere with or preclude other tests, and usually are not amenable to high-throughput application. Examples include metabolic, cardiac, neurologic, or physiology testing that involves surgical manipulations, and usually is done to test specific hypotheses suggested by other phenotype data.

Pathology Evaluations

As in medical and veterinary clinical practice, pathology evaluations can help to characterize deviant or disease phenotypes, and to identify (diagnose) causes and contributors. Pathology evaluations also can contribute critical information to phenotyping, to validating GM models of human disease, to assessing translational applications such as responses to therapies, and to timely identification of research or colony problems that can compromise research outcomes. Diagnostic pathology also complements microbial surveillance in QA and quality control (QC) for phenotyping and translational initiatives. Prompt assessment of illness or other complicating phenotypes (in GM and control animals) can identify problems and their causes early, to minimize loss of animals, money, and time. Model validation assesses if and how the experimental system (in this case, the GM animal) recapitulates the human disease, genetically, mechanistically, and morphologically, at molecular, cell, tissue, system, and organism levels.

Planned strategic application of pathology evaluations should be considered early in study design, and can contribute to phenotyping and other translational studies by:

1. anatomic, histology, and pathology evaluation of phenotypes identified in other tests, to further characterize a phenotype and to assess for confounders and contributors;
2. validation of disease models; and confirmation of the absence of relevant phenotypes, when important to the model;
3. diagnosis of unexpected morbidity or mortality in control and experimental animal, and as part of surveillance and QA measures;
4. preservation/archiving of specimens (tissues, fluids, blocks, slides, and digital slides) that are not evaluated immediately, such that they can be used for later evaluation or other testing.

Table 2.2 summarizes some issues and options to consider early in study design, with an emphasis on pathology phenotyping. The list is not exhaustive, but illustrates the diversity of options and the need for inclusion of specific details in study design, and in reporting results. Strategies also vary to achieve a comprehensive gross necropsy and histology screen that assesses major systems in a reproducible and cost-effective manner. Tables 2.3 and 2.4 offer examples of a 10–12 slide protocol for mice, and a 15–16 slide protocol for rats, respectively, to represent the major systems and examine more than 40 tissues per animal. Note that these examples aim to examine a diversity of tissues on a modest number of slides, and diverge from RENI (RITA NACAD, http://reni.item.fraunhofer.de/reni/trimming/) trimming guidelines for many tissues. A systematic protocol can facilitate training, and improve consistency and quality of slides for tissue examination, but dissection and trimming protocols must also suit the needs of the study, and address the research questions.

Reporting

Communication is mission critical to translational science. International guidelines for mouse, rat, and gene nomenclature are accessible online at http://www.informatics.jax.org/mgihome/nomen. They are linked to the MGI database, the MPD, and the RGD. Correct nomenclature for mice, rats, and genes is important to understand previous studies, in order to design new studies, as well as to report studies accurately and usefully. Terminology for anatomy and phenotype data including pathology are similarly important. Pathbase (http://eulep.pdn.cam.ac.uk) is a mouse anatomy and pathology ontology developed specifically to support GM mouse pathology, and used in IMPC. The toxicologic pathology community has a long history of expertise in rodent pathology. Standardized nomenclature for spontaneous and (primarily chemically) induced lesions has strong precedent in the toxicologic pathology literature, and undergoes extensive peer review in the International Harmonization of

TABLE 2.3 A 10-Slide Mouse Histology Assessment: Example of a Systematic Assessment of More Than 40 Tissues, With Some Common Variations

Cassette/ Slide	Primary Tissue/Organ	Comments/Additional Description (See RENI Guidelines for Additional Options and Information)
1	**Heart, thymus**	
	Heart	Hemisected, both halves: valves, myocardium, epicardium, free walls, septa
	Thymus	Both lobes: cortex, medulla
	Sternum (not decalcified)	Bone, marrow, cartilage, muscle (marrow histomorphology is better than in demineralized bone)
	± Mediastinal lymph nodes	
2	**Lungs**	
	Lungs	Bronchioles, alveoli, interstitium (septa), lymphoid tissue (BALT)
	Trachea	
	Esophagus	
	Thyroid, parathyroid glands	
	± Mediastinal lymph nodes	
	± Aorta	
	± Larynx	
3	**Kidneys, adrenal glands**	
	Kidneys	Left (longitudinal sections), right (cross sections)
	Adrenal glands	
	± Lymph nodes, renal	
	± Ganglion	
4	**Salivary glands, lymph nodes**	
	Submandibular salivary glands	
	Sublingual salivary glands	
	Parotid glands	
	Lymph nodes (superficial and deep cervical)	
	Fat (adiposa)	Brown and white fat
	± Exorbital lacrimal glands	
	± Mammary glands	
5	**Pancreas, mesentery, lymph nodes**	
	Pancreas	Exocrine, endocrine, ducts
	Mesentery	Vasculature
	Lymph nodes, pancreatic, mesenteric	
	Fat (adipose)	
6	**Gastrointestinal tract**	
	Stomach	Forestomach, glandular stomach
	Small intestine	
	Cecum	
	Large intestine	
	± Mucosa-associated lymphoid tissue (MALT)	
	± Lymph nodes	
7	**Liver, spleen**	
	Liver	Sections of left lateral and median lobes ± smaller lobes
	Gallbladder	In liver median lobe section
	Spleen	Hemisected (one or both halves, depending on size)
	± Lymph nodes	
8 Female	**Reproductive/urogenital**	
	Ovaries	With oviduct; ± epoophoron
	Uterus	
	Vagina ± cervix	
	Urinary bladder	
8 Male	**Reproductive/urogenital**	
	Testes	With epididymis; ± vas deferens
	Seminal vesicle with coagulating gland	
	Prostate	Dorsal, ventral lobes at neck of bladder
	Urinary bladder	
	± Ureters, urethra	± Ureters, urethra
	± Lymph nodes, etc.	± Lymph nodes, etc.
9	**Skin (head/neck, inguinal, any lesions)**	
	Skin	Hair, follicles, adnexae, subcutis
	Preputial or clitoral glands	
	± Mammary glands	

(*Continued*)

TABLE 2.3 A 10-Slide Mouse Histology Assessment: Example of a Systematic Assessment of More Than 40 Tissues, With Some Common Variations (Continued)

Cassette/ Slide	Primary Tissue/Organ	Comments/Additional Description (See RENI Guidelines for Additional Options and Information)
10	**Head (decalcified)**	Four to five cross sections or two sagittal sections
	Brain	Ventricles, olfactory bulbs, forebrain, thalamus, hippocampus, cerebellum, medulla
	Pituitary gland	Pars nervosa, intermedius, distalis, Rathke's pouch
	Temporomandibular joint	
	Bone, marrow	
	Nasal cavity and sinuses	
	Oral cavity and teeth	Gingiva molars incisors
	Eyes	Retina lens cornea chambers
	Harderian gland	
	Ears	Bulla (middle ear), tympanum, ossicles, inner ear, cochlea, ampulla
Other slides	**Spine, decalcified**	Cross sections and longitudinal sections of cervical–thoracic spine, lumbosacral spine
	Hind limb, decalcified	Knee, tarsus, lymph nodes, muscles
	GI tract, rolled ("Swiss Roll")	Closed: gut is rolled with contents, without being opened; Open: gut is opened, and mucosa examined, before rolling, fixing; May require three cassettes: (1) small intestine; (2) large intestine; (3) stomach and cecum (these are difficult to roll)
	Other lesions	

RENI tissue trimming guidelines are recommended for additional or specific guidance.

TABLE 2.4 A 15-Slide Rat Histology Assessment: Example of a Protocol to Assess More Than 40 Tissues

Cassette/ Slide	Primary Tissue/Organ	Comments/Additional Description (See RENI guidelines for additional options and information)
1	**Brain**	
	Brain three to four sections in one cassette (or RENI)	Ventricles, olfactory bulbs, forebrain, thalamus, hippocampus, cerebellum, medulla
	Pituitary gland	Pars nervosa, intermedius, distalis, Rathke's pouch
2	**Endocrine**	Place in cassette at initial dissection
	Adrenals	Tumors may require additional cassettes/slides
	Thyroids	Tumors may require additional cassettes/slides
	Pituitary	Tumors may require additional cassettes/slides
3	**Hematopoietic/immunopoietic**	
	Thymus	One or both lobes—depending on size
	Spleen	Representative cross section
	Bone marrow	Collect and fix promptly from opened femur, save/fix in cassette
4	**Salivary glands, lymph nodes;** right side from ear to midline, or lesions—should include:	
	Submandibular salivary gland	
	Sublingual salivary gland	
	Parotid gland	
	Lymph nodes (superficial and deep cervical)	
	Fat (adiposa)	Brown and white fat
	± Exorbital lacrimal gland	
	± Mammary glands	
5	**Pancreas, mesentery, lymph nodes**—representative region should include:	
	Pancreas	Exocrine, endocrine, ducts
	Mesentery	Vasculature
	Lymph nodes, pancreatic, mesenteric	
	Fat (adiposa)	
6	**Heart**	
	Heart	Hemisected, both halves if they fit: valves, myocardium, epicardium, free walls, septa
	Aorta	Cross section aortic arch
7	**Lungs**	
	Lungs	Cross section thru L/R lobes and lesions; bronchioles, alveoli, interstitium (septa), lymphoid tissue (BALT)
	Trachea	With esophagus in single section
	Esophagus	Separately if abnormal (e.g., mega esophagus)
	Thyroid, parathyroid glands	
8	**Kidneys**	One section of each kidney usually fit
	Kidneys	Left (one longitudinal section, or part of longitudinal section to fit in cassette); right (one cross section)

(*Continued*)

TABLE 2.4 A 15-Slide Rat Histology Assessment: Example of a Protocol to Assess More Than 40 Tissues (Continued)

Cassette/ Slide	Primary Tissue/Organ	Comments/Additional Description (See RENI guidelines for additional options and information)
9	**Liver**	Two sections usually fit
	Liver	One left lateral; one median lobes ± smaller lobes
10	**Gastrointestinal tract; Proximal**	
	Stomach	Forestomach, glandular stomach
	Small intestine	Three cross sections proximal, mid, distal
11	**Gastrointestinal tract; Distal**	
	Cecum	Longitudinal or cross section, including GALT
	Colon	Two to three cross sections proximal, mid, distal
	± Mucosa-associated lymphoid tissue	
	± Lymph nodes	
12 Female	**Reproductive/urogenital**	Representative cross sections—see RENI
	Ovaries	with oviduct; ± epoophoron
	Uterus	
	Vagina ± cervix	
	Urinary bladder	
12 Male	**Reproductive/urogenital**	Representative cross sections—see RENI
	Testes	with epididymis; ± vas deferens
	Seminal vesicle with coagulating gland	Representative cross section
	Prostate	Dorsal, ventral lobes at neck of urinary bladder
	Urinary bladder	
	± Ureters, urethra	Often included, associated with other tissues
	± Lymph nodes, etc.	Often included, associated with other tissues
13	**Skin (head/neck, pinna, any lesions)**	
	Skin	Hair, follicles, adnexae, subcutis
	Preputial or clitoral glands	
	± Mammary glands	
14	**Head (decalcified)**	Two to three cross sections
	Ear level	Includes middle/inner ears, associated glands, palate, maxillary molars
	Eye level	Includes eyes, Harderian gland, proximal nose
	Mid-distal nose	Includes nasal cavity, turbinates, vomeronasal organ
	Also includes bone, marrow, muscle, teeth	
Other slides	Lesions or additional tissues of interest require additional slides	
	Record any lesions in necropsy report	
	Spine, decalcified	Cross sections and longitudinal sections of cervical–thoracic spine, lumbosacral spine
	Leg, muscle + sciatic nerve or	Knee, tarsus, lymph nodes, muscles, nerves
	Leg, decalcified	
	GI tract, rolled ("Swiss Roll")	Closed method usually is not practical for rats
	(see also RENI guidelines)	Open: gut is opened, and mucosa examined, before rolling, fixing.
		Rat requires multiple cassettes: (1) small intestine; (2) large intestine; (3) stomach and cecum

In this example softer tissues are earlier in the numbering sequence. Sectioning of softer tissues before harder tissues preserves microtomy blades and can improve sections.

Nomenclature and Diagnostic Criteria (INHAND) initiatives (https://www.toxpath.org/inhand.asp). The National Toxicology Program (NTP) has published an online Nonneoplastic Lesion Atlas (NNLA) for rats and mice (http://ntp.niehs.nih.gov/nnl/). The National Cancer Institute's Mouse Models of Human Cancers Consortium has published GM mouse and rat cancer resources, including whole slide images hosted by NCIP HUB (https://nciphub.org/groups/cgp) and the Center for Genomic Pathology at UC Davis (http://imagearchive.ucdavis.edu), and consensus papers on diagnostic criteria and terminology for neoplasia of the hematopoietic system, nervous system, breast (mammary gland), prostate, lung, and intestine, as well as precancers. MMHCC terminology is especially useful when mechanisms, morphology, and behavior of GM mouse lesions differ from those of spontaneous and chemically induced lesions. In planning for phenotyping, or any translational research, early standardization of terminology and data handling should aim to facilitate comparisons across studies and evaluators, and improve communication and reporting.

Conclusion

Coordinated systematic phenotyping of thousands of GM mice with mutations in every protein coding gene though IMPC, phenotyping of inbred and GM mice through MPD, and phenotyping of inbred and GM rats through RGD already make data and protocol detail accessible to the scientific community. Together with improved reporting and accessibility of data from hypothesis-driven targeted phenotyping, these efforts promise to inform and support diverse translational biomedical research, and enhance the predictive value of work in mice and rats. Since Virchow and Osler the relevance of comparative medicine and pathology has been recognized as fundamental to understanding disease. It is hoped that comparative texts such as this will become essential tools for the design, conduct and reporting of robust, reproducible, relevant, and predictive translational science.

FURTHER READING AND RELEVANT WEBSITES

Barthold SW: Genetically altered mice: phenotypes, no phenotypes, and Faux phenotypes. *Genetica* 122:75–88, 2004.

Brayton C: Spontaneous diseases in commonly used inbred mouse strains ACLAM series. In Fox JG, editor: *The mouse in biomedical research* (ed 3), New York, NY, 2006, Elsevier.

Brayton C: Spontaneous diseases in commonly used mouse strains and stocks, Bar Harbor, ME, 2014, The Jackson Laboratory. MPD: Brayton1. Mouse Phenome Database web site. http://phenome.jax.org.

Brayton C, Justice M, Montgomery C: Evaluating mutant mice: anatomic pathology. *Vet Pathol* 38:1–19, 2001.

Cardiff RD, Rosner A, Hogarth MA, et al: Validation: the new challenge for pathology. *Toxicol Pathol.* 32(Suppl 1):31–39, 2004.

Cardiff RD, Hubbard NE, Engelberg JA, et al: Quantitation of fixative-induced morphologic and antigenic variation in mouse and human breast cancers. *Lab Invest* 93(4): 480–497, 2013.

Center for Genomic Pathology (CGP), University California Davis. Mouse models image archive. http://imagearchive.ucdavis.edu/#.

Cook MJ: The anatomy of the laboratory mouse, New York, NY, 1965, Academic Press. http://www.informatics.jax.org/cookbook.

Elmore SA, Peddada SD: Points to consider on the statistical analysis of rodent cancer bioassay data when incorporating historical control data. *Toxicol Pathol* 37:672–676, 2009.

Frith CH, Ward JM: *A color atlas of the neoplastic and nonneoplastic lesions of aging mice*, New York, NY, 1988, Elsevier. http://www.informatics.jax.org/frithbook/.

Hrabé de Angelis M, editor: *Standards of mouse model phenotyping*, Weinheim, Germany, 2006, Wiley-VCH.

International Harmonization of Nomenclature and Diagnostic Criteria (INHAND). https://www.toxpath.org/inhand.asp.

International Mouse Phenotyping Consortium (IMPC). http://www.mousephenotype.org/.

International Mouse Strain Resource (IMSR). http://www.findmice.org/index.jsp.

Keenan C, et al: Best practices for use of historical control data of proliferative rodent lesions. *Toxicol Pathol* 37: 679–693, 2009.

Maronpot RR, Boorman GA, and Gaul BW, (Eds) *Pathology of the mouse: reference and atlas*, Vienna, IL, 1999, Cache River Press.

Mouse Genome Informatics (MGI). http://www.informatics.jax.org/mgihome/nomen.Inbred Strains of Mice and Rats. http://www.informatics.jax.org/external/festing/search_form.cgi.Mouse Tumor Biology Database. http://tumor.informatics.jax.org/mtbwi/index.do.Nomenclature Home Page. http://www.informatics.jax.org/mgihome/nomen.

Mouse Phenome Database (MPD). http://phenome.jax.org.

National Cancer Institute (NCI), eMICE: Electronic Models Information, Communication, and Education. http://emice.nci.nih.gov.

National Institutes of Health (NIH) Principles and Guidelines for Reporting Preclinical Research. http://www.nih.gov/science/reproducibility/principles-guidelines.htm.

National Research Council (NRC) *Guidance for the description of animal research in scientific publications*, Washington, DC, 2011, National Academies Press. Reprinted in the ILAR J 55(3):536–540. doi:10.1093/ilar/ilu070. http://www.ncbi.nlm.nih.gov/pubmed/22379656.

National Toxicology Program (NTP). Nonneoplastic lesion atlas (NNLA) for rats and mice. http://ntp.niehs.nih.gov/nnl/.

Papaioannou VE, Behringer RR: *Mouse phenotypes: a handbook of mutation analysis*, Cold Spring Harbor, NY, 2004, Cold Spring Harbor Laboratory Press.

Pathbase: European Mutant Mouse Pathology Database. http://eulep.pdn.cam.ac.uk.

Rat Genome Database (RGD). http://rgd.mcw.edu/.

RENI Registry Nomenclature Information System. Revised guides for organ sampling and trimming in rats and mice: Morawietz G, et al: Revised guides for organ sampling and trimming in rats and mice—Part 3. A joint publication of the RITA and NACAD groups. *Exp Toxicol Pathol*, 2004. Kittel B, et al: Revised guides for organ sampling and trimming in rats and mice—Part 2. A joint publication of the RITA and NACAD groups. *Exp Toxicol Pathol*, 2004.Ruehl-Fehlert C, et al: Revised guides for organ sampling and trimming in rats and mice—Part 1. *Exp Toxicol Pathol*, 2003.Available online (English, French, German) (http://reni.item.fraunhofer.de/reni/trimming/).

Scudamore CL, Soilleux EJ, Karp NA, et al: Recommendations for minimum information for publication of experimental pathology data: MINPEPA guidelines. *J Pathol*, 2015. https://www.ncbi.nlm.nih.gov/pubmed/26387837.

Shao Y, Guan Y, Wang L, et al: CRISPR/Cas-mediated genome editing in the rat via direct injection of one-cell embryos. *Nat Protoc* 9(10):2493–2512, 2014.

Shimoyama M, De Pons J, Hayman GT, et al: The Rat Genome Database 2015: genomic, phenotypic and environmental variations and disease. *Nucleic Acids Res* 43(Database issue):D743–D750, 2015.

Ward JM, Rehg JE: Rodent immunohistochemistry: pitfalls and troubleshooting. *Vet Pathol* 51(1):88–101, 2014.

Zeiss CJ, Ward JM, Allore HG: Designing phenotyping studies for genetically engineered mice. *Vet Pathol* 49(1):24–31, 2012.

This page intentionally left blank

NECROPSY AND HISTOLOGY 3

SUE E. KNOBLAUGH
The Ohio State University College of Veterinary Medicine, Columbus, OH, United States

JULIE RANDOLPH-HABECKER
Fred Hutchinson Cancer Research Center, Seattle, WA, United States

Introduction

Necropsy and autopsy are both postmortem examinations of bodies after death. They are scientific examinations conducted in a systematic manner and include careful dissection and observation of the body and organs with collection of samples for additional testing. The specific goals of the examination differ depending on the nature of the case. In rodent models of human disease, necropsies are usually performed at the end of studies (research necropsy) or as part of the veterinary clinical care (diagnostic necropsy). For human autopsy, the examinations often generate both medical and legal information. In biomedical research, systematic, well-conducted anatomic and histologic evaluations provide researchers with morphologic data that document the changes in cells, tissues, organs, and the whole body. Interpretation of these changes, along with laboratory medical and molecular changes, can provide insight into physiologic or disease mechanisms present in the particular rodent model. Data generated by anatomic and histologic evaluation of a cohort are essential to model validation.

Anatomic assessment begins with developing a plan for the necropsy, in light of the experimental or diagnostic goals. Often, the collection of one type of sample, such as bacterial culture of the inner ear, is at odds with another, such as whole-body perfusion fixation for optimal nervous system histology. Plans should be made to triage the collection of clinical laboratory, microbiologic, molecular, and histologic samples according to the importance of each sample to the study.

In this chapter, we outline and discuss the variables to consider prior to performing a rodent model anatomic assessment. The chapter begins with a section on tissue fixation, which is critical to consider before the collection of histologic samples, whether for routine hematoxylin and eosin (H&E) stained sections, for special stains, or for immunohistochemistry (covered in detail in Chapter 4: Microscopy, Immunohistochemistry, Digital Imaging, and Quantitative Microscopy). Dissection and sample collection techniques are outlined in a basic necropsy protocol, and the chapter concludes with histologic techniques and considerations. The topics covered in this chapter are, in their own right, subjects of entire books. The goal of this chapter is to introduce the new rodent investigator to the anatomic assessment of rodent models, including the importance of proper planning to optimize the morphologic data generated. In-depth resources are provided in the Further Reading and Relevant Websites section.

Comparative Anatomy and Histology. DOI: http://dx.doi.org/10.1016/B978-0-12-802900-8.00003-8
© 2018 Elsevier Inc. All rights reserved.

Fixation Considerations Prior to Necropsy

Optimal fixative choice depends on study goals. Certain fixatives may yield superior morphology but interfere with a special stain or antibody protocol. Because tissue samples are valuable, choice of fixative should be carefully considered prior to tissue procurement. It can be valuable to consult with the pathologist reviewing and the laboratory processing your tissue for guidance on fixative choice. It is important that initial fixation, usually performed during necropsy, be done properly because poor fixation or incorrect fixative choice cannot be remedied at a later stage in tissue preparation.

Many chemical fixatives are currently in use; however, most cross-link insoluble with soluble proteins. Cross-linking of the cellular components creates a gel that preserves proteins in their fundamental positions within cells. In addition, fixation enables the tissue to undergo processing, embedding, sectioning, and staining while maintaining its structure. Fixation, if performed correctly, also preserves the tissues from autolysis and bacterial destruction.

MAJOR GROUPS OF FIXATIVES

Each group of fixatives creates characteristic morphologic changes visible within tissue samples. Most available texts and resources use formaldehyde-fixed tissue to illustrate microanatomy and histology. In addition, most staining and immunohistochemistry protocols are optimized for formalin-fixed tissue.

Aldehydes

Aldehydes, such as formaldehyde, paraformaldehyde, and glutaraldehyde, are the fixatives of choice for standard morphologic analysis. The most common formaldehyde solution, known as formalin, is prepared with water and phosphate buffer to create 10% neutral buffered formalin (4% formaldehyde in phosphate-buffered saline). Formalin is the most commonly used fixative for light microscopy and is an ingredient in many other fixatives.

Aldehyde fixatives cross-link proteins and are therefore known as “cross-linking” fixatives. Formaldehyde in solution will quickly polymerize, decreasing its activity. In order to stabilize the solution, formalin contains methanol, which inhibits polymerization. Paraformaldehyde does not contain stabilizing methanol and must be made fresh before each use.

Paraformaldehyde is preferred to formalin when tissue is prepared for electron microscopy. The methanol added to formalin may coagulate cellular components, altering fine tissue ultrastructure. The subtle changes produced by methanol are not visible at the level of light microscopy. Paraformaldehyde is also preferred when briefly fixing tissue prior to use with labeled lectins. Methanol appears to inhibit lectin binding.

Karnovsky’s fixative, 2% buffered glutaraldehyde, fixes tissue quickly and gives excellent overall cytoplasmic and nuclear detail in electron microscopy. However, Karnovsky’s fixative alters protein structure and is not recommended for immunoperoxidase staining or light microscopy.

Davidson’s and modified Davidson’s are frequently used for testes and eyes in toxicologic studies as a replacement fixative for Bouin’s fluid: modified Davidson’s—30% of a 37–40% solution of formaldehyde, 15% ethanol, 5% glacial acetic acid, and 50% distilled H_2O; and Davidson’s—2% of a 37–40% solution of formaldehyde, 35% ethanol, 10% glacial acetic acid, and 53% distilled H_2O.

Mercuric Chloride

Mercuric-chloride-based fixatives include B-5 and Zenker's. These penetrate tissue relatively poorly and require thin sections for adequate fixation (2 mm). Mercuric chloride fixatives provide excellent nuclear detail and in the past were commonly used for fixation of hematopoietic and reticuloendothelial tissues. Due to the inherent toxicity of mercury, these fixatives have been discontinued in most laboratories.

Alcohols

Alcohols, including methanol and ethanol, denature proteins and rapidly dehydrate tissues. Alcohol fixatives are not commonly used for standard tissue histology. Alcohols are used routinely to fix cytologic preparations and frozen tissue because they work quickly and render good nuclear detail.

Picric Acid

Picric acid fixatives represent mixtures of fixatives. The most common among these is Bouin's, which provides excellent nuclear detail. Bouin's fixative contains aqueous picric acid, 40% formaldehyde, and glacial acetic acid. Although not commonly used in histology, it is occasionally used for fixing of testicular, hematopoietic, gastrointestinal, or endocrine tissue, where exceptional nuclear detail may be diagnostically important.

Oxidizing Agents

Oxidizing agents cross-link but cause extensive protein denaturation. Oxidizing agents are primarily used in electron microscopy. The well-known oxidizing agents include osmium tetroxide, potassium permanganate, and potassium dichromate.

TISSUE FIXATION VARIABLES TO CONSIDER

Temperature

Fixation at room temperature maintains excellent morphologic detail and is usually the best choice. Increasing fixative temperature can increase not only the rate of fixation but also the rate of tissue autolysis. Conversely, reducing fixative temperature will not only slow the rate of autolysis but also greatly slow fixation.

Size

Fixative penetration is directly proportional to tissue thickness. Formalin penetrates tissue at approximately 0.5 mm per hour. If a specimen is large, it may take hours or even days for full fixative penetration. As a helpful guideline, tissue prepared for fixation should be no thicker than a nickel (2 or 3 mm) and no larger than a postage stamp (2 cm).

Volume Ratio

The fixative volume should be at least 10–20 times greater than the tissue volume. As fixative molecules bind to the tissue, they are depleted. Inadequate fixative volume will result in inadequate tissue fixation.

Time

Regardless of fixative type, tissue should be placed immediately in fixative to obtain optimal tissue quality. The topic of fixation time continues to generate considerable controversy. Historically, overfixation was perceived as deleterious to tissue. Although overfixation by mercury-containing and coagulative fixatives (alcohols) can cause tissue degradation, it is not clear that formalin overfixation damages tissue. Indeed, formalin underfixation may

TABLE 3.1 Artifacts From Improper Fixation

Problem	Resulting Artifact
Overfixation	Denatured proteins form precipitates within tissue. Tissue becomes very hard and shrinks
Underfixation	Alcohol fixation can occur during dehydration stage of tissue processing resulting in poor histologic morphology and inconsistent immunohistochemistry
Inadequately buffered formalin	Black formalin pigment precipitate appears adjacent to tissue (acid-hematin)
Alcoholic fixatives	Alcohol severely denatures proteins. Immunohistochemistry and histologic morphology compromised
Mercuric chloride fixatives	Inadequately removed mercury may form a precipitate

cause more problems than overfixation. Underfixed tissue is susceptible to fixation by alcohol in the dehydrating step of tissue processing (see Table 3.1 and the section on tissue processing), resulting in protein loss and epitope damage.

A minimum formalin fixation time of 24 h is recommended prior to processing. Whereas formalin penetrates tissue at 0.5 mm per hour, free aldehydes cross-link proteins more slowly. Studies by Fox and Helander (see Further Reading and Relevant Websites) demonstrate that a minimum of 24.5 h is required for complete fixation of a 5-mm-thick tissue section and 25 h for a 4 × 4 × 4-mm tissue cube as the time for fixation would be longer for thicker tissue. One concern regarding prolonged formalin fixation time is its effect on subsequent immunohistochemical studies (see Chapter 4: Microscopy, Immunohistochemistry, Digital Imaging, and Quantitative Microscopy). With the advent of heat-mediated and enzyme antigen retrieval, the majority of antigens can be detected in tissue that has been formalin fixed for several days to months or even years (see Chapter 4: Microscopy, Immunohistochemistry, Digital Imaging, and Quantitative Microscopy).

pH

In order to preserve fine ultrastructure and reduce the appearance of artifactual fixative pigment, fixative pH should be between 7.2 and 7.4. Fixatives may be poorly buffered, so care should be taken to add or exchange fixative if the samples contain excess fluid, which may require more buffering.

Osmolarity

Cells fixed in hypertonic or hypotonic solution may shrink or swell and burst, respectively. A phosphate-buffered saline-based fixative solution will not only address pH issues but also prevent osmolarity issues.

DECALCIFICATION OF BONE SAMPLES

Bone samples must be decalcified to ensure quality paraffin sectioning (see section “Histology”). Acids and chelating agents are two major types of decalcifying agents. Chelating agents such as ethylenediamine tetraacetic acid (EDTA) are gentler but require a relatively long time to completely decalcify bone. For convenience and speed, acid decalcifiers are more widely used. Strong inorganic acids such as nitric and hydrochloric acids are very efficient decalcifying agents; however, they cause tissue damage, hydrolyze nucleic acids, and often render tissue inadequate for immunohistochemistry. Weak organic acids, such as formic acid, still hydrolyze nucleic acids but allow rapid decalcification with better tissue and epitope preservation.

To reduce tissue damage, samples should be completely fixed prior to decalcification. There are several commercial formulations that add varying formic acid concentrations to formalin but these products should be used with great caution. Combining the two agents can decrease the time between tissue harvest and paraffin processing but exposing proteins to acid before they are completely fixed can damage antigens and alter morphology.

Because excess time in acid can severely damage tissue, a decalcification endpoint test, such as

radiography or calcium oxalate test, can be used to determine when to stop decalcification. Alternately, the extent of decalcification can be determined by measuring the flexibility of samples with gentle bending or sectioning. A simple method to monitor rodent tissue during decalcification is to include a section of mouse or rat tail with the decalcifying sample. Easy sectioning through the bone of the tail indicates sufficient decalcification.

Decalcification can be expedited by placing samples on a slow rocker and removing surrounding soft tissue. Although increased temperature increases the speed of decalcification, it also accelerates tissue damage. Thus, room temperature is recommended for decalcification.

Acid should be rinsed completely from decalcified samples. A water rinse of 20 min is generally sufficient. Follow the manufacturer's recommendations for commercial products.

If immunohistochemistry is required on decalcified tissue, ensure preparation of decalcified controls to test for loss of antigenicity during decalcification. For example, to use soft tissue as a control for immunohistochemistry on mouse bone, add the soft tissue control to decalcification solution at the same time as the bone sample.

FROZEN TISSUE FOR HISTOLOGIC EVALUATION

Some histologic studies require no or limited fixation. The cross-linking activity of aldehydes inactivates most enzymes, including esterases and alkaline phosphatase. Fixation and paraffin processing also dissolves tissue lipids. Finally, some antigens are permanently altered by formalin fixation and cannot be retrieved. In these cases, unfixed frozen tissue is required.

Tissue to be frozen should be processed quickly to decrease autolysis. If there will be delay between tissue acquisition and freezing, fresh tissue should be quickly submerged in cold-buffered saline and kept on wet ice. Do not place fresh tissue directly on dry ice or into liquid nitrogen because cell membranes will rupture, destroying tissue architecture. Optimally, tissue should be embedded in a freezing media such as optimal cutting temperature compound or Cryo-Gel prior to freezing.

Tissue should be trimmed (see section "Necropsy") and any excess fluid gently removed prior to application of freezing media. Embedded tissue can then be safely frozen in an isopentane (2-methyl butane) bath over liquid nitrogen or on an aluminum block surrounded by a moat of liquid nitrogen. It is not advised to plunge tissue directly into a slurry of dry ice and alcohol because the alcohol can contaminate the freezing media and alter cutting properties. If the tissue is frozen too slowly, such as in a −20°C freezer or cryostat, significant tissue damage and artifact can result from the formation of ice crystals in the tissue. Embedded samples should be stored at −80°C and protected from desiccation.

NECROPSY

There is no one correct way to perform a rodent necropsy; the research or diagnostic questions at hand will drive the dissection procedure and samples collected, and pathologists often develop their own preferred methods and fixatives. Written for the new rodent investigator, the protocol within this section provides a basic rodent necropsy technique. While it is illustrated primarily with mouse figures, the protocol is suitable for rats. It is a modified Virchow autopsy method (organs removed one by one rather than en bloc) and uses the common and easy fixation technique of immersion in 10% neutral buffered formalin. Variations of this protocol are prevalent in rodent diagnostic laboratories, and phenotyping cores will often have multiple and complex necropsy methods depending on target organ or disease model. Regardless of necropsy

method or fixative used, all instruments, sample collection materials, cameras, and other supplies, along with checklists, should be prepared in advance. It is critical that a unique identifier for each rodent is used and that all samples are properly labeled and all findings recorded. Developing a necropsy checklist tailored to the intended research is important and recommended. An important component is tissue trimming, which is the postfixation dissection of tissues to fit into embedding cassettes (also called "grossing"). Standardized trimming of tissues is needed in research studies to maintain consistency in organ sampling across individual mice; see Further Reading and Relevant Websites for additional references for detailed trimming protocols (http://reni.item.fraunhofer.de/reni/trimming) and videos of necropsy techniques (Treuting and Snyder; Parkinson et al.).

RECOMMENDED MATERIALS

Working in a fume hood or other type of ventilated workstation is important and will protect against inhalants from fixatives or the animal. A good work surface, such as a dissecting board with a cork or rubber surface, works best. Other suitable materials include Styrofoam box lids or multiple layers of paper towels. It is a good idea to wrap the board in paper towel both to keep work surfaces clean and to wrap up the carcass upon completion of the necropsy. Pins are optional and will depend on the preference of the prosector. Pinning creates a stable work foundation, but if the animal is not pinned, there is more freedom to move it. A plastic cutting board is recommended for any tissue trimming that is performed at the time of necropsy. This will prevent artifacts arising from sticky tissues. The ideal instruments include forceps, sharp blades such as razor or scalpel blades, and a few pairs of scissors—one pair dedicated for cutting bone and a fine-tipped pair for delicate soft tissues. Larger scissors are recommended for rats. Phosphate-buffered saline or saline is important for rinsing tissues such as the gastrointestinal (GI) tract and for keeping tissue moist. As noted previously, 10% neutral buffered formalin is an overall good fixative for most tissues, with exceptions for certain tissues, research protocols, and investigator's or pathologist's preference. A syringe and needle are ideal for infusing tissues such as the lung. A metric scale is important for weighing the mouse and individual tissues, and a metric ruler allows recording of size. Specimen containers, tissue cassettes, and labels are essential and keep tissues organized. Certain rodent organs, such as adrenal glands and lymph nodes, are very small and can easily be lost; biopsy bags or mesh screen cassettes are recommended for them.

Prior to euthanizing the mouse or rat, ensure that your supplies are labeled with the mouse's or rat's identification, strain, and any other pertinent information for your research or project. A unique identifier for each mouse or rat is recommended. If terminal blood collection is required, this should be performed immediately after euthanasia because coagulation may occur rapidly and reduce the blood volume obtained. Blind cardiac puncture can be performed using one of two approaches—either via the thoracic inlet or from the left side of the xyphoid process angling toward the right side of the chest. For a rat, a 10–20 mL syringe fitted with a 20- to 25-gauge needle or for a mouse, a 1–3 mL syringe should be fitted with a 23- to 25-gauge needle and the plunger retracted slightly to break the slight vacuum present in new syringes. Blind cardiac puncture is a learned skill and should be practiced on nonessential rodents prior to collecting research samples. Blood should be placed in the appropriate sample tube immediately after collection to prevent clotting. Serum from animals euthanized using carbon dioxide will have aberrantly high potassium levels, possibly as a result of blood pH shifts due to the gas.

EXTERNAL EXAMINATION

The carcass should be weighed after blood collection, and a thorough external examination should be performed. During the external examination, note the rodents' body condition (hydration or body mass index); look for any discharge from eyes, nose, mouth, and urogenital tract; and verify the sex and identification of the rodent (Fig. 3.1). Look for any lesions, wounds, or masses associated with the skin or subcutaneous structures. Examine the oral cavity, including the teeth.

If a skin sample is needed, cut a rectangular piece and place it on an index card (see Further Reading and Relevant Websites and also Chapter 24: Skin and Adnexa for specialized techniques) to avoid curling of the tissue during fixation. Depending on the lesion and researcher's preference, the hairs may be removed via shaving to ease sectioning of the paraffin block.

Large masses may be excised, leaving adjacent normal tissue attached. Large tissue samples should be sectioned prior to placing them into formalin, which aids in rapid penetration of formalin into the deeper portion of the tissue (see section "Histology"). Next, palpate the abdomen for any masses or fluid.

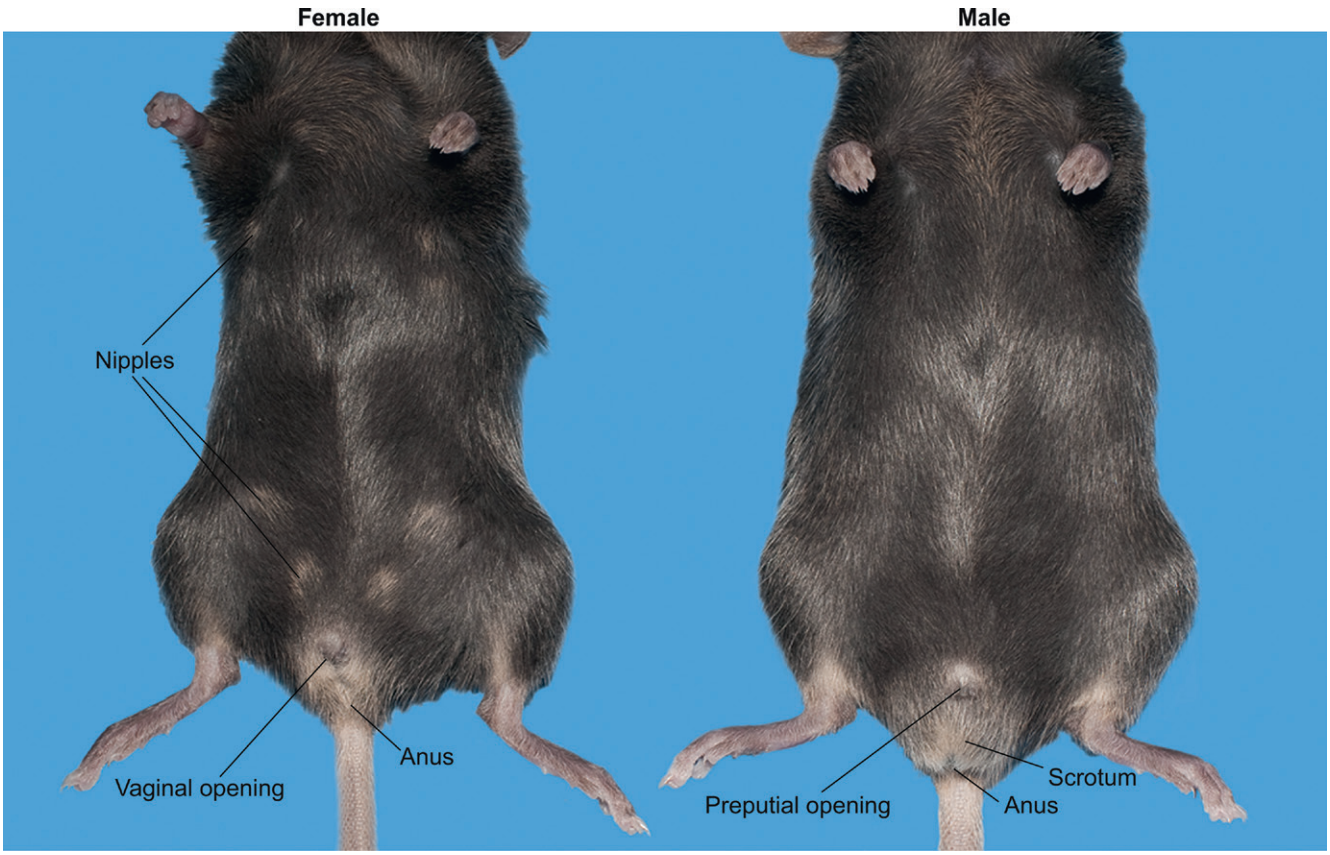

FIGURE 3.1 Female and male rodent external anatomy. For the female, there is a short distance between the anus and the genital (vaginal) opening. Nipples are present; size is dependent on parity and lactation. For the male, there is a long distance between the anus and the genital (preputial) opening.

Need-to-know

- Rodents may be sexed by the length of the anogenital distance, which is longer in the male.
- Male rodents lack nipples.

FIRST INCISION

After all skin and external samples are collected, dampen the hair with 70% ethanol either by spraying or by dipping. This will help keep hair out of the dissection field. Alternatively for the mouse, the entire pelt may be removed by making a small transverse incision at midventral abdomen and then exerting gentle pressure and pulling on the cut skin both cranially and caudally (degloving technique described in Treuting and Snyder). This should be done until the carcass is degloved, with the pelt everted and covering the head and lower limbs. Note that the mammary fat pads and possibly the subcutaneous lymph nodes will remain with the pelt.

Secure the carcass using dissection pins or tacks, exposing the ventrum (Fig. 3.2). If the carcass was not degloved, grasp the skin with forceps and make an incision along the ventral midline from chin to pubis and extend the dissection from the groin or pubis down each leg to about the knee. A razor blade may be used to help remove the tightly adhered rat pelt. Gently reflect the skin back without entering the peritoneal cavity (Fig. 3.3).

FIGURE 3.2 Pinned necropsy position. The pelt is wet with 70% ethanol, and the carcass is positioned ventral side up and secured to the dissection board with pins. Alternatively, the carcass may remain unpinned.

Subcutaneous Structures

Once the pelt is removed, subcutaneous structures may be examined and collected. These include the salivary glands, exorbital lacrimal glands, subcutaneous lymph nodes, mammary fat pads, Zymbal's gland (rat), and clitoral glands in females and the preputial glands in males. In the ventral cervical subcutaneous region lie the submandibular, sublingual, and parotid salivary glands, and cervical lymph nodes (see Chapter 8: Salivary Glands). These may be removed *en bloc* and placed into a cassette (Fig. 3.4).

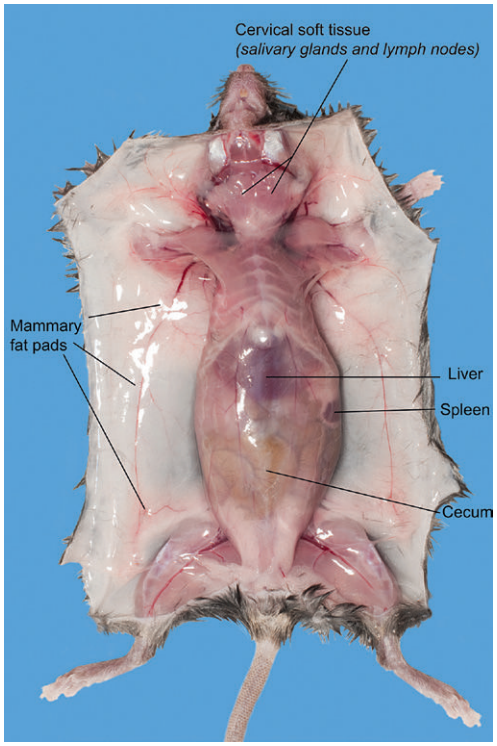

FIGURE 3.3 Ventral subcutis and abdomen. The skin has been dissected away and reflected to expose the subcutaneous and intraabdominal structures. The mammary fat pads in this female mouse remain with the skin. Note the relationship of the abdominal organs through the thin but intact abdominal musculature.

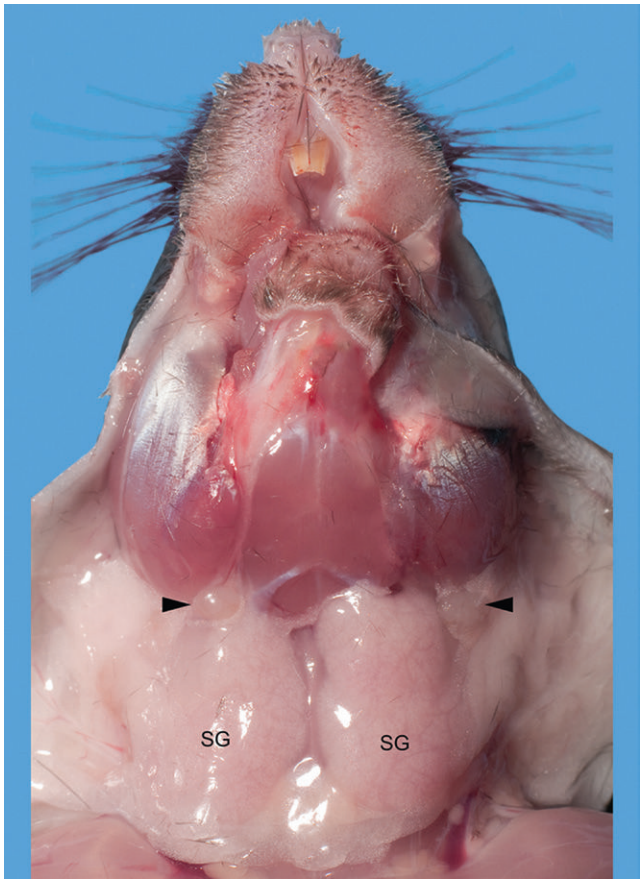

FIGURE 3.4 Subcutaneous ventral cervical region. The ventral cervical region has abundant subcutaneous soft tissues containing the submandibular, sublingual, and parotid salivary glands (SG) and cervical lymph nodes (arrowheads). These tissues may be removed *en bloc*.

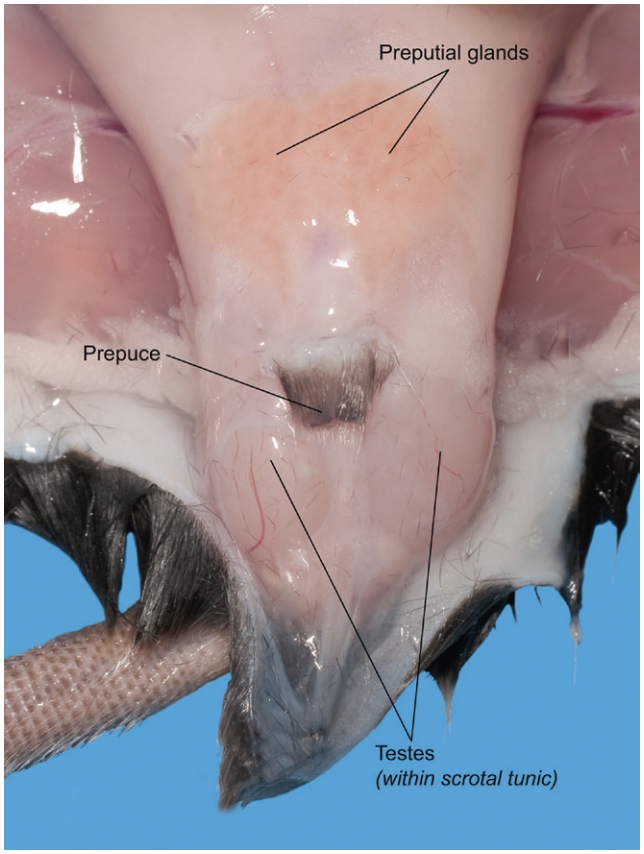

FIGURE 3.5 Male preputial glands and penis. In a female rodent, the clitorial glands are located in this region.

Need-to-know

- Male rodents have larger submandibular salivary glands than female rodents.

The Zymbal's gland and exorbital lacrimal glands lie ventrolaterally near the base of the ear.

In the inguinal subcutaneous region of males lie the preputial glands. In females, this region has the clitoral glands. To sample these glands, bluntly dissect between the gland and the abdominal muscles and connective tissue (Fig. 3.5).

Mammary Glands

The mammary glands are located within subcutaneous fat pads on both sides of the female (Fig. 3.6). Male rodents lack nipples and glands because the majority of the mammary tissue regresses during embryonic development (see Chapter 23: Mammary Gland). The mammary chain consists of five pairs of glands in mice. There are three pairs in the cervicothoracic area and two pairs in the inguinoabdominal area. The rat mammary chain has six pairs of glands. There are three pairs in the cervicothoracic area and three pairs in the inguinoabdominal area. It is important to note that rodent mammary fat pads are extensive and when completely developed extend from the inguinal area and base of the tail to the salivary gland region of the neck and around to the dorsum (see Chapter 23: Mammary Gland). Mammary glands are most obvious in lactating rodents where they may occupy most of the thoracic and abdominal ventral subcutaneous area. The subiliac lymph node may be seen associated with the inguinal mammary gland (Fig. 3.7).

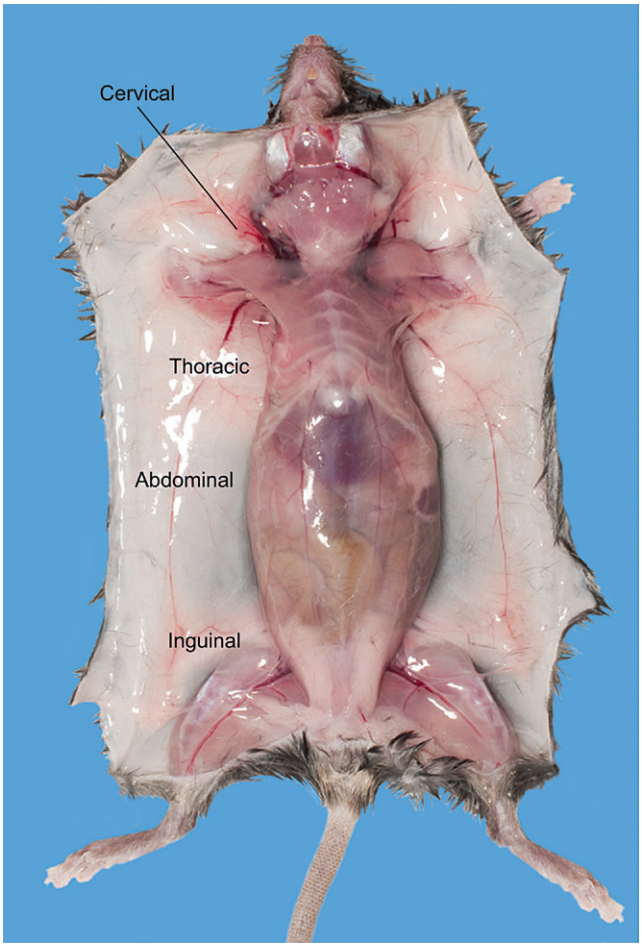

FIGURE 3.6 Ventral mammary fat pads reflect back with the skin. The paired rodent mammary glands are located in the fat pads in the subcutaneous tissues. The mouse mammary chain consists of five pairs of glands. There are three pairs in the cervicothoracic area and two pairs in the inguinoabdominal area. The rat mammary chain has six pairs of glands; three pairs in the cervicothoracic area and three pairs in the inguinoabdominal area. Mammary glands are most obvious in lactating rodents and, when sectioned, may secrete milk.

Need-to-know

- In adult female rodents, the mammary fat pads are extensive, extending dorsally to the intrascapular region and caudoventrally to the perineal region.

The mammary glands may be removed individually and placed flat on paper or index cards or in cassettes, or they may be removed *en bloc* from each side with skin attached. Lay dissected mammary fat pad, skin side up, on a labeled index card. The entire card may be rolled and placed in formalin. This allows proper orientation and labeling of the entire chain on each side. For whole mount techniques, see Chapter 23, Mammary Gland.

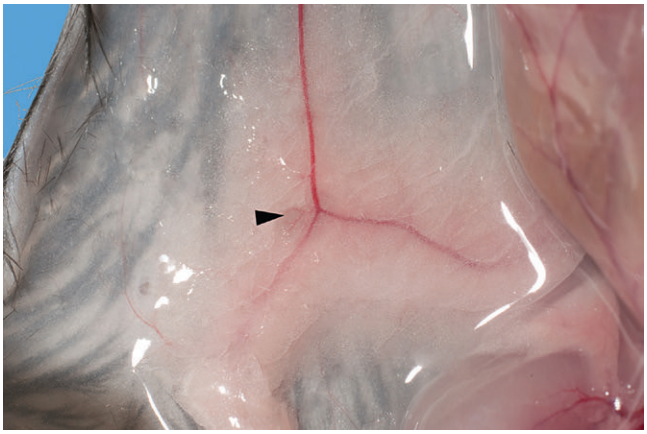

FIGURE 3.7 Left inguinoabdominal mammary fat pad. The subiliac lymph node (arrowhead) may be seen associated with the inguinal mammary gland and branches of the subcutaneous abdominal vein.

Subcutaneous Lymph Nodes

Lymph nodes in normal rodents are small and can be challenging to see without a dissection scope or magnifying glass. Prior knowledge of typical location is needed to locate lymph nodes, especially in obese rodents (see Chapter 19: Hematopoietic and Lymphoid Tissues). Normal lymph nodes are round to bean shaped and light cream to white, and are easily obscured by white adipose tissue. Once collected, lymph nodes should be placed in biopsy bags or into mesh screen cassettes prior to placing into formalin. The internal (deep) lymph nodes are located within the body cavity; therefore, they will be collected later during the necropsy.

INTERNAL EXAMINATION

Abdominal Cavity

To open the abdominal cavity, incise the abdominal musculature on the midline by gently grabbing the musculature with forceps and retracting up so that the abdominal organs are not adjacent to the muscles, and then snip with scissors to make a small opening into the peritoneal cavity. Extend the incision caudally toward the pubis and cranially toward the xyphoid process. Divide the pelvis at the pubic symphysis with scissors to facilitate the removal of the lower abdominal and pelvic contents (Fig. 3.8).

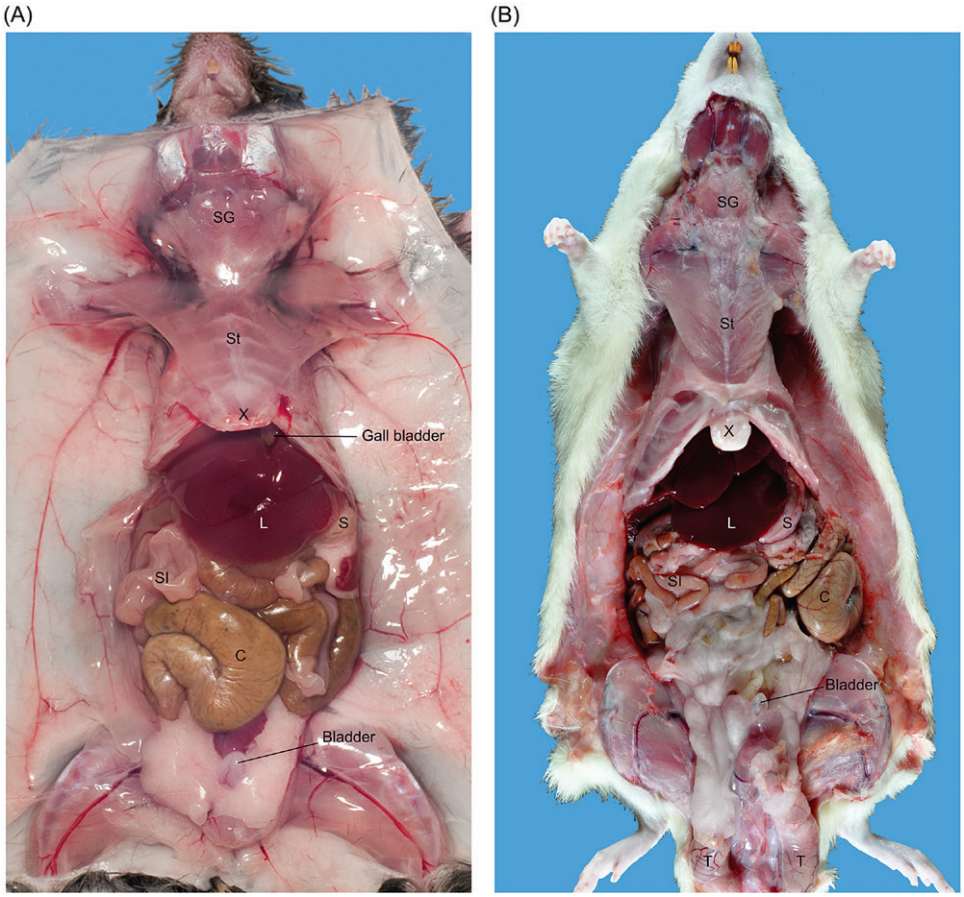

FIGURE 3.8 Internal abdominal regional anatomy. The abdominal contents are exposed after dissection of the abdominal musculature and splitting of the pubic symphysis in the female mouse (A) and in the male rat (B). Salivary glands (SG), sternum (St), xiphoid (X), small intestine (SI), stomach (S), cecum (C), liver (L), and testes (T) are indicated. Note that the rat does not have a gallbladder.

Spleen and Pancreas

The spleen is the first visceral organ of the abdominal cavity to be extracted. Use forceps to hold and then cut the hilum and the gastrosplenic ligament (Fig. 3.9). The pancreas in rodents is diffuse (mesenteric type) and embedded in fat (see Chapter 14: Pancreas). A large portion of the pancreas is located under and attached to the spleen. Thus, due to its intimate connection with the spleen, the pancreas can easily be removed at the same time (Fig. 3.10). Alternatively, a section of the proximal duodenum, to which a portion of the pancreas is attached, may be submitted to examine the head of the pancreas, associated ducts, and duodenal papillae.

Liver

The rodent liver consists of four lobes designated as right, median, left, and caudate. The right lobe has a transverse septum that nearly bisects it in half. The median lobe is the most prominent and is seen first upon entry into the abdomen. The mouse liver median lobe is divided into right and left portions by a bifurcation containing the gallbladder. The rat liver median lobe has an obvious central cleft, but the rat does not have a gallbladder. The left lobe is the largest and is a frequent site of sampling for histology in mice; in the rat it is less prominent. The caudate lobe is small and has two distinct ear-shaped segments that are best viewed by simultaneously reflecting the main body of the liver cranially and the stomach caudally during prosection. The small caudate lobe is located craniodorsal to the stomach. Care should be taken so that it is removed with the bulk of the liver (see Fig. 3.9). The liver is excised by cutting the diaphragm free from the thoracic wall and

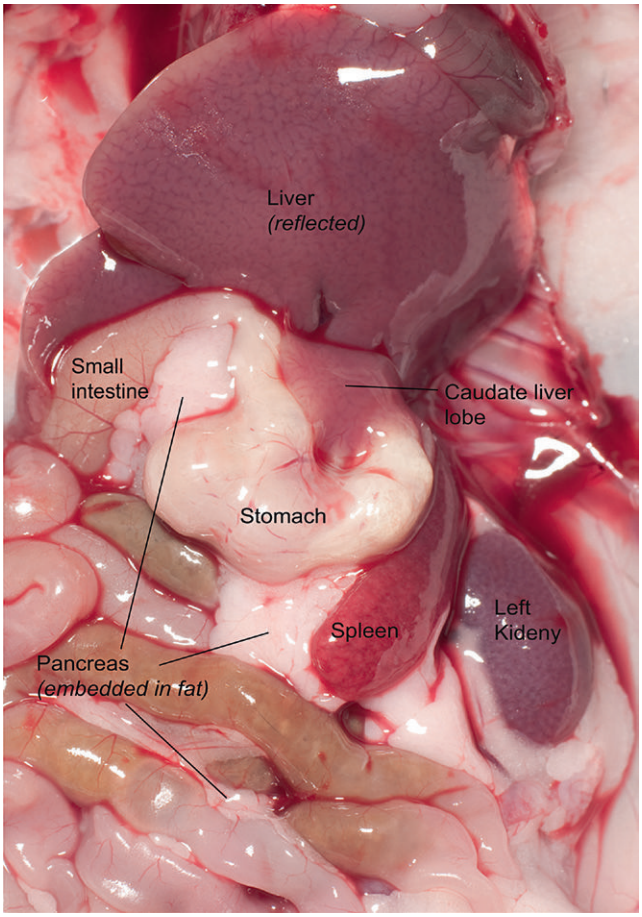

FIGURE 3.9 Left cranial abdomen. The spleen will be the first visceral organ of the abdominal cavity to be extracted. To facilitate visualization of the spleen, the liver should be reflected craniodorsally.

Need-to-know

- Rodents have a diffuse mesenteric type of pancreas.

then gently grasping the connective tissue under the median lobe with forceps and exerting tension posteriorly while severing the esophagus, blood vessels, and any remaining connections to free the liver (Fig. 3.11). All lobes should be separated or all large lobes cut through before placing them in formalin to ensure proper fixation. This facilitates full examination of the organ (Fig. 3.12). Sectioning of the liver for routine diagnostic histology usually includes one section of the median lobe, with centrally located gallbladder in the mouse, and one section of the left lateral lobe. Standardized trim guides for toxicology studies are available (http://reni.item.fraunhofer.de/reni/trimming).

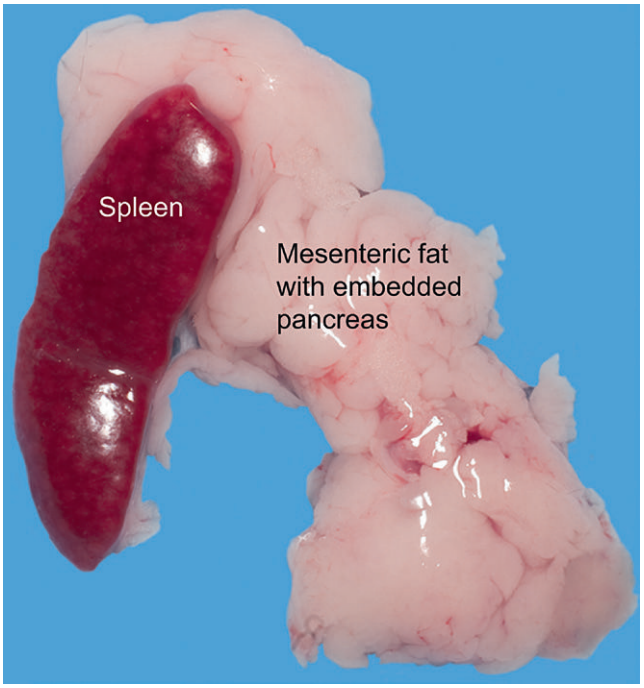

FIGURE 3.10 Spleen and pancreas removed en bloc. The pancreas is located under and attached to the spleen. It is diffuse and embedded in variable amounts of mesenteric fat. A sample of pancreas can routinely be obtained with the spleen.

GI Tract

There are several methods for examining, fixing, and trimming the intestinal tract. The intestinal tract may be fixed closed or opened. Typically, the GI tract is removed from the carcass while bluntly dissecting the mesenteric attachments to release to intestinal coils linearizing the tract. After removing the tract from the carcass, it may be opened to allow for inspection of mucosal surfaces and complete removal of contents. This technique is often performed for intestinal carcinogenesis studies. The closed method is faster, and contents may be removed by flushing if desired. Using a blunt needle placed into the duodenum, phosphate-buffered saline or formalin is injected to flush the contents. Intestinal tissues (either opened or closed) may be prepared using the Swiss roll technique, in which portions of the tract prior to fixation are rolled from proximal to distal and placed into cassettes (see Chapter 12: Lower Gastrointestinal Tract).

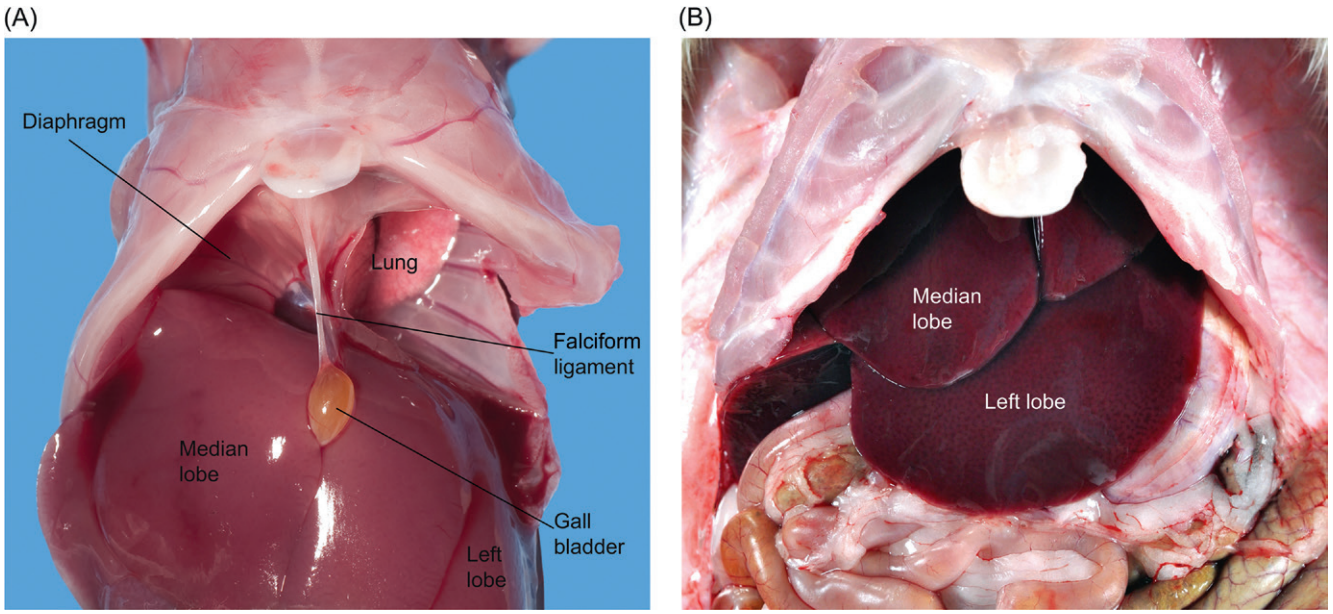

FIGURE 3.11 Liver and gallbladder. (A) Mouse. Note the unusually prominent falciform ligament in this dissection. In most dissections, the ligament is inconspicuous. The lung is visible through the sectioned diaphragm. (B) Rat. The rat does not have a gallbladder.

Need-to-know

- Rats do not have a gallbladder.

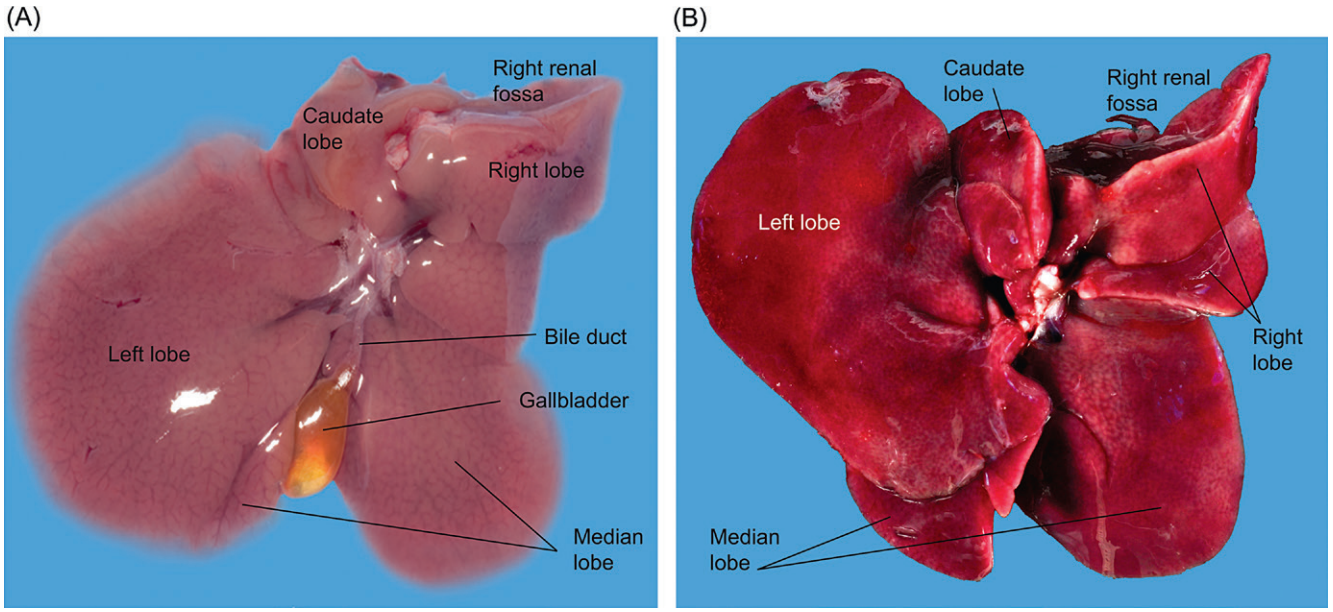

FIGURE 3.12 Ventral aspect of rodent liver. The ventral aspect of the rodent liver demonstrates the four liver lobes. (A) The mouse liver median lobe is divided into right and left portions by a bifurcation containing the gallbladder. (B) The rat liver median lobe has an obvious central cleft, but the rat does not have a gallbladder.

Once the liver has been removed, the stomach should be free from its connection to the liver and esophagus. If it is not, grasp the stomach with forceps and sever the esophagus approximately 0.5 cm above the stomach (Fig. 3.13). Maintaining tension on the stomach, sever the mesenteric attachments between the intestines using blunt dissection and elevation of the freed proximal intestinal tract from the abdominal cavity. Proceed from the stomach toward the anus until the

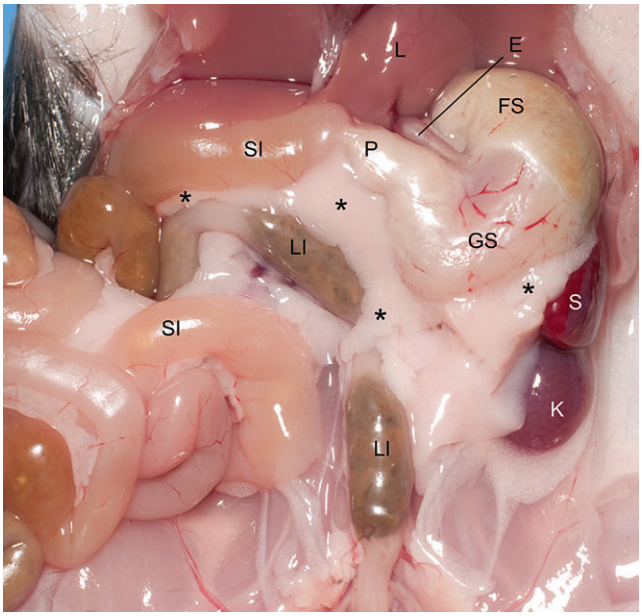

FIGURE 3.13 Left cranial abdomen. The stomach and associated cranial abdominal organs are displayed in a ventrodorsal. The esophagus (E) is located at the cranial midline region of the lesser curvature of the stomach and is easily visualized once the liver (L) is reflected. The pancreas is diffusely dispersed in the mesenteric fat (asterisks). Forestomach (FS), glandular stomach (GS), pylorus (P), spleen (S), small intestine (SI), large intestine (LI), and kidney (K) are indicated.

mesentery along the entire length of the intestinal tract is removed. This stripping of the mesentery will allow inspection of all segments and relatively flat fixation as the intestinal loops are relaxed (Fig. 3.14). Dissect around the anus to free the entire tract and place on a moistened towel or cutting board for further dissection and/or removal of intestinal content. Alternatively, the entire unopened tract may be placed into formalin. A relatively large cluster of mesenteric lymph nodes is often seen in the mesentery close to the ileocecal junction. They are usually seen as the mesentery is stripped from the distal ileum/cecum and should be collected (Fig. 3.15).

The stomach may be fixed using an open or closed method, depending on the preference of the researcher or the experimental protocol. The open method is preferred for evaluation of the stomach mucosa lining and proper flat fixation. Open the stomach by inserting scissors tips into

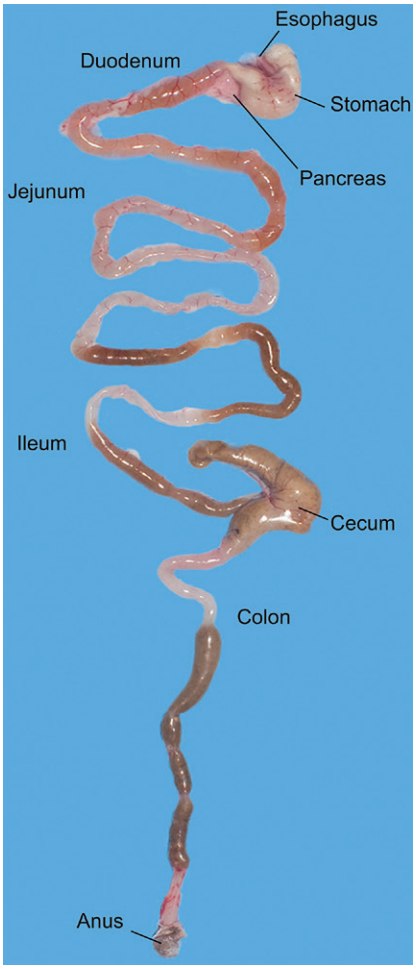

FIGURE 3.14 GI tract after removal of the mesentery. The approximate regions of the GI tract are indicated.

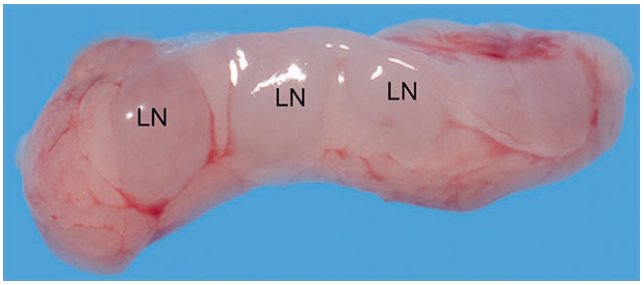

FIGURE 3.15 Mesenteric lymph nodes removed en bloc. The mesenteric lymph nodes (LN) are a group of lymph nodes embedded in the mesenteric fat near the ileocecal junction. The lymph nodes are slightly paler and raised from the surrounding fat.

the nonglandular (white or transparent) region near the diaphragmatic end and dissect along the greater curvature to the pylorus. At this point, the stomach contents may be removed and the stomach rinsed with phosphate-buffered saline or

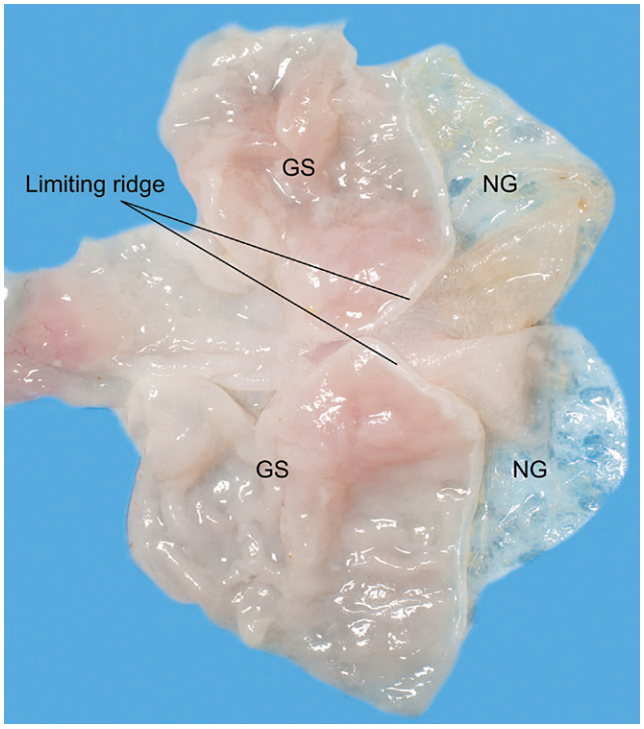

FIGURE 3.16 Opened stomach. The squamous or nonglandular (NG) portion is white-to-translucent, and the glandular (GS) portion is opaque and pink. The limiting ridge it the demarcation between the compartments.

saline (Fig. 3.16). Lay the opened stomach, serosal side down, on an index card to ensure flat fixation. The entire GI tract, especially the muscular stomach, will curl during fixation, which may lead to poorly orientated histology sections.

The closed method traps the stomach contents and allows for distension. Place tight ligatures around the duodenum and esophagus to trap the contents, and inject approximately 1 mL of formalin (Fig. 3.17). In mice, enough of the injected fixative will remain in place without ligatures.

Dissect the cecum from the ileum and proximal colon. Contents may be flushed or washed out with phosphate-buffered saline or formalin. Alternatively, the intact cecum and small and large intestine may be placed into formalin (Fig. 3.18).

Urogenital System

The reproductive tract is located between the urinary bladder and the large intestine. If the large intestine has not been removed, reflect the colon

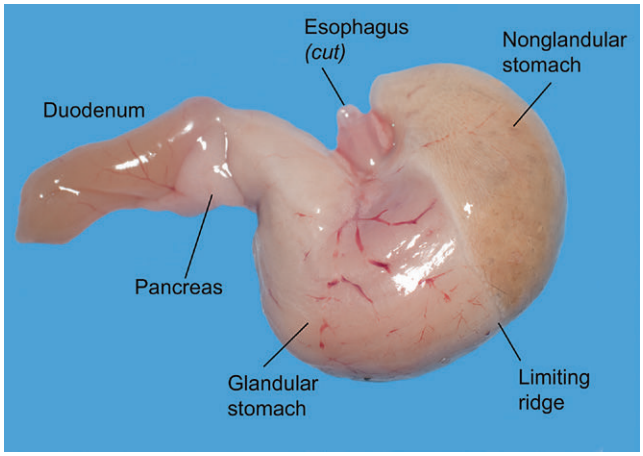

FIGURE 3.17 Closed stomach. The closed method traps the stomach contents and allows for distension.

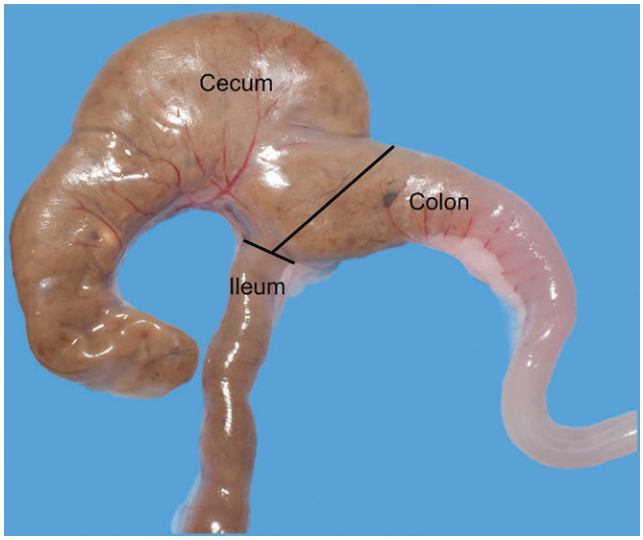

FIGURE 3.18 Ileocecalcolic junction. Dashed lines indicate approximate incision lines to separate the structures.

cranially to visualize the entire urogenital tract for both sexes.

Male The male tract consists of the paired testes with epididymis, seminal vesicles with attached coagulating glands, prostate, the bulbourethral glands, a single bladder, and penis. The testes may be located within the abdomen or scrotum because rodents have open inguinal canals. The prostate is divided into four distinct lobes in the mouse: anterior, dorsal, ventral, and lateral, and three distinct lobes in the rat: anterior, dorsolateral, and ventral (see Chapter 18: Male Reproductive System) (Fig. 3.19).

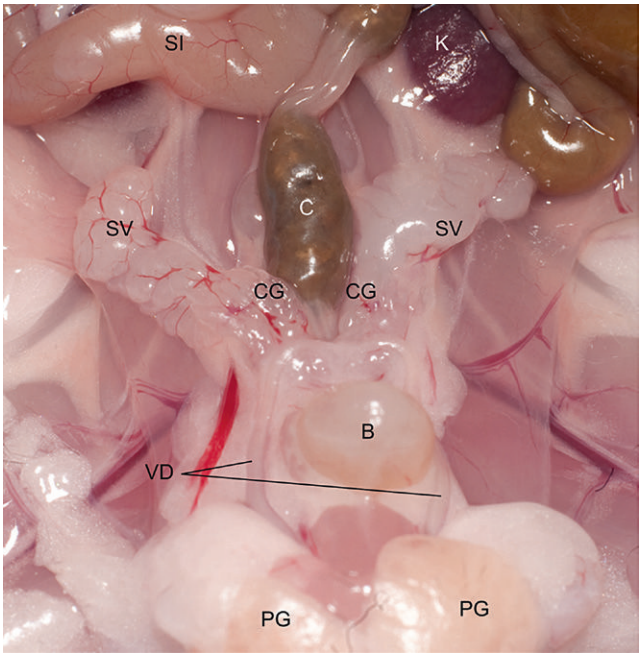

FIGURE 3.19 Male urogenital system (cranial aspect). The male reproductive tract in this figure (mouse) contains paired seminal vesicles (SV), coagulating glands (CG; also called the anterior prostate), vas deferens (VD), and preputial gland (PG). Small intestine (SI), kidney (K), colon, and bladder (B) are indicated.

Need-to-know

- The lobes of the rodent prostate encircle the urethra.
- The coagulating gland is also known as the anterior prostate.
- The coagulating gland is attached to the concave side of the seminal vesicle.

Pull both testes out of the scrotum and sever the vas deferens. Place both testes with attached epididymis into fixative. Alternatively, the reproductive tracts may be left in the carcass and fixed en bloc, which will be sectioned post fixation. Do not section unfixed testes because this will cause the seminiferous tubules to widely separate (Fig. 3.20).

Dissect the skin away from the penis and gently pull on the urethra and bladder to remove the entire lower urogenital tract (Fig. 3.21). The entire tract may be fixed flat on paper or an index card or placed directly into a cassette. See Further Reading and Relevant Websites and Chapter 18, Male Reproductive System, for details regarding specialized fixation and trimming.

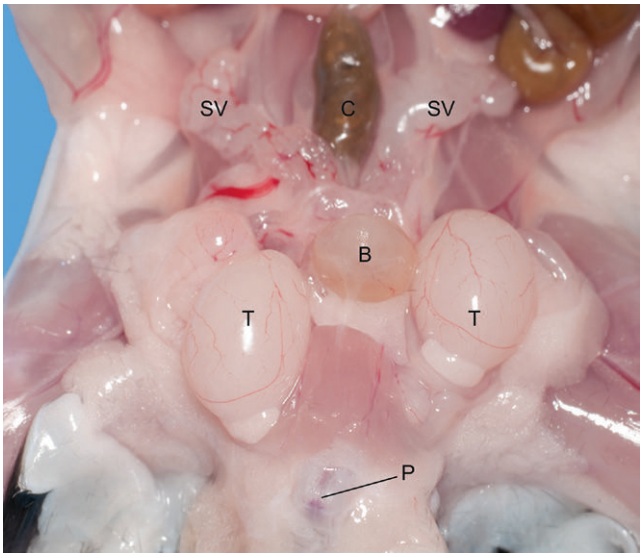

FIGURE 3.20 Male urogenital system (caudal aspect). The male rodent has open inguinal rings. The testicle (T) may be either in the scrotal sac or within the lower pelvic region. The testes should be fixed whole. Special fixatives such as Davidson's are preferred for detailed histologic examination of testes. The colon (C), bladder (B), seminal vesicles (SV), ventral prostate (VP), and penis (P; surrounded by fat) are indicated.

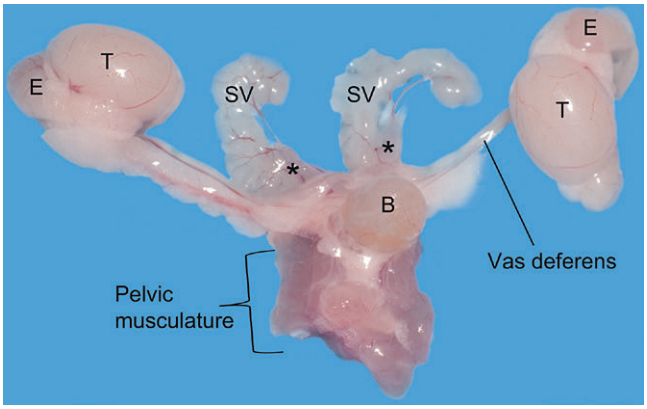

FIGURE 3.21 Dissected male urogenital tract. Once free, the entire tract should be placed flat on paper or in a cassette prior to fixation. Alternatively, the urogenital system may be left intact in the carcass and fixed en bloc. The epididymis (E), testicle (T), seminal vesicles (SV), coagulating gland (asterisks), and bladder are indicated.

Female The female tract consists of paired ovaries, single uterus, cervix, vagina, and bladder. The ovaries are located near the renal caudal poles and are often embedded in fat. The use of a dissecting scope or handheld magnifying glass may aid in ovary identification. The ovaries have a light orange coloration relative to adipose

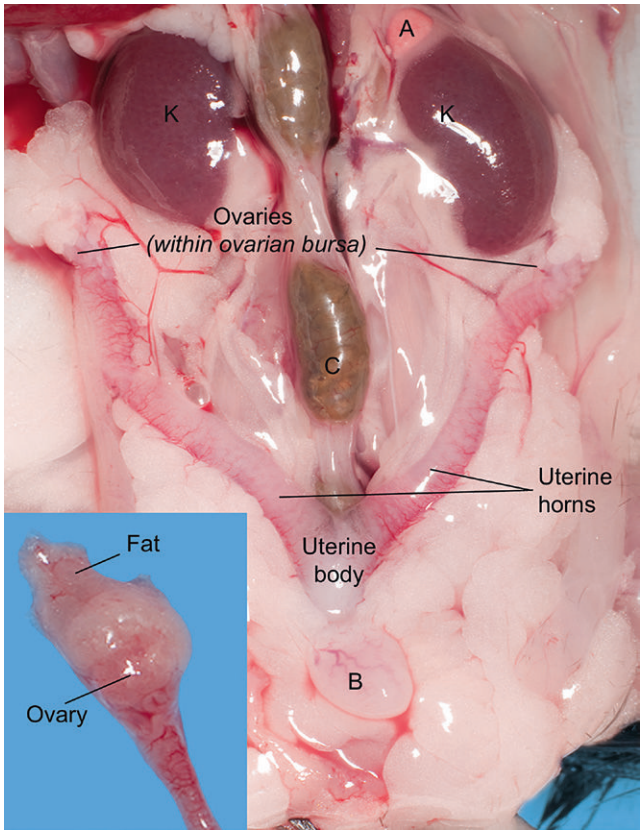

FIGURE 3.22 Female urogenital system. The female tract consists of paired ovaries, single uterus, and bladder (B). The ovaries are located near the caudal pole of the kidneys and are often embedded in fat. They have a light orange coloration relative to adipose tissue due to steroid hormone production (inset). The kidneys (K), adrenal (A), bladder (B), and colon (C) are indicated.

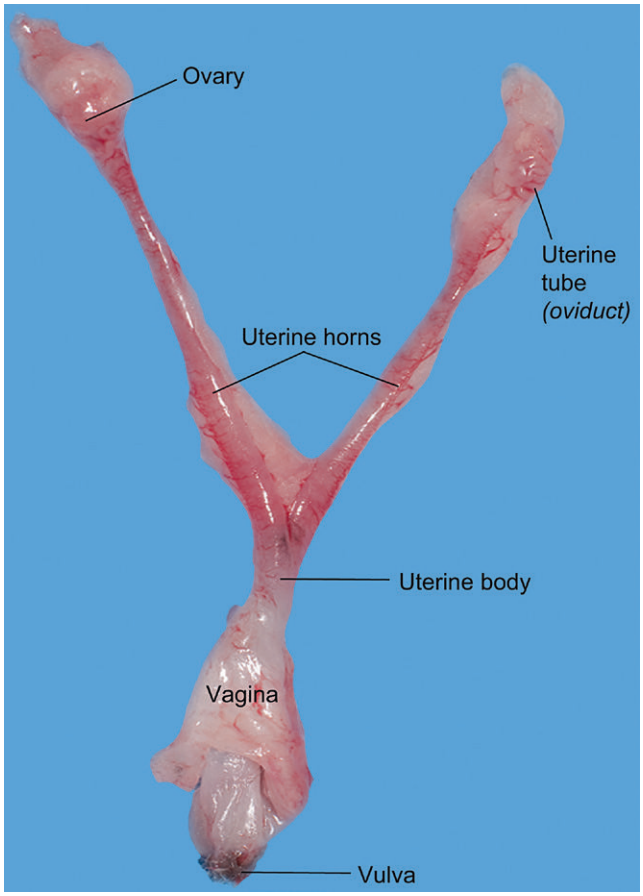

FIGURE 3.23 Dissected female urogenital tract. Once free, the entire tract should be placed flat on paper or in a cassette prior to fixation. Alternatively, the urogenital system may be left intact in the carcass and fixed en bloc.

tissue resulting from steroid hormone production (Fig. 3.22).

Dissect the skin between the vulva and anus, and carefully free the vagina. Grasp the external orifice of the vagina, and pull gently upward to bluntly dissect the surrounding connective tissue. Continue dissecting cranially/anteriorly along the broad ligament and mesovarium to free the uterine horns and ovaries. Once free, fix the entire tract flat on paper or in a cassette. Alternatively, the urogenital system may be left intact in the carcass and fixed en bloc prior to trimming (Fig. 3.23).

Kidneys and Adrenals

The kidneys will be readily visible once the abdominal contents are removed. The bilateral adrenal (suprarenal) glands are in close proximity to each cranial pole of the kidney. The right kidney is cranial to the left kidney (Fig. 3.24).

The kidneys and the attached adrenal glands may be removed from the retroperitoneal region with gentle dissection. The adrenal glands may be fixed attached to the kidneys or, preferably, fixed separately within a biopsy bag or mesh screen cassette to prevent loss (Fig. 3.25). Bisect the left kidney longitudinally and the right kidney transversely to distinguish right from left (Fig. 3.26).

Thoracic Cavity

To open the thoracic cavity, grasp the xiphoid process and lift and cut on either side of the

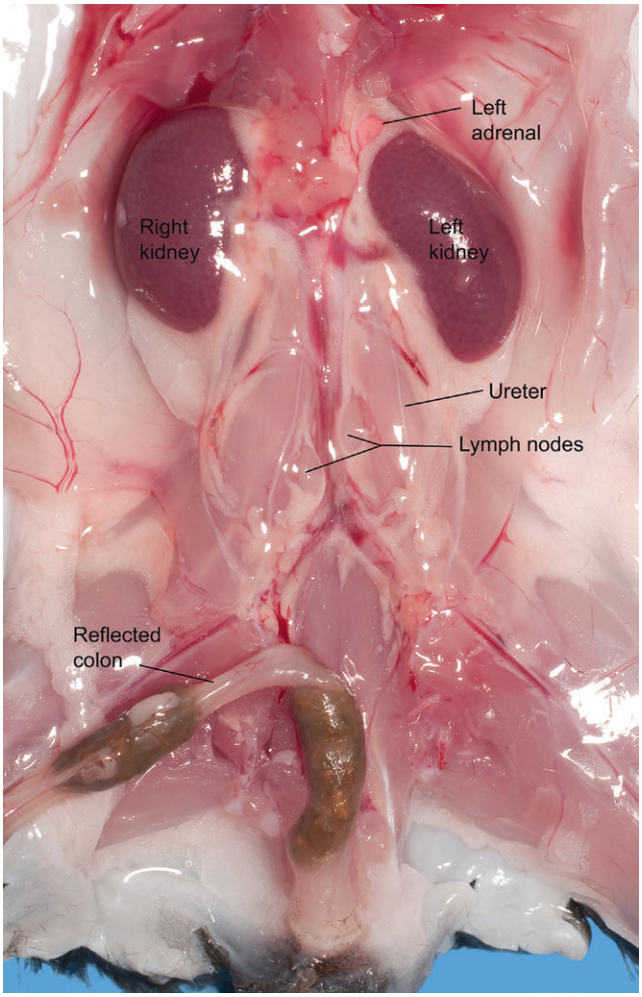

FIGURE 3.24 Abdomen with gastrointestinal and reproductive tracts removed to expose the urinary system. The kidneys are located in the upper abdomen. The adrenal glands are in close proximity to the cranial pole of the kidneys and may be obscured by fat as in this case for the right adrenal. The right kidney is positioned cranial to the left.

FIGURE 3.25 Left adrenal gland and kidney. The adrenals may be surrounded by fat and can be distinguished by the light orange coloration due to steroid hormone production.

Need-to-know

- The adrenal glands of female rodents are larger than those of males.

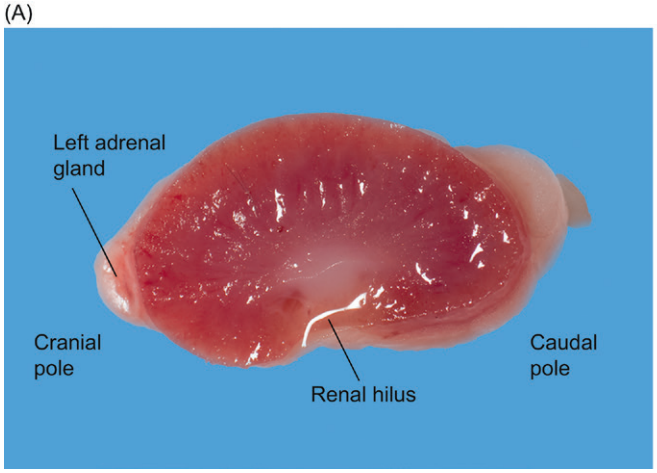

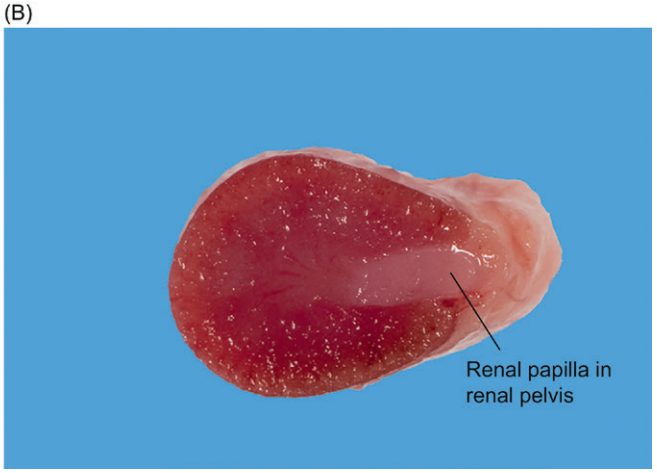

FIGURE 3.26 Kidney. (A) Longitudinal section of left kidney. (B) Transverse section of the right kidney with the caudal pole removed.

sternum at midrib level, extending the bilateral cuts toward the thoracic inlet. This allows removal of the ventral section of the rib cage and examination of thoracic cavity contents. Place the removed sternum into formalin (Fig. 3.27). The sternum may be submitted for bone marrow examination. Make two lateral cuts up each side of the rib cage to remove and allow clear examination of the heart and lungs.

Removal of the Thoracic Organs En Bloc

Split the mandibular symphysis with scissors, grasp the tongue with forceps, and retract gently to aid in bluntly dissecting the tongue, larynx, trachea, and esophagus. Continue retracting with blunt dissection to remove the heart, thymus, and lungs from the thorax. An alternative method is to leave the mandible and oral cavity contents intact, cutting the trachea, esophagus, and associated soft tissues at the level of the larynx/pharynx. The thyroid and parathyroid glands are located immediately caudal to the larynx on either side of the trachea (Fig. 3.28) and may be challenging to see without the aid of a dissecting scope (see Chapter 15: Endocrine System). Collect thyroid and parathyroid glands by cutting a 2-mm section of trachea immediately caudal to the larynx. The tongue and cranial esophagus should be placed into formalin if they were removed from the carcass.

Lungs

The lungs should be inflated with fixative to near physiologic volume prior to immersion fixation. If the lung is not inflated at the start of fixation, the alveolar spaces may collapse, inducing artifacts that may be overinterpreted as an interstitial pneumonia. In contrast, overinflation of the lung with fixative may expand and even rupture alveolar walls, creating an emphysematous appearance. For pulmonary studies in which these artifacts must be avoided, inflating the lungs to specific pressures is recommended (see Chapter 9: Respiratory System). For basic lung inflation, use a 3- to 5-mL syringe with a 25- to 27-gauge needle

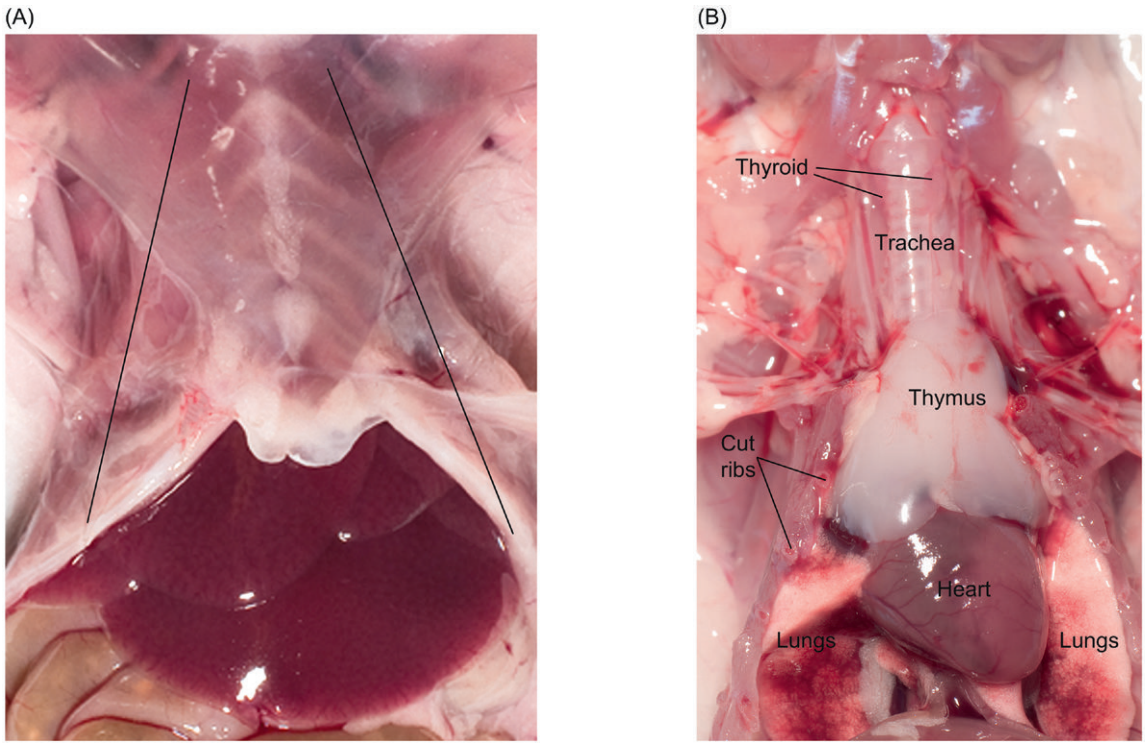

FIGURE 3.27 Thorax. (A) The lines indicate the approximate incision lines to aid in removal of the rib cage. (B) Once the ventral rib cage is removed, the thoracic contents will be exposed.

Need-to-know

- In young animals, the thymus is prominent.
- The red discoloration on the lungs is often a result of euthanasia.

in mice and a 5-mL (mice) or 10-mL (rat) syringe with an 18-gauge needle in rats. Gently thread the needle into the trachea and slowly expand the lung with formalin. Gently inflate the lungs until they appear fully expanded and would fill the chest. Often, bubbles of formalin mixed with pulmonary secretions are present after inflation. It is important not to overinflate or underinflate.

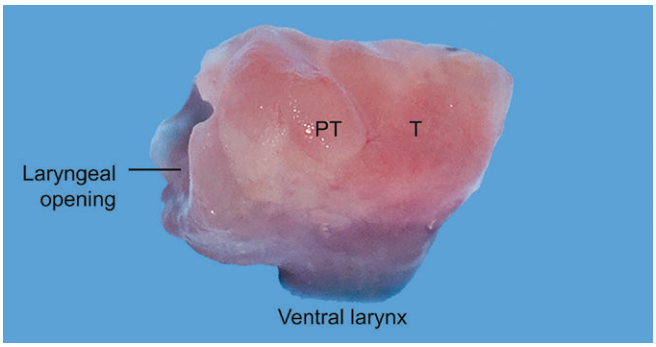

FIGURE 3.28 Laryngeal region. The thyroid (T) and parathyroid (PT) glands are located immediately caudal to the larynx on either side of the trachea and may be challenging to see without a dissecting scope.

Underinflated lungs appear flat and not as full; whereas overinflation is indicated by larger amounts of seeping fluid and foam from the trachea and lungs. Lung inflation may be done *in situ* before removal of the thoracic organs from the carcass (Fig. 3.29).

Heart and Thymus

Remove the heart and thymus from the lungs by transection at the base of the heart above the great vessels. The thymus should be dissected away from the heart (Fig. 3.30). If the internal structures of the heart need to be inspected, bisect from the base to the apex, incorporating the aorta and exposing chambers and valves (Fig. 3.30). For some studies, multiple cross sections of the heart or fixation of the unopened heart may be preferred.

Head

Remove pins and place the mouse or rat onto its ventral side. Remove the skin from the snout to

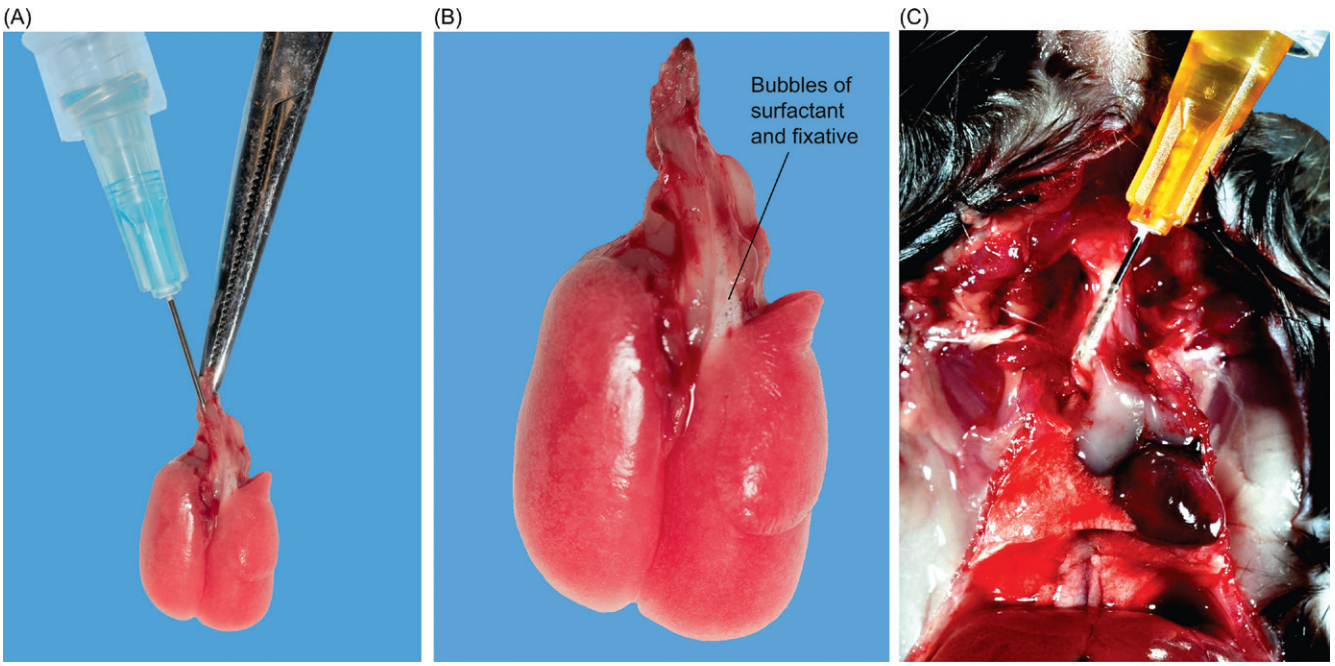

FIGURE 3.29 Inflation of mouse lungs with fixative. (A) After removal, rodent lungs should be infused with fixative to prevent the collapse of the alveoli, which may be misinterpreted as a lesion on histologic assessment. Overinflation may result in rupture of the alveolar walls, which must be distinguished from true emphysema. (B) Note that bubbles of fixative mixed with pulmonary secretions may be present after inflation. (C) Inflation may also be performed with the lungs *in situ*.

Need-to-know

- Lung underinflation leads to artifactual atelectasis.

the back of the head with blunt dissection and transection of the external ear canals and eyelids (Fig. 3.31). Flex the head and cut through the dorsal muscles of the neck at the level of the first cervical vertebrae through the cervical spine and ventral cervical muscles to free the head from the rest of the body (Fig. 3.32).

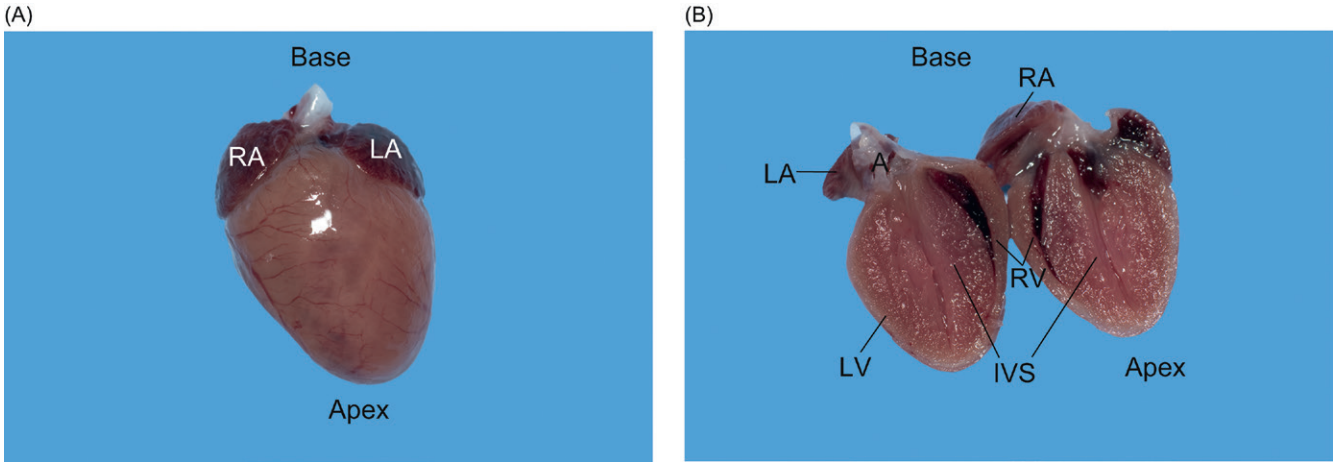

FIGURE 3.30 Heart. (A) The whole heart after removal of the thymus and lungs. (B) Longitudinally sectioned heart exposing chambers and valves. The heart may be placed whole into fixative or sectioned. Left ventricular (LV) and right ventricular (RV) walls, interventricular septum (IVS), left auricle (LA), right auricle (RA), and root of the aorta (A) are indicated.

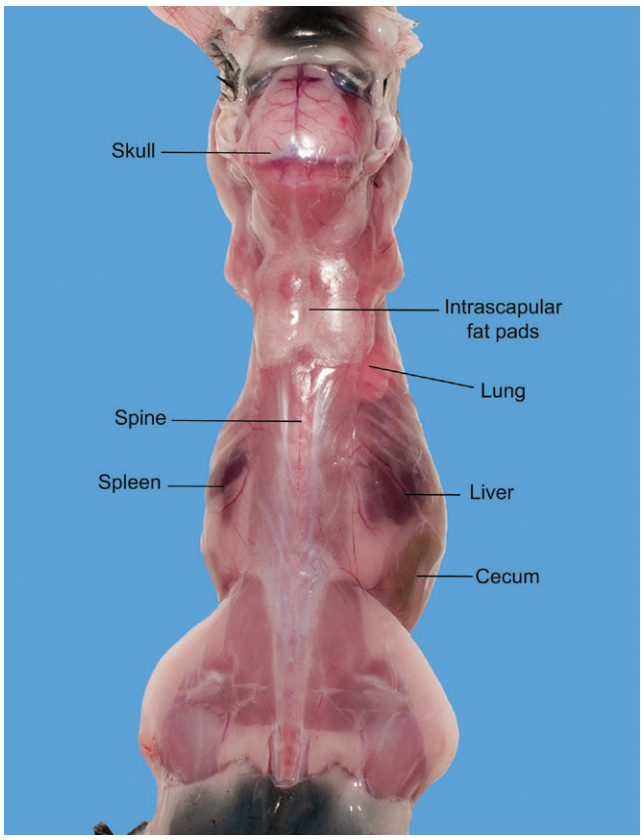

FIGURE 3.31 Dorsal aspect of the carcass post pelt removal. The intrascapular fat pads contain both brown and white adipose tissue.

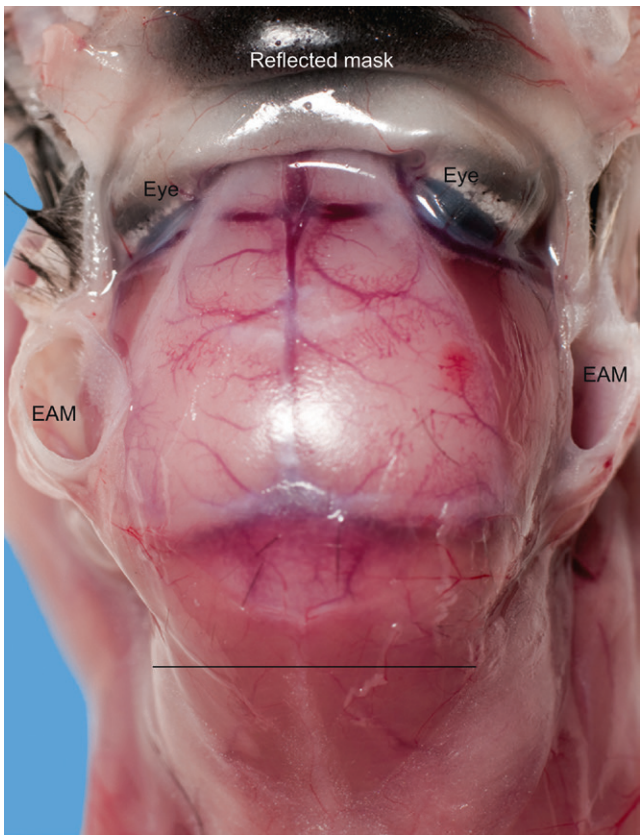

FIGURE 3.32 Removal of the head. The dorsal skull with reflected mask. The line indicates the transection site to expose the foramen magnum. The eyes and external acoustic meatus (EAM) are indicated.

This will expose the foramen magnum. The eyelids and periorbital skin may be left intact for histologic evaluation. Once the skin is removed, the discrete, exorbital lacrimal gland and Zymbal's glands are seen ventrolaterally near the base of the ear (see Chapter 22: Special Senses: Ear). The entire mouse head may be placed directly into fixative and then decalcified.

In the rat and alternatively in the mouse, the brain may be removed separately from the skull. Insert the tip of small scissors into the foramen magnum and cut the skull just above the opening to the ear and repeat on the other side (dashed line in Fig. 3.33). Extend both incisions toward the nose and cut across the frontal bones (Fig. 3.33). Lift and remove the top of the cranium exposing the brain (Fig. 3.33). Artifacts are common in nervous system tissue and are most frequently imparted by removal of the brain and fixation by immersion in 10% neutral buffered formalin. Leaving the exposed brain in the calvarium reduces the incidence of artifacts; however, maximal reduction of artifacts and optimal fixation may be achieved using vascular perfusion (see Chapter 20: Nervous System). The exposed brain can be gently removed from the skull by turning the head over (Fig. 3.34). Starting at either the olfactory lobes or the brain stem, bluntly dissect away the meninges and optic and cranial nerves to release the brain from the cranial vault. The brain may be placed in fixative for immersion fixation. The pituitary gland remains in the base of the skull (Fig. 3.34) for fixation, as removing the unfixed gland particularly in mice often results in tissue damage. To isolate the fixed pituitary gland, utilize pins to scrape around the sulcus to free it from its connections and then gently remove it. Alternatively, the pituitary may be evaluated *in situ* after decalcification. Place the base of the skull directly into fixative and then decalcify. Once decalcified, a transverse section at the level of the ethmoidal bullae will allow examination of the pituitary gland and Zymbal's glands. For whole head sections, once decalcified, it may be trimmed into five coronal sections that will contain most cranial structures (Figs. 3.35 and 3.36). Excellent detailed descriptions of how to prepare the nasal cavity of laboratory rodents have been described (see Chapter 6: Nose, Sinus, Pharynx, and Larynx).

Skeletal System

Skeletal tissues will need to be decalcified prior to routine processing and sectioning. Special techniques are discussed in Chapter 5, Skeletal System.

Bone Marrow

Bone marrow may be evaluated *in situ* on decalcified histology sections of the sternum, long bones, and/or skull. For techniques to collect bone marrow aspirates from the femur for cytology, see Further Reading and Relevant Websites.

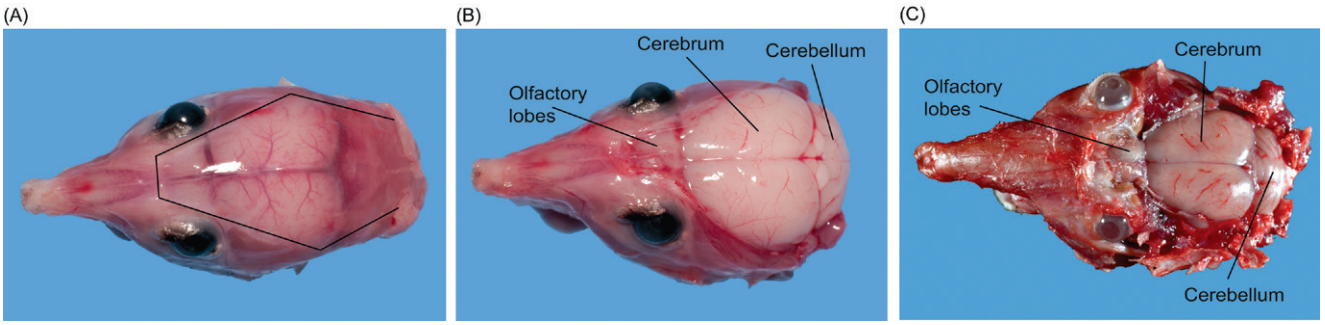

FIGURE 3.33 Head removed from the carcass. (A) Once the skin is removed, the entire head can be placed *en bloc* directly into fixative. Once fixed, the head may be placed into the decalcification (decal) solution. The dashed lines indicate the approximate placement of incisions into the skull to expose the brain. (B) The mouse brain exposed by removal of the calvarium. (C) The rat brain exposed by removal of the calvarium.

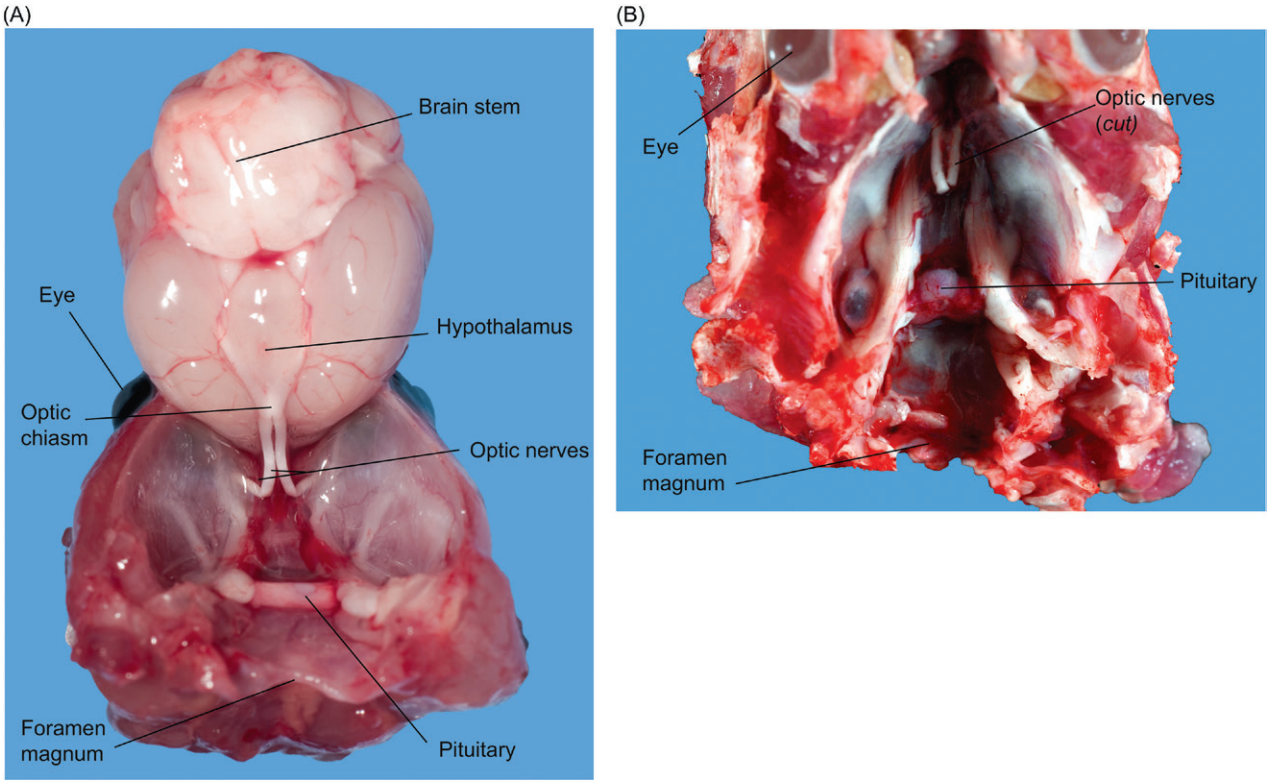

FIGURE 3.34 Ventral aspect of the brain and pituitary. (A)The mouse brain stem is reflected cranially to expose the optic chiasm, still-attached optic nerves, and hypothalamus. The brain should be handled gently and placed immediately into fixative. The pituitary is left in the base of the skull. (B) The rat brain has been removed. The pituitary is left in the base of the skull.

Vertebral Column and Spinal Cord

These may be kept intact with the carcass or dissected away. Remove the ribs and extra muscle and soft tissue. The spinal column may then be placed into decalcification fixative after removal or may be stretched out using tongue depressors and tied with gauze to aid in preventing contraction of the column while fixing.

NEXT STEPS

After the necropsy is completed, fixed tissue can be submitted to a histology laboratory for processing, embedding, and sectioning. Submission paperwork and protocols vary among histology laboratories. As discussed in the next section, rodent tissues require special processing and handling to obtain optimal histology. Prior to beginning the anatomical assessment, it is advisable to discuss the study's histology needs with the laboratory director to ensure the best quality outcome, especially for new projects.

HISTOLOGY

Histology, the study of the microscopic anatomy of cells and tissues, is similar in all three species. A glass slide containing a thin section of stained tissue is examined under a microscope. High-quality histologic sections are vital for the accurate diagnosis of disease, treatment of patients, and conduct of research. Obtaining these sections requires a series of steps: tissue processing, embedding, sectioning, and staining.

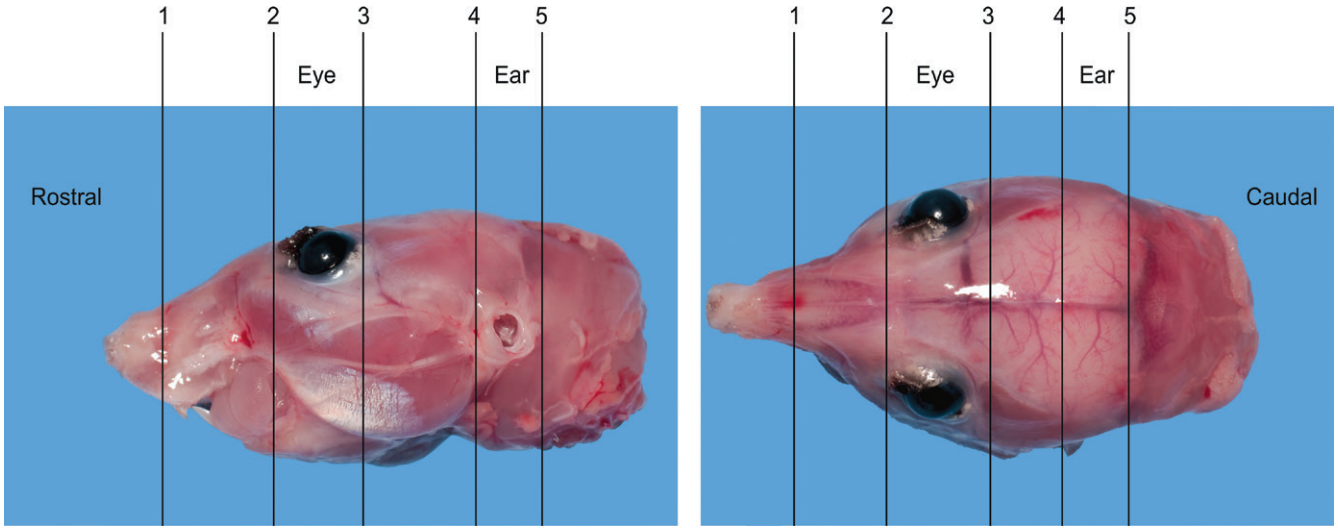

FIGURE 3.35 Sectioning guide for the decalcified whole head preparation. Coronal sections 1, 2, and 3 are placed caudal down into the cassette and sections 4 and 5 are placed rostral down into the cassette.

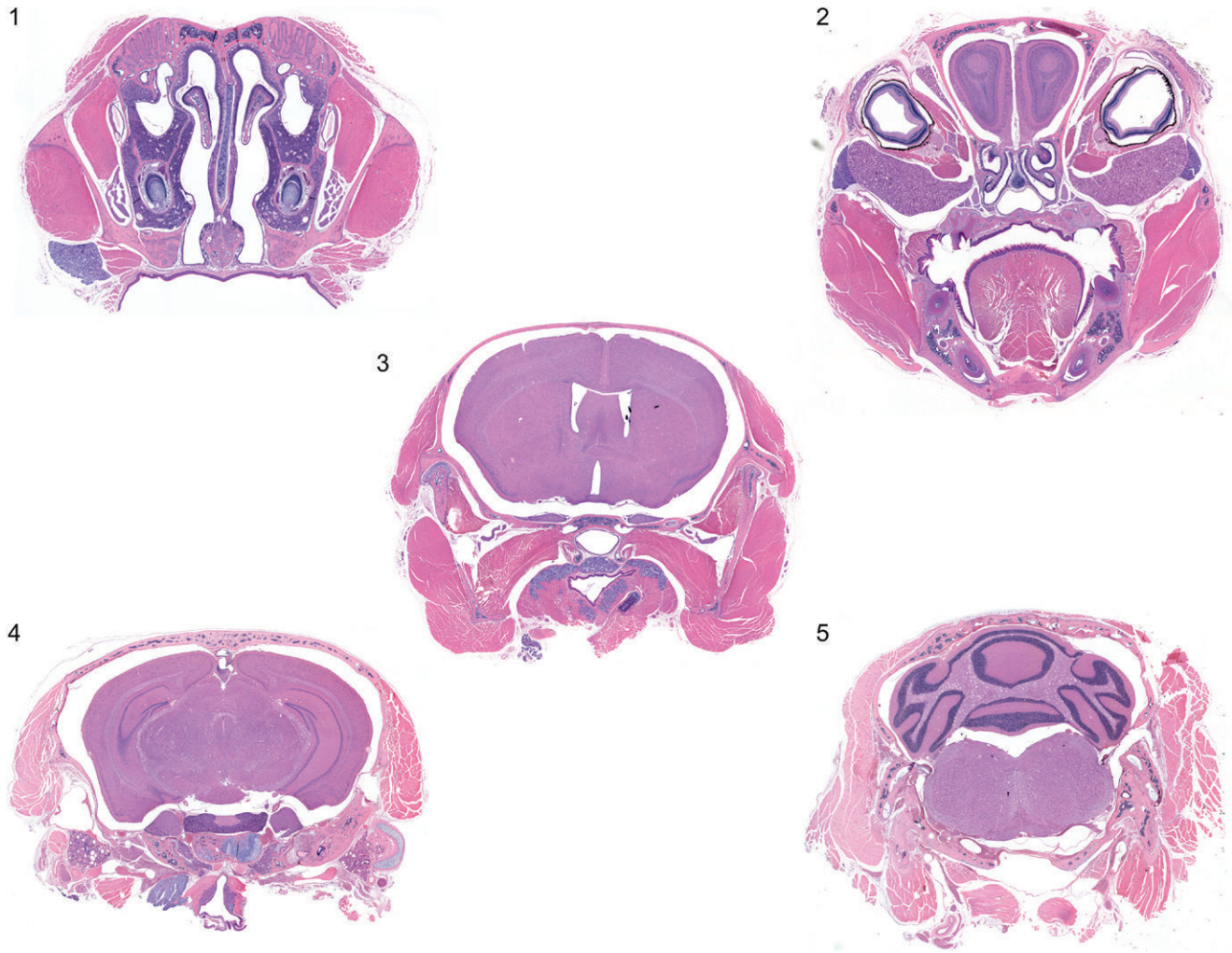

FIGURE 3.36 Example sections of a decalcified mouse head. Panel 1, nose; panel 2, eyes; panel 3, cerebrum; panel 4, ear/pituitary; panel 5, cerebellum. Other cranial structures may be visualized by selection of different regions of the decalcified head, serial, or step sections.

PROCESSING

Before fixed tissue can be processed, it may require additional trimming to fit properly into the cassette. Trimming human tissue is usually referred to as "grossing." Specimens should be cut to no larger than 2.5 × 2.0 × 0.4 cm (Fig. 3.37A). Care must be taken not to overfill the cassette (Fig. 3.37B) which can lead to one of several artifacts resulting from improper trimming (Table 3.2). Processing prepares the tissue for embedding in a rigid medium that provides support and allows thin sectioning. For most routine histology, paraffin wax is the preferred embedding medium because it is rigid enough to allow thin sectioning but flexible enough for most staining protocols. However, before fixed tissue can be embedded in paraffin, it must be processed to remove water, both from the tissue and from aqueous-based fixatives such as formalin.

There are several stages and many steps in tissue processing. It is usually performed on an automated processor that accurately controls processing time and temperature. Processing is usually described as consisting of three stages: dehydration, clearing, and infiltration with paraffin.

Dehydration

Dehydration removes fixative and water from samples. Tissue cassettes are soaked in alcohol, usually ethanol, in graded steps from 70% to 100%. It is important that tissue is completely fixed before it is placed in alcohol to avoid alcohol fixation artifacts (see Table 3.1).

Clearing

The clearing agent must be miscible with both the dehydrating and the infiltrating agents in order to remove one and be replaced by the other. Xylene is the most commonly used clearing agent, and the tissue cassette is soaked in xylene three or more times to completely remove the dehydrating agent. Once the dehydrating agent has been completely removed, clearing agents render the tissue translucent.

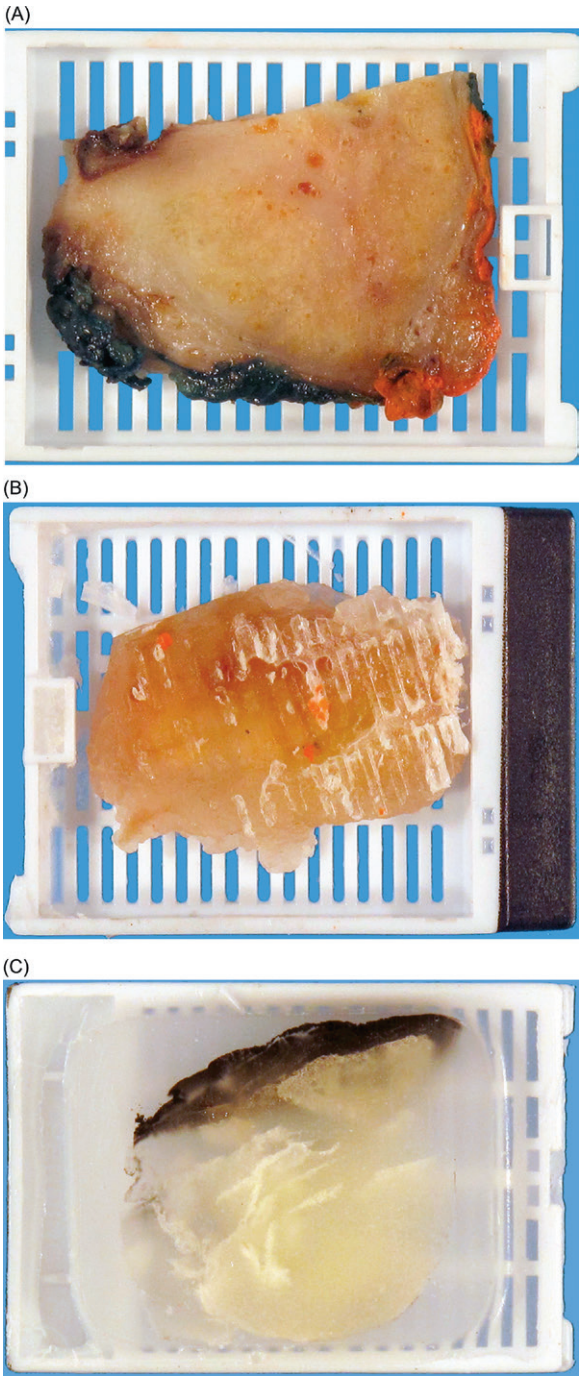

FIGURE 3.37 Tissue cassettes. (A) Appropriate tissue section size. Tissue slices should not exceed 2.5 × 2.0 × 0.4 cm in a standard tissue processing cassette. Note that appropriately sized tissue should not touch the sides or closed lid of the cassette. (B) Excessive tissue placed in cassette. When the cassette lid is closed on a section that is too thick, the tissue squeezes through the perforations in the cassette, causing this raised rib artifact. (C) Underprocessed tissue. Notice the white lines that appear in the wax when the tissue in not completely infiltrated with paraffin. When underprocessed tissue is cut on the microtome, a hole will be present in the ribbon in the vicinity of these white lines.

Need-to-know

- Tissue trim (grossing in) and processing, if done improperly, generates numerous artifacts.

TABLE 3.2 Artifacts From Improper Trimming or Grossing

Problem	Resulting Artifact
Tissue too thick	Tissues may not fix or process completely or may be imprinted with cassette gridlines
Tissue touches cassette sides	Sectioned tissue will not fit on glass slide
Sutures or staples present in tissue	Tears and holes during cutting
Brain or liver tissue placed in mesh bags or on sponges	Numerous holes formed in the tissue
Tissue fragment too small	Embedding and sectioning difficult. The tissue may become lost or destroyed during processing
Bone not properly decalcified	Very difficult to cut, and sections may shatter

TABLE 3.4 Human Tissue: Normal Processor Times for Each Solution

		Process Time[a]	
Stage	Solution	2 h	8 h
Dehydration	95% ethanol	1 min	20 min
Dehydration	95% ethanol	1 min	20 min
Dehydration	100% ethanol	1 min	20 min
Dehydration	100% ethanol	11 min	40 min
Dehydration	100% ethanol	30 min	60 min
Clearing	Xylene	1 min	30 min
Clearing	Xylene	11 min	30 min
Clearing	Xylene	25 min	60 min
Infiltration	Paraffin	3 min	40 min
Infiltration	Paraffin	5 min	40 min
Infiltration	Paraffin	15 min	60 min

[a]Determined by size and density of tissue.

TABLE 3.3 Rodent Tissue: Normal Processor Times for Each Solution

		Process Time[a]			
Stage	Solution	2 h	4 h	6 h	8 h
Dehydration	70% ethanol	10 min	20 min	30 min	40 min
Dehydration	95% ethanol	10 min	20 min	30 min	40 min
Dehydration	95% ethanol	10 min	20 min	30 min	40 min
Dehydration	100% ethanol	10 min	20 min	30 min	40 min
Dehydration	100% ethanol	10 min	20 min	30 min	40 min
Clearing	Xylene	10 min	20 min	30 min	40 min
Clearing	Xylene	10 min	20 min	30 min	40 min
Clearing	Xylene	10 min	20 min	30 min	40 min
Clearing	Xylene	10 min	20 min	30 min	40 min
Infiltration	Paraffin	10 min	20 min	30 min	40 min
Infiltration	Paraffin	10 min	20 min	30 min	40 min
Infiltration	Paraffin	10 min	20 min	30 min	40 min
Infiltration	Paraffin	10 min	20 min	30 min	40 min

[a]Determined by size and density of tissue.

Infiltration

The tissue then undergoes another fluid replacement; this time, the clearing solution is replaced with molten wax (infiltration). Paraffin wax is the most widely used reagent for infiltration and embedding, and it comes in many forms with a variety of melting temperatures and additives to produce quality sections. Some practitioners advocate the use of lower melting point wax to speed the infiltration step. The infiltrating reagent maintains cells and ultrastructural components in their functional orientation during sectioning.

Considerations for Processing

The timing of each step depends on the size and density of the tissue. Complete dehydration and clearing must be achieved in order for uniform infiltration of paraffin. If the tissue is incompletely infiltrated with paraffin (underprocessed), the tissue will shrink when placed in a paraffin mold and be difficult to section (Fig. 3.37C). In general, 2- or 3-mm biopsies are placed on a "2-h" process time, small tissue samples 4–6 mm on a "4-h" process time, and larger tissue samples may be on an "8-h" process time. Some laboratories may have specialized processes for certain tissue samples, such as brain and eye, or for large or fatty samples.

In general, rodent tissue contains less fat than human tissue. For this reason, rodent tissue may dehydrate and clear more quickly than human tissue. The inclination is to process rodent tissue for shorter times than human tissue of the same size (Tables 3.3 and 3.4). Use caution when

TABLE 3.5 Artifacts From Improper Processing

Problem	Resulting Artifact
Solutions not changed regularly	Tissue will not process and may be severely damaged
Tissue cassettes packed too closely in metal baskets	Solutions will not circulate freely around the tissue, and tissue may not process evenly

decreasing processing time because the risk of incomplete paraffin infiltration increases. It is often a better strategy to process tissue for longer times and compensate for the ensuing tissue dehydration by soaking the paraffin blocks in a water bath prior to sectioning.

Care must be taken to maintain fresh reagents on the tissue processor (Table 3.5). Alcohols will absorb water over time, leading to incomplete tissue dehydration. Caution is also required when using different formulations of clearing agents. Some clearing agents can damage antigens and impact the quality of special stains.

EMBEDDING

After infiltration by molten paraffin wax, tissue specimens are ready to be embedded into molds. Specimens unloaded from the processor are removed from their cassettes and placed into molds, into which molten paraffin is poured. During the embedding step, the tissue should be oriented in the mold to provide optimal sectioning (Fig. 3.38). Tissue can be oriented on edge, on end, or on face, depending on the tissue type. When tissue orientation is critical to histologic assessment, it is important to convey clear embedding directions for the desired orientation (Table 3.6).

SECTIONING

Once the tissue has been embedded, the paraffin block must be cut into thin sections of 4–5 µm using a microtome and each section placed on a glass slide. Additional soaking of the paraffin block in a water bath prior to sectioning may be required to rehydrate rodent tissue. Thin sections may optimize

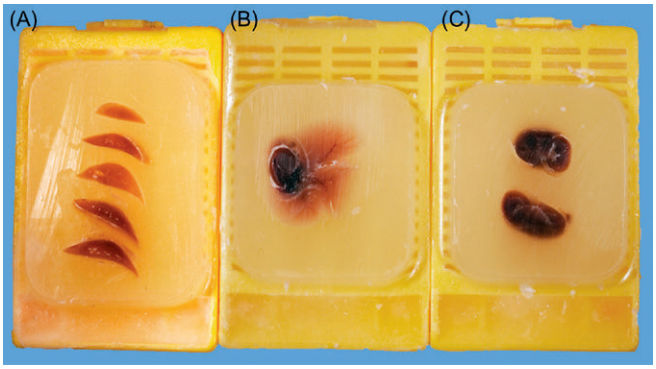

FIGURE 3.38 Proper embedding and orientation of tissue. Paraffin-embedded mouse liver (A), heart with lungs (B), and kidney (C). These blocks show appropriate spacing of tissue and correct orientation for optimal sectioning.

TABLE 3.6 Artifacts From Improper Embedding

Problem	Resulting Artifact
Tissue not oriented correctly	Important structures may be lost during sectioning
Tissue not embedded flat in the bottom of the mold	Complete tissue cross section may not be possible

TABLE 3.7 Commonly Used Histologic Stains

Stain	Target
Hematoxylin	Stains nucleus blue. Usually paired with eosin (H&E)
Eosin	Stains cytoplasm pink. Usually paired with hematoxylin (H&E)

fine morphologic detail. For example, kidney is often cut to 2 µm and bone marrow to 3 µm.

STAINING

Routine and Special Staining

Tissue stains allow for visualization and differentiation of cellular structures. H&E stain, a combined cytoplasmic and nuclear stain, is the most commonly used stain in histology (Table 3.7). Special stains identify specific cellular constituents, such as carbohydrates, lipids, connective tissue, and proteins, as well as microorganisms, pigments, and minerals in tissue and cells (Table 3.8). The general staining protocol is the same for rodent and human tissue. Protocols should be optimized for reagents, instrumentation, and requirements of the reviewing pathologist.

TABLE 3.8 Special Stains

Stain	Target
Pigments and Minerals	
Alizarin red S	Calcium
Bile–Hall's bilirubin stain	Bilirubin
Copper stain	Copper; commonly used to diagnosis Wilson's disease
Fontana–Masson silver method	Argentaffin granules (present in carcinoid tumors) and melanin
Prussian blue	Iron
Turnbull's blue (iron stain)	Ferrous iron in tissue
Sudan black B stain (for lipochrome)	Lipofuscins
Gomori's methenamine silver	Urate crystals
Von Kossa stain for calcium	Calcium
Carbohydrates	
Alcian blue	Acid mucopolysaccharides, acetic mucins
Alcian blue/periodic acid–Schiff (PAS) stain	Differentiates neutral and acetic mucosubstances
Colloidal iron	Mucopolysaccharides
Congo red	Amyloid
Mucicarmine stain	Mucin
PAS stain	Glycogen
Periodic acid–Schiff, digested stain with diastase (PAS-D)	Detects glycogen by digesting out sugars, followed by PAS staining
Thioflavin S stain	Amyloid deposits in tissue
Lipids	
Oil red O stain	Lipids in frozen sections
Sudan black B stain (for fat)	Lipids
Connective Tissue	
Verhoeff–Van Gieson stain	Elastin fibers
Weigert's resorcin–fuchsin	Elastin fibers
Fraser–Lendrum method	Fibrin
Jones' silver stain	Basement membrane of the glomerulus in kidney
Phosphotungstic acid–hematoxylin, Mallory's (PTAH stain)	Muscle cross-striations and fibrin
Reticulin stain	Reticular fibers
Trichrome stain, Masson's method	Differentiates between collagen and smooth muscle in tissue
Proteins and Nucleic Acids	
Methyl green pyronin (MGP) stain	Stains DNA green and RNA red
Microorganisms	
Ziehl–Neelsen stain	Acid-fast mycobacterium
Ziehl–Neelsen stain for Leprae and Nocardia	Acid-fast mycobacterium (sensitive for leprosy)
Fite's acid-fast stain	Acid-fast mycobacterium (sensitive for leprosy)
Auramine–rhodamine fluorescence	Acid-fast mycobacterium
Giemsa (modified May–Gruenwald) stain	*Helicobacter* (gram-negative spiral bacteria) in blood and lymph nodes
Giemsa	*Helicobacter* (gram-negative spiral bacteria) in tissue
Brown and Brenn	Gram-negative and gram-positive bacteria in tissue
Gridley's stain for amoeba	Eosin-stained ingested erythrocytes in amoeba
Grocott's, modified methenamine silver	Fungi
Orcein stain	Hepatitis B antigen that presents itself as cytoplasmic inclusion bodies in liver cells
Spirochete stain (Steiner and Steiner method; Warthen Starry)	Spirochetes
Nervous Tissue	
Bielschowsky technique (silver stain)	Neurofibrillary tangles and senile plaques in Alzheimer's disease
Bodian's method	Nerve fibers
Holzer's stain	Glial fibers
Hortega's stain	Pineal gland/tissue
Nissl stain	Nissl substance
Modified thioflavin S stain	Neurofibrillary tangles and senile plaques in Alzheimer's disease
Special Tissues and Cells	
Grimelius–Pascual's	Neuroendocrine carcinoma
Toluidine blue stain	Mast cells

FURTHER READING AND RELEVANT WEBSITES

Bahnemann R, Jacobs M, Karbe E, et al: RITA—Registry of Industrial Toxicology Animal-Data: guides for organ sampling and trimming procedures in rats. *Exp Toxicol Pathol* 47:247–266, 1995.

Bancroft JD, Gamble M: *Theory and practice of histological techniques*, Edinburgh, UK, 2002, Churchill Livingstone.

Cardiff RD: The mammary pathology of genetically engineered mice: the consensus report and recommendations from the Annapolis meeting. *Oncogene* 19:968–988, 2000.

Cardiff RD, Miller CH, Munn RJ: Limited mouse necropsy. *Cold Spring Harb Protoc* 2014, 2014.

Cardiff RD, Miller CH, Munn RJ: Mouse tissue fixation. *Cold Spring Harb Protoc* 2014, 2014.

Carson FL: *Histotechnology: a self-instructional text*, Chicago, IL, 2009, ASCP Press.

Charles Louis Davis Foundation for the Advancement of Veterinary and Comparative Pathology: *Syllabi from the pathology of genetically engineered rodents and aquatic species, an introduction to phenotyping*: http://www.cldavis.org/syllabi/archive/downloads.html?id=13.

Covelli V: *Guide to the necropsy of the mouse*: http://eulep.pdn.cam.ac.uk/Necropsy_of_the_Mouse/printable.php.

Davis BJ, Travlos G, McShane T: Reproductive endocrinology and toxicological pathology over the life span of the female rodent. *Toxicol Pathol* 29:77–83, 2001.

Feldman DB, Seely JC: *Necropsy guide: rodents and the rabbit*, Boca Raton, FL, 1988, CRC Press.

Fiette L, Slaoui M: Necropsy and sampling procedures in rodents. *Methods Mol Biol* 691:39–67, 2011.

Fox CH, Johnson FB, Whiting J, et al: Formaldehyde fixation. *J Histochem Cytochem* 33:845–853, 1985.

Fraunhofer: *Revised guides for organ sampling and trimming in rats and mice*: http://reni.item.fraunhofer.de/reni/trimming.

Hedrich H, Bullock G: *The laboratory mouse*, New York, NY, 2004, Elsevier.

Helander K: Kinetic studies of formaldehyde binding in tissue. *Biotech Histochem* 69:177–179, 1994.

Jones ML: How formalin affects the outcome of routine and special stains. *Biotech Histochem* 82:155–159, 2007.

Kittel B, Ruehl-Fehlert C, Morawietz G, et al: Revised guides for organ sampling and trimming in rats and mice—Part 2: A joint publication of the RITA and NACAD groups. *Exp Toxicol Pathol* 55:413–431, 2004.

Latendresse JR, Warbrittion AR, Jonassen H, et al: Fixation of testes and eyes using a modified Davidson's fluid: comparison with Bouin's fluid and conventional Davidson's fluid. *Toxicol Pathol* 30(4):524–533, 2002.

Lester SC: *Manual of surgical pathology*, Philadelphia, PA, 2006, Saunders.

Luna LG: *Histopathologic methods and color atlas of special stains and tissue artifacts*, Gaithersburg, MD, 1992, American Histolabs.

Maronpot RR, Boorman GA, Gaul BW, editors: *Pathology of the mouse*, St. Louis, MO, 1999, Cache River Press.

Morawietz G, Ruehl-Fehlert C, Kittel B, et al: Revised guides for organ sampling and trimming in rats and mice—Part 3: A joint publication of the RITA and NACAD groups. *Exp Toxicol Pathol* 55:433–449, 2004.

Olds R, Olds J, Joan R: *A color atlas of the rat: dissection guide*, New York, NY, 1979, Wiley.

Ovalle WK, Nahirney PC: *Netters essential histology*, Philadelphia, PA, 2008, Saunders.

Parkinson CM, O'Brien A, Albers TM, et al: Diagnostic necropsy and selected tissue and sample collection in rats and mice. *J Vis Exp* 54:2966, 2011.

Ruehl-Fehlert C, Kittel B, Morawietz G, et al: Revised guides for organ sampling and trimming in rats and mice: Part 1. *Exp Toxicol Pathol* 55:91–106, 2003.

Scudamore CL, Busk N, Vowell K: A simplified necropsy technique for mice: making the most of unscheduled deaths. *Lab Anim* 48:342–344, 2014.

Scudamore CL: *A practical guide to the histology of the mouse*, New Work, NY, 2013, John Wiley & Sons.

Shappell SB: Prostate pathology of genetically engineered mice: definitions and classification. The consensus report from the Bar Harbor meeting of the Mouse Models of Human Cancer Consortium Prostate Pathology Committee. *Cancer Res* 64:2270–2305, 2004.

Sheehan DC, Hrapchak BB: *Theory and practice of histotechnology*, Columbus, OH, 1987, Battelle Press.

Sundberg JP, Boggess D, editors: *Systemic approach to evaluation of mouse mutations*, Boca Raton, FL, 2000, CRC Press.

Suwa T, Nyska A, Haseman JK, et al: Spontaneous lesions in control B6C3F1 mice and recommended sectioning of male accessory sex organs. *Toxicol Pathol* 30:228–234, 2002.

The Mouse Brain Library: *Mouse brain atlases*: http://www.mbl.org/atlas/atlas.php.

Treuting PM, Snyder JM: Mouse necropsy. *Curr Protoc Mouse Biol* 5(3):223–233, 2015. http://dx.doi.org/10.1002/9780470942390.mo140296.

University of California at Davis: *Mouse virtual necropsy*: http://tvmouse.compmed.ucdavis.edu/virtualnecropsy.

Van den Broeck W, Derore A, Simoens P: Anatomy and nomenclature of murine lymph nodes: descriptive study and nomenclatory standardization in BALB/cAnNCrl mice. *J Immunol Methods* 312:12, 2006.

van der Loos CM: A focus on fixation. *Biotech Histochem* 82:141–154, 2007.

This page intentionally left blank

4 MICROSCOPY, IMMUNOHISTOCHEMISTRY, DIGITAL IMAGING, AND QUANTITATIVE MICROSCOPY

PAUL C. GOODWIN
GE Healthcare, Issaquah, WA, United States

BRIAN JOHNSON
University of Washington School of Medicine, Seattle, WA, United States

CHARLES W. FREVERT
University of Washington School of Medicine, Seattle, WA, United States

INTRODUCTION

Advances in microscopy including improvements in objectives, light sources, computational power, and digital cameras, with the ability to obtain images of regions of interest or whole slides, have led to the resurgence of the light microscope in biomedical research. Similarly, advances in immunohistochemistry (IHC), such as heat-induced epitope retrieval, have increased the use of this technique to obtain important information about specific molecules in tissues. Finally, advances in digital pathology and software programs that objectively analyze digital images have resulted in the increased use of quantitative microscopy—either stereology or image analysis—to efficiently obtain data from studies using histopathology or IHC. The goal of this chapter is to provide the fundamental information required to successfully use microscopy, IHC, digital imaging, and quantitative microscopy to obtain objective nonbiased data from histology sections.

Key Elements of Microscopy

For a microscope to allow visualization of detail, it must provide adequate levels of three key elements: magnification, resolution, and contrast.

MAGNIFICATION

Consider for a moment the process of looking at this page. The height and breadth of the scene that you see without moving your head or eyes is the field of view (FOV) of your eyes. We will call that a magnification of one times (1x). If you take a FOV that is smaller and project it onto your eyes, you will introduce magnification. This can be easily accomplished with a simple lens like a magnifying glass. If height and breadth are each magnified one-fifth of the original, then the magnification is five times (5x) and the total FOV is 1/25th (i.e., 1/5th × 1/5th) of the unaided FOV. If we

Comparative Anatomy and Histology. DOI: http://dx.doi.org/10.1016/B978-0-12-802900-8.00004-X
© 2018 Elsevier Inc. All rights reserved.

take a FOV that is larger than the unaided eye and project that onto the eyes, then the scene is demagnified, and the magnification is less than 1x. In a microscope, magnification is generated by a system of lenses constructed such that the distance from the lens to the detector (your eye for example) is different than the distance from the lens to your object. In the example above, a magnification of 5x is achieved by the distance from the lens to the eye being five times larger than the distance between the lens and the object. In general, magnification is easy and inexpensive to produce, but if it is not accompanied by resolution and contrast, it has little value, because detail is lost.

RESOLUTION

Resolution is the ability to distinguish objects. When two small objects are moved closer together while observing them in a microscope, at some point they will be indistinguishable as separate objects. The separation distance at which the individual objects are no longer seen is one definition of resolution. Regardless of how perfect an optical system, the resolution is limited by the wavelength of light and the numerical aperture.

Optical systems that achieve this theoretical limit of resolution are said to be diffraction limited. Some examples of the theoretical lateral (i.e., in the plane of focus) for common lenses are given in Table 4.1.

TABLE 4.1 Influence of Numerical Aperture (N.A.) and Wavelength on Resolution

Magnification	N.A.	Wavelength (nm)	Resolution (µm)
1x (human eye)	0.16	540	1.72
2x	0.10	540	2.70
4x	0.20	540	1.35
10x	0.45	540	0.60
20x	0.75	540	0.36
40x	0.95	540	0.28
60x	0.95	540	0.28
60x	0.95	460	0.24

CONTRAST

Contrast is the ability to detect objects from background or other features/objects. There are two forms of contrast: the detection of a specific signal in the presence of random noise (signal to noise (SNR) ratio) and the ability to detect a specific signal in the presence of background (signal to background (SBR) ratio). Random noise adds uncertainty to measurements. Some sources of noise are statistical and unavoidable. Only increasing the number of photons by increasing the signal intensity can decrease the relative contribution of noise to the total signal. Other sources of noise can be reduced. Some of these are a function of the quality of the detector (camera, photomultiplier tube, etc.) and the illumination source and can be minimized by deploying higher quality components.

The signal detected at each point in the image is the product of the actual number of events and the noise sources. In comparison, background is additive. Background is an offset in the number of events. Background can be caused by microscope or by the sample preparation. Sample preparation–induced background will be considered in the section on IHC. Microscope-induced background is most often caused by stray light in the microscope. For example, when using an inverted microscope (objective lens pointing up) any light in the room can be picked up by the objective lens and become detected. Microscope ports, faulty filters and shutters, and other poor mechanical designs or optical defects can increase background.

Fig. 4.1 illustrates these principles with different images of a section of rat pancreas to highlight positive immunostaining for insulin in beta cells of the islet. In the first column, we see the effects of magnification. Panel B (1x) is the native image, captured at 20x magnified. Doubling magnification to 40x (2x) yields the image in panel C. Panel A is the islet captured at 10x (0.5x). Notice in panel C that increasing the magnification without increasing the resolution makes the image blurry, that is, the additional

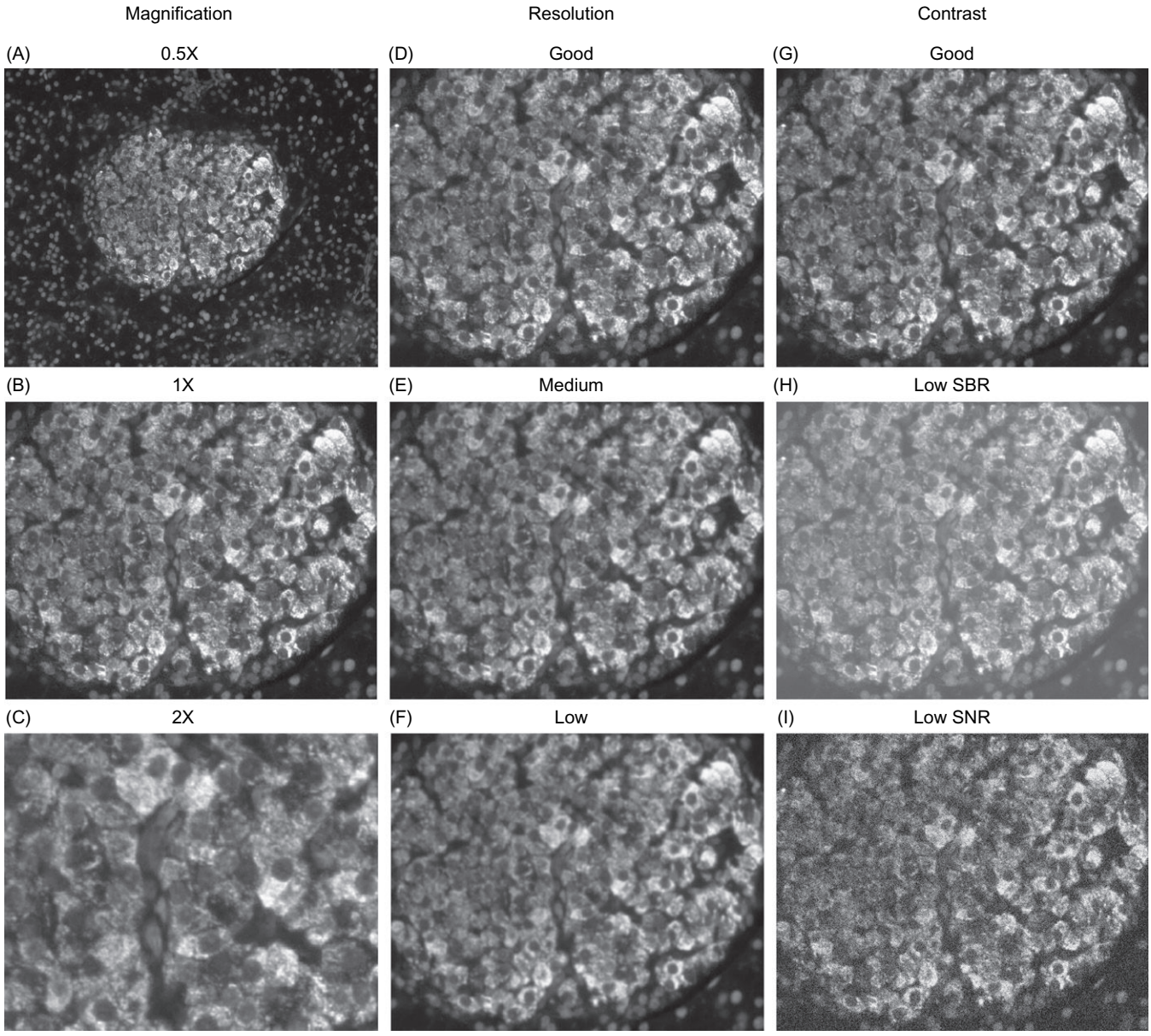

FIGURE 4.1 Microscope functions. To provide a high-quality image, microscopes must accomplish three functions: magnification, resolution, and contrast. (A–C) The left hand column demonstrates the effects of magnification while holding contrast and resolution constant. (B) In the middle panel we see the "native" magnification of the image (1x). (A) If the area projected onto the detector (in the image) is increased, the image is demagnified (0.5x). (C) If the area projected onto the detector (in the image) is decreased, we magnify the image (2x). (D–F) In the middle column we see the effects of resolution while holding magnification and contrast constant. (D) The top panel demonstrates the native resolution of the optical system. (E) A loss of resolution (middle panel) causes less certainty as to the actual shape and borders of features in the image. (F) As we further decrease resolution (bottom panel) these shapes and features become more difficult to delineate. (G–I) The right hand column shows the effects of loss of contrast while maintaining magnification and resolution. (G) The top panel shows the native contrast in the image. (H) Contrast is then degraded by a loss of SBR ratio in the middle panel or (I) degradation of the SNR ratio in the bottom panel.

Need-to-know

- Magnification, resolution, and contrast are the three functions of microscopes that are responsible for the quality of the final image.

magnification is "empty" and contains no new information. In panel D we see the same section at the native resolution for 20x objective (roughly 0.4 μm). In panel E we have the same section at one half of the native resolution (0.8 μm) and in panel F we see it again at one quarter of the native resolution (1.6 μm). In panel G we see the same image at full contrast. In panel H we have

added 25% of the maximum signal as background and in panel I we have added 25% Gaussian noise to the image. Notice in panels H and I that decreasing the SBR or SNR produces an apparent loss of resolution. Panels H and I have the same resolution as panel G, but that resolution cannot be realized due to the lack of contrast.

Key Elements of IHC

BACKGROUND

Histochemical stains and IHC provide spatial information about cells and structures in tissues. Histochemical stains (see Chapter 3: Necropsy and Histology, for details) are able to identify specific molecules (e.g., hematoxylin binding to DNA) or structures in tissues; however, they do not provide the molecular specificity of IHC. The specificity of IHC was first realized in 1942 when fluorescently-labeled antibodies were used to detect pneumococcal antigen in tissues.

Antibodies are able to identify specific molecules, cells, and structures through the binding of the antigen binding site, also called the paratope, to an antigen (i.e., epitope) in tissue. The specificity of this interaction allows a number of scientific applications including IHC, western blots, flow cytometry, and enzyme-linked immunosorbent assay (ELISA). As biological reagents, antibodies have considerable variability in binding affinity and specificity, which can even be evident in lot-to-lot differences. The four key elements of IHC are tissue processing, validation of antibody specificity, optimization of the IHC protocol, and the use of antibody and tissue controls (Fig. 4.2).

TISSUE PROCESSING

Tissue processing includes fixation to stabilize the tissue, dehydration, and then infiltration of the tissue with molten paraffin (≅60°C). Processing produces artifacts, such as the destruction of the epitope for the primary antibody used in an IHC protocol. Considerations for proper tissue collection, fixation, and processing are described in detail in Chapter 3, Necropsy and Histology. Investigators need to carefully consider the requirements for proper tissue collection, fixation, processing, and storage of tissues samples when performing IHC.

VALIDATION OF ANTIBODY SPECIFICITY

The specificity of the acquired immune system has allowed for the production of antibodies to a vast number of antigens, including (but not limited to) proteins, peptides, lipids, amines, sugars, amino acids, drugs, phosphorylated proteins, and the inactive and active forms of proteases. Unfortunately, researchers often obtain an untested antibody to use for IHC without validating its specificity under conditions specific for IHC, such as the detection of antigens in formalin fixed paraffin embedded (FFPE) tissues. When an antibody is not tested prior to use or when appropriate controls are not performed, the staining dictated by the binding of the primary antibody in tissue may not represent the actual location of the target epitope. To minimize the development of erroneous data, which can lead to incorrect conclusions and wasted effort, investigators need to validate antibodies used for IHC. Antibody validation for IHC should include the following: (1) validation of antibody specificity through biochemical analysis; (2) optimization of the IHC protocol; and (3) the use of proper antibody and tissue controls. A suggested list of manuscripts to provide further detail on each of these subjects can be found at the end of this chapter.

When evaluating a new antibody for IHC, it is important to validate the specificity of the antibody (Fig. 4.2). The most common biochemical analysis used for the initial evaluation of antibody specificity is the western blot. It is not uncommon to see western blot analysis of an antibody performed using the recombinant proteins or the

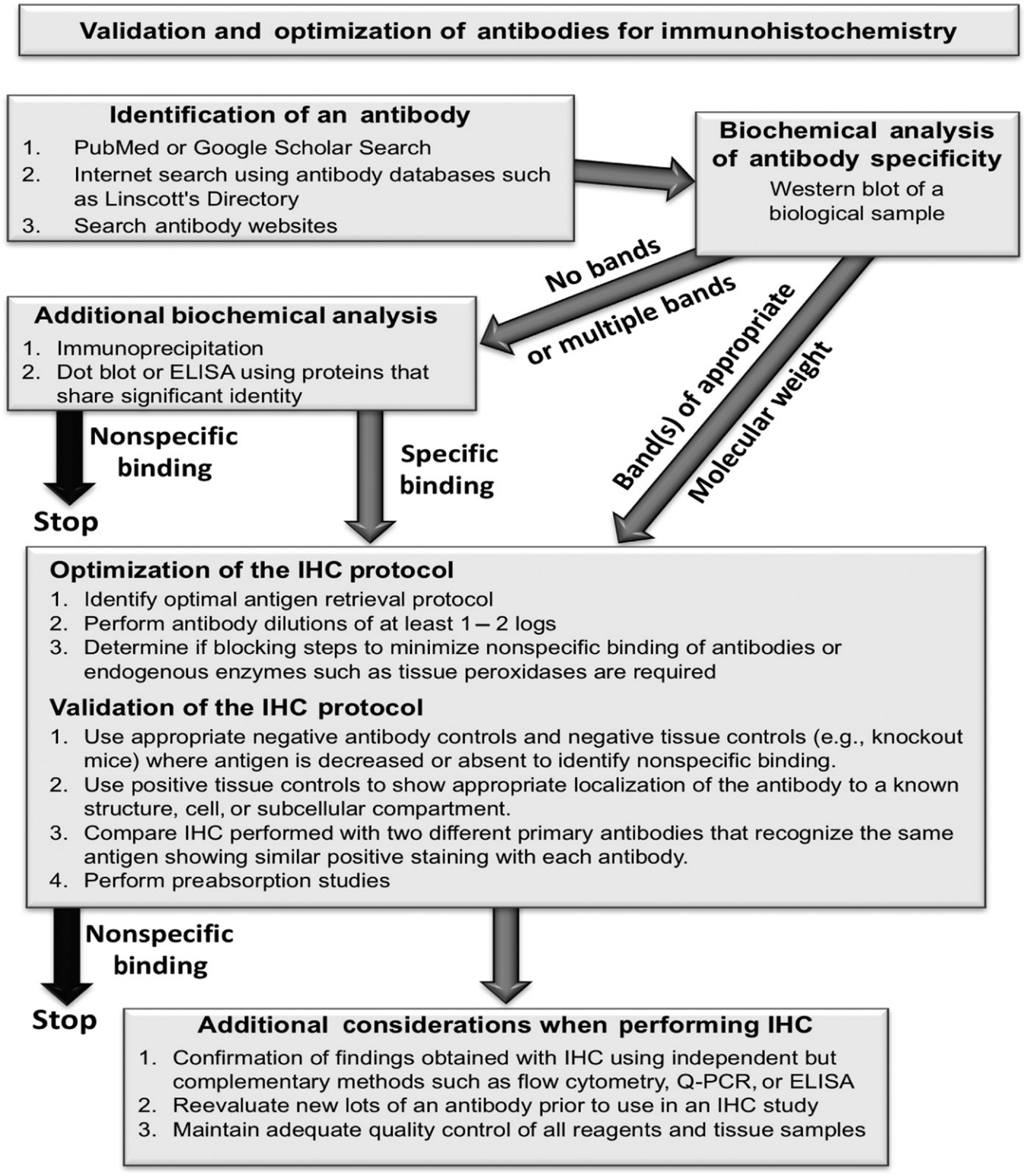

FIGURE 4.2 Guidelines for the validation and optimization of antibodies for IHC.

Need-to-know

- Validation of the primary antibody and optimization of an IHC protocol are critical steps to ensure that an antibody is binding specifically to its epitope.

peptide used to develop an antibody. Binding of an antibody to the antigen used for immunization does not ensure that the antibody specifically binds to its epitope in tissue. An appropriate sample to use to evaluate antibody specificity would be homogenates of the tissue(s) of interest or at minimum a cell lysate from a cell known to express the antigen being evaluated.

The desired outcome of a western blot using a tissue homogenate would be a single band at the expected molecular weight of the antigen. This is not always the case, and on occasion the western blot has either no bands or multiple bands. When this happens, it is important to consider the potential cause of these results. If protein bands are absent on a western blot, it may be due to the reducing conditions used for a western blot that alter a conformational epitope (i.e., 3D structure). Multiple bands on a western blot could be the result of specific and/or nonspecific binding of the antibody. Specific binding of an antibody to its epitope could result in multiple bands on a western blot if multimerization of the target protein or peptide occurs or because of degradation of the target antigen. If linearization of a conformational epitope results in a false negative or if multiple bands are observed on the western blot, then an alternate analysis may need to be considered. Examples include immunoprecipitation, dot blots, and ELISA. Following the biochemical analysis of antibody specificity, the next step is to optimize the antibody protocol.

PROTOCOL OPTIMIZATION

When using an antibody for the first time—even if others have used and published the antibody for IHC—it is important to optimize the IHC protocol yourself in order to identify conditions that enhance the ability of an antibody to detect its epitope in tissue and at the same time minimize nonspecific binding. This involves consideration of antigen retrieval and minimizing nonspecific interactions.

Antigen Retrieval

Antigen retrieval is used to enhance the ability of a primary antibody to bind a specific epitope in FFPE tissue. There are a number of methods used for achieving successful antigen retrieval in FFPE tissue. Proteinase digestion either at ambient "room temperature" or 37°C was commonly used until the development of heat-induced epitope retrieval (HIER), which is probably the single most significant advance in IHC in the last 70 years. While the mechanism is unknown, it is believed that HIER breaks aldehyde induced protein and enzyme crosslinks, as well as possibly returning proteins to their original 3D structure. The development of HIER has greatly increased the number of antibodies capable of detecting their epitope in FFPE, which has expanded the use of IHC in experimental and clinical pathology. Rigorous techniques to validate primary antibody specificity must be employed as antigen retrieval may lead to nonspecific or "off target" binding of the primary antibody to an unintended tissue antigen (Fig. 4.3A). It is recommended that IHC laboratories develop standardized methods when evaluating antigen retrieval for the development of a new IHC protocol. An example of the conditions evaluated when working up a new antibody in the Histology and Imaging Core at the University of Washington is provided in Table 4.2. If an optimal condition is not identified with this initial workup, then other conditions such as proteinase digestion or other HIER techniques are evaluated.

Minimizing Nonspecific Interactions

To minimize nonspecific binding due to ionic or hydrophobic interactions, IHC protocols require thorough washing of tissue sections at all steps of the protocol. On occasion, protein blocks using serum, antibodies, or casein are required to minimize nonspecific binding. The use of serum or antibodies will not only diminish ionic and/or hydrophobic interactions of the primary antibody in tissue, they will also decrease the binding of

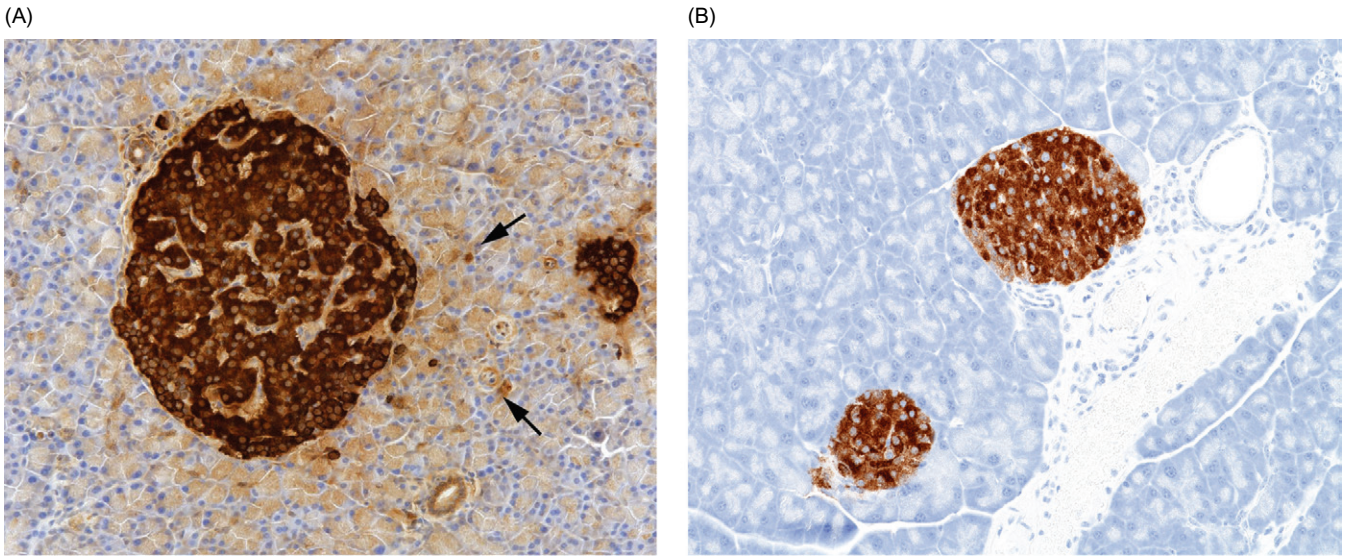

FIGURE 4.3 Immunohistochemical staining of insulin within β-cells in pancreatic islets. The goal of IHC is to develop a protocol where the primary antibody binds specifically to its epitope in tissue. (A) Antigen retrieval with citrate buffer results in nonspecific staining (arrows) of the anti-insulin antibody in the exocrine tissue of this mouse pancreas. (B) When antigen retrieval was not performed, positive immunostaining for insulin using the same antiinsulin antibody as in (A) is localized specifically to β-cells in islets. Brown = immunostaining for insulin and blue = hematoxylin.

Need-to-know

- Antigen retrieval, especially heat-induced epitope retrieval (HIER), on formalin-fixed paraffin-embedded tissues has increased the number of antibodies available.
- During optimization of an IHC protocol, it is important to ensure that antigen retrieval does not increase nonspecific binding of the antibody in a tissue.

TABLE 4.2 Protocol for Initial Evaluation of Antigen Retrieval

Antigen Retrieval Method	pH	Time	Temperature
No antigen retrieval	Not applicable	Not applicable	Room temperature
Citrate buffer	pH 6	10 minutes	100°C
Citrate buffer	pH 6	20 minutes	100°C
EDTA buffer	pH 9	10 minutes	100°C
EDTA buffer	pH 9	20 minutes	100°C

antibodies to cells through native Fc receptors. Antibodies in the protein block should be from the same species from which the secondary antibody is obtained. This will ensure that the secondary antibody does not bind to the antibodies used for this blocking step. On occasion, IHC protocols are developed that require the use of a mouse primary antibody on mouse tissue. To minimize the binding of the secondary antibody to endogenous antibodies in mouse tissue, a number of companies have developed mouse-on-mouse blocking kits that are commercially available.

Endogenous peroxidases and alkaline phosphatases in tissue can result in nonspecific staining when performing IHC using chromogenic stains. When using IHC protocols where peroxidase or alkaline phosphatase are part of the detection system, an important consideration is the addition of a blocking step with hydrogen peroxide to quench the effect of endogenous peroxidases or with levamisole to block the effect of endogenous alkaline phosphatases.

Performing a proper dilution series, typically over one to two logs of antibody concentrations, is a critical step in IHC protocol optimization. The goal of performing an antibody dilution series is to find the concentration of antibody where the high affinity binding of an antibody to its epitope in tissue is maintained but lower affinity nonspecific

ionic and hydrophobic interactions do not occur. Due to the lot-to-lot variability observed with antibodies, it is also recommended that a dilution series be performed when a new lot of a previously validated antibody is obtained.

ANTIBODY CONTROLS

IHC is no different than any other biological assay in that appropriate negative and positive controls need to be included as part of each experiment, in this case to ensure that the primary antibody is specifically binding its epitope in tissue and to account for the day-to-day variability inherent to biological assays.

Negative Controls

Replacement of the primary antibody with another antibody is the simplest test of antibody specificity when performing IHC. Negative control antibodies maintain many of the nonspecific binding characteristics of primary antibodies, but do not detect the epitope of interest. They also identify nonspecific staining caused by tissue enzymes such as endogenous peroxidases when performing chromogenic IHC or tissue autofluorescence when using fluorescent detections systems. For polyclonal antibodies, the negative control antibody should be preimmune serum or commercial sera from the same species used to raise the primary antibody. For monoclonal antibodies, a control antibody of the same species, isotype and concentration needs to be used. All too often investigators replace the primary antibody with phosphate buffered saline (PBS) as the negative control, which does not control for nonspecific binding of the primary antibody in tissues. PBS in place of the primary antibody should only be used to identify nonspecific binding of the secondary antibody in tissue.

Positive Controls

This antibody control is not for use on a daily basis when performing IHC, but rather as a way to evaluate the specificity of antibodies. The positive antibody control uses the comparison of two different antibodies raised against the same antigen as a way to evaluate the immunostaining of each antibody in sequential or adjacent tissue sections. This type of comparison works best if the two antibodies recognize completely different epitopes on the same antigen. By performing IHC with two different antibodies in consecutive tissue sections, one would expect to have identical staining in both sections. If the two antibodies are made in different species, the ability to colocalize them on the same tissue section is an even stronger way to evaluate the specificity of antibodies for IHC. If the positive staining of the two antibodies overlap, this provides additional evidence that the antibodies are binding the same antigen in tissue and that this binding is specific.

Absorption Controls

Preabsorption of an antibody with an excess of antigen is commonly used to validate the specificity of an antibody by blocking the binding of the antibody to its antigen in tissue. The limitation of the absorption control is that reabsorbing the antigen binding site with the peptide used to generate the antibody will be high affinity, which will prevent it from binding to lower affinity binding sites in tissue that cause nonspecific interactions. Absorption controls are most useful in identifying the nonspecific binding of monoclonal and polyclonal antibodies through the binding of antibodies to Fc receptors, ionic and hydrophobic interactions, or the binding of naturally occurring antibodies in a polyclonal antibody to tissue. Finally, absorption controls can cause a false positive if the antigen used for the preabsorption of the antibody binds to tissue, resulting in antigen–antibody complexes binding in tissue. Due to these concerns, absorption controls are best used in conjunction with other methods to validate the specificity of an antibody for IHC.

TISSUE CONTROLS

Negative Controls

The use of FFPE cell pellets or tissues known to lack expression of an antigen can be used as

negative tissue controls when working up and optimizing a new antibody. It is easiest to obtain cell lines that naturally lack the antigen, but, if necessary, cells can be transfected in culture with siRNA to make a cell line deficient in the target antigen. When using cell pellets as a negative or positive tissue control, cell pellets should be fixed and processed into paraffin to allow antibodies to be evaluated under conditions similar to those of the tissue being studied.

Knowing the location of your antigen in tissue or in a cell (e.g., cell surface, cytoplasmic, or nuclear) will assist in assessing the specificity of an antibody. For example, in the pancreas the only cells producing insulin are β-cells in the islets (Fig. 4.3B). Positive immunostaining for insulin in the exocrine pancreas would suggest nonspecific staining of an antiinsulin antibody (Fig. 4.3A). Use of genetically engineered mice lacking the epitope of interest as a test of antibody specificity and as negative control tissue is increasing. Unfortunately, knockout mice are not always available, and this negative tissue control is not applicable to human or other nonmurine tissues.

Positive Controls

Positive controls may be internal tissue controls (i.e., positive immunostaining within the experimental tissue) or separate slides of tissue where the antigen is known to be expressed. They are first used when optimizing a new antibody to determine the appropriate antigen retrieval technique and antibody concentration required for positive immunostaining. For the initial workup of an antibody, one must rely on what is known about the location of an epitope in a tissue. If positive staining for an antibody is observed in a structure, cell, or subcellular compartment (e.g., plasma membrane, cytoplasm, or nucleus) where the target antigen is known to be located, then confidence that antibody binding is specific to its epitope in tissue is increased. For example, the specific immunostaining for insulin within β-cells in the Islets of Langerhans of the pancreas provides evidence of the specificity of this antibody (Fig. 4.3B). When positive tissue controls are not available for the initial workup of an antibody or if the location of an antigen in tissue is not known, it is possible to use FFPE cell pellets that have known expression of an antigen as a positive control. It is easiest to obtain cell lines that naturally express the antigen, but, if necessary, cells can be transfected in culture with DNA to make a positive cell line. A second purpose of positive control tissues is for quality control and to ensure that all the reagents used for the IHC protocol on a given day are working as expected. Ideally, positive and negative tissue control sections would be fixed and processed under the same conditions as the experimental tissue sections.

Key Elements of Digital Imaging

Digital imaging is the conversion of a signal by a sensor into a digital signal that can be processed by a computer to a digital image for viewing. Digital imaging provides a way to convert the various types of electromagnetic radiation, including visible light (bright field and fluorescent microscopes), x-rays (digital x-rays and CT scans), and gamma rays (scintigraphy, SPECT, and PET imaging), into a digital image viewed on a computer monitor. Digital imaging provides several advantages, one of which is the ability to integrate imaging platforms over a wide range of resolutions (Fig. 4.4). For example, the ability to integrate digital images from a radiologic CT scan with information obtained with digital imaging of a tissue section on a glass slide is becoming an important component of experimental and translational research, as it increases the information obtained from a study. A discussion of the cameras and specifically the sensors required for obtaining digital images from microscopes is beyond the scope of this chapter. Information related to digital cameras has been provided in the suggested reading list.

An important addition to digital imaging has been the development of microscopes, such as

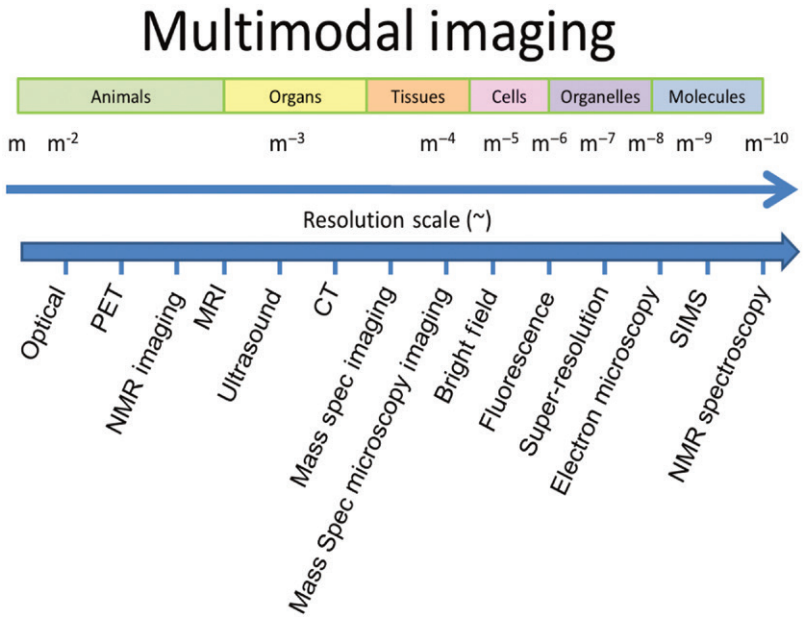

FIGURE 4.4 Multimodal imaging. Digital imaging makes it possible to perform multimodal imaging, which is the integration of data collected from imaging platforms traversing resolutions ranging from mm with optical imaging to ≅200 nm with bright field and/or fluorescent microscopy.

the Hamamatsu Nanozoomer Digital Pathology System (Fig. 4.5), that are used to convert stained tissue on glass slides into whole slide digital images, allowing for viewing and analysis on a computer monitor. Whole slide digital imaging has resulted in the rapid growth of digital pathology as a field that uses this technology for telepathology, research and clinical consultations, teaching, archiving of glass slides, and quantitative microscopy. As costs of memory decrease and with continued improvements in the resolution, speed, and fidelity of the digital sensors, software, and computers, digital pathology may one day become the facsimile of the glass slide and microscopes used today. An example of the ability of digital pathology to improve efficiency and productivity in the workplace is the use of whole slide digital images for quantitative microscopy, providing a means to obtain objective data from IHC (Fig. 4.5).

Key Elements of Quantitative Microscopy

BACKGROUND

The automation and integration of IHC, whole slide digital imaging, and analysis software has enhanced our ability to efficiently obtain quantitative objective data from studies using IHC to understand complex biological processes occurring in organs. For the purpose of this chapter, we have focused on two key elements: stereology and image analysis. The advantages and limitations of each technique are shown in Table 4.3. Note that quantitative microscopy is only accurate when it is performed on high quality tissue samples using validated and optimized antibodies.

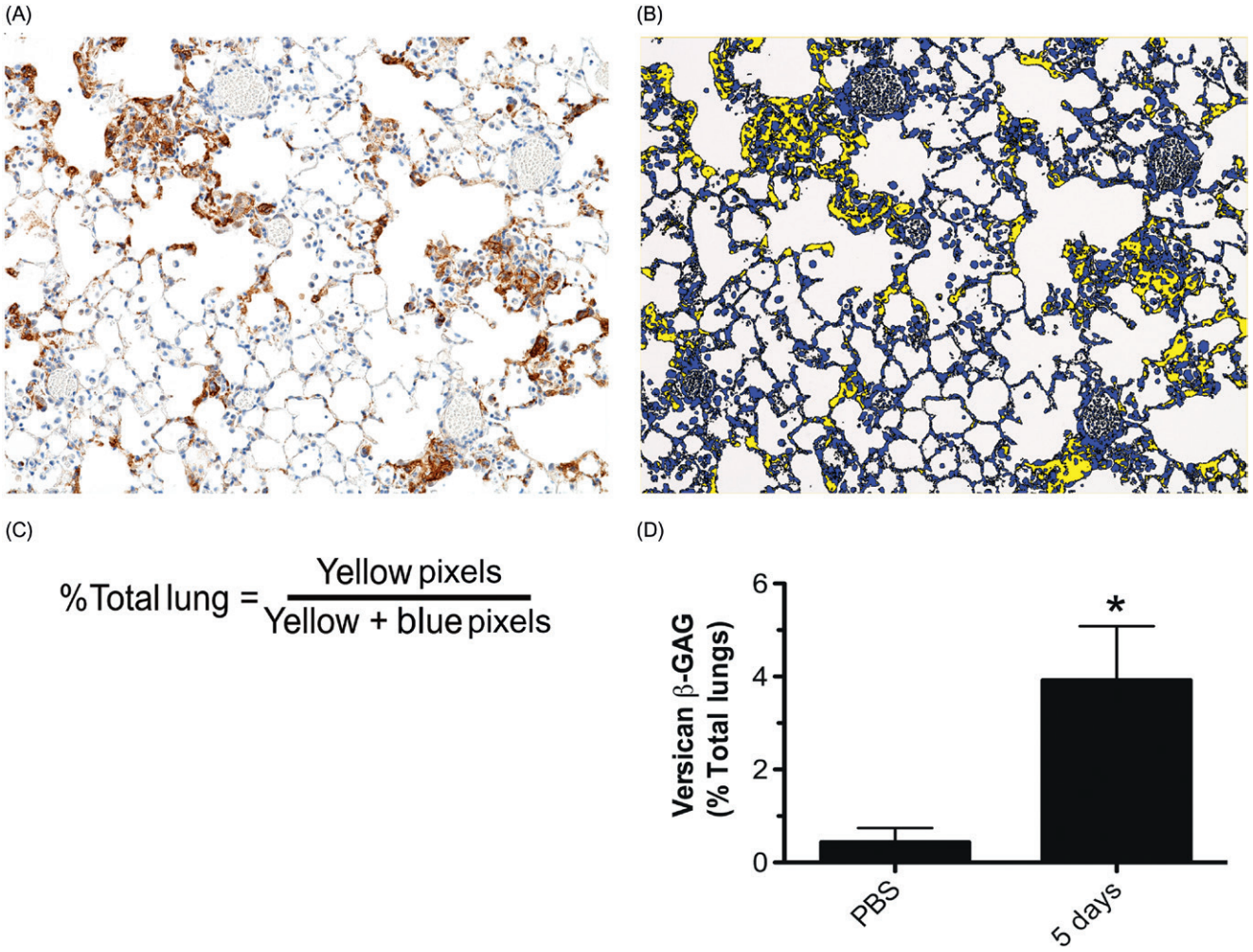

FIGURE 4.5 Image analysis of positive immunostaining in lung tissue. Image analysis using whole slide digital imaging (Hamamatsu NDP System) and automated image analysis software provides quantitative data on the relative amount of versican immunostaining (%total tissue) in lungs of mice treated with PBS or live *Pseudomonas aeruginosa*. (A) Positive immunostaining for versican (brown) in lung tissue obtained from a mouse 5 days after intratracheal instillation of *P. aeruginosa*. The hematoxylin counterstain is blue. (B) Segmentation of the digital image shown in (A) using Visopharm Image Analysis Software (Hoersholm, Denmark) where yellow pixels designate lung tissue that stains positive for versican and blue pixels define lung tissue not stained with the antiversican antibody. (C) Formula used to determine the relative area of lung tissue stained positive for versican. (D) Accumulation of versican is significantly increased in the lungs of mice treated with live *P. aeruginosa*. Values are the mean ± SEM with n=3–4 for each group. (*) significantly different (P<0.05) than mice treated with PBS using Student's T-test.

STEREOLOGY

Computed tomography uses two-dimensional (2D) x-ray images to reconstruct 3D structures in organs. In contrast, stereology does not provide information about the relationships of cells and structures in tissue as a 3D reconstruction, but rather provides precise quantitative measurements of cells and structures in organs using 2D planar tissue cross sections. To make precise measurements of 3D structures in organs, stereology uses a number of techniques that statistically extrapolate quantitative data on the following: total volume of an organ, surface area or length of structures in an organ, the volume

TABLE 4.3 Comparisons Between Stereology and Image Analysis

	Stereology	Image Analysis
Advantages	No assumptions More precise than image analysis Able to accurately measure volumes, numbers of cells, surface area, etc.	Easily automated Rapid Excellent for IHC and special stains where there is contrast between the regions of interest (ROI) and the background, allowing for easy segmentation of an image
Limitations	Considerable increase in time required to perform stereology Typically requires the investigator to obtain an initial reference volume and monitor changes to this during tissue processing	Assumptions required in many instances Less precise than stereology Can only provide measurements of relative change (%), which is typically a ratio of the ROI to the total tissue Does not provide accurate counts of objects (e.g., cells) in tissues

of specific populations of cells within an organ, cell size, and/or number. Stereology statistically extrapolates data about the cellular and structural make-up of an organ or tissue biopsy using rigorous sampling and counting techniques. Therefore, planning for stereology needs to begin before tissue samples are obtained. In addition, in order to obtain an unbiased sampling of tissue and/or digital images, it is critical that all components of the tissue or digital image have a chance of being sampled through a process known as uniform random sampling. When performed correctly, stereology is able to provide precise, unbiased data, which is why it is considered the gold standard for those who perform quantitative microscopy.

IMAGE ANALYSIS

Image analysis is a morphometric technique used to obtain information from digital images using processing tools that segment pixels in a digital image based on color or density (Fig. 4.5A and B). The segmented image is then used to quantitate an area (defined by pixels) of specific features such as the area of positive IHC staining. Most processes required to obtain objective unbiased data can be automated when integrated with whole slide digital imaging, making image analysis an efficient and effective tool. Image analysis is not as precise as stereology and only provides measurements of relative changes to the object(s) of interest (Table 4.3). Image analysis can be used to measure the relative area of positive immunostaining for a protein, cell, or structure in tissue (Fig. 4.5C and D). Whereas it is tempting to perform cell counts when using image analysis, image analysis visualizes profiles of 3D structures in 2D tissue sections, which when counted result in the number of objects (e.g., cells) in tissues being overrepresented. In addition, when comparing objects of different size, counting cellular profiles results in larger objects being counted more often than smaller objects. Therefore, if the goal of a study is to obtain the number of cells or structures in an organ or biopsy, one must use stereology. Even though image analysis has recognized limitations, it is a powerful tool when used correctly to obtain unbiased quantitative data. In addition, quantitative data from IHC studies can be used to increase confidence in the specificity of the IHC protocol by correlating results from IHC with other measurements of the molecule of interest, such as measurements made with flow cytometry, ELISA, or quantitative PCR.

IHC AND IMAGING REPRODUCIBILITY

Reproducibility of scientific studies is an important issue that needs to considered when performing IHC, imaging, and quantitative microscopy. Articles in the Economist, Nature, and other scientific journals have highlighted reproducibility as a significant concern and identified animal models and antibodies as problem areas. Therefore, it is imperative when performing IHC that the concerns raised about the reproducibility of antibodies be addressed. This includes paying close attention to the validation of antibodies, optimization of IHC protocols, and use of appropriate controls when developing and using IHC for research purposes. In addition, particular

attention to the description of experimental details in materials and methods section need to be included to assist individuals that are replicating your work. A list of a number of resources including the ARRIVE (Kilkenny et al.) and MINPEPA (Scudamore et al.) guidelines, as well as recommendations from FASEB, are provided in the Further Reading and Relevant Websites to provide details about information that should be included when reporting your research findings.

Acknowledgments

We would like to acknowledge the excellent technical support from the University of Washington Histology and Imaging Core and Megan Larmore for her assistance with imaging and image analysis. Supported in part by NIH grant: P30DK089507.

Further Reading and Relevant Websites

Tissue Processing

Paavilainen L, Edvinsson A, Asplund A, et al: The impact of tissue fixatives on morphology and antibody-based protein profiling in tissues and cells. J Histochem Cytochem 58(3):237–246, 2010.

Xie R, Chung JY, Ylaya K, et al: Factors influencing the degradation of archival formalin-fixed paraffin-embedded tissue sections. J Histochem Cytochem 59(4):356–365, 2011.

Validation and Optimization of Antibodies for IHC

Baker M: Antibody anarchy: a call to order. Nature 527(7579):545–551, 2015.

Frevert CW, Johnson B, Stahl WL: *Immunohistochemistry: antibody specificity* Pathobiology of human disease: a dynamic encyclopedia of disease mechanisms [internet], Kidlngton, Oxford, UK, 2014, Elsevier Ltd.

Lorincz A, Nusser Z: Specificity of immunoreactions: the importance of testing specificity in each method. J Neurosci 28:9083–9086, 2008.

Pradidarcheep W, Labruyère WT, Dabhoiwala NF, et al: Lack of specificity of commercially available antisera: better specifications needed. J Histochem Cytochem 56:1099–1111, 2008.

Ramos-Vara JA, Miller MA: When tissue antigens and antibodies get along: revisiting the technical aspects of immunohistochemistry—the red, brown, and blue technique. Vet Pathol 51(1):42–87, 2014.

Rhodes KJ, Trimmer JS: Antibodies as valuable neuroscience research tools versus reagents of mass distraction. J Neurosci 26:8017–8020, 2006.

Saper CB: A guide to the perplexed on the specificity of antibodies. J Histochem Cytochem 57:1–5, 2009.

Controls

Burry RW: Specificity controls for immunocytochemical methods. J Histochem Cytochem 48:163–166, 2000.

Hewitt SM, Baskin DG, Frevert CW, et al: Controls for immunohistochemistry: the Histochemical Society's standards of practice for validation of immunohistochemical assays. J Histochem Cytochem 62(10):693–697, 2014.

General Immunohistochemistry

Coons AH, Creech HJ, Jones RN, et al: The demonstration of pneumococcal antigen in tissues by the use of fluorescent antibody. J Immunol 45(3):159–170, 1942.

Nakane PK, Pierce GB:Jr., Enzyme-labeled antibodies: preparation and application for the localization of antigens. J Histochem Cytochem 14(12):929–931, 1966.

Rehg JE, Bush D, Ward JM: The utility of immunohistochemistry for the identification of hematopoietic and lymphoid cells in normal tissues and interpretation of proliferative and inflammatory lesions of mice and rats. Toxicol Pathol 40:345–374, 2012.

Shi SR, Shi Y, Taylor CR: Antigen retrieval immunohistochemistry: review and future prospects in research and diagnosis over two decades. J Histochem Cytochem 59(1):13–32, 2011.

Ward JM, Rehg JE: Rodent immunohistochemistry: pitfalls and troubleshooting. Vet Pathol 51:88–101, 2014.

Ward JM, Erexson CR, Faucette LJ, et al: Immunohistochemical markers for the rodent immune system. Toxicol Pathol 34:616–630, 2006.

Ward JM, Rehg JE, Morse HC:III, Differentiation of rodent immune and hematopoietic system reactive lesions from neoplasias. Toxicol Pathol 40:425–434, 2012.

Microscopy

Goodwin PC: A primer on the fundamental principles of light microscopy: optimizing magnification, resolution, and contrast. Mol Reprod Dev 82(7–8):502–507, 2015.

Hogg J: *The microscope, its history, construction, and application,* London, 1911, George Routledge & Sons.

Milestones in light microscopy. *Nat Cell Biol.* 2009;11(10):1165.

Murphy DB, Davidson MW: *Fundamentals of light microscopy and electronic imaging*, 2nd ed., Hoboken, NJ, 2013, Wiley-Blackwell. xiii, 538 pp.

Digital Imaging/Pathology

Malarkey DE, Willson GA, Willson CJ, et al: Utilizing whole slide images for pathology peer review and working groups. Toxicol Pathol 43:1149–1157, 2015.

Sedgewick J: *Scientific imaging with Photoshop: methods, measurement, and output*, Berkeley, CA, 2008, New Riders.

Sluder G, Wolf DE: *Digital microscopy* Methods in cell biology, 4th ed., Amsterdam; Boston, 2013, Elsevier/AP.

Webster JD, Dunstan RW: Whole-slide imaging and automated image analysis: considerations and opportunities in the practice of pathology. Vet Pathol 51:211–223, 2014.

Quantitative Microscopy

Boyce JT, Boyce RW, Gundersen HJ: Choice of morphometric methods and consequences in the regulatory environment. Toxicol Pathol 38(7):1128–1133, 2010.

Boyce RW, Dorph-Petersen KA, Lyck L, et al: Design-based stereology: introduction to basic concepts and practical approaches for estimation of cell number. Toxicol Pathol 38(7):1011–1025, 2010.

Gonzalez RC, Woods RE: *Digital image processing*, 3rd ed., Upper Saddle River, NJ, 2008, Prentice Hall, xxii. 954 pp.

Howard V, Reed MG: *Unbiased stereology: three-dimensional measurement in microscopy*, New York, 1998, Springer, xvii. 246 pp.

Hsia CC, Hyde DM, Ochs M, et al: An official research policy statement of the American Thoracic Society/European Respiratory Society: standards for quantitative assessment of lung structure. Am J Respir Crit Care Med 181(4):394–418, 2010.

Hyde DM, Tyler NK, Plopper CG: Morphometry of the respiratory tract: avoiding the sampling, size, orientation, and reference traps. Toxicol Pathol 35(1):41–48, 2007.

Russ JC: *The image processing handbook*, 6th ed., Boca Raton, 2011, CRC Press,xviii. 867 pp.

Reproducibility

Collins FS, Tabak LA: Policy: NIH plans to enhance reproducibility. Nature 505:612–613, 2014.

FASEB website on “Enhancing Research Reproducibility” (see below).

Freedman LP, Cockburn IM, Simcoe TS: The economics of reproducibility in preclinical research. PLoS Biol 13(6):e1002165, 2015.

Kilkenny C, Browne WJ, Cuthill IC, et al: Improving bioscience research reporting: the ARRIVE guidelines for reporting animal research. PLoS Biol 8:e1000412, 2010.

Scudamore CL, Soilleux EJ, Karp NA, et al: Recommendations for minimum information for publication of experimental pathology data: MINPEPA guidelines. J Pathol 238:359–367, 2016.

The Economist. Trouble at the lab. Vol 409, pp 26-30 Oct 19, 2013.

Relevant Websites

Antibody RegistryAntibody Registry Site (http://antibodyregistry.org).

Linscott’s Directory: a searchable website to identify antibodies to use for IHC (http://www.linscottsdirectory.com).

Human Protein Atlas (http://www.proteinatlas.org).

FASEB: Enhancing Research Reproducibility (http://www.faseb.org/Portals/2/PDFs/opa/2016/FASEB_Enhancing%20Research%20Reproducibility.pdf).

SKELETAL SYSTEM 5

CHRISTOPHER JEROME
Wake Forest Innovations, Winston-Salem, NC, United States

BENJAMIN HOCH
University of Washington School of Medicine, Seattle, WA, United States

CATHY S. CARLSON
University of Minnesota College of Veterinary Medicine, St. Paul, MN, United States

Introduction

The primary functions of the skeleton are to provide structural support, maintain calcium homeostasis, and replace old or compromised bone so as to maintain structural integrity under normal loading conditions. These functions are carried out by bone-resorbing cells (osteoclasts) and bone-forming cells (osteoblasts) that may change the size, shape, and mass of the bone, particularly during growth, through the process of modeling. During modeling, bone resorption and formation occur independently of one another on different surfaces. As the skeleton matures, the process of remodeling predominates, in which osteoclasts and osteoblasts work in coordinated groups called bone remodeling units to maintain bone mass and structure while replacing old bone. Modeling and remodeling processes respond to the biomechanical environment of the bone and are also modified by endocrine and other influences.

An example of modeling is the continuous formation of bone on outer surfaces and the preponderance of resorption on inner surfaces that together cause the gradual enlargement of bones and of their medullary cavities with age. Another example is the higher rate of resorption than formation in the metaphysis of long bones, which causes a gradient of declining bone mass with distance from the growth plate. Remodeling and modeling processes probably represent a continuum rather than distinct processes.

The skeleton contains 99% of the body's calcium and is crucial to maintaining extracellular calcium levels within the very narrow limits essential to life. Whereas bone resorption and formation processes play a role in liberating and sequestering calcium to maintain calcium homeostasis, it is likely that osteocytes embedded in bone and the calcium exchange mechanisms within the canalicular network that connects them are responsible for short-term calcium exchange.

Bones of the skeleton are classified in several ways. The axial skeleton comprises the skull, spine, and ribs, and the appendicular skeleton comprises the limbs and their attachments to the axial skeleton. Most bones are formed during development

Comparative Anatomy and Histology. DOI: http://dx.doi.org/10.1016/B978-0-12-802900-8.00005-1
© 2018 Christopher Jerome and Elsevier Inc. All rights reserved.

by endochondral ossification, in which bone is formed on a preexisting cartilage model. The bones of the calvarium form by intramembranous ossification in which bone forms directly from an immature fibrous stroma, whereas the bones at the base of the skull form by endochondral ossification. Bones may also be classified as long bones (e.g., femur), flat bones (e.g., ilium), short tubular bones (e.g., proximal phalanx), small bones of the hands and feet (e.g., navicular bone), or sesamoid bones—small oval-shaped bones present in tendons passing over certain joints. A summary of the skeletal system of rodents and humans is shown in Table 5.1.

Skeleton

GROSS ANATOMY

The major anatomical differences between the rodent and human skeleton are related to the adaptation of the rodent skull to a relatively smaller brain and to relatively larger olfactory structures and incisors, as well as to the presence of a long tail (Figs 5.1 and 5.2). Unlike humans, rodents do not have deep orbits. In rodents the pelvic and shoulder girdles are adapted for quadrupedalism, but both rodents and humans exhibit plantigrade locomotion. Other than the difference in size, the skeletons of mice and rats are similar except for minor differences such as a relatively wider and more rounded cranium in mice compared to rats.

Most bones have an outer shell called the cortex, which encloses a network of cancellous (or trabecular) bone composed of plates and rods (trabeculae). The orientation of the trabeculae depends on the applied load forces. The outer or periosteal surface of bone is covered by a thick, fibrous membrane (the periosteum) that contains cells that can form bone by intramembranous ossification. The medullary cavity of bone is lined by a thin layer of cells known as the endosteum.

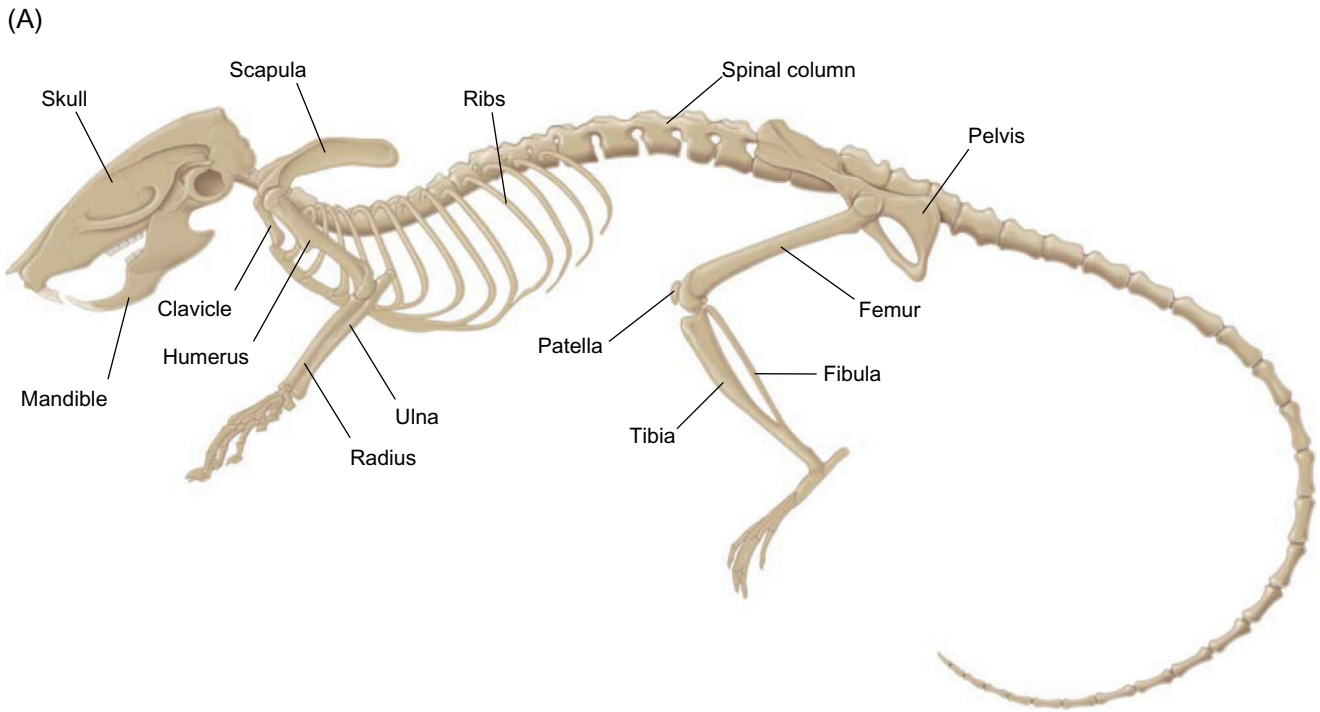

FIGURE 5.1 Regional anatomy of the skeleton. (A) The rodent (mouse) skeletal structure reflects quadrupedalism. (B) The human skeleton is adapted for bipedal locomotion. Source: ©Elsevier, Inc., www.netterimages.com.

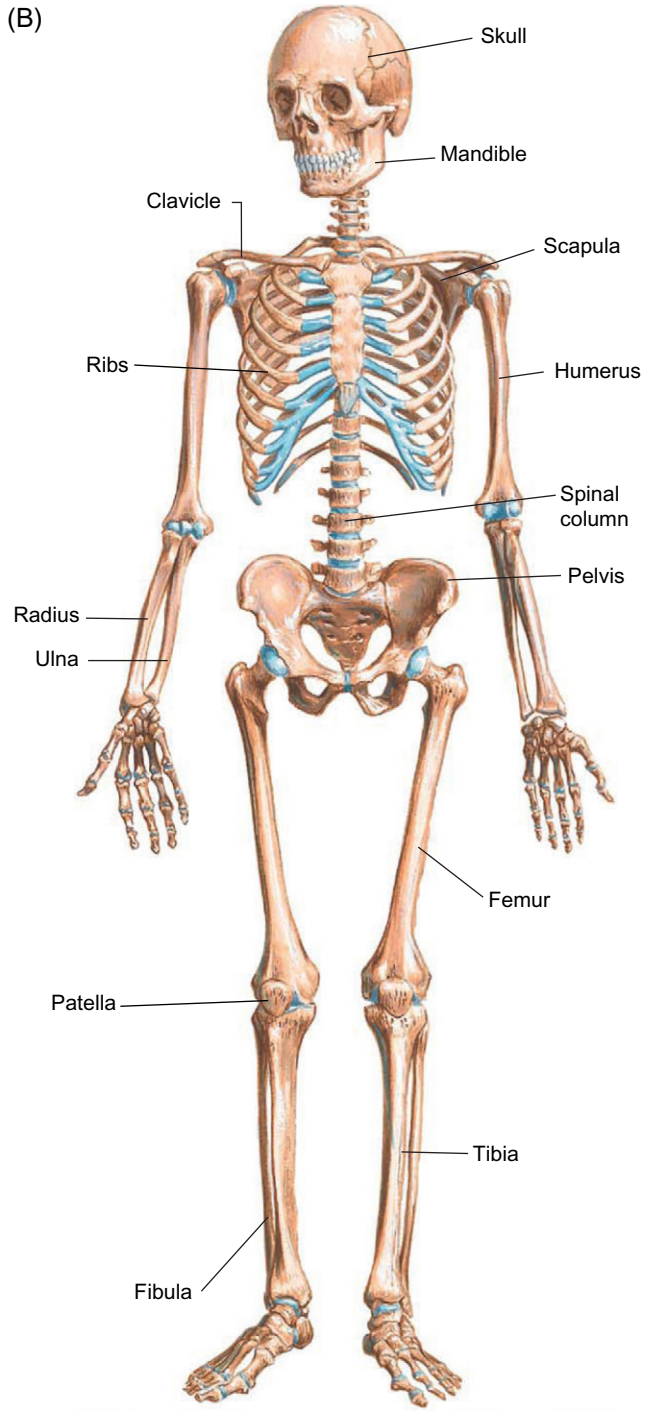

FIGURE 5.1 (Continued)

Need-to-know

- The rodent fibula is half the length and/or fuses with the tibia, whereas the human fibula articulates with the ankle.
- The human skeleton has only 4 coccygeal vertebrae; the rodent has 27 or more.

The thickness of cortical bone varies both within a bone and between bones. Differences between bones are exemplified by comparing the thick cortex of large long bones to the thin cortex of the vertebrae and small bones of the hands and feet. The surface of individual bones is marked by various landmarks (bony prominences) that represent insertion sites of tendons and ligaments (e.g., insertion of the patellar ligament on the tibial tuberosity). There are minor differences in these bony prominences between rodents and humans, such as the greater prominence of the rodent deltoid tuberosity.

Sesamoid bones include the patella and the pisiform bone of the carpus. They are commonly found adjacent to the distal portion of the first metacarpal bone of the forelimb within the adductor pollicis and abductor pollicis brevis tendons, as well as adjacent to the first metatarsal bone of the hind limb within the flexor hallucis brevis tendon. While most sesamoid bones are common to rodents and humans, the fabella (a sesamoid bone in the lateral head of the gastrocnemius muscle behind the lateral femoral condyle) usually seen in rodents is relatively rare in humans.

HISTOLOGY

General Histologic Methods

Bones are commonly prepared for histological evaluation by formalin fixation and decalcification in formic acid or other reagents, followed by embedding in paraffin and sectioning at 5–10 µm. Although these methods are suitable for most purposes, it can be diagnostically or experimentally useful to embed undecalcified bone specimens in methyl methacrylate–based plastic, followed either by sectioning at 5–10 µm using a suitable microtome (typically for longitudinal sections) or by collecting thicker sections using sawing and grinding techniques

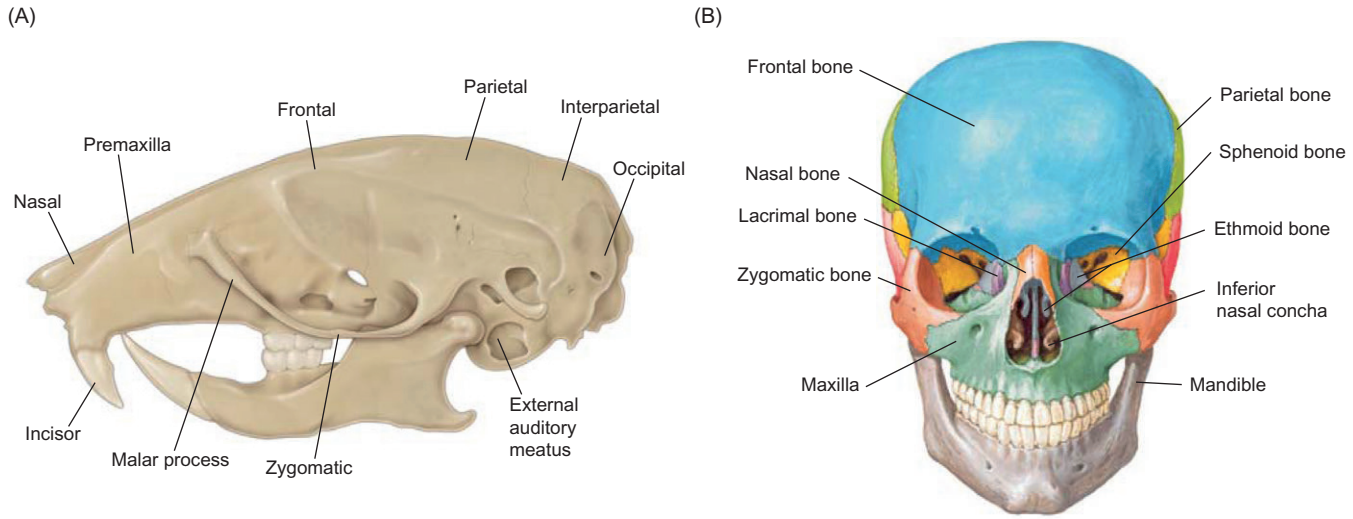

FIGURE 5.2 Gross anatomy of the skull. (A) The rodent (mouse) skull structure reflects the importance of olfaction and large tooth size. (B) The human skull is adapted for large brain size. Source: ©Elsevier, Inc., www.netterimages.com.

Need-to-know

- In the rodent skull, the nasal cavity and jaws predominate.
- In the human skull, the cranial vault predominates.

TABLE 5.1 Skeletal System

Feature	Rodent	Human
	Gross	
Vertebrae	Greater number of thoracic, lumbar, and coccygeal (tail) vertebrae than human	24 articulating cervical, thoracic, and lumbar vertebrae and 9 fused sacral and coccygeal vertebrae
Cervical	7	7
Thoracic	13; T2 large prominent spinous process, varies by strain	12
Lumbar	6	5
Sacral	4	5
Coccygeal	27–31	4
	Histologic	
Cortical bone	Osteons absent; porosities develop with age	Osteons present
Cancellous bone	Secondary spongiosa present during first several months of life and decreases thereafter	Secondary spongiosa absent after skeletal maturity
Growth plate	Persists throughout life	Present only during growth and development
Articular cartilage	Thinner than human; variability in thickness of subchondral plate; no clear tidemark (in skeletally immature animals)	Thickness depends on joint; uniform subchondral plate; tidemark present
Bone marrow	Hematopoietic marrow in axial and appendicular skeleton throughout life	Hematopoietic marrow during development and in adult axial spine; fatty in adult appendicular skeleton
Woven bone	Present	Present
Lamellar bone	Present	Present
Osteoblasts	Present	Present
Osteoclasts	Present	Present
Brown fat	Present in adulthood largely in dorsal intrascapular region	Mostly involutes but can persist in adulthood in neck region

(for cross sections of cortical bone). The advantage of undecalcified specimens is that mineralized and unmineralized bone matrix can be distinguished (Fig. 5.3). This can be of diagnostic or experimental significance, such as in osteomalacia, a disease in which an increased amount of unmineralized bone matrix is present.

In addition, bone-seeking fluorochromes such as tetracycline or calcein can be administered in vivo on a pulsed schedule (typically 2 weeks apart in humans and 4 or 5 days apart in rodents) prior to collection of bone samples. These labels are incorporated into bone as it undergoes primary mineralization soon after osteoblasts lay down the unmineralized osteoid bone matrix (Fig. 5.3B). When undecalcified sections are viewed under epifluorescence following such labeling, the sites of active bone formation exhibit double fluorescent lines corresponding to the location of the mineralization front at the time the labels were administered.

Sections of bone can be subjected to histomorphometric analysis to derive quantitative indices of bone mass, structure, and modeling/remodeling activity. Such measurements typically include relative areas of bone and marrow tissue as a measure of bone mass, as well as proportions of bone surface covered by osteoclasts and osteoblasts as a measure of bone remodeling activity. In undecalcified fluorochrome-labeled sections, the proportion of surface with underlying fluorescent labels, distance between labels, and relative volume and thickness of osteoid and bone can be measured and used as indices of bone formation and mineralization activity.

Other methods for evaluating bone include plain film or digital radiography, bone densitometry (bone mass measurement) by dual-energy X-ray absorptiometry or by quantitative computed tomography (CT), high-resolution structural analysis by micro-CT, and the use of serum and urine biomarkers as indices of bone resorption and bone formation activities. All of these methods have been developed for and applied in both rodent and human bone.

Bone Formation and Maturation

In both rodents and humans, bone forms initially as woven (immature or fiber) bone during early development. Woven bone forms by endochondral

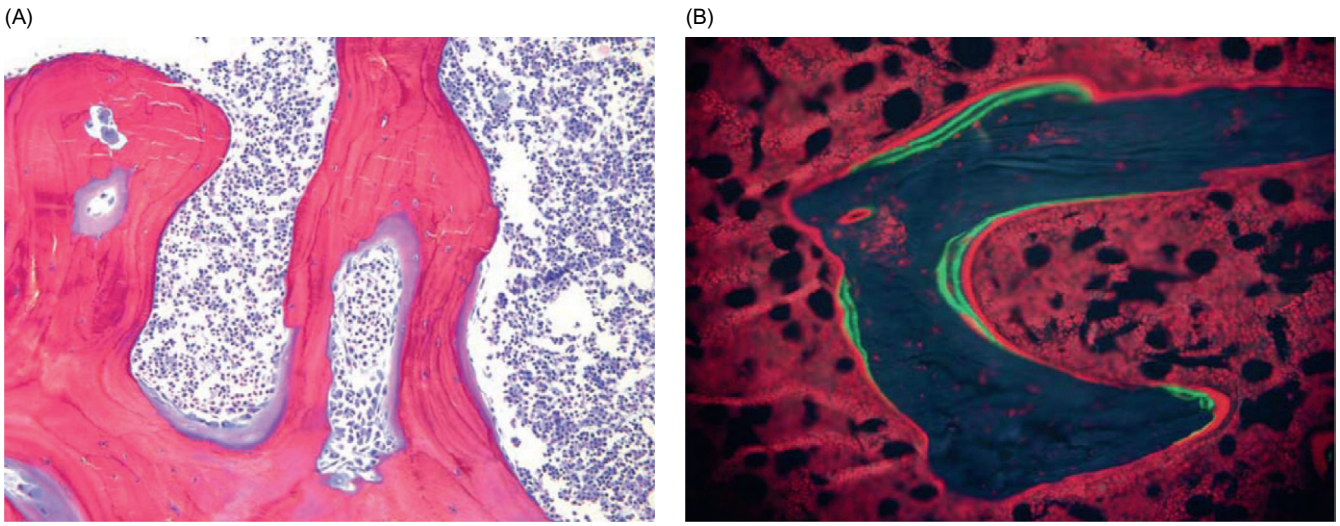

FIGURE 5.3 Undecalcified primate bone. (A) In undecalcified sections, mineralized bone (red) stains differently from unmineralized osteoid seams (newly formed bone matrix; light purple) that line part of the bone surface. Scalloped cement lines that separate bone packets stain dark red in this preparation. (B) In undecalcified sections of lamellar bone, vital double labeling with fluorochromes (green) can be used to visualize bone mineralization sites. Double labels are typically seen underneath the unmineralized osteoid seams (red).

or intramembranous ossification or in response to injury (e.g., fracture). Woven bone has a collagenous matrix that is characterized by an irregularly arranged pattern of collagen fibrils similar to woven fabric, with a cellular population of plump, "activated" osteoblasts that are responsible for bone matrix synthesis and that line the surfaces of the bone (Fig. 5.4). Subsequently, woven bone is replaced by mature lamellar bone over time as a consequence of modeling and remodeling.

Osteoblasts are derived from pluripotential fibroblastic stromal cells. During bone formation, some osteoblasts are incorporated into lamellar bone, at which point they are termed osteocytes. Each osteocyte occupies a lacuna and contains cytoplasmic processes that pass through canaliculi (branching, tubular passages within bone) and communicate with other osteocytes. Mature lamellar bone has fewer and more regularly spaced osteocytes than woven bone and is composed of a collagen matrix arranged in layers (lamellae). Within each layer, the collagen bundles lie parallel to each other. This lamellar structure is analogous to the layers of wood in plywood and provides much greater strength than is exhibited by woven bone; however, it cannot be formed as quickly. The lamellar architecture of mature bone is generally apparent by routine light microscopy (Fig. 5.5). Lamellar bone may be lined by quiescent (flattened) or active (plump and cuboidal in shape) osteoblasts, depending on whether the bone surface is undergoing bone formation. More definitive distinction between lamellar bone and woven bone can be observed using polarized light microscopy, which better defines the arrangement of the collagen fibrils.

Osteoclasts are derived from circulating precursors of the monocyte–macrophage cell line and are multinucleated cells with foamy cytoplasm. They express enzymes that degrade bone matrix, including tartrate-resistant acid phosphatase and cathepsin K. Osteoclasts become polarized and adhere to the surface of the bone where resorption takes place. Resorption occurs through a specialized brush border that appears at the bone–osteoclast interface, and the enzymes remain localized through the formation of a sealing zone around the outer margins of the osteoclast–bone

(A)

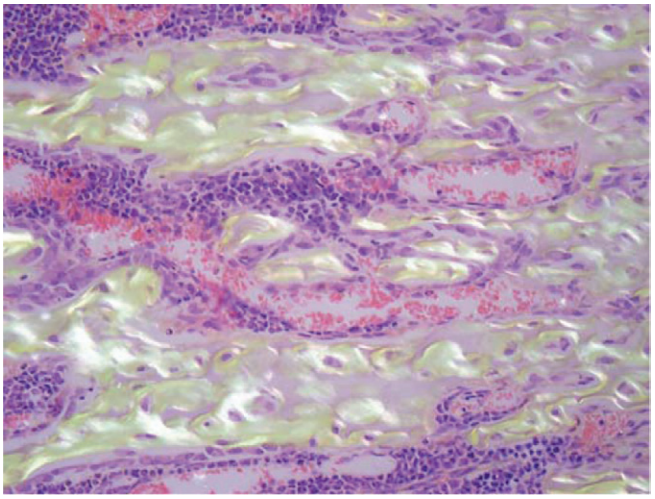

(B)

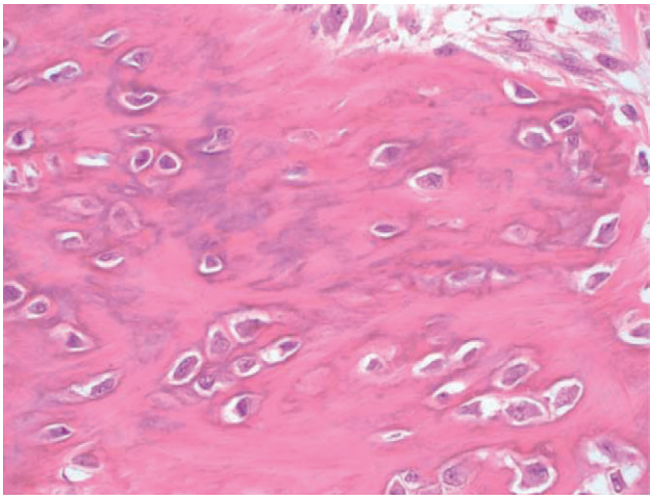

FIGURE 5.4 Woven bone. (A) Rodent (mouse). In both rodents and humans, woven bone has a disorganized arrangement of collagen fibers (seen here as bright white/yellow under polarized light), and osteocytes are rounder, larger, and less regularly spaced than in lamellar bone. (B) Human. The irregular cellular spacing and large round osteocyte nuclei are evident in this example.

Need-to-know

- Woven bone is formed in situations in which rapid bone formation occurs (e.g., growth or fracture repair) and has a far less regular structure than lamellar bone.

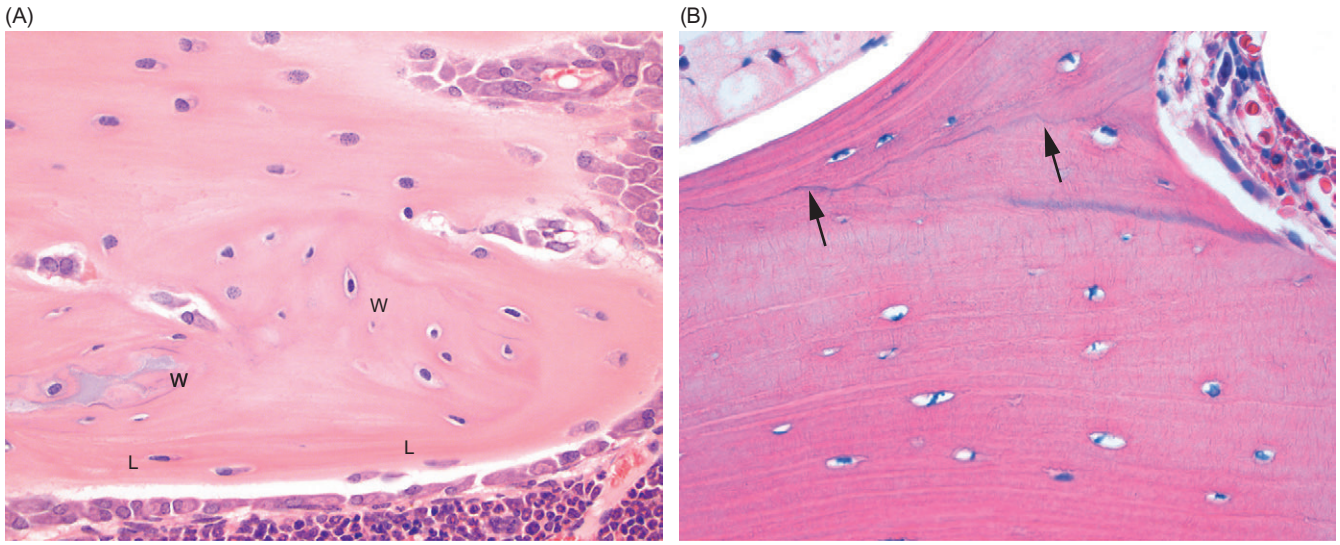

FIGURE 5.5 Lamellar cancellous bone. (A) Rodent (mouse) lamellar bone is similar in structure to human, but packets usually are smaller and have fewer collagen lamellae. In this example in a 6-week-old mouse, a lamellar bone packet (L) has been laid on top of a cartilage and woven bone trabecular core (W). As rodents mature, the trabeculae come to comprise exclusively lamellar bone, as in humans. (B) Human lamellar bone contains osteocytes within lacunae, which are flattened parallel to the collagen lamellae. Distinct packets of lamellar bone are created by remodeling events, and collagen orientation is often different in adjacent packets, which may be separated by distinctly stained cement lines (arrows).

Need-to-know

- Lamellar bone consists of parallel layers of collagen lamellae in which osteocytes are embedded.
- Lamellar bone packets are formed by remodeling events and are separated by cement lines.

interface. The erosion that is formed at this interface by enzymatic removal of mineralized bone matrix is known as Howship's lacuna and often is visible in histological sections (Fig. 5.6). The hallmark of remodeling is the presence of scalloped cement lines between packets of bone formed by bone remodeling units, which represents the scalloped surface left by osteoclasts when they have completed the bone resorption process. The osteoclastic–osteoblastic remodeling units respond to stresses on bone to maintain its structural integrity and can release calcium from bone to help maintain calcium homeostasis.

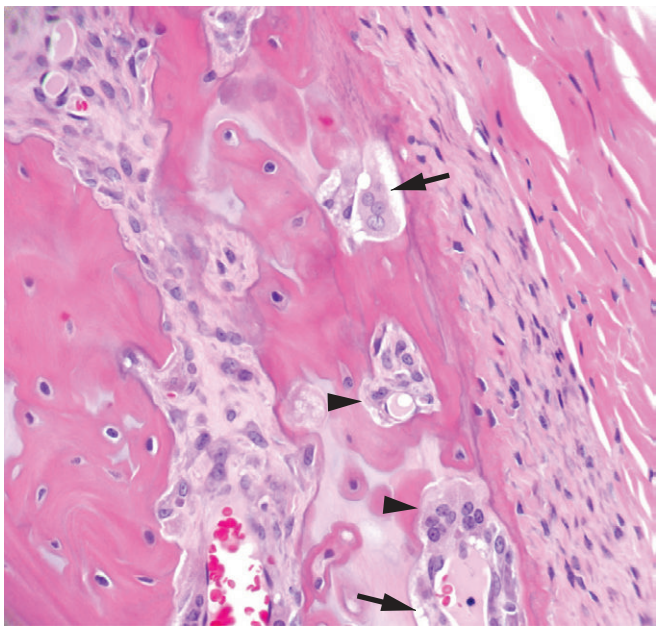

FIGURE 5.6 Bone resorption in rodent (rat). Multinucleated osteoclasts lie on bone surfaces, where the brush border may be evident (arrows), or in scalloped erosions on the bone surface known as Howship's lacunae (arrowheads).

Long Bones

Gross Anatomy

In both rodents and humans, the long bones have three major regions (Fig. 5.7): the epiphysis (end

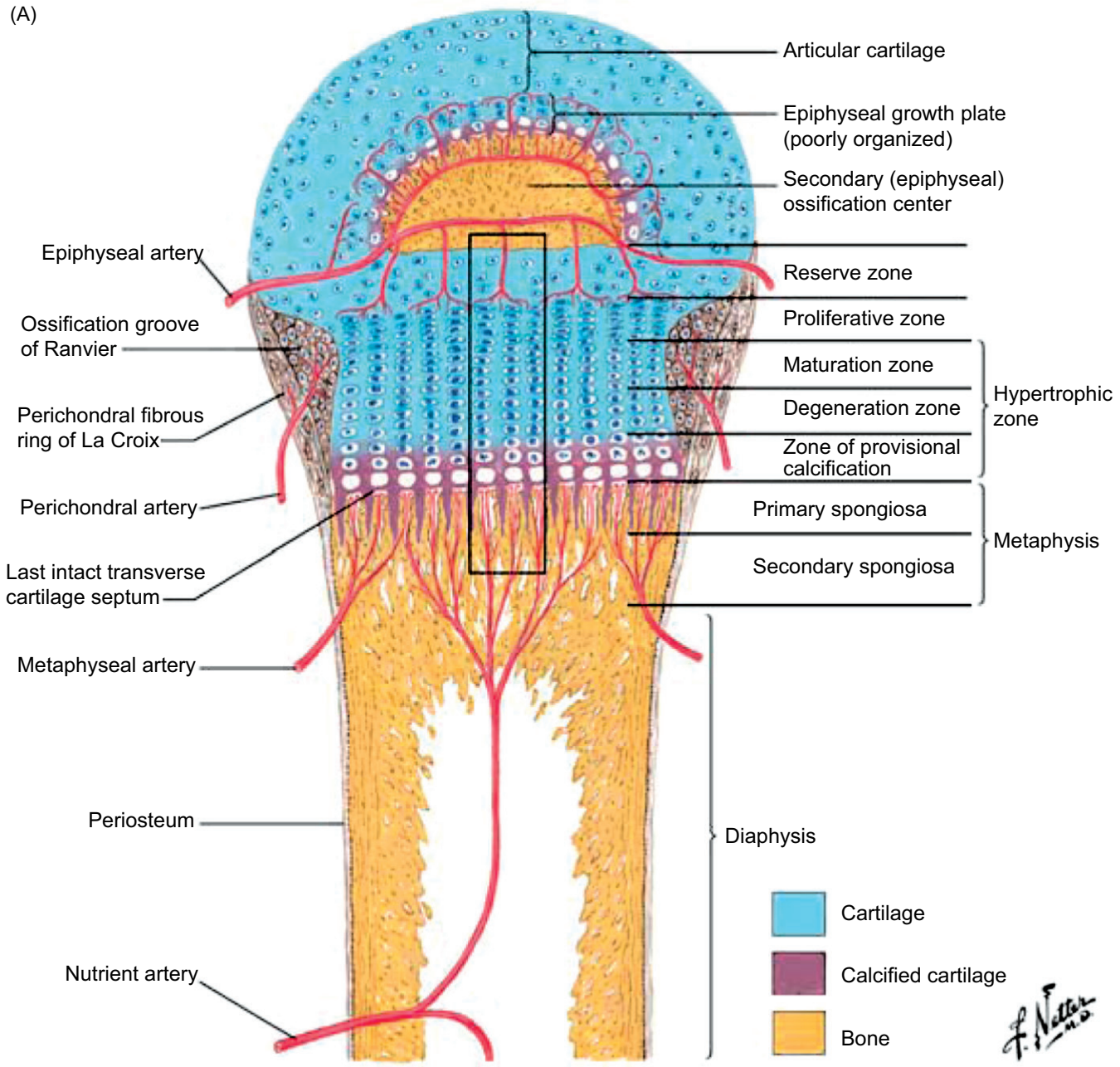

FIGURE 5.7 Long bone. (A) Netter schematic of mammalian long bone. (B) Rodent (mouse) articular cartilage (AC) and calcified cartilage (CC; black line roughly delineates AC from CC) are thin and the subchondral plate (SP) is relatively thick and variably-oriented. (C) Human articular cartilage (AC) is 2 or 3 mm thick in weight-bearing joints and contains three zones: superficial (SZ), middle (MZ), and deep (DZ). It is supported by a relatively thin subchondral plate (SP). The zone between the articular cartilage and calcified cartilage/subchondral bone is marked by a line known as the tidemark (arrows). (D) In rodents (rat), there is a relatively thick calcified cartilage zone containing vacuolated chondrocytes (arrowheads); the tidemark, which may not be obvious in young rodents, is indicated by arrows. Source: (A) ©Elsevier, Inc., www.netterimages.com.

of the bone), the diaphysis (shaft of the bone), and the metaphysis (flared region between the epiphysis and diaphysis). The growth plate (physis), separates the epiphysis from the metaphysis and is the structure responsible for longitudinal growth of the bone. In long bones, the cortex is thickest in the diaphysis, in which bending forces predominate. In the metaphysis and epiphysis, the cortex is thin, and cancellous bone makes up more of the bone in order to support compressive forces from the joints.

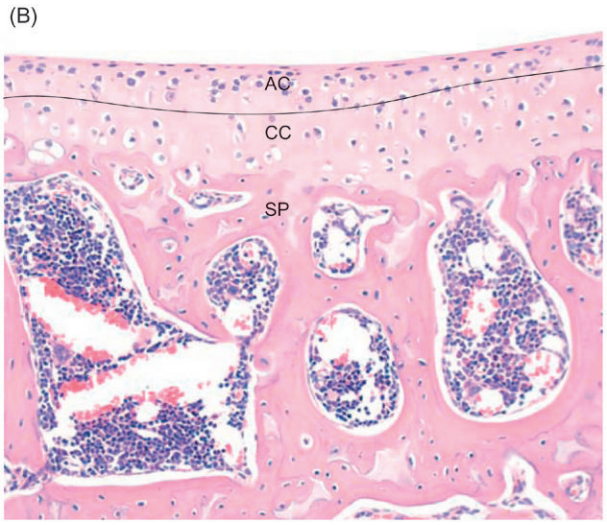

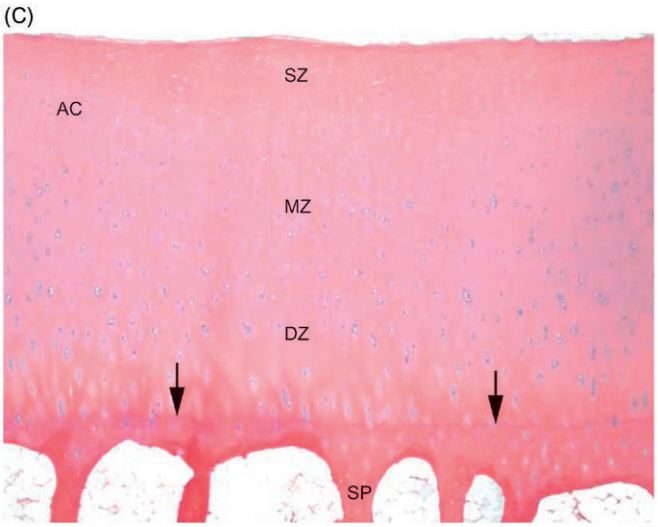

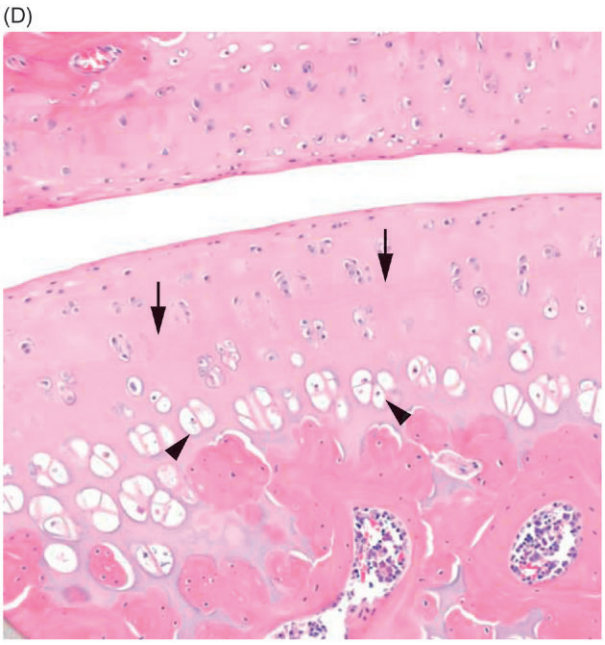

FIGURE 5.7 (Continued)

Need-to-know

- Rodents have much thinner articular cartilage with fewer cellular layers than humans.
- A clearly defined tidemark is not seen in young rodents.

In rodents and humans, most tubular bones develop with growth plates at both ends although some bones, such as the phalanges and the metacarpal and metatarsal bones, ordinarily form this structure only at one end of the bone.

In rodents the fibula fuses with the tibia just below midshaft rather than extending distally to articulate with the ankle as it does in humans.

HISTOLOGY

Epiphysis

A bony nucleus (secondary center of ossification) forms in the center of most epiphyses during development. An exception is the proximal femur in rodents, which undergoes a prolonged phase of mineralization through chondrocyte-, not osteoblast-, dependent mechanisms and lacks a

secondary center of ossification. The knee joint and other diarthrodial synovial joints are lined by articular (joint-related) cartilage, under which is a layer of bone called the subchondral plate (Fig. 5.7). In rodents the subchondral plate is highly variable in thickness, and in some places is very thin. In most human bones the normal subchondral plate is thin and of uniform thickness. Bone making up the subchondral plate is approximately the same thickness as the trabeculae of cancellous bone. However, in some human bones the subchondral plate thickness is more variable. For example, the middle region of the acetabular area of the innominate bone is thicker than the more peripheral areas and subchondral bone of the opposed femoral head.

Growth Plate

In all three species the cartilaginous growth plate can be divided into four zones. From the epiphyseal end to the metaphyseal end, the growth plate is composed of an undifferentiated/resting zone, a proliferative zone, a zone of hypertrophy, and a zone of calcification/ossification that transitions to the subchondral bone. Chondrocytes multiply in the proliferative zone, creating columns of cells that enlarge/undergo hypertrophy. Deep to the hypertrophic zone, the cartilage matrix becomes calcified and chondrocyte columns are invaded by capillaries arising from the metaphysis. The chondrocyte at the base of each column of cells either undergoes apoptosis or is converted to an osteoblast. Calcified cartilage matrix is then resorbed by cells resembling osteoclasts. Finally osteoid (unmineralized bone matrix) is laid down by osteoblasts on the cartilage spicules that remain and becomes mineralized to form the trabeculae of the primary spongiosa, which often have a calcified cartilage core. These trabeculae are subsequently remodeled and, in the secondary spongiosa, they consist almost entirely of bone and are thinner than those in the primary spongiosa. This general structure of the growth plate is shared between humans and rodents.

In rodents the growth plate or remnants thereof may be present in long bones throughout life (Fig. 5.8). However, growth plate thickness, which is generally proportional to longitudinal growth rate, declines in thickness with age. For example, the average growth plate thickness in the distal femur of mice is reported to be 560 µm at day 12 and 100 µm at 4 months of age. Active longitudinal growth ceases in mice after approximately 3 months of age and in rats after approximately 6 months of age. The rodent growth plate then gradually involutes and is characterized by horizontal deposition of bone, similar to the human epiphyseal scar, on persistent but nonproliferating cartilage. During involution, the chondrocytes in the rodent growth plate remnant are arranged in clusters rather than columns and there may be acellular areas within the cartilage as well as intralacunar bone formation.

In humans the growth plate becomes clearly defined when the epiphysis has developed a secondary center of ossification after birth (Fig. 5.8). Even during the period of active growth, the growth plate is never more than 1–3 mm in thickness. This thickness varies from bone to bone. In addition, the thickness of each growth plate is different within a single bone. The growth plate is always thicker at the more actively growing end of the bone (e.g., the proximal end of the tibia more than the distal end). With increasing age, the growth plate becomes thinner. Obliteration of the growth plate defines skeletal maturity and occurs at approximately 15–18 years of age (generally earlier in females than in males). The beginning of this process is marked by lack of cartilage proliferation and by mineralization of the remaining matrix. At this point the growth plate becomes more irregular and wavy in appearance. Subsequently there is endochondral ossification of the cartilage remnant and remodeling of the bone to produce a fusion line between the epiphysis and metaphysis, also known as an epiphyseal scar. This scar represents trabeculae that run at more or less right angles to the longitudinally directed trabeculae of

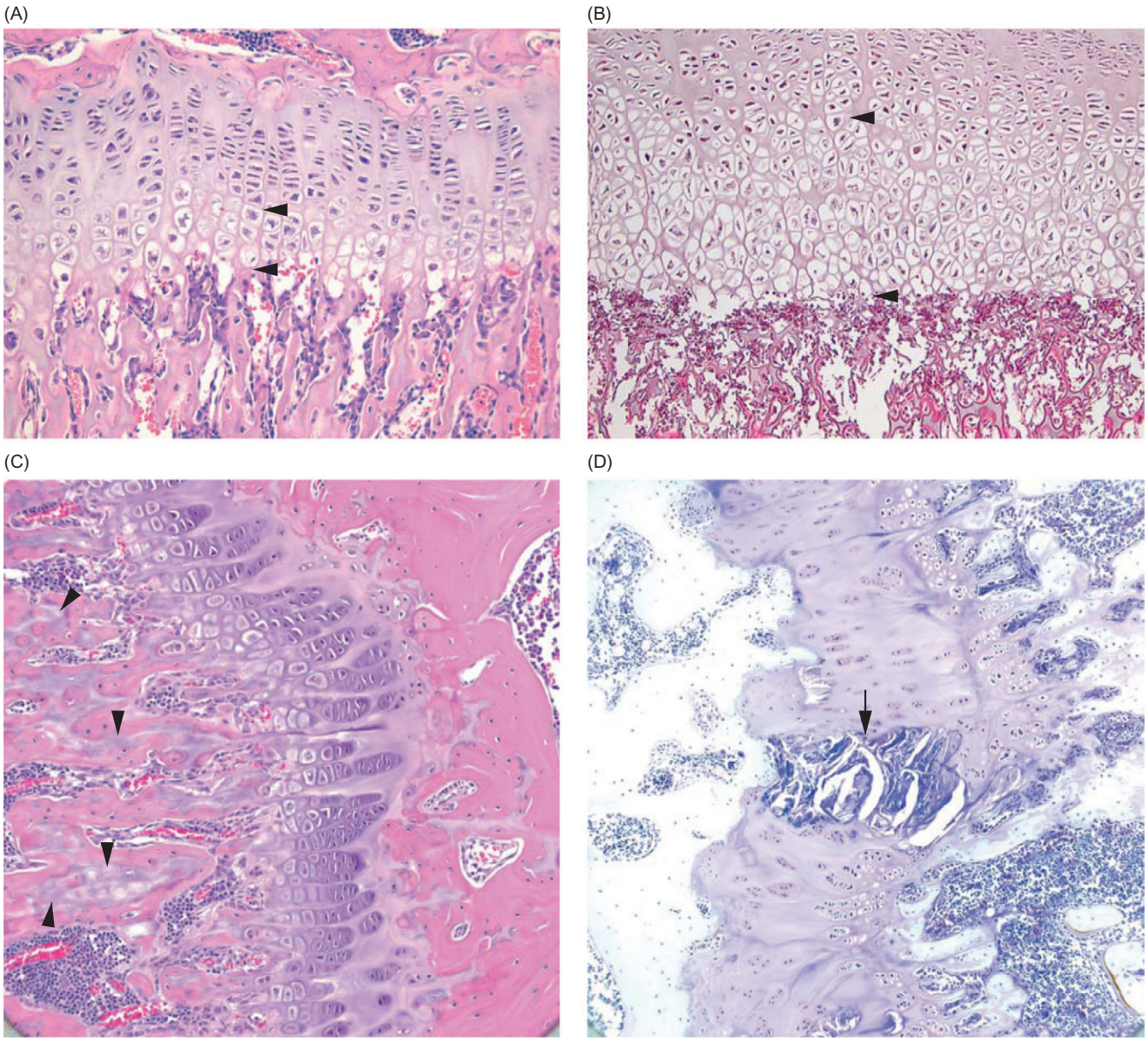

FIGURE 5.8 Growth plate. (A) In the rodent growth plate (mouse), the hypertrophic zone (between arrowheads) is relatively thin. Growth plate remnants persist throughout life, although longitudinal growth largely ceases by 3 (mice) to 6 (rats) months of age. (B) The human growth plate has a thick hypertrophic zone (between arrowheads) with an abrupt transition to bone of the primary spongiosa. In adult humans the growth plate is completely remodeled and replaced by bone. (C) In this rodent (rat) image retention of cartilage cores (arrowheads) in the trabeculae of the primary spongiosa is evident. (D) In early growth plate involution, zonal organization is lost, and transphyseal mineralization occurs (arrow). Source: Nonhuman primate, toluidine blue stain.

the bone. Fusion lines may persist until late in life, particularly in locations such as the distal femur and proximal tibia, but there is eventually complete remodeling of the epiphyseal scar.

Need-to-know

- Growth plate remnants persist in skeletally mature rodents.
- The growth plate completely disappears in human adults.

Metaphysis

In all three species metaphysis contains two regions, the primary and secondary spongiosa. In rodents, the primary spongiosa (immature trabecular bone) lies in the first 250 µm or so below the cartilage growth plate (Fig. 5.9). Osteoblasts and osteoclasts line most of the bone surfaces in this area. The relative amount of marrow increases,

whereas the amount of embedded cartilage in trabeculae and the proportions of osteoclast and osteoblast surface decrease progressively into the secondary spongiosa (mature trabecular bone). The marrow spaces contain predominantly hemopoietic marrow and remain highly cellular throughout life (Fig. 5.10).

Similarly in humans, during development and growth of long bones, the metaphysis is composed of

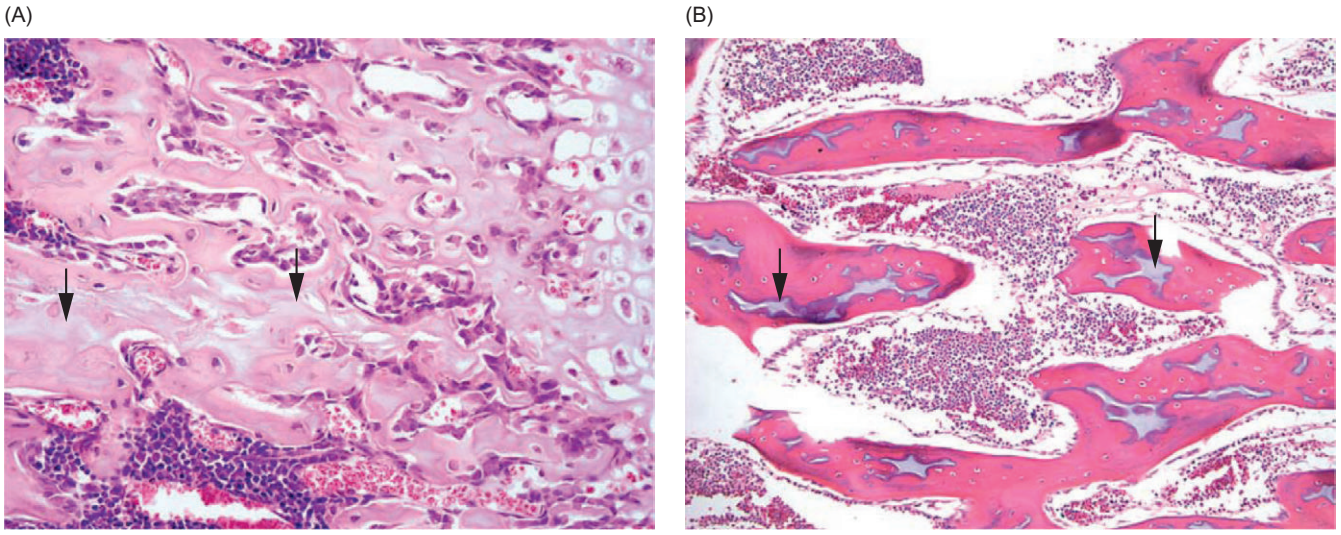

FIGURE 5.9 Metaphyseal immature trabecular bone (primary spongiosa). (A) In 6-week-old mice, cartilage cores (arrows) are present in trabeculae of the primary spongiosa. The marrow cavity is predominantly filled with hemopoietic tissue. (B) Human fetal bone trabeculae have cartilage cores (arrows) that are cartilage anlagen or growth plate remnants.

Need-to-know

- Trabeculae of the primary spongiosa in young rodents resemble human fetal trabeculae.

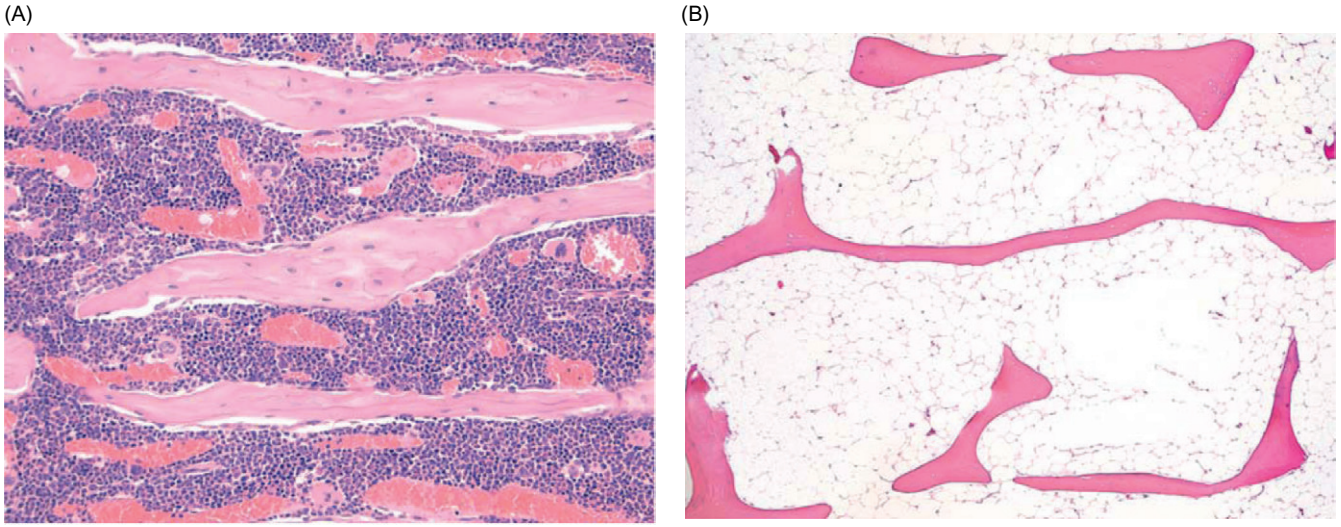

FIGURE 5.10 Metaphyseal mature trabecular bone (secondary spongiosa). (A) In the secondary spongiosa of rodents (mouse), trabeculae are predominantly composed of lamellar bone, although some cartilage persists in the trabecular cores. The marrow cavity is predominantly hemopoietic tissue in the long bones of the limb, but fatty marrow is present in the coccygeal vertebrae. (B) Human adult trabeculae are composed entirely of lamellar bone, and the marrow cavity is filled predominantly with adipose tissue.

Need-to-know

- Secondary spongiosa in the appendicular skeleton of rodents contains predominantly hemopoietic marrow.
- Trabeculae of mice (<50 μm) and rats (<80 μm) are thinner than those of humans (100 μm).

primary spongiosa extending from the growth plate with an associated rich capillary vasculature between trabeculae (Fig. 5.9). The primary trabeculae are lined by numerous active osteoblasts and osteoclasts. From the growth plate toward the diaphysis, there is a progressive increase in the amount of bone surrounding the cartilage cores of the trabeculae in the secondary spongiosa. Osteoblastic and osteoclastic modeling is still occurring, but the cells lining the trabeculae are less readily apparent. The intertrabecular space away from the growth plate is composed of hematopoietic marrow during development that is later replaced by fatty marrow (Fig. 5.10). The cortex of the developing metaphysis is composed of a thin cuff of woven bone (called the bone collar) formed by intramembranous ossification from the periosteum. In adult humans the metaphysis is composed predominantly of cancellous (trabecular) bone that consists of osseous plates and rods that cross each other at more or less right angles marking out the intertrabecular marrow space. The plates may appear thicker or longer depending on the axis of orientation. Fine apertures are present in the trabeculae to allow for communication between marrow spaces. In rodents, there is similar cancellous bone architecture. After skeletal maturity in humans (usually between 15 and 18 years), cancellous trabeculae are composed entirely of lamellar bone without cartilage cores and generally do not contain vascular channels (Haversian systems) as seen in cortical bone. Rodent cancellous bone may contain residual cartilage cores during the first several months of life that gradually decrease over time, with residual cores present only in proximity to the persistent growth plate in older animals. The adult metaphyseal cortex is thin compared to the diaphysis in both rodents and humans. The structure and flared shape of metaphyseal bone allows for support against compressive forces across the adjacent joint in both species.

Cutback Zone

Long bone growth is complex in both rodents and humans. The bones must grow in length and width while maintaining the shape and structure of the metaphysis and diaphysis. Immediately below the growth plate, osteoclast activity on the periosteal surface reduces the outer diameter of the bone to produce the characteristic flare at the end of the bone. As the flared ends grow, what was previously part of the metaphysis must be modeled into the narrow diaphysis. This is accomplished when growth in length is accompanied by osteoclastic resorption of bone from the external surface of the metaphysis in the region not involved in active growth, known as the cutback zone. In the cutback zone of the metaphysis, resorption of the periosteal surface is accompanied by bone formation on the endosteal (inner) surface in order to maintain the mechanical strength of the bone. In contrast, growth in the diaphysis involves addition of bone to the external surface and removal of the endosteal surface.

Diaphysis

In both rodents and humans the shaft of long bones such as the femur consists almost entirely of cortical bone. In very young rodents, the diaphyseal cortex contains a high proportion of woven bone. The diaphysis grows by apposition of circumferential lamellar bone on the periosteal surface, whereas resorption predominates on the endocortical (inner) surface. This causes the outer and medullary cavity diameters to increase and the proportion of woven bone to decrease. By 3 or 4 months of age in mice, and 5 or 6 months of age in rats, the femoral cortex is largely lamellar bone and nonporous except for small vascular spaces in the remaining woven bone. Rodent diaphyseal cortical bone rarely undergoes the Haversian remodeling seen in human bone and thus does not usually contain osteons. However, with age, large marrow-filled intracortical porosities develop that appear to arise from endocortical resorption and tunneling from the marrow cavity (Figs. 5.11 and 5.12).

(A)

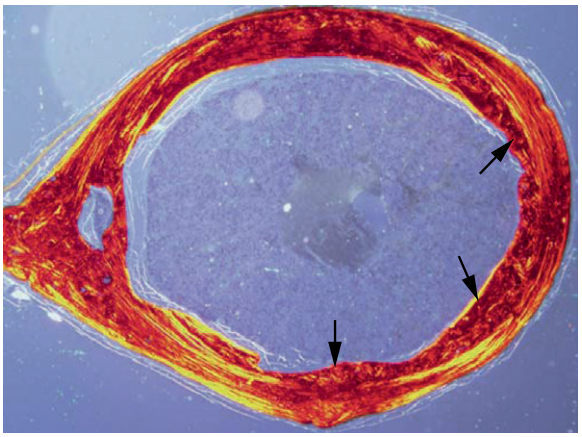

FIGURE 5.11 Cortical bone. (A) In rodents (mouse), cortical bone remodeling is rare, and most of the cortex comprises circumferential lamellae laid down on the outer (periosteal) surface as the bone grows. On the inner aspect, remnants of the less well-organized bone formed during endochondral ossification are seen (arrows) in this cross section of a long bone viewed under polarized light. (B) As shown in this illustration, human adult cortical bone consists mostly of osteonal bone. Osteons are the product of bone remodeling and in cross section comprise a central vascular channel surrounded concentrically by bone lamellae. Source: Elsevier, Inc., www.netterimages.com.

Need-to-know

- In rodent cortical bone, circumferential lamellae predominate and osteons are rare or absent.
- Human cortical bone consists primarily of Haversian osteons.
- Rodent cortical bone is rarely remodeled, and the cortex consists primarily of circumferential lamellae.
- Human cortical bone reflects continuous remodeling throughout life.

(B)

Structure of Cortical (Compact) Bone

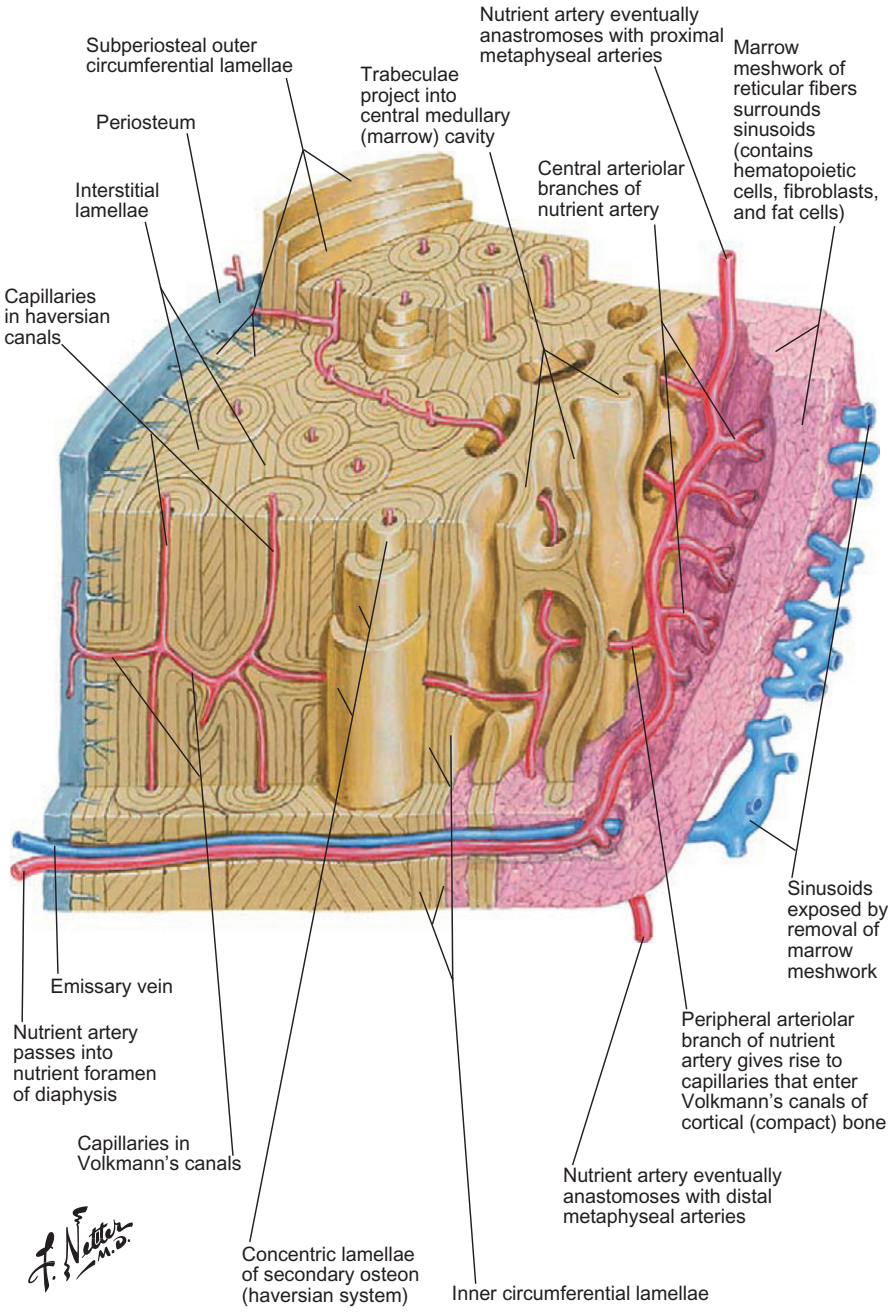

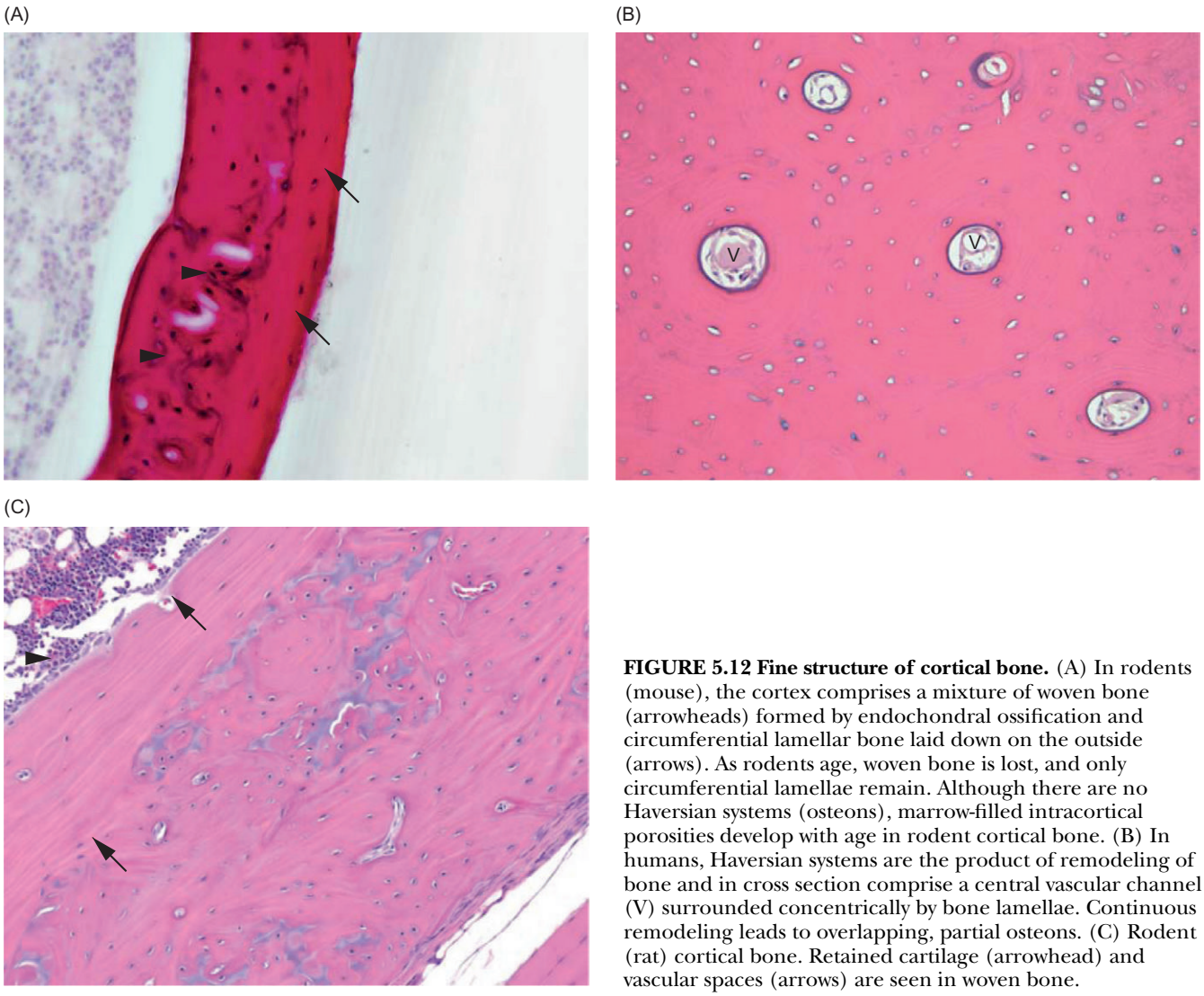

FIGURE 5.12 Fine structure of cortical bone. (A) In rodents (mouse), the cortex comprises a mixture of woven bone (arrowheads) formed by endochondral ossification and circumferential lamellar bone laid down on the outside (arrows). As rodents age, woven bone is lost, and only circumferential lamellae remain. Although there are no Haversian systems (osteons), marrow-filled intracortical porosities develop with age in rodent cortical bone. (B) In humans, Haversian systems are the product of remodeling of bone and in cross section comprise a central vascular channel (V) surrounded concentrically by bone lamellae. Continuous remodeling leads to overlapping, partial osteons. (C) Rodent (rat) cortical bone. Retained cartilage (arrowhead) and vascular spaces (arrows) are seen in woven bone.

Human cortical bone is composed of osteons, circumferential lamellae on the outer and inner surfaces, and interstitial lamellae between osteons. Osteons comprise layers of bone formed around a vascular core (Haversian canal). In cross section, osteons are circular with a diameter of approximately 180–250 µm. Osteons are not discrete units; rather, they divide, rejoin, and interconnect with other osteons to form a complex network analogous to a three-dimensional jigsaw puzzle or the interconnecting roots of a plant. The cortex is formed during development and remodeled throughout life via appositional growth of bone on the outer surface by the periosteum. These layers of bone on the surface are histologically characterized as circumferential lamellae. Throughout the growth period and into adulthood, the circumferential lamellae are remodeled into osteonal bone. As such, circumferential lamellae make up a great proportion of the cortex in younger individuals. Osteonal bone also undergoes remodeling throughout development and adulthood. Remodeling occurs by the formation of a cutting cone consisting of an advancing edge of osteoclasts that form a tunnel in the bone. This is immediately followed by osteoblasts laying down new bone around a vascular core to form a new osteon. Surrounding each osteon is a cement line representing where osteoclastic resorption ended and new bone was laid down. Interstitial lamellar bone between osteons is essentially the remnants of previously remodeled osteons. During cortical remodeling throughout life,

as new circumferential lamellar bone is laid down on the outer surface, there is resorption of bone on the endosteal surface. As with all remodeling, new bone is laid down following resorption, forming circumferential lamellae on the endosteal surface. A Volkmann canal is a vascular channel that runs perpendicular to the long axis of Haversian canals and connects adjacent Haversian systems.

Marrow

Bone marrow comprises hematopoietic and adipose tissues. In rodents there is hematopoietic marrow throughout the long bones accompanied by low numbers of adipocytes. There is more adipose tissue in some marrow sites, such as the medullary cavities of the distal limbs and of the vertebrae. In general hematopoietic marrow is retained in older rodents and occupies a larger area than is occupied by adipocytes. In adult humans hematopoietic marrow resides in the axial skeleton (vertebrae and pelvic bones) and occasionally in the proximal humerus and femur. The remainder of the appendicular skeleton contains fatty marrow.

SPINE

GROSS ANATOMY

Rodent and human lumbar vertebrae differ in several respects, such as relative vertebral body size (Fig. 5.13). Rodents also usually have more

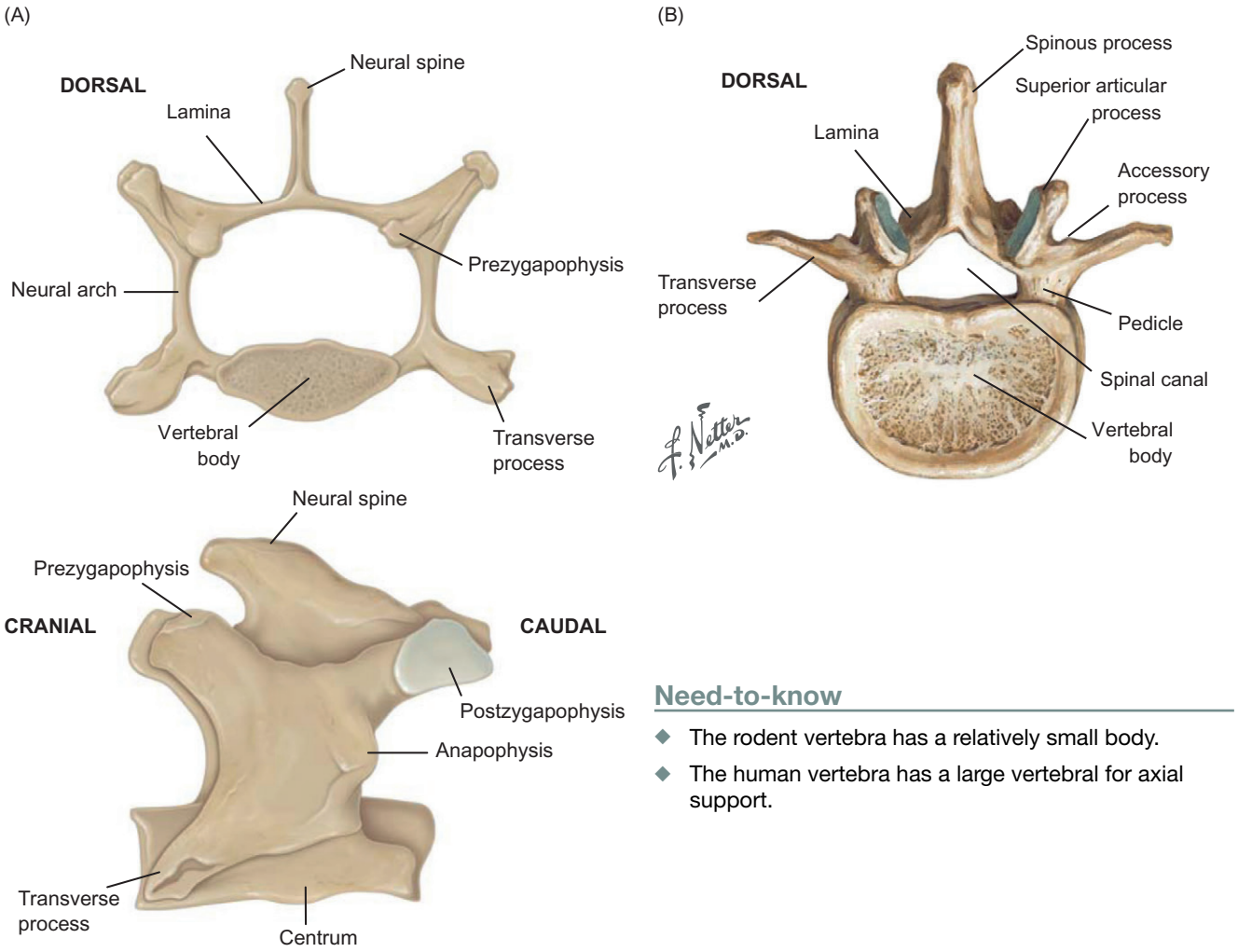

Need-to-know

- The rodent vertebra has a relatively small body.
- The human vertebra has a large vertebral for axial support.

FIGURE 5.13 Gross anatomy of the lumbar vertebra. (A) The rodent (mouse) lumbar vertebra has a relatively small vertebral body (centrum) and ventrally directed transverse processes. (B) The human lumbar vertebra has a large vertebral body for axial support. The transverse processes are located dorsally on the neural arch. Source: ©Elsevier, Inc., www.netterimages.com. (A) Adapted with permission from M.J. Cook. *The anatomy of the laboratory mouse*, 143 pages. Elsevier. Copyright © 1965.

presacral vertebrae as well as more tail (coccygeal) vertebrae than humans (Table 5.1). The total number of precoccygeal vertebrae rarely varies within a species, but it is not uncommon to observe "sacralization" or fusion of the last lumbar vertebra with the sacrum in rodents or to have one extra thoracic vertebra accompanied by one fewer lumbar vertebra in either rodents or humans. In humans the fifth lumbar vertebra may also be fused with the sacrum.

HISTOLOGY

Vertebrae

In rodents and humans the vertebrae have terminal growth plates that are thinner and less well organized than in the long bones because longitudinal growth is very slow or absent. However, the flared metaphysis, gradually decreasing amount of trabecular bone, and thickening cortex with distance from the growth plate all resemble the structure of long bones.

Intervertebral Discs

Rodent and human intervertebral discs are similar and are composed of a fibrocartilaginous structure that forms the articulation (amphiarthrodial joint or symphysis) between vertebral bodies, allowing for mobility and stability of the spine, as well as transmission of load through it. There are two components to the disc: an outer fibrocartilage ring (annulus fibrosus) and a central gelatinous core (nucleus pulposus) (Fig. 5.14). The annulus fibrosus contains collagen fibers arranged in concentric circles that attach to hyaline cartilage end plates on the adjacent vertebral bodies. In contrast the nucleus pulposus is composed of a loose myxoid cartilaginous matrix. The cells of the disc are chondrocytes, as well as stellate to fusiform fibroblastic-appearing cells. It is noteworthy that disc height is not the same in all spine segments. Disc height in the lumbar spine is greater than that in the cervical or thoracic spine.

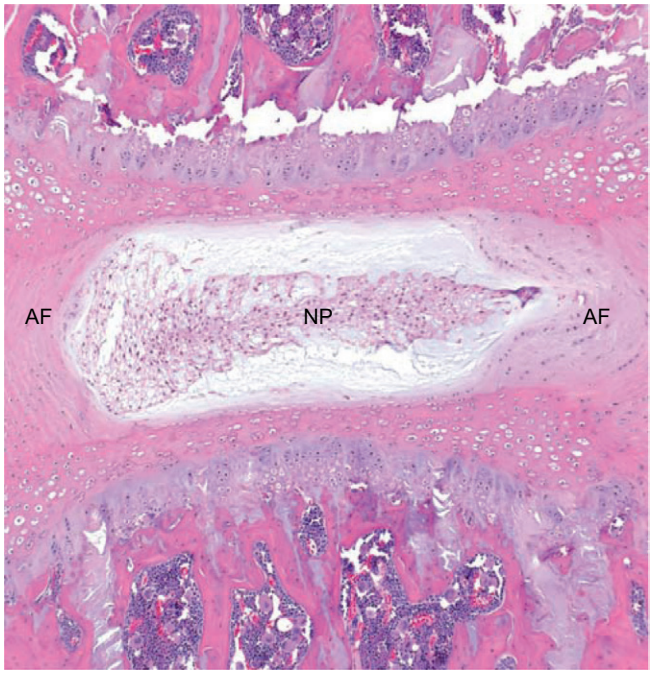

FIGURE 5.14 Intervertebral disc. Rodent (rat) thoracic intervertebral disc. Central nucleus pulposus (NP) comprises loose myxoid cartilaginous matrix. Surrounding collagenous annulus fibrosus (AF) attaches to cartilage end plates of the vertebrae.

JOINTS

GROSS ANATOMY

Bones are connected by joints, which may be classified structurally (based on tissue types) and functionally (based on range of movement). Fibrous and cartilaginous joints permit no movement (synarthrosis) or only slight movement (amphiarthrosis). Synovial joints such as the knee (Fig. 5.15) and shoulder permit extensive movement (diarthrosis). The soft tissues of synovial joints, including synovium, meniscus, joint capsule, tendons, and ligaments, are similar between rodents and humans.

HISTOLOGY

Articular cartilage

In rodents articular cartilage varies between joints, being thicker in larger, more weight-bearing joints. However, overall the cartilage is thinner relative to

(A)

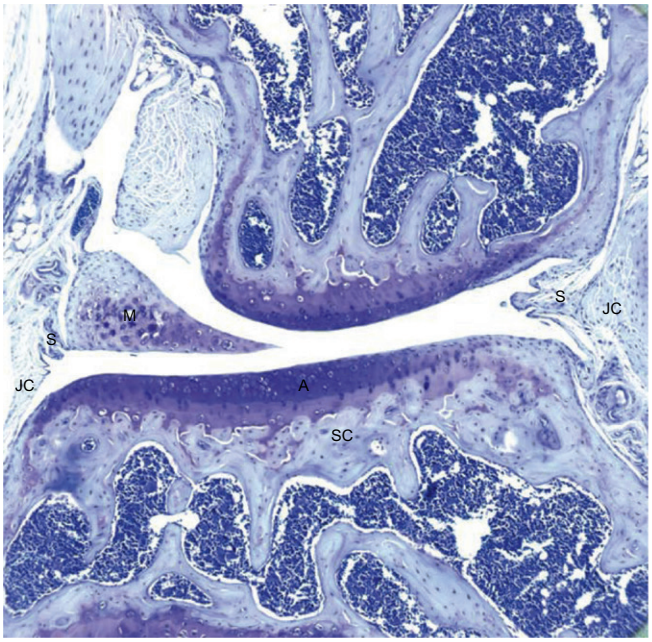

FIGURE 5.15 Knee joint. (A) Rodent (mouse) knee: Coronal section, toluidine blue stain. The major soft tissue structures of synovial joints—synovium (S), meniscus (M), joint capsule (JC), tendons (not shown), and ligaments (not shown)—are similar between humans and rodents. Articular cartilage (A); subchondral bone (SC). (B) Human knee. The knee is a complex structure classified as a diarthrodial joint in both humans and rodents. Source: ©Elsevier, Inc., www.netterimages.com.

Need-to-know

- Menisci commonly ossifiy in rodents.
- Differences between rodents and humans exist in the articular cartilage and subchondral bone (see Fig. 5.7).

(B)

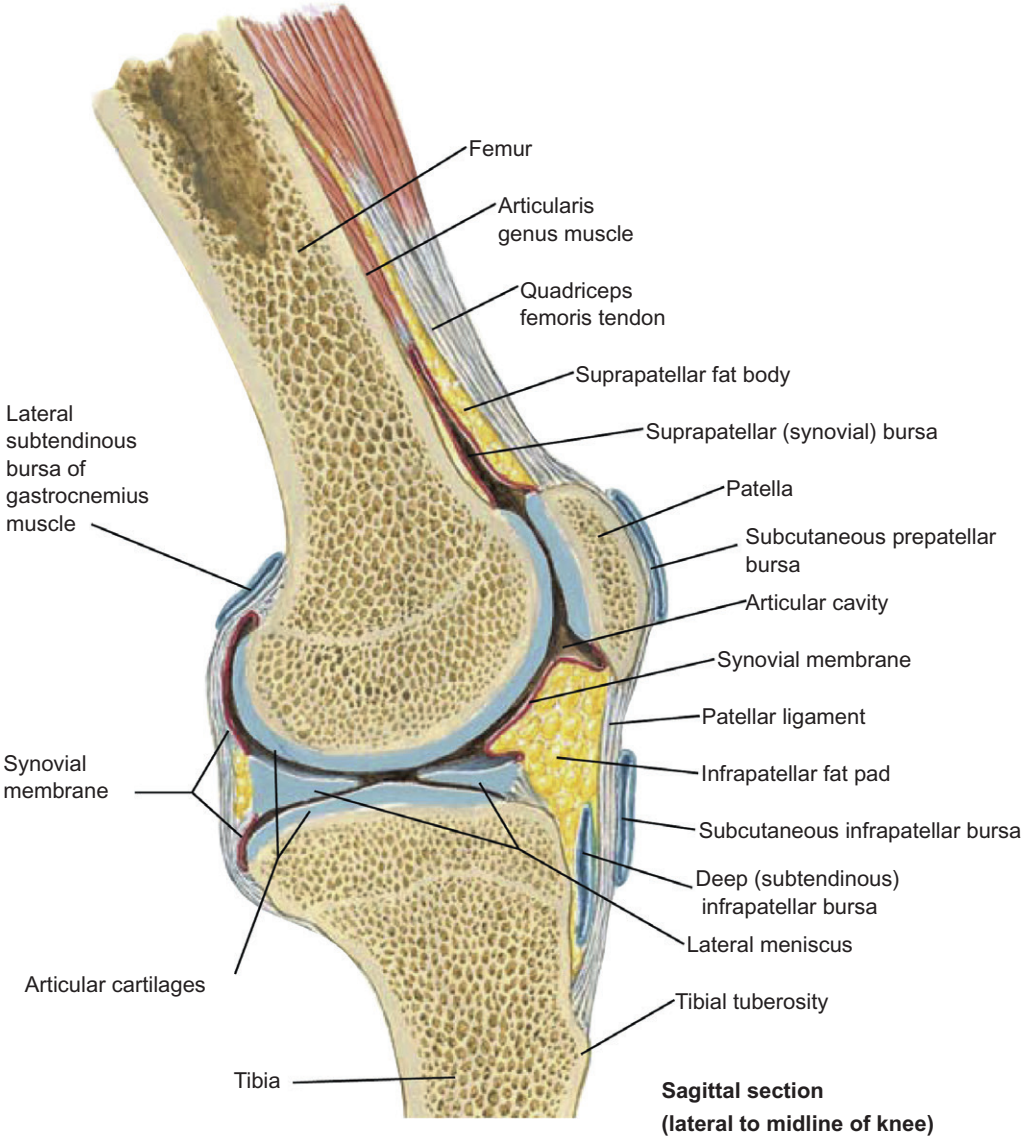

Sagittal section (lateral to midline of knee)

that in humans. The thickness of normal articular cartilage in adult humans is generally 2 or 3 mm, with the major exceptions being the phalanges, in which it is particularly thin (usually not more than 1 mm thick), and the patella, in which it is particularly thick (up to 5 or 6 mm). In both species thickness may also vary within a given joint; e.g., the articular cartilage of the femoral head is thicker over the convexity than at the margins of the joint. In addition, the thickness of articular cartilage tends to be greater in large joints compared to small joints and in parts of the joint where there is considerable pressure (weight). In both rodents and humans microscopic examination shows that articular cartilage is characterized by an abundant glassy matrix containing isolated chondrocytes in lacunae. In both rodents and humans cartilage matrix consists of a meshwork of type II collagen molecules that are cross-linked and smaller amounts of type XI and type IX collagen. The interstitium is filled with aggregates composed of the proteoglycan aggrecan bound to hyaluronan chains. The admixture of collagen, proteoglycan aggregates, and high water content endows articular cartilage with its characteristic mechanical properties.

Human articular cartilage can be divided into four zones. In zone 1, the superficial layer, the cells are relatively small and flat, with their long axis oriented parallel to the articular surface. In zone 2, the intermediate layer, the cells are larger and more sparsely and randomly distributed. In zone 3, the deep layer, the cells are even larger and form radially oriented groups following the collagen fibers in this region. In the calcified zone 4 adjacent to subchondral bone, the matrix is heavily mineralized and the cells are nonviable. These zones are present in adult articular cartilage and are most evident in larger joints. The mineralized matrix at the junction of zones 3 and 4 forms an irregular line known as the tidemark. Articular cartilage is considerably thinner in mice (average thickness = 0.03 mm) and rats (average thickness = 0.1 mm) than in humans and does not contain the distinct superficial, intermediate, and deep zones found in human joints (Figs. 5.7 and 5.15). The calcified zone is present in rodents and is much thicker than that of humans, being approximately equal to or even thicker than the noncalcified articular cartilage. The calcified cartilage zone in rodents also often contains large vacuolated chondrocytes that appear to be normal morphological features of this tissue.

Meniscus

Histologically the matrix of the meniscus is more eosinophilic in H&E stained sections than articular cartilage, reflecting the higher collagen content. Collagen fibers can be readily identified on light microscopy. Rodent menisci commonly exhibit central ossification. The human meniscus is composed of fibrocartilage, primarily containing type I collagen and having a small proportion of proteoglycan. The orientation of the collagen fibers is predominantly circumferential to withstand the loading forces on the meniscus.

Soft Tissues

Comparing rodents to humans, most soft tissues, such as skeletal muscle, tendons, fascia, and ligaments, are histologically similar. Soft tissues such as skin and blood vessels are covered in other chapters.

Adipose tissue of both rodents and humans is organized into subcutaneous and visceral compartments and is composed of white adipose tissue (WAT) and brown adipose tissue (BAT) (Fig. 5.16). Adipose tissue of all three species meets the physiological requirements of energy storage (WAT) and heat production (BAT). BAT is involved in thermoregulation by its ability to uncouple oxidative phosphorylation to produce heat. In rodents adipose tissue of the anterior subcutaneous compartment has a pyramidal shape and lies in the interscapular region, and adipose tissue of the posterior subcutaneous compartment

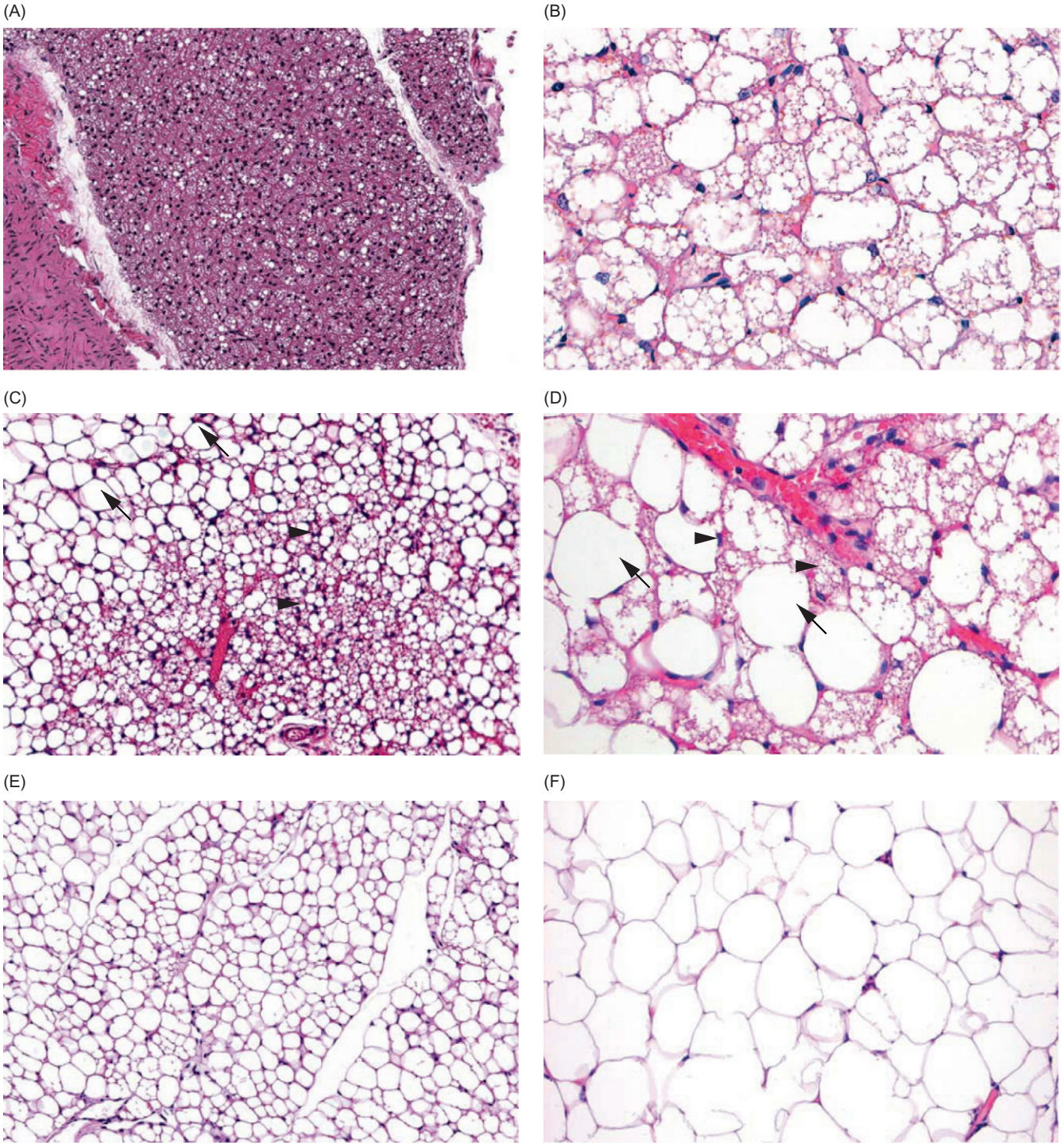

FIGURE 5.16 Adipose tissue. (A) Rodent (mouse) mediastinal (periaortic) brown adipose tissue (BAT). (B) Human BAT. (C) Rodent (mouse) epididymal BAT (arrowheads) admixed with white adipocytes (arrows). (D) Human BAT (arrowheads) admixed with white adipocytes (arrows). (E) Rodent (mouse) white adipose tissue (WAT). (F) Human WAT.

Need-to-know

- Although rodent and human adipose tissues are histologically similar, their distribution is different.
- Brown adipose tissue persists into adulthood to a much greater degree in rodents than in humans.

lies at the base of the hind legs and involves the lumbar, inguinal, pubic, and gluteal regions. Adipose tissue deposits are also found in the limbs, particularly the thigh and popliteal fossa regions of the hind legs. The visceral compartment consists of mediastinal, abdominal, and retroperitoneal deposits. Rodent adipose tissue is composed of both WAT and BAT into adulthood, with the anterior subcutaneous compartment predominantly composed of BAT.

In humans adipose tissue is also organized into subcutaneous and visceral compartments. However, the subcutaneous compartment consists of a continuous sheet of fat around virtually all parts of the body, with larger deposits found in the gluteal and mammary regions of females. The human visceral compartment is similar to that of rodents. In humans BAT represents approximately 5% of body weight in neonates and gradually declines with age. This is in contrast to rodent BAT, which represents approximately 1–2% of body weight but increases to 11–12% of body weight several days after birth. Partial BAT regression occurs several weeks after birth, but this tissue is retained in rodents in adulthood. Although it had previously been thought that adult humans lack BAT, it is now confirmed that BAT can persist into adulthood, predominantly in the neck and supraclavicular region.

FURTHER READING

Aguila HL, Rowe DW: Skeletal development, bone remodeling, and hematopoiesis. *Immunol Rev* 208:7–18, 2005.

Bab I, Hajbi-Yonissi C, Gabet Y, et al: *Micro-tomographic atlas of the mouse skeleton*, New York: Springer, 2007.

Bullough P: Normal bone structure and development. In Bullough P, editor: *Orthopaedic pathology* (ed 4), New York: Mosby, 2004.

Chan EF, Harjanto R, Asahara H, et al: Structural and functional maturation of distal femoral cartilage and bone during postnatal development and growth in humans and mice. *Orthop Clin North Am* 43:173–185, 2012.

Cole HA, Yuasa M, Hawley G, et al: Differential development of the distal and proximal femoral epiphysis and physis in mice. *Bone* 52:337–346, 2013.

Eriksen EF: Normal and pathological remodeling of human trabecular bone: three dimensional reconstruction of the remodeling sequence in normals and in metabolic bone disease. *Endocr Rev* 7:379–408, 1986.

Fazzi R, Galimberti S, Testi R, et al: Bone and bone marrow interactions: hematological activity of osteoblastic growth peptide (OGP)-derived carboxy-terminal pentapeptide II. Action on human hematopoietic stem cells. *Leuk Res* 26:839–848, 2002.

Ferguson VL, Ayers RA, Bateman TA, et al: Bone development and age-related bone loss in male C57BL/6J mice. *Bone* 33:387–398, 2003.

Frontini A, Cinti S: Distribution and development of brown adipocytes in the murine and human adipose organ. *Cell Metab* 11:253–256, 2010.

Glasson SS, Chambers MG, Van Den Berg WB, et al: The OARSI histopathology initiative—Recommendations for histological assessments of osteoarthritis in the mouse. *Osteoarthr Cartil* 18:S17–S23, 2010.

Halloran BP, Ferguson VL, Simske SJ, et al: Changes in bone structure and mass with advancing age in the male C57BL/6J mouse. *J Bone Miner Res* 17:1044–1050, 2002.

Hansson LI, Menander-Sellman K, Stenström A, et al: Rate of normal longitudinal bone growth in the rat. *Calc Tiss Res* 10:238–251, 1972.

Hughes PCR, Tanner JM: The assessment of skeletal maturity in the growing rat. *J Anat* 106:371–402, 1970.

Interlichia JP, Williams NG, Rodgers BD: A rapid, valid and inexpensive assay for measuring epiphyseal plates in mouse tibia. *Growth Horm IGF Res* 20:171–173, 2010.

Isern J, Méndez-Ferrer S: Stem cell interactions in a bone marrow niche. *Curr Osteoporos Rep* 9:210–218, 2011.

Johnson DR, Kida MY: Development of the spinous process of the second thoracic vertebra of the mouse in the late fetal and early postnatal period. *Okajimas Folia Anat Jpn* 72(1):45–49, 1995 May.

Johnson DR, McAndrew TJ, Oguz O: Shape differences in the cervical and upper thoracic vertebrae in rats (*Rattus norvegicus*) and bats (*Pteropus poiocephalus*): can we see shape patterns derived from position in column and species membership? *J Anat* 194(Pt 2):249–253, 1999 Feb.

Martin RB: Toward a unifying theory of bone remodeling. *Bone* 26:1–6, 2000.

McCoy AM: Animal models of osteoarthritis: comparisons and key considerations. *Vet Pathol* 52:803–818, 2015.

Morini S, Pannarale L, Franchitto A, et al: Microvascular features and ossification process in the femoral head of growing rats. *J Anat* 195:225–233, 1999.

Parfitt AM, Drezner MK, Glorieux FH, et al: Bone histomorphometry: standardization of nomenclature, symbols, and units. Report of the ASBMR Histomorphometry Nomenclature Committee. *J Bone Miner Res* 2:595–610, 1987.

Roach HI, Mehta G, Oreffo RO, et al: Temporal analysis of rat growth plates: cessation of growth with age despite presence of a physis. *J Histochem Cytochem* 51:373–383, 2003.

Sengupta P: The laboratory rat: relating its age with human's. *Int J Prev Med* 4:624–630, 2013.

Somerville JM, Aspden RM, Armour KE, et al: Growth of C57Bl/6 mice and the material and mechanical properties of cortical bone from the tibia. *Calcif Tissue Int* 74:469–475, 2004.

Suttie AW, Leininger JR, Bradley AE, editors: *Boorman's pathology of the rat* (ed 2), San Diego: Academic Press, 2017.

Travlos GS: Normal structure, function, and histology of the bone marrow. *Toxicol Pathol* 34:548–565, 2006.

Turner CH, Burr DB: Basic biomechanical measurements of bone: a tutorial. *Bone* 14:595–608, 1993.

White TD, Folkens PA: *Human osteology* (ed 2), San Diego: Academic Press, 2000.

NOSE, SINUS, PHARYNX, AND LARYNX 6

JACK R. HARKEMA, STEPHAN A. CAREY AND JAMES G. WAGNER
Michigan State University, College of Veterinary Medicine, East Lansing, MI, United States

SUZANNE M. DINTZIS AND DENNY LIGGITT
University of Washington School of Medicine, Seattle, WA, United States

Introduction

For all mammalian species, the nose serves as the portal of entry for the air they breathe. This complex organ of the respiratory system is important not only for smell but also for conditioning the inhaled air before it enters the lungs. The nose is well structured to perform these functions, but to differing degrees in rodents and primates, including humans. Despite obvious postural and body size differences, the rodent and human pharynx and larynx share many functional and structural similarities. These include reasonable consistency in the types of covering epithelium, including the presence of intermediate zones, and subepithelial structures. Differences of note involve portions of the structure of the Eustachian (pharyngotympanic or auditory) tube, some laryngeal and vocal cord components, submucosal lymphoid elements, and taste buds.

In the past three decades, major scientific advances have been made in the field of nasal toxicology by using laboratory rodents in short- and long-term inhalation studies. This field of toxicology has grown exponentially since the first published reports by Swenberg et al. (1980) stating that long-term inhalation exposures to high concentrations of formaldehyde induce nasal tumors in laboratory rodents. This previously underexamined part of the respiratory tract has also been the recent focus of reported research efforts in a variety of other scientific disciplines, including neuroscience, molecular biology, respiratory biology, and even paleontology. The tremendous discoveries made during the past decade in the area of olfactory science were highlighted worldwide when Drs. Linda Buck and Richard Axel were awarded the 2004 Nobel Prize in Biology for their pioneering work on the cellular and molecular mechanisms of olfaction. Many of their discoveries were made with in vivo studies using laboratory mice.

This chapter provides a detailed description of the macro- and microscopic anatomy of the rodent nose, sinuses, larynx, and pharynx, and it highlights similarities and differences in structure and function between rodents and humans who are represented by non-human primates (NHP) in many figures. The similarities and differences are important to understand when utilizing rodent models of human nasal airways and associated paranasal sinuses diseases or toxicology.

Comparative Anatomy and Histology. DOI: http://dx.doi.org/10.1016/B978-0-12-802900-8.00006-3
© 2018 Elsevier Inc. All rights reserved.

Nose and Sinus

GROSS ANATOMY

In both rodents and humans, the nose is the portal of entry for the respiratory system. In addition to serving as the sensory organ for smell (olfaction), the nose also functions as an air conditioner and a defender of the lower respiratory tract by filtering, humidifying, and heating the inhaled air. In addition, it protects the delicate gas-exchange regions of the lung by effectively absorbing water-soluble and reactive gases and vapors, trapping inhaled particles, and metabolizing airborne xenobiotics. In general, rodents have much more complex turbinate structures than do primates, including humans. In addition, the nasal cavity of primates is lined by much less olfactory epithelium (OE) than that of rodents. The cellular composition of the nasal mucosa is dependent on both the intranasal location and the animal species.

Both the rodent and the human nasal cavity are divided into two main air passages by the nasal septum. Each nasal passage extends from the nostril openings (nares) to the nasopharynx (Fig. 6.1 and Table 6.1). The nasopharynx is defined as the airway posterior to the termination of the nasal septum and proximal to the termination of the soft palate. Inhaled air flows through the nares into the vestibule, which is a slight dilatation just inside the nares before the main chamber of the nose. Unlike the more distal main chamber that is surrounded by bone, the nasal vestibule is surrounded by flexible cartilage. The luminal surface is lined by a squamous epithelium (SE) similar to that of external skin (Fig. 6.1). In humans, unlike in laboratory rodents, the nasal vestibule also contains varying numbers of hair follicles near the nares.

After passing through the nasal vestibule, inhaled air courses through the narrowest part

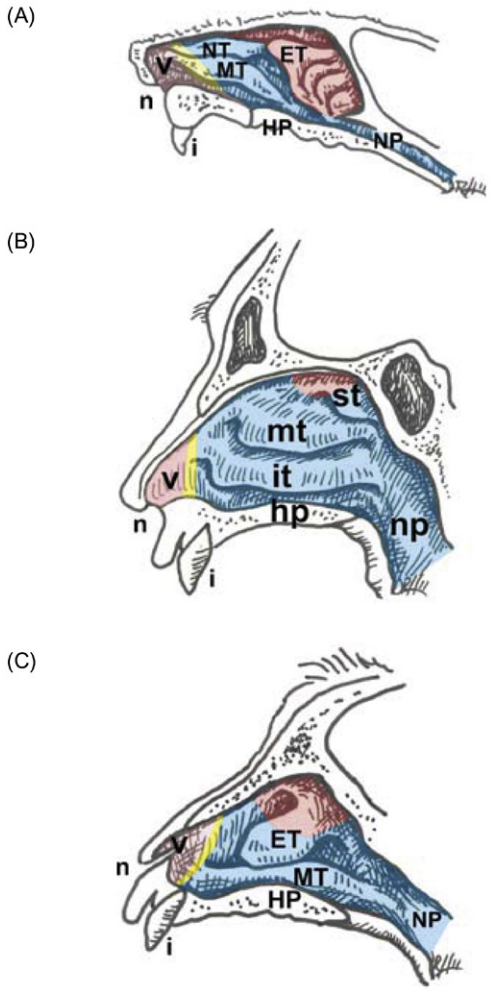

FIGURE 6.1 Schematic drawings of the right nasal passages. (A) Rodent (mouse). (B) Human. (C) NHP. The septum has been removed, exposing the lateral wall. Colors represent the intranasal distribution of surface epithelial types lining the nasal airways. Pink, yellow, blue, and red represent the squamous, transitional, respiratory, and OE, respectively. ET, ethmoid turbinate(s); hp, hard palate; i, incisor tooth; it, inferior turbinate; mt, middle turbinate; MT, maxilloturbinate; n, nostril (naris); NT, nasoturbinate; st, superior turbinate; v, nasal vestibule.

Need-to-know

- The anatomy of the rodent nasal passage is complex relative to that of humans.
- Unlike humans, rodents are obligate nose breathers.
- Nasal function is primarily olfactory in rodents and primarily breathing in humans.
- The surface of the nasal vestibule is lined by squamous epithelium in both rodents and humans, although in humans hair follicles are present near the nares.

TABLE 6.1 Nose And Sinus

Feature	Rodent	Human
	Gross	
Nasal passage	Complex anatomy with olfaction as primary function	Relatively simple anatomic structure with breathing as primary function
Breathing	Obligate nose breathers	Both nasal and oral breathing possible
Nasal vestibule	Surface lined by SE; Lacks hair follicles	Surface is lined by SE; Hair follicles are present near nares
Nasal turbinates	Complex structure with total surface area of approximately 2.9 cm^2 (relative surface area about 5X greater than humans) provides better protection to lower respiratory tract	Relatively simple structure with total surface area of 150–200 cm^2 provides less protection from airborne particles and gases
Paranasal sinuses	Bilateral maxillary sinus only	Multiple paranasal sinuses, including maxillary, frontal, ethmoid, and sphenoid
Accessory olfactory organs	VNO, septal organs of Masera, and Grüneberg Present within the main nasal chamber of rodents	Not well developed or functional
Lymphoid tissues	Focal aggregates with limited distribution. Represented by LE and NALT	More abundant than in rodents. Represented by tonsillar tissues and other aggregates of Waldeyer's ring
	Histologic	
Nonolfactory nasal epithelia (squamous, transitional, and respiratory)	Squamous is relatively thin, transitional is one or two cell layers thick and composed of three cell types, and the majority is respiratory. Together they account for less than 50% of the mouse nasal cavity	Squamous is relatively thick. Transitional is similar to rodent but is four or five cell layers thick and composed of at least five cell types, and respiratory covers most of the nasal cavity and is much thicker. Distribution of cell types varies between species
OE	Lines approximately 50% of the nasal cavity. Facilitates heightened olfactory function	Lines approximately 3% of nasal cavity. Cellular composition of similar to rodent

of the entire respiratory tract, the nasal valve (ostium internum), before entering the main nasal chamber. A lateral wall, septal wall, roof, and floor define each nasal passage of the main chamber. The lumen of the main chamber is lined by the nasal mucosa, well-vascularized and innervated mucous membranes that are covered by a continuous layer of mucus. The nasal mucous layer is moved distally by the synchronous beating of motile cilia to the oropharynx, where it is swallowed into the esophagus.

Turbinates, bony structures lined by the well-vascularized mucosal tissue, project into the airway lumen from the lateral walls into the main chamber of the nose in rodents, nonhuman primates, and humans (Fig. 6.1). The human nose has three turbinates: superior, middle, and inferior (Fig. 6.1). These structures are relatively simple in shape compared to turbinates of rodents, which have complex folding and branching patterns. Nasal turbinates increase the inner surface area of the nose, which is important in filtering, humidifying, and warming of the inspired air. The nasal airway of 16-week-old male B65C3F1 mice is 5 mm long, 0.03 cm^3 (30 µL) in total volume (both passages), and has a total surface area of 2.90 cm^2 (compared to 1.34 cm^2 for 16-week-old Fischer 344 (F344) rats). The turbinated main chamber in humans is approximately 5–8 cm long, 6–10 cm^3 in volume (one passage), and has a total surface area (both passages) of 150–200 cm^2. Relative surface area (i.e., surface area/volume) of the nasal cavity, however, is approximately five times greater in rodents than in humans, due principally to the greater complexity of their nasal turbinates.

Although there are some general similarities between the nasal passages of rodents, nonhuman primates, and humans, there are also striking species differences in nasal architecture (Fig. 6.1). From a comparative viewpoint, rodents have more

complex noses with olfaction as the primary function (macrosmatic), whereas humans have relatively simple noses with breathing as the primary function (microsmatic). In addition, rodents are obligate nose breathers due to the close apposition of the epiglottis to the soft palate. The nasal and oral cavities of humans (and most nonhuman primates) are arranged in a manner to allow for both nasal and oral breathing. Interspecies variability in nasal gross anatomy has been emphasized in previous reviews listed in Further Reading.

The marked difference in nasal airflow patterns between rodents and humans is primarily due to the species-specific variation in number and shape of the nasal turbinates. In rodents, evolutionary pressures concerned chiefly with olfactory function and dentition have defined the shape of the turbinates and the type and distribution of the cells lining these structures. In the proximal nasal airway, the complex naso- and maxilloturbinates of rodents are thought to provide better protection of the lower respiratory tract due to enhanced filtration, absorption, and disposal of airborne particles and gases compared to the simple structure of the middle and inferior turbinates in the human nose. The highly complex shape of the ethmoid turbinates, lined predominantly by olfactory neuroepithelium, in the distal half of the nasal cavity of rodents is suitably designed for acute olfaction. Differences in the complexity of the gross turbinate structure throughout the nasal airway of the rodent are illustrated in Fig. 6.2.

In all three species, luminal surfaces of the nasal mucosa (with the exception of the most proximal regions of the nasal vestibule) are lined by a watery, sticky material (mucus) that is secreted from mucous (goblet) cells in surface epithelium and from underlying glands in the lamina propria. Its physical and chemical properties are well suited for its role in upper airway defense: trapping inhaled particles and scrubbing out certain reactive gases. The synchronized beating of airway surface cilia propels the nasal mucus at different speeds and directions depending on the intranasal location. Mucus covering the olfactory mucosa moves very slowly, with a turnover time of probably several days. In contrast, mucus covering the respiratory mucosa is driven along rapidly (1–30 mm/min) by synchronized beating of cilia, with an estimated turnover time in laboratory rats of approximately 10 min. Similar comprehensive measurements have not been made in mice or humans.

Nasal mucus containing entrapped materials is ultimately propelled by beating cilia to the naso- and oropharynx, swallowed into the esophagus, and cleared through the digestive tract. The nasal mucociliary apparatus (i.e., mucus and cilia) exhibits a range of responses to inhaled xenobiotic agents and can be a sensitive indicator of toxicity. Because this upper airway apparatus is one of the first lines of defense against inhaled pathogens, dusts, and irritant gases, toxicant-induced compromises in its defense capabilities can lead to increased nasal infections and increased susceptibility to lower respiratory tract diseases.

PREPARATION OF NASAL TISSUES FOR MICROSCOPIC EXAM

Excellent detailed descriptions of how to prepare the nasal cavity of rodents for light microscopic examination have been published (see Further Reading). Special attention to fixation, decalcification, and uniform sampling is required due to the anatomical complexity of this organ and its encasement within bone. The first systematic approach for sectioning the nasal passages of laboratory rodents for toxicologic studies was described by Young (1981). Although others have made minor variations to this methodology, it still serves as the best scheme for consistent tissue sampling of rodent nasal passages for routine histopathologic evaluation. Similar tissue selection approaches for the microscopic examination of the nasal airways of nonhuman primates have been used by others (Fig. 6.2C and D). More sections may be needed under certain research or diagnostic circumstances.

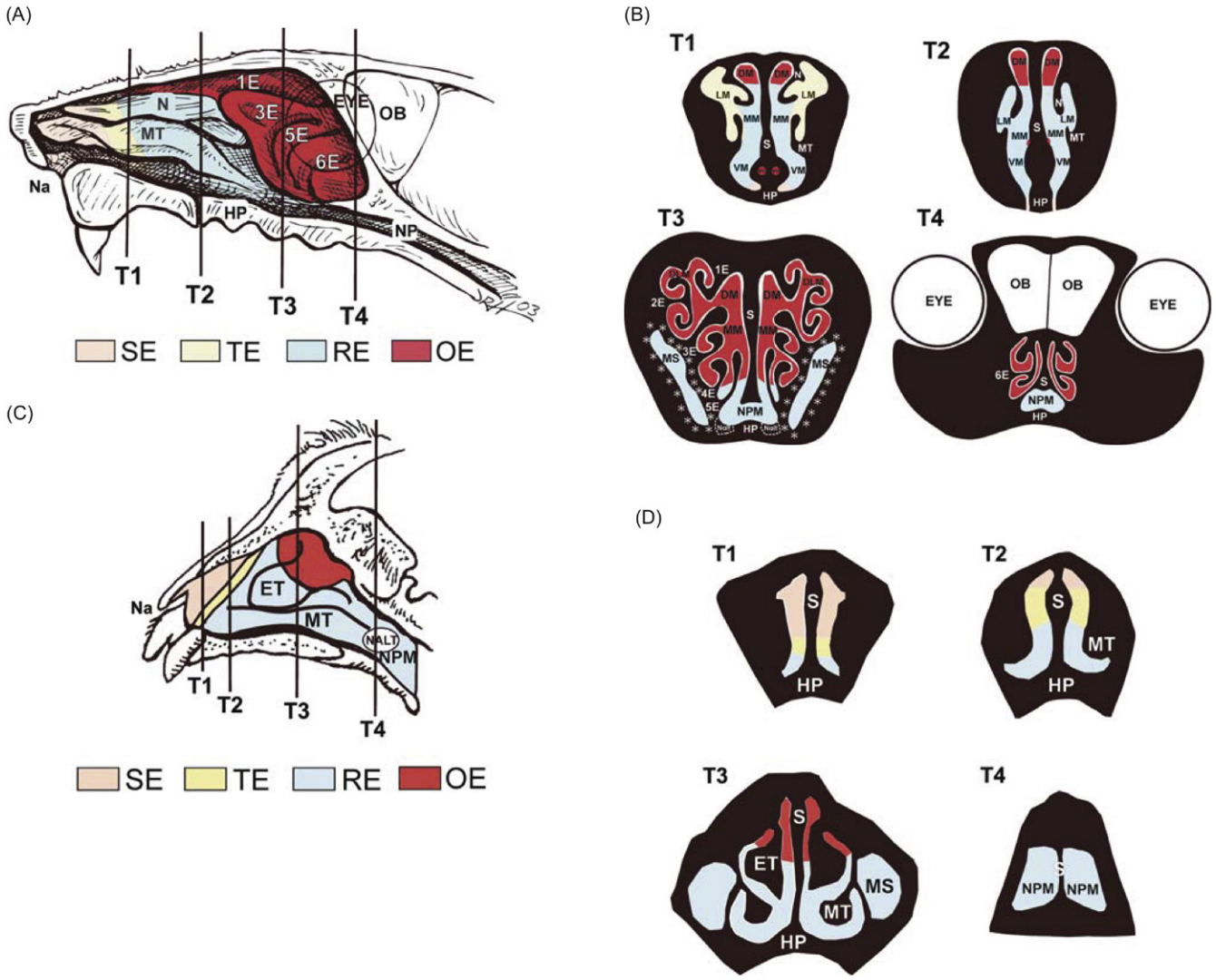

FIGURE 6.2 Nasal passage. (A) Diagrammatic representation of the right nasal passage of a rodent (mouse). Nasal septum has been removed to expose the turbinates (N, nasoturbinate; MT, maxilloturbinate; 1E, 3E, 5E, and 6E, ethmoid turbinates). Vertical lines represent the rostral surfaces of transverse sections (T1–T4) taken at different levels throughout the nasal passage. Colored areas represent the intranasal regions lined by different surface epithelia: tan, SE; yellow, TE; blue, RE; red, OE. (B) Transverse sections at different levels of the rodent (mouse) nasal cavity (T1–T4). DM, dorsal medial meatus; HP, hard palate; LM, lateral meatus; MM, medial meatus; MS, maxillary sinus; MT, maxilloturbinate; N, nasoturbinate; NPM, nasopharyngeal meatus; OB, olfactory bulb of brain; S, septum; VM, ventral meatus; VO, vomeronasal organ; 1E–6E, ethmoid turbinates. (C) Schematic representation of the lateral wall of the right nasal passage from the nose of a primate (Rhesus macaque). The nasal septum has been removed to expose the turbinates (maxilloturbinate and ethmoid turbinate). Vertical lines represent the rostral surfaces of transverse sections T1–T4 taken at different levels throughout the nasal cavity. Colored areas represent the intranasal regions lined by different surface epithelia: tan, SE; yellow, TE; blue, RE; red, OE. (D) Cross sections at different levels of the primate nasal cavity (T1–T4). ET, ethmoid turbinate; HP, hard palate; MS, maxillary sinus; MT, maxilloturbinate; NPM, nasopharyngeal meatus; S, septum.

Need-to-know

- The structure of the nasal turbinates is more complex in rodents than in humans.
- The relative turbinate surface area is approximately five times greater in rodents.

Fig. 6.2A and B illustrates four transverse sections of the rodent nose routinely sampled for light microscopic examination. These nasal tissue sections are taken at specific anatomic locations that are identified by dental or palatine landmarks. The most proximal tissue section, T1, is taken immediately posterior to the upper incisor teeth and contains the proximal aspects

of the nasal septum, naso- and maxilloturbinates, and the intranasal vomeronasal organ (VNO) as its prominent morphologic features. Tissue section 2 (T2) is taken at the level of the incisive papilla and duct that connects the nasal and oral cavities. The principal morphologic features in T2 are the distal aspects of the naso- and maxilloturbinates and the midseptum. Sometimes, a cross section of the very proximal tip of the third ethmoid turbinate is also present in the dorsomedial aspect of one or both of the nasal passages, depending on the cut of this section. The third transverse tissue section (T3) is taken at the level of the second palatal ridge and contains the elaborate ethmoid turbinates, an intramural maxillary sinus adjacent to each nasal passage, and the distal nasal septum that incompletely separates the two nasal passages at this level. The last is called the "septal window" or opening that joins the two nasal airways with the entrance to the nasopharyngeal meatus.

The most distal nasal tissue section (T4) is taken at the level of the first molar teeth and contains the cross-sectional profiles of the distal aspects of nasal septum and ethmoid turbinates and the proximal nasopharyngeal meatus. Fig. 6.2 also provides a general map of the intranasal distribution of the principal nasal epithelia that line the luminal surfaces of the nasal airways of the rodent and primate.

HISTOLOGY

In addition to differences in the gross architecture of the nose in rodents and humans, there are also species differences in the surface epithelial cell populations lining the nasal passages. These differences are found in the distribution of nasal epithelial populations and in the types of nasal cells within these populations. However, both rodents and humans have four distinct nasal epithelial populations: (1) SE, which is primarily restricted to the nasal vestibule; (2) respiratory epithelium (RE), the ciliated, pseudostratified, cuboidal/columnar epithelium found in the main chamber and nasopharynx; (3) transitional epithelium (TE), the poorly ciliated cuboidal/columnar epithelium, lying between SE and RE in the proximal aspect of the main chamber; and (4) OE, located in the dorsal or dorsoposterior aspect of the nasal cavity. Figs. 6.1 and 6.2 illustrate the distribution of nasal epithelia in the rodent nasal cavity. The reader is also referred to other reports in Further Reading for a more thorough and detailed description of the intranasal distribution of airway surface epithelia in rodents and nonhuman primates.

Squamous Epithelium

The nasal vestibule in both rodents and humans is completely lined by stratified SE. It is composed of basal cells along the basal lamina and several layers of squamous cells, which become progressively flatter toward the luminal surface of the airway (Fig. 6.3). This region of the nasal mucosa probably functions similarly to the epidermis of skin to protect the underlying tissues from potentially harmful environmental agents. T1 of rodents contains a small amount of SE lining the floor of the ventral meatus in each nasal passage. Although the cellular composition is similar among rodent and primate species, SE is much thicker in primates (Fig. 6.4).

Transitional Epithelium

Between the stratified SE and the ciliated RE is a narrow zone of poorly or nonciliated, microvilli-covered cuboidal/columnar surface epithelium, which has been referred to as nasal nonciliated or scantly ciliated RE, or nasal TE (Figs. 6.3 and 6.4). Common, distinctive features of TE in rodents and primates include (1) an anatomic location in the proximal aspect of the nasal cavity between the SE and RE, (2) the presence of numerous nonciliated cuboidal or columnar surface cells and basal cells, (3) few ciliated cells and a scarcity of goblet cells, and (4) an abrupt morphologic

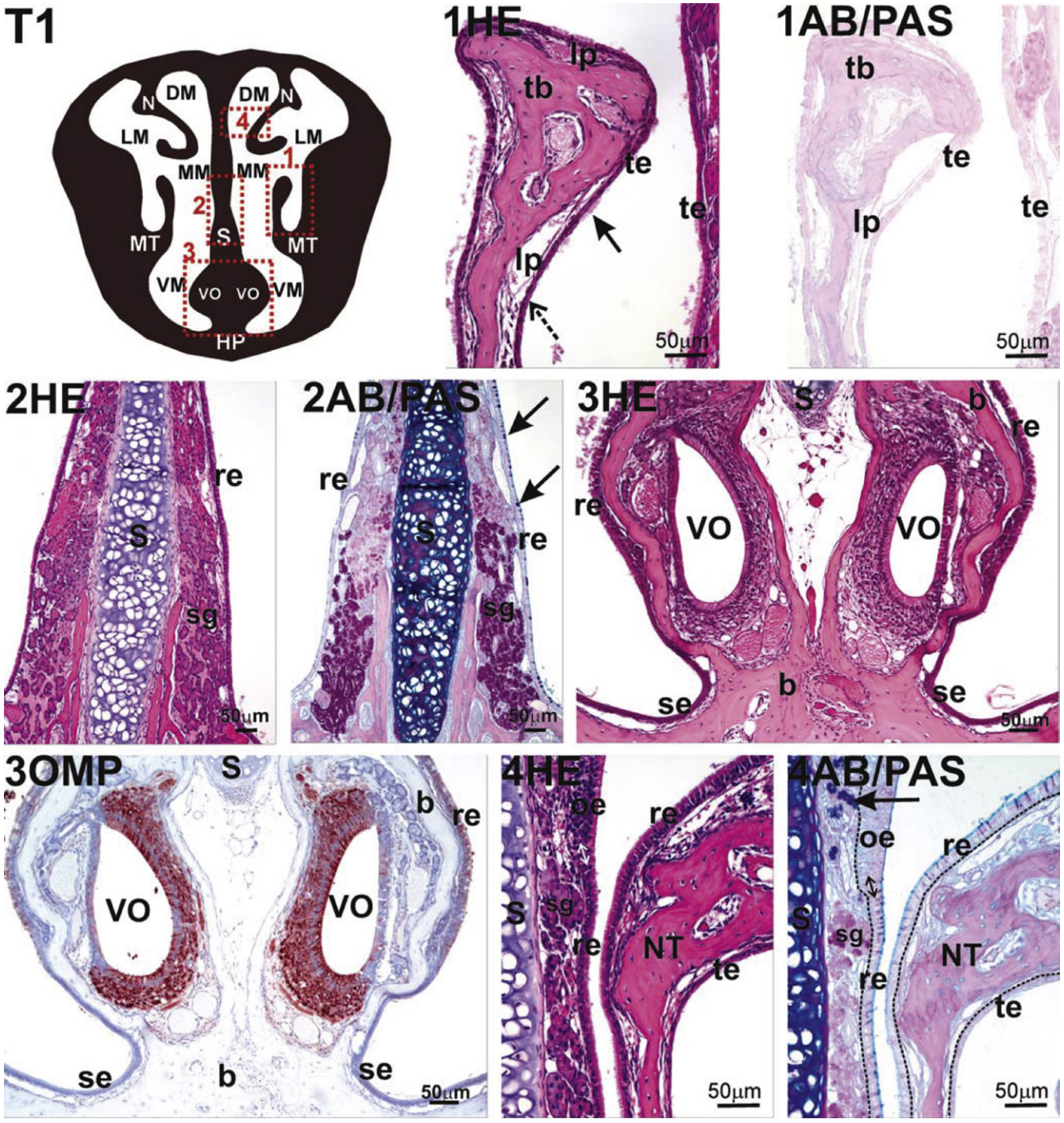

FIGURE 6.3 Rodent (mouse) nose. (T1) Schematic representation of the cross-sectional profile of the proximal aspect of the nose (T1 level). Rodents have several accessory olfactory organs that are missing or poorly developed in humans. DM, dorsomeatus; HP, hard palate; LM, lateral meatus; MM, middle meatus; MT; maxilloturbinate; N, nasoturbinate; S, septum; VM, ventral meatus; VO, vomeronasal organ. Rectangles 1–4 are the intranasal locations for the light photomicrographs of the maxilloturbinate (1), midseptum (2), ventral septum (3), and nasoturbinate/dorsal septum (4). The remaining figures are light photomicrographs of nasal tissues stained with hematoxylin and eosin (HE), Alcian blue (pH 2.5)/periodic acid–Schiff (AB/PAS; stains for mucosubstances in mucous cells; magenta chromagen), or immunohistochemically for OMP (marker of mature olfactory sensory cells; brown chromagen). (1HE and 1AB/PAS) lp, lamina propria; tb, turbinate bone, te, transitional epithelium; solid arrow, a few ciliated epithelial cells; stippled arrow, nonciliated epithelial cells. There are no AB/PAS-stained mucous cells in te. (2HE and 2AB/PAS) re, respiratory epithelium; S, septal cartilage; sg; septal gland; solid arrows, AB/PAS-stained mucous cells in re. (3HE and 3OMP) b, bone; re, respiratory epithelium; S, septal cartilage; se, squamous epithelium; VO, vomeronasal organ. OMP-stained OSNs in the medial aspect of the VO are lined by OE. (4HE and 4AB/PAS) NT, nasoturbinate; oe, olfactory epithelium; S, septal cartilage; sg; septal gland; solid arrow, AB/PAS-stained Bowman's glands underlying oe; double ended arrow, transition between surface epithelial types.

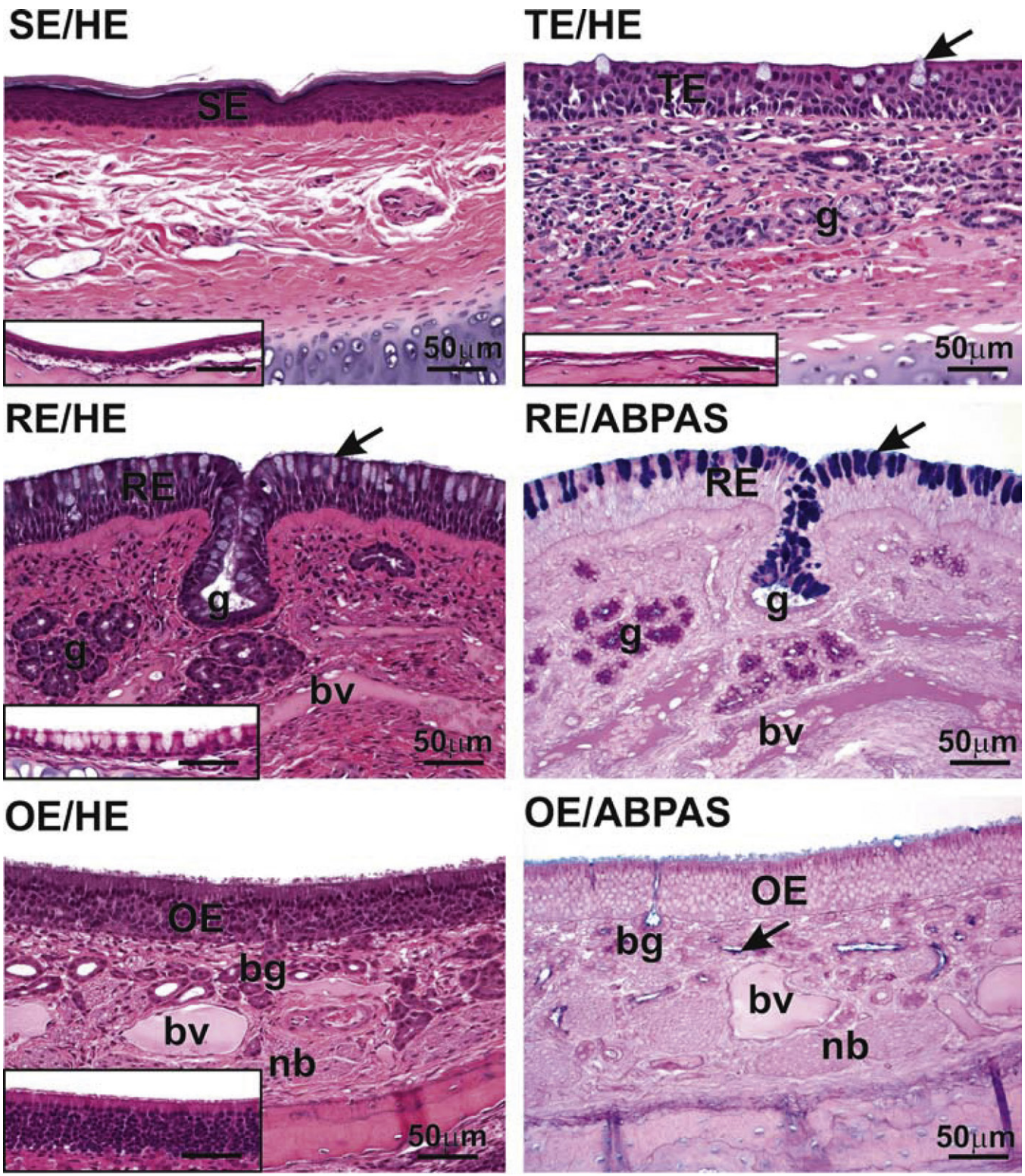

FIGURE 6.4 Nasal epithelia. Light photomicrographs from a rhesus macaque NHP stained with hematoxylin and eosin (HE), Alcian blue (pH 2.5)/periodic acid–Schiff (ABPAS; stains for mucosubstances in mucous cells; magenta chromagen), or immunohistochemically for OMP (marker of mature olfactory sensory cells; brown chromagen). Images from a mouse at the same magnification are present in the small insets. bg, Bowman's glands in lamina propria underlying OE; bv; blood vessels; g, glands in lamina propria underlying RE or TE; nb; nerve bundles containing axons of olfactory sensory cells in lamina propria.

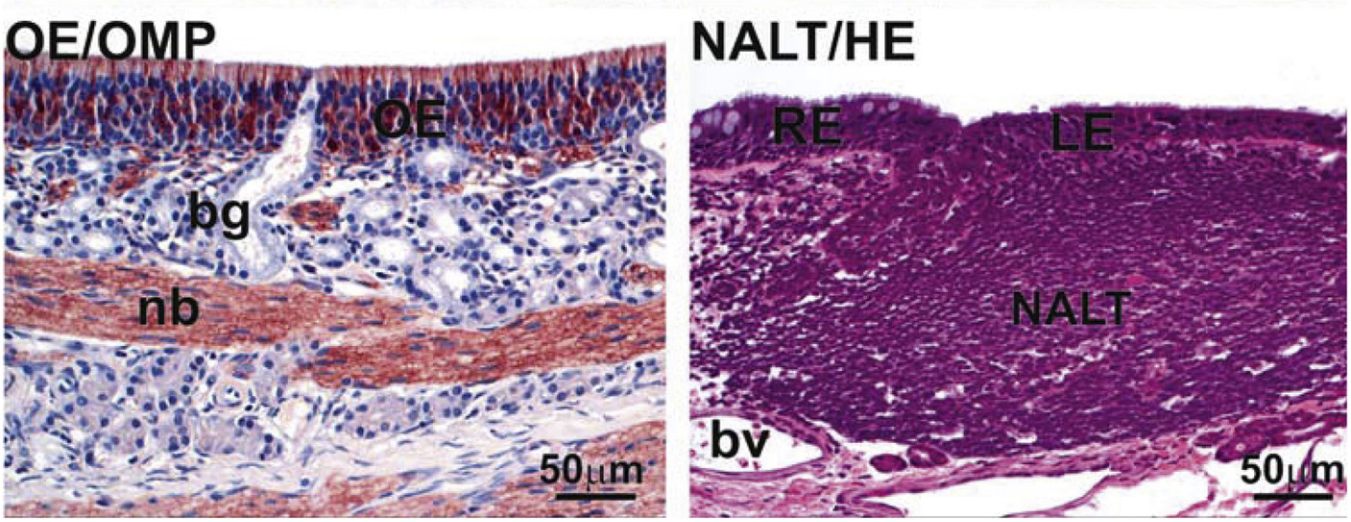

FIGURE 6.4 (Continued)

border with SE, but a less abrupt border with RE. In T1 of rodents, TE lines the luminal surfaces of the lateral wall, maxilloturbinate, and medial aspect of the nasoturbinate. These epithelial surfaces border the lateral meatus in the proximal nasal airways. Rodent TE is thin (one or two cells thick), pseudostratified, and composed of three nonciliated cell types (basal, columnar, and cuboidal) and scattered ciliated cells. In contrast, TE of primates is thick (four or five cells), stratified, and composed of at least five different epithelial cell types including goblet cells (Fig. 6.4).

Luminal, nonciliated TE cells in rodents rarely contain secretory granules, but do have abundant smooth endoplasmic reticulum (SER) in their apices. SER is an important intracellular site for xenobiotic-metabolizing enzymes, including cytochrome P450. The prominence of SER in these cells, as well as in the sustentacular cells of OE, suggests metabolizing capability for certain inhaled and noninhaled xenobiotics.

In both rodents and humans, the lamina propria beneath the TE and RE is a highly vascularized and innervated, loose fibroelastic connective tissue containing serous and seromucous secretory glands. Cavernous venous plexuses, sometimes referred to as "swell bodies," are also present in the

Need-to-know

- Nasal squamous epithelium is relatively thin in rodents compared to humans.
- Olfactory epithelium is the predominant epithelium in the rodent nasal cavity, whereas in primates, it is respiratory.

lamina propria of the nasal mucosa and located in distinct regions along the nasal airway. Dilation of these vessels is thought to alter nasal airflow by thickening the mucosa, narrowing air passages, and diverting inhaled air. Prominent swell bodies in rodents are found in the maxilloturbinates and lateral wall in the proximal nasal passage.

Respiratory Epithelium

The majority of the nonolfactory nasal epithelium of rodents and primates is RE (Fig. 6.1). RE is a pseudostratified, cuboidal/columnar, ciliated epithelium (Figs. 6.4–6.7). Most of the nasal cavity in primates is lined by RE (Fig. 6.1). In laboratory rodents, however, less than half of the nasal cavity is covered by RE (see the following section on OE). In both rodents and primates, the maxillary sinus is also lined by RE. Like SE, RE in primates is much thicker than in rodents (Fig. 6.4).

RE in the nasal cavity of rodents is composed of morphologically distinct cell types that include numerous ciliated (which are most abundant), goblet, and basal cells and lesser numbers of nonciliated columnar/cuboidal cells, including

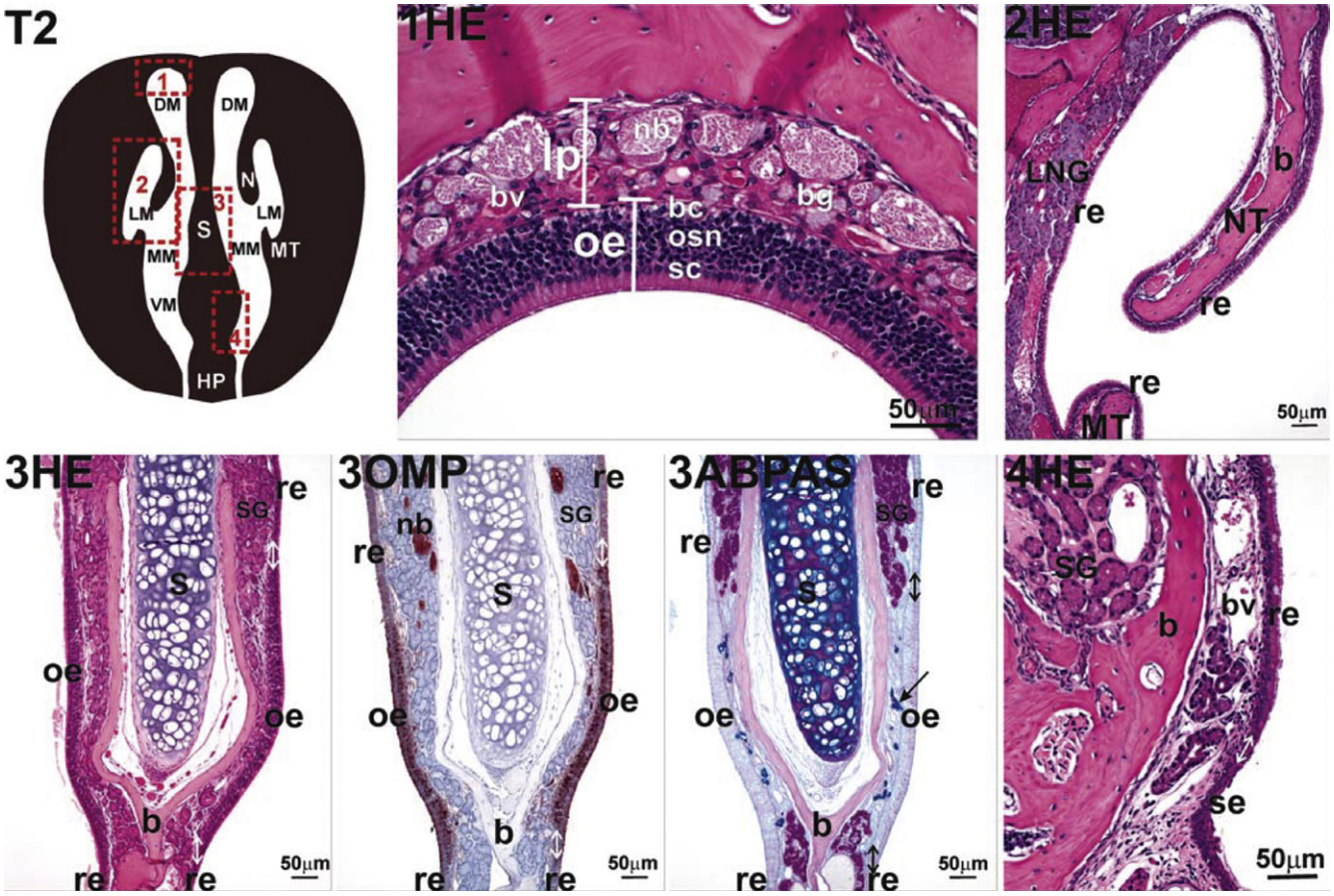

FIGURE 6.5 Rodent (mouse) nose (T2). Schematic representation of the cross-sectional profile of the nose at level T2. DM, dorsomeatus; HP, hard palate; LM, lateral meatus; MM, middle meatus; MT, maxilloturbinate; N, nasoturbinate; S, septum; VM, ventral meatus. Rectangles are the intranasal locations for the light photomicrographs of nasal epithelium lining the dorsal meatus (1), lateral meatus (2), midseptum (3), and ventral septum (4). The remaining figures are light photomicrographs of nasal tissues stained with hematoxylin and eosin (HE), Alcian blue (pH 2.5)/periodic acid–Schiff (ABPAS; stains for mucosubstances in mucous cells; magenta chromagen), or immunohistochemically for OMP (marker of mature olfactory sensory cells; brown chromagen). b, bone; bc; basal cell layer; bg, Bowman's glands; bv, blood vessel; lp, lamina propria; nb, nerve bundles; oe, olfactory epithelium; osn, nuclear layer of OSNs; re, respiratory epithelium; S, septal cartilage; sc, nuclear layer of sustentacular cells; SG, septal glands; double arrows, transition between epithelial types; arrow, ABPAS-stained Bowman's glands.

solitary chemoreceptor and brush cells that have distinctive apical microvilli. In both rodent and primate RE, the thickness and number of ciliated and goblet cells vary according to intranasal location. In rodents, for example, goblet cells are conspicuous in RE lining the proximal, mid-, and ventral septum (T1; Fig. 6.3) and the nasopharyngeal meatus (T4; Fig. 6.7). Goblet cells, however, are scarce in RE lining the more distal midseptum, lateral wall, nasoturbinate, and maxilloturbinate in T2 and maxillary sinus in T3 (Fig. 6.6). In RE of primates, there is a gradual anterior-to-posterior increase in goblet cell density along both nasal septal and lateral walls.

Numerous secretory glands that contain serous and/or goblet cells are located in the lamina propria beneath RE predominantly in the proximal septum and lateral walls of rodents. The largest nasal secretory gland in rodents is the bilateral lateral nasal gland (LNG), also referred to as Steno's gland, which surrounds the maxillary sinus located in the lateral wall adjacent to each nasal passage (T3; Fig. 6.6). Similar nasal glands are also found in the primate nose.

Secretory contents of the LNG drain into the nasal vestibule. The LNG is a major site for the synthesis and secretion of odorant-binding proteins that serve as odorant carriers in nasal

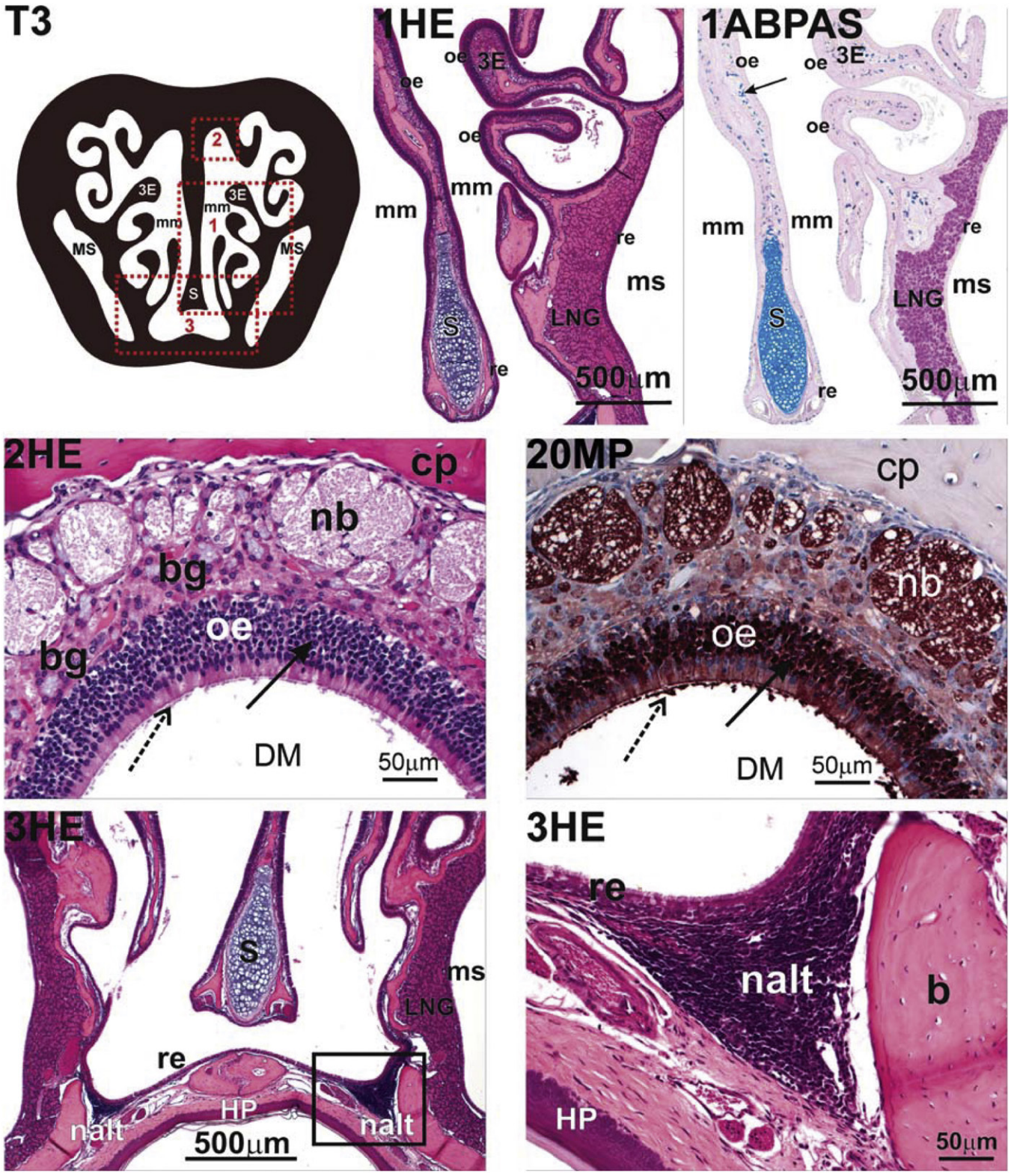

FIGURE 6.6 Rodent (mouse) nose (T3). Schematic representation of the cross-sectional profile of the nose at level T3. 3E, third ethmoid turbinate; mm; middle meatus; MS, maxillary sinus; S, septum. Rectangles are the intranasal locations for the light photomicrographs of nasal epithelium lining the septum (1), medial dorsal meatus (2), and nasopharyngeal meatus (3). The remaining figures are light photomicrographs of nasal tissues stained with hematoxylin and eosin (HE), Alcian blue (pH 2.5)/periodic acid–Schiff (ABPAS; stains for mucosubstances in mucous cells; magenta chromagen), or immunohistochemically for OMP (marker of mature olfactory sensory cells; brown chromagen). b, bone; bg, Bowman's glands; cp, bony cribriform plate; DM, dorsal medial meatus; HP, hard palate; nalt, nasal-associated lymphoid tissue, nb, nerve bundle composed of olfactory sensory cell axons; oe, olfactory epithelium; re, respiratory epithelium; S, septal cartilage; arrow in 1ABPAS, bg in lamina propria underlying oe; arrows in 2HE and 2OMP, nuclear layer of olfactory sensory cells; stippled arrows in 2HE and 2OMP, dendritic ciliary layer of the oe.

Need-to-know

- NALT is more abundant in humans than in rodents.

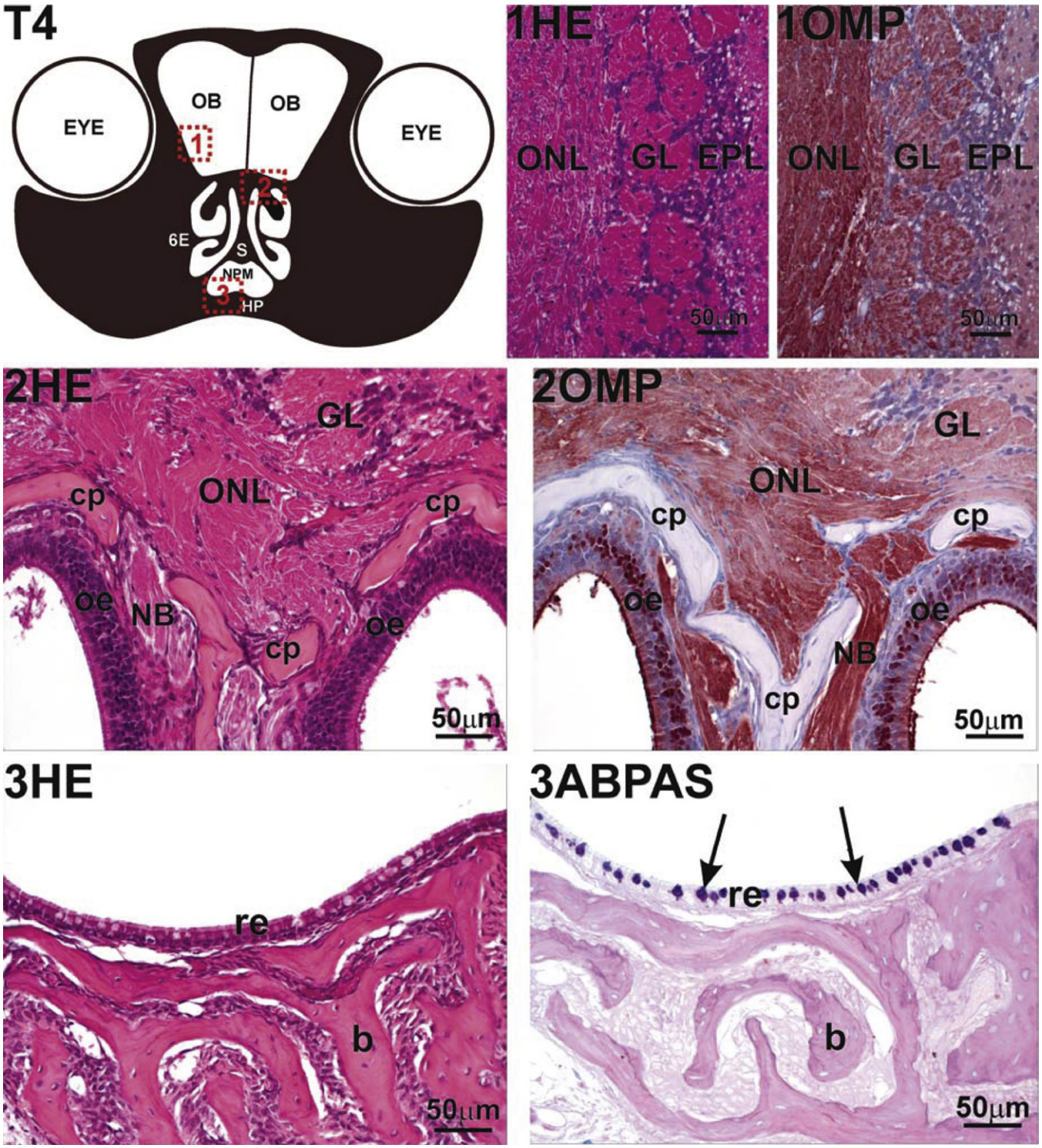

FIGURE 6.7 Rodent (mouse) nose (T4). Schematic representation of the cross-sectional profile of the nose at level T4. 6E, sixth ethmoid turbinate; HP, hard palate; NPM, nasopharyngeal meatus; OB, olfactory bulb of the brain; S, septum. Rectangles are the intranasal locations for the light photomicrographs of OB (1), OE lining the dorsal meatus (2), and RE lining the floor of the NPM (3). The remaining figures are light photomicrographs of tissues stained with hematoxylin and eosin (HE), Alcian blue (pH 2.5)/periodic acid–Schiff (ABPAS; stains for mucosubstances in mucous cells; magenta chromagen), or immunohistochemically for OMP (marker of mature olfactory sensory cells; brown chromagen). b, bone; bg, Bowman's glands; cp, bony cribriform plate; EPL, external plexiform layer of OB; GL; glomerular layer of OB; NB, nerve bundle composed of olfactory sensory cell axons; oe, olfactory epithelium; ONL, olfactory nerve layer of the OB; re, respiratory epithelium; arrows in 3ABPAS, bg in lamina propria underlying olfactory epithelium.

mucus. It also synthesizes large amounts of immunoglobulin A, which is important for immune defense of the upper respiratory tract, and testosterone and salivary androgen-binding proteins, which are likely important in olfaction and reproductive behavior. Because of its high metabolic capacity, the LNG is also a potential target for chemical toxicity caused by secondary metabolites of inhaled or ingested xenobiotic compounds.

Olfactory Epithelium

The most prominent difference between rodent and human nasal epithelium is the amount of nasal airway chamber that is lined by OE (Fig. 6.1). A much greater percentage of the nasal cavity of rodents, which have an acute sense of smell, is lined by OE compared to that of primates, whose sense of smell is not as well developed. Gross et al. (1982) morphometrically determined that approximately 50% of the rodent nasal cavity is lined by this unique sensory neuroepithelium. OE lines most of the ethmoid turbinates, roof, lateral wall, and septum in the distal nasal airways of rodents (T2, T3, and T4; Figs. 6.5–6.7). OE lines only a small area of approximately 500 mm^2 in the middorsal nasal passages of humans, which is 3% of the total surface area of the nasal cavity. In both rodents and humans, OE is a pseudostratified, columnar neuroepithelium containing three principal epithelial cell types: olfactory sensory neurons (OSNs), basal cells, and sustentacular cells (Fig. 6.5).

Olfactory Sensory Neurons

OSNs are bipolar neuronal cells interposed among the sustentacular cells. Mature OSNs express olfactory marker protein (OMP), which is used for immunohistochemical detection of these unique neuroepithelial cells (Figs. 6.4, 6.6, and 6.7) found in both rodents and primates. The cellular composition and epithelial thickness are remarkably similar among rodent and primate species (Fig. 6.4).

The dendritic portions of OSNs extend above the epithelial surface and terminate into a bulbous olfactory knob from which protrude 10–15 immotile cilia (Fig. 6.6). These long and thin cilia, approximately 50 µm in length and 0.1–0.3 µm in diameter, are enmeshed with each other and with microvilli in the surface fluid, and they provide an extensive surface area for reception of odorants. The ciliary membranes of the OSN contain the odorant receptors (ORs) responsible for the chemical interaction with and initial detection of inhaled odors. ORs are G-protein-coupled, seven-transmembrane receptor proteins, which make up the largest gene families known to exist. OR genes were discovered by Linda Buck and Richard Axel, who were awarded the 2004 Nobel Prize in Physiology or Medicine for their landmark work in the cellular and molecular biology of olfaction. Their elegant and novel work was one of the first applications of degenerate polymerase chain reaction (PCR). It is estimated that there are 500–1000 OR genes in rodents and approximately 1000 sequences in humans. They reside in multiple clusters spread throughout the genome, with more than half being pseudogenes.

A single OR gene is expressed in a minute subset of OSNs; it is believed that each OSN expresses only a single OR (the one receptor–one neuron rule). Interestingly, rodent OR genes are expressed in OSNs within one of four even-sized, distinct topographical zones in the OE lining the nasal cavity. OSNs expressing a given OR are distributed in a random, punctate manner within a zone. There are approximately 2 million OSNs within the rodent nasal cavity.

The axon of the OSN originates from the base of the cell and passes through the basal lamina to join axons from other OSNs, forming nonmyelinated nerve bundles (fascicles) in the lamina propria. These olfactory nerves perforate the bony cribriform plate, which separates the nasal cavity from the brain, and form the outer olfactory nerve layer of the olfactory bulb. OSN axons that

express the same OR gene converge with extreme precision on approximately 2000 signal-processing modules called glomeruli that reside in distinct locations within the olfactory bulb (Fig. 6.6). Glomeruli are relatively large spherical neuropils (100–200 µm in diameter) in which OSN axons form synaptic connections on the dendrites of mitral and tufted cells, the output neurons of the olfactory bulb. Transmission of olfactory information is sent through the axons of the mitral and tufted cells to the olfactory cortex.

Basal Cells

The OE also contains two types of basal cells—horizontal basal cells (HBCs) and globose basal cells (GBCs). HBCs are thin cells located along the basal lamina and share many morphologic and histochemical features with the basal cells of nasal RE, such as keratin, as detected by immunohistochemistry. In contrast, GBCs are morphologically more round or oval and are located above the HBCs. These cells have a more electron-lucent cytoplasm than HBCs and are not immunohistochemically reactive for keratin. HBCs are the progenitor cells for GBCs, some of which give rise to OSNs.

Sustentacular Cells

Sustentacular (supporting) cells are columnar epithelial cells that span the entire thickness of the OE from the airway surface to the basal lamina. They likely arise from multipotent basal cells within the OE or in Bowman's gland ducts. The distinct oval nuclei of the sustentacular cells are aligned in a single row along the OE apical aspect and are the most apically located epithelial nuclei within the mammalian OE (Fig. 6.5). The supranuclear portion of the cell is broad, whereas the portion below the nucleus tapers to a thin foot-like process that attaches to the basal lamina. Sustentacular cells surround the OSNs and make multiple contacts with them through fine cellular extensions. The apical surfaces of sustentacular cells are lined by numerous long microvilli that intermingle with the thin cilia of the OSNs along the surface of the airway lumen. The supranuclear cytoplasm of sustentacular cells has abundant SER and xenobiotic-metabolizing enzymes (e.g., cytochrome P450, flavin-containing monooxygenases, and *N*-acetyltransferases). The metabolism in these cells may be important in the detoxification of inhaled xenobiotics and in the function of smell. Sustentacular cells are also thought to contribute to the regulation of the ionic composition of the overlying mucous layer, which undoubtedly affects chemical interactions between odors and their ORs. Mammalian sustentacular cells do not contain the mucin glycoproteins characteristic of columnar mucus-secreting epithelial cells in the nasal RE (e.g., goblet cells).

Other OE Cells

In addition to these principal epithelial cells in the OE of rodents and humans, there are substantial numbers of several different types of apically located microvillous cells whose function(s) is(are) not fully understood. One subgroup of microvillous cells in the OE is morphologically similar to microvillous sensory neurons of the VNO (described later), with an axonal component projecting to the olfactory bulb. These cells also express transient receptor potential channel C2 (TRPC2). Members of the TRP ion channel superfamily function as diverse cellular sensors. Another group of microvillous cells are non-neuronal and lack a basal/axonal segment. In rodents, this subgroup expresses TRPC6, phospholipase C (PLC)-β_2, and inositol trisphosphate receptor type 3, suggesting a function as secondary chemosensory cells. Some of these cells also express TRPM5. These solitary chemosensory cells may interface with peptidergic nerve fibers immunoreactive for neuropeptides (e.g., substance P), suggesting that they may transmit sensation of chemical irritants via the trigeminal nerve.

The production and secretion of mucus covering the OE luminal surface is restricted to

subepithelial Bowman's glands (Figs. 6.4 and 6.6). These glands are located in the underlying lamina propria and interspersed among the olfactory nerve bundles. They are simple tubular-type glands composed of small, compact acini. Ducts from these glands transverse the basal lamina at regular intervals and extend through the OE to the luminal surface. Bowman's glands contain copious amounts of neutral and acidic mucosubstances that contribute to the mucous layer covering the luminal surface of the OE. Like the sustentacular cells, both the acinar and duct cells of Bowman's gland also contain many xenobiotic-metabolizing enzymes.

OTHER NASAL CAVITY FEATURES

Accessory Olfactory Organs in Rodents

In addition to the OE in the main nasal chamber, there are three accessory olfactory organs found in the nasal airways of rodents that are not well developed or functional in the human nose: the VNO, the septal organ of Masera (SOM), and the septal organ of Grüneberg (SOG).

Vomeronasal Organ

The VNO, also referred to as the organ of Jacobson, is a paired tubular diverticulum located in the ventral portion of the proximal septum (T1) of rodents (Fig. 6.3). The lateral wall of each diverticulum is lined by thick, nonsensory columnar epithelium, whereas the medial wall is lined by neuroepithelium. The sensory nerves in the VNO have long microvilli but lack the cilia found in OSNs of the OE (i.e., neuronal microvillous cells described previously). Like OSNs in the main nasal chamber of rodents, these olfactory neurons contain OMP (Fig. 6.3).

The axonal portions of OE in VNO synapse with glomeruli located in the accessory olfactory bulb rather than those in the olfactory bulb. A small duct extends from each diverticulum to the proximal nasal airway lumen near the nasal opening of the nasopalatine canal that connects the nasal cavity with the oral cavity. A primary function of the VNO is to detect pheromones—airborne chemical messages or signals—sent between individual rodents and essential for normal reproductive physiology and behavior. Initial pheromone detection in VNO is triggered by pheromone binding to G-protein-coupled receptors followed by the activation of TRPC2.

Septal Organ of Masera

Another small but distinct chemosensory structure found in the rodent nose is the SOM. It is a small patch of OE with OMP-positive OSNs surrounded by RE and lying bilaterally in the ventral nasal septum near the entrance of the nasopalatine ducts (T2; Fig. 6.5), which connects the oral and nasal cavities. It constitutes approximately 1% of the OE in the main chamber of the rodent nose. Neuronal projections from the SOM connect to distinct regions in the main olfactory bulb. SOM has not been identified in the human nose. For rodents, it has been suggested that the SOM may have an alerting function by sensing airborne odors during quiet breathing, when intranasal airflows do not reach the main OE in the more dorsal regions of the nasal cavity. It may also detect odors from the mouth and act as a chemosensory surveyor of foods.

Septal Organ of Grüneberg

A third accessory population of OMP-expressing sensory neurons is found in the SOG. The SOG is located bilaterally in a discrete area of the dorsorostral tip of the nasal septum in rodents. Because it is located rostral to the routine T1 nasal section, this accessory olfactory organ would not be seen with routine tissue sectioning of the rodent nasal cavity for light microscopy.

Like the SOM, the axons of the SOG project to a distinct subset of glomeruli in the main olfactory bulb. Unlike OSNs of the OE, VNO, and SOM,

which are all part of a luminal surface epithelium, the OSNs of the SOG are located in clusters in the lamina propria beneath OMP-negative surface epithelium. Although the function of SOG is unknown, its rostral location suggests that it may be involved in early detection of distinct odorants.

Lymphoepithelium and Nasal-Associated Lymphoid Tissue

In addition to the four principal nasal epithelia previously described, lymphoepithelium (LE) is another type of specialized epithelium in the nasal airways of rodents that covers discrete focal aggregates of nasal-associated lymphoid tissue (NALT) in the underlying lamina propria (Figs. 6.4 and 6.6). In rodents, LE and NALT are restricted to the ventral aspects of the lateral walls at the opening of the nasopharyngeal duct (T3). The overlying LE is composed of cuboidal ciliated cells, a few goblet cells, and numerous nonciliated, cuboidal cells with luminal microvilli (membranous or M cells) similar to those in gastrointestinal- and bronchus-associated lymphoid tissues in the intestinal and lower respiratory tracts, respectively. M cells are thought to be involved in the uptake and translocation of inhaled antigens from the nasal lumen to the underlying lymphoid structures.

LE and NALT have also been described in the nasopharyngeal airways of nonhuman primates, where they are more abundant than in rodents and are located on both lateral and septal walls of the proximal nasopharynx (Fig. 6.4). The correlate of NALT in humans is Waldeyer's ring, the oropharyngeal lymphoid tissues composed of the adenoids, and the bilateral tubule, palatine, and lingual tonsils.

The location of NALT at the entrance of the nasopharyngeal duct is a very strategic position because most nasal secretions and inhaled air, both presumably laden with antigenic material, flow over this area. Although the function of NALT and its place in the general mucosal-associated lymphoid system are not fully understood, these mucosal lymphoid tissues may have an important function in regional immune defense of the upper airways.

Nasal Trigeminal Nerves and Solitary Chemoreceptive Cells

Inhaled chemicals may neurogenically stimulate not only the OE in the main chamber and accessory olfactory organs, but also chemoreceptors of nasal trigeminal nerves, which are part of the somatic sensory system for the eyes, nose, and mouth. Trigeminal chemoreceptors are present throughout the nasal epithelium lining the rodent and human nasal cavity. Stimulation of trigeminal nerve fibers produces sensations described as irritating, painful, burning, cooling, tingling, stinging, or pungent. Chemical stimulation of these sensory nerves may also result in protective reflexes causing increased secretions (e.g., nasal mucus), decreased respiration rate (e.g., apnea), and reduction in the nasal airways due to vascular congestion and mucosal swelling. Nasal trigeminal nerve fibers that respond to irritants release neuropeptides, such as substance P and calcitonin gene-related peptides, and are presumably polymodal nociceptors. They mediate irritant responses through TRP channels (e.g., TrpV1 and TrpA1), acid-sensing ion channels (ASICs), and other ion channels. Nasal trigeminal nerve fibers ramify repeatedly in the nasal mucosa, and their intraepithelial nerve endings extend close to the airway surface, just below the apical tight junctions connecting epithelial cells. Interestingly, some of these trigeminal nerve fibers in rodent nasal epithelium, predominantly in RE lining the proximal nasal airways, are intimately associated and synapse with solitary chemoreceptive cells (SCCs), distinct nonciliated epithelial cells with loose apical microvilli. These epithelial cells are morphologically distinct from brush cells, also found in RE, that have a stiff tuft of apical

microvilli. In contrast to nasal trigeminal nerves, SCCs express elements of the taste transduction cascade, including Tas1R and Tas2 receptor molecules, α-gustducin, PLC-β_2, and TrpM5. They detect inhaled irritants and other xenobiotic substances that trigger trigeminally mediated airway reflexes. SCCs in rodents are located in nasal, laryngeal, and tracheobronchial airways. In the nasal airways, they are only found in the nasal epithelium.

Nasal Blood Vessels

The lamina propria in both rodent and human nasal mucosa has a rich and complex network of blood vessels, with each of the epithelial regions receiving blood from a separate arterial supply. The vascular system in the nose is composed of resistance and capacitance vessels. Resistance vessels are small arteries, arterioles, and arteriovenous anatomoses. Blood flow to the mucosa is regulated by resistance vessel constriction and dilatation.

Capacitance vessels, the large venous sinusoids (i.e., venous erectile tissue or "swell bodies"), are a unique feature of the nasal vasculature that are distributed throughout the mucosa (Figs. 6.4 and 6.5). In humans and rodents, capacitance vessels are well developed in specific sites of the anterior or proximal aspects of the nasal passages. These vessels have dense adrenergic innervations, and their congestion and constriction are regulated by the sympathetic nerve supply to the nose. Congestion of blood in capacitance vessels can change mucosal thickness, resulting in an altering of nasal airflow patterns and nasal resistance.

Pharynx and Larynx

Gross Anatomy

The pharynx and particularly the larynx are of comparative interest principally because of inhalation-associated injuries such as those seen following repeated aerosol exposures that may occur naturally or as part of toxicity studies in rodents. The pharynx, consisting of the nasopharynx, oropharynx, and laryngopharynx (sometimes referred to as the hypopharynx), extends from the mouth and nasal cavities to the larynx, where it becomes continuous with the esophagus. The pharynx serves as a common passage for food, fluids, and air. The larynx is located between the pharynx and the trachea, and despite a common functional mission and fundamentally similar design, there is great species diversity in the location and finer gross anatomical structural elements of the larynx (Table 6.2). There are also significant laryngeal maturational changes that occur during early life. Functionally, the pharyngeal structures serve a common purpose in all three species, although because rodents, unlike humans, are obligate nasal breathers, all inhaled air passes through the nasopharynx on its path to the trachea and lungs.

In humans and other primates with upright ambulation, the pharynx is flexed, whereas in rodents with elongated heads, the pharynx is relatively straight. Because of this flexed arrangement, coupled with the diminutive size of rodents relative to humans, there are some minor differences in the somewhat arbitrary landmarks separating the divisions of the pharynx. However, in general, in both rodents and humans the nasopharynx is located beneath the base of the skull and dorsal to the soft palate, the oropharynx lies between the end of the soft palate and tip of the epiglottis, and the laryngopharynx extends from the tip of the epiglottis posterior to the beginning of the esophagus. Because of the indistinct and anatomically difficult location of the nasopharynx and oropharynx, intact gross specimens, especially from humans, are typically unavailable; hence, evaluation tends to be based on focused histologic sampling.

TABLE 6.2 Pharynx/Larynx

Feature	Rodent	Human
	Gross	
Pharyngeal arrangement	Linear	Flexed
Nasopharyngeal portion of Eustachian tube	Lacks cartilagenous support and bone element absent. Lacks significant lymphoid component	Continuous cartilagenous support emanating as torus tubarius. Bone near tympanic cavity. Substantial submucosal lymphoid element accompanies tube
Tonsilar tissue, pharyngeal region	Absent, but some lymphoid aggregates	Widely disseminated, well defined
Laryngeal cartilage	U-shaped cartilage associated with ventral pouch is small. Larger in rats than mice Infrequently calcified/metaplastic	No U-shaped cartilage. Commonly displays age-linked calcification/metaplasia
Ventral pouch	Follows from and posterior to base of epiglottis. Site of injury More prominent in rats than in mice	Absent
Vocal folds	Covered by thin layer of low cuboidal to SE. Less commonly a site of injury. Phonation (vocalization) is limited and ultrasonic or near-ultrasonic	Covered by thick nonkeratinized stratified SE. Common site of injury. Vocalization is audible
	Histologic	
Intermediate epithelium, epiglottis	Laryngeal surface near base. Ciliated epithelial cells are more numerous in mice at the epiglottal base Common site of injury Rats have fewer ciliated cells than mice	Laryngeal surface near base Less common site of injury
Taste buds	Widely distributed in pharynx and larynx including epiglottis, fewer in tongue	Most located in tongue with fewer in other oral/pharyngeal sites
Subepithelial laryngeal glands	Mouse: Approximately 0.7/mm^2 Rat: Approximately 1.8/mm^2	Approximately 0.27/mm^2

PREPARATION OF RODENT PHARYNX AND LARYNX FOR MICROSCOPIC EXAM

In rodents, in which most evaluations are performed on decalcified sections of the intact whole head, it is important to strive for consistency in obtaining sections of pharynx and larynx. Specific approaches have been developed to aid in this process (see Kittel et al., 2004; Sagartz et al., 1992). Similar to the nose, special attention to fixation, decalcification, and uniform sampling is required due to the anatomical complexity of this organ and its encasement within bone.

HISTOLOGY

Pharynx

The mucosa of the nasopharynx in both humans and rodents is covered by stratified SE or ciliated columnar-type epithelium (RE) in roughly equal amounts depending on age and history of exposure to irritants. Where these epithelia transition from one to another, there is an intermediate epithelium that is composed of nonciliated, more cuboidal-to-flattened cells. Similar intermediate epithelium is present on the surface of the epiglottis, arytenoid cartilages, ventral pouch of rodents, and in other pharyngeal/laryngeal sites. The remainder of pharyngeal mucosal surfaces is covered by stratified SE that may be keratinized or nonkeratinized. The submucosa of the nasopharynx contains many seromucinous glands, which are particularly common along the route of the Eustachian tube in all three species (Fig. 6.8). The Eustachian tube opens into the nasopharynx in all three species, although rodents lack cartilage in the nasopharyngeal portion of the tube, as well as the distinct tubal tonsil (Gerlach's tonsil) and other submucosal lymphoid tissues seen in humans (Fig. 6.9). In addition, the bony support of the Eustachian tube present near the tympanic

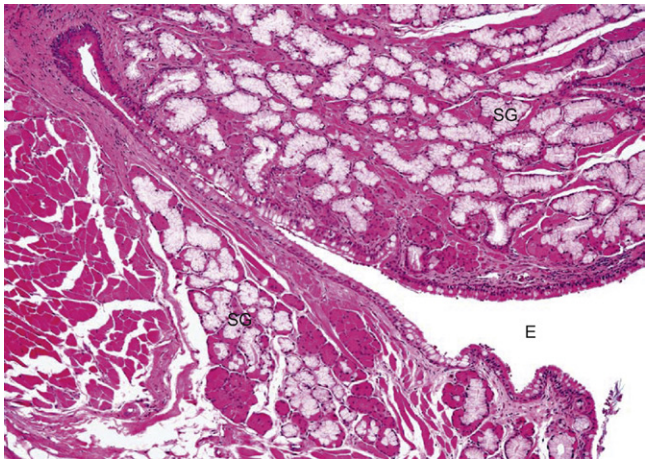

FIGURE 6.8 Rat Eustachian (pharyngotympanic) tube. The Eustachian tube and accompanying seromucinous glands (SG). The tube is lined with ciliated columnar epithelium. (See Chapter 22: Special Senses: Ear, for mouse equivalent.)

Need-to-know

- In contrast to humans, the rodent Eustachian tube lacks substantial cartilagenous support throughout its length and has minimal lymphoid tissue associated with it.

cavity in humans is instead cartilagenous in rodents. Because of the lack of a mucosal-covered cartilaginous extension of the Eustachian tube into the nasopharynx, rodents lack the torus tubarius seen in humans. Intermediate epithelium is present in rodents as the Eustachian tube transitions into the nasopharynx. This transition is from ciliated columnar to stratified SE (Fig. 6.10). The oropharynx of all three species is lined by continuous, nonkeratinizing to partially keratinized stratified SE.

The supporting tissues of the pharynx of all three species, in addition to submucosal glands, also commonly contain connective and elastic tissues and skeletal muscle, and they are richly supplied with blood vessels, lymphatics, and nerves (Figs. 6.9–6.11). Mononuclear cells or aggregates

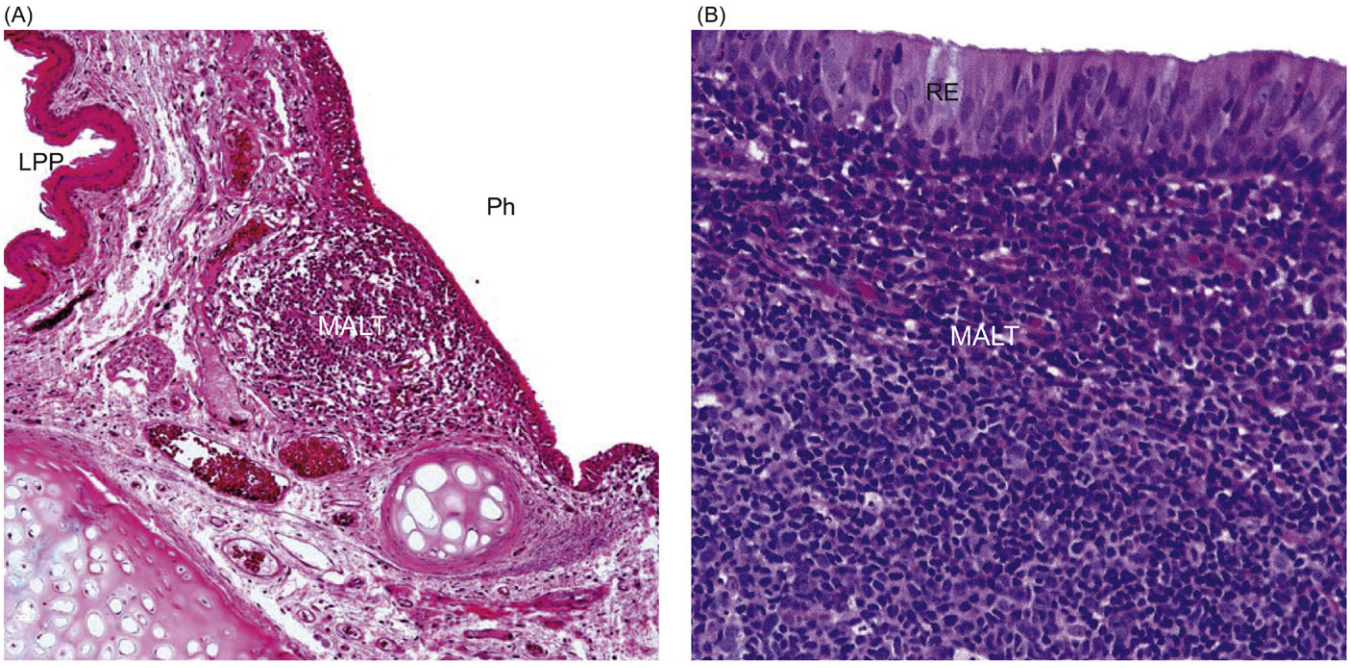

FIGURE 6.9 MALT in the nasopharynx. (A) Rodent (rat). An aggregate of MALT between the lumen of the pharynx (Ph) and the lateral pharyngeal pouch (LPP). These aggregates represent the rodent equivalent of Waldeyer's ring. (B) Human. The human nasopharynx is lined by pseudostratified respiratory mucosa (RE). Unlike in rodents, the underlying lamina propria contains dense aggregates of MALT that protect portals of entry such as the Eustachian tube. Collectively, this lymphoid tissue is known as Waldeyer's ring. Source: Reprinted from Young B, et al: *Wheater's functional histology*, ed 5, 2006, with permission from © Elsevier, www.netterimages.com.

Need-to-know

- Rodents, unlike humans, are obligate nasal breathers, so all inhaled air passes through the nasopharynx on its path to the lungs.
- Rodents lack distinct pharyngeal tonsils but instead have widely dispersed lymphoid aggregates.

and individual mast cells may be present within scattered sites of the submucosa in all three species.

A particular species difference of note is that whereas humans have widely distributed pharyngeal tonsillar tissues, rodents lack distinct tonsils. Humans have a complex collection of nonencapsulated tonsillar lymphoid tissues called Waldeyer's ring. This ring encompasses palatine, pharyngeal, tubal, and lingual tonsils and is composed of distinct aggregates, bands, and follicles of lymphoid tissues, termed mucosal-associated lymphoid tissue (MALT) (Fig. 6.9B). In addition, other tonsillar accumulations can be found within the oropharynx of humans. Mice and rats lack dense lymphoid accumulations consistent with tonsillar structures, although scattered aggregates of submucosal lymphoid cells can be present in some nasal, oral, and pharyngeal locations (Fig. 6.9A). In rodents, NALTs are considered the morphologic equivalent of Waldeyer's ring present in humans (Fig. 6.9B). Also of note is that in rodents, taste buds—or functionally related chemosensory clusters—are widely distributed in the lining epithelium of the epiglottis and other laryngeal and pharyngeal areas (Fig. 6.11B). Although taste buds can be present within the human larynx, they are fewer in number and their distribution is more variable and restricted compared those in rodents.

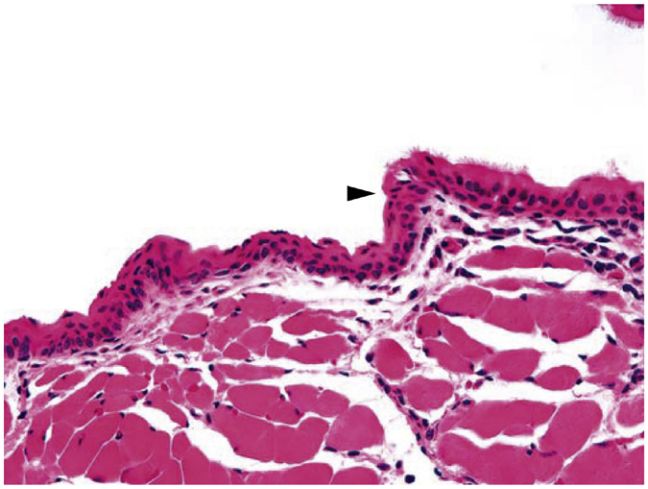

FIGURE 6.10 Rodent (mouse) nasopharynx. Transition (arrowhead) where intermediate epithelium replaces ciliated epithelium.

Need-to-know

- Sites of epithelial transition to intermediate epithelium zones occur in multiple locations within the pharyngeal/laryngeal region in all three species.
- Lesions often manifest in these zones.

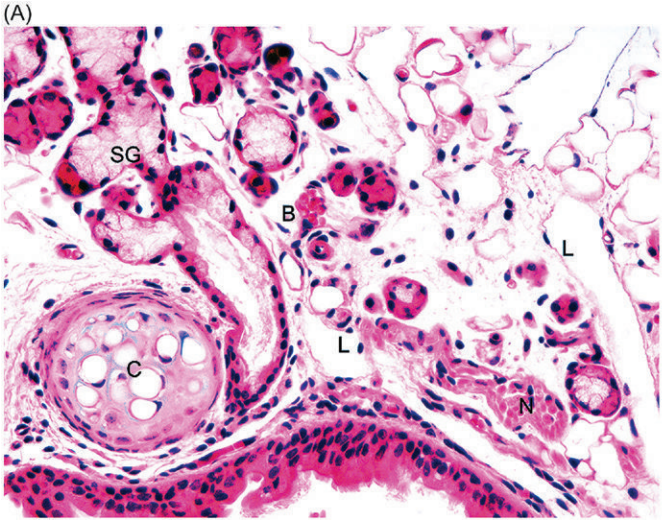

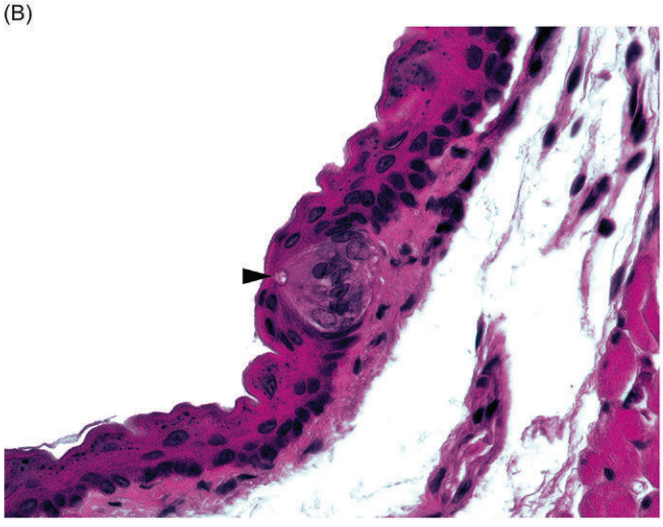

FIGURE 6.11 Rodent (mouse) pharyngeal submucosa. (A) The submucosa is richly supplied with blood vessels (B), lymphatics (L), nerves (N), cartilage (C), and seromucinous glands (SG). (B) A taste bud (arrowhead) within stratified SE of rodent oropharynx in close proximity to the larynx.

Need-to-know

- In rodents, taste buds are more common and widely distributed within the epiglottis, larynx, and pharynx, whereas in human, they predominate in the tongue.

Larynx

The larynx, including the epiglottis, serves the functions of audible phonation and of protection of the respiratory tree from inhalation of food or water during swallowing. Phonation occurs principally in humans, although rodents display some vocalization that extends into the ultrasonic range. Despite a common functional mission and fundamentally similar design, there is great species diversity in the location and finer gross anatomical structural elements of the larynx. There are also significant maturational changes that occur during early life. Comprehensive comparative structural studies of the mouse and rat larynx are few and relatively recent. These studies show that the cartilaginous and muscular organization of the rodent and human larynx is substantially similar. Some minor differences have been noted, including the presence of a small U-shaped cartilage associated with the ventral pouch in rodents (sometimes called the alar cartilage and much more prominent in the rat) that is lacking in humans, as well as some minor differences in musculature and possible variation in ventricular folds in rodents. It is also typical in older humans and some other species for major laryngeal hyaline cartilage structures to calcify and sometimes develop marrow elements, something not commonly reported in normal, wild-type rodents, which typically do not live into old age.

In contrast to the somewhat limited knowledge of the structural organization of the larynx, there is greater understanding of the histology of the rodent epiglottal and laryngeal mucosa because it is a common target of aerosol-mediated injury. The epiglottis (Fig. 6.12) is of importance because it is a common site of injury in all three species (but particularly in rodents) following repeated aerosol or other irritant exposures. The area of the epiglottis susceptible to injury is at the transition from stratified SE to RE in a zone composed of intermediate (sometimes inappropriately called transitional) epithelium (Fig. 6.12C). In both rodents and humans, the anterior or lingual surface of the epiglottis is covered by stratified SE that extends around the tip of the epiglottis to cover portions of the posterior or laryngeal surface (Fig. 6.12). In all three species, the transition from squamous to RE occurs in the intermediate zone near the base of the epiglottis (Fig. 6.12A and D). The intermediate zone is very small and is composed of multilayered nonciliated rounded to cuboidal cells. The thickness and degree of squamous differentiation within the intermediate zone can vary significantly and be much more expansive, especially in humans, who live longer and who may be chronically exposed to environmental irritants such as tobacco or industrial smoke. In spite of minor differences, the distribution of epithelial types in rodents and humans is much more similar than that seen in domestic animals such as the dog. In contrast with the other major laryngeal cartilages, which in rodents and humans are mostly hyaline, the epiglottal cartilage is elastic cartilage. The epiglottis attaches to the hyoid bone and intercalates with the thyroid cartilage (Figs. 6.12 and 6.13). The lamina propria, as in other parts of the pharynx, is composed of loose connective tissue and contains many vascular elements, nerves, and scattered mononuclear cells along with seromucinous glands beneath the laryngeal epithelial surface. The number and location of these glands have been extensively studied in various species. Subepithelial mucous or seromucinous glands are distributed throughout the larynx and trachea of rats and humans (Fig. 6.13B) but only within portions of the larynx in mice. Within the larynx, the numbers of gland orifices per area of mucosa (which directly reflects gland density) is highest in rats ($1.8/mm^2$) followed by mice ($0.7/mm^2$) and humans ($0.27/mm^2$).

Laryngeal structures posterior to the epiglottis (Fig. 6.13A) are defined by a cartilaginous basket formed by three paired cartilages (arytenoid, corniculate, and cuneiform) and two single cartilages (thyroid and arytenoid). Unlike humans, mice and particularly rats have a distinct ventral pouch. This pouch lies between the caudal aspect

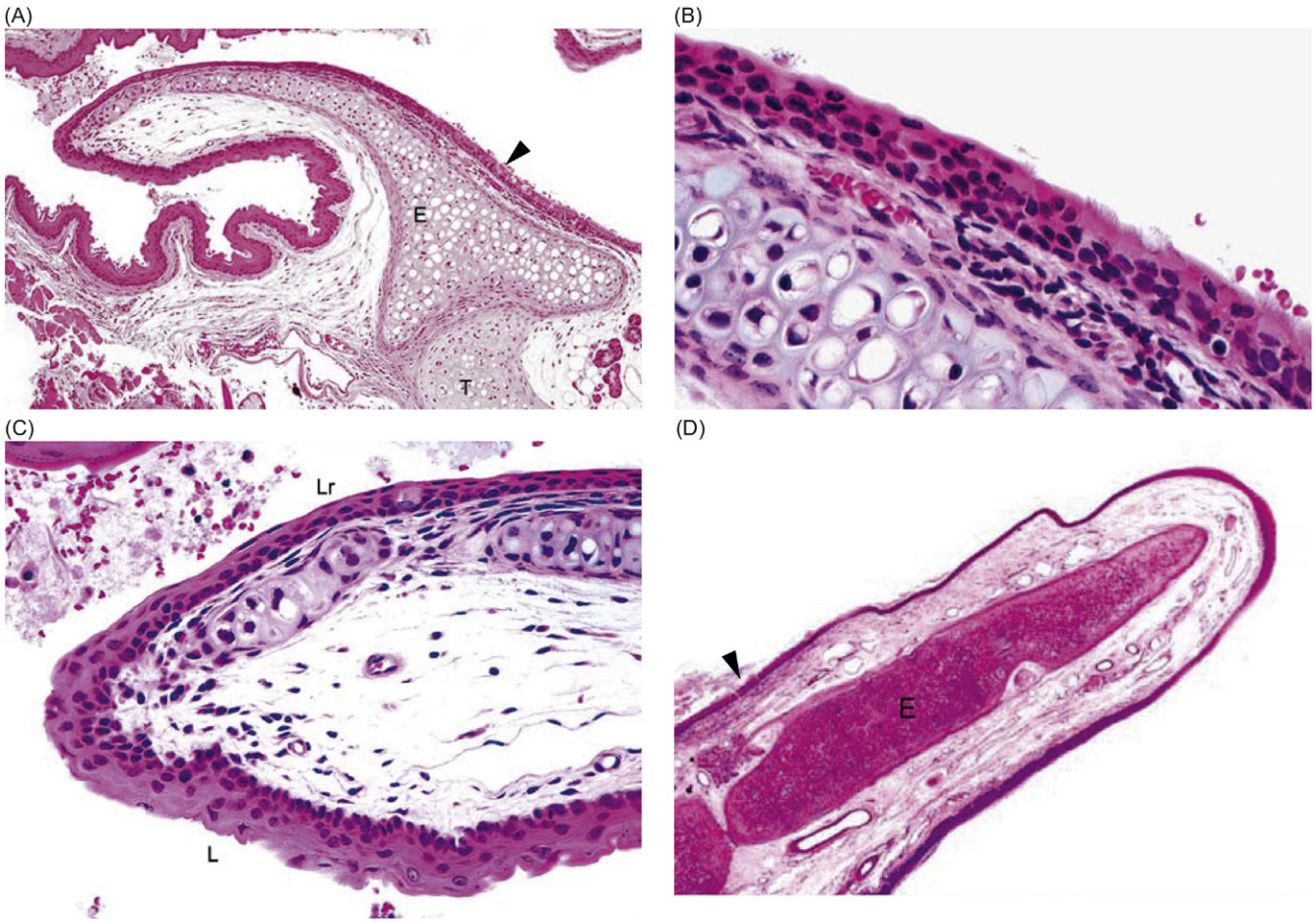

FIGURE 6.12 Epiglottis (A) Rodent (mouse) epiglottis with epiglottal (E) and thyroid (T) cartilages. The epiglottal epithelium transitions from stratified squamous to RE at the intermediate epithelial zone (arrowhead). (B) High magnification view of intermediate zone where epithelium transitions from squamous to ciliated RE. (C) Tip of rodent (mouse) epiglottis. Stratified SE extends from the lingual (L) surface around to the laryngeal (Lr) surface. (D) Human lateral meatus of the tip of the epiglottis at low magnification. The epiglottis has a core of elastic cartilage (E). Its lingual surface (bottom) and free margin (top right) are covered by nonkeratinized stratified SE. Halfway along the laryngeal surface (arrowhead), the epithelium undergoes a transition; it eventually becomes RE. Source: © Reprinted from Ovalle WK, Nahirney JC: *Netter's essential histology*, 2008, with permission from © Elsevier, www.netterimages.com.

of the epiglottis and the tracheal opening and is positioned above the thyroid cartilage. The ventral pouch is lined ventrally by ciliated, mostly columnar, epithelium, which as it progresses laterally changes to cuboidal and (in a few sites) SE. This is important because, as previously noted, there is a predilection for injury at these sites of epithelial transition, as seen with intermediate epithelium covering the epiglottis and arytenoid cartilages, among others. The muscles (all skeletal)

Need-to-know

- The intermediate epithelial zone of the epiglottis is in a generally similar location in rodents and humans.
- It is a common site of injury in rodents, but less so in humans.
- The epiglottal cartilage is elastic in all three species.
- Rodents, unlike humans, have a distinct ventral pouch caudal to the epiglottis.

of the laryngopharynx have complex arrangements because they are closely related to those of the laryngeal cartilages and hyoid bone and can vary in subtle ways between species. In mice, the epithelium covering the vocal folds is thin and low cuboidal to squamoid (Fig. 6.14A) with rats having a slightly thicker cell layer. The vocal folds of humans are covered with a thick layer of nonkeratinized stratified SE (which transitions from RE) and are supported by skeletal muscles and elastic fibers in the submucosa (Fig. 6.14B). In humans, the vocal folds are a common site of injury, in contrast to rodents, in which epiglottal injury predominates.

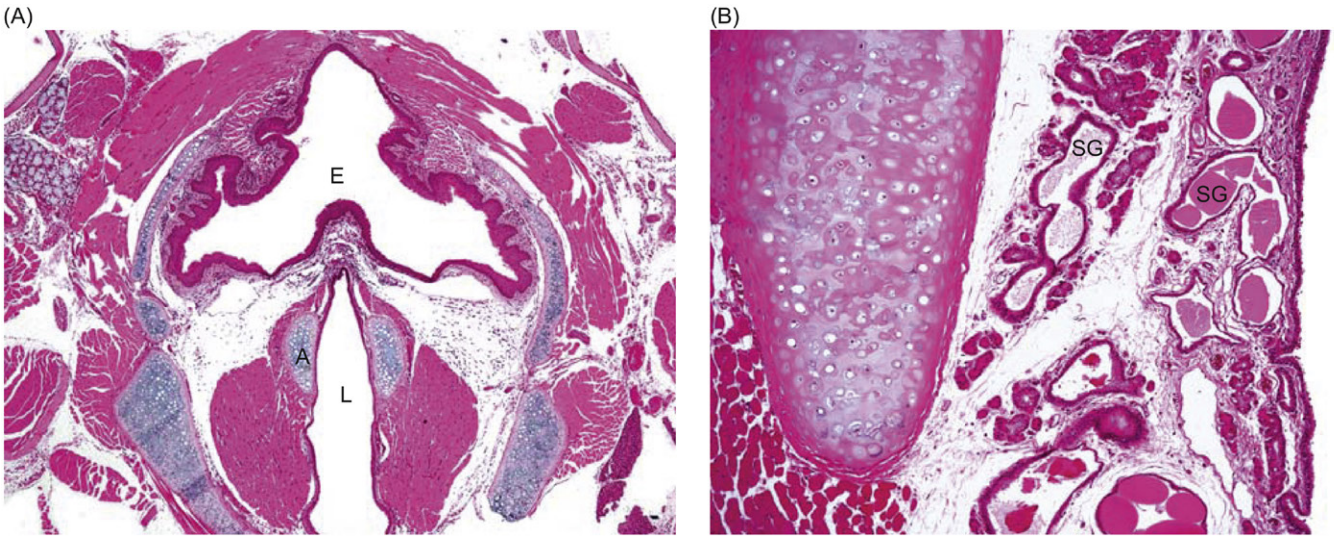

FIGURE 6.13 Rodent larynx. (A) Mouse larynx (L) with arytenoid cartilages (A) and beginning of esophagus (E). There is significant skeletal muscular and cartilagenous support. (B) Rat submucosal seromucinous glands (SG), some here distended with secretory product, found between laryngeal cartilage and the ciliated columnar epithelium covering this area of the larynx of an aged rat.

Need-to-know

- Mice have a small U-shaped (alar) laryngeal cartilage, which is large in rats and lacking in humans.
- Laryngeal cartilages from older humans are commonly mineralized.

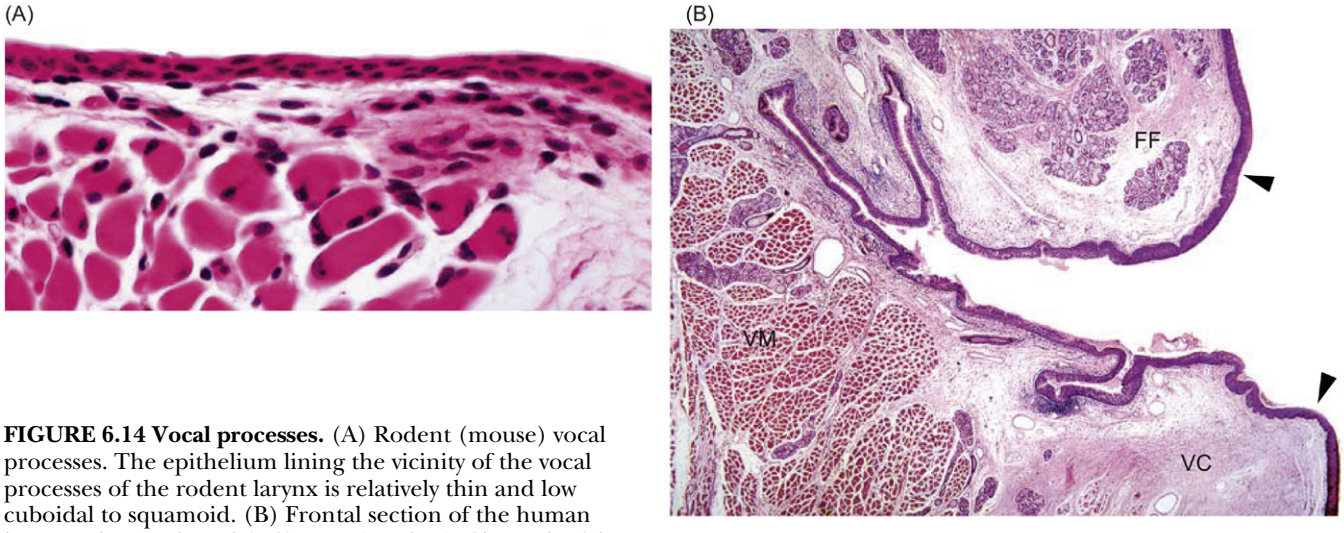

FIGURE 6.14 Vocal processes. (A) Rodent (mouse) vocal processes. The epithelium lining the vicinity of the vocal processes of the rodent larynx is relatively thin and low cuboidal to squamoid. (B) Frontal section of the human larynx. The vocal cord (VC) contains elastic fibers; the false vocal fold (FF) contains seromucous glands. Nonkeratinized stratified SE covers both folds (arrows). An intervening laryngeal ventricle (LV) and the vocalis muscle (VM) are shown. The epithelium covering the vocal cord is much thicker in humans than in rodents. Source: Reprinted from Ovalle WK, Nahirney JC: *Netter's essential histology*, 2008, with permission from © Elsevier, www.netterimages.com.

Need-to-know

- Rodent vocal folds are covered by a very thin, low cuboidal to squamous epithelium, whereas vocal folds are covered with a thick layer of nonkeratinized squamous epithelium.
- The vocal folds in humans are a common site of injury, but not so in rodents.
- Phonation in rodents is limited and ultrasonic or near-ultrasonic.

FURTHER READING

Nose and Sinuses

Bojsen-Moller F: Topography of the nasal glands in rats and some other mammals. Anat Rec 150:11–24, 1964.

Bojsen-Moller F: On the anatomy of the anterior nasal glands in man. Rev Laryngol Otol Rhinol (Bord) 88(Suppl):71–75, 1967.

Brandtzaeg P: Immune function of human nasal mucosa and tonsils in health and disease. In Bienenstock J, editor: Immunology of the lung and upper respiratory tract, New York, NY, 1984, McGraw-Hill, pp 28–95.

Buck L, Axel R: A novel multigene family may encode odorant receptors: a molecular basis for odor recognition. Cell 65:175–187, 1991.

Buck LB: The olfactory multigene family. Curr Opin Neurobiol 2:282–288, 1992.

Carey SA, Minard KR, Trease LL, et al: Three-dimensional mapping of ozone-induced injury in the nasal airways of monkeys using magnetic resonance imaging and morphometric techniques. Toxicol Pathol 35:27–40, 2007.

Ding X, Dahl AR: Olfactory mucosa: composition, enzymatic localization, and metabolism. In Doty RL, editor: Handbook of olfaction and gustation, New York, NY, 2003, Dekker.

Elsaesser R, Montani G, Tirindelli R, et al: Phosphatidylinositide signaling proteins in a novel class of sensory cells in the mammalian olfactory epithelium. Eur J Neurosci 21:2692–2700, 2005.

Gross EA, Morgan KT: Architecture of nasal passages and larynx. In Parent RA, editor: Comparative biology of the normal lung, Boca Raton, FL, 1992, CRC Press, pp 7–25.

Gross EA, Swenberg JA, Fields S, et al: Comparative morphometry of the nasal cavity in rats and mice. J Anat 135:83–88, 1982.

Grüneburg H: A ganglion probably belonging to the N. terminalis system in the nasal mucosa of the mouse. Z Anat Entwicklungsgesch 140:39–52, 1973.

Guilmette RA, Wicks JD, Wolff RK: Morphometry of human nasal airways in vivo using magnetic resonance imaging. J Aerosol Med 2:365–377, 1989.

Harkema JR, Morgan KT: Histology, ultrastructure, embryology, function: normal morphology of the nasal passages. In Jones TC, Dungworth DL, Moher U, editors: Monographs on pathology of laboratory animals: respiratory system, New York, NY, 1996, Springer-Verlag, pp 3–17.

Harkema JR, Wagner JG: Non-allergic models of mucous cell metaplasia and mucus hypersecretion in rat nasal and pulmonary airways. Novartis Found Symp 248:181–200, 2002. 277–282

Harkema JR, Plopper CG, Hyde DM, et al: Regional differences in quantities of histochemically detectable mucosubstances in nasal, paranasal, and nasopharyngeal epithelium of the bonnet monkey. J Histochem Cytochem 35:279–286, 1987.

Harkema JR, Plopper CG, Hyde DM, et al: Nonolfactory surface epithelium of the nasal cavity of the bonnet monkey: a morphologic and morphometric study of the transitional and respiratory epithelium. Am J Anat 180:266–279, 1987.

Harkema JR, Carey SA, Wagner JG: The nose revisited: a brief review of the comparative structure, function, and toxicologic pathology of the nasal epithelium. Toxicol Pathol 34:252–269, 2006.

Hegg CC, Jia C, Chick WS, et al: Microvillous cells expressing IP3 receptor type 3 in the olfactory epithelium of mice. Eur J Neurosci 32:1632–1645, 2010.

Herbert RA, Leininger JL: Nose, larynx, and trachea. In Maronpot R, Boorman GA, Gaul BW, editors: Pathology of the mouse: reference and atlas, Vienna, IL, 1999, Cache River Press, pp 259–292.

Jang W, Youngentob SL, Schwob JE: Globose basal cells are required for reconstitution of olfactory epithelium after methyl bromide lesion. J Comp Neurol 460:123–140, 2003.

Kepler GM, Joyner DR, Fleishman A, et al: Method for obtaining accurate geometrical coordinates of nasal airways for computer dosimetry modeling and lesion mapping. Inhal Toxicol 7:1207–1224, 1995.

Kiselyov K, van Rossum DB, Patterson RL: TRPC channels in pheromone sensing. Vitam Horm 83:197–213, 2010.

Kuper CF: Histopathology of mucosa-associated lymphoid tissue. Toxicol Pathol 34:609–615, 2006.

Ling G, Gu J, Genter MB, et al: Regulation of cytochrome P450 gene expression in the olfactory mucosa. Chem–Biol Interact 147:247–258, 2004.

Ma M, Grosmaitre X, Iwema CL, et al: Olfactory signal transduction in the mouse septal organ. J Neurosci 23: 317–324, 2003.

Mery S, Gross EA, Joyner DR, et al: Nasal diagrams: a tool for recording the distribution of nasal lesions in rats and mice. Toxicol Pathol 22:353–372, 1994.

Mombaerts P: The human repertoire of odorant receptor genes and pseudogenes. Annu Rev Genomics Hum Genet 2:493–510, 2001.

Mombaerts P: Love at first smell—the 2004 Nobel Prize in Physiology or Medicine. N Engl J Med 351:2579–2580, 2004.

Mombaerts P: TrpC2: expression outside the mouse VNO. Chem Senses:33, 2008. ISOT Abstr. S28

Morgan KT, Jiang XZ, Patterson DL, et al: The nasal mucociliary apparatus: correlation of structure and function in the rat. Am Rev Respir Dis 130:275–281, 1984.

Morgensen C, Tos M: Density of goblet cells in the normal adult human nasal turbinates. Anat Anz 142:322–330, 1977.

Negus VE: *Comparative anatomy and physiology of the nose and paranasal sinuses*, Edinburgh, UK, 1958, E&S Livingstone.

Olsson P, Bende M: Sympathetic neurogenic control of blood flow in human nasal mucosa. Acta Otolaryngol 102:482–487, 1986.

Ressler KJ, Sullivan SL, Buck LB: A molecular dissection of spatial patterning in the olfactory system. Curr Opin Neurobiol 4:588–596, 1994.

Sorokin SP: The respiratory system. In Weiss L, editor: Cell and tissue biology: a textbook of histology, Baltimore, MD, 1988, Urban & Schwarzenberg, pp 751–814.

Storan MJ, Key B: Septal organ of Grüneberg is part of the olfactory system. J Comp Neurol 494:834–844, 2006.

Suzuki Y, Takeda M: Basal cells in the mouse olfactory epithelium after axotomy: immunohistochemical and electron-microscopic studies. Cell Tissue Res 266:239–245, 1991.

Swenberg JA, Kerns WD, Mitchell RI, et al: Induction of squamous cell carcinomas of the rat nasal cavity by inhalation exposure to formaldehyde vapor. Cancer Res 40:3398–3402, 1980.

Tizzano M, Cristofoletti M, Sbarbati A, et al: Expression of taste receptors in solitary chemosensory cells of rodent airways. BMC Pulm Med 11:3, 2011.

Uraih L, Morgan KT, Maronpot RR: Symposium on toxicologic pathology of the upper respiratory system. Environ Health Perspect 85:161–352, 1990.

Young JT: Histopathologic examination of the rat nasal cavity. Fundam Appl Toxicol 1:309–312, 1981.

Zhou X, Zhang X, Weng Y, et al: High abundance of testosterone and salivary androgen-binding protein in the lateral nasal gland of male mice. J Steroid Biochem Mol Biol 117:81–86, 2009.

Zufall F: The TRPC2 ion channel and pheromone sensing in the accessory olfactory system. Naunyn Schmiedebergs Arch Pharmacol 371:245–250, 2005.

Pharynx and Larynx

Bak-Pedersen K, Nielsen KO: Subepithelial mucous glands in the adult human larynx. Studies on number, distribution and density. Acta Otolaryngol 102:341–352, 1986.

Bluestone CD, Klein JO: Otitis media and Eustachian tube dysfunction. In Bluestone CD, editor: Pediatric otolaryngology (ed 4), Philadelphia, PA, 2003, Saunders, pp 474–685.

Cesta MF: Normal structure, function and histology of mucosa-associated lymphoid tissue. Toxicol Pathol 34:599–608, 2006.

Harrison DFN: *The anatomy and physiology of the mammalian larynx*, Cambridge, 1995, Cambridge University Press.

Hoyt RF, Hawkins JV, St Claire MB, et al. Mouse physiology. In Fox JG, et al. editor: *The mouse in biomedical research* (vol 3), *Normative biology, husbandry and models* Ed 2, Burlington, MA, 2007, pp 23–90.

Jowett A, Shrestha R: Mucosa and taste buds of the human epiglottis. J Anat 193:617–618, 1998.

Kaufmann W, Bader R, Ernst H, et al: 1st international ESTP expert workshop: "Larynx squamous metaplasia". A reconsideration of morphology and diagnostic approaches in rodent studies and its relevance for human risk assessment. Exp Toxicol Pathol 61:591–603, 2009.

Kittel B, Ruehl-Fehlert C, Morawietz G, et al: Revised guides for organ sampling and trimming in rats and mice—Part 2. Exp Toxicol Pathol 55:413–431, 2004.

Laitman JT, Reidenberg JS: Evolution of the human larynx. In Fried MP, Ferlito A, editors: The larynx (ed 3), San Diego, CA, 2009, Plural Publishing, pp 19–38.

Lewis DJ: Morphological assessment of pathological changes within the rat larynx. Toxicol Pathol 19:352–357, 1991.

Maronpot RR, Boorman GA and Gaul BW: Pathology of the mouse. Reference and atlas, 1999, Cache River Press; Vienna, IL.

Mills SE: Larynx and pharynx. In Mills SE, editor: Histology for pathologists (ed 3), Philadelphia, PA, 2007, Lippincott Williams & Wilkens, pp 431–444.

Nakano T, Iwama Y: Intermediate epithelium lining the mouse auditory tube. Acta Anat 136:134–138, 1989.

Nakano T, Muto H: Anatomical observations in the pharynx of the mouse with special reference to the nasopharyngeal hiatus. Acta Anat 121:147–152, 1985.

Nakano T, Muto H: The transitional zone in the epithelium lining the mouse epiglottis. Acta Anat 130:285–290, 1987.

Nakano T, Yoshioka I, Muto H: Structure and postnatal transformation of the intermediate epithelium lining the mouse nasopalatine duct. Acta Anat 132:132–136, 1988.

Negus VE: *The comparative anatomy and physiology of the larynx*, London, 1949, Heinemann Medical Books.

Ovalle WK, Nahirney PC: *Netter's essential histology*, Philadelphia, PA, 2008, Saunders.

Renne RR, Gideon KM: Types and patterns of response in the larynx following inhalation. Toxicol Pathol 34:281–285, 2006.

Renne RR, Miller RA: Microscopic anatomy of toxicologically important regions of the larynx of the rat, mouse and hamster. In Jones TC, Dungworth DL, Mohr U, editors: Monographs on pathology of laboratory animals, respiratory system (ed 2), Berlin, 1996, Springer, pp 43–51.

Renne RR, Gideon KM, Miller RA, et al: Histologic methods and interspecies variations in the laryngeal histology of F344/N rats and B6C3F1 mice. Toxicol Pathol 20:44–51, 1992.

Renne RR, Gideon KM, Harbo SJ, et al: Upper respiratory tract lesions in inhalation toxicology. Toxicol Pathol 35:163–169, 2007.

Renne RR, Brix A, Harkema J, et al: Proliferative and nonproliferative lesions of the rat and mouse respiratory tract. Toxicol Pathol 37:5S–73S, 2009.

Sagartz JW, Madarasz AJ, Forsell MA, et al: Histological sectioning of the rodent larynx for inhalation toxicity testing. Toxicol Pathol 20:118–121, 1992.

Sbarbati A, Merigo F, Benati D, et al: Laryngeal chemosensory clusters. Chem Senses 29:683–692, 2004.

Thomas LB, Stemple JC, Andreatta RD, et al: Establishing a new animal model for the study of laryngeal biology and disease: an anatomic study of the mouse larynx. J Speech Lang Hear Res 52:802–811, 2009.

Widdicombe JH, Chen LL-K, Sporer H, et al: Distribution of tracheal and laryngeal mucous glands in some rodents and the rabbit. J Anat 198:207–221, 2001.

ORAL CAVITY AND TEETH 7

PIPER M. TREUTING
University of Washington School of Medicine, Seattle, WA, United States

THOMAS H. MORTON JR.
University of Washington School of Dentistry, Seattle, WA, United States

PETER VOGEL
St Jude Children's Research Hospital, Memphis, TN, United States

Introduction

The oral cavity of rodents and humans has similar functions in digestion and sound production (speech) (Table 7.1). Major differences are primarily in the dentition, which reflects the divergence in diets among species. The basic components of the rodent and human oral cavity are the same: the lips, oral mucosa, teeth, tongue, and salivary glands all begin the process of digestion.

Oral Cavity

GROSS ANATOMY

The rodent oral cavity is delineated externally by the lips, which are covered by labial skin composed of an external epithelium containing abundant hairs and adnexa. Rodents have numerous vibrissae on the muzzle, the large sinus tactile hairs (see Chapter 24: Skin and Adnexa) most prominent on the upper lip (Fig. 7.1A). Humans do not have vibrissae. Rodent lips are normally cleft, with a midline fissure between the upper incisors (Fig. 7.1A). Caudal/posterior to the incisors, the lips fold into a space (diastema) located bilaterally between the incisors and first molars. Here, the external haired epithelium is in contact with the tongue. In humans (but not rodents), the vermillion (red) zone serves as the transition between the skin and oral mucosa of the lips (Fig. 7.1B). It has a rich vascular supply and does not contain the adnexa found in skin except for occasional Fordyce spots (visible sebaceous glands). Human maxillary and mandibular lips have central labial frena (frenum labii superior/inferior) that attach to the alveolar mucosa; these are not present in rodents. In some individuals, the maxillary labial frenum may extend between the maxillary central incisors to the palate, resulting in a gap (diastema).

The lateral boundary of the oral cavity is the cheeks; the posterior limits are the epiglottis and the soft palate. The hard and soft palates form the roof, and the tongue completes the base (Figs. 7.2 and 7.3). Because human oral cancers arise in specific anatomic locations, the oral mucosa in humans has been regionally defined in great

Comparative Anatomy and Histology. DOI: http://dx.doi.org/10.1016/B978-0-12-802900-8.00007-5
© 2018 Elsevier Inc. All rights reserved.

TABLE 7.1 Oral Cavity and Teeth

Feature	Rodent	Human
	Gross	
Lips	Cleft between maxillary incisors	Cleft lip abnormal, if present
Vermillion zone	Absent	Present
Diastemata	Space filled by upper lip folding inward between first molar and incisors	Common between the deciduous incisors and cuspids of both jaws in children; uncommon between the maxillary central incisors in some adults
Tongue	Based at epiglottis to lower incisors, distal portion attached to floor of mouth. Dorsal roughened appearance, ventral and sides smooth	Based in the oropharynx, extending anterior to the incisors, attached to the floor of the mouth along the lateral and anterior by a lingual frenum at the anterior midline
Hard palate	From incisors to the posterior of the third molars; eight ridges	From incisors, the incisive papilla posterior to the tuberosities
Soft palate	Relatively short	Midline adjacent to molars posterior into oropharynx forming ulula at midline
Uvula	Absent	Present
Dental formula	2(I1/1, C0/0, PM0/0, M3/3)=16	2(I2/2, C1/1, P2/2, M3/3)=32
Tooth color	Yellow incisors from iron present in enamel	Normal enamel color white to off-white
Deciduous teeth	Absent	2(2CI, 2LI, 2C, 4M)=20
Incisors	Two upper and lower. Grow continuously	Four upper and lower deciduous replaced by four upper and lower adult teeth
Molars	Six upper and lower	Four upper and lower deciduous molars replaced by adult premolars: six upper and lower adult molars
Alveolar bone	Grows with development and eruption of teeth and regresses with loss of teeth	Grows with development and eruption of teeth and regresses with loss of adult teeth
	Histologic	
Labia	External, haired. Internal, variably keratinized squamous epithelium. No labial frena present	Orthokeratinized vermillion starting anterior at skin with transition to nonkeratinized or parakeratinized labial mucosa. Frenum labii superior/inferior present
Buccal mucosa	Variably keratinized squamous epithelium	Nonkeratinized to parakeratinized
Gingiva	Variably keratinized squamous epithelium	Parakeratinized
Ventral tongue	Variably keratinized squamous epithelium, smooth appearance	Nonkeratinized
Dorsal tongue	Heavily keratinized papillae (circumvallate, foliate, fungiform), rough, except for anterior to epiglottal attachment. Posterior tongue has numerous laminal proprial mucous glands; serous glands are deeper within the skeletal muscle fibers and open at the circumvallate papillae	Heavily parakeratinized or orthokeratinized papilla (circumvallate, foliate, fungiform) rough from tip into oropharynx. Serous glands in the circumvallate papilla, submucosal mucoserous glands lateral border and intramuscular mucoserous glands anterior ventral tongue
Lingual tonsil	Absent	Present posterior third, a portion of Waldeyer's ring
Hard palate	Eight ridges of dense connective tissue; anterior midline to first ridge are two openings to nasal cavity	Orthokeratinized, anterior fibrous ridges (rugae), incisive papilla above the incisive foramen, submucosal mucous glands at junction of hard/soft palate into soft palate
Soft palate	Variably keratinized squamous epithelium	Nonkeratinized to parakeratinized
Deciduous teeth	Absent	Enamel on all oral surfaces that may wear on the incisal/occlusal with age, revealing dentin. Roots resorb with development and eruption of the adult teeth
Incisors	Consist of crown-only "open rooted." Enamel presents only on labial surface. Lingual surface thin layer of cementum. Tip is filled with dentin and secondary dentin	Enamel on all oral surfaces
Molars	Crown, cervical margin (neck) and roots. Enamel-free areas on the cusps	Enamel on all oral surfaces to cervical (cemento-enamel junction)
Periodontium	Cementum, periodontal ligaments, alveolar bone, and junctional gingiva	Below cemento-enamel junction, junctional epithelium, cementum, periodontal ligament attached to cementum and alveolar bone

detail (see Further Reading). In contrast, the rodent oral and gingival mucosa has not been not formally defined by region. The hard palate is covered by attached palatal mucosa, which has anterior transverse rugae and is similar in all three species. Rodents lack a uvula, the soft cone-shaped projection of the soft palate seen in humans (Fig. 7.2).

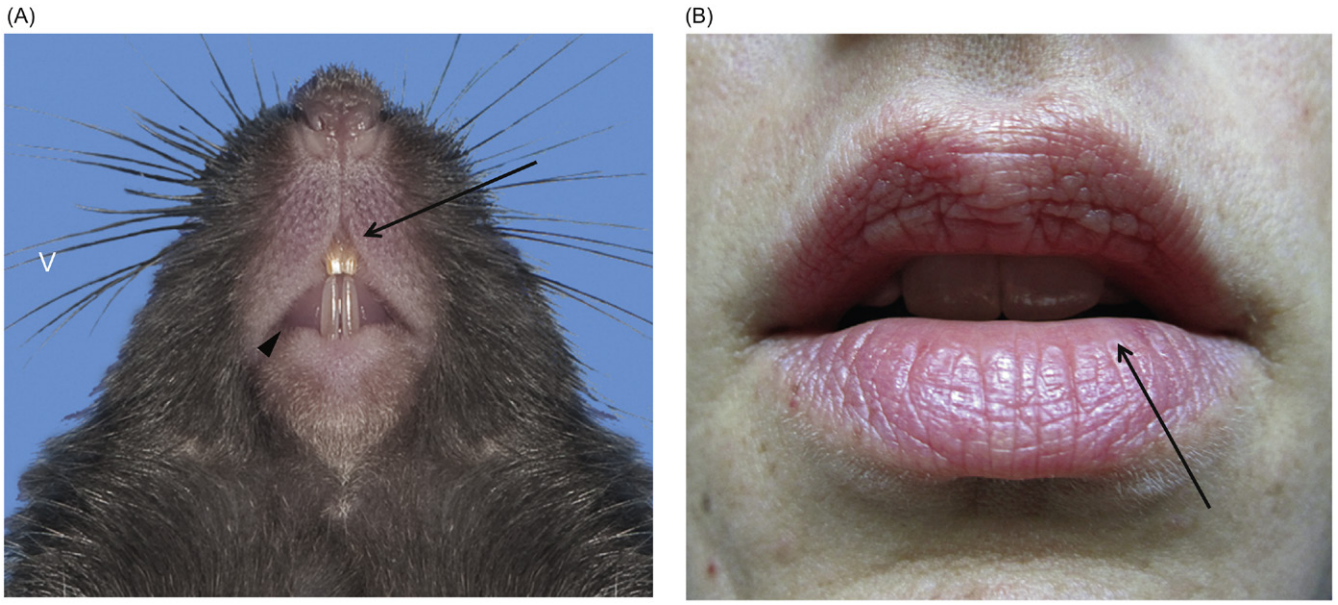

FIGURE 7.1 Muzzle and lips. (A) Rodent (mouse) muzzle. The lips (arrow) are cleft, exposing the prominent incisors. They fold into the oral cavity at the diastemata (arrowhead) between the incisors and molars. Vibrissae (V), the large sinus tactile hairs, project far from the head and are not present in humans. (B). Human lips. The vermillion zone (arrow) is a highly vascular region between the skin and the mucocutaneous junction.

Need-to-know

- Rodent incisors are prominent, exposed by the cleft lip, and yellow tinged due to high iron content in the outer and surface enamel layers.

The rodent tongue base is attached from the epiglottis to the third molar, where it becomes unattached and extends to the lower incisors. In humans, there is a lingual frenum that usually attaches to the floor of the mouth, but may attach to the alveolar mucosa or, in some individuals, to the attached gingiva. Rodents lack a lingual frenum. The dorsal surface of the tongue in all three species is visibly roughened by three types of papillae—the fungiform, filiform, and V-shaped circumvallate—located in the postmolar region. At the rodent epiglottis, there is a smooth region devoid of papillae. At the tip of the rodent tongue, there is a dorsal median groove that ends shortly before a marked elevation at the intermolars (called the intermolar eminence). The sides and ventral aspect of the rodent tongue are covered by typical oral mucosa and are grossly smooth. In contrast, humans have bilateral foliate papillae on the lateral border of the tongue that appears as vertical leaf like folds.

HISTOLOGY

The lips in all three species have a cutaneous portion with hairs (see Chapter 24: Skin and Adnexa) (Fig. 7.4) and a mucocutaneous junction. At the mucocutaneous junction, labial skin transitions to nonhaired keratinized squamous epithelium (mucous membrane). The vermillion zone of human lips is covered by a thin layer of orthokeratinized squamous epithelium with a corrugated surface and a highly vascular dermis (Fig. 7.4B). The epithelium increases in thickness posteriorly, where it transitions in rodents to thickened orthokeratinized mucosa (Figs. 7.4A,C and 7.5A) and in humans to nonkeratinized or slightly parakeratinized stratified squamous epithelium of the labial mucosa (Figs. 7.4B and 7.5C). In rodents, the lips are relatively thin with minimal lamina propria, skeletal muscle, and fat. Rodents do not have the mucoserous labial glands present in the human

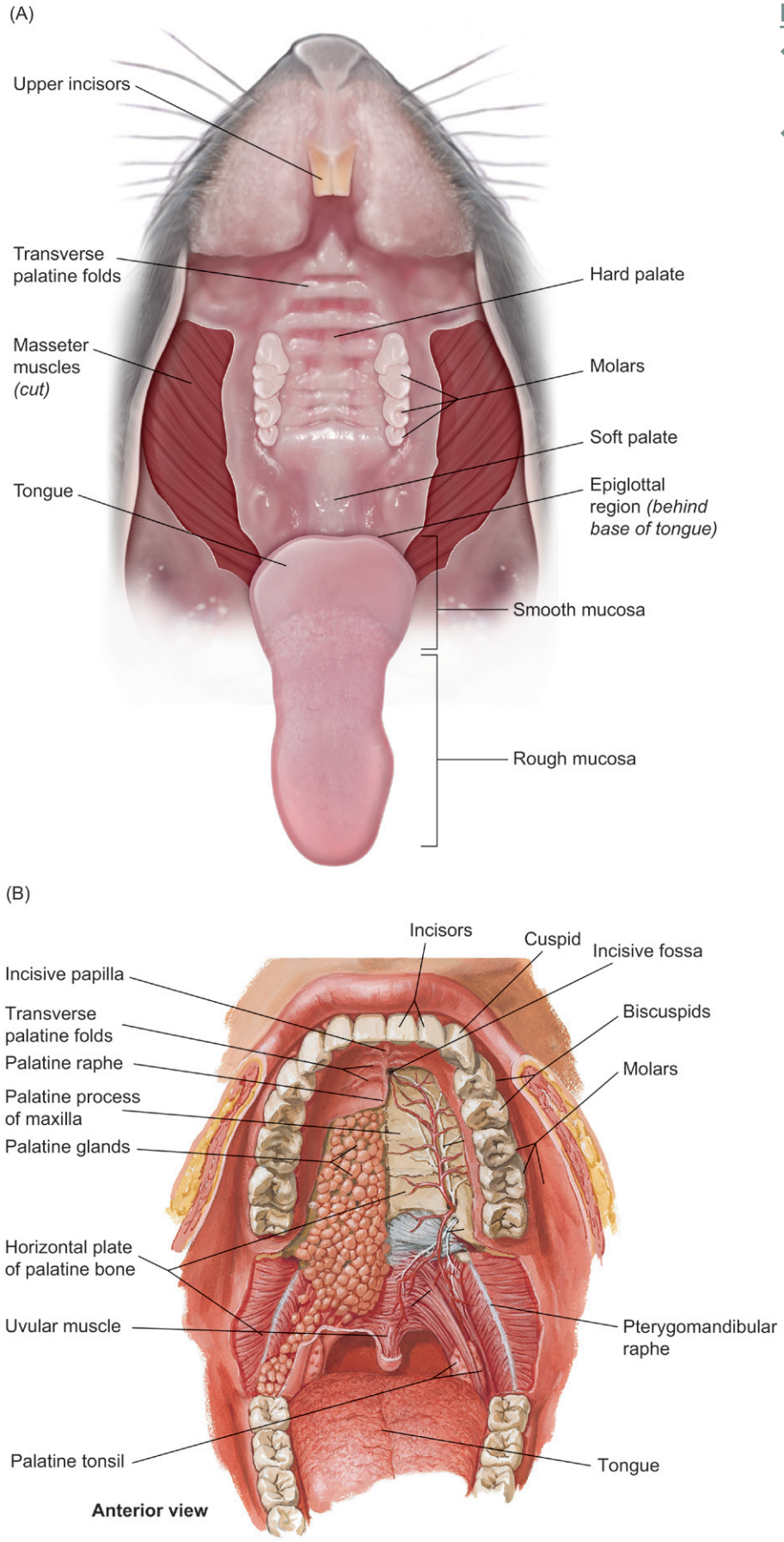

Need-to-know

- The rodent oral cavity should be inspected at necropsy for broken, maloccluded, or overgrown incisors.
- Malocclusion in rodents is a relatively common cause of malnutrition as the incisors grow continuously.

FIGURE 7.2 Regional anatomy of the oral cavity. (A) Rodent (mouse). The hard palate extends from the incisors to the posterior of the third molars and has eight ridges. The rodent dental formula is 2(I1/1, C0/0, PM0/0, M3/3)=16. (B) Human. The anterior hard palate contains the incisive papilla posterior to the central incisors and the transverse palatine folds and extends from the incisors to the posterior of the third molars and the soft palate. Humans have a uvula at the midline of the soft palate. The human dental formula is 2(I2/2, C1/1, P2/2, M3/3)=32. Source: © Elsevier, Inc., www.netterimages.com.

labial lamina propria; however, there are large sebaceous glands located at the angles of the mouth that open to the mucosal surface (Fig. 7.5A). These may be akin to the Fordyce spots seen in humans (Fig. 7.5B,C).

The rodent oral cavity (including the labial, buccal, palatine, and gingival mucosa) is lined by variably orthokeratinized squamous epithelium. The thickness of this keratin layer varies with diet and frequency of ingestion. Fasted or anorexic rodents have increased keratin thickness and occasionally adherent bacterial colonies, especially in the distal esophagus and nonglandular stomach (see Chapter 11: Upper Gastrointestinal Tract).

The human oral mucosa is functionally divided into attached masticatory, lining, and specialized mucosa. The lining mucosa, comprising the buccal mucosa, sulcular mucosa, alveolar mucosa, floor of the mouth, ventral tongue, and soft palatal mucosae, is composed of nonkeratinized-to-slightly parakeratinized stratified squamous epithelium with rete ridges of various lengths. The buccal and labial mucosae are thick and the buccal mucosa may have a spongy appearance. The buccal mucosa may be bilaterally hyperparakeratinized along the bite plane of the teeth, forming what is clinically called the linea alba. The lamina propria of the buccal and labial mucosae has denser collagen and elastin fibers that attach to the underlying muscle. The lamina propria of the alveolar mucosa, sulcus, and floor of the mouth contains loose fibrovascular connective tissue with mixed minor glands. Fordyce granules may be present in the buccal and labial mucosa extending posteriorly to the retromolar region and rarely onto the soft palate.

The bulk of the tongue in all three species is composed of interwoven bands of skeletal muscle interspersed with lingual salivary glands, vessels, nerves, supportive connective tissue, and white adipose tissue (Figs. 7.6–7.8). Mast cells may be present in the interstitial connective tissue of the rodent tongue. In all three species, the serous glands (von Ebner's) are located in the posterior/caudal tongue lamina propria underlying the circumvallate papillae and within the superficial muscle; the ducts of these glands empty into the base of the invaginations between the papillae. There are mucous glands present in all three species; however, in rodents these are restricted to the caudal aspect (Figs. 7.6 and 7.8C). In humans, there are lobules of mixed mucous and serous salivary glands within the muscle of the anterior ventral tongue that forms the glands of Blandin–Nuhn. Their ducts extend to the ventral surface mucosa medial to the plica fimbriata on either side of the lingual frenum. Within the lamina propria along the posterior lateral human tongue are mucous glands of Weber. In all three species, the dorsal tongue is covered by grossly roughened mucosa composed of filiform and fungiform papillae (Figs. 7.8). In rodents, this mucosa, like other areas of the oral cavity, is heavily orthokeratinized. In humans, the dorsal lingual mucosa is covered by parakeratinized and sometimes orthokeratinized stratified squamous epithelium that may have superficial aggregates of bacteria. In all three species, the ducts of the serous glands open at the circumvallate papillae, providing lubrication for the taste buds (Figs. 7.8 and 7.9). Taste buds are morphologically similar between rodents and humans, but vary in location. They are present at the circumvallate papillae in all three species, and in humans, they are also present along the lateral lingual border within the foliate papillae. The majority of human taste buds are found on the tongue, with a high number also on the soft palate and a few on the epiglottis, larynx, and pharynx. Rodent taste buds are found on the soft palate, larynx, and pharynx.

The rodent hard palate has eight grossly visible ridges composed of dense connective tissue. These

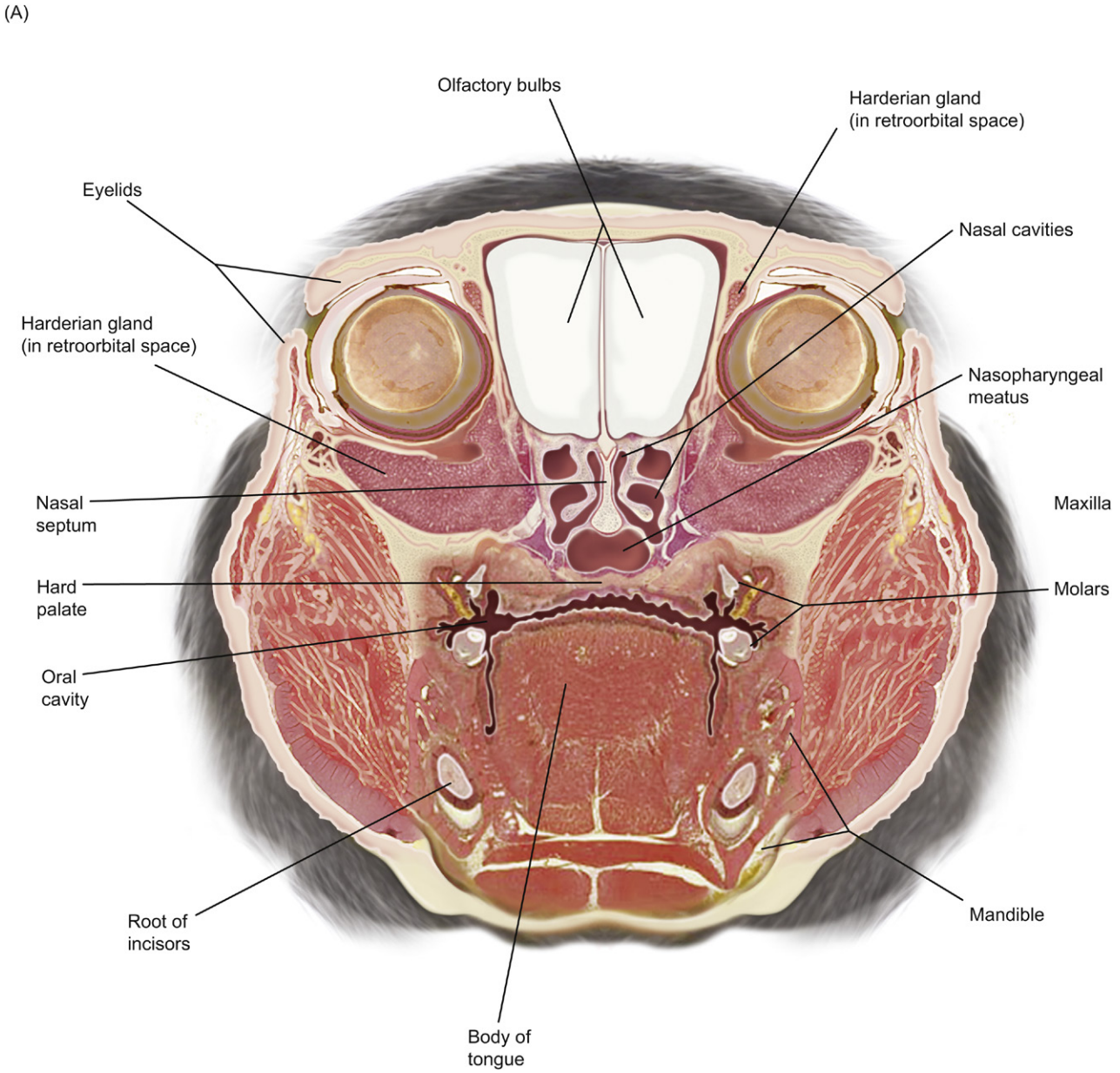

FIGURE 7.3 Coronal sections of the head. (A) Rodent (mouse). The lateral boundary of the oral cavity is the cheeks; the posterior limits are the epiglottis and the soft palate. The hard and soft palates form the roof; the tongue is the base (see Fig. 7.2). (B) Human. The human oral cavity is bounded superiorly by the hard palate and maxillary alveolar bone, laterally by the buccal mucosa that covers the buccinator muscles, and inferiorly by the mucosa of the floor of the mouth that overlies the sublingual glands. The buccal mucosa extends superiorly and inferiorly to become the maxillary and mandibular sulci with transition to the alveolar mucosa and the gingiva. The floor of the mouth becomes the ventral surface of the tongue, which transitions to the specialized mucosa of the lateral and dorsal tongue. Source: © Elsevier, Inc., www.netterimages.com.

ridges blend with the periosteum of the palatine process of the premaxillary, maxillary, and palatine cranial bones (Figs. 7.7 and 7.10). The rodent hard palate transitions to the soft palate (Fig. 7.11), which is composed of mucosa overlying connective tissue, mucous glands, and skeletal muscle. The soft palate is contiguous with the pharynx and contains taste buds (Fig. 7.11B). The histological structures of the human hard palate (Fig. 7.10B) and soft palates are similar to that of rodents.

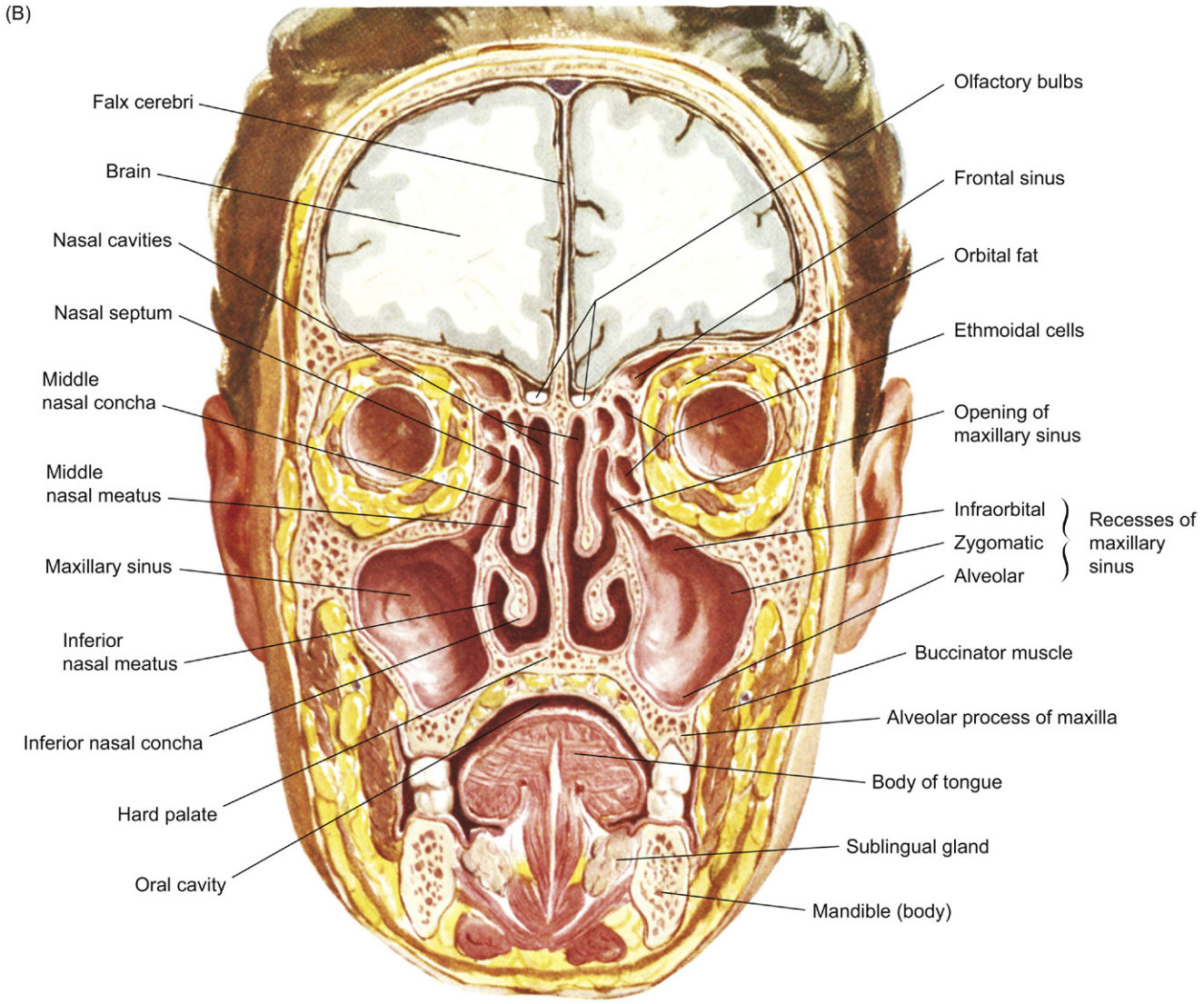

FIGURE 7.3 (Continued).

TEETH

GROSS ANATOMY

Rodents are monophyodont, meaning they develop only one set of teeth throughout life. In contrast, humans are diphyodont, developing two successive sets of teeth known as deciduous and permanent. Rodent incisors are prominent, exposed by the cleft lip, and yellow-tinged due to high iron content in the outer and surface enamel layers (Fig. 7.1A). Humans do not normally have cleft lips and teeth do not normally contain high levels of iron. The rodent dental formula is 2(I1/1, C0/0, PM0/0, M3/3)=16, with the three molars and one incisor separated by a toothless region called the diastema (Fig. 7.2A). In rodents, both the top and bottom incisors grow continuously throughout life and consist of only a crown (both intra- and extra-alveolar portions). This is in contrast to their molars, which have roots, a connecting neck region, and an extra-alveolar crown. The cusps of

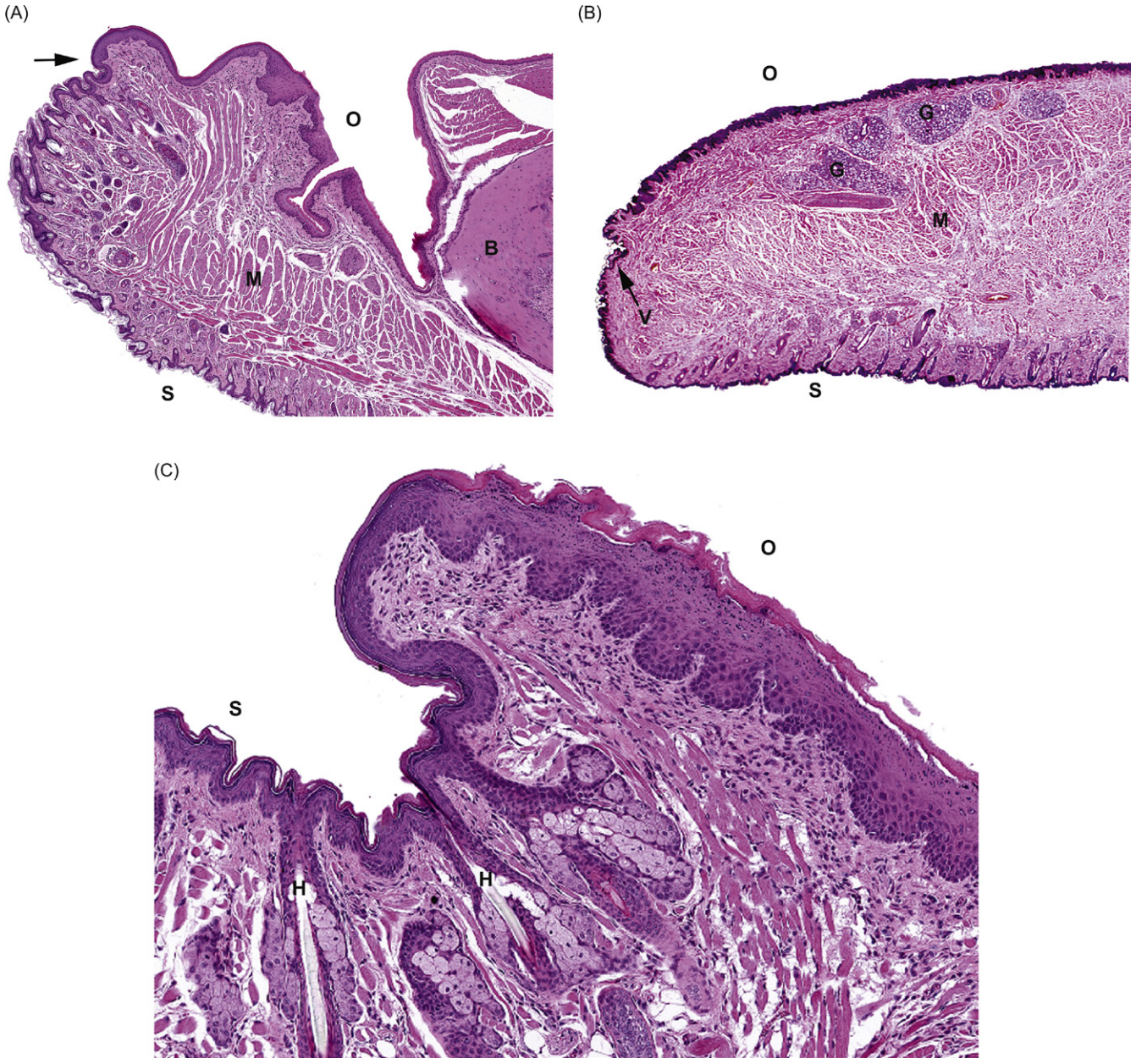

FIGURE 7.4 Longitudinal section of the lip. (A) Rodent (mouse) lip. At the mucocutaneous junction (arrow), the labial skin transitions to the typical oral nonhaired mucous membrane composed of variably keratinized squamous epithelium (arrow). Muscle (M), oral mucosa (O), skin (S), and bone (B) are indicated. (B) Human lip. The bulk of the lower lip is made up of bundles of circumoral skeletal muscle (M) seen in transverse section. The external surface of the lip is covered by skin (S) with adnexa that transitions through the vermillion zone (V) to merge (arrow) with the oral mucosa (O) of the inner surface. This zone derives its color from the richly vascular dermis, which has a thin orthokeratinized epidermal covering. The oral mucosa covering the inner surface of the lip has a thicker nonkeratinized-to-slightly parakeratinized stratified squamous epithelium, and the underlying submucosa contains numerous accessory mixed mucoserous salivary glands (G). (C) Rodent (mouse) mucocutaneous junction. Enlarged from A. The outer skin of the lip (S) contains hair follicles (H) and adnexa. At the mucocutaneous junction, the epithelium transitions to an orthokeratotic stratified squamous epithelium lacking hair follicles and adnexa. Oral mucosa (O) is indicated. Source of B: Reprinted from Young, B. et al: *Wheater's functional histology*, ed 5, Philadelphia, PA, 2006, Churchill Livingstone with permission from Elsevier, www.netterimages.com.

Need-to-know

- The rodent oral mucosal epithelium is orthokeratotic squamous.
- Human oral mucosal epithelium is nonkeratinized to slightly parakeratinized stratified squamous.

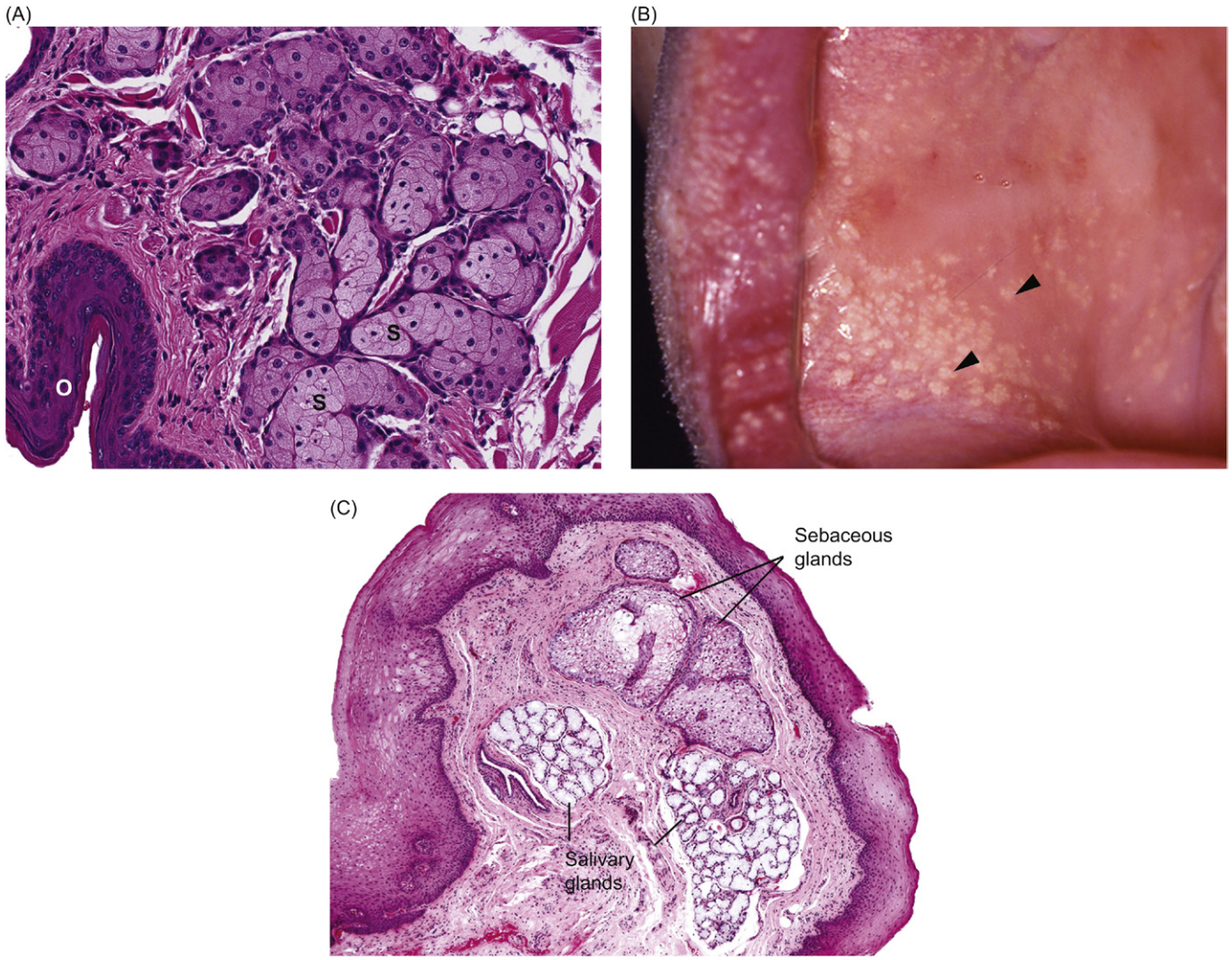

FIGURE 7.5 Sebaceous gland in the oral cavity. (A) Rodent (mouse) sebaceous glands. Large sebaceous glands (S) located at the angles of the mouth open to the oral mucosal surface (O). (B) Sebaceous glands in the mucosa of the human cheek. Known clinically as Fordyce's granules, these sebaceous glands (arrowheads) are present in about 75% of adult humans. (C) Histologic section of human oral mucosa with sebaceous and minor salivary glands. Source of B and C: Reprinted from Nanci, A: *Ten Cate's oral histology*, ed 7, . St. Louis, MO, 2007, Mosby with permission from Elsevier, www.netterimages.com.

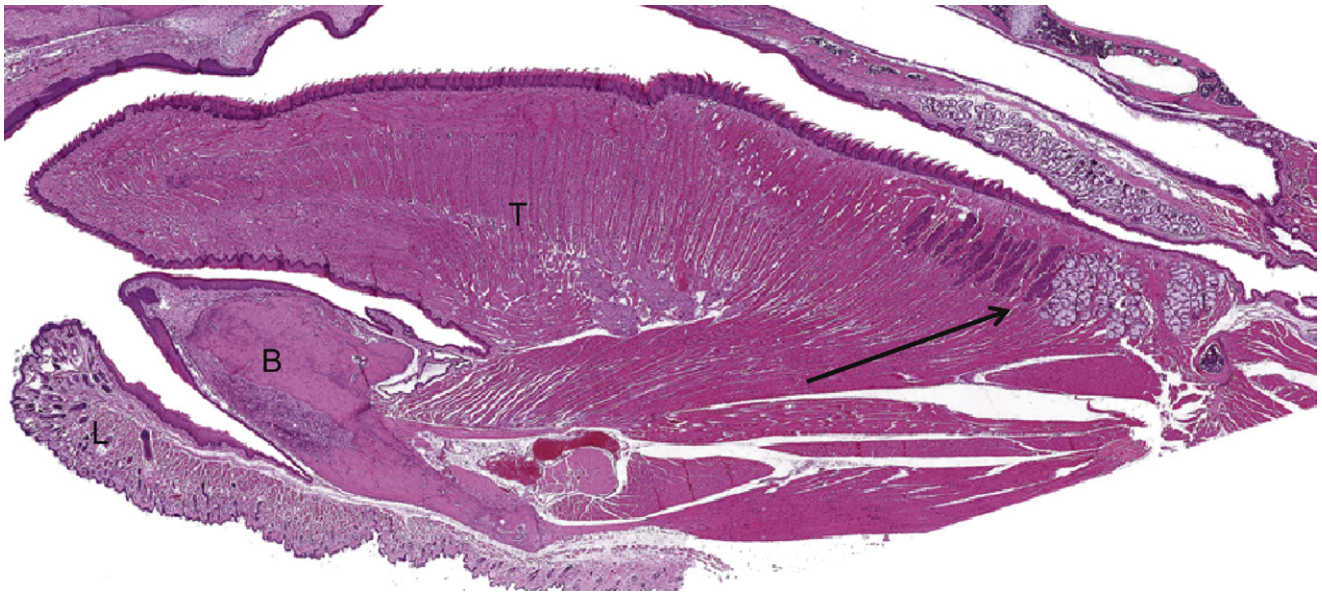

FIGURE 7.6 Longitudinal section of rodent (mouse) tongue. The bulk of the tongue in all species is composed of interwoven bands of skeletal muscle, interspersed by the lingual salivary glands, vessels, nerves, and supportive connective and white adipose tissue. In the rodent, the mixed lingual glands are located caudally (arrow). Tongue (T), lip (L), and bone of mandible (B) are indicated.

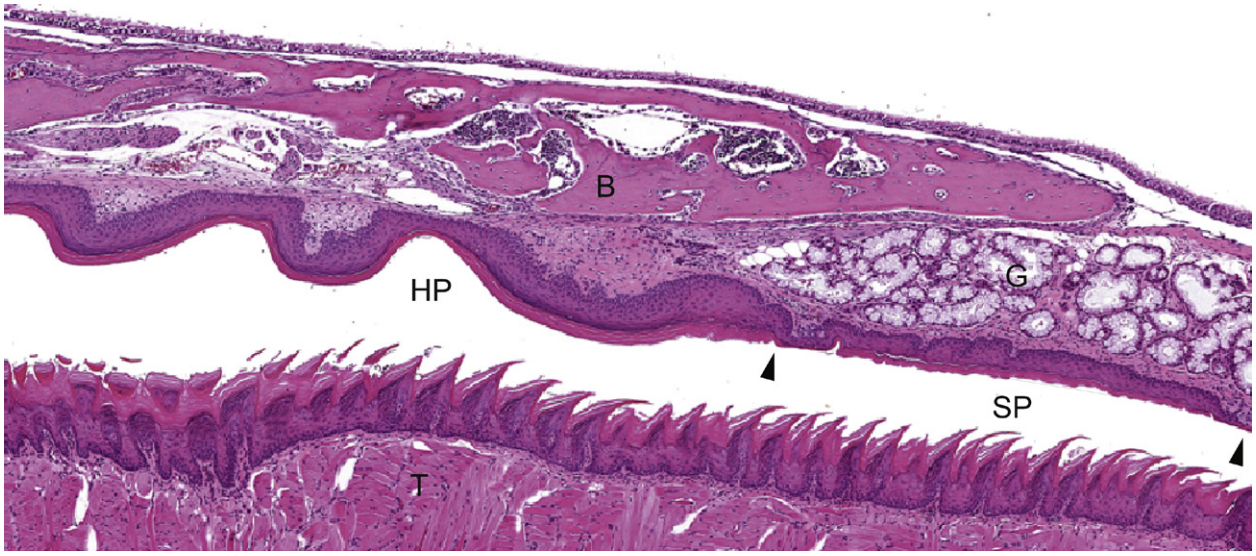

FIGURE 7.7 Longitudinal section of the rodent (mouse) palate and dorsal tongue (T). The hard palate (HP) is firmly attached to the underlying bone (B) with little submucosa. In contrast, the soft palate (SP, between arrowheads) overlies connective tissue, mucous glands (G), and skeletal muscle.

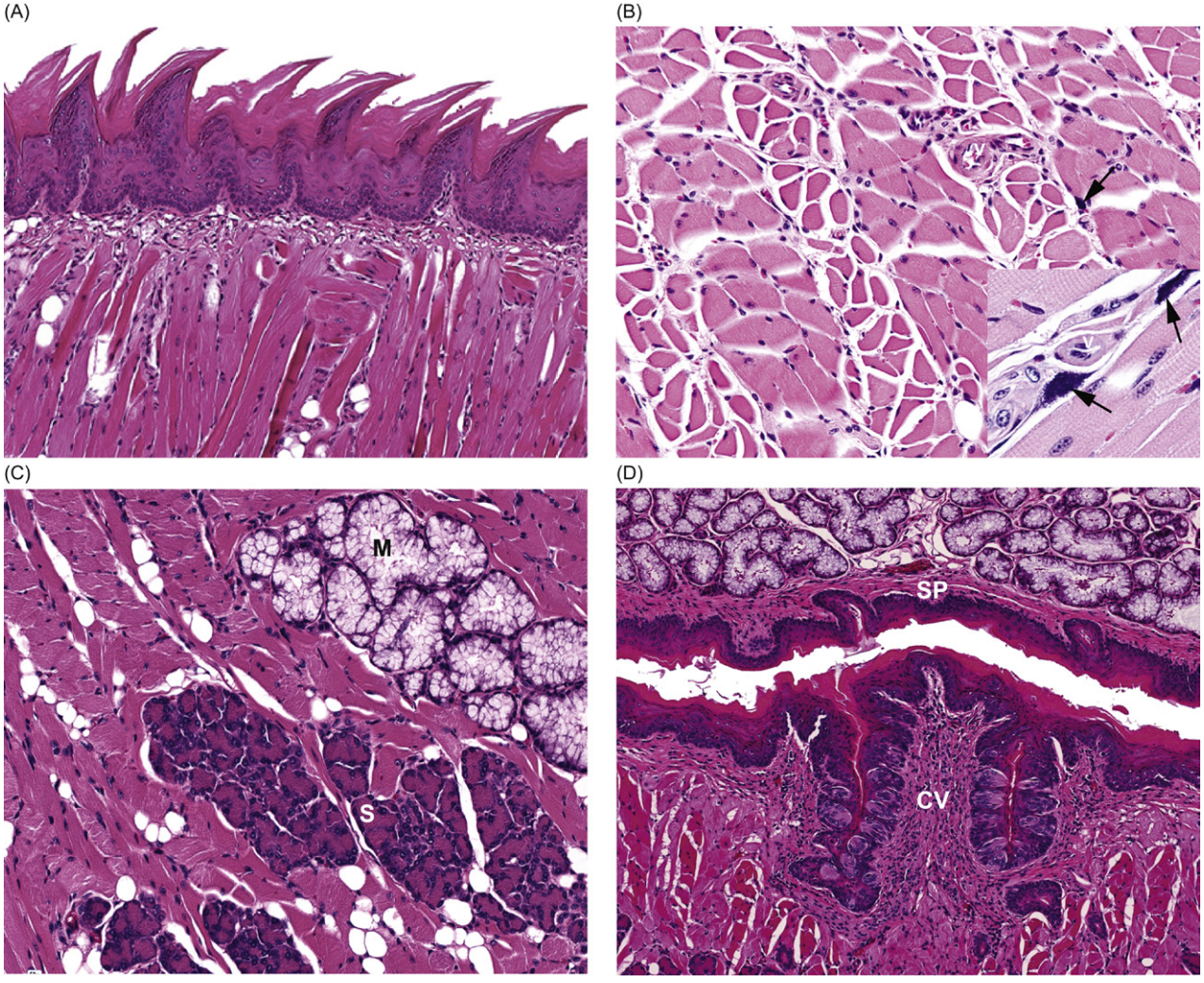

FIGURE 7.8 Rodent (mouse) tongue. (A) The dorsal mucosal surface of the tongue is covered with heavily keratinized papillae that are mechanical and sensory and that are similar to those of other mammals, including humans. The filiform papillae shown are the most numerous in all species. (B) High magnification view of tongue skeletal muscle. The interwoven fibers are typical in all species. Mast cells (arrows; inset) may be present in rodent tongue. (C) Lingual salivary glands. There are numerous mucous (M) and serous (S, von Ebner's) glands located in the lamina propria and between skeletal muscle fibers of the posterior tongue in all species. (D) Caudal tongue. The circumvallate papilla (CV) is sensory with taste buds lining the groove. The ducts of the serous glands open at the circumvallate papillae, providing lubrication for taste buds. The soft palate (SP) is indicated.

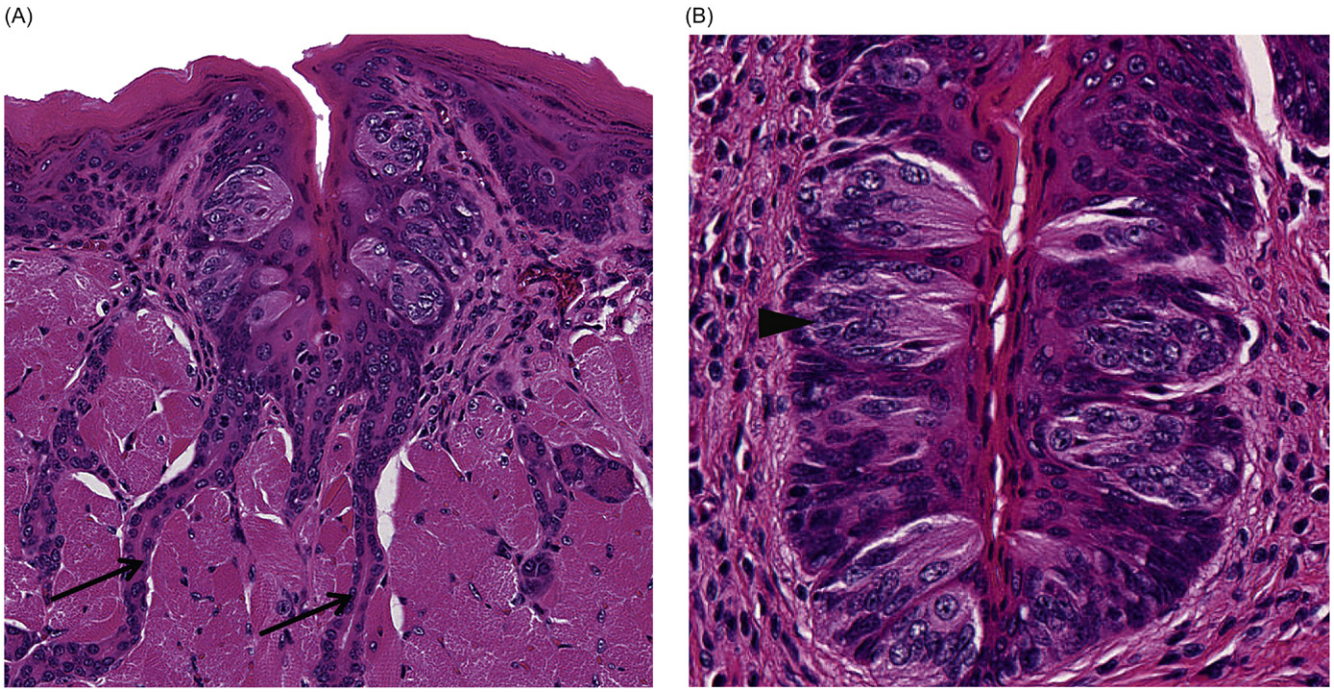

FIGURE 7.9 Rodent (mouse) taste buds. (A) Circumvallate papillae. The ducts of the serous glands open at the circumvallate papillae in all species, providing lubrication for taste buds (arrows). (B) High-power view of the pale-staining taste bud chemoreceptor cells located along the circumvallate trough (arrowhead).

Need-to-know

- Taste buds can be present in the tongue, soft palate, larynx, and pharynx of rodents.
- Histology of the tongue is similar for all the species.

rodent molars lack enamel. Adult humans have a continuous dentition of teeth, and their dental formula is 2(I2/2, C1/1, P2/2, M3/3)=32 (Fig. 7.2B). The crowns of human teeth are entirely covered by enamel, so dentin is not normally visible. The intra-alveolar roots in all three species are composed of dentin covered by cementum, which is attached to the bone by fibrous tissue known as the periodontal ligament, which serves to anchor the teeth to the surrounding bone.

HISTOLOGY

The incisors of rodents are covered by enamel only on the labial surface. The lingual surface of the incisors is covered by thin cementum where periodontal ligament fibers attach. The tips of the incisors are filled with primary dentin, switching to secondary dentin when the primary is worn from gnawing. The incisors are renewed on average every 35–45 days in mice and 40–50 days in rats; however, damage, diet, and genotype may affect this rate. The constant growth of rodent incisors requires proper gnawing in order to both maintain sharpness and prevent growth into the lips or palate. Overgrown incisors are a common cause of malnutrition or failure to thrive; an oral cavity examination is critical in any rodent necropsy. The roots of these incisors extend to the molar roots and thus will often be present in molar sections as well (Fig. 7.12). Although fully mineralized mature enamel is removed during routine preparation of decalcified sections, leaving an empty space, the protein-rich enamel matrix can frequently be seen in decalcified coronal sections of developing incisors (Fig. 7.13). To evaluate mature enamel in histological sections, special techniques are required (see Further Reading).

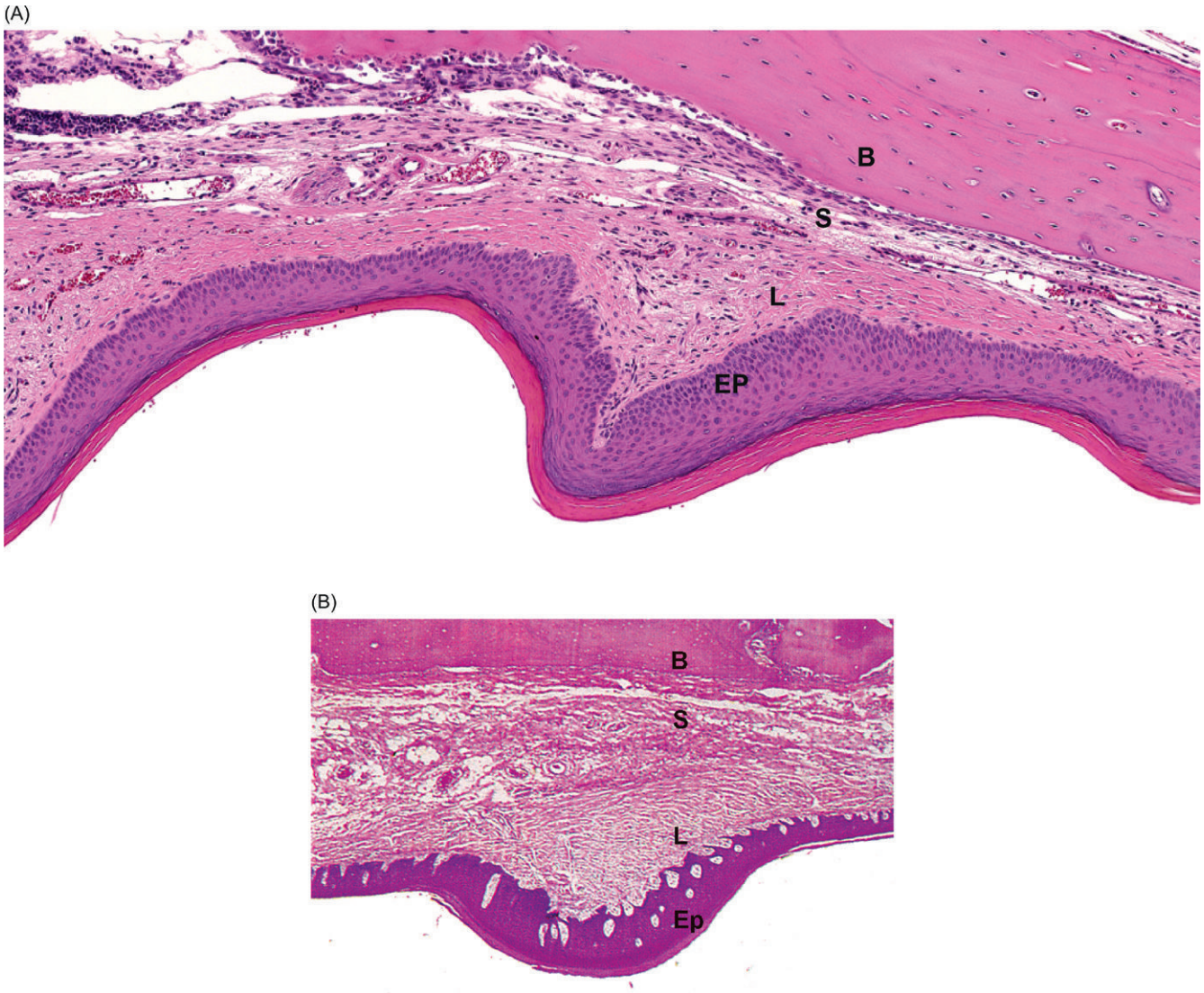

FIGURE 7.10 Hard palate. (A) One of eight grossly visible ridges of the rodent (mouse) hard palate made of orthokeratized squamous epithelium (EP) overlying dense connective tissue (L) that blend with the submucosa (S) and periosteum of the palatine process of the premaxillary, maxillary, and palatine cranial bones (B). (B) The primate hard palate is covered by orthokeratinized stratified squamous epithelium (EP) supported by a densely collagenous lamina propria (L). The anterior palatal mucosa has several transverse folds or rugae, one of which is shown in this micrograph. The mucosa of the hard palate is anchored to the underlying bone (B) by relatively dense submucosal tissue (S) posteriorly containing the palatal glands. Source: Reprinted from Young, B. et al: *Wheater's functional histology*, ed 5, Philadelphia, PA, 2006, Churchill Livingstone with permission from Elsevier.

Importantly, the histological organization of rodent (Figs. 7.13–7.15) and human teeth is very similar. In all three species, blood and lymphatic vessels and nerves pass through the apical foramina to the dental pulp cavity of the tooth, where they are contained in a loose connective tissue. In rodents, the apical foramina of the incisors are wide, in contrast to those of the molars, which gradually narrow with age. In rodents and humans, odontoblasts (dentin-producing cells) line the dental pulp cavity (Fig. 7.14). These tall, columnar cells differentiate from primitive mesenchymal cells. Odontoblasts produce predentin, which mineralizes to dentin, an acellular and avascular substance. As the odontoblasts secrete dentin, they are displaced deeper into the pulp while maintaining connection with the dentin by cytoplasmic processes. These processes are surrounded by the dentin forming the dentinal

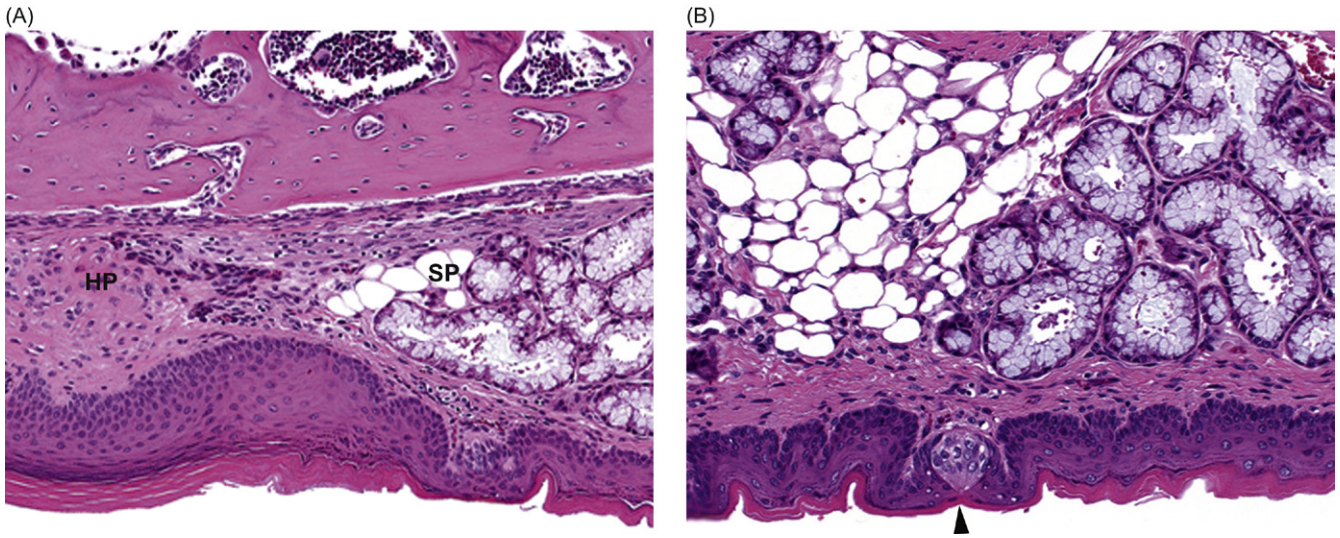

FIGURE 7.11 Rodent (mouse) palate. (A) Transition between hard palate (HP) and soft palate (SP) mucosa. The soft palate continues caudally to the pharynx. (B) The soft palate is composed of squamous epithelium overlying connective tissue, skeletal muscle, numerous mucous glands, and contains taste buds (arrowhead).

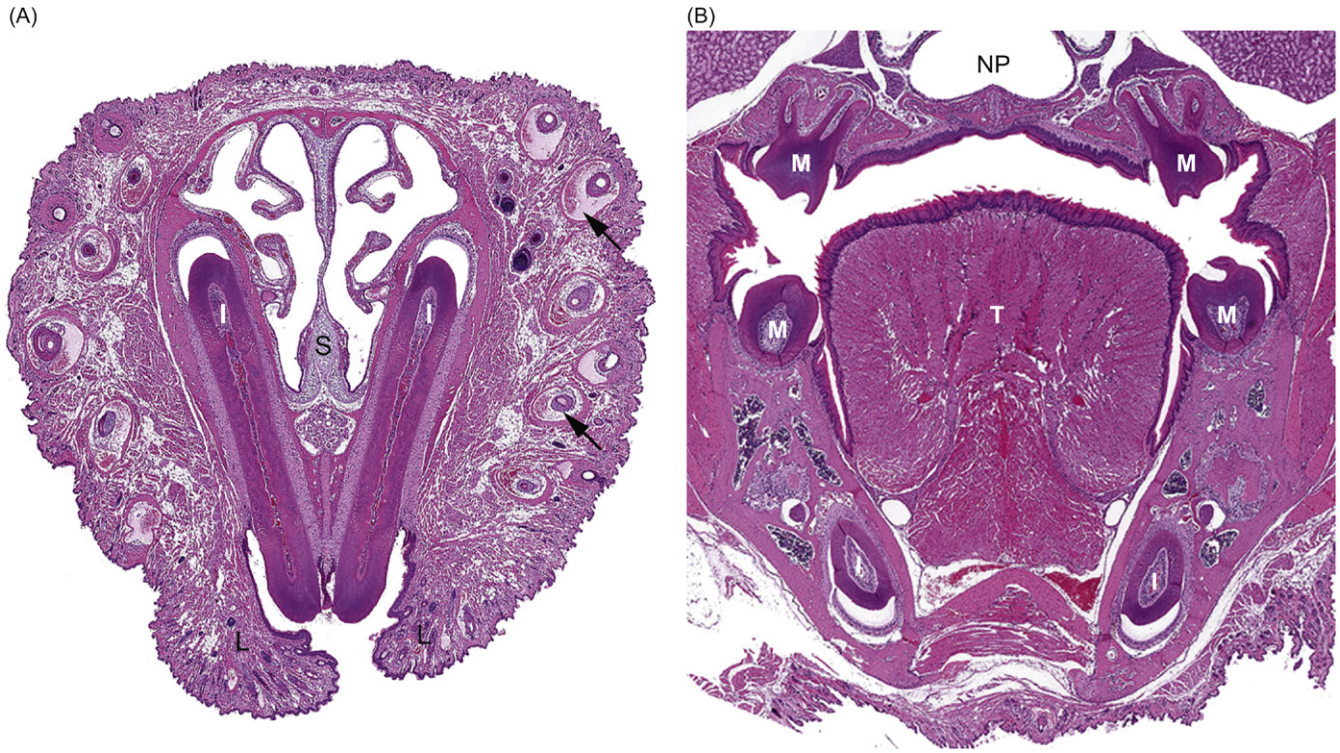

FIGURE 7.12 Rodent (mouse) teeth in situ. (A) Upper incisors. The incisors (I) are visible through the cleft upper lip (L). Vibrissae (arrows) and nasal septum (S) are indicated. (B) Coronal mandible. The incisors (I) have roots that penetrate deeply into the jaw, where they can be seen in section with the molars (M). Tongue (T) and nasopharynx (NP) are indicated. Tissue courtesy Dan Stetson and Tina Gall, University of Washington.

Need-to-know

- In rodents, hair fragments often embed in the gingival sulcus, causing periodontitis that may result in tooth loss and osteomyelitis.
- The constant growth of the incisors of rodents requires proper gnawing in order to both maintain a sharp tooth and to prevent growth into the lips or palate.

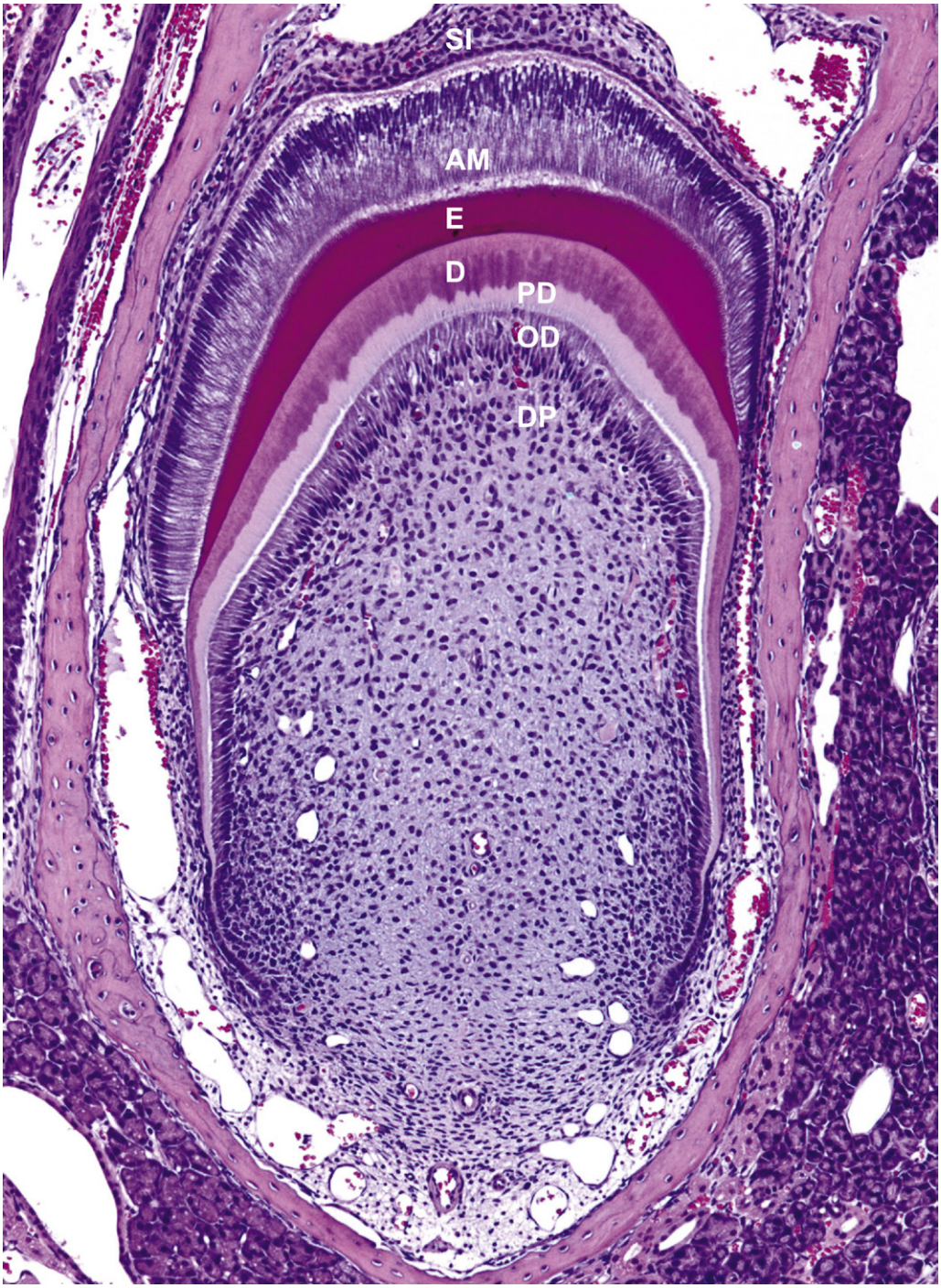

FIGURE 7.13 Decalcified coronal section of developing rodent (mouse) incisor. The histology of growing rodent and human teeth is similar. On the outermost surface of the tooth, a layer of short cuboidal stratum intermedium (SI) cells support elongated ameloblasts (AM) that produce the enamel matrix (E); on the pulp side, dentin (D) and predentin (PD) are produced by odontoblasts (OD) that line the dental pulp (DP) cavity.

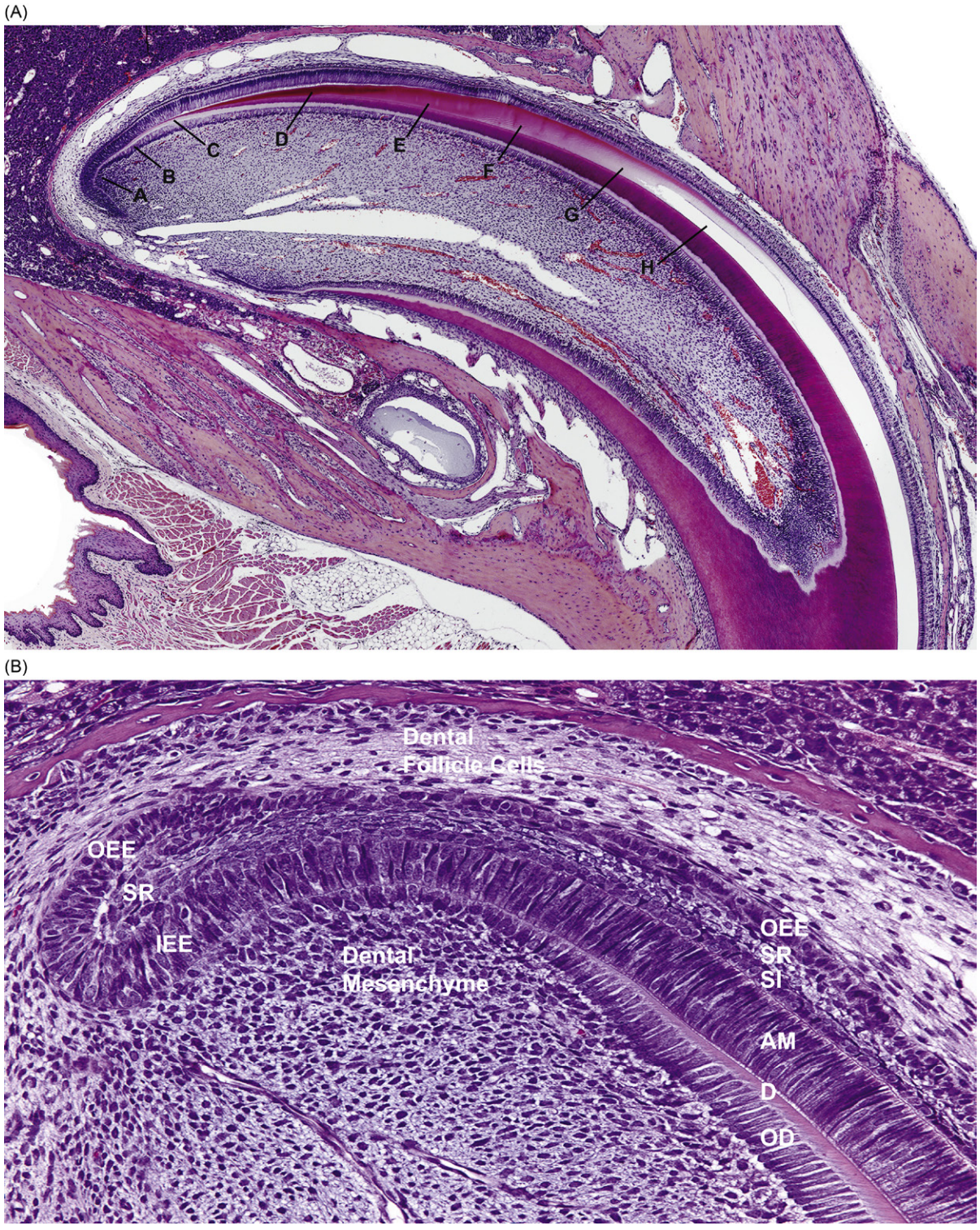

FIGURE 7.14 Decalcified longitudinal section of developing rodent (mouse) maxillary incisors. (A) All stages of amelogenesis (enamel development) can be seen in a single longitudinal section of continuously growing incisor (letters corresponding panels in Fig. 7.15 showing each region). (B) Labial cervical loop of incisor from the incisor apex (region A). This structure contains all the stem and/or progenitor cells that become ameloblasts and odontoblasts. The loosely aggregated stellate reticulum (SR) is between the outer enamel epithelium (OEE) on one side and the stratum intermedium and inner enamel epithelium (IEE) on the other. Also present in this area are stratum intermedium (SI) cells, ameloblasts (AM), dentin (D), and odontoblasts (OD), which line the dental pulp (DP) cavity.

(A) Pre-secretory, cervical loop region

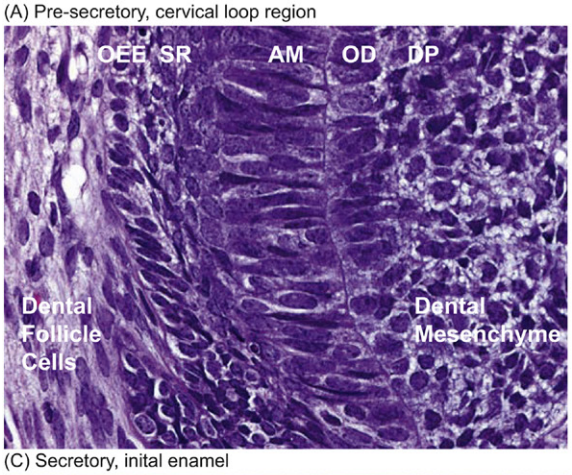

(B) Pre-secretory, dentin region

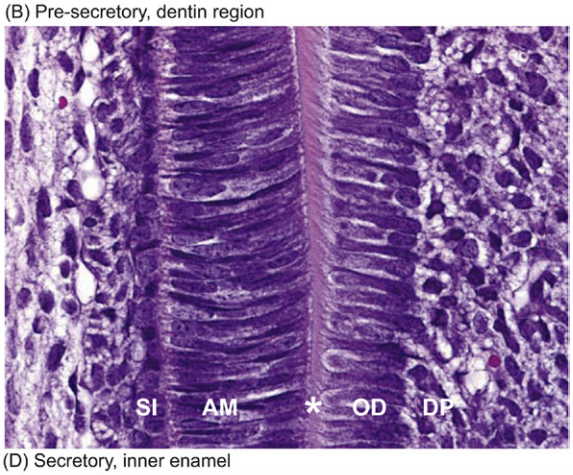

(C) Secretory, inital enamel

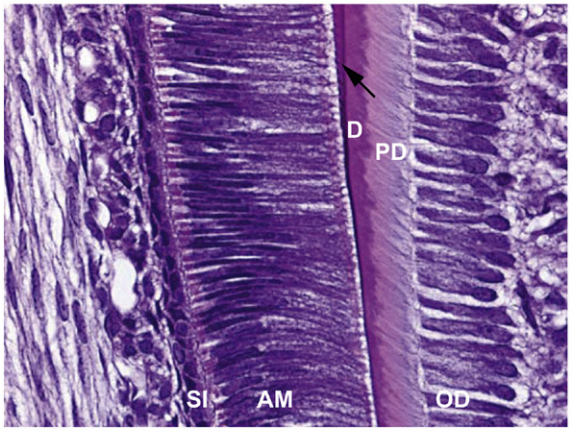

(D) Secretory, inner enamel

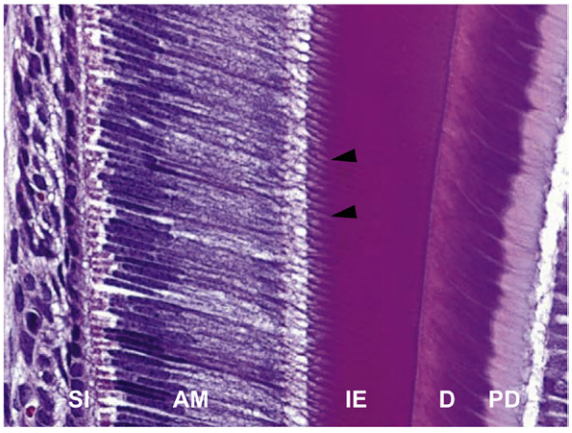

(E) Secretory stage, outer enamel region

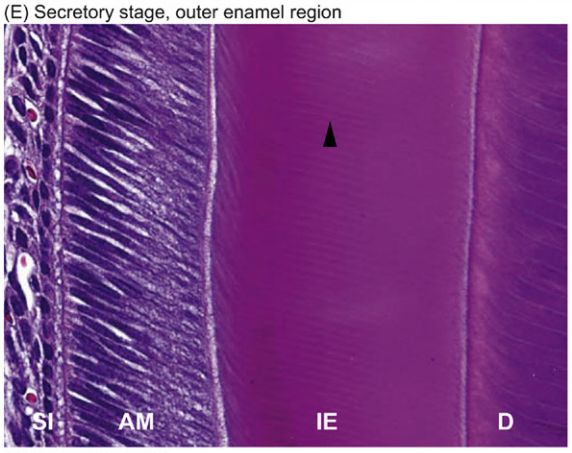

(F) Secretory stage, rodless enamel

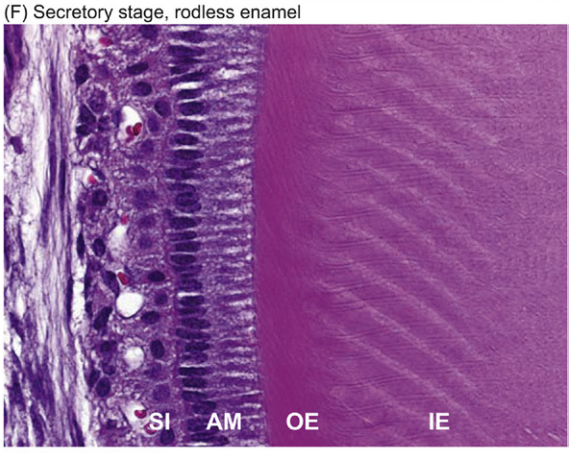

(G) Early maturation

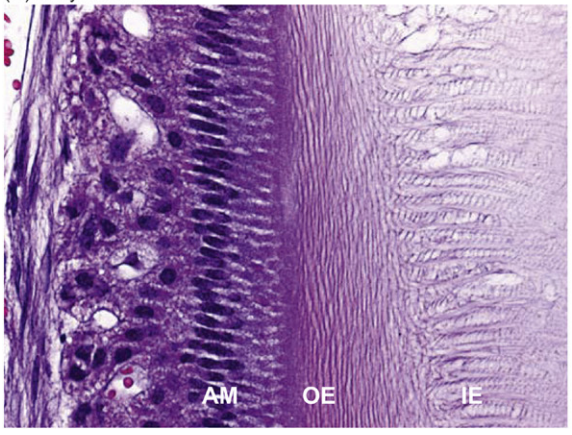

(H) Late maturation

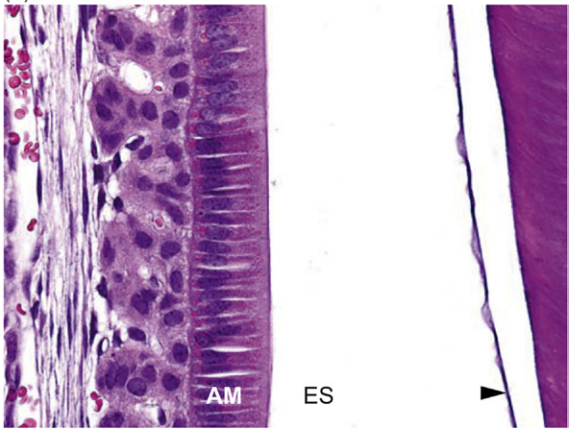

tubules. In early tooth development, dentin production is required for the induction of ameloblasts, the enamel-producing cells of the tooth, which are arranged in a single-cell row supported by the intermediate stratum and the stellate reticulum.

The continuously growing rodent incisor has proven to be an excellent model for investigating tooth development processes. Longitudinal incisor sections (Fig. 7.14A) display all the spatio-temporal steps that occur during amelogenesis (enamel formation) and include the cervical root region containing the stem and/or progenitor cells capable of generating ameloblasts and odontoblasts (Fig. 7.14B).

Histologically, the process of amelogenesis (Fig. 7.14–7.15) on the labial surface of rodent incisor teeth is generally subdivided into presecretory, secretory, and maturation stages, which are located in sequential anatomical regions of the erupting incisors. In the presecretory stage, ameloblasts proliferate, eventually becoming mature columnar secretory cells, and induce the differentiation of odontoblasts into mature columnar secretory cells. The presecretory stage contains two regions, first where ameloblasts face undifferentiated odontoblasts and pulp (Fig. 7.15A) and second where they face dentin (Fig. 7.15B). In the secretory stage, containing four regions, fully differentiated ameloblasts secrete enamel matrix proteins to produce the largely protein framework of secreted enamel. In the first region, a thin layer of lamellar enamel is laid down at the dentino-enamel junction (Fig. 7.15C). The second region is a much longer zone of inner enamel secretion, where ameloblasts have wide, blunt Tomes' processes and form relatively wide decussating enamel rods (Fig. 7.15D). In the third, outer enamel region, Tomes' processes are longer and thinner, and the enamel consists of thin incisically directed parallel rods (Fig. 7.15E). Finally, in the fourth secretory region, ameloblasts retract their Tomes' processes and lay down a thin continuous layer of rodless enamel (Fig. 7.15F). During the maturation stage, the enamel matrix has reached its full thickness and enamel matrix proteins are progressively removed and replaced with mineral. In the earlier part of the maturation stage found in the first region, ameloblasts frequently have ruffled apical borders, reflecting a shift to removal and replacement of enamel proteins via the release of proteolytic enzymes and minerals. Crystals grow to fill the space created by protein matrix removal, with enamel attaining over 95% mineral content when fully mineralized (Fig. 7.15G). Notably, during later stages of maturation in rodents the second region, ameloblasts contain pigmented material and secrete increasing amounts of iron (Fig. 7.15H). Rodent incisor enamel has a much higher iron content than human enamel, with this iron being largely responsible for the orange-yellow color and increased wear-resistance of rodent incisors. The orange-yellow pigmentation

FIGURE 7.15 Amelogenesis in rodent (mouse) incisor. Panels represent regions shown in Fig. 7.14. Abbreviations: *AM*, ameloblasts; *D*, dentin; *DP*, dental pulp; *E*, enamel; *OD*, odontoblasts; *OEE*, outer enamel epithelium; *PD*, predentin; *SI*, stratum intermedium; *SR*, stellate reticulum. (A) Presecretory stage, cervical loop region. Ameloblasts initially facing dental pulp begin to proliferate, change their polarity, and induce the differentiation of odontoblasts from pulp mesenchymal stem cells into a columnar epithelium. (B) Presecretory stage, dentin region. Ameloblasts face dentin (asterisk) produced by fully differentiated odontoblasts. (C) Secretory stage, initial enamel region. In this very short region, a thin layer of lamellar enamel (arrow) is laid down at the dentino-enamel junction by ameloblasts having a relatively smooth apex. (D) Secretory stage, inner enamel region. In this relatively long region, ameloblasts have wide, blunt Tomes' processes (arrowheads) that form relatively wide decussating enamel rods. (E) Secretory stage, outer enamel region. Tomes' processes are long and thin (arrowhead), and the enamel consists of thin incisically directed parallel rods. (F) Secretory stage, rodless enamel region. Ameloblasts retract their Tomes' processes and lay down a thin final continuous layer of rodless enamel (arrowheads). Maturation (progressive mineralization and removal of enamel proteins) begins when the enamel matrix has reached its full thickness and is reflected by increasingly paler staining of the enamel layer. (G) Maturation stage, early region. In this stage, ameloblasts frequently have ruffled apical borders and release proteolytic enzymes and minerals that gradually replace enamel matrix proteins with mineral. (H) Maturation stage, late region. Demineralization of mature enamel creates a clear enamel space (ES), sometimes with a thin layer of residual enamel protein from the dentino-enamel junction present (arrowhead).

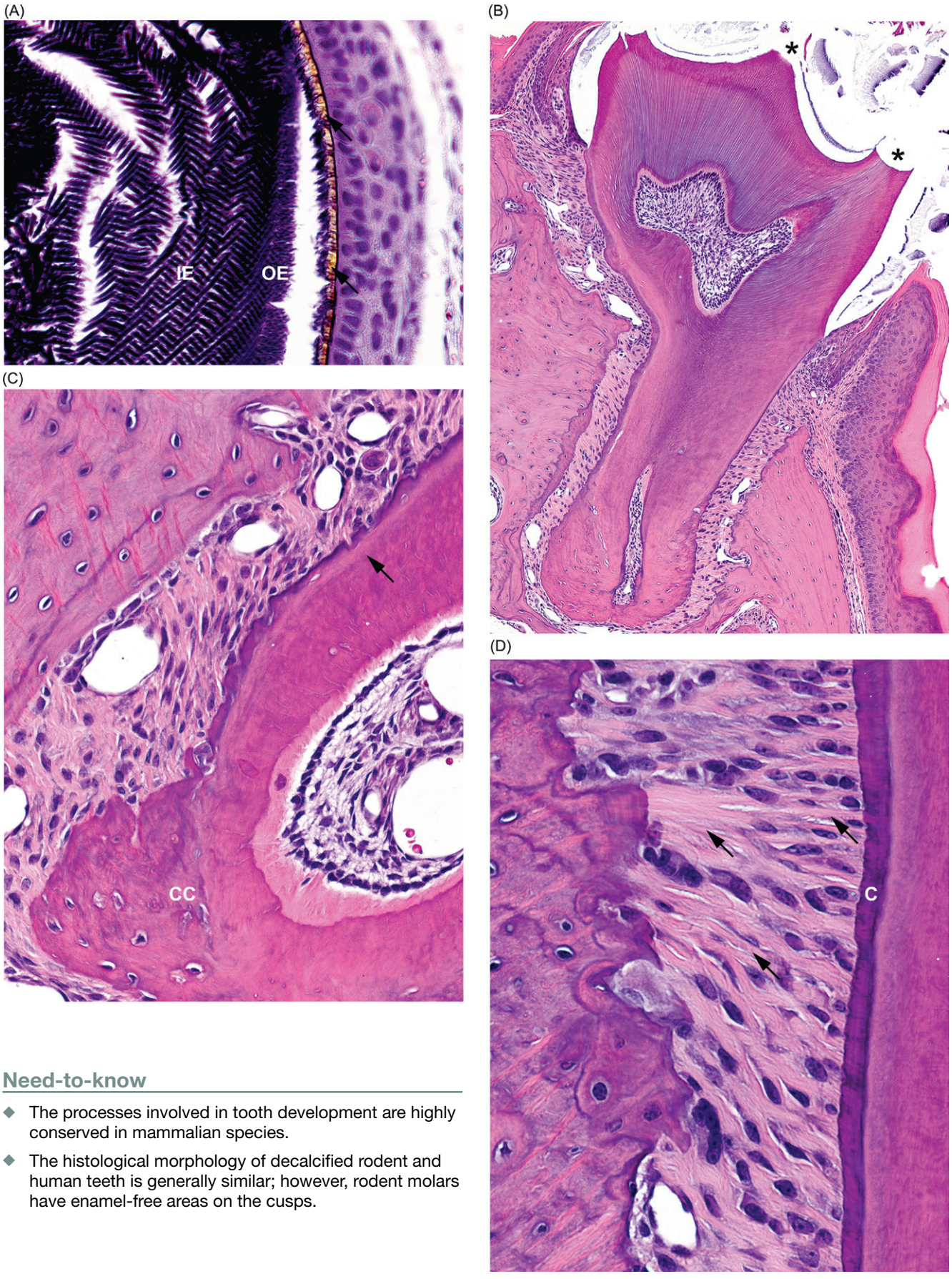

Need-to-know

- The processes involved in tooth development are highly conserved in mammalian species.
- The histological morphology of decalcified rodent and human teeth is generally similar; however, rodent molars have enamel-free areas on the cusps.

of surface enamel can sometimes be detected histologically in partially demineralized tissues (Fig. 7.16A).

The histological presentation of the molars is very similar between the three species, except that in humans all molar surfaces are covered by enamel, whereas in rodents the cusps are devoid of enamel (Fig. 7.16B). Microscopically, two forms of cementum are recognized: cellular and acellular. In all three species, cellular cementum is thickest and most noticeable at the root apex becoming thinner toward the coronal region, where acellular cementum predominates (Fig. 7.16C). With increased age in all three species, there is incisal/occlusal wear of the enamel, and the cellular cementum thickens to maintain occlusion. In all three species, periodontal ligaments anchor the teeth to surrounding bone, with the terminal ends of periodontal ligaments (Sharpey's fibers) extending into both cementum and alveolar bone (Fig. 7.16D).

FURTHER READING

Berkovitz BKB, Moxham BJ, Linden RWA, et al: *Master dentistry volume 3. Oral biology: oral anatomy, histology, physiology and biochemistry*, Philadelphia, PA, 2011, Churchill Livingstone.

Maronpot R, editor: *Pathology of the mouse: reference and atlas*, Vienna, IL, 1999, Cache River Press.

Mills SE, editor: *Histology for pathologists* (ed 4), Philadelphia, PA, 2012, Lippincott Williams & Wilkins.

Nanci A: *Ten Cate's oral histology, development, structure, and function*, ed 7, St. Louis, MO, 2007, Mosby.

Ovalle WK, Nahirney PC: (Netter Basic Science) *Netter's essential histology*, Philadelphia, PA, 2007, Saunders.

Standring S, editor: *Gray's anatomy: the anatomical basis of clinical practice, expert consult—online and print* (ed 40), Philadelphia, PA, 2008, Churchill Livingstone.

Young B, Lowe JS, Stevens A, et al: *Wheater's functional histology: a text and colour atlas*, ed 5., Philadelphia, PA, 2006, Churchill Livingstone.

FIGURE 7.16 Rodent (mouse) tooth features. (A) Incisor with tooth enamel partially demineralized. The surface enamel (arrow) is yellow-orange in color due to high iron content and remains crystalline in partially demineralized tissues because of its higher resistance to acid. Note the thickness of the decussating rods of inner enamel (IE) compared to the thinner outer enamel rods (OE). (B) Molar showing enamel and dentin. Note enamel does not cover the cusps of the rodent molars (asterisk). (C) Molar: cementum. The thick, irregular cellular cementum (CC) layer is most prominent at the apex of the root. A thin layer of acellular cementum (arrow) predominates toward the coronal region of the root. (D) Periodontal ligament of the molar root. These ligaments are anchored into the cementum (C) and alveolar bone (at left) by collagenous Sharpey's fibers (arrows).

This page intentionally left blank

SALIVARY GLANDS 8

RENEE R. HUKKANEN
Eisai US, Andover, MA, United States

SUZANNE M. DINTZIS AND PIPER M. TREUTING
University of Washington School of Medicine, Seattle, WA, United States

INTRODUCTION

In mice, rats, and humans, there are three pairs of major salivary glands and numerous minor glands. Salivary secretions may be serous, mucous, or mixed (both serous and mucous), and they serve similar functions across species—to aid in digestion, taste, protection, and lubrication of the teeth and oral cavity (Tables 8.1 and 8.2). There are abundant similarities among the three types of salivary glands in both rodents and humans. We begin with the shared general anatomy and histology of the major salivary glands. Specific gross and histological characteristics described by gland and species follow.

SALIVARY GLAND FEATURES

GROSS ANATOMY

Rodents and humans both have three paired major salivary glands that are visible grossly—and numerous microscopic minor glands (Figs. 8.1–8.3; Tables 8.1 and 8.2). In rodents, the three major glands are the parotid, submandibular (also called submaxillary or mandibular), and sublingual. These glands must be distinguished from the rodent exorbital lacrimal gland, which is in close anatomical proximity. Humans have the same three major glands. Minor glands in all three species can be found in the lingual, buccal, palatine, pharyngeal, and laryngeal regions (Table 8.2).

GENERAL HISTOLOGY

Salivary glands have a similar anatomic structure across species and type consisting of glandular acini (also termed alveoli) and ducts. Depending on the particular salivary gland, these acini are lined by variable combinations of mucous and serous epithelial cells surrounded by myoepithelial cells, located between the basal plasma membrane and the acinar basement membrane. Secretions from the epithelial cells are contained in apical granules. Mucous cell granules contain mucins, which, when secreted, contribute to saliva viscosity. In contrast, serous cells secretions include water, amylase, ions, and proteins. On contraction, the myoepithelial cells force secretions into the ductal system.

In rodents, the three major salivary gland acini drain to the intralobular intercalated ducts, which connect to the intralobular striated ducts. Several striated ducts drain into an interlobular duct. Secretions then drain to interlobular excretory

Comparative Anatomy and Histology. DOI: http://dx.doi.org/10.1016/B978-0-12-802900-8.00008-7
© 2018 Elsevier Inc. All rights reserved.

TABLE 8.1 Major Salivary Glands

Feature	Rodent	Human
Submandibular Gland		
Gross		
Location	Within ventral cervical subcutaneous region, extending from the mandibular lymph node to thoracic inlet in close association with other glands	In digastric triangle, superior and anterior to digastric muscles and posterior to stylohyoid ligament. Separated into superficial and deep portions by the mylohyoid muscle.
Relative size	Largest major salivary gland	Second largest major salivary gland
Lobulation	Multilobed and lobulated	Similar to rodent
Excretory duct	Duct opens caudal to lower incisors	Similar to rodent
Histologic		
Duct morphology	Unique duct morphology: Granular convoluted ducts connect intercalated and striated ducts. Granular ducts are sexually dimorphic: Male has more and larger ducts with more pink cytoplasmic granules	Not sexually dimorphic
Gland morphology	Compound tubuolalveolar	Similar to rodent
Acinar morphology	Tall pyramidal cells; rat gland may contain oncocytes	Mixed serous and mucous. Serous cells in a crescent-shaped formation on the acini periphery. Mucous cells in direct contact with the duct system.
Secretion	Mouse: predominantly seromucinous Rat: is predominant mucous with serous component	Mixed serous and mucinous
Innervation	Adrenergic innervation	Similar to rodent
Parotid Gland		
Gross		
Location	Within ventral cervical subcutaneous region, extending from submandibular gland, spans region from ear to clavicle	At the base of the zygomatic arch, apex just inferior to the angle of the mandible; extends posterior to ear and anterior to cover masseter
Relative size	Second largest major salivary gland	Largest major salivary gland
Lobulation	Diffuse, multilobulated	Similar to rodent
Excretory duct	Duct opens near mandibular molars	Stensen's duct opens in the mouth by second maxillary molar
Histologic		
Duct morphology	Intercalated duct epithelium is low cuboidal and join directly to intralobular ducts	Intercalated duct epithelium is cuboidal; intralobular ducts are larger in serous glands than in mucous
Gland morphology	Compound tubuolalveolar	Similar to rodent
Acinar morphology	Acinar cells are small and contain apical pink zymogen granules; hyperchromatic basal cytoplasm. Resembles exorbital lacrimal gland and exocrine pancreas; rat gland may contain oncocytes	Similar to rodent
Secretion	Serous	Similar to rodent
Innervation	Adrenergic innervation	Similar to rodent
Sublingual Gland		
Gross		
Location	Within ventral cervical subcutaneous region; close association with submandibular	Above the mylohyoid; below the mucosa of the middle to anterior mouth floor
Relative size	Smallest major salivary gland	Similar to rodent
Lobulation	Single (paired) lobe	Similar to rodent
Excretory duct	Duct opens caudal to mandibular incisors at the sublingual caruncle	Multiple ducts exit caudal to mandibular incisors
Histologic		
Duct morphology	Standard	Similar to rodent
Gland morphology	Compound tubuolalveolar	Similar to rodent
Acinar morphology	Largest salivary acinar cells; tall pyramidal with abundant pale blue cytoplasm (mucous)	Similar to rodent
Secretion	Mucous	Mucous and serous
Innervation	No adrenergic innervation	Adrenergic innervation
Relative size	Smallest major salivary gland	Similar to rodent

TABLE 8.2 Minor Salivary Glands

Gland	Rodent		Human
	Mouse	Rat	
Lingual	von Ebner's gland: mucous and serous	Lingual: serous and mucous Minor sublingual: mucous	von Ebner's: serous Weber's: mucous Blandin–Nuhn: mucoserous
Buccal	Mucous	Buccal: mucous Anterior buccal: serous	Mucoserous
Palatine	Mucous	Mucous	Mucous
Pharyngeal	Mucous	Absent	Mucoserous
Laryngeal	Seromucous	Absent	Mucoserous

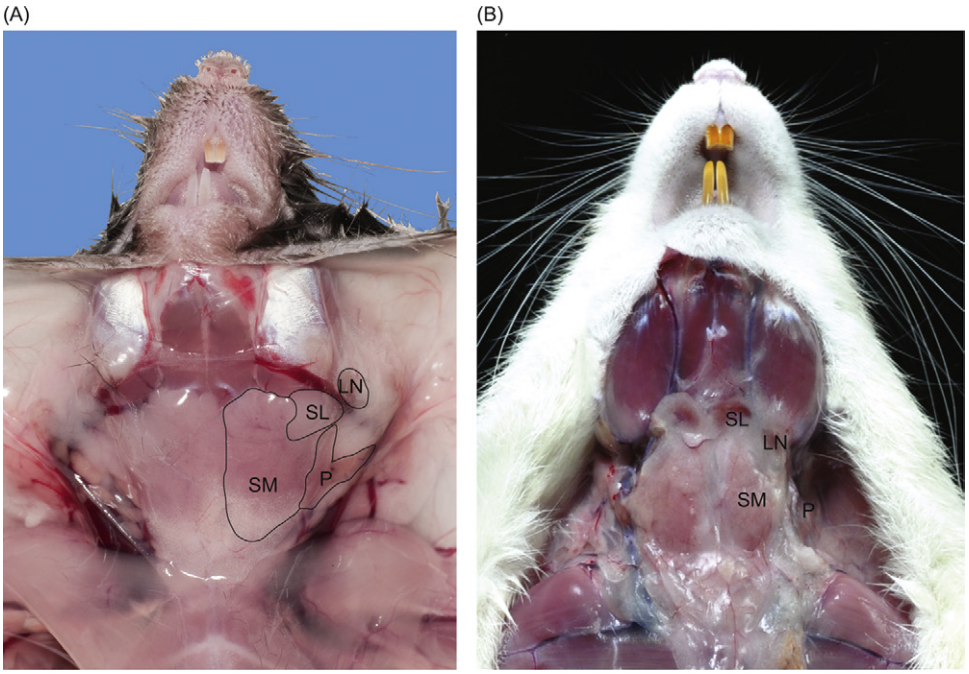

FIGURE 8.1 Rodent regional ventral cervical anatomy. (A) The paired mouse salivary glands are bilaterally located in the cervical neck; regions are outlined in black. (B) Rat ventral head/throat region: submandibular, parotid, and sublingual glands, as well as mandibular lymph nodes, may be removed en block and processed together rather than by separate dissections. Submandibular (SM), sublingual (SL), and parotid (P) salivary glands and lymph node (LN) are indicated. Rat image courtesy Dr. Krista La Perle.

Need-to-know

- Cervical soft tissue contains salivary glands, lymph nodes, and brown and white adipose tissues.
- The thymus is located within the chest cavity.

ducts that empty via the main excretory duct into the oral cavity. The exception is the rodent submandibular gland (as described below), where granular convoluted ducts connect the intercalated to striated ducts (Figs. 8.4 and 8.5). In humans, the duct system of the submandibular and parotid glands is similar to those of rodents, while intercalated and striated ducts are variably present in the sublingual gland. In rodents, the intercalated ducts are often histologically indistinct in all glands, lined by cuboidal-to-flattened epithelium, with minimal surrounding connective tissue. In humans, the intercalated ducts are more distinct, lined by cuboidal epithelium (Fig. 8.6). Striated ducts are more distinct than intralobular ducts in all three species, lined by cuboidal-to-low-

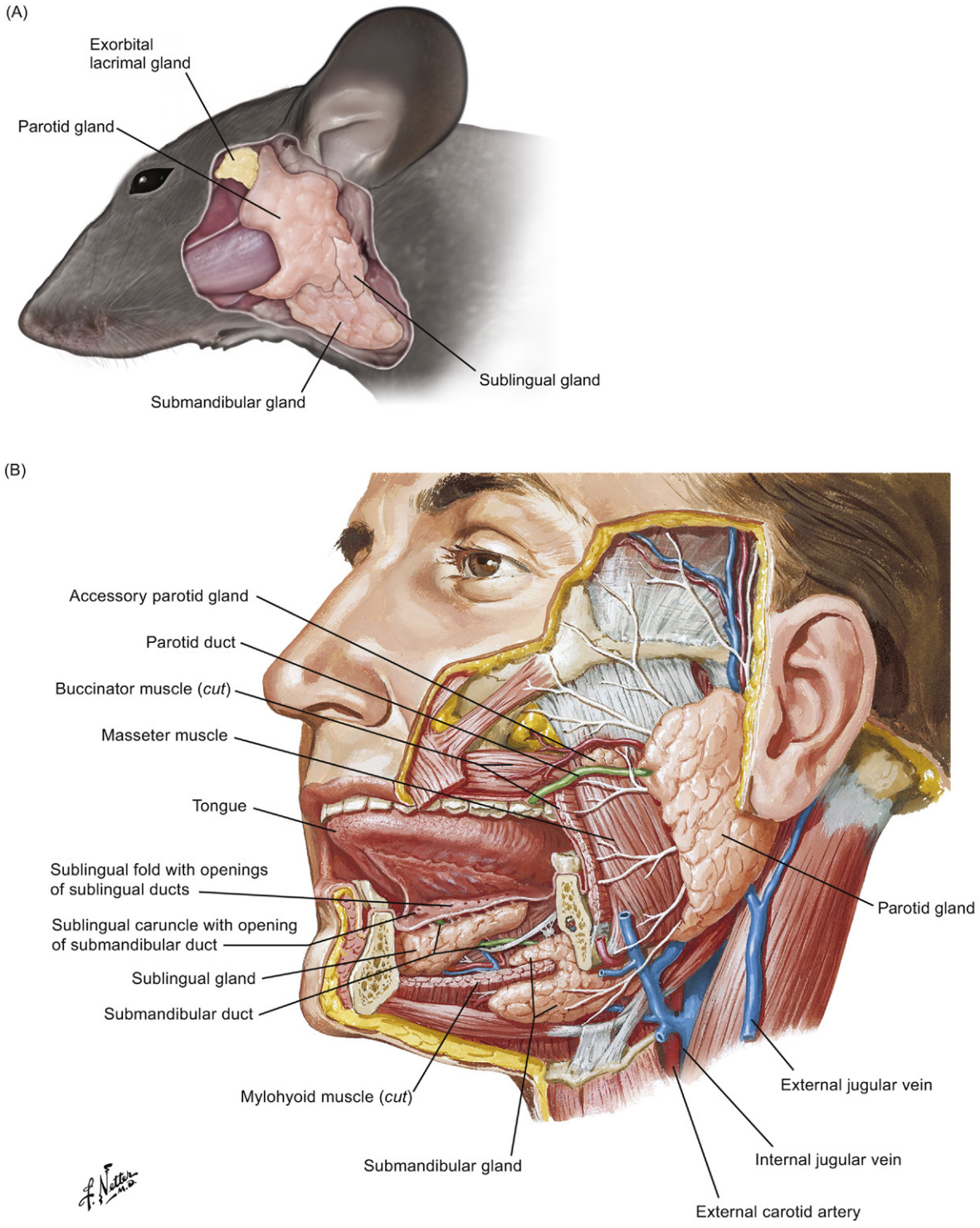

FIGURE 8.2 Regional lateral cervical anatomy. (A) Rodent (mouse). (B) Human.

Need-to-know

- The rodent exorbital lacrimal gland is located near the base of the external ear canal
- The pairs of major salivary glands—parotid, submandibular, and sublingual—combine with numerous minor salivary glands to produce and deliver saliva to the oral cavity.

FIGURE 8.3 Male rodent (mouse) subgross of cervical soft tissues. The submandibular (SM) gland is the largest salivary gland in rodents. Note the proximity of the exorbital lacrimal gland (EL) to the relatively diffuse parotid gland (P). Brown fat (BF), lymph node (LN), and sublingual (SL) gland are indicated.

Need-to-know

- The submandibular salivary gland is the largest of the major glands in the rodent, whereas the parotid is the most diffuse.
- In humans, the parotid gland is the largest.

columnar cells in rodents and by tall columnar cells with large, apically located nuclei in humans, and are surrounded by periductal collagen (Fig. 8.7). All three species have characteristic eosinophilic striations in the basal cytoplasm of the striated ducts (Fig. 8.7). These striations are caused by infolding of the basal plasma membrane. In humans, the striated ducts are larger in serous than mucous glands. Interlobar ducts have cuboidal epithelium, and the main excretory ducts are lined by cuboidal cells that transition to stratified squamous (oral mucosa) at the duct opening.

With the exception of the rodent sublingual gland (see below), salivary acinar cells are richly supplied by adrenergic fibers across species. As such, the glands are responsive to adrenergic stimuli, such as stress, resulting in basophilic cytoplasm (basophilia), cellular hypertrophy, and secondary increases in tissue weight.

Submandibular Gland

Gross Anatomy

Of the major salivary glands in rodents, the submandibular is the largest (Figs. 8.1 and 8.2). It is multilobed and lobulated and is located on the ventral midline of the neck, where the left and right sides are opposed and extend toward the sternum and thoracic inlet. The submandibular gland is bordered by the mandibular lymph node(s) rostrally, where it abuts the sublingual gland and extends dorsally to the parotid gland (Figs. 8.1 and 8.2). It lies superior to the digastric muscles and is separated into superficial and deep portions by the mylohyoid muscle. The main excretory duct of the submandibular gland opens into the oral cavity near the incisors at the sublingual caruncle (Table 8.1).

In humans, the submandibular glands are roughly ovoid in shape and lie on either side of the neck just below the mandible superior to the digastric muscles. They are separated into superficial and deep portions by the mylohyoid muscle. The ducts open into the floor of the mouth, one on each side of the frenulum of the tongue (Table 8.1).

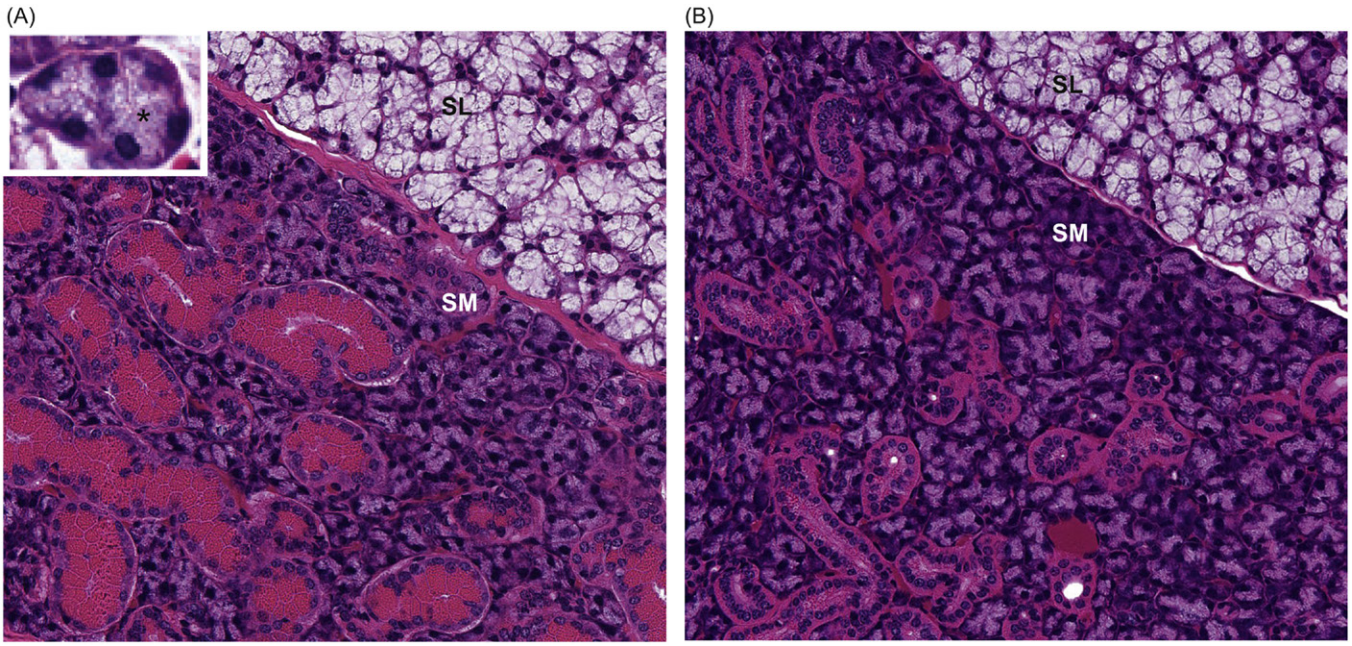

FIGURE 8.4 Rodent (mouse) submandibular glands. (A) Male. The granular convoluted duct cells in the submandibular gland (SM) are larger, with prominent pink granular cytoplasm, than those of female (see B). Note the presence of the sublingual gland (SL). Inset shows higher power view of SM acini with basally located nuclei and apical mucin (asterisk). (B) Female. The sublingual gland (SL) is indicated.

Need-to-know

- Male rodents have prominent granular ducts in the submandibular salivary gland; the weight of the male gland can be twice that of females in mice.

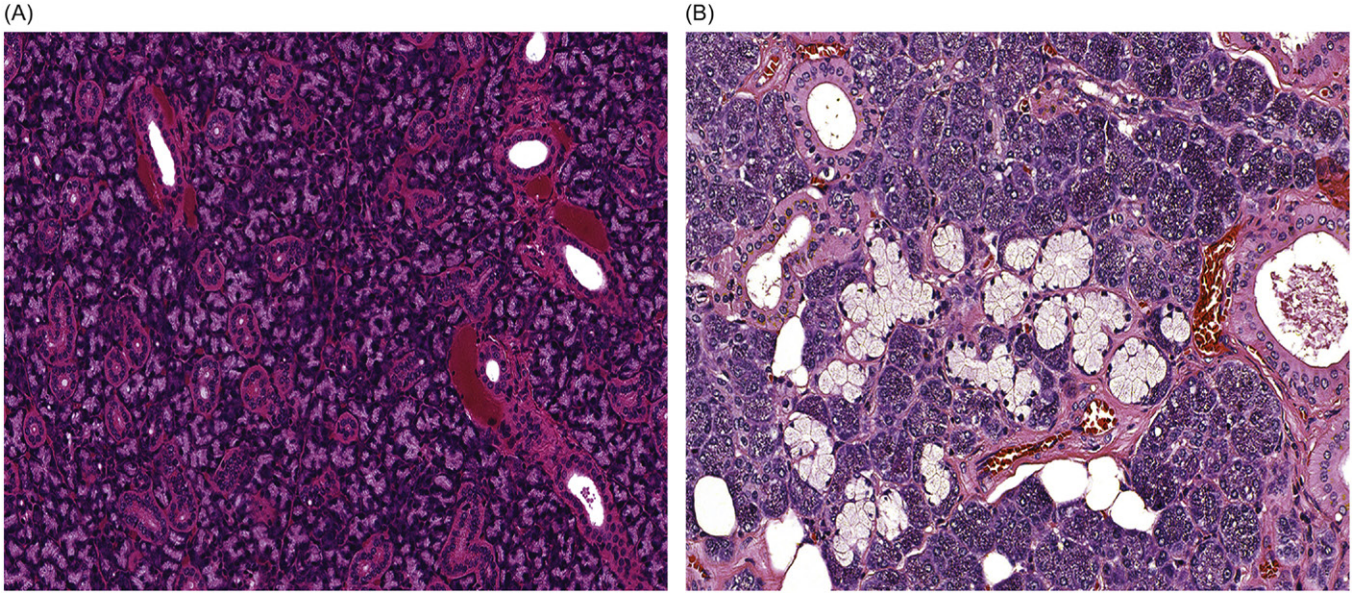

FIGURE 8.5 Submandibular glands. Across species, the secretions are mixed. (A) Female rodent (mouse). Mucous acini are lighter (pale blue staining) in female rodents than in males. (B) Human. Mixed acini are prominent (pale blue staining).

Need-to-know

- In all three species, submandibular secretions are mixed.
- In all three species, secretions increase (cellular hypertrophy) under adrenergic stimulation.

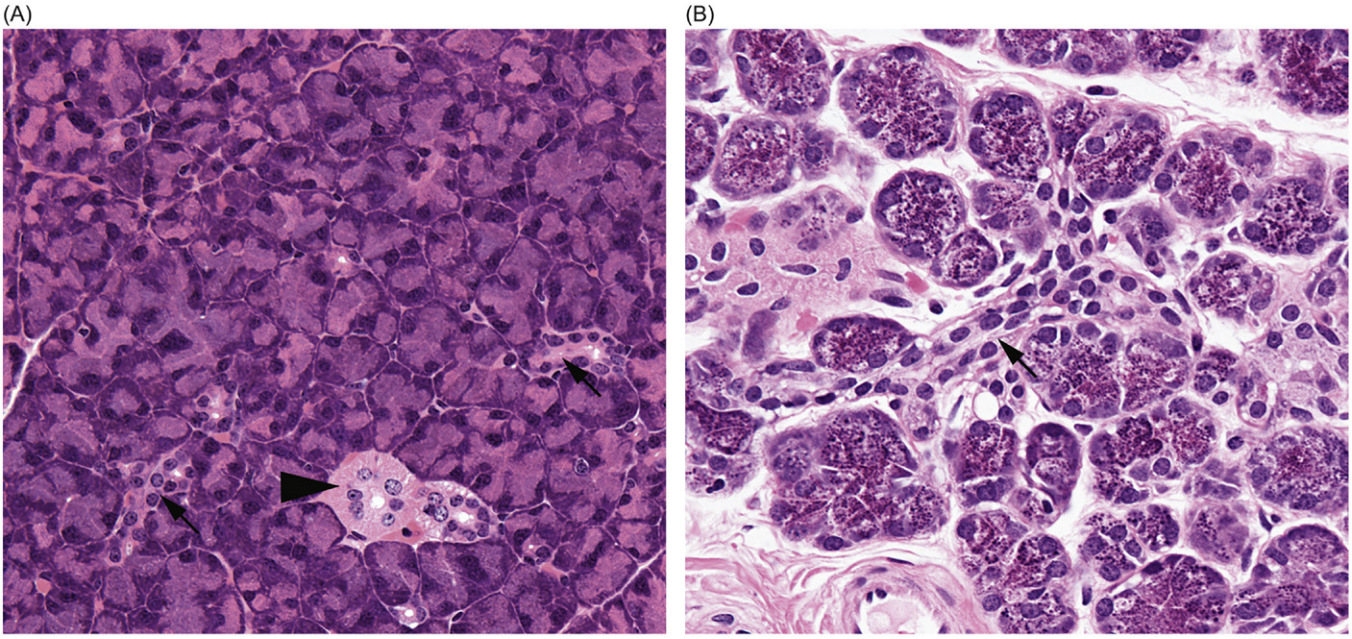

FIGURE 8.6 Parotid glands. (A) Rodent (mouse). The intercalated ducts of the parotid gland (arrows) are lined by low cuboidal epithelium, in contrast to the striated (arrowhead) duct lined by columnar epithelium. Parotid acini in rodents are serous with apical cytoplasmic zymogen granules that stain pink. (B) Human. Each intercalated duct (arrow) is lined by cuboidal epithelium and empties into a larger striated duct. The parotid gland acini are predominately serous and contain abundant cytoplasmic granules.

Need-to-know

- Intercalated ducts are often challenging to identify in rodent tissue sections.
- Rodents and humans have the same basic salivary gland structure.
- The appearance of the striated ducts is a result of basal infolding of the plasma membrane.

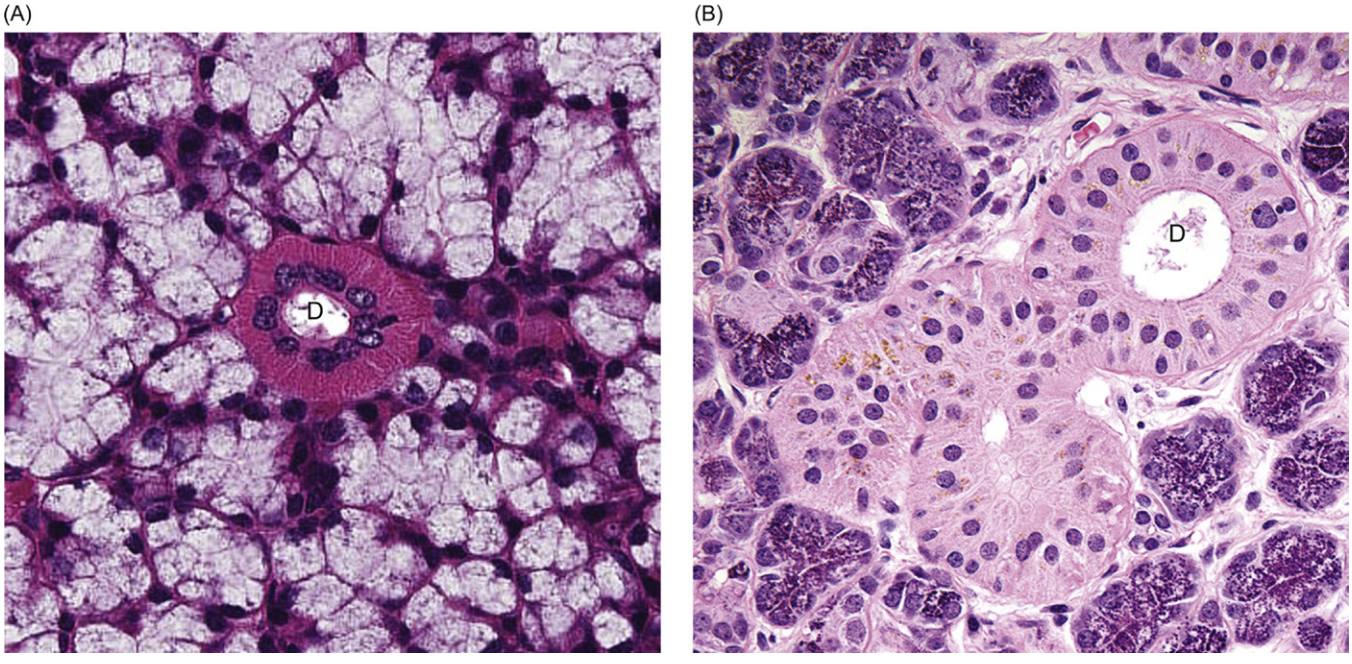

FIGURE 8.7 Striated ducts. (A) Rodent (mouse). The mucous sublingual gland contains intralobular striated ducts (D). Note the similarity to the human striated ducts (see B) within the parotid gland. (B) Human. The intralobular striated ducts (D) are lined by tall columnar cells in which the basal cytoplasm appears striated. These striations are secondary to the many infoldings of the basal plasma membrane.

HISTOLOGY

The acini of the submandibular gland contain both serous and mucous cells in all three species (Figs. 8.4 and 8.5). In mice, the gland is mixed mucoserous, rat is mostly mucous with a serous component, and human is typically mixed, with serous cells predominating. Tall pyramidal acinar cells are basophilic with basal nuclei and may contain apical cytoplasmic mucin droplets (Fig. 8.5). In rodents, the ductular system of the submandibular gland is morphologically unique, containing granular convoluted ducts lined by tall columnar epithelium connecting the relatively short intercalated ducts with the striated intralobular ducts. The granular convoluted duct is sexually dimorphic in rodents (apparent by, 20 days of age in mice, 7 weeks in rats), with male ducts characterized by a larger diameter than female ducts (Fig. 8.4). With age, these ducts occupy a larger percentage of the gland in males, containing prominent, bright pink secretory granules. In female rodents, the ducts are smaller with less distinct granules (Fig. 8.4). This sexual dimorphism is hormone-dependent as the epithelial cells are testosterone-sensitive. In older rats of both sexes, the ductular system of the submandibular gland contains occasional oncocytes, which are characterized by granular eosinophilic cytoplasm containing abundant mitochondria. In humans, the plump serous cells contain prominent basophilic zymogen granules. The mucous cells are pale-staining with abundant clear cytoplasm and are often arranged in duct-like structures, whose blind ends are capped by a crescent of zymogen-rich serous cells. There is no sexual dimorphism within human salivary glands.

Parotid Gland

GROSS ANATOMY

The borders of the rodent parotid gland extend dorsoventrally from the submandibular gland to the base of the ear, rostrally to the morphologically similar exorbital lacrimal gland, and caudally toward the clavicle. The exorbital lacrimal gland is tan-gray, located just anterior and dorsal to the cream-pink parotid (closer to the eye) in rodents (shown in Fig.22.3A; Fig. 8.3). The rodent parotid gland is pyramidal in shape, with the apex positioned inferiorly (downward). The capsule of the parotid gland is well-developed, and septa divide it into lobes and lobules. Its main excretory duct opens into the oral cavity near the molars (Table 8.1). In mice, the parotid gland is diffuse, with multiple lobes separated by connective tissue and fat (both white and brown). In the rat, it is about the same size as the submandibular gland and composed of multiple (three or four) lobes. In humans, the parotid is the largest of the salivary glands, located anterior and inferior to the external ear and overlying the mandibular ramus (Fig. 8.2). The human parotid gland is flat, well-encapsulated, and also pyramidal in shape, with the apex positioned inferiorly as well. The facial nerve divides the gland into superficial and deep portions. The human parotid capsule is also well-developed, and septa divide the gland into lobes and lobule.

HISTOLOGY

The parotid gland acini are serous in all three species, characterized by pyramidal cells surrounding the central acinar lumen (Fig. 8.6). In rodents, the parotid and exorbital lacrimal glands have similar histomorphology, resembling the exocrine pancreas (see Chapter 14: Pancreas). Due to the close anatomic proximity of these two facial glands, the exorbital lacrimal gland is often seen in section with the parotid gland (Fig. 8.8). The parotid and lacrimal glands may be distinguished in rodent tissue section by differences in acini size and nuclear regularity (Figs. 8.6 and 8.8). The parotid acini contain smaller pyramidal cells with regular nuclei, apical pink staining due to zymogen granules, and basal basophilia. In contrast, the lacrimal glands have large cells and

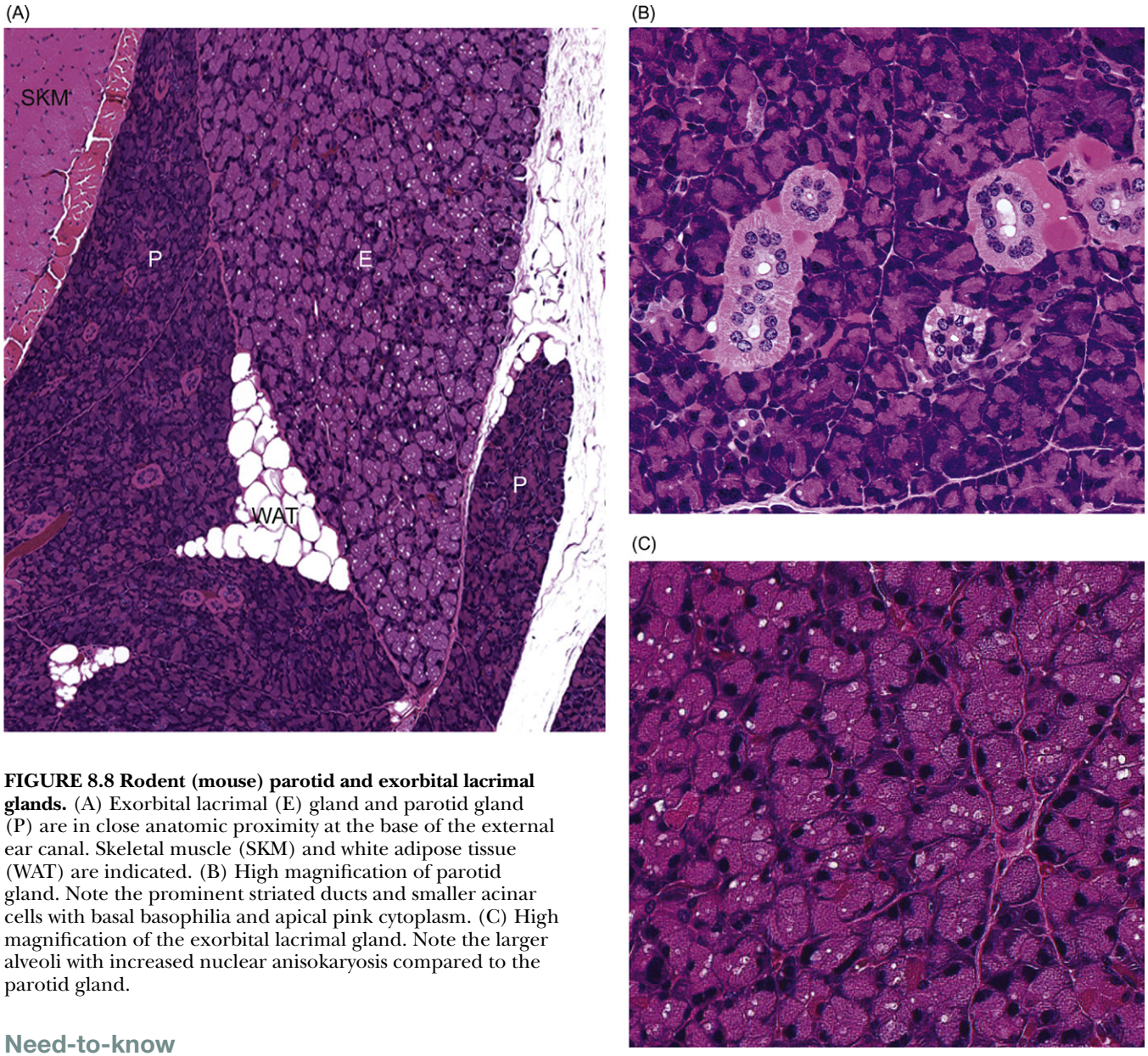

FIGURE 8.8 Rodent (mouse) parotid and exorbital lacrimal glands. (A) Exorbital lacrimal (E) gland and parotid gland (P) are in close anatomic proximity at the base of the external ear canal. Skeletal muscle (SKM) and white adipose tissue (WAT) are indicated. (B) High magnification of parotid gland. Note the prominent striated ducts and smaller acinar cells with basal basophilia and apical pink cytoplasm. (C) High magnification of the exorbital lacrimal gland. Note the larger alveoli with increased nuclear anisokaryosis compared to the parotid gland.

Need-to-know

- Compared with the parotid gland, rodent exorbital lacrimal glands have large acini and distinctive nuclear anisokaryosis that increases with age.
- The exorbital gland does not have striated ducts.
- The rodent parotid gland, exorbital lacrimal gland, and exocrine pancreas acini have a similar histologic appearance.

nuclear anisokaryosis with paler-staining granular cytoplasm (Figs. 8.6 and 8.8). The rodent parotid and submandibular glands are similar in size, acinar cell type, and adrenergic innervation. In rats, the intercalated ducts of the parotid gland are notable for multiple functions, including secretion of electrolytes into the saliva and regenerative capacity for both acinar and ductal cells. In humans, the parotid gland acini are composed entirely of zymogen-rich serous cells, with variable amounts of intervening adipose tissue in the interstitium between parotid lobes.

Sublingual Gland

Gross Anatomy

The sublingual gland in all three species is located anterior to the submandibular gland and under

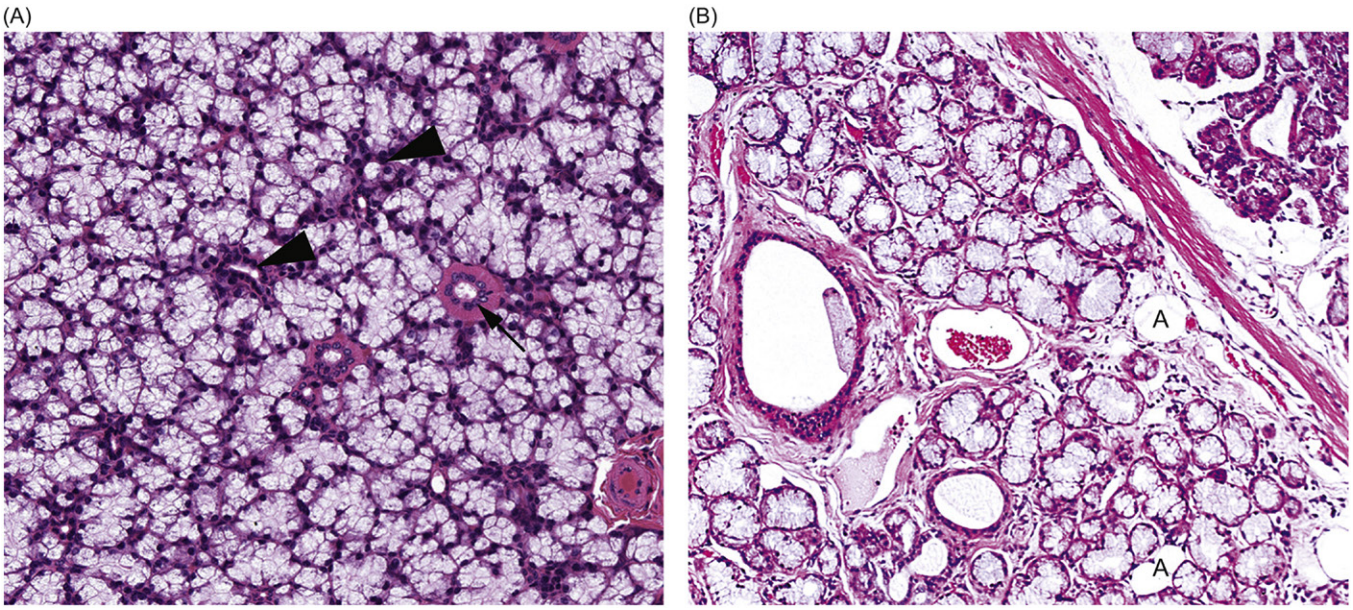

FIGURE 8.9 Sublingual glands. (A) Rodent (mouse). Note the relatively large acinar size and intercalated ducts (arrows). The striated duct (arrowhead) is indicated. (B) Human. Mucous acini predominate. Note that the gland contains occasional adipocytes, a feature found in older individuals. The proportion of fat (A, adipocyte) in the gland generally increases with age. Source (B): Reproduced from Young et al: Wheater's *functional histology: a text and colour atlas*, ed 5, Philadelphia, 2006, Churchill Livingstone with permission from Elsevier.

Need-to-know

- The sublingual gland in the rodent is a single lobe, but has the largest acini of the three salivary glands.
- In rodents, the sublingual gland is mucous; in humans, it is mixed and predominantly mucous.

the tongue, between the mandibular lymph nodes. The sublingual gland is smaller than the other major glands, consisting of a single paired lobe, which, in rodents, is closely adherent to the submandibular gland. In all three species, the main excretory duct of the sublingual gland opens into the oral cavity near the submandibular duct at the sublingual caruncle, adjacent to the incisors (Fig. 8.2 and Table 8.1).

HISTOLOGY

In rodents, sublingual gland acini contain large pyramidal mucous cells with abundant pale blue vacuolated cytoplasm (Fig. 8.9). In contrast to rodent submandibular and parotid glands, the sublingual gland is devoid of adrenergic innervation. In humans, the sublingual gland acini contain predominantly mucous cells admixed with serous. Acinar mucous cells contain flattened basal nuclei and pale eosinophilic cytoplasm.

FURTHER READING

Amano O, Mizobe K, Bando Y, Sakiyama K: Anatomy and histology of rodent and human major salivary glands. *Acta Histochem Cytochem* 45(5):241–250, 2012.

Barthold SW, editor: *Pathology of laboratory rodents and rabbits* (ed 4), Ames, IO, 2016, Wiley Blackwell.

Boorman GA, editor: *Pathology of the Fischer Rat*, San Diego, CA, 1990, Academic Press, Inc.

Chan PC, Mahler JF: NTP technical report on toxicity studies of glyphosate (CAS No. 1071-83-6) administered in dosed feed to F344/N rats and B6C3F1 mice. *Natl Toxicol Progr Tech Rep Ser* 16:1–39, 1992.

Langdon JD: Surgical Anatomy, embryology and physiology of the salivary glands. In Carlson ER, Ord RA, editors: Salivary gland pathology: diagnosis and management, Hoboken, NJ, 2016, John Wiley and Sons, Inc., pp 1–16.

Maronpot R, editor: *Pathology of the mouse: reference and atlas*, Vienna, IL, 1999, Cache River Press.

Martinez-Madrigal F, Bosq J, Casiraghi O: Major salivary glands. In Sternberg SS, editor: *Histology for pathologists* (ed 2), Philadelphia, PA, 1997, Lippincott–Raven, pp 405–429.

Mills SE, editor: *Sternberg's diagnostic surgical pathology* (ed 4), Philadelphia, PA, 2004, Lippincott Williams & Wilkins.

Mills SE, editor: *Histology for pathologists* (ed 3), Philadelphia, PA, 2007, Lippincott Williams & Wilkins.

Ovalle WK, Nahirney PC: *Netter's essential histology*, Philadelphia, 2007, Saunders.

Parker GA, Picut CA: *Atlas of histology of the juvenile rat*, Academic Press, 2016, San Diego, CA.

Silver AR, Som PM: Salivary glands. *Radiol Clin North Am* 36:941–966, 1998.

Young B, Lowe JS, Stevens A, et al: *Wheater's functional histology: a text and colour atlas*, ed 5, Philadelphia, PA, 2006, Churchill Livingstone.

This page intentionally left blank

RESPIRATORY SYSTEM 9

DAVID K. MEYERHOLZ
University of Iowa Carver College of Medicine, Iowa City, IA, United States

CARLOS J. SUAREZ
Stanford University School of Medicine, Palo Alto, CA, United States

SUZANNE M. DINTZIS AND CHARLES W. FREVERT
University of Washington School of Medicine, Seattle, WA, United States

Introduction

The lower respiratory system is a hierarchical system that can be divided into two functional and structural components: the conducting zone and the respiratory zone. The conducting zone consists of airways that transport gases into and out of the lungs and includes the trachea, bronchi, and extends to the terminal bronchioles. The respiratory zone corresponds to the lung parenchyma and includes the respiratory bronchioles, alveolar ducts, alveolar sacs, and alveoli. For the lungs to function properly, the conducting zone must be open to the respiratory zone where gas exchange occurs. Species differences exist in both the gross anatomy (Fig. 9.1) and histology of the lower respiratory system (Table 9.1), and these may compensate for variations in body size and basal metabolic rate.

Trachea

Gross Anatomy

The rodent trachea is the largest structure of the conducting zone and contains C-shaped incomplete cartilaginous rings that vary in number between mice (15–18) and rats (20–25). A total of 15–20 incomplete U-shaped cartilaginous rings support the human trachea. In all three species, the open aspect of these rings is located posteriorly and is closed by a thin fibromuscular membrane that joins the free ends of the rings. The cartilaginous part of the trachea provides rigidity to the airway keeping it from collapsing, and the soft posterior aspect allows the expansion of the esophagus as food passes down to the stomach. In these species, the trachea terminates above the heart at the carina, where it bifurcates and gives rise to the right and left main bronchi. Prior to entry into the lung parenchyma, the main bronchi are also referred to as extrapulmonary bronchi.

Comparative Anatomy and Histology. DOI: http://dx.doi.org/10.1016/B978-0-12-802900-8.00009-9
© 2018 Elsevier Inc. All rights reserved.

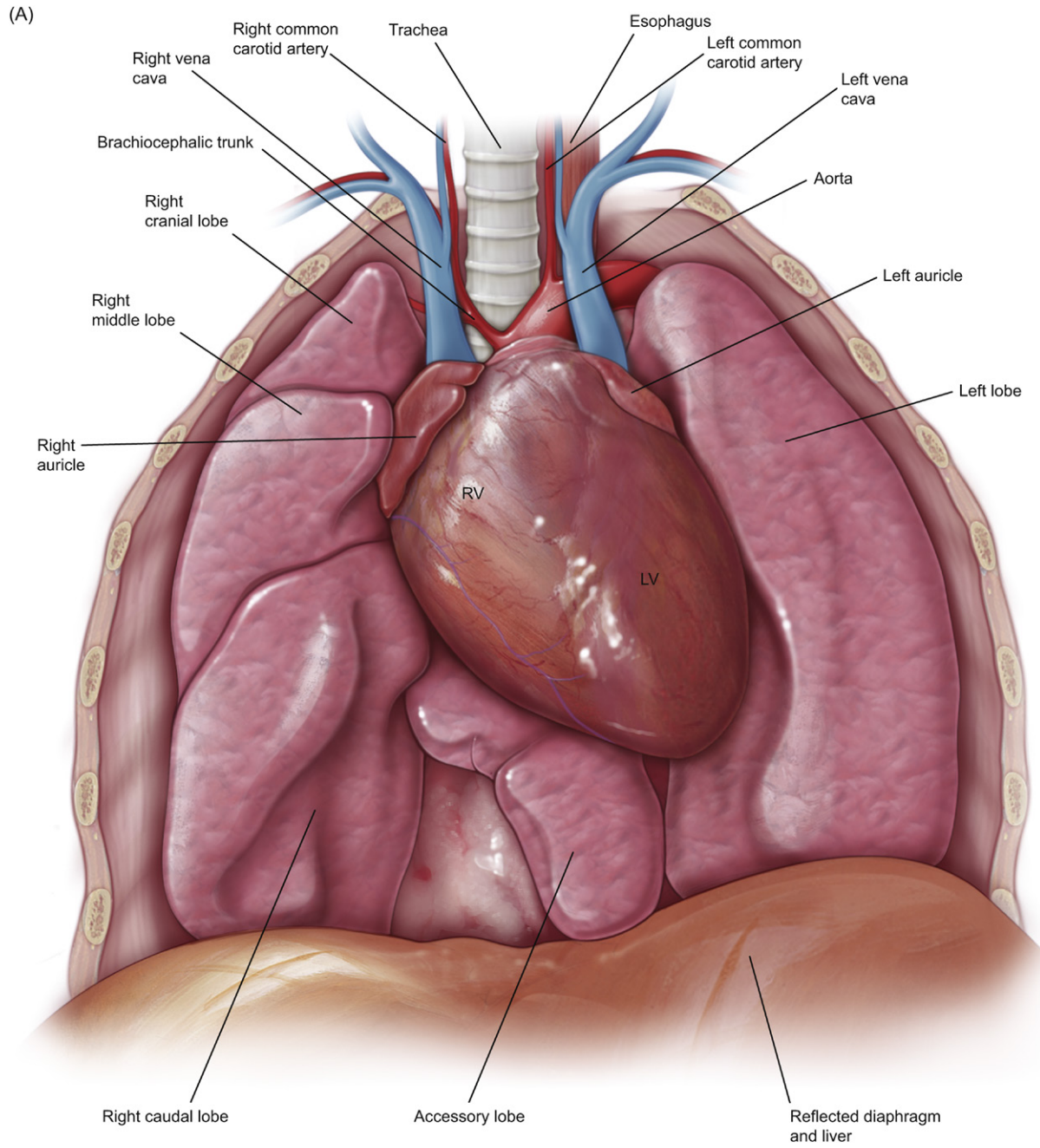

FIGURE 9.1 Regional anatomy of the lungs. (A) In rodents (mouse), the right lung consists of four lobes: cranial, middle, caudal, and accessory. The left lung has only one lobe. (B) In humans, the right lung consists of three lobes: upper, middle, and lower. The left lung consists of two lobes: upper and lower. Source of A and B: © Elsevier, Inc., www.netterimages.com.

HISTOLOGY

The inner surface of the rodent and human trachea is lined by a pseudostratified columnar epithelium (Fig. 9.2). Its pseudostratified appearance is primarily due to variations in shape and position of the nuclei of its different cell types. Mice, rats, and humans have, in comparison, a progressively thicker tracheal epithelium. In humans, the largest population of cells lining of the trachea is ciliated cells, whereas the rodent trachea is mostly lined by nonciliated epithelial cells (Table 9.1). In all three species, nonciliated cells comprise several cell types, including club cells and serous cells (seen preferentially in the rat trachea, but lacking in mice or humans). These nonciliated cells serve several functions in rodent airways that include: producing secretions (liquid, mucus, etc.) and contributing to

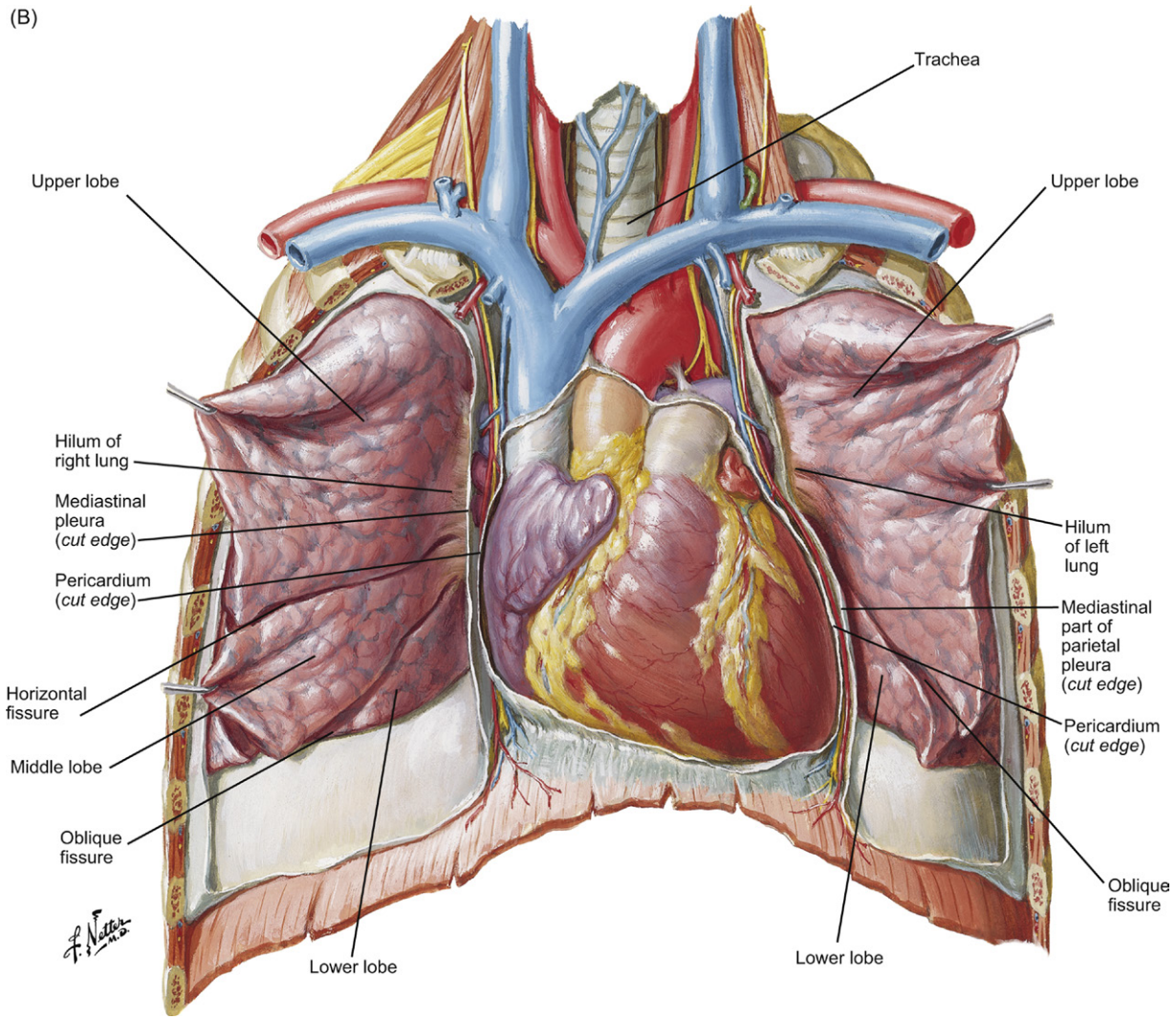

FIGURE 9.1 (Continued)

TABLE 9.1 Respiratory System

Feature	Rodent	Human
	Gross	
Lung lobes	Four right, one left	Three right, two left
Cartilaginous airways	Trachea and primary bronchi (i.e., extrapulmonary only)	Trachea through small intrasegmental bronchi in lung
	Histologic	
Respiratory bronchiole	Absent to rare in mice; if present, more diminutive than that of humans. In rats, absent early in life, but detectable by ~3 weeks postnatally; also more diminutive than that of humans	Present
Airway branching pattern	Monopodial	Dichotomous
	Airway Epithelial Cells (Relative Numbers)	
Trachea	Nonciliated > ciliated > basal. Epithelium is thinner in mice than rats; both thinner than humans	Ciliated > basal > nonciliated and mucous. Epithelial thickness decreases from proximal trachea through bronchi
Primary bronchi	Nonciliated ≥ ciliated > basal	Ciliated > nonciliated > mucous > basal
Terminal bronchioles	Nonciliated > ciliated	Ciliated > nonciliated
Alveoli	In rat, type II cells > type I cells; type I cells are very thin, but have a much greater cell volume than type II cells. Relative cell numbers are not well defined in mice	Type II cells > type I cells; type I cells are very thin, but have a much greater cell volume than type II cells

host defense (via secretion of antimicrobial proteins). Rodent airways typically have low numbers of goblet (mucous) cells compared to humans; however, these numbers can increase in response to inflammation and microbiologic exposures such as that seen in conventional versus specific pathogen free (SPF) facilities. In rodents, this often occurs through club cell transformation to goblet cells. In human trachea, ciliated columnar cells, basal cell, and goblet cells constitute the predominant cell populations (Table 9.1). Basal cells are situated near the epithelial basement membrane without extending to the luminal surface and experimental evidence suggests that these cells may function as stem cells for epithelial tissue repair.

The lamina propria, a layer of highly vascularized loose connective tissue subjacent to the epithelium, provides nutritional and mechanical support to the overlying epithelium, and together with the respiratory epithelium forms the respiratory mucosa. In humans, the superficial portion of the lamina propria is populated by numerous lymphocytes part of the mucosa-associated lymphoid tissue. Rodents originating from SPF facilities have very few lymphocytes in the lamina propria. The number of lymphocytes often increases with age and exposure to particulates or pathogens. In all three species, toward the deep aspect of the lamina propria, the elastic fibers that are present throughout the connective tissue gradually condense, creating a membrane-like boundary between the lamina propria and the underlying submucosa. This elastic band replaces the muscular layer commonly present beneath mucosae in other anatomic sites.

The submucosa is composed of loose connective tissue and glands (Fig. 9.2). In rodents, these submucosal glands are restricted to the proximal (closest to the larynx) trachea. Distribution of submucosal glands in rodents is strain dependent. In mice, these are typically found within the first 1–8 cartilage rings and in the rat, submucosal glands may extend up to the carina in some strains. In humans, the submucosa contains numerous tightly packed seromucinous glands; thus, the number of mucus-producing cells found in major airways differs substantially between rodents and humans.

Below the submucosa are the tracheal cartilaginous rings. Histologically, these are similar between the species and consist of hyaline cartilage surrounded by a thin fibrous membrane, the perichondrium. Fibroelastic tissue and smooth muscle bundles

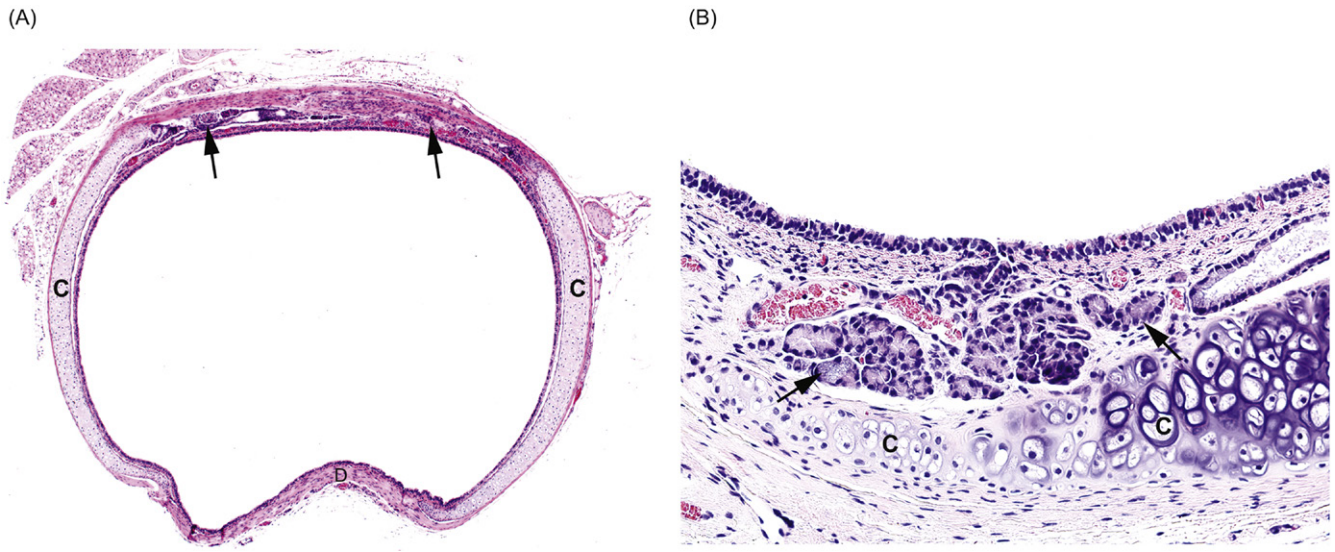

FIGURE 9.2 Rodent (rat) trachea. (A) Oblique cross section of trachea demonstrates submucosal glands (arrows) preferentially along the ventrilateral tracheal wall and preferentially within the intercartilaginous space. Note the lack of submucosal glands along the dorsal membrane D and the overlying the cartilaginous rings C. (B) Oblique cross section of trachea shows submucosal glands (arrows) adjacent to the edges of the cartilage ring C along the ventrilateral wall.

run transversely between the posterior ends of the U-shaped cartilage rings. The outer aspect of the trachea is covered by the adventitia, a loose connective tissue that connects the trachea to surrounding organs.

Lung

Gross Anatomy

In rodents, the right lung is divided into four lobes, whereas the left lung has one lobe. The four right lung lobes are the cranial, middle, caudal, and accessory (Fig. 9.1). In some nomenclature schemes, the accessory lobe is subdivided into the intermediate accessory and the diaphragmatic lobes, with the right lung described as having five lobes.

The right lung of humans is divided into three lobes—upper, middle, and lower—by two interlobar fissures, the oblique and the horizontal. In contrast, the left lung is divided into two lobes, upper and lower, by one interlobar fissure, the oblique fissure (Fig. 9.1). Although there are only two lobes, the anteroinferior portion of the left upper lobe, located over the left side of the heart, constitutes a distinct anatomic area called the lingula.

Bronchi to Terminal Bronchioles

Gross Anatomy

Bronchi are defined as conducting airways that have cartilage (rings or plates) whereas those conducting airways without cartilage are termed bronchioles. In each of the three species, the two extrapulmonary bronchi enter the right and left lungs where they subdivide into the intrapulmonary bronchi, which supply the different anatomical regions of the lungs. The branching of the conducting airways in rodents occurs as an asynchronous, monopodial branching pattern in which smaller airways branch off of the larger parent airway through the lung. Size and shape of rodent airways can vary between strains (Fig. 9.3). Humans also have asynchronous branching, but undergo what is called dichotomous branching, in which the larger parent airway segment divides at an approximately 45° angle into two smaller daughter segments.

After entering the rodent lung, the right intrapulmonary airway divides to supply the cranial, middle, caudal, and accessory lobes. Likewise, the left intrapulmonary airway branches to supply the left lung. It is worth noting that the conducting airways within the lung parenchyma of rodents are composed of only bronchioles, as defined by their lack of cartilage, while in human they include both bronchi and bronchioles. However, this terminology in rodents is not without some controversy as some authors still refer to large intrapulmonary airways in rodents as "bronchi," although use of "bronchioles" is anatomically and functionally most correct. Even so, some have advocated that the intrapulmonary bronchioles in rodent lungs be subdivided into large (i.e., main stem) and small (i.e., branching) bronchioles. This approach may be useful to describe preferential lesion distribution, but consistent definitions for these are difficult in the monopodial branching system seen in rodent airways.

In humans, the right main bronchus is shorter, wider, and more vertical in direction than the left. The right bronchus divides into three lobar bronchi that respectively supply the three right lung lobes. In contrast, the left bronchus divides into two lobar bronchi. Each lobar bronchus then subdivides into various segmental or tertiary bronchi; these airways supply discrete anatomical units of the lung called bronchopulmonary segments that are separated from each other by a layer of connective tissue known as the intersegmental septum. The bronchopulmonary segments contain a centrally located segmental bronchus running together with a pulmonary artery and are drained by pulmonary veins that run peripherally within the intersegmental septum. There are 10 bronchopulmonary segments in the

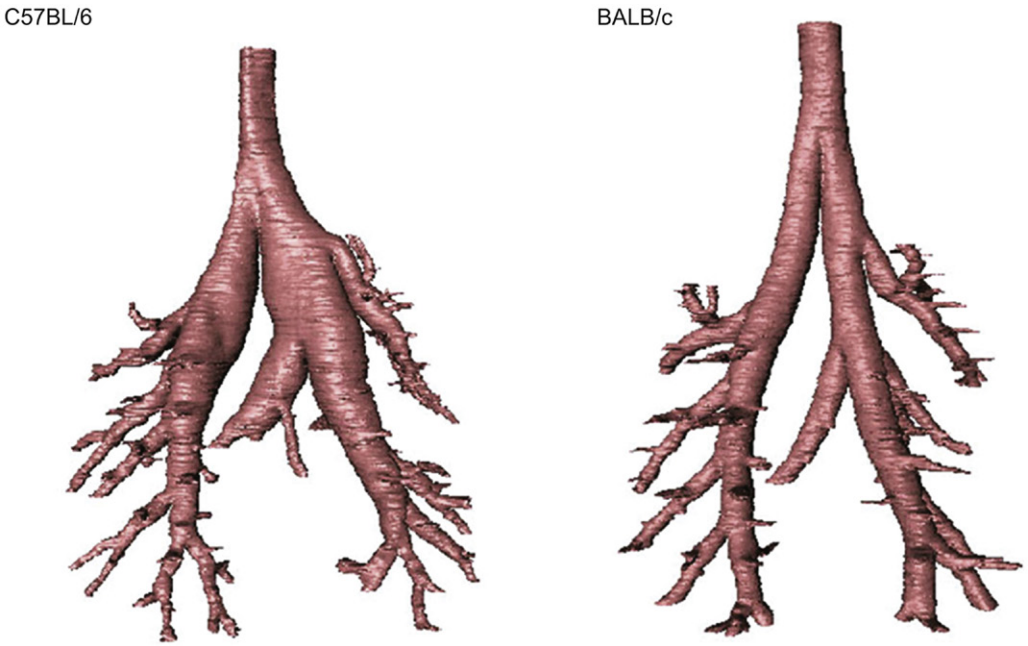

FIGURE 9.3 Reconstructed computed tomography images of rodent (mouse) trachea and airways. Rodent airways have monopodial branching pattern with a large main bronchus that gives rise to smaller airways. However, as evidenced in laboratory mice, strain variations can produce significant variations in airway size and shape as seen by the large bulbous airways of C57BL/6 mice (left) compared to BALB/c mice (right). Reproduced with permission from Thiesse et al: Lung structure phenotype variation in inbred mouse strains revealed through in vivo micro-CT imaging, *J Appl Physiol (1985)* 109(6): 1960–1968, 2010.

right lung and 8–10 in the left lung. The segments are designated according to their anatomic location in each lobe. Examples include apical, anterior, and posterior in the right upper lobe; lateral and medial in the right middle lobe; and superior, medial basal, anterior basal, lateral basal, and posterior basal in the right lower lobe.

Human segmental bronchi, which by definition contain cartilage, undergo branching into primary bronchioles lacking cartilage (Fig. 9.4). Within the pulmonary lobe, the primary bronchioles subdivide into terminal bronchioles that constitute the end of the conducting zone

HISTOLOGY

The histologic transformations that occur in the conducting tract of the lungs are gradual, as opposed to the abrupt changes that take place in other organ systems, such as the gastrointestinal system. The histologic modifications that occur mirror changes in the functional demands along the respiratory tract. Briefly, the major function of the proximal airways is to clean and humidify the inspired air and to remain open despite the collapsing forces induced by respiratory mechanics. Therefore, proximal airways of rodents contain numerous nonciliated cells (Table 9.1) and human proximal airways contain submucosal glands and goblet cells that serve, respectively, to produce a protective layer that moisturizes the inhaled air and traps potentially harmful airborne particles. In contrast, the main function of the distal (farthest from larynx) airways is to distribute the inspired air in a manner that provides the most efficient gas exchange. More distal airway walls have a thick muscle layer that regulates the airflow to different areas of the respiratory zone and a prominent elastic network in the lamina propria that permits recoiling of the mucosa after muscle contraction.

Bronchi

In rodents, the trachea bifurcates at the carina into two extrapulmonary bronchi that enter the

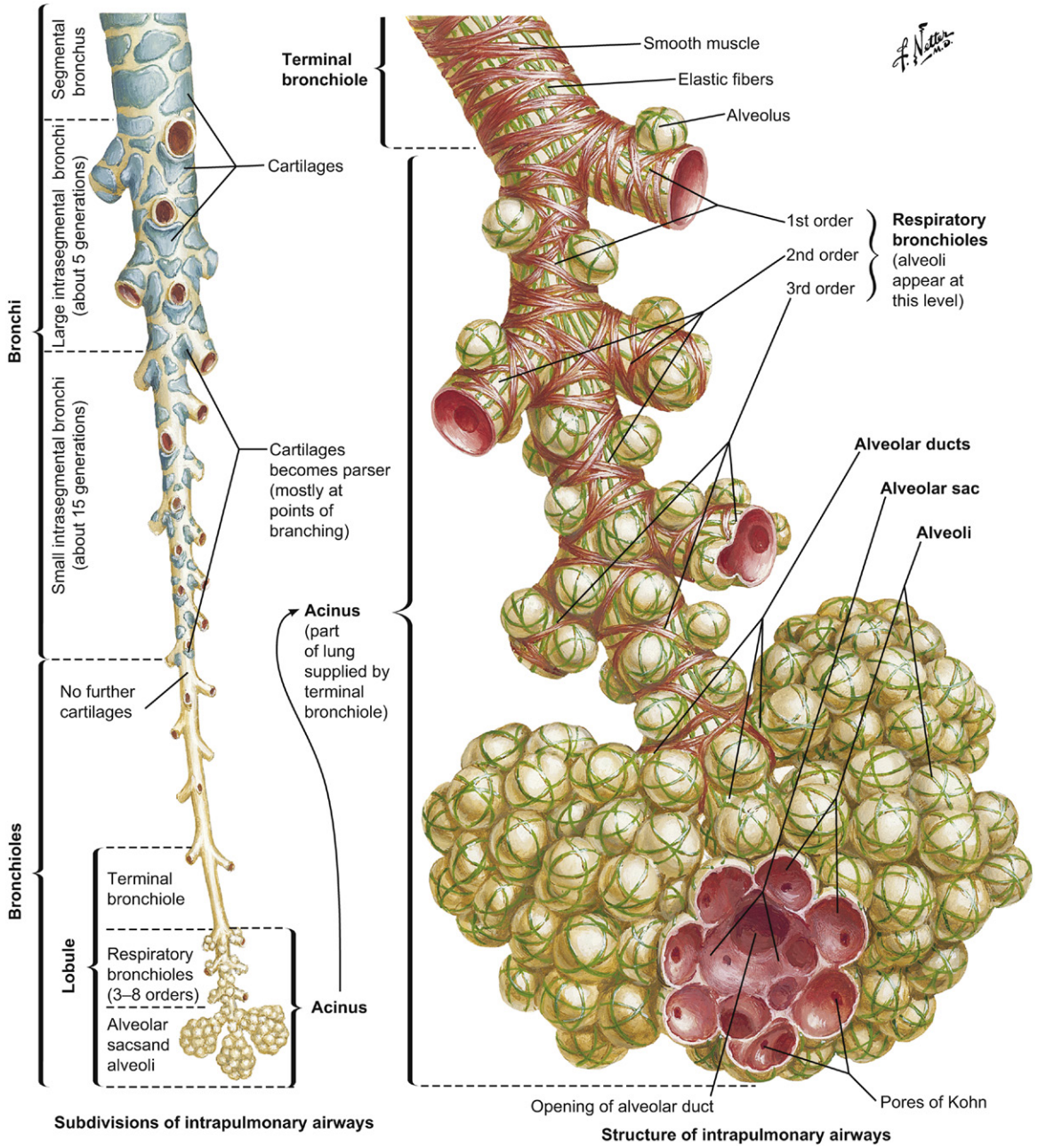

FIGURE 9.4 Conducting airways and respiratory zone of human lung. The airways are a succession of branching tubes that divide and become smaller and more numerous as they transition from bronchi to bronchioles and, finally, the terminal bronchiole, which supplies the respiratory zone where gas exchange occurs. The portion of the lung supplied by the terminal bronchiole is known as the acinus in all three species. Source: © Elsevier, Inc., www.netterimages.com.

Need-to-know

- Rodents have monopodial airway branching, whereas humans have dichotomous branching.
- Intrapulmonary airways in rodents lack cartilage and submucosal glands and so are structurally and functionally similar to human bronchioles.
- Rodents lack well-developed respiratory bronchioles.

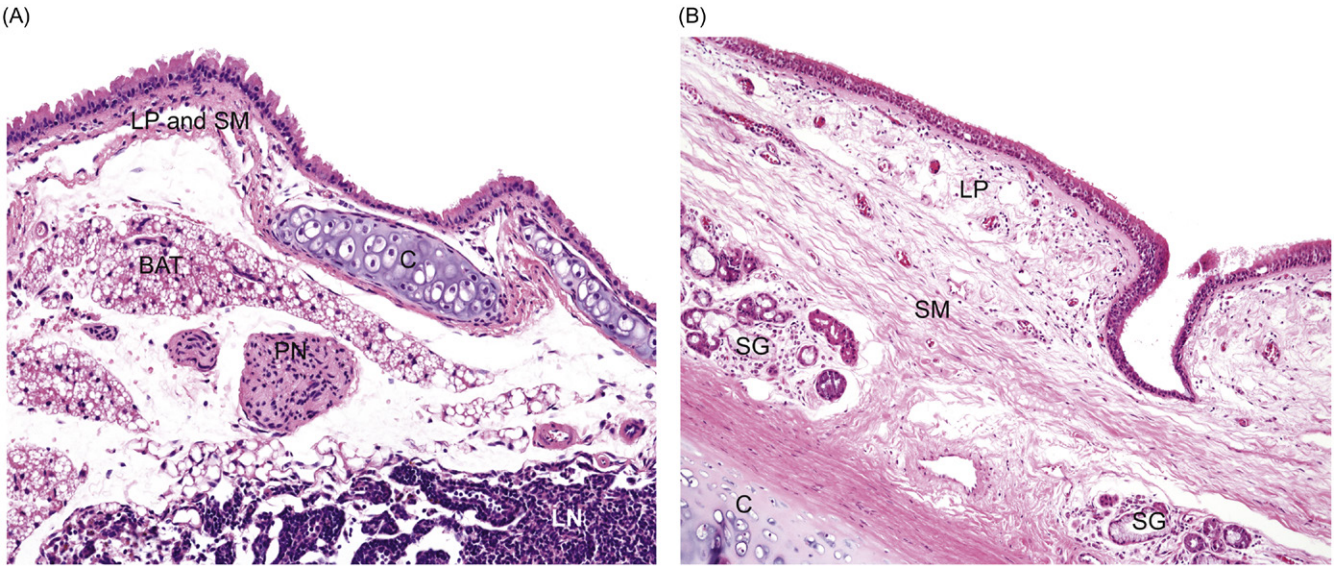

FIGURE 9.5 Extrapulmonary airways. A main stem (extrapulmonary) bronchus from rodent (mouse) lung with regional mediastinal soft tissues (A) and trachea from human lung (B). The surface epithelium in rodents overlays a thin lamina propria and a submucosa without glands. Cartilaginous rings C are found in the extrapulmonary bronchi of both rodents and humans. In humans, there is a much thicker lamina propria and a submucosa that contains submucosal glands. Cartilaginous rings are found in the extrapulmonary bronchi of rodents and humans. *C*, cartilage; *LP*, lamina propria; *SG*, submucosal glands; *SM*, submucosa; *PN*, peripheral nerve; *LN*, lymph node; *BAT*, brown adipose tissue.

right and left lung lobes. Differences in epithelial cell thickness and composition of cell types between rodents and humans are present in the primary bronchi (Fig. 9.5, Table 9.1). The most common cell in the proximal airways of rodents is the nonciliated cell followed by ciliated cells. While several phenotypes of nonciliated cells have been reported, in mice, club cells are the most common, whereas in rats it is serous cells. In contrast, humans largely lack club or serous cells in their proximal airways, and contain mucous and other nonciliated cells (e.g., eccrine and rare serous) instead. Underlying the epithelium of the intrapulmonary bronchi, rodents have very thin lamina propria, a submucosa that lacks submucosal glands, and no cartilaginous rings (Fig. 9.6).

In humans, the main bronchi are histologically similar to the trachea, but the segmental or tertiary bronchi are not. As the bronchi undergo successive divisions, they also undergo gradual histologic changes. The epithelium diminishes in height, becoming simple columnar with little pseudostratification; the number of goblet cells

Need-to-know

- Rodents lack submucosal glands and have less than 1% mucous goblet cells in the epithelium of extrapulmonary bronchi.

decreases; the density of elastic fibers in the lamina propria increases; and the elastic fiber distribution becomes more uniform throughout the connective tissue. A muscular layer between mucosa and submucosa appears, first as a discontinuous layer and later as a continuous spiral layer. The tightly packed glands in the submucosa progressively become sparse and ultimately vanish distally in the segmental bronchi. The cartilage rings become discontinuous plates interconnected by a membrane of fibrous connective tissue. As the bronchi become smaller, the cartilaginous plates become scattered and thinner. Finally, the adventitia—now called the peribronchial layer—acquires more elastic fibers.

Bronchioles

The transition from bronchi to bronchioles involves the reduction of airway cartilage,

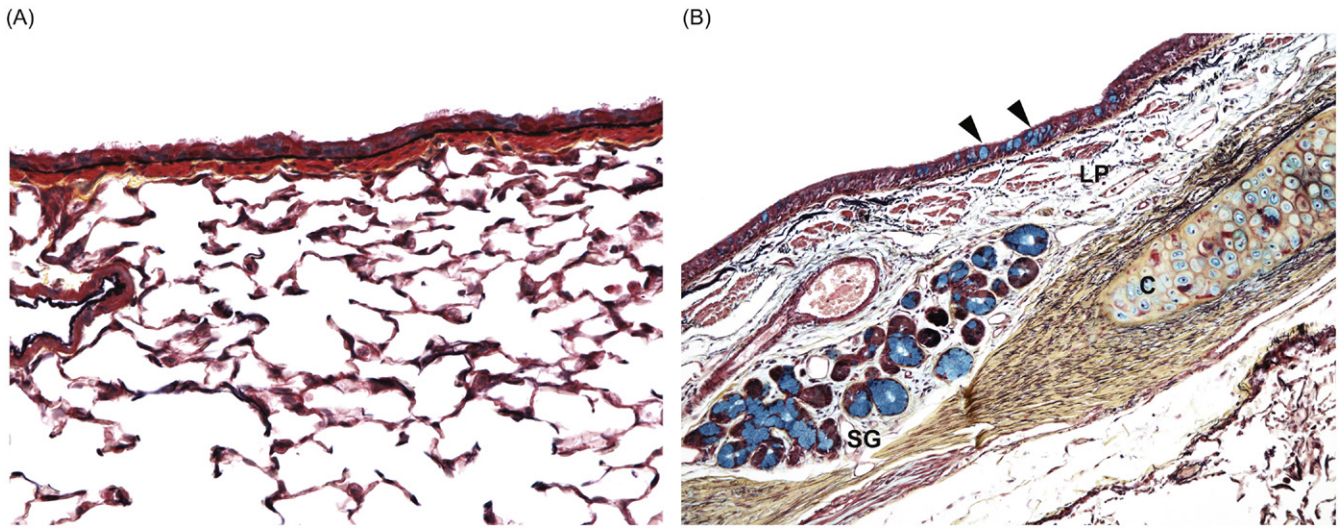

FIGURE 9.6 Large intrapulmonary airways. A large rodent (mouse) bronchiole (A) and a large human bronchus (B) stained with Movat's pentachrome. The proximal intrapulmonary bronchioles in rodents are lined with columnar to cuboidal epithelium. In the large bronchioles of rodents, elastic fibers (black stain) within the very thin lamina propria and submucosa separate epithelial cells from the muscular layer. The intrapulmonary airways of rodents lack cartilage, and submucosal glands thus are appropriately termed "bronchioles." Humans have considerably more mucus-producing goblet cells (arrowheads). Underlying the epithelium is the lamina propria, which contains elastic fibers (black) and loose connective tissue. A discontinuous smooth muscle layer separates the mucosa from the submucosa where submucosal glands are evident. The cartilaginous rings in the human bronchus consist of hyaline cartilage surrounded by fibroelastic tissue. *C*, cartilage; *LP*, lamina propria; *SG*, submucosal glands.

submucosal glands, and surface epithelial height. As mentioned above, all intrapulmonary airways of rodents lack cartilage and submucosal glands so are defined as bronchioles. Conducting bronchioles undergoes gradual histologic changes as they approach the respiratory zone. The bronchiolar epithelium transitions from uncommon low pseudostratified to simple columnar and then to simple cuboidal with a decrease in ciliated cells and an increase in nonciliated (e.g., club) cells. Species differences are shown in Table 9.1.

In human bronchioles, the goblet cells gradually disappear, and increase in numbers of nonciliated (e.g., club) cells. The lamina propria acquires more elastic fibers, and sparse smooth muscle bundles begin to populate the connective tissue. The muscle layer underlying the mucosa thickens significantly relative to airway size, becoming the thickest layer of the airway wall. Also, the submucosa and cartilage plates are lost, distinguishing bronchioles from small bronchi. The peribronchial (outer) layer thins and remains as a simple fibroelastic membrane that anchors the bronchiolar wall to the lung parenchyma. Due to the lack of the submucosa and cartilage plates, the bronchioles have a wall composed of only three histologic layers: mucosa, muscular layer, and outer layer.

Need-to-know

- Rodent interpulmonary airway (bronchioles) lack cartilage and submucosal glands and have few mucus-producing cells in the surface epithelium.
- In rodent airways, nonciliated cells are the principal sources of secretions.

Bronchus-Associated Lymphoid Tissue

Bronchus-associated lymphoid tissue (BALT) is a localized accumulation of lymphoid cells that participate in airway immune responses. This lymphoid tissue, located within the airway submucosa, is composed predominantly of T and B lymphocytes, but also contains plasma cells, dendritic cells, and macrophages. Although the distribution of BALT along human airways appears random, some reports have suggested increased localization to airway bifurcations. BALT is also frequently found between airways and arteries.

The use of the term BALT in rodents has been questioned by some for two reasons: rodents have intrapulmonary bronchioles (not bronchi), and rodents that have been housed in barrier/SPF facilities have less BALT-like structures than those exposed to pathogens or antigenic challenges. This phenomenon has given rise to the term inducible BALT. The use of BALT as a morphological descriptor in rodents that correlates to human BALT seems appropriate in function.

Respiratory Zone

GROSS ANATOMY

The conducting airways transition into the respiratory zone at the level of terminal and respiratory bronchioles (Fig. 9.4). The lung parenchyma distal to the terminal bronchiole is known as the acinus, and it constitutes the functional unit of the lung where gas exchange occurs. The acinus is morphologically composed of the terminal bronchiole, alveolar duct, alveolar sac, and lastly the alveolus, the terminal portion of the respiratory zone.

In rodents, the respiratory bronchiole is not well-developed (Table 9.1) and thus the initial anatomic segment of the rodent acinus is either the alveolar duct (e.g., mice) or a diminutive respiratory bronchiole (e.g., adult rats). In humans (Fig. 9.4), the terminal bronchioles become respiratory bronchioles that give rise to 2–11 alveolar ducts, from which roughly six alveolar sacs derive. Alveoli line the wall of alveolar sacs and represent the terminal end of the respiratory zone.

HISTOLOGY

The histologic structure of the respiratory bronchiole resembles that of the terminal bronchiole except for occasional alveoli in the respiratory bronchiole wall (Fig. 9.7). The alveolar

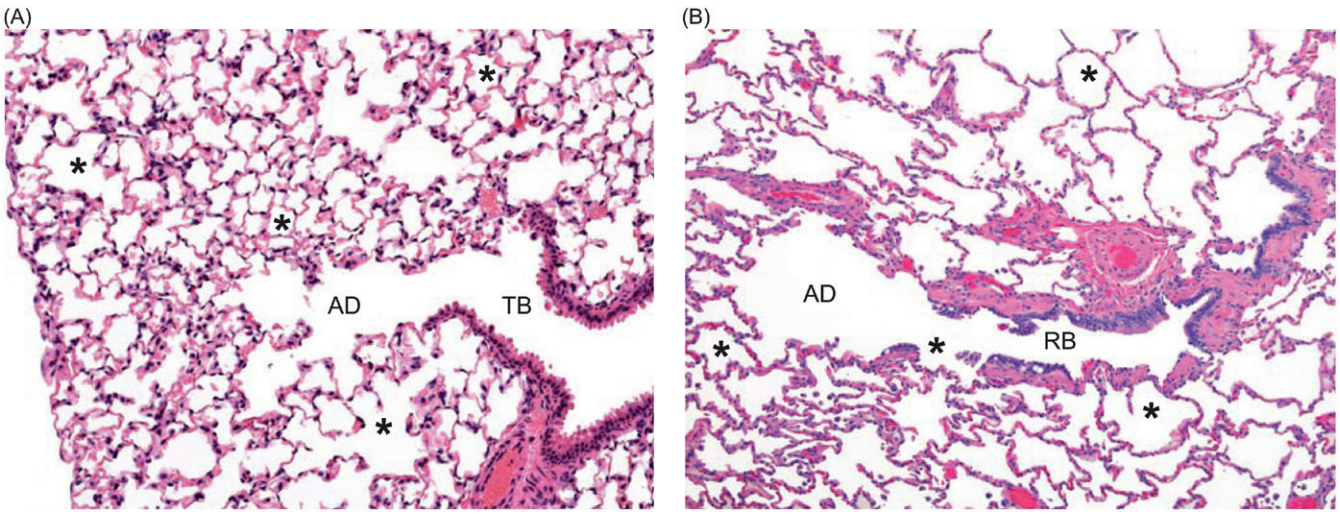

FIGURE 9.7 Respiratory zone bronchioles. (A) Respiratory bronchioles are absent to rare in mice, so air typically flows sequentially from terminal bronchioles (TB) to alveolar ducts (AD) to alveoli (*). In contrast, rats have diminutive respiratory bronchioles that can appear several weeks after birth. (B) The human respiratory zone contains respiratory bronchioles (RB) that open into alveolar ducts (AD) and then into alveoli (*). Respiratory bronchioles are lined by epithelium similar to the terminal bronchiole, but with occasional saccular outcropping (alveoli) in their walls.

Need-to-know

- Rodents lack well-developed respiratory bronchioles; the respiratory zone includes diminutive respiratory bronchioles (if present), alveolar ducts, and alveoli.
- The respiratory zone of the human includes respiratory bronchioles, alveolar ducts, and alveoli.

duct wall is formed by alveoli and sparse bundles of smooth muscle that run through the thin alveolar duct wall and condense around the openings of the alveoli, creating a sphincter-like structure. In contrast, alveolar sacs have a wall formed completely by alveolar septa. Alveoli emanating from neighboring alveolar ducts and alveolar sacs are connected through pores in the alveolar septa, known as pores of Kohn (Fig. 9.8). These pores provide collateral ventilation, which maintains an equal pressure across neighboring alveoli to prevent atelectasis (Fig. 9.4). They also allow for the passage of immune cells, fluid, and infectious agents.

The alveolus serves as the functional and structural components of the respiratory zone and is similar in structure at light microscopy for each of the three species, but the alveolar size is proportional to body mass and so is largest in humans and smallest in mice. The alveolar wall is composed of a thin epithelial layer of simple squamous cells termed type I pneumocytes (type I cells) and low cuboidal cells known as type II pneumocytes (type II cells) that predominantly sit along the alveolar opening (Fig. 9.9). Rats have another prominent alveolar cell type called type III pneumocytes (brush cells), but these cells are only distinguishable by electron microscopy. Type I cells are directly involved in gas exchange, whereas type II cells produce surfactant and function as reserve cells for the alveolar epithelium. Morphometric analysis shows that the human and rat alveolar epithelium is composed of more type II than type I cells (Table 9.1). While type I cells in these species form a very thin lining of the alveolus, the cellular volume of type I cells is actually much larger than type II cells. Mice have both type I and type II cells, but the relative numbers are not as well defined.

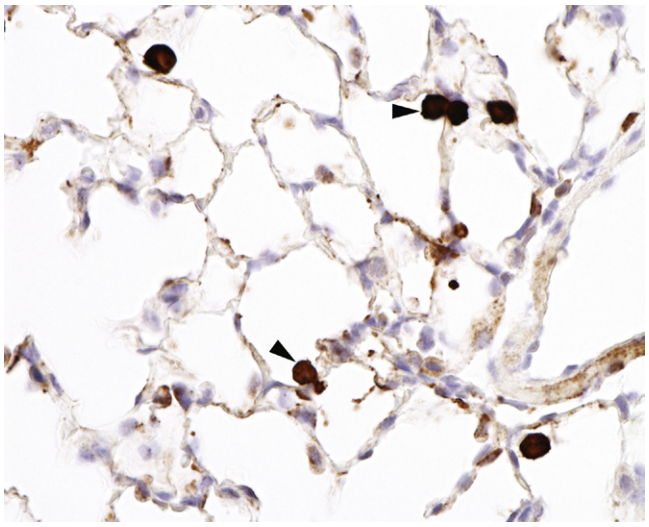

FIGURE 9.8 Pores of Kohn (mouse). The pores of Kohn are holes in the alveolar septa that connect one alveolus to another and are present in each of the three species. These pores provide collateral ventilation, which equalizes pressure between neighboring alveoli. Immune cells, fluid, and infectious agents are also able to transit between alveoli through these pores. Two macrophages (arrowheads, brown-stained cells) can be visualized transiting from one alveolus to another through pores of Kohn in this mouse lung.

Within the alveolar spaces are alveolar macrophages (Fig. 9.9), which scavenge airborne particles and serve as the first line of defense against microorganisms that reach the epithelial surfaces of the respiratory zone. Alveolar macrophages sometimes sit along the walls of alveoli, which make them difficult to differentiate from type II cells by routine histochemical stains in each of the species.

In both rodents and humans, a rich capillary network embedded in loose connective tissue sits beneath the alveolar epithelium. It is composed of elastic and reticular fibers, fibroblasts, myofibroblasts, pericytes, resident macrophages, lymphocytes, mast cells, and a few collagen fibers. The connective tissue and capillary network intervening between two apposed alveolar walls are called the alveolar septum. There are multiple sites along the alveolar epithelium where the alveolar epithelium and endothelium lack intervening connective tissue. At these sites, the basement membranes of the alveolar wall and endothelium fuse (Fig. 9.9) maximizing gas exchange between blood flowing through the capillaries and air in the alveolus.

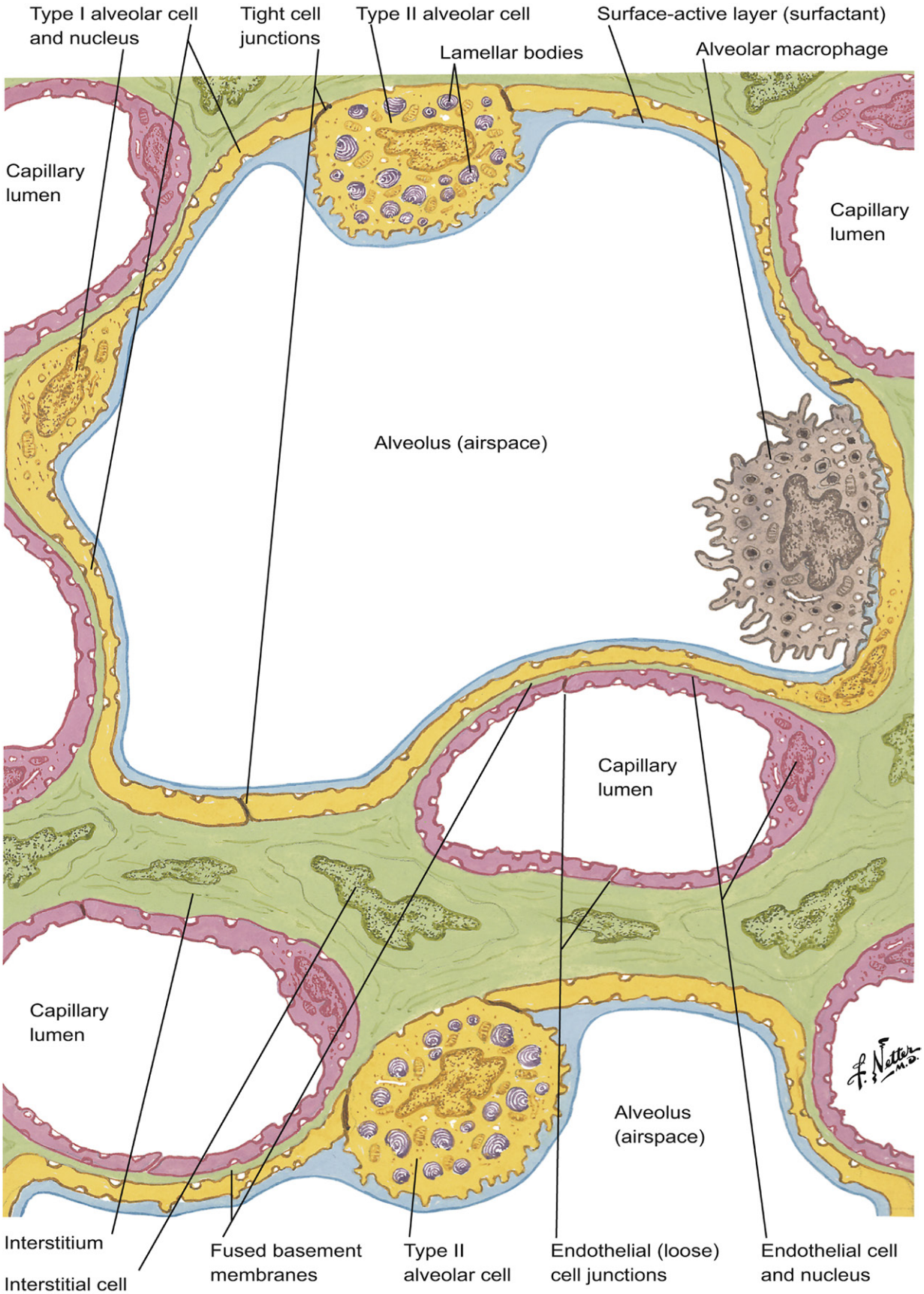

FIGURE 9.9 Alveolus. Type I and type II cells line the alveolar surface of the lungs in all three species. Gas exchange occurs across the thin part of the alveolar septum, which is composed of type I epithelial cell lining, a basement membrane, and the endothelium of the pulmonary capillary. Source: © Elsevier, Inc., www.netterimages.com.

Lung Circulatory System

GROSS ANATOMY

Lung circulation is composed of two distinct circulatory systems that supply blood to the lungs in all three species. The bronchial system, which arises from the aorta and intercostal arteries, provides oxygenated blood to the bronchi, large blood vessels, hilar lymph nodes, and visceral pleura. It terminates at the level of the terminal bronchioles, where it joins with pulmonary capillaries and venules. The pulmonary system arises from the pulmonary artery, which originates from the right ventricle and it transports poorly oxygenated blood from the right heart to the alveoli, where carbon dioxide is removed from the blood and oxygen added. Pulmonary capillaries empty into pulmonary veins, which carry freshly oxygenated blood back to the heart. In rodent lungs, the veins within the lung parenchyma follow the bronchial tree, while in human lungs, these veins course along the connective tissue between lobules (i.e., interlobular septa).

HISTOLOGY

In rodent lung, elastic arteries are large arteries with a medial layer consisting of alternating layers of concentric elastic lamina and smooth muscle cells. There is a gradual transition from elastic arteries to the smaller muscular arteries, in contrast to other species, in which branching of the arteries is associated with abrupt changes in wall thickness or lumen size. In rodent lungs, it is normal to see small arteries having a smooth muscle wall. This is in contrast to humans, where muscularization of arterioles is suggestive of pulmonary hypertension.

Cardiomyocytes are seen in the wall of pulmonary veins in several species including humans and rodents. Rodents commonly have cardiomyocytes seen as a prominent layer around veins within the lung. Studies in mice show that cardiomyocytes are localized in pulmonary veins extending from the hilum of the lungs into lung parenchyma and the surrounding veins, which are 70–250 µm in diameter. In fact, the prominent cardiomyocyte layer can cause some observers to misidentify pulmonary veins as muscular arteries or as evidence of pulmonary hypertension. However, most pulmonary arteries and veins can be distinguished on routine H&E stained sections (Fig. 9.10 and Table 9.2). In humans, these cardiomyocytes quickly disappear after leaving the heart and are only associated with intrapulmonary veins during disease (e.g., atrial fibrillation).

The human pulmonary circulatory system is histologically different from its systemic counterpart. First, the pulmonary arteries have thin walls and large diameters—features that contribute to the creation of a low-pressure system. Second, the muscular layer (i.e., tunica media) of the elastic arterial wall is relatively small due to a lower number of elastic fiber layers. In addition, the elastic structure extends deep into the pulmonary parenchyma. Only a distal and short portion of the pulmonary arterial system corresponds to muscular arteries, which are still rich in elastin and have a thin muscular layer. The wall of pulmonary veins is formed of collagen fibers, smooth muscle, and a discontinuous, rather indistinct elastic layer; these components are haphazardly arranged and are less constant than in systemic veins.

Pleura

GROSS ANATOMY

In humans and rodents, the serous membrane lining the thoracic cavity and surrounding the lungs is referred to as the pleura. This is subdivided into two anatomic components: the visceral pleura encases the lung parenchyma, whereas the parietal pleura lines the inner chest wall.

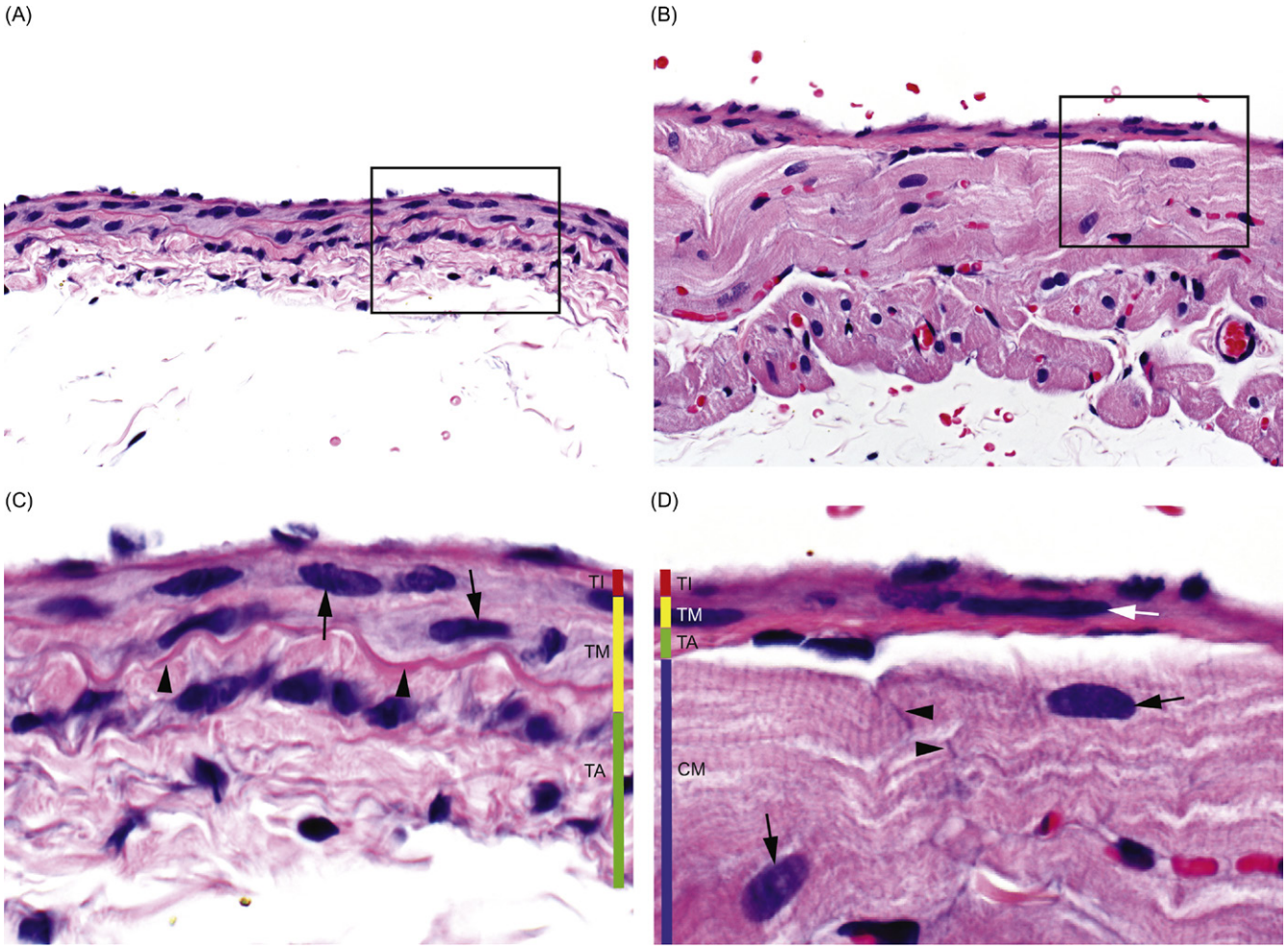

FIGURE 9.10 Rodent (rat) lung vasculature. Large branches of pulmonary artery (A, C) and vein (B, D) are shown. (A, B) At similar magnification, the pulmonary vein (B) will often appear to have a thicker wall (especially in large caliber vessels) due to a prominent layer of 1–5+ cardiomyocytes, which have larger sarcoplasm than smooth muscle cells. (A, C) The pulmonary artery wall is composed of a tunica intima (TI, red line), tunic muscularis (TM, yellow line), and tunica adventitia (TA, green line). The arterial wall is distinguished from veins by a thicker TM composed of smooth muscle cells with elongate nuclei (arrow) and in larger arteries elastic fibers (arrowhead) may be seen. Additionally, the TA is commonly seen with its collagen fibers. (B, D) In contrast, the pulmonary vein has a comparatively thin TM (yellow line) that is preferentially seen only in large veins. The TA (green line) is often loose and ill-defined due to the prominent cardiomyocytes (CM, blue line) lining the TA. Note the contrast between elongate smooth muscle nuclei with blunted edges (white arrow) and cardiomyocytes with their plump oval nuclei (arrows) and abundant eosinophilic sarcoplasm with cross-striations and uncommon intercalated discs (arrowheads). These cardiac muscle cells form a prominent layer exterior to the TA. This thick TM has caused some to mistakenly identify these vessels as pulmonary arteries.

Need-to-know

- The rodent pulmonary artery is distinguished from veins by examination of vessel wall, myocyte nuclei, and sarcoplasm.
- Sarcoplasmal cross-striations and intercalated discs should not be the sole source for distinction, as finding smaller cardiomyocytes around smaller calibre vessels is notoriously difficult.

HISTOLOGY

Both visceral and parietal pleurae have a superficial layer of simple cuboidal mesothelial cells resting on a layer of connective tissue rich in collagen and elastic fibers. The visceral pleura of rodents is thin compared to that of humans (Fig. 9.11). The rodent visceral pleura is almost imperceptible by light microscopy and consists of a flattened to simple squamous layer of mesothelial cells resting on a thin layer of loose collagenous fibrous tissue overlying dense fibroelastic tissue. In contrast, the rodent parietal pleura, while thin compared to humans, is slightly thicker, has fewer elastic fibers, and may contain adipose cells.

TABLE 9.2 Morphological Features to Distinguish Arteries and Veins in Rodent Lung

Vessel Wall Layer	Pulmonary Arteries	Pulmonary Veins
Tunica intima (TI)	Composed of simple squamous endothelial cells and minor connective tissue for support	Composition is generally similar to arteries
Tunica media (TM)	Exterior (abluminal) to TI and composed of: (1) smooth muscle cells with elongate and (2) elastic fibers that are preferentially seen in large caliber arteries	Exterior to TI and composed of: smooth muscle cells form a comparatively *thin* TM to similar caliber arteries. Elastic fibers are not present.
Tunica adventitia (TA)	Found exterior to the TM and composed of loose collagen fibers with scattered nuclei of fibrocytes	Typically not seen due to prominent cardiomyocytes that sit exterior to the TM. Cardiomyocytes (1–5+ cell layers) have plump oval nuclei and comparatively abundant eosinophilic sarcoplasm with cross-striations and rare intercalated disks.

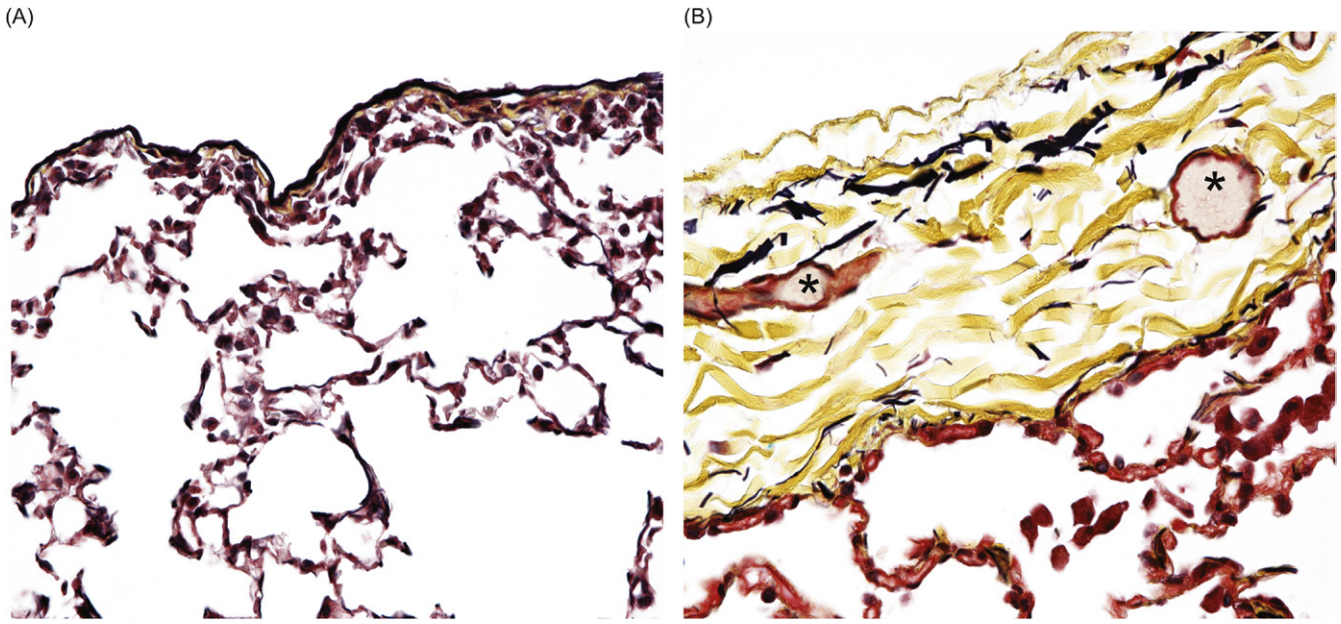

FIGURE 9.11 Visceral pleura of the lungs. In all three species, the fibroelastic layer is composed of collagen (yellow) and elastic fibers (purple to black). (A) The rodent (mouse) visceral pleura, which is composed of mesothelial cells overlying a fibroelastic layer, is very thin. (B) Humans have much thicker visceral pleura. Note the lymphatic vessels (asterisks) incidentally seen in this section. Images are of similar magnification.

The connective tissue of the human visceral pleura contains a network of lymphatic vessels that prevent the accumulation of fluid in the pleural space, the tiny area between the visceral and parietal pleurae. This network, known as the superficial lymphatic network, is drained by lymphatic vessels that run through the interlobular septa. These lymphatic vessels, together with the lymphatic vessels that follow the bronchial tree and the pulmonary vessels, form the deep lymphatic network. The superficial lymphatic network in rodent lungs is not as well characterized. The deep network of pulmonary lymphatics consists of two separate components: lymphatic vessels that connect interacinar regions and a rich plexus of peribronchiolar lymphatic vessels.

The collagen and elastic fibers of the visceral pleura merge with the fibroelastic framework of the lung parenchyma. In rodents, the very thin visceral pleura is in direct contact with, but distinct from, the underlying lung parenchyma. In contrast, a distinct elastic layer separating the two structures can be seen in humans (Fig. 9.11).

FURTHER READING

Cesta MF: Normal structure, function, and histology of mucosa-associated lymphoid tissue. *Toxicol Pathol* 34:599–608, 2006.

Dixon D, Herbert RA, Sills RC, et al: Lungs, pleura, and mediastinum. In Maronpot RR, editor: *Pathology of the mouse*, Saint Louis, MO, 1999, Cache River Press, pp 293–323.

Fox JG: The mouse in biomedical research, Boston, MA, 2007, Elsevier.

Hsia CC, et al: An official research policy statement of the American Thoracic Society/European Respiratory Society: standards for quantitative assessment of lung structure. *Am J Respir Crit Care Med* 181(4):394–418, 2010.

Irvin CG, Bates JH: Measuring the lung function in the mouse: the challenge of size. *Respir Res* 4:4, 2003.

Jeffery PK, Reid L: New observations of rat airway epithelium: a quantitative and electron microscopic study. *J Anat* 120(Pt 2):295–320, 1975 Nov.

Mueller-Hoecker J, Beitinger F, Fernandez B, et al: Of rodents and humans: a light microscopic and ultrastructural study on cardiomyocytes in pulmonary veins. *Int J Med Sci* 5:152–158, 2008.

Peake JL, Reynolds SD, Stripp BR, et al: Alteration of pulmonary neuroendocrine cells during epithelial repair of naphthalene-induced airway injury. *Am J Pathol* 156:279–286, 2000.

Peao MN, Aguas AP, de Sa CM, et al: Scanning electron microscopy of the deep lymphatic network of the mouse lung as viewed in corrosion casts. *Lymphology* 26:42–48, 1993.

Pinkerton K, Herring MJ, Hyde DM, et al: Normal aging of the lung. In Pinkerton K, Hardin R, editors: *The lung: development, aging and the environment* (ed 2), New York, NY, 2015, Elsevier, pp 265–283.

Plopper CG, Hyde DM: The non-human primate as a model for studying COPD and asthma. *Pulm Pharmacol Ther* 21:755–766, 2008.

Rock JR, Onaitis MW, Rawlins EL, et al: Basal cells as stem cells of the mouse trachea and human airway epithelium. *Proc Natl Acad Sci USA* 106:12771–12775, 2009.

Sorokin SP: The respiratory system. In Weiss L, editor: *Cell and tissue biology: a textbook of histology* (ed 6), Baltimore, MD, 1988, Urban & Schwarzenberg, pp 751–814.

Thiesse J, Namati E, Sieren JC, et al: Lung structure phenotype variation in inbred mouse strains revealed through in vivo micro-CT imaging. *J Appl Physiol (1985)* 109(6):1960–1968, 2010.

Vanpeperstraete F: The cartilaginous skeleton of the bronchial tree. *Adv Anat Embryol Cell Biol* 48(3):1–80, 1973.

Widdicombe JH, Chen LL, Sporer H, et al: Distribution of tracheal and laryngeal mucous glands in some rodents and the rabbit. *J Anat* 198(Pt 2):207–221, 2001.

Xu B, Wagner N, Pham LN, et al: Lymphocyte homing to bronchus-associated lymphoid tissue (BALT) is mediated by l-selectin/PNAd, alpha4beta1 integrin/VCAM-1, and LFA-1 adhesion pathways. *J Exp Med* 197:1255–1267, 2003.

CARDIOVASCULAR 10

BERNARD S. BUETOW
Pfizer, Inc., San Diego, CA, United States

MICHAEL A. LAFLAMME
University Health Network, Toronto, ON, Canada

Introduction

The structure and organization of the mouse, rat, and human cardiovascular systems are all generally similar (Table 10.1). As is true in all mammals, rodents and humans have four-chambered hearts: left and right atria, a dominant left ventricle, and a thinner-walled right ventricle (Figs. 10.1–10.4). The rodent heart is obviously far smaller than the human heart; however, the ratio of heart to body weight is similar, as are the relative thicknesses of the right and left ventricular walls.

In both rodents and humans, the majority of heart mass is composed of cardiomyocytes, but significant numbers of other cell types are present, including endothelial cells, fibroblasts, and leukocytes. Differences between the rodent and human hearts include the general shape of the heart; location of the coronary arteries; structure of the valves; thickness of the pericardial sac, epicardium, and endocardium; and prominence of the cardiac skeleton. The anatomy and histologic structures of the vasculature also share many features; differences include thinner walls of rodent arteries and the prominence of cardiomyocytes around rodent pulmonary veins (Table 10.2). Here, mice will generally be used to represent rodents and compare with humans. For structures that are distinct in rats, those differences will be discussed.

As noted in Chapter 1, Introduction, differences in body orientation between quadruped rodents and upright humans may use different terminology to describe the location of an organ or structure. Thus, it is important to distinguish between differences in terminology and true differences in anatomy between species. To review, cranial is used in rodents to indicate toward the head, and caudal to indicate away from the head (toward the tail). Superior is used in humans to indicate toward the head and inferior to indicate away from the head. Thus, cranial in rodents is generally analogous to superior in humans, and caudal in rodents is generally analogous to inferior in humans. Dorsal is used in rodents to indicate toward the back or spinal column, and ventral to indicate toward the underside or ground (in a normal standing posture). Posterior is used in humans to indicate toward the back and anterior to indicate toward the front. Thus, dorsal in rodents is generally analogous to posterior in humans, and ventral in rodents is generally analogous to anterior in humans.

Comparative Anatomy and Histology. DOI: http://dx.doi.org/10.1016/B978-0-12-802900-8.00010-5
© 2018 Elsevier Inc. All rights reserved.

TABLE 10.1 Heart

Feature	Rodent	Human
	Gross	
Heart weight	Mouse: ~0.10–0.15 g Rat: ~0.5–2.5 g	~250–350 g in adult males ~200–300 g in adult females
Heart weight (% of body weight)	Mouse: ~0.40–0.60% Rat: ~0.20–0.50% (decreases with age)	~45% in adult males ~40% in adult females
Left ventricular wall thickness	Mouse: ~1.5–1.8 mm Rat: ~1.5–2.7 mm	~1.2–1.5 cm
Right ventricular wall thickness	Mouse: ~0.5–0.6 mm Rat: ~0.5–0.9 mm	~0.4–0.5 cm
Interventricular septum (IVS) thickness	Mouse: ~1.5–1.8 mm Rat: ~1.5–2.5 mm	~1.2–1.5 cm
Heart rate	Mouse: ~350–700 beats/min Rat: ~300–400 beats/min	~60–100 beats/min
Left ventricular cardiac output	Mouse: ~11–19 mL/min Rat: ~70–80 mL/min	~5 L/min in adult males ~4.5 L/min in adult females
Left ventricular stroke volume	Mouse: ~30–36 μL/beat Rat: ~175–225 μL/beat	~70 mL/beat in adult males ~60 mL/beat in adult females
Heart shape	Oval to spherical	Conical
Rests on diaphragm	No	Yes
Distinct interventricular groove	Absent	Present
Pericardial sac	A few cell layers thick	~1–3 mm thick
Epicardial fat	None to scant	Moderate to abundant along coronary arteries
Anterior (cranial) vena cava	Two (left and right)	One
No. of primary coronary arteries	Mouse: Typically two, occasionally three Rat: Typically two	Typically two branches off of the proximal aorta, with the left branch bifurcating into two major arteries
Origin of coronary arteries	Within or above coronary sinus	Within coronary sinus
Septal coronary artery	Present	Absent (most of the IVS is supplied by septal perforators arising from the left anterior descending coronary artery)
Location of coronary arteries	Intramyocardial	Usually epicardial proximally and becoming mid-myocardial distally
Extracoronary blood supply	Mouse: Absent Rat: Present	Absent
Location of sinoatrial node	Junction of right cranial vena cava and right atrium	Junction of the superior vena cava and the right atrial appendage
Location of atrioventricular node	Interatrial septum	Similar to rodent
Location of bundle of His	Basal interventricular septum (IVS)	Central fibrous body to basal IVS
Location of left and right bundle branches	Subendocardially along the left and right faces of the IVS, respectively	Similar to rodent
Atrioventricular valves	Continuous curtain; chordae tendinae present	Distinct leaflets; chordae tendinae present
Semilunar valves	No chordae tendinae	Similar to rodent
	Histologic	
Epicardium	Thin	Prominent
Endocardium	Thin	Prominent
Subendocardial connective tissue	None to scant	Prominent, particularly on left side of heart; may contain blood vesssels, nerve fibers, adipose, and bundles of smooth muscle
Cardiac skeleton	Mouse: Indistinct Rat: Slightly more distinct than mouse	Distinct
Valve layers	Distinct layers absent; areas of fibrosa and spongiosa present	Three distinct layers: atrialis/ventricularis, fibrosa, and spongiosa
Binucleate cardiomyocytes	Majority (>75%)	Minority (<25%)

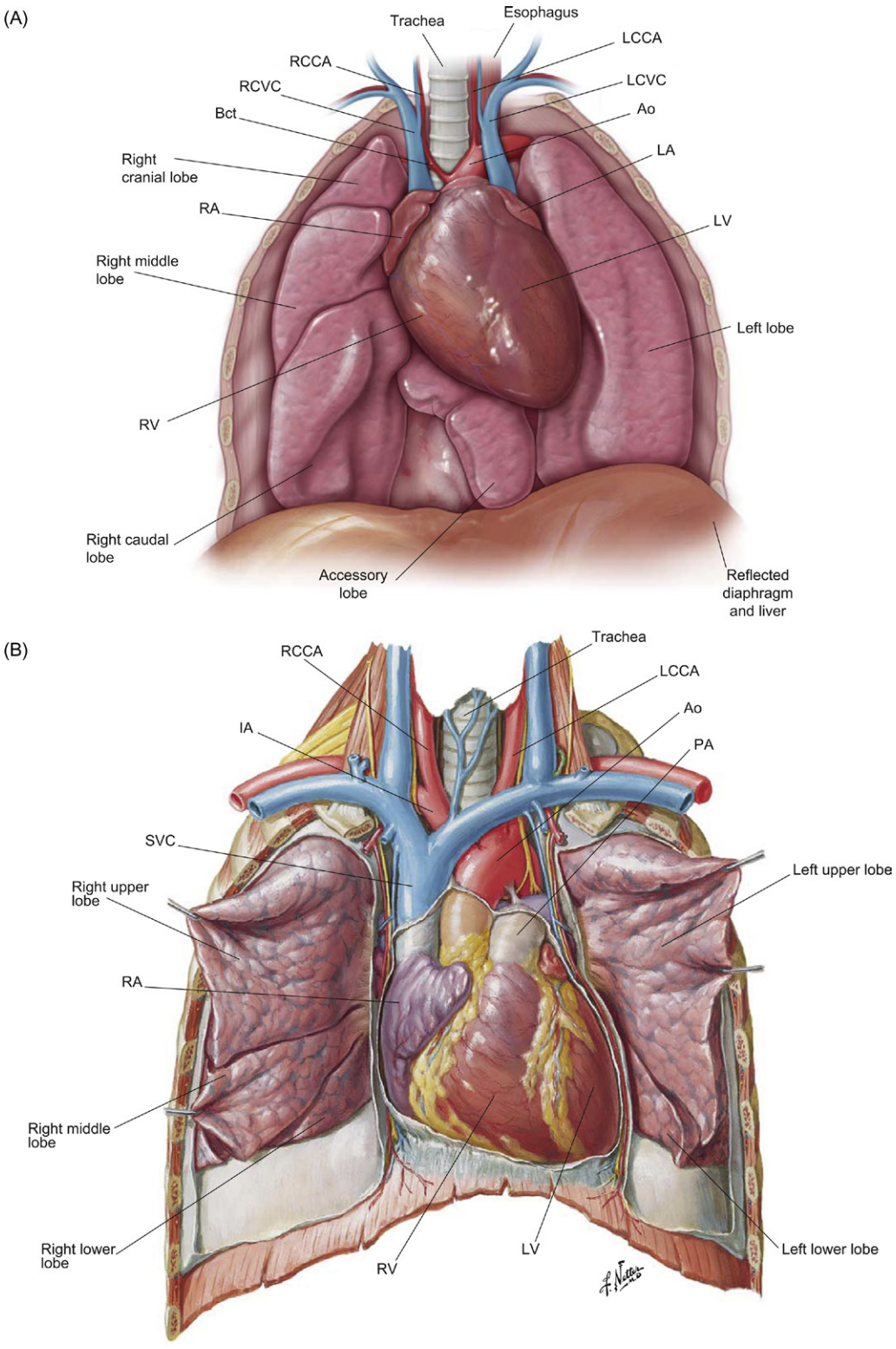

FIGURE 10.1 Regional anatomy of the heart. (A) Ventral view of the rodent (mouse) heart showing its relationship to other thoracic organs. The pericardial sac has been removed. Note the generally spherically shaped and its slight rightward rotation (clockwise from apex to base). The basal right ventricle (RV) is positioned slightly ventrally to the basal left ventricle (LV). The heart does not rest on the diaphragm. Epicardial fat and a distinct interventricular groove are lacking. The right atrium (RA), left atrium (LA), aorta (Ao), brachiocephalic trunk (Bct; equivalent to the human innominate artery), right common carotid artery (RCCA), left common carotid artery (LCCA), left cranial vena cava (LCVC), and right cranial vena cava (RCVC) are indicated. (B) Anterior view of the human heart showing its relationship to other thoracic organs. The pericardial sac has been partially removed. Note the vaguely conical shape of the heart and its slight rightward rotation, resulting in the RV and pulmonary artery (PA) being positioned anteriorly. The inferior face of the heart rests on the diaphragm. *IA*, innominate artery; *LA*, left atrium; *SVC*, superior vena cava. Sources of A and B: © Elsevier, Inc., www.netterimages.com.

Need-to-know

- The rodent pericardium is very thin and is easily lost during necropsy.

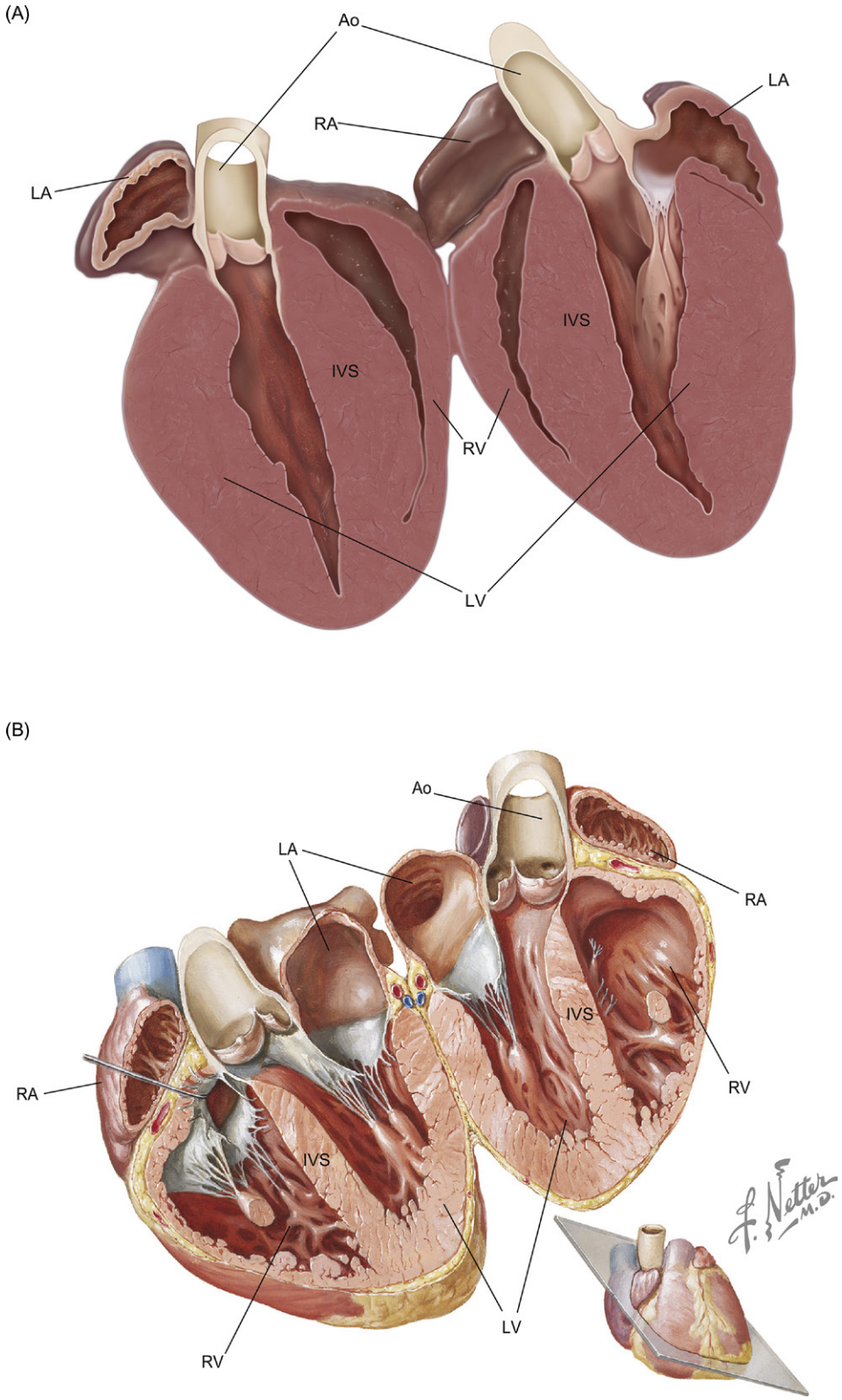

FIGURE 10.2 Heart. (A) This rodent (mouse) heart has been bisected to reveal the interior chambers. Because of the small size, it is difficult to examine structures (such as valves) or measure wall thicknesses grossly. (B) In this view, the human heart has been bisected into its anterior and posterior halves to reveal all four chambers and cardiac valves. *Ao*, aorta; *LA*, left atrium; *LV*, left ventricle; *RA*, right atrium; *RV*, right ventricle. Sources of A and B: © Elsevier, Inc., www.netterimages.com.

Need-to-know

- Rodent valves are typically evaluated microscopically.
- Rodent wall thicknesses are typically evaluated with specialized imaging techniques.
- Measurements can be done microscopically if contraction state and level of sectioning are standardized.

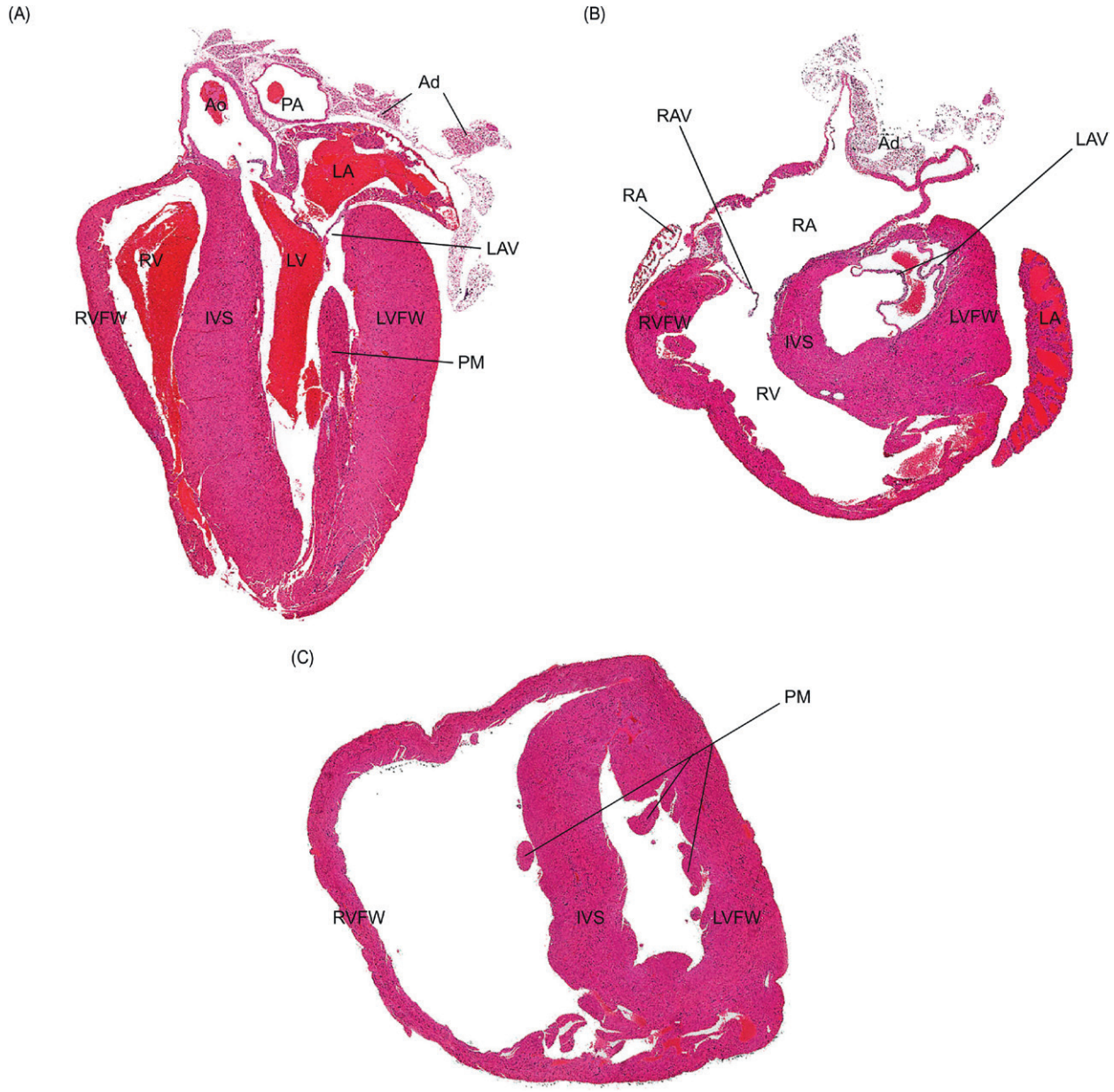

FIGURE 10.3 Subgross anatomy of the rodent (mouse) heart. Bisected (A) and cross-sectioned (B and C) heart (B at the heart base and C at approximately the basal third of the heart). The left ventricular free wall (LVFW) and interventricular septum (IVS) are approximately the same thickness; the right ventricular free wall (RVFW) is approximately one-third the thickness of the LVFW. The atrial walls are much thinner than the ventricular walls. There is virtually no epicardial adipose (Ad) on the ventricular walls, although adipose (primarily brown fat) is readily apparent at the heart base. For a thorough microscopic valve examination, it is best to perform step cross sections through the base of the heart to ensure the valves are captured. The red material within the right and left ventricles, left atrium, aorta, and pulmonary artery is blood; this is frequently seen in rodent hearts because they are often fixed whole. *Ao*, aorta; *AV*, aortic valve; *IVS*, intraventricular septum; *LA*, left atrium; *LV*, left ventricle; *LAV*, left atrioventricular valve; *PA*, pulmonary artery; *PM*, papillary muscle; *RA*, right atrium; *RV*, right ventricle; *RAV*, right atrioventricular valve.

Finally, because of the size of the rodent cardiovascular system, in examination of the rodent heart features is often better done at the microscopic level, despite some of these features being readily examined at the macroscopic level in humans.

Heart

Gross Anatomy

In both rodents and humans, the heart resides in the mediastinum. It is overlaid ventrally (anteriorly in humans) by the sternum, ribs, and

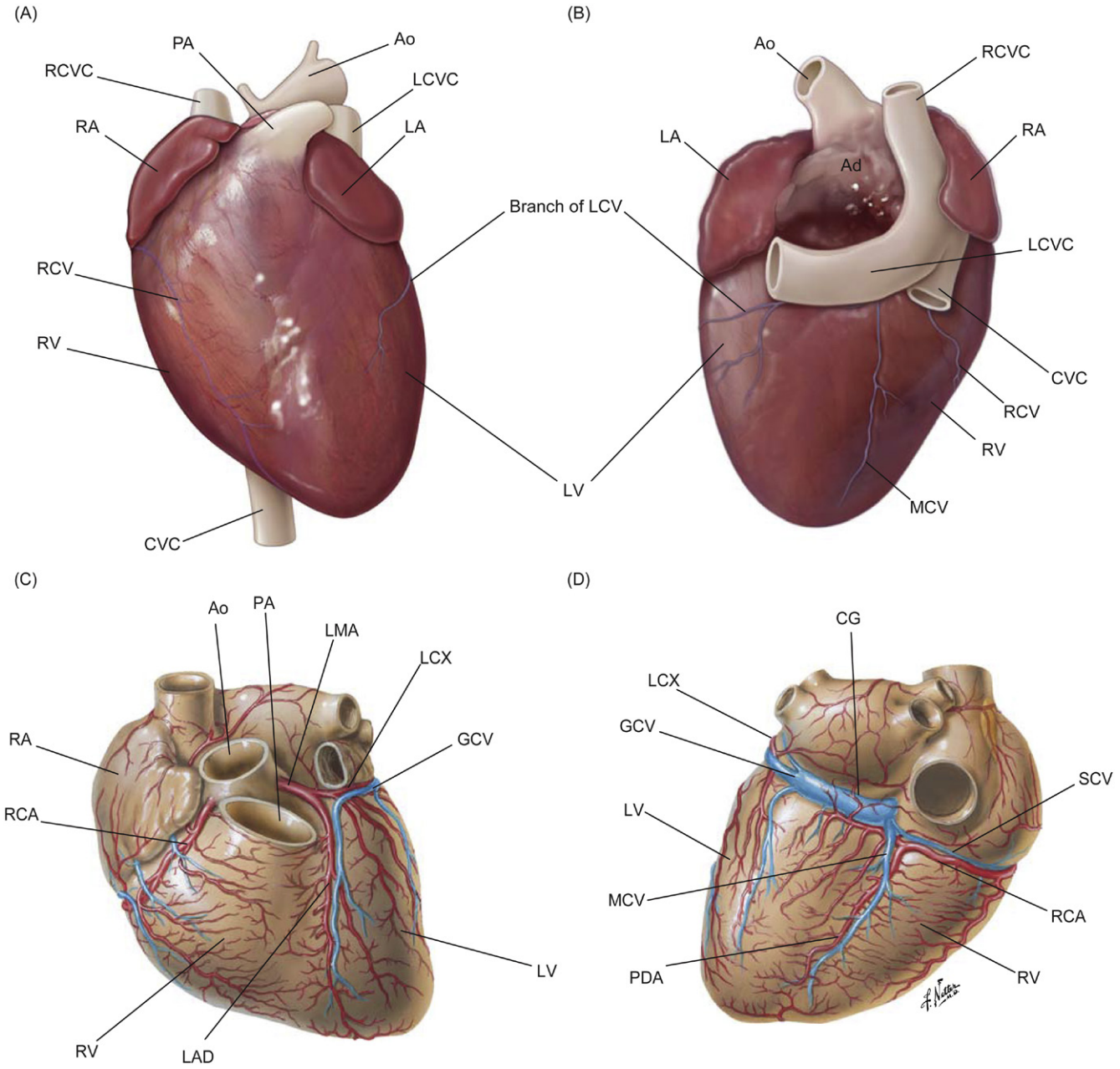

FIGURE 10.4 Exterior surface of heart and cardiac vasculature. Ventral (A) and dorsal (B) surfaces of the rodent (mouse) heart. The vessels that are readily apparent on the surface of the heart are primarily cardiac veins. The coronary arteries are intramyocardial and are not readily apparent on the surface. (C and D) Sternocostal (C) and diaphragmatic (D) surfaces of the human heart. In contrast to the rodent, many of the large vessels in the human heart are epicardial, and this can be viewed externally. In the diagrams, coronary arteries are highlighted in red and veins in blue. *RCVC, LCVC*, right and left cranial vena cavae; *CVC*, caudal vena cava; *RCV, LCV*, right and left coronary veins; *LA*, left atria; *RV*, right ventricle; *Ad*, adipose tissue; *Ao*, aorta; *CG*, coronary groove; *GCV*, great cardiac vein; *LAD*, left anterior descending coronary artery; *LCX*, left circumflex coronary artery; *LMA*, left main coronary artery; *LV*, left ventricle; *MCV*, middle coronary vein; *PA*, pulmonary artery; *PDA*, posterior descending coronary artery; *RA*, right atrium; *RCA*, right coronary artery; *RV*, right ventricle; *SCV*, small cardiac vein.

Need-to-know

- Vessels on the surface of rodent hearts are primarily veins.
- The rat left atrium can be supplied by branches from the internal mammary and/or subclavian arteries.
- There is interindividual variability in the heart vasculature in both rodents and humans.

TABLE 10.2 Vasculature

Feature	Rodent	Human
Artery layers	Tunica intima, tunica media, and tunica adventitia	Similar to rodent
Elastic artery	Contains elastic laminae	Similar to rodent
Muscular artery	Tunica media composed of smooth muscle cells; elastic lamellae confined to EEL and IEL	Similar to rodent
Arterioles	Thin (1–2 cell) muscular layer; lack an EEL and often lack an IEL	Similar to rodent
Capillaries	No IEL or smooth muscle cell layer; intermittent pericytes present	Similar to rodent
Subendothelial connective tissue	Usually absent	Present in varying amounts; typically found in larger vessels
Vasa vasorum	Infrequently to rarely seen	Occasionally seen
Pulmonary veins	Have a thick media composed of cardiomyocytes	Occasionally surrounded by cardiomyocytes near the heart base

intercostal muscles, and it is abutted laterally by the lungs, pleura, and hilar structures and dorsally (posteriorly in humans) by the descending aorta and esophagus (Fig. 10.1). In both rodents and humans, the heart is divided into four chambers: the left and right atria, which are separated by the interatrial septum, and the left and right ventricles, which are separated by the interventricular septum (IVS) (Figs. 10.2 and 10.3). The ventral aspect of the rodent heart corresponds to the sternocostal aspect of the human heart, whereas the dorsal aspect of the rodent heart roughly corresponds to the diaphragmatic aspect of the human heart. In both rodents and humans, the heart comes to a point at its caudal (inferior in humans) pole, called the apex. The opposite end (cranial or superior), where the great vessels originate, is called the base. Hence, the long axis of the heart runs from apex to base.

The rodent heart sits within a very thin pericardial sac, typically only a few cell layers thick. An outer and inner mesothelial layer is separated by a scant fibrous layer. The inner mesothelial layer is also called the parietal pericardium and is continuous with the visceral pericardium (which is the most superficial layer of the epicardium). The pericardial sac is continuous with the mediastinum and attaches to the heart at the base. Within the connective tissue where the pericardial sac attaches to the heart, adipose tissue (primarily brown fat) is present. The pericardial sac is usually inadvertently removed from the heart during necropsy, but occasionally there are small remnants of it histologically. If the pericardial sac is of interest, great care should be taken to avoid removing and discarding it during necropsy. By contrast, the human pericardial sac is a much more substantial structure that has been better characterized. It is composed of two layers: an outer fibrous layer and an inner serous layer. The fibrous pericardium measures 1–3 mm in thickness and generally comprises compact connective tissue. It is attached to the central tendon of the diaphragm caudally and to the tunica adventitia of the great vessels cranially. The serous pericardium is fused to the fibrous pericardium and lines both the inner surface of the pericardial sac (parietal pericardium) and the surface of the epicardium (visceral pericardium). Between the parietal and visceral pericardia is the pericardial cavity, which typically contains 15–50 mL of clear, straw-colored fluid that lubricates and helps protect the heart. Between the visceral pericardium and the myocardium proper is a layer of white adipose tissue of variable thickness; collectively this compartment forms the epicardium. Brown adipose tissue has been described in the human epicardium, but it is not typically a conspicuous feature. A smaller quantity of white adipose tissue can also be found in some regions of the pericardium (adjacent to the parietal pericardium).

The overall shape and surface of the heart are somewhat different between rodents and humans (Figs. 10.1–10.4). In the quadruped rodent, the heart does not sit on the diaphragm and is more freely movable within the pericardial sac; thus, the organ tends to be oval-to-spherical. In the upright human, the heart essentially rests on the

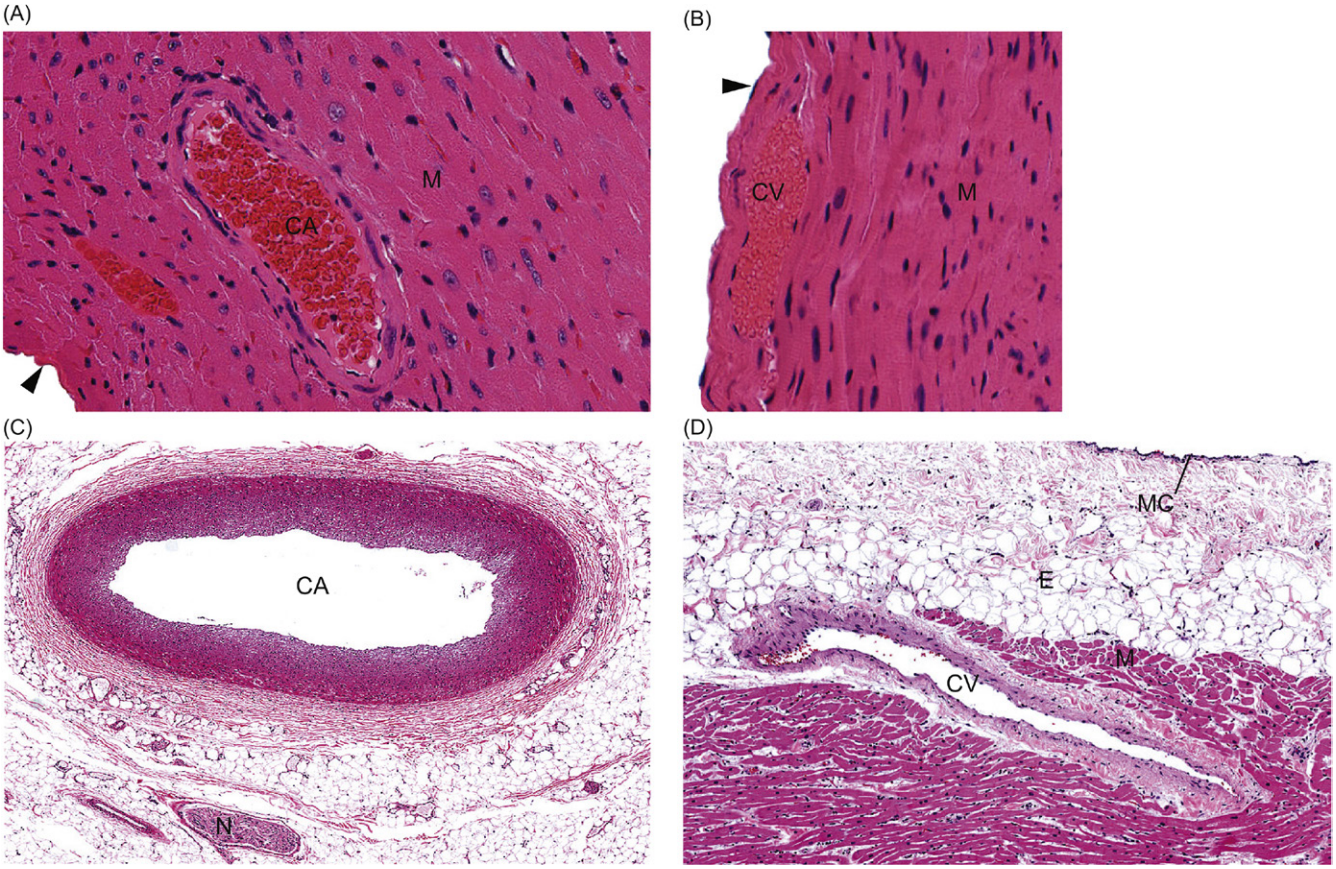

FIGURE 10.5 Location of cardiac vasculature. (A and B) Rodent (mouse) coronary artery (A) and vein (B). The coronary arteries (CA) are intramyocardial and not readily apparent upon gross examination of the heart. The cardiac veins (CV) are much more superficial. Little or no adipose surrounds the coronary arteries or cardiac veins. The epicardium (arrowhead) and myocardium (M) are indicated. (C) Human coronary artery (CA). Most of the proximal coronary arterial tree is located within the fibroadipose tissue of the epicardial compartment. More distally, the coronary arteries branch at sharp angles and dive into the underlying myocardium. Note that this section also includes a cardiac nerve (N). Cardiac nerves are often found running adjacent to the larger vessels. (D) Human cardiac vein (CV), in this case located on the border between epicardial fat (E) and myocardium (M). Note also the flattened layer of mesothelial cells (MC) surfacing the epicardium.

Need-to-know

- Coronary arteries are intramyocardial in rodents and difficult to visualize macroscopically.

diaphragm, and this configuration is reflected by its conical shape and flat inferior surface. In rodents, the right ventricle sits slightly basal relative to the left ventricle, and both ventricles spiral slightly in a clockwise direction as viewed from apex to base. The human heart has an overall similar conformation. In rodents, the heart surface is smooth as the coronary arteries enter the myocardium and traverse the heart within the myocardium; there is no prominent interventricular groove, and no-to-little epicardial fat is present (Figs. 10.4–10.6). In the human heart, the anterior and posterior interventricular grooves are more conspicuous, and, as noted above, the epicardial layer surrounding the heart typically contains a significant amount of fibrofatty tissue (Figs. 10.4 and 10.5).

RELATIVE SIZE CONSIDERATIONS

For routine examination, the rodent heart is weighed after removal, and frequently only the exterior is examined grossly. After fixation, the rodent heart is typically bisected longitudinally, cut midway through the right and left ventricular free walls and through the origin of the great vessels (Figs. 10.2 and 10.3). Examination of the

valves and measurements of wall thicknesses are often done with in-vivo imaging methods and can also done microscopically. Because the state of contraction and level at which measurements are taken can affect wall thickness measurements, care should be taken to standardize these factors, particularly for microscopic measurements in the rodent. It can be difficult to capture the valves on any given section, therefore step sectioning is typically necessary to examine the valves. The rodent heart can also be sectioned at 90° relative to the long axis, resulting in sections with the right and left circumferential free walls as well as the IVS (Figs. 10.3, 10.6, and 10.7). Such sectioning is often done for evaluation of the aortic sinus and valves and can be done for wall thickness measurements if contraction state and level of sectioning are standardized. For wall thickness and chamber measurements, functionally specialized imaging techniques have been adapted to the rodent, including echocardiography and magnetic resonance imaging.

The vastly greater size of the human heart obviously necessitates a very different approach to its gross examination, one in which the relevant structures are examined individually and sequentially. Many standardized approaches to human heart dissection have been described, and a detailed description of these is beyond the scope of the present discussion. Importantly, there is no single best approach, and the heart should be examined using whichever approach best reveals the structure(s) of interest. In most cases, the following general sequence of steps is employed: (1) removal of the organ from the chest and separation from surrounding thoracic organs and the pericardium, (2) external examination, (3) dissection of the major coronary arteries, (4) cross sectioning (bread-loafing) of the ventricles from the apex to a level corresponding to the midpoint of the papillary muscles, and (5) examination of the remaining basal portions of the heart following the direction of blood flow (i.e., right atrium→right ventricle→pulmonary artery→left atrium→left ventricle→aorta).

Rodent heart weights and wall thickness measurements can vary by body weight, age, sex and strain; fixation also affects both weight and wall thickness. The interpretation of experimental effects on heart weight and/or wall thickness should always be interpreted by comparing with proper age, sex, and strain matched controls. Heart weight is often expressed as percent body weight or as heart:body weight ratio. This allows for normalization of heart weight among rodents of different innate or acquired body weights. Normalization should always be performed when evaluating heart weights to help differentiate a systemic difference (e.g., lower heart weights simply because rodents are smaller and have a lower body weight) from a heart-specific difference. Even with normalization, comparisons are best done with intra-study rodents of the same age, sex, and strain. Heart:brain weight ratio is also used for normalization.

Mouse and rat hearts weigh approximately 0.10–0.15 and 0.5–2.5 g, respectively. The mouse heart is approximately 0.40–0.6% of body weight while rat is 0.20–0.50% (lower end of range in older animals). The left ventricular free wall is approximately 1.5–1.8 mm thick in mice and 1.5–2.7 mm thick in rats. As previously mentioned, measurements vary by age, sex, and strain. In both mice and rats, the IVS is approximately the same thickness as the left ventricular free wall, and the right ventricular free wall is typically approximately one-third as thick as the left ventricular free wall. In contrast, both atrial walls are much thinner than the ventricular walls, and in some areas may only be a few cell layers thick (Figs. 10.3 and 10.7).

Proportionately, the human heart is similar in size to the rodent heart. Its weight is approximately 200–350 g or approximately 0.4–0.45% of lean body weight. The left ventricular free wall, right ventricular free wall, and IVS are 1.2–1.5, 0.4–0.5, and 1.2–1.5 cm thick, respectively. The mitral valve circumference and aortic valve circumference (measurements not typically made in rodents) are approximately 8–10 and 6–8.5 cm, respectively.

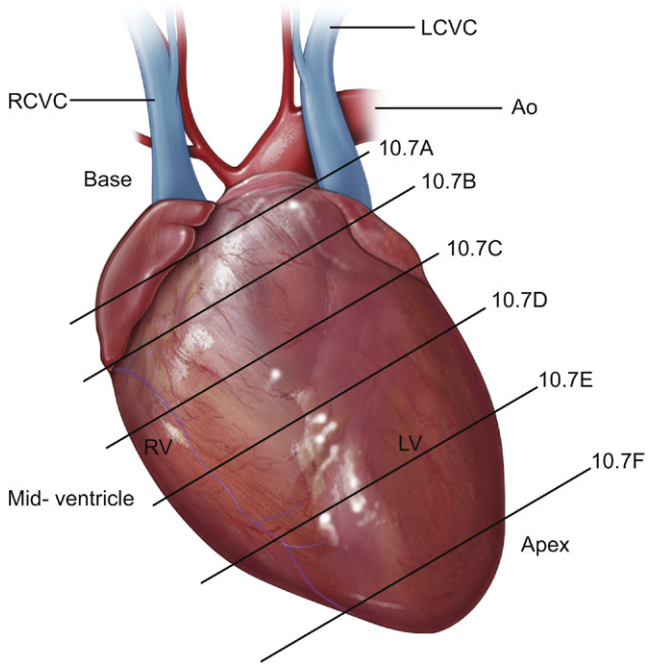

FIGURE 10.6 Rodent (mouse) heart. This figure indicates the approximate plane of section for the corresponding Fig. 10.7A–F. The individual cross sections in Fig. 10.7 demonstrate differences in cross-sectional anatomy present at different levels. Orientation and definitive histologic identification of cardiac structures may require serial proximal and distal sections to reference the relative location of a particular structure. Fig. 10.7A and B covers the base region, Fig. 10.7C–E covers the ventricular region, and Fig. 10.7F covers the apex region. *Ao*, aorta; *LCVC*, left cranial vena cava; *LV*, left ventricle; *RCVC*, right cranial vena cava; *RV*, right ventricle.

Need-to-know

- The rodent has two cranial (anterior) venae cavae.

HISTOLOGY

Myocardium

Myocardium shows similar features at the light microscopic level in rodents and humans (Fig. 10.8). Atrial and ventricular myocardium have generally similar histologic features; however, atrial walls are thinner, and atrial cardiomyocytes tend to be smaller, thinner, and more elongated than their ventricular counterparts. In both rodents and humans, most of the cross-sectional area is occupied by cardiomyocytes, the predominant parenchymal cell type. Cardiomyocytes have a rectangular shape and show a pattern of cross-striations similar to that of skeletal muscle, with alternating light I (isotropic under polarized light) bands and dark A (anisotropic under polarized light) bands. Cardiomyocytes may contain one or two centrally located nuclei. Although the majority of rodent cardiomyocytes are binucleate, most human cardiomyocytes are mononucleate. Nuclei have a granular chromatin pattern and one or two prominent nucleoli. Cardiomyocytes occasionally branch at acute angles. They are connected by specialized junctional complexes called intercalated disks. Intercalated disks represent the undulating double membranes where two cells are tightly bound together by desmosomes and connected by gap junctions, allowing electrical impulse conduction from cell to cell. In histologic sections, the intercalated disks appear as faint lines running perpendicular to the long axis of the myofibers. In adult human and occasionally rodent hearts, cardiomyocytes may contain golden brown lipofuscin pigment in a perinuclear location (Fig. 10.9). Lipofuscin is composed of lipids, phospholipids, and proteins that accumulate secondary to lipid peroxidation. It is generally more commonly seen in humans than in rodents and is considered a “wear-and-tear” pigment, in that it is also more common in older humans or rodents.

Most of the preceding features are best visualized when cardiomyocytes are examined in longitudinal section—that is, oriented from end-to-end parallel to plane of section. Invariably, in some microscopic fields, the cardiomyocytes will be sectioned transversely (Fig. 10.10). In this view, striations and intercalated disks are inconspicuous, but the cardiac interstitium and non-myocyte cell types therein are better revealed. Similar to the analogous structure in skeletal muscle, the endomysium is a collagen network that surrounds individual muscle fibers. The perimysium is a slightly thicker collagen network that surrounds groups of cardiomyocytes. Because these collagen networks are relatively thin and the bundling of cardiomyocytes is often

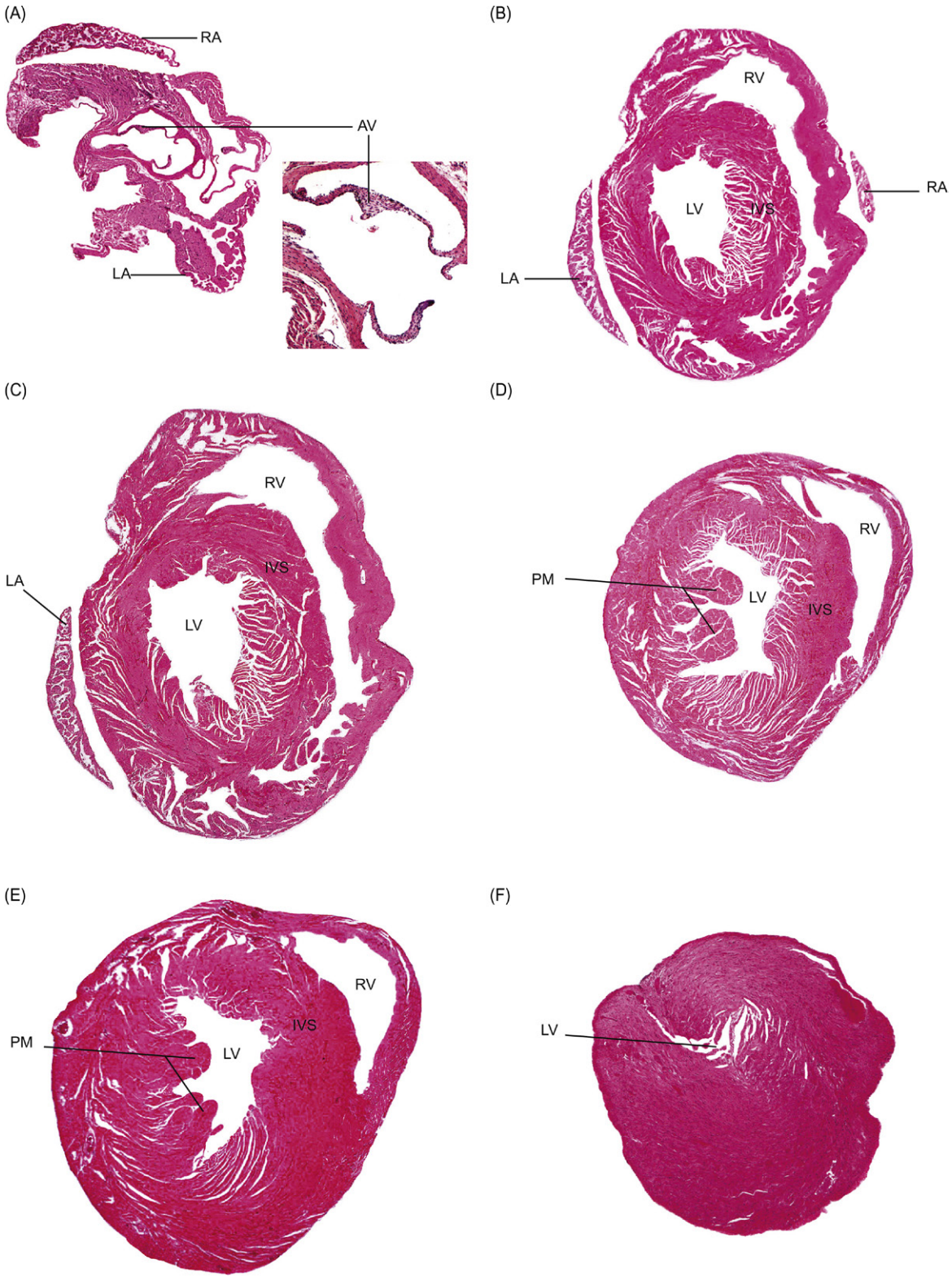

FIGURE 10.7 Rodent (mouse) heart. Cross sections from the base to the apex of the heart illustrate the major landmarks present at different levels. Due to the hearts' general spherical shape, cross sections near the base and apex are smaller than mid-ventricular cross sections. The papillary muscles and the presence and relative size of the ventricular lumens serve as robust landmarks. Capturing the valves or other specific structures on a given section often requires step or serial sections of the heart. (A) Heart base. The valves and part of the atria are visible. (Insert) Aortic valves. Melanocytes may be present within valve leaflets of pigmented rodent strains. (B) Lower heart base (below aortic valve). Cross section of the ventricles and both atria. (C) Upper ventricular region. Cross section of the ventricles and left atria. The lumen of the right ventricle is larger than that of the left. (D) Mid-ventricular region. The papillary muscles in the left ventricle are prominent. (E) Lower ventricular region. Cross section of the ventricular lumens. Note that compared with D, the left ventricular lumen size has changed little, whereas the right ventricular lumen is smaller. (F) Apex. The lumen of the left ventricle is considerably smaller than that in B–E, and the IVS and right ventricle are not present in this plane. *AV*, aortic valve; *IVS*, interventricular septum; *LA*, left atrium; *LV*, left ventricle; *PM*, papillary muscles; *RA*, right atrium; *RV*, right ventricle.

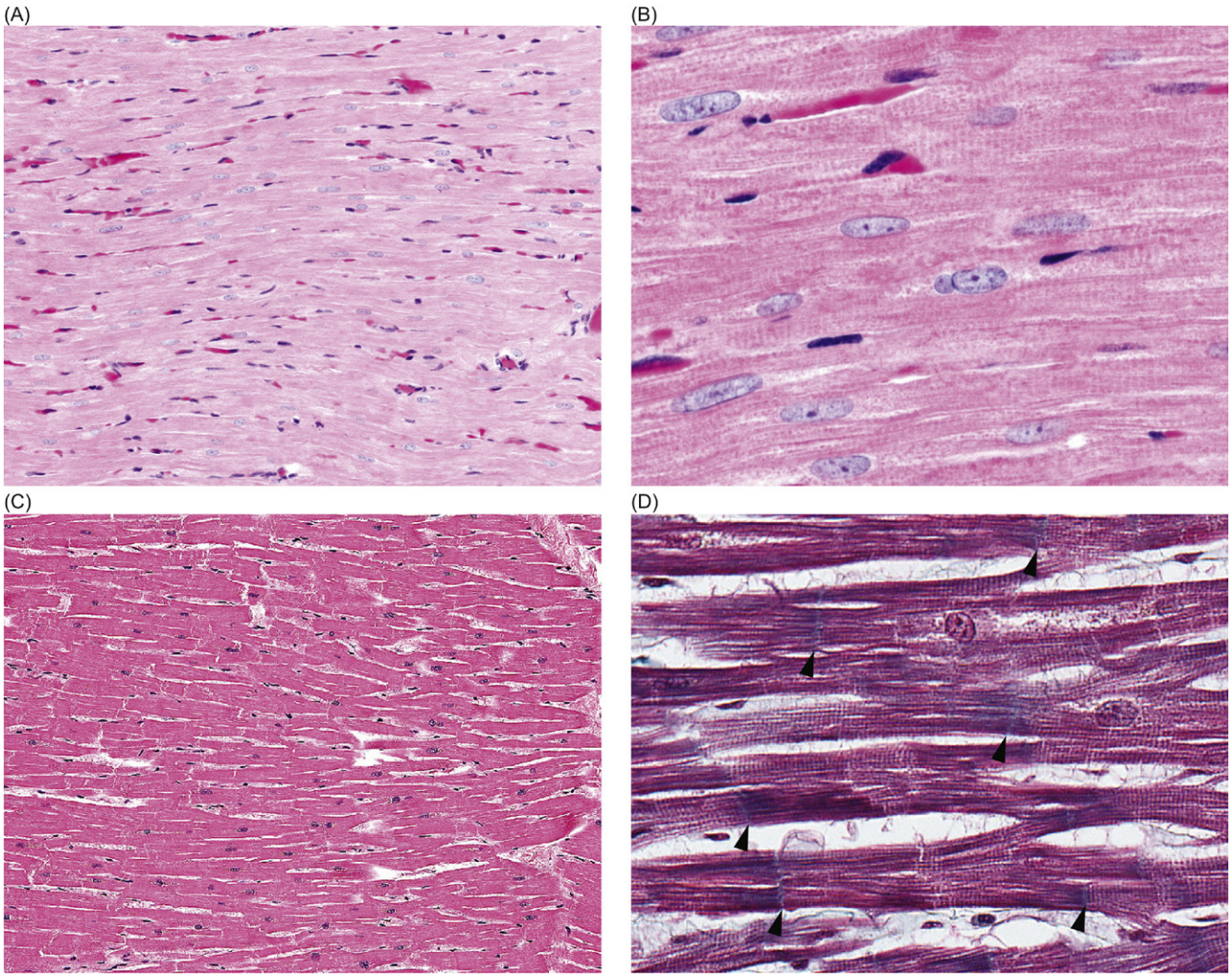

FIGURE 10.8 Longitudinally oriented cardiomyofibers. (A, B) Left ventricular myocardium of the rodent (rat) at low (A) and high (B) magnification. The majority of the area is occupied by the large cardiomyocyte eosinophilic cytoplasm. In these photomicrographs, most cardiomyocytes are oriented longitudinally, and the faint cross-striations are evident at high power in B. Cardiomyocyte nuclei are large, oval-to-rectangular, and contain granular chromatin with one or two nucleoli. Between cardiomyocytes is a delicate interstitium containing fibroblasts and capillaries lined by endothelial cells. Fibroblast and endothelial cells appear similar: Both have scant cytoplasm and small oval-to-flat densely basophilic nuclei. Erythrocytes are present within capillaries. (C) Human left ventricular myocardium at low magnification. Microscopically, human myocardium is very similar to that of rodents. (D) Human left ventricular myocardium at high magnification and stained with Gomori trichrome. This special stain is useful in highlighting the cross-striations, as well as the intercalated disks (arrowheads). The latter are specialized electromechanical junctions between adjacent myocytes and are similar in all three species.

indistinct, they are frequently lumped together as part of the "cardiac interstitium," which includes all components between cardiomyocytes. Within the interstitium is a rich vascular network so that each cardiomyocyte is surrounded by multiple capillaries. Cell types present in the interstitium include abundant fibroblasts and endothelial cells, both of which have scant cytoplasm and oval-to-flat nuclei with a dense chromatin pattern. In addition, the interstitium contains low numbers of leukocytes (primarily macrophages and lymphocytes, both of which are best visualized with immunohistochemistry) and low (human) to extremely low (rodent) numbers of adipocytes.

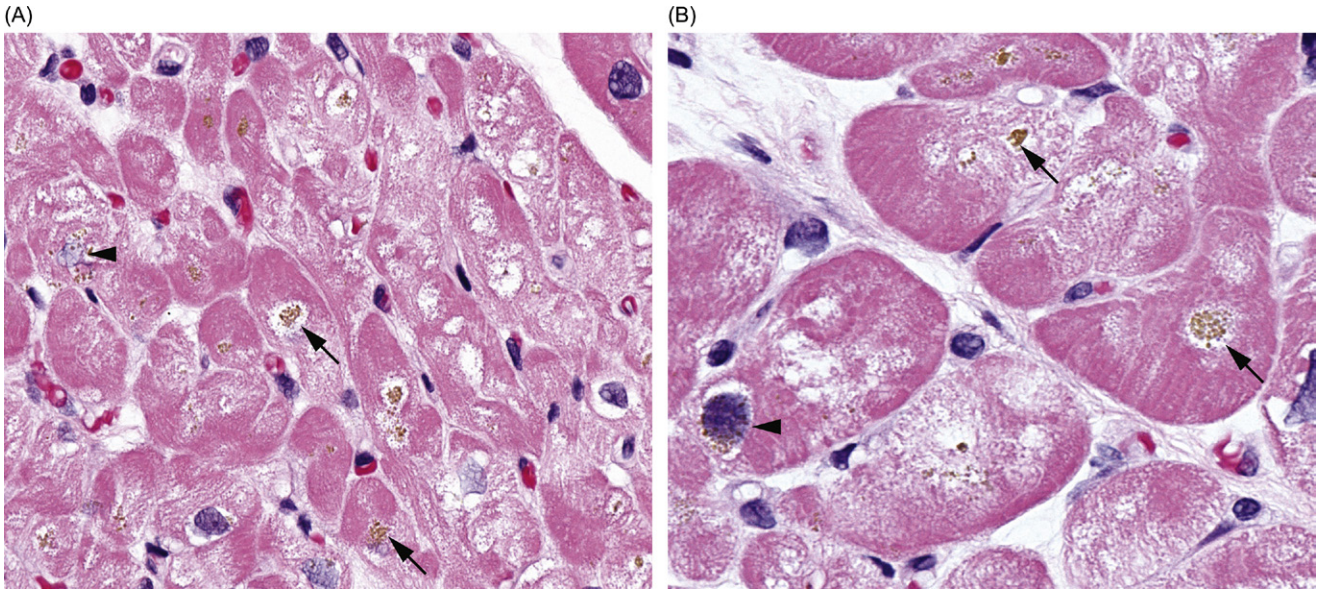

FIGURE 10.9 Lipofuscin. Examples of lipofuscin accumulation in the human heart. In all three species, lipofuscin is a granular golden brown pigment accumulation within cardiomyocytes. (A) Cross-sectional myocardium with cytoplasmic lipofuscin (arrows); when present it is often seen adjacent to cardiomyocyte nuclei (arrowheads). (B) High magnification of lipofuscin accumulations.

Although interstitial cells occupy only a small fraction of the cross-sectional area of the heart, they represent the majority of the total cell population present. The interstitium also contains a delicate network of extracellular matrix, and special histochemical (e.g., trichrome) stains can be used to highlight the collagen present in this compartment.

Microscopic fields in which cardiomyocytes are variably caught in longitudinal, transverse, or oblique section reflect the real organization of cardiomyocytes across the ventricular wall, where the mean axis of cardiomyocytes gradually transitions across the different layers of the ventricular wall. In the left ventricle, inner myofibers tend to be oriented longitudinally so as to form trabeculae and papillary muscles, whereas myofibers in the middle portions of the wall are generally oriented circumferentially and thereby form a cylinder around the ventricular chamber from apex to base. The orientation of myofibers in the outer portions of the ventricular wall is more variable by region.

Endocardium, Epicardium, and Pericardial Sac

The inner surface of the heart is lined by the endocardium, which covers the inside of both ventricles, both atria, and all the valves. The endocardium is continuous with the tunica intima of the great vessels (described below). The endocardium has three components: a single layer of flat endothelial cells in direct contact with the blood-filled chamber, a dense inner connective tissue layer, and a loose outer connective tissue layer (Fig. 10.11). The last two layers are sometimes lumped together and referred to as the subendocardium. In rodents, the three distinct layers are not typically seen by light microscopy. Rather, a single-cell layer of endothelium is visible, occasionally with a small amount of connective tissue beneath it. Although still surfaced by only

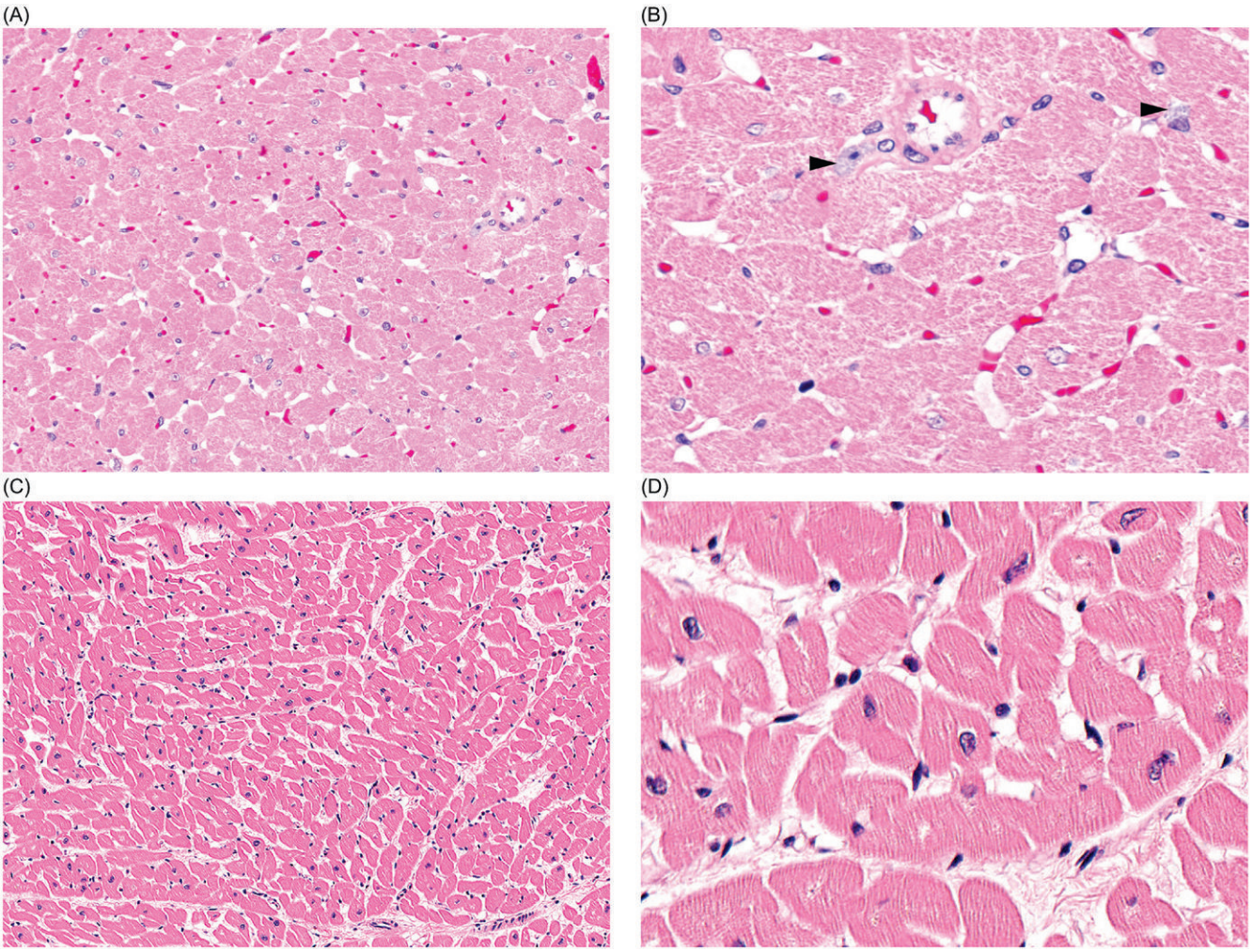

FIGURE 10.10 Cross-sectioned cardiomyofibers. (A, B) Left ventricular myocardium of the rodent (rat) at low (A) and high (B) magnification. In these photomicrographs, the cardiomyocytes are primarily cross-sectioned and the cardiac interstitium can be better visualized (compare to Fig. 10.8). The higher magnification (B) of cross-sectioned cardiomyofibers illustrates how the cross-striations that were evident on longitudinal section are no longer seen, whereas the fibroblasts and endothelial cells of the interstitium are more prominent. When cardiomyofiber nuclei are sectioned in this orientation, they appear more round. Frequently, the plane of section does not include the cardiomyocyte nucleus; if the nucleus is present, typically only one nucleolus is visible. Erythrocytes are present within capillaries. Mast cells (arrowheads) are also commonly seen. (C, D) Left ventricular myocardium of the human at low (C) and high (D) magnification. In both transverse and longitudinal sections, the microscopic features of human myocardium are very similar to those of rodents.

Need-to-know

- Binuclear cardiomyocytes are common in the rodent.

a single layer of endothelium, the subendocardial compartment is thicker and more prominent in humans, especially on the left side of the heart. In addition to collagen, elastic fibers, and fibroblasts, the human subendocardium may contain blood vessels, nerve fibers, adipose tissue, and bundles of smooth muscle. Specialized cells of the peripheral cardiac conduction system, the Purkinje fibers, are also found at this site in both rodents and humans.

The outer surface of the heart is covered by a specialized compartment termed the epicardium. The free surface of the epicardium is lined by a single layer of flattened mesothelial cells (i.e., the visceral layer of the serous pericardium). In rodents, the epicardium is thin and consists of this single-cell mesothelial layer with a small amount of fibrous connective tissue beneath it (Fig. 10.11). The epicardium is a much more

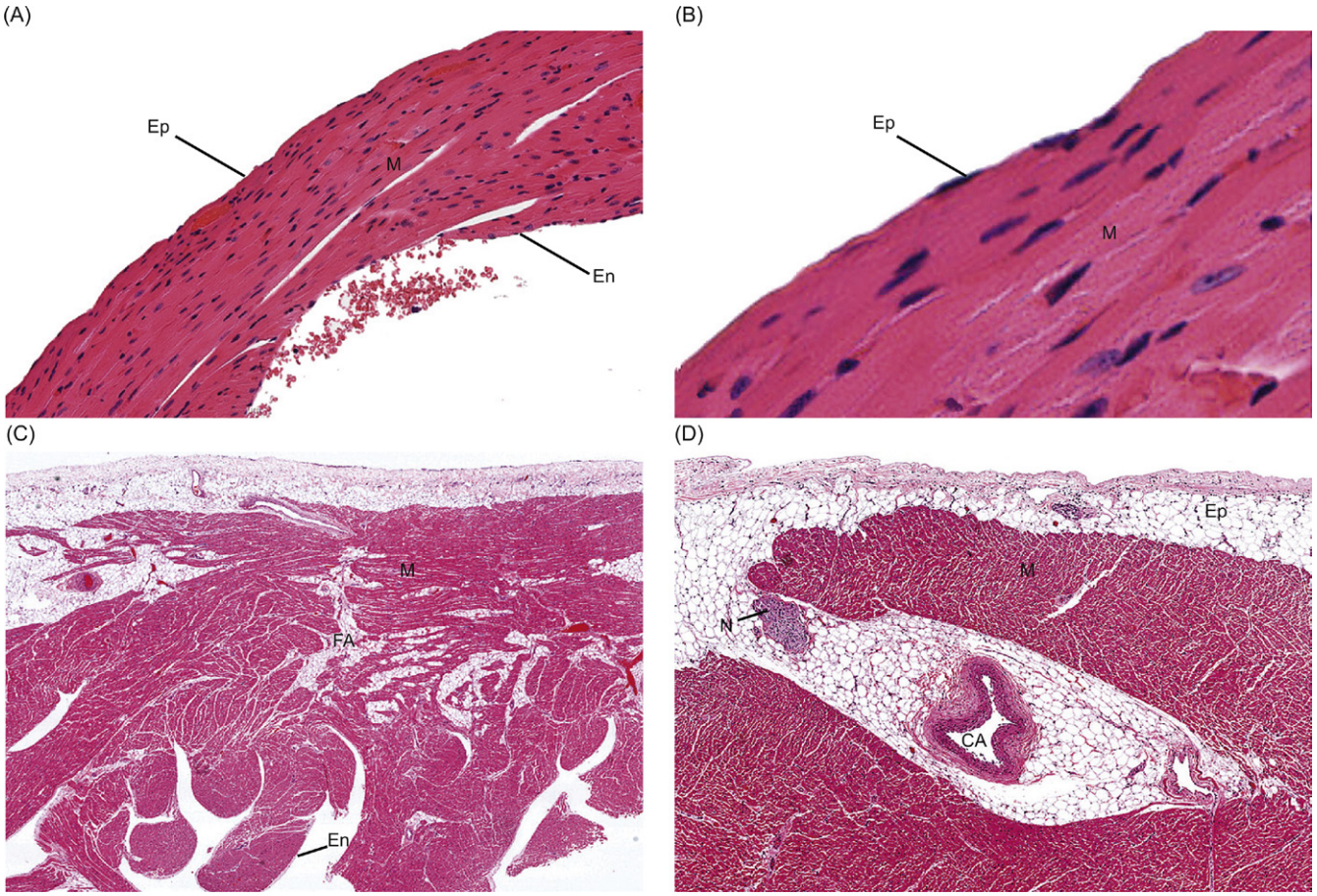

FIGURE 10.11 Epicardium and endocardium. (A, B) Rodent (mouse) right ventricular free wall at low (A) and high (B) magnification. The epicardium (Ep) and endocardium (En) are very thin, often only one cell layer thick. The rodent epicardium, endocardium, and myocardium (M) contain no significant adipose tissue, although the myocardium of older rodents occasionally has small amounts. (C) Human right ventricular free wall, full thickness and viewed at low magnification. The right ventricle differs from rodent in that it normally contains a significant amount of fibroadipose tissue (FA), especially in the anterolateral and apical regions. Fatty infiltration is less extensive in the left ventricle and septum. Endocardium (En), epicardium (Ep), and myocardium (M) are indicated. (D) Outer portions of the human ventricular wall. Unlike rodent, the epicardium forms a wide compartment. Similar to rodent, it is surfaced by a single layer of mesothelial cells, but also contains abundant fibroadipose tissue, which helps to cushion the many coronary vessels and cardiac nerves (N) found in this region. *CA*, coronary artery.

Need-to-know

- The rodent has thin epi- and endocardial layers with scant epicardial fat or subendocardial connective tissue.

substantial structure in humans. Here, the single layer of mesothelium is supported by a layer of fibrous or fibroadipose tissue that may measure up to several millimeters in thickness. Indeed, in our experience, individuals who are used to examining only rodent hearts are often surprised to see the extent of adipose tissue found on the human heart. Epicardial adipose tissue is usually most prominent along the atrioventricular and interventricular grooves, where it surrounds and cushions the major coronary vessels and nerves, but in some individuals it may envelope the entirety of both ventricles.

The visceral pericardium of the epicardium is continuous with the parietal pericardium of the pericardial sac at the base of the heart. In rodents, small fragments of pericardial sac can occasionally be found in histological sections taken from near the base of the rodent heart. The pericardial sac

of rodents is very thin; it is composed of an outer mesothelial cells layer, an inner mesothelial layer, and a scant intermediate fibrous layer. At the light microscopic level, it is frequently difficult to distinguish these layers. These structures are somewhat easier to recognize histologically in humans, although the mesothelium of the visceral pericardium may rub off during handling of the organ. The fibrous pericardium consists of dense bands of wavy collagen with interspersed elastic fibers (that can be visualized only with special histochemical stains), infrequent stromal cells, and scant thin-walled blood vessels. Its inner surface is lined by a single layer of mesothelial cells.

Cardiac Valves

GROSS ANATOMY

In rodents and humans, there are four cardiac valves: the left atrioventricular (mitral) valve, aortic valve, right (tricuspid) atrioventricular valve, and pulmonic valve. These valves separate the left atrium and left ventricle, left ventricle and aorta, right atrium and right ventricle, and right ventricle and pulmonary artery, respectively. Valve structure is generally similar in rodents and humans. However, rodent valves form more of a continuous curtain compared with human valves, which are divided into more distinct leaflets. The human right atrioventricular valve has three leaflets and is also known as the tricuspid valve. The left atrioventricular valve has two leaflets and is also known as the bicuspid or mitral valve. The pulmonic and aortic valves both have three leaflets and are also known as semilunar valves. In rodents, the valves are typically examined microscopically (or functionally by specialized imaging techniques, i.e., echocardiography). As noted above, generating properly oriented sections of valve tissue from rodents can be challenging and may require multiple step sections at the heart base to ensure the valves are captured (Figs. 10.7). In humans, the cardiac valves are easily studied intact by opening the heart in a manner that preserves their anatomic relationships.

The bases of the valves are anchored in fibrous connective tissue at the heart base. In mice, the amount of connective tissue is minimal, while in rats there is slightly more. In older rodents, the amount of connective tissue is often increased compared with younger rodents, and occasionally contains a small amount of cartilage or bone (Fig. 10.12). A low number of mast cells may be present within the connective tissue. In humans, each of the four valves is situated within a dense fibrous ring known as the annulus. The aortic, tricuspid, and mitral annuli abut one another, whereas the pulmonary annulus is separated by conus muscle. Together, the four annuli contribute to the fibrous skeleton, the so-called "cardiac skeleton" that isolates the atria from the ventricles and provides support for the valves and cardiac conduction system. In rodent heart, especially mouse, the fibrous connective tissue does not form a distinct fibrous skeleton.

The atrioventricular valves are distinguished by the presence of multiple thin fibrous structures called chordae tendineae that project from near the free edge of the valve. These structures, which are far less prominent in rodents, attach on their opposite end to specialized papillary muscles. Chordae tendineae anchor the valves to the ventricle wall and prevent them from inverting. They arise from papillary muscles of the ventricular walls or directly from the ventricular walls; there are no papillary muscles on the right ventricular free wall. The rodent left atrioventricular valve attaches to two papillary muscles, one anterior and the other posterior, which both arise near the apex of the heart. The pulmonic and aortic valves do not have chordae tendinae.

HISTOLOGY

In both rodents and human, flow surfaces of the cardiac valves are lined by a continuous layer of

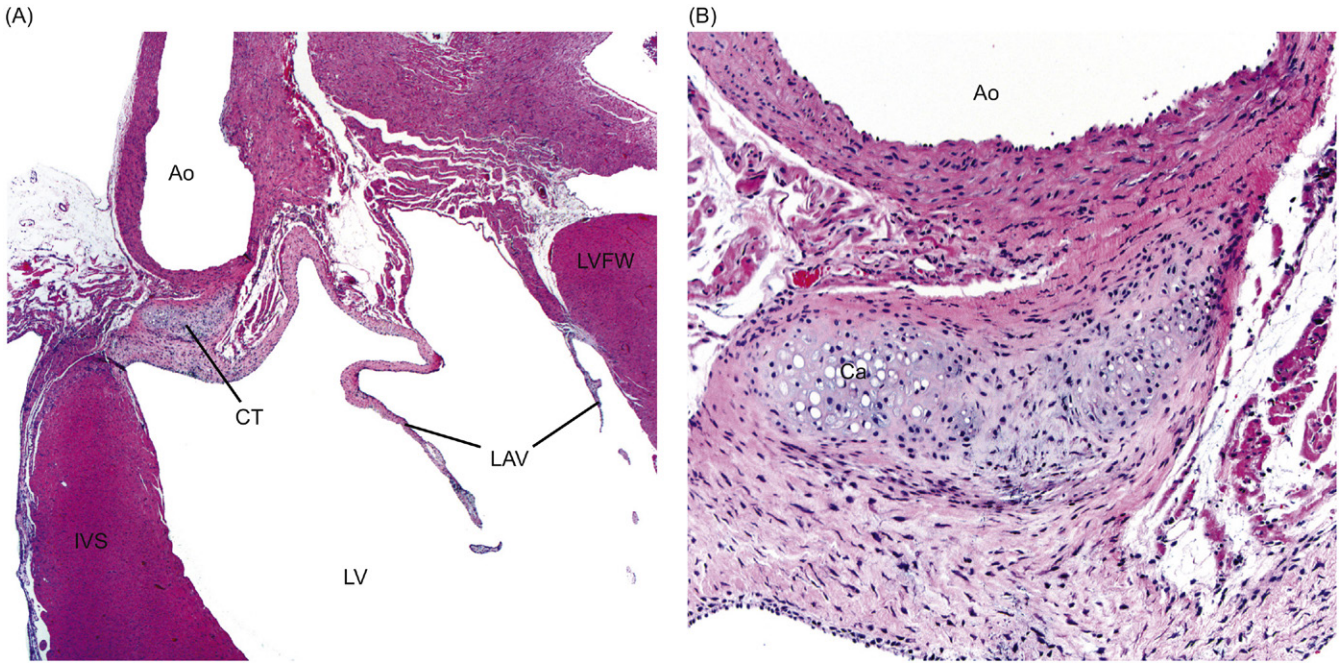

FIGURE 10.12 Connective tissue at the base of the rodent (rat) heart. Heart base at low (A) and high (B) magnification. Rodent hearts do not have a distinct cardiac skeleton. Occasionally one is observable in rats and older mice as a small amount of connective tissue (CT) present at the base of the heart near where the valves are anchored. Within the connective tissue, there is occasionally a small amount of cartilage (Ca) or bone. *Ao*, aorta; *IVS*, interventricular septum; *LAV*, left atrioventricular valve; *LV*, left ventricle; *LVFW*, left ventricular free wall.

Need-to-know

- The rodent cardiac skeleton is indistinct.

flattened endothelial cells. However, the internal structure of cardiac valves from rodents and humans appears quite different, with human cardiac valves exhibiting a distinct, trilaminar architecture that is far less conspicuous in rodents.

Rodent valve leaflets have distinct areas, but these areas do not form the distinct layers seen in humans (described below). Instead, there are areas of dense organized fibrous connective tissue, analogous to the fibrosa of humans, and areas of disorganized collagen and myxomatous (proteoglycan-containing) extracellular matrix, analogous to the spongiosa of humans (Fig. 10.13). The basal aspect of valves is typically almost all fibrosa, with spongiosa often only being visible in the more apical aspects of the valves. Note that the plane of sectioning can cause areas of the valve (particularly the loose myxomatous areas) to appear irregularly thickened, thus care should be taken to distinguish this finding from the pathologic process of valvular myxomatous degeneration (valvular endocardiosis).

Given the complex structure of human valve tissue, special histochemical stains for collagen and elastin (e.g., Movat's pentachrome) are routinely used to evaluate them. Human leaflets have three major layers that are recognizable in histological sections properly oriented from proximal to distal: the atrialis/ventricularis, the spongiosa, and the fibrosa (Fig. 10.13). The first layer, the atrialis for atrioventricular valves and ventricularis for semilunar valves, is continuous with the subendocardium of the preceding chamber and contains prominent elastic fibers. Near the opposite face of the valve is the third layer, the densely collagenous fibrosa, which is continuous with the fibrous annulus of the valve and provides structural support to the leaflet. The fibrosa extends the full length of the valve leaflet, and in the case of the atrioventricular valves, inserts into the chordae tendinae and the papillary

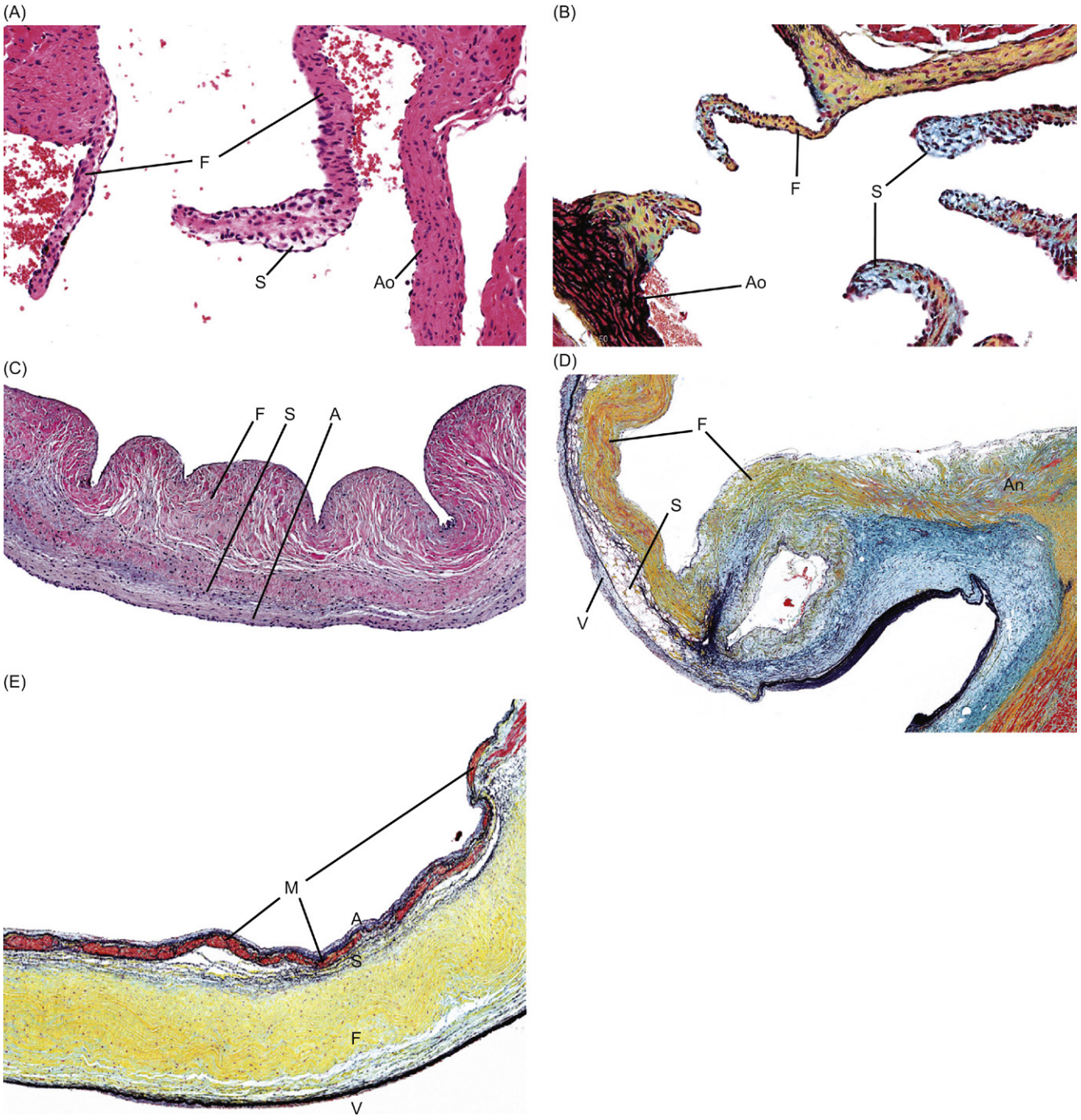

FIGURE 10.13 Valves. (A, B) Rodent (mouse) aortic valve and proximal aorta. The valves are covered by endothelium and internally are composed of areas of fibrosa (F) and spongiosa (S) without distinct layering. With an H&E stain (A), the fibrosa is dense and eosinophilic, whereas the proteoglycan-rich spongiosa is light blue. Special stains such as Movat's pentachrome (B) better distinguish different areas of the valve, with the fibrosa staining yellow and the spongiosa staining blue. Movat's pentachrome also clearly stains elastic fibers, as evidenced by the numerous dark elastic lamellae in the aorta. The valves lack significant elastic lamellae. (C–E) Human aortic (C and D) and mitral (E) valves. Unlike the rodent, the valves have an obvious layered architecture, including the collagen-rich fibrosa (F), and proteoglycan-rich spongiosa (S), as well as the elastin-rich atrialis (A) or ventricularis (V) layers of the atrioventricular and semilunar valves, respectively. The main structural component of cardiac valves is the collagen-rich fibrosa, which is directly continuous with the fibrous valve annulus (An). In the mitral valve, leaflet tissue located close to the annulus may also contain smooth muscle cells (M) and even cardiomyocytes. These cell types are typically not encountered in rodent leaflets.

Need-to-know

- The rodent atrioventricular valves are generally a continuous curtain and lack the three distinct histological layers seen in humans.

muscle tips. Separating the atrialis/ventricularis and fibrosa compartments is the second layer, the spongiosa, which contains abundant proteoglycans, giving it a loose, "spongy" appearance by routine histochemical staining. In the human mitral valve, tissue located close to the valve insertion in the annulus may also contain capillaries, smooth muscle cells, and cardiomyocytes.

Conduction System

In rodents and humans, the sinoatrial (SA) node, the atrioventricular (AV) node, the atrioventricular bundle (bundle of His), and the right and left bundle branches represent the main parts of the conduction system of the heart. Although the human conduction system has been described in greater detail than that of rodents, the organization of the conduction systems is similar. In both rodents and humans, the SA node lies at the junction of the cranial vena cava (right cranial vena cava in rodents) and the right atrium, and the AV node lies in the interatrial septum. The AV node is continuous with the bundle of His, the next structure in the central cardiac conduction system. In rodents, the transition from AV node to the bundle of His is ill-defined anatomically. In both rodents and humans, the bundle of His separates into left and right bundle branches that travel beneath the endocardium toward the apex on the left and right side of the IVS, respectively.

Cells of the nodes and bundle branches are smaller in diameter than ventricular cardiomyocytes, have an oval shape, a centrally located nucleus with a prominent nucleolus, and an eosinophilic, slightly granular cytoplasm without striations (Fig. 10.14). Capturing sections of the conduction system in rodents can be challenging and typically requires step sectioning. Immunohistochemistry can be used to better visualize the conduction system, particularly in rodents.

Although careful dissection and a good knowledge of cardiac anatomy are required, these structures can be readily sampled and identified in histological sections from the human heart. In humans, a component of this fibrous skeleton, the central fibrous body, is an important landmark that helps locate the AV node and the bundle of His. As previously noted, the fibrous skeleton of the rodent is less conspicuous, and thus the central fibrous body is not well-defined in rodents. The central fibrous body is formed by the convergence of the membranous septum and the right fibrous trigone (the rightward portion of the fibrous continuity between the mitral and aortic valves). It is penetrated by the central cardiac conduction system, and electrical propagation proceeds from the atria to the crest of the IVS along this axis. The compact AV node is located between the "working" atrial myocardium (proximally) and the central fibrous body (distally) and connected to the former by transitional nodal cells. Thus, AV nodal myocytes are morphologically distinct from their counterparts in the neighboring working myocardium but not insulated from them by fibrous tissue. The next structure along the central conduction system axis is the bundle of His (Fig. 10.14), which resembles the compact AV node, but is located within the central fibrous body. The bundle of His then emerges from the central fibrous body, enters the crest of the IVS, and gives rise to the left and right bundle branches. These structures retain the insulating fibrous sheath that they assumed in the bundle. Subsequent components of the peripheral cardiac conduction system are morphologically similar in mouse and human.

Great Vessels and Coronary Vasculature

Gross Anatomy

The great vessels bring blood to and from the heart, and the coronary vasculature supplies blood to the heart itself. The great vessels comprise the aorta, vena cavae, pulmonary artery, and pulmonary

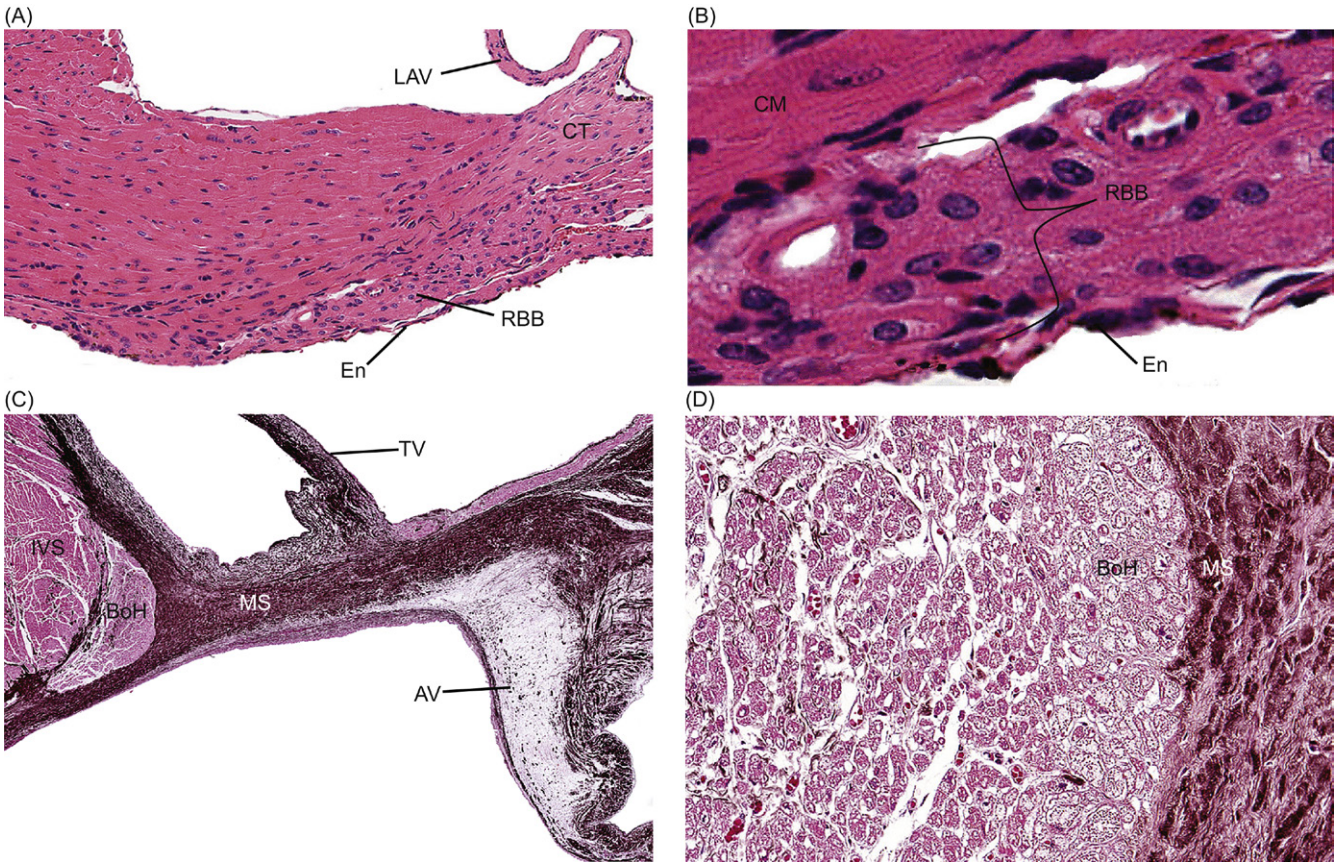

FIGURE 10.14 Conduction system. (A, B) Rodent (mouse) apical IVS and central cardiac conduction system. The right bundle branch (RBB) is present within the wall of the IVS immediately subjacent to the right ventricular endocardium (En). Cells of the conduction system appear similar to cardiomyocytes but lack striations and are smaller. In B, faint striations are evident in cardiomyocytes (CM), whereas cells of the RBB lack striations and are smaller, as evidenced by a shorter internuclear distance. Obtaining portions of the conduction system can be very challenging and can require step sections through the area of interest. Also present in A are the left atrioventricular valve (LAV) and a small focus of connective tissue (CT) at its base. (C, D) Human central cardiac conduction system at low (C) and high (D) power; Jones' methenamine silver stain. Although much larger, the histological anatomy of the central cardiac conduction system is very similar to that of rodents. The bundle of His (BoH) is captured in this plane of section. Note the close relationship of this structure to landmarks including the tricuspid valve (TV), aortic valve (AV), interventricular septum (IVS), and the collagenous membranous septum (MS). The membranous septum is part of the central fibrous body, which insulates the bundle. As illustrated by the higher power view of the bundle in D, the myocytes also lack conspicuous cross-striations, but instead show prominent cytoplasmic vacuolization. Source: Slide courtesy of Dr. Dennis Reichenbach, University of Washington.

veins. In both rodents and humans, oxygenated blood exits the left ventricle when it passes through the aortic valve. The systemic circulation returns to the heart via the vena cavae. In rodents, there are left and right cranial vena cavae and one caudal vena cava. The corresponding vasculature in humans is composed of the superior vena cava (only one) and inferior vena cava. Blood exits the right ventricle via the pulmonary artery, which originates at the pulmonic valve, and returns to the heart via the pulmonary veins.

In rodents, the anatomy and nomenclature of the coronary vasculature vary by strain and can even vary within the same strain. Rodent coronary vasculature has not been characterized to the degree as human coronary vasculature. See Further Reading section for more detailed descriptions of the various rodent coronary patterns that have been reported.

Rodents typically have two major coronary arteries, both of which originate in or slightly

above the aortic sinus (the bulge at the origin of the ascending aorta). Humans also typically have two major coronary arteries that originate within, not above, the aortic sinus. Soon after leaving the aortic sinus/aorta, rodent coronary arteries enter the myocardium and traverse the heart within the myocardium, typically at a depth of approximately 200–400 μm beneath the epicardium. Thus, in contrast to humans, the coronary arteries of rodents are intramyocardial and therefore often not readily visible when examining the surface of the heart (Figs. 10.4 and 10.5).

In mice, the right coronary artery courses over and supplies the right ventricle. It gives off several branches, one of which is comparable to the posterior descending artery of humans. Another branch is the septal artery, which does not have a human counterpart. The septal artery also has been reported to originate from either the coronary sinus or the left coronary artery; in addition, there can be two septal arteries with different origins. The left coronary artery generally crosses obliquely over the left ventricle and gives off variable branches. Some authors refer to the primary branches as the left circumflex and obtuse marginal arteries. In this schema, the obtuse marginal artery is considered comparable to the left human anterior descending coronary artery.

In rats, the right coronary artery gives off a branch, the septal artery. The right coronary artery supplies the right ventricle, most of both the left and right atria, most of the IVS, and sometimes a small portion of the left ventricle. The left coronary artery gives off two (infrequently three) more branches. One branch, the interventricular artery, runs roughly parallel to the IVS, supplies a portion of the IVS and has anastomoses with the septal artery. Another branch, the circumflex artery, runs beneath the ventral surface of the left ventricle toward the apex and supplies most of the left ventricle. In addition to the coronary arteries described above, the rat left atrium can be supplied by branches from the internal mammary and/or subclavian arteries.

The vessels that are grossly visible on the surface of the rodent heart are primarily the cardiac veins, running slightly beneath the epicardium. Parallels between the venous anatomy of rodents and humans are less obvious than for the major coronary arteries. Although variable, the typical primary veins of rodent ventricles can be categorized as follows: (1) the right ventricular vein, which courses over the right ventricle and drains into the right atrium; (2) the left cardiac vein, which courses over the left ventricle and drains into the coronary sinus; (3) the major caudal vein on the posterior surface, which either drains into the coronary sinus, left cardiac vein or right atrium; and (4) the left and right conal veins, which run circumferentially around the base of the ventricles near the atrioventricular junction, drain into the right atrium or right cranial vena cava.

Considerable variation has been described in terms of the origin, number, course, and size of coronary arteries in the human heart (Fig. 10.4). In most cases, there are two major coronary branches, which arise from two of the three aortic sinuses and extend for most or all of their length within the epicardial fat. After arising in its aortic sinus, the right coronary artery typically courses in a rightward direction around the orifice of the tricuspid valve, where it gives rise to multiple branch vessels to the right ventricle and important elements of the pacemaker and cardiac conduction system. In most hearts, the right coronary artery crosses the acute margin of the heart and extends fully to the intersection of the atrioventricular and posterior interventricular grooves on the lower posterior face of the heart (a landmark also known as the crux of the heart). In approximately 80% of human hearts, the right coronary artery continues as the posterior descending coronary artery, a vessel that runs in the posterior interventricular groove from the crux toward the apex of the heart and that supplies

additional branches to the posterior aspect of both ventricles. This common anatomic configuration is termed right coronary dominance. A minority of hearts show either a left dominant circulation, in which the posterior descending artery is instead a continuation of the left circumflex artery, or a codominant circulation, in which the posterior descending artery is supplied by both the left circumflex and right coronary arteries.

There is considerable variation in the branching of the left coronary artery in humans. In most individuals, the undivided left main coronary artery runs approximately 2 or 3 cm beyond the left aortic sinus before it bifurcates into the left anterior descending and left circumflex coronary arteries. The left anterior descending artery then runs in the anterior interventricular groove toward the apex. It gives rise to a variable number of septal branches, which perforate into and supply the IVS, and to diagonal branches, which extend along the lateral surface of the left ventricle. Note that these portions of the vasculature are commonly intramyocardial rather than epicardial in location. The other major branch off of the left main coronary artery, the left circumflex coronary artery, usually runs in the left atrioventricular groove before ramifying into the obtuse marginal branches, which are frequently intramyocardial as well.

In the human heart, the cardiac veins follow a course roughly parallel to the major arteries. Most veins ultimately drain into the coronary sinus, a wide venous channel that opens into the right atrium between the inferior vena cava and the tricuspid valve. Among the major tributaries of the coronary sinus are the great, middle, and small cardiac veins. The great cardiac vein typically arises near the apex and runs along the anterior interventricular groove to the base of the heart. It then turns laterally, wraps around the mitral orifice in the left atrioventricular groove to the posterior face of the heart, and widens to form the coronary sinus. The middle cardiac vein runs opposite to the posterior descending artery from apex to base in the posterior interventricular groove, whereas the small cardiac vein tracks alongside branches of the right coronary artery in the right atrioventricular groove. Both middle and small cardiac veins drain into the coronary sinus near the crux.

A macroscopic description of the systemic vascular tree of rodents and humans is beyond the scope of this text. See Further Reading section for descriptions of the systemic vasculature of rodents and/or humans.

HISTOLOGY

The great vessels and cardiac vasculature, along with the rest of the vasculature, can be broken down into the following components: arteries, arterioles, capillaries, venules, and veins. The systemic direction of blood flow is heart→elastic artery→muscular artery→arteriole→capillary→venule→vein→heart. Except for being considerably smaller in rodents, the microscopic anatomy is generally similar in rodents and humans, i.e., the vessel wall components are essentially the same.

Arteries can be divided into two categories: elastic (e.g., aorta, pulmonary artery, and common carotid artery) and muscular (e.g., the vast majority of the named arterial tree). Both types have three layers known as tunica: the tunica intima, the tunica media, and the tunica adventitia (also called tunica externa). The tunica intima is the inner layer and represents the interface between the vessel wall and the lumen. It consists of a single layer of flattened endothelial cells that are continuous and histologically equivalent to those in the endocardium and a small amount of supporting loose connective tissue (Figs. 10.15 and 10.16). In rodents, subendothelial connective tissue is virtually nonexistent, and, at the light microscopic level, the endothelium rests on the internal elastic lamina (IEL), a compact layer of elastic fibers. In humans, the thickness of this

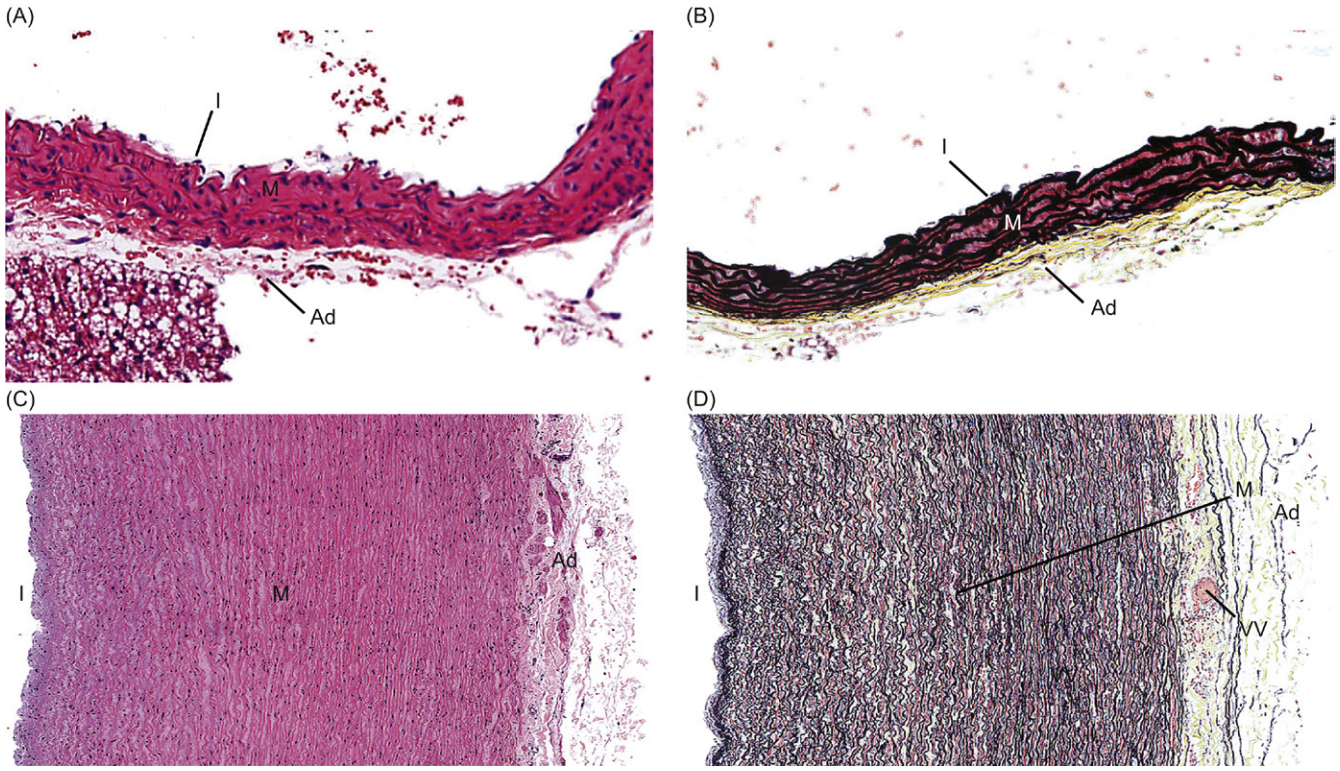

FIGURE 10.15 Elastic artery. (A, B) Rodent (mouse) aorta stained with H&E (A) or Movat's pentachrome (B). The aorta is shown here as an example of an elastic artery. It is composed of the tunica intima (I), a flattened layer of endothelium; the tunica media (M), a layer of elastic fibers (black in B) and smooth muscle cells; and the tunica adventitia (Ad), fibrous connective tissue. In the rodent, there are typically fewer than 10 elastic lamellae (with somewhat more lamellae near the aortic root). (C, D) Human aorta stained with H&E (C) or Movat's pentachrome (D). The histologic features are similar to those of the rodent, but with more prominent vasa vasorum (VV), which are vessels that arise in the adventitia and periodically extend into the adjacent media, and far more elastic lamellae (~50).

subendothelial connective tissue varies with artery size, age, and disease state. The tunica media is the middle portion of the vessel wall and contains smooth muscle cells and connective tissue, whereas the tunica adventitia is composed of connective tissue that is often continuous with the surrounding soft tissues. The intimal and medial compartments are separated by the IEL. IEL prominence varies considerably with the caliber and location of the vessel. Similarly, the tunica media and adventitia are separated by a layer of elastic fibers known as the external elastic lamina (EEL), which is generally less distinct than the IEL.

Elastic arteries are distinguished from muscular arteries by the former's relative abundance of elastic fibers, which are organized into concentric fenestrated sheets (Fig. 10.15). In two-dimensional histologic sections, these sheets appear as compact, parallel-oriented elastic lamellae separated by smooth muscle cells and collagen. Although elastic lamellae are best evaluated using special histochemical stains (e.g., Movat's pentachrome), they are also highly refractile and can usually be appreciated by routine stains as well. In humans, the breadth of the elastic artery wall typically exceeds the diffusion limit, so the inner portions of the wall are sustained by small arteries called vasa vasorum that arise in the tunica adventitia. In rodents, vasa vasorum are infrequently seen in the adventitia and rarely seen in the inner portions of normal vessels.

Muscular arteries are similar histological structures to elastic arteries but are defined by their relative paucity of medial elastic content (Fig. 10.16). The tunica media of muscular arteries is composed of a thick layer of smooth muscle cells, which provide vasomotor tone. Elastic fibers are largely confined

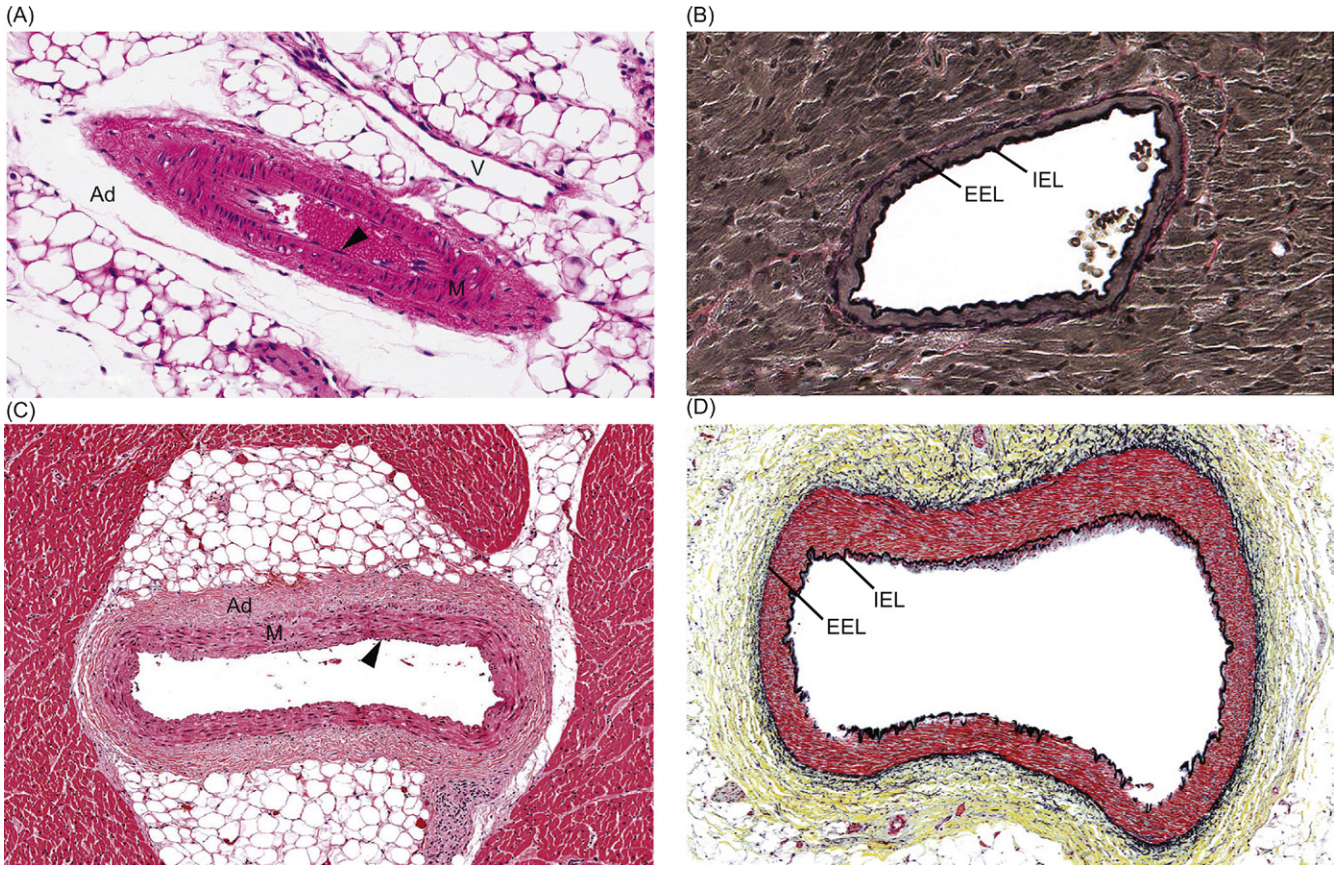

FIGURE 10.16 Muscular artery. (A, B) Cross section of rodent (mouse) mesenteric artery stained with H&E (A) and a coronary artery stained for elastin (B). Both are muscular arteries single flattened endothelial cell layer (intima; arrowhead), a smooth muscle wall (media; M), and an external fibrous connective cell layer (adventitia; Ad). Veins (V) are much thinner-walled. The intima and media are separated by the internal elastic lamina (IEL), and the tunica media and adventitia are separated by the external elastic lamina (EEL). (C, D) Cross sections of human coronary arteries stained with either H&E (C) or Movat's pentachrome (D). The histologic features are very similar to those of rodent.

Need-to-know

- General vascular structure is similar between rodents and humans, except that in rodents, subendothelial connective tissue is rarely seen.

to the IEL and EEL. In humans, vasa vasorum tend to be more confined to the tunica adventitia, except in the largest of muscular arteries, whereas in rodents they are rarely seen.

In arterioles, the muscular layer is much thinner than in muscular arteries, measuring only one or two cell layers in thickness, even in humans. Arterioles do not have an EEL, and smaller arterioles lack even an IEL. The tunica adventitia is correspondingly thin as well.

Capillaries are the smallest branch of the vascular tree. They are composed of a single endothelial cell layer resting on a basement membrane. No IEL or smooth muscle cell layer is present. Pericytes, which are smooth muscle-like cells, are interspersed along capillaries. Capillaries are divided into three types based on the continuity of the vessel wall: continuous, fenestrated, and sinusoidal. Venules are slightly larger than capillaries and may also have interspersed pericytes along their walls.

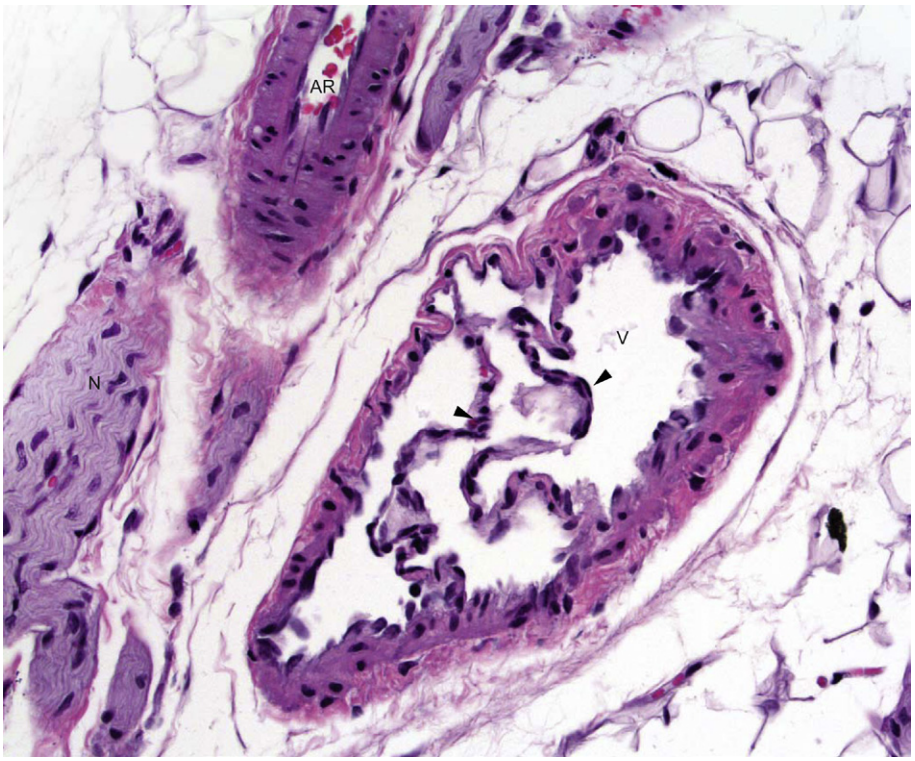

FIGURE 10.17 Vein. Rat mesenteric veins. Veins (V) have a similar appearance to arteries (AR), but have thinner walls containing less smooth muscle and elastic laminae than arteries. Additionally, veins have paired valves (arrowheads) throughout the venous system. *N*, nerve.

Veins generally have a similar appearance to arteries. However, they are distinctly thinner-walled due to having far less smooth muscle and elastic fibers. Veins contain paired valves throughout the venous system (Fig. 10.17). A unique feature of rodent pulmonary veins is that they are surrounded by cardiac muscle, a feature not normally present in humans (Fig. 10.18).

Common Incidental Findings in Rodents

Abnormal findings are beyond the scope of this chapter. However, because a given finding in a single rodent might be expected in a population of rodents (i.e., an incidence rate for a given finding of 10% may be normal for a population of mice), a few such incidental (background) findings are worth mentioning. It should be kept in mind that the incidence for these findings varies by strain and age. Cardiovascular incidental findings in mice and/or rats include atrial thrombosis, cardiac amyloidosis, cardiac mineralization (both epicardial and myocardial), perivascular lymphoid infiltrates, cysts, cardiomyopathy, small myocardial inflammatory foci, endocardiosis, and polyarteritis nodosa.

In addition to incidental findings, care should be taken to distinguish genuine antemortem changes from perimortem changes and handling artifacts. Common findings caused by euthanasia or handling of rodent tissues include areas of increased cardiomyocyte eosinophilia, sometimes with a prominent banding pattern (not to be confused with contraction band necrosis), and slight separation of cardiomyocytes (not to be confused with edema).

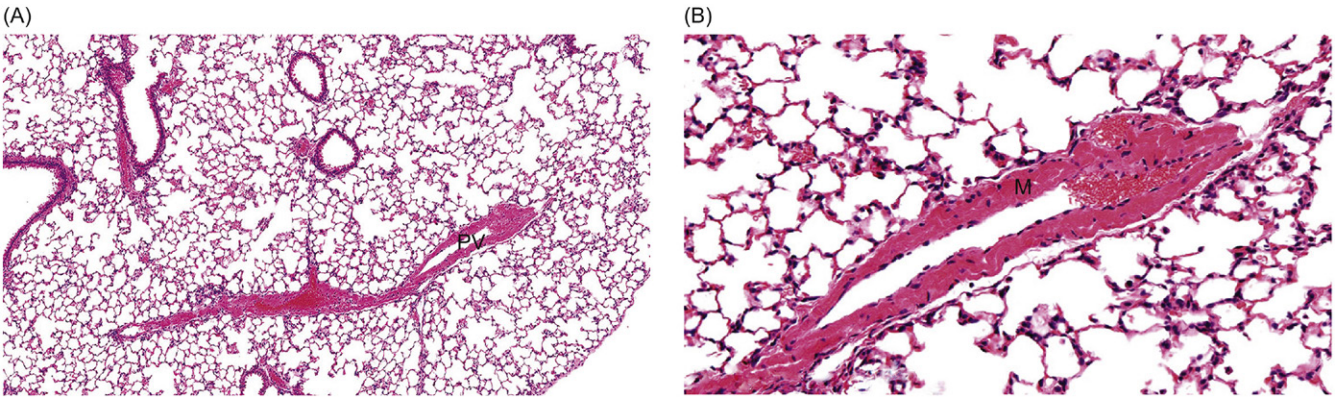

FIGURE 10.18 Cardiomyocytes of rodent pulmonary veins. Rodent (mouse) lung at low (A) and high (B) magnification. A unique feature of rodents is that the thick media (M) of their pulmonary vein (PV) is composed of cardiomyocytes. Compare the mesenteric vein media in Figure 10.16A or Figure 10.17 with the pulmonary vein media in 10.18B (Figures 10.16A and 10.18B are at the same magnification).

Need-to-know

- The rodent pulmonary veins are surrounded by cardiomyocytes deep into the lung parenchyma.

FURTHER READING

Ahmed SH, Rakhawy A, Abdalla A, et al: The comparative anatomy of the blood supply of cardiac ventricles in the albino rat and guinea-pig. J Anat 126(1):51–57, 1978.

Akhter SA: The heart and pericardium. Thorac Surg Clin 21(2):205–217, 2011.

Anderson RH, Ho SY, Becker AE: Anatomy of the human atrioventricular junctions revisited. Anat Rec 260:81–91, 2000.

Baker HJ, Lindsey JR, Weisbroth SH: *The laboratory rat, Volume 1, Biology and diseases*, Orlado, FL, 1979, Academic Press.

Ciszek B, Skubiszewska D, Ratajska A: The anatomy of the cardiac veins in mice. J Anat 211:53–63, 2007.

Colvee E, Hurle JM: Maturation of the extracellular material of the semilunar heart values in the mouse. A histochemical analysis of collagen and mucopolysaccharides. Anat Embryol (Berlin) 162:343–352, 1981.

Fernandez B, Duran AC, Fernandez MC, et al: The coronary arteries of the C57BL/6 mouse strains: implications for comparison with mutant models. J Anat 212:12–18, 2008.

Gude W, Cosgrove G, Hirsch P: *Histological atlas of the laboratory mouse*, New York, 1982, Plenum.

Halpern MH: Extracoronary cardiac veins in the rat. Am J Anat 92(2):307–327, 1953.

Halpern MH: The sino-atrial node of the rat heart. Anat Record 123(4):425–435, 1955.

Halpern MH: The dual blood supply of the rat heart. Am J Anat 101(1):1–16, 1957.

Hew KW, Keller KA: Postnatal anatomical and functional development of the heart: a species comparison. Birth Defects Res B Dev Reprod Toxicol 68:309–320, 2003.

Icardo JM, Colvee E: Atrioventricular valves of the mouse: III. Collagenous skeleton and myotendinous junction. Anat Rec 243:367–375, 1995.

Icardo JM, Colvee E: Origin and course of the coronary arteries in normal mice and in iv/iv mice. J Anat 199:473–482, 2001.

Icardo JM, Arrechedera H, Colvee E: The atrioventricular valves of the mouse: I. A scanning electron microscope study. J Anat 182:87–94, 1993.

Junqueira L, Carneiro J: *Basic histology*, ed 11, New York, 2005, McGraw-Hill.

Kresakova L, Purzyc H, Schusterova I, et al: Variability in the cardiac venous system of wistar rats. JAALAS 54(1):10–16, 2015.

Kumar D, Hacker TA, Buck J, et al: Distinct mouse coronary anatomy and myocardial infarction consequent to ligation. Coron Artery Dis 16:41–44, 2005.

Lev M, Thaemert JC: The conduction system of the mouse heart. Acta Anat (Basel) 85:342–352, 1973.

Maronpot R: *Pathology of the mouse*, Vienna, IL, 1999, Cache River Press.

Mora F, Callahan MF, Eckman DM, et al: Cardiac output (co), stroke volume (sv) and heart rate (HR) in exercising rats. FASEB 20:A395, 2006.

Olivetti G, Cigola E, Maestri R, et al: Aging, cardiac hypertrophy and ischemic cardiomyopathy do not affect the proportion of mononucleated and multinucleated

myocytes in the human heart. J Mol Cell Cardiol 28:1463–1477, 1996.

Percy DH, Barthold SW: *Pathology of laboratory rodents and rabbits*, ed 3, Ames, IA, 2007, Blackwell.

Popesko P, Rajtova V, Horak J: *A colour atlas of anatomy of small laboratory animals*, Oxford, 1992, Elsevier.

Sheppard M, Davies MJ: Practical cardiovascular pathology, New York, 1998, Oxford University Press.

Silver MM, Silver MD: Examination of the heart and of cardiovascular specimens in surgical pathology. In Silver MD, Gotlieb AI, Schoen FJ, editors: Cardiovascular pathology (ed 3), Philadelphia, PA, 2001, Churchill Livingstone.

Venoit JP, Ghadially FN, Walley VM: Light microscopy and ultrastructure of the blood vessels and heart. In Silver MD, Gotlieb AI, Schoen FJ, editors: Cardiovascular pathology (ed 3), Philadelphia, PA, 2001, Churchill Livingstone.

Webb S, Brown NA, Anderson RH: The structure of the mouse heart in late fetal stages. Anat Embryol (Berlin) 194:37–47, 1996.

Webster SH, Liljegren EJ: Organ:body-weight ratios for certain organs of laboratory animals: III. White Swiss mouse. Am J Anat 97:129–153, 1955.

Wessels A, Sedmera D: Developmental anatomy of the heart: a tale of mice and man. Physiol Genom 15:165–176, 2003.

Young B, Lowe JS, Stevens AS, et al: *Wheater's functional histology: a text and colour atlas*, ed 5, Philadelphia, PA, 2006, Churchill Livingstone.

This page intentionally left blank

UPPER GASTROINTESTINAL TRACT 11

PIPER M. TREUTING
University of Washington School of Medicine, Seattle, WA, United States

MARK J. ARENDS
University of Edinburgh, Edinburgh, Scotland, United Kingdom

SUZANNE M. DINTZIS
University of Washington School of Medicine, Seattle, WA, United States

Introduction

The upper gastrointestinal (GI) tract (Tables 11.1–11.3) is composed of the oral cavity (see Chapter 7: Oral Cavity and Teeth), salivary glands (see Chapter 8: Salivary Glands), and the esophagus, stomach, and small intestine (comprising the duodenum, jejunum, and ileum). In all three species, the basic mural structure of the tract is maintained. The entire tract is essentially a smooth muscle-enveloped tube with an innermost mucosa (comprising the epithelium, lamina propria, and muscularis mucosae), submucosa, tunica muscularis (also known as the muscularis propria), and a variable outer layer of serosa or adventitia. The functions of the upper GI tract include transport of the swallowed food bolus, enzymatic digestion, and absorption of nutrients, in addition to protective barrier function against the external environment. The morphologic appearance of the different sections reflects the primary function of each segment and is variable between rodents and humans.

Esophagus

Gross Anatomy

The esophagus functions to transport masticated and swallowed food boli through the mediastinum from the pharynx (see Chapter 6: Nose, Sinus, Pharynx, and Larynx) to the stomach (Table 11.1 and Figs. 11.1 and 11.2). In all three species, the esophagus has upper and lower esophageal sphincters at the proximal and distal ends, which prevent retrograde movement of food by contracting and closing the lumen of the esophagus. During swallowing, these sphincters relax to allow forward passage of food. Rodents, unlike humans, cannot vomit. The esophagus in rodents is a straight tube that lies dorsal to the larynx in the cervical region, traverses the thorax to the left of the trachea, and passes through the esophageal hiatus in the diaphragm slightly left of midline. It enters the midpoint of the rodent stomach at the lesser curvature near the limiting ridge (also known as the margo

Comparative Anatomy and Histology. DOI: http://dx.doi.org/10.1016/B978-0-12-802900-8.00011-7
© 2018 Elsevier Inc. All rights reserved.

TABLE 11.1 Esophagus

Feature	Rodent	Human
	Gross	
Location	Dorsal and slightly left of the trachea	Posterior to trachea
Constrictions	Minimal constrictions Mouse: lower circular band of smooth muscle serve as sphincter Rat: upper and lower circular band of smooth muscle serve as sphincters	Upper sphincter derived from cricopharyngeus muscle; lower sphincter less well-defined; zone of increased intraluminal pressure
Enters stomach at	Midpoint lesser curvature	Superior aspect of lesser curvature
Mucosal folds	Longitudinal	Plicated, longitudinal folds at rest
	Histologic	
Z-line	Absent	Abrupt transition from esophageal squamous mucosa to gastric glandular mucosa at gastroesophageal junction
Mucosa	3–5 cells thick; keratinized squamous epithelium	Nonkeratinized squamous epithelium; 300–500 µm; smooth proximally transitions to plicated distally
Lamina propria	Thin; no glands	Superficial glands at proximal and distal ends
Submucosa	Thin; typically visible at the distal esophagus only, no glands	Submucosal glands diffusely scattered
Muscularis mucosae	Present; at the distal esophagus only, smooth muscle	Thicker in esophagus than in other parts of digestive tract
Muscular tunic	Primarily skeletal and distal band of smooth muscle	Transition from skeletal (proximal) to smooth muscle (distal); outer muscular layer slightly thicker than inner
Serosa	Adventitia only	Adventitia only in mediastinum; serosa mainly below diaphragm (in peritoneal cavity)
Squamous epithelium	Keratinized	May become keratinized if subject to trauma
Skeletal muscle	Primary	Upper one-third; contraction involuntary
Smooth muscle	Secondary; band just proximal to stomach	Gradual transition to smooth muscle only in lower one-third
Mucous glands	No	Superficial and submucosal

plicatus), the region where the nonglandular forestomach meets the glandular mucosa elevated by thickened forestomach lamina propria (Fig. 11.3). In humans, the esophagus begins at the cricoid cartilage, traverses the thoracic cavity in the posterior mediastinum, and penetrates through the diaphragm for several centimeters before entering the stomach (Table 11.1 and Fig. 11.2). At the gastroesophageal junction, the nonkeratinizing esophageal squamous mucosa abruptly transitions to compact glandular secretory gastric mucosa. This transition is seen macroscopically as a sharply demarcated squamocolumnar junction, or line of contrast, called the Z-line (Fig. 11.3).

HISTOLOGY

With the exception of the epithelium, the general organization of the esophagus is similar in all three species (Figs. 11.4 and 11.5). The esophageal wall is organized similarly to other part of the GI tract; except for the outermost layer, which is primarily adventitial rather than serosa. The esophageal wall is organized as a muscular tube surrounding a hollow central lumen and is composed of multiple layers: the mucosa (epithelium, lamina propria, and muscularis mucosae), submucosa, and tunica muscularis. In rodents, the serosa, submucosa, and muscularis mucosae are absent from the upper esophagus (Fig. 11.4).

The inner luminal (inner) surface of the rodent esophagus is lined by keratinized stratified squamous epithelium 3–5 cells thick (Fig. 11.4), whereas in humans it is lined by nonkeratinized stratified squamous epithelium approximately 0.5-mm thick (Fig. 11.4). In both cases, the mucosa is longitudinally folded at rest. The thickness of the keratin layer in rodents is diet-dependent, and fasting animals often show adherent bacterial colonies and increased keratin layers (Fig. 11.5A).

TABLE 11.2 Stomach

Feature	Rodent	Human
	Gross	
Forestomach	Present; keratinized squamous epithelium; thin-walled left half	Absent
Glandular stomach	Right half of stomach; thick mucosa; cardiac, fundus, pyloric regions	Present; cardiac, fundus corpus, antrum, pylorus
Rugal folds	Mouse: Not prominent Rat: more prominent	Prominent when stomach empty; most prominent in corpus and fundus
Areae gastricae	Not described	Mucosal shallow grooves that do not flatten with distention
Limiting ridge/margo plicatus	Present projection between glandular and nonglandular gastric mucosa	Absent
	Histologic	
Mucosa	Keratinized squamous or glandular; simple compact straight glands; cell composition varies with region	Simple compact straight glands; cell composition varies with region
Lamina propria	Present	Similar to rodent
Submucosa	Present	Similar to rodent
Muscularis mucosae	Present	Similar to rodent
Muscular tunics	Inner oblique; middle circular; outer longitudinal	Similar to rodent
Serosa	Present	Similar to rodent
Squamous epithelium	Amount of keratin is diet- and fasting-dependent; increased keratin with decreased food; can see adherent bacterial colonies	No
Foveolar (cardiac) cells	Simple columnar; mucus-secreting; line top portion of mucosa	Similar to rodent
Parietal cells	Eosinophilic; acid-secreting; midportion of glands	Similar to rodent
Chief cells	Basophilic; zymogen-secreting; near base of glands	Similar to rodent
Cardiac glands	Mucous glands near limiting ridge; smallest portion	Similar to rodent
Fundic glands	Parietal and chief cells; top portion lined with foveolar cells	Similar to rodent
Pyloric glands	Near duodenum; mucous cells only	Mucous cells and some parietal cells; chief cells absent
Enterochromaffin	Visualized with argyrophilic or IHC stains Mouse: located between basement membrane and chief cells Rat: located between mucus cells in pylorus, between chief, parietal and mucus cells in fundus	Diffusely scattered in epithelium; visualized with argyrophilic or IHC stains

The limiting ridge is present in rodents but not humans (Fig. 11.6). At the distal end of the human esophagus, there is an abrupt transition from nonkeratinizing squamous to columnar glandular epithelium. The Z-line is visible grossly and is often asymmetric (Fig. 11.6).

In all three species, the esophageal lamina propria underlies the barrier epithelium and consists of loose connective tissue, capillaries and lymph vessels, inflammatory cells, and (in humans) esophageal mucous glands (Fig. 11.5). A single thin layer of longitudinally oriented smooth muscle, immediately beneath the lamina propria makes up the muscularis mucosae (Fig. 11.5). In humans, the esophageal submucosa is more abundant than the lamina propria and contains submucosal mucous glands and nerve plexi. In all three species, the esophageal tunica muscularis consists of two roughly perpendicular layers of muscle: the thicker outer longitudinal muscular layer and the thinner and transverse inner circular muscular layer (Figs. 11.4 and 11.5). In rodents, the tunica muscularis is principally skeletal, with a band of smooth muscle present proximal to the lower esophageal sphincter. A unique feature of the human esophageal tunica muscularis is the gradual shift from proximal skeletal to distal smooth muscle. Between the muscular layers in all three species are nerve plexi known as Auerbach's plexus. The adventitia consists of a thin connective tissue layer and surrounds the majority of the

esophagus. Short portions of the distal thoracic and intraabdominal esophagus are covered by mesothelium, derived from the serosa of the pleural and peritoneal cavities. This serosal lining covers the majority of the distal GI tract.

Stomach

Gross Anatomy

The stomach is the dilated portion of the GI tract responsible for storing food, processing it into chyme, and then delivering measured amounts to the duodenal portion of the small intestine. In rodents, the stomach is located in the left proximal abdomen and is partially covered by the left lateral hepatic lobe (Fig. 11.1). The rodent gastric mucosa is grossly divided into two distinct regions that are visible even from the serosal aspect: the forestomach and the glandular stomach (Fig. 11.3), whereas humans lack a forestomach. The forestomach is lined by keratinizing squamous mucosa, which accounts for approximately two-thirds of the stomach and lies to the left of the limiting ridge, encompassing the entrance of the lower esophagus. The rodent glandular stomach is divided into three anatomic regions: the small cardia (cardiac region) adjacent to the limiting ridge; the fundus, where the mucosa has prominent large folds termed rugae (and is more prominent in rats); and the antrum, which has relatively smooth mucosa.

In humans, the stomach begins proximally at the gastroesophageal junction several centimeters distal to the diaphragm and ends at the pyloric sphincter, where the duodenal portion of the small intestine begins near the midline (Fig. 11.2). The human stomach is crescent- or J-shaped and has lesser and greater curvatures attached to fatty tissues called the lesser omentum and greater omentum, respectively. The inner surface of the human stomach has prominent rugae, which flatten on distention, and much smaller shallow grooves termed areae gastricae.

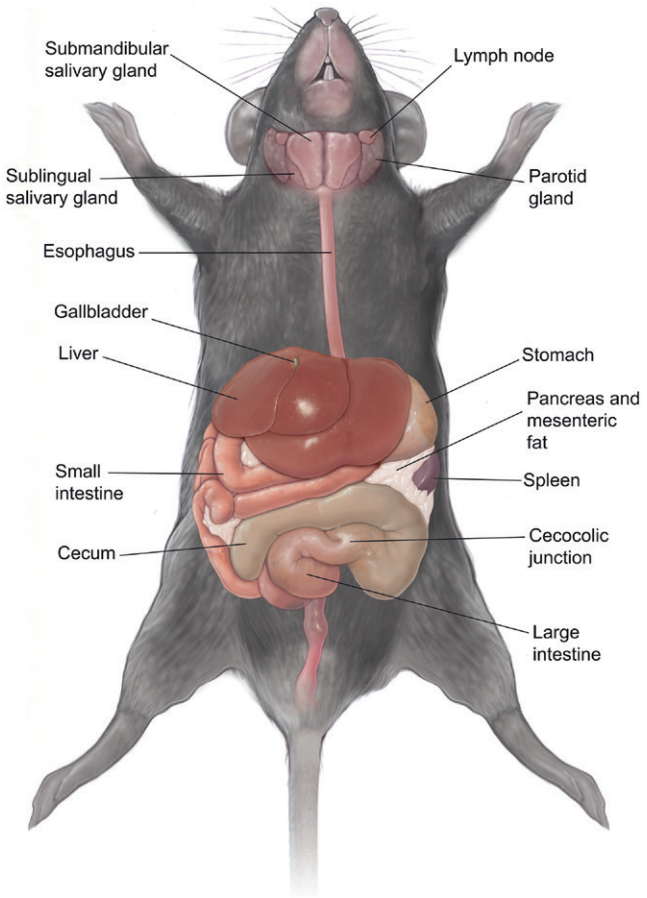

FIGURE 11.1 Rodent (mouse) regional abdominal anatomy. The esophagus enters the diaphragm to the left of the midline. The majority of the stomach is covered by the liver, which, along with the cecum, occupies the majority of the rodent abdomen. Source: © Elsevier, Inc., www.netterimages.com.

Need-to-know

- Rodent intestines have a smooth serosal surface.
- The regional placement of the intestines, especially the cecum, is dependent on the amount of distension by ingesta.

Similar to rodents, the human gastric mucosa grossly appears homogeneous, but is divided into anatomic regions: in addition to the cardia, fundus, and antrum found in rodents, there is also a body (corpus) and pylorus (Fig. 11.3C). The cardia extends 1–3 cm immediately distal to the gastroesophageal junction. The fundus is the upper portion of the stomach that lies superior (cephalad) to the level of this junction. The corpus is the midportion and makes up the majority of the stomach. The antrum and pylorus are the distal portion of the stomach proximal to the pyloric sphincter and duodenum.

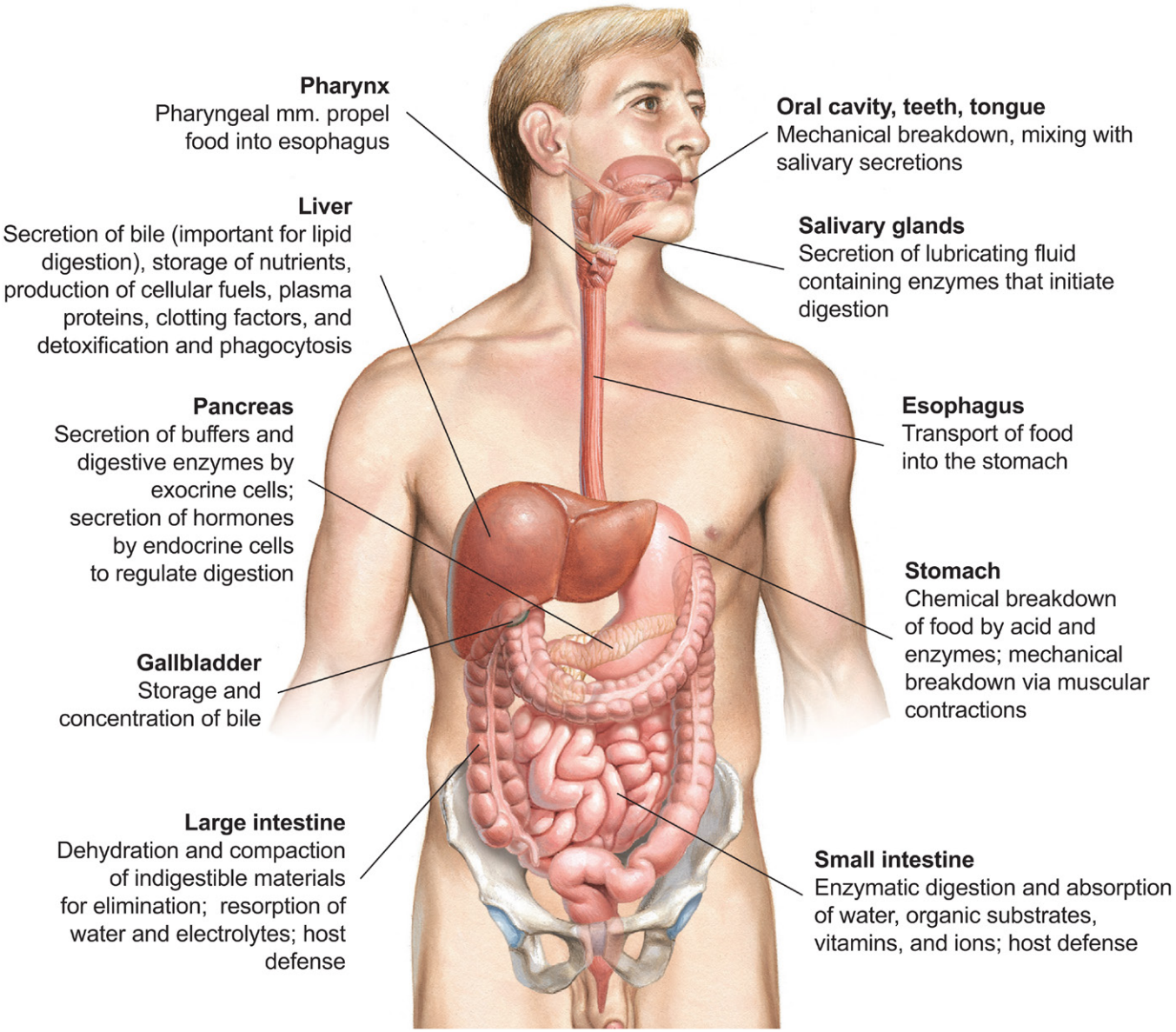

FIGURE 11.2 Human regional abdominal anatomy. The esophagus begins at the cricoid cartilage, traverses the thorax in the posterior mediastinum, and then penetrates the diaphragm and courses several centimeters before entering the stomach. The J-shaped stomach ends at the midline where the duodenal portion of the small intestine begins. Note that in this artist's rendition of the relative positions of the abdominal organs, there appears to be an empty space between the lower edge of the liver and the lesser curve of the stomach. This space does not exist in life as the liver overlies and is in contact with the lesser curve of the stomach and parts of the duodenum. Source: © Elsevier, Inc. www.netterimages.com.

In all three species, the muscles of the gastric wall include three layers: an innermost oblique, a middle circular, and an outer longitudinal. The oblique layer is best developed in the cardia. In rodents, there is a thin inner oblique, wide middle circular, and thin outer longitudinal layer. The middle circular layer is most prominent at the pylorus in all species.

HISTOLOGY

As with the esophagus, the basic cellular components and glandular distribution of the stomach are similar in all three species. There are the two types of gastric mucosa are fundic (oxyntic) and pyloric (mucinous). Fundic type glands predominate and are found in the rodent

TABLE 11.3 Small Intestine

Feature	Rodent	Human
	Gross	
Length	Pylorus to cecum in mouse: ~35 cm and in rat: ~170 cm	~7000 cm
Duodenum	Relatively short segment; Brunner's glands present	From pylorus to ligament of Trietz
Duodenal papillae	Present; pancreatic (one or multiple) and common bile ducts	Pancreatic and common bile duct join at the ampulla of Vater
Jejunum	Peyer's patches most prominent, longest segment	Two-fifths of small intestine, prominent plicae circularis
Ileum	Terminates at the ileocecal valve	Peyer's patches most prominent; longest segment
GALT	Peyer's patches antimesenteric; most prominent in jejunum	Peyer's patches most prominent in distal ileum
	Histologic	
Mucosa	Lack plicae; have relatively tall villi; height and shape vary by region, diet, pregnancy	Have plicae; relatively short villi
Duodenal villi	Leaflike; tall	Short; leaflike and densely packed
Jejeunal villi	Cylindrical; tall	Taller and frondlike
Ileal villi	Cylindrical; short	Thinner and more sparse
Lamina propria	Projects into villi; central lacteal	Similar to rodent
Submucosa	Mouse: relatively thin, except for proximal duodenum with Brünner's glands Rat: thicker	Brünner's glands prominent in proximal duodenum and slowly disappear distally
Muscularis mucosae	Relatively thin	Similar to rodent
Muscular tunics	Inner circular; outer longitudinal smooth muscle; Mouse: thinner than rat or human Rat: thicker than mice	Similar to mouse, but thicker
Nervous plexi	Submucosal and myenteric	Similar to rodent
Serosa	Thin, single layer of mesothelial cells; absent on upper esophagus	Similar to rodent
Enterocytes	Most abundant; have microvilli; in ileum may have adherent large segmented filamentous G+ bacteria; nonpathogenic	Most numerous proximally; decrease distally; have apical microvilli
Mucous/goblet cells	Increase in the ileum	Numbers increase distally
Enteroendocrine cells	Near basement membrane	Diffusely scattered in epithelium
Paneth cells	Exocrine serous; antimicrobial functions; granules increase in size with fasting; more prominent in the ileum; limited to small intestine	Most numerous in ileum; also present in appendix and cecum; found at crypt base
M cells	Modified lymphoepithelium overlying GALT; antigen sampling	Similar to rodent
Caveolated cells	Present, but not apparent in routine sections	Similar to rodent

glandular fundus and in the fundus and body of the human stomach. Pyloric type glands are found in the rodent pyloric region, and in the human cardia, antrum, and pyloric regions (Fig. 11.8).

The rodent cardia is relatively small and adjacent to the limiting ridge (Fig. 11.6). Rodent cardia glands are lined by abundant mucous cells that lack granules. In rodents, the gastric pits appear straight in section and are simple branched tubules, similar to human fundic mucosa (Fig. 11.7).

In all three species, in the larger fundic region, glandular mucosa is lined by regular straight gastric pits containing mucous neck cells (foveolar neck cells), eosinophilic parietal (acid-producing) cells, and basophilic chief (zymogen-producing) cells, which are found at the base of the crypts (Fig. 11.7). Human fundic-type mucosa is characterized by short gastric pits lined by simple columnar epithelium composed of surface mucous cells. The gastric pits are connected to multiple deeper gastric glands, which are located in the loose vascular connective tissue of the lamina propria (Fig. 11.7). The gastric glands in the fundic-type mucosa are composed primarily of parietal (oxyntic) cells, with fewer mucous neck and deeper chief (zymogenic) cells and scattered enteroendocrine cells.

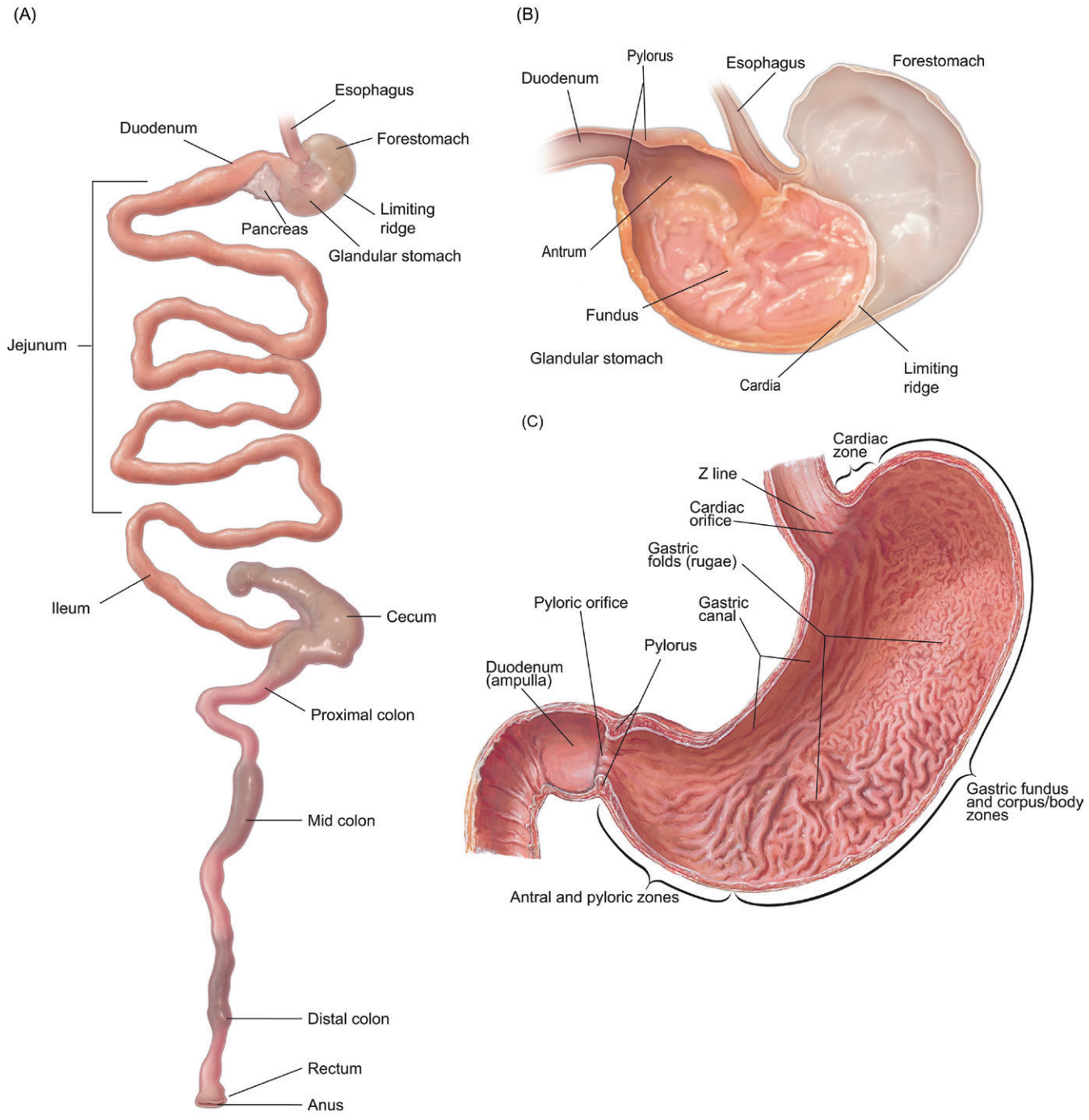

FIGURE 11.3 Upper GI tract. (A) Rodent (mouse) GI tract ex vivo. The majority of mesenteric attachments have been dissected away. A small amount of pancreas normally is tightly adherent to the duodenum at the level of the pancreatic duct. The two gastric regions are recognizable through the gastric serosa. (B) Bisected rodent (rat) stomach. The rodent stomach is divided into two regions, nonglandular forestomach and glandular stomach. The glandular stomach is divided into the small cardia adjacent to the limiting ridge; the fundus, where the mucosa is folded with rugae which are more prominent in the rat; and the antrum, which has relatively smooth mucosa. The limiting ridge is the visible, slightly raised division between the nonglandular and glandular regions and is homologous to the human Z-line. (C) Human stomach. The Z-line is a sharply demarcated line of contrast at the gastroesophageal junction. The human stomach has large folds (rugae) that are most prominent in the corpus and fundus. Source: © Elsevier, Inc., www.netterimages.com.

Need-to-know

- The rodent stomach has two grossly distinct regions that are separately by the limiting ridge.
- Rodents have a nonglandular forestomach and a glandular portion that is composed of the small cardia, large fundus, and pyloris.
- The duodenum is very short in rodents.

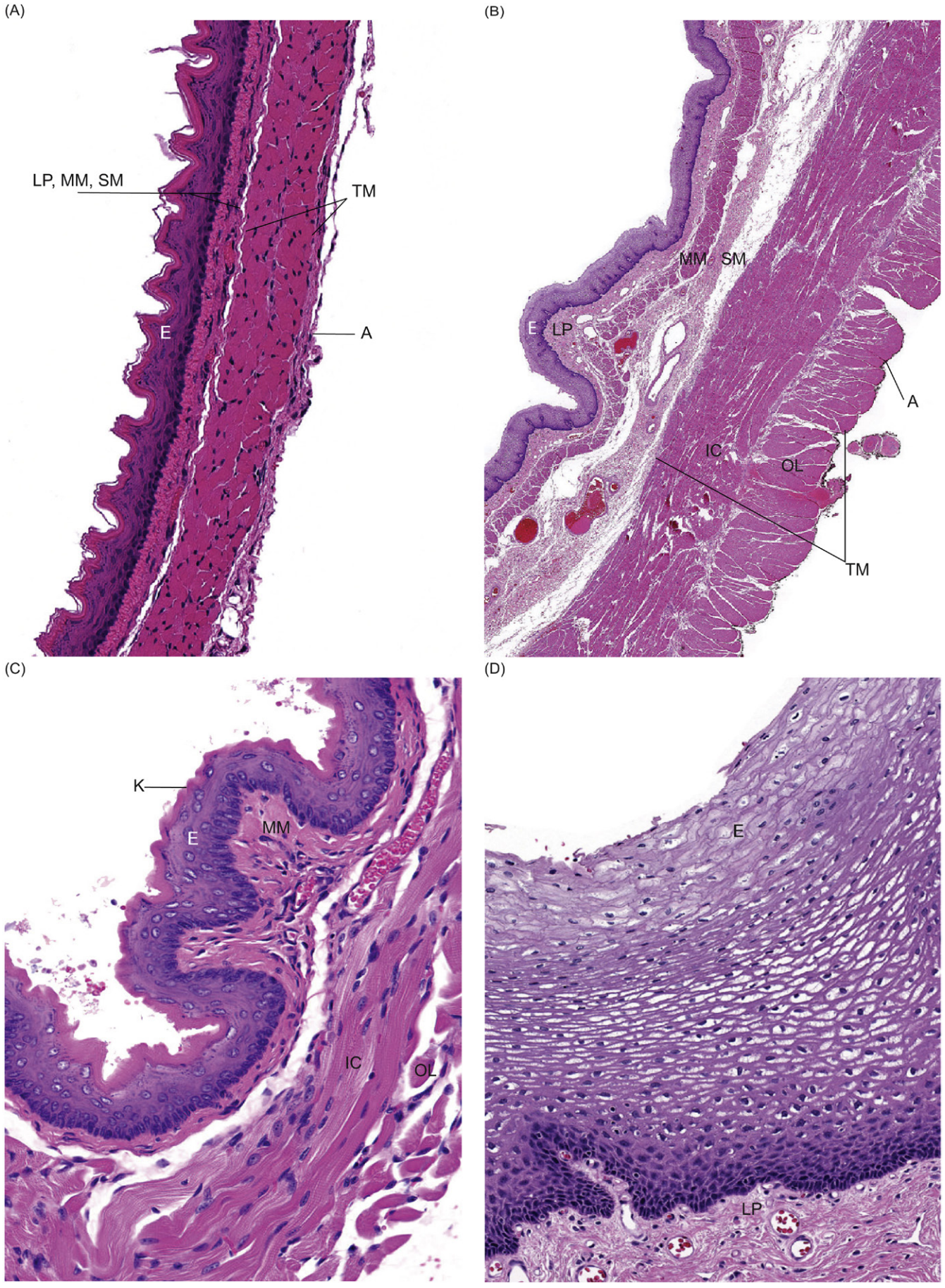

FIGURE 11.4 Esophagus. (A) Rodent (mouse). The mucosa of the rodent esophagus is composed of epithelium (E), lamina propria (LP), and muscularis mucosae (MM). In this section of mid to upper esophagus, the lamina propria, muscularis mucosae,

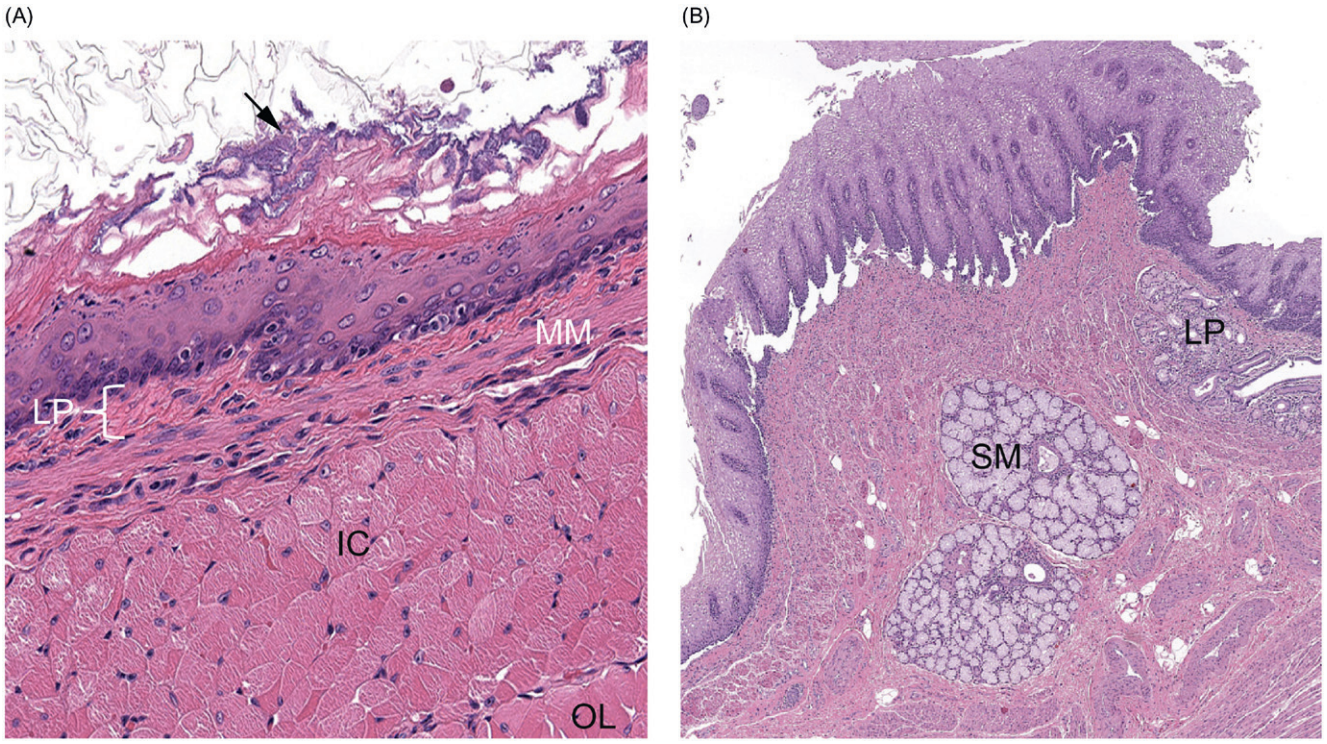

FIGURE 11.5 Lower esophagus. (A) Rodent (mouse). Mucosal hyperkeratosis with adherent bacteria (arrow) is a common finding in anorexic rodents. This particular immunodeficient mouse also has mild inflammation and prominent keratohyaline granules within the epithelium. Note the prominent lamina propria (LP) and muscularis mucosae (MM) in this lower esophagus, in contrast to those shown in Fig. 11.4. The muscularis externa is composed of inner circular skeletal muscle (IC) and outer longitudinal skeletal muscle (OL). (B) Human esophagus with submucosal and superficial glands. Submucosal glands (SM) are composed predominately of mucus-secreting cells with a minor serous component and are present beneath the muscularis mucosae in normal human esophagus. Simple tubular mucous glands are also present within the lamina propria (LP) of the proximal and distal esophagus, where they are named superficial glands. Adjacent chronic inflammation is common.

Need-to-know

- The muscularis mucosae and the submucosa are absent in the cranial portion of the rodent esophagus; these layers are more easily distinguished in the rodent lower esophagus.
- Rodent esophageal epithelium is keratinized.
- Rodents lack submucosal mucous glands.
- Rodent muscularis propria is predominately skeletal muscle.
- Rodents cannot vomit.
- The amount of keratin is dependent on diet and fasting; adherent bacterial colonies can also be seen.

◄ and submucosa (SM) are indistinct, in contrast to the lower esophagus (see Figs. 11.4C and 11.5A). Rodent tunica muscularis (TM) is predominately skeletal muscle. Adventitia (A) is indicated. (B) Human esophagus. The following are indicated: epithelium (E); lamina propria (LP); muscularis mucosae (MM), which is thicker in the esophagus than in other portions of the digestive tract; submucosa (SM); tunica muscularis (TM) with inner circular (IC) and outer longitudinal (OL) muscle layers; and adventitia (A). (C) Rodent (mouse) mucosa. The rodent esophageal mucosa contains keratinized (K) stratified squamous epithelium (E). In this section of mid-esophagus, there is an island of muscularis mucosae (MM) composed of smooth muscle. Inner circular (IC) and outer longitudinal (OL) muscle layers are indicated. (D) Human mucosa. The human mucosa contains nonkeratinizing stratified squamous epithelium. The basal layer occupies the lower 10% of the epithelium. As they approach the surface, squamous cells become glycogen-rich and flatten.

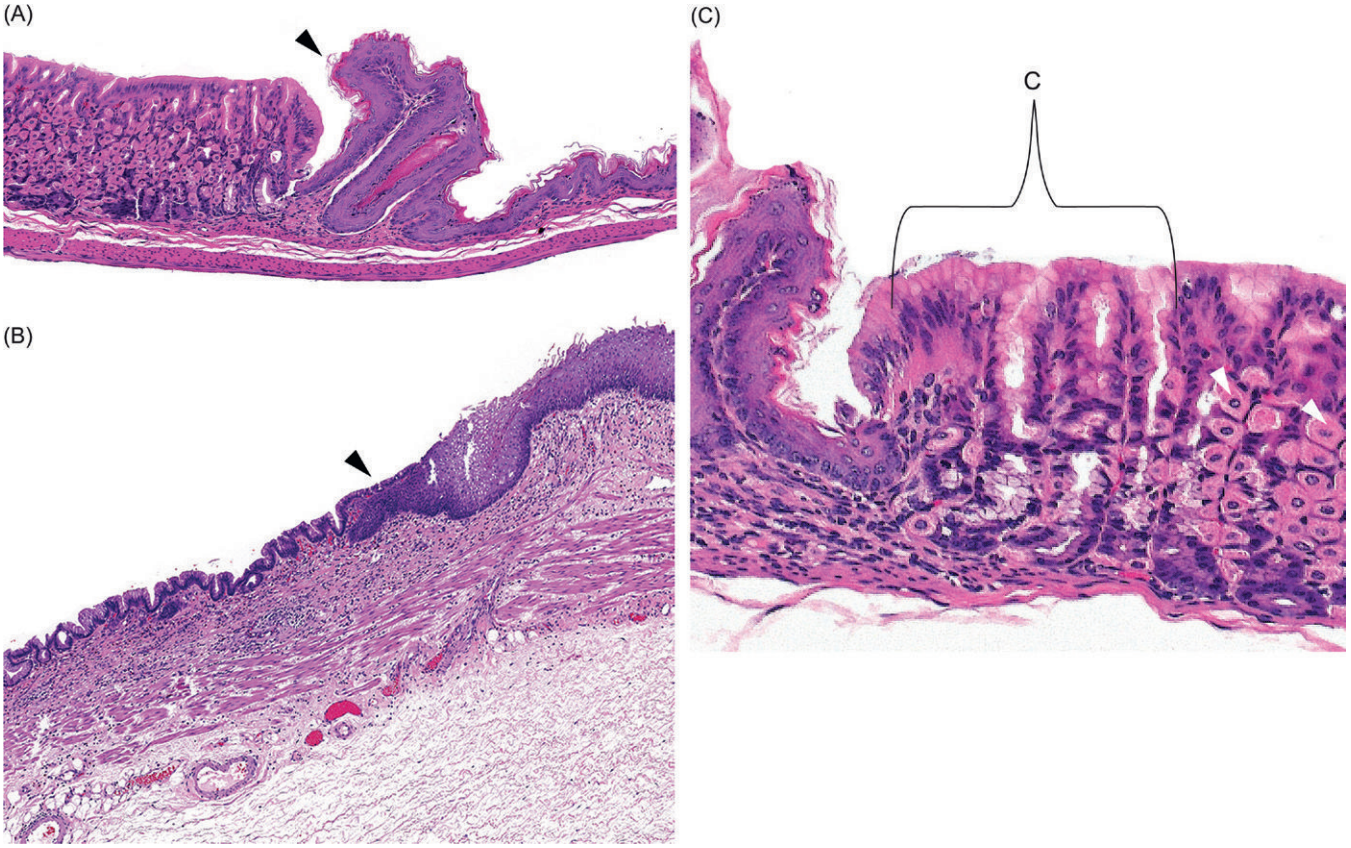

FIGURE 11.6 Gastric squamocolumnar junction. (A) Rodent (mouse) gastric limiting ridge. Rodents lack a Z-line in the esophagus but have a similar junction called the limiting ridge (arrowhead) between the nonglandular forestomach, which makes up the proximal two-thirds of the rodent stomach, and the glandular distal region. (B) Human Z-line. The abrupt mucosal transition at the junction of the human esophagus and cardia (arrowhead) is known as the Z-line. There is normally mild inflammation in this region in most Western adults. (C) Rodent (mouse) gastric limiting ridge and cardia. The cardia (C) is the smallest region of the rodent glandular mucosa. The straight gastric glands have abundant pale-staining mucous cells. In contrast, parietal cells (white arrowheads) of the fundic region are granular and pink-staining.

Need-to-know

- Humans lack a forestomach.
- Rodents lack as esophageal Z-line.
- Rodents have a raised mucosal fold (limiting ridge) at the junction between the nonglandular and glandular stomach.
- There is often inflammation at the limiting ridge.
- Inflammation increases with certain diseases and age.

At the pylorus (Fig. 11.8), the rodent glands are composed of only mucous cells, with a lack of chief and parietal cells. Human pyloric-type mucosa is characterized by long gastric pits lined by surface mucous cells and short convoluted gastric glands (Fig. 11.8). As in rodents, the predominant cell types in pyloric-type mucosa are surface mucous neck cells, with a relative lack of parietal cells and no chief cells. In all three species, enterochromagraffin cells are present along with the glandular mucosa adjacent to the basement membrane; however, special stains are required to identify them. The gastric glandular regions in all three species are not sharply demarcated, and transitional mucosa with pyloric and fundic features may be seen.

The gastric submucosa connective tissue layer has prominent vascular and lymphatic networks and scattered nerve plexi. The gastric tunica muscularis has three layers of muscle depending on the location, and serosa covers the stomach in all three species.

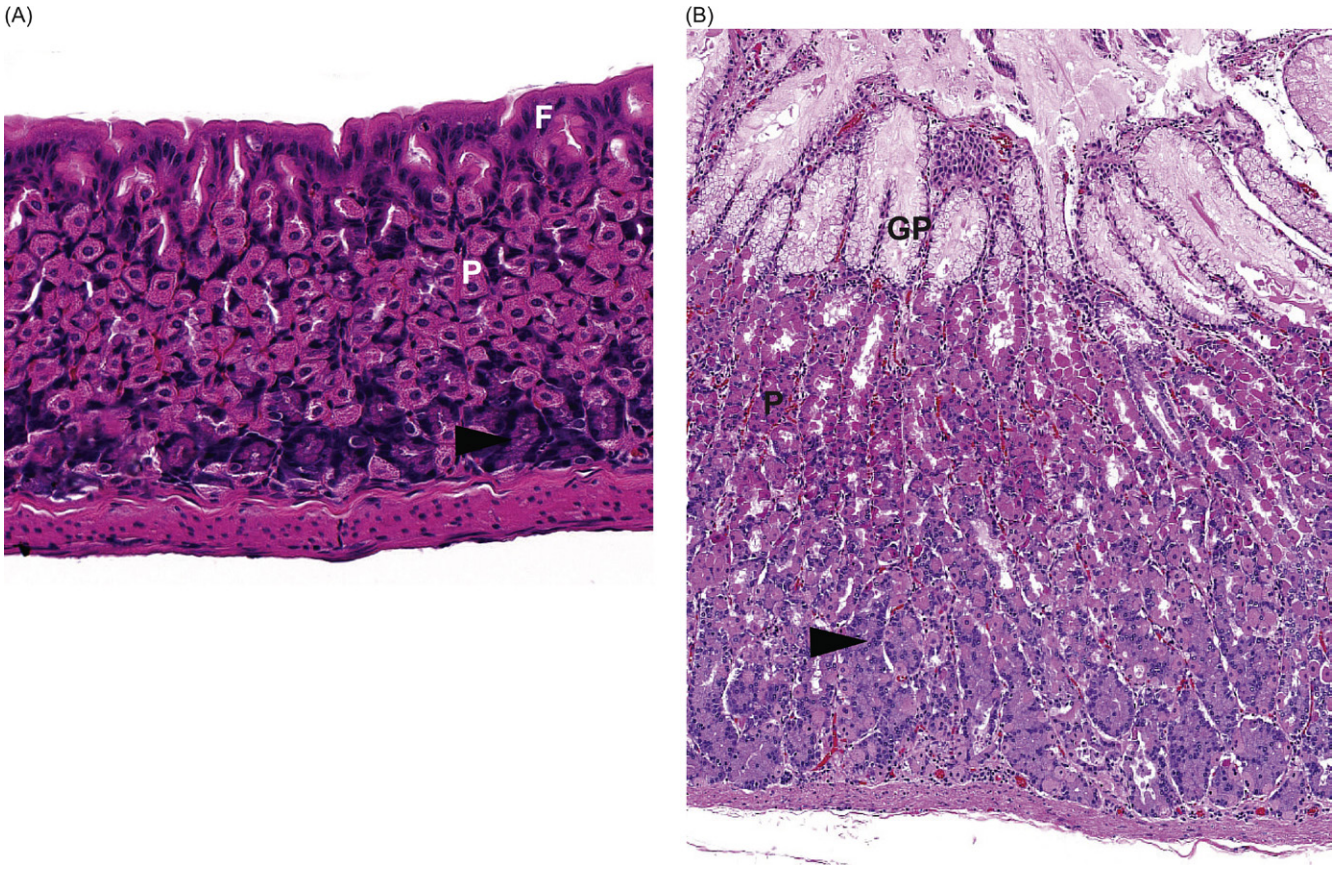

FIGURE 11.7 Fundic mucosa. (A) Rodent (mouse). The rodent fundic region is the largest portion of the glandular stomach. It is lined by simple branched gastric glands that appear relatively straight in section. The foveolar columnar (F) mucus-secreting cells line the superficial upper gastric gland, the pale eosinophilic acid-secreting parietal cells (P) occupy the middle sections, and the darker-staining zymogen-secreting chief cells (arrowhead) line the basal region of the simple straight glands. (B) Human. Short gastric pits (GP) lined by mucous cells lead to long, tubular, tightly packed gastric glands. The eosinophilic parietal cells (P) predominate in the upper part of the glands, and the bluish chief cells (arrowhead) predominate at the base. Fundic glands make up approximately 75% of the human gastric mucosa (in the fundus and corpus/body).

Need-to-know

- In all three species, the fundic-type glands are the most numerous.

Small Intestine

Gross Anatomy

The small intestine is the longest portion of the GI tract (approximately 35 cm in mice, 170 cm in rats, and 700 cm in humans) and is responsible for the absorption of nutrients. The small intestine begins at the pyloric sphincter (Figs. 11.3 and 11.9) and continues distally to the ileocecal valve. The three regions—duodenum, jejunum, and ileum—each contains the same layers found throughout the upper GI tract. Of these, the small intestine mucosa is the most variable in appearance.

In rodents, its gross appearance is smooth. In contrast, human small intestine mucosa contains permanent circular folds called plicae that run perpendicular to the long axis of the bowel and serve to increase absorptive surface area. The surface of all three species is covered by tiny (0.5–1.5 mm) fingerlike projections called villi that maximize nutrient absorption by greatly increasing the surface area. In rodents, the villous heights are nearly double those of human, providing increased surface area despite lack of plicae.

The duodenum is the most proximal region, is very short in rodents, and in humans includes all

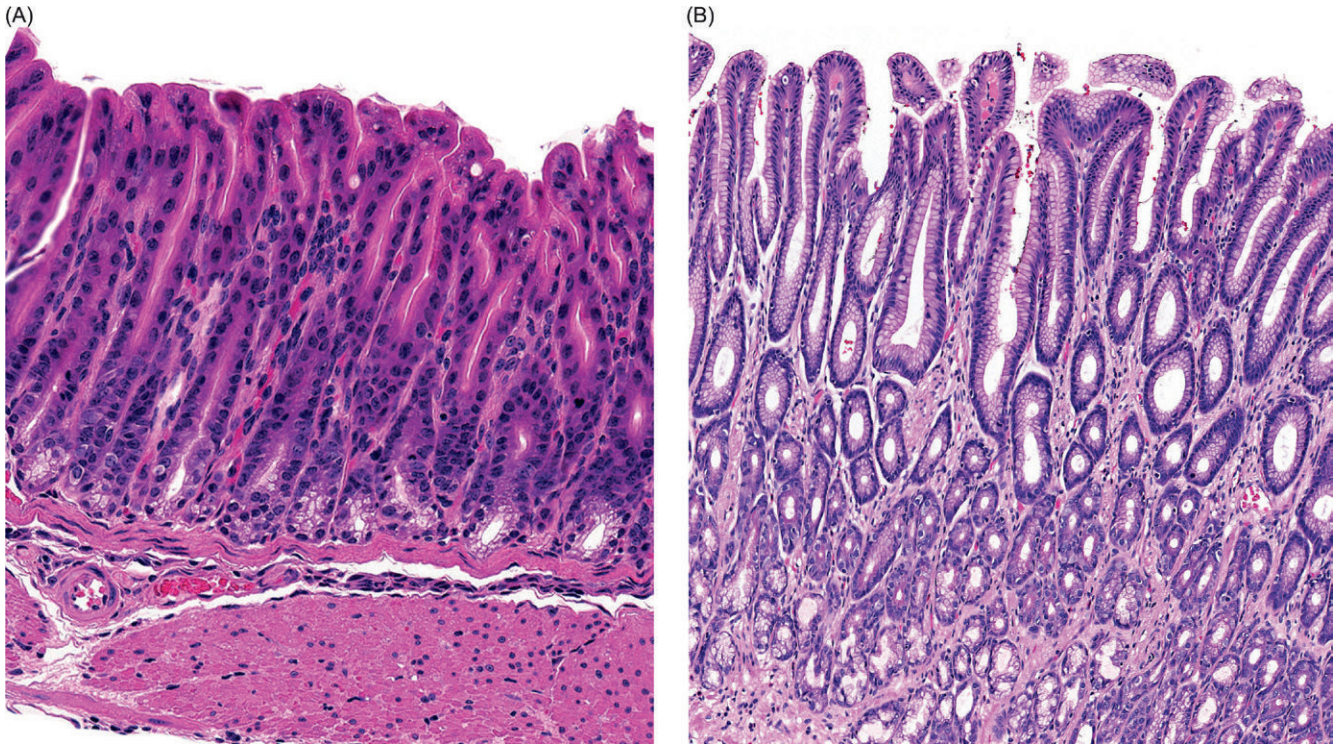

FIGURE 11.8 Pyloric mucosa. (A) Rodent (mouse). The rodent pyloric mucosa is primarily lined by mucus-producing cells and similar to the human pyloric region. (B) Human. The pyloric region close to the duodenum contains pyloric glands characterized by slightly villous surface epithelium. As in rodents, the glands are lined predominately with mucus-secreting cells, with scattered parietal cells present.

of the small intestine to the ligament of Trietz, a strip of fibromuscular tissue that attaches the distal duodenum to the posterior abdominal wall near the midline. In all three species, the duodenum receives bile produced by the liver through the common bile duct and digestive juices produced by the pancreas through the pancreatic duct. In rodents, the main pancreatic duct may be single or multiple (see Chapter 14: Pancreas) and enters the duodenum at the papillae. Often, the pancreas will be more tightly adherent to the duodenum in this region and may be present in duodenal sections (Fig. 11.10). In the majority of humans, the bile duct and pancreatic ducts join at the ampulla of Vater and empty via the duodenal papilla into the duodenal lumen.

The remainder of the small intestine is divided between the jejunum (proximal two-fifths) and ileum (distal three-fifths). In humans, the jejunal wall is thick, with up to twice as large diameter as the ileum. In all three species, the small intestine is attached to the posterior abdominal cavity by the mesentery and derives its blood supply primarily from the superior mesenteric artery. In rodents, raised oval and pale foci may be noted along the serosal antimesenteric border. These collections of lymphoid cells are known as gut-associated lymphoid tissue (GALT) and include lymphoid aggregates and Peyer's patches. In humans, GALT is most prominent in the ileum (Fig. 11.10). Peyer's patches are also grossly apparent in human terminal ileal mucosa at the antimesenteric border.

HISTOLOGY

The basic structure of the small intestinal mucosa is similar in all three species. Intestinal crypts (crypts of Lieberkühn) are located at the base of the villi and represent simple or branched glands (Figs. 11.10 and 11.11). In all three species,

FIGURE 11.9 Pylorus. (A) Rodent (mouse) pylorus and duodenum. The duodenum of the rodent contains numerous submucosal (Brünner's) glands (arrow). Note the thickness of the pyloric sphincter muscle region (M, musculature). (B) Human. The pyloric sphincter (PS) consists of a markedly thickened circular layer of the tunica muscularis and marks the transition from stomach to duodenum. The glandular mucosa of the stomach abruptly transforms to the villous mucosa of the duodenum, which contains mucus-secreting Brünner's glands (arrow).

Need-to-know

- Rarely, ectopic pancreas may be seen in duodenal mucosa in all three species.
- The bile and pancreatic ducts open at the duodenal papillae and should not be misinterpreted as a hyperplastic lesion.

FIGURE 11.10 Small intestine. (A) Mouse jejunum (magnification ×2.5). Note the lack of mucosal folds, relatively long villi, abundant intraluminal ingesta (plant material), and very thin muscular tunics. (B) Rat jejunum (×2.5). Rat intestinal tract is similar to mouse, lacking mucosal folds with relatively longer villi than humans. (C) Human jejunum (magnification ×1.5). The muscular tunics of the small intestine comprise an outer longitudinal layer (OL) and an inner circular layer (IC). The thick submucosa (SM) forms connective tissue cores supporting the mucosal folds (PC, plica circularis) on which the villi (V) rest. Serosa (S) is indicated. (D) Mouse ileum (magnification ×200). Note the extremely thin submucosa (SM) and muscular tunics (IC, OL). Peyer's patch (PP) and villi (V) are indicated. (E) Rat ileum (magnification ×200). The submucosa (SM) is discernable in the rat and the muscular tunics (IC, OL) can be distinguished. Note the isolated lymphoid follicle (ILF) and villi (V). (F) Human ileum (×1.5). The submucosa (SM) is prominent with fat and blood vessels observable even at this low magnification. Peyer's patch (PP) and villi (V) are indicated.

Need-to-know

- Villous height and shape are highly variable in all three species; thus histologic distinction between regions can be difficult.
- Distention with fixatives, overexuberant flushing, and autolysis may artefactually alter villous height.
- Rodent intestine has an extremely thin submucosa and tunica muscularis compared to humans. In mice, the submucosa is difficult to discern.

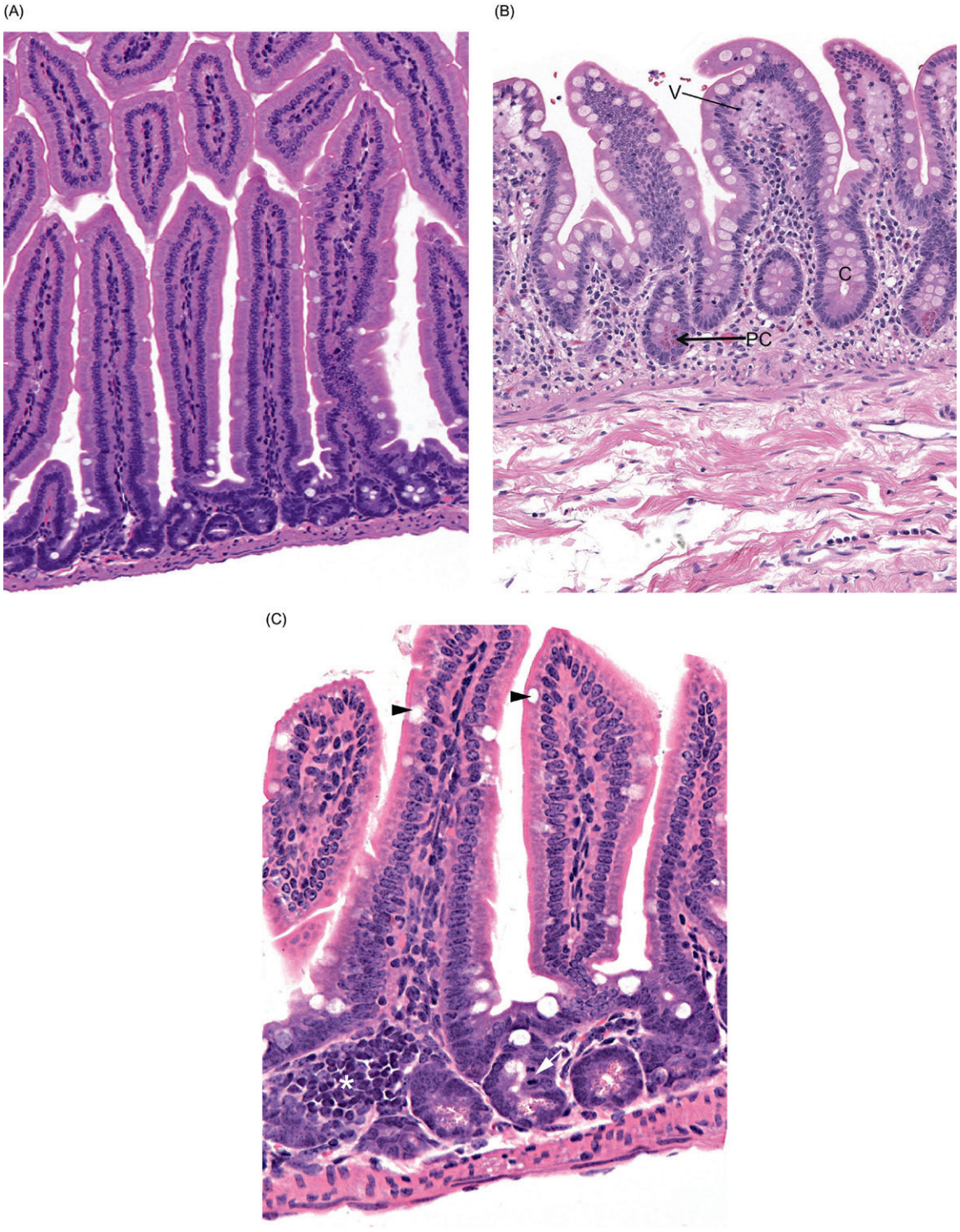

FIGURE 11.11 Small intestinal villi. (A) Rodent (mouse). Rodent small intestines have significantly taller villi than human small intestine, allowing increased surface area despite lack of mucosal folds. This image is ×200 magnification to demonstrate relative length of mouse villi compared to human villi shown in B. (B) Human. Human small intestinal villi are shorter than those of rodents. The villi (V) are lined by simple columnar epithelium that is continuous with that of the crypts (C), which contain Paneth cells (PC). (C) High magnification of rodent (mouse) small intestinal villi. Villi in all three species are primarily lined by absorptive enterocytes with scattered goblet cells (arrowheads). Paneth cells are present at the base of the crypts and contain abundant bright eosinophilic granules. Stem cell progenitors are located between and above the Paneth cells (arrow indicates mitotic figure, region of stem cells which is adjacent to a granule-containing Paneth cell). Note the isolated lymphoid aggregate in the lamina propria (asterisk).

Need-to-know

- In general, the villous length decreases from duodenum to ileum.
- Villous height in rodents will increase with certain diets, pregnancy and lactation, and experimental intestinal resection.
- In rodents, Paneth cells are present only in the small intestine.

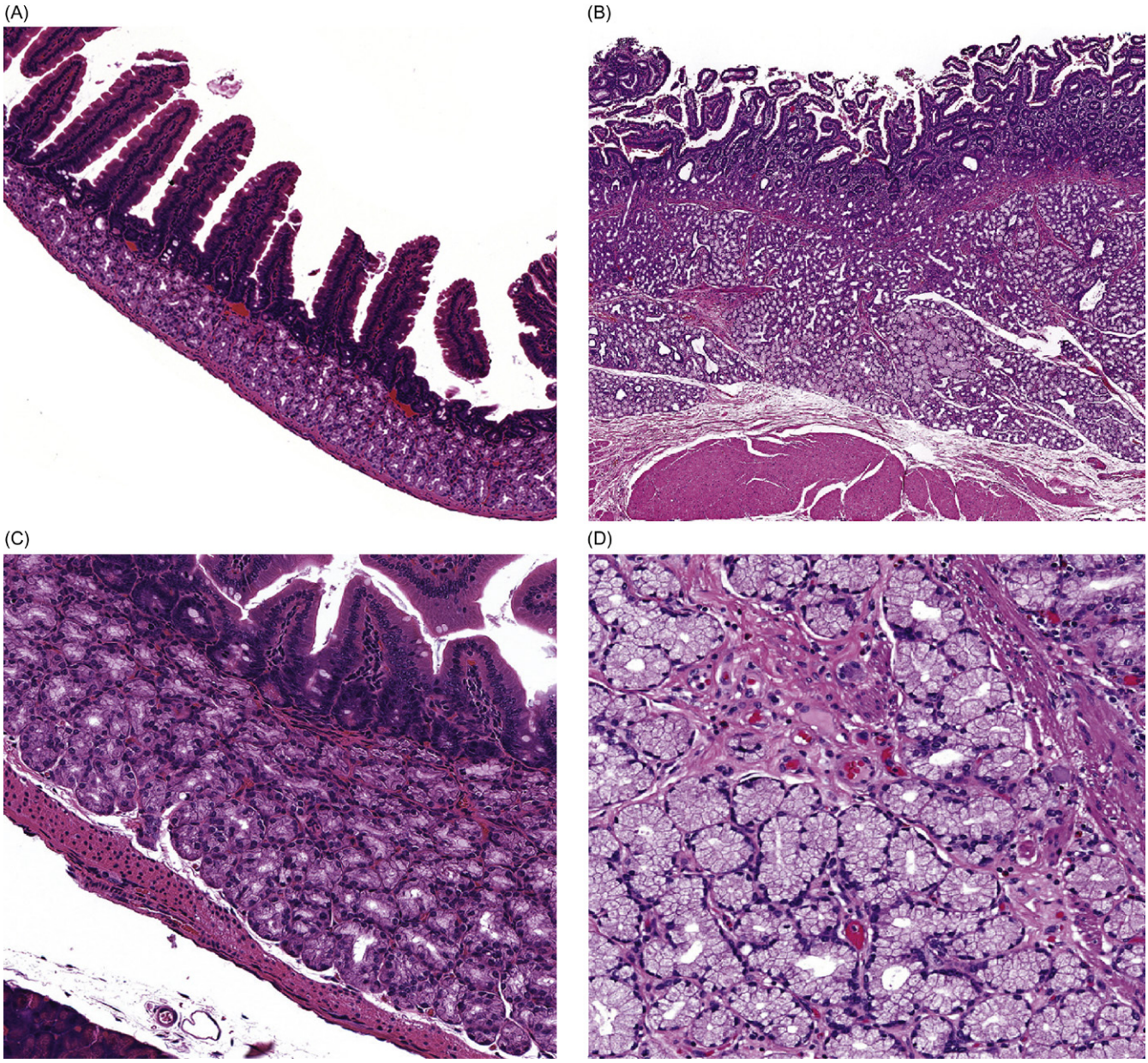

FIGURE 11.12 Brünner's glands. (A) Rodent (mouse). Note the presence of Brünner's glands and tall villi. (B) Human. Brünner's glands are predominately submucosal but can extend into the overlying mucosal lamina propria. (C) High magnification of rodent (mouse). In all three species, the glands produce a periodic acid–Schiff reagent positive secretion that serves as a buffer to acidic gastric secretions and pancreatic enzymes. (D) Human Brünner's glands. The glands are similar in all three species and are tubuloalveolar, which are modified extensions of the crypts of Lieberkühn.

the villous epithelium is contiguous with crypt epithelium, which is composed of several cell types: enterocytes (surface absorptive cells), goblet cells, stem cells, Paneth cells, and enteroendocrine cells (Fig. 11.11).

The villous architecture of the mucosa differs along the length of the intestine in all three species (Figs. 11.10 and 11.11). Although it is often challenging to distinguish the jejunum from the ileum, in general, the villous length decreases from duodenum to ileum. Specialized structures such as Brünner's glands (Fig. 11.12), Peyer's patches (Fig. 11.13), and Paneth cells (Fig. 11.11) can offer additional landmarks along the intestine. Villous height in rodents will increase

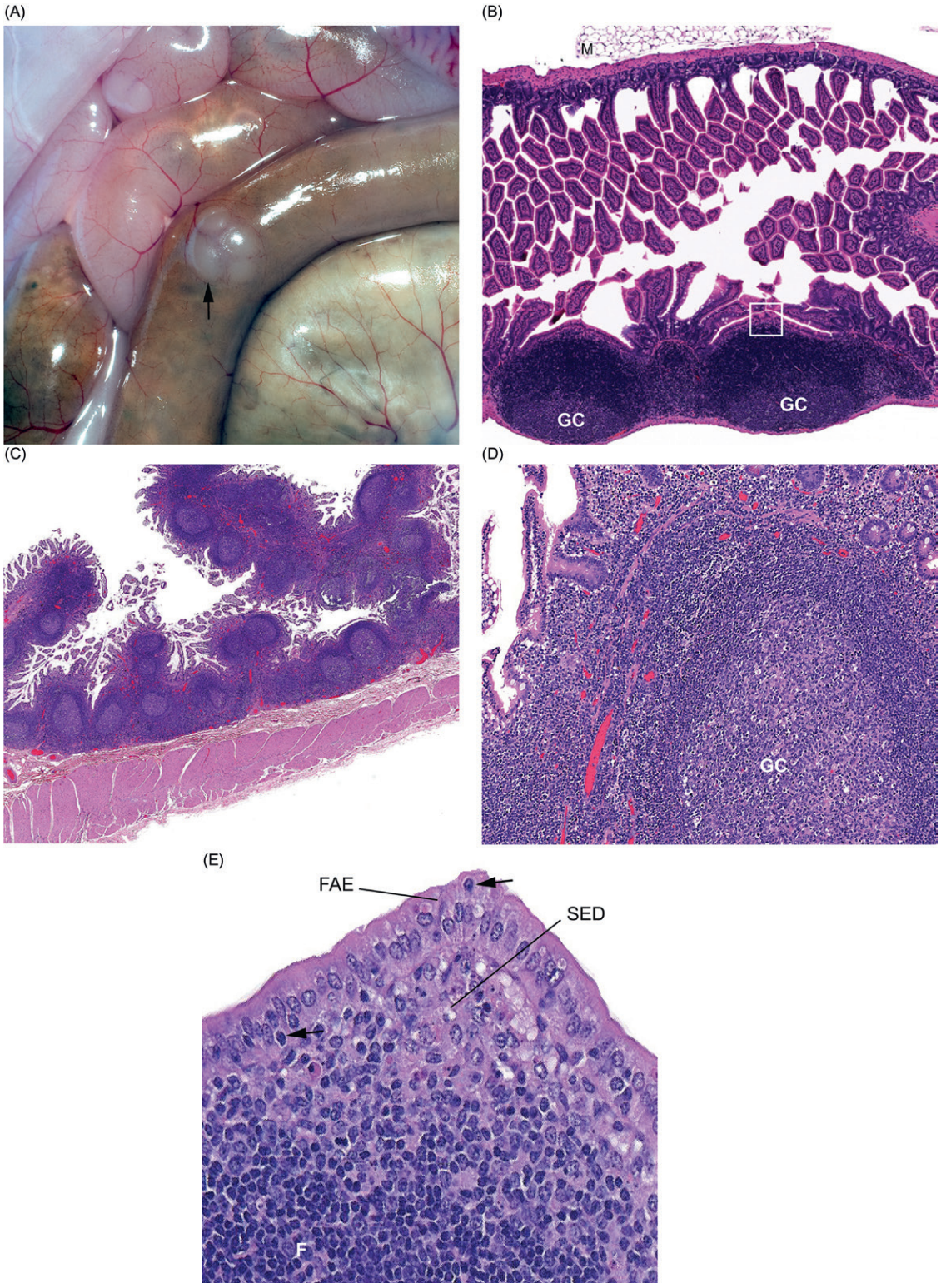

FIGURE 11.13 Gut-associated lymphoid tissue. (A) Rodent (mouse) jejunal GALT. In rodents, they are located on the antimesenteric border of the small intestine. Peyer's patches appear as raised foci on the serosal surface. (B) Rodent (mouse). Notice the germinal centers (GC) and the antimesenteric location. Mesentery (M) is indicated. Boxed region indicates region of follicle-associated epithelium (FAE), magnified in E. (C) Human ileal GALT. Confluent lymphoid aggregates with germinal center formation are located along the antimesenteric border and are present within the lamina propria, often extending into the submucosa. The number of lymphoid follicles can vary from a few to hundreds. (D) High magnification of human GALT. The germinal center (GC) is surrounded by the mantle zone of small lymphocytes that merges with the upper submucosa and lamina propria, which are diffusely infiltrated by lymphocytes. The overlying epithelium is flattened and shows goblet cell loss. (E) High magnification of rodent (mouse) follicle-associated epithelium. There are numerous lymphocytes (arrows) associated with the epithelium and subepithelial dome region. The follicle (F) is indicated.

Need-to-know

- Germinal centers in large aggregates of GALT are a consistent finding in all segments of the GI tract.

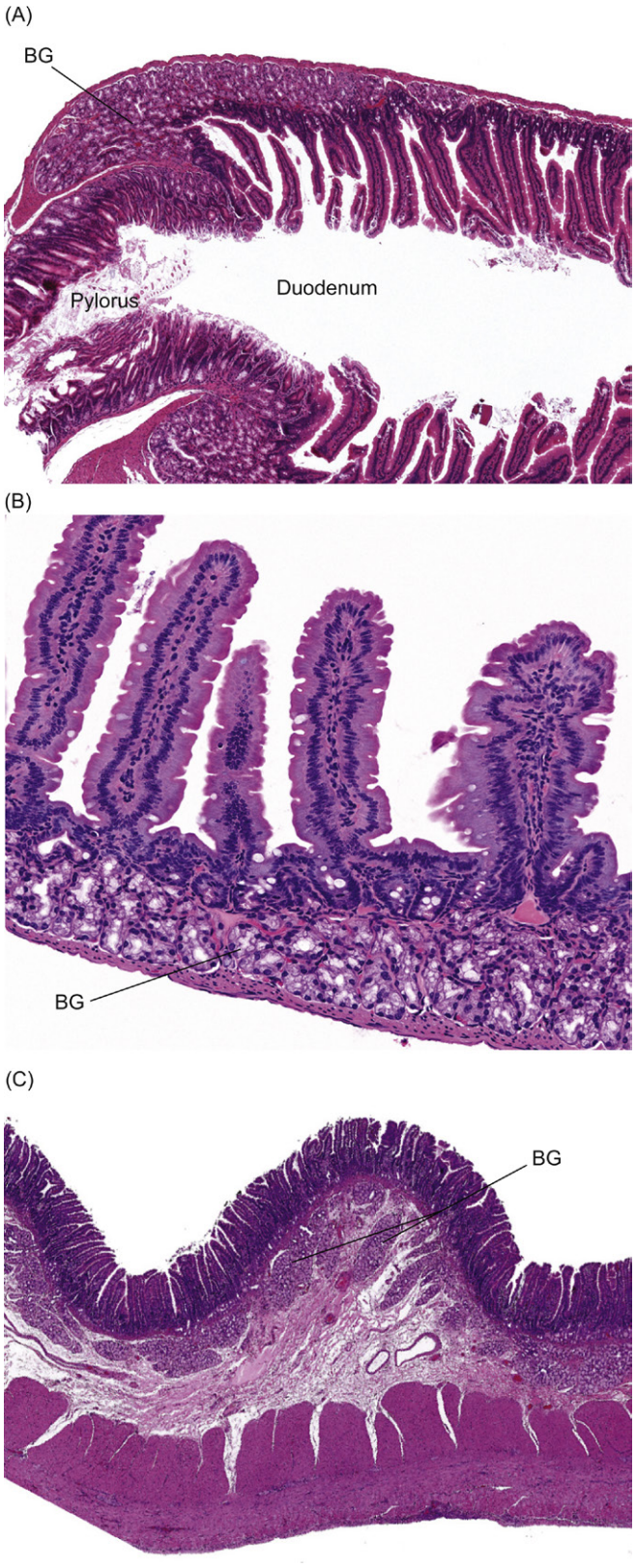

FIGURE 11.14 Duodenum. (A) Rodent (mouse) duodenum and pylorus. Rodent duodenum may be identified in section by the tall and leaflike villi. (B) High magnification of rodent (mouse) duodenal villi. (C) Human duodenum. Note the villous projections of the mucosa that characterize the entire small intestine. In all three species, Brünner's glands (BG) are prominent in the proximal duodenum.

with certain diets, pregnancy and lactation, and experimental intestinal resection. Distention with fixatives, overexuberant flushing, and autolysis may artifactually alter villous height. In rodents, duodenal villi are tall and leaflike (Fig. 11.14), jejunal villi are tall and cylindrical (Fig. 11.15), and ileal villi are short and cylindrical (Fig. 11.16). In humans, the duodenal villi are short, leaflike, and densely packed (Fig. 11.14); jejunal villi become taller and frondlike (Fig. 11.15); and ileal villi are thinner and sparser than those of the proximal small intestine (Fig. 11.16).

Stem cells divide rapidly to replenish the small intestinal epithelium, renewing it every 2 or 3 days in rodents and every 3–5 days in humans—rendering its mucosa one of the most rapidly dividing tissues in the body. The stem cell compartment is located around the base of the crypt, adjacent to Paneth cells (Fig. 11.11). Paneth cells are exocrine serous and secrete a variety of substances with antibacterial and other innate immunity functions. They have abundant brightly eosinophilic cytoplasmic granules within their cytoplasm. In rodents, Paneth cells are most prominent in the ileum and are not found in the rodent large intestine (Fig. 11.16). Paneth cells are normal constituents of the human small intestine, occasionally noted in the appendix, and cecum.

Enterocytes are tall columnar cells with an apical (luminal) surface covered with closely packed microvilli (brush border). Goblet cells are responsible for producing mucin and in all species increase in number from duodenum to ileum. Intraepithelial lymphocytes, plasma cells, macrophages, eosinophils, and mast cells are also present in the intestine of all three species. Enteroendocrine cells exist throughout the rodent GI tract near the basement membrane, usually within the glands or crypts, and secrete various hormones and peptides to regulate gut physiology. In humans, in addition to being near the basement membrane, enteroendocrine cells may also be seen scattered higher up the crypts and villi in small numbers. Special staining techniques are required

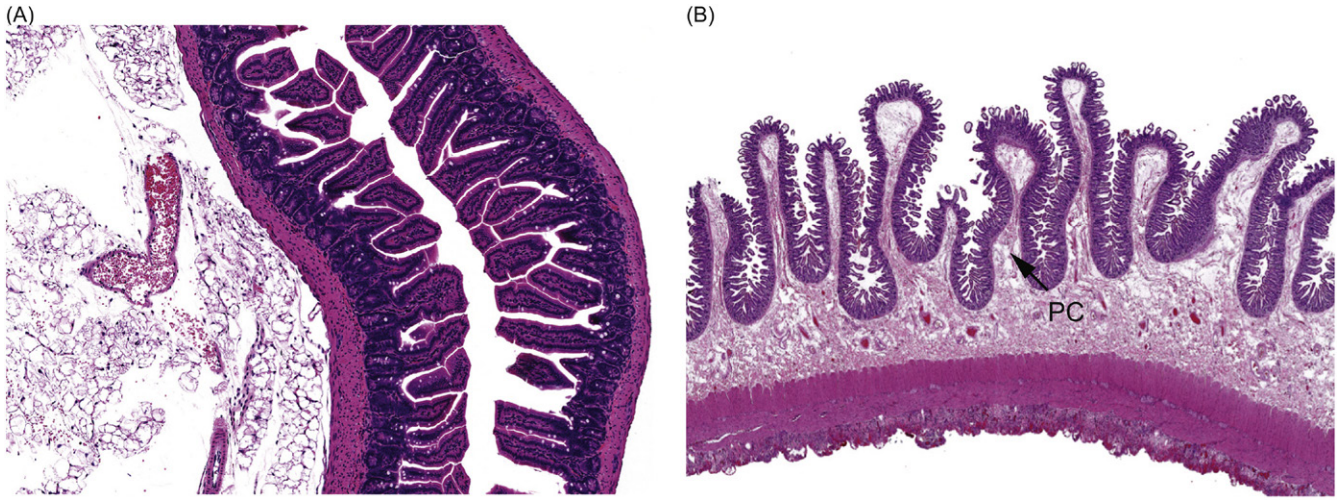

FIGURE 11.15 Jejunum. (A) Rodent (mouse). Rodent jejunal villi are tall and cylindrical. (B) Human showing plica circularis (PC). The human small intestine mucosa contains prominent transverse folds formed by cores of submucosal connective tissue lined by villous mucosa, which serve to increase absorptive surface area.

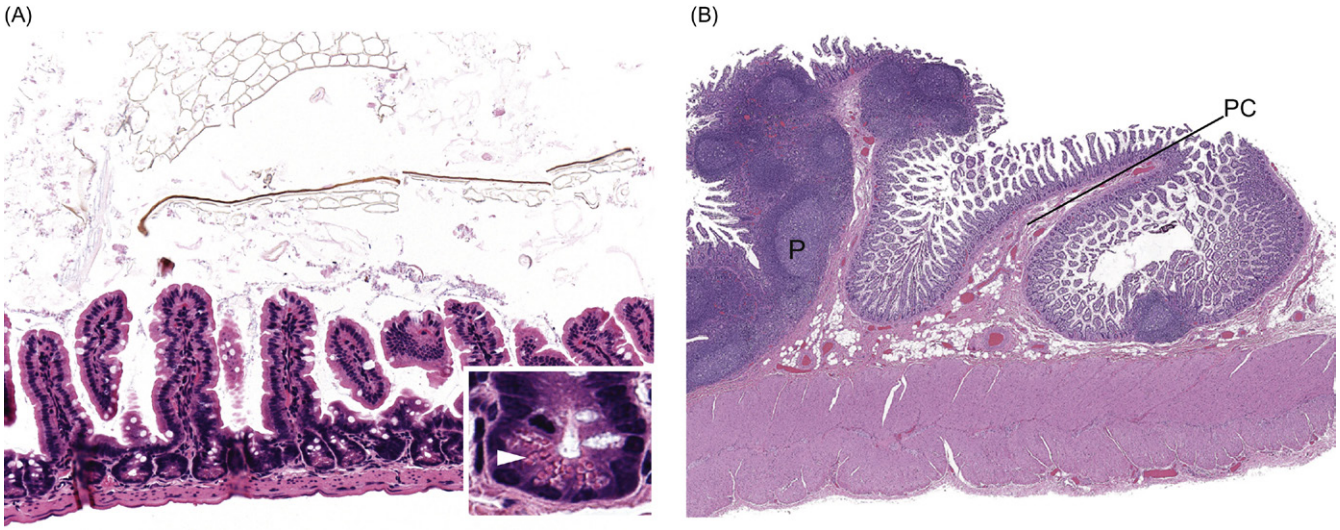

FIGURE 11.16 Ileum. (A) Rodent (mouse). In the rodent ileum, villi are short and cylindrical and Paneth cells (inset, arrowhead) may be prominent. (B) Human. The human ileum contains the plica circularis (PC). Peyer's patches (P) are prominent in the lamina propria.

to visualize these neuroendocrine cells. For more detail regarding the structure and function of enteroendocrine cells, see Gunawardene et al. (2011) (Further Reading).

In all three species, the mucosa-associated lymphoid tissue (GI-associated lymphoid tissue/GALT) includes the primary inductive sites: Peyer's patches (primarily in small intestine) and lymphoglandular complexes (large intestine). Smaller lymphoid structures include isolated lymphoid follicles (Fig. 11.10) and cryptopatches. Peyer's patches (Fig. 11.13) are covered by follicle-associated epithelium containing specialized microfold (M) cells that transport antigens, molecules, and microorganisms from the intestinal lumen. GALT contains B-cells in the follicles, T-cells in the interfollicular regions, and efferent lymphatics. Germinal centers are a frequent finding in Peyer's patches. Peyer's patches in rodents, while diffusely distributed, are most notable in the jejunum, and present mostly on the antimesenteric side of the small intestine (Fig. 11.13). For more detail regarding the

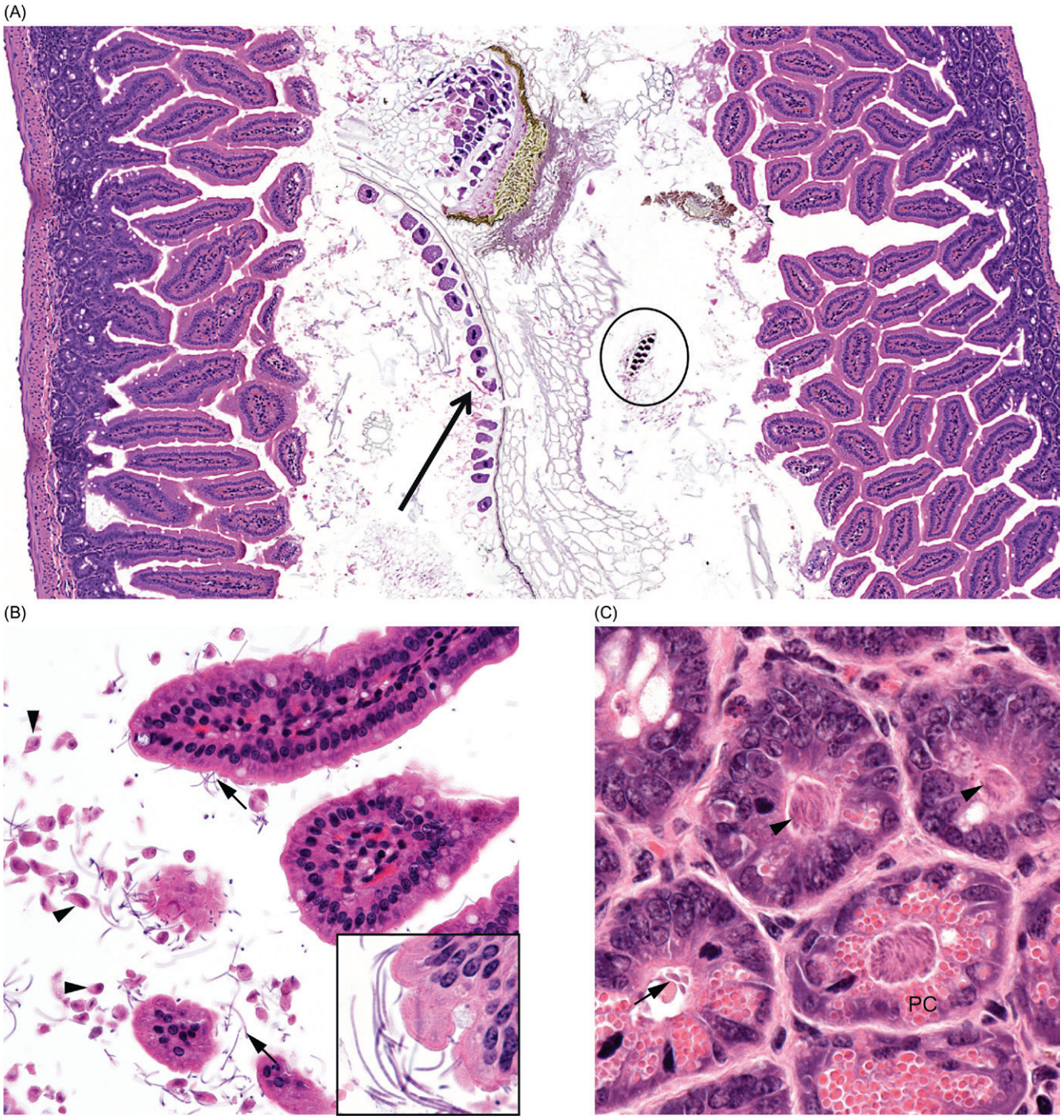

FIGURE 11.17 Rodent (mouse) small intestinal contents. (A) Ingesta is often retained in rodent intestinal tract. In the upper GI tract, there are often recognizable plant fragments with refractile cell walls and cellular material (arrow) that can be pigmented. Hair fragments (circled) and, less often, skeletal muscle (not shown) are also seen. Skeletal muscle may presumably be ingested with cannibalism of pups, fighting, or contaminated feed. (B) Organisms may also be assessed when ingesta is retained. Numerous protozoa (trichomonads, arrowheads) are present admixed with segmented filamentous bacteria (arrows and inset). (D) Abundant *S. muris* trophozoites fill intestinal crypts (arrowheads). Arrow indicates the characteristic 7–9 ×2–3 µm, piriform-shaped organism. Paneth cell (PC) is indicated.

Need-to-know

- Plant and hair fibers should not be confused with intestinal parasites.

structure and function of MALT, see Cesta (2006) (Further Reading).

The submucosa of the small intestine is composed of loose fibroelastic connective tissue in rodents and dense connective tissue in humans. It contains blood vessels, lymphatics, and nerve plexi. The proximal duodenal submucosa contains Brünner's glands (Fig. 11.12), tubuloalveolar glands that secrete alkaline mucous fluid to help neutralize chyme from the stomach. Brünner's glands gradually disappear distally. The small intestine tunica muscularis consists of two smooth muscle tunics (Fig. 11.10). In all three species, the inner circular one is thicker than the outer longitudinal, with nerve plexi in between. Mice have very thin intestinal walls relative to humans, with rats in-between (Fig. 11.10). Small intestine serosa, known as the visceral peritoneum, is composed of a single-celled layer of mesothelium covering a small amount of loose fibroelastic connective tissue.

Methods

In rodents, the GI tract may be fixed unopened with contents intact. This allows for examination of ingesta, including plant material and visible microbiota such as protozoa and segmented filamentous bacteria (Fig. 11.17). In most modern specific pathogen free facilities, nematodes such as pinworms (*Syphacia obvelata, Spironucleus muris*, and *Aspiculuris tetraptera*) are excluded agents; hence it is important to be able to distinguish them from plant material.

In rodents, small intestine segments can be difficult to distinguish histologically, therefore, if accurate location (e.g., duodenum vs jejunum) is required, small intestine sections should be collected in a systematic manner at necropsy using regional anatomic landmarks. Either cross sections or short longitudinal segments can be collected for routine histology from the intestinal tract after it is removed from the carcass and mesenteric attachments. For example, the duodenum should be sectioned at less than 0.5–1 cm from the pylorus, the jejunum at the midpoint of the small intestine (between the pylorus and ileocecal region), and the ileum collected at 0.5–1 cm proximal to the ileocecal region and samples placed into properly labeled tissue or multiwell cassettes for processing. For additional details on phenotyping, fixation, necropsy, and histologic considerations, see Chapter 2, Phenotyping, and Chapter 3, Necropsy and Histology.

Further Reading

Cesta M: Normal structure, function and histology of mucosa-associated lymphoid tissue. Toxicol Pathol 34:599–608, 2006.

The mouse in biomedical research (ed 2) Fox J.G.Barthold S, Davisson M, editors: Normative biology, husbandry, and models, vol 3, San Diego, CA, 2006, Academic Press.

Gunawardene AR, Corfe BM, Staton CA: Classification and functions of enteroendocrine cells of the lower gastrointestinal tract. Int J Exp Pathol 92(4):219–231, 2011.

Lewin KJ, Riddell RH, Weinstein WM: *Gastrointestinal pathology and its clinical implications*, New York, 1992, Igaku Shoin.

Madara JL, Trier JS: Functional morphology of the mucosa of the small intestine. In Johnson LR, editor: Physiology of the gastrointestinal tract (ed 2), New York, 1987, Raven Press, pp 1209–1249.

Maronpot RR, Boorman GA, and Gaul BW, et al: *Pathology of the mouse: reference and atlas*, Vienna, IL, 1999, Cache River Press.

Mills SE, editor: Histology for pathologists (ed 3), Philadelphia, PA, 2007, Lippincott Williams & Wilkins.

Netter FH: Upper digestive tract *Digestive system*, Part I of CIBA collection of medical illustrations vol. 3, Summit, NJ, 1957, Ciba-Geigy.

Ovalle WK, Nahirney PC: *Netter's essential histology*, Philadelphia, PA, 2007, Saunders.

Rishniw M, Fisher PW, Doran RM, et al: Smooth muscle persists in the muscularis externa of developing and adult mouse esophagus. J Muscle Res Cell Motil 28:153–165, 2007.

Rubin W, Ross LL, Sleisenger MH, et al: The normal human gastric epithelia. A fine structural study. Lab Invest 19:598–626, 1968.

Scudamore CL: *A practical guide to the histology of the mouse*, New York, 2013, Wiley.

Suttie AW, Leininger JR, Bradley AE: *Boorman's pathology of the rat: reference and atlas*, ed 2, New York, 2017, Academic Press.

Young B, Lowe JS, Stevens A, et al: *Wheater's functional histology: a text and colour atlas*, ed 5, Philadelphia, PA, 2006, Churchill Livingstone.

This page intentionally left blank

LOWER GASTROINTESTINAL TRACT 12

PIPER M. TREUTING
University of Washington School of Medicine, Seattle, WA, United States

MARK J. ARENDS
University of Edinburgh, Edinburgh, Scotland, United Kingdom

SUZANNE M. DINTZIS
University of Washington School of Medicine, Seattle, WA, United States

Introduction

The lower gastrointestinal tract, commonly referred to as the large intestine, begins at the cecum and also includes the appendix (humans only) colon, rectum, and anus. The primary function of the large intestine in all three species is to dehydrate and store fecal material. Extensive reabsorption of water and salt occurs in the right/proximal colon and continues throughout. Movement of the increasingly solid colonic contents from proximal to distal is supported by abundant mucus-secreting goblet cells that serve to lubricate and protect the colonic mucosa from trauma. All three species have abundant bacterial flora within the colon, which carry out a rumen-like function that is more prominent in rodents. Commensal protozoa are frequently present in rodent intestines. The large intestine of all three species is divided regionally into the cecum, appendix (humans), colon, rectum, and anus (Table 12.1 and Figs. 12.1–12.6). The anatomic division of the human large intestine (right and left colon) is based on configuration and location. Rodent and human large intestines are similar in mural structure, including the mucosa, submucosa, and inner circular and outer longitudinal tunica muscularis and serosa. For techniques, see Chapter 3, Necropsy and Histology, and Moolenbeek and Ruitenberg (1981).

Cecum

Gross Anatomy

In rodents, the cecum is a curved, blind sac that represents up to one-third of the large intestine (Figs. 12.1 and 12.3). The apical blind end typically demonstrates visible gut-associated lymphoid tissue (GALT; see last section) and is narrower than the base that includes the region of the ileocecal and cecocolic junctions. The rodent cecum is a functional fermentation vat containing a high concentration of bacterial and lesser protozoal organisms. In the cecum, bacterial load can be 10^{11}/g feces. Bacterial fermentation, and thus cecum size, is diet-dependent. The commensal bacteria produce free fatty acids, vitamin K, and some of the B vitamins. Rodents recapture these vitamins through coprophagy. In humans, the

Comparative Anatomy and Histology. DOI: http://dx.doi.org/10.1016/B978-0-12-802900-8.00012-9
© 2018 Elsevier Inc. All rights reserved.

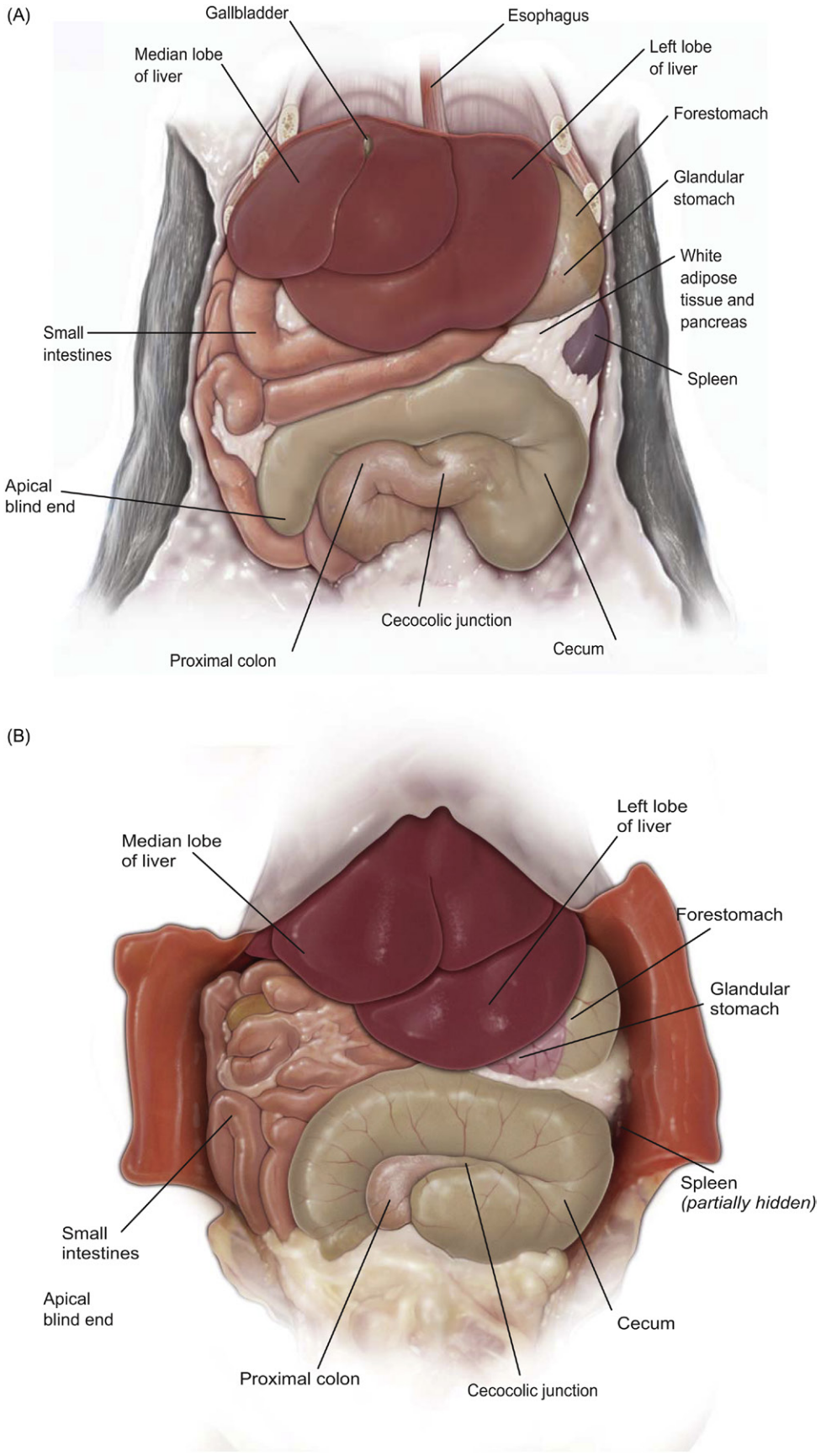

FIGURE 12.1 Regional anatomy of the rodent abdomen. (A) Mouse. (B) Rat. The large cecum is quite prominent; depending on the amount of ingesta, it can sometimes occupy a majority of the lower abdomen. Source: © Elsevier, Inc., www.netterimages.com.

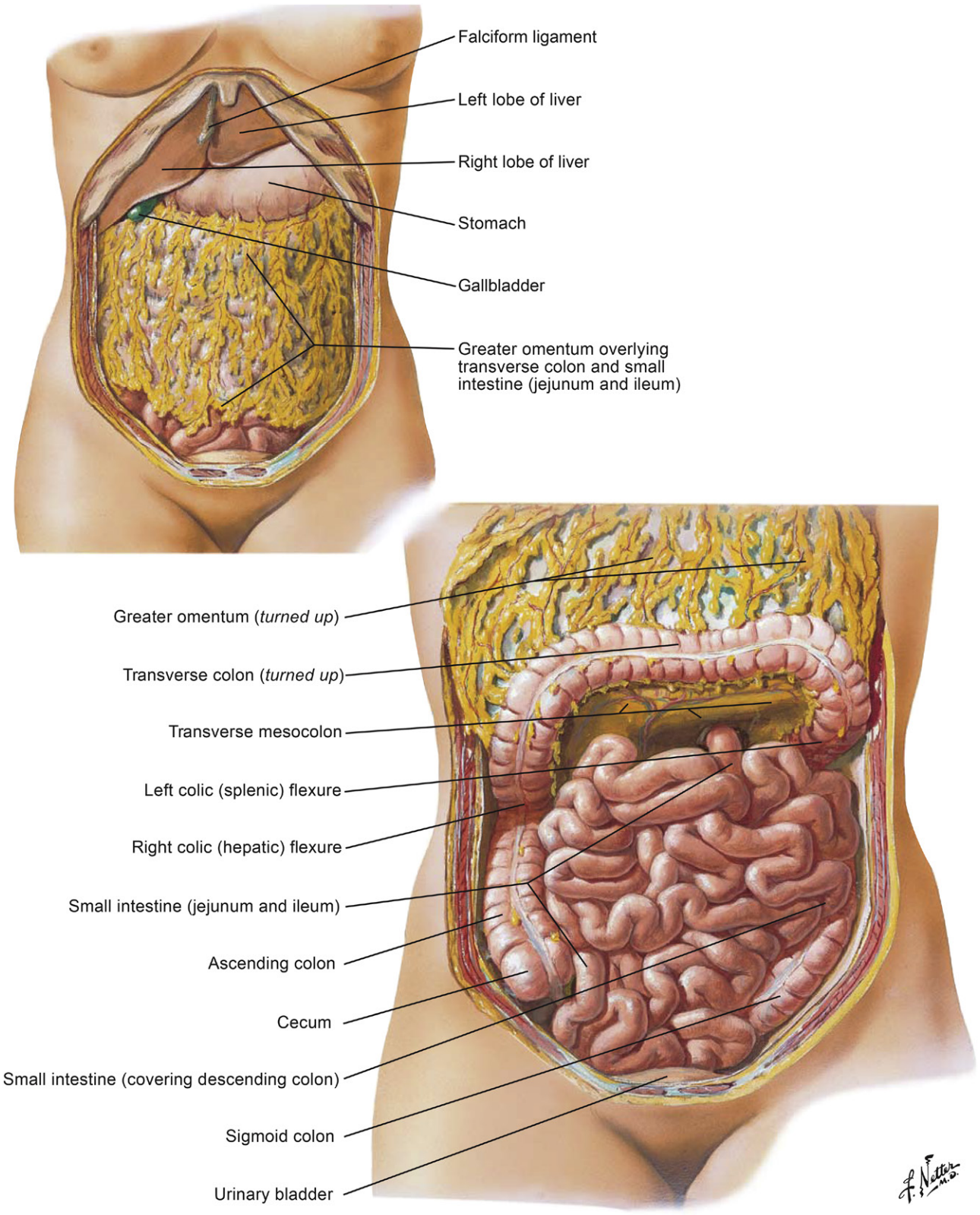

FIGURE 12.2 Regional anatomy of the human abdomen. The human large intestine measures approximately 1–1.5 m and constitutes the terminal section of the digestive tract. The transverse and sigmoid colon lie within the abdominal cavity and are covered by mesothelium. The cecum, ascending colon, and descending colon are partly retroperitoneal and partly invested with peritoneal mesothelium, except for the distal third of the rectum which is surrounded by adventitia, fascia, and fat. Source: © Elsevier, Inc. www.netterimages.com.

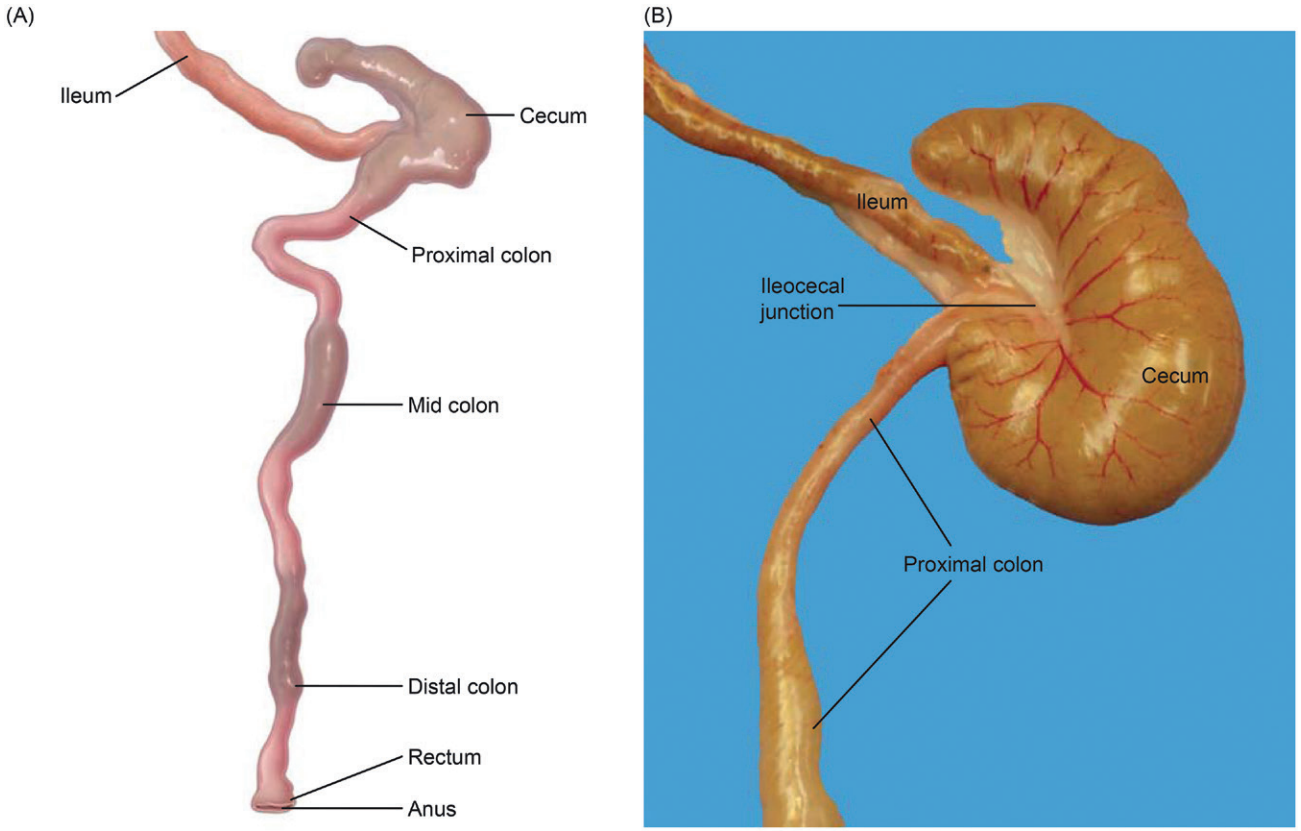

FIGURE 12.3 Rodent large intestine. The large intestine is similar in mice (A) and rats (B). The ileum enters the cecum, a large J-shaped blind sac, at the ileocecal junction. The proximal colon exits at the cecocolic junction near the ileocecal junction. Fecal pellets are formed by consolidation and dehydration in the mid and distal colon. Note the visible transverse mucosal folds in the proximal colon of the rat (B). Source for (A): © Elsevier, Inc., www.netterimages.com.

Need-to-know

- Rodent serosa is smooth, lacking taenia and haustra.
- Rodents have a large cecum and lack an appendix.
- Healthy rodent gastrointestinal tract will have formed fecal pellets in the distal colon.

cecum is a continuous part of the proximal colon that lies distal to the ileocecal valve and is much reduced in relative size compared with rodents (Figs. 12.3 and 12.4).

HISTOLOGY

The mucosa of the rodent cecum and proximal colon demonstrates transverse folds (Fig. 12.7). The human cecum is in continuity with the ascending colon and has the same histological mucosal structure.

APPENDIX

GROSS ANATOMY

Rodents do not have an appendix. The human appendix arises from the cecum, inferior to the ileocecal junction, and is a small blind-ended tube (worm-shaped or vermiform) measuring ~9 cm in average length (range 2–20 cm). It contains abundant GALT and has been proposed to be involved in immune system support of beneficial bacteria growth that allows the appendix to act as a haven for useful bacteria to repopulate the colon if disease flushes out the bacterial contents.

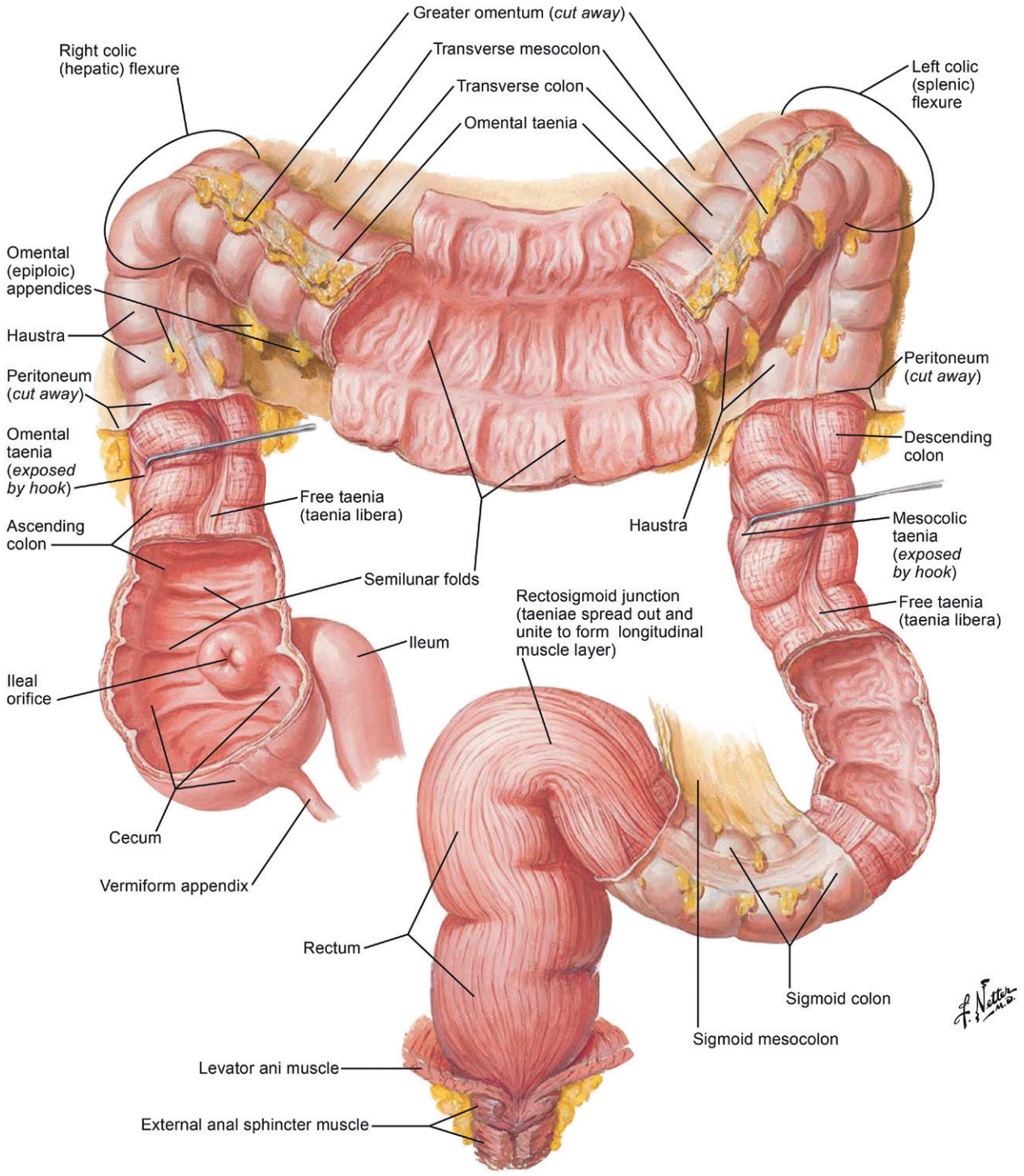

FIGURE 12.4 Human large intestine. The anatomic division of the human colon is based on its configuration and location. The right colon is composed of the appendix, cecum, ascending colon, and transverse colon to the midline. The left colon begins at the midline transverse colon and includes the descending and sigmoid colon and rectum. The outer longitudinal layer of the tunica muscularis proximal to the rectum forms three distinct longitudinal bands called taenia coli. The colon becomes sacculated between the taenia, forming the haustra. Source: © Elsevier, Inc., www.netterimages.com.

Need-to-know

- The human cecum is smaller and the rectum is larger than rodents.
- Humans have taenia coli and haustra.

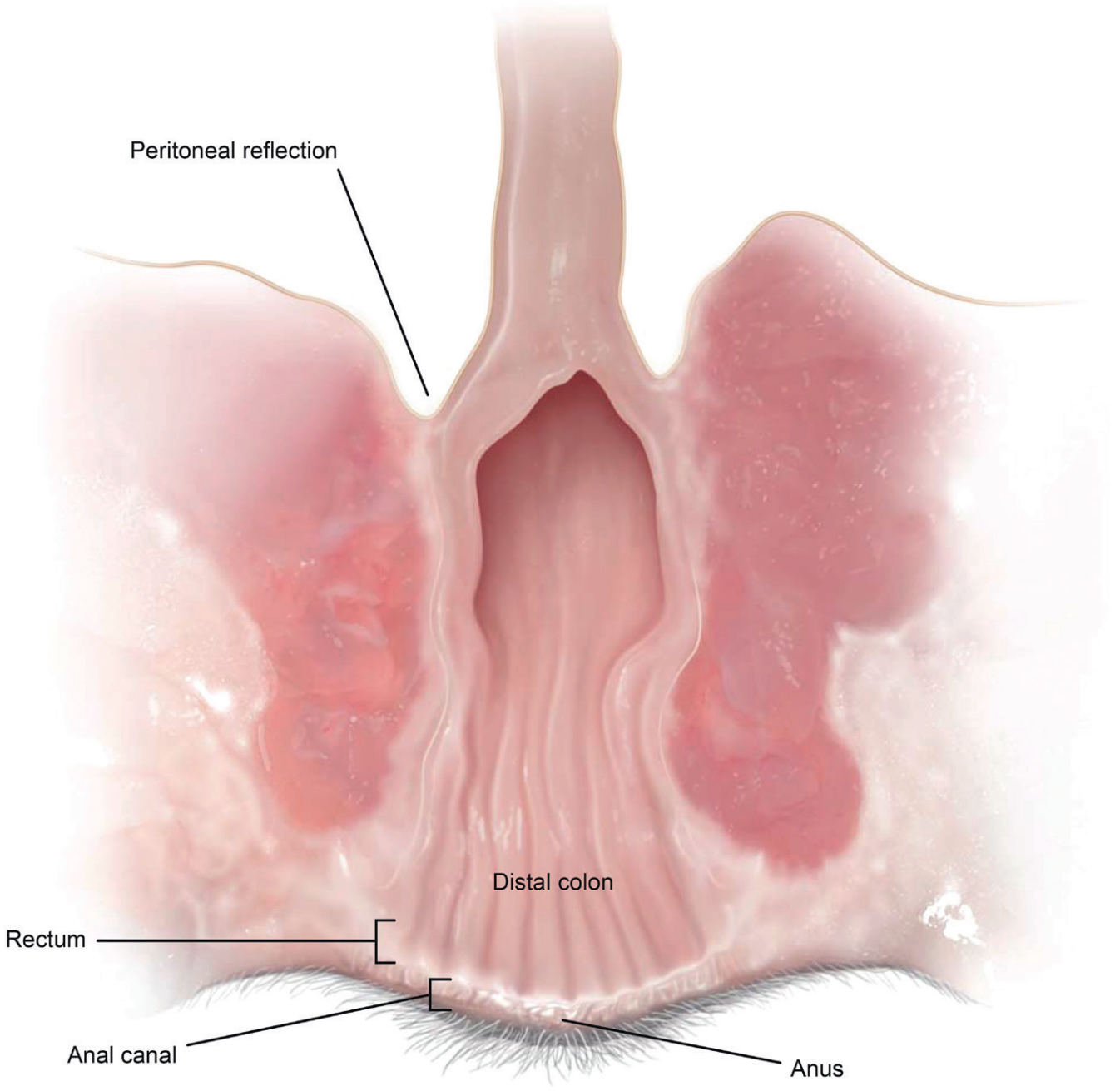

FIGURE 12.5 Rodent (mouse) anorectal junction.
Source: © Elsevier, Inc., www.netterimages.com.

Need-to-know

- The mouse rectum is very short and indistinct; it is prone to prolapse, especially when inflamed.

HISTOLOGY

The human appendix contains all of the anatomic layers of the large intestine. The appendix characteristically also has multiple, often back-to-back, lymphoid follicles forming extensive GALT within its submucosa, with an accompanying dense lymphocytic infiltrate extending into the lamina propria (Fig. 12.7).

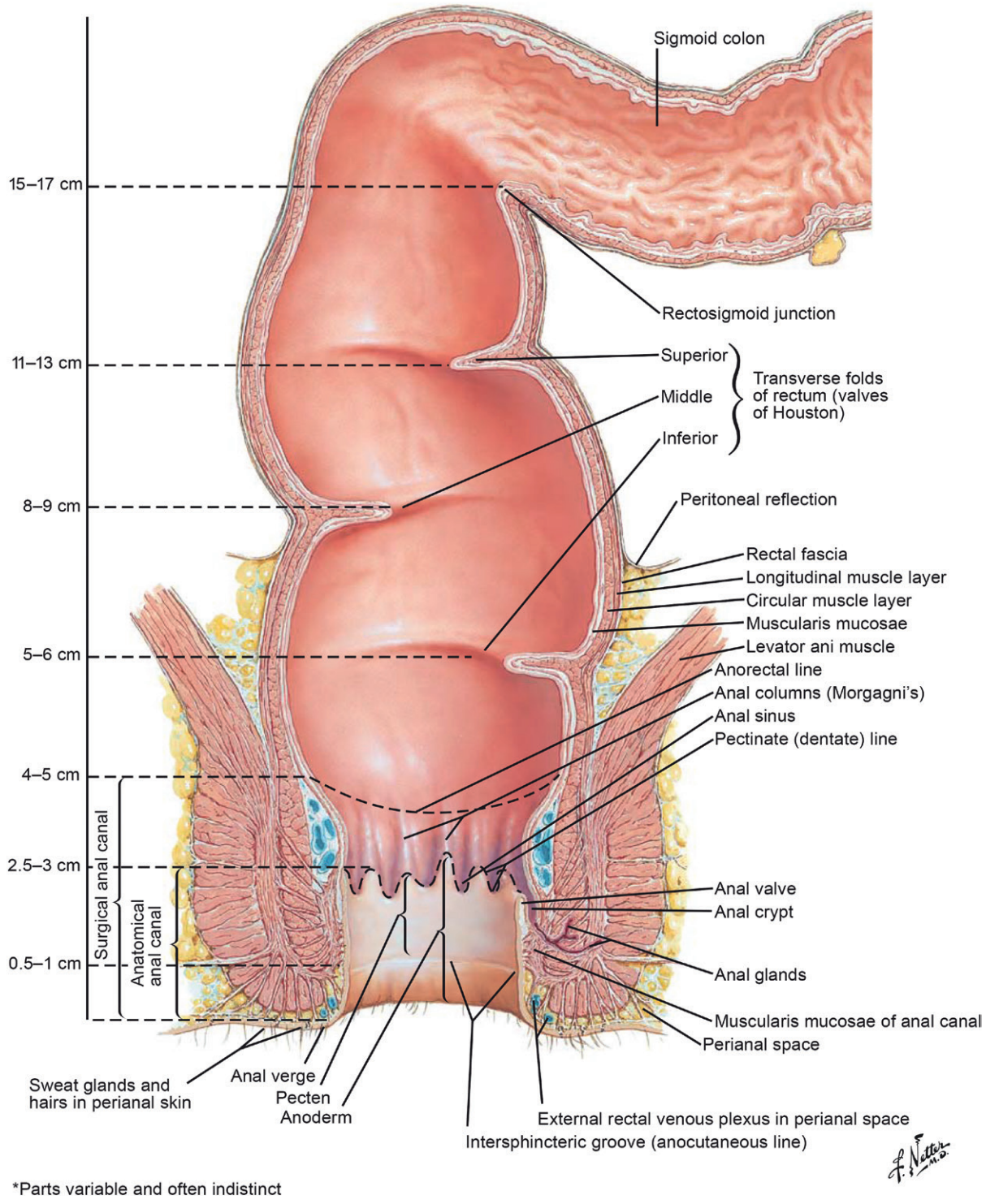

FIGURE 12.6 Human anorectal junction. The rectum is approximately 12–15 cm long, and the distal third is covered by adventitia, fascia, and fat within the deep pelvis, rather than mesothelium. The "anatomical anal canal" is 2 or 3 cm long and contains squamous mucosa only, whereas the "surgical anal canal" (4–5 cm) also includes the 5–10 vertical glandular mucosal folds known as the anal columns of Morgagni. The glandular-squamous junctional mucosa has serrated appearance known as the pectinate (dentate) line. Source: © Elsevier, Inc. www.netterimages.com.

TABLE 12.1 Lower Gastrointestinal Tract

Feature	Rodent	Human
	Gross	
Cecum to rectum	Mouse: ~14 cm; rat: ~25 cm	~100–150 cm
Taenia coli and haustra	None; smooth serosa; may have fecal pellets	Present
Appendix	Absent	Present, vermiform, ~9 cm
Cecum	Fully functional blind sac; transverse mucosal folds; thin submucosa and muscular tunics; straight crypts; may have simple branching at base; size dependent on diet, flora. Large GALT on apical greater curvature; Mouse: ~3–4 cm; rat: ~3–7 cm	Continuous with the proximal colon, lying adjacent to the ileocecal valve
Functional cecum	Present; fermentation, vitamins K and B	Absent
Corprophagy	Present	Absent
Proximal/ascending/right	Transverse folds in the mucosa, from cecum to mid colon; Mouse: folds are typically not visible through serosa Rat: folds are visible through serosa	Colon from ileocecal valve to the hepatic flexure
Mid/transverse	Very short; lumen narrows; no mucosal folds	Connects the hepatic to the splenic flexure
Distal/descending/left	Fecal pellets may be seen	Splenic flexure to left lower quadrant; S-shaped sigmoid colon extends from descending colon to rectosigmoid junction; sigmoid colon may be redundant
Rectum	Indistinct from distal colon; Mouse: very short ~5 mm and straight; prone to prolapse Rat: ~50–80 mm, prolapse is rare	12–15 cm curved; proximal two-thirds of rectum has a mesothelial covering within the peritoneal cavity, whereas the distal third of rectum is extraperitoneal, lying within the deep pelvis, surrounded by adventitia, fascia, and fat
Anus	At ventral base of tail	Anal canal is ~3–5 cm, traverses the pelvic floor to anal opening
Circumanal glands	Modified sebaceous glands around anal canal	Apocrine glands, perianal
	Histologic	
Mucosa	Mucosal folds vary by region. Cecum and proximal colon: transverse; mid colon: flat with no folds; distal colon and rectum: longitudinal	Transverse folds at all regions
Absorptive colonocytes	Present	Similar to rodent
Mucous/goblet cells	Present	Similar to rodent
Enteroendocrine cells	Present	Similar to rodent
Paneth cells	Absent	Cecum and appendix
Microfold (M) cells	Present	Similar to rodent
Lamina propria	Lymphocytes, plasma cells, macrophages, eosinophils, mast cells	Similar to rodent
Muscularis mucosae	Thin	Variable thickness; traversed by lymphoid follicles; poorly developed in appendix
Submucosa	Rodents thinner than humans Mouse: very thin Rat: thicker than mouse	Contains adipose tissue, arterioles, venules, lymphatics, and Meissner's plexus
Muscular tunics	Muscular tunics thicken distally	Auerbach's plexus between the two muscle bands
Cecum	Abundant lymphoid tissue at apical greater curvature	Paneth cells may be present
Proximal colon	Transverse mucosal folds	Transverse folds
Mid colon	Flat mucosa	Transverse folds
Distal colon	Longitudinal mucosal folds	Transverse folds
Rectum	Indistinguishable from distal colon	Transverse folds
Anus	Keratinized stratified squamous epithelium	Nonkeratinized stratified squamous epithelium

Colon

GROSS ANATOMY

In all three species, the colon maintains the same mural structure as the rest of the gastrointestinal tract: mucosa, submucosa, and inner circular and outer longitudinal tunica muscularis and serosa (Fig. 12.8). The rodent colon has a smooth serosal appearance throughout (Figs. 12.1 and 12.3). In humans, the outer longitudinal layer, proximal to the rectum, forms three distinct

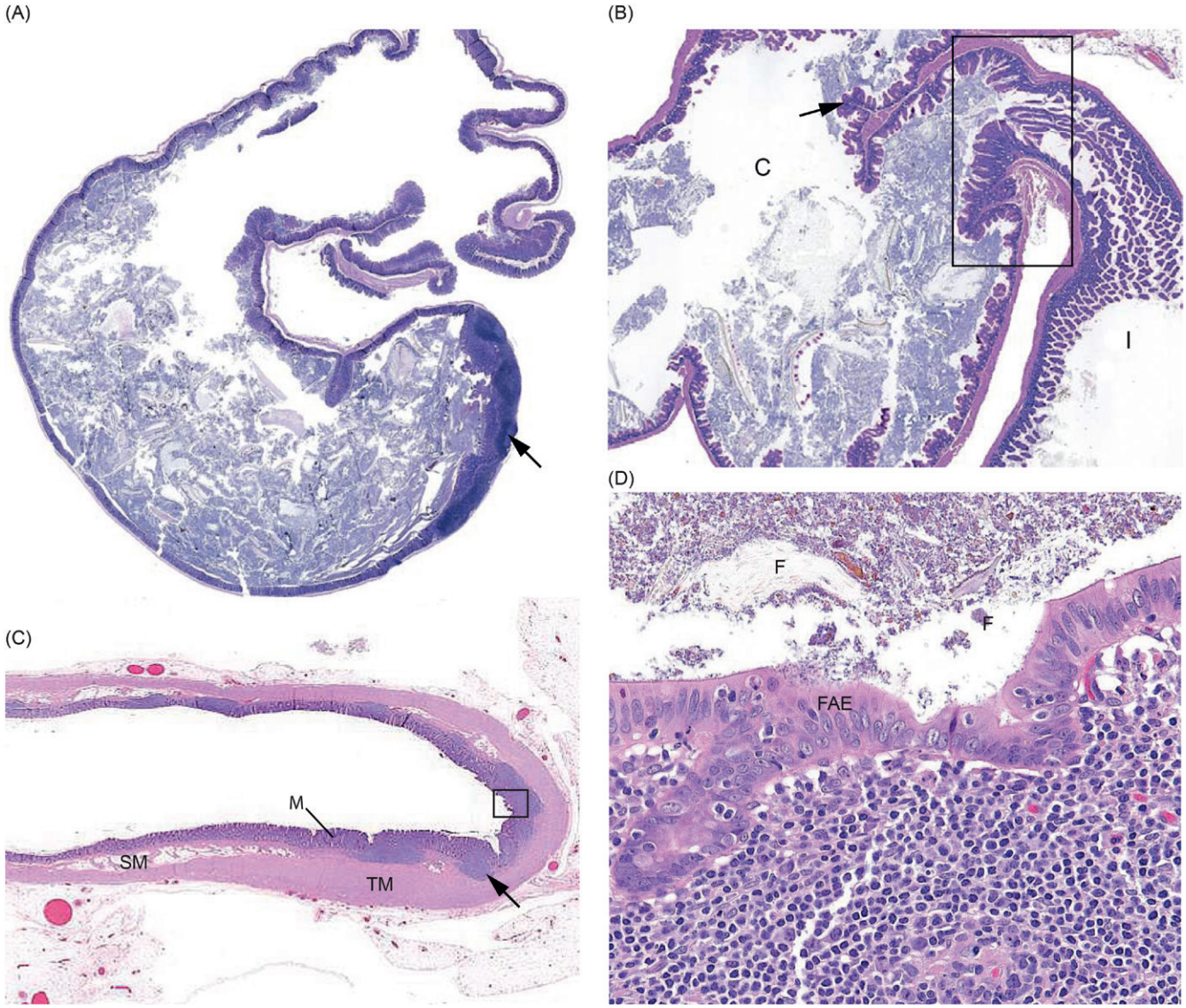

FIGURE 12.7 Cecum and appendix. (A) The rodent (mouse) cecum is a large blind J-shaped sac that ferments ingesta. At the narrow tip of the cecum is a large region of GALT (arrow). Retention of feces in the cecum is common, unless intentionally removed at necropsy. (B) The rodent (mouse) ileocecal junction (boxed region). The ileum enters the dilated end of the cecum (C). The cecal mucosa has transverse folds (arrow), whereas the distal ileum (I) has typical small intestinal villi. (C) Human appendix. The appendix contains all of the anatomic layers of the colon: the mucosa (M) with associated and often prominent lymphoid aggregates (arrow and box), the fatty submucosa (SM), and two layers of the tunica muscularis (TM). (D) High magnification (box in C) of a human appendiceal lymphoid aggregate and lumen. The appendiceal lumen is often filled with fecal material (F), which may form concretions known as fecaliths. The follicle-associated epithelium (FAE) is indicated.

longitudinal bands called taenia coli. Because the taenia are slightly shorter than the large intestine, the human colon becomes sacculated between the taenia, forming the haustra (Fig. 12.4). Fecal pellets can be seen in the distal rodent colon and can impart a segmented appearance that should not be confused with haustra. In the proximal colon of rats, the transverse mucosal folds may be evident through the serosa; this is less frequent in mice despite the presence of similar mucosal folds.

The rodent cecum empties into the proximal (also termed right) colon (Fig. 12.1). The colon continues toward the pyloric region of the stomach, and begins a short middle (also termed transverse) segment to the distal (also termed descending) colon. The rectum is relatively short in

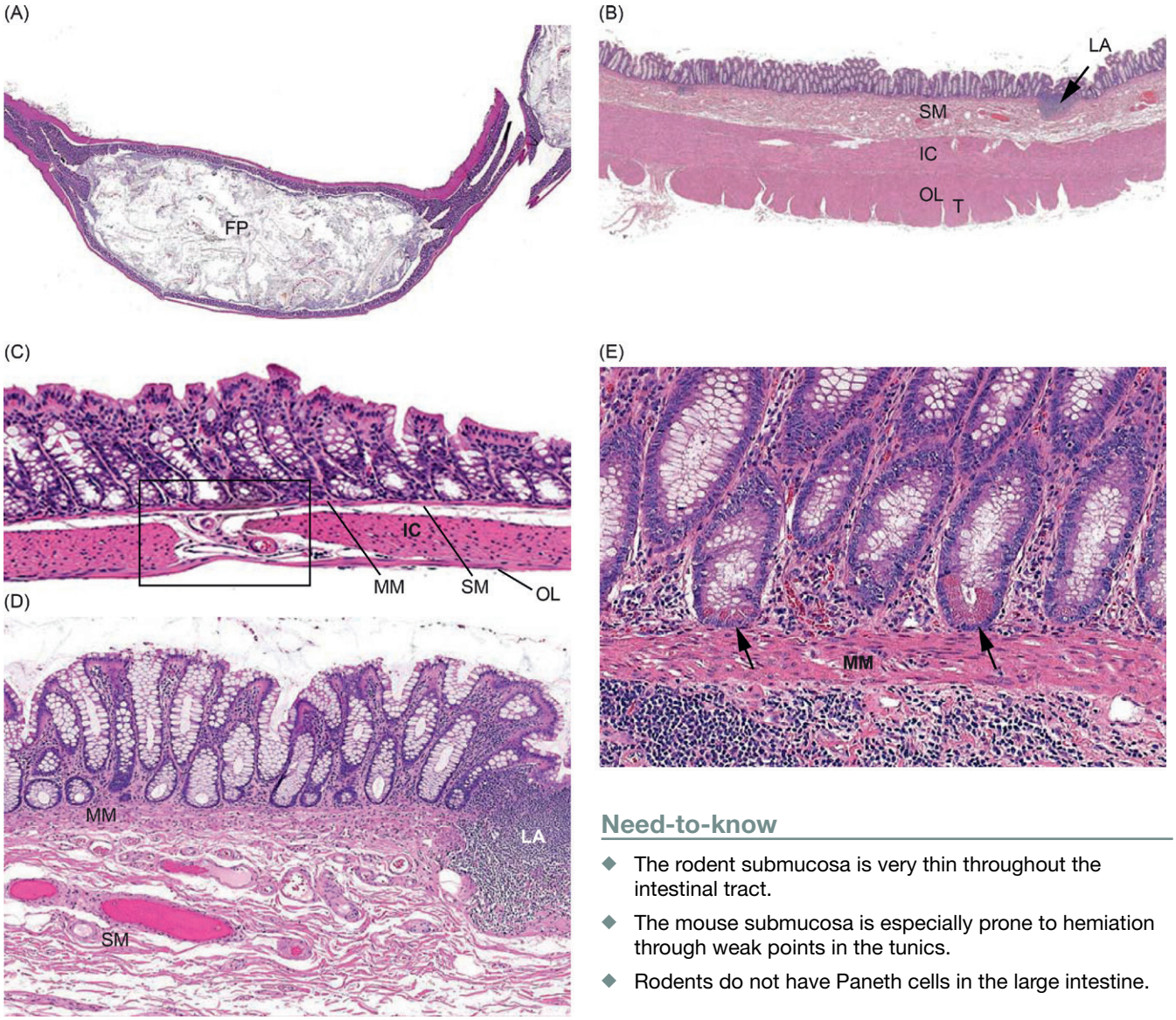

Need-to-know

- The rodent submucosa is very thin throughout the intestinal tract.
- The mouse submucosa is especially prone to hemiation through weak points in the tunics.
- Rodents do not have Paneth cells in the large intestine.

FIGURE 12.8 Colon. (A) Subgross rodent (mouse) colon with a fecal pellet (FP) magnified to ×12.5. The rodent intestinal wall is considerably thinner than human, with little or no discernable submucosa. (B) Subgross human colon magnified to ×12.5. The muscular wall is thick to allow peristaltic movement of solid intestinal contents with fusion of the bundles of the outer longitudinal (OL) muscularis forming the taenia coli (T). The inner circular (IC) muscular tunic, submucosa (SM), and lymphoid aggregate (LA, arrow) are indicated. (C) Rodent (mouse). Rodents lack taenia coli, the fused bundles of the outer longitudinal muscularis. Notice the thinning of the tunica muscularis at the entrance of serosal blood vessels, lymphatics, and nerves (box). This region is a common area for herniation of the mucosa, especially when colitic. Note the muscularis mucosae (MM), under which is the very thin connective tissue of the mouse submucosa (SM). Inner circular (IC) and outer longitudinal (OL) tunica muscularis are indicated. Note there is artefactual separation of the SM from the tunica muscularis. (D) Human. The submucosa (SM) is relatively thick and contains adipose tissue, blood vessels, lymphatics, lymphoid aggregates (LA), nerves, collagen fibers, and inflammatory cells. (E) Human. The appendix and cecum are usually the only areas of the large intestine that may contain Paneth cells (arrows) at the crypt base. Muscularis mucosae (MM) is indicated.

rodents, especially mice, where it is easily prolapsed under certain pathological conditions; rats seem to be relatively resistant to rectal prolapse (Fig. 12.5).

The anatomic division of the human colon is based on its configuration and location. The right colon is composed of the appendix, cecum, ascending colon, and transverse colon to the midline (Figs. 12.2 and 12.4), roughly corresponding to the cecum and proximal colon of rodents. The human left colon begins around the midline of the transverse colon, includes the descending colon, sigmoid colon and rectum, and ends at the anorectal junction. The human left colon roughly

corresponds to the mid and distal rodent colon (Figs. 12.2 and 12.4).

The rectum in rodents is straight and relatively short and indistinct from the distal colon (Fig. 12.5). There is little description of the formal anatomical boundaries of rectum versus distal colon in rodents. The rectum in mice has been reported as ~0.5 cm and rats ~ 5–8 cm. This is in contrast to humans, where the rectum is 12–15 cm and curved following the shape of the sacrum and coccyx. The definition of the human anorectal boundaries varies by medical discipline and impacts colorectal cancer treatment. The human rectum is divided into three parts: upper, middle, and lower (Fig. 12.6). The upper rectum is a continuation of the sigmoid colon. The transition from colon to rectum, the rectosigmoid junction, is typically defined anatomically at the level of the third sacral vertebrae. The proximal two-thirds of the human rectum has a serosal covering by peritoneal mesothelium, whereas the distal third is covered by adventitia, fascia, and fat within the deep pelvis, rather than mesothelium. The glandular rectal mucosa transitions to the squamous mucosa of the anal canal (2–3 cm long) at the pectinate (dentate) line.

HISTOLOGY

The rodent colon regions—proximal, mid, and distal–each have characteristic mucosal folds (proximal and distal) or lack thereof (mid) which help to distinguish the segments histologically (Figs. 12.9 and 12.10). The proximal rodent colon has transverse mucosal folds (usually V-shaped); the mid-colonic mucosa is flat, and the distal rodent colonic mucosa has longitudinal folds. The human colonic mucosa has transverse folds throughout, with increasing prominence from proximal to distal. In all three species, the mucosa is composed of tubular glands, known as crypts of Lieberkühn, oriented perpendicular to the long axis of the colon. There are no villi in the large intestine. The crypts of Lieberkühn are lined by simple columnar absorptive colonocytes, goblet cells, and enteroendocrine cells (Fig. 12.8). As the intestinal contents become increasingly solid, mucin is required to lubricate their passage. In rodents, goblet cells are abundant along the entire length of the crypt in the proximal colon. Goblet cells show a relative decrease in number at the base of the crypts in the distal colon and rectum. In the human colon, goblet cells predominate, and the ratio of goblet cells to enterocytes increases from cecum to rectum. Paneth cells, found in the small intestine, can also be seen in the human appendix and cecum (Fig. 12.8) but are normally absent from the more distal colon and are entirely absent from rodent colonic mucosa.

The lamina propria, which forms the investing stroma of the colonic mucosa in all three species, contains capillaries and lymphatic vessels, as well as lymphocytes and plasma cells. Eosinophils, mast cells, and macrophages are normal constituents of the lamina propria, but are relatively rare compared to lymphocytes and plasma cells (see below for GALT). Even rarer, scattered neutrophils may be a normal component of the lamina propria but should not be present within the normal colonic surface or crypt epithelium.

The human submucosa has abundant adipose tissue that is absent in rodents. Indeed, the mucosa and submucosa are very thin in mice, increasing the incidence of mucosal herniation. Herniation is especially prevalent when inflammation is present and at anatomically weaker points in the tunica muscularis, such as at the insertion of serosal blood vessels, lymphatics, and nerves (Fig. 12.8).

In all three species, the tunica muscularis has inner circular and outer longitudinal layers. The rodent distal colon muscular layers are thicker than those found in the cecum. The tunica muscularis increases in thickness progressively in the distal colon where the mucosa has longitudinal folds, resulting in a characteristic cross-sectional appearance. In humans, the smooth muscle bundles of the outer layer fuse to form longitudinally oriented bands (taenia coli) that are absent in rodents.

FIGURE 12.9 Subgross of a rodent (mouse) colon in a Swiss roll preparation. (A) Closed technique with retained fecal pellets. The proximal colon (PC) is in the center. Notice the transverse mucosa folds (arrow). The mid colon (MC) has fecal pellets, and the distal colon (DC) has longitudinal folds of mucosa (arrowhead). (B) Open technique with contents removed. The opened colon is fixed flat and then rolled on edge prior to processing. Anus (A) is indicated. Image courtesy of Dr. J. M. Ward.

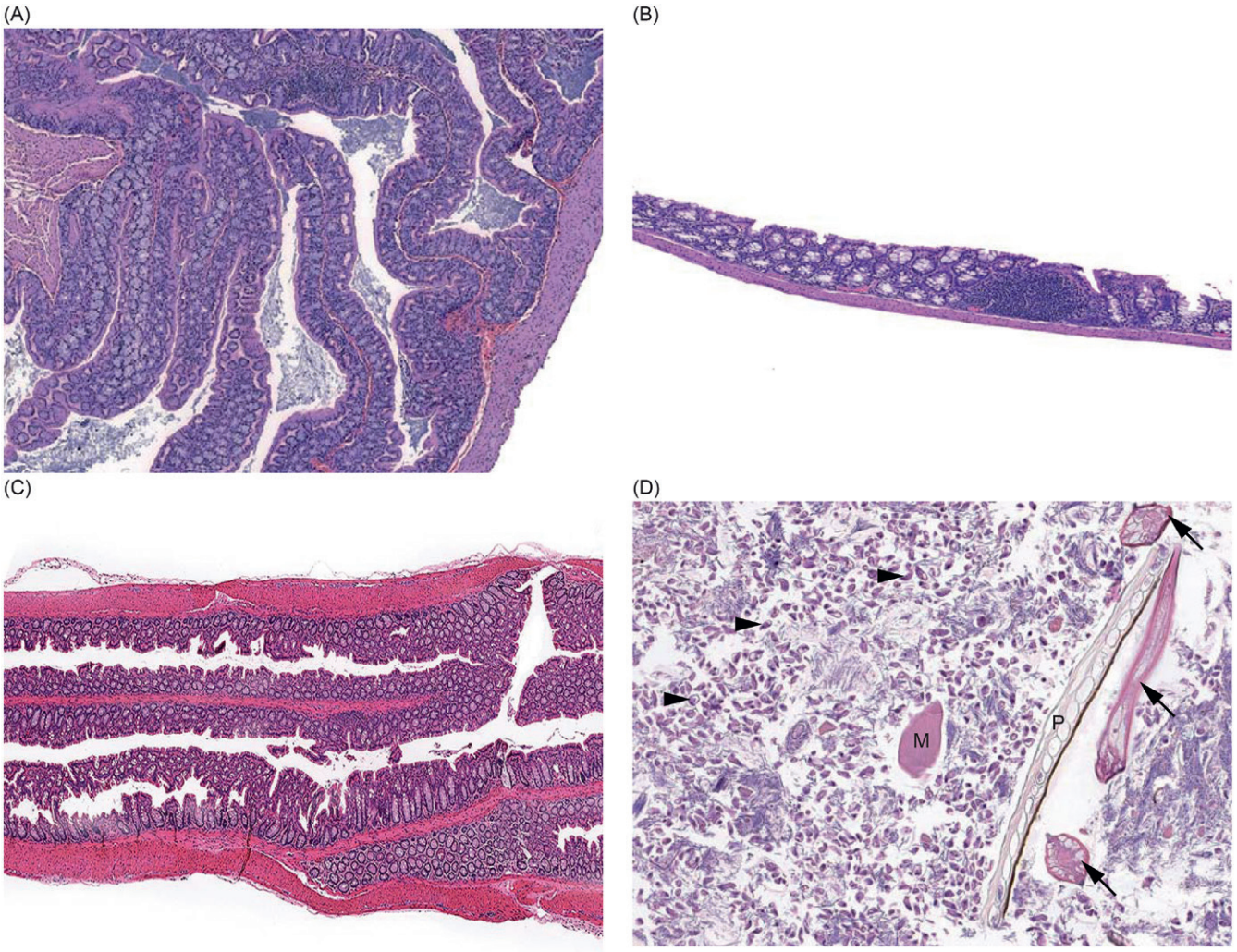

FIGURE 12.10 Rodent (mouse) colon mucosa. (A) The proximal colon mucosa has transverse folds that are longer than those present in the cecum. (B) The mid colon lacks mucosal folds. (C) The distal colon has longitudinal mucosal folds that are prominent when devoid of fecal pellets. (D) Feces contain abundant flora, including mixed bacterial colonies and protozoa. The composition of the microflora depends on pathogen status, diet, housing, and genotype. Nematodes such as pinworms may be present (arrows, longitudinal and cross sections); however, they are not normally found in SPF mice. Trichomonad protozoa appear tear-to-pear-shaped (arrowheads), are often seen, and are usually considered commensals, but may have impact on certain disease models. Occasionally muscle fragments (M) may be seen.

The enteric nervous system in all three species contains aggregates of ganglion cells and associated nerve fibers called plexi, which are prominent within the submucosa (Meissner's plexus) and between the inner and outer muscular layers of the tunica muscularis (Auerbach's plexus).

Need-to-know

- The appearance of the large intestine in tissue section varies with the fixation method, presence of fecal material, and bowel distension.
- The regions of the rodent large intestine can be distinguished histologically, whereas human colonic regions are indistinguishable.

Feces are often present in sections of rodent colon and consist of plant material, sloughed enterocytes, bacteria, variable protozoa, and, rarely, fragments of bone and skeletal muscle (Fig. 12.10). In conventionally housed, nonspecific pathogen free (non-SPF) animals, cross sections of rodent pinworms *Aspiculuris tetraptera* and *Syphacia obvelata* may be seen, although they are excluded from most rodent research colonies. Protozoa including ciliates and flagellates such as *Spironucleus muris* and *Trichomonas muris* are often present in the

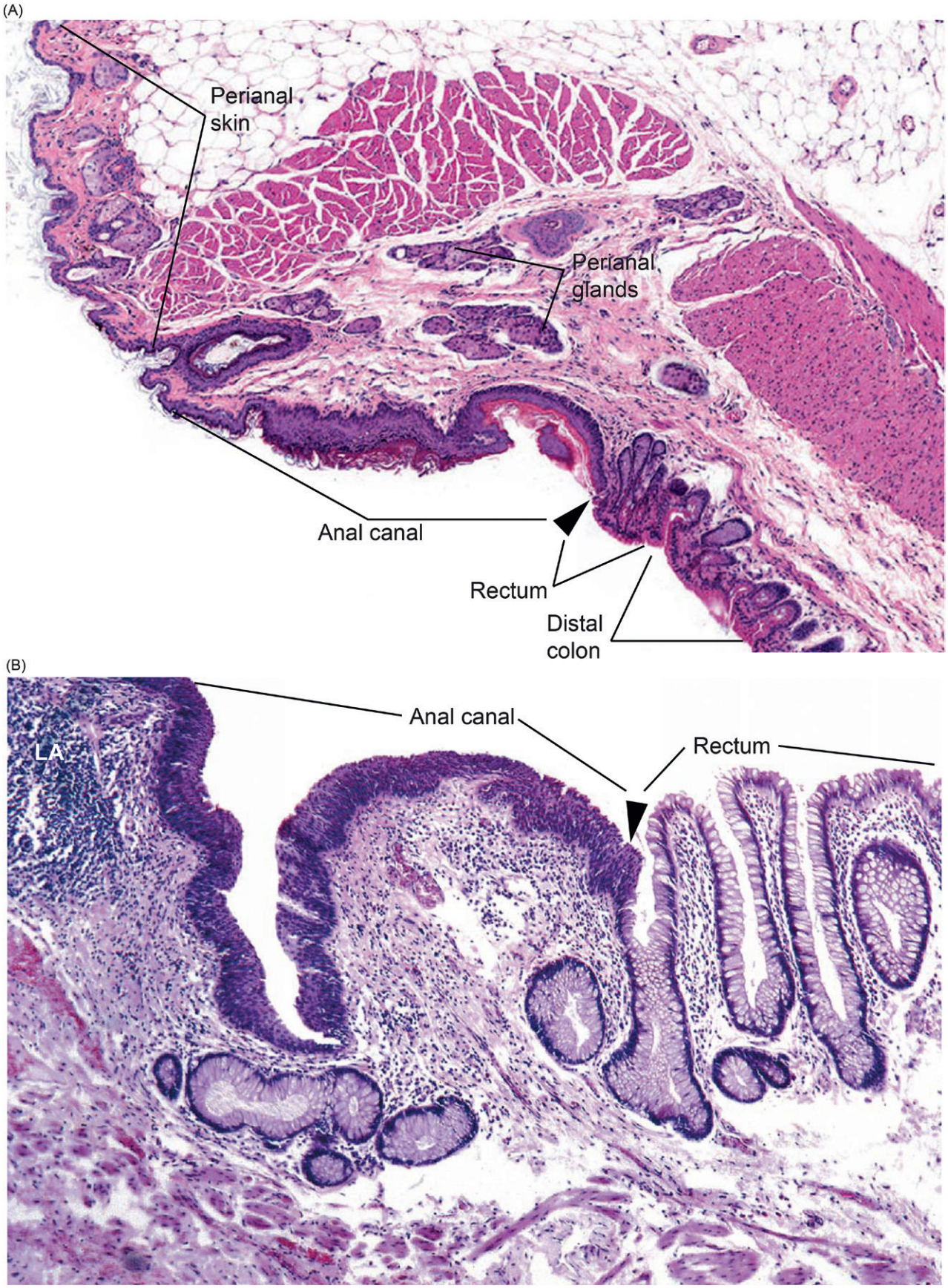

FIGURE 12.11 Anorectal junction. (A) Rodent (mouse) anorectal junction. An abrupt transition occurs from the colonic and rectal glandular mucosa to the keratinized stratified squamous epithelium of the anal canal (arrowhead). Circumanal sebaceous (perianal) glands are present beneath the anal epithelium. Image courtesy of Dr. J. M. Ward. (B) Human anorectal junction. An abrupt transition (arrowhead) occurs from surface and crypts lined by simple columnar (right) to stratified columnar (left) epithelium at the pectinate (dentate) line. This stratified columnar epithelium rapidly changes to the nonkeratinized stratified squamous epithelium lining the anal canal. Mucus-secreting goblet cells predominate on the rectal mucosal surface and in rectal crypts. Highly cellular lamina propria under the epithelium contains lymphoid aggregates (LA). Source: Reprinted from Ovalle WK and Nahirney JC: *Netter's essential histology*, 2013, with permission from © Elsevier, www.netterimages.com.

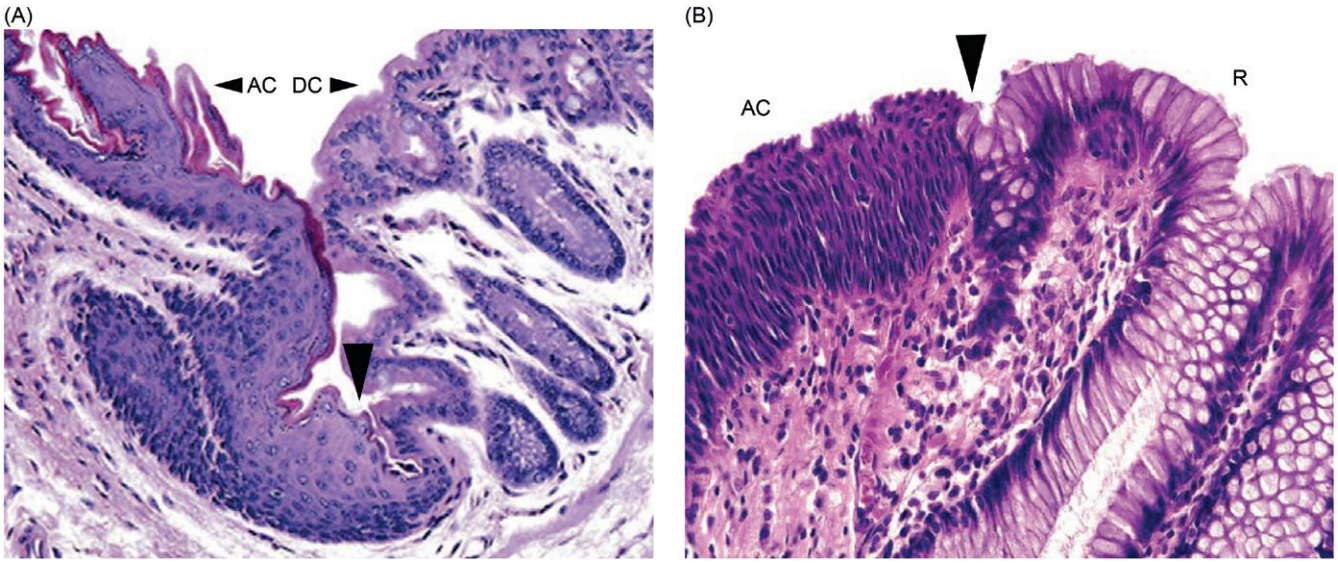

FIGURE 12.12 Higher magnification of the anorectal junction. (A) Rodent (mouse) anorectal junction. An abrupt transition (larger arrowhead) occurs from simple columnar (right) to stratified squamous (left) epithelium. There is no columnar epithelial transition zone, and the anal canal mucosa is keratinized squamous epithelium. Image courtesy of Dr. J. M. Ward. (B) Human anorectal junction. An abrupt transition (arrowhead) occurs from rectal simple columnar (right) to anal canal stratified columnar (left) epithelium at the pectinate (dentate) line. Developmentally, this line represents the hindgut-proctodeum junction. Anal canal (AC) and rectum (R) are indicated. Source: Reprinted from *Netter's essential histology*, Ovalle, W.K., and Nahirney, J.C. 2013, with permission from © Elsevier, www.netterimages.com.

Need-to-know

- Prolapse can lead to severe mucosal hyperplasia, subsequent mucosal herniation, and fibroplasias that can mimic invasive carcinoma.
- The rodent anorectal junction has no stratified columnar epithelium, and the rodent anal canal is lined by keratinized stratified squamous epithelium.
- The human anal canal is lined by nonkeratinized stratified squamous epithelium.

gastrointestinal tract and are not excluded in most rodent research colonies. The ileum may contain large segmented filamentous bacteria (SFB) adhered to the tips of the villi (see Chapter 11: Upper Gastrointestinal Tract). Most protozoa and SFB are considered nonpathogenic commensals except in certain circumstances. The microflora of mice is highly dependent on husbandry, pathogen status, genotype, and diet. For example, immunocompromised mice often have a bloom of protozoal flagellates and ciliates, whereas mice fed a high-fat diet will have a reduction in plant material. Hair fragments and skeletal muscle may also be present as a result of normal grooming, excessive grooming (barbering), or fighting.

In rodents, the rectum is short with an abrupt transition from the rectal crypt containing glandular mucosa to the squamous mucosa of the anal canal (Figs. 12.11 and 12.12). Unlike humans, rodents have no transitional zone of stratified columnar epithelium; rectal mucosa is indistinguishable from distal colon (Figs. 12.11 and 12.12). In humans, the distal third of the rectum is covered by adventitia, fascia, and fat, rather than mesothelium. The human rectum terminates at the pectinate (or dentate) line, becoming the anal canal, which in all three species is lined by squamous epithelium. In humans, the "anatomical anal canal" is 2 or 3 cm long and includes only squamous mucosa, whereas the "surgical anal canal" is 4–5 cm long and also contains 5–10 glandular mucosal folds known as the anal columns of Morgagni, giving the anorectal mucosal junction a serrated appearance called the pectinate (or dentate) line (Figs. 12.5, 12.6, 12.11, and 12.12). Rodents have large modified sebaceous glands in the zone surrounding the anus, whereas humans have large apocrine sweat glands present within the dermis of the skin adjacent to the anus; both are known as circumanal glands.

Gut-Associated Lymphoid Tissue

GROSS ANATOMY

In rodents, GALT is present in the colon principally at the narrow apical tip of the cecum (Fig. 12.7). GALT is grossly visible throughout the entire gastrointestinal tract, most prominently within the small intestinal antimesenteric border. Rodent GALT is also found scattered throughout the colon within the lamina propria and submucosa as smaller crytopatches and isolated lymphoid follicles (see also Chapter 11, Upper Gastorintestinal Tract, and Further Reading).

HISTOLOGY

Lymphocytes are distributed diffusely through the lamina propria and occur as isolated lymphoid follicles. These follicles can occur within the lamina propria and submucosa or can extend from the lamina propria through the muscularis mucosae and into the underlying submucosa. The largest follicles, called lymphoglandular complexes or lymphoid patches, may be visible macroscopically and are typically located at the cecal tip. Smaller aggregates, visible microscopically, include cryptopatches and isolated lymphoid follicles (Figs. 12.7, 12.8, and 12.10). For additional information, see Chapter 11, Upper Gastrointestinal Tract, and Further Reading (below).

FURTHER READING

Boivin GP, Washington K, Yang K, et al: Pathology of mouse models of intestinal cancer: consensus report and recommendations. *Gastroenterology* 124:762–777, 2003.

Cesta M: Normal structure, function and histology of mucosa-associated lymphoid tissue. *Toxicol Pathol* 34:599–608, 2006.

Hamilton SR: Structure of the colon. *Scand J Gastroenterol* 19:13–23, 1984.

Kararli TT: Comparison of the gastrointestinal anatomy, physiology, and biochemistry of humans and commonly used laboratory animals. *Biopharm Drug Dispos* 16(5): 351–380, 1995.

Kenig J, Richter P: Definition of the rectum and level of the peritoneal reflection—still a matter of debate? *Wideochir Inne Tech Maloinwazyjne* 8(3):183–186. 2013.

Levine DS, Haggitt RC: Colon. In Sternberg SS, editor: Histology for pathologists, ed 2, Philadelphia, PA, 1997, Lippincott-Raven, pp 519–550.

Maronpot RR, Boorman GA, Gaul BW, editors: *Pathology of the mouse: reference and atlas.*, Vienna, IL, 1999, Cache River Press.

Moolenbeek C, Ruitenberg EJ: The "Swiss roll": a simple technique for histological studies of the rodent intestine. *Lab Anim* 15:57–59, 1981.

Mowat AM, Agace WW: Regional specialization within the intestinal immune system. *Nat Rev Immunol.* 14(10): 667–685, 2014.

Neutra MR, Padykula HA: The gastrointestinal tract. In Weiss L, editor: Modern concepts of gastrointestinal histology, New York, 1984, Elsevier, pp 696–702.

Ovalle WK, Nahirney PC, Netter FH: Netter's Essential Histology, 2013, Elsevier Saunders.

Percy D, Barthold S: Pathology of laboratory rodents & rabbits, ed 4, Ames, IA, New York, 2016, Wiley.

RENI Registry Nomenclature Information System. Revised guides for organ sampling and trimming in rats and mice. http://reni.item.fraunhofer.de/reni/trimming.

Rudling R, Hassan AB, Kitau J, editors: A simple device to rapidly prepare whole mounts of mouse intestine. *Cell Proliferation* 39:415–420, 2006.

Shamsuddin AM, Phelps PC, Trump BF: Human large intestinal epithelium: light microscopy, histochemistry, and ultrastructure. *Hum Pathol* 13:790–803, 1982.

Scudamore C: A practical guide to the histology of the mouse, New York, 2013, Wiley.

Suttie AW, Leininger JR, Bradley AE: Boorman's pathology of the rat: reference and atlas, ed 2, New York, 2017, Academic Press.

Treuting PM, Clifford CB, Sellers RS, editors: Of mice and microflora: considerations for genetically engineered mice. *Vet Pathol* 49(1):44–63, 2012.

Young B, Lowe JS, Stevens A, editors: Wheater's functional histology: a text and colour atlas, ed 5, Philadelphia, PA, 2006, Churchill Livingstone.

Ward JM, Maronpot RR, Sundberg JP: Pathology of genetically engineered mice, Ames, IA, 2000, Iowa State University Press.

HEPATOBILIARY SYSTEM 13

ARLIN B. ROGERS
Tufts University, North Grafton, MA, United States

RENEE Z. DINTZIS
Johns Hopkins School of Medicine, Baltimore, MD, United States

Introduction

The liver is a regulatory center for nutrient processing, protein production, energy homeostasis, and detoxification. Nutrients are collected from blood arriving from the gastrointestinal tract via the portal vein, while toxins from intestinal bacteria and other sources are cleared. The rodent liver, which comprises a greater percentage of total body mass than human, spans the subdiaphragmatic space; in contrast, the human liver is limited to the right upper quadrant of the abdomen (Table 13.1). The rodent liver has a relatively smooth, uninterrupted surface, while the human liver is traversed and suspended by thick surface ligaments. Lobe patterns also differ between species. However, functional lobules are highly conserved in structure. In all three species, mixed arterial and portal venous blood enters the lobule through portal triads (which actually are tetrads consisting of arterioles, venules, bile ductules, and often-neglected lymphatics). Nutrients and macromolecules are freely exchanged between hepatocytes and plasma across sinusoids lined by fenestrated endothelium, while resident cells including hepatic stellate cells, Küpffer cell macrophages, and T and NK cells maintain immune surveillance. Physiologic function between the three species is similar, although some key differences are reflected at the microscopic level (Table 13.1). Rodents rapidly store dietary glucose from a recently ingested meal as glycogen in centrilobular hepatocytes. This increases cytoplasmic osmotic potential, resulting in increased water uptake and cytoplasmic clearing producing a wispy eosinophilic network. This normal response to feeding is sometimes referred to as "hydropic degeneration" or "cloudy swelling." Differences in molecular processing and detoxification also may manifest at the morphologic level. For example, mice challenged with compounds metabolized via peroxisome proliferator-activated receptor-α are highly susceptible to the formation of liver tumors, whereas humans routinely take PPAR-α agonists to improve lipid profiles with few untoward side effects. At the structural level, rodent hepatocytes may present as a homogeneous field, especially in midzonal and centrilobular areas of the mouse whereas, the human liver exhibits distinct hepatocyte cords one cell thick from portal triad to centrilobular vein. Compared with humans, the rodent liver has much less discernible collagen and other connective tissues. In response to chronic injury, bridging cords of collagen and nodular regeneration characteristic of cirrhosis are readily apparent in the human liver and to a lesser extent in the rat, but rarely occur in the mouse despite enthusiastic claims of "cirrhosis." Indeed, special stains such as picrosirius red often are required to

Comparative Anatomy and Histology. DOI: http://dx.doi.org/10.1016/B978-0-12-802900-8.00013-0
© 2018 Elsevier Inc. All rights reserved.

TABLE 13.1 Liver and Gallbladder

Feature	Rodent		Human
	Mouse	Rat	
Gross			
Location	Subdiaphragmatic; spans entire cranial abdomen	Similar to mouse	Upper R abdominal quadrant
Liver lobes	4: Median, L (largest), R (bisected), caudate	4: Median (right wing larger), L, R (bisected), caudate	4: R (largest), L, caudate, quadrate
Gallbladder	Protrudes from central isthmus of medial lobe	Not present	Beneath R lobe
Ligaments	Not apparent	Not apparent	Prominent
Histologic			
Hepatic plates	Not apparent; generally most prominent in periportal and midzonal regions (acinar zones 1 and 2)	Distinct single-cell	Similar to rat
Portal triads	Larger triads apparent, small ones often not apparent	More distinct than mouse	All sizes are apparent
Bi- and multinuclear hepatocytes	Can account for 25% of cells	Similar to mouse	Similar to rodent
Cytoplasmic clearing (hydropic degeneration, cloudy swelling)	Routine after meal; most evident in centrilobular hepatocytes	Uniformly stained from portal to central regions	Uncommon
Collagen in and between triads	Not prominent even in disease; special stains required	More prominent than in mouse; may be seen with H&E in portal region	More prominent than in rodent; distinct on H&E in portal regions
Sinusoid structure	Fenestrated and discontinuous	Similar to mouse	Similar to rodent
Küpffer cells	15% of total liver cells	Similar to mouse	Similar to rodent
Hepatic stellate (Ito) cells	Present in sinusoids	Similar to mouse	Similar to rodent
Bile canaliculi	Not easily detectable in normal liver on H&E	Similar to mouse	Similar to rodent

detect fine collagen fibrils in the injured mouse liver. These differences must be borne in mind when using mice as models of drug-induced liver injury. Bile salt composition is species-specific. Mice and humans have a gallbladder, whereas the rat lacks this structure without apparent harm. Overall, similarities in structure and function between the three species far outweigh the differences, and rodents remain the most widely applied laboratory models of human hepatobiliary injury and disease.

Liver

Gross Anatomy

Rodent liver weights vary by species and strain but typically fall in the 2–3 g range (3–5% body weight, BW) in mice, and 4–5 g range (2–3% BW) in rats. As a percentage of total body mass, the mouse liver is more prominent than that of rats or humans. This is reflected by the larger proportional volume of abdominal cavity occupied by the liver in mice. In rodents, the liver spans most or all of the subdiaphragmatic region, whereas in humans it is restricted to the right superior (cranial) abdominal quadrant (Fig. 13.1). Abdominal ligaments that traverse and distinctly delineate lobes of the human liver are not evident in rodents. The four lobes of the rodent liver are right, median, left, and caudate (Fig. 13.2A and B). Older literature designates right and left lobes as right lateral and left lateral, but these redundant designations are omitted in more recent classifications. In rodents, the right lobe has a transverse septum that nearly bisects it, leading to subclassification by some of right cranial (anterior) and right caudal (posterior) lobes. The median lobe lies most ventrally and is the first one encountered when the abdominal cavity is approached from

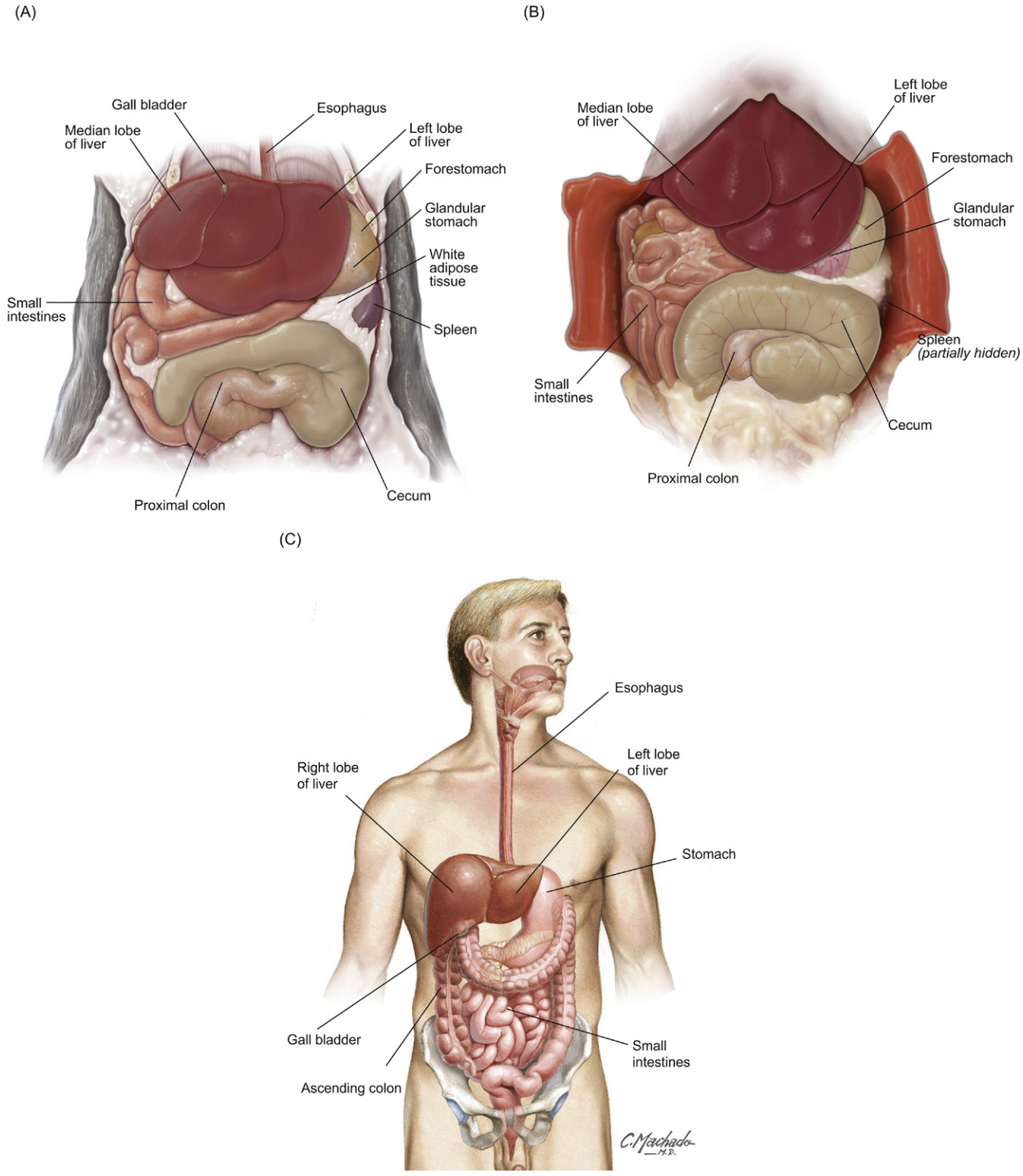

FIGURE 13.1 Regional anatomy of the liver. (A) Mouse and (B) rat. The rodent liver spans the entire subdiaphramatic space in the cranial abdomen, and does not have prominent surface ligaments. (C) Human. The human liver occupies the upper right quadrant of the abdominal cavity, prominently septated near the left lobe by the falciform ligament.

Need-to-know

- The human liver is in the upper right abdominal quadrant and is smaller as a percentage of total body mass than the rodent.
- Mouse and rat livers occupy the entire subdiaphragmatic region.

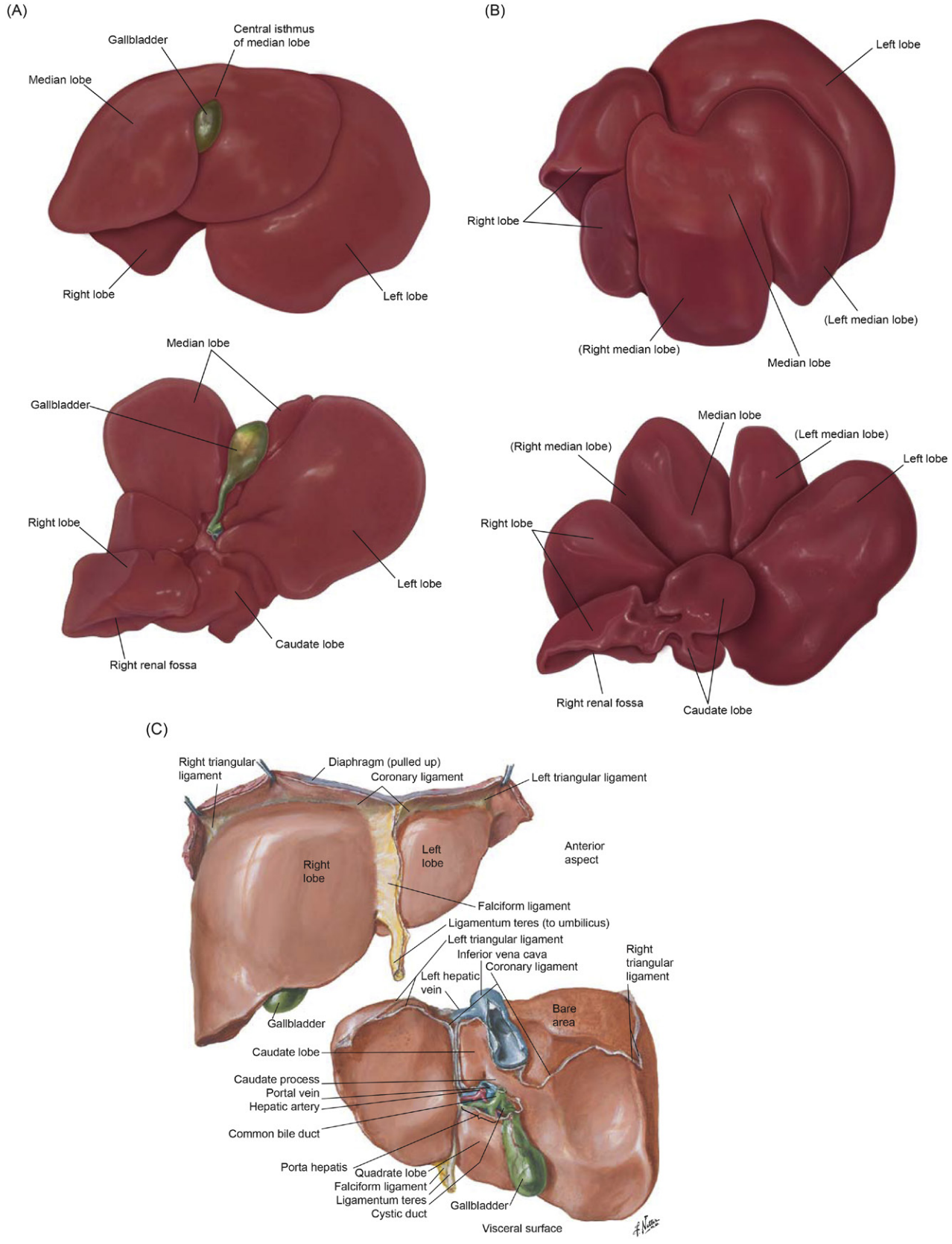

FIGURE 13.2 Gross anatomy of the liver and gallbladder. (A) The mouse liver has four lobes: Left (largest), right (hemisected), median, and caudate. The gallbladder fundus protrudes below the central isthmus of the medial lobe when viewed from the usual ventral perspective. (B) The rat liver also has four lobes: Left, right (hemisected), median, and caudate. The right wing of the medial lobe is larger than the left. (C) The human liver also has four lobes: right (largest), left, caudate, quadrate, with several prominent surface-associated ligaments.

Need-to-know

- The mouse gallbladder protrudes below the central isthmus of the median lobe.
- The rat does not have a gallbladder.
- The human liver is marked by numerous prominent surface ligaments.

the usual ventral aspect. In the mouse, it has two symmetrical pyriform wings connected by a narrow central isthmus beneath, which protrudes the blind ventral sac of the gallbladder (Fig. 13.2A). In the rat, the right wing of the median lobe is larger than the left and there is no gallbladder (Fig. 13.2B). The left lobe is the largest and is a frequent site of sampling for histology in the mouse, whereas in the rat it comprises less total hepatic volume. The caudate lobe is small and has two distinct ear-shaped segments that are best viewed by simultaneously reflecting the main body of the liver cranially and the stomach caudally during prosection. In the rat, caudate lobe wings sometimes are subclassified as anterior and posterior.

The human liver weighs approximately 1500 g and comprises ~2% of total BW, making it the largest gland in the body. It is located below the diaphragm on the right side of the abdominal cavity (Fig. 13.1C). It has four incompletely separated lobes. On the anterior surface are the large right and smaller left lobes; on the visceral surface, the upper caudate, and the lower quadrate lobes are exposed, situated between the right and left lobes (Fig. 13.2C). Separating the quadrate lobe from the caudate lobe is the porta hepatis, or liver hilus, the region where the portal vein and hepatic artery enter the liver, and the hepatic duct exits. Hepatic veins, carrying blood leaving the liver, emerge from the caudate lobe and empty almost directly into the inferior vena cava. This attachment of the hepatic veins to the inferior vena cava helps to secure the liver position in the upper abdominal cavity. The human liver is surrounded by a collagenous capsule, known as Glisson's capsule, and the capsular connective tissue becomes continuous with the internal stroma of the liver at the hilus. The peritoneal ligaments are recognizable surface landmarks of the liver. The most prominent of these are the falciform ligament, between the right and left lobes, and the coronary ligament, which attaches the liver to the inferior surface of the diaphragm. The gallbladder is present on the undersurface of the right liver lobe.

HISTOLOGY

Hepatic microscopic architecture in all three species can be described in the context of "classical liver lobules." These are polygonal structures with portal tracts at the periphery circumscribing a central vein. The human liver is estimated to contain approximately 1 million classical hepatic lobules.

Plates of hepatocytes are supported by reticulin and other stromal elements and appear to be radiating out from the central artery; blood and bile travel in opposite directions (Fig. 13.3). Mixed arterial and venous blood moves from portal regions to the central vein through sinusoids, whereas bile secreted into canaliculi is directed to portal regions by specialized hepatocellular microvilli. Hepatic cords or plates comprise columns of hepatocytes extending from the portal region to central vein. The spaces between the plates contain the liver sinusoids, or "capillaries" of the liver. The walls of sinusoids are reduced to a bare minimum, with fenestrations and large discontinuities between the endothelial cells. Between the sinusoid and the liver cell is the pericapillary space of Disse, where blood plasma is in direct contact with the hepatocytes, permitting free exchange of macromolecules.

Hepatic lobular architecture is similar across species, with stromal support by reticulin and countercurrent bile flow relative to blood flow (Fig. 13.3). Due to their smaller size and decreased amount of connective tissue, some rodent portal regions may be overlooked in histologic sections, especially in the mouse (Fig. 13.4). Human hepatic portal structures are supported by a greater amount of collagen, as well as thin reticular fibers (consisting of type III collagen), that form a loose network supporting the sinusoids. Due to their size and associated connective tissue, portal regions in the human liver are readily apparent even at low magnification.

The Rappaport system of lobule division from the periportal (acinar zone 1) to midzonal (acinar zone 2) to centrilobular (acinar zone 3) regions is based on hepatocellular enzymatic function and

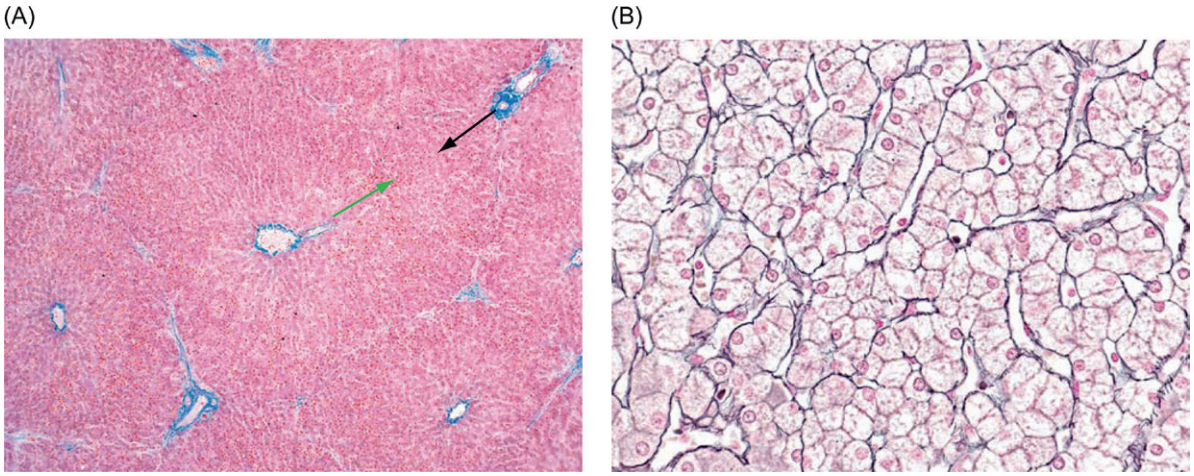

FIGURE 13.3 Human hepatic lobules and cords. (A) Azocarmine/aniline blue stain of human liver highlighting lobules bounded by connective tissue (blue). Black arrow shows direction of blood flow; green arrow shows direction of bile flow. (B) Hepatic plates (or cords) are supported by reticulin (black) and separated by sinusoids lined with fenestrated endothelium.

Need-to-know

- In all three species, blood and bile flow in opposite diections through the hepatic lobule.
- Hepatic plates, in all three species, are columns of hepatocytes extending from the portal regions to central veins and are lined by porous sinusoidal endothelium.

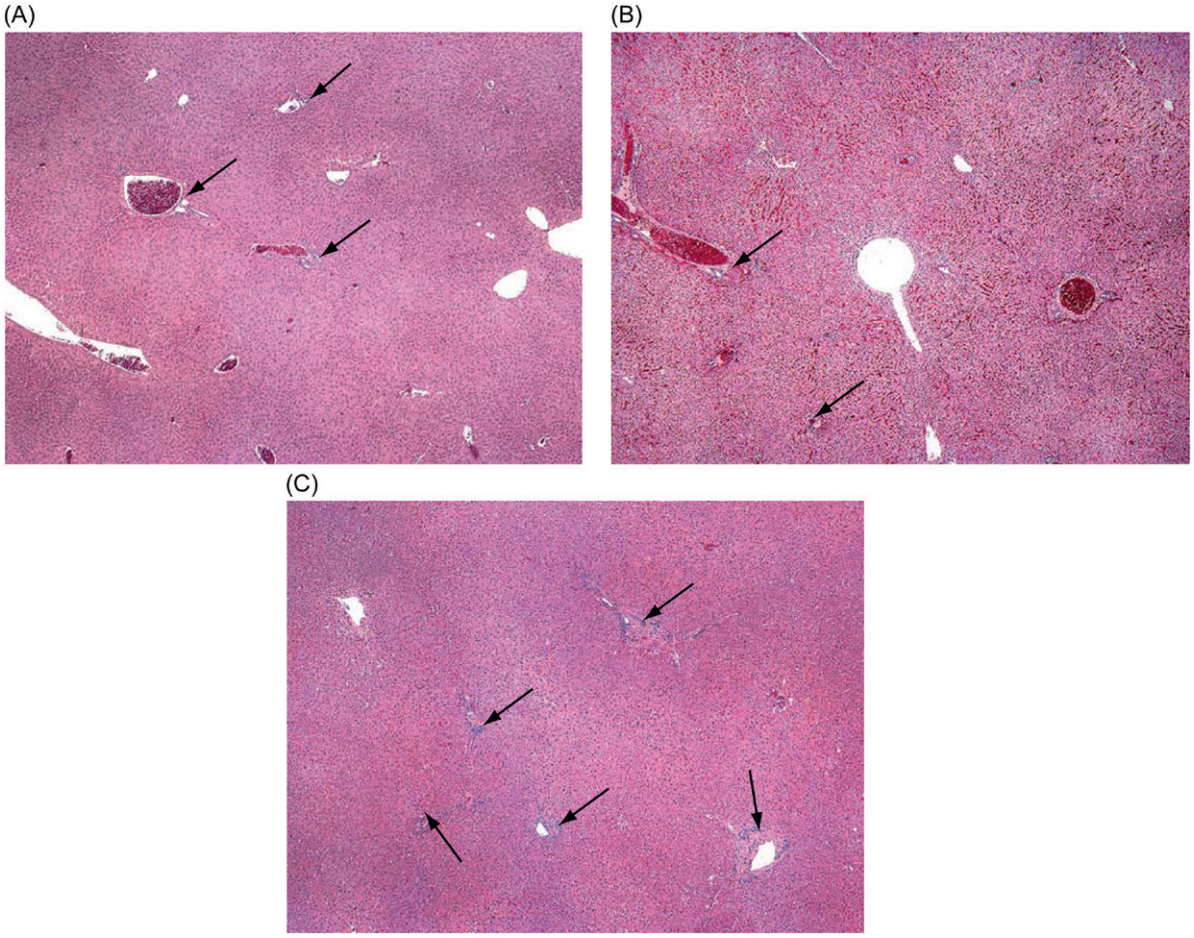

FIGURE 13.4 Portal regions (arrows) at low magnification. (A) Mouse portal regions are less apparent than rat (see B) at the same magnification. The absence of glycogen-associated cytoplasmic clearing in centrilobular hepatocytes indicates this animal did not eat a recent meal. (B) In rat portal regions, hepatocytes stain slightly paler than human. However, postprandial glycogen clearing is not as prominent as in the mouse. (C) Human portal regions are readily identified at low magnification (×4 objective). Uniform eosinophilic staining of hepatocytes is normal.

Need-to-know

- Portal units may be difficult to discern in the mouse; lobular organization may be best recognized by the pale staining of centrilobular hepatocytes in animals following a recent meal.
- Portal regions are larger and more readily identified at low magnification in the human liver.

blood oxygenation. It is equivalent between all three species (Fig. 13.5). Although often referred to as "portal triads," in all three species, the portal regions actually comprise four components: arterioles, venules, bile ductules, and lymphatics (Fig. 13.6). Single-cell hepatic plates extending the length of the lobule are typical in the rat and in humans, whereas in mice hepatocytes may swell and compress together after a meal due to glycogen-associated water imbibition. This results in loss of distinct cord delineation in the mouse, especially in the midzonal and centrilobular regions (Figs. 13.7 and 13.8). Indeed, clearly delineated single-cell hepatic cords across the entire length of the lobule may suggest anorexia or chronic disease in the mouse liver. In rats, single-celled plates are more common. In mice that have eaten a recent meal, lobular architecture may best be discerned by the staining pattern with H&E. Centrilobular hepatocytes will appear pale due to water imbibition in association with glycogen storage, whereas periportal hepatocytes will retain more homogeneous eosinophilic staining and cell separation. Rat hepatocytes stain more uniformly from portal to central regions than the mouse, and are often paler staining than human hepatocytes.

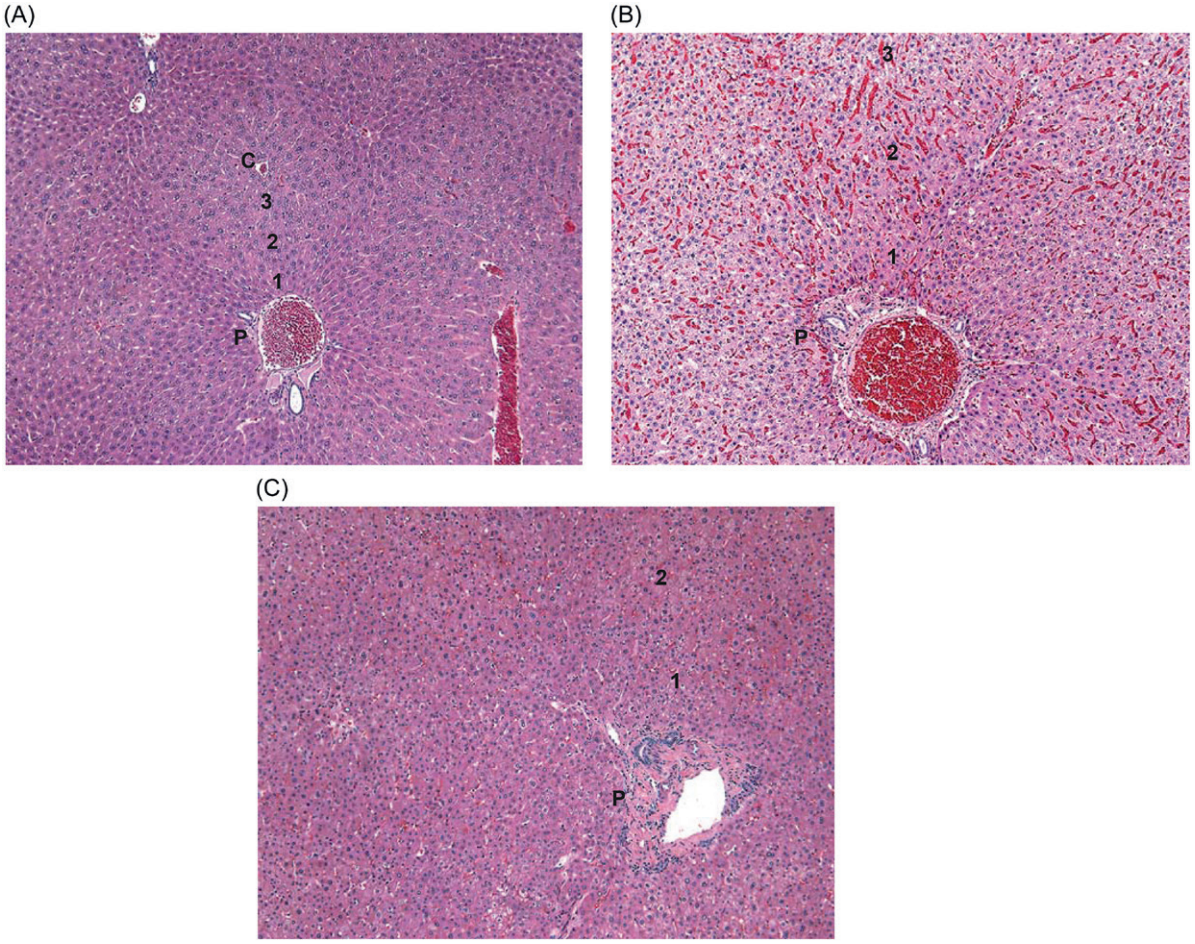

FIGURE 13.5 Lobules. (A) In the mouse lobule, multiple portal regions (P) and central veins (C) are evident at the same magnification. Note the transition of hepatocyte staining from dark to light across the periportal (1), midzonal (2), and centrilobular (3) regions due to glycogen accumulation and cytoplasmic clearing of centrilobular hepatocytes following a meal. (B) The rat liver has lobules intermediate in size between human and mouse, since glycogen storage following a meal does not result in as much hepatocyte clearing in the rat as it does the mouse. (C) In this higher magnification view of human liver, the portal region (P) is readily identified. Note the uniform staining of hepatocytes in 1 and 2.

Need-to-know

- Although individual cell sizes are the same, the rodent lobule is smaller than the human.
- Human portal regions have more abundant fibrous connective tissue than mice.

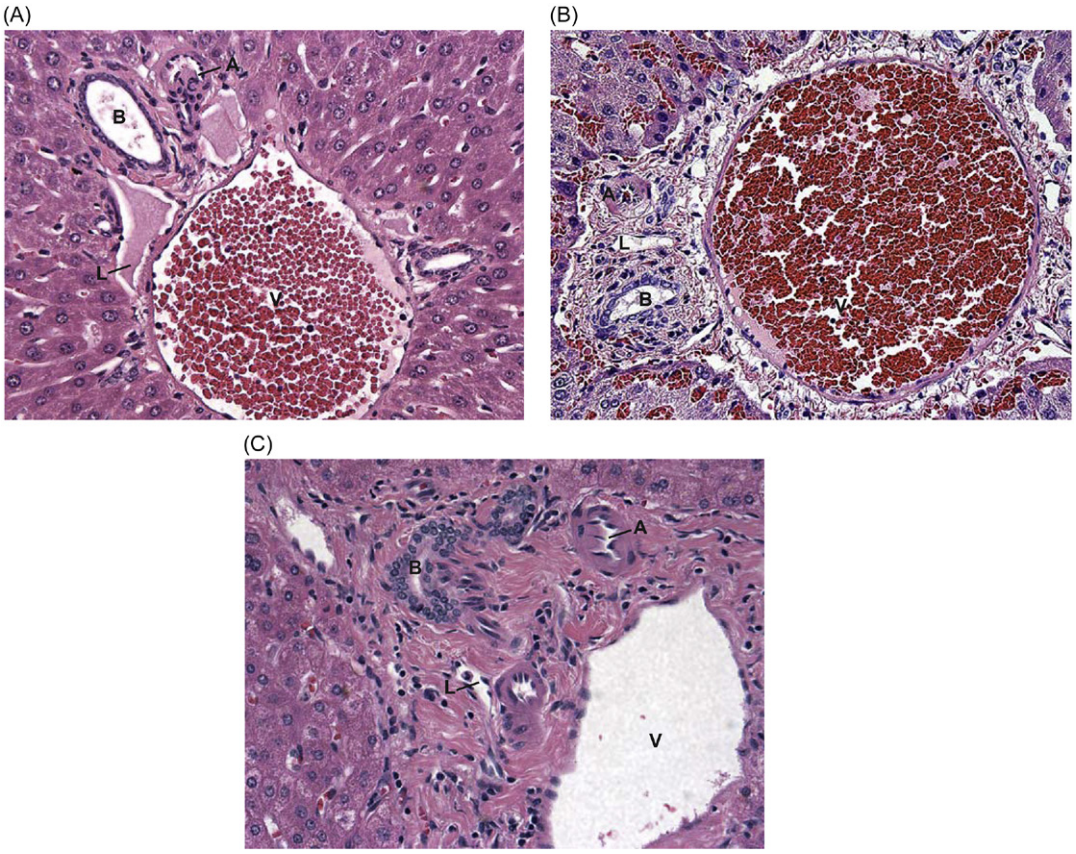

FIGURE 13.6 Portal region. Although frequently called the "portal triad," there are actually four components to the portal region: arterioles (A), venules (V), bile ductules (B), and lymphatics (L). (A) The four components in mouse; note the significantly lower amount of collagenous connective tissue compared with rat and human. (B) The rat has an intermediate amount of supporting collagen between the human and mouse. (C) Human. Note the dense connective tissue and scattered mononuclear cells.

Need-to-know

- Portal "triads" actually comprise four elements: arterioles, venules, bile ductules, and lymphatics.
- Human and rat portal regions have more associated collagen than mouse.

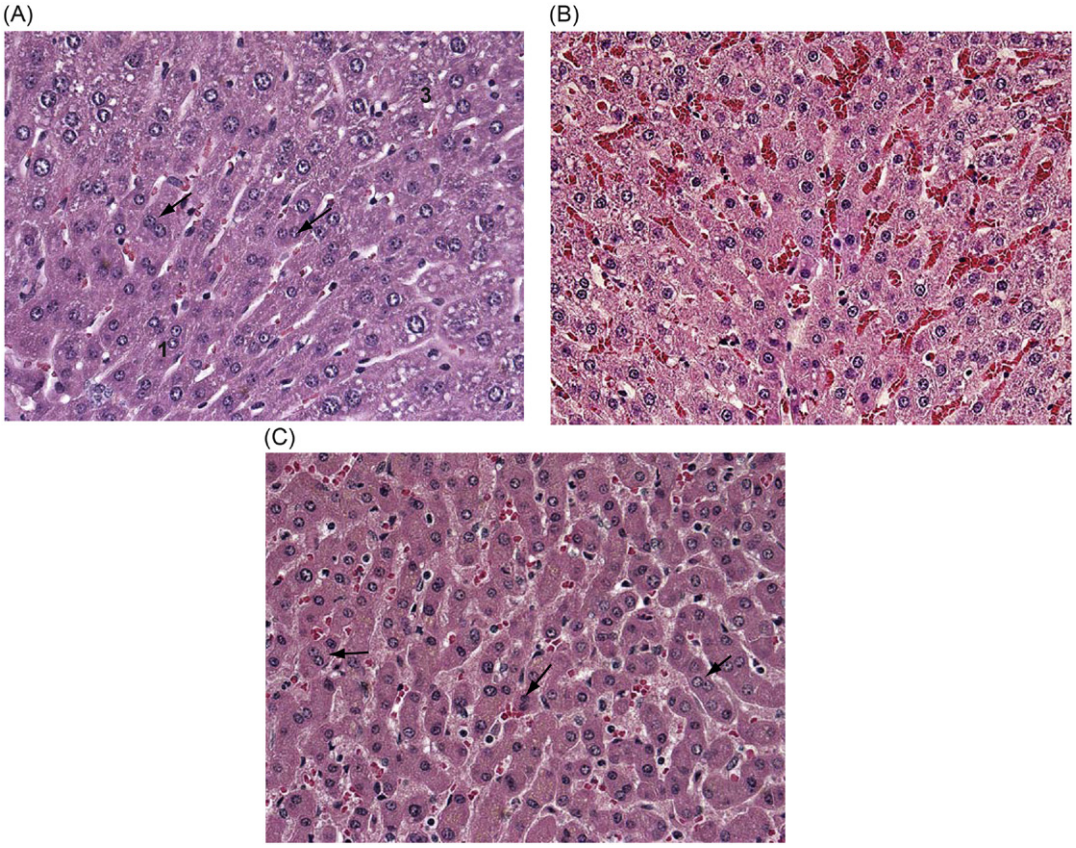

FIGURE 13.7 Midzonal region. (A) Mouse hepatic cords are less well defined than human, and hepatocyte staining in the centrilobular region is paler than the periportal region owing to centrilobular postprandial glycogen accumulation; binucleate cells (arrows) also are common. (B) Rat hepatocytes exhibit generally uniform staining across the regions like the human, although it is usually somewhat paler. (C) The human liver exhibits well-defined hepatic cords one cell thick, relatively uniform cell staining, and frequent binucleate hepatocytes (arrows).

Need-to-know

- Binucleate hepatocytes are common in all species.

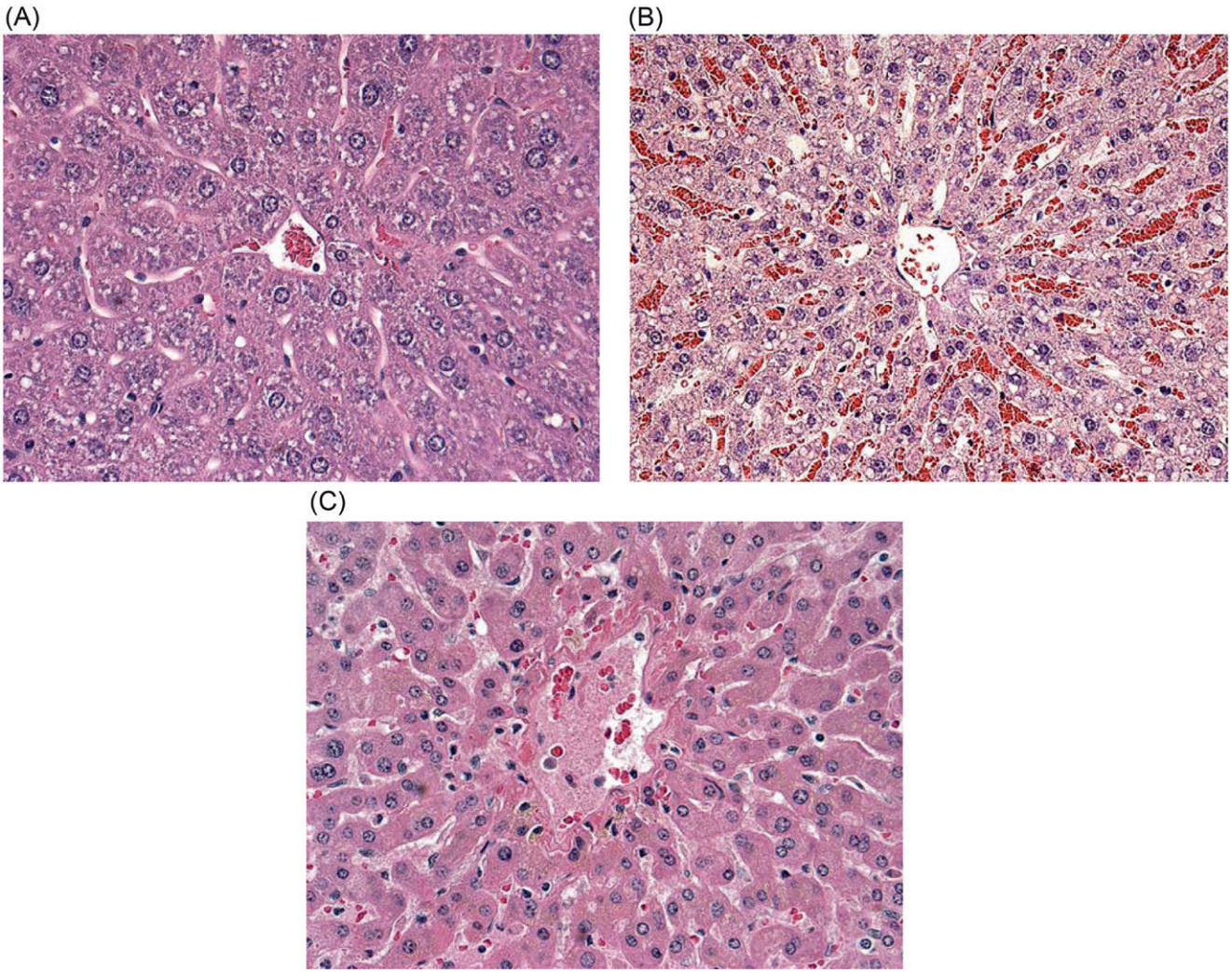

FIGURE 13.8 Centrilobular region. (A) Centrilobular mouse hepatocytes often exhibit a motheaten staining pattern due to normal postprandial glycogen storage; distinct cords are not as apparent as human. (B) Centrilobular rat hepatocytes exhibit uniform moderate-to-pale staining. Glycogen clearing is not as prominent as in the mouse. (C) Centrilobular hepatocytes in the human liver converge on the central vein, and generally retain distinct organization in cords.

Need-to-know

- Centrilobular mouse hepatocytes accumulate glycogen and water following a meal, resulting in pale irregular cytoplasmic staining. This is less apparent in rat.

In health, there is little difference in staining intensity between human hepatocytes in the periportal, midzonal, or centrilobular regions. Midzonal regions are comprised of parallel and interdigitating columns of hepatocytes. Centrilobular hepatocytes have the lowest oxygen tension and are a frequent target of oxidative and/or toxic injury, which may contribute to the increased amount of gold-brown lipofuscin. Lipofuscin, also called aging or wear-and-tear pigment, is composed of indigestible cell debris that accumulates over the years, is seen in all three species, and is more apparent in adult humans due to the longer human life span.

Although most hepatocytes have one nucleus, it is not uncommon to find binucleated and/or polyploidy cells in any given field in all three species (Fig. 13.7).

In all three species, resident macrophages known as Küpffer cells project into the sinusoid lumen. They constitute one of the principal filters for foreign particulate matter entering the liver, and make up about 15% of total liver cells. T cells and NK-T cells also are abundant in liver

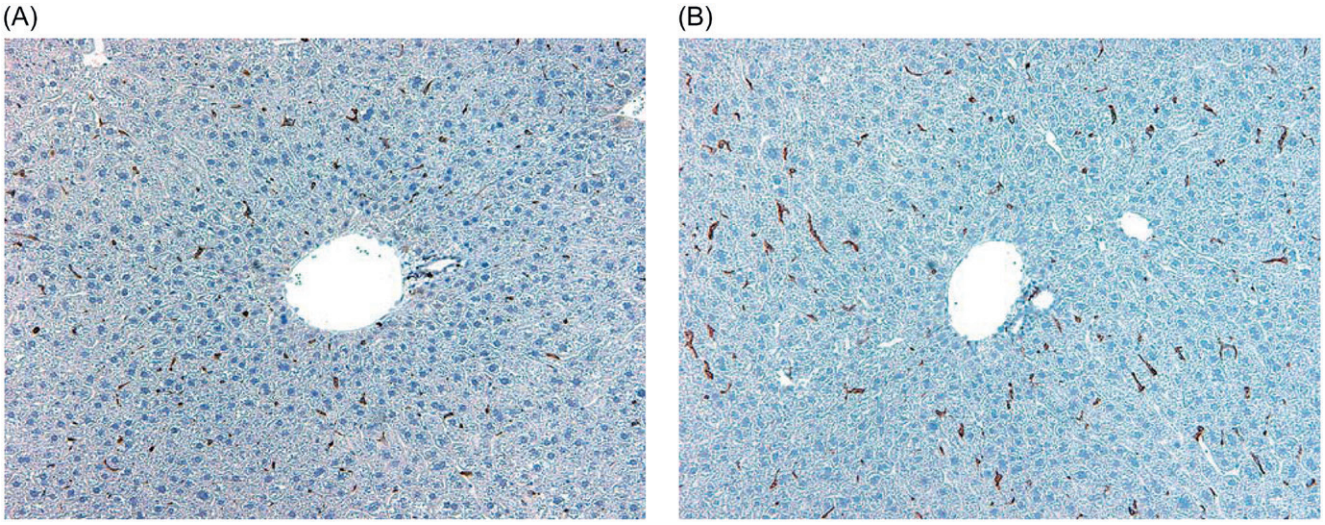

FIGURE 13.9 Immune cells of the rodent (mouse) liver. (A) CD3 IHC demonstrates many T and NK-T cells in normal mouse liver. (B) F4/80 IHC of mouse liver reveals sinusoid-associated resident macrophages (Küpffer cells).

sinusoids, reflecting the major role of this organ in immunosurveillance. Like Küpffer cells, $CD3^+$ T and NK-T cells require immunohistochemistry (IHC) for visualization (Fig. 13.9). The hepatic stellate cell, or Ito cell, which stores lipids and vitamin A in health and is involved in collagen induction in fibrosing liver diseases, also is present in the sinusoid and can be visualized by glial fibrillary acidic protein IHC.

Bile canaliculi are minute tubular spaces between liver cells in all three species, and receive the bile secreted by the hepatocyte. Their walls are lined by polarized hepatocyte plasma membranes enriched with bile exporters and microvilli that direct secretions toward portal outflow tracts. Tight junctions prevent bile leakage into the hepatic parenchyma. The canaliculi traverse the lobule and eventually empty into tiny ducts called canals of Hering, which deliver the bile to the bile ducts located in the portal tracts at the periphery of the lobule countercurrent to the flow of blood. Canals of Hering also are the site of indistinct progenitor or "hepatic stem" cells that may proliferate in response to injury. Bile ductules join in progressively larger interlobular bile ducts, eventually forming left and right hepatic ducts that empty into the mouse and human gallbladder.

Need-to-know

- In all three species, the liver has a significant function in immunosurveillance.
- Resident nonhepatocyte cell populations in the liver of all three species include NK cells, T cells, NKT cells, MØ (Küpffer cells), and hepatic stellate (Ito) cells.

Gallbladder

The gallbladder protrudes from the central isthmus of the medial lobe of the liver in mice and is found beneath the right liver lobe in humans (Fig. 13.1). Rats do not have a gallbladder (Fig. 13.2). The gallbladder serves as a site of bile storage until expressing its contents through the common bile duct into the small intestine under the influence of the digestive enzyme cholecystikinin. The mouse gallbladder is similar to the human, except that there is less smooth muscle and connective tissue, and the surface epithelium is cuboidal rather than columnar (Fig. 13.10). The wall of the human gallbladder contains a readily apparent surface epithelium, lamina propria, muscularis, and serosa. The epithelium is simple columnar, and there is no muscularis mucosa or submucosa. The serosal coat is fairly thick. Diverticula, or invaginations of surface epithelium, sometimes extend quite deeply into the wall and can retain bacteria resulting in chronic inflammation (cholecystitis).

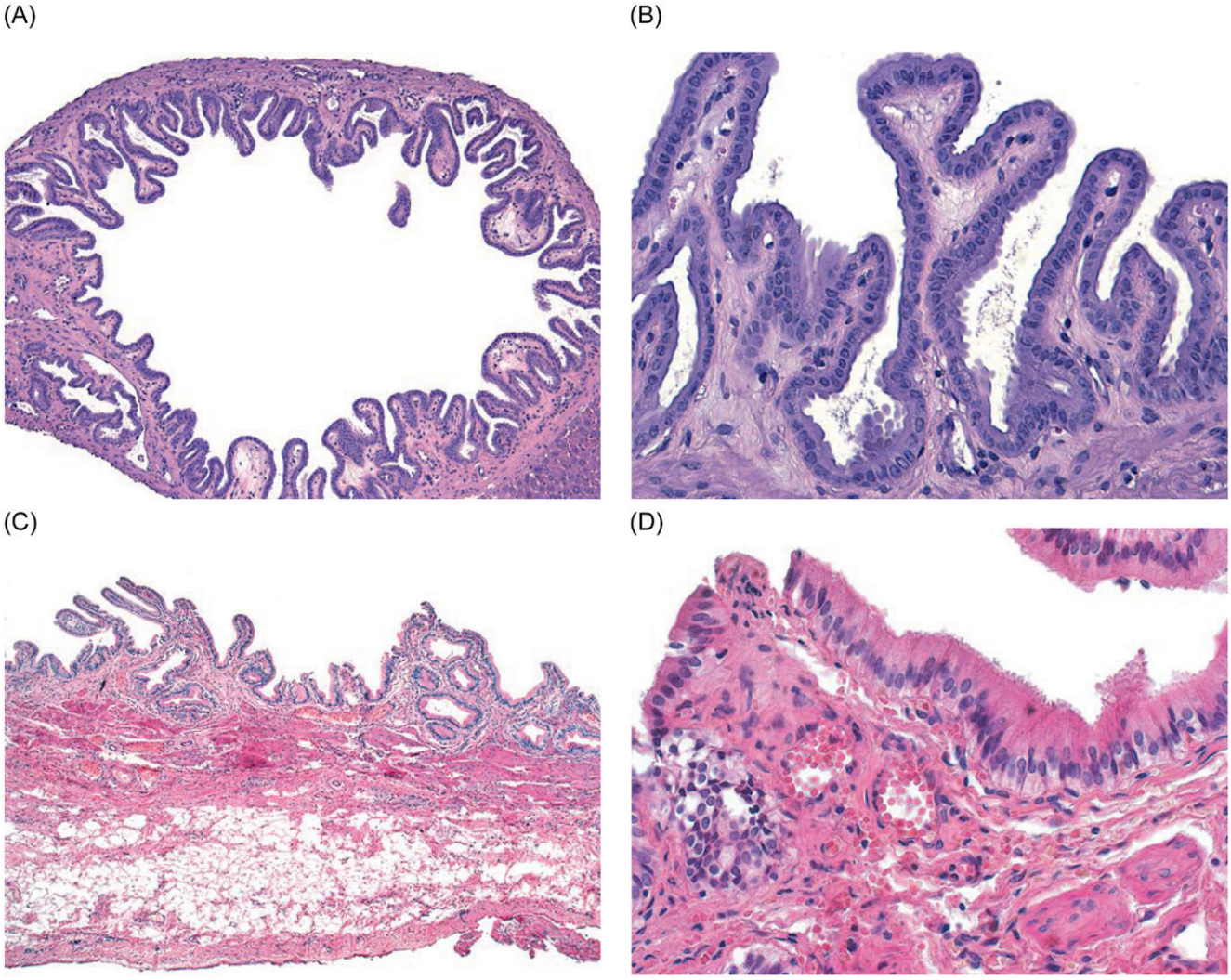

FIGURE 13.10 Gallbladder. (A) Low magnification view of mouse gallbladder; layers are the same as human, but with less smooth muscle and connective tissue. (B) Mouse gallbladder mucosa is lined by cuboidal-to-low columnar epithelium. (C) Human gallbladder with surface epithelium supported by lamina propria connective tissue, with subjacent submucosa, muscularis propria, and adventitia. (D) High magnification of human gallbladder mucosa lined by tall columnar epithelium.

Need-to-know

- The mouse gallbladder has scant stroma and the epithelium is cuboidal.
- The human gallbladder has abundant supporting stroma and columnar epithelium.

FURTHER READING

Burt AD, Portmann BC, Ferrell LD: *MacSween's pathology of the liver*, ed 5, Philadelphia, PA, 2007, Churchill Livingstone-Elsevier.

Friedman SL: Hepatic stellate cells: protean, multifunctional, and enigmatic cells of the liver. *Physiol Rev* 88:125–172, 2008.

Kumar V, Abbas AK, Fausto N: *Robbins and Cotran pathologic basis of disease*, Philadelphia, PA, 2005, Elsevier-Saunders.

Maronpot RR, Boorman GA, Gaul BW, editors: *Pathology of the mouse*, St. Louis, MO, 1999, Cache River Press.

Motta P, Muto M, Fujita T: *The liver: an atlas of scanning electron microscopy*, New York, 1978, Igaku-Shoin.

Ovalle WK, Nahirney PC: *Netter's essential histology*, Philadelphia, PA, 2008, Saunders-Elsevier.

Rogers AB, Houghton J: Helicobacter-based mouse models of digestive system carcinogenesis. *Methods Mol Biol* 511: 267–295, 2009.

Suttie AW, Leininger JR, Bradley AE: *Boorman's pathology of the rat*, ed 2, San Diego, CA, 2017, Academic Press.

Young B, Lowe JS, Stevens A, et al: *Wheater's functional histology*, Philadelphia, PA, 2006, Churchill Livingstone-Elsevier.

This page intentionally left blank

PANCREAS 14

DENNY LIGGITT AND SUZANNE M. DINTZIS
University of Washington School of Medicine, Seattle, WA, United States

Introduction

The pancreata of mice and rats (rodents) and humans have many more similarities than differences although much remains to be discovered and understood in all three species. A major structural difference between the species is that the rodent pancreas is locally dispersed throughout the mesentery adjacent to the duodenum while in humans the pancreas, while generally in the same location, is more compact. Other significant differences include the finding that the islets of Langerhans, the endocrine portion of the pancreas, are on average larger and mostly interlobular in rodents, compared to the smaller, mostly intralobular islets seen in humans. In addition, beta cells predominate in rodents, whereas in humans beta cells are fewer and alpha cells are more numerous than those in rodents. There are also distinct differences in the arrangement of the rodent and human pancreatic duct as it enters into the duodenum, as well as the blood vascular system and the course it takes to supply and exit the exocrine and endocrine portions of the pancreas.

Pancreas

Gross Anatomy

The pancreas is a relatively flat to slightly plump, white-to-pink colored organ that develops from an outgrowth of the primitive foregut and represents approximately 0.1% or less of an adult animal's body weight. It is a combined endocrine and exocrine gland in close physical association with the upper duodenum and adjacent tissues. During development, exocrine and endocrine elements are both derived from differentiation of duct epithelium. Depending on the species, the gross anatomical pattern of the pancreas presents as either a "mesenteric" or a "compact" type (Fig. 14.1). As implied by the name, the mesenteric pattern describes the pancreas's relatively diffuse dispersion within the duodenal mesentery. In this pattern, lobules and segments are separated, sometimes widely, by abundant mesenteric fat and stromal elements including lymphoid aggregates in rodents. This dispersion of pancreatic elements makes it difficult to accurately collect and weigh a complete mesenteric pancreas. This mesenteric pattern is present in the rabbit and in rodents in a

Comparative Anatomy and Histology. DOI: http://dx.doi.org/10.1016/B978-0-12-802900-8.00014-2
© 2018 Elsevier Inc. All rights reserved.

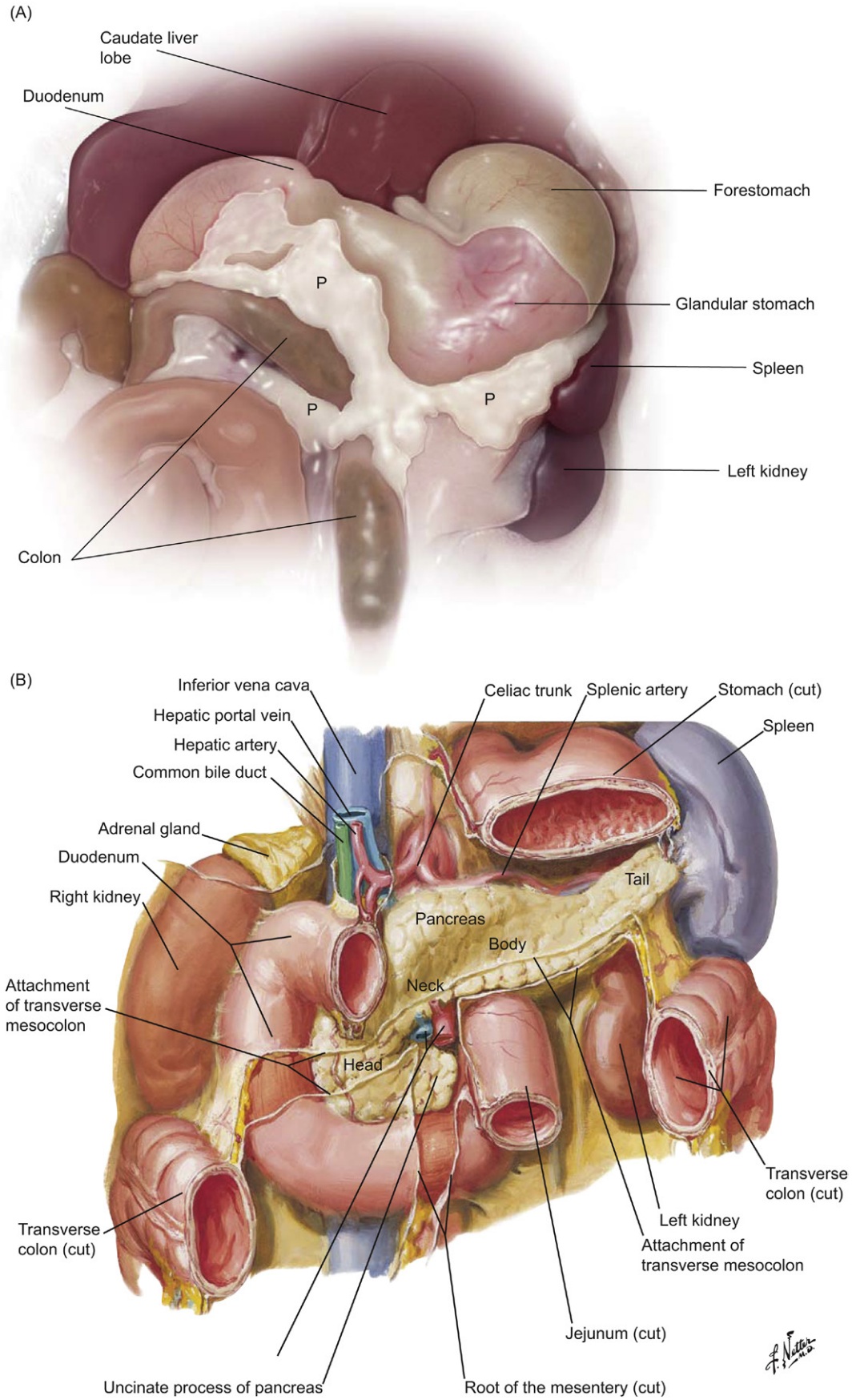

FIGURE 14.1 Regional anatomy of the pancreas. (A) Gross view of the mesenteric rodent (mouse) pancreas. The wide distribution of the pinkish white tissue demonstrates the diffuse nature and lack of distinction between adipose and pancreatic tissues. Distinct divisions are difficult to identify. (B) Gross view of the compact human pancreas shows distinct head, neck, body, and tail regions. Source: © Elsevier, Inc., www.netterimages.com.

TABLE 14.1 Pancreas

Feature	Rodent		Human
	Mouse	Rat	
Gross anatomic pattern	Mesenteric	Similar to mouse	Compact
Lobule size	Small	Similar to mouse	Large
Islet size (average diameter)	116 ± 80 μm	100–200 μm	50 ± 29 μm
Islet location	Unevenly distributed through organ; most interlobular	Similar to mouse	Evenly distributed through organ; most intralobular
Islet number	Proportional to body mass	Similar to mouse	Similar to mouse
Islet cells	Beta cells predominate (±75%), alpha cells lower (±18%); beta cells central, alpha and gamma cells peripheral	Similar to mouse but % varies based on anatomical region	Beta cells less dominant than mouse (±55%), alpha cells higher than mouse (±37%); islet cells scattered and randomly distributed along vessels
Pancreatic ducts	Primary duct joins bile duct prior to entry into duodenum; multiple accessory ducts are common	Similar to mouse	Primary duct joins bile duct at greater duodenal papillae; single accessory duct is common
Islet microvasculature	Blood vessels drain into both the insulo-acinar portal system and insulo-venous efferent system; in islets, basal lamina accompanies vessels only	Similar to mouse. Basal lamina status uncertain	Blood vessels primarily drain into the insulo-acinar portal system; in islets, basal lamina accompanies endocrine cells and vessels ("double" basement membrane)

slightly more compacted form where divisions can be recognized as duodenal, gastric, and splenic (the largest and most easily recognized) segments. In the typical compact presentation—which occurs in human, monkey, dog, and hamster—the organ is denser and more closely confined within the curve of the upper duodenum. This compact presentation permits distinct regions of the pancreas to be recognized more readily by the gross anatomic terms head, neck, body, and tail.

HISTOLOGY

Pancreata from rodents and humans share many histological and functional similarities, but also display some potentially important differences (Table 14.1). The pancreas is invested by a variably thin connective tissue capsule (Fig. 14.2) and divided into lobules, which are formed from dense accumulations of exocrine glands that often surround the islets. Individual lobules are defined by the thin connective tissue capsule extending into the parenchyma in the form of septa. These septa and associated interlobular connective tissues support blood and lymph vessels, nerves, ganglia, and pancreatic ducts. As animals normally age, septal, and parenchymal connective tissue increases, particularly as an accompaniment to spontaneously occurring focal duct dilation and acinar cell atrophy (Fig. 14.2E). Arteries that supply the pancreas divide into arterioles within the septal space and distribute to individual lobules similarly in rodents and humans. Lymphatics are not obvious in normal histologic preparations, but with ultrastructural studies they are shown to be more prominent and widely distributed in mice compared to rats and are little-examined in humans. The size of the lobules is roughly relative to the size of the species; hence, lobules are small in rodents and larger in humans. A similar size association does not exist with islets.

The exocrine portion of the pancreas consists of lobules formed from tightly packed clusters of branched, interdigitating compound tubuloacinar glands. The acini are groups of large pyramidal secretory epithelial cells that surround and define a lumen. The luminal orientation of acini will only occasionally be clearly recognizable (Fig. 14.3), due to the two-dimensional nature of histologic sections and the complexity of the acinar architecture. Acinar cells are attached at the luminal surface by apical tight junctions; at the basal surface, they are supported by a basal lamina. They have a basal-to-centrobasal nucleus and in rodents may have two nuclei. Acinar cells have prominent endoplasmic reticula and Golgi complexes, and their cytoplasm may contain large quantities of zymogen (secretory) granules

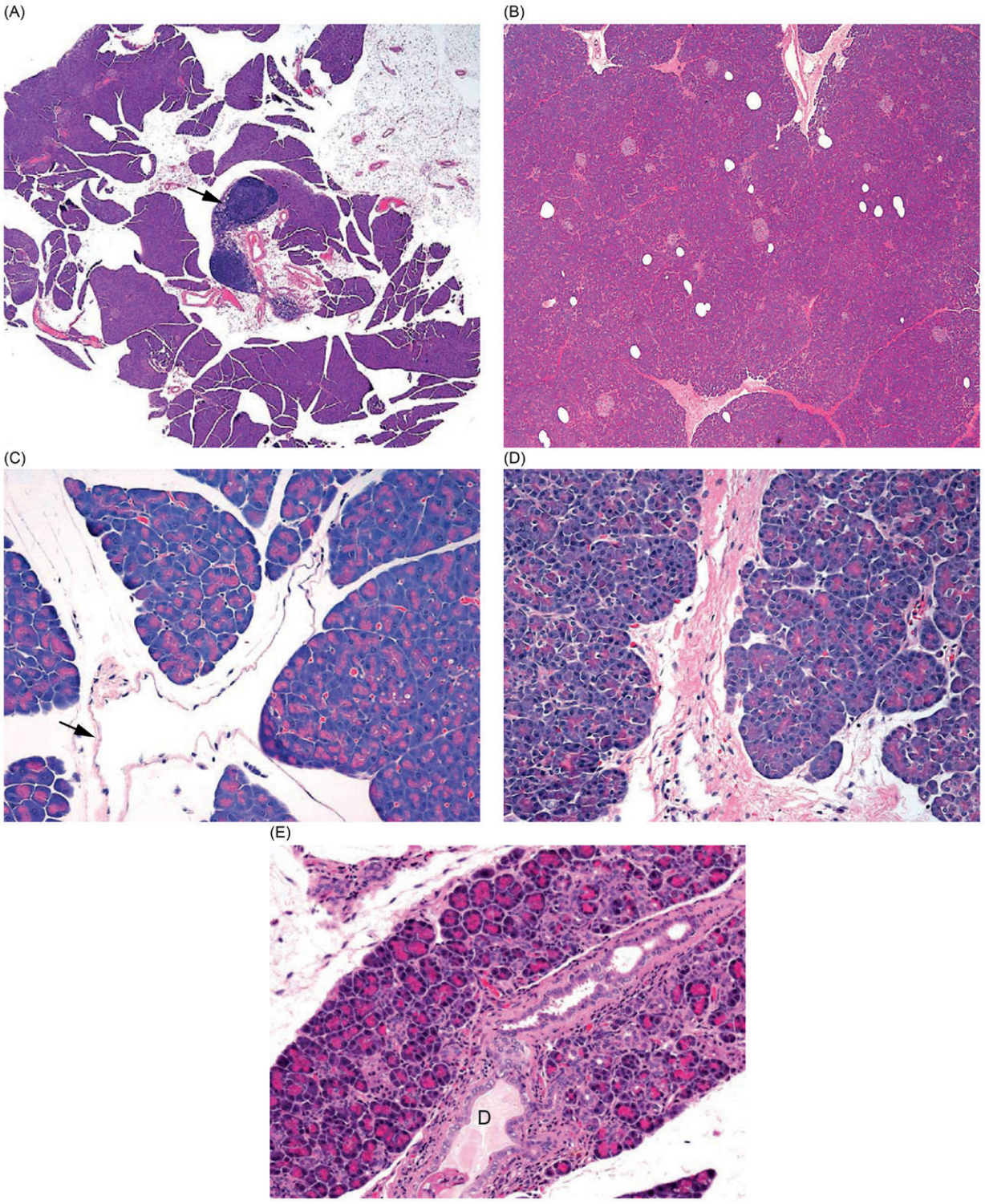

FIGURE 14.2. Mesenteric and compact pancreas.
(A) Mesenteric rodent (mouse) pancreas. Lobes and lobules are dispersed and separated by mesenteric fat, connective tissue, and lymphoid aggregates (arrow). (B) Compact human pancreas. Pancreatic structure is denser in humans. Individual or small clusters of adipocytes are also present as small clear foci. These can be seen in older or obese rodents and humans. (C) Mesenteric rodent (mouse) pancreas. A thin fibrous capsule invests the pancreas and extends into the parenchyma to divide it into lobes and lobules (arrow). The intralobular stroma supports blood vessels, lymphatics, and nerves. (D) Compact human pancreas from older human. The interlobular stroma and capsule are prominent. (E) Pancreas from an aged rat. Focal acinar atrophy with duct dilation (D) and fibrosis are common age-associated changes.

Need-to-know

- Rodent pancreas is loosely dispersed in a "mesenteric" pattern, whereas the human pancreas has a "compact" presentation with distinct head, neck, body, and tail regions.
- The pancreatic capsule extends via septa to divide the parenchyma into lobes and lobules.
- The capsule and accompanying septa are typically thin but can thicken with age and eventually may be accompanied by other age-associated atrophic and degenerative changes.

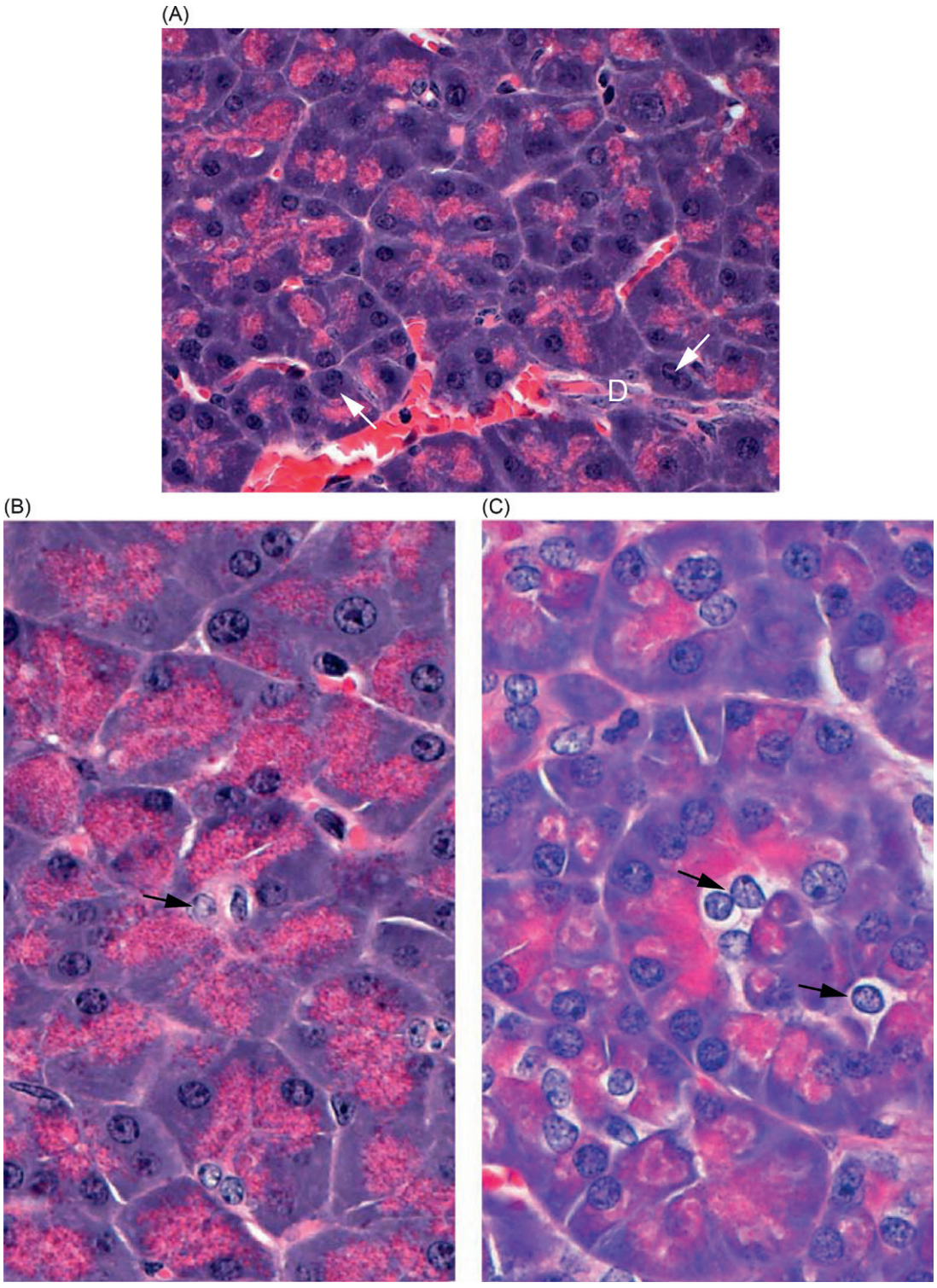

FIGURE 14.3 Acini and granules. (A) Zymogen granule-rich acinar epithelial cells from rodent (mouse). Vascular and intercalated ductal (D) elements are also present. Multinucleated acinar cells can be observed (arrows). (B) Rodent (mouse) centroacinar cells (arrow) are indistinct. (C) Human centroacinar cells (arrows) are more distinct than in the rodent.

Need-to-know

- Acinar structure in humans, rats, and mice is similar, although rodent acinar cells may be multinucleated.
- In rodents, the primary pancreatic duct joins the bile duct prior to emptying into the duodenum, and multiple accessory ducts are common.
- In humans, the primary pancreatic duct joins the bile duct at the greater duodenal papillae, and only a single accessory duct is common.

clustered toward the apical surface of the cell. Zymogen granules are refractile and stain intensely red with H&E. They contain a variety of digestive enzymes, most of which become activated upon entry into the duodenum. In both rodents and humans, acinar cells appear histologically similar and relatively uniform, but they are actually composed of a rather heterogeneous population. For instance, acinar cells in close proximity to islets tend to be larger and to contain more digestive enzymes than more distant ones. Other functional and structural markers confirm acinar cell heterogeneity, but clear species differences remain to be described.

The large zymogen granule-rich epithelial cells lining the acinar glands merge at the luminal surface with relatively clear-staining flattened oval-to-cuboidal centroacinar cells, which may be somewhat indistinct in rodents (Fig. 14.3). Centroacinar cells are continuous with the lumen of the intercalated duct. The progression of excretory ducts from smallest to largest is: intercalated → intralobular → interlobular → main pancreatic duct. As ducts increase in size, their lining changes from cuboidal to low columnar to columnar epithelium, which lines the main pancreatic duct. Ductal epithelial cells, which are present as a single layer, may have cilia or microvilli, and goblet cells are also occasionally present in main pancreatic ducts. In humans, the main pancreatic duct enters the duodenum at the greater duodenal papilla (papilla of Vater) along with the common bile duct. Most people have a small accessory duct that opens into the proximal duodenum. In rodents, pancreatic exocrine secretions typically drain into the duodenum via the common bile duct. Multiple accessory ducts, such as those associated with the dispersed mesenteric lobules, may also be present and drain directly into the duodenum. Interestingly, pancreatic acinar and ductal cells remain pluripotent and can give rise to both functional exocrine and endocrine cells (and possibly neoplasia) following some types of pancreatic injury.

The endocrine portion of the pancreas is represented by the islets of Langerhans, which account for 1% or 2% of pancreas volume in rodents and 1–4% in humans. Numbers of islets are proportional to body weight for all species. Islets vary in size, location, and composition within and among species. The average rodent islet is approximately twice the diameter of a human islet, but sizes in all three species (particularly in mice) are widely distributed and may overlap. Exceptionally large islets can occasionally be seen in humans as well as in pregnant, obese, or aged rodents (Fig. 14.4). In rodents, islets tend to be unevenly distributed throughout the pancreas. As such, it is possible to view sections that have very few or entirely lack islets. This makes it particularly important to properly and thoroughly sample the rodent pancreas when doing histologic evaluation of islets. An additional important difference is that in rodents, islets are present in both interlobular/periductal and, occasionally, intralobular locations (Fig. 14.4C). This contrasts with humans—as well as monkeys, cows, pigs, dogs, rabbits, and cats—where islets are mostly intralobular (Fig. 14.4D).

Rodent and human and islets are composed of various combinations of the three primary endocrine cell types and supporting stromal elements: alpha cells, which secrete glucagon; beta cells, which secrete insulin and amylin; and gamma cells, which secrete somatostatin. Also present in much lower numbers are several additional subtypes of islet cells and mediators; including epsilon cells, which secrete ghrelin; and PP or F cells, which secrete pancreatic polypeptide. Species differences in islet cells are not obvious in H&E-stained sections (Fig. 14.5). Accurate identification of islet cell type and distribution depends on the use of appropriate immunohistochemical or other special staining techniques. The composition and distribution of endocrine cells within individual islets varies greatly among and within species and with the physiologic state; however, some basic differences exist. For instance, in rodents, islets are composed primarily of beta cells whereas in

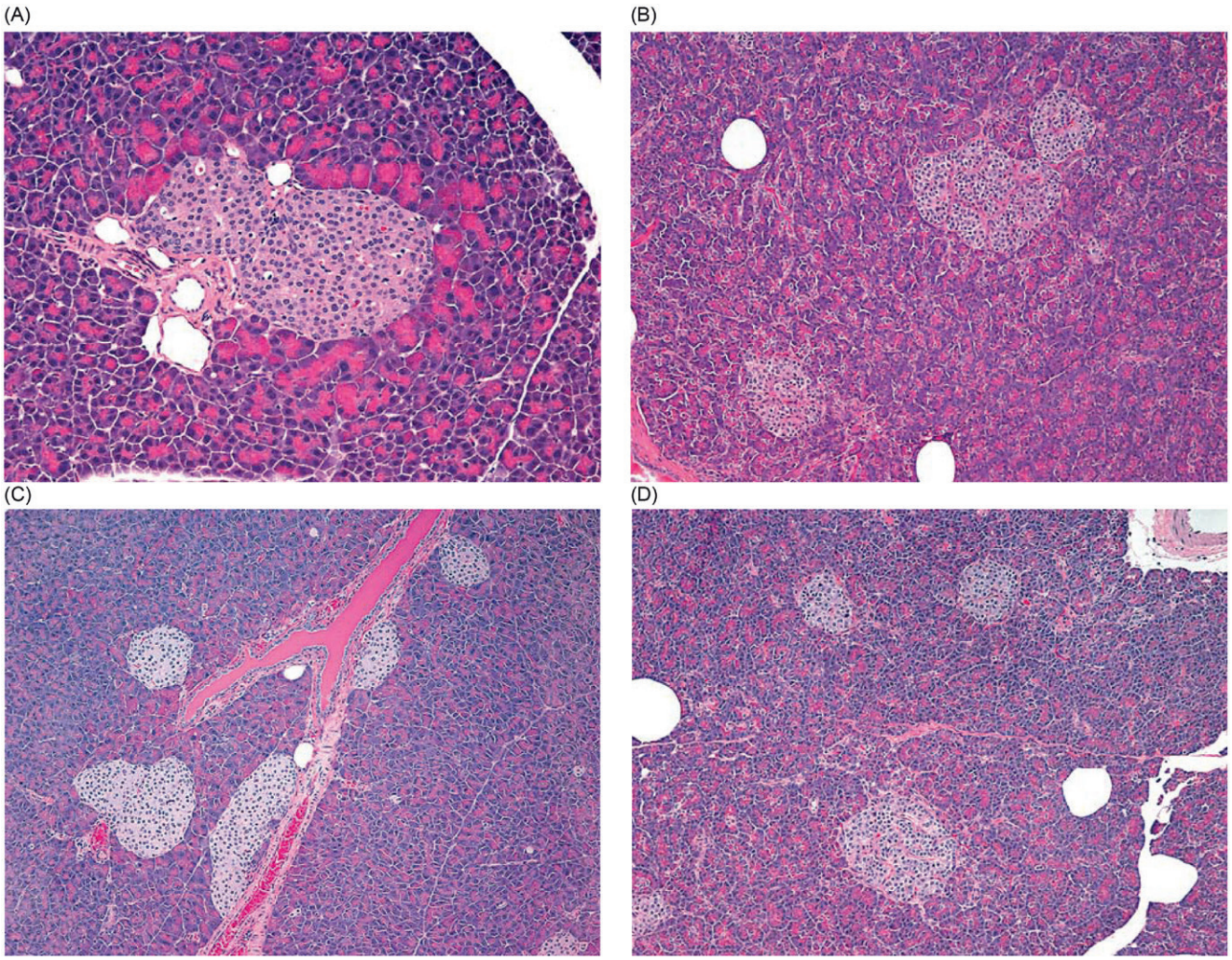

FIGURE 14.4 Islets. (A) Example of a large interlobular islet from a mouse. A corona of enlarged acinar cells surrounds this islet. (B) Section of human pancreas showing three intralobular islets. Note the normal variation in islet size, with the two small islets being more typical. Clear foci are adipocytes. (C) Rodent (mouse) islets. As most islets in the mouse are located in interlobular spaces and are often periductal or perivascular. In this figure, the interlobular duct contains pink secretory material, and the artery is filled with red blood cells. (D) Human islets. In the human, islets are principally found in intralobular locations, lack a close association with larger ducts and vessels, and are closely surrounded by acinar cells.

Need-to-know

- Islets vary greatly in size, particularly in mice.
- Islets tend to be distributed unevenly throughout the rodent pancreas, in contrast to the more evenly distributed pattern in the human pancreas.

humans, islets more typically contain a mixture of endocrine cell types with relatively fewer beta cells overall (Fig. 14.5C and D). In addition, in rodents, these dominant beta cell populations are typically clustered in the center of the islet and surrounded by other islet cell types, whereas in humans the various islet cell populations are intermingled and closely, but randomly, associated with islet blood vessels.

Understanding of pancreatic microvascular anatomy in general and of islet microvascular anatomy in particular remains incomplete. Islets are highly vascularized and have sinusoidal

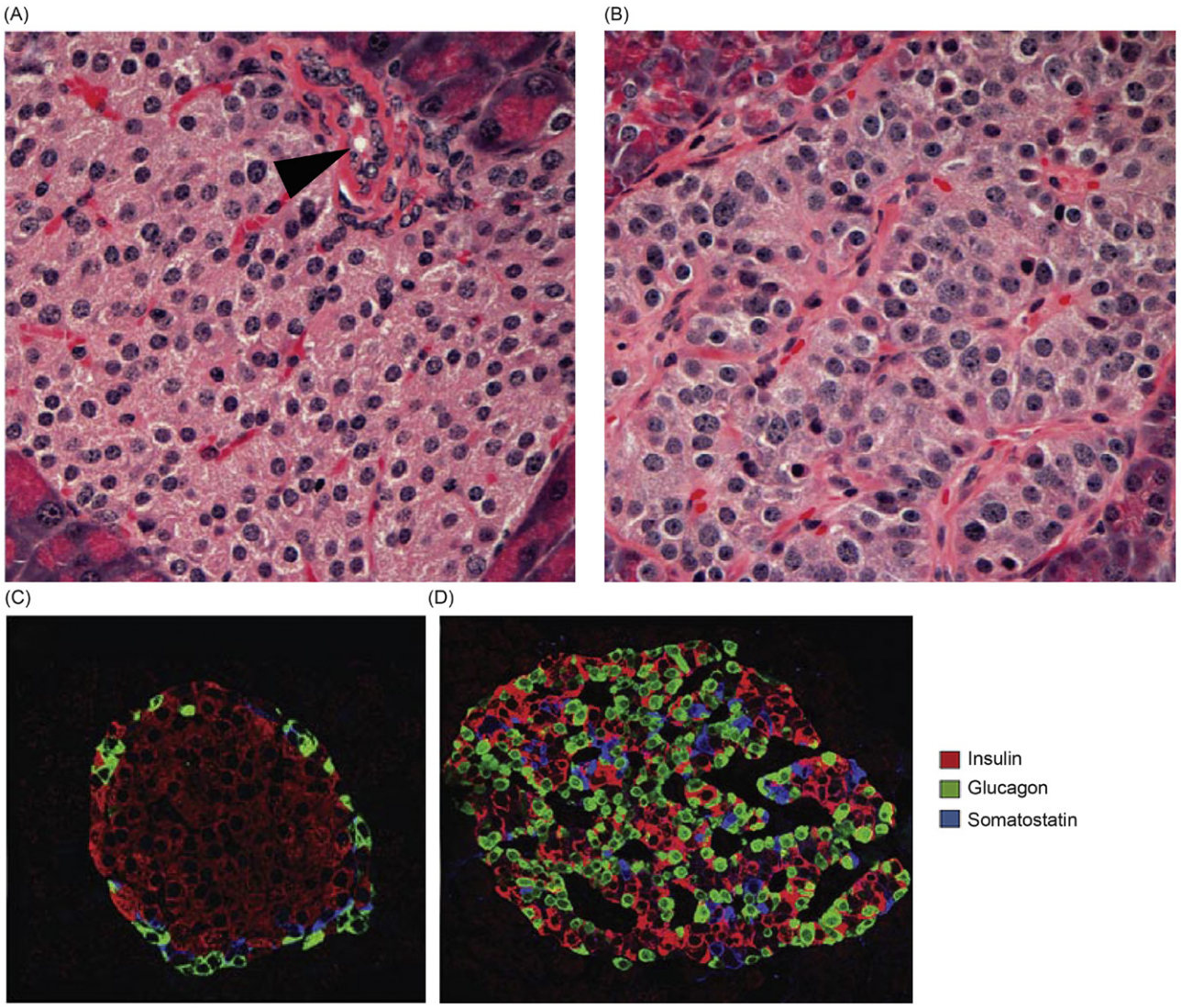

FIGURE 14.5 Islet characteristics. Comparison of islets from a rodent (mouse) (A) and an older human (B). Stromal elements are more prominent in the human islet, which is a reflection of age rather than a fundamental histologic difference. Also note the pancreatic duct (arrowhead) in close proximity to the mouse islet, which is typical for this species. As seen by immunohistochemistry, beta (red) cells predominate in rodents (mouse) (C) and tend to be more centrally located than in humans (D), where beta cells are less predominant and more randomly distributed. Source: Cabrera et al.: The unique cytoarchitecture of the human pancreatic islet has implications for islet cell function. *Proc Natl Acad Sci USA* 103(7):2334–2339, 2006; © (2006) National Academy of Sciences USA.

Need-to-know

- In rodents, islets are mostly interlobular, whereas human islets are most commonly intralobular.
- Some lobules in rodents may have few or entirely lack islets.
- Comparing islet cell composition between the species requires special stains or immunohistochemical methods to differentiate cells.

capillaries with similarities to renal glomeruli (Fig. 14.6). Capillaries that serve the islets are 5 times denser and have approximately 10 times more fenestrations than those serving the exocrine pancreas. In mice, a single basement membrane is present, which accompanies blood vessels. In humans, both islet cells and islet vessels have basal lamina, resulting in a "double" basement membrane. It is uncertain which occurs in rats. The manner in which blood flows through an islet may have significant functional consequences, and several blood flow models have been proposed

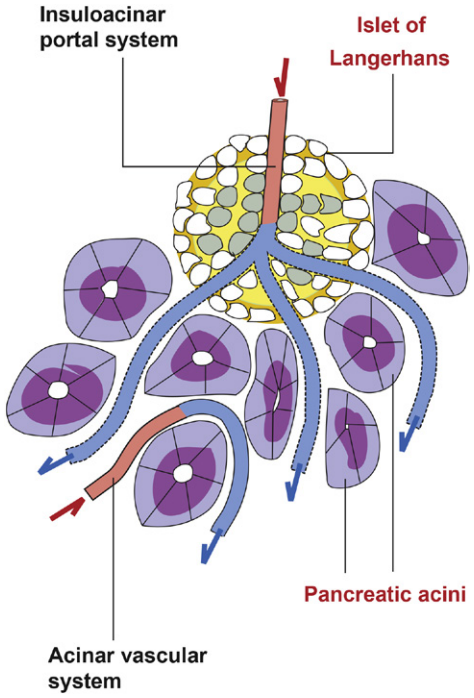

FIGURE 14.6 Pancreatic blood supply. Blood supplying islets continues on to supply acini via the insulo-acinar portal system. In addition, acini may be supplied directly via an independent arterial-venous system known as the acinar vascular system. In rodents, because many islets are interlobular, blood emanating from these islets may flow directly into veins without passing through acinar tissues. Source: Modified from Kierszenbaum: *Histology and cell biology*, Philadelphia, PA, 2007, Mosby, p. 492.

and continue to be refined. Despite differences, each of these models accounts for the concept of an insulo-acinar portal system whereby blood that passes through an islet then perfuses acinar tissue (Fig. 14.6). Functionally, this may account for the presence of the relatively larger acinar cells around the islets (Fig. 14.4A). Species differences that do exist are to some degree related to the predominance of interlobular islets compared to intralobular islets, as well as to distribution of cell types within islets, islet size, and other variables. In rodents, where the vast majority of islets are interlobular, the islets are supplied by lobular vessels that drain into the insulo-acinar portal system as well as directly into lobular veins (insulo-venous efferent system). This contrasts with humans, where most islets are intralobular, and the insulo-acinar portal system dominates. Although species differences in pancreatic circulation are recognized, none are absolute; they can vary based on islet size, metabolic state, association (or lack thereof) with lobular tissue, and location within the pancreas.

The pancreas receives innervation from sympathetic, parasympathetic, and afferent fibers that follow blood vessels. For a recent in-depth review of innervation of the pancreas, as well as other comparative aspects of human and mouse pancreata, see Dolensek et al.

Because of ease of access to tissue, a great deal of what is known about the pancreas has been derived from experimental animals, particularly young normal rodents. This presents a challenge in that comparisons are typically made with human autopsy tissue that is often from older, medically compromised individuals. In addition, throughout the years, investigations of pancreatic structure and function involving different species have naturally merged into hybrid models or prototypes. It is important to consider known and emerging differences when making translations between species. It is increasingly obvious that although there are great similarities, some significant species differences are emerging and dependence on either structural or functional prototypes may not always be reliable.

FURTHER READING

Barreto SG, Carati CJ, Toouli J, et al: The islet–acinar axis of the pancreas: more than just insulin. *Am J Physiol Gastrointest Liver Physiol* 299:G10–G22, 2010.

Brissova M, Fowler MJ, Nicholson WE, et al: Assessment of human pancreatic islet architecture and composition by laser scanning confocal microscopy. *J Histochem Cytochem* 53:1087–1097, 2005.

Brunicardi FC, Stagner J, Bonner-Weir S, et al: Microcirculation of the islets of Langerhans. *Diabetes* 45:385–392, 1996.

Cabrera O, Berman DM, Kenyon NS, et al: The unique cytoarchitecture of human pancreatic islets has implications for islet cell function. *Proc Natl Acad Sci USA* 103:2334–2339, 2006.

Dolensek J, Rupnik MS, Stozer A: Structural similarities and differences between the human and mouse pancreas. *Islets* 7:1–16, 2015.

Go VLW, Dimagno EP, Gardner JD, et al: *The pancreas: biology, pathobiology and disease*, New York, 1993, Raven Press.

Greaves P: *Histopathology of preclinical toxicity studies*, San Diego, CA, 2007, Elsevier.

Haschek WM, Rousseaux CG: *Haschek and Rousseaux's handbook of toxicologic pathology*, ed 3, San Diego, CA, 2013, Academic Press.

In't Veld P, Marichal M: Microscopic anatomy of the human islet of Langerhans. *Adv Exp Med Biol* 654:1–19, 2010.

Kharouta M, Miller K, Kim A, et al: No mantle formation in rodent islets—the prototype of islet revisited. *Diabetes Res Clin Pract* 85:252–257, 2009.

Kierszenbaum AL: *Histology and cell biology*, ed 2, Philadelphia, PA, 2007, Mosby.

Kim A, Miller K, Jo J, et al: Islet architecture: a comparative study. *Islets* 1:129–136, 2009.

Maronpot RR, editor: *Pathology of the mouse*, Vienna, IL, 1999, Cache River Press.

Motta PM, Macchiarelli G, Nottola SA, et al: Histology of the exocrine pancreas. *Microsc Res Tech* 37:384–398, 1997.

Murakkami T, Hitomi S, Ohtsuka A, et al: Pancreatic insulo-acinar systems in humans, rats and some other mammals: scanning electron microscopy of vascular casts. *Microsc Res Tech* 37:478–488, 1997.

Suttie AW, Leininger JR, Bradley AE: *Boorman's pathology of the rat: reference and atlas*, ed 2, New York, 2017, Academic Press.

Virtanen I, Banerjee M, Palgi J, et al: Blood vessels of human islets of Langerhans are surrounded by a double basement membrane. *Diabetologia* 51:1181–1191, 2008.

Ziv O, Glaser B, Dor Y: The plastic pancreas. *Dev Cell* 26:3–7, 2013.

ENDOCRINE SYSTEM 15

KRISTA MARIE DUBRAY LA PERLE
The Ohio State University College of Veterinary Medicine, Columbus, OH, United States

SUZANNE M. DINTZIS
University of Washington School of Medicine, Seattle, WA, United States

Introduction

Endocrine organs are richly vascularized ductless organs that produce hormones (Table 15.1). The epithelial cells of each organ secrete their hormone product directly into the bloodstream where, upon binding with specific receptors in target organs, cellular functions are affected. The endocrine system includes not only the endocrine glands (thyroid, parathyroid, adrenal, pituitary and pineal) but also single cells and small clusters of neuroendocrine cells in various organs such as the lung and gastrointestinal tract, and the paraganglia. This chapter addresses the thyroid, parathyroid, adrenal, pituitary and pineal glands, as well as the paraganglia; the endocrine pancreas is covered in Chapter 14: Pancreas.

Thyroid Gland

Gross Anatomy

In rodents and humans, the thyroid gland typically lies under the sternohyoid and sternothyroid muscles and lateral to the trachea near the base of the laryngeal cartilages (Figs. 15.1 and 15.2). It is a reddish-brown, butterfly-shaped organ with right and left lobes joined by a thin isthmus, which forms a bridge across the ventral and anterior aspect of the trachea, respectively. It typically extends from the posterior larynx along the first three or four tracheal cartilage rings in mice (Figs. 15.1 and 15.3), and the first four or five tracheal rings in rats. Due to its very small size, collection and weighing of the mouse thyroid gland may produce artifacts that can complicate or preclude histologic evaluation. Although mouse thyroid gland weights are conspicuously absent from the Mouse Phenome Database, published weights range from 1.5 to 2.6 mg with lobe measurements of approximately 2 × 1 × 0.5 mm. Rat thyroid lobes measure up to 7 × 3×3 mm, with published thyroid weights ranging from 13 to 28 mg, and increasing with age. It is recommended for thyroid gland weights in rats to be obtained postfixation and dissection, and evaluated relative to body weights. In humans, the thyroid gland usually weighs 15–25 g, and measures approximately 5–6 × 2–2.5 × 2 cm (Fig. 15.4).

In mammalian development, the thyroid gland derives from endoderm from the foramen cecum

Comparative Anatomy and Histology. DOI: http://dx.doi.org/10.1016/B978-0-12-802900-8.00015-4
© 2018 Elsevier Inc. All rights reserved.

TABLE 15.1 Endocrine System

Feature	Rodent	Human
	Gross	
Thyroid gland	One pair (two glands) connected by a thin isthmus; ectopic tissue common	Similar to rodent
Parathyroid gland	One pair (two glands); ectopic tissue common	Two pairs (four glands); ectopic tissue common
Adrenal gland	One pair (two glands); accessory tissue common	One pair (two glands)
Pituitary gland	One gland composed of anterior (adenohypophysis) and posterior (neurohypophysis) lobes; the pars distalis cradles the pars intermedia and pars nervosa	Similar to rodent
Pineal gland	Small and round; located on the external surface of the brain at the interface between the cerebral hemispheres and cerebellum	Resembles a pine cone due to incomplete lobules formed by intralobular stroma extending from the capsule; located within the posterior wall of the third ventricle near the center of the brain
Paraganglia	Variably discrete aggregates distributed along the central axis of the body in the neck, thorax and abdomen	Similar to rodent
	Histologic	
Thyroid gland follicles	Spherical structures lined by nonciliated cuboidal epithelial cells with lumens containing eosinophilic colloid; occasional spherical structures lined by ciliated and nonciliated, often keratinizing, epithelial cells of ultimobranchial origin that may form cysts	Similar to rodent
Thyroid gland C cells	Mouse: Inconspicuous by routine staining; fewer than in rats; present centrally in the lobe Rat: Polygonal cells between thyroid follicular epithelial cells and basal lamina of follicle; more prominent and frequent than in mice; present centrally in the lobe	Polygonal cells between thyroid follicular epithelial cells and basal lamina of follicle
Parathyroid gland	Composed of chief cells (active, light; inactive, dark)	Composed of adipose tissue, chief cells, and oxyphil cells
Adrenal cortex	Two discrete zones: glomerulosa and fasciculata	Three zones: glomerulosa, fasciculata, and reticularis
Adrenal X-zone (corticomedullary junction)	Mouse: Develops postnatally and regresses by puberty in males; regresses in pregnancy in females Rat: Inconspicuous	Fetal zone undergoes apoptosis after birth
Adrenal medulla	Composed of chromaffin cells and scattered ganglia	Similar to rodent
Pituitary gland pars distalis	Composed of acidophil and basophil secretory cells and chromophobes	Similar to rodent
Pituitary gland pars intermedia	Thick band of polygonal cells; adjacent to residual lumen of Rathke's pouch lined by cuboidal epithelium	Thin; adjacent to residual lumen of Rathke's pouch lined by cuboidal epithelium
Pituitary gland pars nervosa	Unmyelinated axons from hypothalamic neuron cell bodies supported by modified glial pituitcytes	Similar to rodent
Pineal gland	Composed primarily of pinealocytes with fewer glial cells	Similar to rodent
Paraganglia	Variably discrete aggregates distributed along the central axis of the body in the neck, thorax and abdomen.	Similar to rodent
	Product(s)/function(s) of cells	
Thyroid gland follicles	Produce triiodothyronine (T3) and tetraiodothyronine (T4)	Similar to rodent
Thyroid gland C cells	Produce calcitonin	Similar to rodent
Parathyroid gland	Produces PTH	Similar to rodent
Adrenal cortex	Glomerulosa produces mineralocorticoids; fasciculata primarily produces corticosterone; no sex steroids produced due to lack of 17α-hydroxylase	Glomerulosa produces mineralocorticoids; fasciculata primarily produces cortisol; reticularis produces sex steroids
Adrenal medulla	Primarily produces epinephrine	Produces epinephrine and norepinephrine
Pituitary gland pars distalis	Acidophils produce GH and prolactin; basophils produce LH, FSH, ACTH, and TSH	Similar to rodent
Pituitary gland pars intermedia	Primarily produces ACTH with lesser amounts of α-MSH and β-endorphin	Unknown
Pituitary gland pars nervosa	Stores oxytocin and vasopressin produced by the hypothalmus	Similar to rodent
Pineal gland	Pinealocytes produce melatonin	Similar to rodent
Paraganglia	Aortic and carotid body chemoreceptors detect alterations in oxygen, carbon dioxide tension, and pH	Similar to rodent

region at the base of the tongue and from the ultimobranchial bodies of the IV and V branchial pouches. Ectopic thyroid tissue may come to rest anywhere along this cervical midline path, including the anterior mediastinum and base of heart in humans and rodents. A midline triangular extension at the superior aspect of the isthmus may be seen in approximately 40% of humans and is referred to as a pyramidal lobe. The thyroid gland of rodents and humans is enveloped by a thin fibrous capsule. Fine fibrous septae extend from this capsule into the thyroid gland producing a lobulated parenchymal architecture (thyromeres). The vascular supply is primarily provided from the inferior and superior thyroidal arteries. A venous plexus in the thyroid capsule gives rise to superior, medial, and inferior thyroid veins that drain into the internal jugular vein and brachiocephalic vein.

HISTOLOGY

In rodents and humans, the two primary cell types of the thyroid gland are follicular cells and C cells. Although most thyroid tissue is endodermally derived, the C cells are of neural crest origin. Follicular cells predominate and form roughly spherical structures—the thyroid follicles (Figs. 15.5 and 15.6). Follicular cells form a single layer of low columnar-to-flattened cuboidal epithelium (Fig. 15.6A and B). Nuclei are round-to-oval, and chromatin is coarsely granular. Rodents and humans have an additional follicular structure of ultimobranchial origin that is lined by ciliated and nonciliated cells, the latter of which are predisposed to keratinize, and often forms cysts (Fig. 15.6C).

The base of the follicular cells rests on the basement membrane at the peripheral aspect of the follicle, and the apical ends contain microvilli along the luminal surface. Within the follicles is colloid, which consists of the glycoprotein thyroglobulin and other substances, including proteolytic enzymes. Follicular cells are responsible for thyroglobulin synthesis, sodium iodide symporter-mediated uptake of iodide, and oxidization of iodide to iodine by thyroperoxidase. They actively concentrate iodide to levels 30–40 times those in serum and release iodine into the follicular lumen, where it iodinates thyroglobulin. Iodinated thyroglobulin is the storage form of the two thyroid hormones, triiodothyronine (T3) and tetraiodothyronine (T4). The thyroid gland is unique among endocrine organs in its ability to store its synthesized hormones. Hydrolysis of stored iodinated thyroglobulin releases T3 and T4 into the bloodstream. Thyroid-stimulating hormone (TSH) from the anterior pituitary stimulates T3 and T4 release, the levels of which stimulate a negative feedback loop to inhibit additional release of TSH. When low blood levels of thyroid hormone are detected in the hypothalamus, it releases thyrotropin-releasing hormone (TRH), which acts on the anterior pituitary to effect release of TSH. The serum half-life of T3 and T4 is significantly shorter in rodents than in humans due to distinct differences in thyroid hormone transport proteins: the half-life of T4 and T3 in rats is 12–24 and 6 h, respectively, compared to humans in which the half-life is 5–9 and 1 days, respectively. The availability of corresponding data is more limited in mice and restricted to a T4 half-life in Swiss Webster mice of 8–10 h. Thyroid hormones in rodents exist primarily in an unbound state, which is more prone to metabolism and excretion. Limited binding of thyroid hormone in rodents occurs with albumin, postalbumin, and transthyretin (prealbumin). In contrast, thyroid hormones in humans are primarily bound to high-affinity T4- and T3-binding globulins, which are not present in rodents.

The appearance of the follicular epithelial cells and colloid is affected by many variables, including age, diet, sex, and especially endocrine status. In active glands, epithelial cells tend to be columnar, with basophilic colloid containing absorption droplets near the epithelial interface. In contrast, inactive glands are lined by flattened epithelial

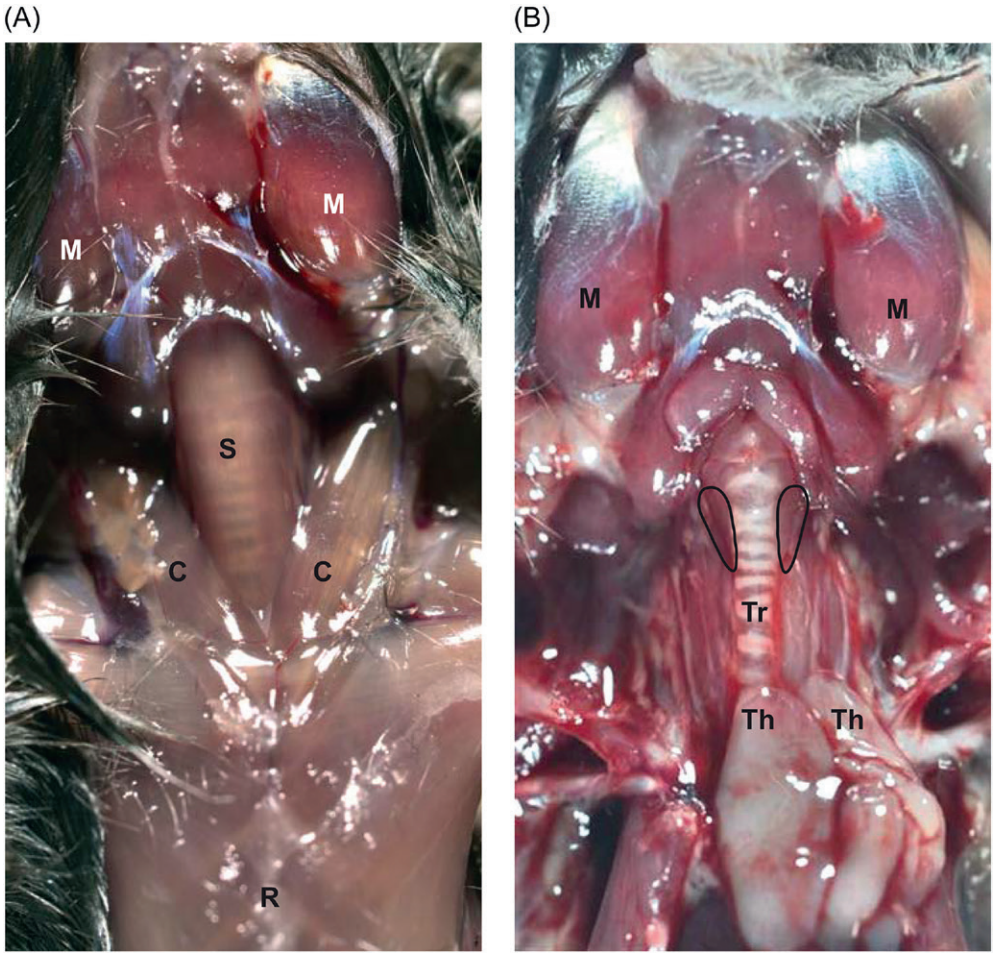

FIGURE 15.1 Rodent (mouse) regional cervical anatomy. Ventral aspect of the thyroid gland in vivo. (A) Regional anatomy after the skin is removed. The sternohyoid/sternothyroid (S) and sternocephalicus (C) muscle, as well as the rib cage (R) must be removed to visualize the laryngeal region. (B) Upon removal of the overlying musculature and rib cage, the two reddish-brown lobes (outlined) of the thyroid gland are visible, nestled along each lateral aspect of the trachea (Tr), spanning the first three or four tracheal cartilage rings. The lobes are connected by a thin isthmus that is not apparent. Two thymic lobes (Th) and masseter muscles (M) are indicated.

cells, and the follicular lumen is distended with eosinophilic colloid. With age, follicles also tend to become larger and more variable in size, with a concomitant decrease in the amount of interfollicular connective tissue.

The C cells (parafollicular cells) of the thyroid gland are foci of less than 10 cells scattered throughout the gland in the connective tissue between thyroid follicles or within the follicular epithelium adjacent to the basal lamina at the base of follicular cells. C cells account for only 0.1% of thyroid epithelial cells. Without the aid of argyrophilic histochemical or immunohistochemical stains, it is difficult to identify C cells in a thyroid gland, particularly in mice. Calcitonin immunohistochemical staining demonstrates the tendency of C cells to cluster centrally in the lobe, typically at the level of the parathyroid glands (Fig. 15.7). Ultrastructurally, the C cells contain dense secretory granules that contain the peptide hormone calcitonin. By inhibiting bone resorption by osteoclasts, calcitonin serves as an antagonist of parathyroid hormone (PTH, see next). Calcitonin aids in decreasing serum calcium levels, whereas PTH influences processes leading to increased serum calcium levels.

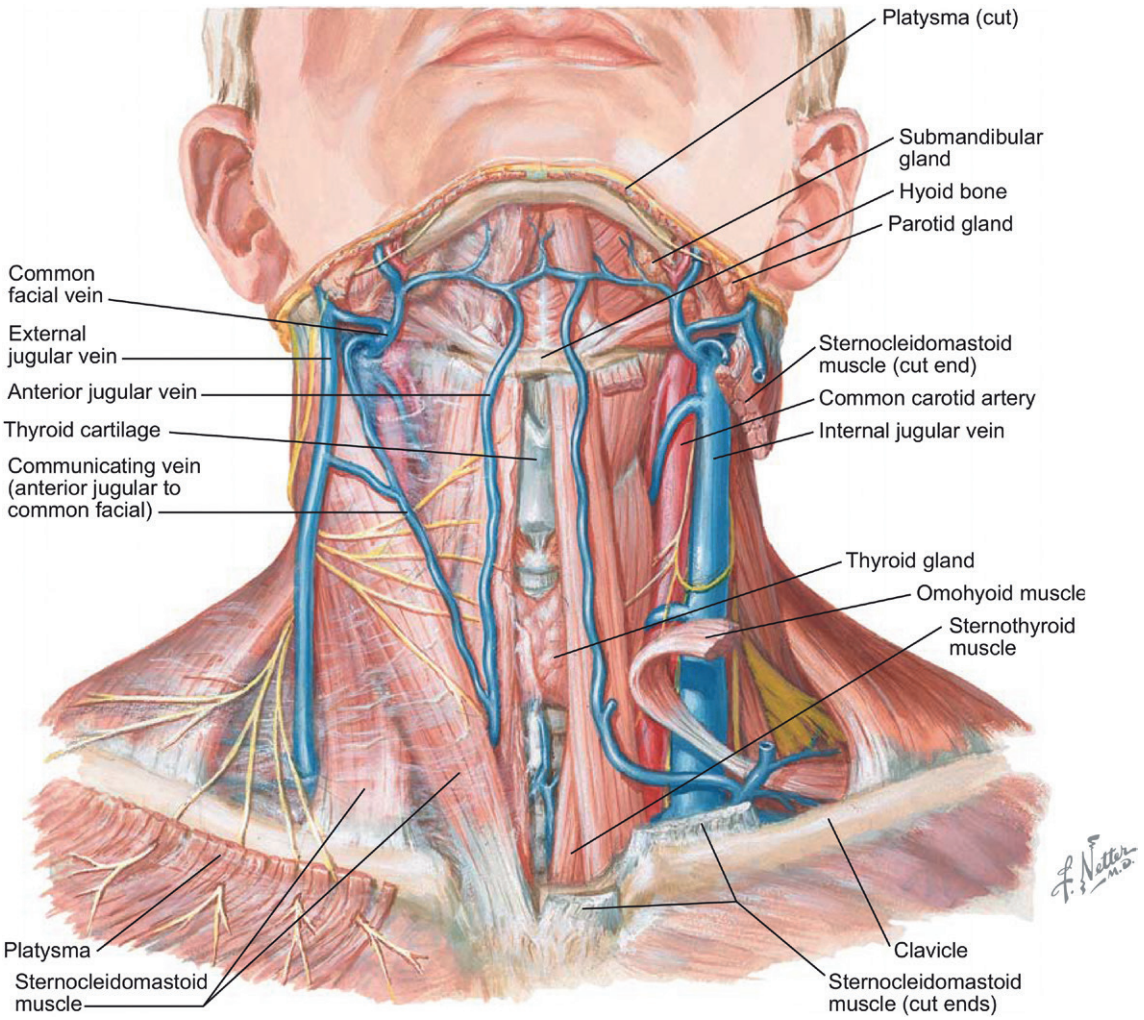

FIGURE 15.2 Human regional cervical anatomy. Source: © Elsevier, Inc., www.netterimages.com.

Parathyroid Gland

Gross Anatomy

Rodents have a single pair of parathyroid glands, which are believed to be derived from the dorsal component of the third pharyngeal pouch (Figs. 15.3 and 15.5). They are typically subcapsular at the cranial-lateral aspect of the thyroid gland, with the glands more superficially located within the thyroid gland in mice than rats. However, they are seldom at the same level, are not uniformly transected, and are frequently difficult to locate, particularly in mice. They are likely to be more visible in rats, where they cumulatively appear as oval white structures that measure approximately 2 mm^3 and weigh 2–4 mg, with some reports documenting female rat parathyroid glands as 50% larger than male. Humans typically have four parathyroid glands (two pairs), which are most frequently embedded in the posterior connective tissue capsule of the thyroid gland, and referred to as the superior and inferior parathyroid glands (Fig. 15.8). As in rodents, human ectopic parathyroid glands may also be found embedded in thyroid parenchyma, thymus, mediastinum, and retroesophageal connective tissue. Up to 10% of people have more than four parathyroid glands. Human parathyroid glands are yellow to orange-tan, weigh on average 40 mg, and measure 3–6 × 2–4 × 0.5–2 mm.

HISTOLOGY

The parathyroid glands have thin fibrous capsules and are composed of epithelial chief and oxyphilic cells supplied by a rich intraglandular capillary network. The chief cells are arranged in sheets, cords, trabeculae, and follicles. In both rodents and humans, chief cells produce PTH, which is involved in calcium homeostasis through its effects on calcium levels in bone, kidneys, and intestines. Chief cells are spherical with round vesicular nuclei and have ample amphophilic-to-pale eosinophilic cytoplasm (Fig. 15.9). They measure approximately 7–12 µm in diameter and contain intracytoplasmic fat droplets, as well as PTH secretory granules, which are responsible for cellular staining upon immunohistochemistry with antibodies to chromogranin. In humans, oxyphil cells constitute a minor epithelial cell population in the parathyroid gland that is thought to derive from the chief cells and to be an inactive stage. Oxyphil cells are larger (12–20 µm in diameter) than chief cells and have deeply eosinophilic, granular cytoplasm that contains abundant mitochondria and lacks secretory granules (Fig. 15.9B). In rodents, although chief cells are categorized as active dark or inactive light cell by their functional state, oxyphil cells have not been observed. The prepubescent human parathyroid gland contains very few intraglandular interstitial fat cells, but this progressively increases to 40–70% of the gland's volume as humans age.

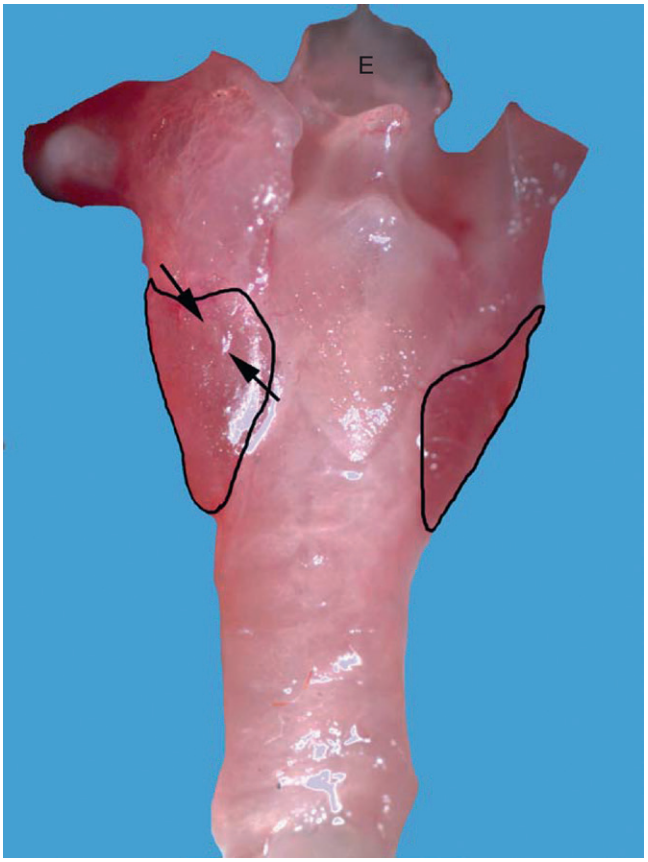

FIGURE 15.3 Rodent (mouse) regional thyroid anatomy. Dorsal aspect of the larynx and thyroid gland ex vivo. The two reddish-brown lobes (outlined) of the thyroid gland are positioned laterally along the trachea, caudal to the epiglottis (E). Arrows delineate the left parathyroid gland.

ADRENAL GLAND

GROSS ANATOMY

The paired adrenal glands, also referred to as suprarenal glands, are located cranial (rodents) or superior (humans) to the upper pole of the kidneys (Figs. 15.10 and 15.11). Cumulatively, mouse adrenals measure approximately 1 mm^3 and weigh 5–7.2 mg. Rat adrenals each measure approximately 6 × 5 × 3 mm and weigh 21–32 mg; rat adrenal weights should be evaluated relative to brain weights. Many reports document rodent adrenal weights up to 25% larger in females than in males. In humans, each adrenal weighs 8–13 g and has an approximate size of 5 × 3 × 1 cm. Grossly, the right gland is usually roughly triangular and the left more crescent-shaped. On cut section (Fig. 15.12), the adrenal gland is divided into a pale tan cortex seen beneath the fibrous adrenal capsule and a central darker reddish-brown medulla. Cortical:medullary:cortical width in rodents and humans is approximately 1:2:1 (Fig. 15.13A). The cortex is derived from mesoderm. It secretes corticosteroids, mineralocorticoids, glucocorticoids, and small amounts of sex hormones. Corticosteroid production occurs in response to

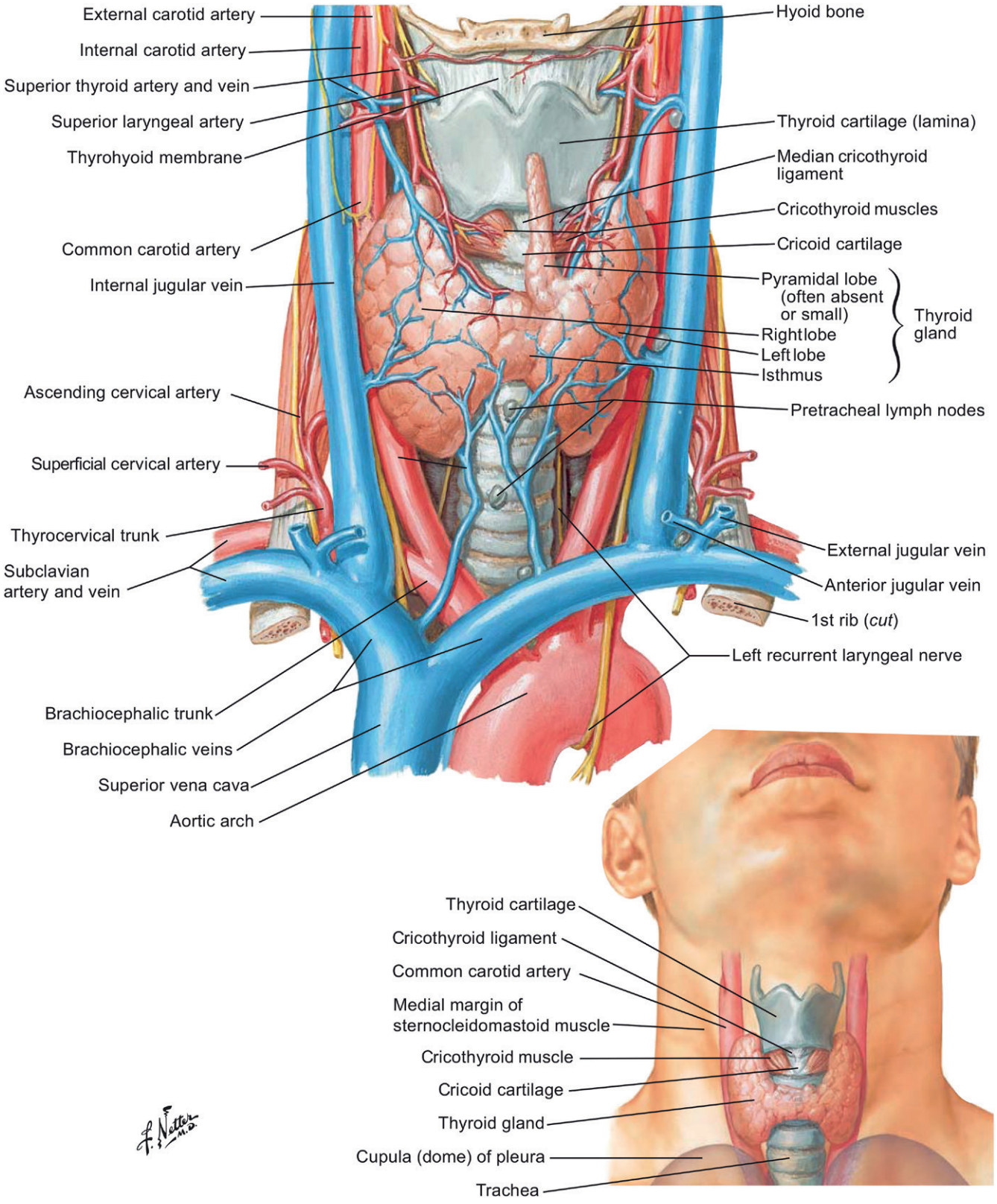

FIGURE 15.4 Human regional thyroid anatomy. Source: © Elsevier, Inc., www.netterimages.com.

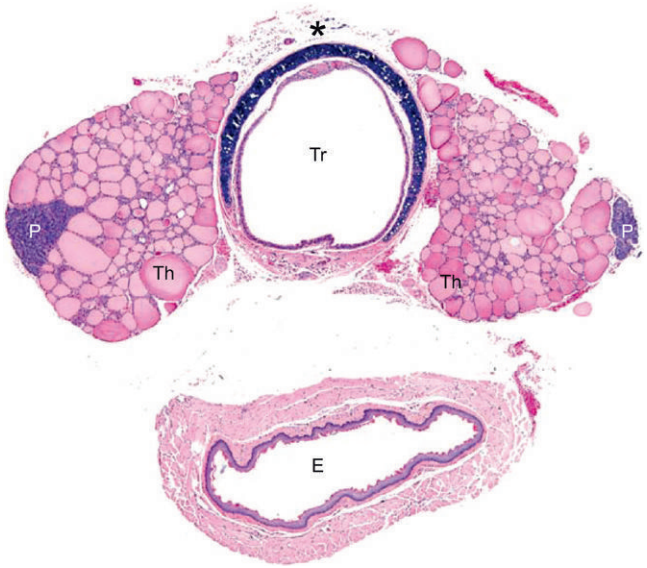

FIGURE 15.5 Rodent (mouse) subgross cervical regional anatomy. A transverse section through the trachea (Tr) and esophagus (E), including bilateral lobes of the thyroid (Th) and parathyroid (P) glands. The isthmus, if located in the plane of section (asterisk), would connect the two lobes of the thyroid gland.

adrenocorticotropic hormone (ACTH) produced by the anterior pituitary gland. Glucocorticoid production varies between rodents and humans: the major glucocorticoid in rodents is corticosterone, whereas humans predominantly produce cortisol. The adrenal medulla is derived from the neural crest. It is controlled by the sympathetic nervous system and produces the catecholaimes epinephrine and norepinephrine.

HISTOLOGY

There are four layers in the rodent adrenal cortex (Fig. 15.13B): the zona glomerulosa, zona fasciculata, zona reticularis, and the X-zone. The zona glomerulosa (mineralocorticoid production) is thin, with the cells arranged in indistinct arches. The zona fasciculata (corticosteroid production) consists of columns that make up the majority of the cortex in rodents. In contrast, the zona reticularis (sex steroid production) is not clearly distinguishable, albeit more distinct in rats than in mice, and does not synthesize androgens due to the absence of 17α-hydroxylase. The basophilic X-zone is comparable to the human fetal zone in its corticomedullary location, steroidogenic cell composition, and adrenal primordial origin. There is considerable variation in the degree of X-zone development in mice with regard to extent and duration. In contrast to the human fetal zone, which undergoes apoptosis and disappears soon after birth, the mouse X-zone develops postnatally, starting on approximately day 10, is fully developed at weaning, and then undergoes a sexually dimorphic pattern of regression. In female mice, the X-zone persists until pregnancy, when it rapidly regresses, or until approximately 9 weeks of age, when it slowly regresses, in some strains via lipid vacuolization (Fig. 15.14A). In male mice, the X-zone disappears by puberty without undergoing lipid vacuolization. It sometimes persists in either sex, particularly with castration. The appearance and disappearance of the X-zone in both male and female mice directly correlates with the enzymatic activity of 20α-hydroxysteroid dehydrogenase, which was initially described as a progesterone-metabolizing enzyme of the ovary critical for progesterone homeostasis in rodent pregnancies. The X-zone is essentially inconspicuous in rats, with the exception of a single documented case in a male rat, castrated at 3 weeks of age.

Three additional unique features of the rodent adrenal cortex are frequently observed during histologic evaluation. First, nodules of accessory cortical tissue, attached to the cortex or dispersed in the retroperitoneal adipose tissue, are commonly seen in rodents (Fig. 15.14A). Second, lipogenic pigmentation of the adrenal gland appears as yellowish-brown, granular-to-foamy, intracellular ceroid pigment at the corticomedullary junction (Fig. 15.14B). This pigment accumulates during regression of the X-zone in mice and as a senile change in both mice and rats. Lastly, type A spindle cells and type B polygonal cells proliferate in mice, parallel to the capsule initially and then expanding vertically and horizontally between columns of the zona

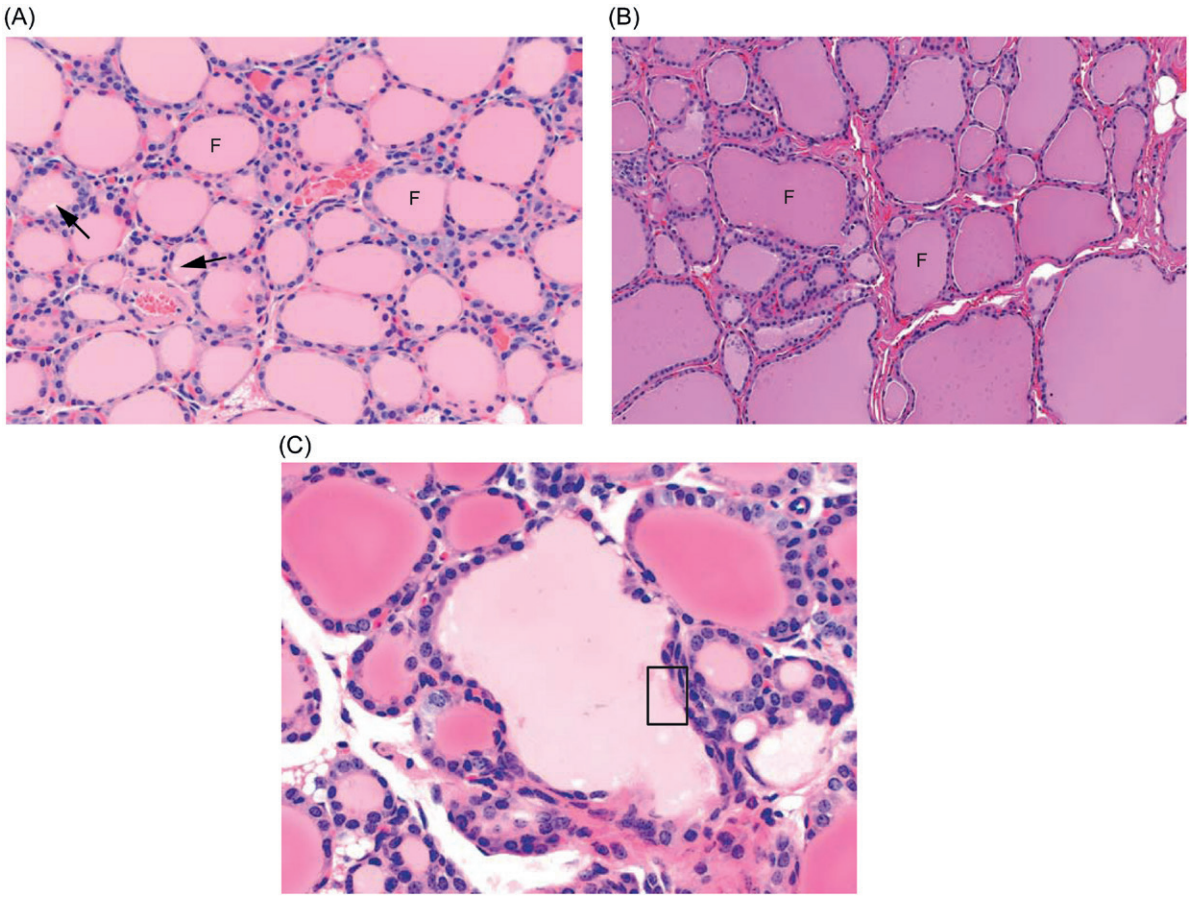

FIGURE 15.6 Thyroid gland. (A) Rodent. Spherical follicles (F) within the mouse thyroid gland are composed of a single layer of low cuboidal thyrocytes lining a lumen filled with eosinophilic colloid. Contained within the colloid is the prohormone thyroglobulin and iodine, which is an essential component of thyroid hormone. Clear vacuoles (arrows) within the colloid of some follicular lumens represent thyroglobulin endocytosis for proteolysis and thyroid hormone release. (B) Human. The active thyroid gland shows variably sized follicles (F) lined by a single layer of cuboidal epithelium. The follicles contain homogeneous eosinophilic colloid. (C) Rodent (mouse) thyroid follicles. The follicular structure is of ultimobranchial origin, lined by both ciliated (box) and nonciliated epithelial cells, which often form cysts.

Need-to-know

- The height of thyroid follicular epithelium and the tinctorial properties of the colloid are variable and highly dependent on endocrine status in rodents and humans.
- Follicular size becomes more variable with age in rodents and humans.

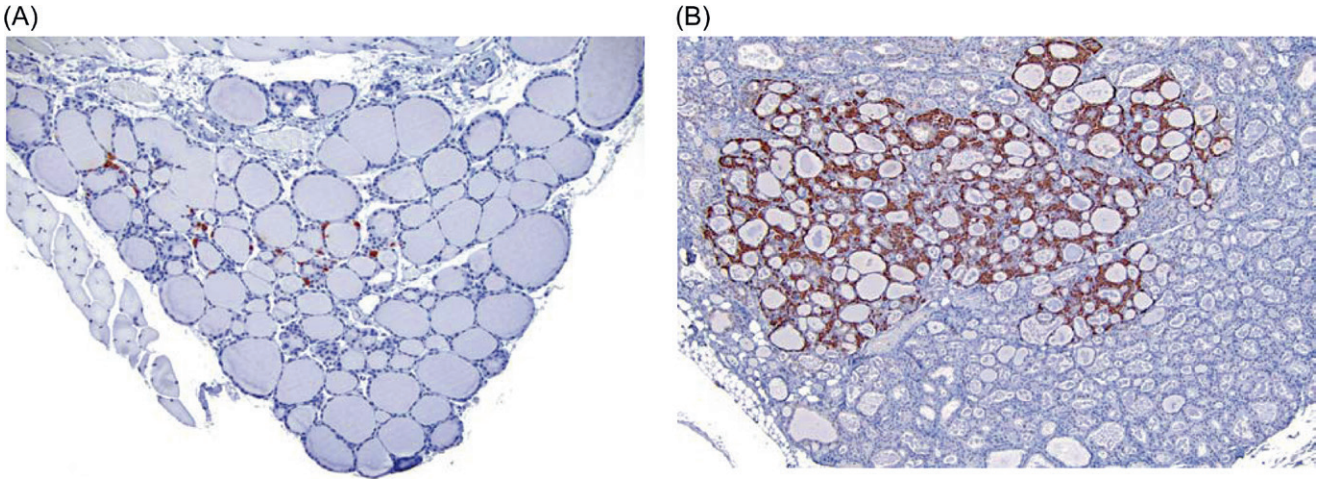

FIGURE 15.7 Calcitonin immunohistochemical staining of rodent thyroid gland. (A) Mouse. (B) Rat. Clustered centrally within the thyroid gland, there are variable numbers of C cells between follicles, greater in rats (B) than mice (A). DAB chromogen (brown) with hematoxylin counterstain.

Need-to-know

- C cells are inconspicuous in the mouse without special histochemical or immunohistochemical staining.
- The density of C cells is higher centrally within the thyroid gland, and greater in rats than in mice.

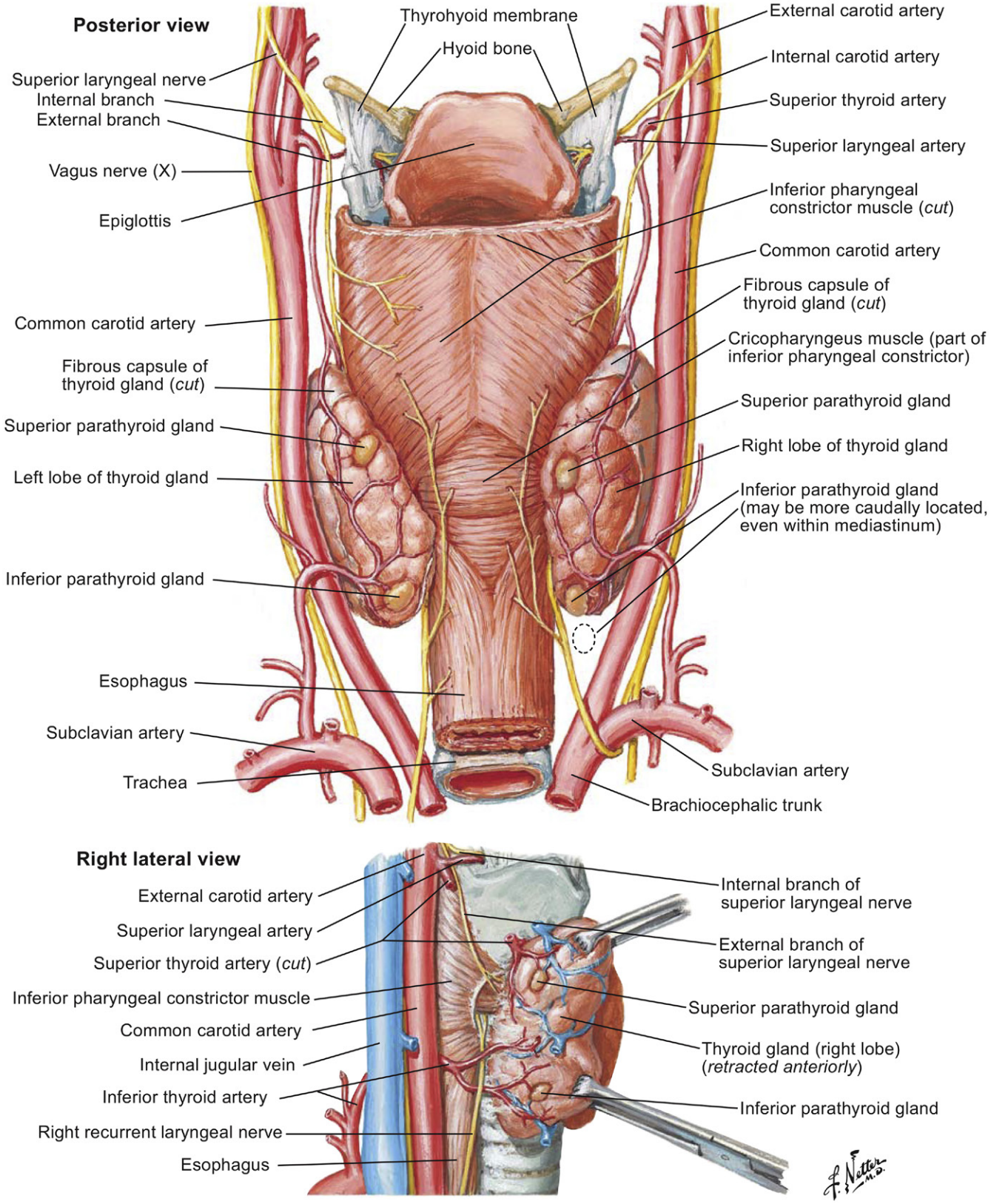

FIGURE 15.8 Human regional parathyroid anatomy. Source: © Elsevier, Inc., www.netterimages.com.

Need-to-know

- There is only one pair of parathyroid glands in rodents.

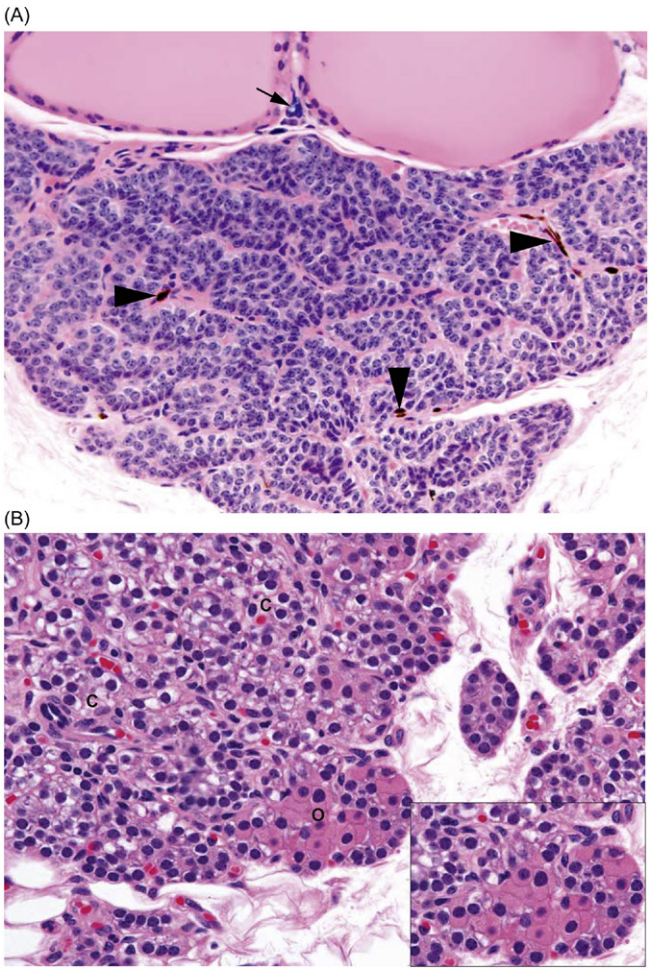

FIGURE 15.9 Parathyroid gland. (A) Rodent (mouse). Noted here subjacent to two large, colloid-filled thyroid follicles and composed entirely of neuroendocrine chief cells that produce PTH. Mast cells (arrow) are commonly observed in histologic sections of numerous rodent tissues. The presence of scattered melanocytes (arrowheads) is consistent with pigmented strains. (B) Human. Glandular elements supported in a bed of adipose tissue. The glandular cells are of two cell types, chief cells (C) and oxyphil cells (O). Oxyphil cells usually form nodules and have abundant eosinophilic cytoplasm (inset, high magnification).

Need-to-know

- Oxyphil cells have not been described in rodents.

fasciculata to the corticomedullary junction (Fig. 15.14C). The extent of this subcapsular proliferation varies with mouse age, strain, hormonal status, and housing conditions.

The human adrenal cortex has the same three zona layers as rodent, but as mentioned above, lacks the X-zone, except as a fetal form (Fig. 15.15). The zona glomerulosa may be incomplete and lies immediately under the fibrous adrenal capsule. It is composed of polygonal cells with round, darkly basophilic nuclei and small amounts of pale eosinophilic cytoplasm with few intracellular fat droplets that are arranged in rounded clusters or trabeculae. The zona glomerulosa is continuous with the zona fasciculata, which is made up of polygonal cell columns arranged perpendicular to the capsule. These cellular columns are often two cells thick and are separated from one another by a loose fibrovascular stroma. Individual cells are large with spherical pale-staining nuclei and vacuolated acidophilic cytoplasm that contains abundant lipid droplets and substrates for steroid hormone synthesis. The zona reticularis accounts for approximately one-fourth the thickness of the adrenal cortex and lies between the columns of the zona fasciculata and the adrenal medulla. Its cells are polygonal, smaller than those of the zona fasciculata, and arranged predominantly in single cell-wide cords separated by dilated capillaries. The cytoplasm is dense, and lipid-poor. Lipofuscin granules may be visible in those cells closest to the adrenal medulla.

In both rodents and humans, the junction between the adrenal cortex and medulla is rather irregular; no fibrous zone or capsule separates the cells of the zona reticularis from the medulla. Indeed, sometimes cords of cortical cells may extend deep into the medulla.

The medulla accounts for approximately 10% of the weight and volume of the adrenal gland in rodents and humans. It is composed of large polygonal pheochromocytes, also known as chromaffin cells and scattered ganglion cells (Fig. 15.16). Pheochromocytes are arranged in trabeculae and balls of cells (Zellballen) surrounded by flattened sustentacular cells that are not readily observed by light microscopy but easily identified by immunohistochemistry with antibodies to S100 protein. Pheochromocytes are large epithelioid cells that have abundant

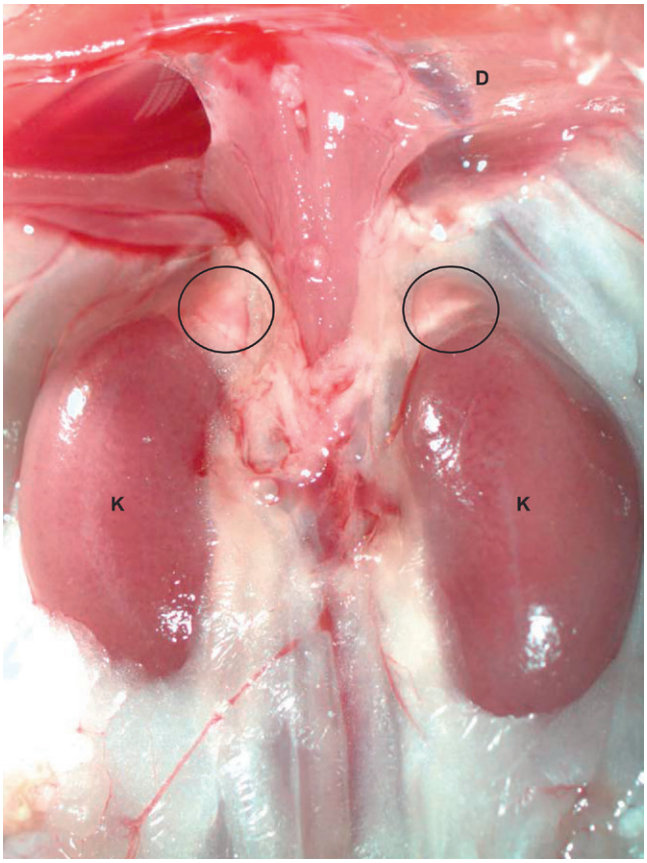

FIGURE 15.10 Rodent (mouse) regional adrenal anatomy. Upon removal of the liver, spleen, pancreas, and gastrointestinal tract, the adrenal glands (circled) can be seen anterior and medial to the cranial poles of the kidneys (K). Diaphragm (D) is indicated.

amphophilic cytoplasm and round-to-oval nuclei with coarsely clumped chromatin. Ultrastructurally, pheochromocyte cytoplasm contains abundant storage granules. In rodents, approximately 75–85% of pheochromocytes produce epinephrine and 15–25% produce norepinephrine, as opposed to humans where an individual pheochromocyte can produce both epinephrine and norepinephrine. Pheochromocytes essentially serve as modified (i.e., without dendrites or axons) postganglionic catecholamine-producing neurons of the sympathetic nervous system. Preganglionic cholinergic splanchnic sympathetic nerves innervate the adrenal medulla and stimulate release of catecholamines from pheochromocytes into the bloodstream.

Pituitary Gland

GROSS ANATOMY

The pituitary gland, along with the pineal gland (see below), is found within the central nervous system. It has a notably different location in rodent and human brain due to differences in regional anatomy (Fig. 15.17). In rodent brain, it is possible to capture both the pituitary and pineal glands in a single coronal (transverse) section (Fig. 15.18). The pituitary gland, also known as the hypophysis, remains in the skull of rodents and humans upon removal of the brain due to its residence within the sella turcica on the dorsal surface of the basisphenoid bone between the trigeminal nerves (Fig. 15.19). It is composed of an anterior lobe, or adenohypophysis, and a posterior lobe, or neurohypophysis, which are morphologically distinct, yet are collectively attached to the median eminence of the hypothalamus in the overlying brain via an infundibular stalk. The adenohypophysis consists of the pars distalis, the histologically inapparent pars tuberalis, and the pars intermedia, while the neurohypophysis consists of the pars nervosa and histologically inapparent infundibulum. In rodents, the peripheral pars distalis appears tan to reddish-tan and cradles the more central pars intermedia and pars distalis, which appear white (Fig. 15.19A and B). The pituitary gland in mice measures approximately 3 × 2×1 mm and weighs 1–3 mg, while in rats it measures approximately 6 × 5.5 × 3 mm and weighs 7–16 mg. The human pituitary gland measures approximately 13 × 10 × 6 mm and weigh 500 mg. Pituitary glands are larger in multiparous female rodents and humans than males.

HISTOLOGY

The pars distalis of the adenohypophysis is the largest and most functionally diverse region of the pituitary gland in both rodents and humans. It is composed of several different endocrine cell

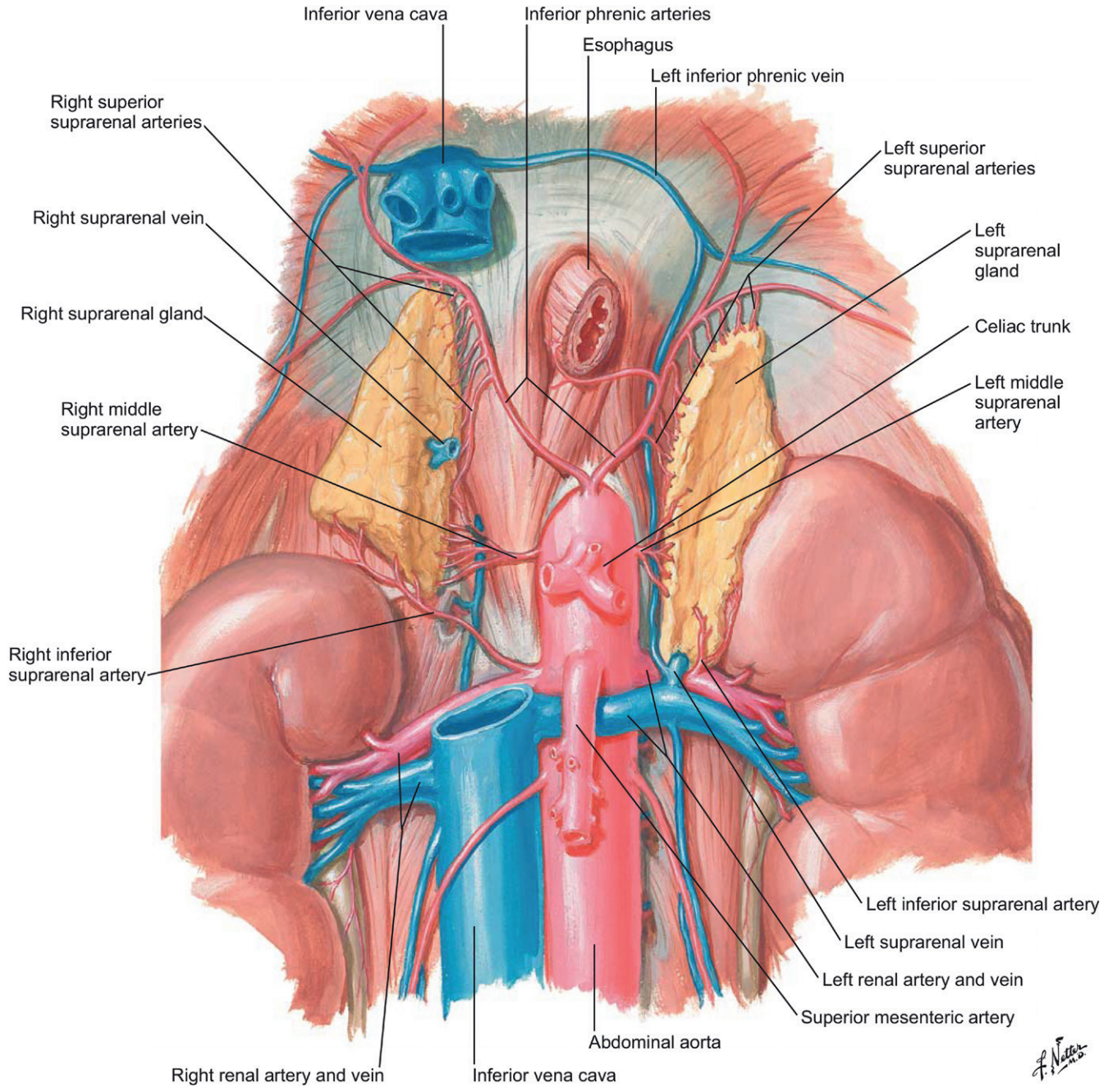

FIGURE 15.11 Human regional adrenal anatomy. Source: © Elsevier, Inc., www.netterimages.com.

populations that secrete pituitary tropic hormones under the control of specific releasing hormones or factors from the hypothalamus (Figs. 15.19C and 15.20). The secretory cells are arranged in cords and nests separated by abundant capillaries to facilitate release of hormones into the peripheral circulation. Secretory cells in the adenohypophysis are classified as the chromophilic acidophils and basophils and the chromophobes based on the reactions of their secretory granules with H&E (Fig. 15.20) or Orange-Fuschin-Green (OFG) stains, and further subclassified based on contemporary specific immunohistochemical staining. Acidophils can be further subclassified functionally into somatotrophs that secrete growth hormone (GH; somatotropin) in response to GH-releasing and

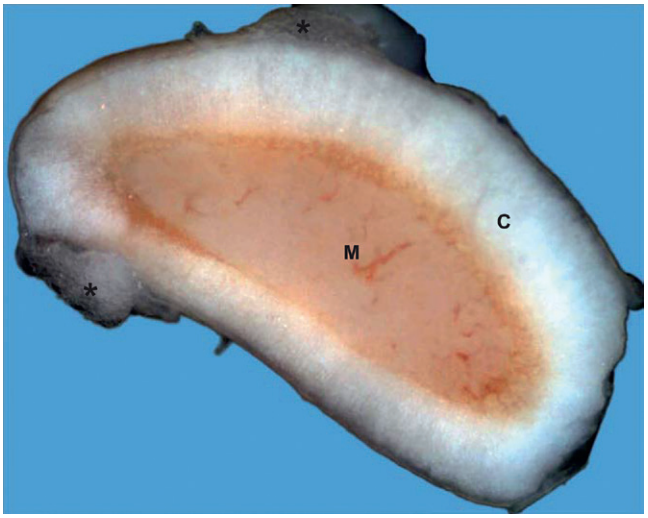

FIGURE 15.12 Sagittal section of rodent (mouse) adrenal gland. In this ex vivo and fixed specimen, the cortex (C) is whitish-tan, in contrast to the orange-tan medulla (M). Small amounts of brown adipose tissue (asterisks) remain on the capsular surface.

-inhibiting hormones; luteotrophs that secrete luteotropic hormone (luteotropin; prolactin) in response to prolactin-releasing hormone and prolactin-inhibiting factor (dopamine); and corticotrophs that secrete ACTH in response to corticotroph-releasing hormone. Basophils include gonadotrophs that secrete both luteinizing hormone (LH) and follicle-stimulating hormone (FSH) in response to gonadotropin-releasing hormone, as well as thyrotrophs that secrete TSH in response to TRH. While most cells actively synthesize and secrete a single hormone, a small number of bihormonal cells such as gonadotrophs are documented in rodents and humans.

Chromophils can also be distinguished ultrastructurally according to size of secretory granules. Chromophobes are pituitary cells that by light microscopy lack stainable cytoplasmic secretory granules, and represent degranulated chromophils, inactive reserve cells, and/or undifferentiated stem cells. The numbers of chromophil subpopulations and their distribution within the gland vary, particularly between rodents. For example, the typical mouse pars distalis stained with OFG is composed primarily of equal numbers of individualized acidophils and chromophobes with

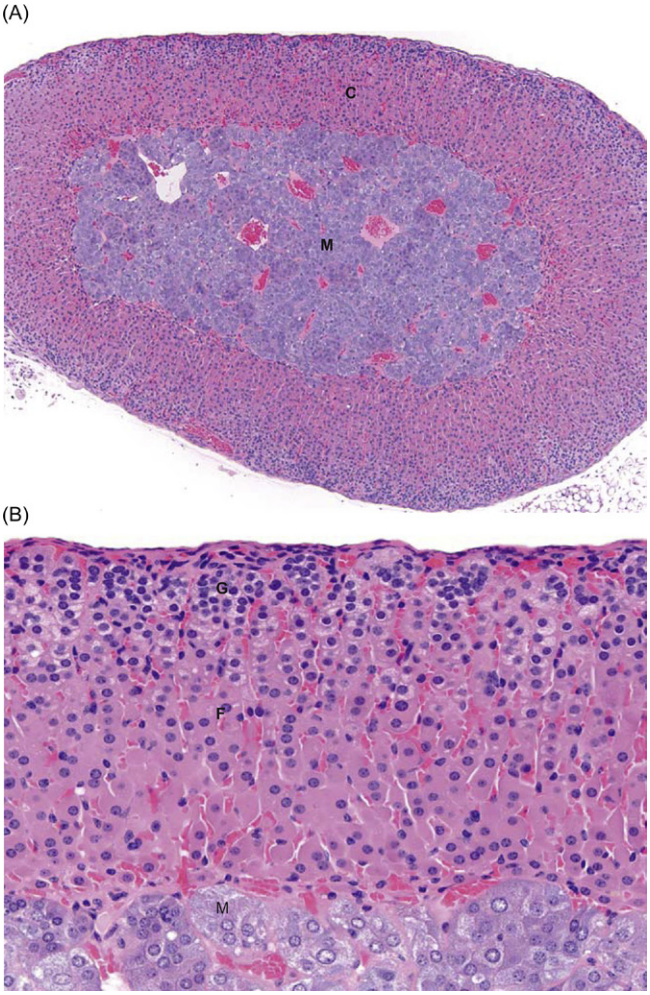

FIGURE 15.13 Rodent (mouse) adrenal gland. (A) Peripheral cortex (C) surrounding a central medulla (M), yielding a cortical: medullary: cortical width of approximately 1:2:1. (B) Adrenal cortex. Only two zones are consistently distinguishable in the mouse adrenal cortex: the thin zona glomerulosa (G), characterized by subtle arches, and the wider zona fasciculata (F) with cells arranged in columns that are eosinophilic to foamy, depending on the level of steroid production. The medulla (M) is indicated.

Need-to-know

- Normal cortical:medullary: cortical width is approximately 1:2:1 in rodents and humans.
- In contrast to humans, who produce cortisol, corticosterone is the major glucocorticoid produced by the rodent adrenal cortex.
- The zona reticularis is indistinguishable in rodents due to the absence of 17 α-hydroxylase and associated androgen production.

rare scattered basophils. In contrast, the typical rat pars distalis stained with OFG is composed primarily of sheets of chromophobes with scattered acidophils and fewer basophils. In addition, the number of mammotroph acidophils tends to be greater in

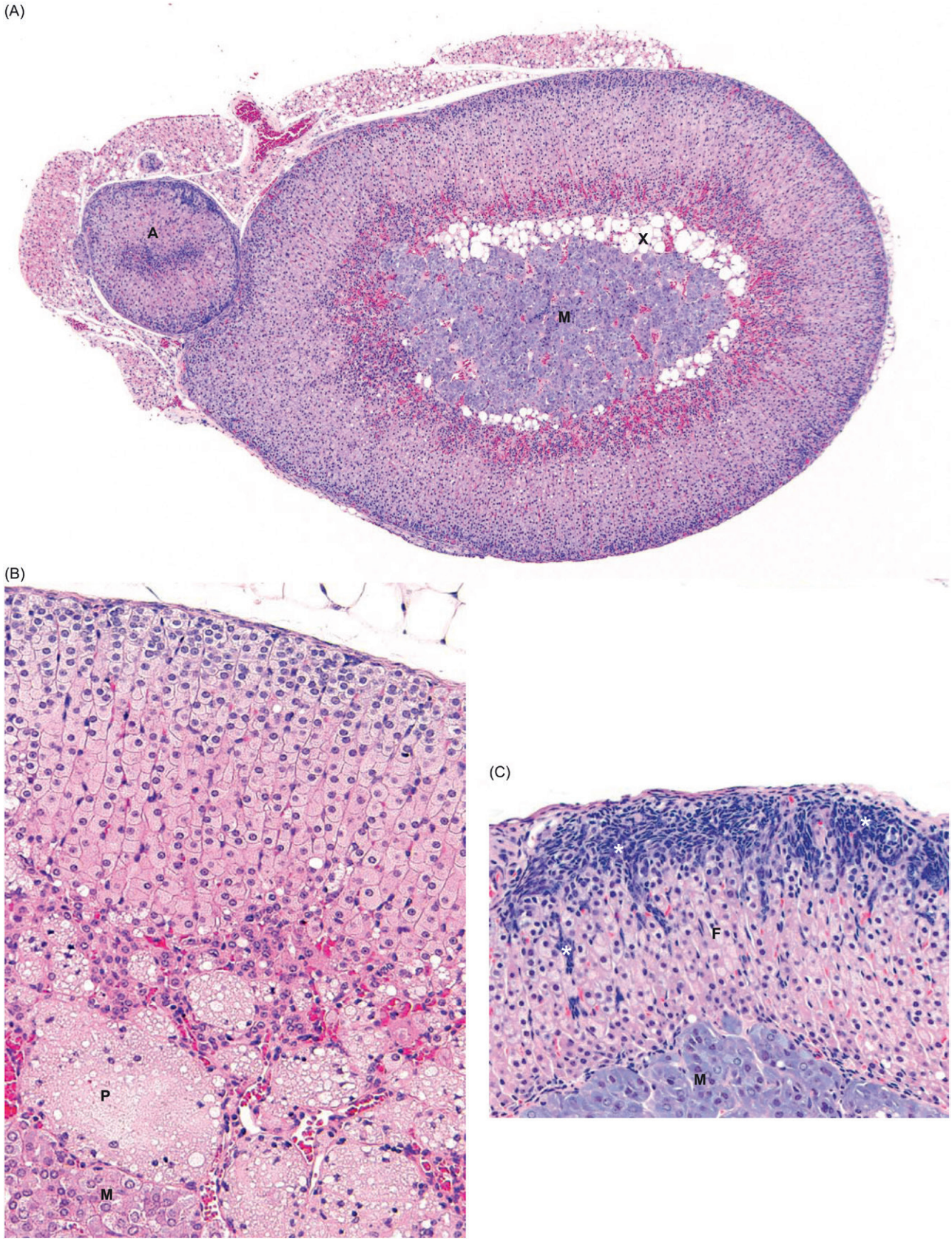

FIGURE 15.14 Rodent (mouse) adrenal gland. (A) X-zone in a female. The X-zone (X) in the mouse adrenal cortex is located adjacent to the medulla (M), similar to the fetal zone of the human adrenal cortex. Accessory adrenocortical nodules (A) are also commonly seen in mice. (B) Lipogenic pigmentation of aged mouse adrenal. A common senile change at the adrenocorticomedullary junction is the accumulation of yellowish-brown, foamy pigment (P) within cortical cells, noted here adjacent to islands of medullary chromaffin cells (M). (C) Subcapsular spindle cells in aged mouse adrenal. Proliferation of spindle cells (asterisks) subjacent to the capsule and vertically between columns of the zona fasciculata (F) is also commonly seen. The medulla (M) is indicated.

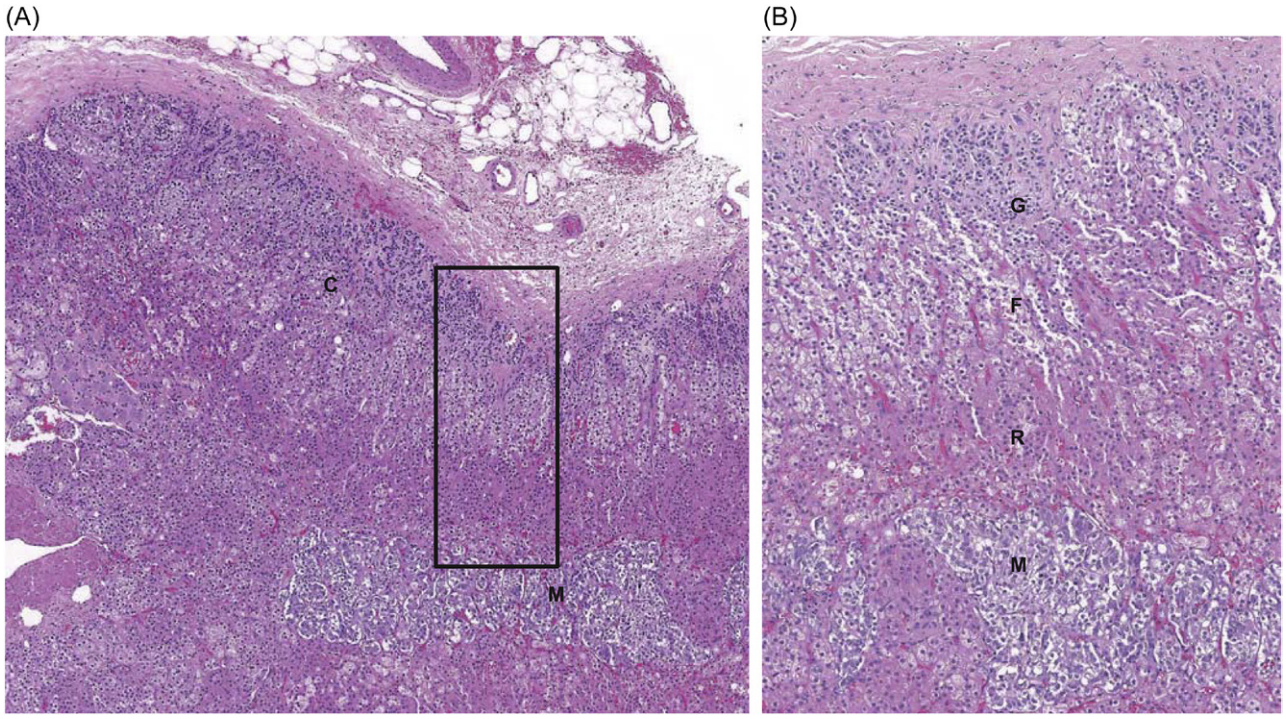

FIGURE 15.15 Human adrenal gland. (A) A dense fibrous capsule contains an outer cortex (C) that makes up approximately 90% of the gland and inner medulla (M). (B) Three histologic zones: the zona glomerulosa (G), zona fasciculata (F), and zona reticularis (R). The glomerulosa represents approximately 10% of the cortex and is located subjacent to the capsule. The fasciculata is the broadest of the three zones and is composed of large cells filled with lipid droplets imparting a pale cytoplasm. The reticularis is the thin innermost zone whose cells contain less lipid.

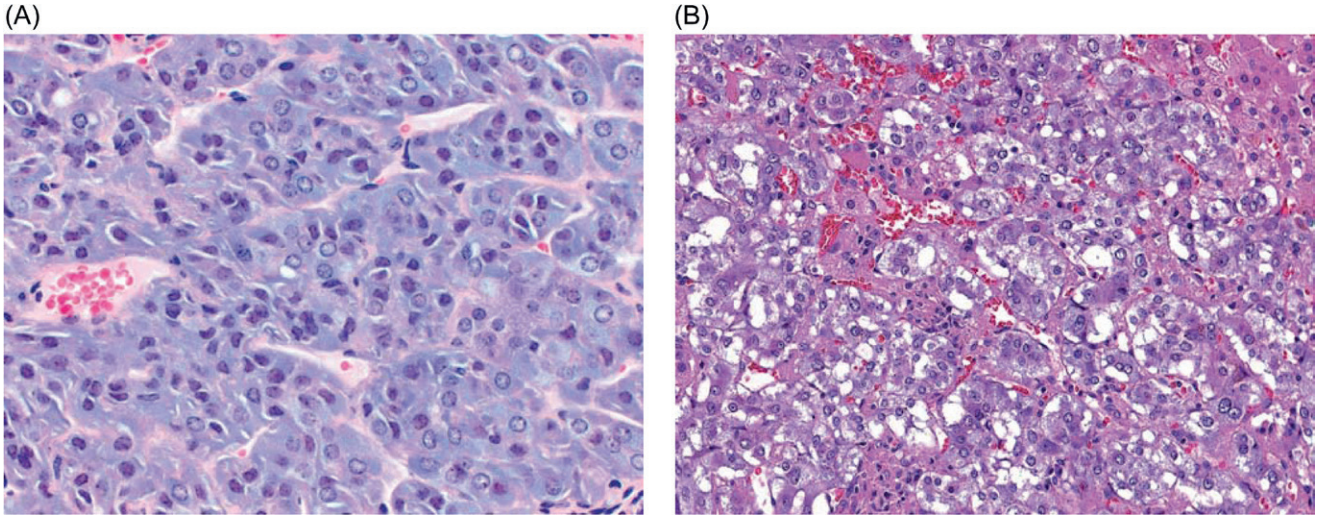

FIGURE 15.16 Adrenal medulla. (A) Rodent (mouse). The medulla is composed of basophilic, neuroendocrine chromaffin cells that produce catecholamines. (B) Human. The medulla secretes epinephrine and norepinephrine under the control of the sympathetic nervous system.

Need-to-know

- Most chromaffin cells in rodents produce epinephrine, whereas in humans they produce both epinephrine and norepinephrine.

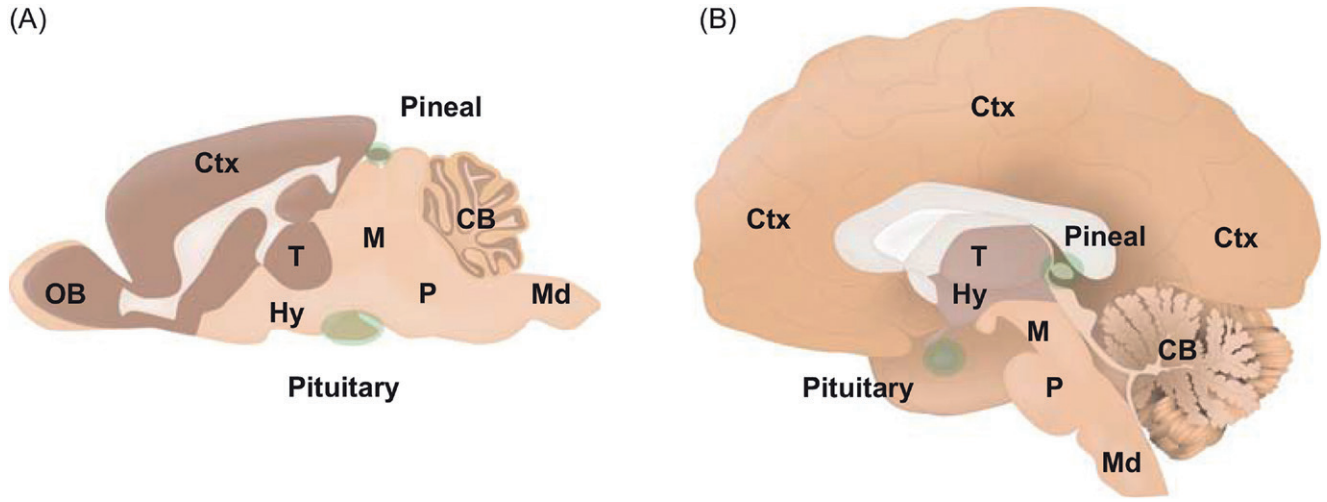

FIGURE 15.17 Comparative locations of the pituitary and pineal glands. Pituitary and pineal glands in the rodent (mouse) (A) and human (B) are highlighted (green ovals) on sagittal schematic diagrams of the brain. CB, cerebellum; Ctx, cerebral cortex; Hy, hypothalamus; M, midbrain; Md, medulla oblongata; OB, olfactory bulb; P, pons; T, thalamus. Source: Figure by Sara Samuelson, S. S. Illustrations.

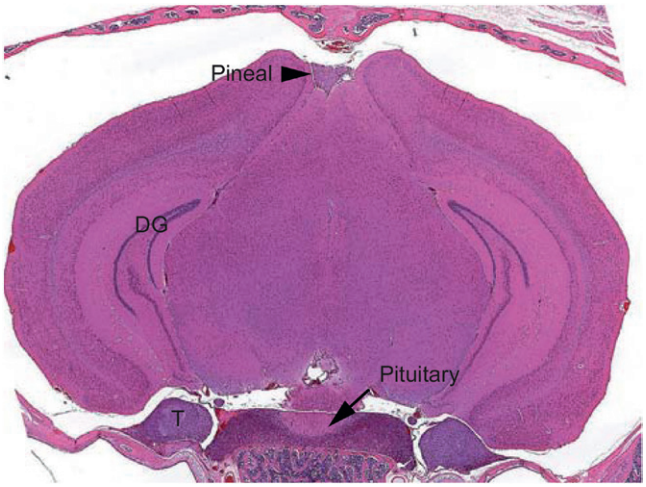

FIGURE 15.18 Locations of the pituitary and pineal glands in the rodent (mouse). In coronal (transverse) sections, both glands may be found in the same plane. Note the marked retraction of the brain within the cranial vault, indicating soft tissue shrinkage during processing. DG, dentate gyrus of the hippocampus; T, trigeminal ganglion.

females, while reports indicate that the number of somatotroph acidophils as well as thyrotroph and gonadotroph basophils tends to be greater in males. It should also be noted that spontaneous proliferative pituitary lesions (i.e., adenomas) in rodents are most commonly derived from active prolactin-secreting lactotrophs ± corresponding chromophobes.

The pars intermedia of the adenohypophysis is located between the pars distalis and the pars nervosa (Fig. 15.20). It is adjacent to the residual lumen of Rathke's pouch, which is lined by a single layer of low cuboidal epithelial cells. The pars intermedia is thicker and subsequently more pronounced in rodents than humans, due to an irregular band of polygonal cells with round-to-oval nuclei and abundant pale eosinophilic foamy cytoplasm. Unlike in humans, the rodent pars intermedia is the source of proopiomelanocortin-derived peptides—ACTH with lesser amounts of α-melanocyte stimulating hormone (α-MSH) and β-endorphin. In humans, the pars intermedia is thin, poorly developed, and often contains colloid-filled cysts that are lined by flattened epithelium. Individual cells are cuboidal or columnar and sit on a slightly fibrous stroma.

The pars nervosa of the neurohypophysis is eosinophilic, fairly homogenous, and relatively hypocellular (Fig. 15.20). It is composed of unmyelinated axons from hypothalamic neurons that terminate on capillaries supported by modified glial cells known as pituicytes. The neurohypophyseal hormones, oxytocin and vasopressin or antidiuretic hormone (ADH), are

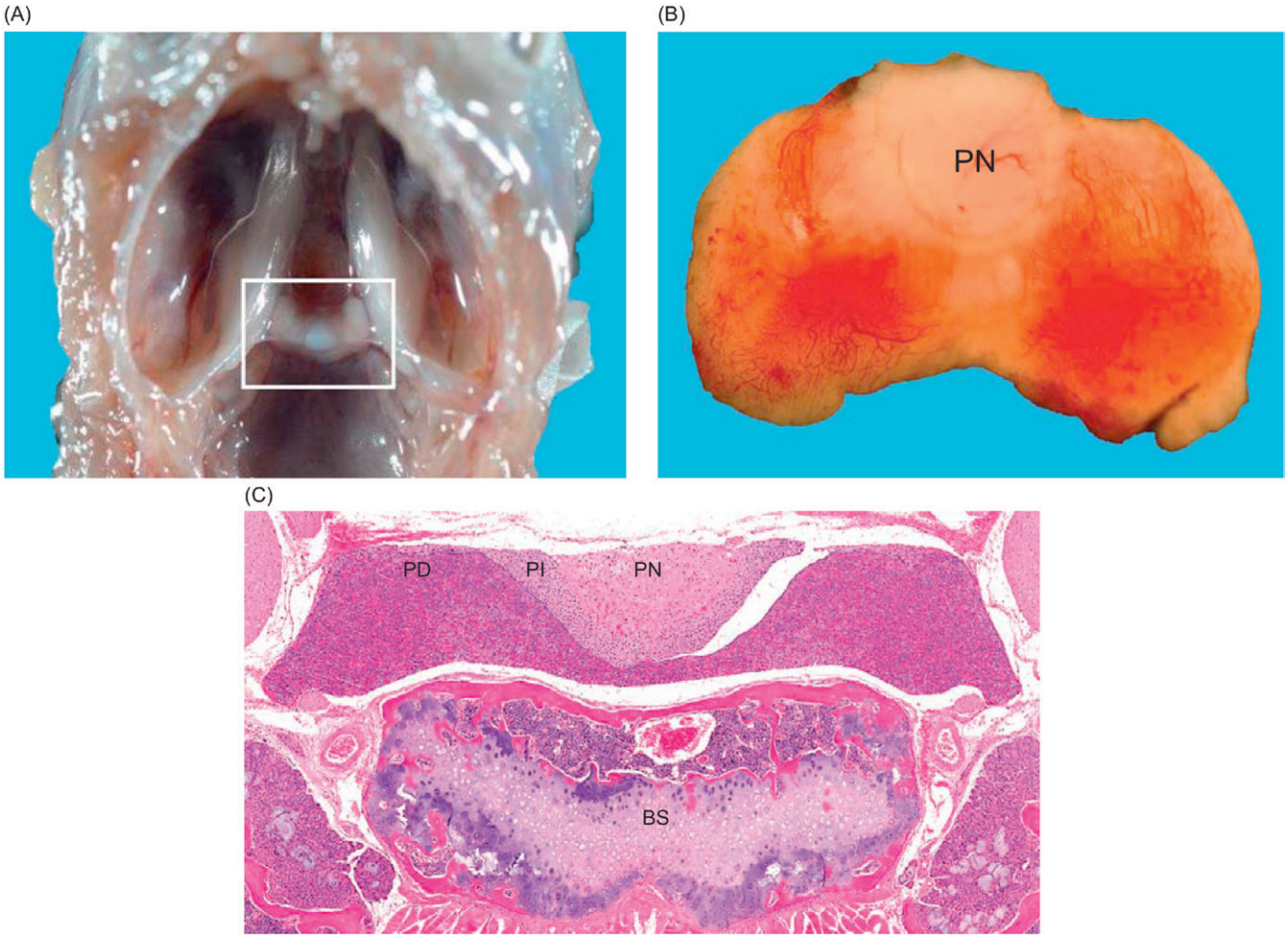

FIGURE 15.19 Rodent (rat) pituitary gland in vivo and ex vivo. (A) The pituitary gland (square) remains in the skull upon removal of the brain. Grossly, the pars distalis is tan to reddish-tan and cradles the centrally located pars intermedia and pars nervosa (PN), which appear white in A and B. (C) The pituitary gland resides within the sella turcica on the dorsal aspect of the basisphenoid bone (BS). PN, pars nervosa; PI, pars intermedia; PD, pars distalis.

synthesized in the cell bodies of hypothalamic neurons within the supraoptic and paraventricular nuclei, packaged into secretory granules, and transported by long axonal processes of the hypothalamo-hypophyseal tract to axons in the pars nervosa where they are released into the associated rich capillary bed.

Pineal Gland

Gross Anatomy

Similar to the pituitary gland, the pineal gland has notably different locations in rodent and human brain (Fig. 15.17); in rodents it can be seen with the pituitary gland in a single coronal (transverse) section (Fig. 15.18). The rodent pineal gland is found on the external surface of the brain on midline at the interface between the cerebral hemispheres and the caudal (inferior) colliculi (Fig. 15.21). It is encapsulated by an extension of the pia mater, and as such, frequently remains attached to the meninges when the skull cap is removed for extraction of the brain. Rodent pineal glands are round and pale tan. The exceedingly small size of the mouse pineal gland typically restricts its observation to histologic sections; the published volumes in sexually mature mice ranges from 97 to 105 $\times 10^6 \mu m^3$. The rat

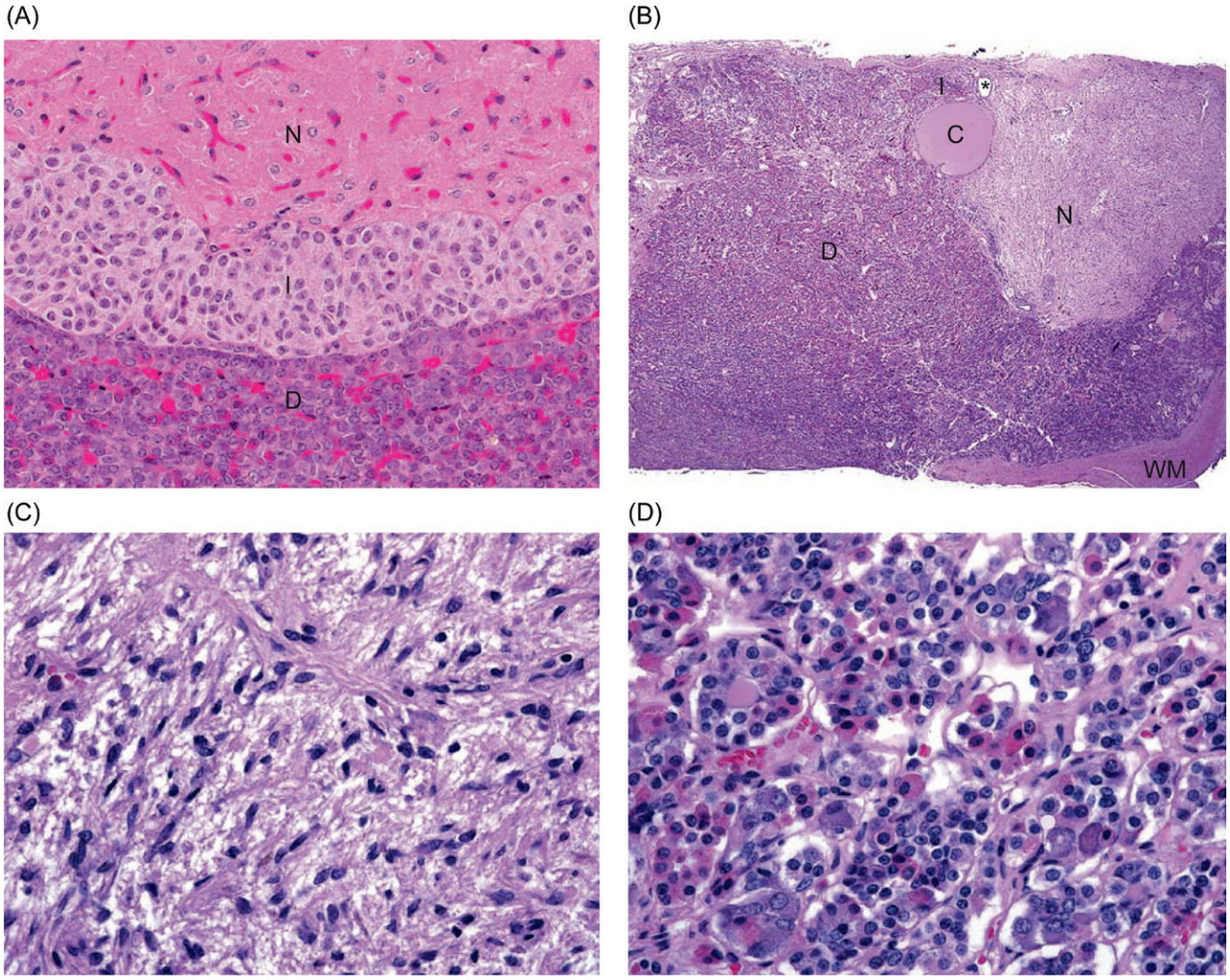

FIGURE 15.20 Pituitary gland. (A) Rodent (mouse). (B–D) Human. The pituitary gland has three distinct zones, which are functionally diverse. The pars distalis (D) in A, B and D exhibits nests and cords of chromophilic and chromophobic secretory cells. The pars intermedia (I), as shown in A and B, is separated from the pars distalis by a residual cleft of Rathke's pouch lined by cuboidal epithelial cells; it is thicker and more prominent in rodents than in humans. The pars intermedia of humans (B) typically has epithelial-lined cysts that are empty (asterisk) or contain colloid (C). The pars nervosa in A–C is composed of unmyelinated axons from hypothalamic neurons that terminate on capillaries supported by modified glial cells known as pituicytes.

Need-to-know

- The pars intermedia in rodents is thicker and more pronounced than in humans.
- Unlike in humans, the rodent pars intermedia is the source of POMC-derived peptides.

pineal gland measures 1–2 mm^3 and weighs 0.5–1 mg, with larger weights documented in males. The human pineal gland is located within the posterior wall of the third ventricle near the center of the brain, measures 5–8 × 3–5 × 3–5 mm, and weighs 100–200 mg. Its configuration in humans resembles a pine cone, hence the name pineal, due to the formation of incomplete lobules by prominent intralobular fibrovascular stroma extending from the pineal gland capsule.

HISTOLOGY

Cells in the pineal gland of both rodents and humans derive from two populations. The majority (~95%) are parenchymal modified neurons known as pinealocytes that originate from neuroectoderm. Pinealocytes are round cells that frequently form clusters, rosettes, and/or linear arrays intimately associated with a rich capillary network (Fig. 15.22). They have round, euchromatic nuclei with a single

FIGURE 15.21 Rodent (rat) pineal gland ex vivo. The pineal gland (circle) can be readily identified on the external surface of the brain at the interface between the cerebral hemispheres and cerebellum, in instances when it does not remain attached to the meninges of the skull cap during removal.

prominent nucleus and moderate amounts of pale eosinophilic granular cytoplasm. Variable numbers of cytoplasmic processes may be apparent by silver histochemical staining methods. Pinealocytes are photosensitive and secrete melatonin, a regulator of circadian rhythm, in response to light-dark cycle signals transmitted along the retinohypothalamic tract. Basal plasma melatonin levels are elevated during dark periods and correspond to histologic changes such as pinealocyte hypertrophy, multiple nucleoli, and cytoplasmic lipid droplets. The remaining cells are interstitial glial cells that resemble classical and fibrous astrocytes. They can be differentiated from pinealocytes by their smaller size, more elongated shape, and hyperchromatic nuclei. Mineralized concretions (corpora amylacea, corpora arenacea, psammoma bodies, or "brain sand") accrue with age in the human pineal gland (Fig. 15.22B and D).

Paraganglia

Gross Anatomy

Paraganglia are groups of chromaffin neurosecretory cells of neural crest origin that are dispersed throughout the body of both rodents and humans as gray-to-pink masses. They are classified as sympathetic or parasympathetic according to their location and neural association. Sympathetic paraganglia, of which the adrenal medulla is the prime example, are distributed along paravertebral sympathetic chains and nerves that innervate retroperitoneal and pelvic organs. Parasympathetic paraganglia serve as chemoreceptors, are distributed primarily along the cervicothoracic branches of the glossopharyngeal and vagus nerves and include the jugulotympanic, orbital, vagal, laryngeal, and subclavian paraganglia, as well as the carotid and aortic bodies. These chemoreceptors are sensitive to changes in carbon dioxide level, pH, and oxygen tension in the blood, thereby aiding in the regulation of respiration and circulation. Carotid and aortic bodies can initiate an increase in the depth, minute volume, and rate of respiration via their effect on parasympathetic nerves or an increase in heart rate and elevation of arterial blood pressure via their effect on the sympathetic nervous system. With the exception of the bilateral carotid bodies located at the carotid bifurcation, paraganglia are highly variable in number and location, but typically distributed along the central axis of the body. Determining their location is aided by the relatively high permeability of their blood vessels to Evans blue dye. The weight of the carotid bodies in humans, which correlates with body weight, has been estimated according to the following equation: combined weight of carotid bodies (mg) = 0.29 × body weight (kg) + 3.0. Because of variability, weights for other paraganglia have not been estimated.

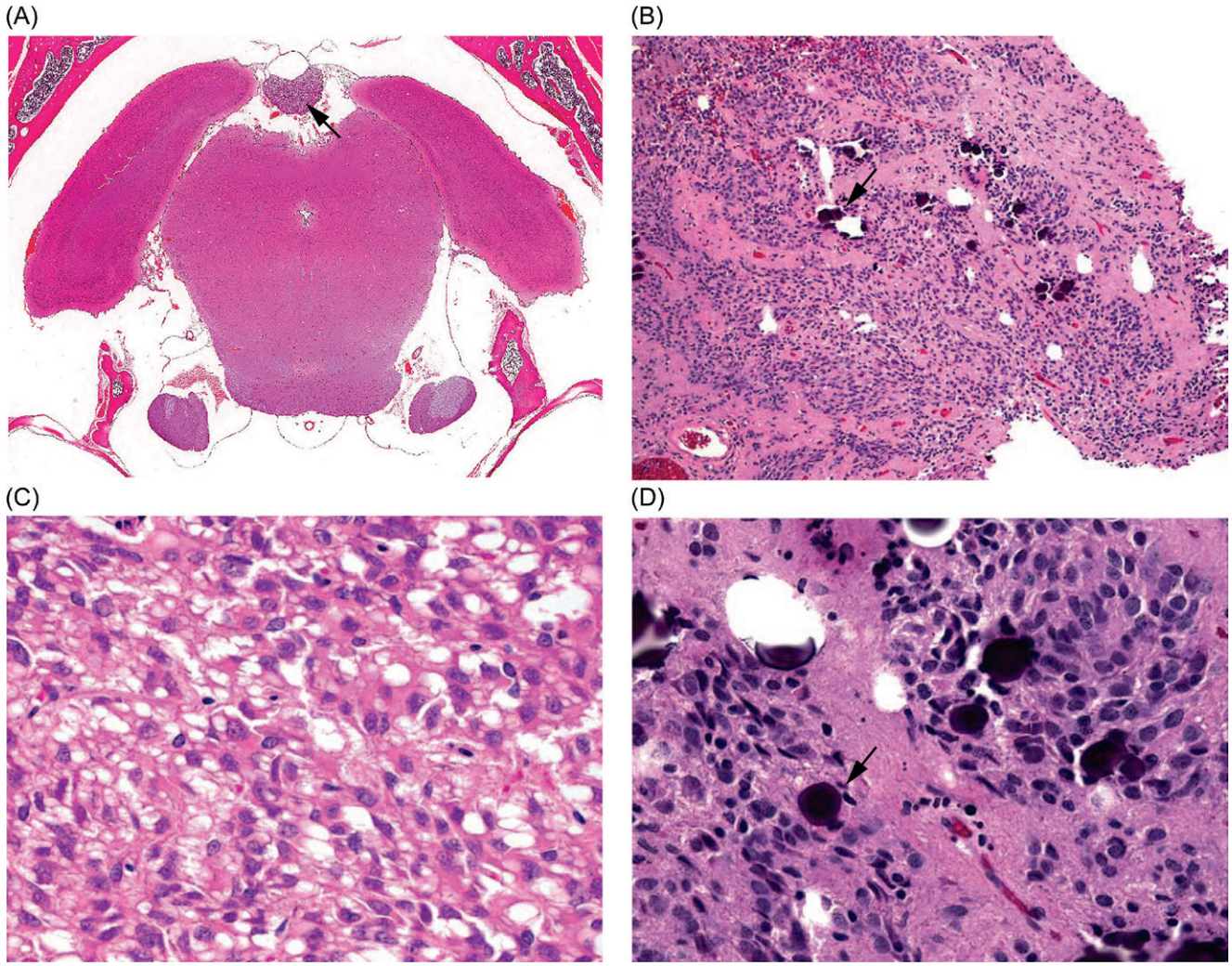

FIGURE 15.22 Pineal gland. (A, C) Rodent (rat). (B, D) Human. (A) The rat pineal gland (arrow) is on the midline between the cerebral hemispheres and the caudal colliculi, irregularly round and surrounded by a thin capsule. (B) The human pineal gland is centrally located in the brain and composed of incomplete lobules due to prominent fibrovascular stroma. The majority (~95%) of cells in rodent (C) and human (D) pineal glands are pinealocytes with round nuclei and pale eosinophilic, often vacuolated, cytoplasm. Glial cells are smaller, elongated, and have hyperchromatic nuclei. As shown in B and D, calcification (arrows) is a normal age-related change in the human pineal gland. Note the retraction of the brain within the cranial vault in A, indicating soft tissue shrinkage during processing.

Need-to-know

- The rodent pineal gland is round and located on the external surface of the brain at the interface between the cerebral hemispheres and caudal colliculi.
- The human pineal gland is incompletely lobulated and positioned centrally in the brain along the posterior wall of the third ventricle.

HISTOLOGY

In all three species, the paraganglia are composed of chromaffin cells, polygonal neuroendocrine cells, with basophilic cytoplasm containing numerous membrane-bound granules, and supporting glial cells, which are arranged into discrete lobules separated by connective tissue septae (Fig. 15.23). Nerve endings with synaptic vesicles, as well as nerve fibers and mast cells, are in close association. In rodents, the carotid and aortic bodies and abdominal paraganglia have been studied the most extensively. Carotid and aortic body size and subsequent hypoxic ventilatory response can vary between individual animals and strains. Abdominal paraganglia are maximally developed at birth and then variably disperse, degenerate, or both such that discrete masses are no longer apparent after 1 week.

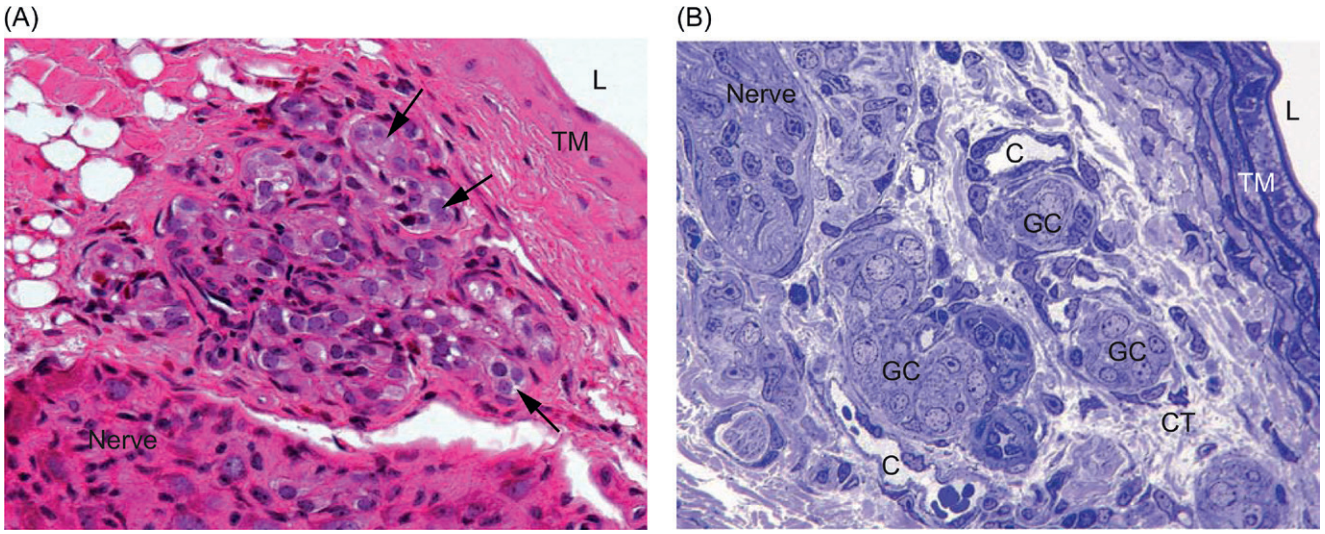

FIGURE 15.23 Paraganglia. (A) Rodent (mouse) carotid body. Discrete, whorl-like arrangement of glomus cells (arrows) of the carotid body interspersed between a ganglia and nerve, and the tunica media (TM) of the mouse carotid. Lumen is indicated (L). (B) Human carotid body. This richly vascularized structure is close to the lumen (L) and tunica media (TM) of the internal carotid artery. Groups of spherical glomus cells (GC) with euchromatic nuclei are embedded in connective tissue (CT). These cells are close to a network of sinusoidal capillaries (C). Afferent nerve fibers of cranial nerve IX (N) are seen. Plastic section, toluidine blue. Source of A: Dr. Piper Treuting. Source of B: Reprinted from Ovalle WK, Nahirney JC: *Netter's essential histology*, 2008, with permission from © Elsevier, www.netterimages.com.

Need-to-know

- Paraganglia are distributed as aggregates of neurons along the central axis of the body in the neck, thorax, and abdomen.
- The size, number, and physiologic response of paraganglia vary between strain and individual.

FURTHER READING

Bailey SA, Zidell RH, Perry R: Relationships between organ weight and body/brain weight in the rat: what is the best analytical endpoint? *Toxicol Pathol* 32:448–466, 2004.

Baker BL, Gross DS: Cytology and distribution of secretory cell types in the mouse hypophysis as demonstrated with immunocytochemistry. *Am J Anat* 153:193–216, 1978.

Beatriz M, Lopes S, Pernicone PJ, et al: Pituitary and sellar region. In Mills SE, editor: *Histology for pathologists* (ed 4), Philadelphia, PA, 2012, Lippincott Williams & Wilkins, pp 343–374.

Bilezilian JP, Levine MA, Marcus R, editors: *The parathyroids*, New York, 1994, Raven Press.

Biscoe TJ, Pallot DJ: The carotid body chemoreceptor: an investigation in the mouse. *Q J Exp Physiol* 67:557–576, 1982.

Carcangiu ML: Thyroid. In Mills SE, editor: *Histology for pathologists* (ed 4), Philadelphia, PA, 2012, Lippincott Williams & Wilkins, pp 1185–1208.

Carney JA: Adrenal gland. In Mills SE, editor: *Histology for pathologists* (ed 4), Philadelphia, PA, 2012, Lippincott Williams & Wilkins, pp 1231–1254.

Cernuda-Cernuda R, Huerta JJ, Muñoz Llamosas M, et al: Age-related morphometric changes in the pineal gland. A comparative study between C57BL/6J and CBA mice. *Histol Histopathol* 15:1087–1092, 2000.

Daughaday W: A comparison of the X-zone of the adrenal cortex in two inbred strains of mice. *Cancer Res* 1:883–885, 1941.

Deane BM, Howe A, Morgan M: Abdominal vagal paraganglia: distribution and comparison with carotid body, in the rat. *Acta Anat (Basel)* 93:19–28, 1975.

DeLellis RA, Dayal Y: The neuroendocrine system. In Mills SE, editor: *Histology for pathologists* (ed 4), Philadelphia, PA, 2012, Lippincott Williams & Wilkins, pp 1255–1276.

Easton J, Howe A: The distribution of thoracic glomus tissue (aortic bodies) in the rat. *Cell Tissue Res* 232:349–356, 1983.

Goormaghtigh N: On the existence of abdominal vagal paraganglia in the adult mouse. *J Anat* 71(Pt. 1):77–93, 1936.

Hardisty JF, Boorman GA: Thyroid and parathyroid glands. In Maronpot RR, editor: *Pathology of the mouse*, Vienna, IL, 1999, Cache River Press, pp 537–554.

Hershkovitz L, Beuschlein F, Klammer S, et al: Adrenal 20α-hydroxysteroid dehydrogenase in the mouse catabolizes progesterone and 11-deoxycorticosterone and is restricted to the X-zone. *Endocrinology* 148:967–988, 2007.

Holmes PV, Dickson AD: X-zone degeneration in the adrenal glands of adult and immature female mice. *J Anat* 108:159–168, 1971.

Howard E: The representation of the adrenal X zone in rats, in the light of observations on X zone variability in mice. *Am J Anat* 62:351–373, 1938.

Karasek M, Reiter RJ: Functional morphology of the mammalian pineal gland. In Jones TC, Capen CC, Mohr U, editors: *Monographs on pathology of laboratory animals: endocrine system* (ed 2), New York, 1996, Springer-Verlag, pp 193–204.

Kaufman M, Nikitin AY, Sundberg JP: *Histologic basis of mouse endocrine system development: a comparative analysis*, Boca Raton, FL, 2010, CRC Press.

Keane KA, Parker GA, Regan KS, et al: Scientific and regulatory policy committee (SRPC) points to consider*: histopathology evaluation of the pubertal development and thyroid function assay (OPPTS 890.1450, OPPTS 890.1500) in rats to screen for endocrine disruptors. *Toxicol Pathol* 43:1047–1063, 2015.

Kittel B, Ernst H, Kamino K: Anatomy, histology, and ultrastructure, parathyroid, mouse. In Jones TC, Capen CC, Mohr U, editors: *Monographs on pathology of laboratory animals: endocrine system* (ed 2), New York, 1996, Springer-Verlag, pp 328–330.

Kittel B, Ernst H, Kamino K: Anatomy, histology, and ultrastructure, parathyroid, rat. In Jones TC, Capen CC, Mohr U, editors: *Monographs on pathology of laboratory animals: endocrine system* (ed 2), New York, 1996, Springer-Verlag, pp 330–333.

Kus I, Sarsilmaz M, Ozen OA, et al: Light and electron microscopic examination of pineal gland in rats exposed to constant light and constant darkness. *Neuro Endocrinol Lett* 25:102–108, 2004.

Marino DJ: Age-specific absolute and relative organ weight distributions for Fischer 344 rats. *J Toxicol Environ Health A* 75:1484–1516, 2012.

McDonald DM, Blewett RW: Location and size of carotid body-like organs (paraganglia) revealed in rats by the permeability of blood vessels to Evans blue dye. *J Neurocytol* 10:607–643, 1981.

Møller M, Rath MF, Klein DC: The perivascular phagocyte of the mouse pineal gland: an antigen-presenting cell. *Chronobiol Int* 23:393–401, 2006.

Monkhouse WS: The effect of *in vivo* hydrocortisone administration on the labelling index and size of chromaffin tissue in the postnatal and adult mouse. *J Anat* 144:133–144, 1986.

Neepa YC, Jahnke GD, St. Hilaire C, et al: Role of thyroid hormones in human and laboratory animal reproductive health. *Birth Defects Res B Dev Reprod Toxicol* 68:479–491, 2003.

Nyska A, Maronpot RR: Adrenal gland. In Maronpot RR, editor: *Pathology of the mouse*, Vienna, IL, 1999, Cache River Press, pp 509–536.

Osamura RY: Histology, ultrastructure, and immunochemistry, pituitary gland, rat. In Jones TC, Capen CC, Mohr U, editors: *Monographs on pathology of laboratory animals: endocrine system* (ed 2), New York, 1996, Springer-Verlag, pp 33–41.

Pihlajoki M, Dörner J, Cochran RS, et al: Adrenocortical zonation, renewal, and remodeling. *Front Endocrinol (Lausanne)* 6:27, 2015.

Poole MC, Kornegay III WD: Cellular distribution within the rat adenohypophysis: a morphometric study. *Anat Rec* 204:45–53, 1982.

Quimby FW, Luong RH: Clinical chemistry of the laboratory mouse (ed 2), Fox JG, Barthold SW, Davisson MT, Newcomer CE, Quimby FW, Smith AL, editors: *The mouse in biomedical research: normative biology, husbandry, and models*, vol 3, Burlington, MA, 2007, Elsevier.

Rao-Rupanagudi S, Heywood R, Gopinath C: Age-related changes in thyroid structure and function in Sprague Dawley rats. *Vet Pathol* 29:278–287, 1992.

Rehm S, Nitsche B, Deerberg F: Non-neoplastic lesions of female virgin Han:NMRI mice, incidence and influence of food restriction throughout life span. I: Thyroid. *Lab Anim* 19:214–223, 1985.

Rosol TJ, DeLellis RA, Harvey PW, et al: Endocrine system (ed 3), Haschek WM, Rousseaux CG, Wallig MA, editors: *Haschek and Rousseaux's handbook of toxicologic pathology*, vol 3, Waltham, MA, 2013, Academic Press.

Rosol TJ, Yarrington JT, Latendresse J, et al: Adrenal gland: structure, function, and mechanisms of toxicity. *Toxicol Pathol* 29:41–48, 2001.

Ross MH, Pawlina W: Endocrine organs. In Pawlina W, editor: *Histology: a text and atlas with correlated cell and molecular biology* (ed 7), Philadelphia, PA, 2016, Wolters Kluwer Health, pp 742–789.

Roth SI, Sadow PM, Johnson NB, et al: Parathyroid. In Mills SE, editor: *Histology for pathologists* (ed 4), Philadelphia, PA, 2012, Lippincott Williams & Wilkins, pp 1209–1230.

Schachner M, Huang S-K, Ziegelmüller P, et al: Glial cells in the pineal gland of mice and rats: a combined immunofluorescence and electron-microscopic study. *Cell Tissue Res* 237:245–252, 1984.

Sucheston ME, Cannon MS: The transient-zone in the human and mouse adrenal gland. *Ohio J Sci* 72:120–126, 1972.

Tischler AS: Paraganglia. In Mills SE, editor: *Histology for pathologists* (ed 4), Philadelphia, PA, 2012, Lippincott Williams & Wilkins, pp 1277–1300.

Wills PI, Schindler WJ: Radiothyroxine turnover studies in mice: effects of temperature, diet, sex and pregnancy. *Endocrinology*:1272–1280, 1970.

Wollman SH, Hilfer SR: Embryologic origin of the various epithelial cell types in the second kind of thyroid follicle in the C3H mouse. *Anat Rec* 191:111–121, 1978.

Yamaguchi S, Balbir A, Schofield B, et al: Structural and functional differences of the carotid body between DBA/2J and A/J strains of mice. *J Appl Physiol* 94:1536–1542, 2003.

Zak FG, Lawson W: *The paraganglionic chemoreceptor system.* Physiology, pathology and clinical medicine, New York, 1983, Springer-Verlag.

This page intentionally left blank

URINARY SYSTEM 16

MARTHA A. DELANEY
University of Washington School of Medicine, Seattle, WA, United States

JOLANTA KOWALEWSKA
Eastern Virginia Medical School, Norfolk, VA, United States

PIPER M. TREUTING
University of Washington School of Medicine, Seattle, WA, United States

Introduction

The urinary system in the three species is composed of bilateral paired kidneys and ureters, a single midline pelvic bladder, and a urethra (Table 16.1 and Figs. 16.1–16.3). The urinary system is responsible for a variety of physiologic processes, including osmoregulation, blood pressure and volume regulation, stimulation of red blood cell production, calcium absorption, toxin metabolism, and excretion. The nephron is the functional unit of the kidney and is composed of the glomerulus and the renal tubule. The products of the kidney include urine, the enzyme hormone renin, and the hormones erythropoietin and calcitriol, which is the active form of vitamin D. These common mammalian renal functions, as well as overall gross and histologic structure, are quite similar between rodents and humans. Species differences in renal physiology are reflected in the nephron ratio and number, and also the morphology of vascular bundles, renal papillae, and medulla. Rodents, especially males, make highly concentrated urine with a high protein content. Sexual dimorphism can be present in the rodent kidney. Ultrastructural differences also exist between rodents and humans.

Kidney size, as well as responses to various drugs and compounds, can differ significantly depending on rodent sex within and between strains. These potential differences must be considered during study design, interpretation of clinical data, and postmortem evaluations. Rodent strain differences in renal weight, function, and disease susceptibility are also well-documented. Please see the Further Reading section for additional information.

Kidney

Gross Anatomy

The rodent kidney is located retroperitoneally, often surrounded by white adipose tissue with pockets of brown adipose tissue within the pelvis and occasionally surrounding the renal capsule. Both kidneys are located in the upper midabdomen (Fig. 16.1). The right kidney is relatively cranial, adjacent to the right lobe of the liver; the left is more caudal. The human kidney is also located retroperitoneally in the posterior abdomen and, like the rodent kidney, is surrounded by adipose tissue. The upper pole of the human kidney is at the level of the upper edge of the 12th thoracic rib, whereas the lower pole extends to the 3rd lumbar rib. The right kidney is usually slightly lower (inferior/caudal) than the left one (Fig. 16.2).

Comparative Anatomy and Histology. DOI: http://dx.doi.org/10.1016/B978-0-12-802900-8.00016-6
© 2018 Elsevier Inc. All rights reserved.

TABLE 16.1 Urinary System

Feature	Rodent	Human
	Gross	
Kidney structure	Bilateral, unilobar, smooth	Bilateral, multilobar, smooth, may be lobulated
Kidney location	Retroperitoneal; right more cranial; next to liver, adrenals closely opposed to cranial poles	Retroperitoneal; right more caudal; adrenals above the upper poles
Kidney sexual dimorphism	Male larger than female	Similar to rodent
Papillae	Unipapillary and unipyramidal; can extend into proximal ureter	Multipapillary and multipyramidal (4–18)
White adipose tissue	Perirenal	In pelvis, perirenal
Brown adipose tissue	Renal pelvis and perirenal	Usually absent
Ureters	Mouse: very small, retroperitoneal; enter bladder at trigone Rat: small (0.3 mm diam.), retroperitoneal; enter bladder at trigone	Retroperitoneal; enter bladder at trigone
Bladder location	Lower abdominal cavity, ventral to the colon; orientation allows for accumulation of protein and crystalline debris at apex	Lower abdominal cavity, anterior to colon (male) or uterus (female)
Urethra	Male: prostatic, membranous, and penile portions, exits at urethra fossa Female: runs through the clitoris, exits at the clitoral fossa	Male: prostatic, membranous, and spongy Female: exits in front of the vaginal opening and ~2.5 cm behind the glans clitoridis
Os penis	Present, dorsal to urethra	Absent
Predominant nephron loops	Long 3:1	Short 7:1
	Histologic	
Renal cortex	Outer zone contains glomeruli and proximal convoluted tubules; inner zone has rayed appearance due to straight tubules	Subcapsular zone contains proximal convoluted tubules; the remaining cortex contains glomeruli, proximal and distal convoluted tubules, and thick portions of Henle's loops
Average glomerular diameter	Mouse: 73 µm Rat: 90 µm	200 µm
Bowman's capsule lining	Mouse: in males cuboidal epithelium, testosterone dependent Rat: in both male and females, low cuboidal parietal epithelium	Simple squamous epithelium (rarely cuboidal)
Number and size of glomeruli	Numbers do not increase with age; size may get larger	Similar to rodent
Sexual dimorphism of glomeruli	Female rats have smaller but more numerous glomeruli than male rats	Absent
Mesangium (with H&E)	Prominent	Less prominent
Proximal tubules	Mouse: proximal tubular epithelial cell (PCT) cytoplasm is granular and eosinophilic due to large amount of mitochondria. Proximal convoluted cortical tubular epithelium in males may contain lipid vacuoles Rat: PCT cytoplasm is similar to mouse and the epithelium in young male rats can contain hyaline (alpha-2u-globulin) droplets	PCT cytoplasm similar to rodent. Tubular cells contain small apical cytoplasmic vacuoles, which are most prominent in the proximal tubular segments
Sexual dimorphism of proximal tubules	Present at EM level in proximal convoluted tubule (PCT) segments	Absent
PCT	Cuboidal with prominent periodic acid–Schiff-positive (PAS+) brush border	Low columnar with granular and eosinophilic cytoplasm due to large amount of mitochondria; prominent PAS+ brush borders
Distal convoluted tubule	Similar to PCT with less prominent brush border	Cuboidal; less eosinophilic; brush border absent
Juxtaglomerular apparatus	Renin-producing cells prominent in afferent arteriole; PAS+ granules	Similar to rodent
Medulla	Outer medullar with outer and inner stripe; inner medulla (papillae)	Similar to rodent
Vascular bundles of the inner stripe of medulla	Complex: loops of Henle intermingle with large bundles of ascending and descending vasa recta	Simple: loops of Henle separate from vascular bundle that contains only the loops of vasa recta
Renal pelvis	Lined by urothelium; can have intraepithelial eosinophilic droplets or vacuoles	Similar to rodent

(*Continued*)

TABLE 16.1 Urinary System (Continued)

Feature	Rodent	Human
	Histologic (continued)	
Renal pelvic fornices	Lined by single layer of epithelium	Absent
Interstitium	Increased in medulla	Similar to rodent
Ureter lining	Urothelium	Urothelium: upper two-thirds, 2–3 cell layers; lower one-third, 4–5 cell layers
Bladder lining	Mouse: five layers of urothelium, fixation dependent Rat: three layers of urothelium; fixation dependent	5–7 layers of urothelium; fixation dependent
Urethra	Mouse: lined by urothelium; abundant mucous glands; urethral orifice is lined by stratified squamous epithelium Rat: similar to mouse, and urethral glands regress in older female rats; remnant glandular tissue referred to as paraurethral glands	Similar to mouse
Interstitial cells	Mouse: oriented horizontally in medulla Rat: similar to mouse with three described types: Type 1 (stellate); Type 2 (monocytic); Type 3 (pericytic)	Cortical interstitial cells: fibroblast-like and lymphocyte-like cells. Medullary interstitial cells: lipid-containing cells, lymphocyte-like cells and pericytes
	Ultrastructural	
Average basement membrane thickness	Mouse: 80–200 nm Rat: 335–414 nm	320–340 nm
Glomerular capillary basement membrane layers	Mouse: very distinct Rat: distinct	Less distinct
	Other	
Specific gravity	Relatively high; strain and sex dependent; normal ranges depend on lab	Relatively low; normal range depends on lab, 1.020–1.028
Proteinuria	Present normally, especially in males; strain dependent; normal ranges depend on lab	Physiologic proteinuria: <150 mg/24 h in adults, <140 mg/m^2 in children; human urinary protein is Tamm–Horsfall protein (uromodulin)
Creatinuria	Strain dependent; normal ranges depend on lab	Normal range 500–2000 mg/dL
Seminal plugs (coagulum)	Frequent perimortem occurrence in males, commonly found in bladder	Absent

Like humans, adrenal glands of rodents are closely associated with the cranial poles of the kidneys. The rodent kidney is mahogany-colored, smooth, bean-shaped, and relatively thin dorsoventrally (Fig. 16.3). Male rodents have relatively larger kidneys than females, and kidney weight varies between inbred strains. The human kidney is reddish-brown and usually has a smooth surface. In children, and occasionally in adults, the kidney surface may have fissures of various depths that represent remnants of fetal lobulation (Fig. 16.3). Similar to rodents, the human male kidney is slightly larger than the female (125–170 vs 115–155 g). In all three species, blood vessels, lymphatics, and nerves enter and exit the kidney at the renal hilum, which contains the renal sinus, a fat-filled space occupied by renal calyces.

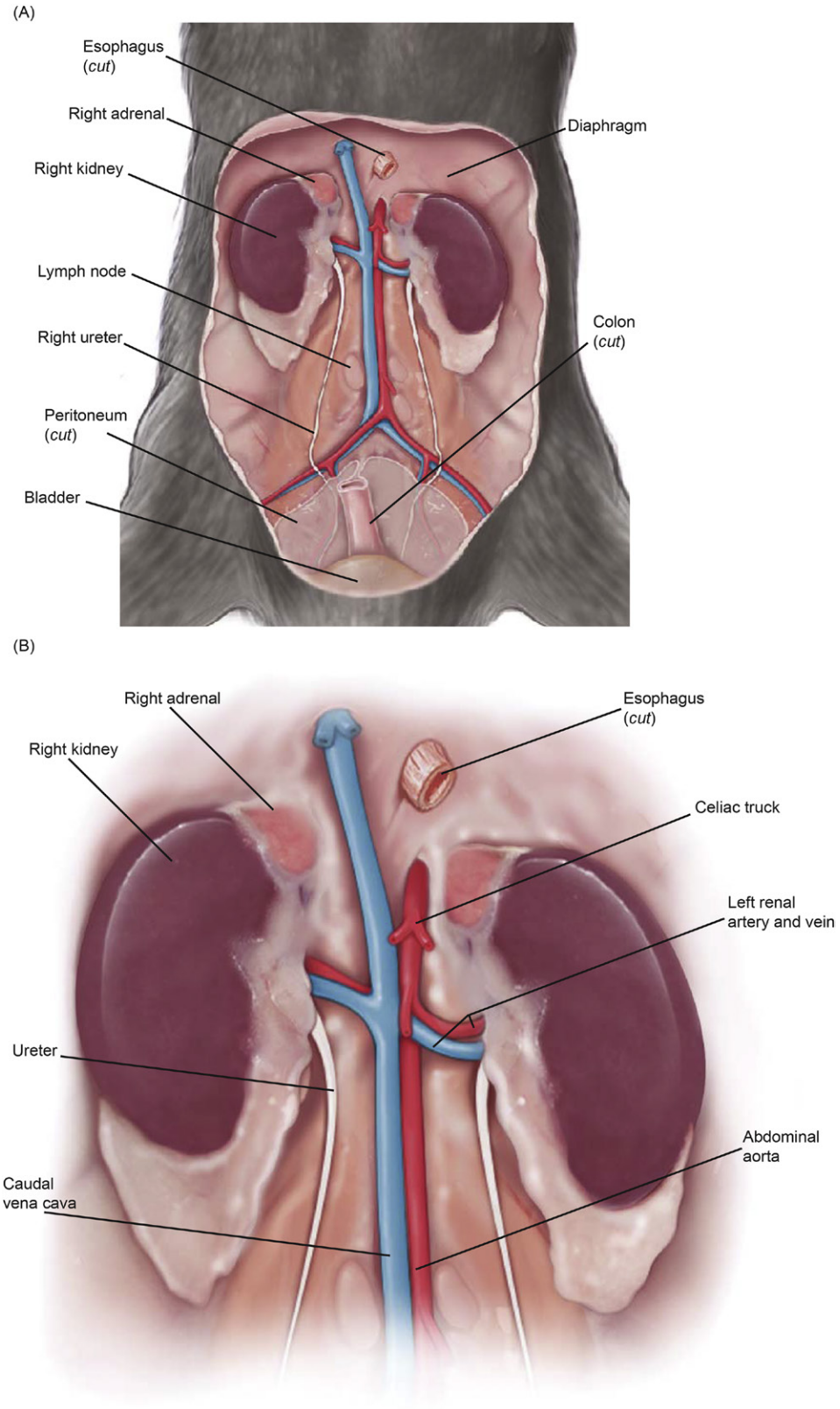

FIG. 16.1 Rodent (mouse) regional anatomy. (A) Retroperitoneal space. (B) Kidneys and perirenal soft tissues. Rodent kidneys are retroperitoneal, located in the cranial midabdomen. In well-conditioned rodents, they are surrounded by white adipose tissue with pockets of brown adipose tissue. The right kidney is relatively cranial, located adjacent to the right lobe of the liver within the renal fossa. The left kidney is lower in the abdomen. The adrenal glands are located at the cranial poles of the kidneys. Rodent ureters are small and in animals with abundant fat stores may be challenging to locate grossly. Mice and rats produce 0.5–1.0 and 8.25–16.5 mL of highly concentrated urine per day, respectively. Source: © Elsevier, Inc., www.netterimages.com.

Need-to-know

- Rodent ureters are very small, often embedded in fat, and may be difficult to identify grossly without the aid of magnification.
- The right kidney in rodents is positioned cranially, in close opposition with the right lobe of the liver.
- In humans the left kidney is slightly superior.

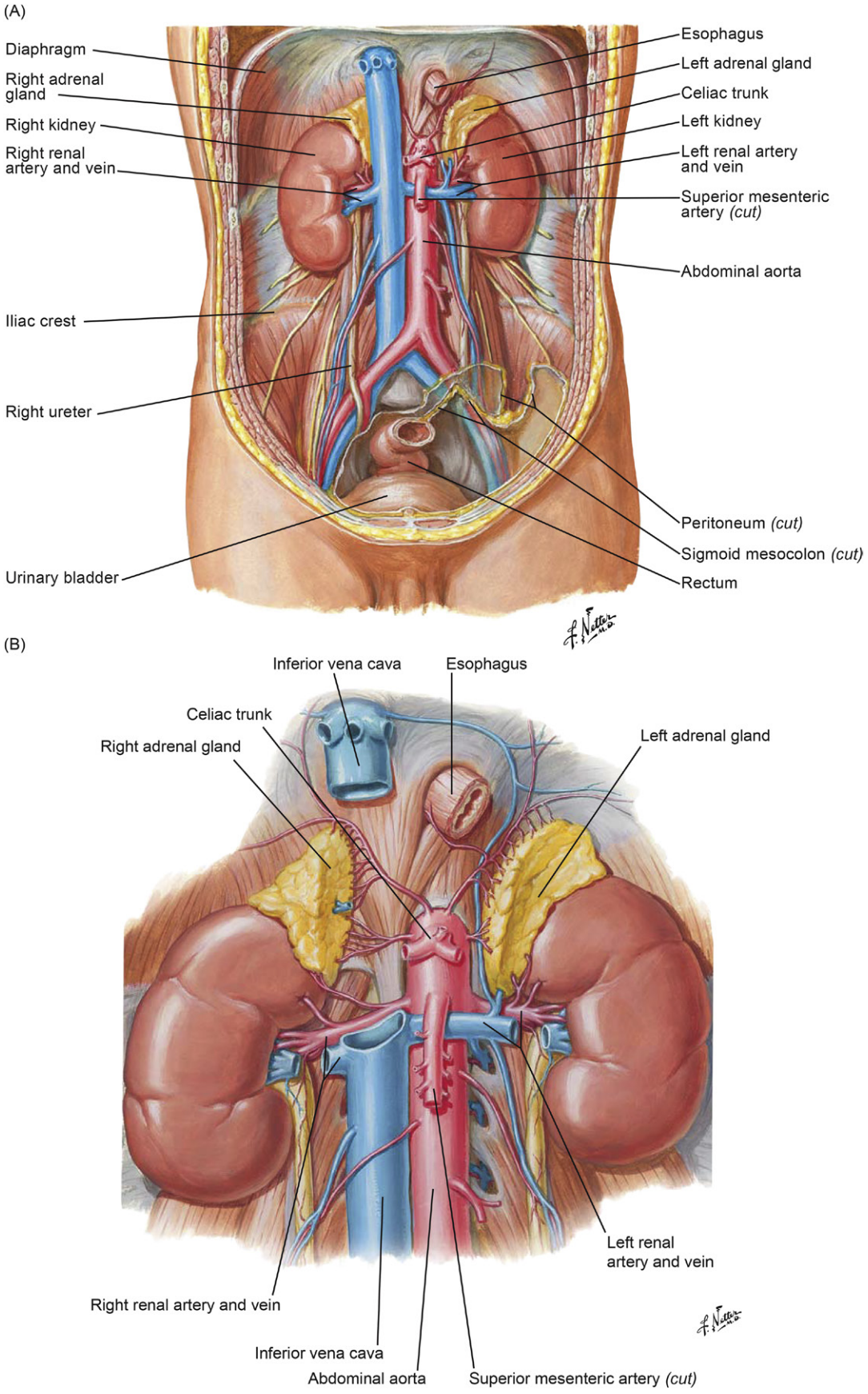

FIGURE 16.2 Human regional anatomy. (A) Retroperitoneal space. (B) Kidneys and perirenal soft tissues. The fat-embedded kidneys lie in retroperitoneal position just anterior to the muscles of the posterior abdominal wall. Humans produce between 1 and 2 L of urine per day. Source: © Elsevier, Inc., www.netterimages.com.

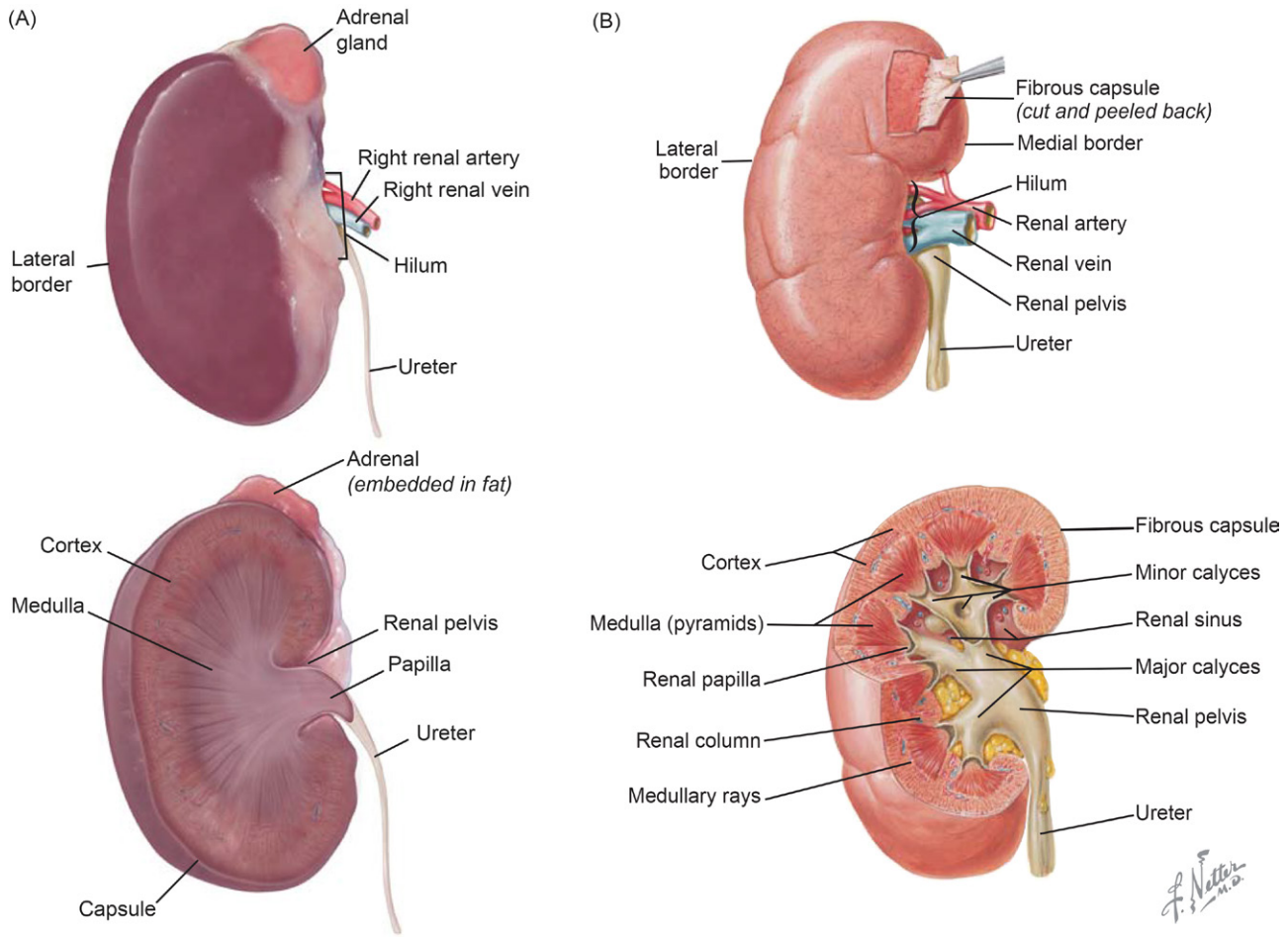

FIGURE 16.3 Right kidney (A) Rodent (mouse). The unilobar kidney has a smooth, capsular surface and is dorsoventrally flattened. The medially located hilum contains blood vessels, nerves, and the ureters. The single medullary papilla extends deep into the renal pelvis, which often contains both white and brown adipose tissue. On cross or longitudinal sectioning, the cortex appears as cone-shaped cortical labyrinths and medullary rays that extend from the outer medulla, which is divided into an outer and inner stripe. The papilla is the inner portion of the medulla. The small ureters are located in the retroperitoneal space, dorsal to the reproductive tract and bladder, and enter obliquely at the trigone of the bladder. (B) Human. The kidney has multiple papillae, and they do not deeply extend into the pelvis. Source: © Elsevier, Inc., www.netterimages.com.

Rodent kidneys are unilobar (unipyramidal) with only a single papilla that extends deep into the renal pelvis (Fig. 16.3). The cortices have cone-shaped cortical labyrinths and medullary rays that extend from the outer medulla, which is divided into an outer and inner stripe. The inner-most portion of the medulla is the renal papilla, which extends into the renal pelvis and ureter.

Need-to-know

- The rodent kidney is unilobar with one renal papilla; the medulla and cortex are easily discernible grossly.
- Humans have multipapillary (multipyramidal) kidneys, usually with 7–9 papillae (range, 4–18). Papillae can be simple (drain one lobe) or compound (drain multiple lobes).

Humans kidneys are multipapillary (multipyramidal) (Fig. 16.3) with 7–9 papillae (range, 4–18). There are two main types of papillae: simple, which drain only one lobe, and compound, which drain two or more adjacent fused lobes. Each papilla is surrounded by a minor calyx. Two or three minor calices join together to form major calices, which in turn open into the renal pelvis.

The blood supply to the kidney is similar in all species. The designation of interlobar arteries is used for the portion of the vasculature connecting the segmental to arcuate arteries (Fig. 16.4).

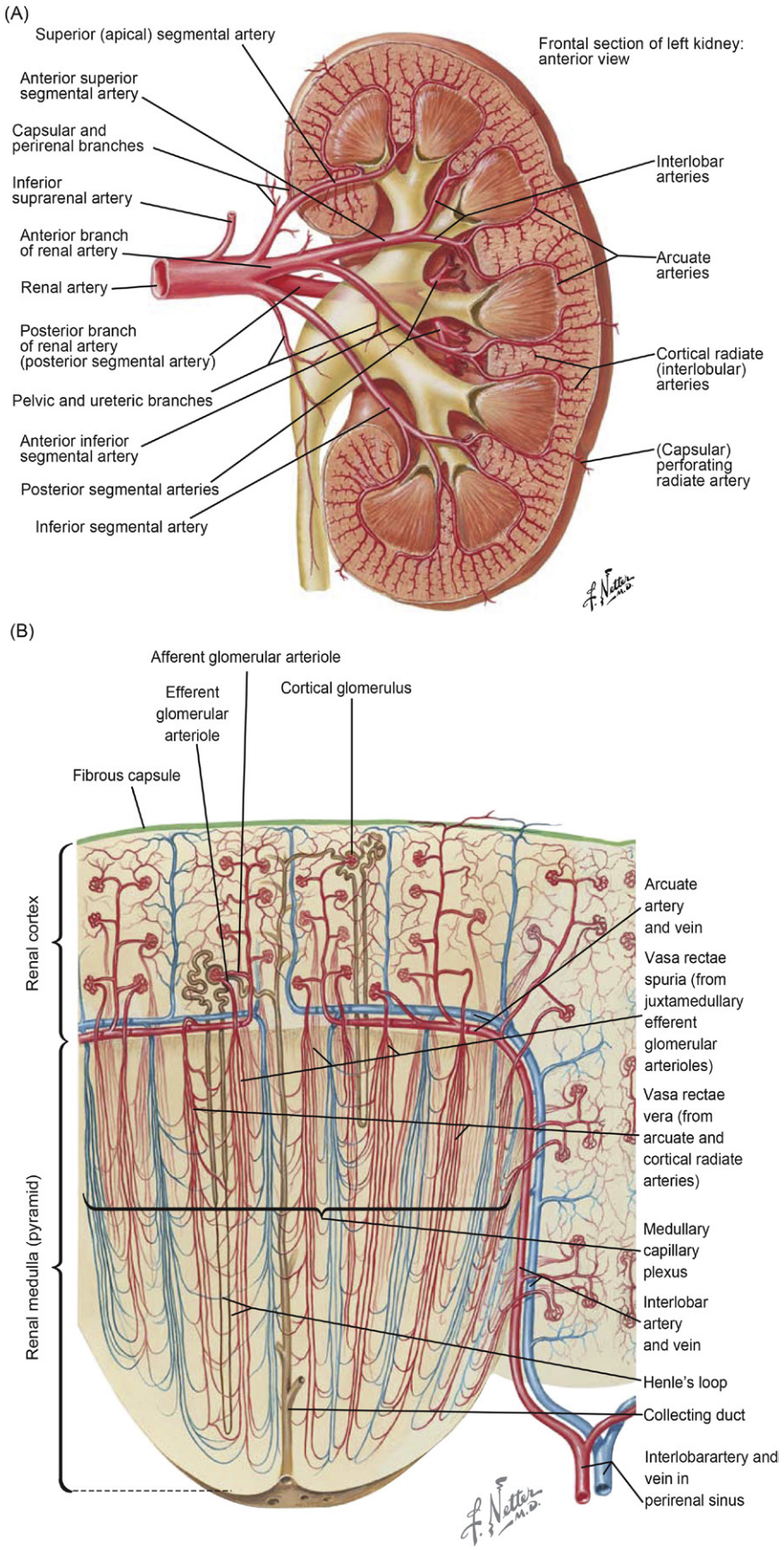

FIGURE 16.4 Renal vasculature diagram. In all three species, the kidneys receive ~25% of cardiac output. Urine production is dependent on the glomerular filtration rate, which is defined by the amount of blood flowing to the kidneys. Arterial blood flows directly to the glomerulus via the afferent arterioles, the site of ultrafiltration. The glomerulus contains afferent and efferent arterioles; afferent arterioles comprise the majority of fenestrated capillaries of the glomerular tuft. Efferent arterioles carry filtered blood to the vasa recta of the juxtamedullary nephrons, which then drain the blood to the venous system. In rodents, the vasa recta coalesce to form giant vascular bundles that aid in their increased ability to form highly concentrated urine. Source: Reprinted from Netter's Essential Histology, Ovalle, W.K., and Nahirney, J.C., 2008, with permission from © Elsevier, Inc., www.netterimages.com.

HISTOLOGY

Nephron

The nephron is the functional unit of the mammalian kidney (Fig. 16.5). In mice, rats, and humans, the nephron is composed of the glomerulus, proximal tubule (convoluted and straight), descending and ascending loops of Henle, straight segment, macula densa, and convoluted distal tubule. Nephrons are classified by location in the cortex: superficial or juxtamedullary in mice; and superficial, midcortical, or juxtamedullary in rats and humans (Fig. 16.5). An additional nephron classification scheme is by loop of Henle length, described as either short- or long-segment. Rodents have more long-segment nephrons than short (3:1), whereas humans have more short-looped segments than long (7:1). This difference accounts for the overall greater concentrating ability of the rodent kidney, in which yields urine with high specific gravity (ranging from 1.030 to 1.060 g/ml) and proteinuria which is most prominent in males.

There are ~14,000 nephrons in mice and 30,000–35,000 in rats. Humans have ~1 million per kidney. In all three species, the number does not change with age, although the glomeruli do increase in size, and the density of glomeruli decreases from the outer to inner zones of the cortex.

Glomeruli

Rodent kidney tissue (Fig. 16.6) closely resembles that of a juvenile human (Fig. 16.7), with a relatively thin cortex corticis (the subcapsular zone devoid of glomeruli) and significantly smaller glomerular size (average 73.4 and 90 µm in mice and rats vs 200 µm in adult humans) (Fig. 16.8). In all three species, the juxtamedullary glomeruli may appear larger than those in the superficial cortex. The glomerular corpuscle comprises a network of capillaries surrounded by Bowman's capsule (Fig. 16.9). The glomerular vascular network is supported by myoepithelial cells (mesangial cells) embedded in extracellular matrix. Usually, there are one or two cells per mesangial area. The luminal surface of the capillaries is lined by specialized fenestrated endothelium, whereas the urinary surface is covered by visceral epithelial cells (podocytes), with characteristic foot processes seen ultrastructurally. The glomerular basement membrane in both species is present between endothelial cells and podocytes. Special stains, including periodic acid–Schiff (PAS) and Jones' methenamine silver, are part of a routine examination in human renal pathology to highlight the glomerular basement membrane (Fig. 16.9). Bowman's capsule is normally lined by a layer of flat parietal epithelial cells (Fig. 16.9–16.11).

Rodents display variable sexual dimorphism in the kidney, including within the glomeruli, which is strain- and age-dependent (Fig. 16.10). In male rodents, the parietal epithelium of Bowman's capsule may be cuboidal, in contrast to the usually flat squamous epithelium in humans and female rodents. This finding is less appreciated in rats, though when present does not indicate pathology. In addition, female rats tend to have smaller but more numerous glomeruli than males.

Ultrastructural features of the mouse, rat, and human glomerulus are mostly similar, with the major difference in the thickness of the glomerular basement membrane (Figs. 16.12 and 16.13). The glomerular capillary basement membrane is composed of three layers: Lamina rara interna, lamina densa, and lamina rara externa. The lamina densa is thicker in humans than in mice, resulting in an average basement membrane thickness of 320–340 nm, compared to 80–200 nm in mice. The rat glomerular basement membrane thickness is closer to that of humans than mice, with an average thickness of 335–414 nm. In mice, the basement membrane layers are more distinctly visible than in humans (Fig. 16.13). Other ultrastructural features, such as fenestrated endothelium and gaps between glomerular podocyte processes, are similar in all three species.

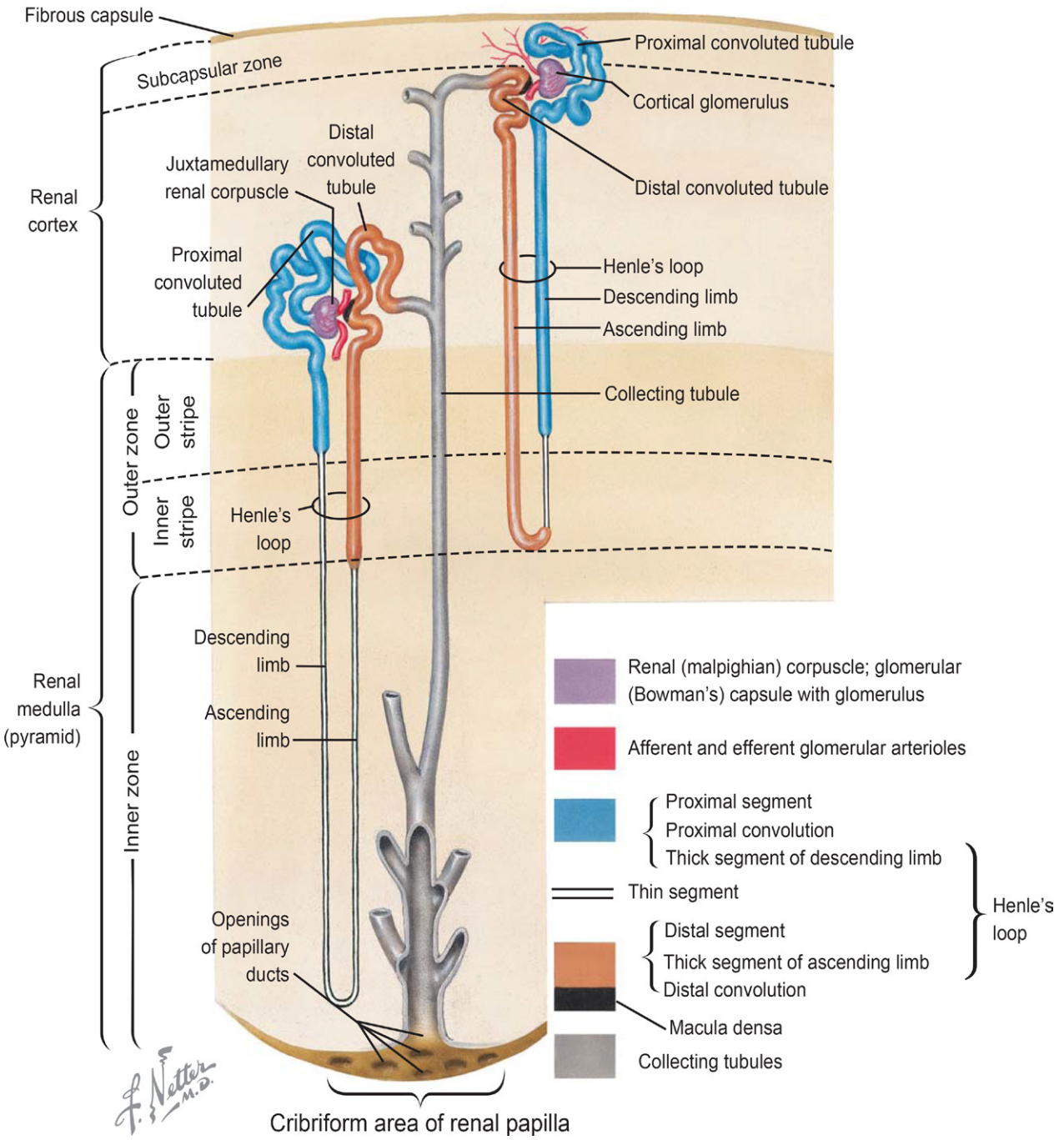

FIGURE 16.5 Diagram of a nephron. In all three species, the nephron is the functional unit of the kidney and is composed of the renal corpuscle (the glomerular capillary tuft and enclosing epithelial Bowman's capsule) and the proximal and distal tubules, which are connected by the loop of Henle. Filtrate empties to the collecting tubules, which drain to the larger collecting ducts that exit at the cribriform region of the renal papilla. Nephrons in both species are classified by cortex location and loop of Henle length. Compared to humans, rodents have greater numbers of long-segment nephrons than short ones (3:1), reflecting the overall greater concentrating ability of the rodent kidney. In all three species, the proximal convoluted tubule is divided morphologically and functionally into three segments (P1–3). Source: Reprinted with modifications from Netter's Essential Histology, Ovalle, W.K., and Nahirney, J.C., 2008, with permission from © Elsevier, Inc., www.netterimages.com.

Need-to-know

- Rodents have more long-segment nephrons.
- Rodent urine is highly concentrated, with protein and creatinine present normally.

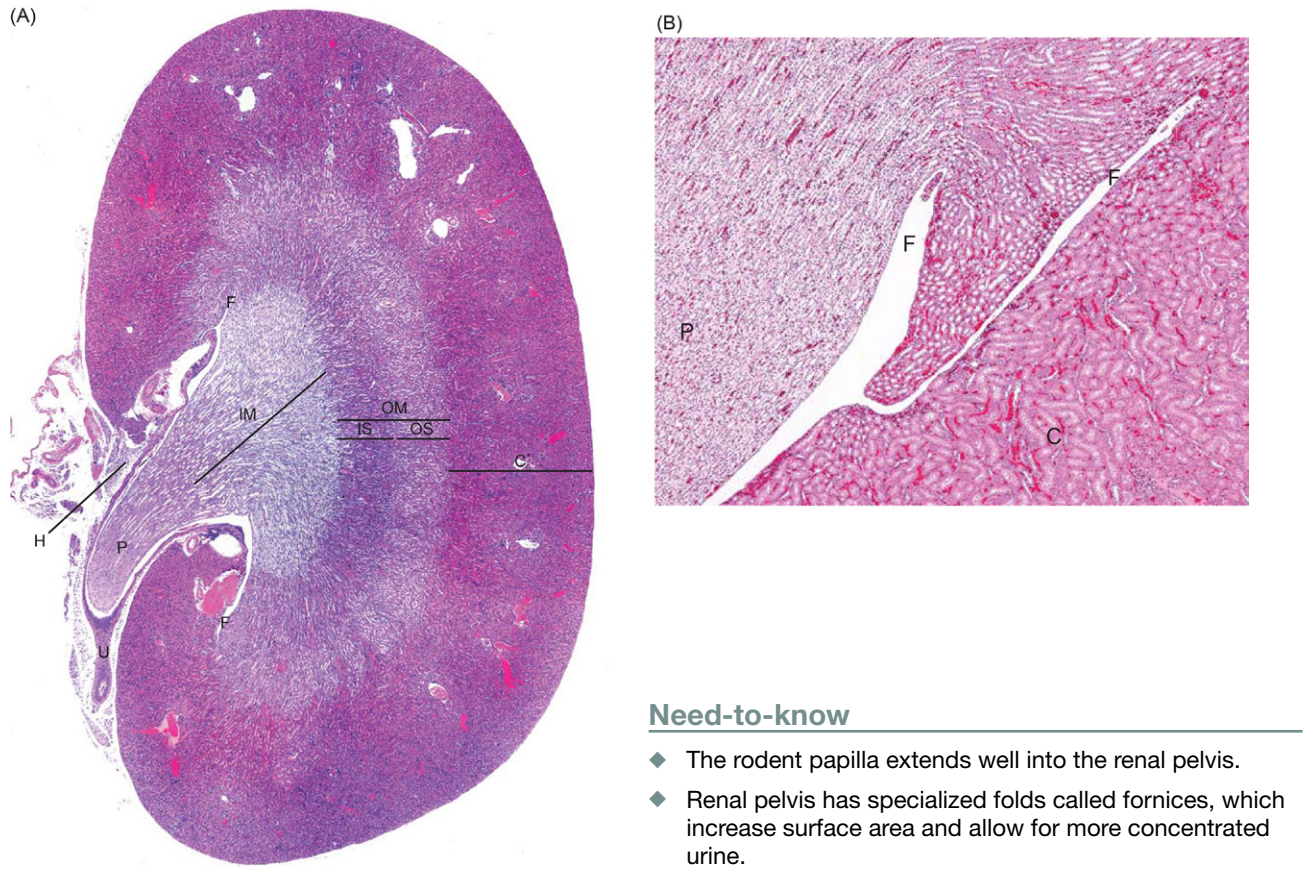

Need-to-know

- The rodent papilla extends well into the renal pelvis.
- Renal pelvis has specialized folds called fornices, which increase surface area and allow for more concentrated urine.

FIGURE 16.6 Rodent (mouse) kidney subgross. (A) The capsular surface of the kidney is smooth. The cortex (C), medulla (M), and hilus (H) are easily discernable. A single papilla (P) extends deep into the renal pelvis. The upper portions of the pelvises have folds called fornices (F), which increase surface area. The renal hilus (H) contains abundant brown fat. The cortex (C), outer medullar (OM), inner stripe (IS), outer stripe (OS), inner medullar (IM), and ureter (U) are indicated. Source: Courtesy of Dr. Julie Randolph-Habecker. (B) High magnification demonstrating the relationship with fornix (F), cortex (C), and papilla (P).

Cortical labyrinths

The cortical labyrinths of rodents contain mostly proximal convoluted tubules (PCT) (Figs. 16.5 and 16.14) that terminate at the medullary rays. In the medulla, the tubules are the pars recta, straight descending limb, and the thin loops of Henle. There are four parts to the loop of Henle: (1) Thick descending limb (pars recta of the PCT), (2) thin descending limb, (3) thin ascending limb, and (4) thick ascending limb (pars recta of the distal convoluted tubule). Distal convoluted tubules are present within the medullary rays, where they empty into collecting ducts and drain to the medulla, and can be discerned histologically due to their pale staining and lack of brush borders (Fig. 16.14). Segments of the renal tubules of rodents can be routinely identified on histologic section and highlighted with special stains and ultrastructural exam as in humans. The proximal tubular epithelium is similar between the three species, with the PCT and straight segments divided by functional capacity into three segments: P1, P2, and P3 (Fig. 16.5). These segments are also known by S1, S2, and S3 and can be identified by histochemical and ultrastructural microscopy. At the level of the light microscope, the proximal convoluted tubule brush border has a prominent, relatively thick brush border, which is highlighted by PAS staining (Fig. 16.14). P2 extends into the first part of the straight segment and has a less prominent brush border. P3 runs within the medullary rays and into the outer stripe of the outer medulla. In rodents, these segments have sexual dimorphism; for example, male rats have increased smooth endoplasmic reticulum in P1

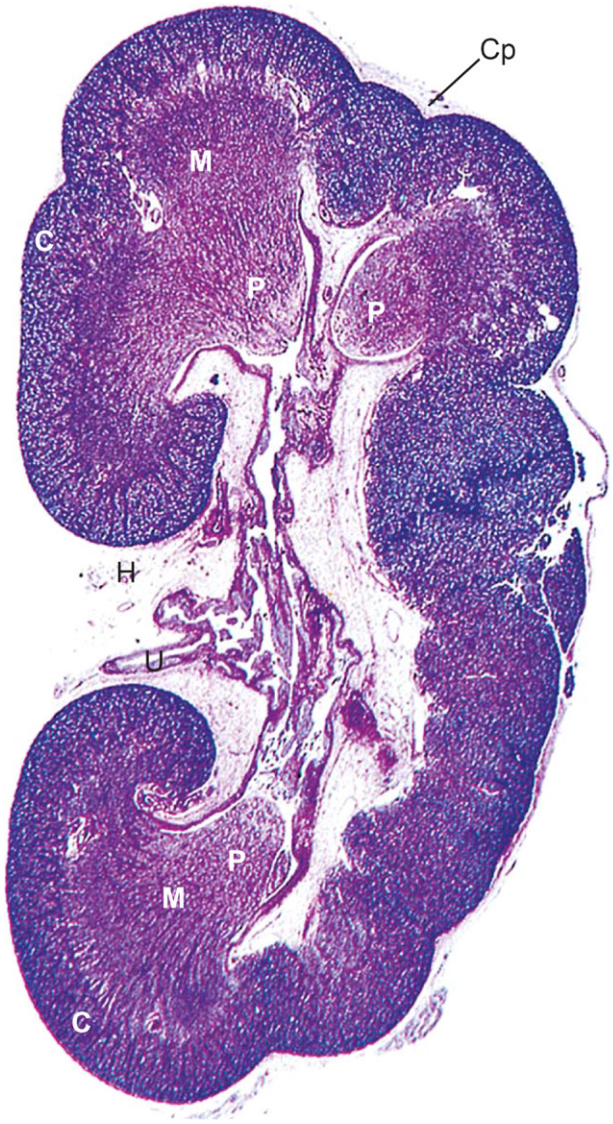

FIGURE 16.7 Human kidney subgross. The surface of this infant kidney is convex and irregular, reflecting multipyramidal development. In histologic section, only a single plane through the pelvicalyceal system can be visualized. This plane of section includes the axes of three lobes, the papilla (P) of each one projecting into the central pelvicalyceal space; this drains into the ureter (U) that leaves the kidney via the hilum (H). The darker-stained cortex (C) can be clearly differentiated from the paler-stained medulla (M). The fibrous capsule (Cp) of the kidney is continuous at the hilum with fatty supporting tissue, which packs the space (renal sinus) between the hilar structures. Source: Reprinted from Wheater's Functional Histology, 5th Edition, Young, B. et al. 2006, with permission from © Elsevier, Inc.

Need-to-know

- The human papillae project into minor calices.

and P2, which can be appreciated ultrastructurally. Similarly, male mouse P2 mitochondria are larger and more electron-lucent, and there are more autophagic vacuoles. These sex differences in structure reflect functional differences (see Further Reading).

Proximal tubule cuboidal-to-columnar epithelial cells are brightly eosinophilic with granular cytoplasm due to high numbers of mitochondria, and a dense PAS-positive brush border (Fig. 16.14). In rodents, the distal convoluted tubule lacks the prominent brush border of the PCT, but it may otherwise be difficult to distinguish in H&E–stained sections (Fig. 16.14). Sexual dimorphism of the rodent glomeruli and tubules is present at both light and electron microscopic levels (Figs. 16.14 and 16.15). For instance, male mouse outer cortical tubular cells are variably vacuolated. These vacuoles are typically small, discrete, and colorless, consistent with microvesicular lipid accumulation. The proximal tubules of sexually mature young male rats often contain eosinophilic (α-2u-globulin) granules, which are well visualized with Mallory–Heidenhain stain and referred to as hyaline droplets (Fig. 16.15). These alpha-2u-globulin granules are of unknown significance, but can accumulate in apical portions of renal tubular epithelial cells in normal young male rats. They may also be detected in higher quantities following exposure to certain chemicals and in the context of various renal and other diseases. In contrast, female rodents do not typically have vacuolation of proximal tubular cells, and cells of female and older male rats do not contain abundant eosinophilic granules (Figs. 16.8 and 16.15). In humans, small cytoplasmic apical vacuoles and granules are seen predominately in the proximal tubular epithelial cells and correspond to a well-developed endocytic-lysosomal apparatus. In the outer medulla of rodents, the thin loops are enveloped in large vascular bundles, which assist in the profound concentrating ability of the rodent nephron (Figs. 16.16 and 16.17). The descending thick limb of the distal tubule reenters the cortex at the juxtaglomerular apparatus (JGA), which is similar in both species (Fig. 16.17). The JGA is composed of the

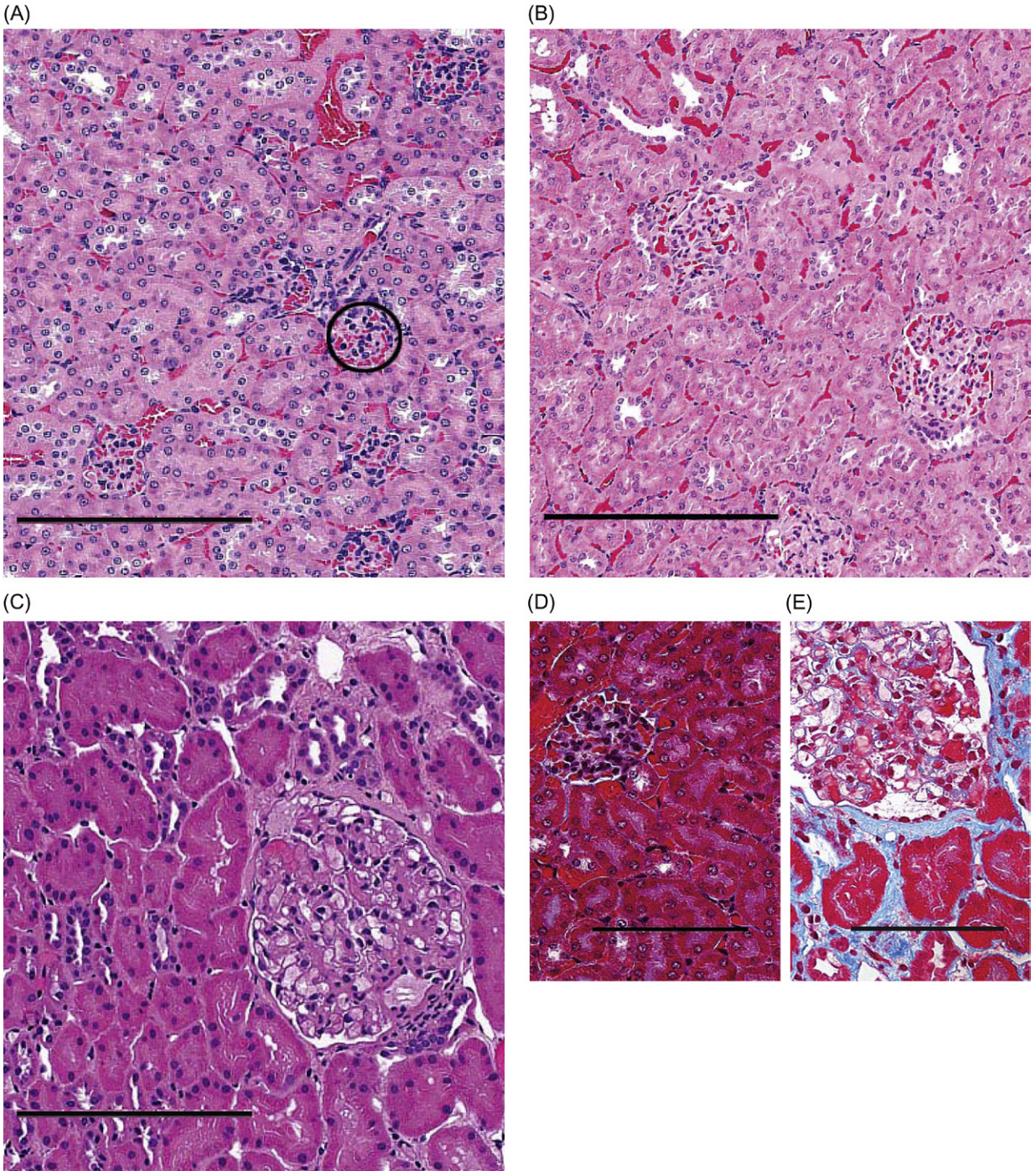

FIGURE 16.8 Cortex. (A) Mouse. Glomeruli (circle) are considerably smaller than in humans, with an average diameter of 73.4 µm. (B) Rat. Glomeruli (circle) are larger than in mice but smaller than in humans, with an average diameter of 90 µm. (C) Human. Renal cortex biopsy. The average diameter of the glomeruli is 200 µm. (D) Mouse. Kidney stained with Masson's trichrome. Kidney has little interstitial connective tissue, with only the perivascular areas and capsule staining strongly blue. (E) Human. Renal cortex biopsy stained with Masson's trichrome. As in most human tissues, the supporting parenchymal connective tissue (blue) is more prominent than in mouse. Figures A, B, and C are the same magnification; scale bar = 250 µm; figures D and E are the same magnification; scale bar = 50 µm.

Need-to-know

- The rodent glomerulus is much smaller than the human.
- Rodents have thin cortex corticis, the subcapsular zone devoid of glomeruli.
- The approximate number of nephrons per kidney is 14,000 for mice, 30,000 for rats, and 1 million for humans.
- Human kidneys have more prominent parenchymal connective tissue.

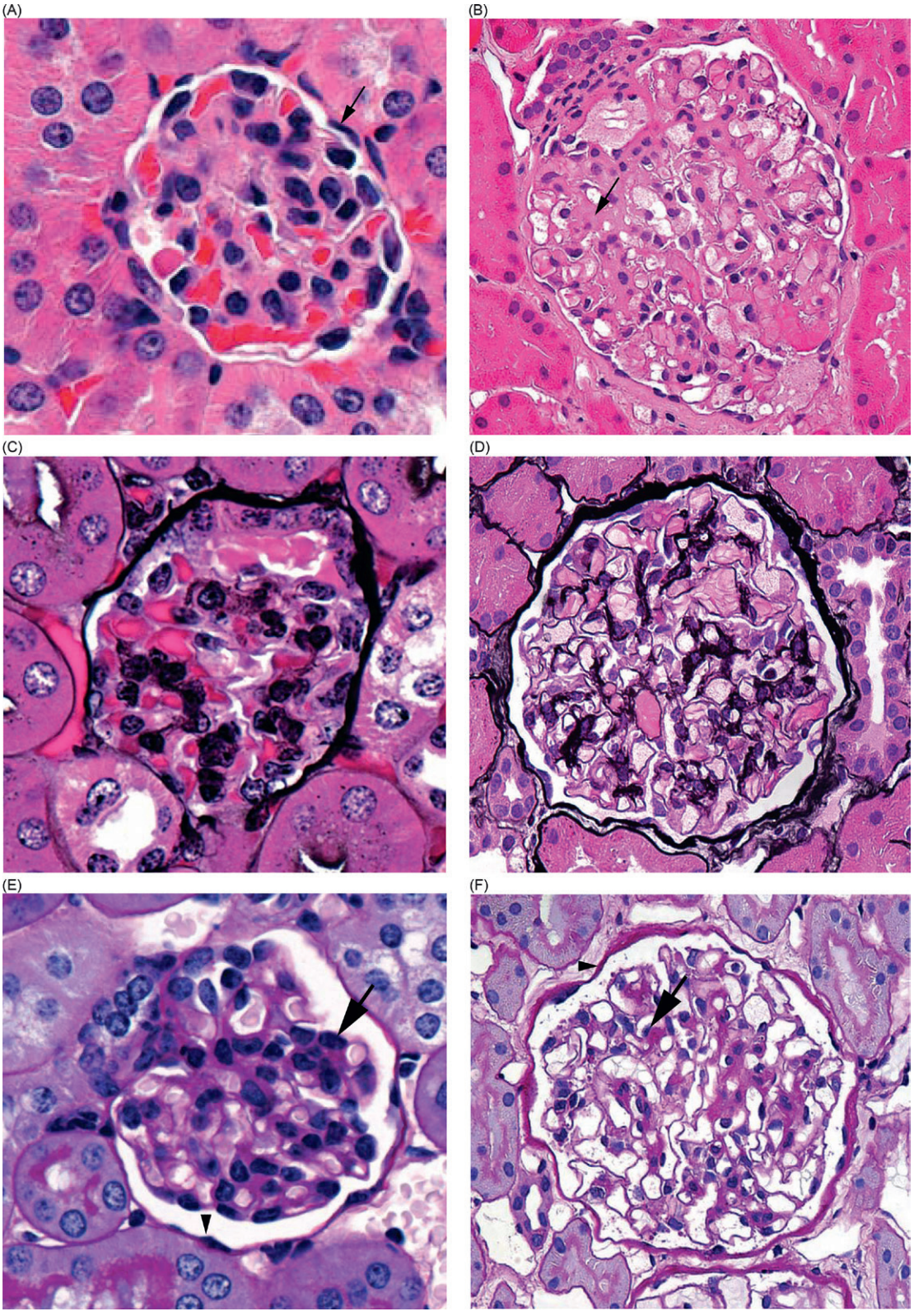

FIGURE 16.9 Glomeruli. (A) Rodent (mouse). The basic structure of the glomerular corpuscle is a network of capillaries supported by the mesangium and surrounded by Bowman's capsule (arrow). (B) Human. The glomerular vascular network is supported by myoepithelial (mesangial) cells embedded in extracellular matrix. Usually, there are one or two cells per mesangial area (arrow). (C) Male rodent (mouse) stained with Jones' methenamine silver to highlight the glomerular basement membrane. Note the low cuboidal parietal epithelium. (D) Human stained with Jones' methenamine silver to highlight glomerular and tubular basement membranes. Mesangial cell nuclei are poorly visible because of the dark-stained matrix. (E) Female rodent (rat). PAS stain. Podocytes (arrow) and parietal epithelium (arrowhead) are indicated. (F) Human. PAS stain. Endothelial cell nuclei bulge into glomerular capillaries. Capillary loops (arrow) are lined by visceral epithelial cells (podocytes). Flat parietal epithelial cells line the Bowman's capsule (arrowhead). The space between parietal and visceral layers of epithelial cells, Bowman's space, contains primary glomerular filtrate.

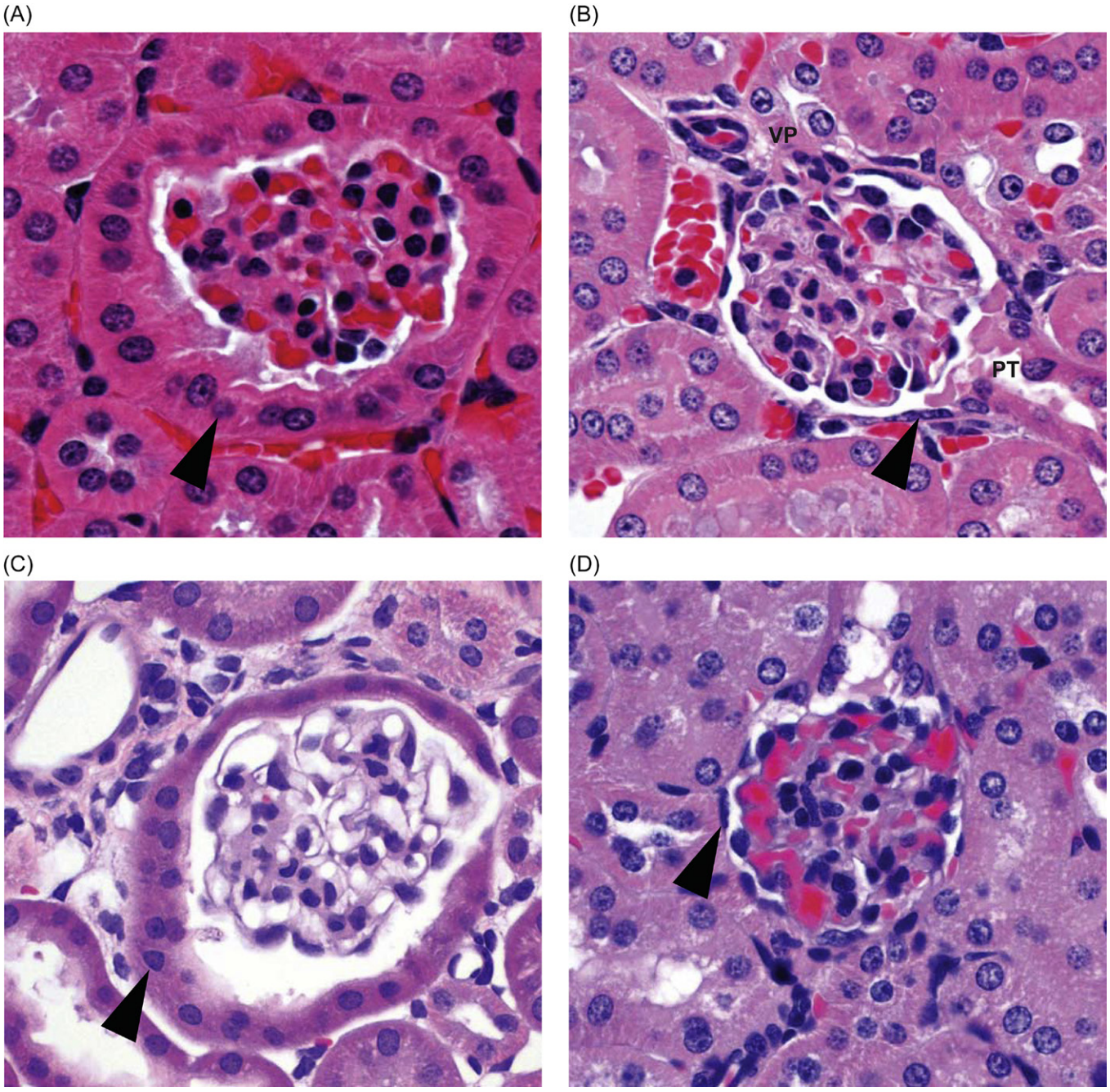

FIGURE 16.10 Sexual dimorphism in rodent glomeruli. (A) Male mouse. The cuboidal parietal epithelium resembles proximal convoluted tubule (PCT) epithelium (arrowhead). This change is variable depending on strain and increases with the age. Immature male glomeruli resemble those of the female. (B) Female mouse. The parietal epithelium is thin (arrowhead); however, low cuboidal epithelium may occasionally be present in females. Proximal tubule (PT) and vascular pole (VP) are indicated. (C) Male rat. Note the cuboidal parietal epithelium (arrowhead). (D) Female rat. Note the thin, flat parietal epithelium (arrowhead).

Need-to-know

- Mature male rodents have cuboidal parietal epithelium.
- Immature male rodent glomeruli resemble those of females.
- Rats and female mice may occasionally exhibit low cuboidal parietal epithelium.

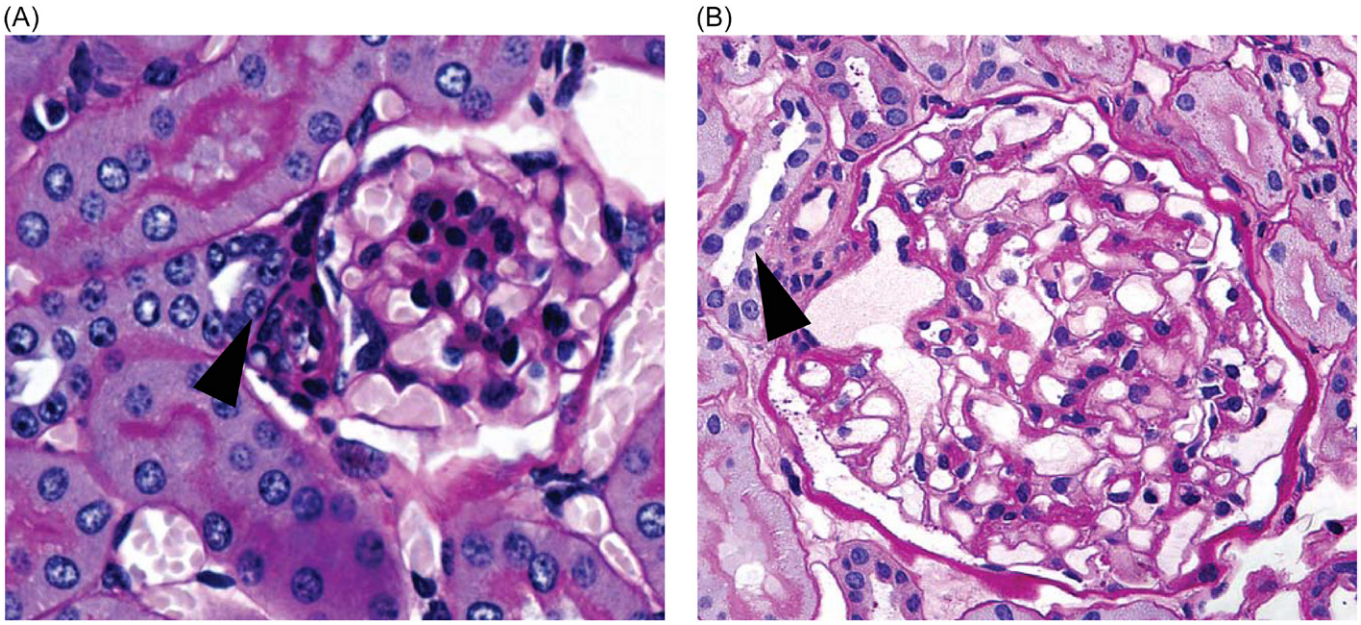

FIGURE 16.11 Juxtaglomerular apparatus. (A) Rodent (mouse). The rodent juxtaglomerular apparatus (JGA), as in humans, contains renin-producing smooth muscle cells of the afferent arteriole that stain with PAS. Macula densa, the low cuboidal cells of the distal convoluted tubules (arrowhead), and extraglomerular mesangial cells all work to control systemic blood pressure. Extraglomerular cells are difficult to visualize in most routine sections. (B) Human. PAS-stained glomerulus with visible juxtaglomerular apparatus (arrowhead). The afferent arteriole may be identified by a relatively thicker media.

afferent and efferent arterioles, macula densa, and extraglomerular mesangial cells, and it is located at the vascular pole of the renal corpuscle. The granular renin-producing cells are most prominent in the afferent arteriole and are PAS-positive (Fig. 16.11).

Medulla

In humans and rodents, the medulla is divided into inner and outer zones, and the outer zone is divided into inner and outer stripes, which are evident by differential staining (Fig. 16.6). Within the medullary rays, the distal convoluted tubules join the collecting tubules, which then combine to larger collecting ducts at the renal papillae making up the inner medulla. The inner medulla and inner stripe of the outer medulla contain collecting ducts, thin ascending and descending limbs of the distal tubule. The outer stripe of the outer medulla contains terminal segments of the proximal tubule, thick ascending limbs of the distal tubule, and collecting tubules. Proportionally, rodents have increased long nephrons, with more extending deep into the renal papilla from the cortex, resulting in an increased ability to concentrate urine compared to humans. Surrounding the distal tubules and collecting ducts are the vasa recta and interstitial cells. The interstitial cells of rodents are fusiform with a horizontal orientation between collecting tubules and capillaries, and they serve to compartmentalize the medulla, allowing for osmotic gradients (Fig. 16.18). Rats have similar histologic features of medullary interstitial cells appearing as columns of cells amongst the collecting tubules. In humans, there are two types of cortical interstitial cells: Fibroblast-like erythropoietin secreting cells and lymphocyte-like cells. The medulla contains three types of interstitial cells: Prominent lipid-containing cells with long cytoplasmic processes, mainly localized to the inner medulla and often arranged in rows between the loop of Henle and the vasa recta;

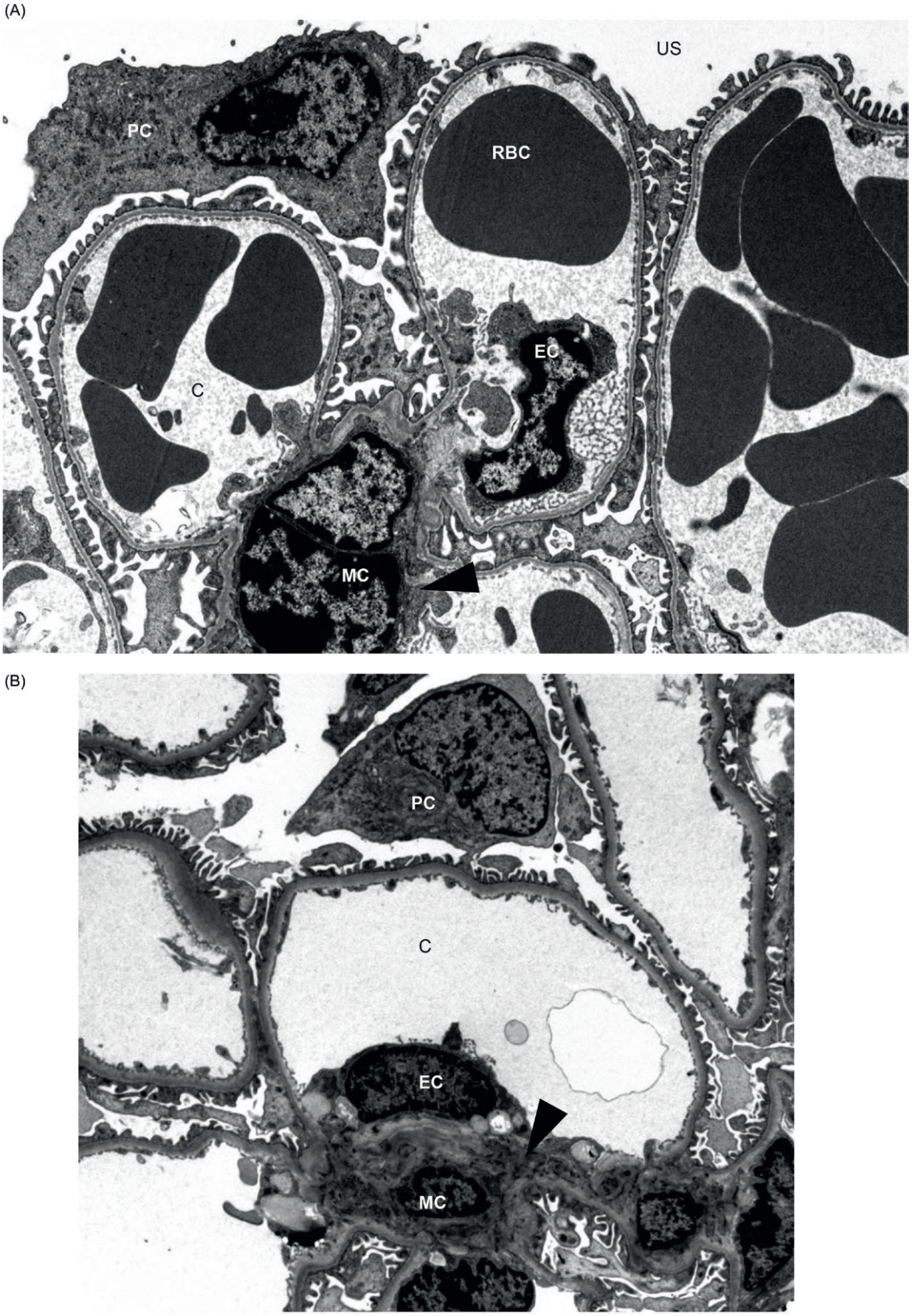

FIGURE 16.12 Glomerular ultrastructure. (A) Rodent (mouse) (8000 ×). The ultrastructure of the glomerulus is similar between the three species, with the exception of the basement membrane, which is thicker in humans. Numerous capillary loops (C) are in section and contain red blood cells (RBC) supported by the mesangial matrix (arrowhead) and cells (MC). Fenestrations in the endothelium and filtration slits in the podocyte (PC) foot processes, along with the glomerular basement membrane, filter the blood, and ultrafiltrate collects in the urinary space (US). (B) Human (3600 ×). The capillary lumina (C) are lined by endothelial cells, with the endothelial cell nuclei (EC) usually located on the mesangium and the flat fenestrated cytoplasm lining the capillary lumina. Mesangial cells (MC) are embedded in the extracellular matrix (arrowhead) and provide support for the glomerular capillaries. Podocytes (PC) are located outside the capillary walls and send their foot processes to the adjacent capillaries. Source: Courtesy of Holly Predd Carlson, University of Washington.

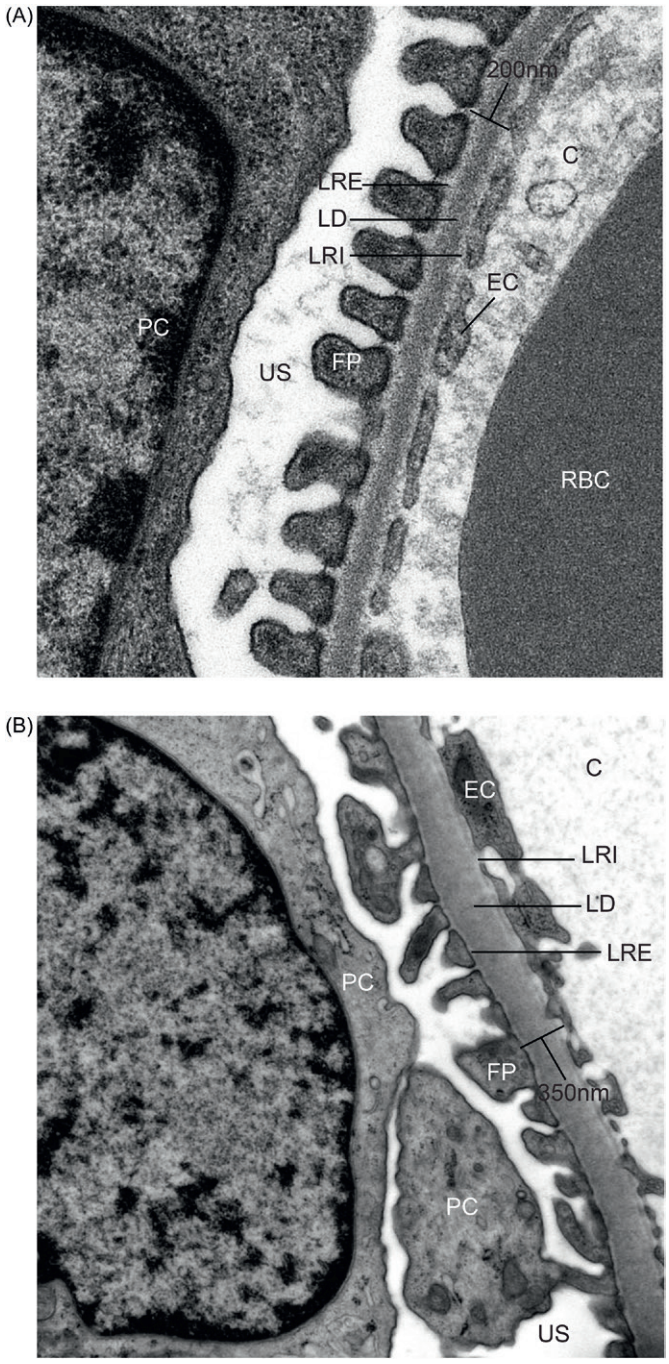

FIGURE 16.13 Glomerular basement membrane (GBM). (A) Rodent (mouse). Higher magnification (20,000 ×). The average thickness of mouse GBM is 80–200 nm. The lamina rara interna (LRI) and externa (LRE) and central core lamina densa (LD) are more distinct in mice than rats. Capillary lumen (C), urinary space (US), foot processes (FP), red blood cells (RBC), podocytes (PC), and endothelial cells (EC) are indicated. (B) Human. High magnifincation (13,000 ×). Note the similar architecture to that seen in rodents. The lamina densa (LD) is relatively thicker, and the adjacent lamina rara interna (LRI) and externa (LRE) are less distinct. The average thickness of human GBM is 320–350 nm. Capillary lumen (C), urinary space (US), foot processes (FP), and endothelial cells (EC) are indicated. Source: Courtesy of Holly Predd Carlson, University of Washington.

lymphocyte-like cells; and pericytes situated near the vasa recta. Ultrastructural characterization of interstitial cells in rats revealed a similar structure to humans with three distinct types of structural attributes related to cell function. Type 1, or stellate, interstitial cells are irregular-shaped with long cytoplasmic processes with abundant lipid vacuoles and rough endoplasmic reticulum. These cells are closely associated with the loop of Henle and capillaries and are involved in prostaglandin production. Type 2 (monocytic) interstitial cells are rounded with scant cytoplasm, sparse endoplasmic reticulum, abundant free ribosomes, and are devoid of long processes. Type 3 interstitial cells are flattened with thin cytoplasmic processes and related to the pars (vasa) recta; these cells are considered to function like a pericyte. Similar interstitial cells types are noted in mouse kidneys, although detailed ultrastructural studies as was done for rats are currently unavailable (Fig. 16.18).

Papilla

The rodent papilla extends well into the renal pelvis, in contrast to the human papillae. The renal pelvis in all species is lined by urothelium, similar to that found in the ureter and bladder (Fig. 16.19). Urothelium in the rodent renal pelvis may have small eosinophilic (hyaline) cytoplasmic droplets or vacuoles of unknown significance (Fig. 16.19).

Ureters, Urinary Bladder, and Urethra

Gross Anatomy

The ureters, urinary bladder, and urethra together make up the conduction system of the lower urinary tract. The ureters of mice are very small and are located in the retroperitoneal space, dorsal to the reproductive tract and bladder; they enter the

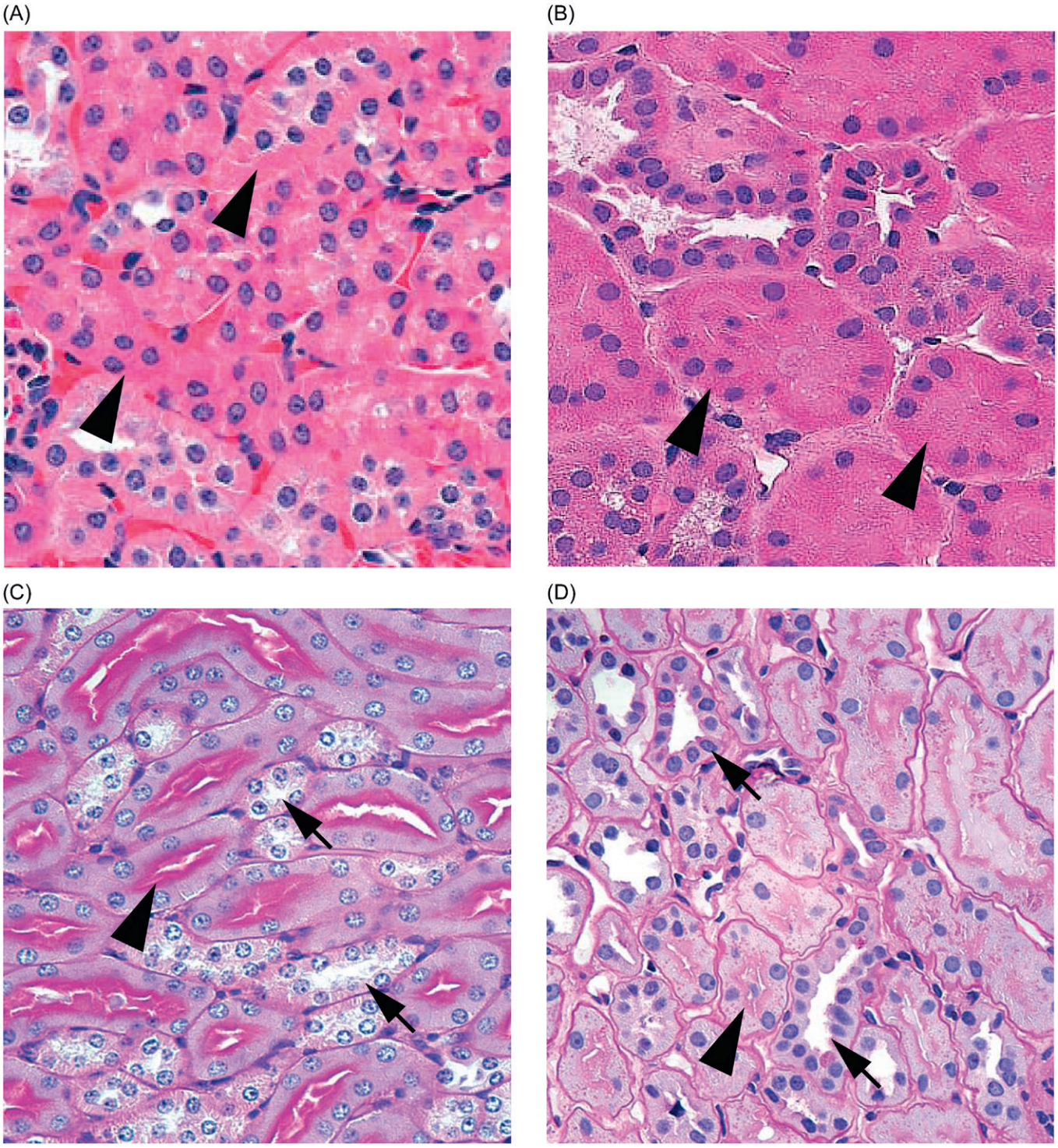

FIGURE 16.14 Cortical tubules. (A) Rodent (mouse) cortex. Proximal convoluted tubules are densely stained pink (arrowheads). Distal convoluted tubules are paler and lack the brush border, which is more readily appreciated on PAS-stained sections. (B) Human cortex. Proximal convoluted tubules are densely stained pink (arrowheads). (C) Rodent (mouse) PAS-stained cortex. Proximal convoluted tubule brush border is prominent (arrowhead), in contrast to distal convoluted tubule (arrow). (D) Human PAS-stained cortex. Similar to rodents, the proximal convoluted tubule brush border is prominent (arrowhead), in contrast to the distal convoluted tubule (arrow).

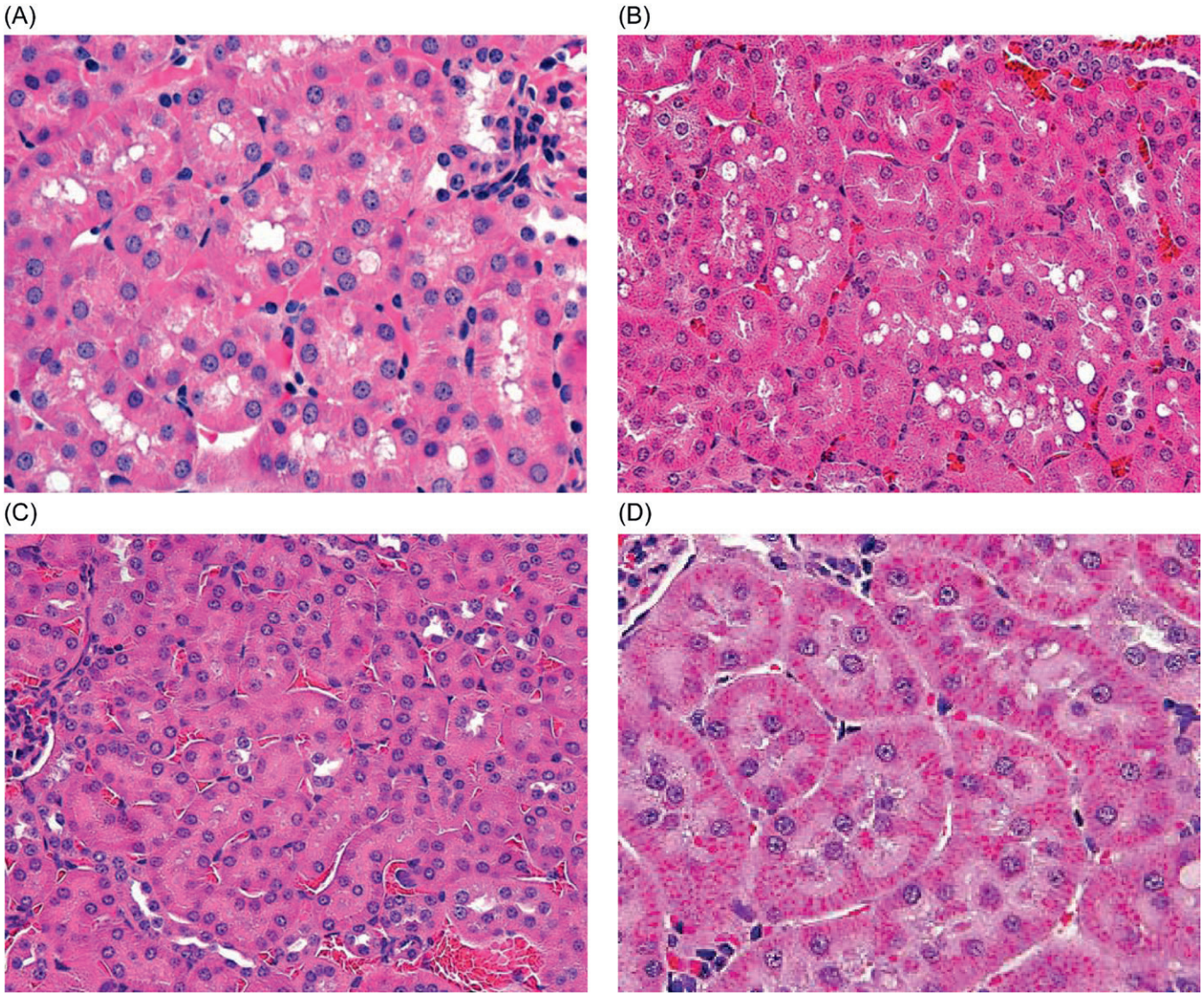

FIGURE 16.15 Cortex sexual dimorphism. (A) Young male mouse. (B) Old male mouse. Outer cortical tubular cells are variably vacuolated. This is an example of moderate vacuolation in an older male. The vacuoles are typically small, discrete, and colorless, consistent with microvesicular lipid accumulation. (C) Female mouse. This is the typical appearance of cortex from either a female or young male. (D) Male rat cortex. Proximal convoluted tubules contain cytoplasmic small eosinophilic hyaline droplets presumed to represent α2u-globulin, seen predominantly in young adult males.

Need-to-know

- Male rodent sexual dimorphism of the kidney includes larger organ size an higher proteinuria than females. These features are variable, depending on strain and age.
- Male rodents may have cuboidal parietal epithelium and superficial cortical tubular vacuolation, which is strain and age dependent.
- Male rats have larger glomeruli and eosinophilic hyaline droplets of the proximal convoluted tubules.

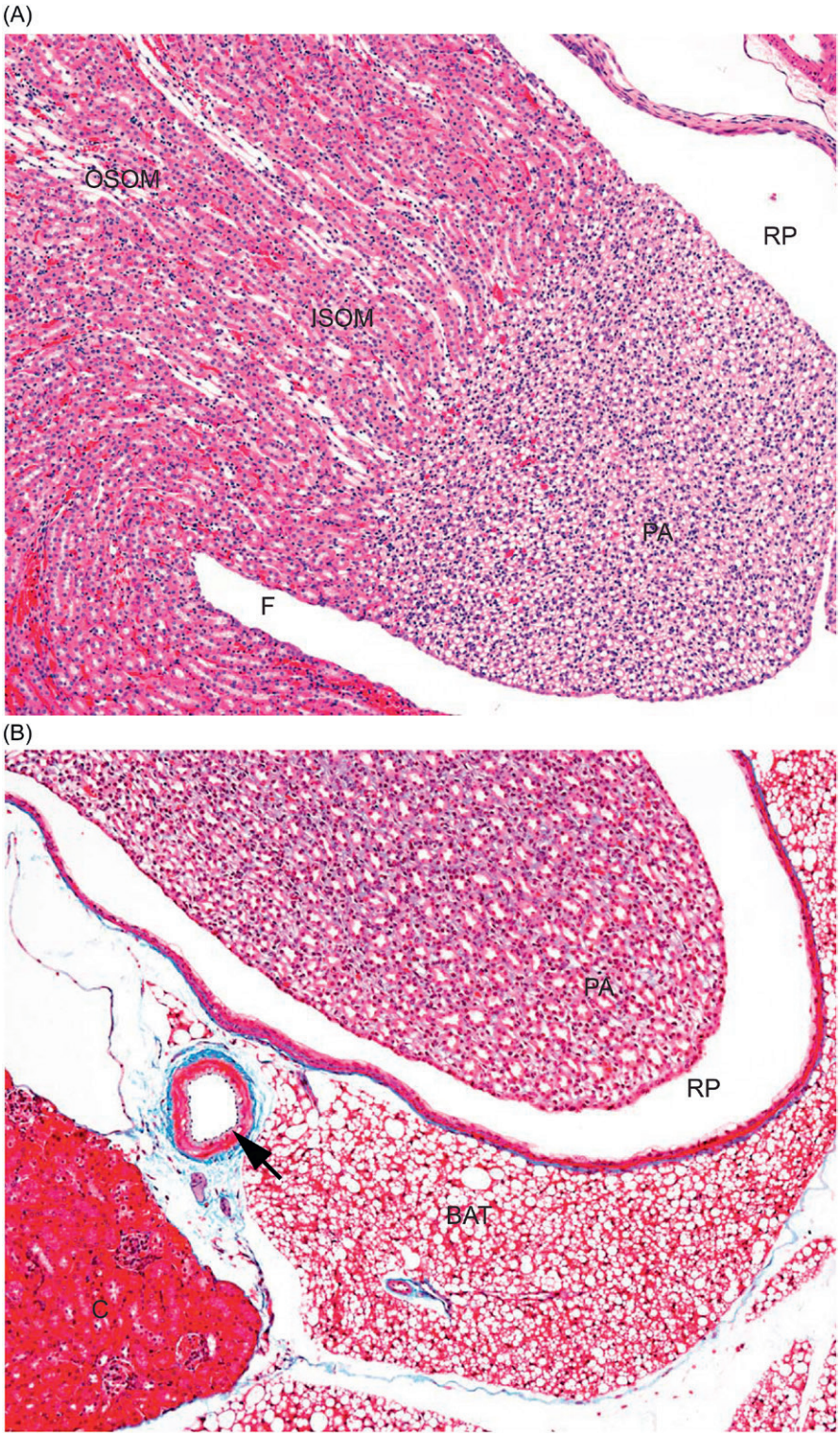

FIGURE 16.16 Papillae and hilus. (A) Rodent (mouse). Note the outer stripe of the outer medulla (OSOM), inner stripe of the outer medulla (ISOM), inner medulla, and the loops of Henle (thick and thin descending limbs, and thin and thick ascending limbs). Fornix (F), renal papillae (PA), and renal pelvis (RP) are indicated. (B) Rodent (mouse) renal hilus. Mason's trichrome stain. The single renal papilla (PA) of mice extends well into the pelvis (RP). The renal sinus contains brown fat (BF) and a renal artery (arrow). Cortex (C) is indicated.

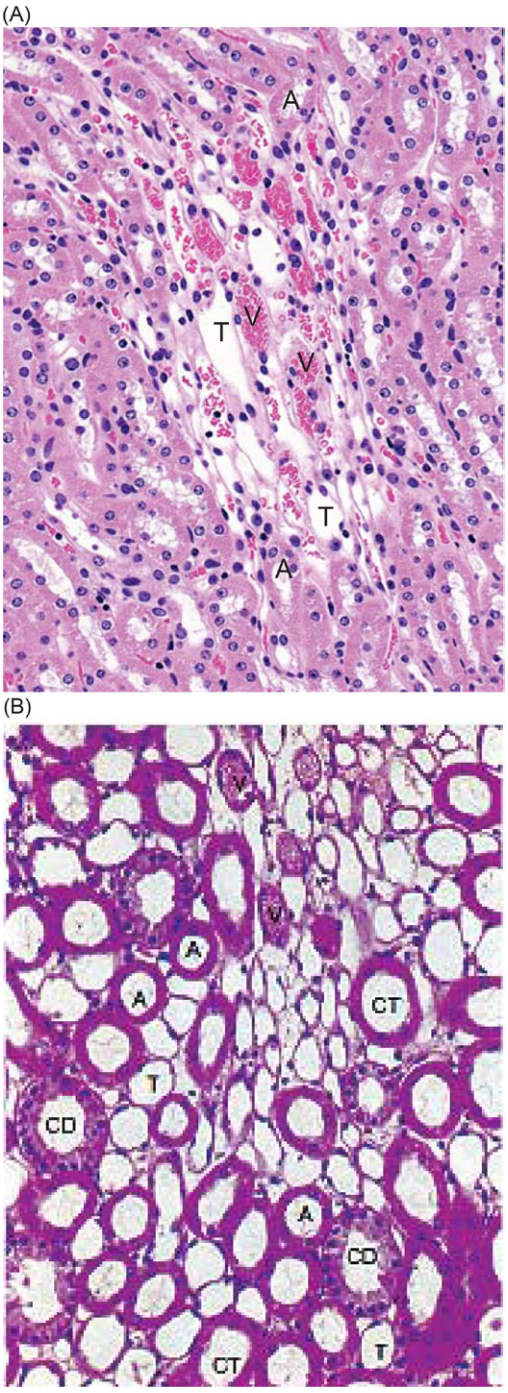

FIGURE 16.17 Medulla. (A) Rodent (mouse). Longitudinally-sectioned inner stripe of the outer medulla contains thick ascending limbs (A), thin limbs (T), and vasa recta (V). Rodents have a complex type of medulla in which large vascular bundles intermingle with the descending thin limbs. (B) Human. In contrast, humans have a simple medulla with separation between vascular bundles and tubules. The thin limbs (T) have a simple squamous epithelium and may be differentiated from the vasa recta (V) by the absence of erythrocytes and their regular rounded shape in transverse section. The thick ascending limbs (A) and collecting tubules (CT) are lined by low cuboidal. The collecting ducts (CD) are easily recognized by their large diameter and pale stained columnar epithelial lining. Source: Reprinted from Wheater's Functional Histology, 5th Edition, Young, B. et al. Copyright 2006, with permission from Elsevier.

bladder obliquely at the trigone (Figs. 16.1 and 16.3). Rat ureters are similarly small; ~0.3 mm in diameter. In both species, the left ureter is slightly shorter than the right ureter due to the more cranial position of the right kidney. If the animal has extensive abdominal and retroperitoneal adipose, locating the ureters at necropsy may be difficult.

The bladder in rodents is ventral to the colon and principally located within the pelvic region, dependent on the amount of distension with urine. The relatively high protein content of urine, especially in males, and the anatomic orientation of the bladder facilitate retention of granular proteinaceous debris within the bladder lumen.

The urethra in male rodents is divided into membranous and penile. The membranous urethra extends from the bladder to the penis, where just prior to entrance it expands to a caudolateral bulbous diverticulum. The penile urethra runs ventral to the os penis, also known as the baculum. It is relatively common to see proteinaceous material along the length of the urethra in male rodents as a result of accessory sex gland secretions. This can vary in appearance from eosinophilic granular material to a large coagulum of accessory sex gland secretions, sometimes admixed with sperm (see Chapter 18: Male Reproductive System for a complete discussion of the accessory sex glands). These coagula are commonly evident at necropsy, but are not associated with inflammation or urothelial damage. In male rodents, the urethra empties at the penile urethral fossa. In female rodents, the urethra is shorter, but it has a similar anatomical structure as that of the male. It travels through the clitoris and empties at the clitoral fossa just ventral to the vaginal orifice.

As in rodents, the ureters of humans are paired bilateral tubes that conduct urine from the renal pelvis to the bladder (Figs. 16.2 and 16.3). They are located in the abdominal retroperitoneal space and enter the bladder obliquely at the trigone. The human male urethra is divided into three

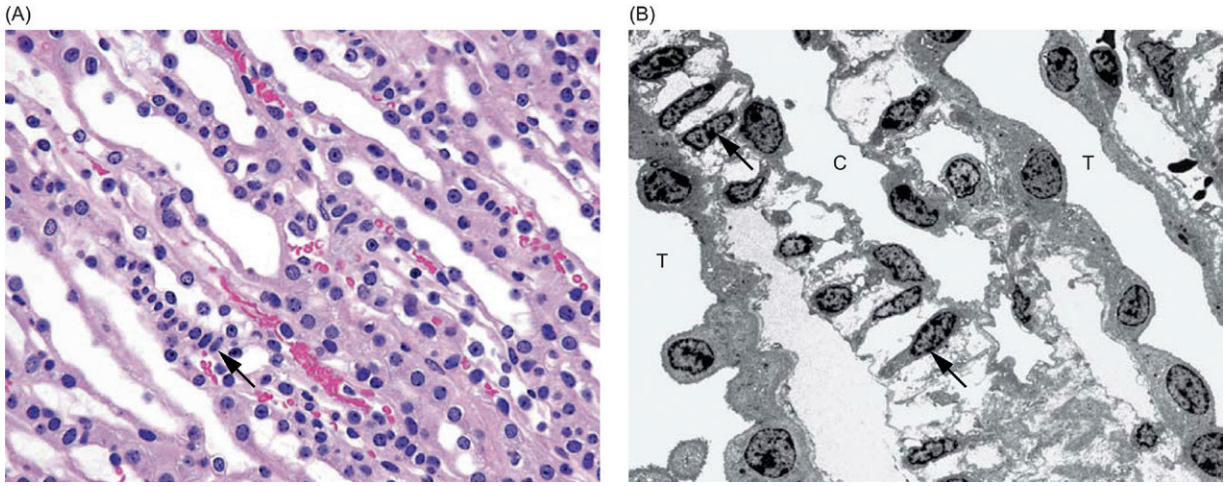

FIGURE 16.18 Papillae. (A) Rodent (mouse). Papilla with distal and collecting tubules, collecting ducts, and horizontal interstitial cells (arrow). (B). Rodent (mouse) (2000 ×). Electron micrograph of interstitial cells (arrow). These cells are fusiform with a horizontal orientation between collecting tubules (T) and capillaries (C), and they serve to compartmentalize the medulla, allowing for osmotic gradients.

Need-to-know

- Humans and rats share similar types of medullary intersitial cells, including lipid-containing cells with long cytoplasmic processes, lymphocyte-like cells, and pericytes.

segments: Prostatic, membranous, and spongy. The female urethra is relatively short and wide.

HISTOLOGY

The ureters, bladder, and urethra are all lined by urothelium, a specialized epithelium also known as transitional epithelium. In mice, the urothelium is generally two or three layers thick and in rats up to four layers—compared to five to seven layers of cells in humans—but this varies with distension (Figs. 16.20 and 16.21). In all three species, it is similarly stratified with superficial, intermediate, and basal cell layers (Fig. 16.19). These cell layers are morphologically distinct, although the distinction is better appreciated in humans (Fig. 16.19). In all three species, the superficial cells, known as umbrella cells, keep the epithelium impermeable to urine even when at full stretch. These large, ovoid cells have plentiful eosinophilic cytoplasm and round nuclei; some are binucleate (Figs. 16.19 and 16.20). The apical cytoplasm is indistinct and intensely stained, and the cell surface outline has a characteristic scalloped appearance. Intermediate layer cells are columnar, with nuclei oriented at a 90° angle to the basement membrane. Basal layer cells are compact and cuboidal in form. The basement membrane beneath urinary epithelium is often too thin to be resolved by light microscopy. Under the urothelium lies lamina propria, composed of collagenous and elastic tissue.

The ureters have similar histologic structures (Fig. 16.20). In humans, the lamina propria may be highly cellular and contain lymphoid aggregates. In the upper two-thirds of the ureter, the human muscularis propria has two cell layers (inner longitudinal and outer circumferential), whereas in the lower third, as well as in the bladder, it has three cell layers.

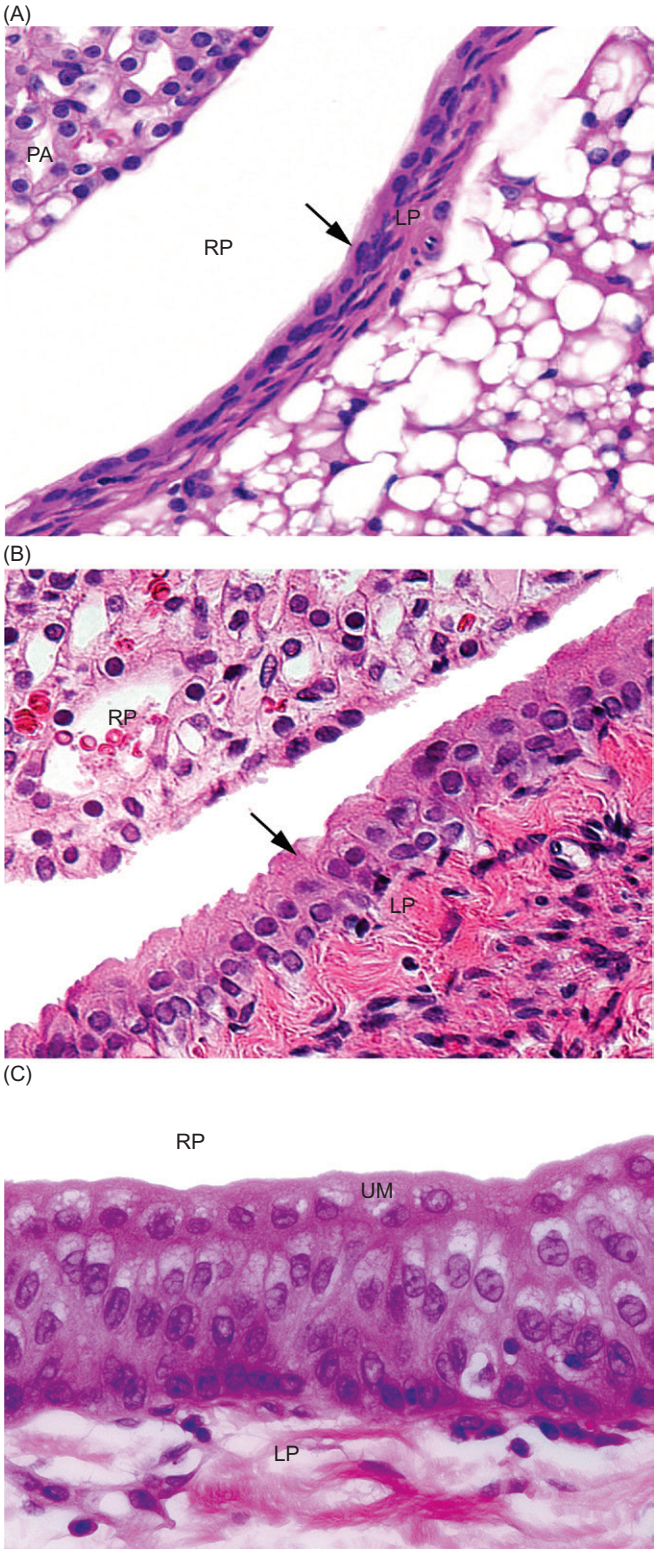

FIGURE 16.19 Urothelium. (A) Mouse; (B) Rat; (C) Human. In all three species, the conducting regions of the urinary system—including the renal pelvis, ureters, bladder, and urethra—are lined by specialized stratified epithelium, the urothelium (arrow). Papilla (PA), renal pelvis (RP), and extremely thin lamina propria (LP) are indicated. The epithelium is stratified into three to six layers of cells and is distension-dependent. The basal layers are compact and cuboidal in form, whereas intermediate-layer cells are more columnar, with their nuclei orientated at 90° to the basement membrane. The surface (superficial) cells are called umbrella (UM) or dome cells; they are large and ovoid with round nuclei and plentiful eosinophilic cytoplasm. The urinary epithelium rests on a basement membrane, which is often too thin to be resolved by light microscopy. The loose lamina propria (LP) is seen underlying the epithelium. The renal pelvis (RP) is indicated. Source: Reprinted from Wheater's Functional Histology, 5th Edition, Young, B. et al. 2006, with permission from Elsevier.

The bladder is very similar, with species differences limited to thickness of the walls and urothelium, and to the lymphoid aggregates often found in the bladder wall of older rodents. Distension of the bladder at necropsy has a major impact on histologic appearance and should be considered when evaluating mucosal morphology. Artifactual thickening of the bladder mucosa will occur if the bladder is not properly distended with fixative. Although this is of minimal impact in most routine diagnostics, it can be misinterpreted as early hyperplasia (Fig. 16.21).

In male rodents, the membranous urethra has abundant mucous glands, known as Littre glands, within the lamina propria, as well as an outer layer of skeletal muscle (Fig. 16.22). At the colliculus seminalis, near the dorsal neck of the bladder, the ducts of the dorsal prostate and accessory sex glands (seminal vesicles and coagulating glands) enter the membranous urethra. Here, the urethral epithelium is low columnar, in contrast to the rest of the urinary outflow tract, which is lined by urothelium until the transition to the urethral orifice. Female rodents may have detectable urethral glands within the submucosal connective tissue, depending predominantly

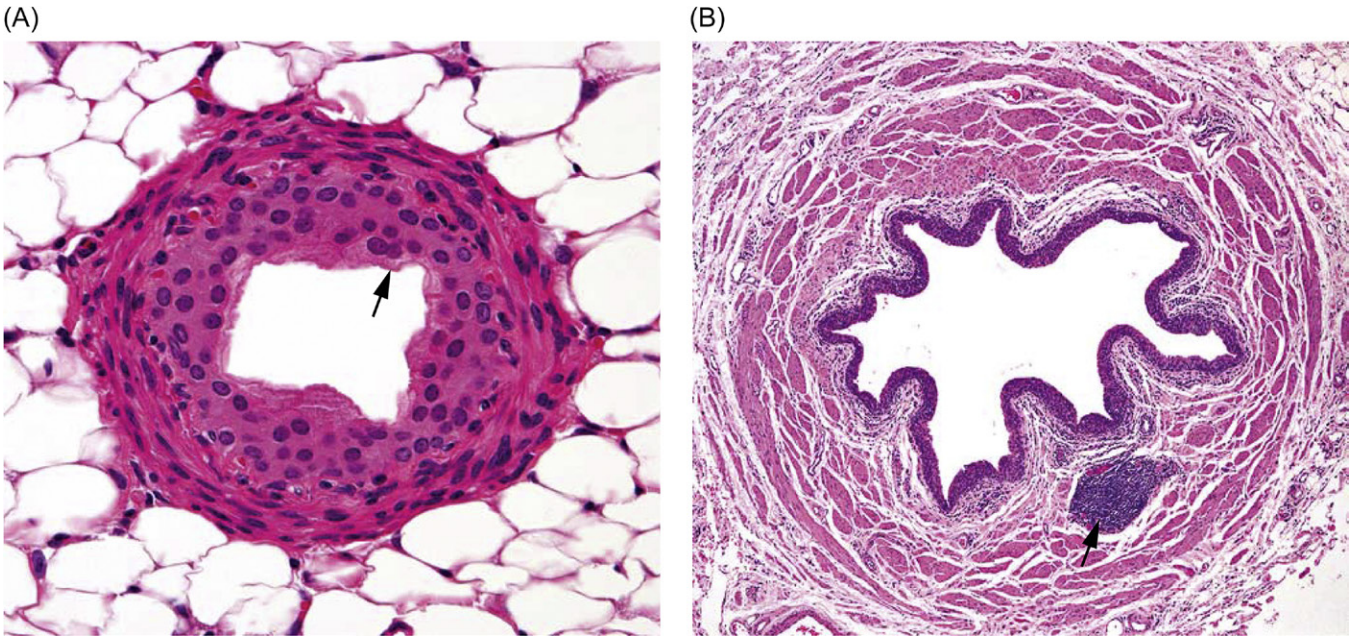

FIGURE 16.20 Ureter. (A) Mouse (rodent). The ureters are bilateral small retroperitoneal tubes lined by urothelium. The lamina propria is indistinct compared to the human ureter. Notice the binucleated superficial urothelial umbrella cell (arrow). (B) Human. The ureter has a star-shaped lumen lined by urothelium. The lamina propria is highly vascular and contains variable amounts of diffuse lymphatic tissue and occasionally small lymphoid nodules (arrow). Interlacing smooth muscle bundles occupy the muscularis externa, which is invested by an outer adventitia.

Need-to-know

- Lymphoid aggregates are seen all three species either in the submucosa of the bladder (rodent) or in the ureter (human).

on age. In female rats, urethral glands are most numerous at 30 days of age, after which they begin to regress. Remnant glandular tissue occasionally found in older female rats is referred to as paraurethral glands.

The human male prostatic urethra is lined primarily by urothelium. The membranous section is lined by stratified columnar epithelium, while at the end of the spongy urethra, the stratified columnar epithelium is gradually replaced by nonkeratinized stratified squamous epithelium. Invaginations of urethral epithelium lead to mucus-secreting Littre glands and the bulbourethral gland. In human females, the urethra near the urinary bladder is lined by urothelium, which is gradually replaced by stratified columnar epithelium, followed by nonkeratinized squamous epithelium as it reaches its opening into the vestibule. Similar to the male urethra, invagination of the epithelium forms mucus-secreting urethral glands. In all three species (and both sexes), the external urethral orifice is lined by stratified squamous epithelium, which is heavily keratinized in rodents (Fig. 16.22).

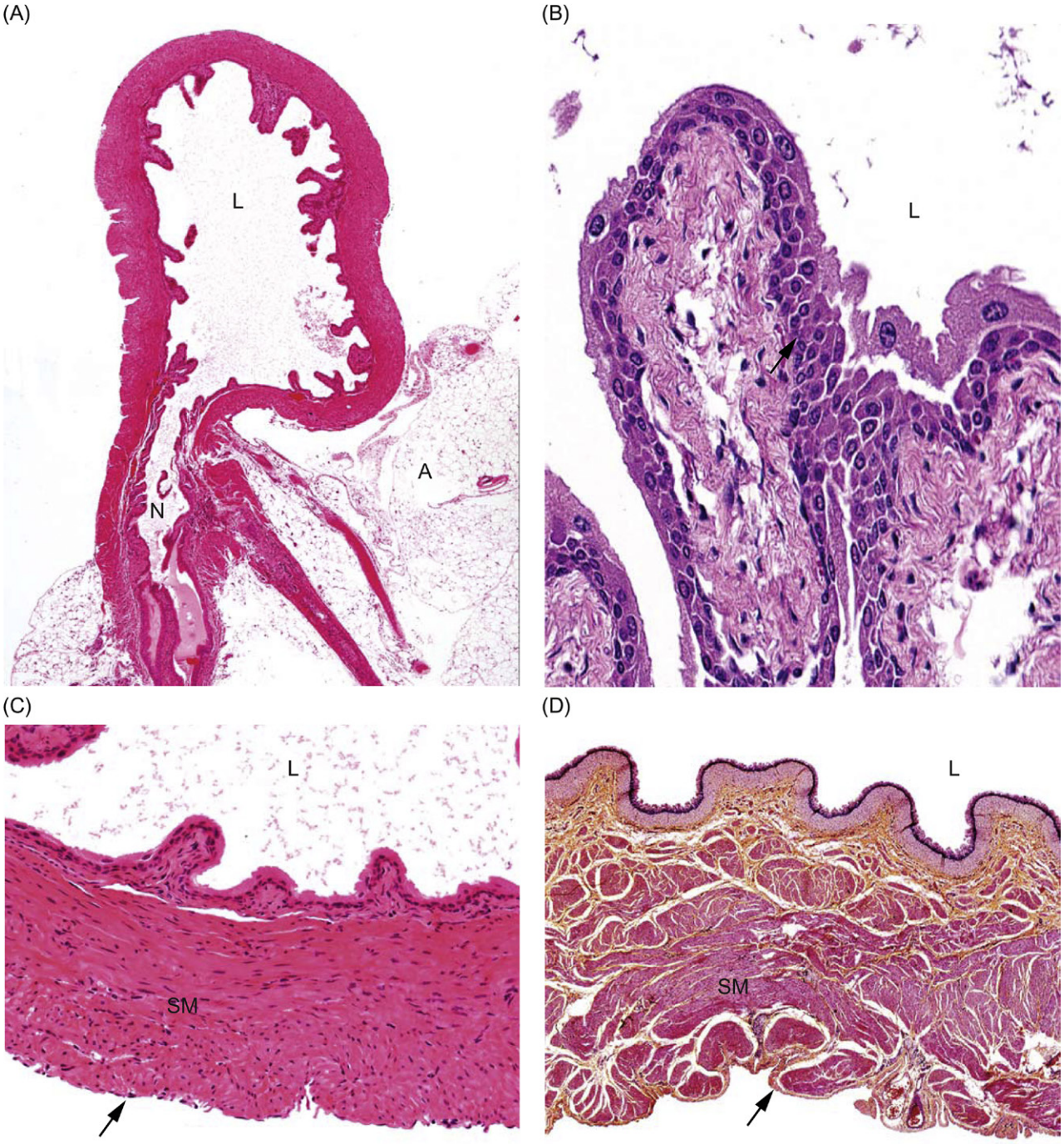

FIGURE 16.21 Bladder. (A) Male rodent (mouse). A low-power overview of a contracted bladder that was not distended with fixative and thus contains folded and thickened mucosa. The presence of intraluminal granular material is a reflection of the high protein concentration of mouse urine, especially male. The lumen (L), bladder neck (N), and white adipose tissue (A) from the pelvic fat pads are indicated. (B) High magnification of bladder mucosa from a male mouse. Notice the dramatic infolding of the mucosa that occurs in some areas making the urothelium appear thickened (arrow). This should not be interpreted as hyperplasia in a contracted bladder. The lumen (L) is indicated. (C) Male mouse bladder wall. Note the mucosal corrugations and intraluminal granular debris. Lumen (L), smooth muscle (SM), and thin serosa (arrow) are indicated. (D) Human bladder wall. The mucosa, according to the degree of distention, may look corrugated, with irregular longitudinal folds created by shape changes. The serosa consists of connective tissue covered externally by thin, simple squamous epithelium made of a continuous layer of mesothelial cells (not seen at this magnification). Lumen (L) and smooth muscle (SM) are indicated. Source: Reprinted from Netter's Essential Histology, Ovalle, W.K., and Nahirney, J.C., 2008, with permission from © Elsevier, www.netterimages.com.

Need-to-know

- The histomorphology of the bladder is highly fixation dependent.
- Male rodent bladders often contain proteinaceous material and sperm within the lumen.

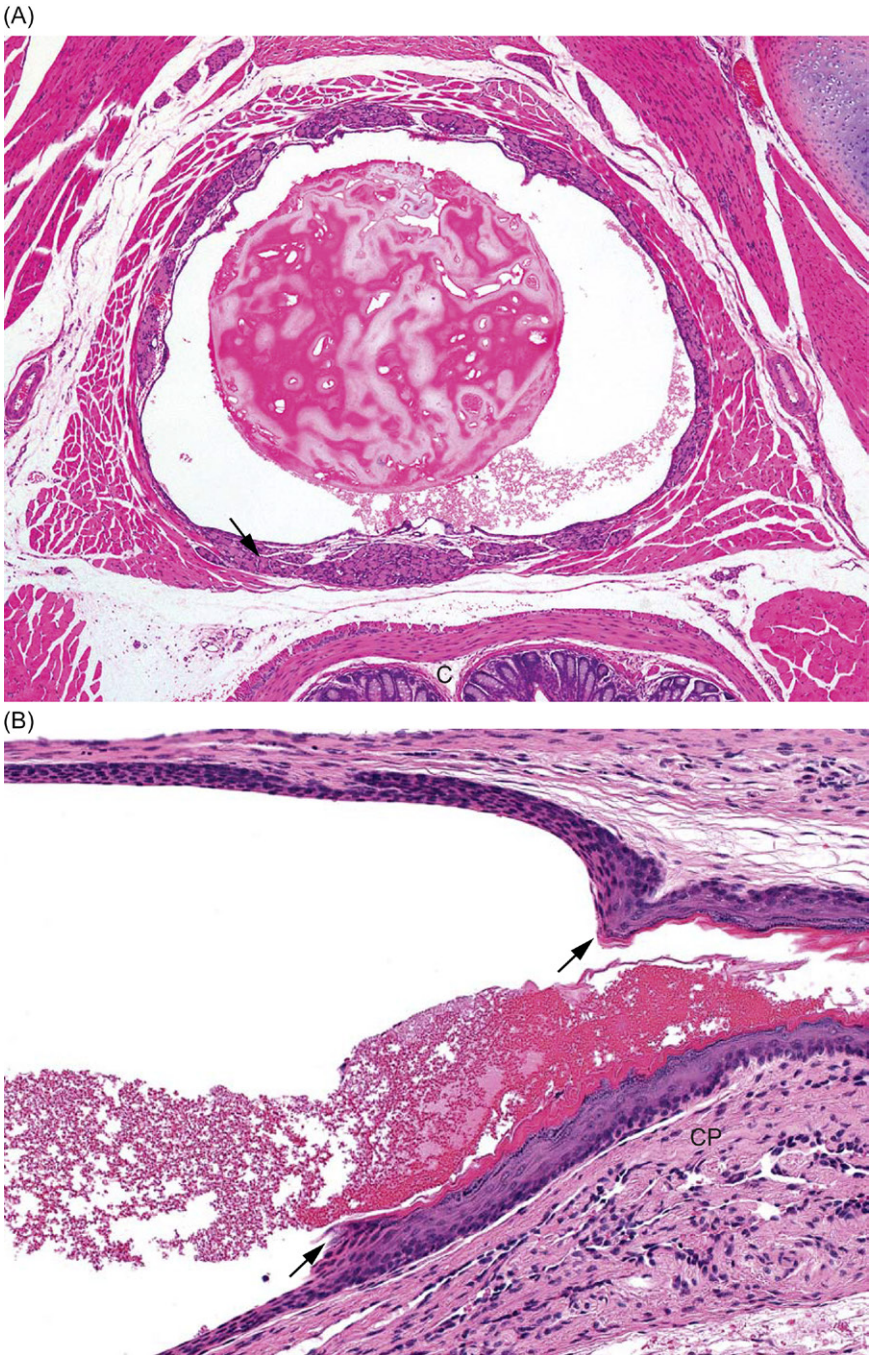

FIGURE 16.22 Urethra. (A) Rodent (mouse). The membranous urethra of a male from a cross section of the pelvis has abundant Littre glands (arrow) within the lamina propria and has an outer layer of skeletal muscle. The large spherical intralumenal structure is a coagulum of accessory sex glandular fluids. Colon (C) is indicated. (B) Rodent (mouse). Longitudinal section of penile urethra. Transition of the urethral urothelium to the external urethral orifice (arrows) to keratinized squamous epithelium is shown. Corpus cavernosum penis (CP) is indicated.

Need-to-know

- The lower urinary tract of male rodents may have intraluneal coagulum, which frequently accumulates perimortem.

FURTHER READING

Greaves P: *Histopathology of Preclinical Toxicity Studies*, London, UK, 2012, Academic Press.

Maronpot RR, Boorman GA, Gaul BW, editor: *Pathology of the Mouse: Reference and Atlas*, Vienna, IL, 1999, Cache River Press.

Mills SE, editor: *Histology for Pathologists* (4th edn.), Philadelphia, 2012, Lippincott Williams & Wilkins.

Ovalle WK, Nahirney PC: *Netter's Essential Histology* (Netter Basic Science), Philadelphia, 2008, Saunders.

Society for Toxicologic Pathology: International Harmonization of Nomenclature and Diagnostic Criteria (INHAND). https://www.toxpath.org/inhand.asp.

Suttie AW, Leininger JR, Bradley AE: *Boorman's Pathology of the Rat: Reference and Atlas*, 2nd edn., New York, 2017, Academic Press.

Young B, Lowe JS, Stevens A, et al: *Wheater's Functional Histology: A Text and Colour Atlas*, 5th edn., Oxford, 2006, Churchill Livingstone.

This page intentionally left blank

FEMALE REPRODUCTIVE SYSTEM 17

KELLI L. BOYD
Vanderbilt University Medical Center, Nashville, TN, United States

ATIS MUEHLENBACHS
Centers for Disease Control and Prevention, Atlanta, GA, United States

MARA H. RENDI AND ROCHELLE L. GARCIA
University of Washington School of Medicine, Seattle, WA, United States

KATHERINE N. GIBSON-CORLEY
University of Iowa Carver College of Medicine, Iowa City, IA, United States

Introduction

The female genital system is dynamic in both rodents and the human, with varying morphologic appearance based on hormonal influences during the estrus (rodent) or menstrual (human) cycle, pregnancy, and ovarian senescence. This chapter focuses on the ovaries, oviduct (uterine or fallopian tube), uterus and cervix, vagina and clitoris of actively cycling adult rodent and human females, as well as the placenta. Although both humans and rodents are mammals with similar ovaries, oviducts, uteri, and placentation, there are several structural and functional differences (Tables 17.1–17.3). In particular, the gross anatomy between the three species varies considerably, whereas the histologic appearance and basic functions tend to be more similar.

Ovary

Gross Anatomy

Rodent and human ovaries are paired, spherical (rodent) or ovoid (human) structures (Figs. 17.1 and 17.2). Rodent ovaries are located at the caudal poles of the kidneys, attached to the dorsal body wall by the mesovarium and enclosed in a transparent elastic bursa. The periovarian space is closed off to the abdominal cavity by the ovarian bursa, with the exception of a small channel in the bursa through which blood vessels and nerves enter and leave the ovarian hilus. Human ovaries float within the pelvis, surfaced by peritoneum that attaches them to the broad ligament anteriorly, to the uterus medially, and to the pelvic sidewalls laterally by associated ligaments (Fig. 17.2). When females become sexually mature, the smooth

Comparative Anatomy and Histology. DOI: http://dx.doi.org/10.1016/B978-0-12-802900-8.00017-8
© 2018 Elsevier Inc. All rights reserved.

TABLE 17.1 Female Reproductive Tract

Feature	Rodent	Human
	Gross	
Ovary	Spherical, enclosed in bursa	Oval, open to peritoneal cavity
Oviduct	18–30 mm; thin tube, tightly coiled	12 cm; muscled-lined tube; not coiled
Oviduct segments	Ampulla, infundibulum, and intramural	Similar to rodents
Oviduct relationship to ovary	Opens directly into the ovarian bursa	Ampulla has fimbriated end that opens directly into peritoneal cavity adjacent to ovary
Uterine type	Mouse: Bicornuate uterus with two lateral horns and a single body Rat: Duplex, bicornuate uterus with two lateral horns	Simplex
	Histologic	
Oviduct epithelium	Diffusely ciliated in ampulla segment	Simple ciliated columnar cells and interspersed peg cells
Ciliated cells	Decrease as the oviduct approaches the uterus	Most numerous the ampulla and infundibulum and decrease in the intramural segment
Myometrium	Inner circular and outer longitudinal smooth muscle layers	Single smooth muscular layer
Myometrial glands	Mouse: Presence varies by strain Rat: Absent	Absent
	Estrus (r)/Menstrual (h) Cyclic Endometrial Changes	
Proestrus/proliferative	Hyperemic and distended with mitoses in the epithelium and leukocytes in stroma	Tubular-shaped glands with columnar cells. Both gland and stromal mitoses are present
Estrus/secretory	Maximum mitoses, leukocytes rare	Epithelium remains columnar but the glands become distended and more tortuous. The cells contain subnuclear vacuoles early in the secretory phase, followed by supranuclear vacuoles with eventual loss of the vacuoles. The stroma becomes increasingly epithelioid during the latter half of the secretory phase under the influence of progesterone
Metestrus/shedding	Epithelium degenerates, uterine wall no longer distended, high numbers of leukocytes	Stroma condenses and there is neutrophilic infiltrate and epithelial breakdown
Diestrus	Collapsed uterus with leukocytes and regeneration	Absent

TABLE 17.2 Sexual Maturity and Ovulation

Feature	Rodent	Human
	Puberty	
Age at onset	Mouse: Approximately 4 weeks Rat: 30–50 days	Approximately 10 or 11 years, lasting approximately 4 years
Estradiol production by ovaries	Effect varies by strain	Leads to breast and uterine development, as well as the pubertal growth spurt and epiphyseal plate closure
Exposure of immature females to male urine	Can hasten puberty	Not studied
Exposure of immature females to urine from group-housed females	Mouse: Can delay puberty Rat: Unknown	Not studied
Day length and temperature	Can affect	No effect
	Estrus (r)/Menstrual (h) Cycle	
Length	Approximately 4–6 days continuous estrus cycles unless interrupted by pregnancy	Approximately 28 days beginning at the onset of puberty until menopause
Phases	Proestrus, estrus, metestrus, and diestrus	Menstrual/shedding, proliferative (follicular), and secretory (luteal)
Follicle development/cycle	Multiple follicles mature simultaneously	Multiple follicles begin the maturation process, with one follicle becoming the dominant follicle
Ova release	Multiple at ovulation	Usually only one ova per menstrual cycle

TABLE 17.3 Gestation and Placentation

Feature	Rodent	Human
Length of gestation	Mouse: 18.5–21 days Rat: 21–24 days	Average 40 weeks (or full term: 39–40 weeks)
Placental size (diameter)	Mouse: 2.0 cm Rat: 2.5 cm	20 cm
Placental shape	Discoid	Similar to rodent
Maternal–fetal interdigitation	Labyrinthine	Villous
Placental barrier	Hemochorial	Similar to rodent
Yolk sac	Minor continued function in maternal–fetal exchange	Nonfunctional remnant at term
Uterine spiral arteries	Mouse: Remodeling minimal and not dependent on NK cells or invasive trophoblasts. Rat: Remodeling directed by NK cells and invasive trophoblasts	Similar to rat
Trophoblast populations	Labyrinth trophoblast, spongiotrophoblast, giant cell trophoblast	Syncytiotrophoblast, cytotrophoblast, extravillous trophoblast, chorionic laeve trophoblast

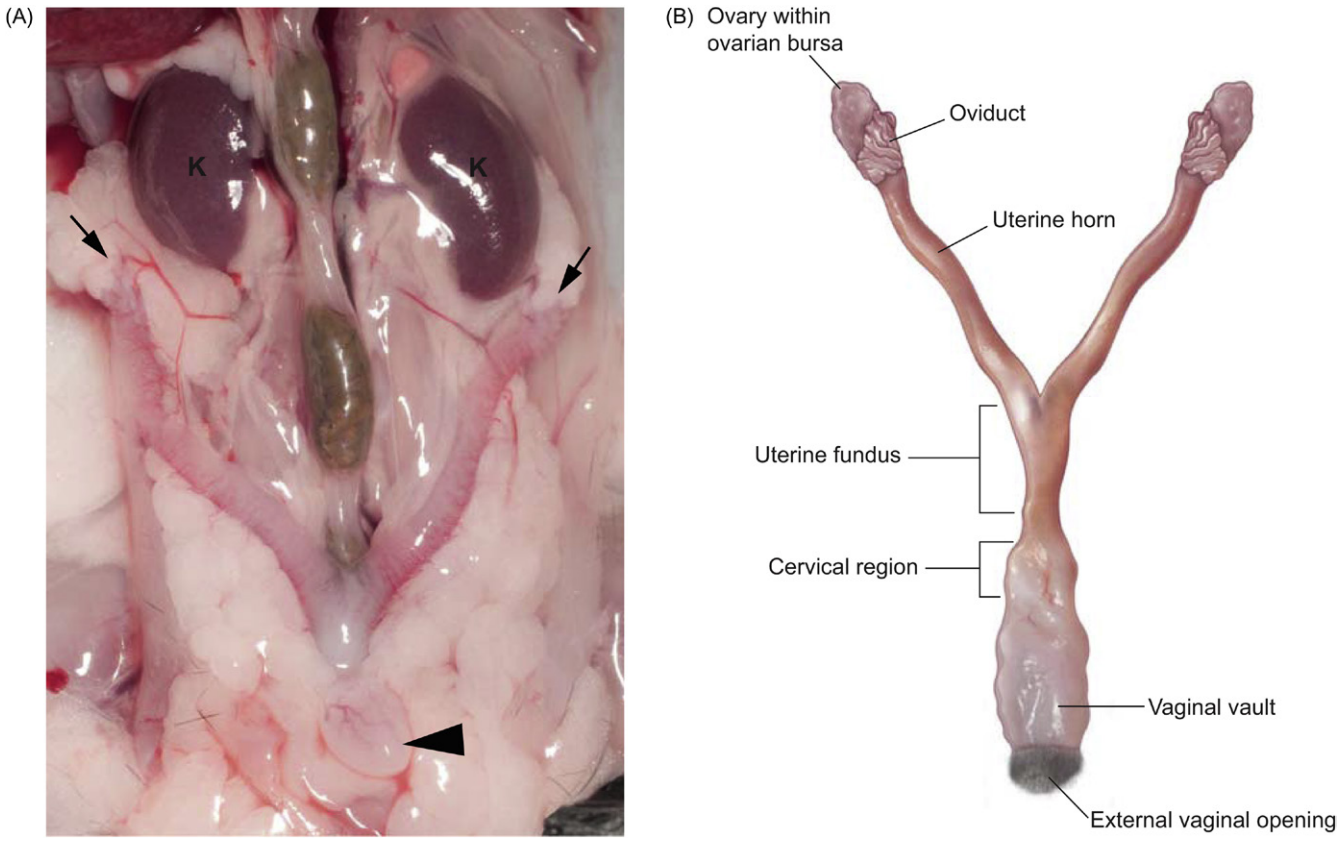

FIGURE 17.1 Rodent (mouse) regional anatomy. (A) Mouse reproductive tract *in situ*. Paired ovaries (arrows) are located at the caudal poles of the kidneys (*K*) embedded in the ovarian fat pad. Paired uterine horns meet at the fundus. Note that the urinary bladder (arrowhead) is present at the ventral surface of the vaginal vault. (B) *Ex vivo* mouse reproductive tract showing paired ovaries and oviducts, duplex uterus, vaginal vault, and external vaginal opening. Melanosis of uterine fundus may be seen in pigmented mouse strains. Rats have similar gross anatomy. Source: © Elsevier, Inc., www.netterimages.com.

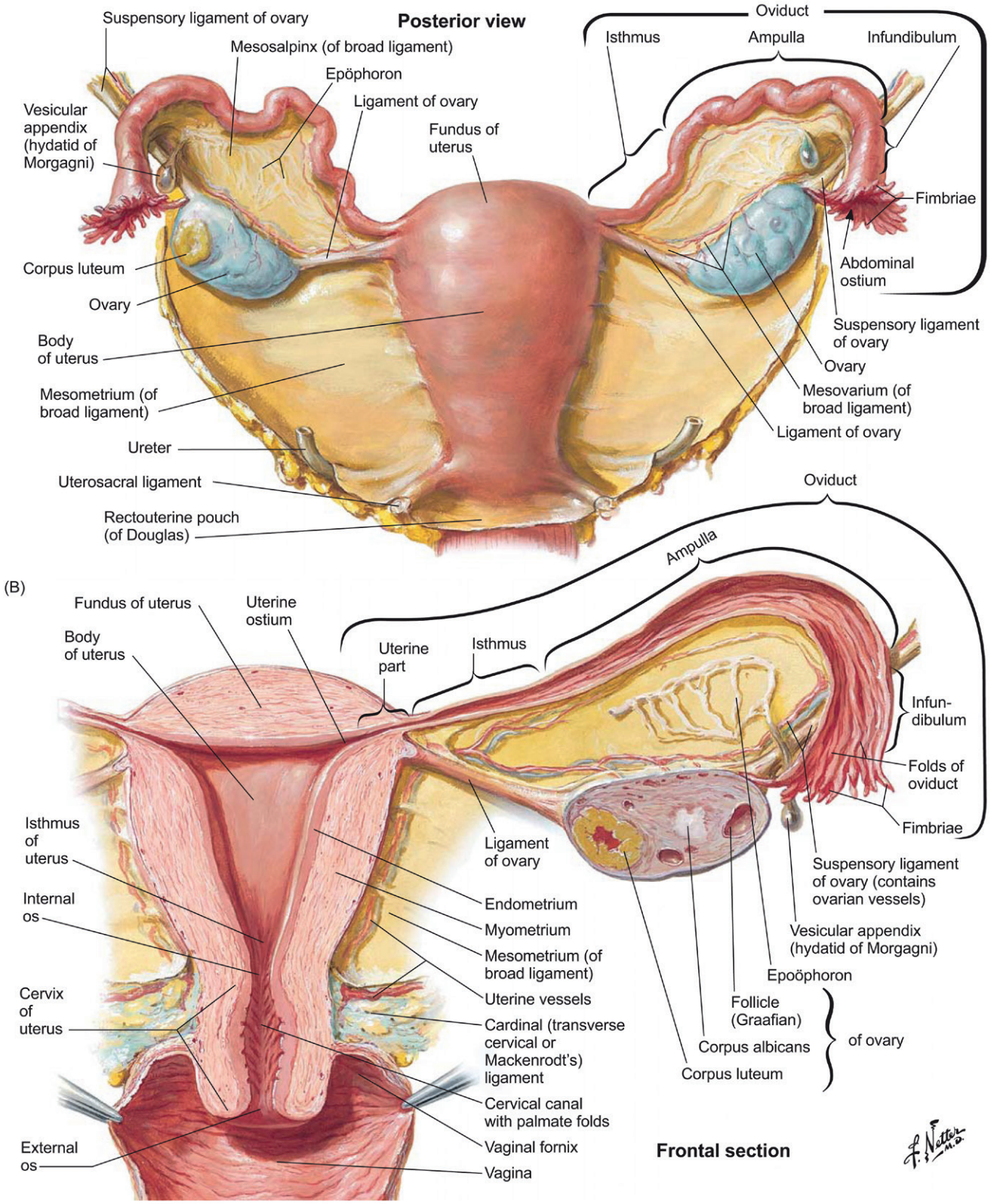

FIGURE 17.2 Human regional anatomy. Diagram of the relationship between the human ovary, oviduct, and uterus including the cervix. The human ovaries are located within the peritoneal cavity and are not encased in a bursa, as in rodents. Source: © Elsevier, Inc., www.netterimages.com.

surface of the ovary becomes nodular as a result of follicles and corpus lutea development during estrus/menstrual cycles.

HISTOLOGY

The rodent ovarian bursa is covered by mesothelium on the inner and outer surfaces which is composed of blood vessels, nerves, and few smooth muscle fibers (Fig. 17.3). An accumulation of adipose tissue referred to as the fat body is present near the hilus. The outer surface of the rodent ovary is covered by the germinal epithelium, which is composed of a single layer of cuboidal-to-columnar epithelium. The human ovary is surfaced by similar-appearing mesothelium (Fig. 17.4). In both rodents and humans, ovarian parenchyma is divided into two poorly defined areas—the central vascular medulla and a compact outer cortex. The medulla consists of dense fibrous connective tissue and blood vessels. The cortex consists of developing follicles, corpus lutea, supporting stroma, and blood vessels (Figs. 17.4–17.6). The primordial follicles lie directly beneath the germinal epithelium in the tunica albuginea. Primordial follicles consist of flat cells surrounding the clear spherical ovum (Figs. 17.5 and 17.6). The nuclei of individual oocytes have open chromatin and a prominent nucleolus. Although most primordial follicles contain a single ovum, polyova are not uncommon in young rodent females but are quite unusual in human females. As primordial follicles are depleted through ovulation or atresia (Figs. 17.5 and 17.6), dense fibrovascular tissue becomes the prominent feature of the tunica albuginea.

Multiple follicles mature simultaneously in both rodents and humans; however, typically only one egg is released in humans, whereas several are released in rodents. Maturation and ovulation are similar in rodents and humans. During maturation, the ovum and the follicle enlarge. As the ovum matures, it is surrounded by the multilayered stratum granulosum composed of small basophilic granulosa cells (Figs. 17.5 and 17.6). The maturing follicle develops a liquid-filled antrum and stromal cell sheath which moves the follicle centrally as it enlarges. The stromal sheath differentiates into the vascular theca interna and the fibrous theca externa during maturation (Fig. 17.6). The theca externa is penetrated by blood and lymphatic vessels to create the vascular plexus within the theca interna. However, the granulosa layers in both rodents and humans remain avascular. The oocyte deposits an acellular material that becomes the zona pellucida, which separates the oocyte from the granulosa cells. As the follicle matures to become a tertiary or Graafian follicle, the follicle bulges into the periovarian space in preparation for ovulation. At ovulation, the germinal or ovarian surface epithelium ruptures and releases the oocyte, zona pellucida, and follicle cells (cumulus oophorus), into the periovarian space. Rodent follicles are further classified by cross-sectional diameter, number of granulosa cell layers, and nature of antral space (see Further Reading for additional details). Small follicles are numerous in all stages of the estrus cycle. Large maturing follicles are most abundant in proestrus and disappear in estrus as a result of ovulation.

Following ovulation in both rodents and humans, the granulosa cells hypertrophy, become vascularized from the theca interna, and form the corpus luteum (Fig. 17.7). Mature lutein cells have clear vacuolated eosinophilic cytoplasm and a large nucleus with open chromatin. In rodents, multiple mature corpora lutea are present post ovulation. Corpora lutea from several generations of ova may be present simultaneously in the same ovary in both rodents and humans. Immature corpora lutea are smaller and basophilic, whereas older and mature corpora lutea are large and eosinophilic with cells arranged in cords around sinusoids.

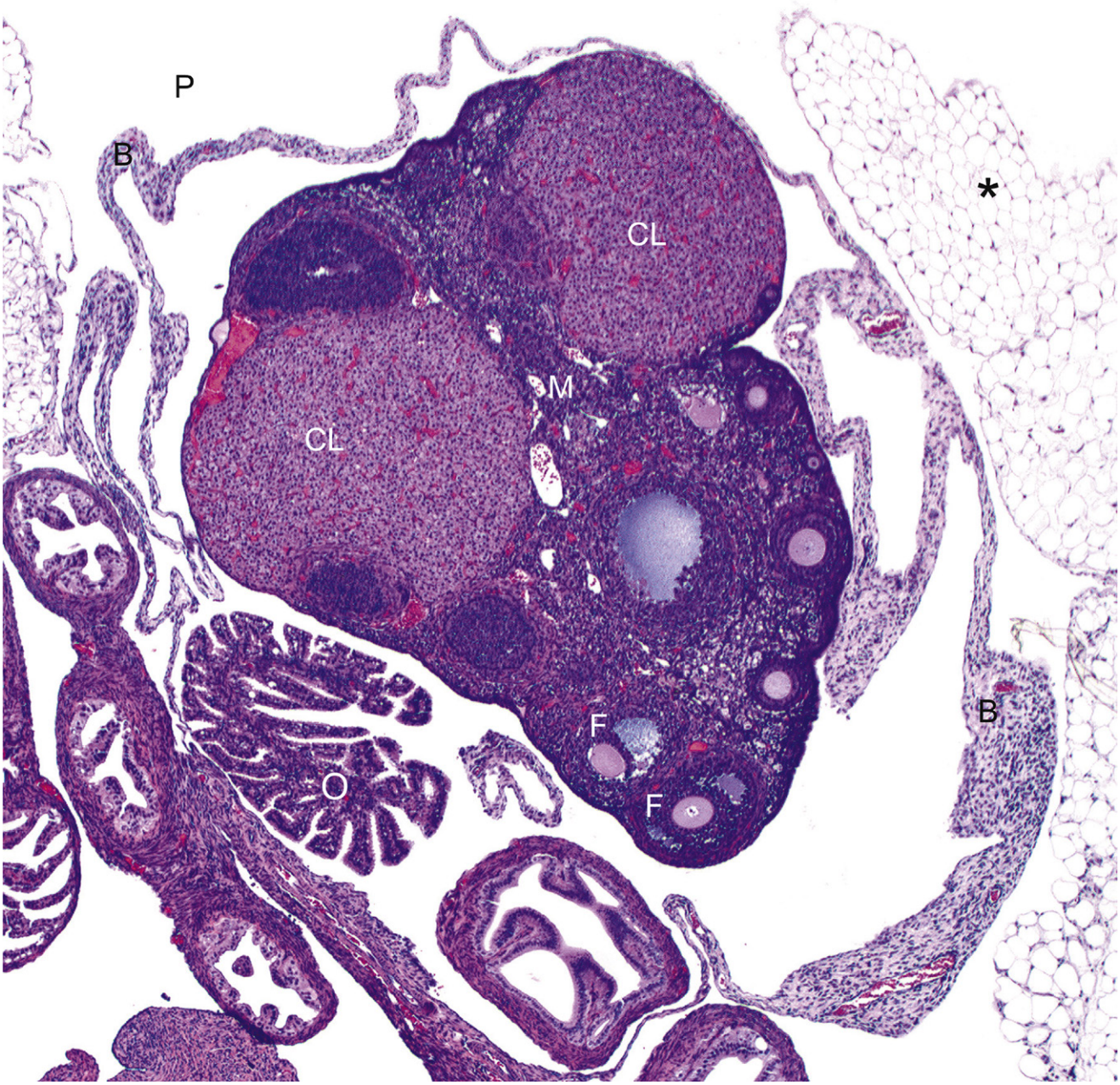

FIGURE 17.3 Rodent (mouse) ovary. Rodent ovaries are paired structures embedded in fat (asterisk) just caudal to the kidneys. They are completely surrounded by the ovarian bursa (B). The rodent estrus cycle is typically 4–6 days, and multiple follicles (F) mature simultaneously. In rodents, maintenance of pregnancy is dependent on progesterone secreted by the corpus luteum (CL). The ovary has two poorly defined areas—a highly vascular central medulla (M) and a more compact outer cortex composed of the developing follicles and corpus lutea. Oviduct (O) and peritoneal cavity (P) are indicated.

Need-to-know

- Rodent ovaries are completely surrounded by the ovarian bursa.
- Maintenance of pregnancy in rodents is dependent solely on the corpus luteum, whereas in humans, pregnancy depends on the corpus luteum during the first trimester and subsequently the placenta.

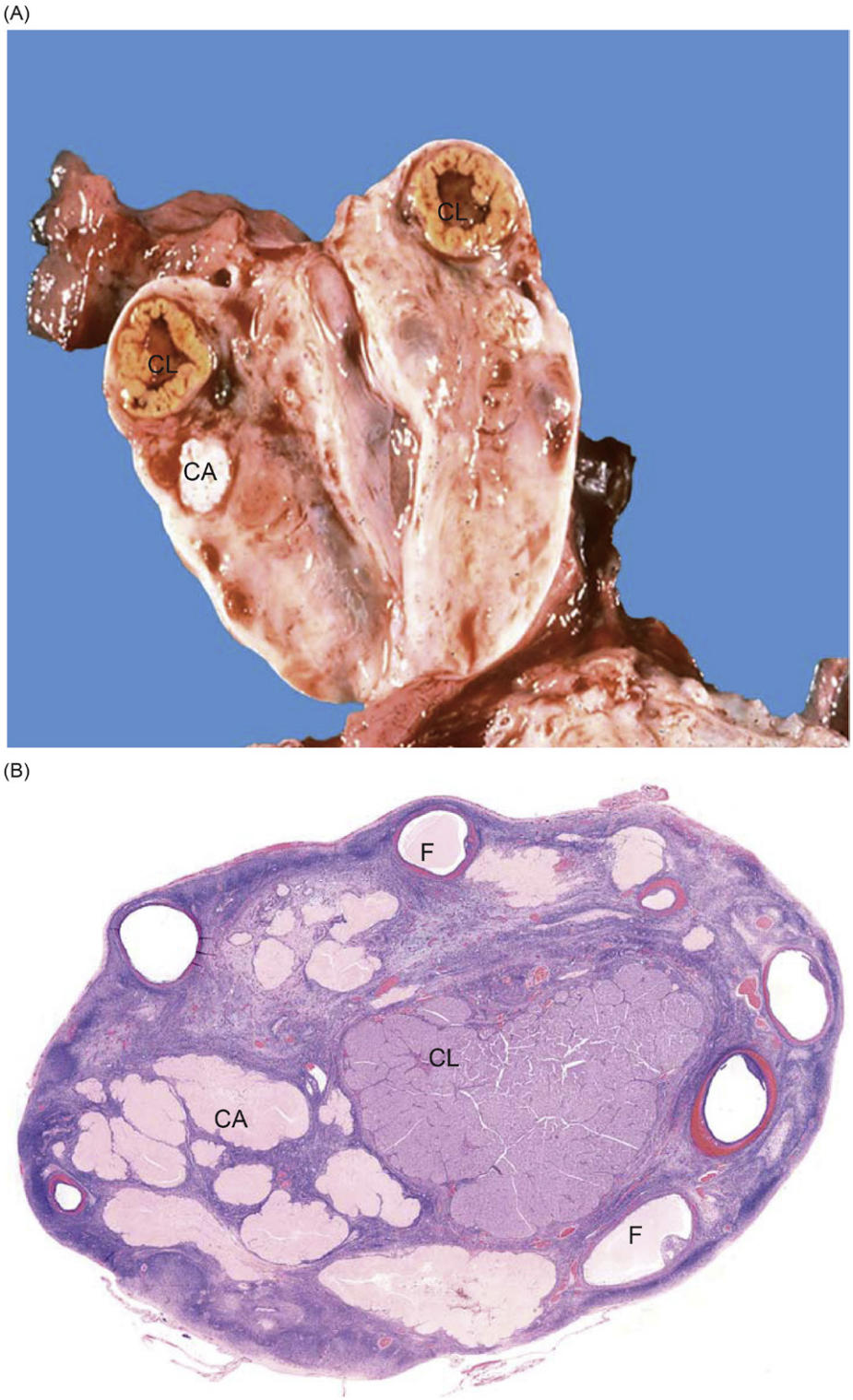

FIGURE 17.4 Human ovary. (A) A gross photo of the human ovary with corpus luteum (CL) and corpora albicans (CA). (B) Part of a corpus luteum (CL) and two developing follicles (F). Similar to rodents, human ovaries are paired structures. However, unlike rodents, human ovaries are covered by mesothelium and essentially float within the peritoneal cavity. There is no bursa surrounding human ovaries. The corpus luteum (CL) supports gestation until the placenta takes over this function.

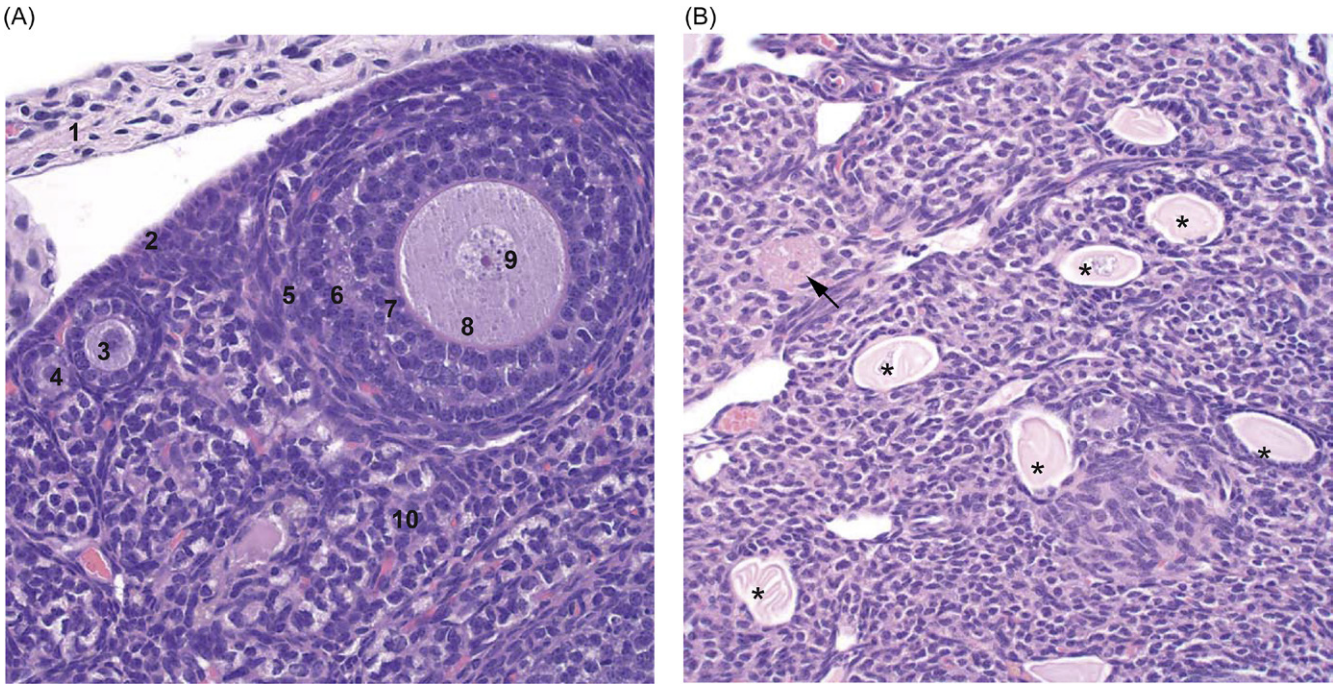

FIGURE 17.5 Rodent (mouse) ovary. The surface of the ovary is covered by a layer of cuboidal cells, the germinal epithelium (2). Primordial follicles (4) are found beneath the germinal epithelium in the tunica albuginea, which is indiscrete until late in life. Polyovular follicles are not uncommon in young mice. At ovulation, the germinal epithelium ruptures and the ovum and its cluster of cells are released into the periovarian space. 1, Ovarian bursa; 2, germinal epithelium; 3, primary unilaminar follicle; 4, primordial follicle; 5, thecal layer; 6, lutein cells; 7, granulosa cells and cumulus oophorus; 8, zona pellucida; 9, oocyte; 10, ovarian stroma. (B) Degenerate or atretic follicles (asterisks) and accumulation of cells with light brown cytoplasmic pigment (arrow) are observed in older mice.

Need-to-know

- Multiple follicles mature simultaneously in both rodents and humans; typically, a single ovum is released in humans, whereas multiple ova are released at ovulation in the rodent.

Not all ova and follicles mature fully, and it is common to see cell death resembling apoptosis in the degenerating follicles. These degenerate follicles, referred to as atretic follicles, are composed of remnants of ovum and zona pellucida (Fig. 17.5). As rodents age, the interstitial tissue formed from degenerating follicles increases and is often characterized by large cells containing brown pigment. As humans age, the ovaries have increasing numbers of scars, referred to as corpora albicans. These corpora albicans represent previous corpus lutea that have undergone involution.

Oviduct (Uterine Tube)

GROSS ANATOMY

The rodent oviduct, also known as the uterine tube, is an approximately 18–30 mm long, narrow coiled tube that connects the uterine horn with the periovarian space (Fig. 17.1). The oviduct is suspended from the dorsal body wall by the mesotubarium, which is continuous with the mesovarium, ovarian bursa, and the uterine mesometrium. The human oviduct is a similar-

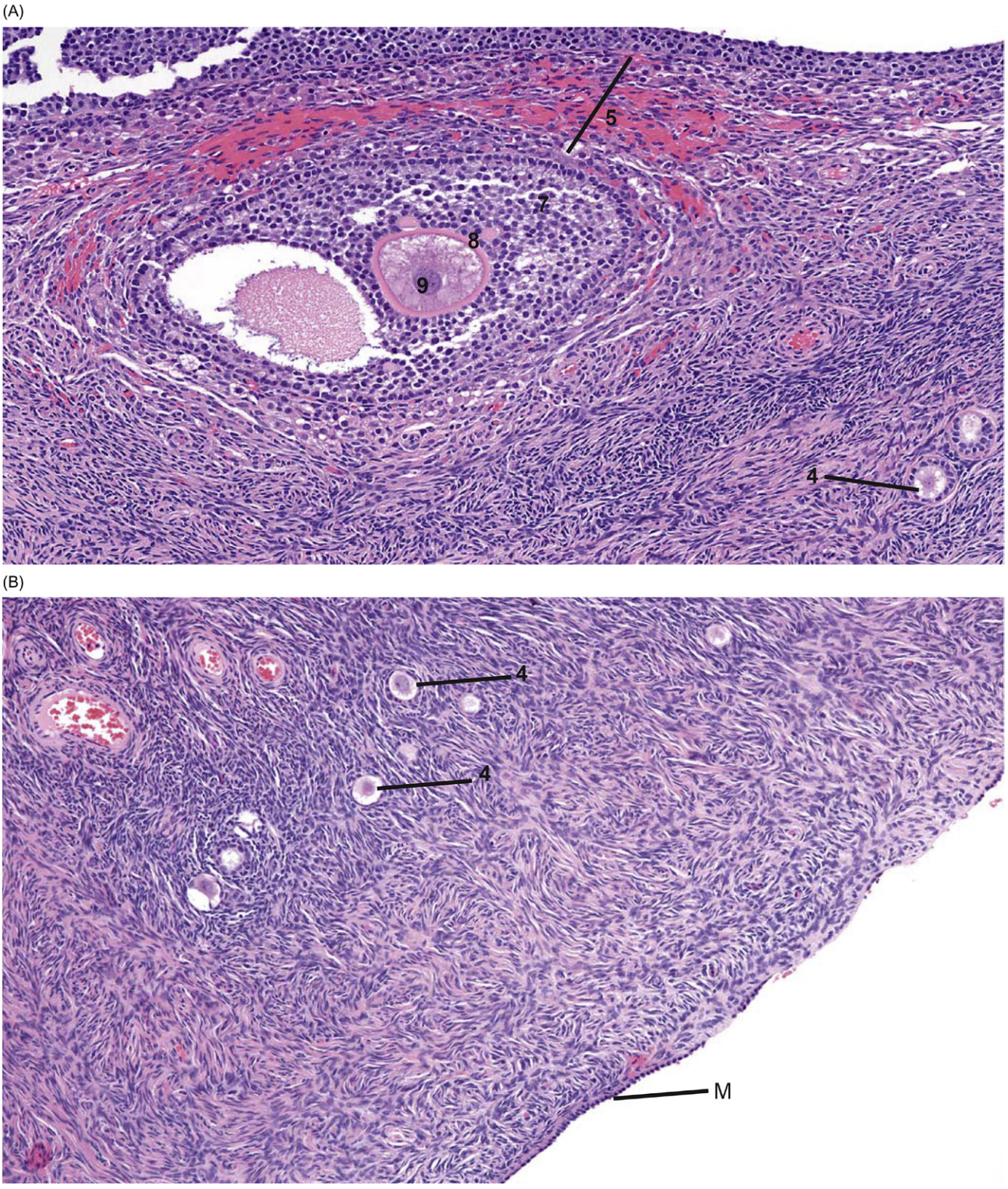

FIGURE 17.6 Human ovary. Oocyte (A) and primordial follicles (B). The surface of the human ovary is covered by a flat layer of mesothelium (M) that is similar in appearance to the germinal epithelium covering the rodent ovary. Basic ovarian structure is similar in mice and humans. 4, Primordial follicle; 5, thecal layer; 7, granulosa cells and cumulus oophorus; 8, zona pellucida; 9, oocyte.

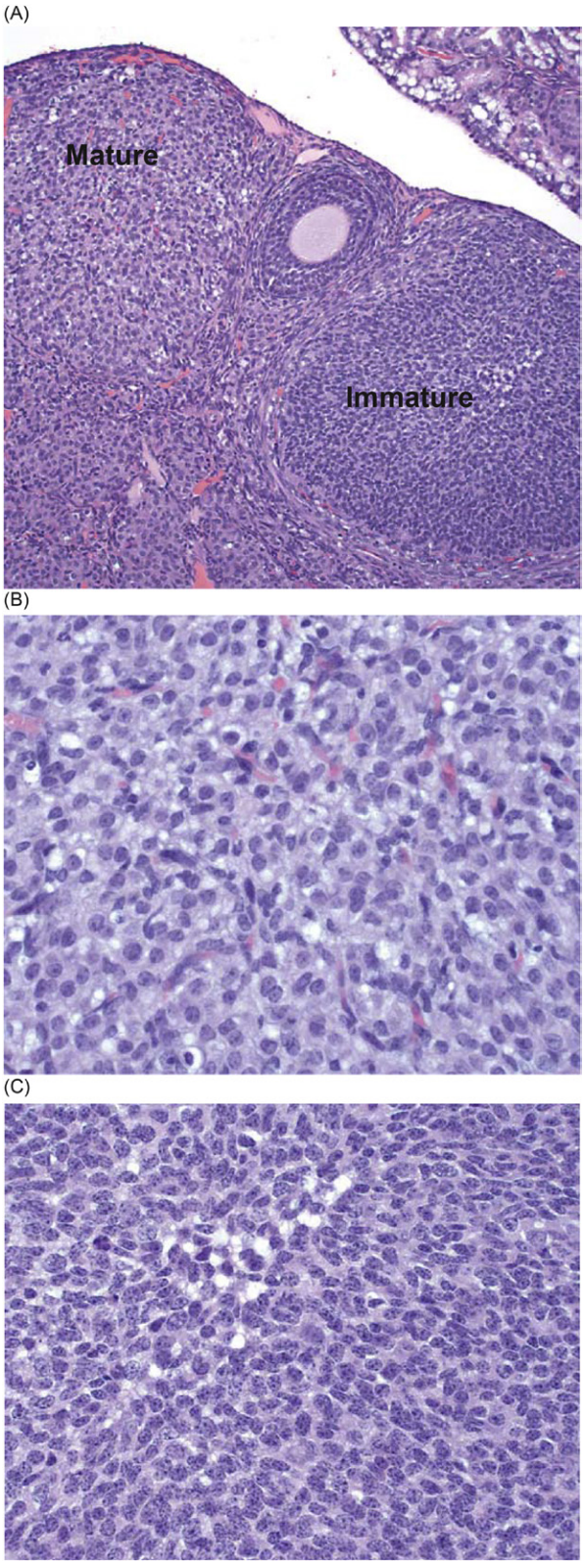

FIGURE 17.7 Rodent (mouse) corpus luteum. (A) Mature rodent corpus luteum with eosinophilic cells arranged in cords around sinusoids. (B and C) High magnification of (B) mature corpus luteum and (C) immature corpus luteum with small and basophilic cells.

appearing, approximately 12 cm long, muscled-lined tube that is not as tightly coiled as that of rodent (Fig. 17.2). Similar to rodents, the human oviduct courses through the corresponding broad ligament from the uterine cornu (horn) to the respective ovary. Both rodent and human oviducts are composed of an intramuscular portion, an isthmus, an ampulla, an infundibulum, and a fimbriated end. The intramuscular portion of the oviduct is located within the uterine wall. In rodents, this segment extends into the dorsolateral uterine wall and forms a slight projection into the uterine cavity referred to as the colliculus tubarius. This projection varies in length but is always less than 1 mm. The intramuscular portion of the human oviduct varies in length depending on uterine size, and it extends from the upper recess of the cornu laterally until it emerges from the uterine wall. The isthmus is the narrow portion of the oviduct that exits the uterine wall and extends laterally to the ampulla. The isthmus in rodents is much more tightly coiled than that of humans. The ampulla is the widened portion of the tube that connects the isthmus to the infundibulum of the oviduct. From the infundibulum, the oviduct forms the fimbriated fringe end that opens into the periovarian space in rodents and into the peritoneal cavity adjacent to the ovary in humans. In humans, one of these fimbriae attaches the oviduct to the ovary (Table 17.1).

HISTOLOGY

The microscopic anatomy of the oviduct is quite similar between rodents and humans (Fig. 17.8). The oviduct mucosa is folded throughout, most elaborately in the ampulla, with diminished folding toward the intramural section (Fig. 17.9). The mucosa of the ampulla and infundibulum is composed of a tall, columnar epithelium with centrally located nuclei, abundant eosinophilic cytoplasm, and prominent long, motile cilia (Figs. 17.9 and 17.10). In the isthmus, the epithelium is composed of low pseudostratified columnar cells with variable numbers of cilia. Peg cells

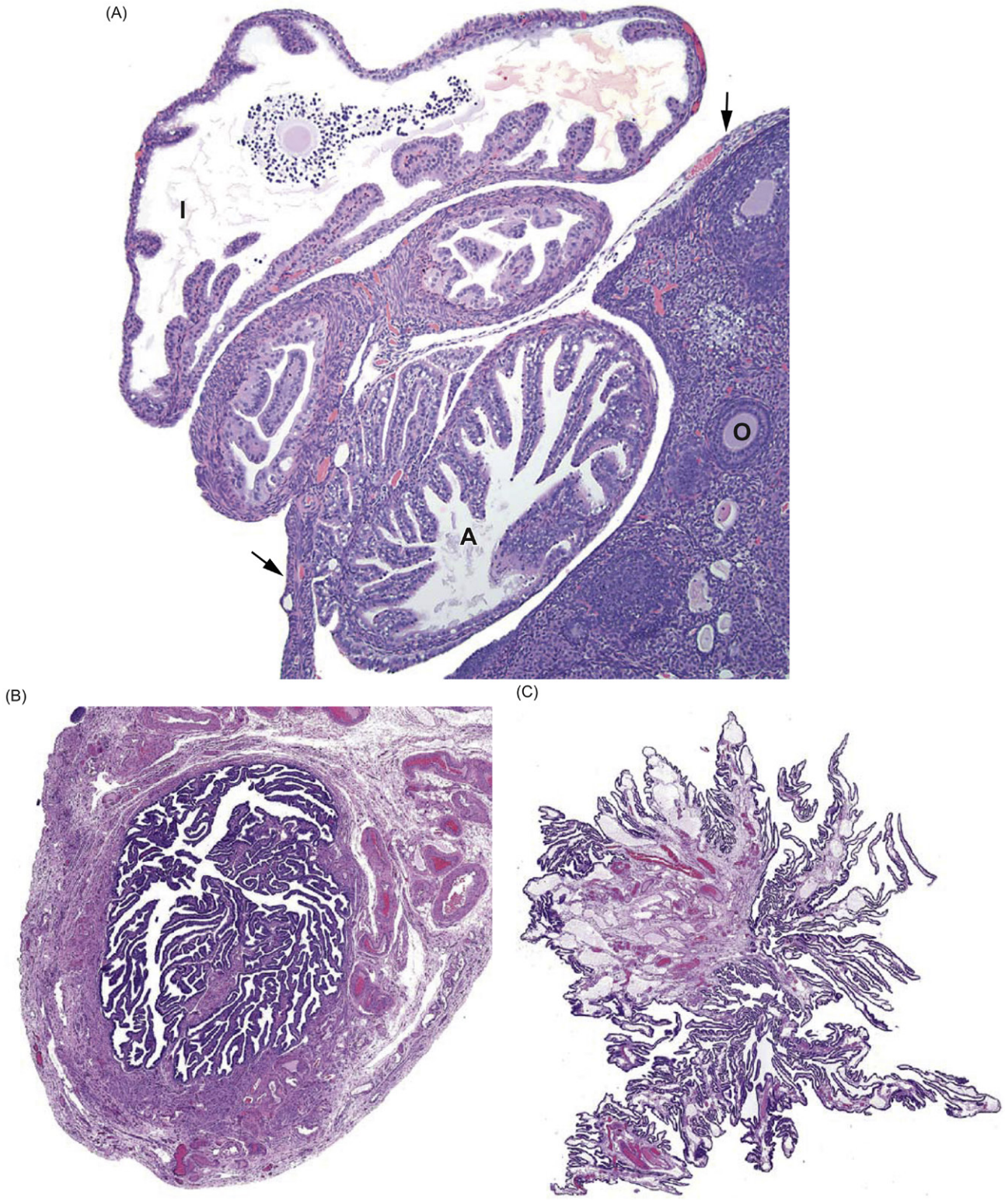

FIGURE 17.8 Oviduct (uterine tube). (A) The rodent (mouse) oviducts have three segments—the infundibulum, ampulla, and intramural segment. The ampulla (A) opens directly into the ovarian bursa (arrows) and is lined by ciliated epithelium. Ciliated cells decrease in the infundibulum and intramural segment. An ovum and associated cells are shown here in the isthmus (I). The ovary (O) is shown. (B and C) Human. The human oviduct opens directly into the peritoneal cavity and is lined by ciliated cells that are greatest in number in the fimbriated end and ampulla and decrease in number toward the intramural segment. (B) Ampulla of human oviduct. (C) Fimbriated end of human oviduct.

Need-to-know

- Corpus lutea from multiple estrus cycles in rodents can be present in the same ovary.
- The ampulla segment of the rodent oviduct opens into the ovarian bursa; in comparison, the human oviduct opens directly into the peritoneal cavity.

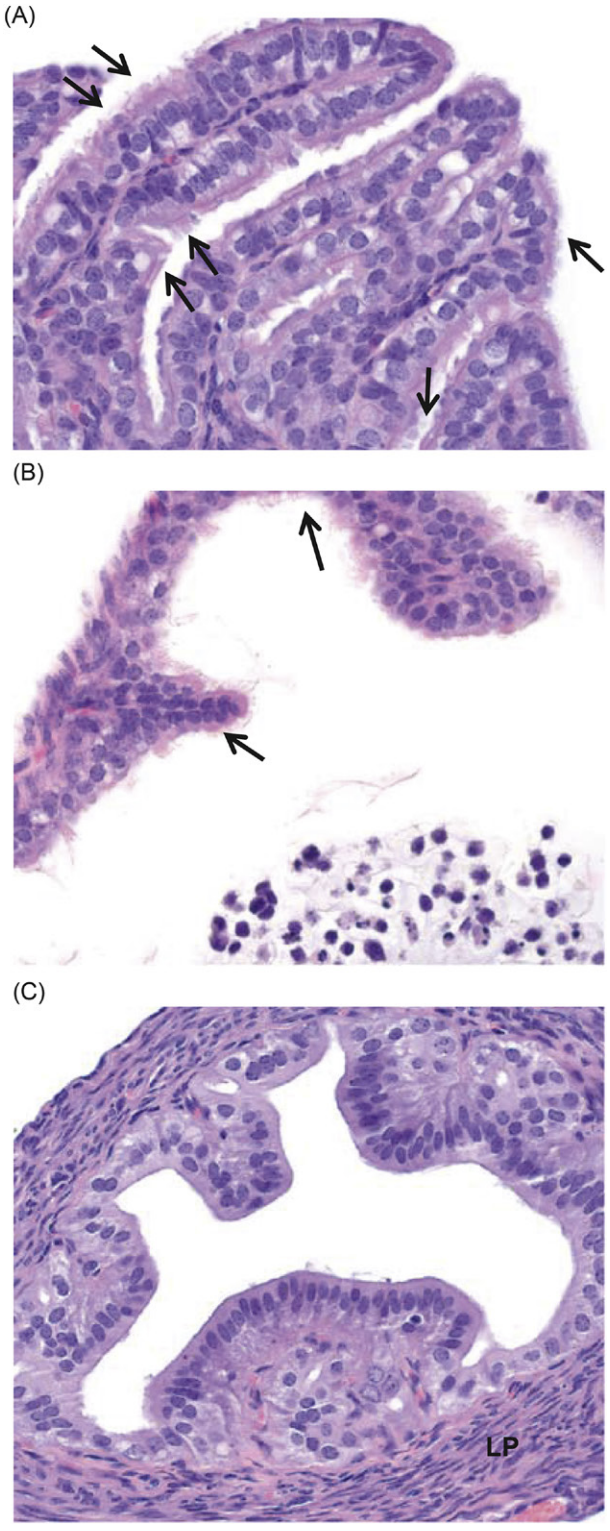

FIGURE 17.9 Rodent (mouse) oviducts (uterine tubes). Ciliated cells decrease in number as the oviduct enters the uterus. (A) In the ampulla segment, the lining columnar epithelium is diffusely ciliated (arrows). (B) In the isthmus, ciliated cells are fewer in number (arrows). (C) The intramural segment is lined by nonciliated low columnar cells. The lamina propria (LP) of the oviduct consists of some elastic fibers and smooth muscle fibers that become thickest in the intramural segment. Rodents and humans are similar in these respects.

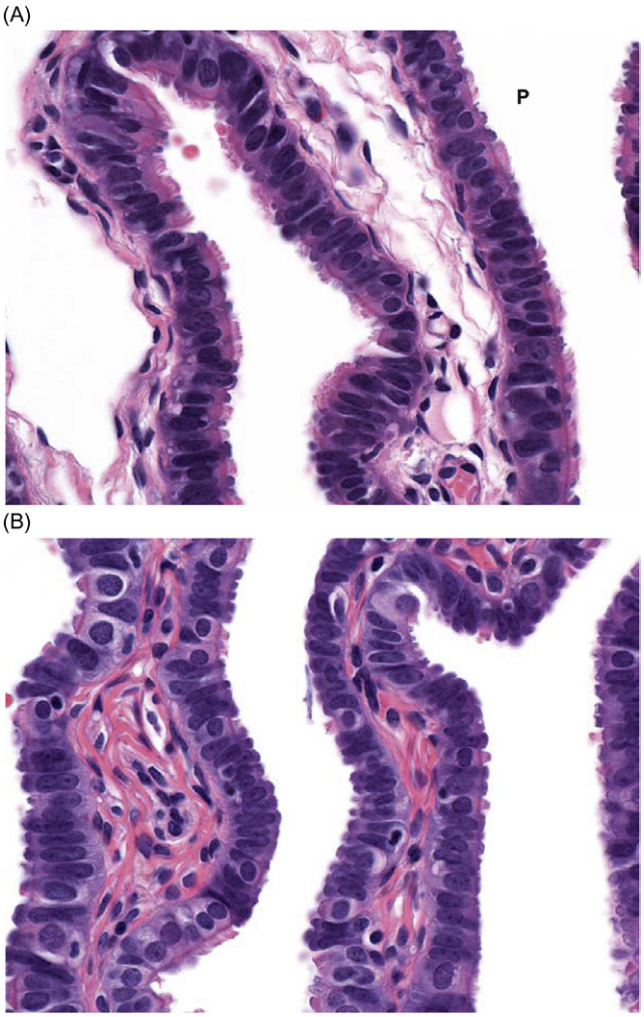

FIGURE 17.10 Human oviduct (uterine tubes). (A) Fimbriated end of human oviduct at high magnification. The fimbria are lined by ciliated cells and are floating in the peritoneal cavity (P) near the surface of the human ovary. (B) Mid-oviduct at high magnification. Note there are fewer ciliated cells than at the fimbriated end.

are nonciliated epithelial cells that are found in increasing numbers from the infundibulum to the isthmus in the oviduct and serve to produce fluid rich in nutrients for the ovum, spermatozoa, and zygotes. Simple columnar cells line the intramural segment. The lamina propria is consistent throughout the oviduct and is composed of a thin connective tissue layer admixed with elastic and smooth muscle fibers. The muscularis layer is composed of smooth muscle fibers arranged circularly. This layer is thinnest at the infundibular end of the oviduct, becoming thickest at the point it joins the muscularis of the uterine wall.

Uterus and Cervix

GROSS ANATOMY

Mice have a bicornuate uterus consisting of two cornua that join distally into a single corpus (body) (Figs. 17.1 and 17.2). Rats have a duplex uterus that consists of two separate uterine horns that are partially fused caudally. Humans have a pear-shaped uterus (Fig. 17.2) with "typical" measurements of 8 cm long by approximately 5 cm from cornu to cornu, with a single triangular-shaped cavity; however, uterine size varies tremendously depending on hormonal status, pregnancy, prior pregnancies, and the presence of leiomyomata. The rodent uterus is suspended from the dorsal body wall by the mesometria, which are heavy broad ligaments carrying blood and lymphatic vessels, as well as abundant nerves. The human uterus is suspended by similar ligaments from the lateral pelvic sidewalls. The mouse and human uterine body comprises the cranial/fundal and caudal/cervical segments. The rat uterus is partially fused but does not have a true uterine body. In mice, the cranial segment of the uterine body is divided into two cavities by a median septum. The caudal segment, or cervix, consists of a single canal that protrudes into the vaginal opening. Rats have a single cervix with two distinct canals for each uterine horn. In rodents, the walls of the cervix and the vagina are continuous both dorsally and ventrally but not laterally. The lateral vaginal walls extend superiorly and form deep fornices on either side. In humans, the cervix protrudes into the vagina (ectocervical portion) with prominent anterior and posterior fornices, as well as somewhat more shallow lateral fornices.

HISTOLOGY

The most striking histologic differences between the gynecologic tracks of rodents and humans are found in the uterine body and supravaginal (upper) portion of the cervix (Figs. 17.11–17.16). The uterine horns in rodents and the uterine fundus in humans both consist of the endometrium, an inner epithelial-lined mucosa, which covers the myometrium (muscular layer) of the uterus (Fig. 17.16). In the nonpregnant rodent uterus, the endometrium is arranged in elevated transverse folds supplied by blood vessels, lymphatics, and nerves. The mucosal epithelium consists of simple columnar cells that extend into branched tubular glands within the endometrial stroma (Figs. 17.11 and 17.12). The rodent endometrial stroma consists of loosely arranged reticular connective tissue with many small polyhedral cells. The myometrium is composed of an inner circular layer and outer longitudinal layer of smooth muscle fibers separated by loose, highly vascular connective tissue, the stratum vasculosum. The outer serosa is continuous with the mesometrium. Although not as striking as the changes seen in the rodent vaginal epithelium, the morphology of the rodent endometrium does change depending on the stage of the estrus cycle (Figs. 17.13 and 17.16). In proestrus, the uterus is distended and hyperemic, mitotic cells are observed in the epithelial cells, and leukocytes infiltrate the stroma. During estrus, mitosis is peaking and leukocytes are rare. In metestrus, the uterine wall is not distended, endometrial cells are undergoing degeneration with no mitoses, and leukocytes are prominent. In diestrus, the uterine wall is collapsed, and leukocyte infiltration and regenerative changes are observed in the endometrium (Table 17.1). Unlike humans, the uterine mucosa is absorbed rather than shed during diestrus.

The human endometrium is composed of glands and specialized stroma. It has an irregular interface with the smooth muscle myometrium, and the endometrial appearance and thickness vary tremendously with menstrual cycle/hormonal status. The endometrial cycle is divided into the proliferative, secretory, and menstrual phases (Figs. 17.12–17.13). The proliferative phase endometrium is found during the first half of the cycle when estrogen levels are high, and it

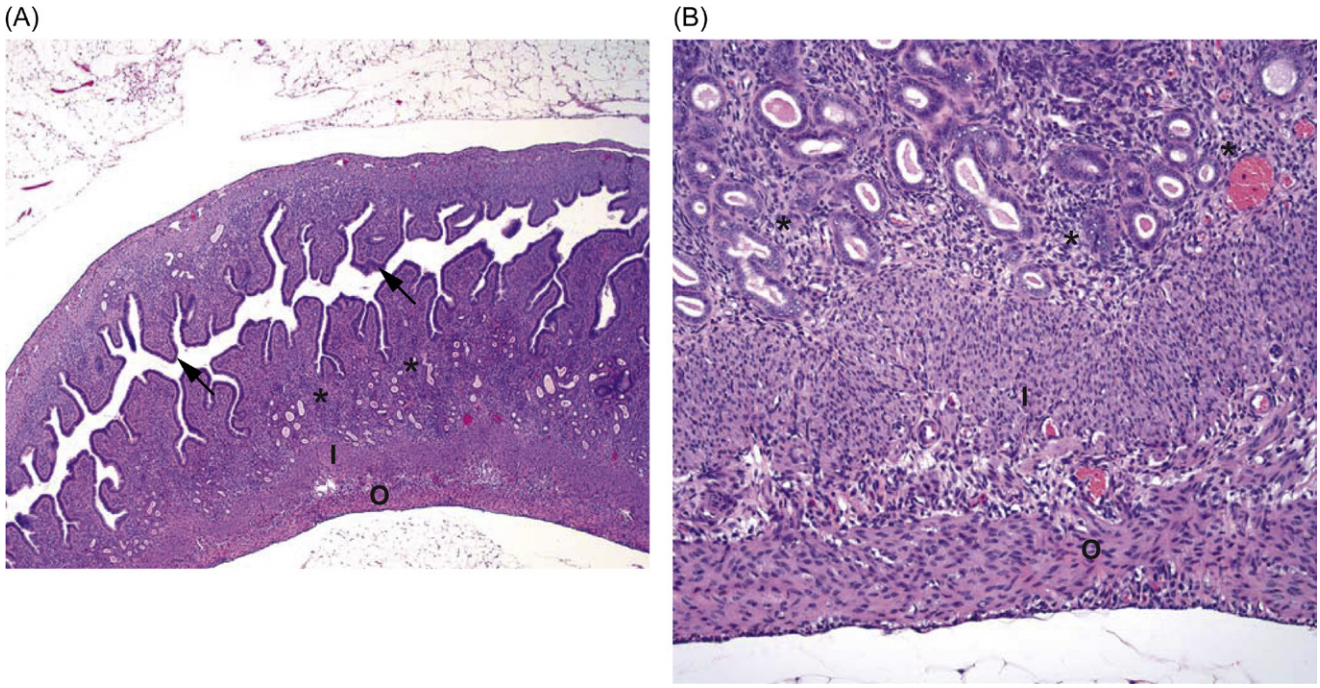

FIGURE 17.11 Rodent (mouse) uterus. Rodents have a bicornuate uterus. (A) The uterine inner lining, the endometrium (arrows), is composed of a simple columnar epithelium that extends to branched tubular glands in the endometrial stroma (asterisks). (B) The myometrium is composed of inner (I) and outer (O) smooth muscle layers. Note that although not shown here, myometrial glands are normal in some mouse strains.

Need-to-know

- Myometrial glands are normal in some mouse strains but are only seen in humans with adenomyosis.
- The human endometrium undergoes three non-gestational phases depending on the hormonal status/phase of the menstrual cycle.

is relatively thin at the beginning of the cycle (immediately following menstruation). It is composed of tubular, narrow, and variably tortuous glands within a cellular stroma. The glands are relatively evenly spaced in the stroma, and the cells lining the glands are crowded/pseudostratified, have scant cytoplasm, and contain numerous mitosis. After ovulation, and with the increase in levels of progesterone, the endometrium becomes secretory. Early secretory endometrial stroma is still relatively cellular; the glands have similar configurations as proliferative glands, but with subnuclear vacuoles. As the cycle progresses, the glands become dilated, serrated, and crowded. After the development of subnuclear vacuoles, the cells develop supranuclear vacuoles and then increasing cytoplasm. Although the glands become more crowded as the secretory phase progresses, the cells lining the glands are less crowded and mitoses are absent. Stromal cells also develop more cytoplasm as the secretory phase progresses and toward the end of the cycle become "decidualized." Decidualized stromal cells develop abundant eosinophilic cytoplasm and have an epithelioid appearance. In addition, in late secretory phase, the spiral arteries become pronounced. Gestational endometrium is similar to late secretory phase endometrium, with pronounced decidualized stroma and abundant secretory cells (Fig. 17.12). Menstrual endometrium is a mixture of late secretory phase endometrium and "sloughing endometrium." Sloughing endometrium is composed of compact stromal balls surrounded by epithelium and, at times, prominent neutrophil infiltration.

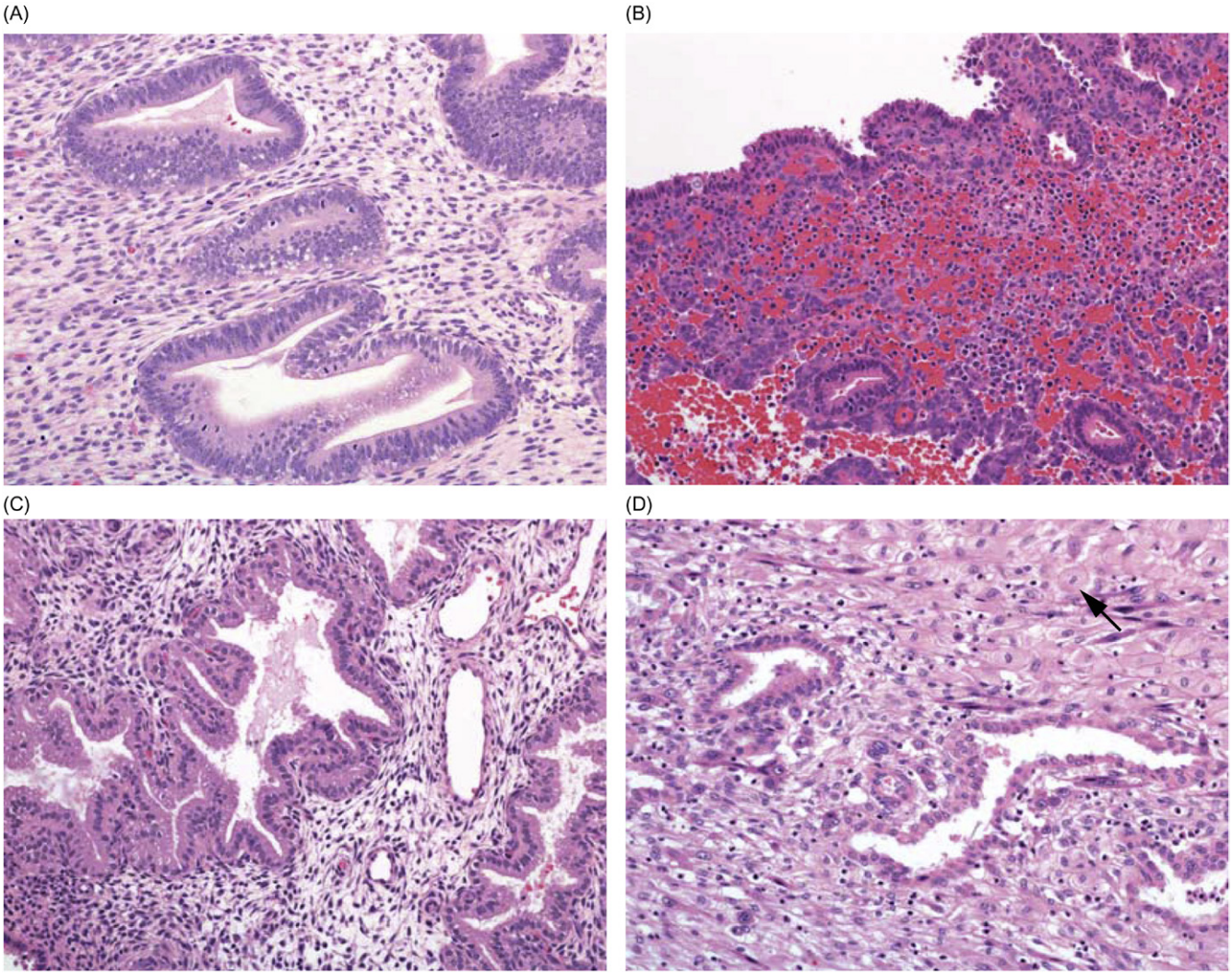

FIGURE 17.12 Human endometrium. The human endometrium has four major phases—proliferative, shedding, secretory, and gestational. (A) Endometrial glands in the proliferative phase are round and tubular with pseudostratified epithelium with many mitoses. (B) During shedding, the stroma and epithelium break down and neutrophils infiltrate the epithelium. (C) Endometrial glands in the secretory phase are convoluted with epithelium that is cuboidal with secretory vacuoles. (D) Gestational endometrium has glands similar to the secretory phase, with decidualized stroma in which the stromal cells are plump and eosinophilic (arrow).

The transition between the uterine corpus and the cervix differs between rodents and humans (Figs. 17.14 and 17.15). In mice, the uterine horns join at the midline, with the medial walls fusing to form the median septum that extends into the lumen of the corpus (Fig. 17.14A). In rats, the uterine horns fuse to form a corpus but maintain separate lumens that pass through a single cervix into the vaginal vault (Fig. 17.14B). As the uterine horns join the corpus in both mice and rats, the columnar epithelium of the endometrium gradually changes to stratified squamous epithelium. The entire corpus and cervical canal in both mice and rats are then lined by stratified squamous endocervical epithelium, which is continuous with the vaginal mucosa. The lamina propria of the corpus is more fibrous compared to the uterine horns. There are circular and longitudinal smooth muscle bundles, as well as serosa, that complete the wall of the corpus and

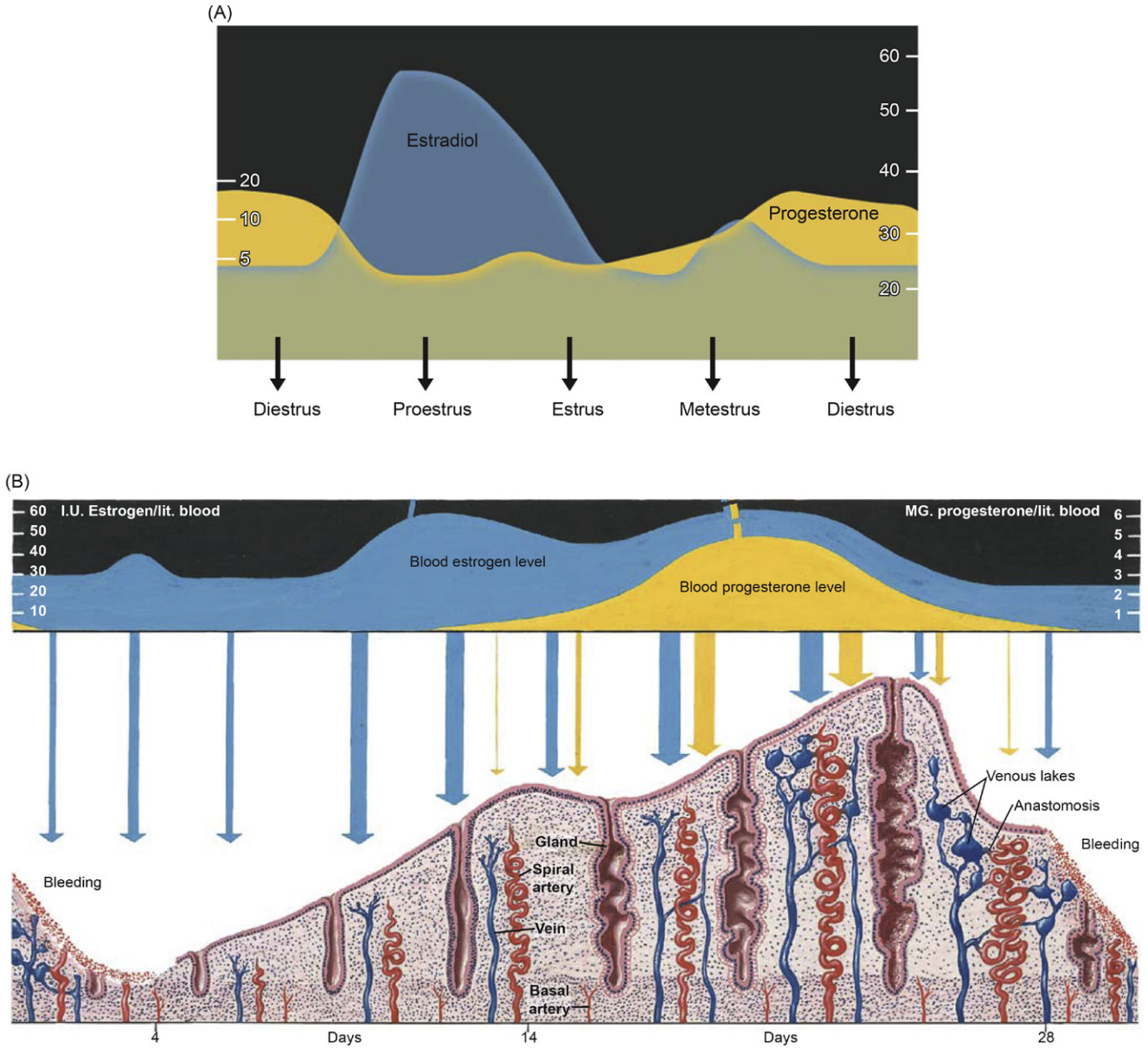

FIGURE 17.13 Hormonal cycle diagrams (A) Rodent estrus cycle. Morphologic changes in the vaginal mucosa are associated with hormonal changes during the rodent estrus cycle. Endometrial morphology also varies with cycle, although not as dramatically as in humans. Source: © Elsevier, Inc., www.netterimages.com. (B) Human menstrual cycle. Diagram illustrating the integration of the hormonal cycle and the corresponding effects on the human endometrium. Estrogen exerts a proliferative effect on the endometrium, whereas progesterone leads to the differentiation of the endometrium. Withdrawal of progesterone and estrogen leads to menstrual sloughing. Source: © Elsevier, Inc., www.netterimages.com.

proximal part of the cervix. However, in the distal portion of the cervix, the wall is composed entirely of collagenous fiber bundles that become loose and separate during gestation and parturition.

In humans, the endometrial epithelium transitions to a mucous-secreting columnar endocervical epithelium. In addition, the cellular endometrial stroma gradually becomes more fibrous, similar to that seen in rodents. The columnar, mucous-secreting epithelium of the endocervical mucosa then transitions to the relatively smooth squamous epithelium, which lines the ectocervical portion (Fig. 17.15). This transformation zone may

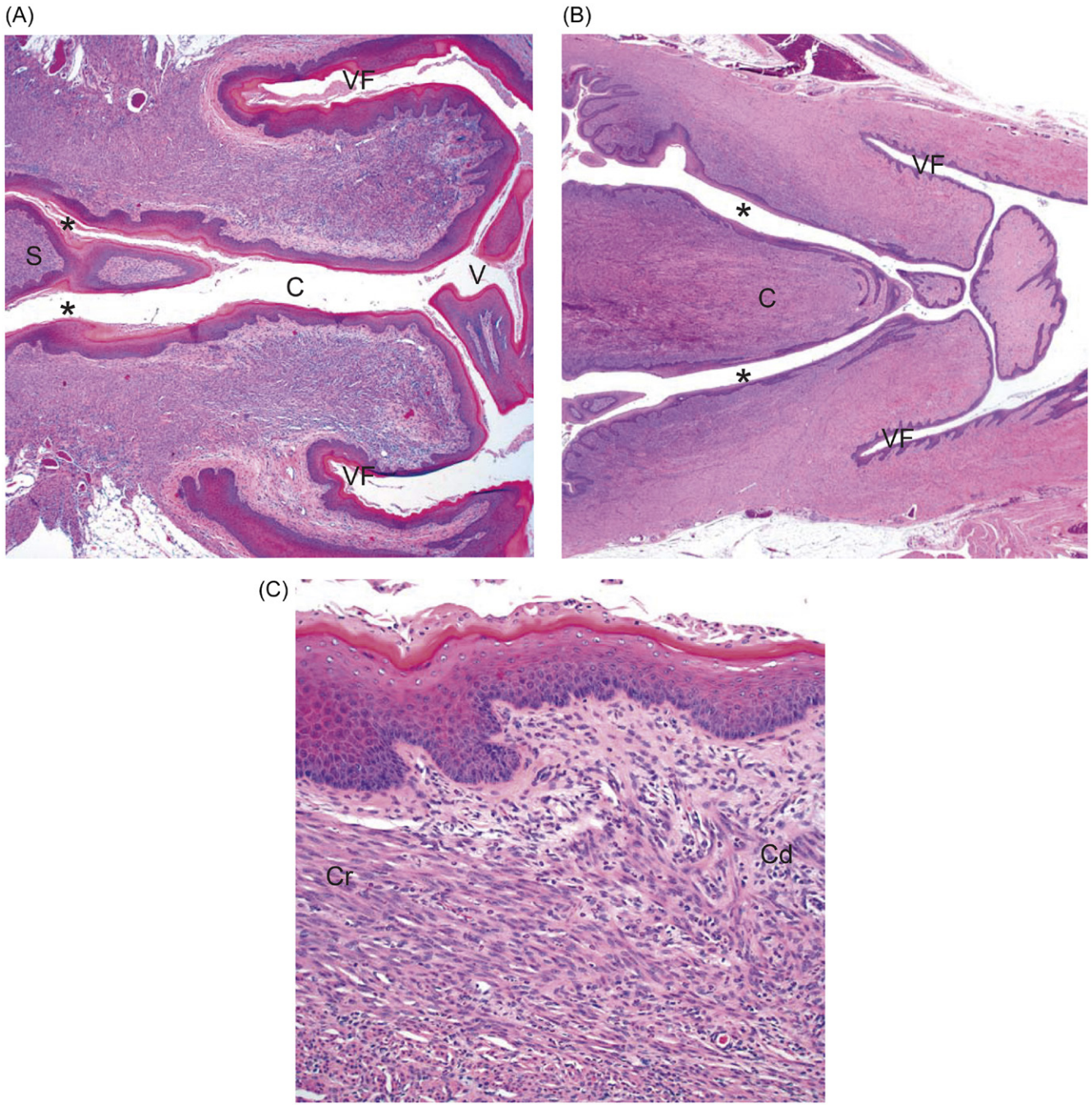

FIGURE 17.14 Rodent uterine body and cervix. (A) The mouse uterine body is lined by stratified squamous epithelium and divided cranially into two canals (asterisks) by a median septum (S). The vaginal fornix (VF) is shown. The caudal undivided portion, the cervix (C), also lined by stratified squamous epithelium, has a single opening into the vaginal lumen (V). (B) The rat uterine horns remain separate but fused to form the uterine body. There are two independent canals (*) that pass through the single cervix into the vaginal lumen. The vaginal fornix (VF) is shown. (C) In rodents, cervical canal epithelium is continuous with the vaginal epithelium. The cranial segment (Cr) of the cervical wall is composed of circularly arranged smooth muscle. The caudal segment (Cd) of the wall is composed primarily of collagen bundles and less smooth muscle that becomes widely spaced and loose during pregnancy.

Need-to-know

- Mice have a single cervix lined by stratified squamous epithelium continuous with the vaginal epithelium.
- Rats have a single cervix with two separate canals from the uterine horns lined by stratified squamous epithelium.

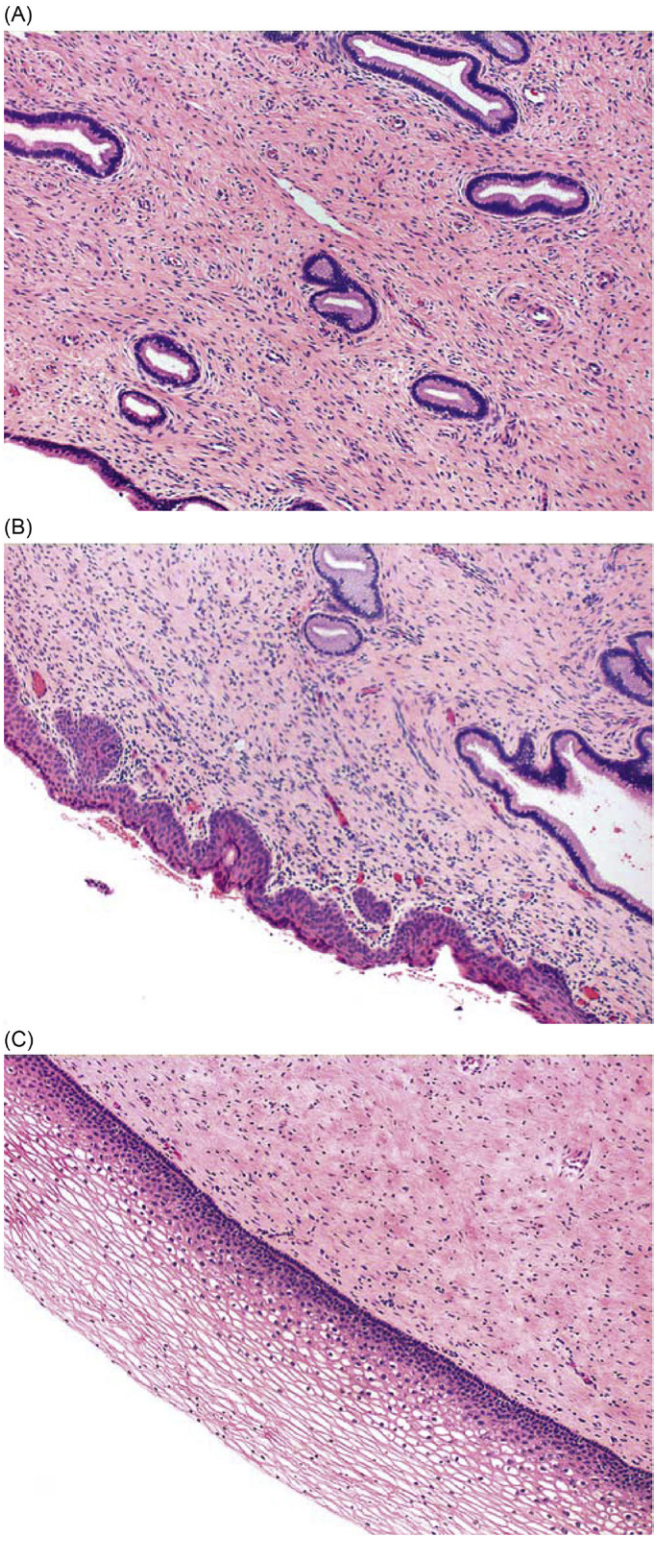

FIGURE 17.15 Human cervix. The human cervix is composed of the ecto- and endocervix. (A) The endocervix is composed of simple columnar mucinous epithelium. (B) The transformation zone changes in position during various hormonal stages but is composed of metaplastic squamous cells and endocervical cells. (C) The ectocervix is composed of stratified squamous epithelium similar to that in the vagina.

be either within the endocervical canal or exposed to the vaginal vault, depending on and hormonal status. The stratified squamous epithelium of the ectocervix is continuous with vaginal squamous epithelium.

Vagina and Clitoris

Gross Anatomy

In rodents, the vagina is short and muscular, and it extends from the cervix to an external opening dorsal to the urethra. The vagina is loosely connected to the rectum dorsally and the urethra ventrally (Fig. 17.1). At the exterior opening of the vagina, the clitoris forms an elevation on the ventral aspect. The paired clitoral glands are sebaceous glands; they are covered by hair and skin, and there is a shallow depression at the tip of the clitoris referred to as the clitoral fossa. The urethra opens into the clitoral fossa. The paired clitoral glands are located anterolaterally in the subcutaneous tissue, each with a single duct that opens into the lateral walls of the clitoral fossa.
In humans, the vagina is 6–7.5 cm in length; it is also muscular and extends from the cervix (Fig. 17.2) to the vulva. In contrast to rodent, there are a series of grossly apparent ridges, referred to as rugae, produced by folding of the wall of the outer third of the vagina. These rugae allow significant extension and stretching during sexual intercourse and parturition. The vagina opens into the vulval vestibule. Anteriorly, the vulva is composed of the mons pubis, which separates into two folds of hair-bearing skin known as the labia majora. Medial to the labia majora are the labia minora, two folds of tissue covered by squamous mucosa that form the anterolateral borders to the vulval vestibule, which contains the clitoris, the urethral opening, and the vaginal introitus (entrance). The clitoris is located in the anterior portion of the vulval vestibule, where the labia minora meet. The urethral opening is immediately posterior to the clitoris and anterior to the vaginal introitus. Posterior to

the vagina is the perineum, the area between the vagina and the anus.

HISTOLOGY

In rodents, the internal end of the vagina (referred to as the vaginal vault) is lined by a keratinized stratified squamous epithelium that undergoes measurable morphologic changes during the rodent estrus cycle (Figs. 17.17 and 17.18). The vaginal mucosa is folded with no glands. The lamina propria is composed of connective tissue with circular and longitudinal muscularis layers, whereas the outermost layer is formed by adventitia that is continuous with the rectal and urethral adventitia (Fig. 17.17). In humans, the vagina is lined by a nonkeratinized squamous epithelium and does not undergo the significant morphologic changes seen in rodents during the estrus cycle (Fig. 17.17). Small changes in the amount of glycogen accumulation and nuclear maturation do occur, but are minor compared with the changes seen in rodents. In rodents, the outer aspects of the labia majora are lined by hair-bearing skin, whereas the inner portions of the labia majora, the labia minora, and the vulval vestibule are lined by nonkeratinized squamous mucosa. The rodent clitoris is covered by skin and hair, whereas that of humans is covered by squamous mucosa. In rodents, the clitoral glands empty into the clitoral fossa via excretory ducts lined by stratified squamous epithelium (Fig. 17.18). Also opening into the clitoral fossa is the urethra, which is lined by transitional epithelium. In humans, there are periurethral (Skene's) glands and major (Bartholin's) and minor vestibular glands, which open into the vulval vestibule. Skene's glands are lined with pseudostratified, mucus-secreting columnar cells that empty via bilateral periurethral ducts that are lined by transitional-type epithelium. Bartholin's glands are lined by mucus-secreting columnar cells and empty via bilateral ducts adjacent to the vaginal introitus that are also lined by transitional epithelium.

The urethra is lined by transitional epithelium that merges with the nonkeratinized squamous epithelium at the urethral orifice. Erectile tissue surrounds the urethra near the tip of the clitoris in mice; similar erectile tissue surrounds the clitoris in humans. The clitoral erectile tissue is composed of a fine vascular network similar to that present in the male penis (Figs. 17.18 and 17.19). Rodents have a small bone in the clitoral connective tissue, homologous to the os penis; humans do not (Fig. 17.19). The lamina propria of the clitoris and urethra consists of connective tissue that blends into the adjacent connective tissue and dermis.

PLACENTA

The placenta is a fetomaternal organ, with a fetal portion, known as the villous chorion, and a maternal portion, known as the decidua basalis. The placenta is the most morphologically diverse organ across mammalian species (Figs. 17.20–17.27). Theories to explain its diversification over evolutionary history include maternal–fetal conflict over nutrient allocation, the number of offspring produced, and lifespan.

GROSS ANATOMY

In rodents, the placenta is discoid and approximately 2 cm × 0.6 cm. The uteroplacental circulation is similar to that of humans, although in rodents the maternal–fetal interdigitation is labyrinthine rather than villous (Fig 17.21 and Table 17.3).

In humans, the placenta is also discoid and approximately 20 cm in diameter. The uteroplacental circulation is composed of a fetal surface and a maternal surface that is attached to the uterus (Fig. 17.22). Maternal blood enters the intervillous space through the spiral arteries, which have been modified by invasive fetal trophoblast cells and transformed into low-resistance vessels. Maternal blood exits the intervillous space through uterine

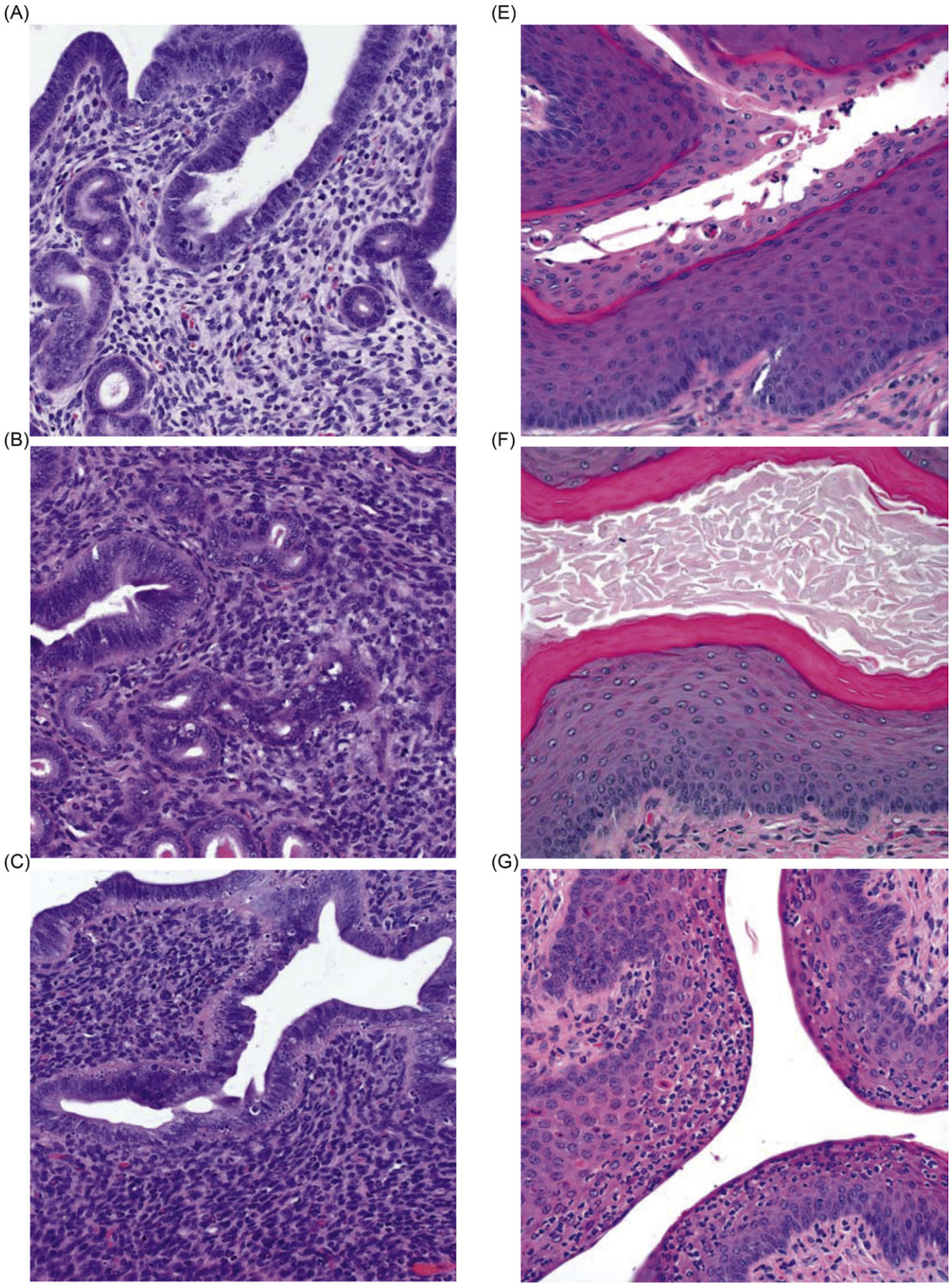

Figure 17.16 (Continued)

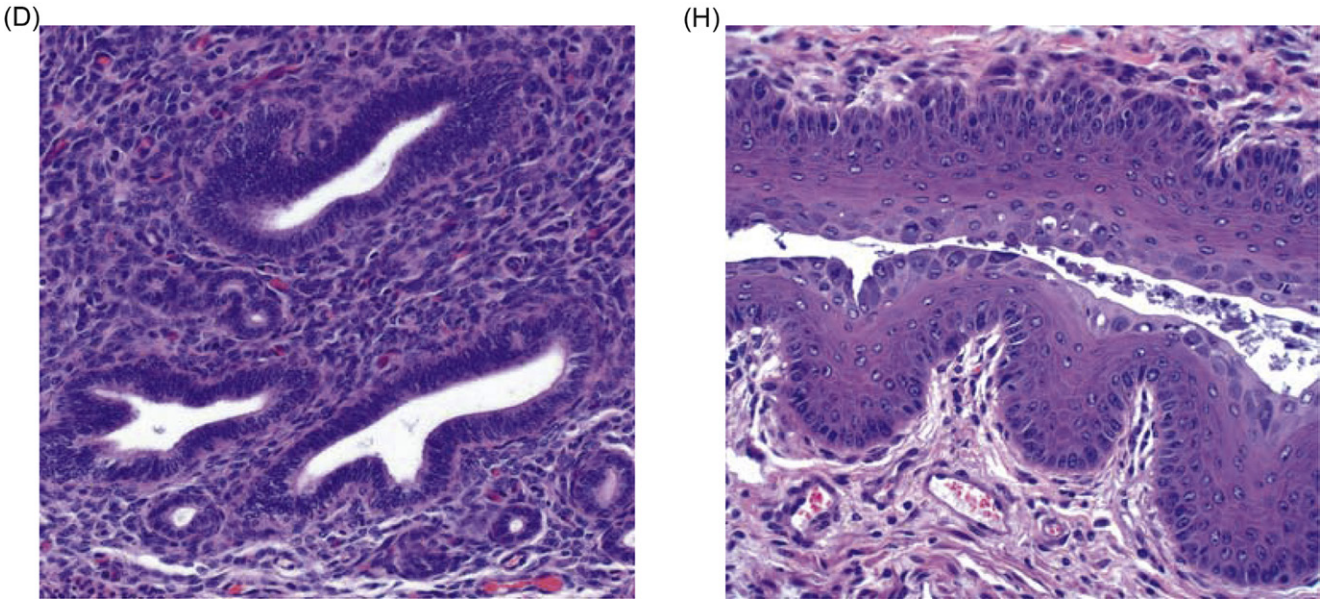

FIGURE 17.16 Rodent (mouse) endometrial and vaginal epithelial changes during the estrus cycle. Endometrial morphology (A–D) and vaginal mucosa morphology (E–H) change during the estrus cycle. Histologically, four stages of the estrus cycle are easily determined: proestrus, estrus, metestrus, and diestrus. Endometrium: (A) In proestrus, the uterus is distended and hyperemic, mitotic cells are observed in the epithelial cells, and leukocytes infiltrate the stroma. (B) During estrus, mitosis is peaking and leukocytes are rare. (C) In metestrus, the uterine wall is not distended, endometrial cells are undergoing degeneration with no mitoses, and leukocytes are prominent. (D) In diestrus, the uterine wall is collapsed, and leukocyte infiltration and regenerative changes are observed in the endometrium. (E) During proestrus, the mucosa is 10–13-cell thick and the outer layers stain lightly with eosin, whereas the granulosa layer shows increasing cornification. Mitoses are frequent, but few leukocytes are present. (F) In estrus, the mucosa is approximately 12-cell thick. The superficial nucleated layer is lost, and the cornified layer is superficial. Mitoses are decreasing, and leukocytes are absent. (G) In metestrus, the cornified layer is delaminated, and leukocytes begin to appear under the epithelium. (H) During diestrus, the mucosa is 4–7-cell thick. Surface epithelial cells are mucified, and mucus, leukocytes, and desquamated cells are present in the lumen.

veins. Fetal blood enters the placenta through the umbilical artery, which branches over the fetal surface of the placenta, branches further as it enters the chorionic villi containing capillary trees, and returns by a venous path to the umbilical vein.

The yolk sac is an extraembryonic membrane that surrounds the developing embryo and is derived from embryonic endoderm and mesoderm and it is the primitive circulatory system and erythropoiesis prior to placenta development. In rodents, the yolk sac plays a minor role in embryonic support following placental development (Fig. 17.23). In humans, the chorionic vessels are entirely derived from the allantois; the yolk sac does not contribute to maternal–fetal exchange and is present only as a small remnant at delivery. The yolk sac is lined by a single endodermal layer of tall columnar cells on a thin basal lamina separating endodermal epithelium from the mesoderm that gives rise to the blood islands. In early development, blood islands lined by elongated endothelial-like cells contain embryonic nucleated erythrocytes (Fig. 17.23). The yolk sac maintains communication with the embryo via intralabyrinth sinuses and the margins of the chorioallantoic plate, which is formed by fusion of the allantois and the chorionic plate (Figs. 17.20 and 17.21) in both rodents and humans. This fusion initiates the formation of the placenta. In rodents, the chorioallantoic plate is composed of umbilical

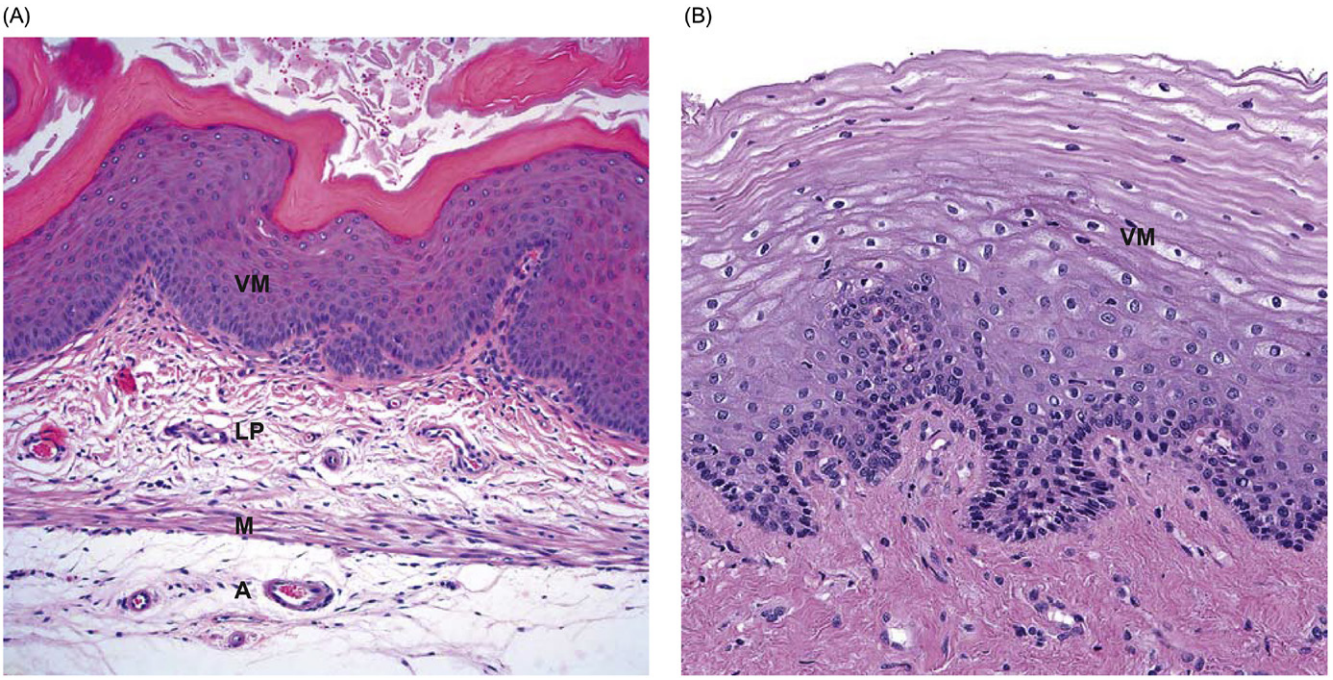

FIGURE 17.17 Vaginal mucosa. (A) Rodent (mouse). The vaginal mucosa (VM) is composed of stratified squamous epithelium and is folded into longitudinal elevations with no glands. The morphology of the vaginal epithelium changes during the different stages of the estrus cycle. The lamina propria (LP) is fibrous, and the muscularis (M) layer is thin admixed with significant fibrous connective tissue. Adventitia (A) makes up the outermost layer. (B) Human. The vaginal mucosa (VM) is composed of stratified squamous epithelium with no glands. Unlike that of rodents, the vagina is not keratinized, and the morphology of the vaginal mucosa does not change significantly during the menstrual cycle.

Need-to-know

- The rodent vaginal mucosa changes morphology at each phase of the estrus cycle, whereas the human vaginal mucosa has a relatively stable morphology.

vessels and loosely arranged spindle cells originating from the extraembryonal ectoderm (Figs. 17.20 and 17.21).

Both humans and rodents have hemochorial placentas, where the fetal trophoblast is directly exposed to maternal blood. The placenta is fully developed in mice by day 12 of the 18.5–21-day gestation period and in rats, by day 14 of the 21–24-day gestation period. In humans, the hemochorial placenta is fully developed by week 5 of the 37–42-week gestation period (Table 17.3).

HISTOLOGY

The embryonic components of the rodent placenta include the chorioallantoic plate, labyrinth layer, Reichert's membrane, and giant cell trophoblasts, spongiotrophoblasts (Fig. 17.21), whereas the embryonic components of the human placenta include the amnion, chorionic plate, intervillous space, and basal plate (Fig. 17.23). In both rodents and humans, the decidua is the only extraembryonic (maternal) component (Figs. 17.21 and 17.23). In rodents, the decidua is divided into the basalis and the capsularis. The heavily vascularized decidua basalis is located on the mesometrial side, where it interacts with spongiotrophoblasts. In contrast, the decidua capsularis is located on the antimesometrial side; it is thinner and less well vascularized. In humans, the decidua basalis is found at the implantation site, which later underlies the placenta. The human decidua also includes the decidua capsularis, which covers the surface of the gestational sac, and the decidua parietalis, found on the opposite uterine wall.

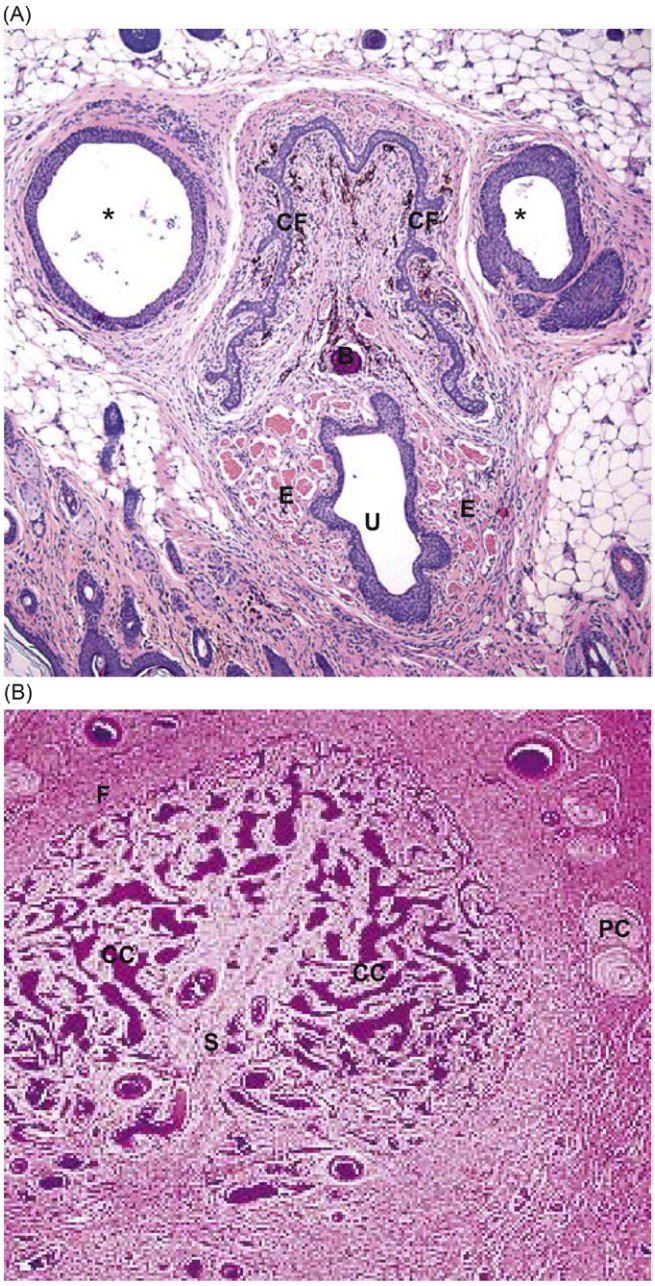

FIGURE 17.18 Clitoris. (A) The rodent (mouse) clitoris is a ventrally extending elevation located on the anterior wall of the vaginal introitus. The tip of the clitoris is covered by stratified squamous vaginal epithelium, and the anterior lateral surfaces are covered by haired skin. The urethra (U) opens near the tip of the clitoris. Erectile tissue (E) similar to penile erectile tissue surrounds the urethra near the tip of the clitoris. A small bone (B) homologous with the os penis is surrounded by connective tissue on the anterior face. The paired clitoral gland ducts (asterisks) open laterally at the clitoral fossa (CF). (B) Human. Note the two corpora cavernosa (CC), arranged side by side and filled with blood, the incomplete central septum (S), and the fibrocollagenous sheath (F), outside which are prominent nerve endings (mainly Pacinian touch corpuscles (PC)). Source: Reprinted from Human Histology, 3e, Stevens, A., Lowe, J.S., 2004, with permission from Mosby, © Elsevier. www.netterimages.com

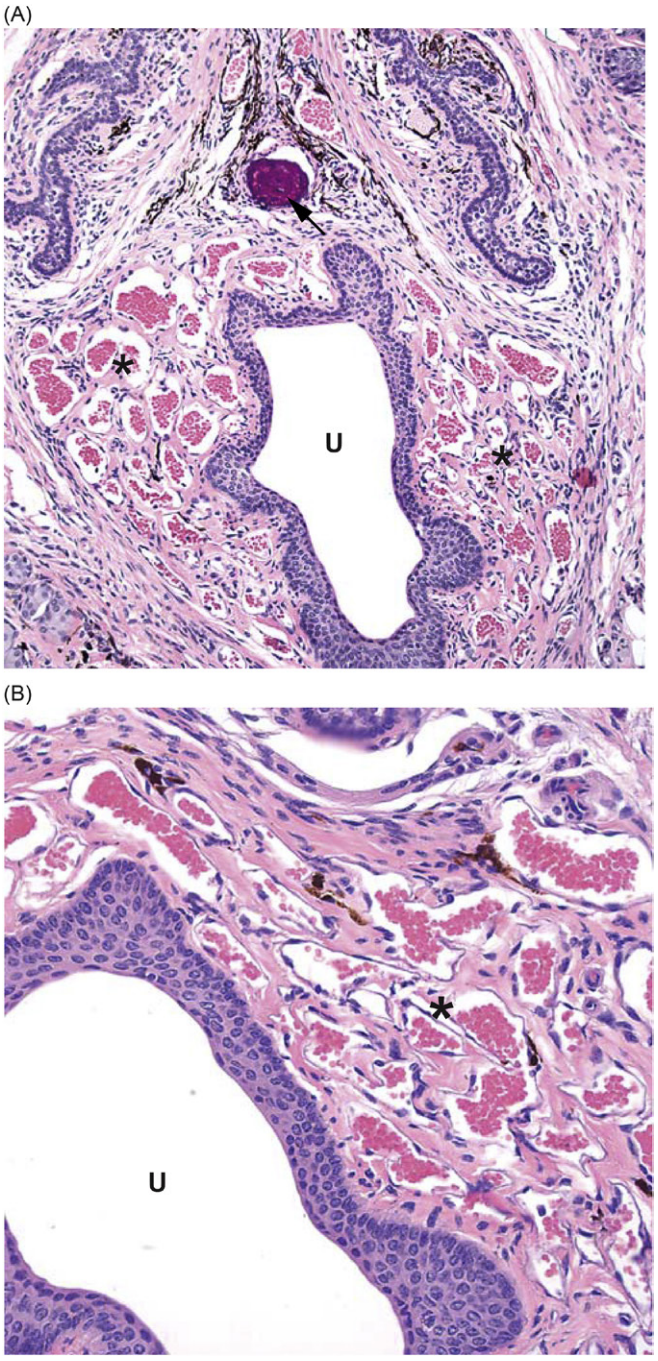

FIGURE 17.19 Rodent (mouse) erectile tissue. Clitoral erectile tissue (asterisks), similar to penile erectile tissue, surrounds the urethra (U) near the tip of the clitoris. (A) A small bone (arrow) homologous with the os penis is surrounded by connective tissue on the anterior face. (B) High magnification view of erectile tissue.

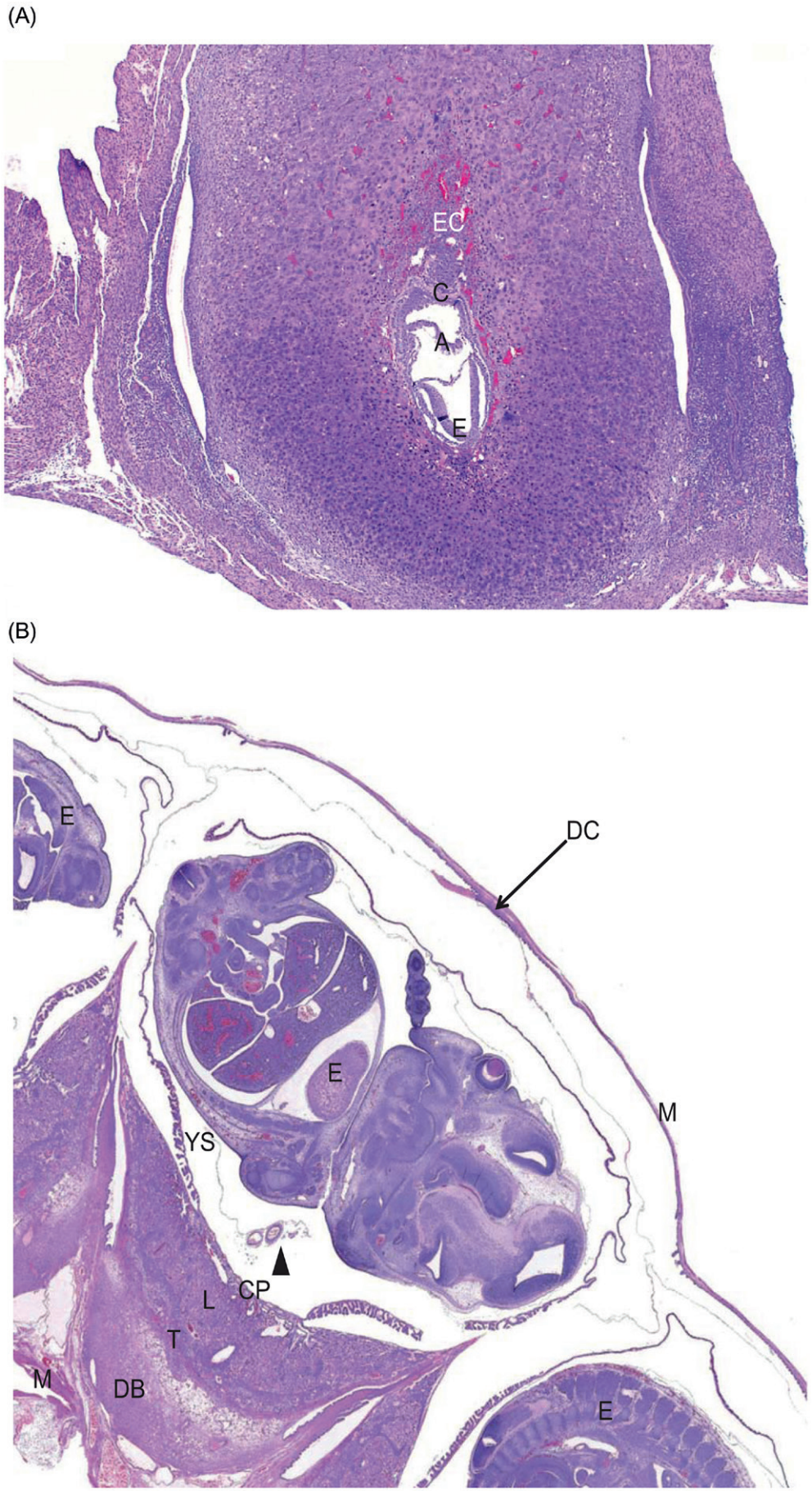

FIGURE 17.20 Developing rodent (mouse) placental layers. (A) At embryonic day (ED) 8.5, the developing placental layers include the ectoplacental cone (EC), the chorion (C), the amnion (A), and the developing embryo (E). (B) Subgross of gravid uterus (ED 12.5). The embryo (E) is contained within the yolk sac (YS). The placental layers partially visible at this low magnification include the chorionic plate (CP); trophoblast (T), which includes spongiotrophoblasts and giant trophoblast cells; the labyrinth (L); decidua basalis (DB), and capsularis (DC). Myometrium (M) and portions of additional embryos (E) are indicated.

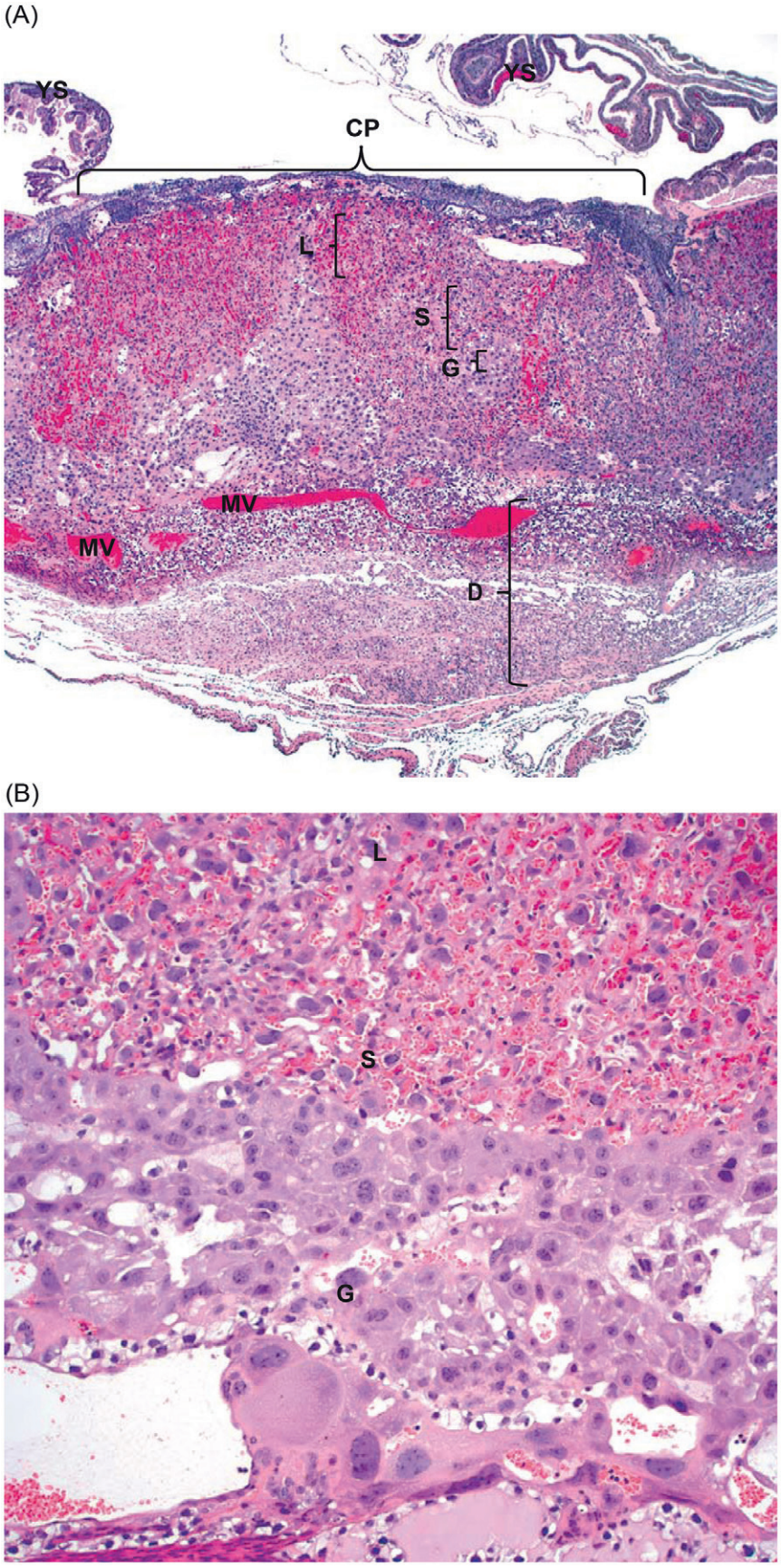

FIGURE 17.21 Rodent (mouse) placenta. (A) Rodents and humans both have hemochorial placentation, where maternal blood comes in direct contact with fetal membranes through a labyrinth layer (L). Embryonic-derived layers include the labyrinth, the spongiotrophoblasts (S), and the giant cell trophoblasts (G). The decidual (D) layer is completely derived from maternal tissue. CP, allantochorionic plate; MV, maternal vessels; YS, yolk sac. (B) Embryonal components of the placenta, the labyrinth layer (L), the spongiotrophoblast layer (S), and the giant cell trophoblast layer (G).

Need-to-know

- Rodents and humans have hemochorial placentation.

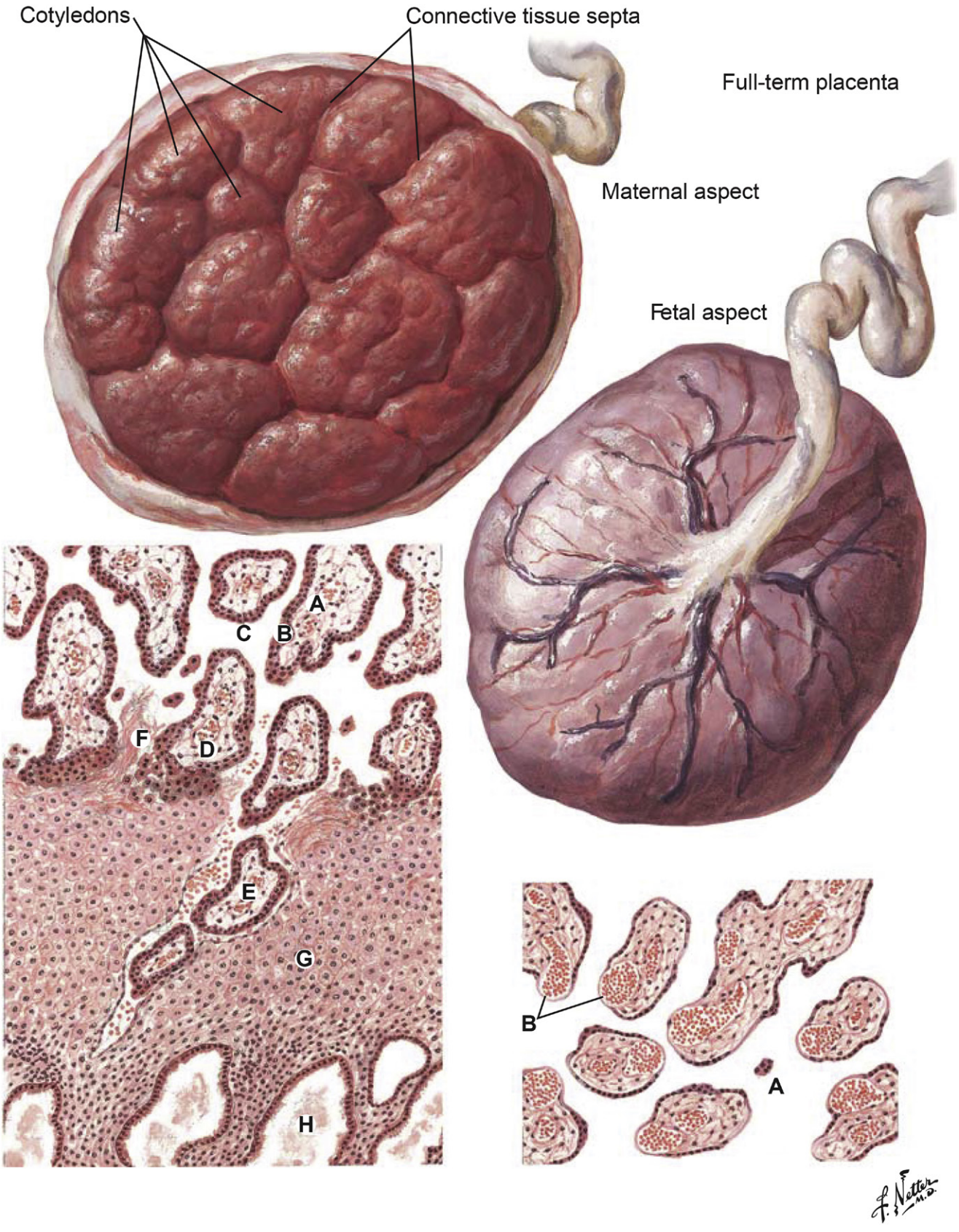

FIGURE 17.22 Human placenta. Diagram showing the maternal and fetal surfaces, as well as the insertion of the umbilical cord. Fetal villi project into the lacuna system, which is filled with maternal blood. (Bottom left) Section through deep portion of placenta, early gestation. *A*, villus; *B*, trophoblast; *C*, intervillous space; *D*, anchoring villus; *E*, villus-invading blood vessel; *F*, fibrinoid degeneration; *G*, decidua basalis; *H*, gland. (Bottom right) Appearance of placental villi at term. *A*, aggregation of trophoblast nuclei into a "syncytial knot"; *B*, fetal blood vessel endothelium against a thinned syncytiotrophoblast, where they share a basal lamina. The cytotrophoblast has disappeared. Source: © Elsevier, Inc., www.netterimages.com.

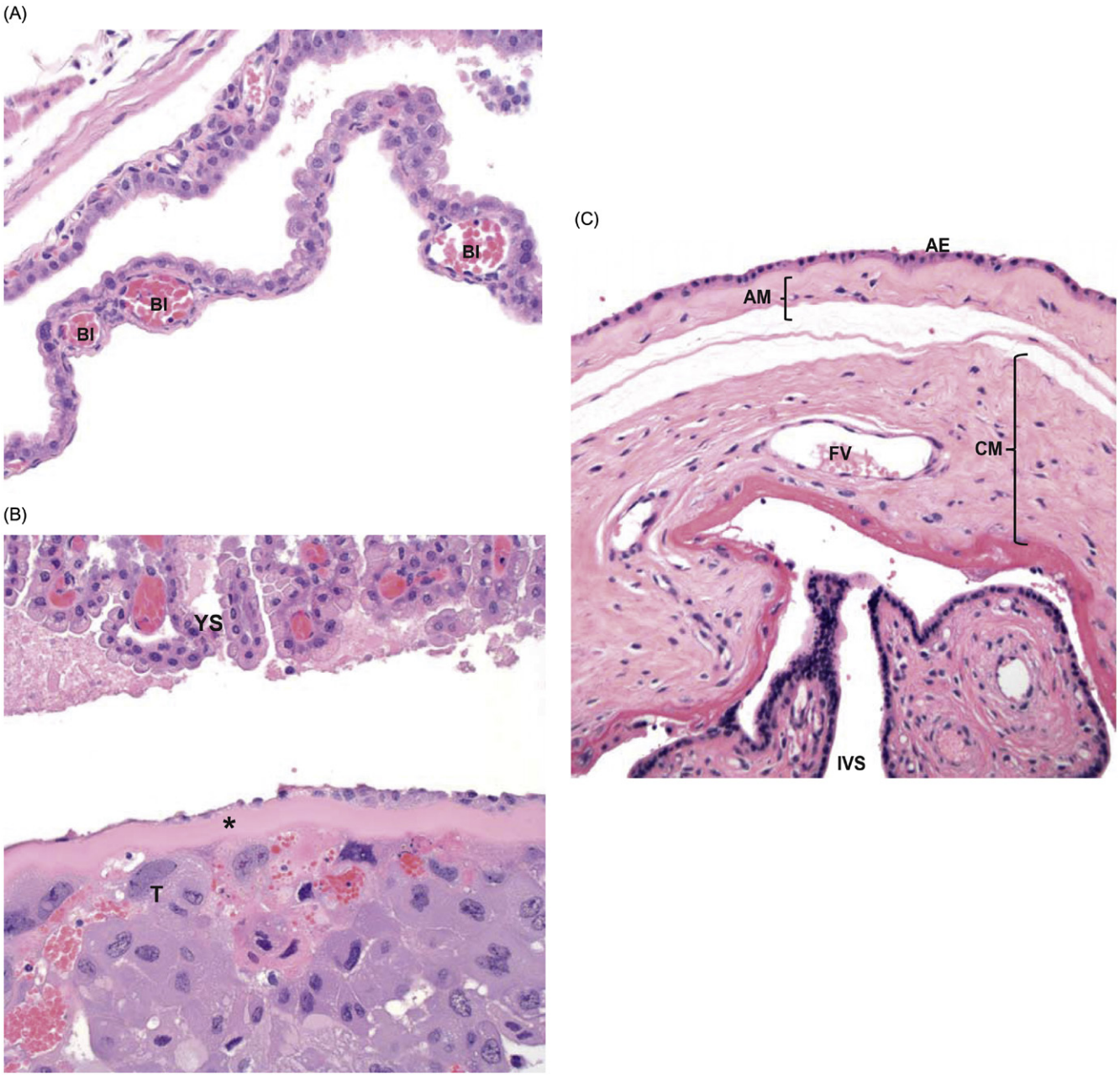

FIGURE 17.23 Placenta. (A) Yolk sac from day 16.5 of gestation in mice. The parietal and visceral layers of the yolk sac are lined by tall columnar cells. A thin basal lamina separates the epithelium from the mesoderm and blood islands (BI), which are lined by endothelial-like cells and contain immature and mature erythrocytes. (B) Mouse. Reichert's membrane (asterisk) is unique to the rodent placenta and forms an acellular basement membrane that separates the trophoblasts (T) and the yolk sac (YS). (C) Human. The chorionic plate is lined by amniotic epithelium (AE), amniotic mesoderm (AM), and chorionic mesoderm (CM). *FV*, fetal vessel; *IVS*, intervillous space.

Need-to-know

- The yolk sac plays a minor role in embryonic support after embryonic day 12.5 (mouse) and 13.5 (rat), when the placenta is fully developed.
- Reichert's membrane is unique to rodents.

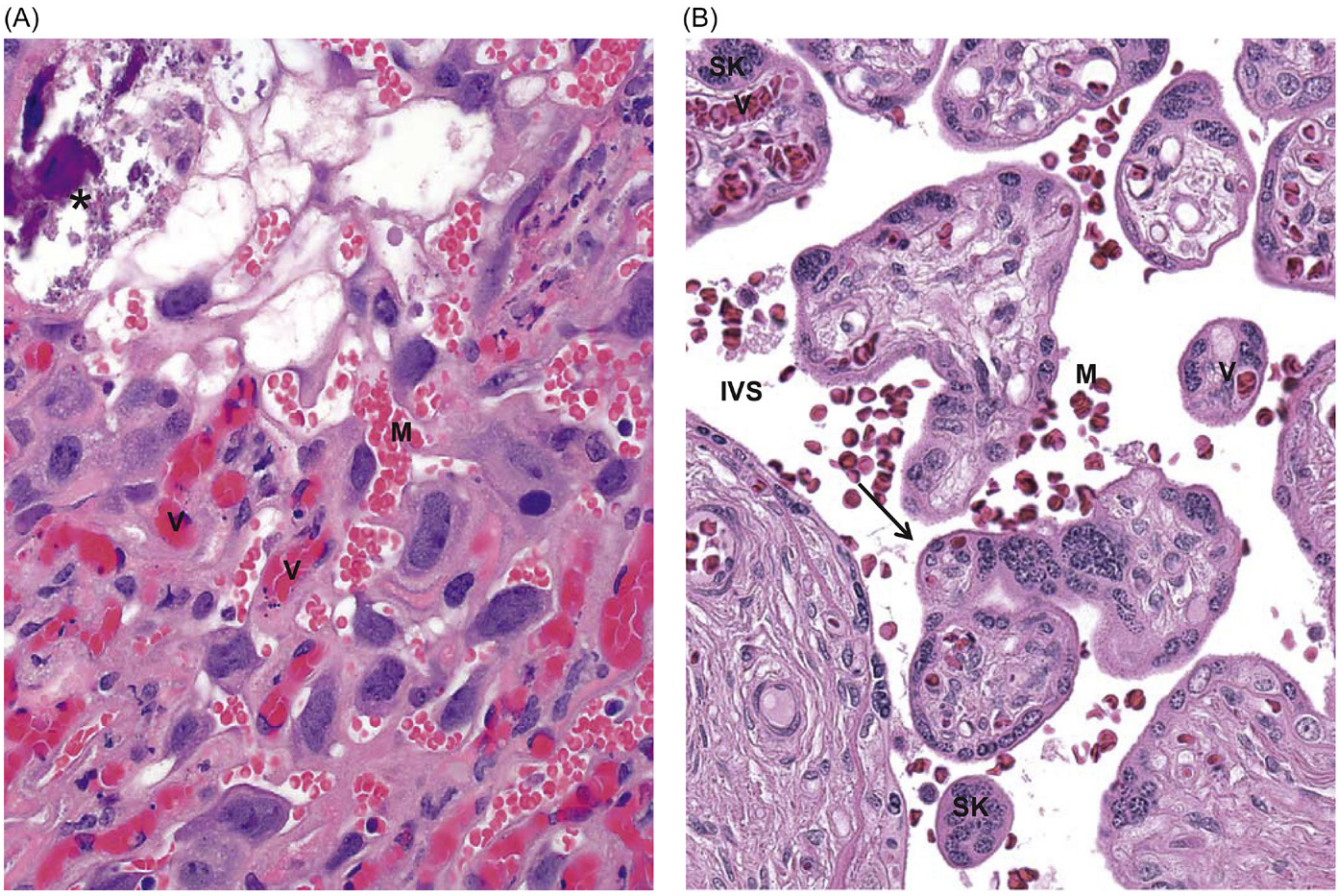

FIGURE 17.24 Placenta. (A) Rodent (mouse). The labyrinth layer is highly vascularized with embryonic and maternal blood. The embryonic blood channels (V) are lined by embryonic endothelial cells and contain immature erythrocytes. Labyrinth trophoblasts line vascular channels filled by maternal blood (M). Mineralization (asterisk) is not uncommon. (B) Human. The intervillous space (IVS) is perfused by maternal blood (M). Highly vascularized fetal villi are lined by villous trophoblast (arrow). *SK*, syncytial knot; *V*, fetal vessel. Source: Courtesy of Tess. B. Treuting.

Need-to-know

- In rodents, mineralization is commonly observed in the labyrinth and trophoblast layers during normal pregnancies.
- In humans, mineralization can also be observed during normal term pregnancies.

In rodents, Reichert's membrane (Fig. 17.23), a thick acellular basement membrane unique to the rodent placenta, divides the giant cell trophoblasts from the yolk sac. The rodent labyrinth layer is a highly vascularized structure composed of labyrinth trophoblasts; embryonal endothelium, which forms blood vessels; and embryonal erythrocytes (Fig. 17.24). Maternal blood cells fill spaces lined by labyrinth trophoblasts. It is not uncommon to see mineralization in the labyrinth layer as a normal finding (Fig. 17.24), or in human placental villi at term. The spongiotrophoblast layer is composed of large cells with abundant, often vacuolated, eosinophilic cytoplasm (Fig. 17.25). This layer forms just below the labyrinth and is traversed by maternal vessels. Spongiotrophoblasts may phagocytize maternal erythrocytes and may have pink hyaline cytoplasmic globules (Fig. 17.25), which may dramatically increase with trophoblast degeneration.

Next to the spongiotrophoblasts is the giant cell trophoblast layer. These cells have abundant eosinophilic cytoplasm and large nuclei and are frequently greater than 100 µm in diameter, with individual nuclei greater than 50 µm in

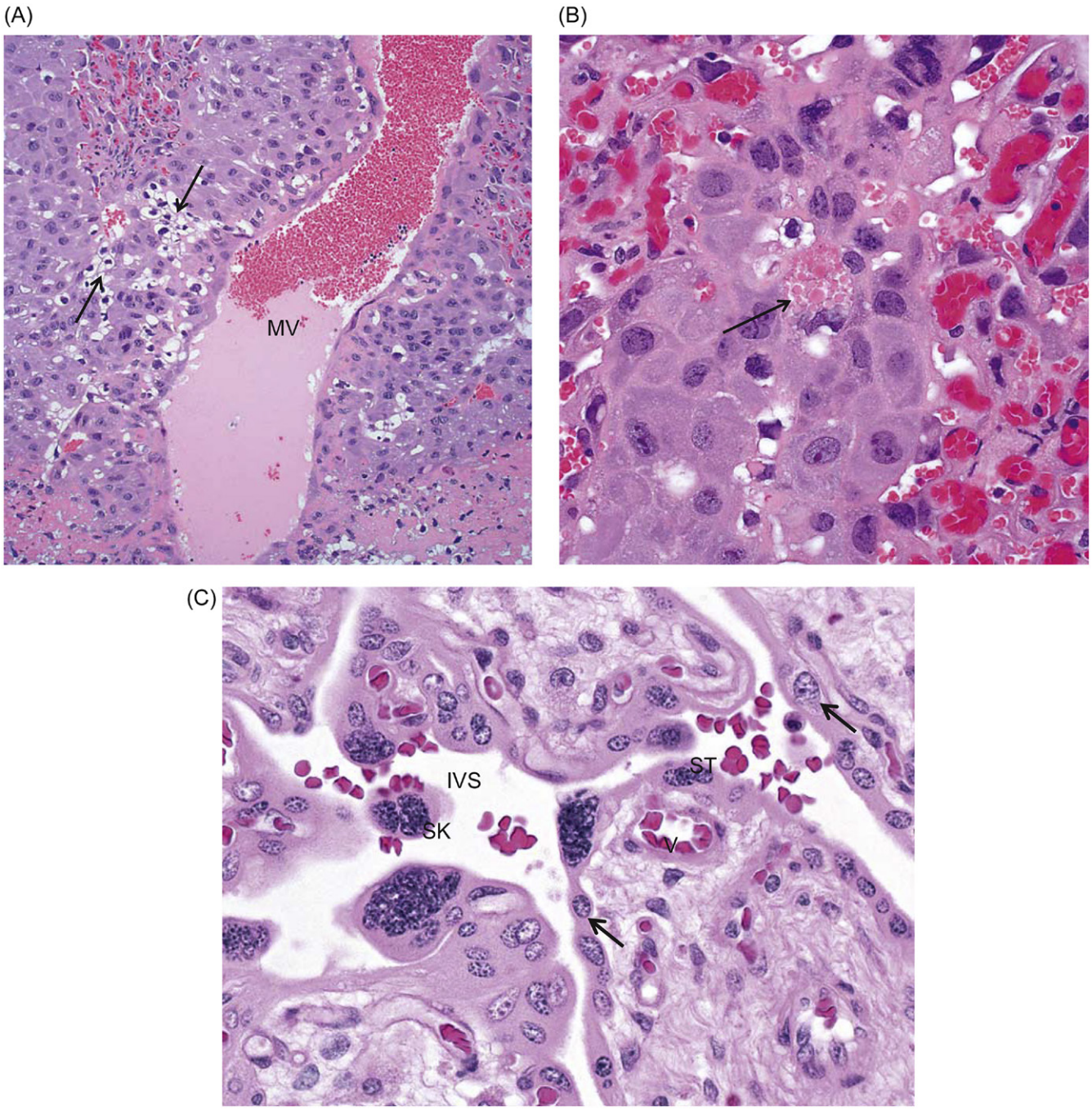

FIGURE 17.25 Placenta. (A) Rodent (mouse). Large maternal vessels (*MV*) traverse the spongiotrophoblast layer. Cells in this layer are often markedly vacuolated (arrows). (B) Rodent (mouse). Spongiotrophoblasts may phagocytize maternal erythrocytes and may have pink cytoplasmic globules (arrow). (C) Human. The villous trophoblast is composed of two layers. The outermost syncytiotrophoblast (ST), which is a multinucleate syncytium, is replenished by the underlying cytotrophoblast (arrows). *IVS*, intervillous space; *SK*, syncytial knot; *V*, fetal vessel. Source: Courtesy of Tess. B. Treuting.

Need-to-know

- Cells in the spongiotrophoblast layer can vary markedly in appearance and can be diffusely vacuolated.
- Spongiotrophoblasts phagocytize maternal erythrocytes.

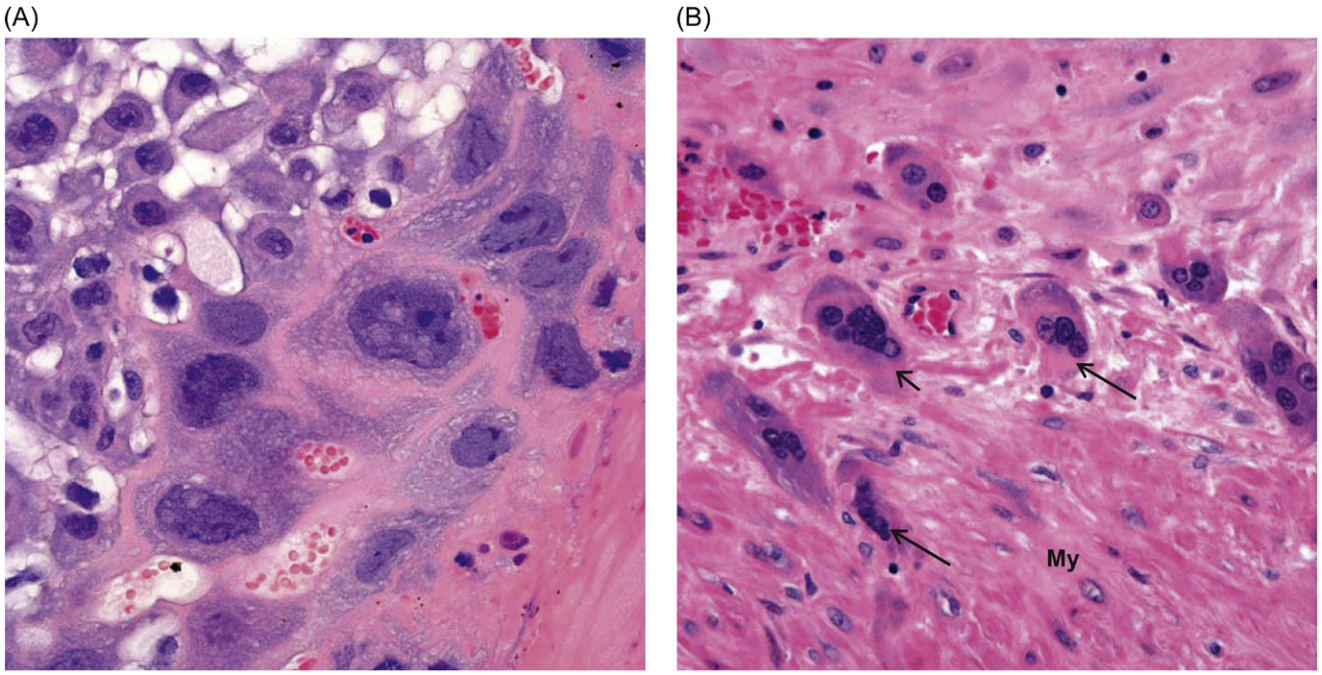

FIGURE 17.26 Trophoblasts. (A) Rodent (mouse) placental giant cell trophoblasts can often be greater than 100 µm in diameter and have individual nuclei that are more than 50 µm in diameter. (B) Human giant cell trophoblasts (arrows) are multinucleated and present at the deep basal plate at the myometrial border. *My*, myometrium.

diameter (Fig. 17.26). At Reichert's membrane, they extend into the decidua, which makes up the maternal portion of the placenta (Fig. 17.27). Cells are haphazardly arranged and typically have diffuse cytoplasmic vacuolation and irregularly shaped nuclei. Large maternal vessels develop to support the pregnancy. The decidua and giant cell trophoblasts form a sinusoidal network, the vitelline meshwork that is filled with maternal blood.

In humans, the chorion laeve or fetal membranes are formed at the edge of the placental disk by fusion of the basal plate and chorionic plate by obliteration of the intervillous space (Fig. 17.24). The fetal surface is lined by amniotic epithelium, a single layer of cuboidal-to-columnar cells, which transition to an unkeratinized stratified squamous epithelium over the umbilical cord. Subjacent to the amnion is connective tissue containing residual trophoblasts, known as chorionic laeve trophoblasts. Subjacent to the chorion laeve is the maternally derived decidua capsularis, which is derived from decidualized maternal endometrium.

In humans, a population of trophoblasts lines the chorionic villi, the site of maternal–fetal exchange (Figs. 17.22–17.24). The outmost layer, the syncytiotrophoblast, is a true multinuclear syncytium (Fig. 17.25) that is replenished by underlying cells with proliferative capacity, the cytotrophoblast (Fig. 17.24). As the cytotrophoblast fuses with the syncytiotrophoblast, its nucleus undergoes apoptosis and clusters with other nuclei. These "syncytial knots" are pinched off into the maternal circulation (Fig. 17.25). Remarkably, the syncytiotrophoblast is approximately 10 m^2 in area and contains more than 10 billion nuclei, through which all nutrient and gas exchange between mother and fetus occurs. A second population present within the basal plate is the extravillous trophoblast (Fig. 17.27), which invades the decidua (Fig. 17.27). The extravillous trophoblast also invades the spiral arteries, destroying smooth muscle and endothelium, and also differentiates into giant cell trophoblasts at the endometrial–myometrial junction (Fig. 17.27), similar to those described above for rodents.

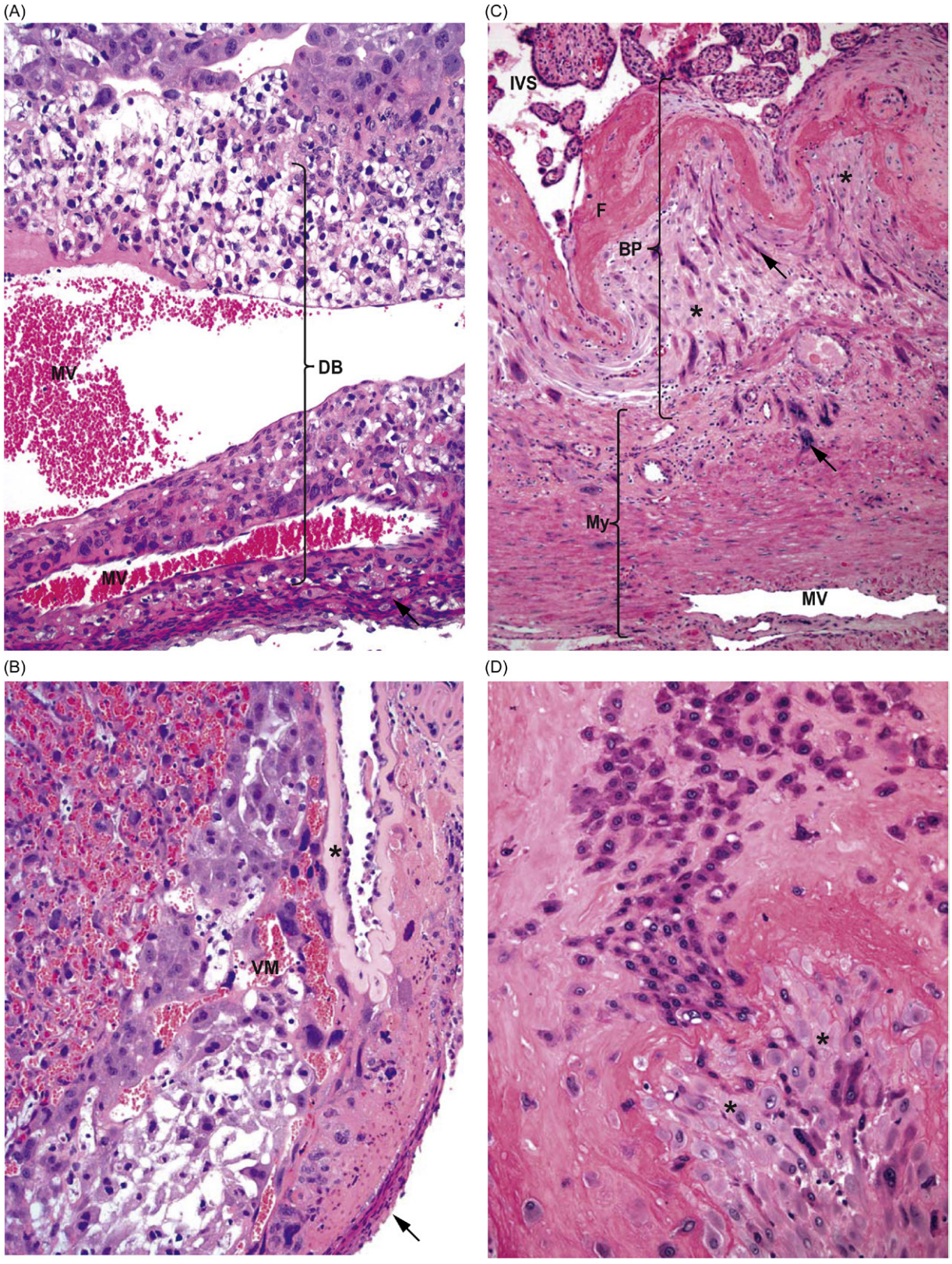

FIGURE 17.27 Decidua basalis and basal plate. (A) Rodent (mouse). Cells in the decidua basalis are haphazardly arranged and typically have diffuse cytoplasmic vacuolation and irregularly shaped nuclei. Large maternal vessels (MV) develop to support the pregnancy. The capsularis (arrow) is a compact layer of the maternal decidua completely surrounding the embryo. (B) Rodent (mouse). At Reichert's membrane (asterisk), giant cell trophoblasts extend into the decidua to the vitelline meshwork (VM), which is filled with maternal blood. (C) Human. The human basal plate (BP) is composed of fibrin (F), extravillous trophoblasts (arrows), and decidua (asterisk) overlying the myometrium (My). *IVS*, intervillous space; *MV*, maternal vessels. (D) Human extravillous trophoblasts present in the upper basal plate migrate into the decidua (asterisk).

FURTHER READING

Benirschke K: *Comparative Placentation.* http://placentation.ucsd.edu.

Benirschke K, Kaufmann P: *Pathology of the Human Placenta*, 4th edn., New York, 2000, Springer.

Bolon B, Bucci TJ, Warbritton AR, et al: Differential follicle counts as a screen for chemically induced ovarian toxicity in mice: Results from continuous breeding bioassays. Fundam Appl Toxicol 39(1):1–10, 1997.

Haig D: Genetic conflicts in human pregnancy. Q Rev Biol 68(4):495–532, 1993.

Kagabu S, Umezu M: Histological analysis of the "critical point" in follicular development in mice. Reprod Med Biol 3:141–145, 2004.

Maronpot RR, Boorman GA, Gaul BW: *Pathology of the Mouse: Reference and Atlas*, Vienna, IL, 1999, Cache River Press.

Mills S: *Histology for Pathologists*, 4th edn., Philadelphia, 2012, Lippincott Williams & Wilkins.

Mossman HW: Comparative morphogenesis of the fetal membranes and accessory uterine structures. Carnegie Contrib Embryol 26:129–246, 1937.

Suttie AW, Leininger JR, Bradley AE: *Boorman's Pathology of the Rat: Reference and Atlas*, 2nd edn., New York, 2017, Academic Press.

The Jackson Laboratory *Biology of the Laboratory Mouse*, 2nd edn., New York:, 1966, Dover. Web-adapted version available at http://www.informatics.jax.org/greenbook

Ward JM, Mahler JF, Maronpot RR: *Pathology of Genetically Engineered Mice*, Ames IA, 2000, Iowa State University Press.

Young B, Lowe JS, Stevens A, et al: *Wheater's Functional Histology: A Text and Colour Atlas*, 5th edn., Oxford, 2006, Churchill Livingstone.

MALE REPRODUCTIVE SYSTEM 18

SUE E. KNOBLAUGH
The Ohio State University College of Veterinary Medicine, Columbus, OH, United States

LAWRENCE TRUE AND MARIA TRETIAKOVA
University of Washington School of Medicine, Seattle, WA, United States

RENEE R. HUKKANEN
Eisai US, Andover, MA, United States

Introduction

Rodents are essential animal models of human disease. They are common models for both cancer studies and toxicological evaluation. The male reproductive system is assessed in toxicologic dose studies with focused evaluation of fertility and development, and mice are often used as models for human prostate cancer. Given the large number of genetically engineered mouse models generated and studied as models for human prostate carcinoma, and the large number of rats used for toxicological evaluation, it is important for researchers and pathologists to know the normal anatomy and histology of the mouse, rat, and the human male urogenital tract and to understand the anatomical differences between rodent and human. The prostate gland exemplifies this point. The rodent prostate gland is divided into lobes, where each lobe is histologically distinct. Conversely, the human prostate gland is a single organ without lobes.

Male rodents also have additional accessory sex glands, such as the ampullary and preputial glands, that are not found in humans. Consequently, the preputial gland and ampullary glands should not be interpreted as an abnormal finding. In addition, as the development and maintenance of accessory sex glands in general are hormonally dependent, progressive atrophy noted with aging and/or decreased production of testosterone may vary. In older rats, epithelial stroma may decrease while cytoplasmic lipofuscin deposits increase. In rodents, the accessory sex glands are frequent sights of inflammatory lesions. It is not uncommon to see a background incidence of lymphocytic infiltrates in any accessory gland or tissue.

Comparative Anatomy and Histology. DOI: http://dx.doi.org/10.1016/B978-0-12-802900-8.00018-X
© 2018 Elsevier Inc. All rights reserved.

Histologic characteristics are important to understanding the phenotype of rodent models of human disease. Thus, a basic understanding of the normal histology of the urogenital organs of rodents and humans and where they differ is essential for proper interpretation and characterization of rodent models of disease.

This chapter highlights such differences in several aspects of the male reproductive system, including the testes, extratesticular ducts (efferent ducts, epididymis, and vas deferens), the accessory sex glands (seminal vesicles, prostate gland, ampullary, bulbourethral, and preputial glands), the urethra, and the penis (Table 18.1 and Fig. 18.1).

Testes

Gross Anatomy

The function of the testes is to produce and release the male gametes, spermatozoa. Both rodent and human testes are paired. In mice, each testis weighs ~0.06 g and measures ~0.66 cm× 0.39 cm × 0.45 cm. In rats, each testis weighs ~1.7 g and measures ~2.4 cm × 1.3 cm × 0.9 cm. In humans, the average testis weighs 21.6 g (right) or 20 g (left), with the right usually 10% heavier than the left. Each human testis measures ~4.6 cm × 2.6 cm × 3 cm. In both rodents and humans, the paired testes are located in the scrotum, covered by a dense fibrous capsule, the tunica albuginea, and a double layer of mesothelium, the tunica vaginalis, which also lines the inner surface of the scrotum.

Rodents are unique in that the testes communicate with the abdominal cavity through patent inguinal canals, which remain open throughout life. The inguinal canals are occupied by the epididymal fat pad when the testes are in the scrotum. Out of the scrotum, each testis is also surrounded epididymal fat pad (Fig. 18.2). In contrast, in humans, inguinal canals are normally closed after descent of the testes from the retroperitoneum into the scrotum after birth. As the testes descend, they carry a layer of peritoneum that once in

TABLE 18.1 Male Reproductive Tract

Feature	Rodent	Human
	Gross	
Testes	Paired; within scrotum; open inguinal canals	Paired; outside body, within scrotum, closed inguinal canals
Epididymis	Head (caput), body (isthmus), tail (cauda); posterior aspect of each testis	Similar to rodent
Vas deferens	Paired; conducts spermatozoa from tail of the epididymis to urethra	Similar to rodent
Seminal vesicles	Attached to coagulating gland (anterior lobe of prostate)	Diverticuli of vas deferens
Prostate	Mouse: Divided into four lobes; coagulating gland (anterior), dorsal, lateral, and ventral Rat: Divided into three lobes; ventral, dorsolateral, and coagulating gland (anterior)	Alobular organ with central, peripheral, and transitional zones
Ampullary glands	Glandular outpouchings of vas deferens	Absent
Bulbourethral glands (Cowper's glands)	Paired; located near base of the penis, embedded within ischiocavernosus and bulbocavernosus muscles	Paired; adjacent to membranous urethra
Preputial glands	Modified sebaceous glands located in the caudal subcutaneous tissue lateral to the base of the penis	Absent
Urethra	Prostatic/membranous, penile	Similar to rodent
Penis	Haired prepuce; os penis	Glabrous prepuce; os penis absent
	Histologic	
Testes	Compound tubular glands covered by tunica albuginea, composed of seminiferous tubules: Sertoli cells, germ cells (spermatogonia, spermatocytes, spermatids), and interstitium (Leydig cells)	Similar to rodent
Spermatogenesis	Mouse: Cycle 8.8 days; spermatogenesis 35 days Rat: Cycle 12.9 days; spermatogenesis 52 days	Cycle 16.0 days; spermatogenesis 70 days

(*Continued*)

TABLE 18.1 Male Reproductive Tract (Continued)

Feature	Rodent	Human
Epididymis	Epididymal ducts are composed of a smooth muscle wall and a principal columnar-to-cuboidal epithelium with microvilli (stereocilia)	Similar to rodent
Vas deferens	Lined by ciliated columnar epithelium surrounded by a thick smooth muscle layer consisting of a thick intermediate circular layer, inner and outer layers of longitudinally oriented smooth muscle, and adventitia	Similar to rodent
Seminal vesicles	Lined by smooth muscle and connective tissue stroma with a columnar epithelium that forms characteristic branching mucosal folds	Lined by smooth muscle wall composed of inner circular layer and outer longitudinal layer with pseudostratified epithelium consisting of tall, columnar cells, some of which have a yellow-brown cytoplasmic pigment and variably sized nuclei. Rare, markedly enlarged, pleomorphic epithelial cell nuclei
Prostate	Lobes separated by a mesothelium-lined thin, delicate capsule; individual glands or acini within each lobe are surrounded by a sparse smooth muscle stroma embedded in loose connective tissue	Prostatic glands (or acini) are irregularly shaped and embedded in a fibromuscular stroma; lined by cuboidal-to-columnar epithelium and a layer of basal cells
Coagulating gland (anterior prostate)	Mouse: Coagulating gland (anterior prostate) lined by cuboidal-to-columnar epithelium, papillary or cribriform, abundant, homogenous, eosinophilic secretions Rat: Similar to mouse with pale pink secretions	Absent
Dorsal prostate	Mouse: Dorsal prostate gland is lined by columnar epithelium with moderate infolding and homogeneous, eosinophilic secretions. Individual glands surrounded by dense fibromuscular stroma Rat: See dorsolateral lobe	Absent
Dorsolateral prostate	Mouse: Absent Rat: Dorsal portion lined by cuboidal-to-tall columnar with cytoplasmic blebs and intermediate staining secretions. Lateral portion lined by cuboidal-to-tall columnar epithelium with distinctive brush border and deep eosinophilic secretions	Absent
Ventral prostate	Mouse: Ventral prostate lined by cuboidal-to-columnar epithelium with sparse infolding and focal tufting, and abundant, homogeneous, pale, serous secretions Rat: Ventral prostate gland composed of closely packed acini, or alveoli surrounded by smooth muscle and lined by single layer of tall columnar epithelial cells with supranuclear clear areas and pale pink secretions	Absent
Ampullary glands	Glands lined by simple columnar epithelium that forms longitudinal folds and are surrounded by dense fibromuscular stroma with vacuolated secretions	Absent
Bulbourethral glands (Cowper's glands)	Mouse: Glandular acini are highly arborized and lined by tall columnar epithelium. In the secretory state, the epithelium has abundant, foamy cytoplasm, and in the resting state, the cytoplasm is eosinophilic and finely granular Rat: Glandular acini lined by a single layer of tall, closely packed pyramidal cells that appear faintly basophilic and contain discrete secretory granules	Glands consist of closely juxtaposed acini composed of polygonal epithelial cells with abundant clear cytoplasm
Preputial glands	Mouse: Glands are lobulated with connective tissue capsule that surrounds large, cavernous ducts lined by stratified squamous epithelium and acini composed of eosinophilic, pale, foamy, secretory sebaceous cells with dark nuclei and peripheral, flat, elongated basal cells Rat: Acini composed of sebaceous cells with characteristic eosinophilic secretory granules; cavernous ducts lined by stratified squamous epithelium	Absent
Urethra	Lined by a transitional epithelium (urothelium). The external penile urethral orifice lined by stratified squamous epithelium	Lined by transitional epithelium (urothelium) and nonkeratinizing stratified squamous epithelium, which becomes more prominent in the distal urethra
Penis	Composed of the penile or distal portion of the urethra, vascular erectile tissue (the cavernae corporum cavernosum and the corpus spongiosum), and the orifice of the penis. Os penis made of bone located proximally and ends distally in the tip of the glans as male urogenital mating protuberance (MUMP) composed of fibrocartilaginous tissue. Covered by prepuce, which encloses the glans and is covered externally by stratified squamous epithelium that contains hair follicles (filiform hairs)	Lined by skin and contains three cylindrical portions of erectile tissue—paired corpora cavernosa and a corpus spongiosum that partially surrounds the penile urethra. Noncircumcised glans penis is variably covered by a prepuce composed of outer keratinized, nonhaired squamous mucosal epithelium, lamia propria, smooth muscle, and inner mucosal epithelium

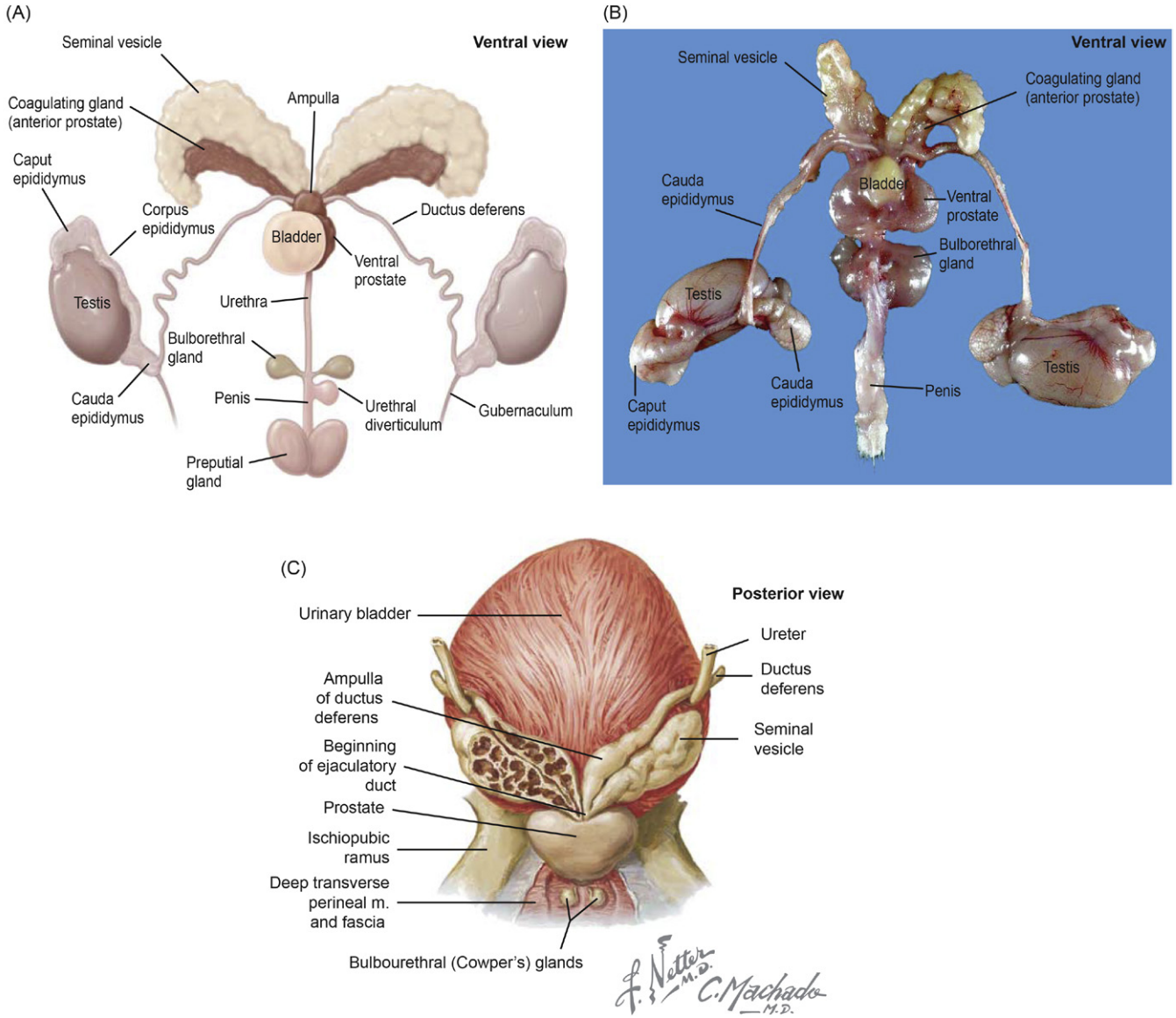

FIGURE 18.1 Regional anatomy of the male reproductive system. (A) Rodent (mouse) schematic. Source: Adapted with permission from Anatomy of a Laboratory Mouse, Cook, M.J., 1965, with permission from Elsevier. (B) Rodent dissection (rat). The rodent male reproductive tract consists of paired testes, extratesticular ducts (efferent, epididymis, vas deferens), the accessory sex glands (seminal vesicles, prostrate lobes, ampullary glands, bulbourethral glands, preputial glands), urethra, and penis. (C) Human. The human reproductive tract consists of paired testes, extratesticular ducts (efferent, epididymis, vas deferens), the accessory sex glands (seminal vesicles, bulbourethral glands, prostate gland), urethra, and the penis. Source: © Elsevier, Inc., www.netterimages.com.

the scrotum, becomes the tunica vaginalis. In rats, the tunica vaginalis is a common sight for mesothelioma; therefore, the surface of the testis, epididymis (see below), and lining of the scrotum should be closely examined in aging animals.

Need-to-know

- Rodents have ampullary and preputial glands, whereas humans do not.
- The rodent prostate is multilobed.

HISTOLOGY

In all three species, the tunica albuginea is continuous with the interlobular septa that divide grouped seminiferous tubules into lobules. As described below, the seminiferous tubules connect, in sequence, to the segments of the ductal system—the rete testis, efferent ducts, epididymis, and the vas deferens.

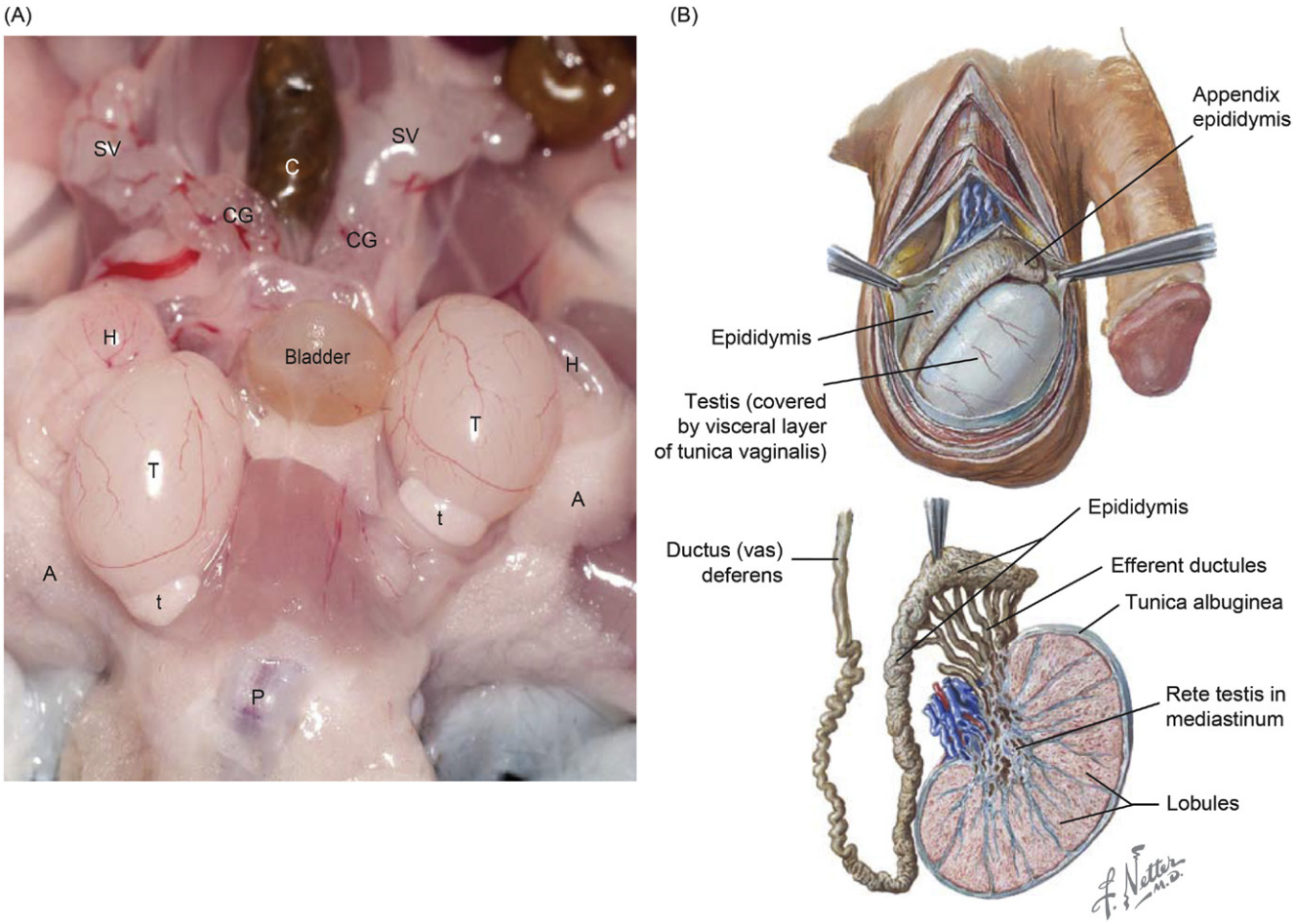

FIGURE 18.2 Testes. (A) Rodent (mouse). Each rodent testis (*T*) is surrounded by the capsule (tunica albuginea) and juxtaposed to the epididymis on the posterior aspect. The epididymis has a head (caput) (H) and a tail (cauda) (t) and is surrounded by adipose tissue (*A*). The coagulating gland (CG), seminal vesicles (SV), penis (P, partially obscured by fat), and colon (C) are indicated. (B) Human. Human testes are paired and located outside the body within the scrotum where each is surrounded by the visceral tunica vaginalis. The tunica vaginalis rests on the capsule (tunica albuginea) which divides the testis into lobules via numerous collagenous septa. The seminiferous tubules within the lobules, **c**onnect, in sequence, to the segments of the ductal system—the rete testis, efferent ducts, epididymis, and within the spermatic cord, the vas deferens. Source: © Elsevier, Inc., www.netterimages.com.

Seminiferous Tubules

In all three species, the bulk of each testis is composed of arrays of convoluted seminiferous tubules and an interstitium (Fig. 18.3), composed of somatic Sertoli and Leydig (interstitial) cells and germ cells. The seminiferous tubules are lined by Sertoli and germ (spermatogonia, spermatocytes, and spermatids) cells arranged in layers and surrounded by a basement membrane

Need-to-know

- The rodent testes can communicate with the abdominal cavity through open inguinal canals.
- Humans have closed inguinal canals.

consisting of an outer thin parietal epithelium overlying peritubular myoid cells, collagen, and an inner layer of extracellular matrix. These germ cells produce the male gametes. Sertoli cells, which have relatively scant cytoplasm and oblong nuclei with small nucleoli, are interspersed with the developing germ cells; and support and nurture the developing spermatozoa. The maturing elongated spermatids are attached to the cell membrane of Sertoli cells, each of which can support up to 50 germ cells. Tight junctions between Sertoli cells form what is known as the "blood–testis barrier."

In all three species, spermatogonia, which are the earliest stage of germ cell maturation,

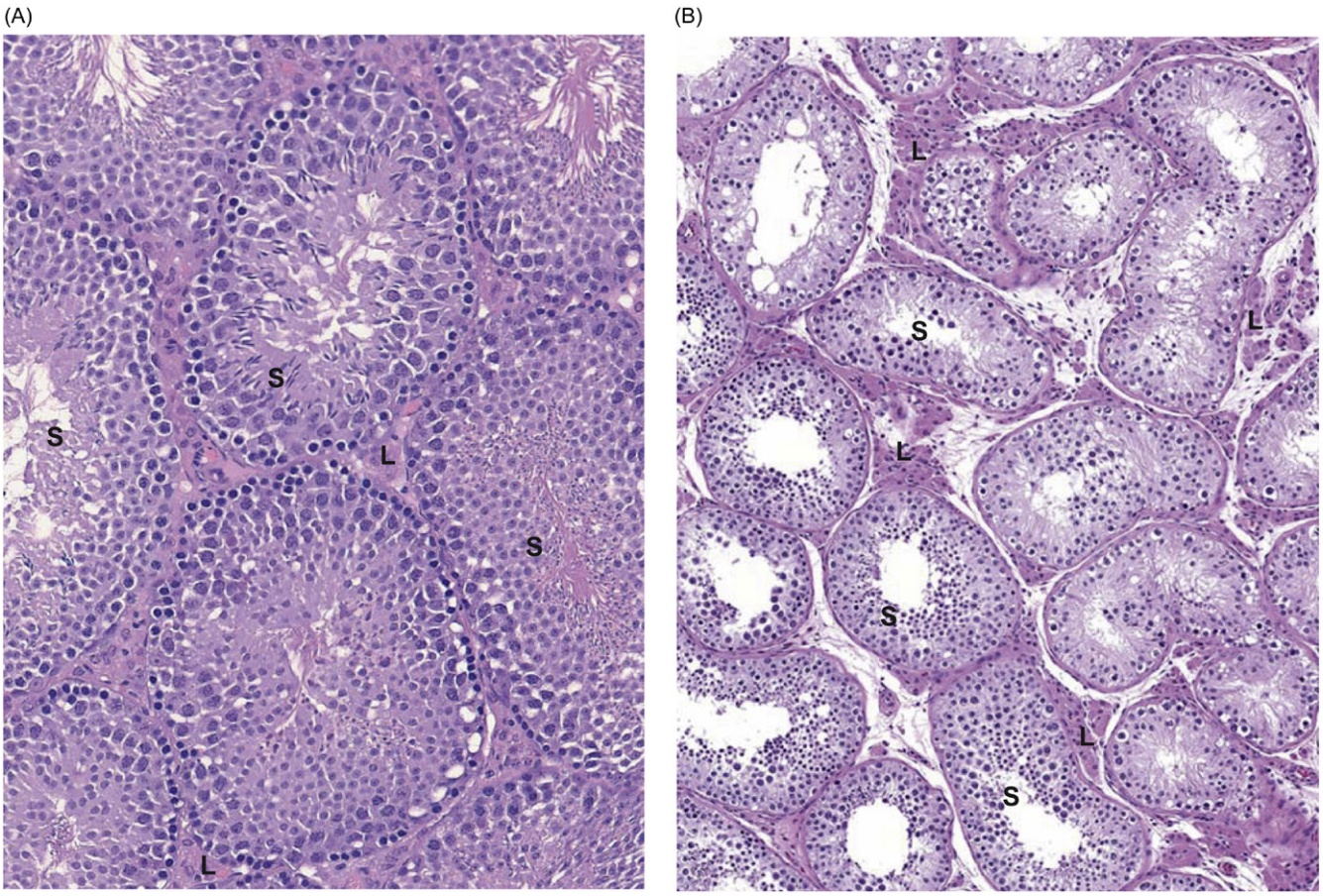

FIGURE 18.3 Testes. (A) Rodent (mouse). The bulk of each rodent testis is composed of convoluted seminiferous tubules (S) and interstitial or Leydig cells (L). (B) Human. Each human testis is composed of convoluted seminiferous tubules (S) and interstitial or Leydig cells (L).

are located at the base of the tubules. During spermatogenesis, germ cells move from the periphery to the lumina of the tubules as they proceed through highly ordered and sequential stages of maturation from spermatogonia to spermatocytes, spermatids, and mature spermatozoa (Fig. 18.4). Final maturation of spermatozoa occurs in the epididymis (see below). In mice, spermatogenesis occurs in 35 days, rats, 52, and in humans, 70. Spermatogenic staging for all three species has been extensively reviewed (see Further Reading). The coordinated maturation and relationships among germ cells is described in stages which are represented by Roman numerals I to XIV in rats and I to XII in mice. A periodic acid-Schiff (PAS) stained section may aid in distinguishing the various stages.

The interstitium between the seminiferous tubules is composed of Leydig cells, rare inflammatory cells, and vessels. Leydig cells synthesize and secrete testosterone under the regulation of pituitary luteinizing hormone. Leydig cells have an abundant, eosinophilic cytoplasm and large, round nuclei with large nucleoli and in humans contain elongated, intracytoplasmic crystals of Reinke. These crystals may be seen under light microscopy and are only found in humans and bush rats (*Rattus fuscipes*); their function remains unknown. Leydig cell proliferation and neoplasia increases with age in rats, reaching nearly 100% incidence by 2 years of age in some strains (F344). Such lesions are commonly bilateral and result in secondary degenerative changes to hormonally dependent secondary sex gland epithelium.

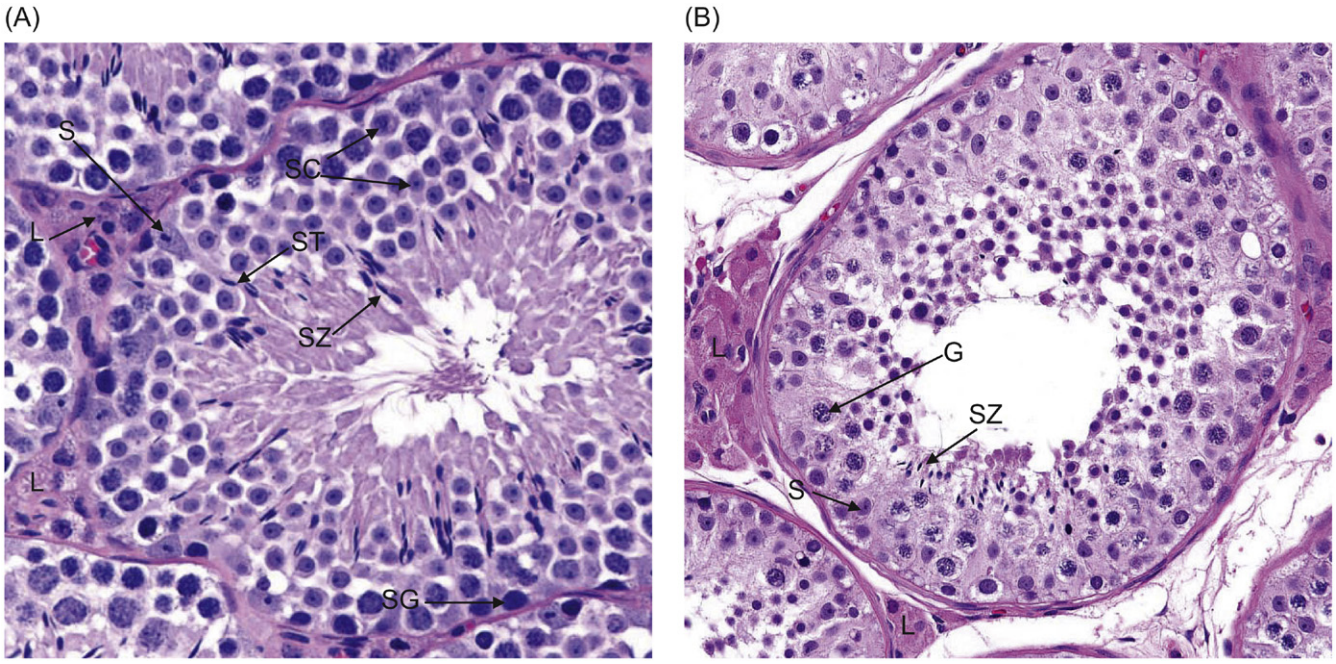

FIGURE 18.4 Seminiferous tubules. (A) Rodent (mouse). The rodent seminiferous tubules are lined by a stratified epithelium which consists of spermatogenic cells (spermatogonia (SG), spermatocytes (SC), spermatids (ST), and spermatozoa (SZ) and nonspermatogenic cells (Sertoli cells (S)). The seminiferous tubules are separated by interstitial cells or Leydig cells (L) which are endocrine cells that produce testosterone. Spermatogenesis and spermiogenesis occur sequentially along the length of each tubule. (B) Human. Human Sertoli cells (S), characterized by oval nuclei with round nucleoli and scant cytoplasm, are between germinal cells (G), which are characterized by large nuclei that have a complex pattern of heterochromatin. The lumen contains mature spermatozoa (SZ). Polygonal Leydig cells (L), which have abundant eosinophilic cytoplasm, are within the interstitium between the tubules.

Need-to-know

- In all three species, the germ cell types from basal location (immature) to luminal location (mature) are spermatogonia, spermatocyte, spermatids, and spermatozoa.
- Spermatogenesis takes approximately 35 days in mice, 52 days in the rat, and 70 days in the human.

In all three species, the seminiferous tubules form loops at either end that end in the excretory ducts, tubuli recti, which are located at the interface of the rete testis. They are lined by transitional cells that look like Sertoli cells and should not be misinterpreted as atrophic seminiferous tubules.

Rete Testis

The rete testis is a dilated intratesticular structure located directly under the tunica albuginea at the cranial pole of the testis (Fig. 18.5). It is also near the arterial supply of the testis which comes from the testicular artery. The testicular artery is convoluted and is surrounded by the venous pampiniform plexus for heat exchange. In rodents, the rete testis is lined by a flattened, cuboidal epithelium and located under the tunica albuginea. In humans, the ducts of the rete testis are lined by cuboidal epithelium (Fig. 18.5). In all three species, the rete testis is located at the testis margin and usually forms an extratesticular portion that connects to the efferent ducts (Fig. 18.5).

Efferent Ducts

Gross Anatomy

The efferent ducts collect and store spermatozoa and conduct it from the rete testis into the head of the epididymis. In rodents, the efferent ducts are located within the epididymal fat pad. Mice generally have 3–5 ducts, whereas rats have 6–9. In humans, up to 15

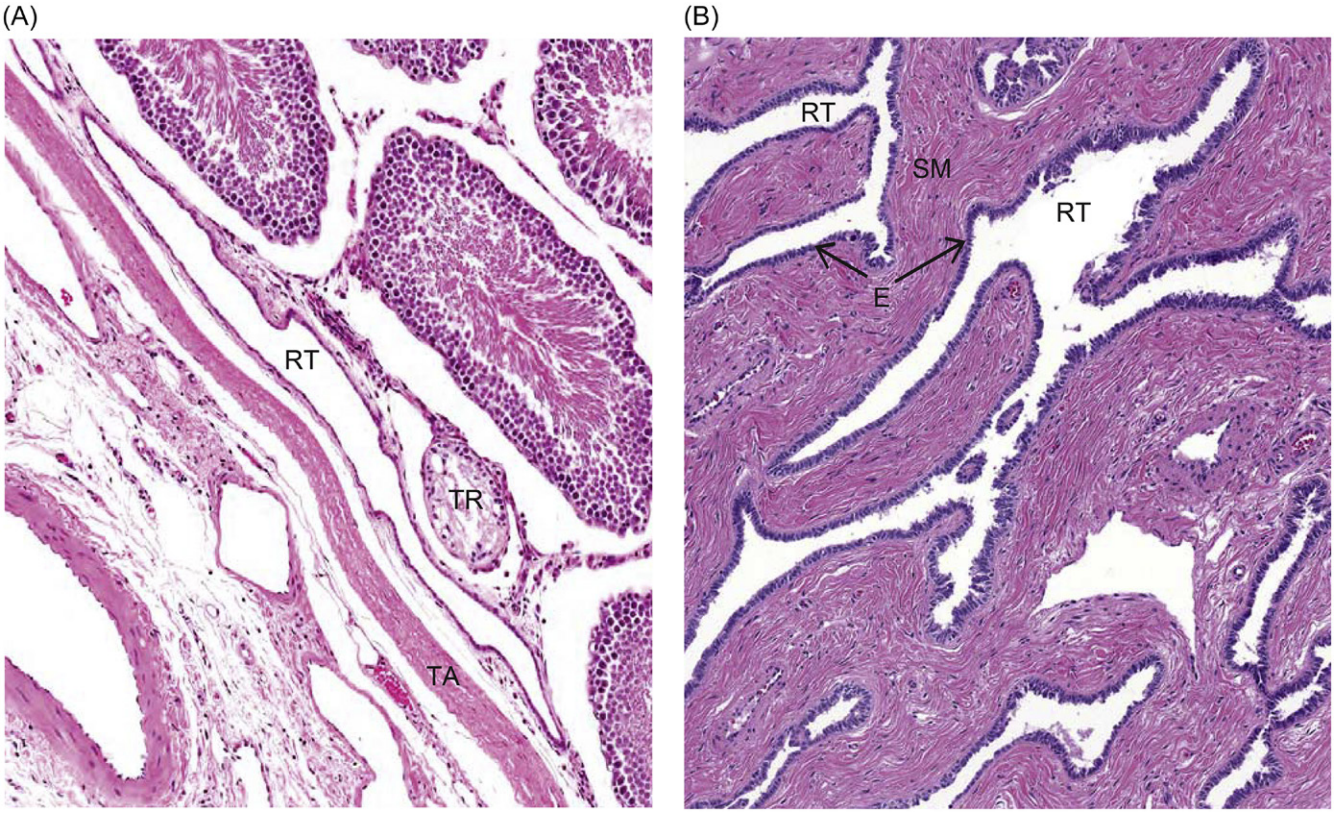

FIGURE 18.5 Rete testis. (A) Rodent (rat). In rodents, the dilated tubules of the rete testis (RT) are located under the tunica albuginea (TA) and lined by a flat-to-cuboidal epithelium. A tubular rectus (TR) is lined by transitional cells. (B) Human. The human rete testis (RT) is a complex of ducts that drain the seminiferous tubules. The epithelium (E) of the rete is cuboidal. Smooth muscle (SM) is indicated.

ducts have been reported. In rodents, the terminal portion of the efferent ducts forms a single tube that transitions into the initial segment of the epididymis whereas in humans, there are multiple entries of the ducts into the epididymis.

HISTOLOGY

In all three species, the epithelium is a single layer composed of ciliated tall columnar cells and short, nonciliated cells. In humans, a minority of epithelial cells contain a yellow-brown pigment. In all three species, cilia propel spermatozoa into the epididymis; the nonciliated cells are thought to reabsorb some of the testicular fluid. Each efferent duct is surrounded by a thin band of smooth muscle that aids in propelling the spermatozoa toward the epididymis (Fig. 18.6).

Need-to-know

- The rodent tubuli recti are lined by transitional cells and should not be mistaken for atrophic seminiferous tubules.

EPIDIDYMIS

GROSS ANATOMY

The major function of the epididymis is the accumulation, final maturation, and storage of mature spermatozoa. In all three species, the paired epididymides are structurally similar, consisting of initial and intermediate segments into which the efferent ducts empty and three main parts that include: The head (caput), body (isthmus), and tail (cauda). The epididymis may be further subdivided based on functionality. It lies on the posterior aspect of the testis, with the caput at the upper pole and cauda at the lower pole. In contrast to the human epididymis, the rodent epididymis is longer and loosely attached to the testis. In rodents, the head of the epididymis is surrounded by the epididymal fat pad.

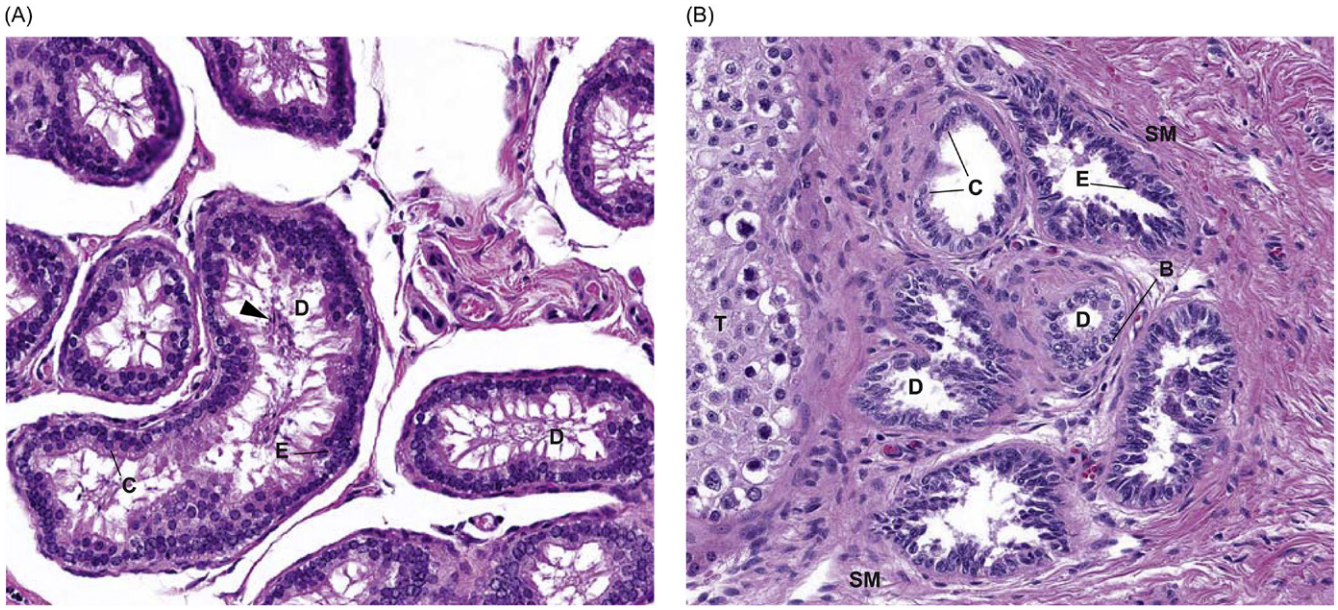

FIGURE 18.6 Efferent ducts. (A) Rodent (mouse). Rodent efferent ducts (*D*) are lined by ciliated (*C*) and nonciliated tall columnar epithelial cells (E). Note spermatozoa (arrowhead) in lumen. (B) Human. Human convoluted efferent ducts (D) of the efferent ducts are lined by a single layer of epithelial cells (E) and surrounded by smooth muscle (SM). Each efferent duct is lined by an epithelium, which varies from tall columnar and ciliated (C) to short and nonciliated with a layer of basal reserve cells (B). Each duct is surrounded by a band of smooth muscle (SM). The ciliated cells and smooth muscle help propel spermatozoa towards the epididymis. Seminiferous tubule (T) is indicated.

HISTOLOGY

In all three species, the epididymal ducts are composed of a smooth muscle wall and a principal columnar-to-cuboidal epithelium with microvilli (stereocilia). The epithelium is composed of principal cells that are tall columnar with apical stereocilia (principal cell type) with a secretory and excretory function, smaller, peripheral basal cells with detoxicant activity, halo cells which are the immune cells, and tall clear cells that are absorptive in function. In the head, the luminal diameter of the tubules is the smallest with the tallest epithelium (pseudostratified columnar) with basally located nuclei. In the tail, tubules have a larger diameter lumen with the shortest epithelium (cuboidal-to-simple columnar) with round to flattened nuclei (Figs. 18.7 and 18.8). In humans, occasional lymphocytes may be seen within the epididymal epithelium. Histologically, in mice, five segments can be distinguished, whereas in rats, there are >6 defined zones characterized by the percentage of cell type(s) present.

In all three species, the head is connected to the efferent ducts; the tail, which stores the mature spermatozoa, is connected to the vas deferens. In rodents, the epididymis often develops spermatoceles and spermatic granulomas. A sperm granuloma develops when spermatozoa penetrate interstitial tissues and incite an inflammatory reaction. Sperm granulomas should not be misinterpreted as a neoplastic process. Neoplasia of the epididymis is rare in all three species. Blockage of the lumen of the secretory ductal system may result in sterility.

VAS DEFERENS

GROSS ANATOMY

In all three species, the vas deferens, also known as the ductus deferens, is paired and conducts

FIGURE 18.7 Rodent (mouse) epididymis. (A) The rodent paired epididymides consist of a head (caput), body (isthmus), and tail (cauda). Histologically, the epididymal ducts are lined by columnar-to-cuboidal epithelium and smooth muscle. (B) The epididymal tubules are smallest and have the tallest epithelium (columnar) in the head (caput). (C) The epididymal tubules are largest and epithelium the lowest (cuboidal) in the tail (cauda).

spermatozoa from the tail of the epididymis to the urethra. It is part of the spermatic cord, along with associated blood vessels and nerves. In rodents, the vas deferens leads from the tail of the epididymis into the ampulla (see below), which opens into the urethra at the level of the colliculus seminalis.

In humans, the vas deferens is connected to the tail of the epididymis at the ampulla, where it connects to a short duct draining the seminal vesicle within the prostate gland to form an ejaculatory duct. The ejaculatory ducts from each side connect to the prostatic urethra.

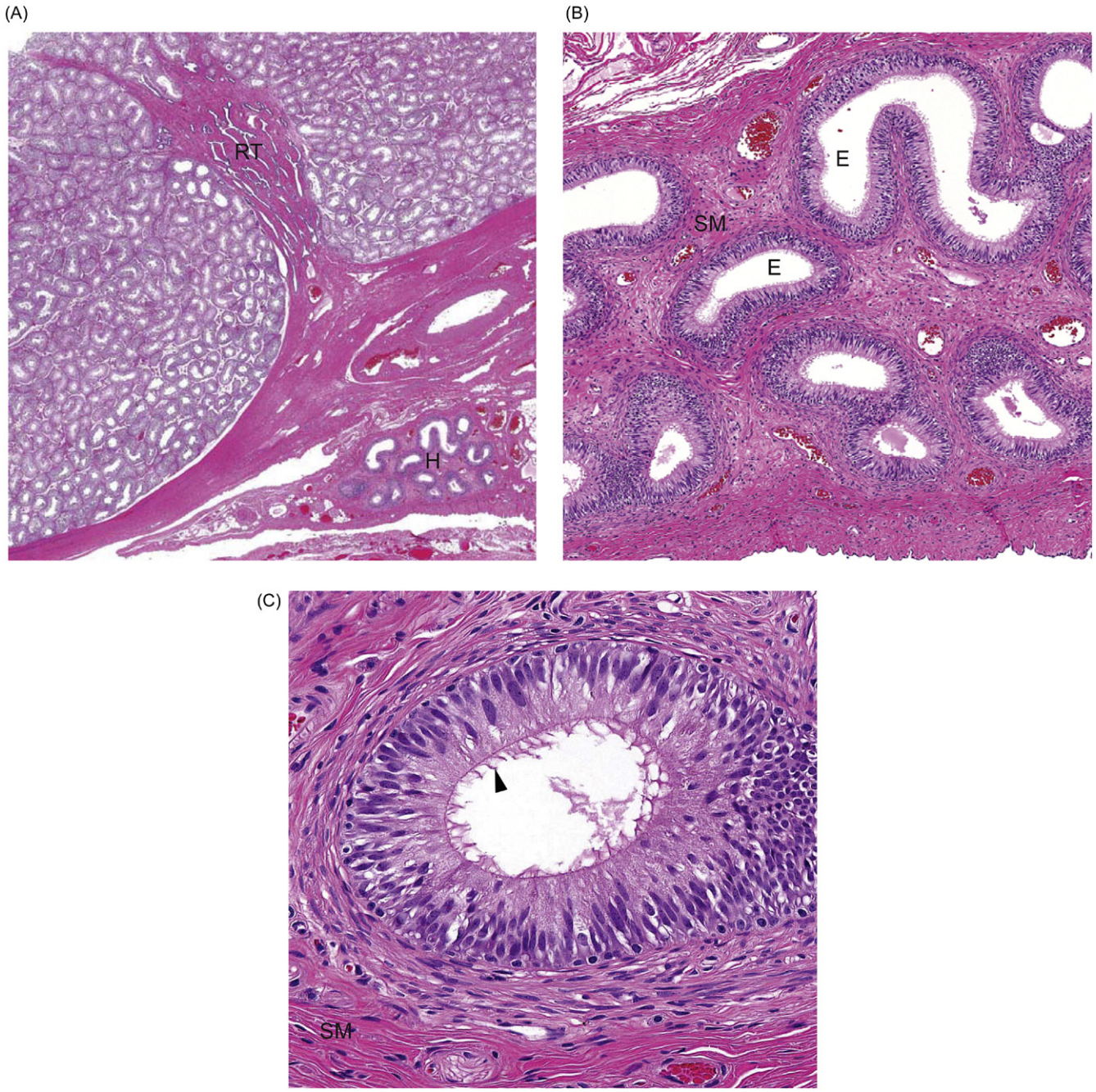

FIGURE 18.8 Human epididymis. (A) The rete testis (RT) drains into the head of the epididymis (H) via the efferent ducts. (B) The epididymal ducts are lined by smooth muscle (SM) and pseudostratified epithelium (E). (C) The tubules are smallest and have the tallest epithelium (columnar) in the head (caput). The principal epithelial cells have very long microvilli (arrowhead), called stereocilia.

Need-to-know

- In all three species, the rete testis drains into the head of the epididymis via the efferent ducts.
- In all three species, the epididymal tubules are smallest and have columnar epithelium in the head and the tubules are largest and cuboidal epithelium the lowest in the tail.
- The epididymal lumen may contain mature spermatozoa.

HISTOLOGY

Histologically in all three species, the vas deferens is lined by ciliated columnar epithelium that is surrounded by a thick smooth muscle layer consisting of a thick intermediate circular layer, inner and outer layers of longitudinally oriented smooth muscle, and adventitia (Fig. 18.9). These thick layers of smooth muscle conduct and expel spermatozoa during ejaculation. In rodents, the

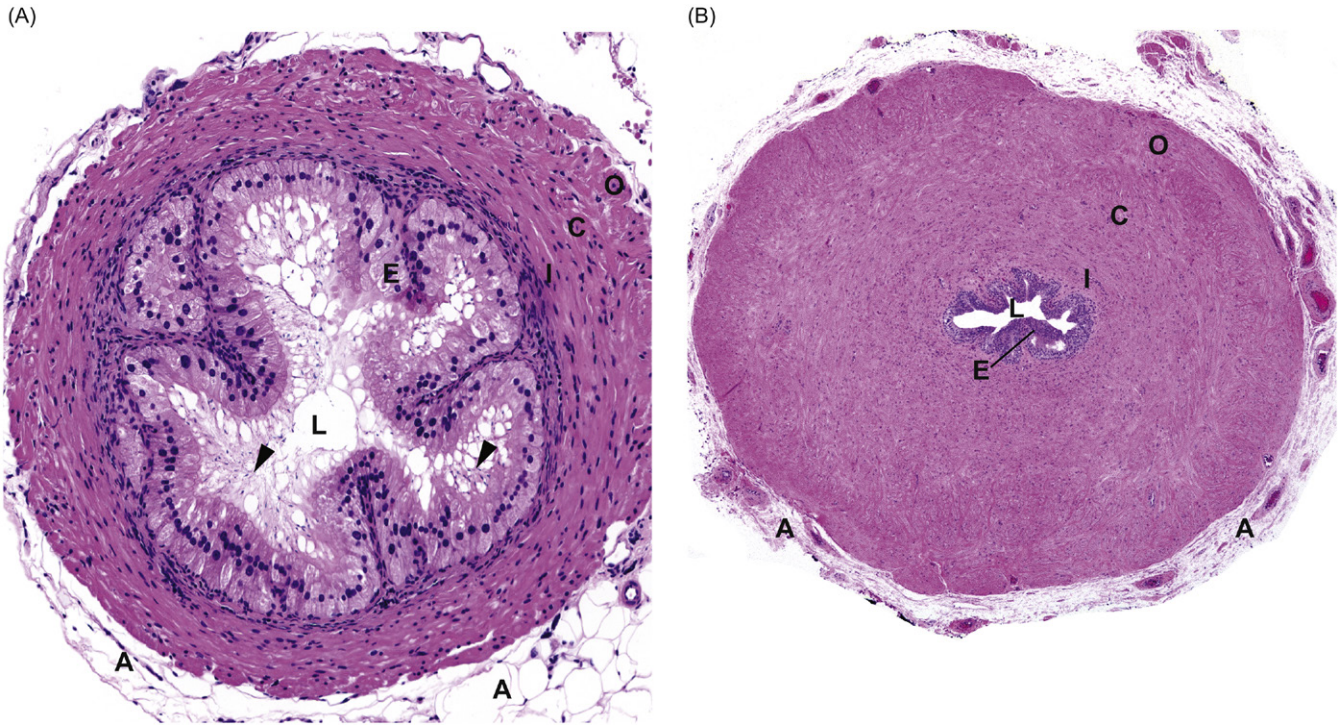

FIGURE 18.9 Vas deferens. (A) Rodent (mouse). The rodent vas deferens is lined by ciliated columnar epithelium (*E*) with a thick middle circular smooth muscle layer (C) and inner (I) and outer (O) longitudinal smooth muscle layers and adventitia (*A*). Sperm (arrowheads) are present in the lumen (L). (B) Human. The human vas deferens is also lined by a ciliated columnar epithelium (E) with a very thick muscle wall with a circular layer (C), inner (I) and outer (O) layer, and adventitia (A).

epithelium often appears crowded. In aged mice, there are cells with large, polyploid nuclei within the epithelium of the vas deferens and epididymis.

Seminal Vesicles (Vesicular Glands)

GROSS ANATOMY

The seminal vesicles are one of the accessory sex glands common to rodents and humans. In all three species, they are large, bilateral, sacculated glands dorsolateral to the urinary bladder. In rodents, each gland is up to 25 mm long, and curled with caudally directed anterior tips. The coagulating gland, which is the anterior prostate in rodents, is bilaterally attached to the lesser curvature of the seminal vesicles (Fig. 18.1). In aged rodents, the seminal vesicles may become very large and may occasionally undergo unilateral or bilateral torsion with compromise of venous or arterial blood flow. The combined secretions of the seminal vesicles, coagulating gland, and contributions from the bulbourethral gland form the seminal fluid in rodents. The combined secretions of the seminal vesicles and coagulating gland form the seminal plug in male rodents. In the human, the seminal vesicles measure 6 cm × 2 cm and, the seminal fluid is composed of the combined secretions of the seminal vesicles and prostate.

Need-to-know

- The thick layers of smooth muscle in the rodent and human vas deferens are used for expelling sperm.

HISTOLOGY

In the rodent, the seminal vesicle is lined by smooth muscle and connective tissue stroma with a columnar epithelium that forms characteristic branching mucosal folds. The branching of the mucosal folds is normal and should not be confused with hyperplasia. The epithelial cells contain conspicuous secretory granules with basal nuclei. The lumen contains characteristic, intensely eosinophilic secretions (Fig. 18.10).

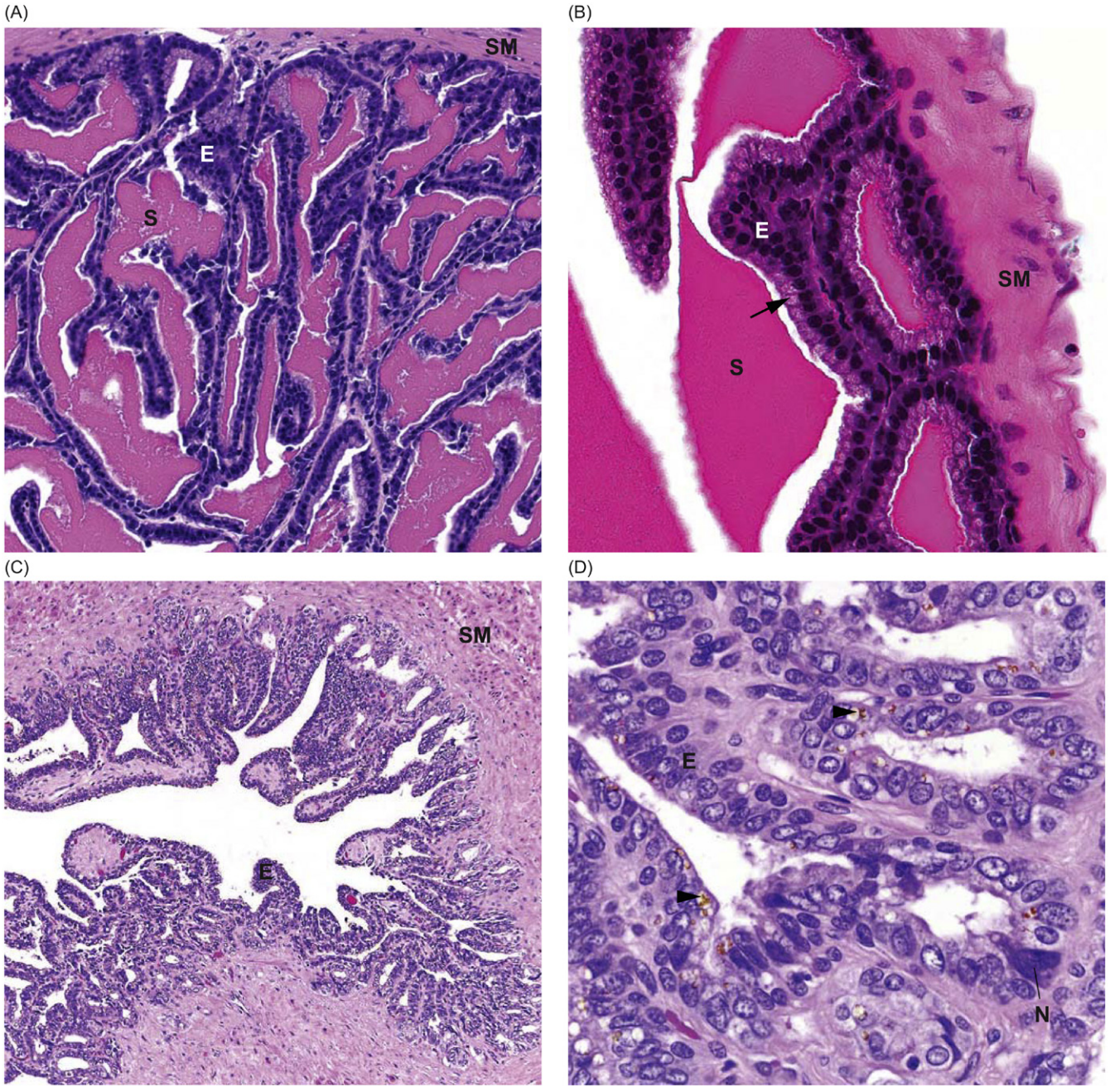

FIGURE 18.10 Seminal vesicles. (A, B) Rodent (mouse). The rodent seminal vesicle wall is composed of smooth muscle (SM) and tall columnar epithelium (E) that forms characteristic branching mucosal folds and intensely eosinophilic intraluminal secretions (S). (B) High magnification of tall columnar epithelium (E) with secretory granules (arrow) and basal nuclei. (C, D) Human. Each human seminal vesicle is composed of a prominent smooth muscular wall (SM) and consists of a lumen with complex outpouchings of folded mucosa with a honeycombed appearance. (D) The epithelium (E) consists of pseudostratified tall columnar, secretory cells that contain intracytoplasmic lipid droplets, often have yellow-brown lipofuscin granules (arrowheads), and variably sized nuclei (N) including aptly named "monster cells."

Need-to-know

- In rodents, the branching of the mucosal folds is normal and should not be confused with hyperplasia.
- In all three species, the lumen contains characteristic, intensely eosinophilic secretions.
- Human epithelial cells often contain lipofuscin granules.

When the gland is distended with secretory material, the folds stretch and shorten. The seminal vesicles of aged mice may retain secretions and enlarge, either unilaterally or bilaterally. They may also become blocked and distended in mouse models of prostatic cancer. This dilatation may result in abdominal distention. Contraction (atrophy) of one or both seminal vesicles is also common. Rodents may present with dilatation of one seminal vesicle and contraction of the other seminal vesicle. In rats, lipofuscin deposits within the epithelial cytoplasm increase with age.

The human seminal vesicles develop as diverticula of the vasa deferentia. They consist of a lumen into which complex outpouchings of mucosa secrete a mucinous product. The pseudostratified epithelium consists of tall, columnar cells, some of which have a yellow-brown cytoplasmic pigment and variably sized nuclei. Rare, markedly enlarged, pleomorphic epithelial cell nuclei are normal, and should not be interpreted as neoplastic. The smooth muscle wall of the seminal vesicles consists of an inner circular layer and an outer longitudinal layer. The muscle conducts secretions into the urethra during ejaculation (Fig. 18.10).

Prostate Gland

Gross Anatomy

The mouse prostate gland is divided grossly into four distinct paired lobes: Anterior, dorsal, ventral, and lateral. The dorsal and lateral lobes are sometimes grouped together as the dorsolateral lobe. The lobes surround the urethra and are invested in a membrane. They can be difficult to identify without the aid of a dissecting microscope; however, once the entire tract, as well as the surrounding membrane, is removed, each has a characteristic shape and location if viewed under a dissecting microscope (Fig. 18.11). The dorsal lobe is around the urethra. It has a butterfly shape. On the ventral aspect of the tract, the ventral lobe appears clear, gelatinous, and leaf-shaped and is located above the urethra and toward midline. It is flanked by both lateral lobes, which start dorsally and then incompletely wrap around the urethra ventrally. The anterior prostate is synonymous with dorsocranial/cranial prostate and is also known as the coagulating gland. The anterior prostatic lobe is located cranial to the other lobes and is attached to the lesser curvature of the seminal vesicles. It is tubular in shape and grossly appears clear and gelatinous.

The rat prostate gland consists of three paired lobes including the ventral, dorsolateral, and anterior. The paired ventral lobes are readily visible grossly. They lie along the ventrolateral surface of the urinary bladder. The dorsolateral lobes are wrapped around the proximal end of the urethra and surround the excretory ducts of the seminal vesicles and coagulating gland at the terminus of the vas deferens. The dorsolateral lobe contains ~50 ducts that open into the prostatic urethra. As in mice, the anterior lobe adheres to the concave side of the seminal vesicles.

The human prostate gland is situated between the base of the urinary bladder and the rectum. It weighs ~20 g in young adults, but may increase to 30–40 g by age 60 due to benign prostatic hyperplasia. The prostate gland measures ~3.5–4 cm × 4.5 cm × 3 cm. The urethra, into which the prostate gland and the ejaculatory ducts drain, passes through the prostate. In contrast to the multilobed rodent prostate, the human prostate gland is a single organ that is organized as histologically similar zones by the pattern of branching of the prostate gland ducts (Fig. 18.11). The zones have a complex three-dimensional structure. The central zone surrounds the urethra. The transition zone, which is the site of the benign condition termed nodular hypertrophy, is predominantly anterior to the urethra. Conversely, the peripheral zone, which is the site of the majority of cases of prostate gland carcinoma, is located posterior to the urethra. Separated from the rectum by no more than a thin fibromuscular stroma, the peripheral zone is relatively accessible for transrectal biopsies to sample the prostate gland for prostatic adenocarcinoma.

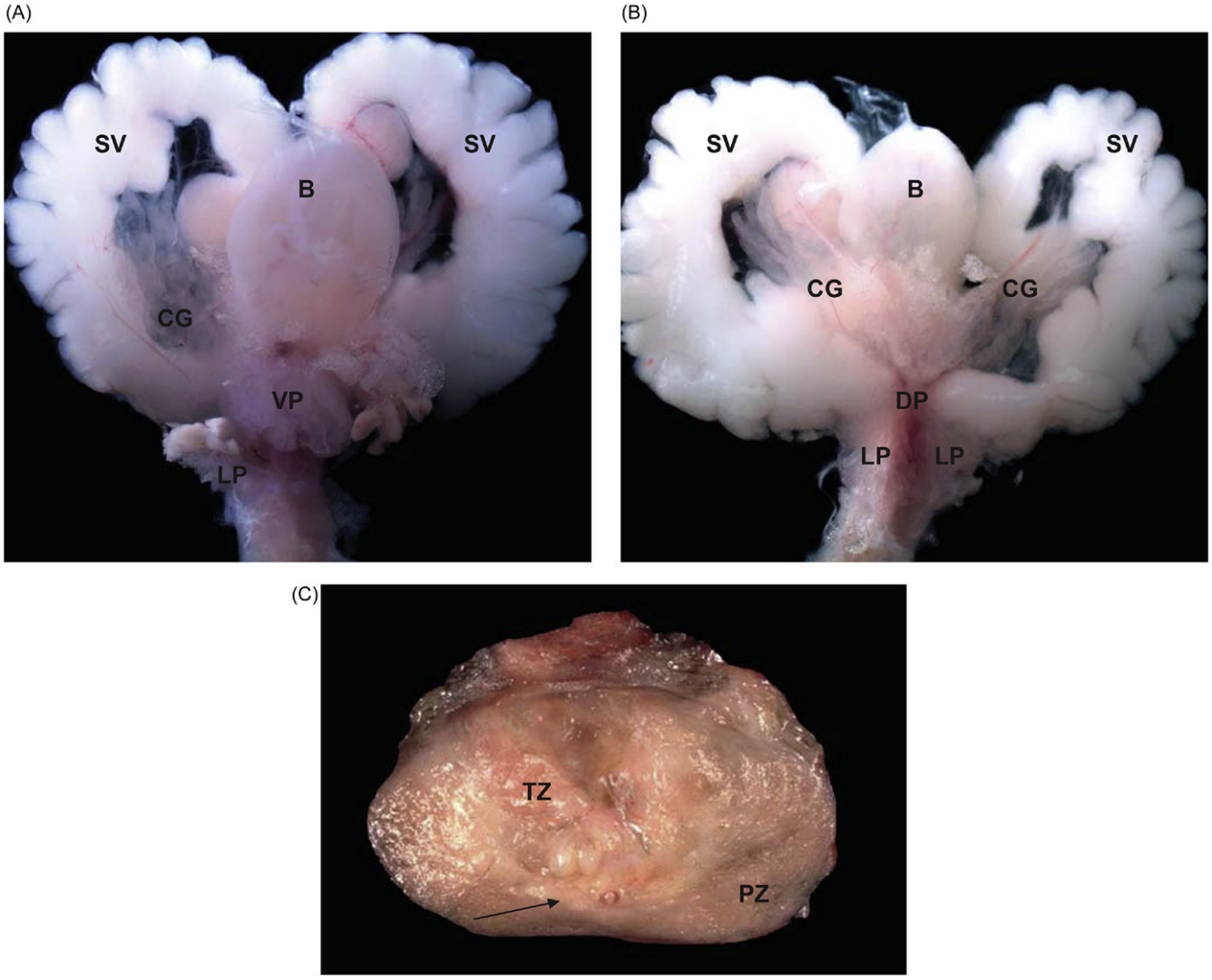

FIGURE 18.11 Gross prostate gland. (A) Rodent (mouse) ventral view. (B) Rodent (mouse) dorsal view. The rodent prostate gland is divided into four distinct lobes: The coagulating gland (CG) (anterior), dorsal prostate gland (DP), lateral prostate gland (LP), and ventral prostate gland (VP). (C) Human prostate. The human prostate gland is a single alobular structure with three zones. The transition zone (TZ) is demarcated from the peripheral zone (PZ) by fibrous tissue (arrow). The central zone (CZ) is located in the posterior and medial aspect of the prostate gland (not pictured).

Need-to-know

- The mouse prostate is composed of four paired lobes located circumferentially around the urethra and caudal to the urinary bladder.
- The rat prostate has three distinct gross lobes: ventral, dorsolateral, and coagulating gland (anterior).

HISTOLOGY

Histologically, the lobes of the rodent prostate gland are separated from one another by a mesothelium-lined thin, delicate capsule.
The glandular prostate is separated from the mesothelium-lined capsule by loose fibroadipose tissue that contains major vessels, nerves, and ganglia. The individual glands or acini within each lobe are surrounded by a sparse smooth muscle stroma embedded in loose connective tissue. The ductules that constitute each lobe are surrounded by a few layers of spindle cells (a mix of fibroblasts and smooth muscle cells) and eosinophilic collagen. Overall, the rodent prostate gland has a modest stromal component compared to that of the human prostate gland (Fig. 18.12).

The individual lobes of the rodent prostate gland have distinctive histological characteristics (Fig. 18.13). In mice, the anterior prostate (coagulating gland) is lined by a cuboidal-to-columnar epithelium with a papillary or cribriform

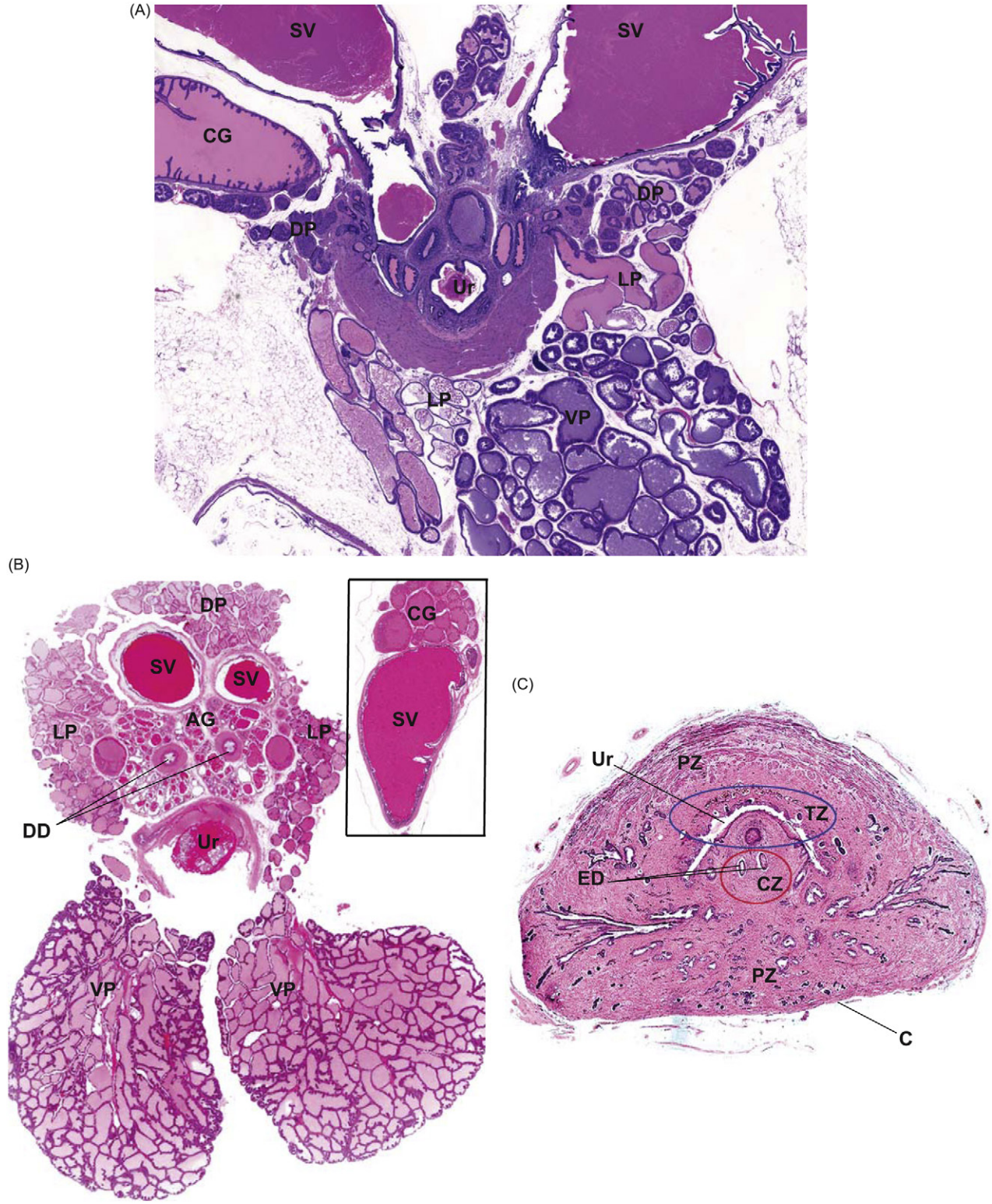

FIGURE 18.12 Prostate gland. (A) Mouse. The mouse prostate gland is divided into histologically distinct lobes which surround the urethra (Ur): Seminal vesicle (SV), coagulating gland (anterior) (CG), dorsal (DP), lateral prostate gland (LP), and ventral (VP) prostrate lobes. (B) Rat. The rat prostate gland is also divided into histologically distinct lobes. Mid-transverse section: Ampullary glands (AG), vas deferens (DD), dorsal prostate gland (DP), lateral prostate gland (LP), and ventral prostate. (Inset) Rat seminal vesicle (SV) and coagulating gland (CG). (C) Human. The human prostrate is alobular, but is divided into three concentric zones. The central zone (CZ, red circle) encircles the ejaculatory ducts (ED), the transition zone (TZ, blue circle), which surrounds the prostatic part of the urethra (Ur), and the peripheral zone (PZ) which makes up the bulk of the gland. The human prostate gland is surrounded by a capsule (C).

Need-to-know

- The human prostate is grossly divided into zones which are not clearly demarcated, but may be characterized by specific predisposition to disease.
- The rodent prostate lobes are invested and separated by a thin mesothelial-lined membrane, whereas the human prostate is surrounded by a capsule.

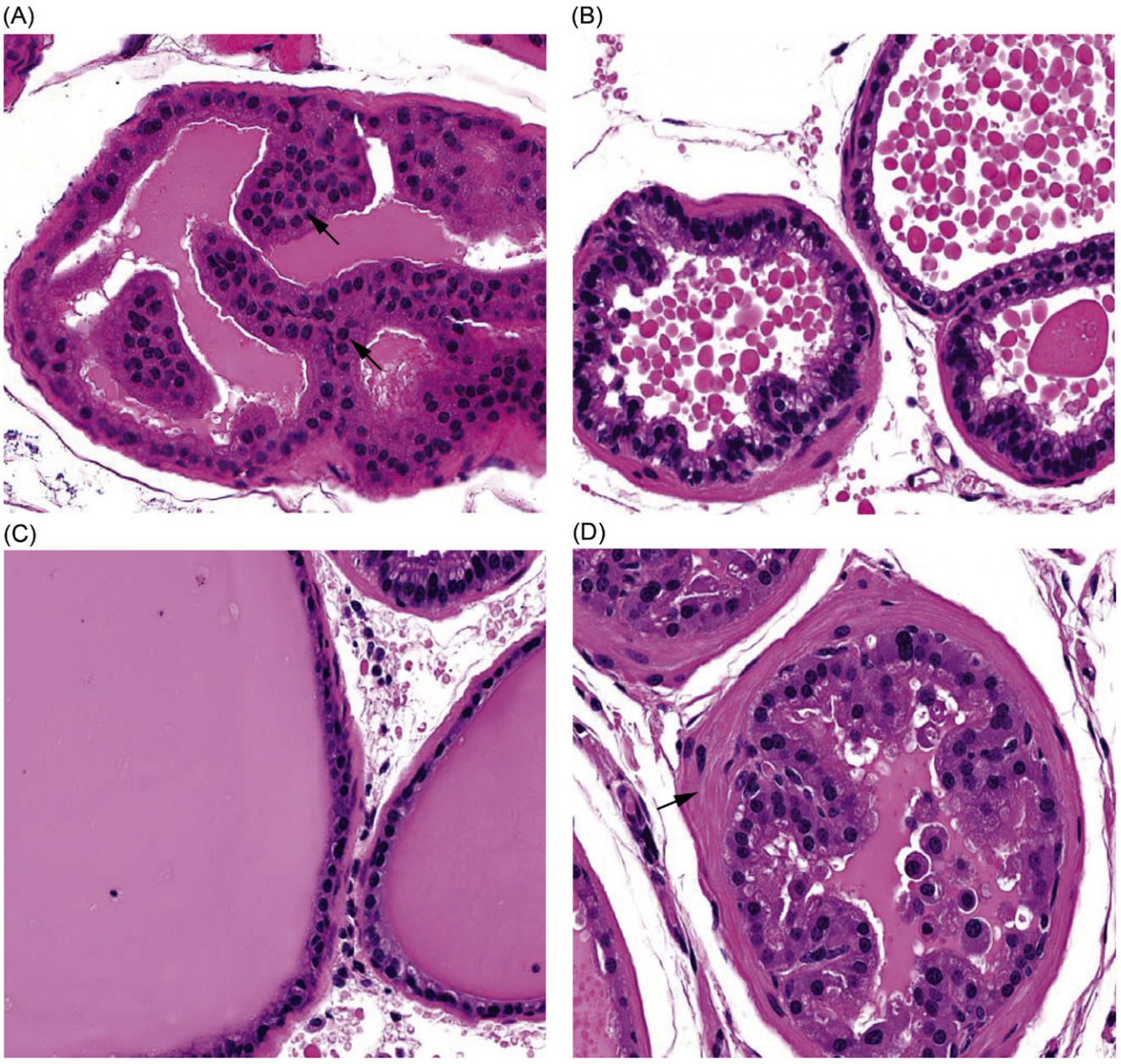

FIGURE 18.13 Mouse prostate gland. (A) Coagulating gland (anterior prostate): The epithelium is cuboidal-to-columnar with a papillary or cribriform growth pattern (arrows). The epithelial cells have an eosinophilic, granular cytoplasm with centrally located nuclei and the lumen contains abundant, homogenous, eosinophilic secretions. (B) Lateral prostate: Lined by mostly cuboidal to low columnar epithelium with sparse infolding, contains granular cytoplasm with amorphous, particulate, eosinophilic secretions. Epithelial cells have small, uniform, basally located nuclei. The glands are surrounded by peripheral loose connective tissue. (C) Ventral prostate: Lined by mostly cuboidal epithelium abundant luminal spaces contain homogenous, pale, serous secretions. Epithelial cells have small, uniform, basally located nuclei. (D) Dorsal prostate: Lined by columnar epithelium, with moderate infolding, which have granular cytoplasm and luminal homogenous, eosinophilic secretions. Epithelial cells contain centrally-to-basally located uniform nuclei. Individual glands are surrounded by a thick fibromuscular stroma (arrow) and peripheral loose connective tissue.

Need-to-know

- The rodent lobes of the prostate can be distinguished histologically, whereas the human prostatic regions are indistinguishable.
- Only the dorsal rodent prostate glands are surrounded by a fibromuscular stroma, whereas there is contractile fibromuscular stroma surrounding all the glands in the human prostate.
- In human prostate, it is common to find lamellated corpora amylacea and prostatic concretions, which are more common with increasing age.

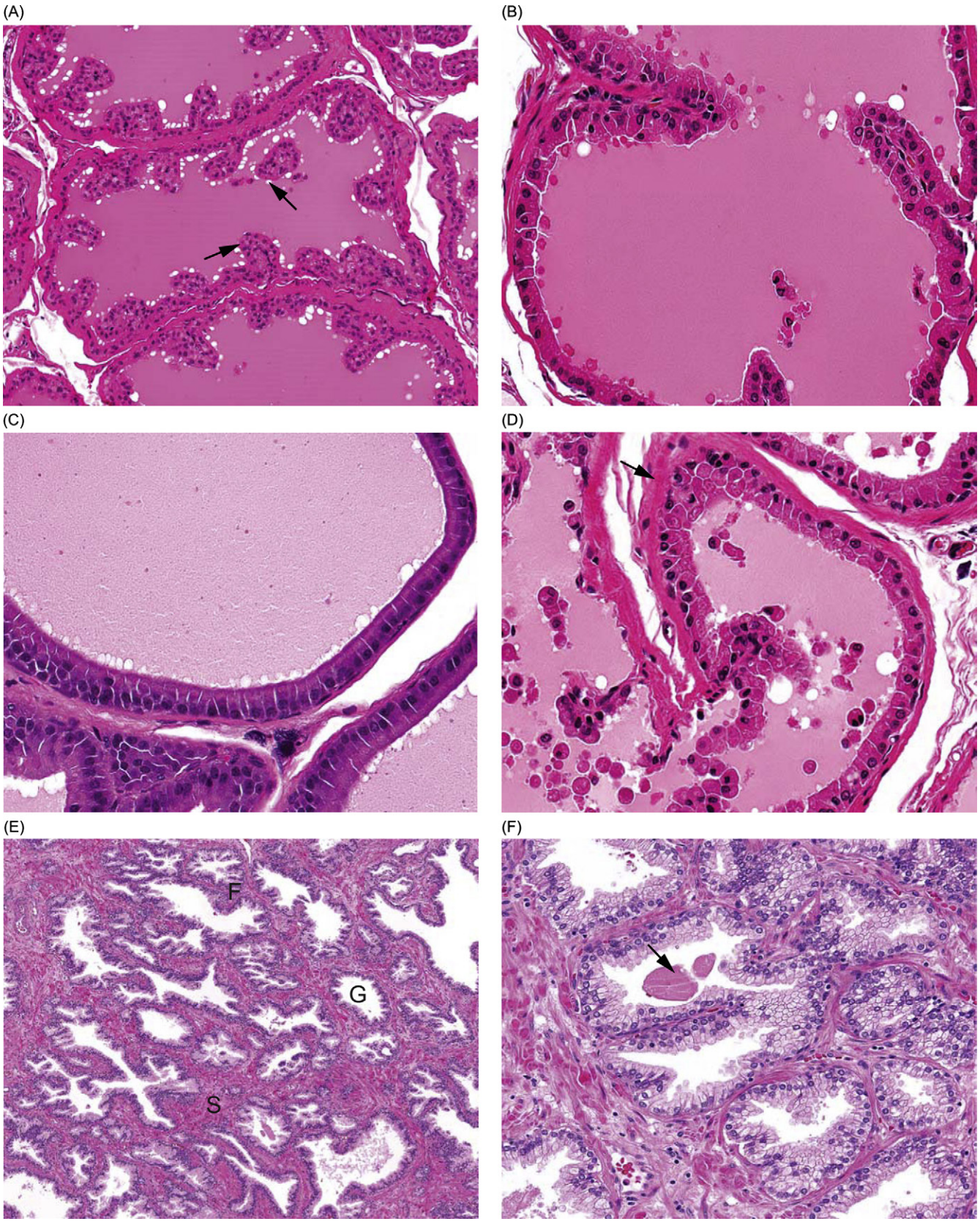

FIGURE 18.14 Rat and human prostate gland. (A–D) Rat. The rat prostrate lobes are histologically distinct. (A) Coagulating gland (anterior prostate): The epithelium is cuboidal-to-columnar with a papillary or cribriform growth pattern (arrows). The epithelial cells have an eosinophilic, granular cytoplasm with centrally located nuclei and lumens contain abundant, homogenous, eosinophilic secretions. (B) Lateral prostate: Lined by mostly cuboidal to low columnar epithelium with sparse infolding, and distinctive brush border with deep, eosinophilic secretions. (C) Ventral prostate: Lined by tall columnar epithelium with sparse infolding, and contain homogenous, pale, eosinophilic secretions. (D) Dorsal prostate: Lined by cuboidal-to-columnar epithelium, with characteristic cytoplasmic blebs and secretions that stain intermediate to the lateral lobe and ventral lobes. Individual glands are surrounded by a thin fibromuscular stroma (arrow). (E, F) Human. (E) The human prostate

growth pattern, with eosinophilic, granular cytoplasm, centrally located nuclei and abundant, homogeneous, eosinophilic secretions. The lateral prostate gland is lined by mostly cuboidal to low columnar epithelium with sparse infolding, and granular cytoplasm, and small, uniform, basally located nuclei, and amorphous, particulate, eosinophilic secretions. The lateral glands are surrounded by peripheral loose connective tissue. The ventral prostate gland is lined by cuboidal-to-columnar epithelium with sparse infolding and focal tufting, basally located nuclei, and abundant, homogeneous, pale, serous secretions. The dorsal prostate gland is lined by columnar epithelium with moderate infolding, and granular cytoplasm, basally located uniform nuclei, and homogeneous, eosinophilic secretions. Individual glands are surrounded by a dense fibromuscular stroma and peripheral loose connective tissue (Fig. 18.13). The height of the epithelium of the glands within the various lobes varies with the stages of the secretory cycle from cuboidal (quiescent) to columnar (active).

The rat prostate gland consists of three paired, anatomically and histologically distinct lobes: Anterior (coagulating gland), ventral, and dorsolateral (Fig. 18.14). As in mice, the coagulating glands are synonymous with the dorsocranial/cranial/anterior prostate. The glands histologically share a capsule with the seminal vesicles and are composed of a series of tubules lined by cuboidal-to-columnar epithelium with papillary or cribriform growth pattern. The epithelial cells have a distinct vacuolated basal cytoplasm. The ventral lobes are composed of closely packed acini, or alveoli surrounded by smooth muscle. Alveoli are lined by a single layer of tall columnar epithelial cells with basal nuclei and supranuclear clear areas, which are secretory, nonsecretory basal cells, and macrophage like cells with many lysosomes. Secretions stain lightly with eosin and appear pale pink. The dorsolateral prostrate lobes are composed of two distinct histological zones: The dorsal portion, which appears most similar to the coagulating gland and the lateral portion which resembles the ventral prostate. Acini from both portions are loosely arranged, separated by fibrous stroma. The epithelium throughout the dorsolateral lobe is cuboidal to tall columnar. The lateral portion has a distinctive brush border and deep eosinophilic secretions. The dorsal lobe has characteristic cytoplasmic blebs that are not seen in other lobes with secretions that stain intermediate to the lateral portion of the dorsolateral lobe and the ventral lobe (Fig. 18.14). In young rats, the dorsal and lateral portions of the dorsolateral lobe may be distinguished; however, as animals age, histological distinctions, such as apical cytoplasmic blebs in the dorsal epithelium, fade. Distinguishing between lobes is necessary when evaluating proliferative and neoplastic lesions as, similar to human, predilection for lobes varies. As in mice, the height of the epithelium of the glands within the various lobes varies with the stages of the secretory cycle from cuboidal (quiescent) to columnar (active).

In the human, prostatic glands (or acini) are irregularly shaped and embedded in a fibromuscular stroma (Fig. 18.14E and F). Histologically, the human prostatic glands consist of cuboidal-to-columnar epithelium composed of a luminal secretory cell layer subjacent to which is a layer of basal cells. Rare basal cells, which have a neuroendocrine phenotype, represent less than 1% of prostate gland epithelial cells. These three cell types have distinct immunophenotypes: Luminal secretory cells—KLK3/prostate-specific

◀ **FIGURE 18.14** (Continued) gland is composed of irregular branching glands (G) which are surrounded by a dense stroma (S) composed of fibroblasts, collagen, and smooth muscle. The mucosa forms branching folds (F) that give a papillary appearance lined by an epithelium composed of a luminal secretory layer of tall columnar cells, and a basal cell layer which lies on a basement membrane. (F) High magnification of the pseudostratified prostatic epithelium. An intralumenal concretion (arrow) is indicated.

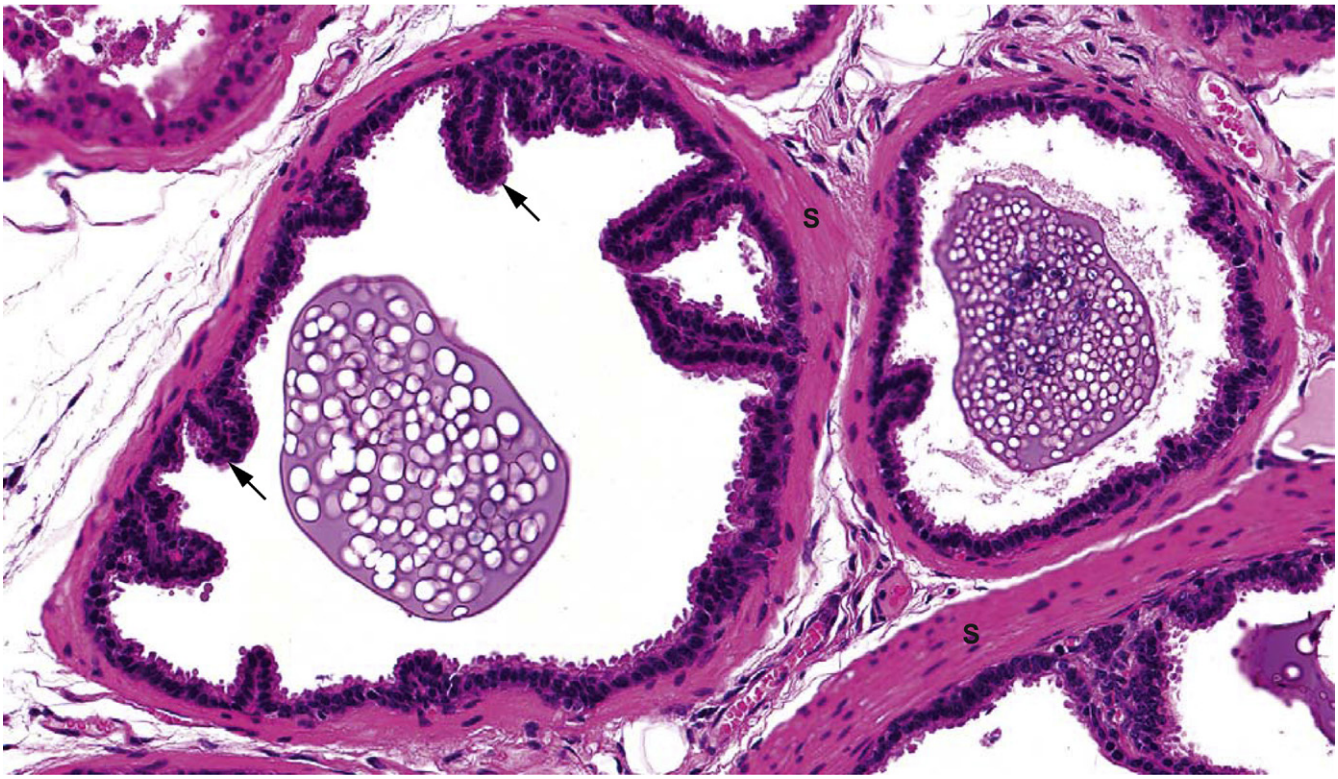

FIGURE 18.15 Rodent (mouse) ampullary glands. The rodent ampullary glands are lined by simple columnar epithelium with large, oval nuclei. The glands are distinct from prostate gland as they are surrounded by a dense fibromuscular stroma (S). The epithelium forms longitudinal folds (arrow). The glands contain homogenous, dense, eosinophilic, secretions with a characteristic vacuolated appearance.

Need-to-know

- Ampullary glands are unique to rodents; there is no human counterpart.
- The glands are distinct from prostate as they are surrounded by a dense fibromuscular stroma with characteristic vacuolated secretions.

antigen and KRT 8 (keratin 8); basal cells—KRT 5/6, KRT 10, KRT 14 (keratins 5/6, 10, and 14, respectively), and TP63/p63; and neuroendocrine cells—neurosecretory granule-associated proteins CHGB/chromogranin B and SYP/synaptophysin. Lamellated variably calcified eosinophilic aggregates of protein, termed corpora amylacea, can be found within some gland lumina. These may obstruct ducts and, quite rarely, predispose to prostatitis. Corpora amylacea are not seen in the rodent prostate.

Ampullary Glands

GROSS ANATOMY

Ampullary glands are found in rodents but not in humans. They are paired accessory, glandular, androgen-dependent outpouchings of the proximal vas deferens, one on each side. They encircle the vas deferens in rodents. Their secretions contribute to the formation of semen. They open into the ampullae at the level of the colliculus seminalis. Although there is no known human counterpart to the ampullary glands of rodents, it is important to be aware of their histologic appearance for proper interpretation when using animal models (Fig. 18.15).

HISTOLOGY

Ampullary glands are lined by cuboidal epithelium with large, oval nuclei. The glands may be distinguished from those of the prostate

gland as they are surrounded by a characteristic, dense, fibromuscular stroma. The epithelium forms longitudinal folds and the glands contain homogeneous, dense, eosinophilic secretions with characteristic vacuolization (Fig. 18.15).

Bulbourethral Glands

GROSS ANATOMY

In the rodent, the bulbourethral glands are androgen-regulated accessory glands that are analogous to Cowper's glands in humans. They are located near the base of the penis, embedded within the ischiocavernosus and bulbocavernosus muscles. They are paired and consist of a main body, tail, and secretory duct. They are located more distally along the urethra and are separated more distinctly from the prostate gland than in humans. The main body is embedded in connective tissue lateral to the urethral diverticulum, and surrounded by the bulbocavernosus muscle. The tail is located between the ischiocavernosus and bulbocavernosus muscles. The excretory ducts open into the urethra cranial to the urethral diverticulum in mice and the urethral bulb in rats. Based on the location of the glands (within and between muscle), it is possible to misinterpret bulbouretheral tissue as metastatic carcinoma.

HISTOLOGY

Histologically, the bulbourethral glands are multilobular. Each lobule is composed of acini that open into a centrally located canal. A thin capsule of fibrous connective tissue surrounds and separates the acini. In mice, the glandular acini are highly arborized and lined by tall columnar epithelium. In the secretory state, the epithelium has abundant, foamy cytoplasm, and in the resting state, the cytoplasm is eosinophilic and finely granular. The secretory cells are found mainly in the body, and the resting cells are found in the tail (Fig. 18.16). The ductular epithelium is cuboidal. Older mice may develop cystic bulbourethral glands that may result in swelling of the perineal region and impaired reproductive performance. Bacterial infections with *Staphylococcus aureus* and *Pasteurella pneumotropica* are also common.

In rats, the bulbourethral gland is a pear-shaped tubuloalveolar gland, producing a mixture of mucous and seromucous material. The epithelium is composed of a single layer of tall, closely packed pyramidal cells that appear faintly basophilic and contain discrete secretory granules (Fig. 18.16).

In humans, mucin-expressing bulbourethral glands (Cowper's glands) are situated adjacent to and drain into the membranous urethra. These glands consist of closely juxtaposed acini composed of polygonal epithelial cells with abundant clear cytoplasm (Fig. 18.16). Although bulbourethral glands are virtually never the site of pathological changes in the human, expression of transgenes in genetically engineered mouse models may produce pathological changes in rodent bulbourethral glands.

Preputial Glands

GROSS ANATOMY

The preputial glands are modified sebaceous glands that are unique to rodents. The paired preputial glands are analogous to clitoral glands in female rodents. Grossly, they are large, flattened, tan-yellow, and located in the caudal subcutaneous tissue just lateral to the base of the penis (Fig. 18.17). Each gland is up to 20 mm long and 5–8 mm wide in the sexually mature rat and weighs ~70–150 mg in older rats.

HISTOLOGY

Glands are lobulated and consist of a connective tissue capsule that surrounds large, cavernous ducts lined by stratified squamous epithelium

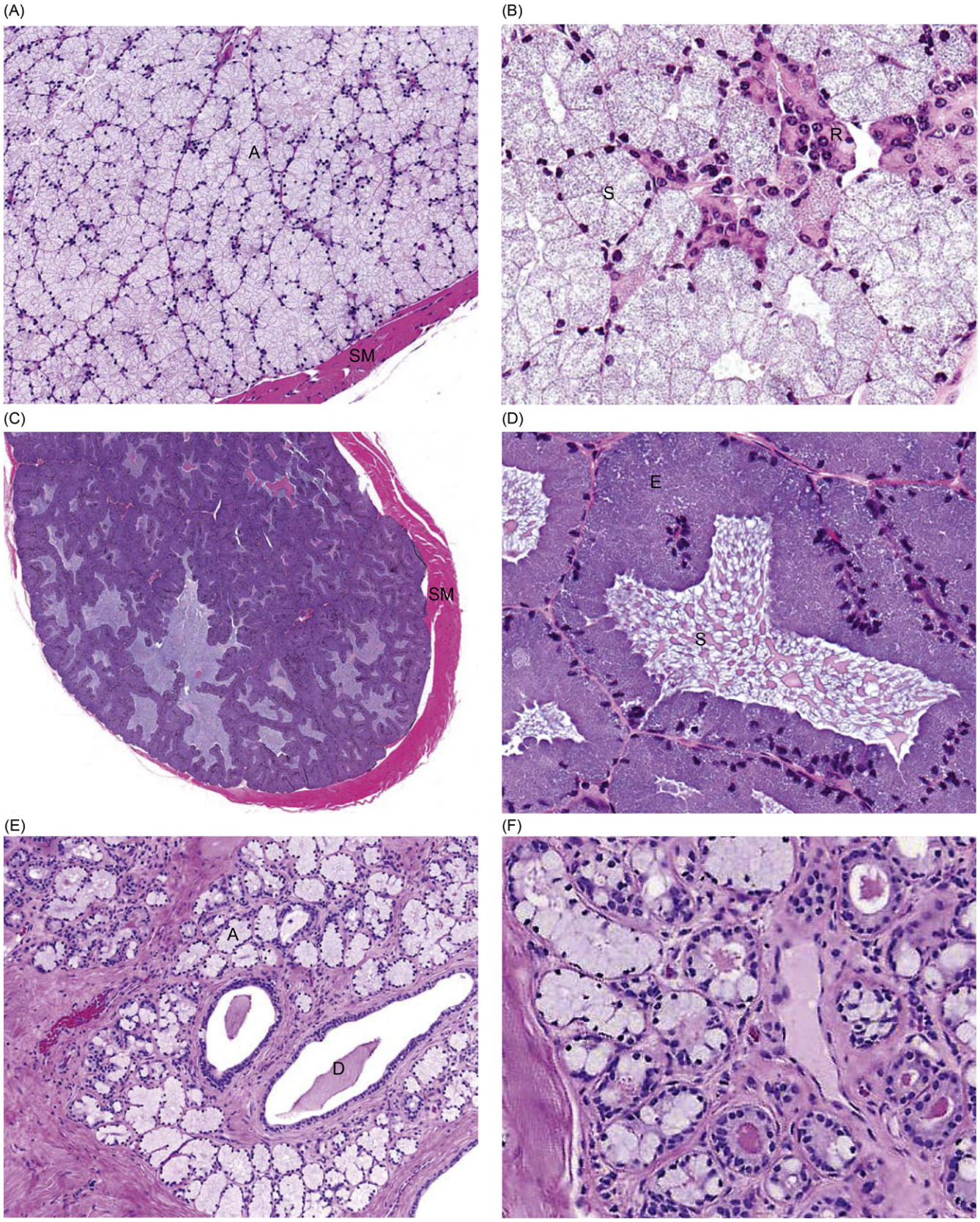

FIGURE 18.16 Bulbourethral gland (Cowper's gland). (A) The mouse bulbourethral gland consists of acini (*A*) lined by tall columnar epithelium embedded in skeletal muscle (SM). (B) High magnification of mouse bulbourethral gland with eosinophilic, foamy cytoplasm in the secretory state (S) and eosinophilic finely, granular cytoplasm in the resting state (R). (C) Rat bulbourethral glands are pear-shaped and embedded in skeletal muscle (SM). (D) High magnification of rat bulbourethral gland with acini composed of a tall pyramidal epithelium (E) that appears basophilic with discrete secretory granules and produces a seromucous secretion (S). (E) The human bulbourethral glands have lobular arrangement of centrally located ducts (D) surrounded by compact acini (A) with foamy or clear cells. (F) High magnification of human bulbourethral gland.

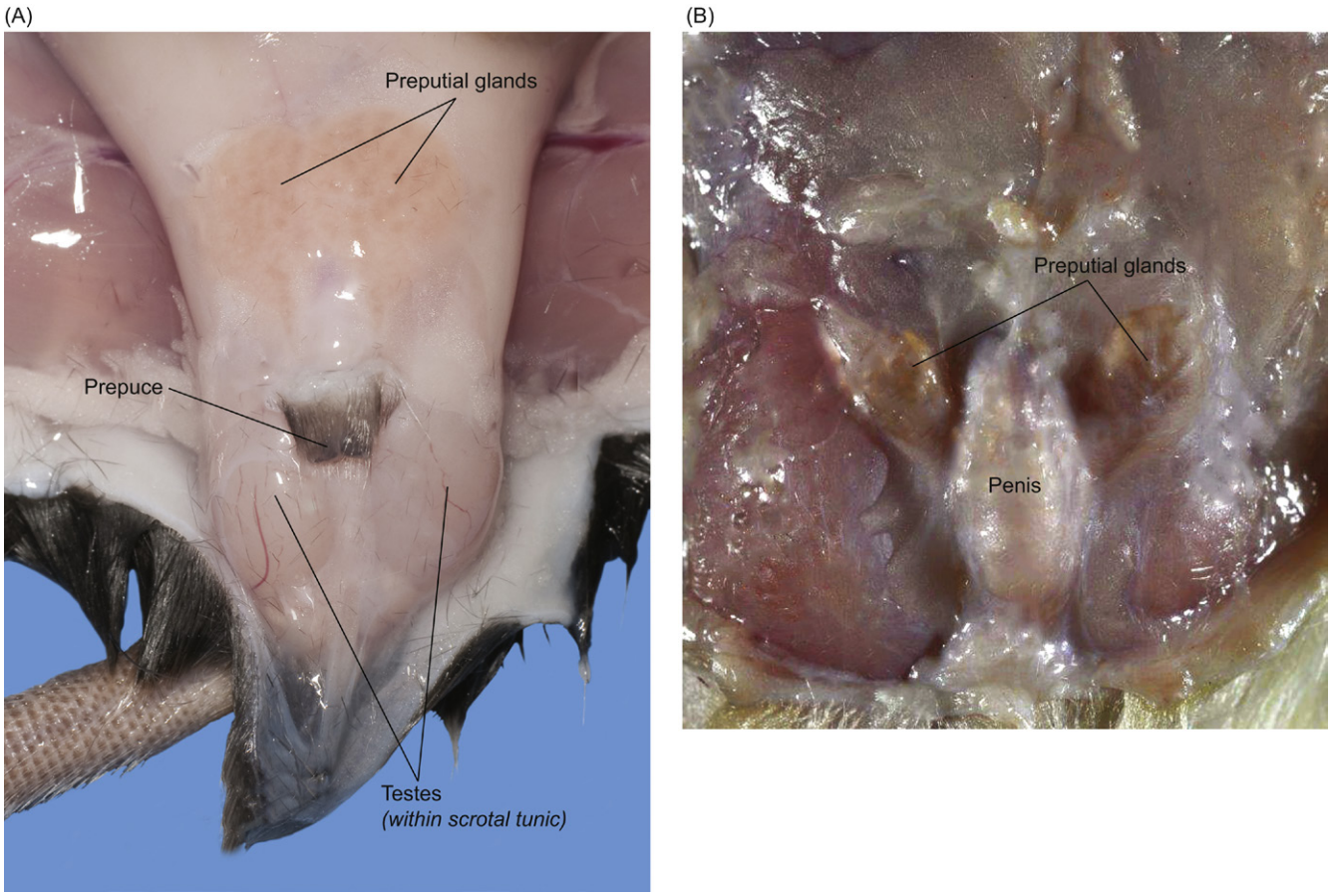

FIGURE 18.17 Rodent preputial glands. (A) Mouse. (B) Rat. Rodents have paired preputial glands located in the subcutaneous tissue lateral to the penis. They are leaf-shaped, flat, and yellow-brown. Scrotal skin has been reflected to reveal the testes in mice.

and acini (Fig. 18.18). The excretory ducts are continuous with a central duct that extends the length of the entire gland. The acini are composed of eosinophilic, pale, foamy, secretory sebaceous cells with dark nuclei and peripheral, flat, elongated basal cells. In rats, the sebaceous cells have characteristic eosinophilic secretory granules (Fig. 18.18). The preputial glands are prone to bacterial infection and subsequent abscessation. Preputial swellings (representing abscesses or proliferative lesions) present as firm masses within the subcutaneous tissues lateral to the penis.

Marked enlargement of the glands due to ductal ectasia, hyperkeratosis, and cyst formation may also occur. The incidence of these changes increases with age. In addition to infectious lesions, a spectrum of proliferative and neoplastic changes develops with age in many strains of rats.

URETHRA

GROSS ANATOMY

In all three species, the urethra extends from the trigone of the urinary bladder to the external urethral orifice (urethral meatus). The rodent urethra is divided into the prostatic/membranous and penile urethra. The prostatic/membranous urethra is thin and may be seen in close proximity to the prostate, seminal vesicles, coagulating gland, and vas deferens in *en bloc* sections (Fig. 18.19).

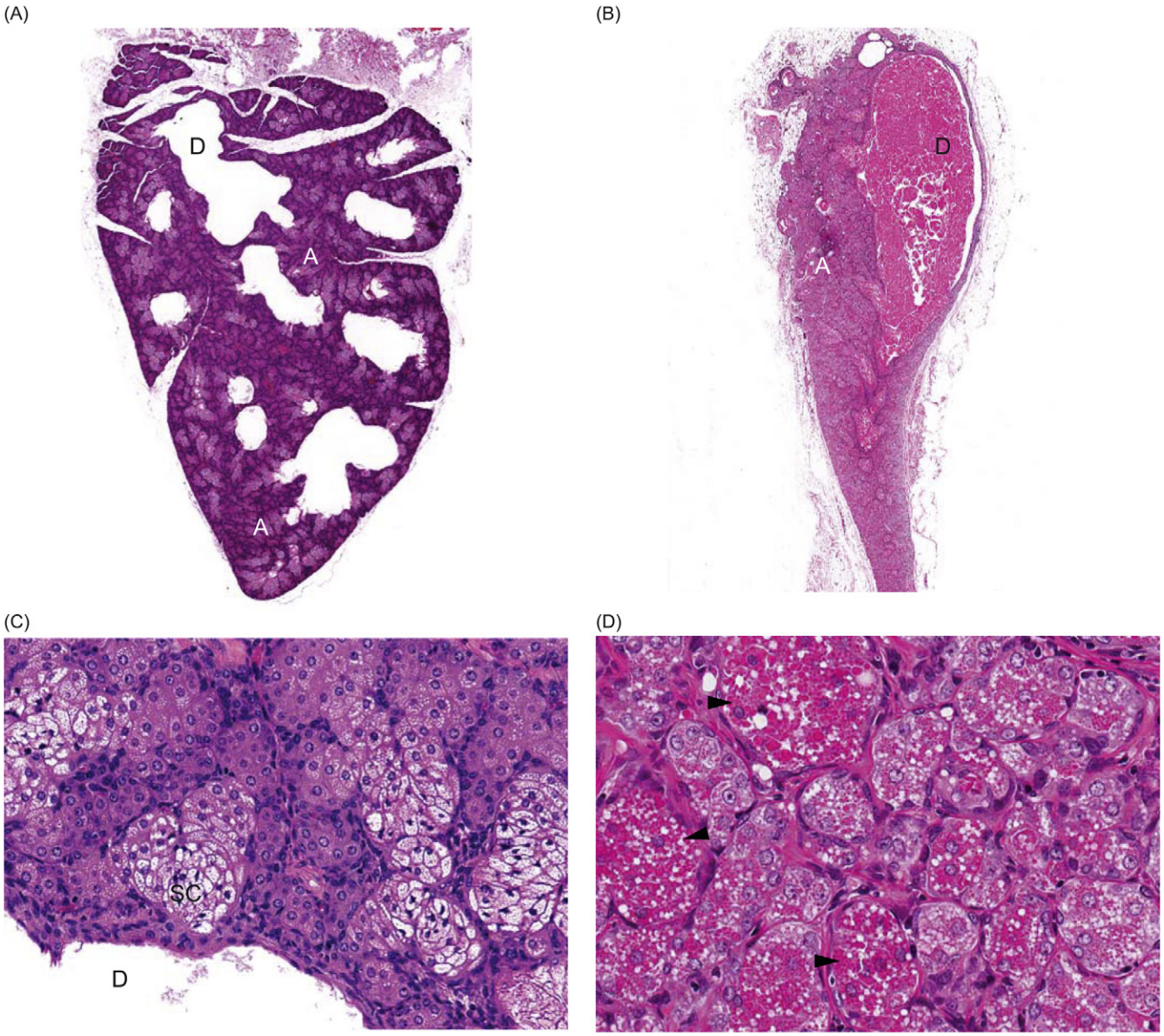

FIGURE 18.18 Rodent preputial glands. (A, C) Mouse. (B, D) Rat. The mouse preputial glands are composed of acini (*A*) and large, cavernous, excretory ducts (D). (C) At high magnification, mouse preputial glands are composed of sebaceous secretory cells (SC) forming acini and large, cavernous, excretory and lateral ducts (D) lined by squamous epithelium. (B) The rat preputial glands are composed of acini (A) and lateral excretory ducts which empty into a large central duct (D). As in mice, the ducts are lined by stratified squamous epithelium. (D) At high magnification, acini are composed of modified sebaceous glands that have prominent eosinophilic granules (arrows).

Need-to-know

- The preputial glands are prone to enlargement and subsequent abscessation, ductal ectasia, hyperkeratosis, and cyst formation.
- There is no human counterpart to the rodent preputial glands.

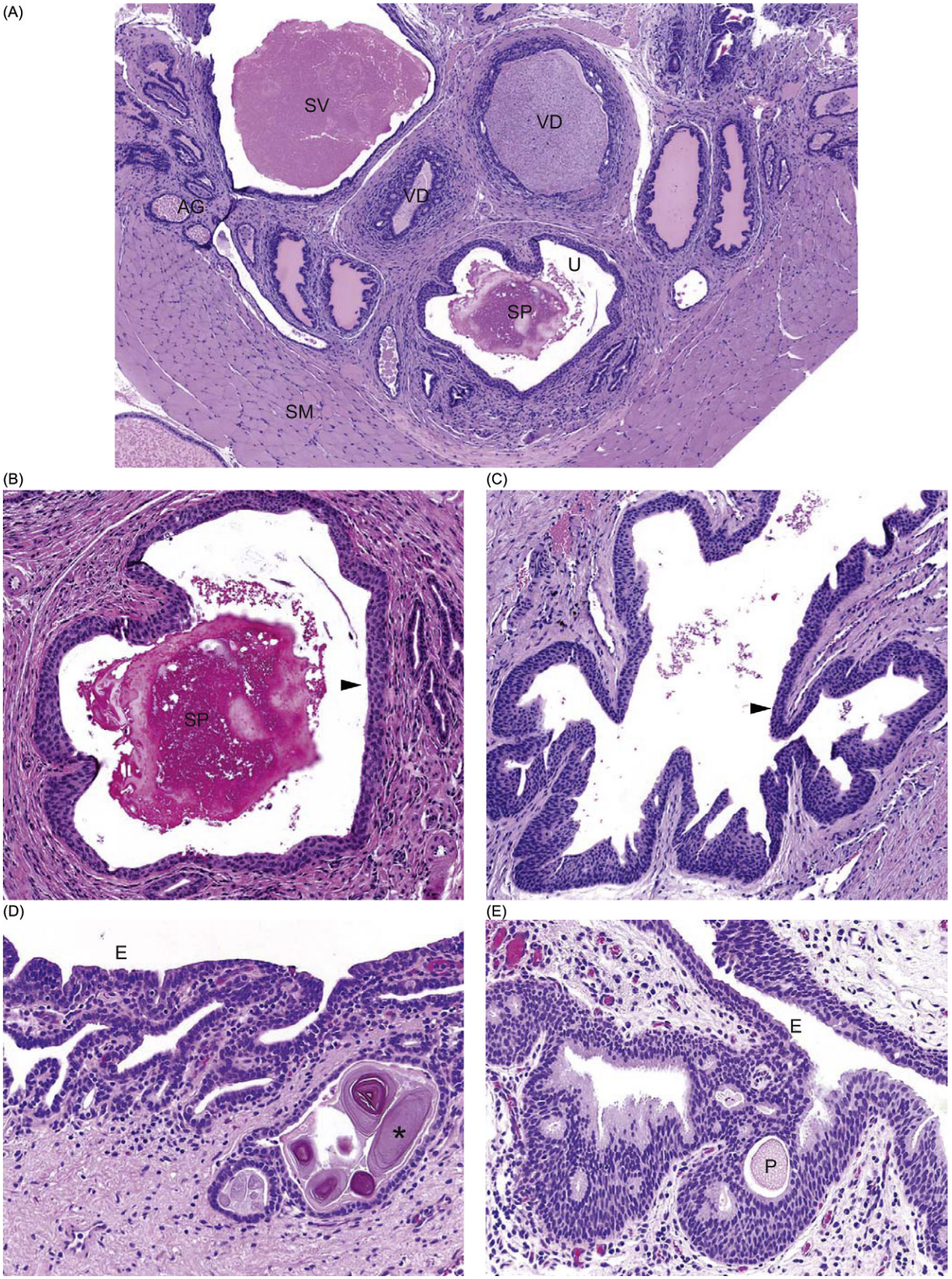

FIGURE 18.19 Urethra. (A) *En bloc* section of rodent (mouse) prostatic urethra (U) with neighboring ampullary glands (AG), vas deferens (VD), seminal vesicle (SV), and seminal plug (SP) within the lumen. The rodent urethra is surrounded by smooth muscle (SM). (B) High magnification of rodent (mouse) prostatic urethra with a seminal plug (SP) within the lumen. The rodent prostatic urethra is lined by transitional epithelium (arrowhead). (C) The rodent (mouse) penile urethra is located below the os penis and is lined by transitional epithelium (arrowhead). (D) The human prostatic urethra is lined by transitional or columnar epithelium (E). The underlying glands contain lamellated corpora amylacea (*). (E) The human penile urethra is lined by stratified columnar or transitional epithelium (E). The external opening (urethral meatus) is lined by stratified squamous epithelium. Periurethral glands (P) secrete mucus into the urethral lumen.

The penile urethra extends through the penis, where it exits at the tip of the glans penis. The human urethra has three segments—the prostatic, membranous, and penile urethra.

HISTOLOGY

The lumen of the rodent urethra is lined by a transitional epithelium (urothelium). The external penile urethral orifice is lined by stratified squamous epithelium. The lamina propria contains loose connective tissue that decussates with striated muscle.

In humans, transitional epithelium (urothelium) and nonkeratinizing stratified squamous epithelium, which becomes more prominent in the distal urethra, line the urethra. The urethral meatus at the distal penis is lined by stratified squamous epithelium. The periurethral glands (glands of Littré) and the bulbourethral glands lubricate the urethra with mucoid secretions (Fig. 18.19D and E).

Periurethral glands are small mucus-secreting glands that drain into the urethra. In rodents, they are located in the suburethral tissue of the membranous urethra distal to the prostatic ducts. They may be found within samples of rodent prostate gland and other accessory tissues. Some mouse strains contain a urethral diverticulum that is located near the posterior aspect of the pelvic canal and is lined by transitional epithelium. This should not be confused with the bulbourethral glands, which are located at the same anatomic level. In the rodent, the combined secretions of the seminal vesicles, coagulating glands form a coagulum or seminal plug that can be found incidentally in any part of the urethra or urinary bladder of the male. The female counterpart is the copulatory plug located in the vagina briefly after mating. The copulatory plug prevents the outflow of semen from the vagina and thus aids in fertilization. The plugs are composed of homogeneous, amorphous to granular, eosinophilic secretory material that often contains mature sperm (Fig. 18.20). In humans, the periurethral glands are adjacent to and drain into the penile urethra.

Penis

GROSS ANATOMY

In all three species, the penis consists of the root, body, and glans covered on its surface by skin. In adult rodents, the proximal body and distal glans meet at a right angle bend. The rodent penis is covered by a prepuce (Fig. 18.17).

HISTOLOGY

In rodents, the penis is composed of the penile or distal portion of the urethra, vascular erectile tissue (the cavernae corporum cavernosum and the corpus spongiosum), and the orifice of the penis. In contrast to humans, rodents have an os penis made of bone that is located proximally and ends distally in the tip of the glans as the male urogenital mating protuberance (MUMP) composed of fibrocartilaginous tissue (Fig. 18.21). In mice, the MUMP extends ~1 mm beyond the urethral meatus. This is in contrast to the rat penis, which is blunt distally as the fibrocartilaginous MUMP is locally internalized. The rodent penis is covered by the prepuce which encloses the glans and is covered externally by stratified squamous epithelium that contains hair follicles (filiform hairs).

In the rodent, focal aggregates of lymphocytes are relatively common in the organs of the male reproductive tract; however, these inflammatory cells are not considered functionally significant.

The human penis is lined by skin and contains three cylindrical portions of erectile tissue—paired corpora cavernosa and a corpus spongiosum that partially surrounds the penile urethra (Fig. 18.21). The human glans penis is variably covered by a prepuce composed of outer keratinized, nonhaired squamous mucosal epithelium, lamia propria, smooth muscle, and inner mucosal epithelium.

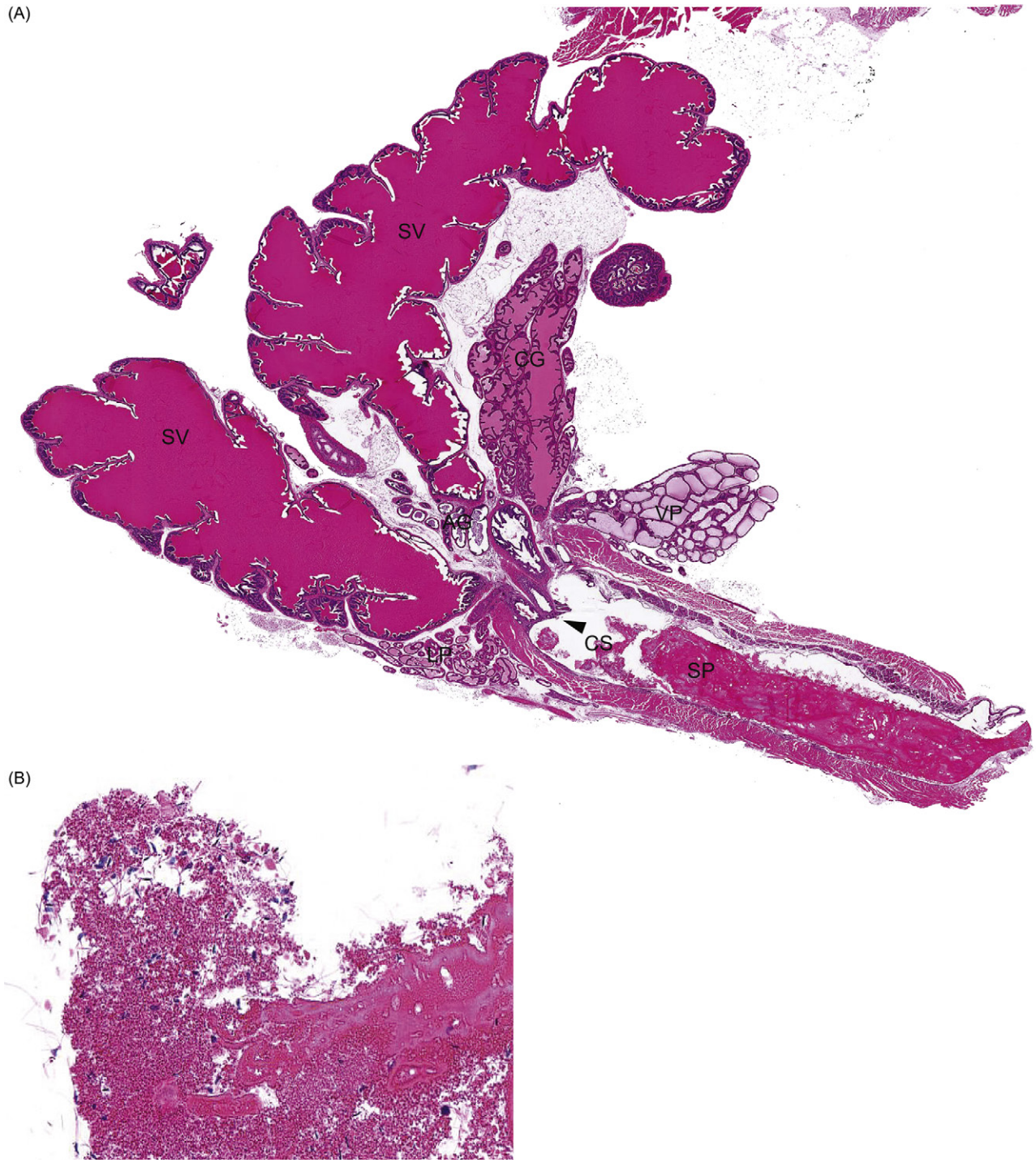

FIGURE 18.20 Rodent (mouse) colliculus seminalis and seminal plug. (A) The rodent (mouse) coagulum (seminal plug) (SP) is composed of secretions from the accessory sex glands. Here, it is shown at the transition of the prostatic/membranous to penile urethra near the colliculus seminalis (CS). The mucosa of the CS is thicker than the rest of the urethra and should not be mistaken for mucosal proliferation. In the rodent, the combined secretions of the seminal vesicles (SV) and coagulating gland (CG) form a coagulum or plug that can be found incidentally in any part of the urethra or urinary bladder of the male and also in the vagina of the female. The ventral prostate gland (VP), lateral prostate gland (LP), and ampullary glands (AG) are indicated. (B) High magnification of the coagulum with acellular eosinophilic secretions admixed with mature sperm.

Need-to-know

- The coagulum (seminal plug) is formed from combined secretions of the seminal vesicles and the coagulating glands (anterior prostate).
- The coagulum is composed of homogenous, amorphous-to-granular, eosinophilic secretory material which often contains mature sperm.

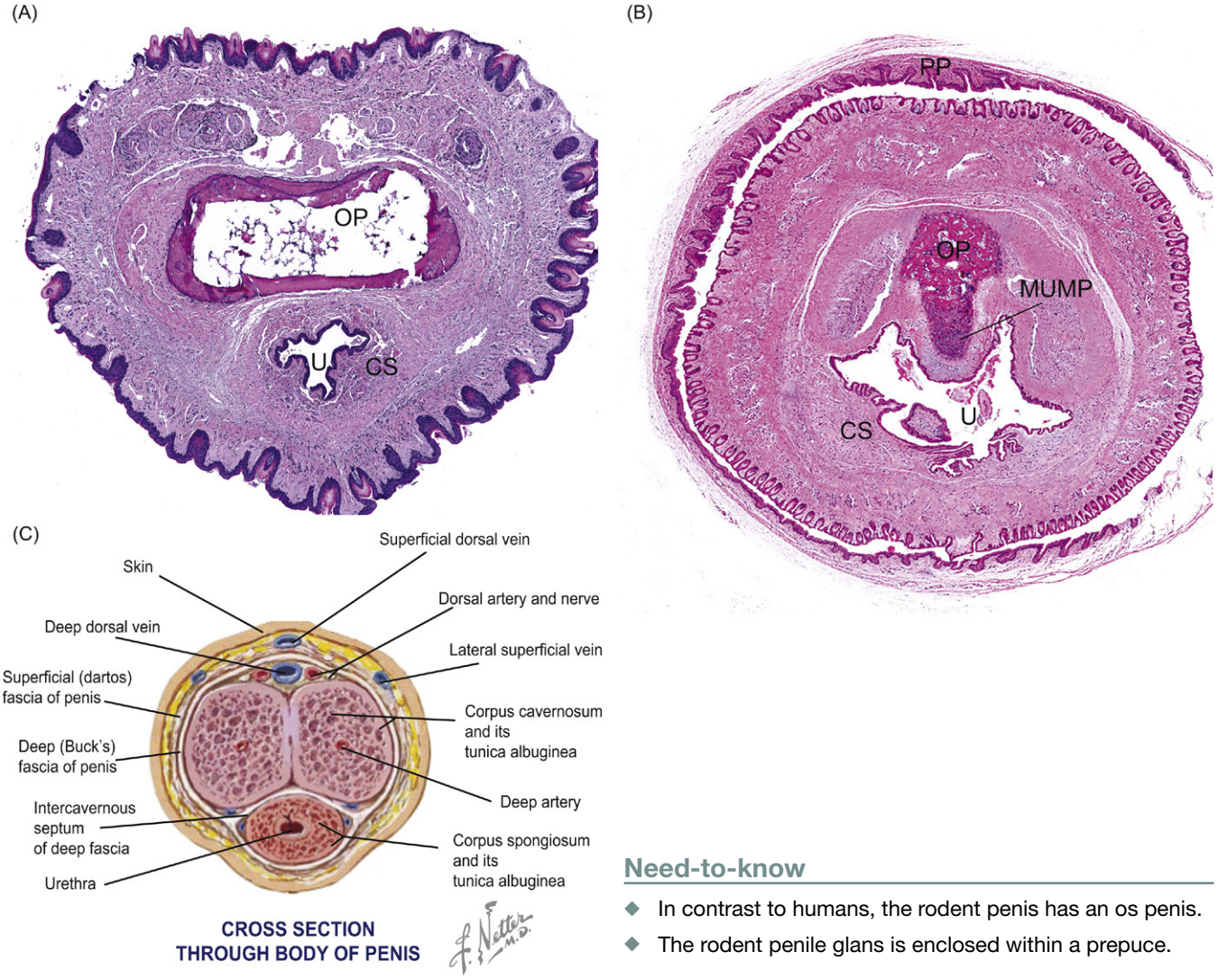

Need-to-know

- In contrast to humans, the rodent penis has an os penis.
- The rodent penile glans is enclosed within a prepuce.

FIGURE 18.21 Penis. (A) Mouse. (B) Rat. (C) Human. The rodent penis is enclosed within a prepuce (PP). In rodents, an os penis made of bone is located proximally and ends distally in the tip of the glans as the male urogenital mating protuberance (MUMP), composed of fibrocartilaginous tissue. The urethra (U) is surrounded by the corpus spongiosum (CS). (C) The human penis consists of three cylindrical masses of erectile tissue. The dorsal aspect comprises the corpora cavernosa penis and the midline consists of the corpus cavernosum urethrae (corpus spongiosum) that surrounds and supports the penile urethra. The cavernous bodies are surrounded and invested by fibroelastic tissue, the tunica albuginea, which is continuous with a loose hypodermis.

FURTHER READING

Burkitt HG, Young B, Heath JW: *Wheater's Functional Histology*, Philadelphia, 1993, Churchill Livingstone.

Creasy D: Evaluation of testicular toxicity in safety evaluation studies: The appropriate use of spermatogenic staging. *Toxicol Pathol* 25:119–131, 1997.

Creasy D, et al: Proliferative and nonproliferative lesions of the rat and mouse male reproductive system. *Toxicol Pathol* 40:40S–121S, 2012.

Creasy DM: Evaluation of testicular toxicity in safety and evaluation studies: The appropriate use of spermatogenic staging. *Toxicol Pathol* 25:119–131, 1997.

Creasy DM, Foster P: Male reproductive system. In Haschek E, Rousseaux C, editors: *Handbook of Toxicologic Pathology*, New York, 1991, Academic Press, pp 829–889.

Creasy DM, et al: Pathogenesis of male reproductive toxicity. *Toxicol Pathol* 29:64–76, 2001.

Cunha GR, et al: Current understanding of hypospadias: Relevance of animal models. *Nat Rev Urol* 12:271–280, 2015.

Hedrich H, Bullock G: *The Laboratory Mouse*, New York, 2004, Academic Press.

Ittmann *Cancer Res* 73(9):2718–2736, 2013.

Keane KA, et al: Regulatory Policy Committee (SRPC) points to consider: Histopathology evaluation of the

pubertal development and thyroid function assay (OPPTS 890.1450, OPPTS 890.1500) in rats to screen for endocrine disruptors. *Toxicol Pathol* 43(8):1047–1063, 2015.

Lanning LL, et al: Recommended approaches for the evaluation of testicular and epididymal toxicity. *Toxicol Pathol* 30:507–520, 2002.

Maronpot RR, Boorman GA, Gaul BW: *Pathology of the Mouse: Reference and Atlas*, Vienna, IL, 1999, Cache River Press.

Mills SE: *Histology for Pathologists*, 3rd edn., Philadelphia, 2007, Lippincott Williams & Wilkins.

Oliveira DS, Dzinic S, Bonfil AI, et al: The mouse prostate: A basic anatomical and histological guideline. *Bosn J Basic Med Sci* 16:8–13, 2016.

Percy DH, Barthold SM: *Pathology of Laboratory Rodents and Rabbits*, 3rd edn., Oxford, 2007, Blackwell.

Rodriguez E, et al: New insights on the morphology of adult mouse penis. *Biol Reprod* 85:1216–1221, 2011.

Shappell SB, et al: Prostate pathology of genetically engineered mice: Definitions and classification. The consensus report from the Bar Harbor Meeting of the Mouse Models of Human Cancer Consortium Prostate Pathology Committee. *Cancer Res* 64:2270–2305, 2004.

Suttie AW, Leininger JR, Bradley AE: *Boorman's Pathology of the Rat: Reference and Atlas*, 2nd edn., New York, 2017, Academic Press.

Suwa T, et al: Spontaneous lesions in control B6C3F1 mice and recommended sectioning of male accessory sex organs. *Toxicol Pathol* 30:228–234, 2002.

Yang JH, et al: Morphology of mouse external genitalia: Implications for a role of estrogen in sexual dimorphism of the mouse genital tubercle. *J Urol* 184:1604–1609, 2010.

This page intentionally left blank

HEMATOPOIETIC AND LYMPHOID TISSUES 19

JERROLD M. WARD
Global VetPathology, Montgomery Village, MD, United States

SINDHU CHERIAN
University of Washington School of Medicine, Seattle, WA, United States

MICHAEL A. LINDEN
University of Minnesota, Minneapolis, MN, United States

Introduction

The hematopoietic and lymphoid tissues give rise to and house erythrocytes (red blood cells), leukocytes (white blood cells), and platelets. The hematopoietic tissues arise from hematopoietic stem cells (HSCs) (Fig. 19.1), and include bone marrow, peripheral blood, and certain lymphoid tissue. The lymphoid tissues make up the lymphatic system and include the primary lymphoid tissues of bone marrow and thymus, and secondary tissues of lymph nodes, spleen, and mucosa-associated lymphoid tissues (MALT). Tertiary lymphoid tissues are those with induced lymphoid cells after inflammation and disease. The hematopoietic and lymphoid systems each contain cellular components of the immune system (innate and adaptive), but immune cells can be present in any tissue normally or induced by disease. Lymphoid and hematopoietic antigens and cells containing such antigens in rodents and humans can be readily demonstrated within formalin-fixed, paraffin-embedded (FFPE) or frozen tissues using polyclonal or monoclonal antibodies. Examples will be illustrated.

Bone Marrow

The bone marrow is the tissue found in the hollow spaces of bones (Figs. 19.2 and 19.3). In adult rodents and humans, the bone marrow is the major site of hematopoiesis, through the three processes of erythropoiesis, myelopoiesis, and megakaryopoiesis. Hematopoiesis that occurs outside the bone, known as extramedullary hematopoiesis (EMH), is discussed in the Spleen section, although it can occur in other tissues. The bone marrow is sometimes described grossly as red (hematopoietic tissue predominant) or yellow (fat predominant) marrow. Microscopically, it is a mixture of hematopoietic elements and fat, with approximately equal proportions of each in a healthy human adult, and primarily hematopoietic cells in rodents. The ratio of cells to fat is described as "cellularity," and this cell:fat ratio decreases progressively with age.

The bone marrow has many stromal/supportive cellular elements, including fibroblasts, histiocytes (macrophages), adipocytes, osteoclasts, osteoblasts, and endothelial cells, which are important in bone remodeling and vascularity. Vascular sinuses are found in the marrow of both rodents and humans.

Comparative Anatomy and Histology. DOI: http://dx.doi.org/10.1016/B978-0-12-802900-8.00019-1
© 2018 Elsevier Inc. All rights reserved.

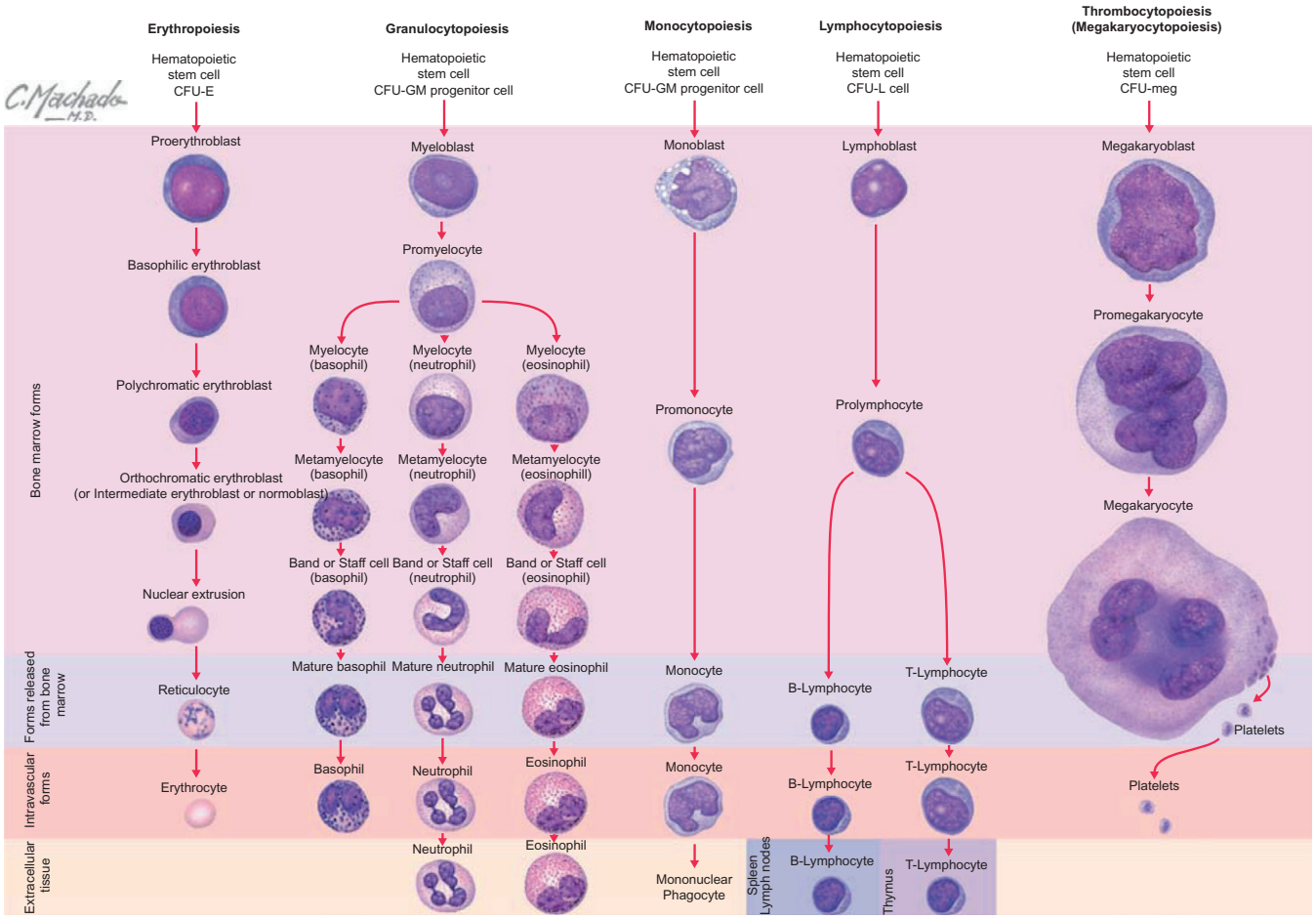

FIGURE 19.1 Maturational sequence of human hematopoietic cells. Source: © Elsevier, Inc., www.netterimages.com.

Need-to-know

- The maturation sequences and morphology of bone marrow cell lineages are similar in rodents and humans.

METHODS

Collection and Processing of Bone Marrow

Rodent bone marrow collection, usually from long bones and in some studies also or only from sternum, is almost always a terminal event. Most typical is for rodents to be sacrificed and the tissues fixed in formalin. Long bones, such as femora, and sternal bones are removed, fixed in formalin or other fixative for 24–48 h, subsequently decalcified in an acid solution and/or ethylenediaminetetraacetic acid (EDTA), and then processed for conventional paraffin-embedded histology with hematoxylin and eosin (H&E) staining. Formic acid–formalin solution or Bouin's solution can be used as both a fixative and decalcifying solution. Sternum does not have to be decalcified in young rodents. Alternatively, long bones can be harvested from sacrificed rodents and flushed with saline to extract marrow elements. The marrow can be smeared on a slide or a cytocentrifuged slide can be prepared. The slides are air-dried, methanol-fixed, and Wright–Giemsa-stained to highlight nuclear and cytoplasmic details.

Human bone marrow is most often collected for diagnostic procedures and infrequently for donation to transplant recipients. Bone marrow biopsies and aspirates are most often collected from the superior posterior iliac crest. Rarely, aspirates are obtained from the sternum. Aspiration removes bone marrow cells and fluid. The aspirate's contents

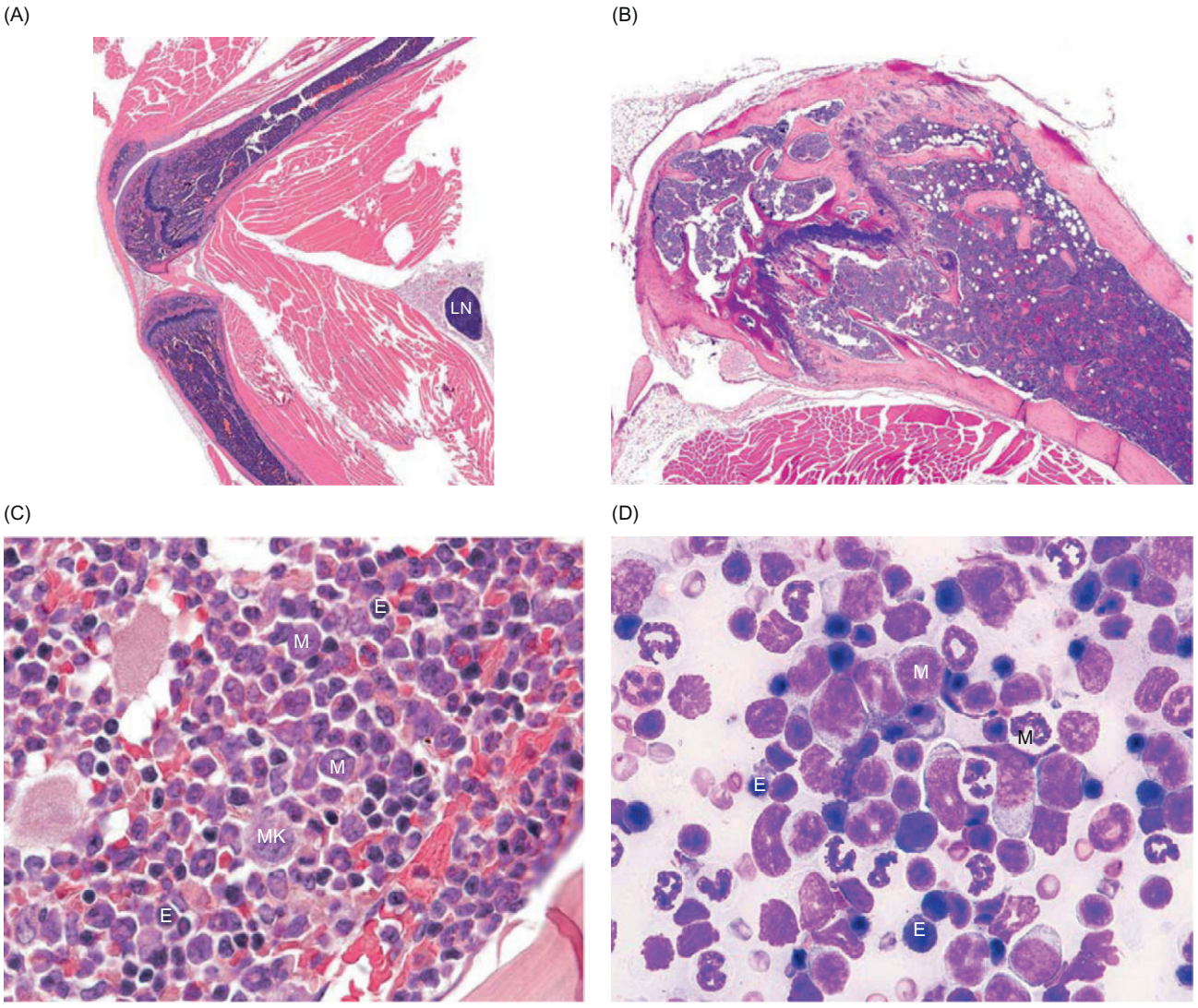

FIGURE 19.2 Rodent (mouse) bone marrow. (A) The bone marrow of the femur and tibia of a young mouse can be seen (left side) in front of the popliteal lymph node (LN). A very small amount of marrow fat is present. (B) High magnification of the end of the femur showing cellular bone marrow. (C) High magnification of bone marrow showing erythroid (E), myeloid (M), and megakaryocytic (MK) elements. (D) Bone marrow aspirate. Cytology of erythroid (E) and myeloid (M) maturation is seen.

Need-to-know

- In rodents, bone marrow evaluation is typically a terminal (necropsy) event, whereas it can be performed as a routine clinical procedure in humans.
- Although aspirate preparations are common in humans, these are more difficult to obtain in rodents. Wright–Giemsa-stained cytospin preparations may provide a viable alternative.
- Normal rodent marrow typically lacks lymphoid aggregates, but many B-cells and fewer T-cells are often found with immunohistochemistry.
- Lymphoid aggregates may be seen in human marrow, where they increase in frequency with age or reactive conditions.

are smeared on a slide and Wright–Giemsa-stained as described previously. Bone marrow biopsies are obtained by taking a "core" biopsy with a large-bore hollow needle. The bone is fixed (usually in formalin or acetic zinc formalin (AZF)), decalcified in acid, and then processed for conventional paraffin-embedded histology with H&E staining. For rodents and human material alike, air-dried Wright–Giemsa-stained material is ideal for cytologic evaluation and morphologic differentiation of cell types. H&E-stained, FFPE material is best for evaluating the morphologic context of the various cell types in relation to one another and to the surrounding bone. In addition, fresh rodent or

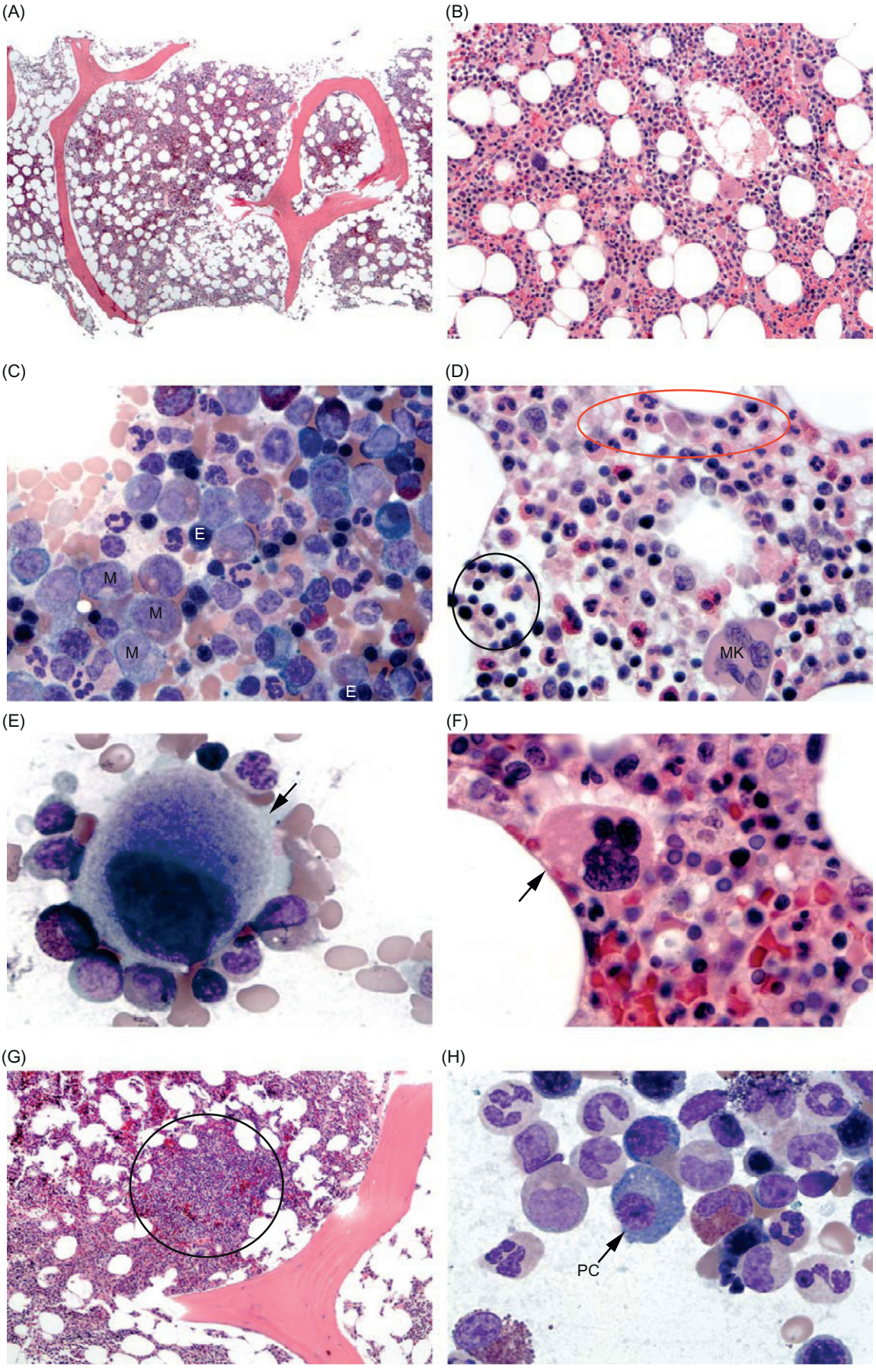

FIGURE 19.3 Human bone marrow. (A and B) Core biopsy; low-power magnification of bone marrow. Cellularity (ratio of cells to fat) and bony trabeculae may be assessed. (C and D) High-power assessment of bone marrow constituents for tri-lineage hematopoiesis. (C) Wright–Giemsa-stained human aspirate smear. Representative myeloid (M) and erythroid (E) cells are indicated. (D) Core biopsy. Areas with a collection of myeloid (red oval) or erythroid (circle) cells are shown. A megakaryocyte (MK) is indicated. (E) Aspirate and (F) core biopsy. Examples of human megakaryocytes (arrows) are indicated. (G) Core biopsy. A benign lymphoid aggregate (circle) is shown. (H) Aspirate. A plasma cell (PC) is shown.

human bone marrow aspirate samples can be profiled by flow cytometry.

Examination of the Bone Marrow

Upon routine histopathological evaluation of the bone marrow, it is important to make an overall assessment in a systematic manner. The first step is to evaluate the ratio of cells to fat, known as cellularity. H&E-stained, FFPE core biopsies at low magnification are best suited for this. While bone marrow cellularity is over 90% for rodents (even old ones), it is lower in humans, with approximately 50% cellularity (Fig. 19.3). The second step is to evaluate for tri-lineage hematopoiesis, which evaluates erythropoiesis, myelopoiesis, and megakaryopoiesis. Maturing forms of each cell line are expected to be present, and this is best evaluated on a high-quality Wright–Giemsa-stained aspirate smear. Tri-lineage hematopoiesis can also be evaluated on H&E-stained, FFPE core biopsies; however, it is difficult to accurately differentiate various maturational stages in such specimens. In humans, bone marrow cellularity decreases with age and is typically equal to 100 minus the age of the patient (and reflected as a percentage ranging from <5% up to 100%). Human marrow cellularity is best estimated using a core biopsy from the iliac crest, although other sites may be utilized as well. Cellularity is often low just under the bony cortex, especially in the elderly; therefore, subcortical marrow alone should not be used to estimate marrow cellularity. The maturation sequences and morphology of bone marrow cell lineages are similar in rodents and humans.

HISTOLOGY AND CYTOLOGY

Erythroid Cells

Erythropoiesis involves a series of maturational steps in the formation of erythrocytes (Fig. 19.1). In the bone marrow, there is typically a spectrum of erythroid differentiation that is best appreciated on a high-quality Wright–Giemsa-stained aspirate smear. The earliest cell in erythropoiesis is the proerythroblast, which is similar to other blasts, with nucleoli and high nuclear:cytoplasmic ratios. The cytoplasm is often a distinct deeply basophilic color on aspirates stained with Wright–Giemsa. Proerythroblasts develop into basophilic erythroblasts, which have coarser chromatin and absent nucleoli. As hemoglobin production increases, the cytoplasm develops a grayish hue. Proerythroblasts develop into polychromatic erythroblasts. These cells have relatively more cytoplasm that stains with both blue and red dyes. The nucleus has condensed chromatin and round nuclear edges. The polychromatic erythroblast then develops into an orthochromatic erythroblast; at this point, the cytoplasm is predominantly red. When the cell is sufficiently mature, the nucleus is extruded, and this anuclear cell is termed a reticulocyte. Reticulocytes leave the bone marrow and develop into mature erythrocytes in the peripheral blood, with loss of the basophilic tinge to the cytoplasm as RNA levels decrease and acquisition of an area of central pallor.

Myeloid Cells

Myelopoiesis involves a series of maturational steps from HSCs to common myeloid progenitor cells through terminal differentiation leading to the formation of granulocytes, including basophils, neutrophils, eosinophils, and monocytes. This is sometimes further divided into granulopoiesis and monocytopoiesis (Fig. 19.1). In bone marrow, there is typically a spectrum of myeloid differentiation with neutrophils and neutrophil precursors predominating. As noted in the previous section, maturation is best appreciated on a high-quality Wright–Giemsa-stained aspirate smear; therefore, the rest of this section refers to this preparation. Myeloblasts are infrequent (<2% of white blood cells) and vary in diameter from 15 to 20 µm, with a high nuclear:cytoplasmic ratio and scant pale blue agranular cytoplasm.

Myeloblasts differentiate into promyelocytes, which have basophilic cytoplasm with distinct magenta-colored primary cytoplasmic granules. Promyelocytes differentiate into myelocytes, which have slightly oval nuclei and pale pink cytoplasm containing small, light ill-defined pink-reddish granules also known as secondary granules. Both promyelocytes and myelocytes may have a perinuclear halo. Myelocytes differentiate into metamyelocytes, which have a kidney-shaped nucleus and granular cytoplasm. Metamyelocytes differentiate into band cells with horseshoe-shaped nuclei. Ultimately, these band cells develop segmented nuclei and exit to the peripheral blood as mature neutrophils. Eosinophils and basophils go through parallel stages of differentiation, but these cell types are significantly less frequent in the marrow. Monocytes are present in the marrow; their precursors are rare and include monoblasts and promonocytes. Once leaving the marrow, monocytes differentiate into macrophages and dendritic cells.

Lymphocytes

Lymphopoiesis involves a series of maturational steps from HSCs to common lymphoid precursors to differentiated T, B, natural killer (NK), and plasma cells. Lymphocytes are often seen in the bone marrow but are infrequent (especially plasma cells) in nonpathologic states. These cell types are further discussed in the blood, thymus, and lymph node sections. A relatively common normal variant in bone marrow sections of adult humans is a lymphoid aggregate, which is not usually seen in healthy mice. These aggregates contain a mixture of B and T cells (with a greater proportion of T cells) and are found between, but usually not abutting, bony trabeculae (nonparatrabecular). Bone marrow plasma cells typically represent less than 3% of bone marrow cellularity. In bone marrow biopsy sections, they are often seen near vessels. Morphologically, they are best identified on bone marrow aspirate smears, where they have abundant cytoplasm, an eccentric nucleus, a perinuclear halo, and clumped nuclear chromatin that are often compared to a "clock face" (Fig. 19.3H).

Megakaryocytes

Megakaryocytes give rise to mature platelets, which are essential to thrombosis and hemostasis (Fig. 19.1). Megakaryoblasts are the earliest forms and develop into promegakaryocytes, which contain granules. Promegakaryocytes subsequently develop into megakaryocytes, which are most often seen in the bone marrow. Megakaryocytes get their name from their large nuclei (Fig. 19.3E) formed by the fusion of multiple nuclei: These cells undergo mitotic divisions multiple times with no cytoplasmic separation. Thus, the nuclei often have two (4N), four (8N), or eight (16N) nuclear lobes and abundant cytoplasm. Their cytoplasm contains factor VIII and von Willebrand factor, which are essential for hemostasis. Ultimately, as megakaryocytes migrate, they liberate portions of their cytoplasm as platelets. The remaining naked nuclei are phagocytosed or disintegrate. Upon review of bone marrow biopsies or aspirates, a pathologist would assess for megakaryocyte number and relationship to the rest of the marrow (Fig. 19.3B). Upon higher magnification, a pathologist would assess nuclear detail on both aspirates and core sections (Fig. 19.3) to rule out hyper- or hypolobated megakaryocytic nuclei.

Peripheral Blood

Peripheral blood is composed of plasma, erythrocytes, leukocytes, and platelets. It functions similarly in rodents and humans to deliver oxygen, nutrients, and to carry waste to sites for disposal or breakdown. In addition, blood carries the leukocytes, platelets, and clotting factors to sites for action. As described in the previous

section, all three cell types originate in the bone marrow and usually migrate as mature cells to the peripheral blood. Plasma proteins are made in the bone marrow, the liver, and other cells in the reticuloendothelial system.

METHODS

Collection of Peripheral Blood

Rodent peripheral blood is often collected for experiments or to evaluate for disease. Given the small size of mouse veins, venipuncture is not routinely performed. Tail sticks can be performed to get small drops of blood, although they may not yield a sufficient volume for blood smear preparations or automated hematology analyzers. Nonterminal blood collection involves a retro-orbital eye or submandibular bleed, which can collect up to 50–100 µL. This involves placing an EDTA- or heparin-coated glass capillary tube behind the eye of the rodent into the retro-orbital space to collect blood. If performed correctly, this can be done multiple times without significant harm to the animal (though some institutions require anesthesia for this procedure). For larger volumes of blood, cardiac puncture is performed: After anesthetization, a needle is placed through the skin, under the sternum, and into the left ventricle. Up to 1–2 mL of blood can be collected; this procedure is a terminal event. Human blood is almost always collected by venipuncture, most often for clinical testing. A needle is placed into the median antecubital vein (upper extremity), and 3–10 mL of blood is collected into a vacuum test tube containing an anticoagulant (EDTA, heparin, or sodium citrate). It should be stressed that for blood cell morphology on stained smears, superior preparations are obtained from blood collected in EDTA.

Automated Cell Counting

Rodent and human blood is often analyzed on automated instruments that use light detectors and impedance sensors to quantify the concentration of nucleated and anuclear cells in blood. A main advantage of automated counters, in addition to their speed, is that they count such a large number of cells that data generated tend to be very precise compared with manual counting. These data are used to calculate reference ranges for individual blood components (Table 19.1).

TABLE 19.1 Comparison of Reference Ranges for Peripheral Blood and Its Components

Parameter	Rodent		Human[a]
	Mouse[b]	Rat[c]	
Blood volume (mL) per kg body weight	70–80	60	70
Average total blood volume (mL)	1.25–1.75	20	4700–5000
Heart rate (beats/min)	400–800	300–500	80–120
Blood pressure (mm Hg)	125/90	116/90	120/80
Hematocrit (packed red blood cell volume as percentage total blood volume)	39–49	39–69	36–45
Red blood cell count (million/µL)	7–13	5.8–10	3.8–5
Hemoglobin (g/dL)	12.2–16.2	13–23	11.5–15.5
Mean corpuscular volume (fL)	42–50	58–77	81–98
Mean corpuscular hemoglobin (pg)	14–17	17–25	27.3–33.6
Mean corpuscular hemoglobin concentration (g/dL)	33–36	27–38	32.2–36.5
Red cell distribution width of coefficient variation (%)	14–20	10–15	11.6–14.4
White blood cell count (per µL)	5,000–12,000	4,000–18,000	4,300–10,000
Platelet count (per µL)	300,000–1,000,000	800,000–2,600,000	150,000–400,000
Neutrophils (%)	20–25	16–54	34–71
Lymphocytes (%)	70–75	38–79	19–53
Monocytes (%)	2–6	3–11	5–13
Eosinophils (%)	0–3	0.1–4.3	0–7
Basophils (%)	0–0.1	0–1.7	0–1

[a]Human reference ranges adapted from data generated at the University of Washington Medical Center.

[b]Mouse reference ranges adapted from McGarry et al. (2010) and http://phenome.jax.org/.

[c]For male Crl:CD (SD) rats, from Otto et al. (2015).

Peripheral Blood Smear

Rodent and human blood smears are made in a similar manner. A drop of blood is placed on a glass microscope slide, and a spreader slide evenly disperses the blood along the slide's surface. This allows the cells to be distributed in such a way that they are far enough apart to be counted and differentiated. Like marrow, the slide is air-dried quickly, methanol-fixed, and stained with a Wright–Giemsa stain. A peripheral blood smear is typically scanned with a 20× objective to assess the distribution of white blood cell types, and a manual differential is typically performed using a 40× or higher objective (Figs. 19.4 and 19.5). Higher objectives, including 100× with oil, are helpful to assess platelet morphology and concentration (Fig. 19.5).

HISTOLOGY AND CYTOLOGY

Erythrocytes

Erythrocytes typically appear as biconcave discs (Figs. 19.4 and 19.5). On stained smears, they are circular with distinct, smooth margins. Rodent erythrocytes are 4–7 µm in diameter and appear similar in morphology to those in humans. Human erythrocytes are 6–8 µm in diameter (similar to the size of the nucleus of a resting lymphocyte) and 1.5–2.5 µm thick, with an area of central pallor comprising approximately one-third of the diameter of the cell. Erythrocyte morphology is best appreciated where cells are well distributed, inside the feathered edge. In young rodents (<4 weeks of age), reticulocytes can be seen as up to 10% of erythrocytes.

Leukocytes

Neutrophils

Neutrophils, also known as polymorphonuclear neutrophilic granulocytes, function in the innate immune system in responses to tissue and cell injury, especially in inflammation and bacterial infections (Fig. 19.4). Neutrophils in both rodents and humans have cytoplasmic granules containing cytotoxic lysosomal enzymes and a nucleus that is separated into distinct lobes with a thin strand (filament) connecting them. In rodents, only 20–25% of peripheral blood leukocytes are neutrophils, compared to 50–70% in humans. When ideally stained, the cytoplasm is light pink, and the numerous, evenly distributed fine granules have a light pink-to-purple color. Human neutrophils typically have three to five nuclear lobes, with three-lobe forms the most abundant (41%). In females of all three species, a small nuclear drumstick-shaped appendage representing an inactivated X chromosome (Barr body) can be seen. Barr bodies are much more common in female rodent blood smears (Fig. 19.4). When activated, neutrophils can develop dark coarse granules; this is termed toxic granulation. In addition, activated neutrophils often contain vacuoles.

Eosinophils

Eosinophils are granulocytes that have band or bilobed nuclei. In mice, 0–3% of the leukocytes are eosinophils and 0.1–4.8% in rats (Fig. 19.5). In humans, eosinophils are roughly the same size as neutrophils and represent between 0% and 7% of white blood cells in the periphery. It has been shown that human eosinophils and eosinophil granules are larger than rodent eosinophils. Eosinophils get their name from their relatively large, spherical granules that have a particular affinity for stains containing acid eosin. The cells stain reddish-orange, sometimes with brownish tints. The granules contain histamine, enzymes, and other proteins. Eosinophils are rarely phagocytic. Typically, they migrate to peripheral sites and degranulate upon stimulation, releasing cytotoxins that are toxic to both parasites and host tissue.

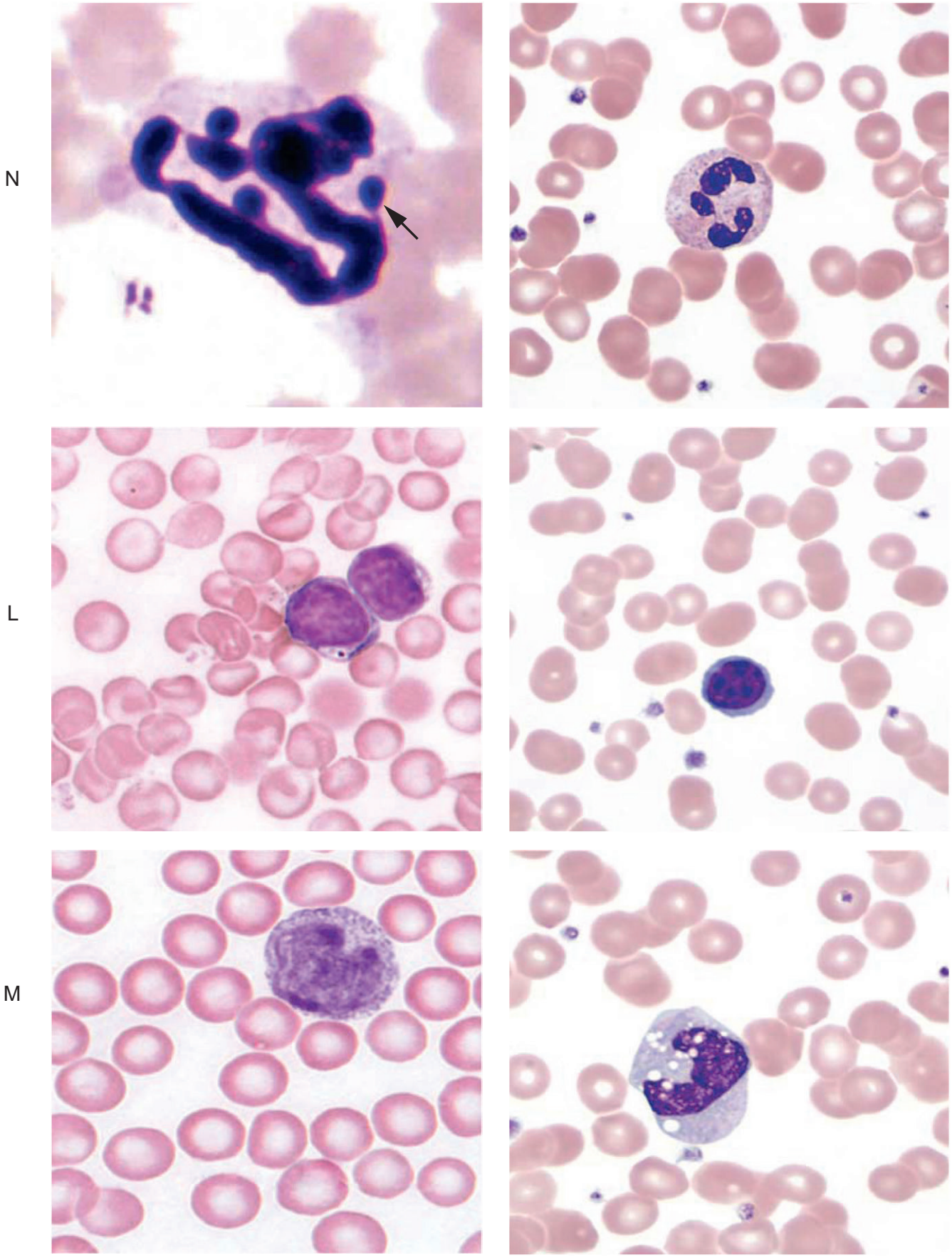

FIGURE 19.4 Neutrophils (N), lymphocytes (L), and monocytes (M). Rodent (mouse) (left); human (right). Note the similar morphology between rodent and human. A Barr body (arrow) is seen in the female mouse neutrophil panel and a cytoplasmic granule in one of the mouse lymphocytes.

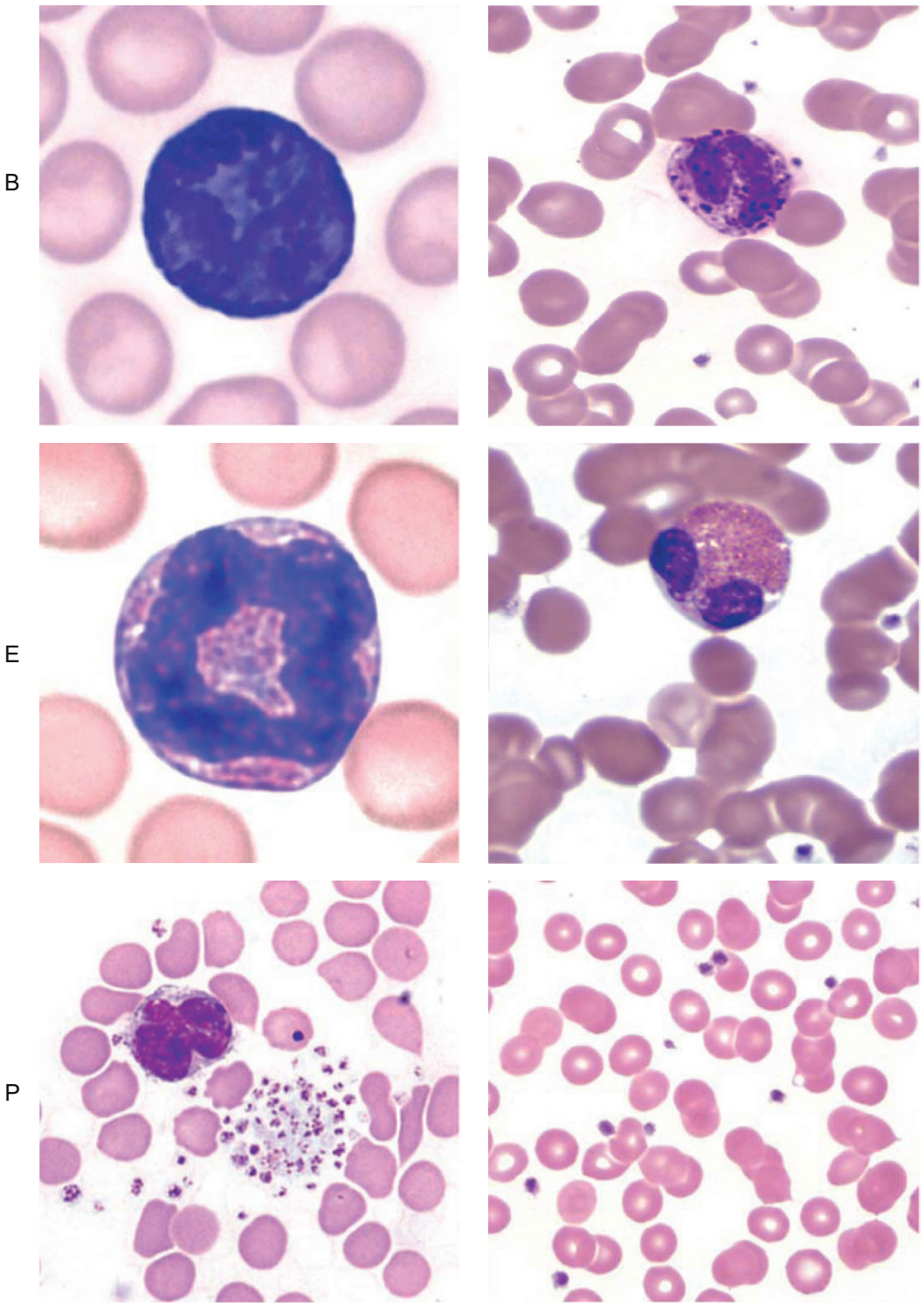

FIGURE 19.5 Basophils (B), eosinophils (E), and platelets (P). Rodent, (mouse) (left); human (right). A monocyte is visible with erythrocytes in the mouse platelet panel. A clump of platelets is also seen. Source: Mouse basophil and eosinophil reproduced from McGarry MP, Protheroe CA, Lee JJ: Mouse Hematology: A Laboratory Manual. Cold Spring Harbor, NY: Cold Spring Harbor Laboratory Press, 2010, by permission of Mayo Foundation for Medical Education and Research. All rights reserved.

Need-to-know

- Eosinophils and basophils are not often seen in peripheral blood smears from rodents, but are seen in low numbers in most human smears.
- There is a higher proportion of lymphocytes in rodent blood than in human blood.
- There is a higher proportion of neutrophils in human blood than in rodent blood.

Basophils

Basophils are granulocytes that have round, indented, band, or segmented nuclei (Fig. 19.5). In mice, less than 1% of the leukocytes are basophils and less than 2% in rats. In humans, basophils are roughly the same size as neutrophils. They are rarely found in the peripheral blood, representing 0% or 1% of leukocytes. They have round-to-oval shapes with smooth edges. Basophils get their name from their prominent (0.2–1 µm) cytoplasmic granules that have an affinity for basic dyes. These granules are numerous and unevenly distributed, with colors varying from deep purplish-blue to dark purple-red. They contain heparin, histamine, and other chemicals. Basophils are not phagocytic; rather, when stimulated, the cells eject the chemicals contained in their granules.

Monocytes

Monocytes are phagocytic leukocytes of the blood that, in conjunction with tissue macrophages and neutrophils, are important cells involved in first-line defense against pathogenic organisms or foreign cells (Fig. 19.4). In mice, monocytes comprise 2–6% of the peripheral blood leukocytes and 3–11% in rats. In humans, monocytes comprise 1–6% of human blood cells. Generally, monocytes are three or four times the size of adjacent erythrocytes. Cell shape is variable, although most are round to oval, with abundant dull blue-gray cytoplasm. Granules are sometimes present, and they are usually fine, lightly staining, and numerous. Cytoplasmic vacuoles are often present. Monocyte nuclei are usually folded or kidney-shaped. This variation in nuclear morphology is also seen in rodents.

Lymphocytes

Lymphocytes are most commonly found in the lymphoid organs (see thymus, lymph nodes, and spleen sections below), but they also circulate in the peripheral blood (Fig. 19.4). In mice (70–75%) and in rats (38–79%) the majority of peripheral blood leukocytes are lymphocytes. In humans, lymphocytes make up 30–70% of the peripheral leukocytes in children; in adults, this number decreases to 20–40%. The majority of lymphocytes in the periphery are small, ranging from 7 to 10 µm in diameter. Their nuclear chromatin is clumped and darkly stained. The cells have high nuclear:cytoplasmic ratios, and the cytoplasm is blue with a variable intensity. NK cells, which often have the appearance of large granular leukocytes (LGLs), can be seen in both rodents and humans. The granules are more prominent in rats than in mice and a large granular lymphocyte leukemia in specific rat strains is common. Reactive lymphocytes can also be seen and tend to be larger, with more abundant cytoplasm and occasionally with reactive granules.

Platelets

Platelets are derived from bone marrow megakaryocytes (see Bone Marrow, Fig. 19.1). In rodents, platelets are often clustered together but may occur as individual platelets. In both species, the diameter of platelets seen on a blood smear ranges from 1 to 4 µm. Platelet edges are irregular, with pointed filaments and tentacle-like protrusions. The cytoplasm stains light blue with small granules. No nucleus is present. Although platelets tend to adhere to one another, clumping can also be indicative of suboptimal anticoagulation at the time of blood collection. Platelets are crucial for thrombosis and hemostasis, and they respond to endothelial cell injury by activating, clumping, and providing a catalytic surface for clotting factors.

Thymus

The thymus is an organ consisting of a network of epithelial cells and associated lymphocytes that function as the center of T cell development. This organ has a similar function, structure, and histology in rodents and humans, and it undergoes similar age-related changes in all three species (Table 19.2).

TABLE 19.2 Thymus

Feature	Rodent		Human
	Mouse	Rat	
		Gross	
Location	Anterior mediastinum	Similar to mouse	Similar to rodent
Normal weight	30–50 mg (2–4-month old)	300–400 mg (2–4-month old)	Range, 10–30 g
Function	T cell development	Similar to mouse	Similar to rodent
		Histologic	
Medulla	Epithelial and reticular cells and lymphocytes; site of Hassall's corpuscles, which are less prominent than in the human	Similar to mouse	Epithelial and reticular cells and lymphocytes; site of Hassall's corpuscles
Cortex	Lymphocytes, reticular and epithelial cells; lymphoid cells predominate	Similar to mouse	Similar to rodent
Age-related changes	Weight changes vary by mouse strain/line; increase in medulla; decrease in cortex	Similar to mouse	Mild decrease in weight; increase in the perivascular space; decrease in the thymic epithelial compartment
Ectopic thymus	Present in up to 90% of some lines of mice in various cervical locations	Common	Uncommon
Ectopic parathyroid	Uncommon	Uncommon	Uncommon

GROSS ANATOMY

The rodent thymus is located ventrally in the anterior portion of the thoracic cavity (Fig. 19.6A). Similarly, the human thymus is located in the anterior mediastinal compartment (Fig. 19.6B). The anatomic structure of this organ is similar in humans, rats, and mice. The thymus is composed of two lobes, typically unequal in size, that are connected by a thin connective tissue bridge designated the isthmus. In rodents, the thymus may reach a peak size (4–8% of body weight) by 3–6 weeks, and then it gradually undergoes age-related atrophy, grossly and microscopically, although rodent strain and sex differences are found. The degree of age-related involution is greater in humans than in rodents. Human thymic weight ranges from approximately 10 to 30 g, with the greatest thymic weight seen in children. Thymic involution peaks at puberty. Although the decrease in thymic weight with age is relatively mild, as discussed later, involution is apparent at the histologic level, where the percentage of thymus volume taken up by thymic epithelial space is replaced by adipose tissue and nonthymic lymphocytes that fill the perivascular space. By the age of 70 years, less than 10% of total thymic tissue in humans consists of what is called thymic epithelial space.

HISTOLOGY

The thymus is enclosed in a thin connective tissue capsule that focally infiltrates into the organ, separating the thymus into lobes. In humans, the perilobular connective tissue gives rise to septae that demarcate sublobules. Sublobulation is not noted in rodents. The histology of the thymus of both species is similar (Figs. 19.7–19.10). The thymus consists of two primary areas, the cortex and medulla. These areas are the site of T cell development and are collectively designated the thymic epithelial space. Perivascular tissue surrounds the functional thymic epithelial space and lies within the thymic capsule.

The thymic cortex underlies the capsule and is located at the periphery of the organ (Fig. 19.7). It is composed of a mixed population consisting primarily of lymphocytes known as thymocytes, with fewer scattered epithelial cells. Thymocytes are small to intermediate in size, with scant cytoplasm and variably condensed chromatin. They show a gradient in nuclear size, with those closest to the capsule showing somewhat larger nuclear size and more open chromatin, whereas the majority of cortical thymocytes have smaller nuclei with condensed chromatin. Cortical

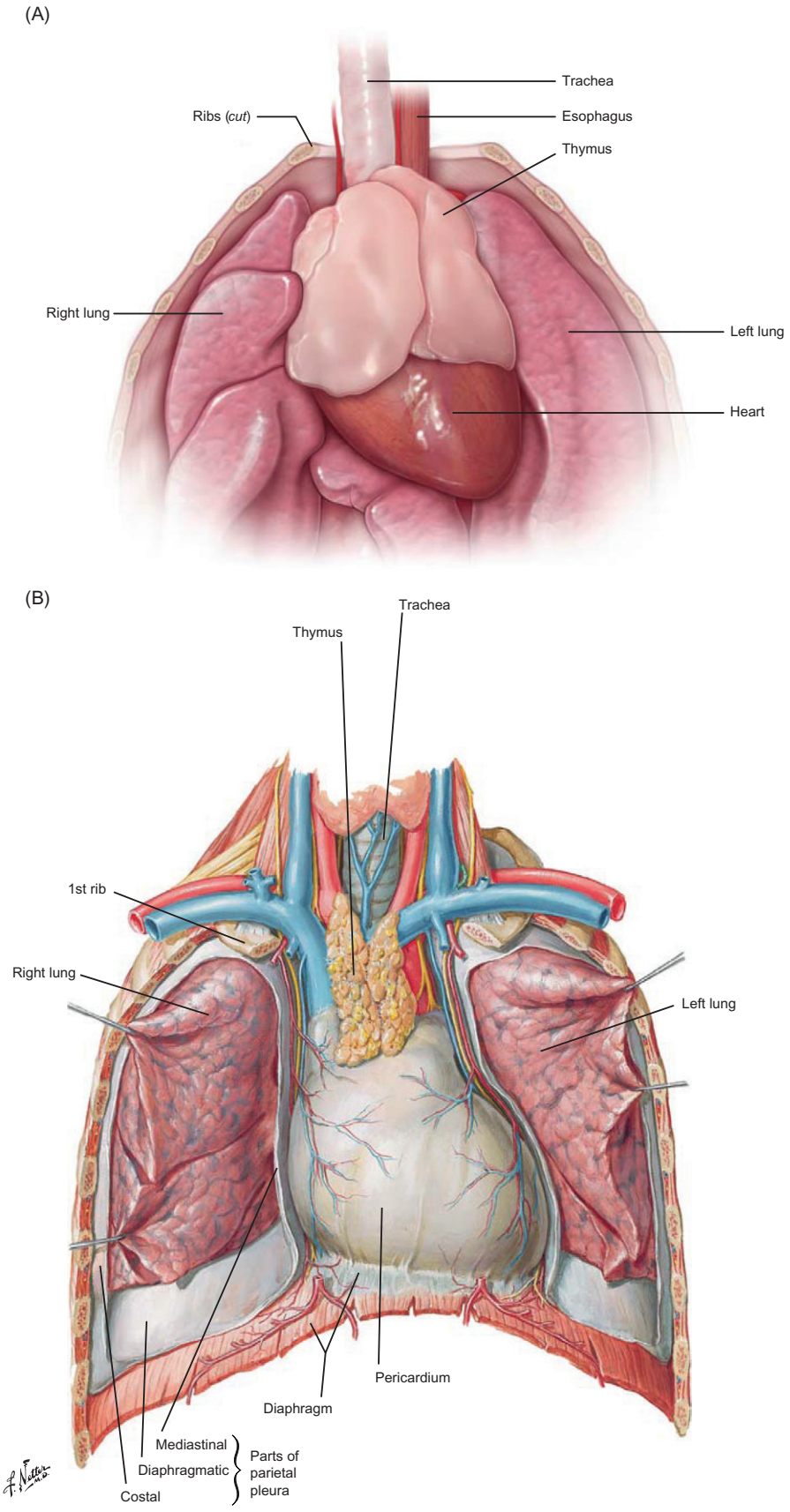

FIGURE 19.6 Thymus schematic. (A) Rodent (mouse) Source: © Elsevier, Inc., www.netterimages.com (B) Human. Note the anatomic location of the thymus in the anterior mediastinum and the relationship of this organ to surrounding structures. Source: © Elsevier, Inc., www.netterimages.com.

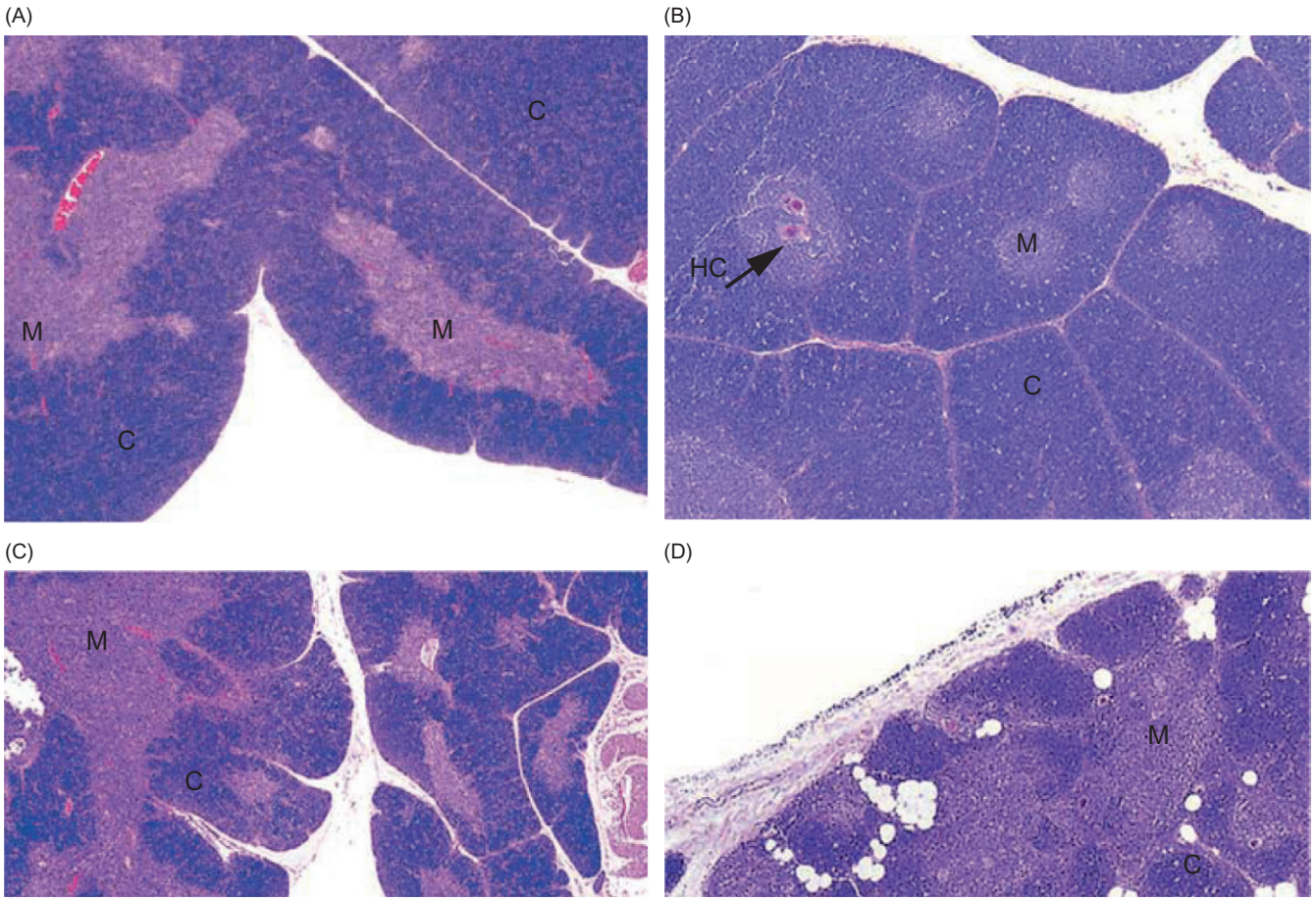

FIGURE 19.7 Low-magnification views of rodent (mouse) and human thymus. Rodent (A and C) and human (B and D) are similar in histologic appearance. At 4 months (A), rodent thymus is mature and has a wide cortex and medulla; by 8 months (C), there is mild lymphocyte depletion from the cortex and widening of the medulla. Human thymus is depicted at 4 months (B) and 16 years (D). The cortex (C) and medulla (M) are easily identified at low power. Note the increase in fat deposition with age. The perivascular space is essentially a potential space in the 4-month-old thymus but begins to expand and fill with adipose tissue in the 16-year-old. Hassall's corpuscles (HC) are also indicated in the medulla of the 4-month-old thymus at this magnification.

thymic epithelial cells are less frequent, are scattered through the cortex, and have projections connecting them to neighboring epithelial cells. These epithelial cells can be distinguished from thymocytes on the basis of their larger nuclei and more open chromatin. Epithelial-free zones have been reported in the rat thymus. Also scattered through the cortex may be macrophages, including tingible body macrophages, which contain apoptotic cell debris. These may be increased in a variety of reactive states, giving rise to a "starry sky" appearance in the cortex. In rodents, the thymic cortex often decreases in size (i.e., narrows, involutes, and atrophies) with age.

The medulla contains epithelial cells, dendritic cells, and lymphocytes; however, in the medulla, epithelial cells predominate, giving this region a pale appearance at low power. The medullary epithelial cells have less prominent cytoplasmic projections and focally form keratinized structures known as Hassall's corpuscles (HCs) (Figs. 19.9 and 19.10). HCs are pathognomonic for thymic tissue in humans. HCs in rodents do not have the typical HC morphology seen in humans and other species. Specifically, they are not as well organized as in humans and some other species; they form clusters of large cells with eosinophilic cytoplasm, and they show little evidence of cell degeneration

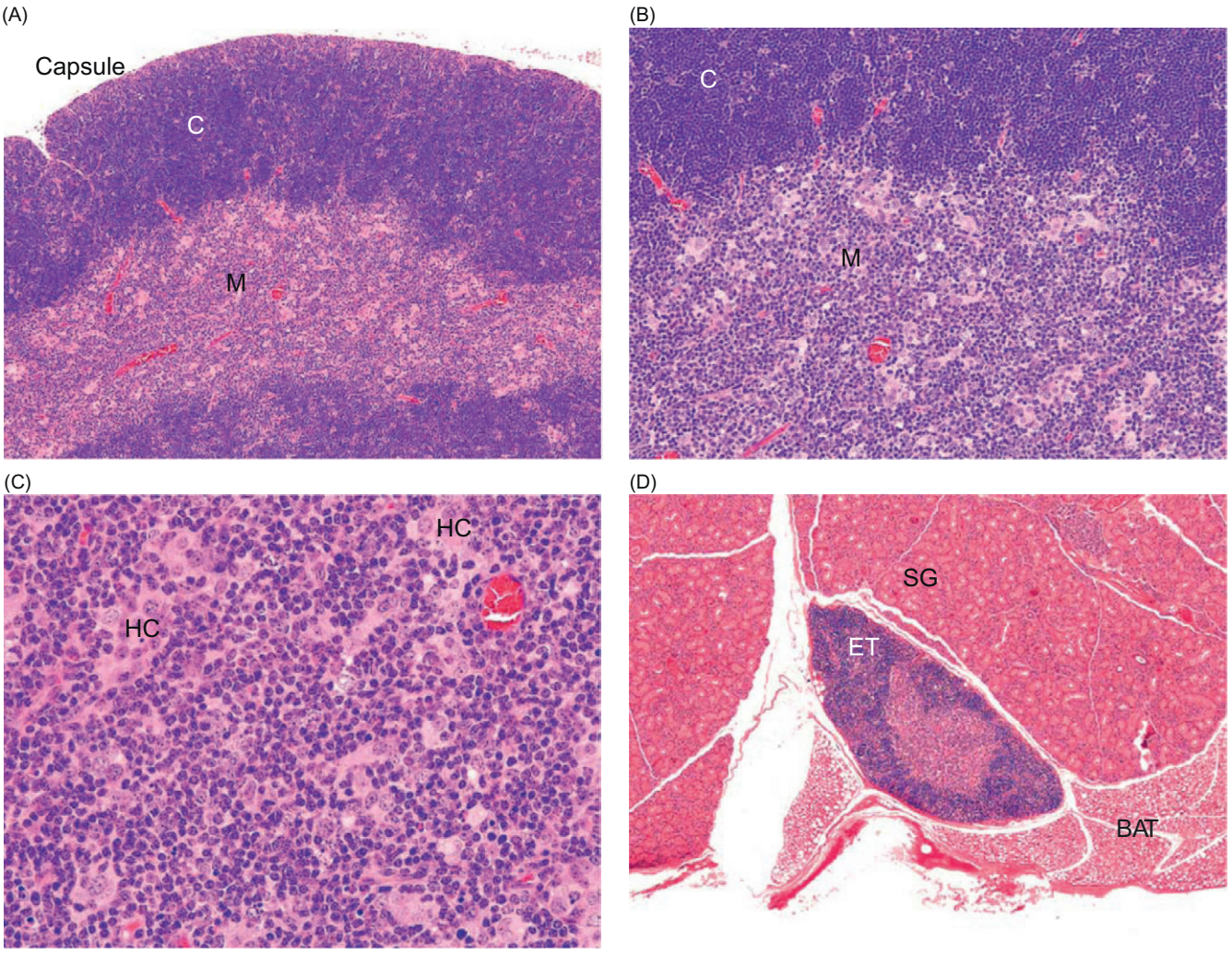

FIGURE 19.8 Higher magnification views of thymus from 4-month-old rodent (mouse) showing thin capsule, with cortex (*C*) and medulla (*M*). (A–C) The medulla contains Hassall's corpuscles (HC), which are not as organized as in human thymus. (D) Ectopic thymus (ET) can be present in various cervical tissues, including tissues adjacent to the salivary gland (SG) and brown adipose tissue (BAT).

Need-to-know

- Rodent thymus does not have sublobules.
- Hassall's corpuscles are not as well developed in the rodent.
- Ectopic cervical thymus is more common in the rodent.

(Fig. 19.10A, B). Thymic cysts, arising from thymic medullary epithelium and with ciliated cells (Fig. 19.10C, D), appear in increasing prevalence and size with age in some strains of rodents, and especially in nude mice. In aging rodents, areas of medullary hyperplasia may often appear after 6 months. Thymic involution in rodents is histologically characterized by decreased depletion of mature lymphocytes in the cortex, with an increase of some types of medullary cells.

The perivascular space present within the thymus is generally devoid of thymic epithelial cells, but rather consists of fat, vessels, and mature B and T lymphocytes. In mice, some thymic epithelial cells are perivascular. In human infants, this compartment is essentially a virtual space consisting primarily of vessels. As noted above, with aging, the percentage of thymus occupied by this compartment increases (due most notably to an increase in perivascular adipose cells). With certain

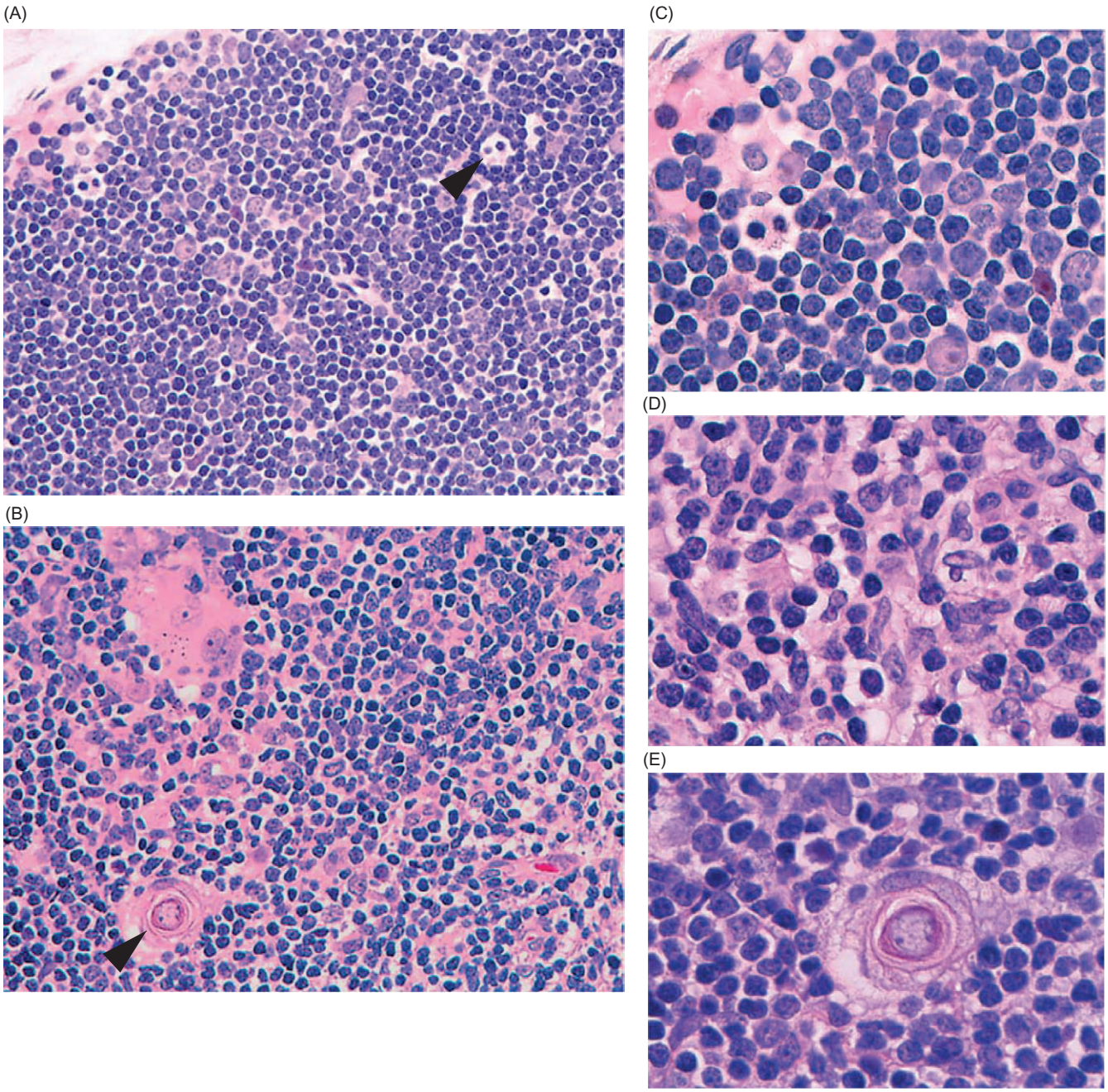

FIGURE 19.9 High magnification views of human thymus. (A) Cortex. At this power, tingible body macrophages (arrowhead) can be seen in the cortex, because this is a site of rapid lymphocyte turnover. (B) Medulla. Hassall's corpuscles (arrowhead) can be seen; the medulla contains more epithelial and fewer lymphoid cells than the cortex. (C) Cortex showing the range in size of thymocytes. Small thymocytes with clumped chromatin predominate. (D) Medulla showing a relative increase in epithelial cells compared to the cortex. (E) Medulla showing a Hassall's corpuscle.

reactive states, the lymphoid component of the perivascular space can increase, with B cell follicles containing germinal centers occasionally observed.

Ectopic cervical thymus (Fig. 19.8D) can be found in up to 90% of some lines of mice in various cervical locations, including the thyroid and salivary gland, less so in rats. Ectopic thymus is also occasionally found in humans in the neck and has been reported in association with the lower parathyroid gland or within the thyroid. Of note, in humans, ectopic parathyroid, sebaceous, or salivary gland tissue may be seen within the thymus. Ectopic parathyroid tissue can also be seen in the thymus of rodents.

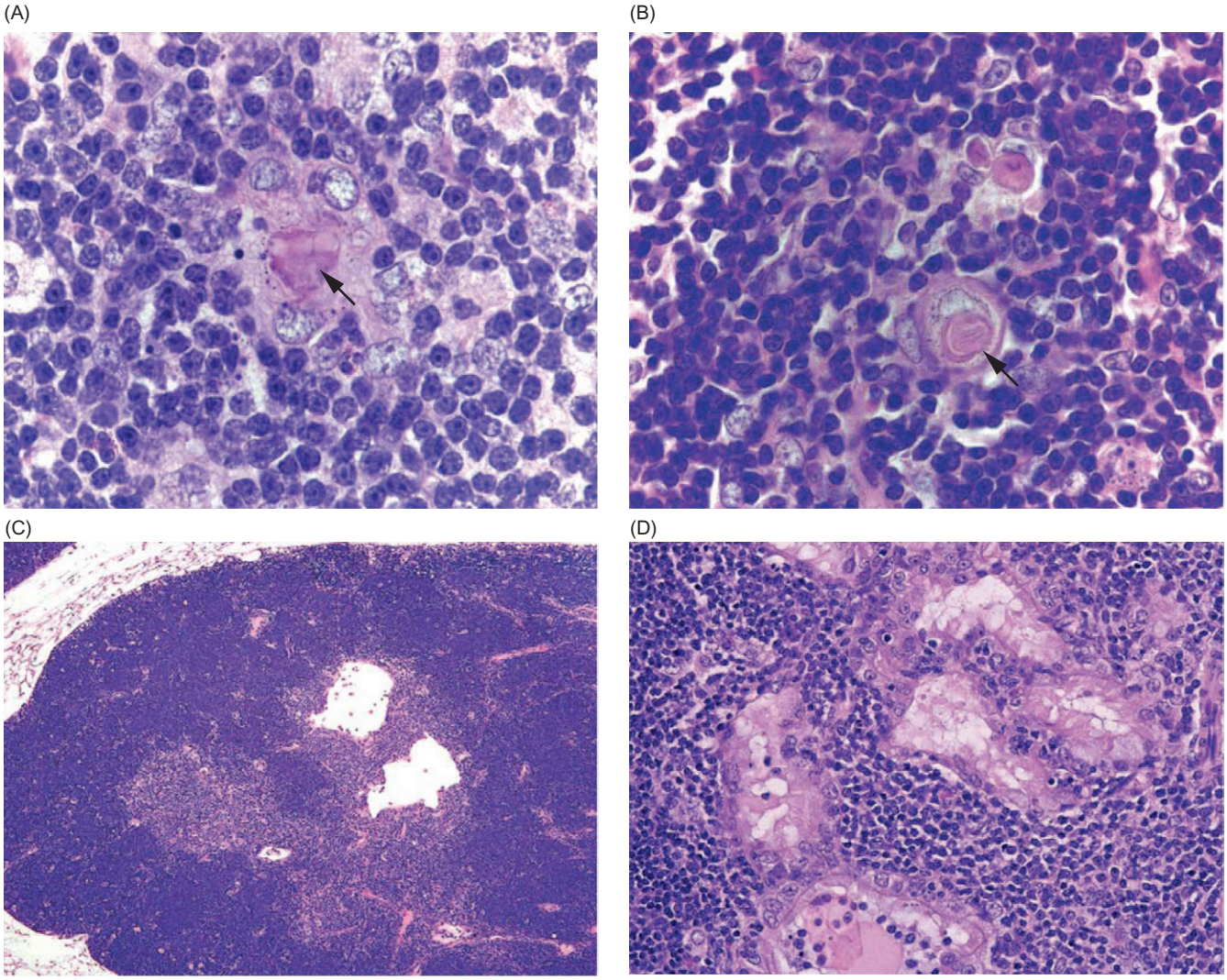

FIGURE 19.10 Comparison of mouse and rat thymic features. (A) Mouse medulla with Hassall's corpuscle (arrow). (B) Rat medulla with Hassall's corpuscle (arrow). (C) Mouse thymus with cysts in medulla. (D) Mouse thymus with cysts in medulla, mucus in epithelial lining, and ciliated epithelial cells.

Lymph Nodes

The lymph nodes are peripheral organs that house a major subset of mature lymphocytes. The lymph nodes serve a similar function in the rodent and human and are critical in mediating immune reactions to exogenous and endogenous stimuli. The lymph nodes are connected by a system of lymphatics that transport lymphatic fluid, circulating tissue fluid generated from drainage of the interstitial tissues. The lymphatic system, serves a transport function for lymphatic fluid, similar to blood vessels for blood, and begins as blind-end vessels in organs and tissues that drain tissues and carry antigenic stimuli to lymph nodes. The lymphatic system eventually drains into the thoracic duct to redistribute the interstitial fluids back to the blood.

REGIONAL ANATOMY

Lymph node distribution in mice has been well described (Fig. 19.11, Table 19.3) and also in rats. There can be inter- and intrastrain differences in the numbers of nodes per rodent. Nodes are generally very small (1–4 mm) and difficult to visualize within fat or other tissues. Rat nodes are

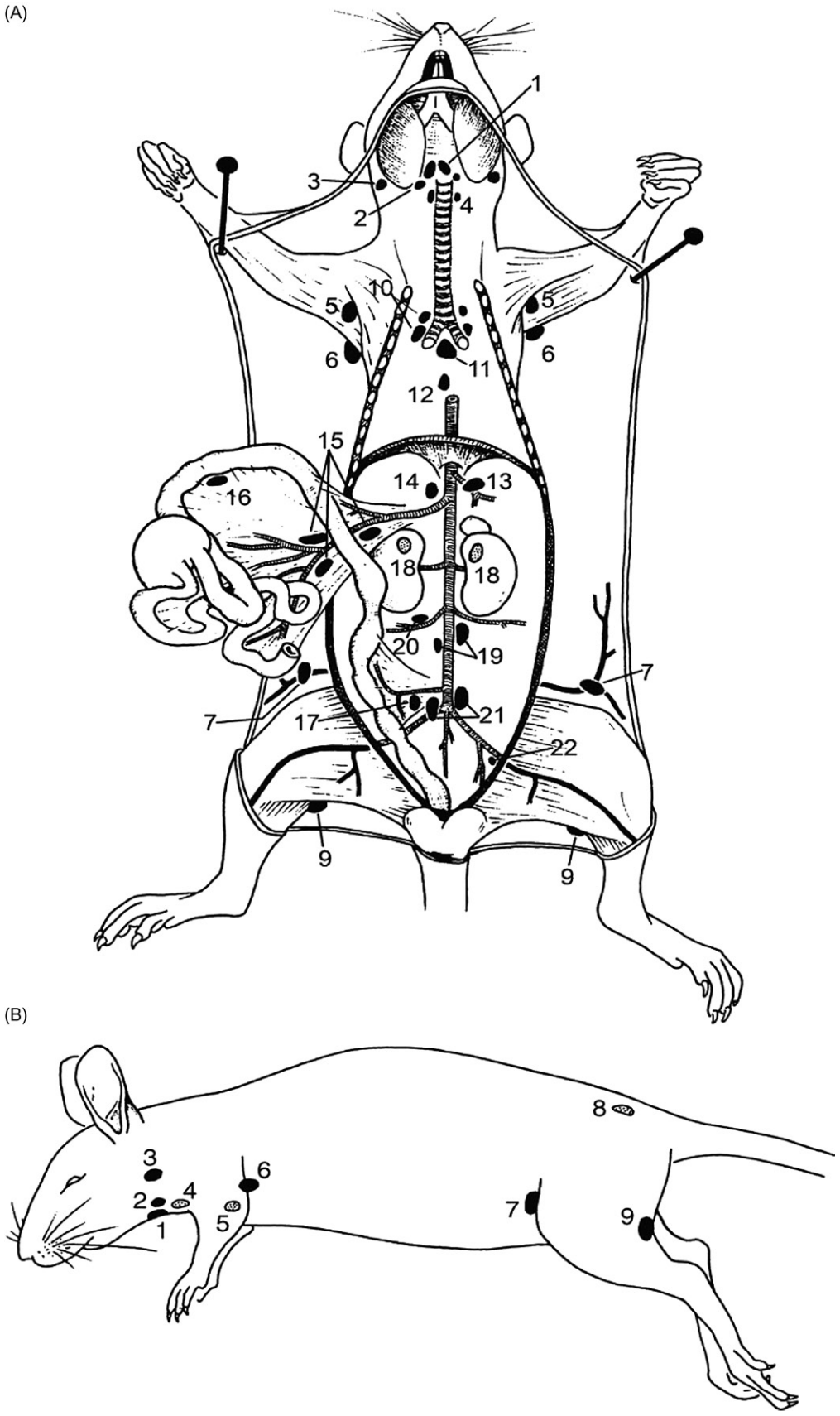

FIGURE 19.11 Anatomical distribution of lymph nodes in the rodent. See accompanying Table 19.3 for lymph node names. Source: Reproduced from Van den Broeck W, Derore A, Simoens P: Anatomy and nomenclature of murine lymph nodes: Descriptive study and nomenclatory standardization in BALB/cAnNCrl mice. *J Immunol Methods* 2006; 312(1–2): 12–19, with permission from Elsevier.

TABLE 19.3 Lymph Nodes Observed in BALB/cAnNCrl Mice (see Figure 19.11)

English Name	Location
1. Mandibular	Rostromedial to the sublingual and mandibular salivary glands
2. Accessory mandibular	Dorsolateral to the mandibular lymph node
3. Superficial parotid	Ventral to the external acoustic pore, caudal to the extraorbital lacrimal gland, cranioventral to the parotid salivary gland, dorsal to the junction between the superficial temporal vein and the maxillary
4. Cranial deep cervical	Medial to the external jugular vein and sternocephalic muscle, lateral to sternohyoid muscle, caudal to digastric muscle, dorsal to the trachea
5. Proper axillary	Medial to the shoulder, dorsolateral to ascending pectoral muscle, at the junction between the lateral thoracic vein and the axillary vein
6. Accessory axillary	Caudal to triceps brachii muscle, lateral to cutaneous trunci muscle, in subcutaneous adipose tissue
7. Subiliac	In the fold of the flank (plica lateralis) cranial to thigh musculature, near the deep circumflex iliac artery and vein
8. Sciatic	Medial to superficial gluteus muscle, caudal to gluteus medius muscle and sciatic nerve
9. Popliteal	In the popliteal fossa between biceps femoris muscle and semitendinosus muscle
10. Cranial mediastinal	Bilaterally two lymph nodes located lateral to the thoracic thymus and along the internal thoracic artery and vein
11. Tracheobronchial	Single (unpaired) lymph node at the tracheal bifurcation
12. Caudal mediastinal	Single (unpaired) lymph node in the caudal mediastinum, ventral to the esophagus, along the ventral vagal trunk
13. Gastric	Single (unpaired) lymph node in the lesser omentum at the minor curvature of the stomach
14. Pancreaticoduodenal	Single (unpaired) lymph node in the mesoduodenum, dorsal to the portal vein, surrounded by pancreatic tissue
15. Jejunal	Large cluster of lymph nodes in the mesojejunum along the cranial mesenteric artery
16. Colic	In the mesocolon at the transition between ascending colon and transverse colon
17. Caudal mesenteric	Single (unpaired) lymph node in the caudal mesentery at the origin of the caudal mesenteric artery
18. Renal	Dorsal to the ipsilateral kidney nearby the renal blood vessels, caudal to the adrenal gland
19. Lumbar aortic	Lateral to (and adjacent with) the abdominal aorta, halfway between the origin of the renal and common iliac arteries
20. Lateral iliac	In adipose tissue caudolateral to the kidney along the deep circumflex iliac artery
21. Medial iliac	Major bilateral lymph node at the terminal segment of the abdominal aorta and the origin of the common iliac artery
22. External iliac	Small lymph node along the initial (intra-abdominal) segment of the external iliac artery, before the latter enters the femoral canal

somewhat larger in size. They are usually grayish in color and elongated or round. The largest rodent lymph nodes are generally the mesenteric and mandibular nodes. Other nodes commonly used for rodent histopathology studies include popliteal (in fat behind the knee), axillary, and subiliac. Human lymph nodes are present in typical external locations, including neck (cervical), axillae, and inguinal regions, and also internal locations, including thoracic, para-aortic, and mesenteric regions (Fig. 19.12). Human lymph nodes vary in size from 0.5 to 2 cm. Even in healthy humans, external lymph nodes may be palpable.

The lymph nodes are important components of the immune system, and their anatomy is similar in rodents and humans. Location and nomenclature of lymph nodes in all three species have been reported in various publications but terminology may differ for nodes located in similar anatomical locations. No official rodent terminology exists for lymph nodes but a publication on mouse nodes suggested proper terms based on international anatomical nomenclature (see Further Reading, Van den Broeck, 2006).

A three-dimensional schematic of a typical human lymph node is outlined in Fig. 19.13. The lymphoid lobule has been described as the basic anatomical and functional lymph node unit. Afferent lymphatics enter the lymph node on the convex edge, and efferent lymphatics exit on the concave edge. A fibrous capsule surrounds the exterior of the lymph node. Blood supply is provided by arterioles and venules, typically entering the node near the efferent lymphatics. Within the node is a cortex, composed of lymphoid nodules, and a medullary sinus, containing cords of lymphocytes and plasma cells with associated macrophages. Lymph flows from the afferent lymphatics into the subcapsular

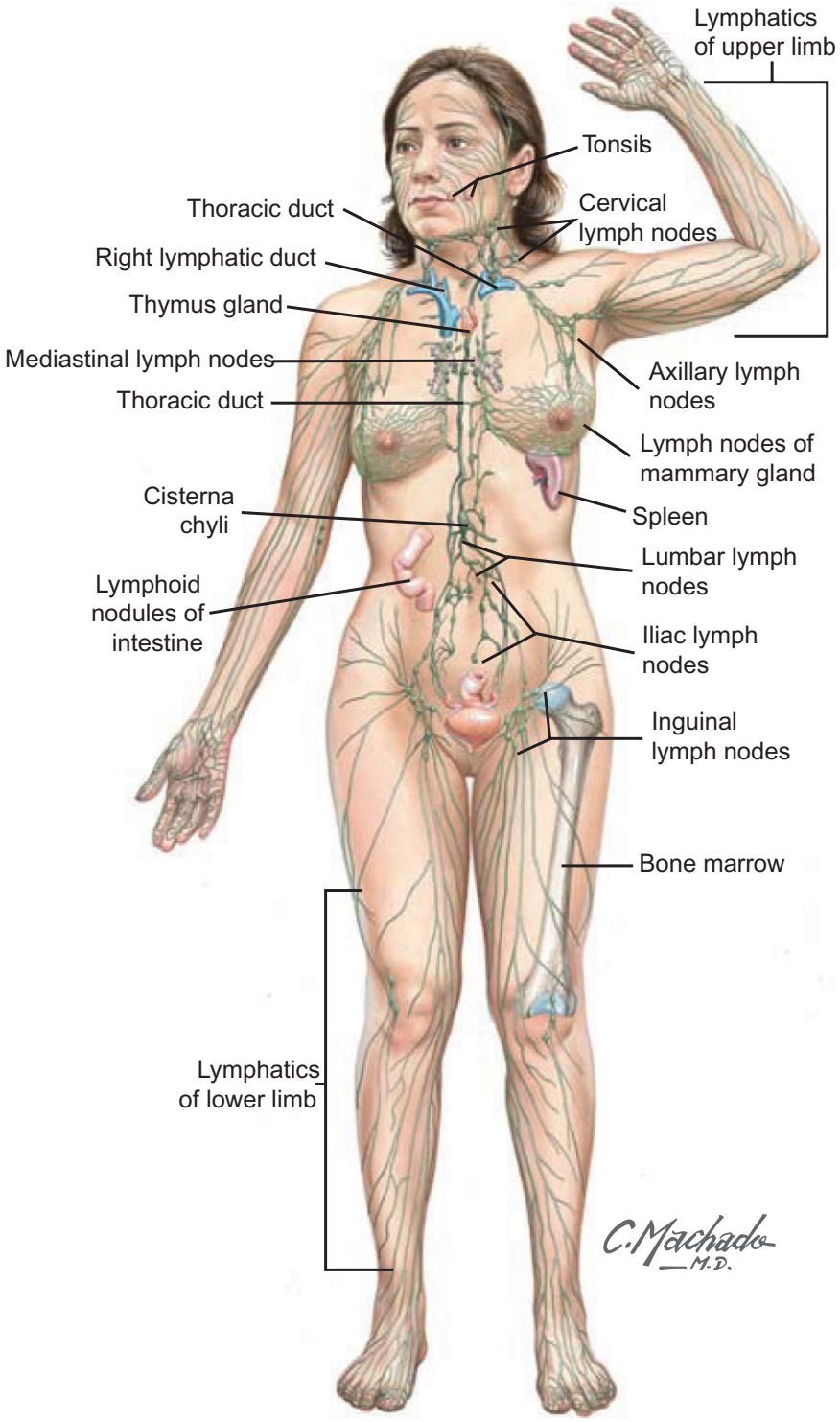

FIGURE 19.12 Common distribution of lymph nodes in adult human. Source: © Elsevier, Inc., www.netterimages.com.

sinuses, cortex, and medulla, exiting through efferent lymphatics. Lymphocytes enter the lymph node through afferent lymphatics or postcapillary venules. Antigens in the lymph or blood enter the node and stimulate lymphocytes in the cortex to produce both effector and memory B and T cells. Tissue drainage patterns are described in one of the references (Tinley et al.) for rat lymph nodes.

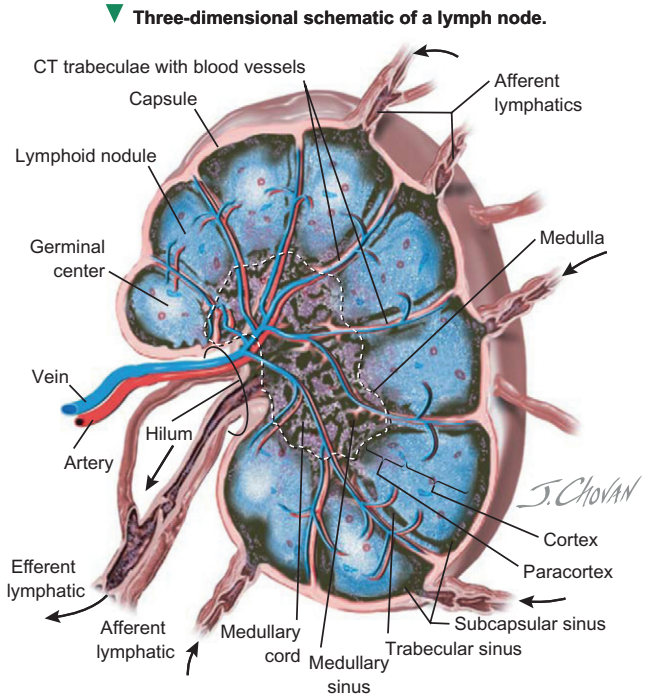

FIGURE 19.13 Three-dimensional schematic of a human lymph node. Source: © Elsevier, Inc., www.netterimages.com.

HISTOLOGY

As the size of rodent lymph nodes is very small, routine histological sections can vary in morphology. For example, sections taken off center on the node, either in a sagittal or transverse plane, will show variable size areas of the cortex, paracortex, and medulla (Figs. 19.14 and 19.15). Thus, although these appearances are normal, they may mimic lesions seen in older rodents, experimentally induced disorders, or mutant rodents. The mandibular lymph node may be the most variable of all in rodents with the mesenteric second. The mandibular node responds to activity in its draining tissues, nasal and oral cavities which are often exposed to outside insults. Thus, reactive changes (germinal center hyperplasia, plasma cell hyperplasia) often occur in this node more so than in others. A typical section and some variable sections are shown in Figs. 19.15 and 19.16. Lymph node compartment size is dependent on the plane of section. The capsule is thin, with underlying subcapsular sinuses. The cortex contains follicles and few small germinal centers in young rodents. The B cells are PAX5$^+$ in rodent nodes (Fig. 19.16C) and CD20$^+$ in human nodes (Fig. 19.16D). Often, germinal centers are not seen in young (<4 months of age) rodent nodes. When germinal centers are present, they typically contain centrocytes, centroblasts, and follicular dendritic cells with tingible body macrophages and apoptotic cell debris (Fig. 19.14A, C). Larger and/or greater numbers of germinal centers indicate response to antigenic stimuli.

The paracortex contains mostly T cells (which are CD3$^+$, Fig. 19.16A, B), dendritic cells, and high endothelial venules (HEVs) with migrating lymphocytes (Fig. 19.17C, D). HEVs have the same general structure in humans and rodents but the endothelial cytology varies among the species (Figs. 19.17C, D). The lumen of the HEVs appears larger in rats and humans (Figs. 19.17C, D and 19.18A). In young rodents, the paracortex has few obvious dendritic cells but they may be more prominent in rats (Fig. 19.18A). HEVs and dendritic cells may become more obvious as the animal ages and in reaction to stimuli.

The medulla is composed of medullary sinuses lined by lining cells and medullary cords containing various cell types including histiocytes, macrophages, mast cells, and pigmented macrophages in mesenteric nodes especially of rats (Fig. 19.18B). Sinus histiocytes have more cytoplasm in rats and humans. Mast cells can be seen more commonly in young rat medullary cords and sinuses than in mice (Fig. 19.18C, D). Mouse mast cells have more basophilic granules than do rats in H&E stains but are more common in older animals. Mast cells can be seen in the lymph nodes in humans, though it is not a common feature. In reactive lymph nodes, myeloid cells, mast cells, and plasma cells can be seen in the medullary cords. Sinuses lined by endothelial cells often contain histiocytes and macrophages. Connective tissue in the lymph node stroma is fairly sparse.

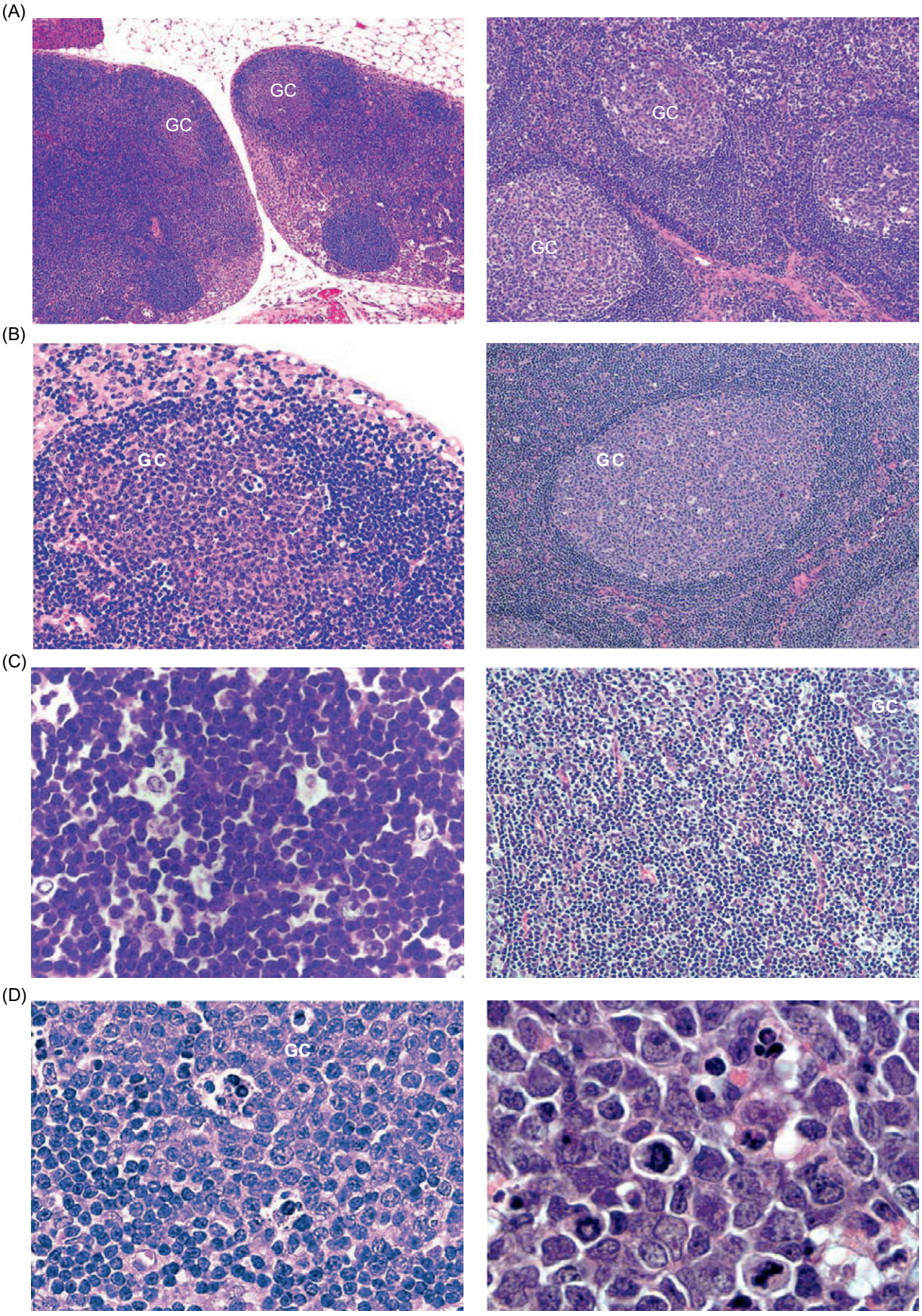

FIGURE 19.14 Rodent (mouse) and human lymph nodes. (A) Lymph node capsule, germinal centers (GC), and interfollicular (paracortical) lymphocytes from mouse (left) and human (right). (B) Germinal center of mouse (left) and human (right). (C) Paracortical/interfollicular zone of mouse (left), and human (right) with hyperplasia in human lymph node. Mouse paracortex shows dendritic cells and mature T cells. Note the germinal center at the right edge of the human image. (D) Close-up of germinal center cells of mouse (left) and human (right), with mitotic figures, and macrophages containing apoptotic debris.

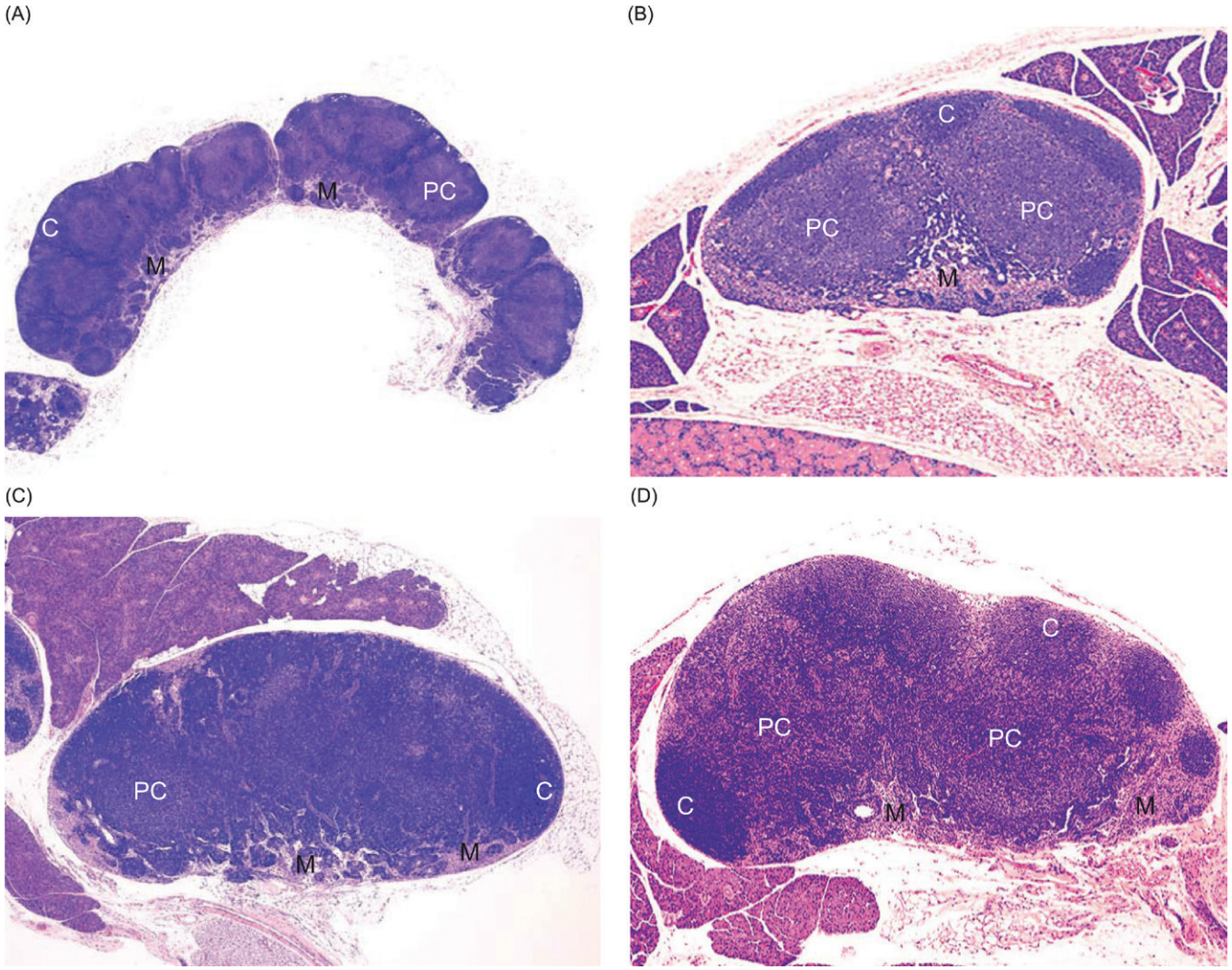

FIGURE 19.15 Variation in lymph node sections in young rodent (mouse). The mesenteric lymph node (A) shows a prominent pale paracortex (PC) with thin rim of cortex (C), whereas the other sections (B–D) show variations in the size of the medulla and paracortex.

Need-to-know

- The lymph nodes of rodents are very small compared to human lymph nodes; therefore, histological appearance varies based on the plane of section in rodents more so than for human nodes.
- Lymph nodes in young rodents do not have well-developed germinal centers, whereas germinal centers are seen in humans at all ages.

Because human lymph nodes are much larger than rodent lymph nodes, it is much easier to routinely cut a full cross section of the human node for examination by light microscopy. Similar to rodent, human lymph nodes are surrounded by a connective tissue capsule; however, it is thicker than that in rodents (Figs. 19.14 and 19.17). Underlying the capsule is the lymph node cortex, which contains primary and secondary B cell follicles. Secondary follicles contain germinal centers, and multiple germinal centers may be seen in a reactive lymph node (Fig. 19.14A, B), even in young humans. Germinal centers are surrounded by a well-formed mantle zone more so in humans (Fig. 19.4B). The germinal center and mantle zone both typically show polarity, with the thicker portion of the mantle zone facing the cortex and the thin portion facing the central portion of the node. Underlying the thin portion of the mantle zone is the dark

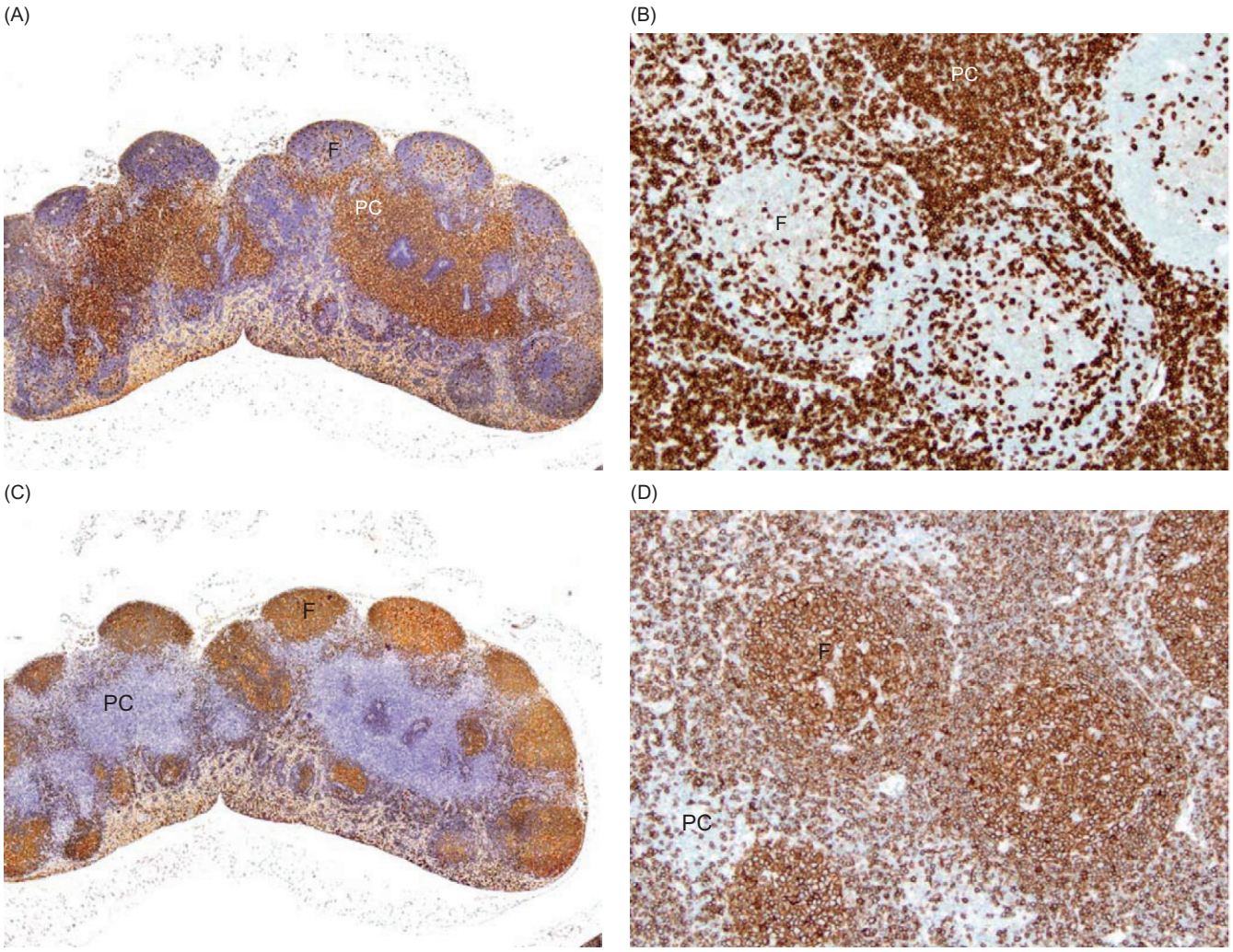

FIGURE 19.16 Immunohistochemical (IHC) detection of T and B cells in lymph nodes. The staining patterns are similar in all three species. Cortical follicles (F) contain the majority of B cells whereas T cells populate the paracortex (PC). (A) Rodent (mouse) lymph node immunolabeled for T cells with CD3; low magnification demonstrates cortical and paracortical staining pattern. (B). Human lymph node immunolabeled for T cells with CD3; high magnification demonstrates cellular staining pattern not present in follicles. (C) Rodent (mouse) immunolabeled for B cells using PAX5 shows follicular pattern. (D) Human lymph node immunolabeled for B cells using CD20 also shows follicular pattern.

Need-to-know

- Distribution of B- and T-cells within lymph nodes is the same in all three species.

zone of the germinal center, which consists primarily of centroblasts, whereas at the opposite pole of the lymph node is the light zone, which contains greater numbers of centrocytes, T cells, and dendritic cells. Of note, at high power, the centroblasts of the germinal center may be mistaken as atypical if viewed out of context of the remainder of the lymph node because they may contain multiple mitotic figures, apoptotic bodies, and activated cells characterized by high nuclear:cytoplasmic ratios, vesicular chromatin, and prominent nucleoli (Fig. 19.14B). In human lymph nodes, a marginal zone may sometimes be seen surrounding the mantle zone of a follicle, but it is less well developed than those seen in other organs, such as the spleen or mucosa-associated lymphoid tissue (MALT). Between the follicles is the paracortical (interfollicular) zone. This zone typically contains small reactive T lymphocytes. When stimulated, dendritic cells present antigens to the adjacent lymphocytes. In antigen-stimulated (reactive) lymph nodes, the mixture of the small lymphocytes and abundant dendritic cells is

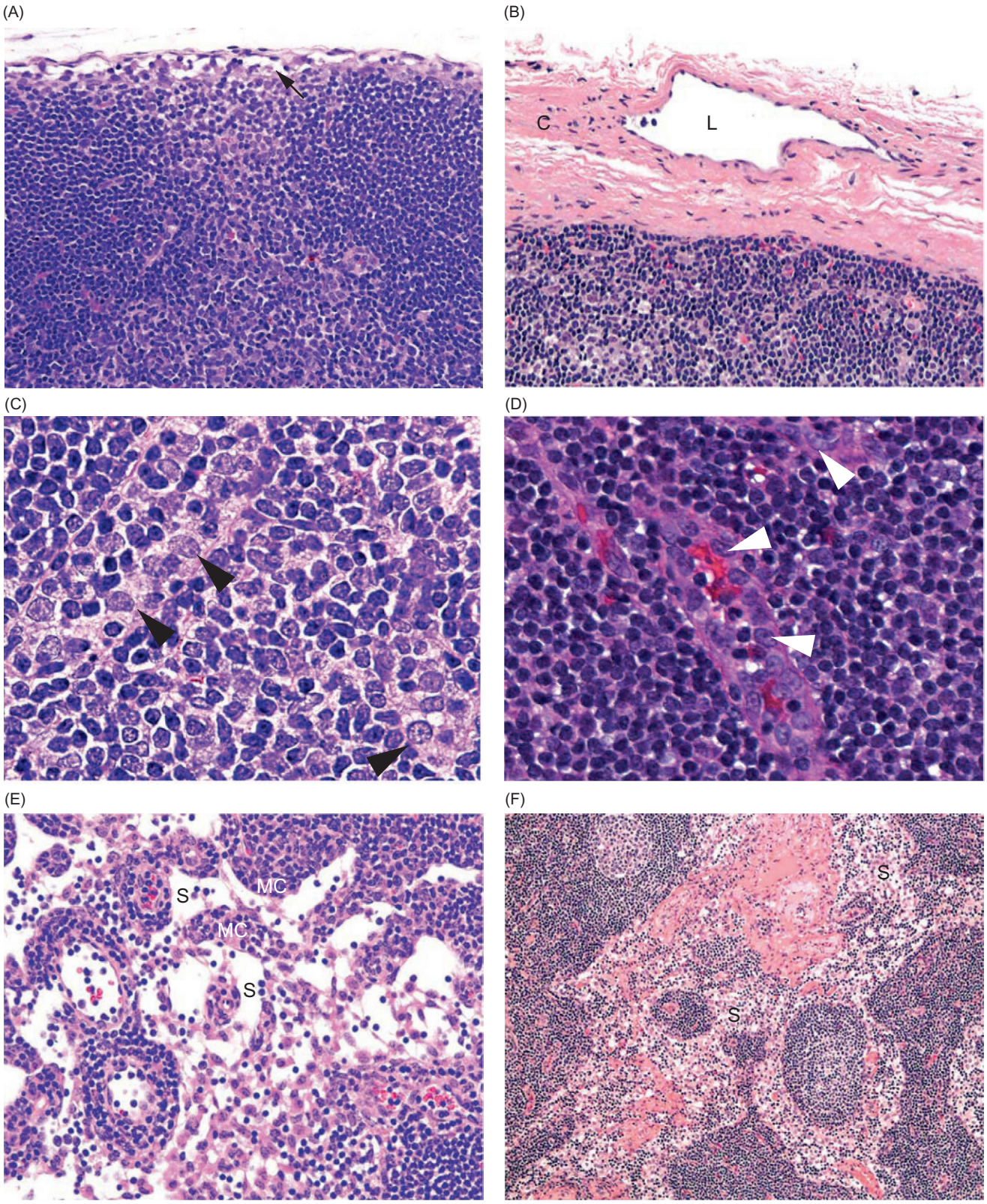

FIGURE 19.17 Lymph node capsule, paracortex, and subcapsular sinus. (A) The rodent (mouse) lymph node capsule is very thin (arrow); (B) the thicker human lymph node capsule is composed of more connective tissue. Lymphatic vessel (L) is indicated. (C, D) High endothelial venules (HEVs) (black arrowheads) in young adult rodent (mouse) are composed of large pale eosinophilic endothelial cells, whereas human (D) HEVs are more cuboidal in appearance (white arrowheads). (E) Medullary sinuses (S) and medullary cords (MC) in rodent (mouse) also have little connective tissue. (F) Medullary sinuses (S) are also seen in human lymph nodes.

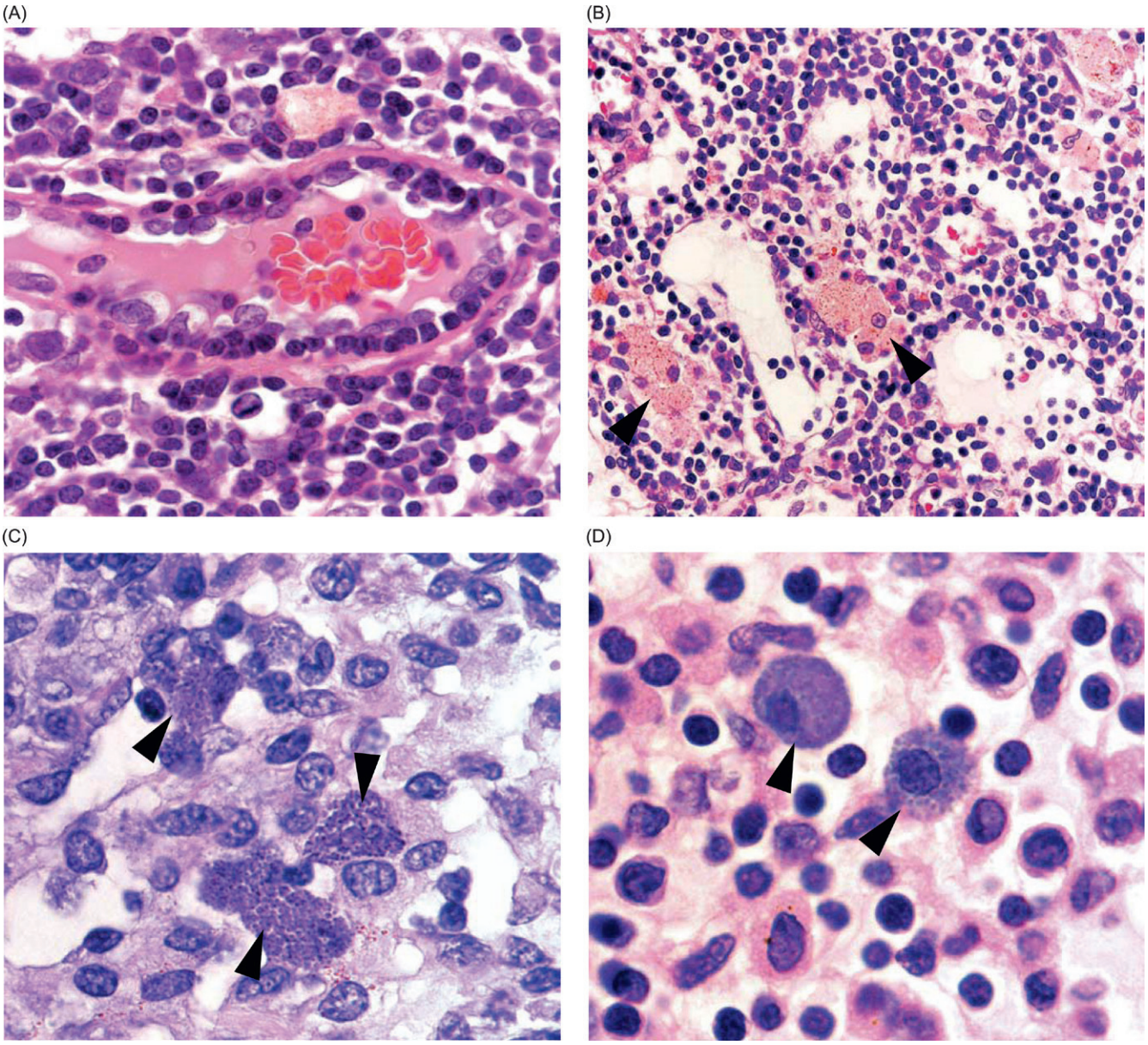

FIGURE 19.18 Rodent lymph node features. (A) Rat paracortical vein resembling a high endothelial vein (HEV), erythrocytes are present. (B) Rat pigmented macrophages with abundant cytoplasm (arrowheads) in medullary cords of mesenteric lymph node. (C) Mouse mast cells (arrowheads) in medullary cords. Note large dark blue granules. (D) Rat mast cells (arrowheads) in medullary cords. Note smaller blue granules.

Need-to-know

- Rodent connective tissue mast cell granules are visible on routine H&E staining.
- Rodent mucosal and neoplastic mast cells and human cells typically required metachromatic stains (toluidine blue, giemsa) to highlight the cytoplasmic granules.

termed nodular paracortical hyperplasia and appears mottled at low power (Fig. 19.14C). In the central portion (medulla) of the lymph nodes, the patent sinuses are visible. In a variety of reactive conditions, these sinuses may fill with histiocytes, a phenomenon designated sinus histiocytosis in rodents and humans (Fig. 19.17E, F).

Spleen

The spleen shows a similar general anatomical structure in both rodents and humans, in which it functions in filtering the blood and mediating immune responses (Table 19.4). In rodents, but not in humans, the spleen also serves as a normal

TABLE 19.4 Spleen

Feature	Rodent		Human
	Mouse	Rat	
	Gross		
Location	Abdomen, left upper quadrant	Similar to mouse	Similar to rodent
Normal weight (adult)	100–200 mg (2–4-month old)	500–900 mg (2–4-month old)	150 g
Function	Filtering, lymphoid organ; hematopoiesis	Same as mouse	Filtering, lymphoid organ
	Histologic		
Capsule	Connective tissue and smooth muscle	Similar to mouse	Similar to rodent
Red pulp	Filtering and transport components; sinusoids and cords compose the filtering apparatus; cords contain macrophages that recognize and remove foreign material and damaged erythrocytes from circulation	Similar to mouse	Similar to rodent
Extramedullary hematopoiesis	Red pulp—normal site of low levels of hematopoiesis, but highly reactive to conditions that also stimulate bone marrow	Similar to mouse	No or minimal hematopoiesis under normal conditions; may be increased with marrow fibrosis or infiltration
Periarteriolar lymphoid sheaths	Cuff of lymphoid cells consisting predominantly of $CD4^+$ T cells surrounding arterioles although may be less developed than human	Similar to mouse	Similar to rodent, but more developed
B cell follicles	Include both resting primary follicles containing naive B cells and activated secondary follicles containing germinal centers	Similar to mouse	Similar to rodent
Marginal zone	Thin in most strains/lines of mice; marginal sinus can be appreciated between the marginal and mantle zones	Very wide and prominent; marginal sinus can be appreciated	Present surrounding primary and secondary B cell follicles; composed of memory B cells with abundant cytoplasm; marginal sinus not well appreciated by light microscopy

site of reactive hematopoiesis throughout life that can provide a hematopoietic response to various stimuli (i.e., diseases, infectious agents, tumors, blood loss, and anemia).

GROSS ANATOMY

In each species, the spleen is located in the left upper quadrant of the abdomen adjacent to the greater curvature of the stomach. The rodent spleens are somewhat more elongated than is the human spleen (Fig. 19.19) and weighs 100–200 mg in 2–4-month-old mice and 500–750 mg in young rats. The rodent spleen is surrounded by a capsule composed of fibrous tissue, elastic fibers, and smooth muscle, with an overlying thin layer of mesothelial cells. The human spleen weighs approximately 150 g and is surrounded by a connective tissue capsule containing collagen and a small amount of smooth muscle. The amount of smooth muscle in the splenic capsule of both rodents and humans is low compared with that in other mammals, reflecting the lower storage/reserve function of the spleen in rodents and humans.

Vessels enter and leave the spleen at the hilum in both species. Blood enters the spleen via the splenic artery and leaves via the splenic vein, which drains into the portal vein. Occasionally, an accessory spleen may be detected in rodents and humans.

HISTOLOGY

The spleen in the three species contains two primary zones, the red pulp and the white pulp (Figs. 19.20–19.23). In all three species, it is possible to appreciate the two zones grossly on cut section (Fig. 19.19). The ratio of red pulp to white pulp in human spleen is higher than that in rodents, because white pulp accounts for a greater proportion of the splenic volume. The red pulp is the primary site of filtering in both species (Figs. 19.21E and 19.22A), with a meshwork of sinusoids and cords serving as a filter. The sinusoids are lined by endothelial cells (littoral cells) that in humans express CD8. These cells are also thought to be present in the rodent spleen but are not as well characterized. The cords of the red pulp contain macrophages in mice marked by F4/80,

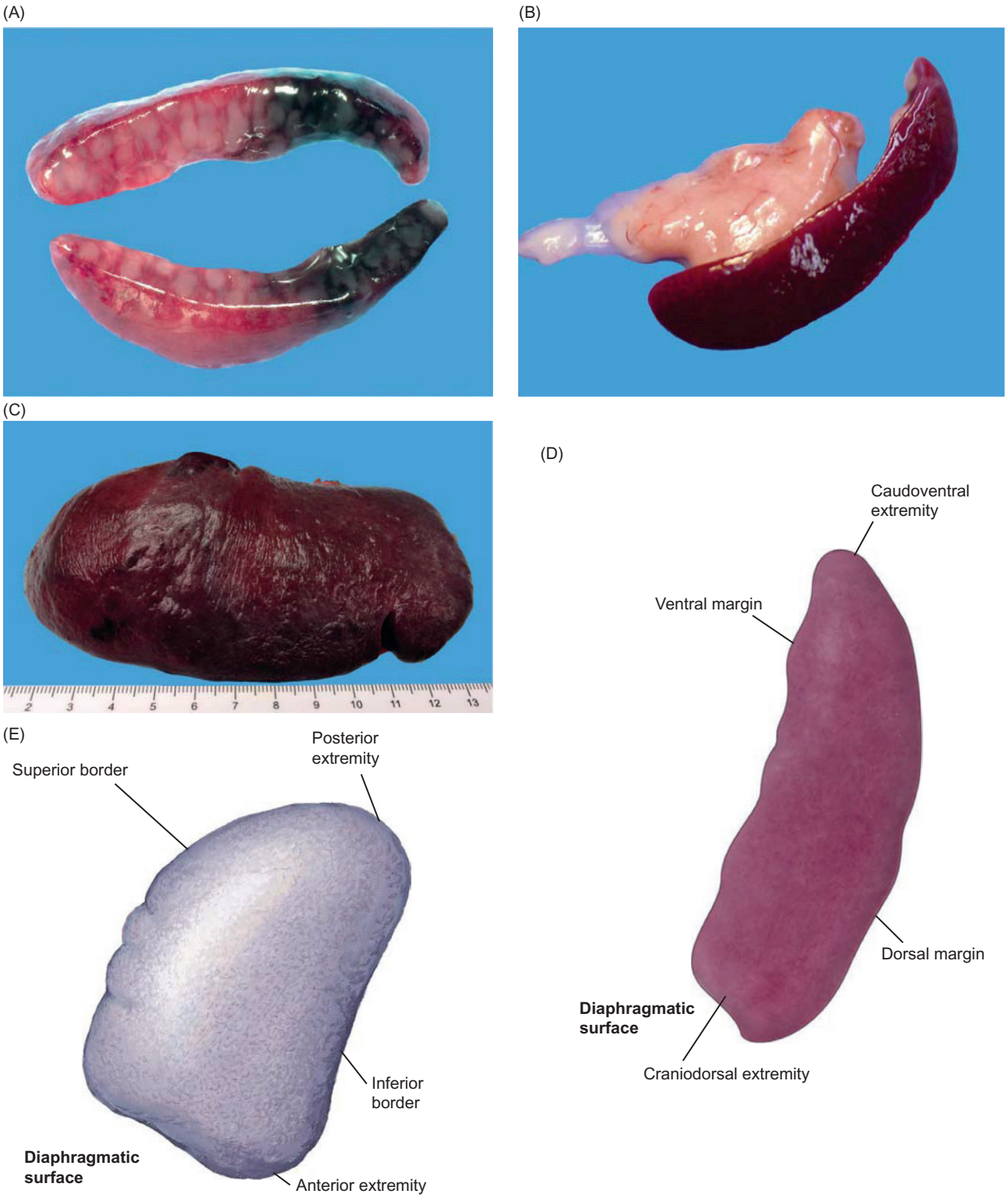

FIGURE 19.19 Spleen regional anatomy. (A) Mouse spleen from a pigmented C57BL6/J mouse with focally extensive melanosis. Note the white pulp is readily visible in this image captured with a dissection microscope. (B) Rat spleen with attached pancreas and mesentery. (C) Human spleen. (D) Schematic of mouse spleen. (E) Schematic of human spleen. D and E. Source: © Elsevier, Inc., www.netterimages.com

Need-to-know

- Melanosis may be seen grossly on the spleen of pigmented rodent strains.

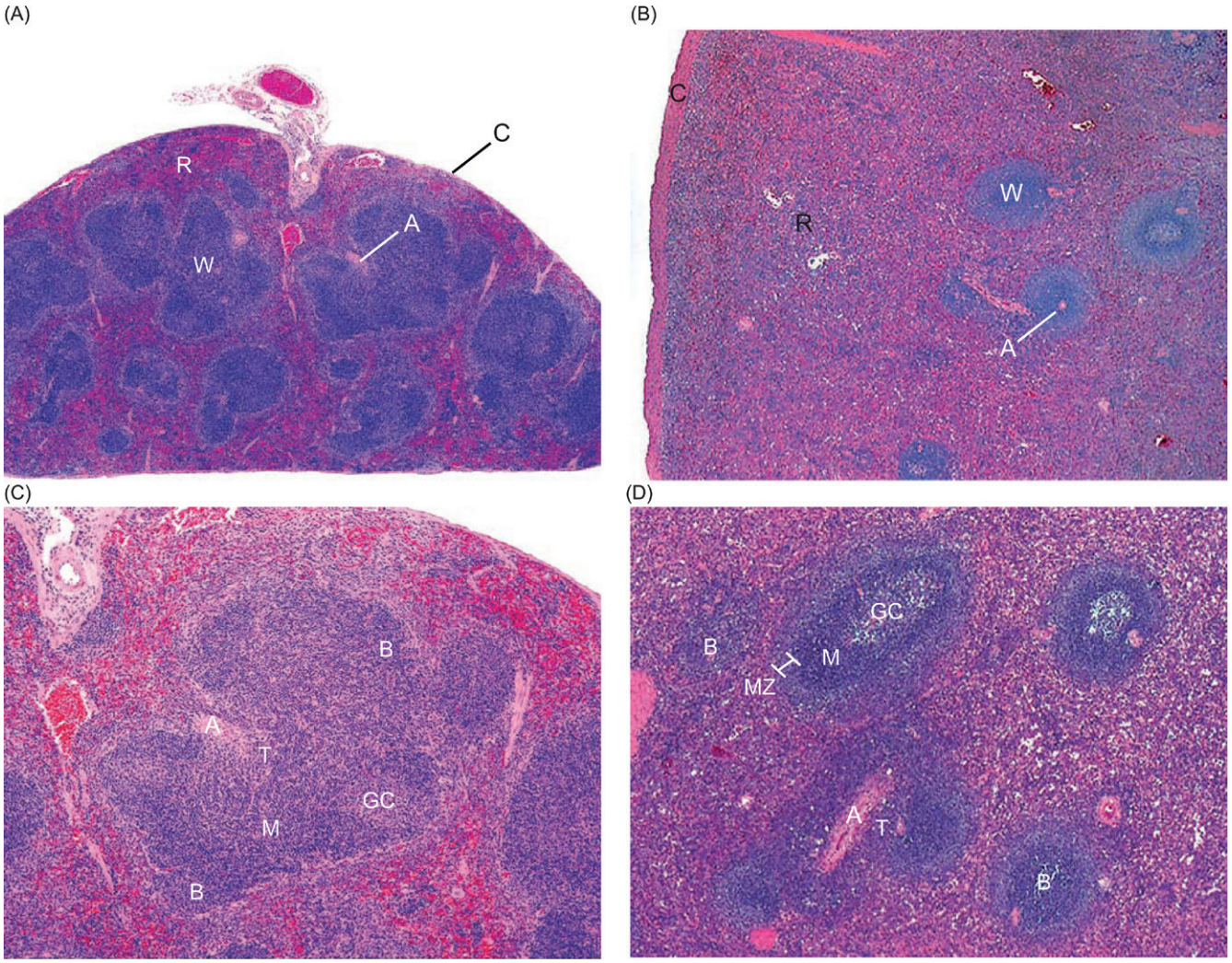

FIGURE 19.20 Low- and medium-magnification views of spleen. Rodent (mouse) (A and C) and human (B and D) are shown. Capsule (C), red pulp (R), white pulp (W), central arteriole (A), T cells area (T), B cell area (B), germinal center (GC), mantle zone (M), and marginal zone (MZ, region noted by bars) are indicated. Note that white pulp makes up a significantly larger proportion of mouse spleen than human spleen. *GCs* and follicles often become more prominent and larger in mice as they age and are exposed to environmental influences.

Need-to-know

- Rodent spleen has more white pulp than human, where red pulp comprises 75–90% of splenic volume.
- Red pulp in the rodent is a site of normal hematopoiesis. In the adult human, significant extramedullary hematopoiesis is not normal.
- The rodent spleen has a discernible marginal sinus, whereas no comparable structure is appreciated in the human spleen by light microscopy.
- The B-cell zone predominates in the rodent white pulp, whereas the T-cell zone predominates in the human spleen.
- Melanin may be present diffusely or focally in the red pulp of the spleen of black-haired mice.

(Fig. 19.23E) and by CD68 in rats (Fig. 19.23F) that continually monitor the contents of blood as it passes through the spleen. Splenic macrophages remove and process material from the bloodstream including blood-borne debris, microorganisms, and damaged erythrocytes. Also present within the cords are structural elements such as fibroblasts. Scattered lymphocytes, predominantly $CD8^+$ T cells, and occasional plasma cells occupy the cords as well. In addition to the splenic sinusoids and cords, the red pulp contains capillaries that do not have filtering capabilities but are involved primarily in moving blood.

In rodents, the splenic red pulp is a normal site of low levels of hematopoiesis and a major site of

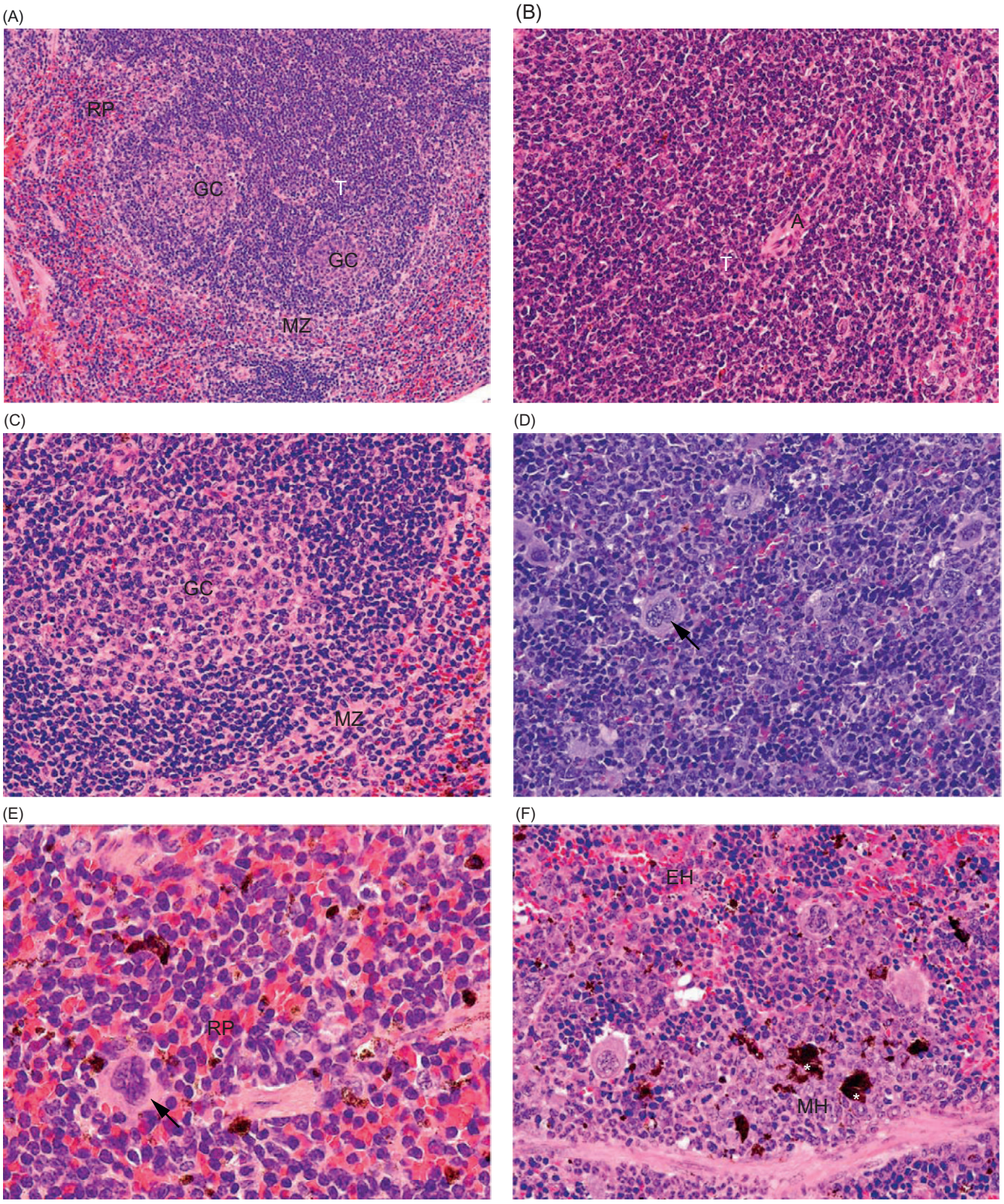

FIGURE 19.21 Rodent (mouse) spleen. (A) Splenic white pulp. Note the periarterial and periarteriolar sheaths of lymphoid cells, T cells area (T), and two germinal centers (GC) with adjacent thin marginal zone (MZ). Red pulp (RP) is also indicated. (B) PALS, T cells area showing small lymphocytes around the central arteriole (*A*). (C) Germinal center with adjacent thin marginal zone. (D) Myeloid and erythroid hyperplasia with megakaryocytes (arrow) in red pulp. (E) Red pulp showing one megakaryocyte (arrow) and a low level of hematopoiesis. (F) Red pulp showing myeloid hyperplasia (MH) and erythroid hyperplasia (EH) with melanin pigment (*).

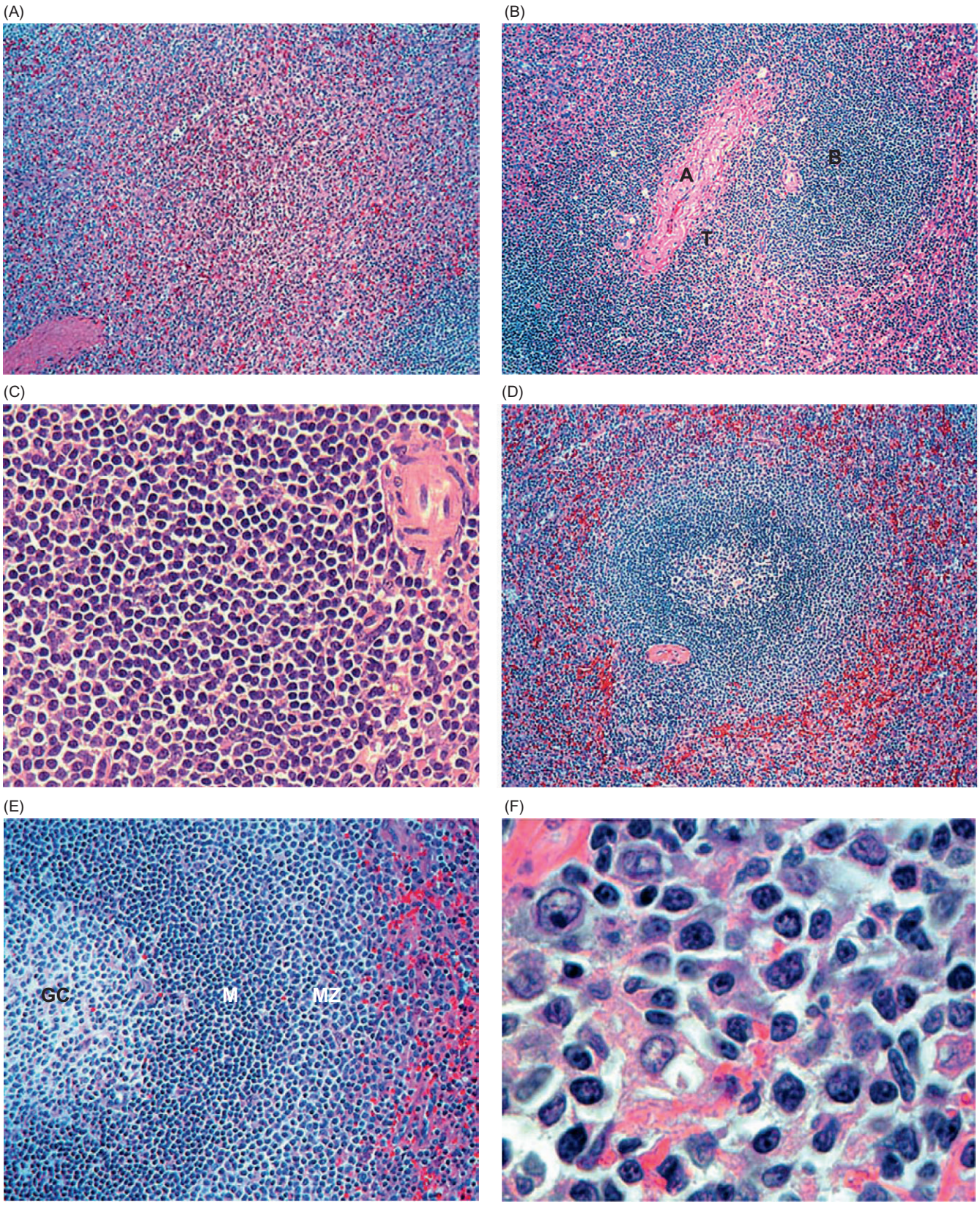

FIGURE 19.22 Human spleen. (A) Red pulp splenic cords and sinusoids. Note the relative paucity of lymphoid cells in this region. A small portion of white pulp is seen in the lower right-hand corner. (B) White pulp central arteriole (*A*) surrounded by small lymphoid cells, which are predominantly $CD4^+$ T cells (T) that make up the PALS. A B cell follicle (*B*) is seen at the periphery of this portion of the PALS. (C) PALS consist predominantly of small lymphoid cells. (D) Germinal center. Note the well-demarcated marginal zone, mantle zone, and central germinal center. As seen in this image, collections of erythrocytes may be seen surrounding reactive B cell follicles (lying within the perifollicular zone), giving the impression of a red halo. (E) Germinal center (GC), highlighting the differences between the GC, mantle zone (M), and marginal zone (MZ). (F) High-power view of the GC showing larger (centroblasts) and smaller (centrocytes) B cells.

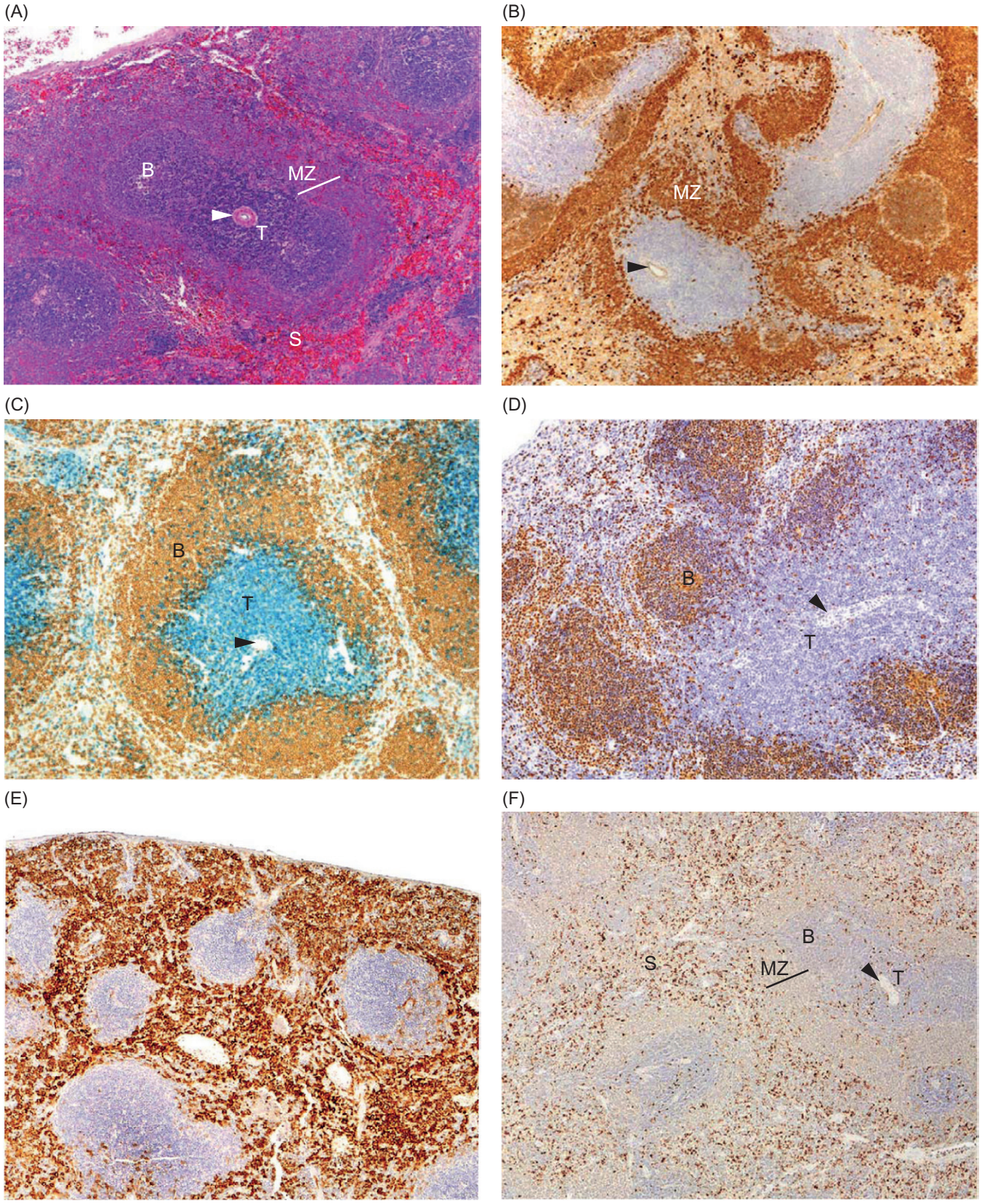

FIGURE 19.23 Immunohistochemical (IHC) labeling of rodent spleen. (A) Rat spleen stained with H&E showing wide marginal zone (MZ, line). B and T cell regions, red pulp sinusoids (S), and arteriole (arrowhead) are indicated. (B) Rat spleen with IgM distribution in wide marginal zones. (C) Double IHC stain showing mouse B (CD45R, brown) and T (CD3, blue) cells. (D) Mouse spleen with PAX5 in B cells (follicles and marginal zones). (E) Mouse spleen with F4/80 expression in the red pulp macrophages. (F) Rat spleen showing CD68 in red pulp myeloid cells (including macrophages). Arteriole (arrowhead) in PALS; B cell regions (B); T cell regions (T).

Need-to-know

- The anatomical distribution of lymphocyte and macrophage cell types within the spleen is similar in all three species.

reactive hematopoiesis (i.e., myeloid, erythroid, and megakaryocytic hyperplasia) (Fig. 19.20). Hematopoiesis in the spleen is referred to as EMH. In humans, EMH is generally minimal; however, small foci of incidental EMH may be seen, particularly in reactive or enlarged spleens. EMH can also occur in the setting of pathologic conditions impacting marrow hematopoiesis, such as myeloproliferative disorders, marrow fibrosis, or marrow infiltration.

Splenic hematopoiesis in rodents involves all three lineages (myeloid, erythroid, and megakaryocytic) and may be more prominent in older animals. As in the marrow, a decrease in hematopoiesis is usually not seen in the spleen as rodents age; however, increases in hematopoiesis (either tri-lineage or an increase in one lineage) may be seen under conditions that cause marrow stress. Melanin pigment can be seen focally or diffusely in the red pulp of rodents with black hair (Fig. 19.21F)

The white pulp in the three species is a lymphoid area consisting of periarterial and periarteriolar sheaths of lymphocytes (PALS) composed primarily of T (predominantly $CD4^+$ and $CD3^+$, Fig. 19.23C) cells and follicular dendritic cells. Associated with these T cell-predominant areas are rodent B cell follicles which are $CD45R^+$ (Fig. 19.23C) and $PAX5^+$ (Fig. 19.23D), that may include primary follicles consisting mostly of naive B cells or secondary follicles containing reactive germinal centers surrounded by a distinct mantle zone (Figs. 19.21 and 19.22). The white pulp in the three species is surrounded by a well-developed marginal zone composed of monocytoid-appearing B cells with abundant pale cytoplasm and marginal zone macrophages. The marginal zones of human (Figs. 19.20D, 19.22D, E) and rat spleen (Fig. 19.23A, B) are more prominent than in most mouse strains and stocks but some mouse strains or stocks may have more prominent marginal zones than other strains or stocks. Marginal zone B cells are often marked by the presence of IgM (Fig. 19.23B). In the human, the marginal zone is more developed in the spleen than in a typical resting lymph node but a similar marginal zone is not found in rodent nodes. The marginal zone of rodent and human spleen differs in that the rodent spleen histologically reveals a marginal sinus that separates a layer of metallophilic macrophages from the B cell layer and marginal zone macrophages, discernible by light microscopy in rodents, but only seen by ultrastructure and immunohistochemistry in humans. The marginal zone in the three species is contiguous with the T cell zone of the PALS and B cell follicles, and in humans both are surrounded by a perifollicular zone containing many capillaries, which may appear congested by light microscopy.

Mucosa-Associated Lymphoid Tissue

Lymphoid tissue is often found in association with epithelial-lined mucosa and, as noted previously, is termed MALT, which includes those found in the nasal cavity (NALT), auditory system (ATALT), lung (BALT), intestine (GALT), and in other sites. In rodents, grossly visible aggregates of lymphoid tissue are found in the small intestine as Peyer's patches (PP) (Fig. 19.24A) that often contain germinal centers (Fig. 19.24B), also noted in Chapter 11, Upper Gastrointestinal Tract. PP in rats are larger than those in mice and often have larger germinal centers. There are more PP in the jejunum of mice than in the ileum and more in the ileum of rats than in their jejunum. A few small grossly visible aggregates may be found in the large bowel of mice, one in the tip of the cecum and others along the ascending and descending colon. In rats, two large grossly visible lymphoid nodules are prominent in the ascending and descending colon and also in the tip of the cecum.

In humans, such tissue is most commonly seen in the palatine and nasopharyngeal tonsils and in the ileum as PP, in which it is referred to as gut-associated lymphoid tissue (GALT). Rodents have

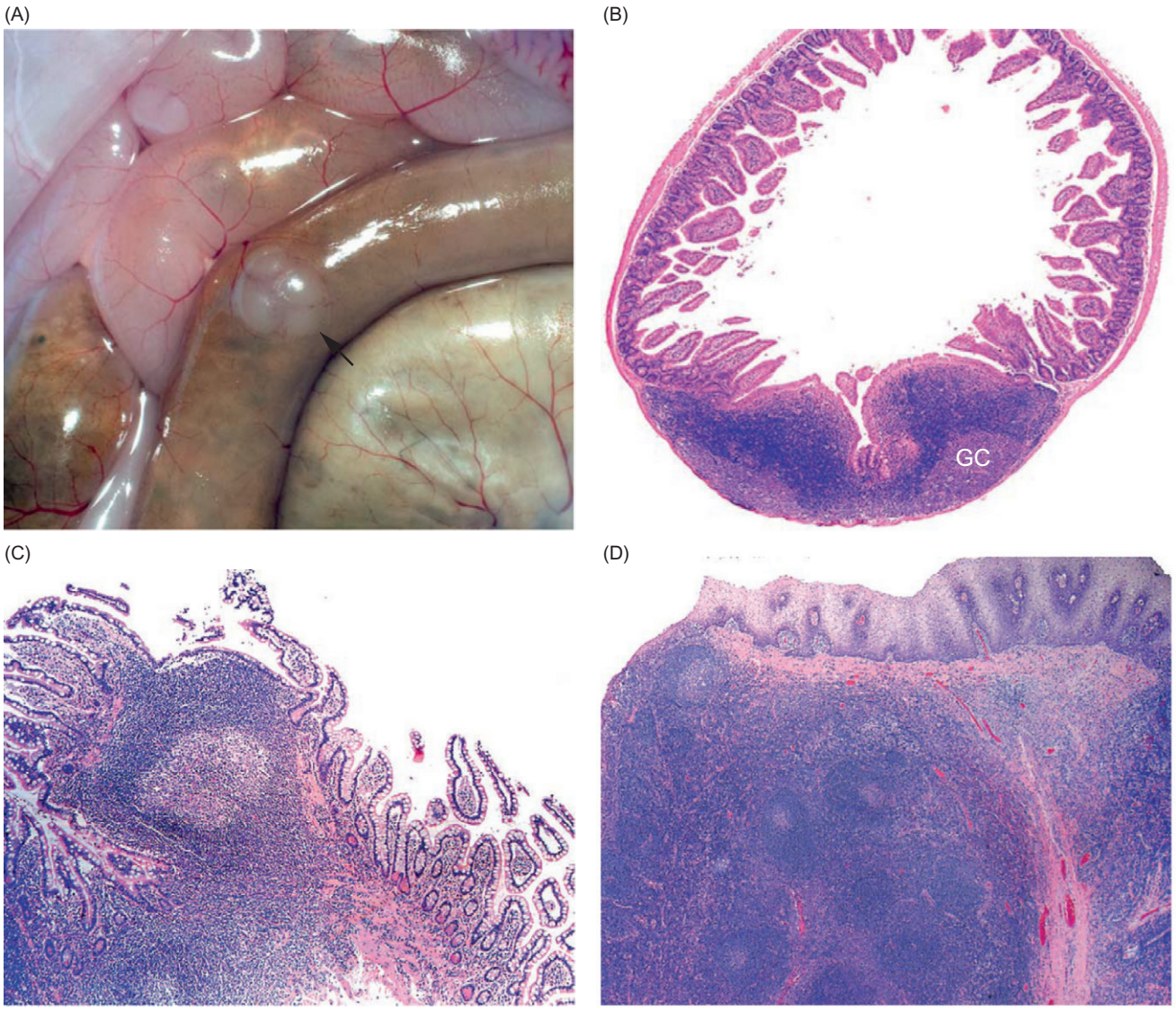

FIGURE 19.24 Mucosa-associated lymphoid tissue (MALT). (A) Rodent (mouse) Peyer's patch (arrow) is grossly visible on the antimesenteric aspect of the small intestine. (B) Histologically, the pale zones in the mouse Peyer's patch are germinal centers (GC). (C) Human Peyer's patch in the ileum with pale germinal centers. (D) Human tonsil showing subepithelial lymphoid tissue with pale germinal centers.

no tonsils but do have nasal-associated lymphoid tissue (NALT).

Humans and mice usually do not have bronchus-associated lymphoid tissue (BALT), although mice from some rare housing facilities may have BALT in their lungs (see Chapter 9, Respiratory System for further discussion). Rats always have BALT. Induced BALT (iBALT) may occur in aging mice (and in humans) and after experimental infections and with exposure to antigens. iBALT is composed primarily of B cells (Fig. 19.25B, C). Tertiary lymphoid tissue is induced by infections and immune-mediated diseases in tissues where lymphoid cells are not normally found (such as in lung and salivary gland in mice). Please see also a discussion of BALT in Chapter 9, Respiratory System.

Gastrointestinal MALT is typically located in the submucosa, adjacent and deep to the epithelium,

Need-to-know

- Tonsils are a normal finding in human oral cavity but are not present in rodents.
- Intestinal MALT is similar in mice and humans.

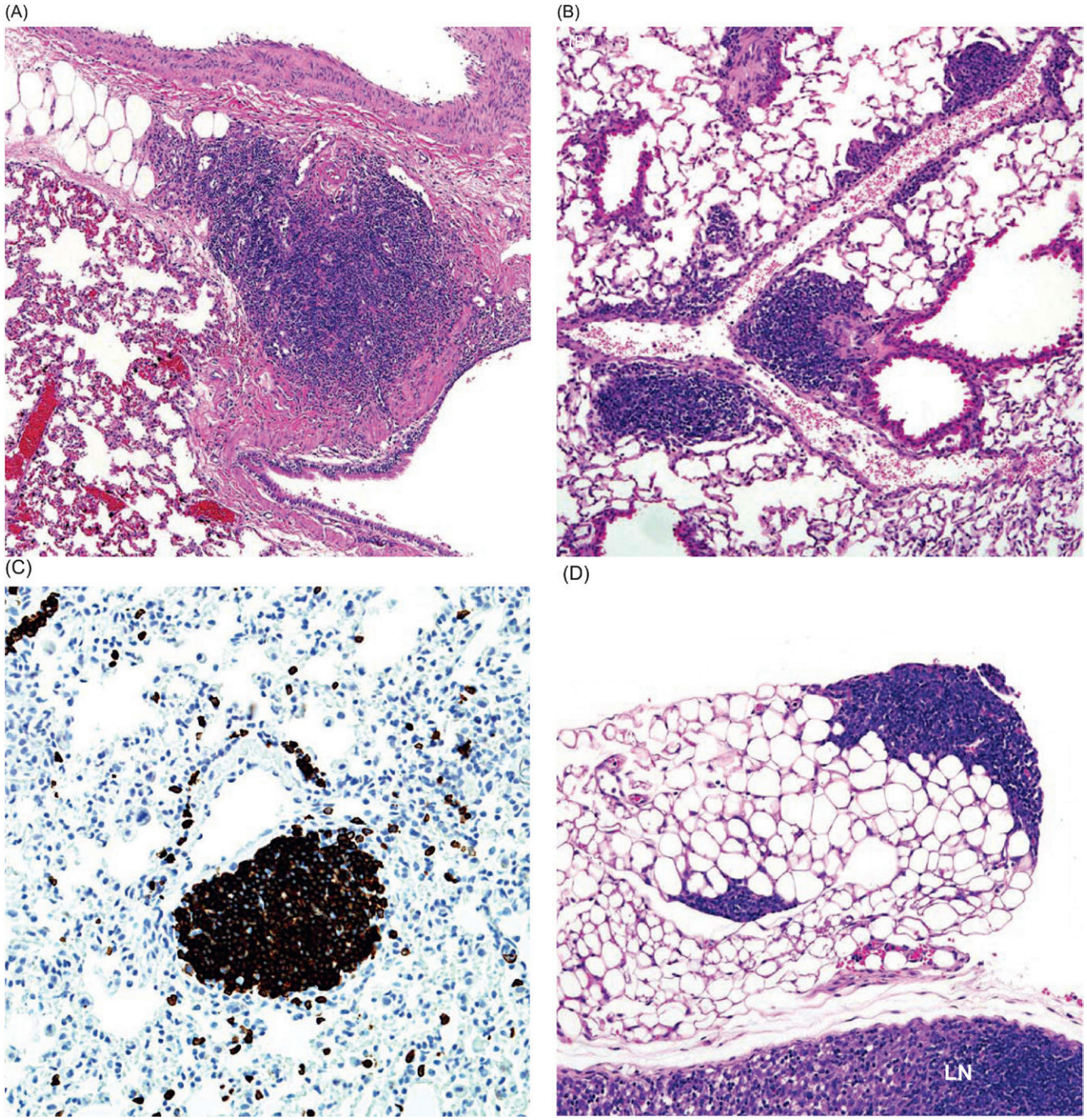

FIGURE 19.25 Secondary and tertiary lymphoid tissues in rodents. (A) Rat lung BALT adjacent to bronchus. (B) iBALT in an aging mouse. (C) Mouse tertiary lymphoid tissue iBALT is composed mostly of B cells ($CD45R^+$). (D) Mouse mesenteric lymphoid tissue, milky spots. Mesenteric lymph node (LN) is indicated.

and shows a similar structure to lymphoid tissue in other organs with primary and secondary follicles noted. As mentioned previously, these follicles are often surrounded by a marginal zone resembling that seen in the spleen and more well developed and distinct than that seen in the lymph nodes. MALT in humans, rodents may expand under exposure to chronic antigenic stimulation. Examples of MALT in normal human tonsil and the bowel of mouse and human are illustrated in Fig. 19.24C, D. The human appendix also has lymphoid nodules (see Chapter 12: Lower Gastrointestinal Tract).

Milky Spots

Foci of lymphocytes and macrophages known as milky spots are normally found in the omentum and mesentery of humans and rodents (Fig. 19.25D). They may be increased in number and size with age and in rodents infected with various infectious agents or in various immune-related diseases. Milky spots may also occur in mediastinal tissue.

Acknowledgments

We thank Dr. Herbert C. Morse (NIAID, NIH) for some of the mouse IHC figures, Christine Dijkstra for rat IHC, and Dr. Alfredo Molinolo (UC San Diego) for some of the rat tissues used to prepare figures. We thank Meghan Pickard and Matt Lurken (Anatomic Pathology, University of Minnesota) for gross images of the human spleen.

FURTHER READING AND RELEVANT WEBSITES

Aspinall R, Andrew D: Thymic involution in aging. *J Clin Immunol* 20(4):250–256, 2000.

Bain BJ: Bone marrow trephine biopsy. *J Clin Pathol* 54(10):737–742, 2001.

Belyaev DK, Gruntenko EV: Strain differences in thymus weight in mice with different predispositions to spontaneous mammary cancer. *Nature* 237(5355):401–402, 1972.

Cesta MF: Normal structure, function, and histology of the spleen. *Toxicol Pathol* 34(5):455–465, 2006.

Cesta MF: Normal structure, function, and histology of mucosa-associated lymphoid tissue. *Toxicol Pathol* 34(5):599–608, 2006.

Chang CC, Osipov V, Wheaton S, et al: Follicular hyperplasia, follicular lysis, and progressive transformation of germinal centers. A sequential spectrum of morphologic evolution in lymphoid hyperplasia. *Am J Clin Pathol* 120(3):322–326, 2003.

Dabbs DJ and Thompson LDR. *Diagnostic Immunohistochemistry: Theranostic and Genomic Applications*, Philadelphia: Saunders, 4th Edition, pp 960.

Diggs LW, Bell A, Sturm D: *The morphology of human blood cells* Wright Stained Smears of Peripheral Blood and Bone Marrow, 3rd edn., North Chicago, IL, 1975, Abbott Laboratories.

Dooley J, Erickson M, Gillard GO, et al: Cervical thymus in the mouse. *J Immunol* 176(11):6484–6490, 2006.

Dunn TB: Normal and pathologic anatomy of the reticular tissue in laboratory mice, with a classification and discussion of neoplasms. *J Natl Cancer Inst* 14(6):1281–1433, 1954.

Elmore SA: Enhanced histopathology of the spleen. *Toxicol Pathol* 34(5):648–655, 2006.

Erlandsen SL, Magney JE: *Color Atlas of Histology*, St. Louis, MO, 1992, Mosby-Year Book.

Frith CH, Ward JM: *Color Atlas of Neoplastic and Non-Neoplastic Lesions in Aging Mice*, New York, 1988, Elsevier. http://www.informatics.jax.org/frithbook.

Garcia CF, Swerdlow SH: Best practices in contemporary diagnostic immunohistochemistry: panel approach to hematolymphoid proliferations. *Arch Pathol Lab Med* 133(5):756–765, 2009 May.

Greaves P: *Histopathology of Preclinical Toxicity Studies: Interpretation and Relevance in Drug Safety Evaluation*, New York, 1990, Elsevier.

Hale LP: Histologic and molecular assessment of human thymus. *Ann Diagn Pathol* 8(1):50–60, 2004.

Harkema JR, Carey SA, Wagner JG: The nose revisited: A brief review of the comparative structure, function, and toxicologic pathology of the nasal epithelium. *Toxicol Pathol* 34(3):252–269, 2006.

Ioachim HL, Medeiros LJ: *Ioachim's Lymph Node Pathology*, 4th edn., Philadelphia, 2009, Wolters Kluwer/Lippincott Williams & Wilkins.

Jones TC, Ward JM, Mohr U, et al: *Hemopoietic System*, Berlin, 1990, Springer-Verlag.

Lee JJ, Jacobsen EA, Ochkur SI, et al: Human versus mouse eosinophils: "That which we call an eosinophil, by any other name would stain as red". *J Allergy Clin Immunol* 130(3):572–584, 2012 Sep.

Lee SH, Erber WN, Porwit A, et al: ICSH guidelines for the standardization of bone marrow specimens and reports. *Int J Lab Hematol* 30(5):349–364, 2008.

Lynch HE, Goldberg GL, Chidgey A, et al: Thymic involution and immune reconstitution. *Trends Immunol* 30(7):366–373, 2009.

Maronpot RR, Boorman GA, Gaul BW: *Pathology of the Mouse: Reference and Atlas*, Vienna, IL, 1999, Cache River Press.

McGarry MP, Protheroe CA, Lee JJ: *Mouse Hematology: A Laboratory Manual*, Cold Spring Harbor, NY, 2010, Cold Spring Harbor Laboratory Press.

Mebius RE, Kraal G: Structure and function of the spleen. *Nat Rev Immunol* 5(8):606–616, 2005.

Merchant HA, Rabbie SC, Varum FJ, et al: Influence of ageing on the gastrointestinal environment of the rat and its implications for drug delivery. *Eur J Pharm Sci* 62:76–85, 2014.

Mikaelian I, Nanney LB, Parman KS, et al: Antibodies that label paraffin-embedded mouse tissues: A collaborative endeavor. *Toxicol Pathol* 32(2):181–191, 2004.

Mills SE: *Histology for Pathologists*, 3rd edn., Philadelphia, 2007, Lippincott Williams & Wilkins.

Moghimi SM: Mechanisms of splenic clearance of blood cells and particles: Towards development of new splenotropic agents. *Adv Drug Deliv Rev* 17:103–115, 1995.

Ohtani O, Ohtani Y: Structure and function of rat lymph nodes. *Arch Histol Cytol* 71(2):69–76, 2008.

Otto GM, Franklin CL, Clifford CB: Biology and Diseases of Rats. In Anderson LC, Otto G, Prtichett-Corning KR, Whary MT, Fox JG, editors: *Laboratory Animal Medicine* (Third Edition), ACLAM, London, 2015, Academic Press, pp 151–207.

Parker GA, Picut CA, Swanson C, et al: Histologic features of postnatal development of immune system organs in the Sprague-Dawley rat. *Toxicol Pathol* 43(6):794–815, 2015.

Pearse G: Normal structure, function and histology of the thymus. *Toxicol Pathol* 34(5):504–514, 2006.

Pinkus GS, Warhol MJ, O'Connor EM, et al: Immunohistochemical localization of smooth muscle myosin in human spleen, lymph node, and other lymphoid tissues. Unique staining patterns in splenic white pulp and sinuses, lymphoid follicles, and certain vasculature, with ultrastructural correlations. *Am J Pathol* 123(3):440–453, 1986.

Rehg JE, Ward JM: Application of Immunohistochemistry in Toxicologic Pathology of the Hematolymphoid System in press. In Parker G, editor: *Immunopathology in Toxicology and Drug Development*, , 2017, Springer.

Rehg JE, Bush D, Ward JM: The utility of immunohistochemistry for the identification of hematopoietic and lymphoid cells in normal tissues and interpretation of proliferative and inflammatory lesions of mice and rats. *Toxicol Pathol* 40:1–30, 2012.

Rehg JE, Rahija R, Bush D, et al: Immmunophenotype of spontaneous hematolymphoid tumors occurring in young and aging female CD-1 mice. *Toxicol Pathol*:1025–1034, 2015.

Sawanobori Y, Ueta H, Dijkstra CD, et al: Three distinct subsets of thymic epithelial cells in rats and mice defined by novel antibodies. *PLoS One* 9(10):e109995, 2014.

Seymour R, Sundberg JP, Hogenesch H: Abnormal lymphoid organ development in immunodeficient mutant mice. *Vet Pathol* 43(4):401–423, 2006.

Shimazaki C, Uchida R, Nakano S, et al: High serum bone-specific alkaline phosphatase level after bortezomib-combined therapy in refractory multiple myeloma: Possible role of bortezomib on osteoblast differentiation. *Leukemia* 19(6):1102–1103, 2005.

Steiniger BS: Human spleen microanatomy: Why mice do not suffice. *Immunology* 145(3):334–346, 2015.

Suttie AW, Leininger JR, Bradley AE: *Boorman's Pathology of the Rat: Reference and Atlas*, 2nd edn., New York, 2017, Academic Press.

Terszowski G, Muller SM, Bleul CC, et al: Evidence for a functional second thymus in mice. *Science* 312(5771):284–287, 2006.

Tilney NL: Patterns of lymphatic drainage in the adult laboratory rat. *J Anat* 109(Pt 3):369–383, 1971.

Travlos GS: Normal structure, function, and histology of the bone marrow. *Toxicol Pathol* 34(5):548–565, 2006.

Van den Broeck W, Derore A, Simoens P: Anatomy and nomenclature of murine lymph nodes: Descriptive study and nomenclatory standardization in BALB/cAnNCrl mice. *J Immunol Methods* 312(1–2):12–19, 2006.

van den Oord JJ, De Wolf-Peeters C, Desmet VJ, et al: Nodular alteration of the paracortical area. An in situ immunohistochemical analysis of primary, secondary, and tertiary T-nodules. *Am J Pathol* 120(1):55–66, 1985.

van Krieken JH, te Velde J, Hermans J, et al: The amount of white pulp in the spleen: A morphometrical study done in methacrylate-embedded splenectomy specimens. *Histopathology* 7(5):767–782, 1983.

Vroegindeweij E, Crobach S, Itoi M, et al: Thymic cysts originate from Foxn1 positive thymic medullary epithelium. *Mol Immunol* 47(5):1106–1113, 2010.

Ward JM, Erexson CR, Faucette LJ, et al: Immunohistochemical markers for the rodent immune system. *Toxicol Pathol* 34(5):616–630, 2006.

Whary MT, Baumgarth N, Fox JG, et al: Biology and Diseases of Mice. In Anderson LC, Otto G, Prtichett-Corning KR, Whary MT, Fox JG, editors: *Laboratory Animal Medicine* (Third Edition), ACLAM, London, 2015, Academic Press, pp 43–149.

Wilkins B, Wright DH:: *Illustrated Pathology of the Spleen*, New York, 2000, Cambridge University Press.

Wilkosz S, Ireland G, Khwaja N, et al: A comparative study of the structure of human and murine greater omentum. *Anat Embryol (Berl)* 209(3):251–261, 2005.

Willard-Mack CL: Normal structure, function, and histology of lymph nodes. *Toxicol Pathol* 34(5):409–424, 2006.

WEBSITES

Frith CH and Ward JM. Color Atlas of Neoplastic and Non-Neoplastic Lesions in Aging Mice. http://www.informatics.jax.org/frithbook.

Jackson Laboratory, Mouse Tumor Biology Database. http://tumor.informatics.jax.org/mtbwi/index.do.

NIEHS. https://www.niehs.nih.gov/research/resources/protocols/protocols-immuno/index.cfm.

This page intentionally left blank

NERVOUS SYSTEM 20

JESSICA M. SNYDER
University of Washington School of Medicine, Seattle, WA, United States

CATHERINE E. HAGAN
The Jackson Laboratory, Sacramento, CA, United States

BRAD BOLON
GEMpath, Inc., Longmont, CO, United States

C. DIRK KEENE
University of Washington School of Medicine, Seattle, WA, United States

Introduction

The central nervous system (CNS, brain and spinal cord) and peripheral nervous system (PNS, ganglia and nerves) together control somatic (sensorimotor or voluntary) and autonomic (involuntary) functions. The CNS is anatomically and functionally the major body system that varies most between rodents and humans (Table 20.1).

The nervous system poses unique challenges for morphologic assessment. Relative to other organs and systems, the domains of the CNS are anatomically diverse across species and even among individuals, exhibiting major structural changes at both gross and microscopic levels over very short distances and in all three dimensions. Specialized histologic techniques are needed to produce highly homologous (i.e., structurally identical) sections among individuals and to minimize structural artifacts that inexperienced morphologists may misinterpret as genuine lesions.

In many neurological diseases of humans, specific neuroanatomic regions are preferentially involved. Primary examples include the cerebral cortex in Alzheimer's disease, the striatum (caudate nucleus and putamen) in Huntington's disease, the substantia nigra in Parkinson's disease, the cerebellum in spinocerebellar ataxias, CNS white matter in multiple sclerosis, and the ventral horn of the spinal cord in amyotrophic lateral sclerosis. Thus, understanding macroscopic and microscopic distinctions in neuroanatomy between humans and rodents is a prerequisite to using spontaneous, induced, or genetically engineered rodent models of disease to investigate such conditions and potential therapeutic options.

The general similarity of the anatomy, biochemistry, and physiology of the nervous system among mammals permits mice and rats to be employed as models of human neurological function and disease. However, the extreme complexity and large size of the human brain and spinal cord relative to the simple form and more primitive function

Comparative Anatomy and Histology. DOI: http://dx.doi.org/10.1016/B978-0-12-802900-8.00020-8
© 2018 Elsevier Inc. All rights reserved.

TABLE 20.1 Nervous System

Feature	Rodent	Human
	Brain	
	Gross	
Lobes defined by external landmarks	Absent	Present
Sulci and gyri	Absent	Present
Olfactory bulb/archicortex	Very large	Small
Cranial lobe of cerebellum	Less lateral spread	More lateral spread
Parafloccular lobule of cerebellum	Large	Insignificant
Middle lobe of cerebellum	Small	Lateral portions larger in humans
	Histologic	
Cerebral cortex	Primarily paleocortex	Primarily neocortex
Cortical interneurons	Less significant	Significant role
Independence of subcortical centers from cerebral cortex control	More independent	Less independent
Visual cortex	More lateral	More midline
Functional cortices	Primary	Primary and associative ("higher thought")
White matter	Relatively scant	Very abundant
Substantia nigra cells	Melanin pigment not obvious	Obvious neuromelanin pigment
Predominant sensory cortex	Olfactory and face—whisker barrels (motor component to whisker barrels, as well)	Hands and face (lips and tongue)
Hippocampus	Dorsal aspect of cerebrum	Ventral aspect of cerebrum
Basal ganglia	Combined caudate nucleus and putamen (rendered as caudate putamen or caudoputamen)	Separate caudate nucleus and putamen
Cerebellar nuclei	Less discrete	More discrete
Medial and lateral lemniscus	Small	Large
Inferior olivary nucleus	Smaller	Large, due to expanded cerebellar hemispheres
Mineralization with age	Mouse: Lateral thalamus Rat: Pineal gland	Pineal gland
Meninges	Thin	Thick, well developed
	Spinal Cord	
	Gross	
Spinal formula	Mouse: C7 T13 L6 S4 Cd 28 Rat: C7 T13 L6 S4 Cd27-30	C7 T12 L5 S5 Cd 4
Predominant motor tract	Rubrospinal	Corticospinal
Lumbosacral enlargement	L_2–L_6	L_2–S_3
Spinal nerves	Approximately 15 dorsal and 15 ventral rootlets per segment (on each side)	6–8 dorsal and 6–8 ventral rootlets per segment (on each side)
Sciatic nerve origin	Mouse: L_3–L_4 Rat: L_4–L_5	L_4–S_3
	Histologic	
Corticospinal tract	Smaller and located in dorsal column, minor role in motor functions	Larger and located in lateral column, major role in motor functions, especially dexterity of distal limbs
Rubrospinal tract	Larger, major role in locomotion and posture	Smaller, cooperative role with corticospinal tract
Lateral horn	Less prominent	More prominent
Segments containing sympathetic nervous system preganglionic cell bodies	Mouse: T_1–L_2 Rat: T_1–L_3	T_1–L_3
Segments containing parasympathetic nervous system preganglionic cell bodies	L_6–S_1	S_2–S_4
Nucleus of Bishoff (tail afferents)	Mouse: Maybe Rat: Yes	Absent
Peripheral nerve connective tissue	Scant	Abundant
	Endocrine	
	Gross	
Pituitary	One gland composed of anterior (adenohypophysis) and posterior (neurohypophysis) lobes; the pars distalis cradles the pars intermedia and pars nervosa	Similar to rodent

(Continued)

TABLE 20.1 Nervous System (Continued)

Feature	Rodent	Human
Pineal gland	Small and round; located on the external surface of the brain at the interface between the cerebral hemispheres and cerebellum	Resembles a pine cone due to incomplete lobules formed by intralobular stroma extending from the capsule; located within the posterior wall of the third ventricle near the center of the brain
	Histologic	
Pituitary gland—pars intermedia	Mouse: Morphologically distinct, larger than in most species Rat: Morphologically distinct, although smaller than mouse	Poorly developed, thin layer of cells, contains colloid cysts
Pineal gland	Not lobulated, more homogenous appearance	Prominently lobulated, cells arranged in rosettes, and clusters, age-related mineralization
	Vasculature, Choroid Plexus, Ependyma, and Circumventricular Organs	
	Gross	
Vasculature	Mouse: Not yet widely characterized, a few studies provide 3D atlases of deep brain vasculature Rat: Characterized	Well-characterized and more complex owing to the sulci, gyri, and lobes of human brain
Callosomarginal artery	No equivalent artery	Runs along cingulate gyrus
Anterior choroid artery	Mouse: Supplies choroid plexus and thalamus Rat: Supplies choroid plexus, thalamus, hypothalamus ± hippocampus	Supplies choroid plexus, thalamus, hippocampus
Ventral corpus callosum	Mouse: Medial orbitofrontal artery Rat: Branches of anterior cerebral artery (septal branches)	Frontopolar branch of anterior cerebral artery
	Histologic	
Choroid plexus	Less extensive folds and fronds	More extensive folds and fronds and connective tissue due to increased volume and surface area
Subcommissural organ	Mouse: Limited vascularization Rat: Vascularized by endothelium, not fenestrated	Vestigial, with no vascularization

of the rodent counterparts have the potential to thwart translational medicine efforts. The best means of ensuring that data extrapolation from rodent to human is performed in a rational manner is for neuroscientists engaged in rodent studies to understand the equivalent and divergent features of the brain and spinal cord for these species. This chapter and the references in the Further Reading and Relevant Websites list provide a thorough introduction of the major points needed for such a nervous system comparison.

Brain
Gross Anatomy

Surface Features

On gross examination, many striking differences are evident between the brains of a rodent and human (Fig. 20.1). The most obvious variations are that rodent brains are tiny (~0.4 g in mice, ~2.0 g in rats), lissencephalic (do not have sulci or gyri), and have little white matter. In contrast, the much larger human brain (approximately 1300 g) has a readily apparent lobular organization, prominent sulci and gyri, and extensive white matter. Viewing the dorsal (superior) surface of the rodent brain in situ, the cerebri, colliculi, and cerebellum are visible (Fig. 20.2A), whereas the same examination in human will demonstrate only cerebral cortex (Fig. 20.2B). Evaluation of the ventral surfaces of mouse (Fig. 20.2C) or rat brain reveals several prominent landmarks, including (but not limited to) the olfactory tubercles, optic chiasm, pituitary gland (or the infundibular stalk where the gland was attached), piriform cortex, pons, and medulla oblongata. Similar ventral landmarks may be observed in human brains (Fig. 20.2D), although the sizes of certain structures differ substantially from those of the

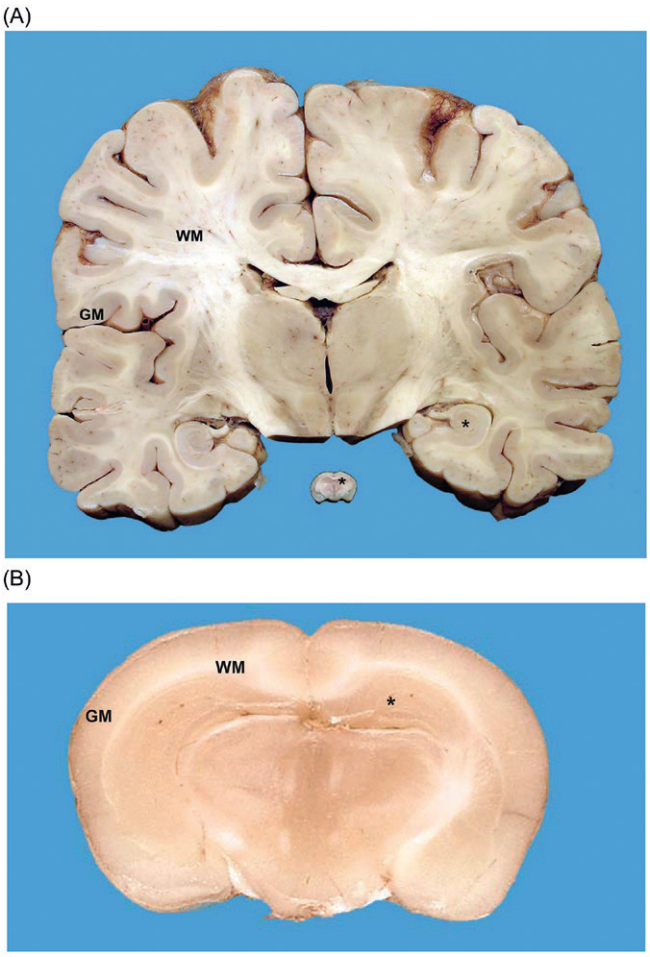

FIGURE 20.1 Brain. (A) Coronal brain slices from rodent (mouse) and human demonstrating the marked differences in organ size and organization. (B) Rodent (mouse) brain, enlarged. Gray matter (GM) includes neuron cell bodies, glia, and blood vessels. White matter (WM) consists of myelinated axons and myelinating cells. The hippocampal formation on the right side of each slice is marked with an asterisk. Many of the photos and diagrams in this chapter have been adjusted in size to provide optimal anatomical and cellular comparisons.

identical rodent features. The main ventral attribute that differs between rodents and humans is the prominence of the olfactory bulbs and tracts. Due to the importance of smell as the main sensory modality in rodents, the olfactory bulbs are extremely large (comprising 6–7% of total brain weight; Fig. 20.3A), and the olfactory tracts (that provide the bridge to the ventral brain) are extremely large protuberances. Humans, who rely far less on their olfactory sense, are equipped with extremely small olfactory bulbs and nerves (Fig. 20.2D).

Gross comparisons of rodent and human brain demonstrate many distinctions in CNS structures between them. Lateral views showcase the marked expansion of the cerebral cortex in humans, which is indicated both by the intricate folding of the cerebrum and by its extension over the cerebellum (Fig. 20.3B). Whereas the neuraxes of rodents (as quadrupeds) are linear from rostral to caudal (Figs. 20.3A and 20.4A), humans (as bipeds) have an upright posture that imparts a curvature between the horizontally oriented cerebrum and the vertically oriented brain stem (Figs. 20.3B and 20.4B). This postural adaptation in bipeds in combination with the proportionally much larger cerebral cortical and white matter volumes in humans has resulted in dramatic differences in positioning of some neuroanatomic structures in humans compared to rodents.

Side-by-side comparisons of the dorsal (superior) and ventral (inferior) brain surfaces of rodents and humans highlight significant differences (Fig. 20.2). The most overt divergence is the absence of fissures, gyri, and sulci on the rodent cerebrum, with the exception of the longitudinal fissure that divides the two hemispheres. Thus, it is impossible to delineate specific regions of the rodent cerebrum on the basis of surface topography, while such subdivisions are readily defined for the human cerebrum using visible gyri and sulci. In contrast to the cerebrum, the features of the dorsal cerebellum surface and overall brain surface are more equivalent in rodents and humans. The cerebellum can be divided dorsally into two lateral hemispheres and a midline vermis. Ventrally, the brain stem is composed of a broad pons rostrally that tapers to form the medulla oblongata caudally. The pyramids of the medulla, formed of descending motor axons, can be seen in both rodents (Fig. 20.2C) and humans (Fig. 20.2D) on the ventral surface of the brain stem.

Internal Landmarks

Key brain divisions also are easily compared using interior characteristics, such as gray and white matter boundaries, observed in cross-sectional slices from rodents (Fig. 20.5) and humans (Fig. 20.6).

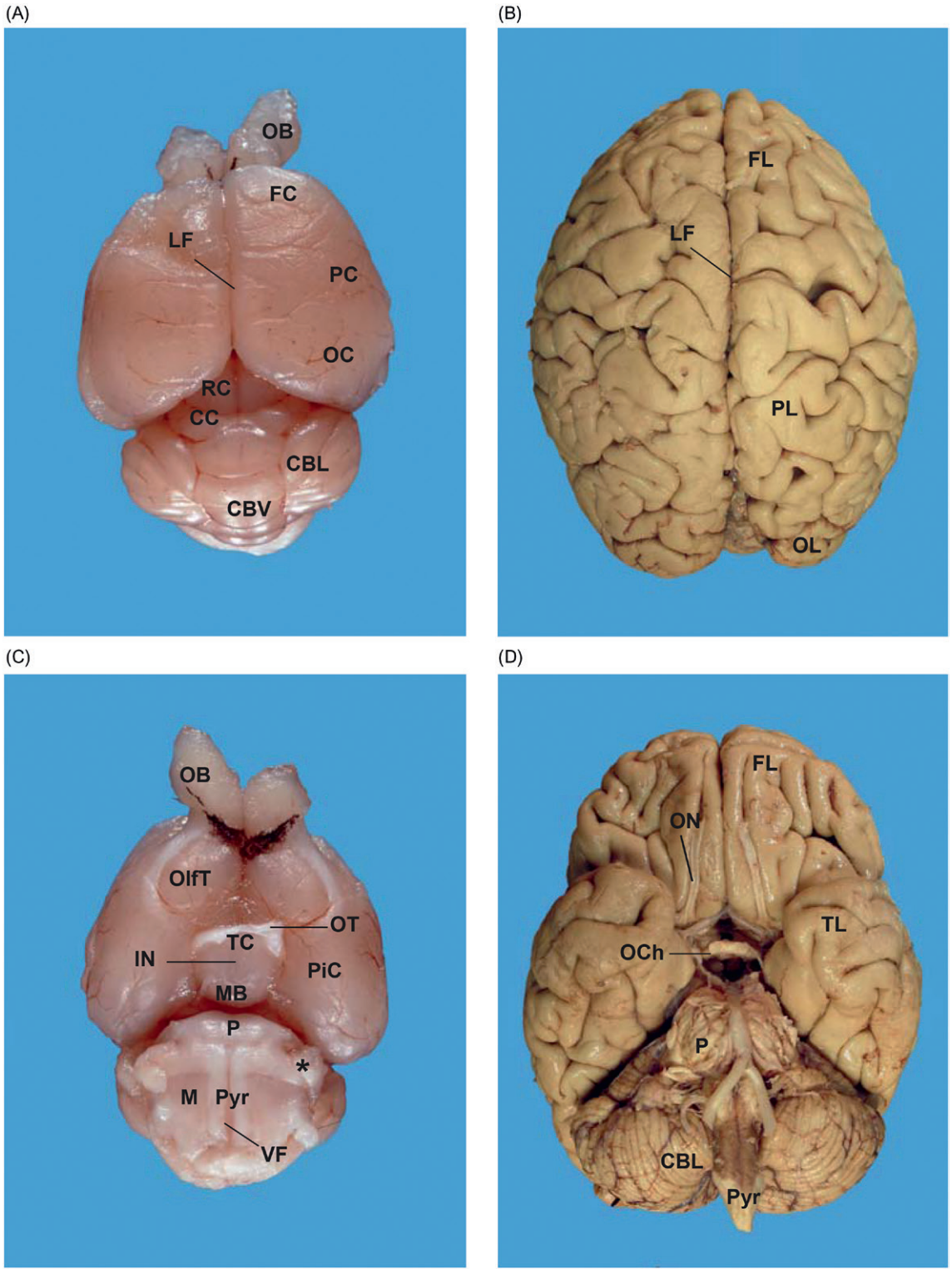

FIGURE 20.2 Brain surface features. Major gross features of the dorsal (A and B) and ventral (C and D) surfaces of fixed brains from a rodent (mouse) (A and C) and human (B and D). The optic chiasm (OC) has been removed from the mouse brain, but the base of the optic tract (OT) is still visible. The ventral mouse brain shows meningeal melanosis (blackening) of the caudal olfactory bulbs, which is a relatively common spontaneous finding in C57BL/6 mice. Meninges have been removed from the human brain. *CBL*, cerebellum—lateral hemisphere; *CBV*, cerebellum—vermis; *CC*, caudal colliculus; *FC*, frontal cortex; *FL*, frontal lobe; *IN*, infundibulum; *LF*, longitudinal fissure; *M*, medulla oblongata; *MB*, mammillary bodies; *OB*, olfactory bulb; *OC*, occipital cortex; *OCh*, optic chiasm; *OL*, occipital lobe; *OlfT*, olfactory tubercle; *ON*, olfactory nerve; *OT*, optic tract; *P*, pons; *PC*, parietal cortex; *PL*, parietal lobe; *PiC*, piriform cortex; *Pyr*, pyramids; *RC*, rostral colliculus; *TC*, tuber cinereum; *TL*, temporal lobe; *VF*, ventral median fissure. The asterisk on the ventral surface of the mouse brain denotes the roots of cranial nerves V (trigeminal), VII (facial), and VIII (vestibulocochlear).

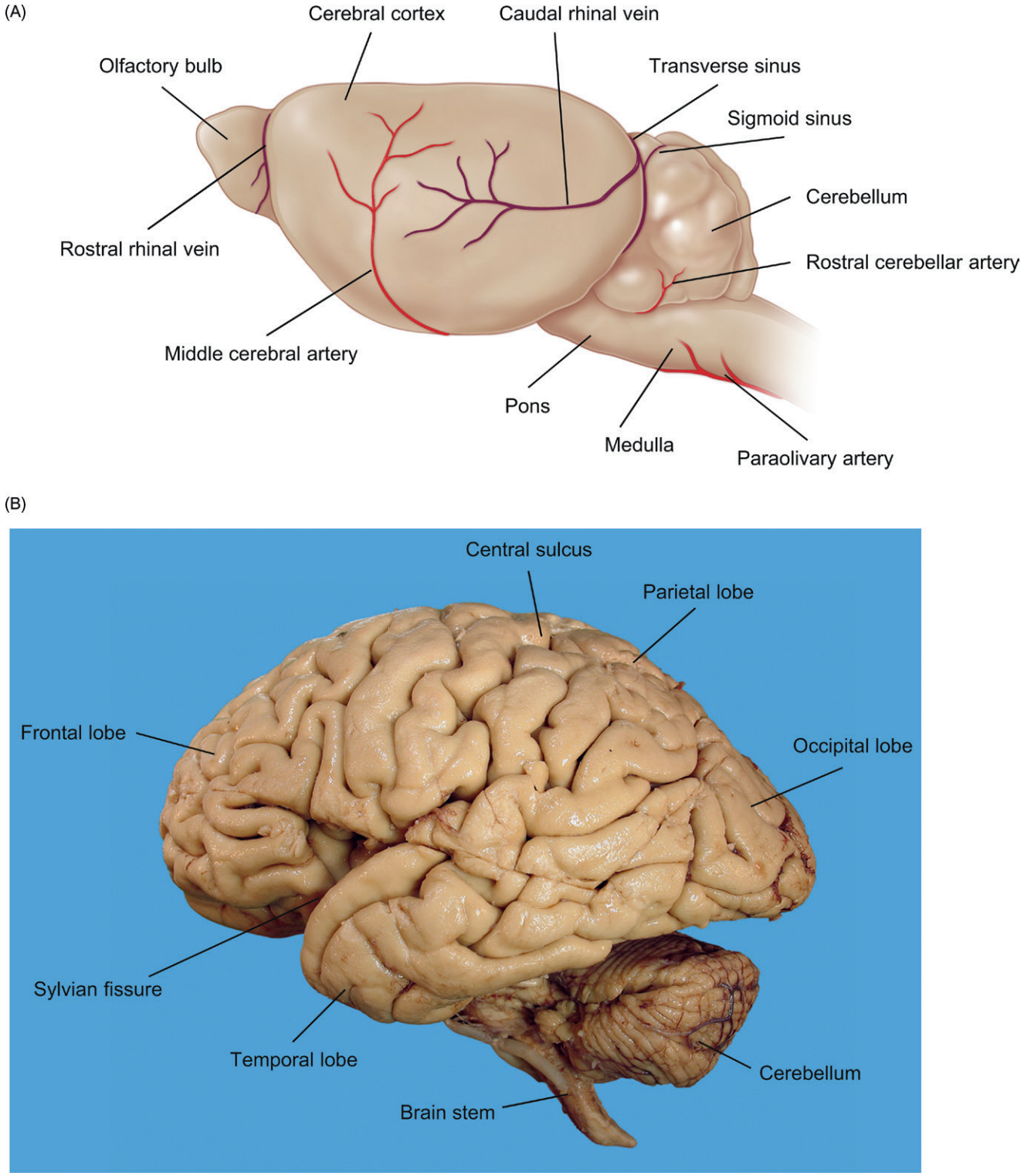

FIGURE 20.3 Brain lateral view. (A) Rodent (mouse) and (B) human showing major differences in anatomical organization. (Meninges have been removed from the human cerebrum but were left intact on the cerebellum.)

Need-to-know

- Main gross structural differences are the small cerebrum (forebrain) and large cerebellum and olfactory lobes of the rodent brain relative to the human brain.
- Rodents lack cerebral gyri and sulci.

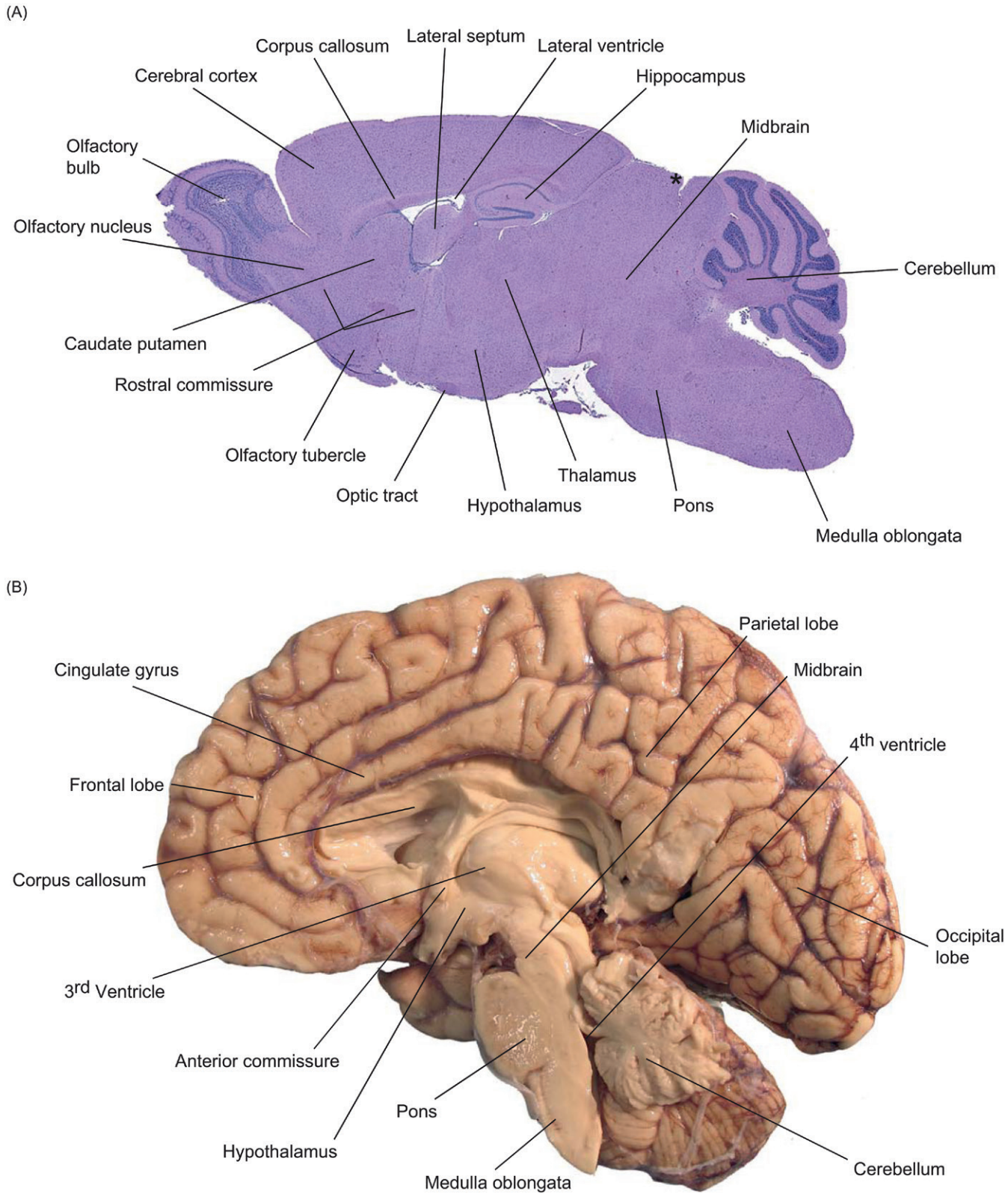

FIGURE 20.4 Brain parasagittal (lateral of midline) view. (A) Subgross of rodent (mouse) brain and (B) mid-sagittal gross preparation of human. The hippocampus is not visible in the sagittal plane of human brain. The asterisk denotes the approximate position of the mouse pineal gland (although the actual gland is not shown in the section).

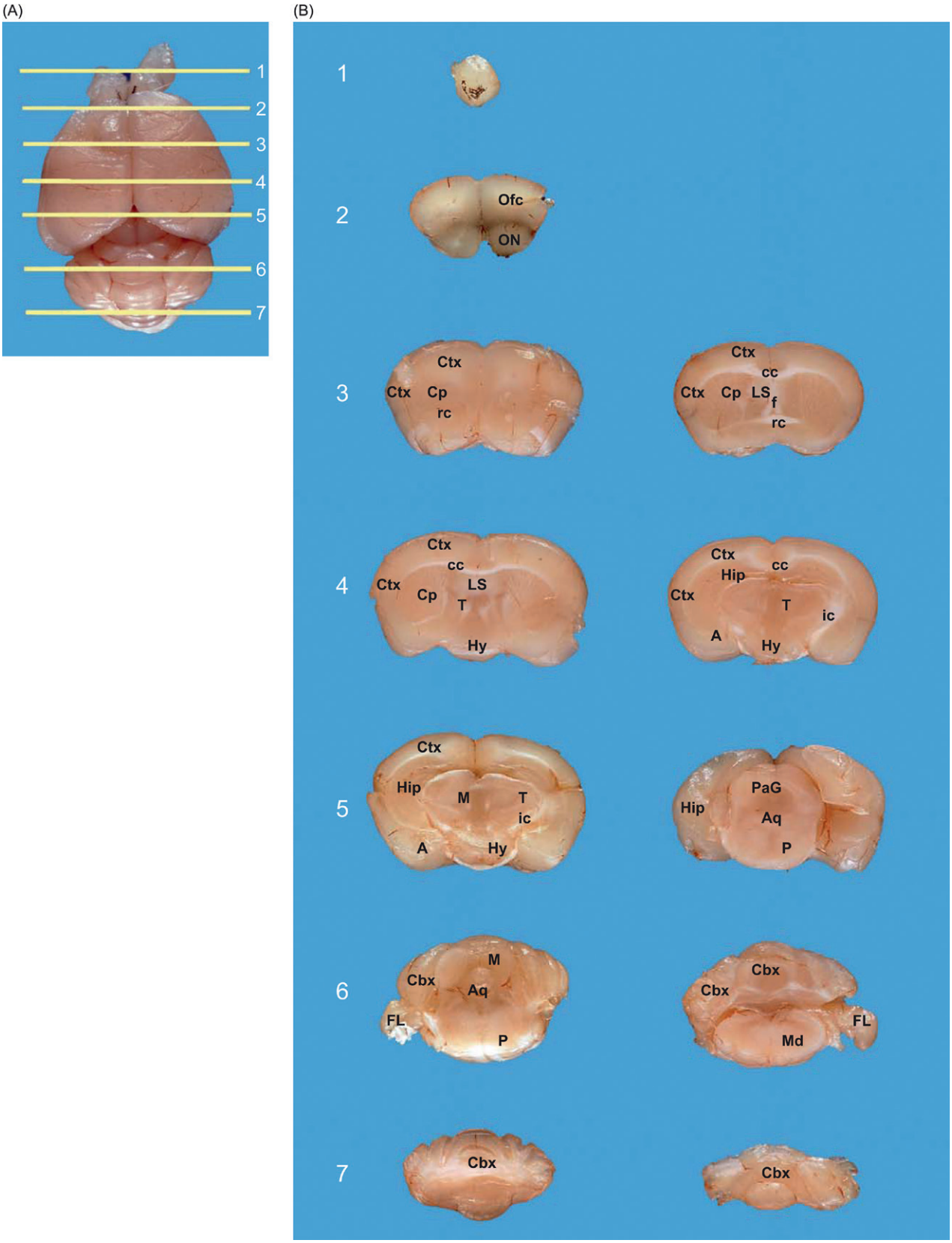

FIGURE 20.5 Brain coronal (cross) sections of rodent (mouse) brain. The numbered levels shown in A correspond to the labeled levels in B. The sections on the left column show the rostral side of each slice, whereas the right column shows the caudal side. Note that only one olfactory lobe is shown for Level 1. *A*, amygdala; *rc*, rostral commissure; *Aq*, mesencephalic aqueduct; *Cbx*, cerebellar cortex; *cc*, corpus callosum; *Cp*, caudate/putamen; *Ctx*, cerebral cortex (neocortex); *f*, fornix; *FL*, flocculus lobe of the cerebellum; *Hip*, hippocampus; *Hy*, hypothalamus; *ic*, internal capsule; *LS*, lateral septum; *M*, mesencephalon (midbrain); *Md*, medulla oblongata; *Ofc*, orbitofrontal cortices; *ON*, olfactory nucleus; *P*, pons; *PaG*, periaqueductal gray matter; *T*, thalamus.

Need-to-know

- Anatomical boundaries of many brain regions differ between rodents and humans.

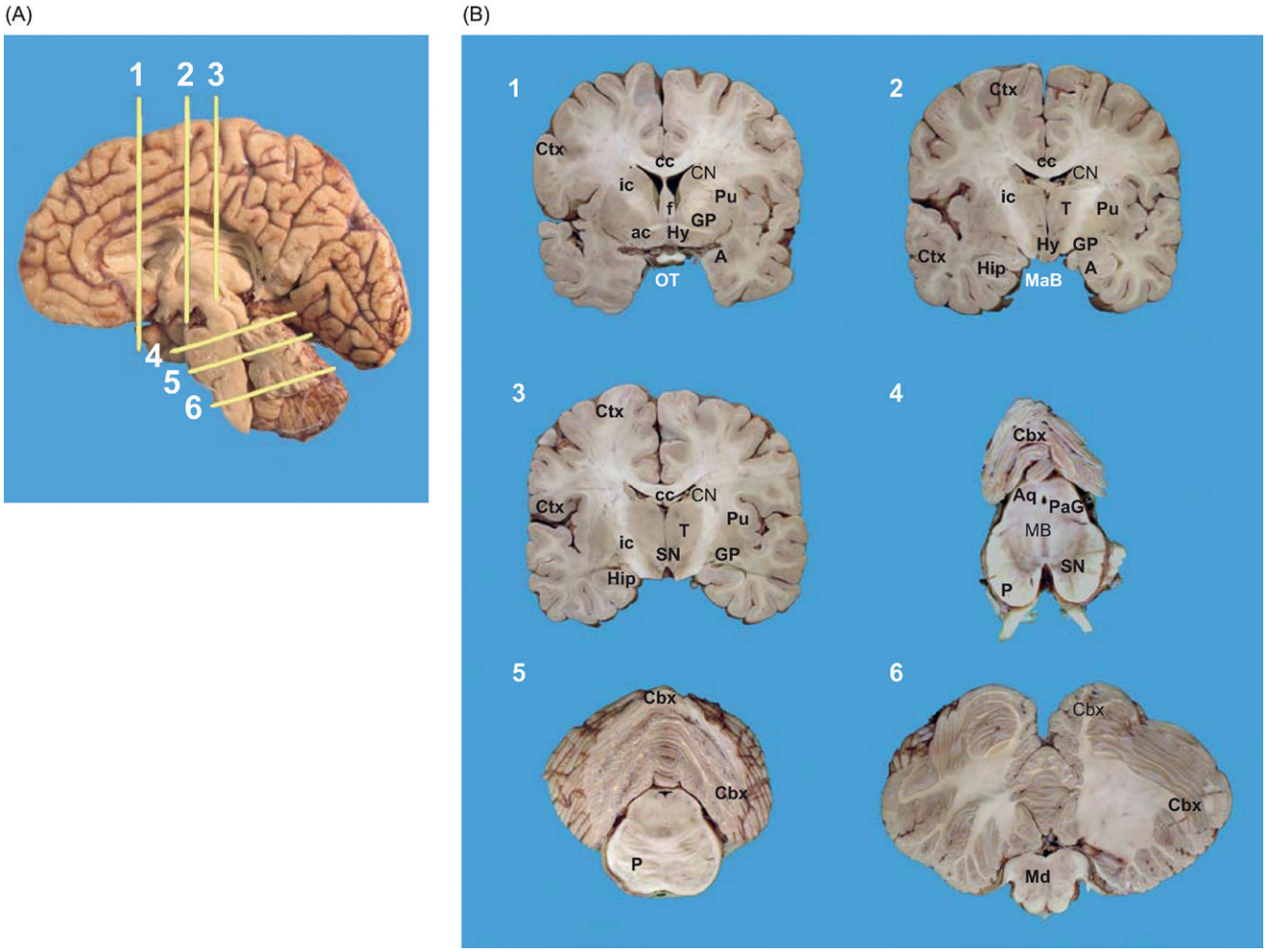

FIGURE 20.6 Brain coronal (cross) sections of a human brain. The numbered levels shown in A correspond to the labeled levels in B. The approximate levels of each (B) image relative to the human neuraxis are depicted on the gross lateral image of human brain (A). The human neuraxis is unique in that it has a 90° bend. Levels may be distinguished by major external and internal features: *1*, striatum, composed of the caudate nucleus (CN), putamen (Pu), and globus pallidus (GP); *2*, mammillary bodies (MaB); *3*, substantia nigra (SN); *4*, mesencephalon (midbrain MB), with the aqueduct of Sylvius (Aq) surrounded by the periaqueductal gray matter (PaG); *5*, pons (P); and *6*, medulla oblongata (Md). *4v*, fourth ventricle; *A*, amygdala; *ac*, anterior commissure; *Cbx*, cerebellar cortex; *cc*, corpus callosum; *Ctx*, cerebral cortex (neocortex); *f*, fornix; *Hip*, hippocampus; *Hy*, hypothalamus; *ic*, internal capsule; *OT*, optic tract; *P*, pons; *T*, thalamus. Images 4–6 are oriented to facilitate comparison with the mouse levels in Fig. 20.5.

The arrangement of major cell types at the microscopic level (as detailed below) is similar for rodents and humans, although the greater degree of functional diversity in humans may result in more apparent cytoarchitectural diversity of basic cell types in humans.

The *cerebral cortex* has an outer layer of gray matter (i.e., neuron-rich regions) and a central core of white matter (i.e., zones comprised chiefly of myelinated neuron processes and various glial support cells). The thickness of the gray matter and the amount of underlying white matter are much greater in humans relative to rodents as a consequence of the greater cerebrocortical intra- and interhemispheric connectivity required to support cognitive processes, as indicated by the many large gyri in the human brain.

The *basal nuclei* (formerly basal ganglia) include the striatum (caudate and putamen), globus pallidus, subthalamic nucleus, and substantia

nigra. These brain regions are deep gray matter masses of the telencephalon and mesencephalon (substantia nigra), the neurons of which serve chiefly as motor control centers. In the human brain, the caudate and putamen are distinct structures separated by the internal capsule, while in rodents the caudate and putamen are fused. The substantia nigra ("black substance") is visible grossly in adolescent and mature humans due to local accrual of neuromelanin, while this nucleus in rodents is pale because neurons do not accumulate this pigment in these species.

The *diencephalon*, the portion of the brain underlying the middle cerebral cortex, is the most primitive portion of the cerebrum. The diencephalon contains many closely linked brain centers (termed the "limbic system") that serve together to regulate emotions and behaviors that are important to socialization; survival (feeding, fighting, and fleeing); and memory. The limbic system also influences multiple visceral functions via efferent nerves of the autonomic nervous system (ANS). The diencephalic centers participating in the limbic system include the amygdala, fornix, habenular nuclei, hippocampus, hypothalamus, septum, and rostral (anterior) thalamic nucleus. Of these, the hippocampus, thalamus, hypothalamus, and amygdala are most often subjected to neuropathology analysis in rodents and humans due to their well-known functional correlations.

The hippocampus has a distinctive C-shaped, tilted profile in three dimensions that is viewed more dorsally in brains of rodents (Figs. 20.5 and 20.7) and more ventrally in those of humans (Fig. 20.6). The anatomic profile of the hippocampus shifts in relation to the central midline, moving laterally and ventrally in more caudal regions of the brain (Fig. 20.8). Recognizable hippocampal zones include Ammon's horn, the dentate gyrus, and the subiculum. Ammon's horn [*Cornu Ammonis* (CA)] is divided into regions CA1–CA4.

The thalamus forms the central part of the diencephalon and is the seat for multiple, often indistinct nuclei that relay sensory information between lower brain centers and the cerebral cortex. Distinct nuclei serve specific functions. Connections between the thalamus and the cerebral cortex are reciprocal. Much of the anatomic connectivity between the thalamus and other CNS domains is conserved among rodents and humans.

The hypothalamus, which lies ventral (inferior) to the thalamus, is positioned near the junction of many major neural pathways as well as the pituitary stalk. It integrates the homeostatic functions of the autonomic, endocrine, and somatosensory systems. Nuclei in this region are poorly delineated in rodents and humans.

The *cerebellum* can be divided into the corpus, which coordinates muscle movements and tone, and the flocculonodular region, which controls equilibrium. Macroscopic differences in cerebellar anatomy distinguish the brains of rodents and humans. Relative to rodents (Fig. 20.2A), humans (Fig. 20.2D) possess expanded lateral cerebellar hemispheres as an adaptation associated with well-developed limbs capable of extensive independent movement, especially of the digits. Cerebellar lobules in humans are much larger than those of rodents due to an increase in the length and number of their folia. The deep cerebellar nuclei in rodents are relatively smaller and less defined compared to those of humans. Despite these quantitative distinctions in cerebellar structure, the quality of the basic functions is similar for both humans and rodents.

The *brain stem* includes the midbrain and pons rostrally and the medulla oblongata caudally. Working together, brain stem nuclei integrate and modulate the activities of other brain centers, coordinate autonomic pathways, and regulate

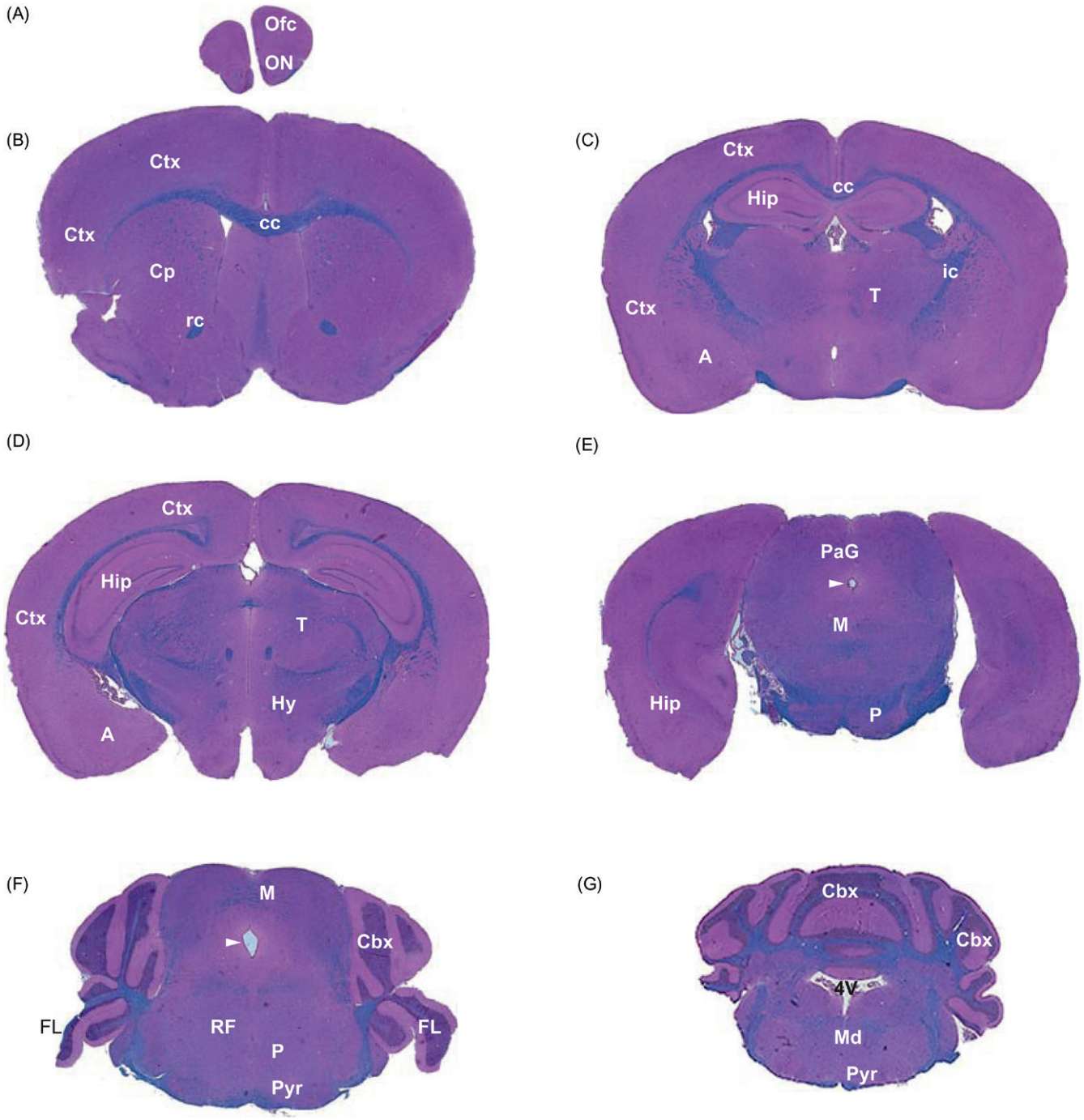

FIGURE 20.7 Coronal (cross) sections of rodent (mouse) brain (H&E and with Luxol fast blue [LFB]). Levels are taken at approximately the same levels as shown in Fig. 20.5. *A*, amygdala; *rc*, rostral commissure; *arrowheads*, mesencephalic aqueduct; *Cbx*, cerebellar cortex; *cc*, corpus callosum; *Cp*, caudate/putamen; *Ctx*, cerebral cortex (neocortex); *FL*, flocculus lobe of the cerebellum; *Hip*, hippocampus; *Hy*, hypothalamus; *ic*, internal capsule; *M*, mesencephalon (midbrain); *Md*, medulla oblongata; *Ofc*, orbitofrontal cortices; *ON*, olfactory nucleus; *P*, pons; *PaG*, periaqueductal gray matter; *Pyr*, pyramids; *RF*, reticular formation; *T*, thalamus.

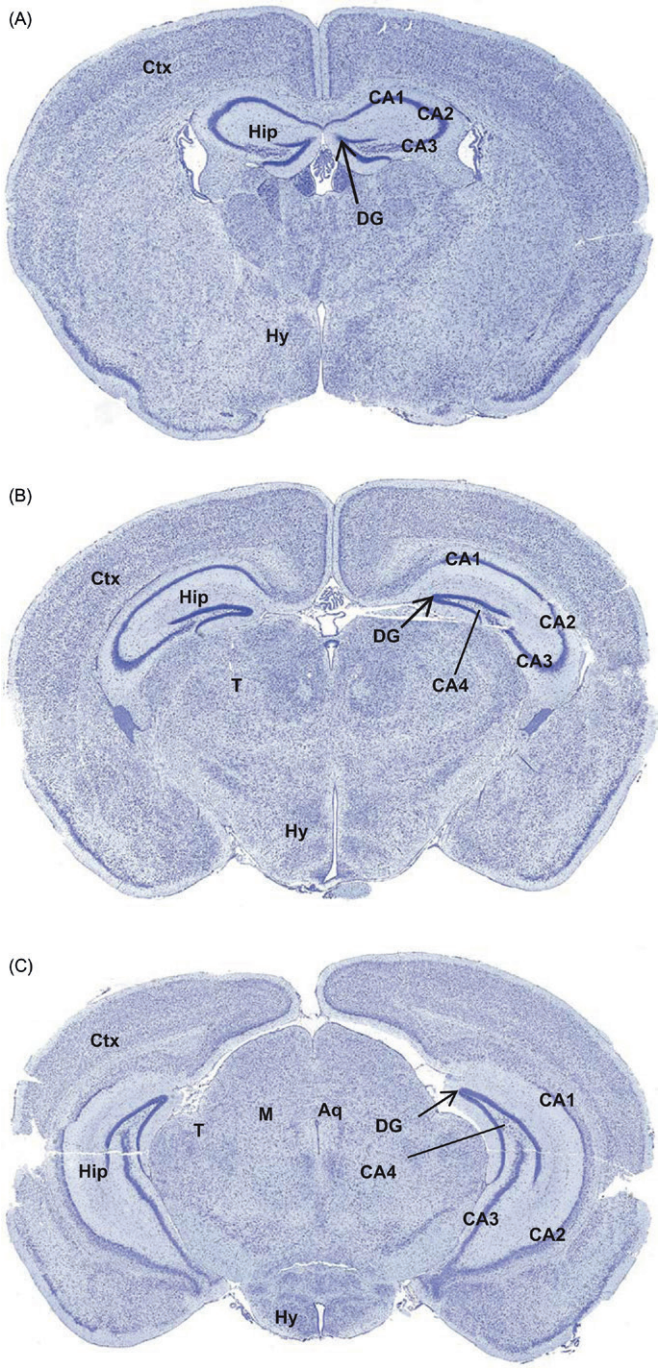

FIGURE 20.8 Coronal (cross) sections of rodent (mouse) brain (Nissl stain). Note the conformation of the hippocampus at its head (A), body (B), and near its tail (C) (Nissl stain). The hippocampus is a set of narrow zones that follow an S-curve starting at the dentate gyrus (DG; meaning for *Cornu ammonis*, "tooth-like"; the arrow points at its apex). The DG is a densely packed layer of granule cells. The hippocampus proper is divided into a series of CA (meaning "ram's horn") subfields containing pyramidal neurons, which are designated CA1–CA4 regions. In the region of the mesencephalon (M), the CA3 field becomes quite narrow. The CA4 subregion does not have pyramidal morphology like other CA regions because it is actually the most superficial layer of the DG and contains mossy fibers. It is also referred to as the hilus, hilar region, or the polymorphic cell layer. *Aq*, mesencephalic aqueduct; *Ctx*, cerebral cortex (neocortex); *Hip*, hippocampus; *Hy*, hypothalamus; *T*, thalamus.

basal homeostatic functions. Brain stem nuclei are arranged in longitudinal columns that represent rostral extensions of the functional zones found in the spinal cord gray matter. Like the cerebellum, brain stem anatomy is conserved between humans and rodents. The olivary nucleus (or inferior olivary nucleus in humans), which is the most distinct cell aggregate in this region in all mammalian species, relays afferent fibers from both higher and lower brain centers to the cerebellum.

The *ventricular system* in rodents and humans is a series of four interconnected cavities and their connecting channels at the core of the brain and spinal cord. In rodents, the sizes of these spaces may vary by strain. These conduits collect and circulate cerebrospinal fluid (CSF) and interstitial fluid (ISF). Specific elements of this system include: two lateral ventricles, residing beneath the cerebral cortex; the third ventricle, located within the diencephalon on the midline and connected to the lateral ventricles via the interventricular foramina; the mesencephalic aqueduct (of Sylvius) that passes through the midbrain; the fourth ventricle, located between the cerebellum dorsally and the pons ventrally; and the central canal within the spinal cord (Fig. 20.9A and B). The CSF is produced by tufts of choroid plexus (CP) in the lateral and fourth ventricles and communicates with the subarachnoid space of the meninges by way of the paired lateral apertures (of Luschka), which drain the fourth ventricle in both rodents and primates, and the median aperture (of Magendie), which connects the fourth ventricle of primates but not rodents to the cisterna magna (Fig. 20.9B). The rates of CSF production and absorption differ among species. The ISF is generated by extravasation of fluid from capillaries (mainly in the brain) before flowing through the neuropil to enter perivascular "glymphatic" channels formed by astrocyte processes. Both CSF and ISF carry many factors (e.g., brain-derived hormones, metabolites) and help equilibrate neuropil pH, and CSF cushions the brain and spinal cord from mechanical trauma.

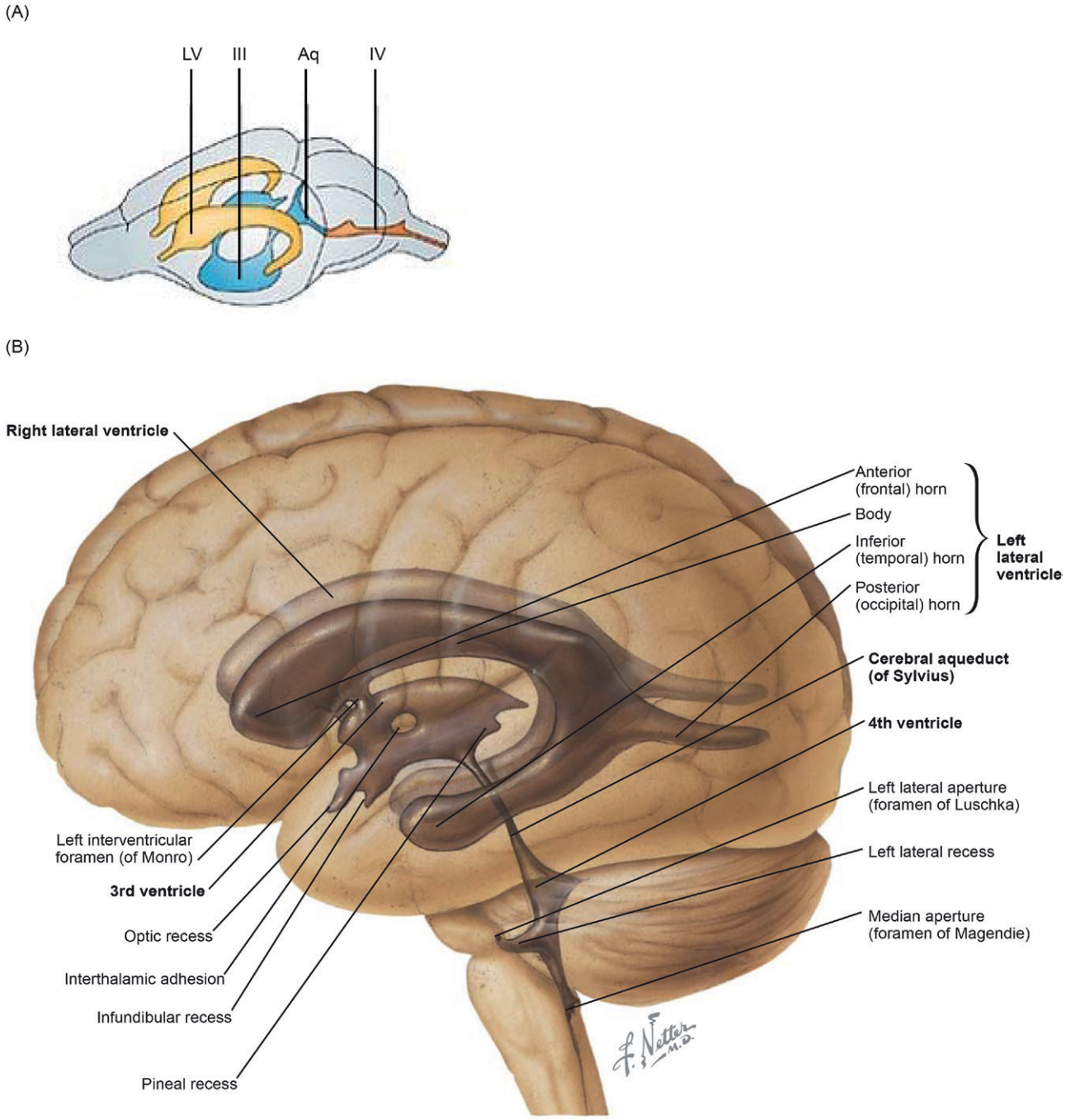

FIGURE 20.9 Lateral views of the ventricular system. (A) Rodent (mouse). Lateral ventricle (LV) and aquaduct (Aq) are indicated. (B) Human. The ventricular system in mice has a more horizontal orientation compared to the human. Sources: A. Fliegauf et al.: When cilia go bad: cilia defects and ciliopathies. *Nat Rev Mol Cell Biol* 8(11), 880–893, 2007 with the permission of Nature Publishing Group. B. © Elsevier, Inc., www.netterimages.com.

The *vascular supply* of the brain in rodents (Fig. 20.10) and humans (Fig. 20.11) is relatively conserved. Blood reaches the rodent brain via the internal carotid arteries (ICs) and to a lesser extent the vertebral arteries (VAs). The ICs supply blood to cortical and subcortical regions directly and via their major branches, while the VAs supply the arteries of the brain stem and cerebellum. The structure of the arterial system is reported to vary by rodent strain; for example, the caudal (posterior) communicating artery is visible in CBA mice (Fig. 20.10) but has

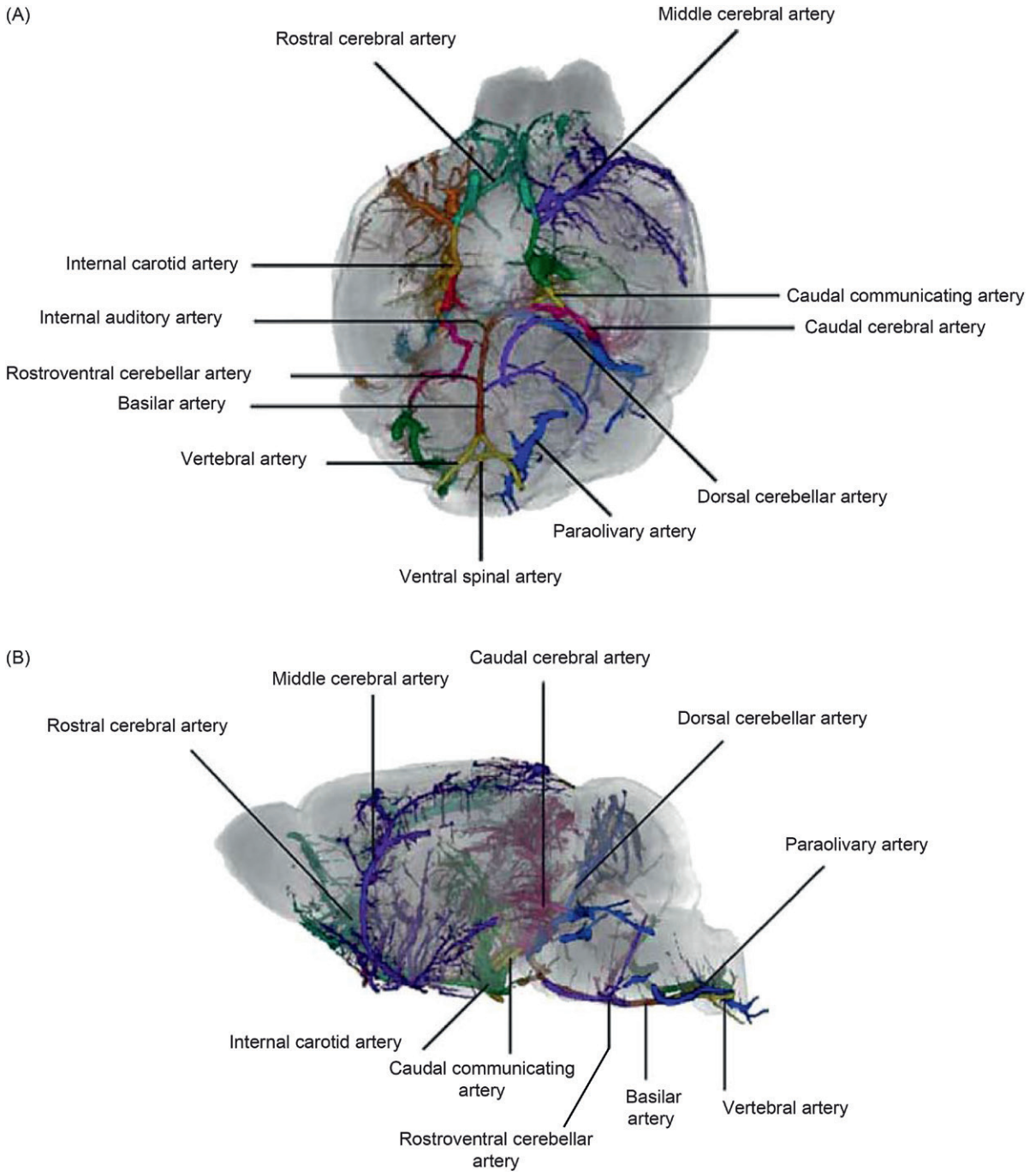

FIGURE 20.10 Rodent (mouse) surface arteries. Ventral (A) and lateral (B) aspects of the rodent (mouse) brain. (A) Ventral arterial ring (circle of Willis) and its branches. These images were acquired by using magnetic resonance imaging and computed tomography to define the vasculature of a CBA mouse, not the C57BL6/J strain used throughout the remainder of the book. This distinction is important because the caudal communicating artery has been reported to be absent or poorly formed in some C57BL/6 lines. Sources: Reprinted from Dorr et al.: Three-dimensional cerebral vasculature of the CBA mouse brain: a magnetic resonance imaging and micro computed tomography study. Neuroimage 35(4):1409–1423, 2007 with the permission of Dr. N. Kabani and Elsevier.

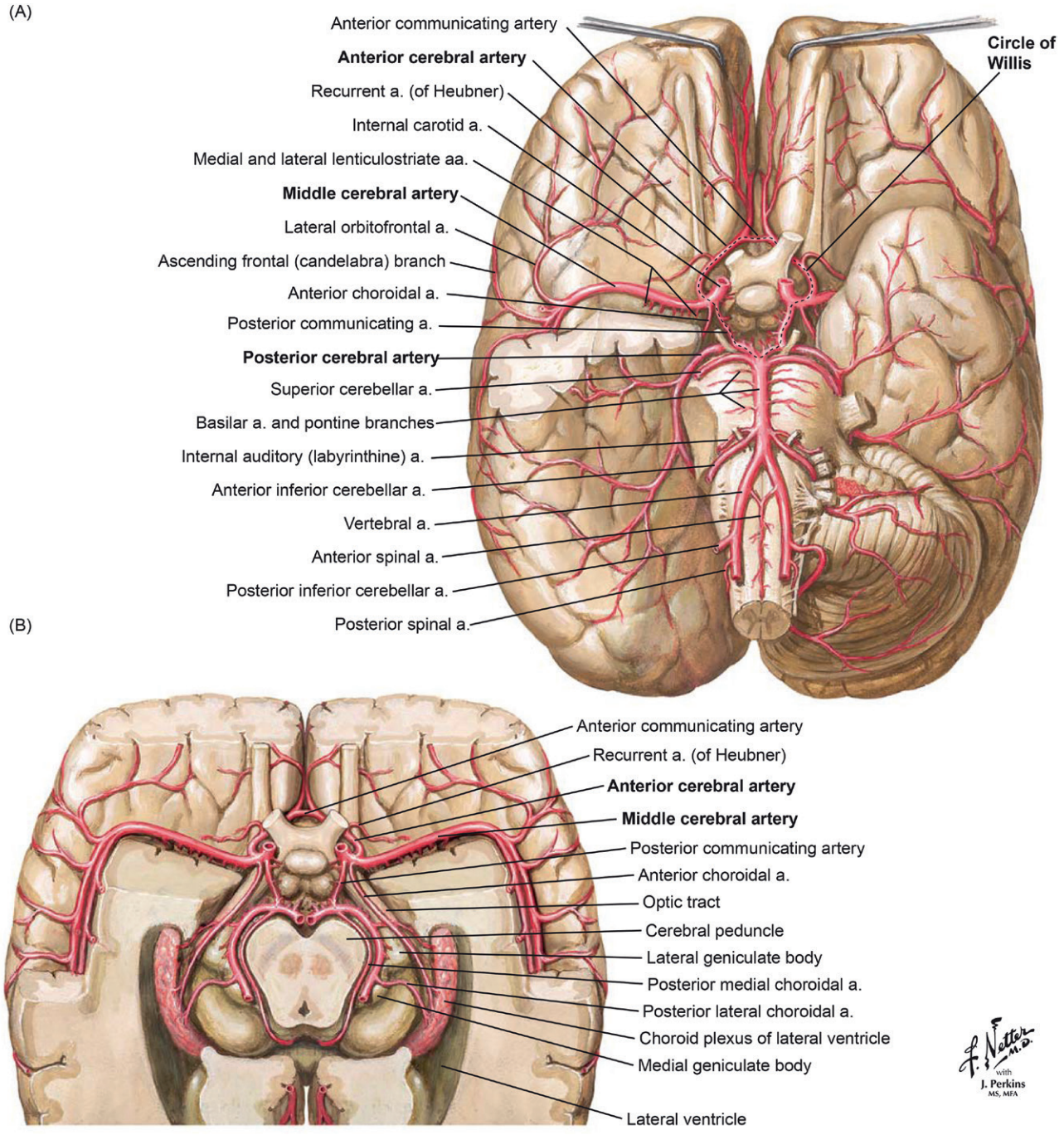

FIGURE 20.11 Human surface arteries. (A) Basal view and (B) lateral view. *a*, artery; *aa*, arteries. Source: © Elsevier, Inc., www.netterimages.com.

been reported to be absent or poorly formed in C57BL/6 mice. In humans, the same major arteries are involved in perfusing the brain. However, the complexity of human brain structure relative to the rodent brain leads to a slightly different arterial pattern. The names of corresponding arteries and veins often bear different names in rodents and humans.

The Endocrine Brain

The two classic endocrine organs within the CNS are the pituitary gland and the pineal gland, which are discussed in detail in Chapter15, Endocrine System. The *pituitary gland* resides in the sella turcica of the skull, and is connected to the brain via the infundibular stalk. In rodents and

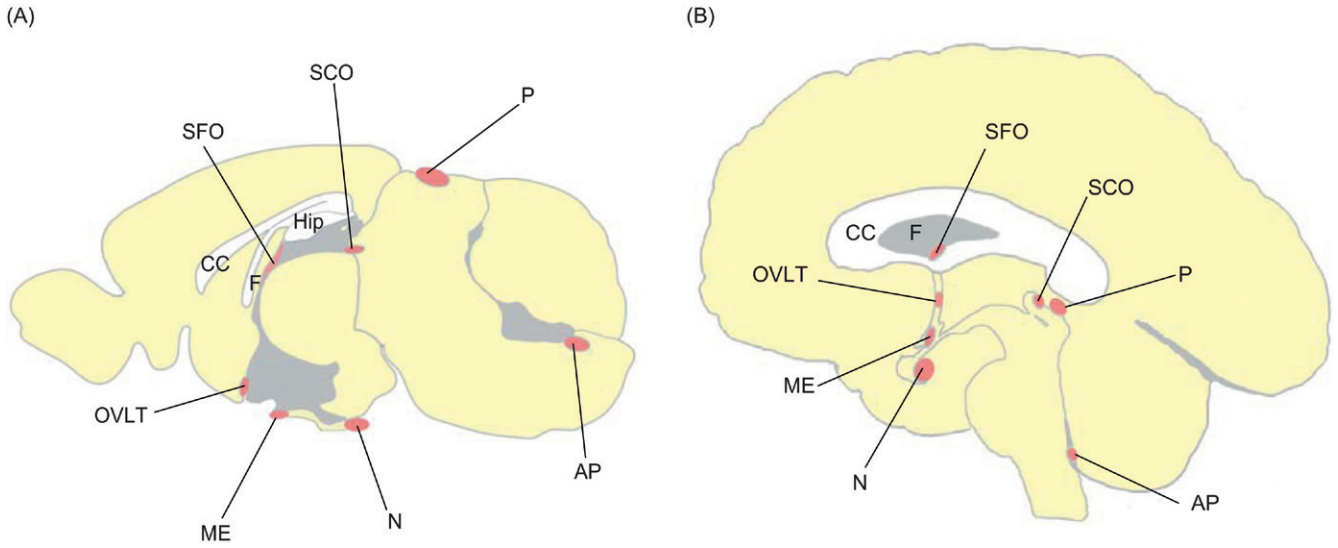

FIGURE 20.12 Circumventricular organs. (A) Rodent (mouse) and (B) human brains. The seven CVOs (shown as poppy-colored ovals) are the area postrema (AP), median eminence (ME), neurohypophysis (N), organum vasculosum of the lamina terminalis (OVLT), pineal (P), subcommissural organ (SCO) and subfornical organ (SFO). *cc*, corpus callosum; *F*, fornix; *Hip*, hippocampus.

humans, the gland typically remains in the skull during brain removal. Its three main lobes—the adenohypophysis (pars distalis, anterior lobe), the intermediate lobe (pars intermedia), and neurohypophysis (pars nervosa, posterior lobe)—are more morphologically discrete in rodents than in humans. The adenohypophysis and the neurohypophysis can both be discerned grossly.

The pineal gland is one of the circumventricular organs (CVOs), which are groups of specialized neurons and supporting glia that are found in small, highly vascularized, midline structures located in the walls of the ventricular system. Because of their highly cellular and/or porous structure, CVOs have a tendency to be interpreted as lesions by inexperienced morphologists.

Five CVOs (listed from rostral to caudal) are found exclusively near the third ventricle (Fig. 20.12): vascular organ of the lamina terminalis (OVLT; Fig. 20.13A), subfornical organ (SFO; Fig. 20.13B), median eminence (ME; Fig. 20.13C), subcommissural organ (SCO; Fig. 20.13D), and pineal gland (Fig. 20.13E). One, the area postrema (AP; Fig. 20.13F), is in the floor of the fourth ventricle. Some researchers also include the choroid plexus and neurohypophysis (i.e., posterior lobe of the pituitary gland) as CVOs. CVO locations differ in rodents and human as a function of ventricular anatomical differences. Some CVOs are situated at the junction between ventricles (SFO, SCO, and AP), whereas others line ventricular recesses (neurohypophysis, ME, OVLT, and pineal).

CVOs may be chemosensory (OVLT, SFO, and AP) or secretory (the neurohypophysis and pineal gland). Their numerous capillary loops lack a blood–brain barrier (BBB), due to the fenestrated nature of the endothelial lining (which is the case for all but the SCO). This allows direct exchange between blood and CVO nervous tissue. However, CVO cells of the ependymal lining have few cilia and are connected by tight junctions (representing a de facto BBB). Only three CVOs—the AP, OVLT, and SFO—contain neurons, whereas two others—the CP and SCO—consist entirely of specialized ependymal cells. These organs function to regulate biological rhythms (pineal and SCO); blood pressure and water balance (AP, CP, OVLT, and SFO); food aversions (AP); and homeostasis (ME and pineal).

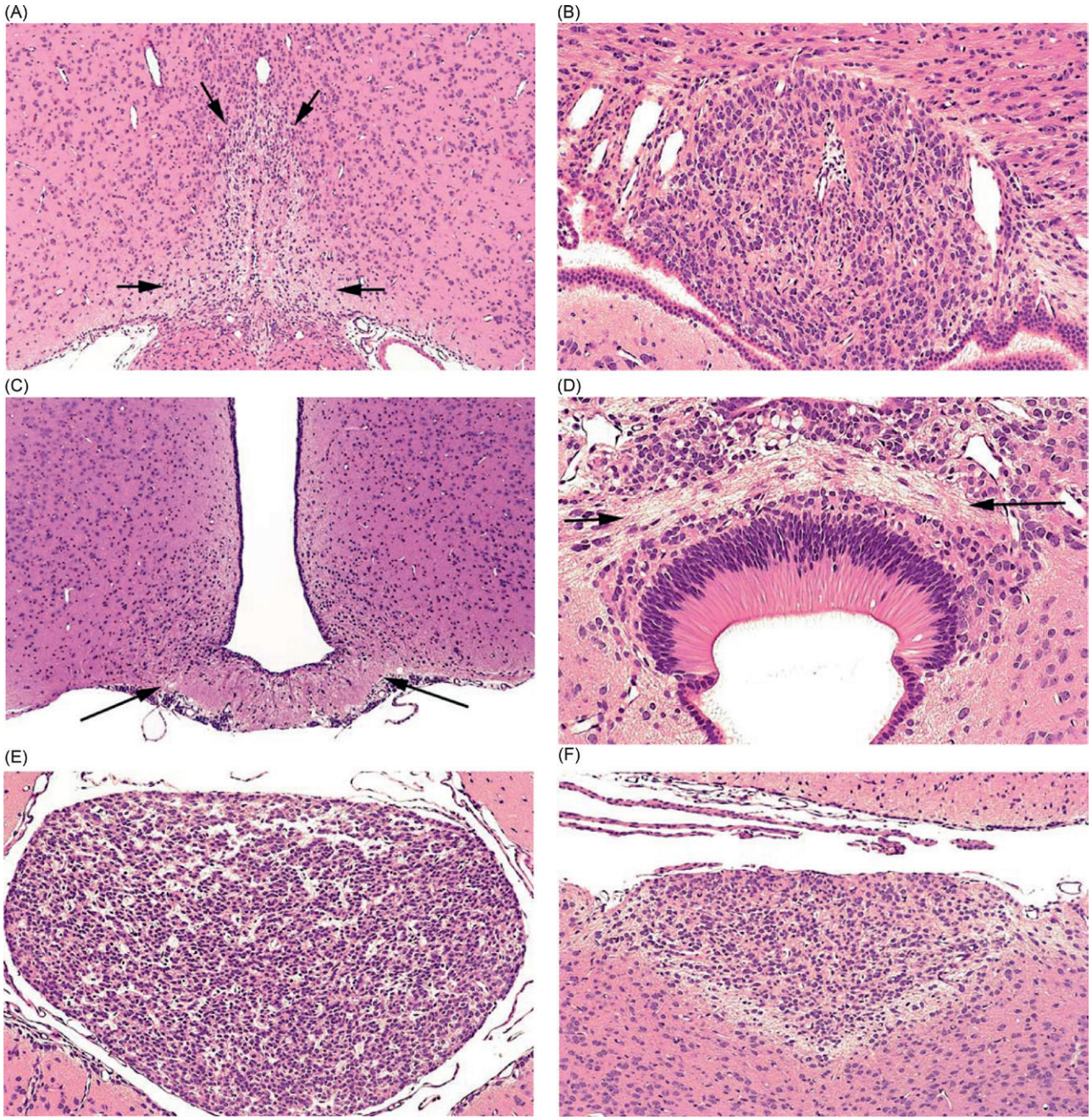

FIGURE 20.13 CVOs in the rodent brain (rat). These six brain regions are the organum vasculosum of the lamina terminalis (A; outlined by arrows), subfornical organ (SFO) (B), median eminence (ME) (C; bracketed by arrows), subcommissural organ (SCO) (D), pineal gland (E), and AP area postrema (AP) (F). Neurons occur only in the CVOs in A, B, and F. The SFO (B) is sometimes mistaken for a lesion (e.g., a subependymal granuloma). The caudal (posterior) commissure (arrows in D) appears pale (hypomyelinated) because this image was taken from the brain of a weanling at postnatal day 21 (i.e., before myelination is complete). H&E. Source: Reprinted from Garman: Histology of the central nervous system. Toxicol Pathol 39(1): 22–35, 2011 with the permission of Dr. Robert Garman and Sage Publications.

Functional Specialization of the Brain

Functional domains of the nervous system correlate with particular anatomic sites in the CNS, and neurons with comparable functions are clustered in regionally stereotypical patterns.

The cerebral cortex can be divided into three regions based on phylogeny. The *archicortex* is the most primitive domain and consists of the olfactory bulbs, olfactory tracts, and olfactory cortex (the piriform lobe of mammals). The *paleocortex*, the next oldest cortical region,

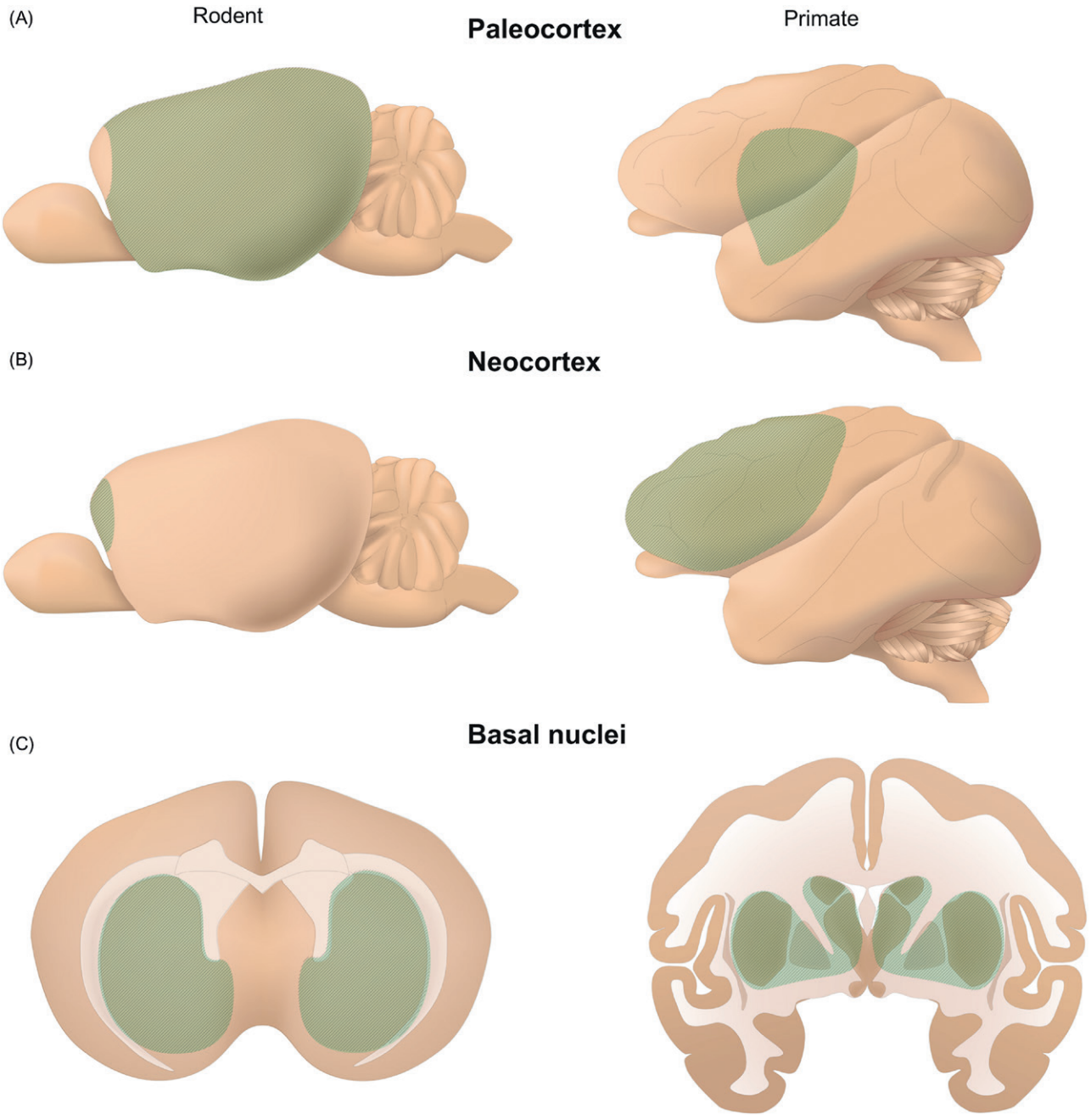

FIGURE 20.14 Brain regions. Schematic representations demonstrating the approximate boundaries of the paleocortex (A), neocortex (B), and the basal ganglia (striatum) (C) in rodents (left) and primates (right). Source: Figure provided by Sara Samuelson, S. S. Illustrations.

Need-to-know

- Rodent paleocortex does not fully recapitulate the human neocortical circuitry and functions.

is the cortical seat of the limbic system. The *neocortex* consists of the frontal (rostral), parietal (dorsolateral), temporal (ventrolateral), and occipital (caudal) lobes. Interspecies differences in cortical function hinge on the ratio of paleocortex (emotion-driven and involuntary functions) to that of neocortex (higher associative and cognitive function). The cerebral cortex of rodents consists chiefly of paleocortex with little neocortex, while the neocortex is extensive in humans (Fig. 20.14).

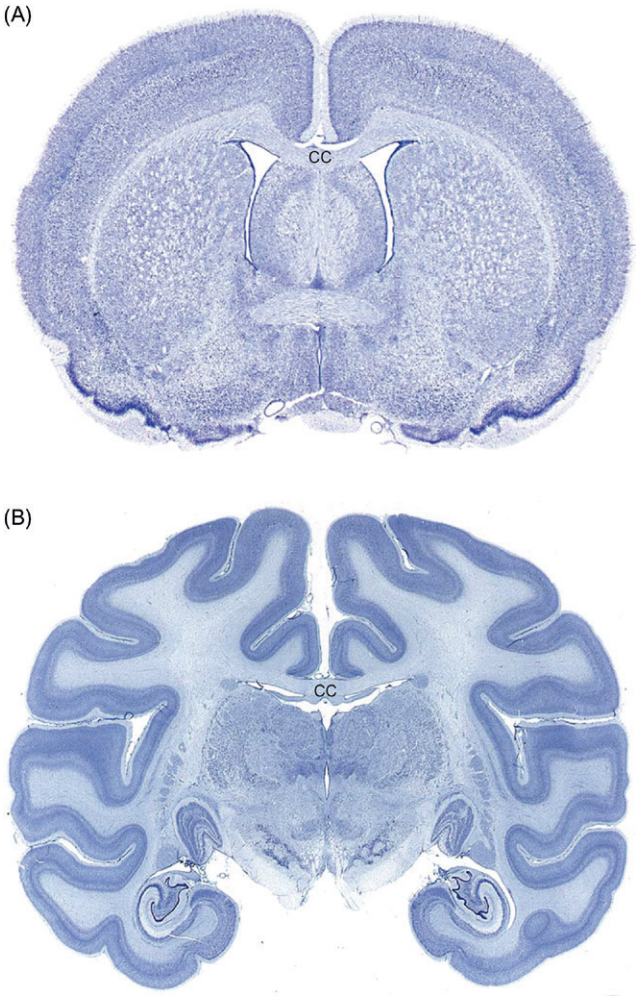

FIGURE 20.15 Brain gray and white matter (Nissl stain). The proportion of gray (dark blue) to white (pale blue) matter is much higher in the rodent (rat) brain (A) relative to its primate (cynomolgus monkey) counterpart (B). The primate brain is shown at a markedly reduced size to facilitate this comparison. *cc*, corpus callosum. Source: Images provided by Dr. Robert Switzer III of Neuroscience Associates (Knoxville, TN).

Need-to-know

- Humans have much more white matter than rodents, because they have more neurons and, therefore, more neuronal process.

The archicortex also is large in rodents relative to humans. Relative to rodents (Fig. 20.15A), the human cerebral cortex (Fig. 20.15B) has more white matter, which is related anatomically to the greater quantity of neocortex and functionally to the more extensive cognitive capabilities of this species.

Functional studies have shown that practically all regions of the cerebral cortex are linked to underlying subcortical centers (e.g., via the thalamus and basal nuclei). Nevertheless, particular cortical areas consistently relate to major functional modalities (Fig. 20.16). Topographical arrangements of these functional areas differ between rodents and humans but are stable within each species. In rodents, the visual cortex is located more laterally than in humans. In human but not rodents, the sense integration areas also have large accessory or associative cortices (Fig. 20.16). These associated cortices do not have direct connections to the senses and are thought to be involved in higher mental processes. Within the somatosensory and motor functional zones, body regions are projected somatotopically. Rodents and humans make different use of their sensory and motor modalities. Therefore, the proportional representation of various body parts on these cortices as a "homunculus" (little man) or "musunculus" (little mouse) differs markedly (Fig. 20.17). Large representations in the sensory cortex do not necessarily translate to large representations in the motor cortex for the same feature (Table 20.1).

Developmental distinctions are important considerations in neuroanatomic analysis because the most rapid changes in neural anatomy and physiology occur *in utero* and during the first few days (or months or years in long-lived species) of postnatal life. New neurons and synapses form widely until early adulthood (three weeks of age in rodents and the first two decades in humans). Neuronal populations in certain areas of the human frontal cortex (related to higher cognitive functions) may continue to mature for decades. Age-related structural differences include the extent of cerebral fissuration, regional differences in brain and spinal cord myelination, and the number of synapses in various brain regions. Age-related functional variations include a more porous BBB in developing

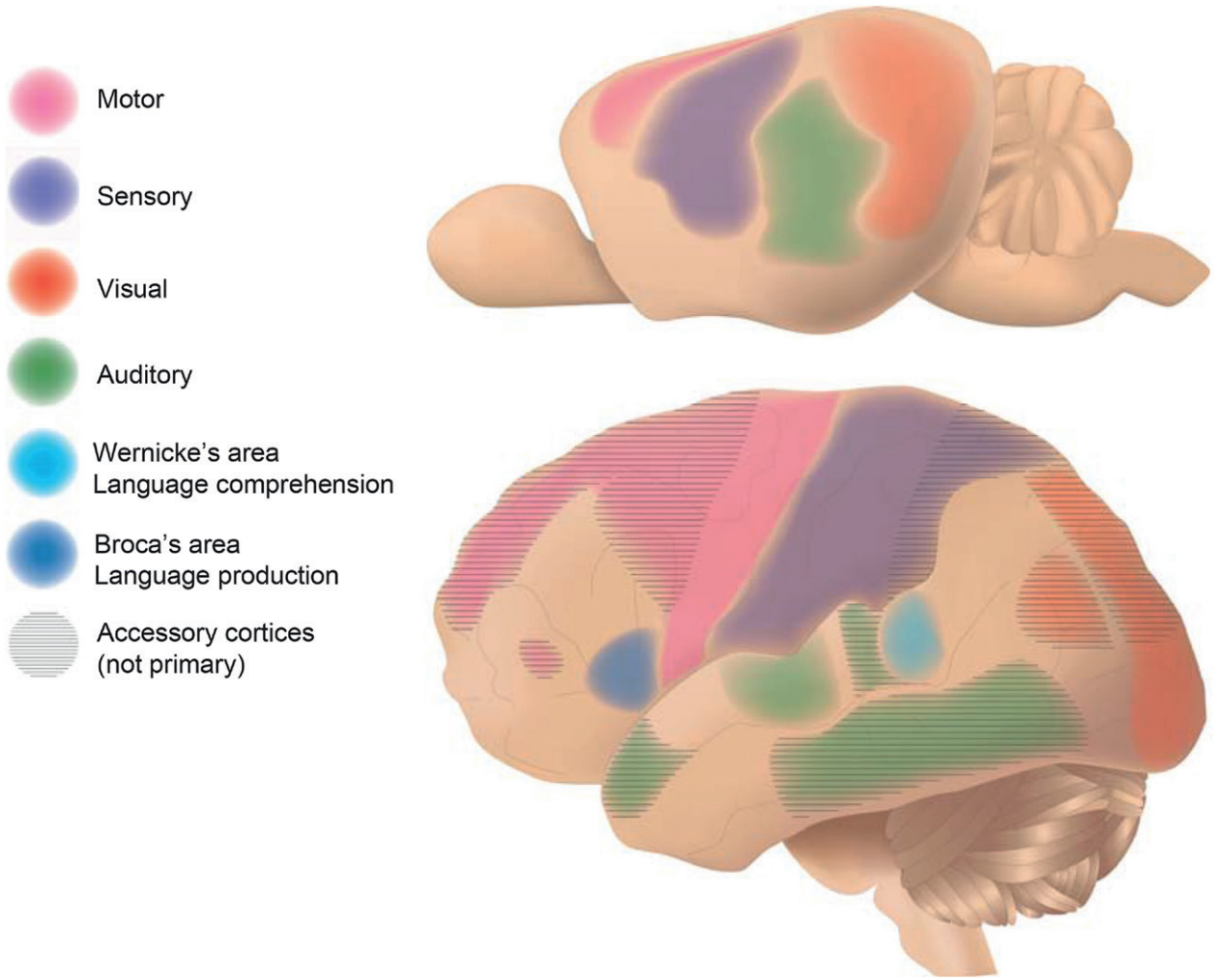

FIGURE 20.16 Brain functional zones. Schematic representations of the brain demonstrating the approximate boundaries of major functional zones as projected on the surface of the cerebral cortex of the rodent (mouse) (top) and human (bottom). Source: Figure by Sara Samuelson, S. S. Illustrations.

Need-to-know

- The mouse lacks accessory cortical areas.

animals and progressive increases in the levels of neurotransmitters, their receptors, and their synthetic pathways.

Within a species, strain and gender effects may impact neural structure and function. Strain differences in regional brain anatomy usually are fairly minor. For example, among different mouse strains, disparities have been documented in brain anatomy (the presence of a corpus callosum), behavior (especially in motor and stereotyped actions), neurochemistry (both hormone production and regional neurotransmitter levels), and responsiveness to drugs. These strain differences may be especially important in comparative behavioral models of disease. Other anatomic variations include the existence of sexually dimorphic nuclei and white matter tracts as well as distinctions in the number and location of sulci and the neuronal density in various brain

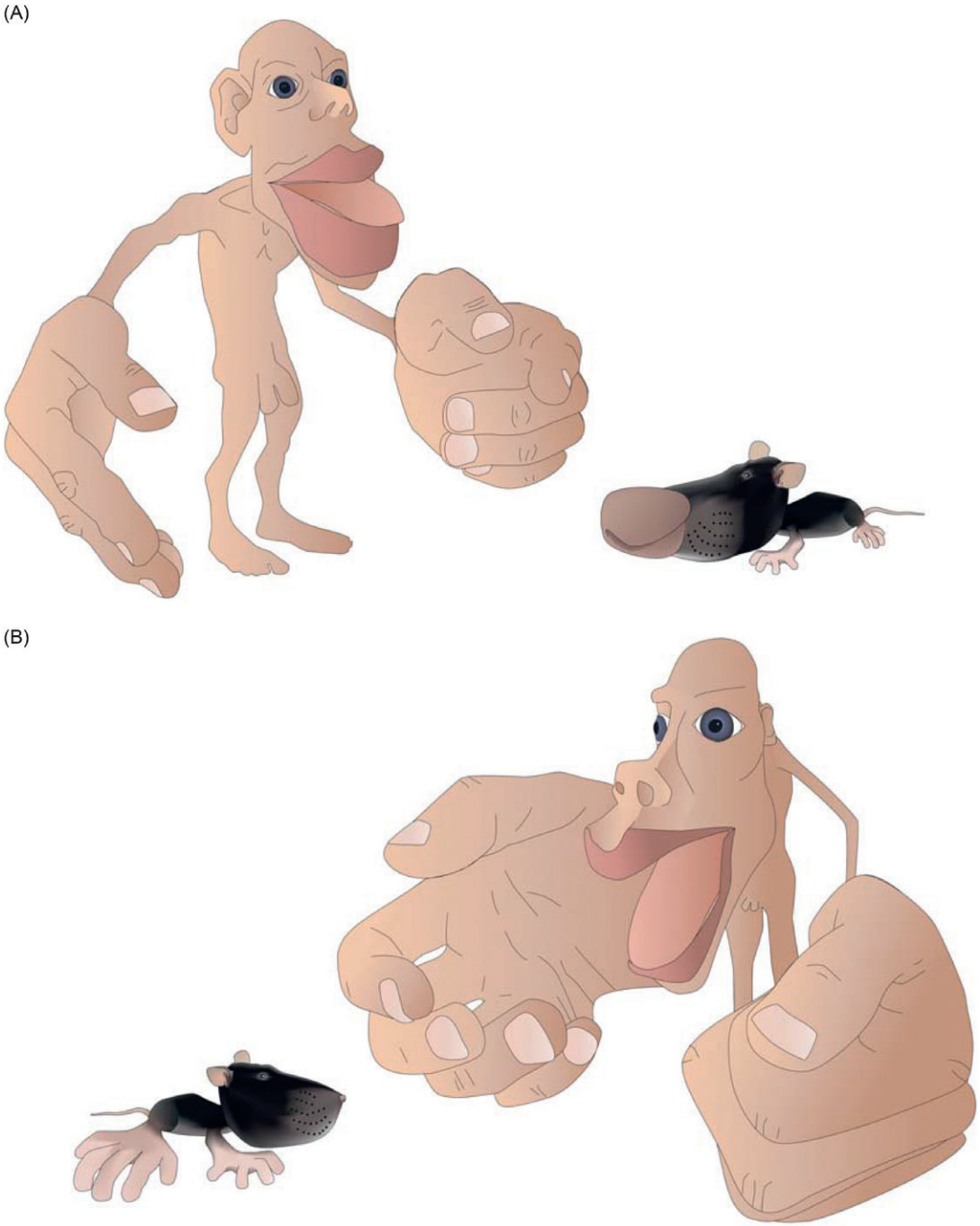

FIGURE 20.17 Sensory (A) and motor (B) "homunculi" (little man) and "musunculi" (little mouse). The sizes of the figures' body parts are proportional to the volume of somatosensory cortex (A) and motor cortex (B) devoted to their control. For somatosensory input, the hands and face are dominant in human, whereas the nose (olfaction) and whisker barrels predominate in mice. For motor output, hands are the dominant structure in humans, whereas in mice motor tasks are divided nearly evenly between the limbs and such facial features as the upper lip, lower jaw, vibrissae (facial whiskers), and eye muscles. The homunculi are based on the models at the Natural History Museum in London. Source: The somatosensory "musunculus" is derived from Vanderhaeghen et al.: A mapping label required for normal scale of body representation in the cortex. Nat Neurosci 3(4):358–365, 2000, whereas the motor maps were defined using data from Pronichev and Lenkov: Functional mapping of the motor cortex of the white mouse by a microstimulation method. Neurosci Behav Physiol 28(1):80–85, 1998. Figures by Sara Samuelson, S. S. Illustrations.

Need-to-know

- Shapes and proportions of body parts encoded in the somatosensory and motor cortices differ markedly.

regions. Gender-specific sex hormones have been shown to cause biochemical disparities, such as regional differences in the quantities and circadian cycling of neurotransmitters and hormones, in rodents and primates. The vascular supply to the brain also differs among mouse strains and between rats and mice, which may impact the relevance of data obtained using rodent models of cerebral ischemia (stroke) with respect to predicting potential human responses to brain ischemia.

HISTOLOGY

Cell Types

Cells of the CNS can be divided into two categories based on their embryonic origin: neuroectodermal or mesenchymal. Cells arising from the neuroectodermal layer include neurons, astrocytes, oligodendrocytes, and ependymal cells. Each neuron is sustained by approximately 10–50 glial cells, a catchall term for astrocytes, oligodendrocytes, and ependymal cells, including CP epithelium. Cells of mesenchymal origin include meningeal fibroblasts and vascular endothelium (discussed below), and microglia, which are not true glia. Rather, microglia are thought to arise from yolk sac progenitors and/or circulating precursors of the macrophage lineage. More detailed descriptions of CNS histology and cytoarchitecture, including common lesions and artifacts, may be found in standard histology and neuropathology texts and also reviews listed in Further Reading.

Neurons

The functional unit of the nervous system is the neuron. Neurons have one or more dendrites through which they receive input from other neurons and one axon that synapses on other neurons or nonneural effector organs, such as the musculature. Within the human brain, there are approximately 130 billion neurons forming 150 trillion synapses.

Neurons can be categorized in many ways, but the principal features used to distinguish populations of neurons are their neurotransmitter phenotype and their morphologic appearance. Neurons typically secrete a single small molecule neurotransmitter, most commonly glutamate (in excitatory cells) or γ-aminobutyric acid (GABA; inhibitory cells), as well as one or a few small peptide neurotransmitters such as enkephalin or parvalbumin. Neurons come in many sizes and shapes, but two common types with specific functional implications are large pyramidal cells and small granule cells. Pyramidal neurons, such as those of the cerebral cortex laminae and the motor neurons of the spinal cord ventral horns, have relatively big cell bodies and abundant Nissl substance (i.e., rough endoplasmic reticulum); they tend to be widely dispersed in the regions in which they occur. Granule neurons, like those populating the inner cerebellar cortex layer and the hippocampus CA fields, have smaller nuclei with scant cytoplasm and are tightly packed within their domains. Pyramidal cells usually function as projection neurons (so called because their long axons link to distant CNS regions or peripheral effector organs), while granule cells serve as interneurons that connect nearby CNS regions. However, this pattern is not universal; in the striatum, some interneurons are larger than the prevalent GABAergic medium spiny projection neurons. Generally, neurons are smaller and populate the neuropil more densely in rodents relative to the same structures of human neural tissues (Fig. 20.18). Common methods to reveal neurons are immunohistochemical procedures that detect neurofilament proteins, neuronal nuclei (e.g., the marker NeuN), or protein gene product 9.5 (PGP9.5) for the cell class as a whole as well

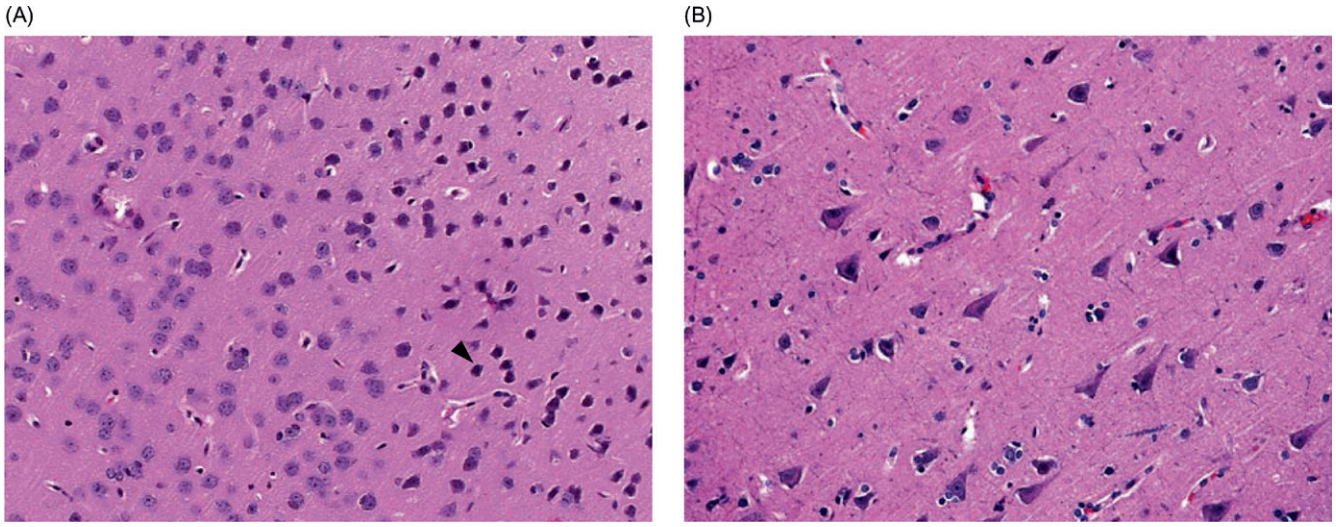

FIGURE 20.18 Brain gray matter. Rodent (mouse) (A) and human (B). Large neurons, astrocytes, and oligodendroglia are surrounded by neuropil, an amorphous expanse of eosinophilic cell processes (sea of pink) filling the space between cell bodies. In the mouse image, the neurons on the right side (black arrowhead) exhibit the contracted, more intensely basophilic appearance of "dark neuron artifact." Such dark neurons are thought to be a consequence of postmortem manipulation/trauma in ischemic brain tissue; they do not represent degenerating or dying neurons.

Need-to-know

- Rodent cerebrocortical neurons appear more compact and are more densely bunched compared to human neurons.

as neurotransmitters or transmitter-producing enzymes for specific neuronal populations.

Astrocytes

Astrocytes are the most common glial cell. Their numbers exceed those of neurons in most brain areas. Astrocytes support neuronal function by producing antioxidants (glutathione), recycling neurotransmitters (glutamate and GABA), and maintaining the BBB (to sustain the microenvironmental equilibrium). Astrocyte foot processes are also major components of the BBB and glymphatic channels.

The cytoarchitecture of astrocytes is characteristic. Their nuclei are approximately the same size as many neuronal nuclei, but are larger than oligodendrocyte nuclei. Astrocytic nuclei are round to ovoid and have small or indistinct nucleoli. Cytoplasmic processes of nonreactive astrocytes are inconspicuous in hematoxylin and eosin (H&E)-stained sections, while astrocytes reacting to injury develop increased cytoplasmic mass and prominent stellate processes with discernable borders (gemistocytic astrocytes). The method most frequently used to find astrocytes is immunohistochemical detection of glial fibrillary acidic protein (GFAP).

Oligodendrocytes

Oligodendrocytes (oligodendroglia or "oligos") form and maintain the myelin that surrounds processes of CNS neurons. Each oligo sheathes multiple axons, while several oligos can serve as "satellite cells" next to neuron cell bodies in gray matter. Oligodendrocytes have round nuclei with condensed chromatin, which stain darker than those of astrocytes and neurons; commonly exhibit a clear "halo" artifact in immersion-fixed but not perfusion-fixed CNS tissues; and lack a basal lamina. Oligodendrocytes are often seen in linear rows between the nerve fibers of white matter tracts (Fig. 20.19). Common markers for oligodendrocytes include carbonic anhydrase II, CNPase (2′,3′-cyclic nucleotide 3′-phosphohydrolase), myelin basic protein (MBP), and myelin oligodendrocyte

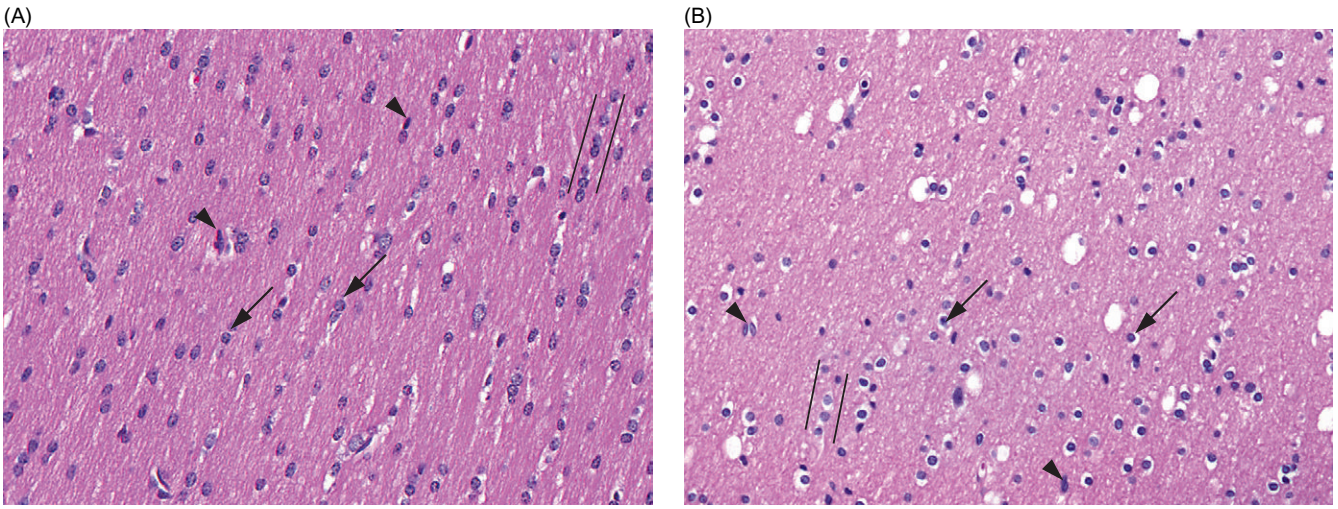

FIGURE 20.19 Brain white matter. Rodent (mouse) (A) and human (B). Oligodendrocytes (arrows) have round, dark nuclei and are arranged in long rows (bracketed by lines) oriented parallel to the axons that they myelinate. In H&E-stained sections, white matter is slightly more eosinophilic and less cellular than gray matter, and the neuropil has a more organized, streaming appearance. The human oligodendrocytes often have a slight perinuclear halo ("fried egg" appearance). This feature occurs as an artifact of immersion fixation and is not prominent in the mouse image because the animal was perfused with fixative. Occasional astrocytes (arrowheads) are evident as oblong, irregularly shaped nuclei. The cytoplasm of astrocytes (and microglia) normally blends with the neuropil and typically cannot be observed unless the cells are activated.

glycoprotein (MOG). Oligodendrocyte damage leading to loss of CNS myelin is not subject to repair in rodents and humans.

Ependyma

These glial cells are arranged in a single layer of cuboidal to columnar cells that line the surface of all of the brain ventricles as well as the central canal of the spinal cord. The cells have a homogeneous appearance, with oval hyperchromatic nuclei and pale eosinophilic cytoplasm. They resemble CP epithelium but are smaller. Ependymal cells are joined by desmosomes, thereby forming a brain–CSF barrier, and have microvilli and are usually ciliated. The motion of the cilia circulates the CSF from the brain through the ventricular system.

Choroid Plexus (CP) Epithelium

CP cells are modified ependymal cells that cover the capillary loops responsible for production of CSF. The cells form a single layer of cuboidal epithelium, the slight apical bulge of which resembles a set of cobblestones. CP cells are found in all of the ventricles. Human CP has more abundant fibrovascular stroma among the vascular channels and a larger surface area relative to the same structures in rodents (Fig. 20.20).

Microglia

Microglia are the innate immune cells of the CNS. These resident histiocyte-like cells arise in part from yolk sac progenitors that colonize the CNS during development, and in part from bone marrow-derived monocytes that enter the damaged CNS during adulthood. Microglia in H&E-stained CNS sections are few in number; such "resting" cells have inconspicuous cytoplasm and dark, rod-shaped nuclei that are smaller than those of astrocytes. Activated microglia have lighter oval nuclei and may appear to be distended by phagocytosed material. The markers often used to demonstrate microglia are CD68 in humans and CD11b or ionized calcium-binding adapter molecule 1 (Iba-1) in rodents.

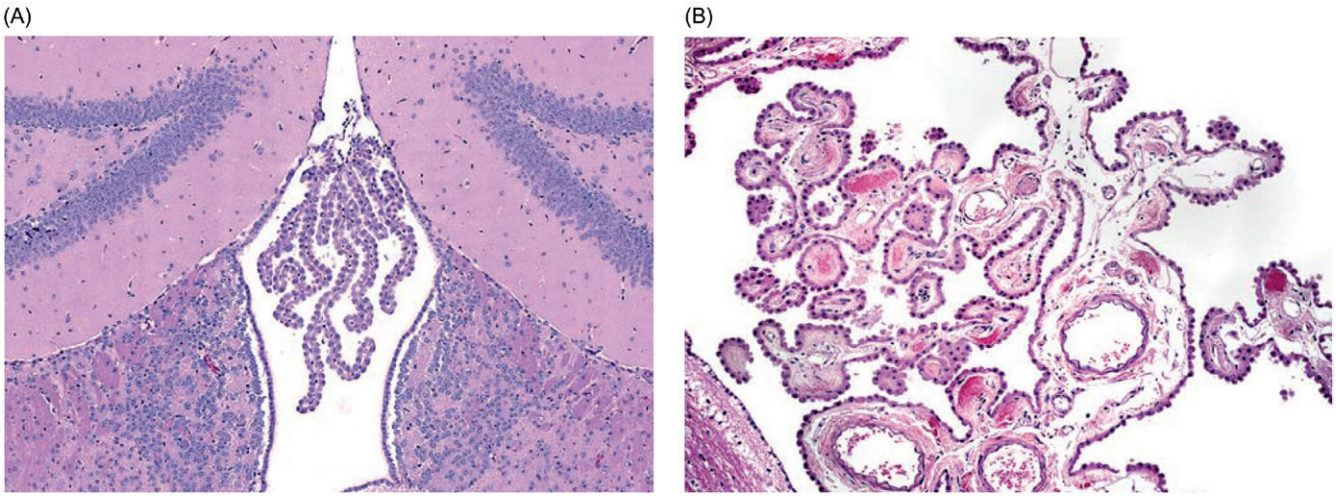

FIGURE 20.20 Choroid plexus. Rodent (mouse) (A) and human (B). This tissue contains branching fronds of specialized secretory epithelial cells that extend into the ventricular cavities. The single layer of epithelium is separated from numerous winding blood vessels by a thin band of connective tissue. Choroid plexus (CP) is the source of cerebrospinal fluid (CSF). (B) Human CP has a larger surface area and more abundant connective tissue relative to that of mice.

Region-Specific Histology

Cerebral Cortex

The gray matter in the cerebral cortex harbors two major types of neurons: small granule cells, which function as intracortical interneurons, and large pyramidal cells, which serve as efferent projection neurons traveling within the cerebral cortex or extending to subcortical structures. Cerebrocortical neurons form six parallel layers in the gray matter (Fig. 20.21), each designated by a Roman numeral. The molecular layer (I), the most superficial lamina, has neuronal processes (neuropil) and glial cell bodies. The next layers are the external granule cell layer (II) and external pyramidal cell layer (III). These laminae are fairly distinct in the human brain but cannot be readily discerned in many regions of the rodent cerebral cortex. The deepest levels are the internal granule cell layer (IV), internal pyramidal cell layer (V), and multiform layer (VI). Afferents to the cerebral cortex arise in the ipsilateral and contralateral cortex (terminating mostly in layers II and III) as well as in the thalamus (terminating in layers I, IV, and VI). Corticocortical efferents arise from layer III, corticostriatal efferents from layer V, and corticothalamic efferents from layer VI. The width and prominence of these layers varies among regions; for comparable regions, layering generally is more evident in human cortex relative to rodent cortex.

Basal Nuclei

The semi-organized gray matter aggregates comprising the basal nuclei are populated by projection neurons (mainly the GABAergic medium spiny neurons) and cortical interneurons, both of which appear predominantly as granule cells. The streaming of white matter tracts through the striatum gives it a striped appearance, hence its name (Fig. 20.22). Bundles of myelinated, small-diameter axons cross the striatum toward the globus pallidus; these axons are called pencil fibers (Wilson's pencils) based on their appearance. As discussed previously, neurons in the human substantia nigra accumulate neuromelanin—a coarse, dark, cytoplasmic pigment formed as a

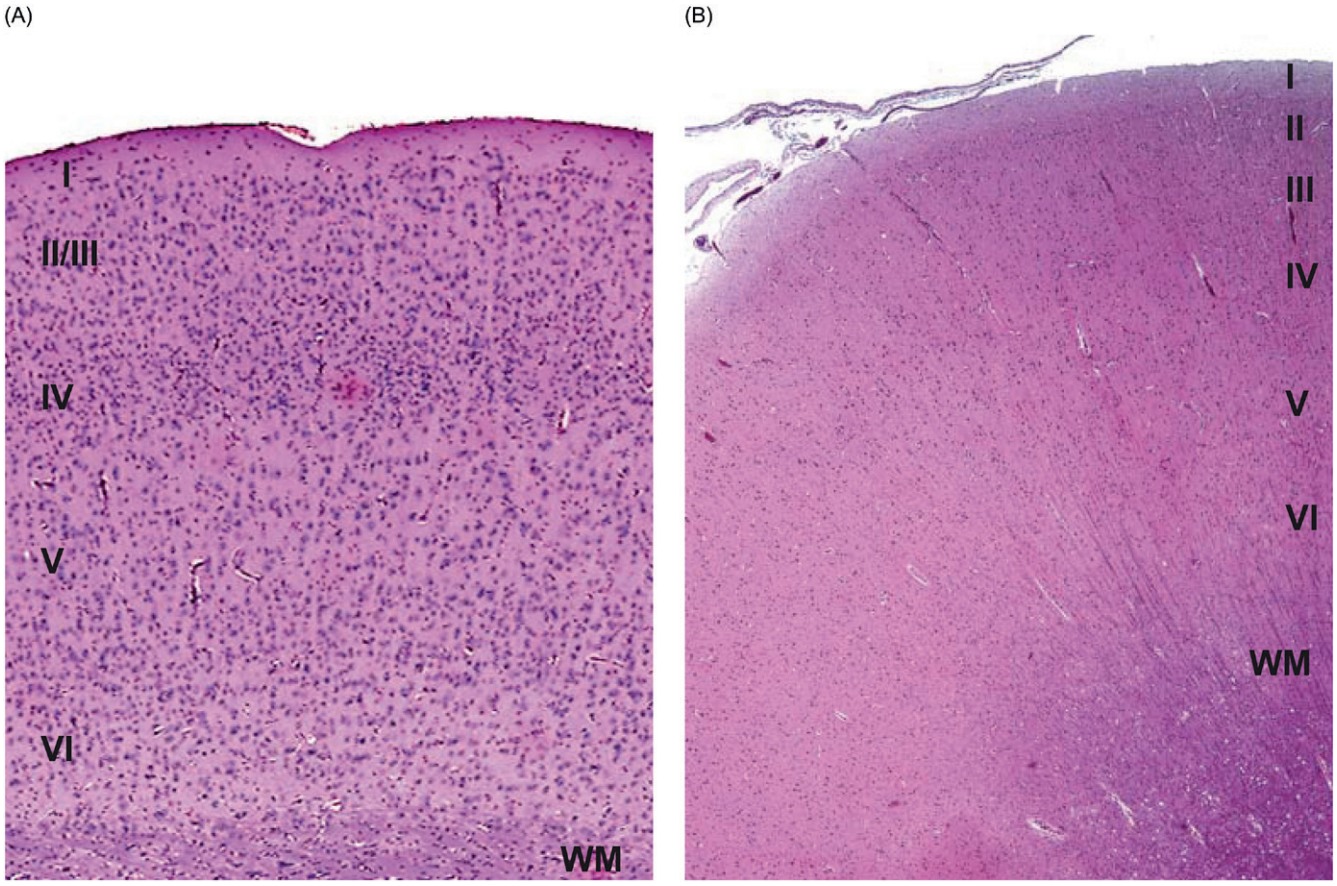

FIGURE 20.21 Neuronal organization in the cerebral cortex. Rodent (mouse) (A) and human (B). The cortex contains six layers, although in mice, layers II and III are merged together as layer II/III. Layer I (molecular layer) lies beneath the meninges and contains neuropil and few neuron cell bodies. The remaining strata are layers II (external granular cell layer), III (external pyramidal cell layer, composed of small pyramidal cells), IV (internal granular cell layer), V (internal pyramidal cell layer, containing large pyramidal cells), and VI (multiforme layer, with elongate fusiform neurons). To highlight cellular detail of each species, the mouse image is presented at a higher magnification. *WM*, white matter.

by-product of catecholamine (dopamine) synthesis (Fig. 20.23). In contrast, the neurons in the rodent substantia nigra exhibit basophilic halos and bands along the cytoplasmic borders but lack neuromelanin (Fig. 20.23).

Diencephalon

Ammon's horn of the hippocampus contains pyramidal neurons exhibiting variable amounts of cytoplasm (more in humans than rodents) and dendritic spines. The dentate gyrus contains granule neurons, and is more densely populated in rodents than humans (Fig. 20.24). Ammon's horn (CA) is divided into regions CA1–CA4 (Fig. 20.24).

The hypothalamus is comprised of many poorly delineated nuclei. In general, parvocellular (small) neurons project to the ME, whereas magnocellular (large) neurons send fibers directly to the neurohypophysis (i.e., the caudal/posterior part of the pituitary gland).

Cerebellum

The cerebellar cortex contains three layers, which are, from deep white matter to cortical surface, termed the granular layer, the Purkinje cell layer, and the molecular layer (Fig. 20.25). The granular layer contains numerous granule neurons whose axons extend superficially into the molecular layer; the rodent granular layer is less densely populated than the human granular layer. The Purkinje cell layer in humans and rodents is composed of a single row of large Purkinje neurons with a single axon that extends deep into the cerebellum and

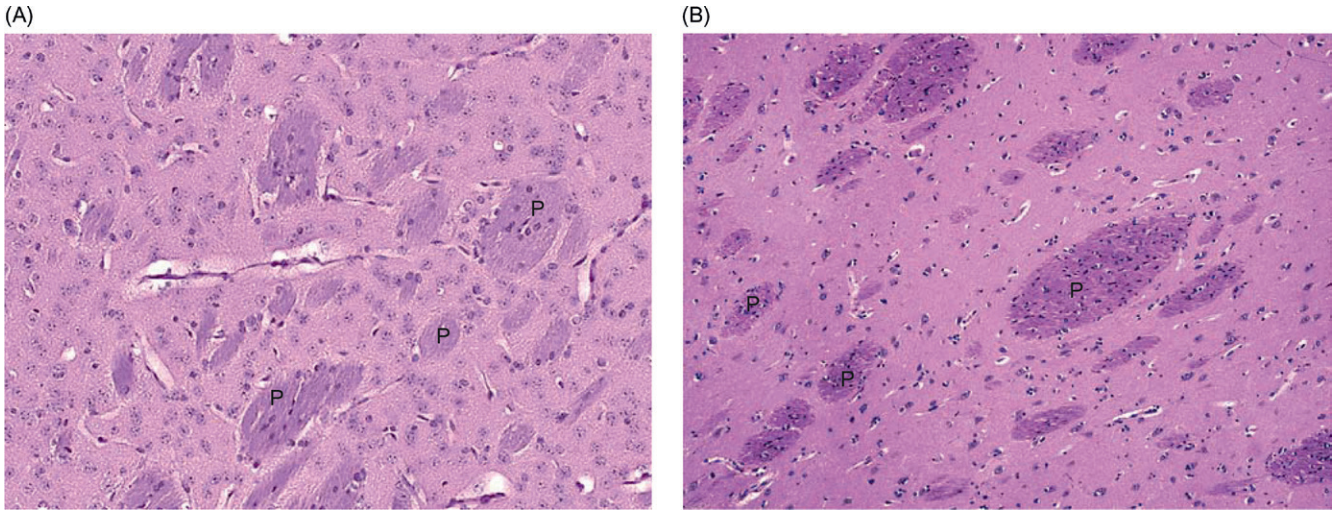

FIGURE 20.22 Caudate/putamen (H&E and LFB). Rodent (mouse) (A) compared to the caudate nucleus of human (B). Bundles of finely myelinated, small-diameter axons (P) crossing the striatum toward the globus pallidus are called "pencil fibers" ("Wilson's pencils" or striatopallidal fibers) in humans; although the term is not frequently encountered in rodent neuroanatomy references, it aptly describes the appearance of white fiber tracts in rodent caudate/putamen. In humans, the caudate nucleus and putamen are separate but semicontinuous brain structures separated by streaming fibers of the anterior internal capsule. The alternating gray and white matter gives the tissue a striped appearance, so the two structures together are referred to as the "striatum" (meaning "striped").

Need-to-know

- Histologically the caudate and the putamen are nearly identical, and they have a common embryologic origin.

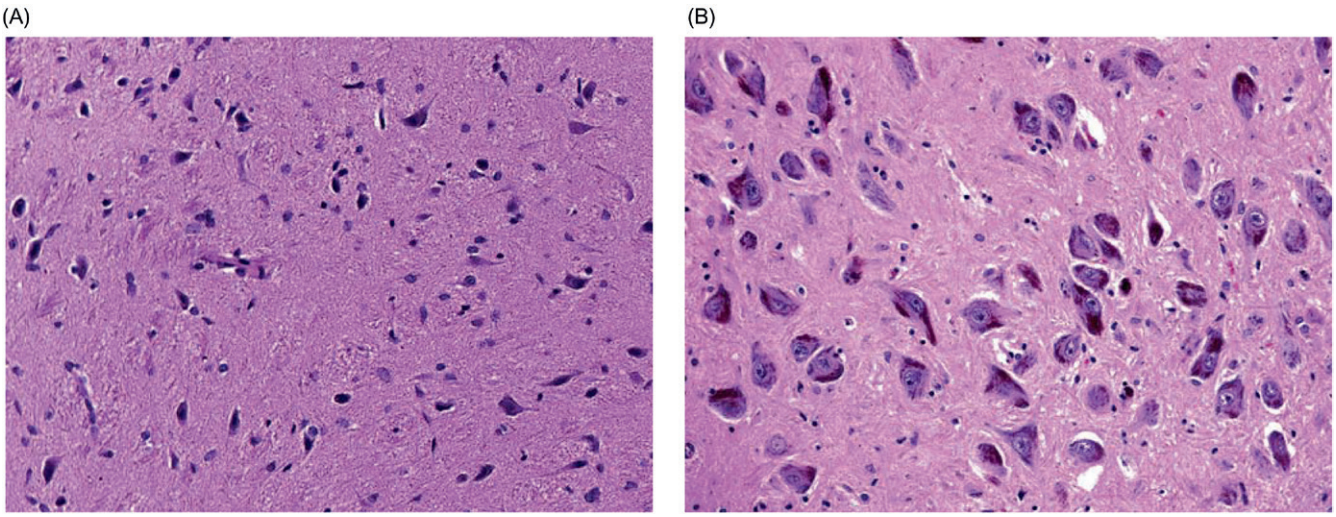

FIGURE 20.23 Substantia nigra. Rodent (mouse) (A) and human (B). The region takes its name from the accumulation of neuromelanin (dark cytoplasmic pigment granules) in the large dopaminergic neurons in human substantia nigra. In mice, the same neuronal population is characterized by a narrow halo of cytoplasm bordered by a basophilic band. The pigment in mice is not visible, as it is in humans. It takes approximately 3 years of accumulation for pigment to become microscopically visible in humans.

numerous dendrites that project into and widely arborize in the molecular layer. Rodent Purkinje cells are smaller and have less cytoplasm than human Purkinje cells. Thus, the molecular layer's abundant neuropil network consists mostly of the granule cell axons and Purkinje cell dendrites. The cell nuclei within the molecular layer are mostly glial cells.

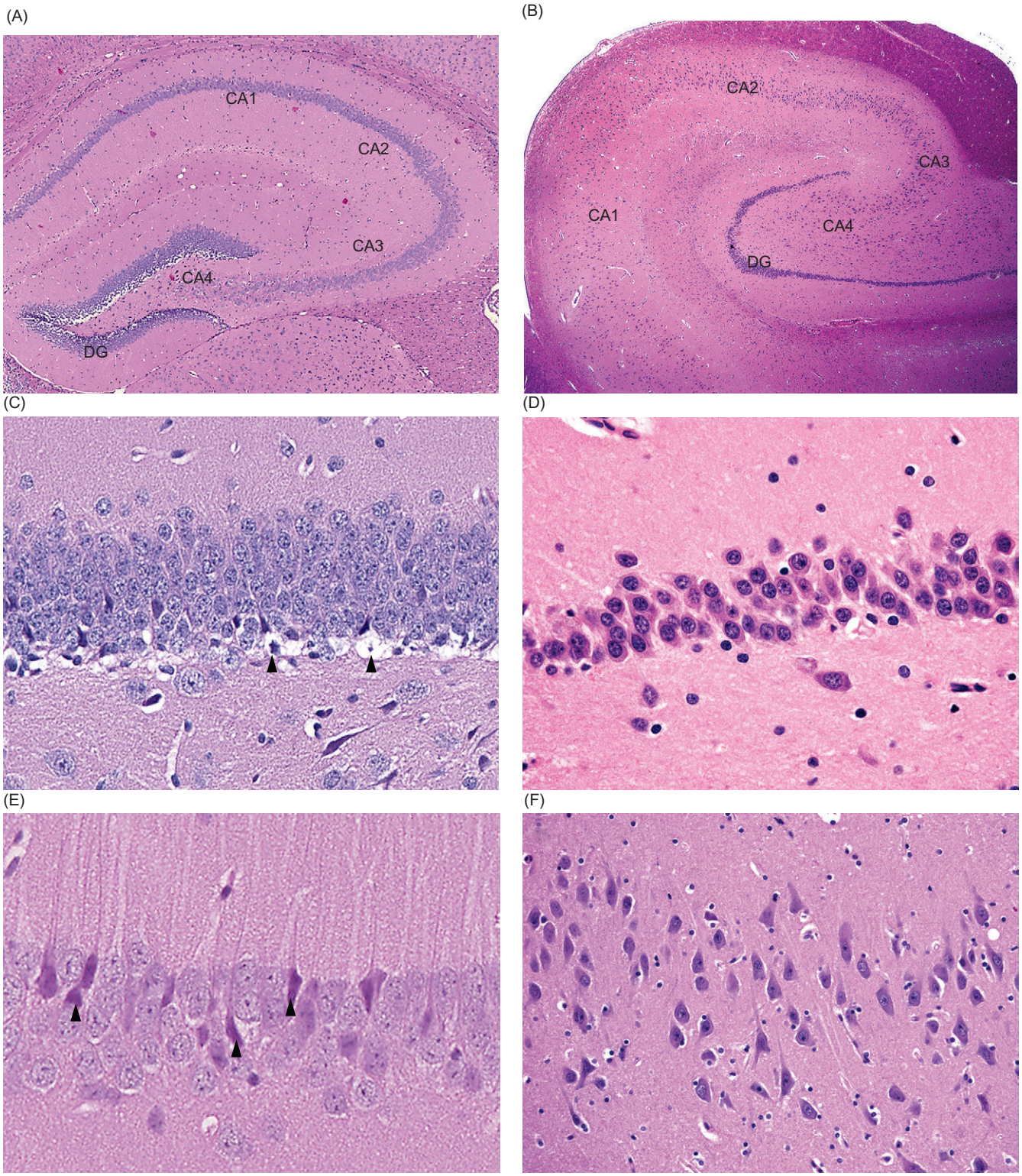

FIGURE 20.24 Organization of the hippocampus. Rodent (mouse) (A, C, and E) and human (B, D, and F). (A) Mouse dentate gyrus (DG) containing dense granule cells and CA1–CA4 regions containing pyramidal neurons. (B) Human DG and CA1–CA4 (hilus or superficial layer of DG) regions. The DG granule cells are more numerous and densely packed in mice (C) relative to human (D). Granule cells project to the mossy fibers of CA4 and pyramidal cells of CA3. Mouse CA1 pyramidal neurons (E) are more densely packed, much smaller, and have less cytoplasm than their human CA1 counterparts (F). Note the presence of "dark neurons" (E; arrowheads)—a common histological artifact characterized by contracted, intensely basophilic neuron bodies—in rodents. This artifact is thought to result from postmortem manipulation or trauma in ischemic brain tissue; it should not be interpreted as evidence of neuronal degeneration or death. The clear band of vacuolated cells is another common processing artifact observed in the hippocampus of immersion-fixed rodent brains (C; arrowheads). Mouse and human micrographs are shown at different magnifications to better illustrate the cytoarchitectural features of each species.

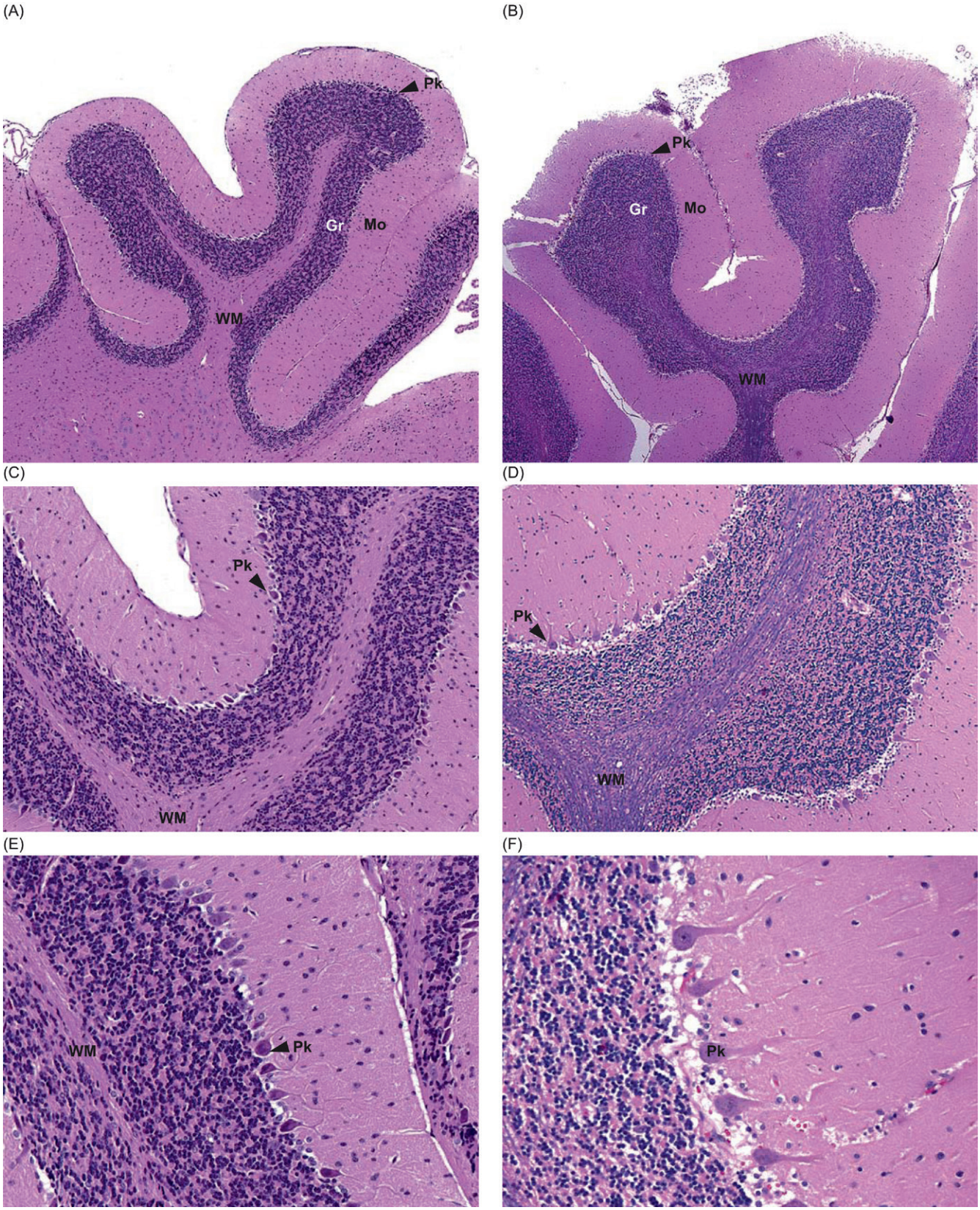

FIGURE 20.25 Cerebellum. Rodent (mouse) (A, C, and E) and human (B, D, and F; H&E with LFB). The region is uniformly organized in three layers, which are (from outside to in) the molecular layer (Mo), Purkinje cell layer (Pk, with arrowheads), and the granular layer (Gr). The molecular layer is a broad expanse of densely packed neuronal processes with few neuronal bodies. The Purkinje cell layer is a single layer of large, torpedo-shaped cells with prominent apical processes extending into the molecular layer; the cells in mice are smaller and have less cytoplasm (E) relative to human cells (F). The granular layer is packed with small, dark, round granule cells, and it is more cellular in human than in mice. The white matter (WM) core of each cerebellar folium (meaning "leaf") is visible in both species. Mouse and human micrographs are shown at different magnifications to better illustrate the cytoarchitectural features of each species.

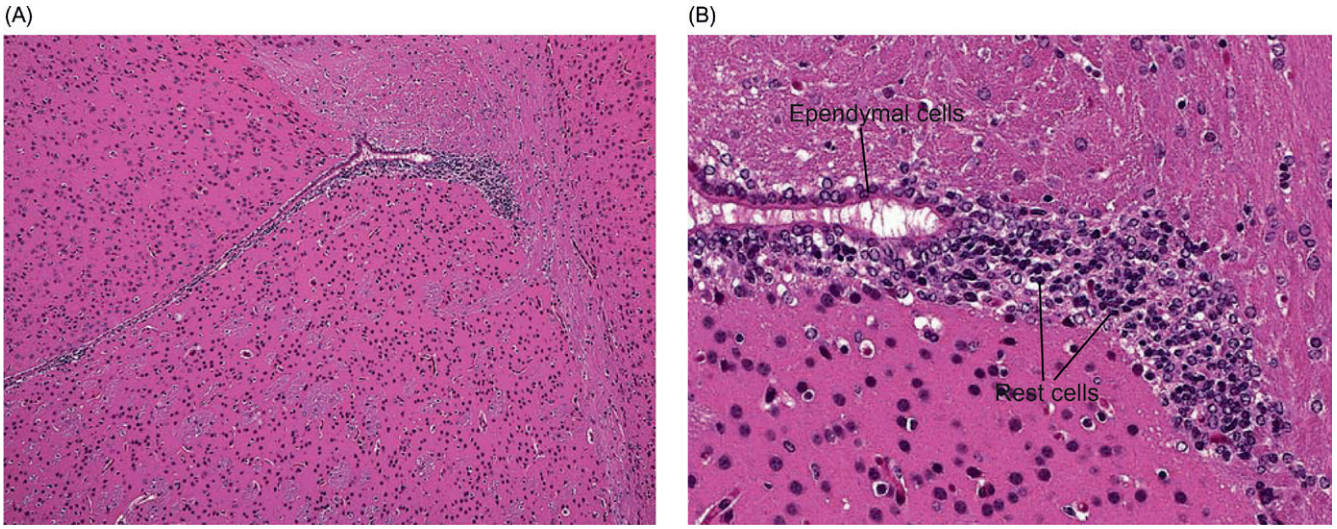

FIGURE 20.26 Rodent (mouse) stem cell rests. The ependymal cells form a simple layer of specialized, ciliated, cuboidal epithelium that covers the surfaces of the brain ventricles and spinal cord central canal. These cells differentiate from germinal cells of the embryonic neural tube. Occasionally, undifferentiated stem cells fail to migrate and are found as clusters known as rests (neural tube remnants) located near the ependyma of ventricles. (A) Rostral extension of the lateral ventricle with adjacent stem cell rest. (B) Rests contain small, dark, round cells with minimal cytoplasm. These cell clusters also occur in humans, in whom the most common site is the floor of the fourth ventricle and the second most common site is the lateral ventricle.

Need-to-know

- Ependymal rests should not be confused with inflammation.

Brain Stem

This brain division consists of poorly delineated nuclei encompassed within intersecting white matter tracts peppered with the randomly scattered neurons of the reticular formation. On transverse sections, the reticular formation is divided into radiating, wedge-shaped zones, oriented with their apices near the floor of the fourth ventricle (Fig. 20.7F). From medial to lateral, these wedges include the raphe nuclei on the midline, the gigantocellular (large cell) zone, the intermediate (medium to large cell) area, and the parvicellular (small cell) region. The lack of readily defined divisions between elements of the brain stem makes histological analysis of this region a formidable task.

Relative to the olivary nucleus in rodents, the human inferior olivary nucleus exhibits substantial craniocaudal and lateral expansion. The increase in size is related to the enhanced connectivity between this nucleus and the enlarged hemispheres of the overlying cerebellum.

Cell Rests

Occasionally, clusters of undifferentiated germinal cells that have failed to migrate can be found adjacent to the ependyma and ventricles (Fig. 20.26). These "stem cell rests" (neural tube remnants) can sometimes be found in the fourth or lateral ventricles. The cells appear small, round, and dark with minimal cytoplasm. They are sometimes mistaken as a lesion. Another common example of this phenomenon in rodents is small clusters of retained external granule cells (i.e., the precursors of the cells in the granular layer) on the surface of the cerebellum.

RELATED STRUCTURES

Meninges

The meninges are the connective tissue coverings of the brain and spinal cord. The outermost layer is the dura mater, a dense and tough tissue that is reduplicated to form the periosteum of the inner skull. Beneath the dura is the arachnoid,

a network of loose connective tissue that lacks blood vessels. The arachnoid is closely adhered to the pia mater, which is the innermost membrane that contains blood vessels; together, these two structures are referred to as the leptomeninges. The very thin leptomeninges of rodents are visible grossly. They are thicker and more vascular in humans due to the increased surface area that must be oxygenated. Meninges have both collagen and elastic fibers. In the vertebral canal, there is an epidural space between the meninges and vertebrae, which is often filled with white adipose tissue. The principal cell types in meninges are fibroblasts within the stroma and the vascular endothelium. The extent of collagen production is greater in the thicker outer dura mater and relatively less in the two thinner leptomeningeal layers, the arachnoid and pia mater. On occasion, a few leukocytes (typically lymphocytes) may be seen near superficial meningeal blood vessels.

Blood–Brain Barrier

The BBB and blood–nerve barrier represent dynamic, tightly regulated interfaces that separate nervous tissue from many blood-borne materials. The BBB consists mainly of specialized capillary endothelial cells in which the presence of complex tight junctions, lack of fenestrae, and low endocytic activity result in decreased permeability. Glial cell processes (mainly astrocytic) are also implicated in the regulation, maintenance, and repair of these barriers. As noted previously, the barrier does not exist in the CVOs of the brain, and it is also lacking in autonomic ganglia. In mice, the BBB becomes functional on embryonic day (E) 16 (where E0 is the day of conception).

Spinal Cord
GROSS ANATOMY

Anatomic Organization

The spinal cord in cross section is oval-shaped and consists of a central, butterfly-shaped zone of gray matter and an outer rim of white matter. Rodent and human spinal cords are anatomically comparable, although subtle differences exist among species.

The cervical, thoracic, and lumbosacral divisions of the spinal cord have characteristic appearances that differ somewhat in rodents compared to humans. The cervical spinal cord is of larger caliber because it contains fiber tracts for both the forelimb and the hind limb. The cervical (brachial) enlargement or intumescence extends from spinal cord segments C_5 to T_1. The lumbosacral enlargement extends from spinal cord segment L_2 to segment L_6 in rodents (vertebral body T_{12} through L_1) and from segment L_2 to segment S_3 in humans. Rodents and humans also have different numbers of vertebrae in their spinal columns. Rodents have 7 cervical, 13 thoracic, 6 lumbar, 4 sacral, and 27–30 caudal (tail) vertebrae; humans have 7 cervical, 12 thoracic, 5 lumbar, 5 sacral, and 4 caudal (coccyx) vertebrae. The number of lumbar vertebrae may vary by mouse strain. The ventral surface of the cord has a longitudinal groove, the ventral median fissure. The posterior (dorsal) surface of the human spinal cord has a sulcus (posterior median sulcus) that is not well-defined in rodents.

The spinal cord gray matter for both rodents and humans is organized in somatotopic fashion for each spinal cord segment. The butterfly-shaped gray matter of the spinal cord can be divided into the dorsal (posterior) horns and the ventral (anterior) horns. Neurons in the dorsal horn receive incoming (afferent) sensory signals, whereas those of the ventral horn distribute outgoing (efferent) motor impulses to various effector organs. The spinal cord white matter contains multiple, bilaterally symmetrical fiber tracts segregated among the dorsal, lateral, and ventral funiculi (columns). For each spinal cord segment, most of the white matter tracts are organized in somatotopic fashion for both rodents and humans. The courses of tracts in the dorsal funiculus do not overlap. In the other

funiculi, however, tracts blend together so that their locations can only be approximated. Distinct white matter tracts often carry functionally similar information that differs only in the location of the body regions that they innervate or the amount of detail that they transmit.

The vascular supply of the spinal cord includes the ventral artery (anterior spinal artery in humans), a single continuous channel that extends from the cervical segments to the filum terminale, and the bilateral dorsal spinal arteries (posterior spinal arteries in humans) located just ventral to the dorsal roots. The dorsal spinal arteries are mostly continuous channels, but often the single vessels are split into two or more parallel elements.

Functional Specialization of the Spinal Cord

The descending spinal cord tracts transmit motor signals to the peripheral effector organs, especially voluntary muscles. The corticospinal tract is the best known fiber tract. In humans, this huge bundle has undergone an evolutionary expansion that parallels the enhancement of dexterity of the distal musculature and the development of "skilled" motor capacities; it is located in the lateral column. Unlike humans, the corticospinal tract in rodents is much smaller and located in the dorsal column. Therefore, the corticospinal tract plays an important role in motor control in humans, but it does not play a major role in locomotion or manipulation in rodents. In contrast, rodents depend on descending signals within the rubrospinal tract, the second most prominent descending tract, for locomotion and posture. The rubrospinal tract originates in the red nucleus in the rostral midbrain. In animals with a prominent lateral corticospinal tract, the rubrospinal tract runs just ventral to the lateral corticospinal pathway. The rubrospinal tract is small in humans because motor functions are mainly managed by the lateral corticospinal tract.

The ascending spinal cord tracts transmit sensory information from the peripheral organs to the brain. Sensory modalities carried from the body surface include pain, position, temperature, and touch, while those carried from internal viscera are limited to pain and pressure. Ascending tracts contain myelinated axons from dorsal root ganglia and axons of spinal neurons. In animals with prominent tails (including rodents), an additional dorsal column nucleus on the midline, the nucleus of Bishoff, contains afferent projections from the tail.

HISTOLOGY

The spinal cord is composed of a central zone of gray matter ensheathed in white matter. The boundaries between the two zones are distinct in routine sections (Fig. 20.27A), but the margins are more easily delineated in sections stained to distinguish white matter (Fig. 20.27B). The neurons in the dorsal horn, which receive afferent (incoming) sensory signals, are chiefly smaller neurons. The neurons in the ventral horns, which supply efferent (outgoing) motor impulses to various effector organs, are large pyramidal neurons. An intermediolateral (lateral) column is located at the boundary of the dorsal and ventral horns in the thoracic and upper lumbar spinal cord; this region contains the preganglionic neurons of the sympathetic nervous system, and it is more pronounced in the human spinal cord. The limits of sympathetic outflow are segments T_1 to L_2 in mice and T_1 to L_3 in rats and humans. The lateral margin of the intermediate zone in the sacral spinal cord is the location of an inconspicuous cell column that contains the preganglionic neurons of the parasympathetic nervous system. The limits of parasympathetic outflow are L_6 to S_1 in rodents, and S_2 to S_4 in humans. Recent research suggests that these sacral autonomic neurons actually serve a sympathetic function.

Spinal cord white matter increases in quantity more rapidly than does the amount of gray matter (when assessed in cross section) as

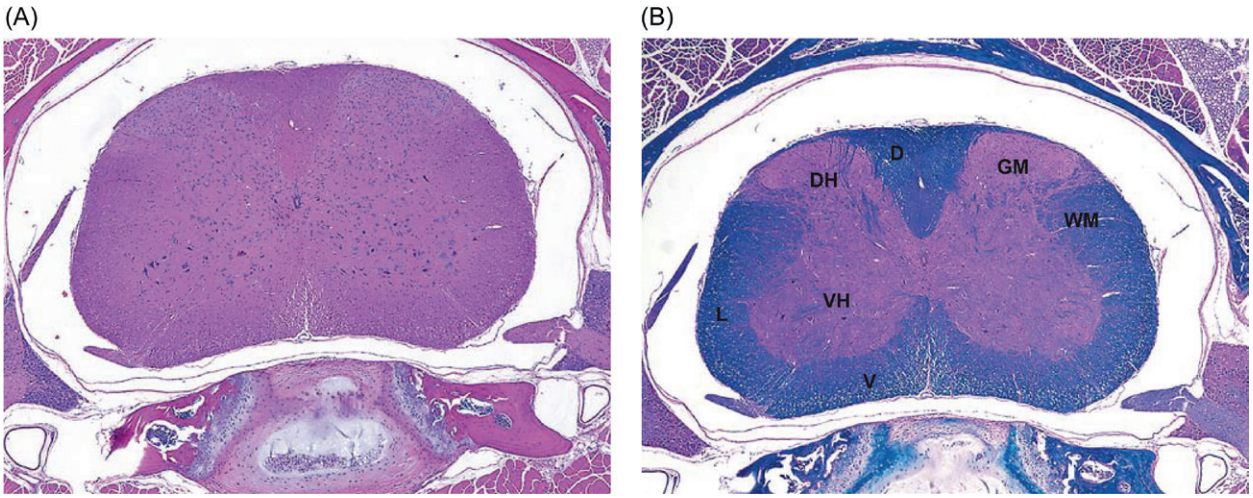

FIGURE 20.27 Rodent (mouse) cervical spinal cord. Stained with H&E only (A) and with H&E and LFB (B). The boundary between gray matter (GM) and white matter (WM) is much better defined by LFB, which stains myelin. Dorsal (D), lateral (L), and ventral (V) funiculi of the white matter and dorsal (DH) and ventral (VH) horns of the gray matter are shown.

Need-to-know

- Quadrupeds may retain "spinal walking" reflex capacity even after spinal cord transaction.

animals increase in size (Figs. 20.28 and 20.29). This finding reflects the greater number of axons needed to innervate a larger body area. This pattern is more pronounced in the dorsal funiculus, the main conduit for transmission of most tactile and proprioceptive impulses, particularly in humans (Fig. 20.29) relative to rodents (Fig. 20.28). In addition, the dorsal funiculus as a percentage of total white matter content is much larger in humans (almost double that of rodents) as a result of higher refinement of fine sensation and advanced evolution of motor skills in the distal limbs.

The caudal end of the spinal cord narrows and terminates in the conus medullaris. The continuation of the conus is the filum terminale (terminal fiber), which is made up of longitudinal collagen bundles, elastic fibers, and an ependymal remnant. The cauda equina, so named because it resembles a horse's tail, is composed of spinal nerves that originate above the conus but extend caudally beyond it within the spinal column prior to exiting (Fig. 20.30). The dorsal root ganglia, which contain cell bodies of sensory spinal nerves, are not uncommonly seen in spinal cord cross sections (Fig. 20.30). The caudal vertebrae continue distally in rodents for approximately 22–26 more segments than in humans, depending on the length of the tail. The nervous system in the tail consists of two large nerves that run dorsolaterally within the tail.

Nerves and Ganglia

Regional Anatomy

Nerves carry information either from the CNS to peripheral effector organs, or from peripheral sensory organs to the CNS; ganglia are nerve-associated collections of cell bodies. The PNS may be divided and subdivided based on functional, and in some cases anatomic, features and includes the somatic (sensorimotor) nervous system and most of the autonomic nervous system (ANS). Anatomic components of these PNS divisions include the dorsal and ventral spinal nerve roots; the spinal, dorsal root, and other sensory ganglia; sensory and motor nerves and their terminals; and cranial nerves III–XII. In general, the somatic

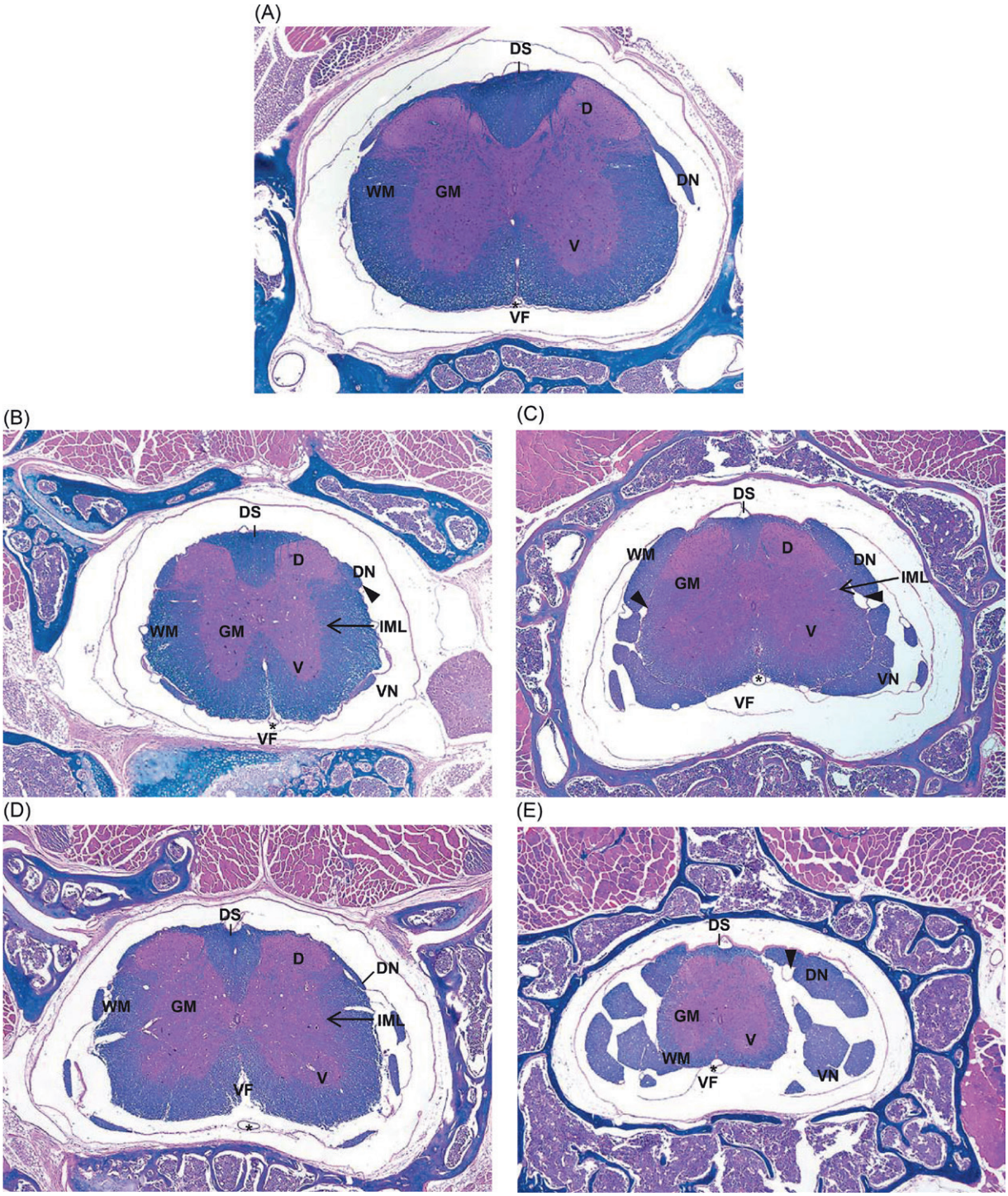

FIGURE 20.28 Rodent (mouse) spinal cord. Regional variation in spinal cord appearance in mice is illustrated in these cross sections taken from (A) cervical enlargement, (B) cranial thoracic cord, (C) caudal thoracic cord, (D) lumbar enlargement, and (E) sacral cord near the cauda equina; H&E with LFB counterstain. The cervical enlargement has an oval profile with large white matter (WM) funiculi and prominent, broad ventral gray horns (V) that contain the motor neurons that innervate the thoracic limbs. Sections at the cranial aspect of thoracic cord (B) have a more rounded, narrow appearance that broadens again at the caudal thoracic level (C) as the lumbar enlargement is approached. (D) Lumbar cord has broad, prominent ventral gray horns that harbor the motor neurons that control the hind limbs. (E) Sacral–caudal cord consists of a small quadrilateral contour, with a narrow mantle of white matter surrounding a relatively large core of gray matter (GM), flanked by multiple nerve roots. The lateral horns, which are formed by the intermediolateral cell columns (IML), are visually less prominent in mice compared with humans. *D*, dorsal horn; *DN*, dorsal (sensory) spinal nerve roots; *DS*, dorsal median sulcus; *VF*, ventral median fissure; *VN*, ventral (motor) spinal nerve roots; *asterisks*, ventral spinal artery; *arrowheads*, dorsal spinal artery.

Need-to-know

- Rodents have 7 cervical, 13 thoracic, 6 lumbar, 4 sacral, and 27–30 caudal segments of spinal cord.
- Humans have 7 cervical, 12 thoracic, 5 lumbar, 5 sacral, and 4 caudal segments.

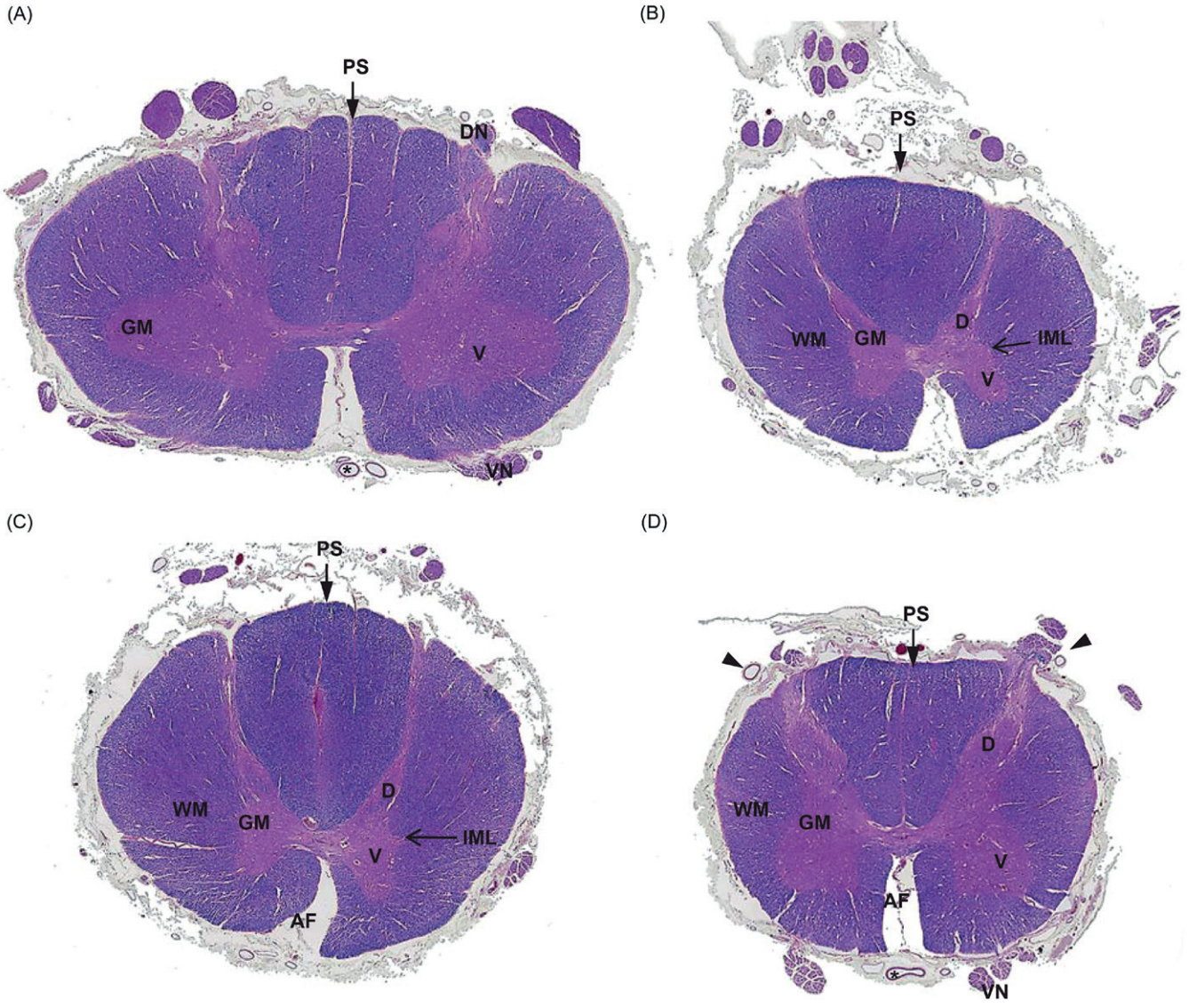

FIGURE 20.29 Human spinal cord. Regional variation in spinal cord appearance in human is illustrated in these cross sections taken from (A) cervical enlargement, (B and C) thoracic cord, and (D) lumbar cord (H&E with LFB counterstain). White matter (WM) appears purple, and gray matter (GM) appears pink. Comparing these images to the mouse sections in Fig. 20.28, it is easy to appreciate the different shapes of the gray matter between mice and humans at the same spinal cord levels. (A) The cervical enlargement has an oval shape with large white matter funiculi and prominent, broad anterior (ventral; V) gray horns that contain the motor neurons that innervate the upper extremities. Thoracic sections have a more rounded appearance and small peglike anterior gray horns (B); they also have pronounced lateral horns formed by the intermediolateral cell columns (IML), which house neurons of the sympathetic nervous system (C). The white matter appears large in relation to the amount of gray matter in the thoracic region relative to the lower amounts of white matter in the cervical and lumbar levels. (D) Lumbar cord has broad prominent anterior gray horns (V) that hold neurons controlling the motor supply to the lower extremities. *AF*, anterior median fissure; *D*, posterior (dorsal) horn; *DN*, posterior (dorsal; sensory) spinal nerve roots; *PS*, posterior median sulcus; *VN*, anterior (ventral; motor) spinal nerve roots; *asterisks*, anterior spinal artery; *arrowheads*, posterior spinal artery.

Need-to-know

- Spinal cord white matter relative to gray matter (when assessed in cross section) is increased in humans compared to rodents as a result of the greater number of axons needed to innervate a larger body area.

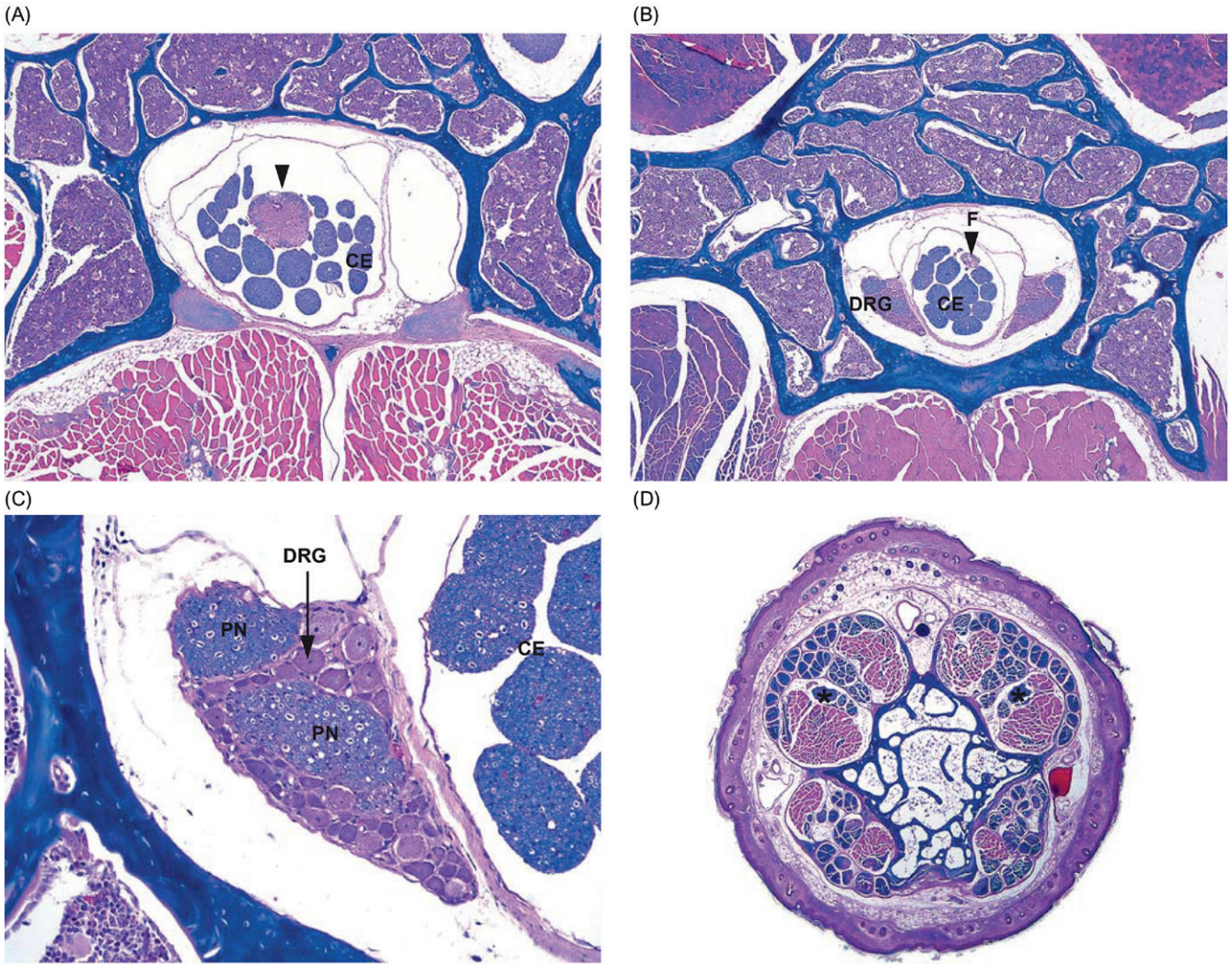

FIGURE 20.30 Rodent (mouse) spinal cord. Regional variation in spinal cord appearance in mice is illustrated in these cross sections taken from the conus medullaris, cauda equina, and tail. (A) The conus medullaris (medullary cone (arrowhead)) is the terminal end of the spinal cord. It is surrounded by the spinal nerve roots that form the cauda equina ("horse's tail"). (B) The filum terminale ("terminal fiber" (F)) is the strand of longitudinally arranged collagen bundles and elastic fibers proceeding caudally from the apex of the conus medullaris. (C) The dorsal root ganglion (DRG) contains neuronal cell bodies that supply axons in sensory spinal nerves and peripheral nerves (PN, blue zones within the DRG). (D) Cross section of tail showing positions of large peripheral nerves (asterisks). H&E with LFB counterstain.

division relays information from the external environment to the brain and controls voluntary motor functions, whereas the autonomic branch transmits signals from the internal environment and regulates involuntary motor activities and the endocrine system. The distribution and function of the PNS and ANS are similar between rodents and humans.

The ANS consists of cranial nerves in the head region; a pair of neural trunks and related ganglia located ventral (anterior) to the vertebral column in the caudal cervical, thoracic, and lumbar regions; sacral nerves; and a complex web of ganglia and nerve plexi located near and within viscera. Anatomically, the ANS consists of two divisions. The sympathetic system resides in the thoracolumbar division, whereas the parasympathetic system is the craniosacral division (although new data suggests the sacral division also may be sympathetic in function).

The main functional elements of any nerve are its axons, the long processes that relay the output

from neurons in the CNS [brain cortices or nuclei, or the ventral (anterior) horns of the spinal cord] or PNS (dorsal root or autonomic ganglia). The conduction velocity of each nerve is dictated by the degree of axonal insulation, which is provided by myelin derived from Schwann cells. In general, axons of the somatic sensory and motor domains are of larger caliber, have thicker myelin sheaths, and possess higher conduction velocities than do autonomic nerve fibers.

Spinal nerves are functionally mixed and carry both sensory and motor fibers. The spinal nerves arise from the spinal cord at each segment by way of two roots, each formed of multiple rootlets. For each spinal cord segment, rodents have approximately 15 dorsal and 15 ventral rootlets, whereas humans have half as many dorsal and ventral rootlets. The dorsal (posterior) or sensory root bears a *dorsal root ganglion* (DRG) containing the cell bodies of the sensory neurons. The ventral (anterior) or motor root consists of axons from the lower motor neurons in the ventral horn of the spinal cord. Relative to the dorsal roots, the ventral roots typically have fewer fibers of larger caliber because the thick axons originate from the lower motor neurons in the ventral horns of the spinal cord. The dorsal and ventral roots unite just distal to the sensory DRG to form a spinal nerve. After leaving the vertebral column via an intervertebral foramen, the spinal nerves divide into a dorsal branch, which feeds the epaxial (back) musculature and adjacent skin; a ventral branch serving the hypaxial (body wall) musculature and adjacent skin (including the limbs); and a communicating ramus, which connects to the sympathetic trunk of the ANS.

Cranial nerves are similar to spinal nerves. However, unlike spinal nerves, cranial nerves are not spaced at equal distances along the neuraxis, and they have no separation of their sensory (dorsal) and motor (ventral) roots. In fact, in mixed cranial nerves, sensory and motor fibers emerge from the brain surface using the same root. Unlike spinal nerves, only a few cranial nerves have sensory ganglia: V, VII, VIII, IX, and X. In addition, some cranial nerves carry only sensory fibers: I, II, and VIII. Cranial nerves that serve almost entirely as motor tracts are III, IV, VI, XI, and XII. The optic nerve (II) is not a true nerve but is actually an extension of a brain tract; in fact, II is myelinated by oligodendrocytes rather than Schwann cells. Therefore, cranial nerves I and II are extensions of the CNS.

Autonomic nerves carry signals controlling involuntary automated functions. The visceral sensory fibers, like the somatic sensory fibers, have neurons of origin located in spinal ganglia. However, the visceral motor fibers are unusual in that a chain of two neurons is involved. The first neuron in the brain (midbrain or brain stem) or spinal cord (intermediolateral zone of the thoracic domain) sends a long preganglionic fiber to a ganglion located near the organ to be innervated. From this site, a second postganglionic fiber proceeds to either the smooth muscle or glands, where they synapse on a second smaller ganglion within the organ being innervated.

HISTOLOGY

Ganglia contain large neurons surrounded by variable numbers of specialized glia known as satellite cells (Fig. 20.31). These cells appear to serve many of the same functions that astrocytes serve in the CNS.

Nerves are organized as bundles of myelinated and nonmyelinated axons. The difference between these fiber types is in myelin thickness: myelinated fibers are encircled by many layers, whereas nonmyelinated fibers are encircled by one or a few layers (Fig. 20.32). The myelin in nerves is made by Schwann cells, which are characterized by elongate, wavy nuclei interspersed within the axon bundles. Each Schwann cell forms the myelin for a single axon. Damaged PNS myelin may be repaired over time by Schwann cell proliferation. Standard immunohistochemical markers for Schwann cells are CNPase, MBP, peripheral myelin protein 22, and S100β.

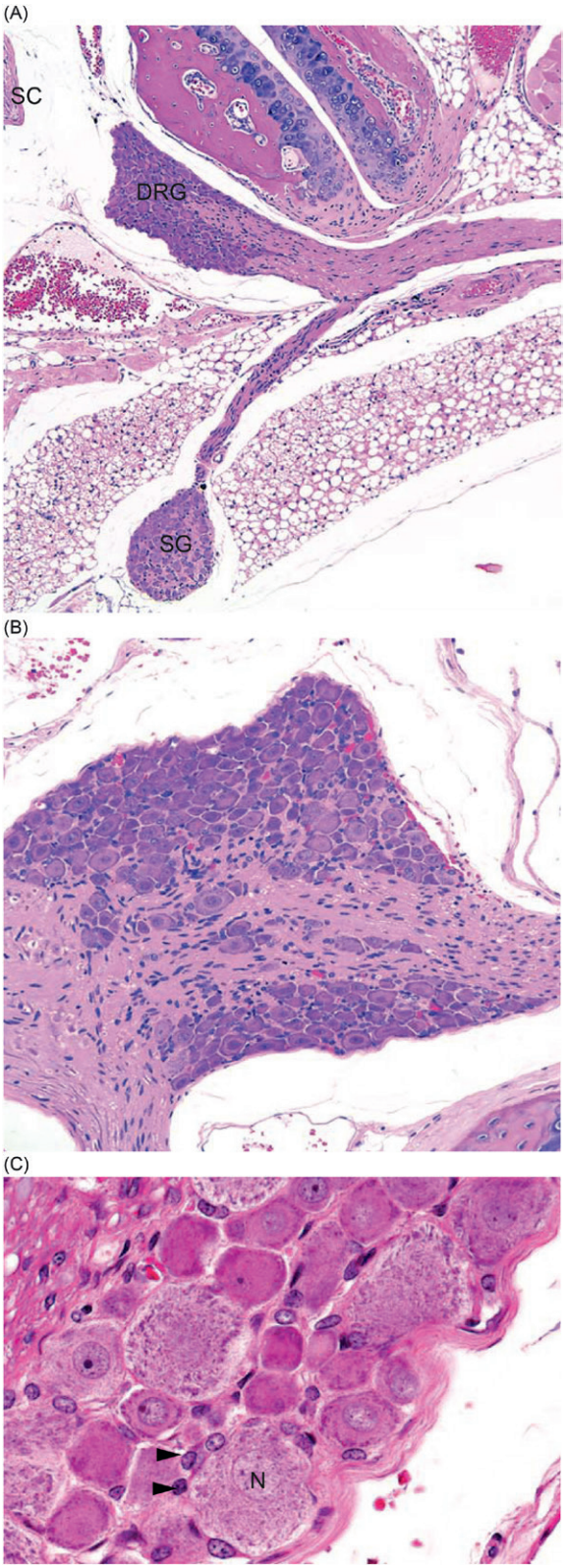

FIGURE 20.31 Rodent DRG. (A) Lower magnification image in a mouse showing the DRG and sympathetic chain ganglion (SG). The spinal cord is indicated (SC). (B) High magnification image of the DRG in a mouse. (C) High magnification image of a DRG in a rat, with neurons (N) and surrounding satellite cells (arrowheads).

Axons within the PNS are surrounded by connective tissue: the endoneurium between individual axons, the perineurium binding large bundles of axons into fascicles, and the epineurium that surrounds the whole nerve. The perineurium originates from fibroblasts, rather than Schwann cells. These connective tissue components are clearly discernible in cross section (Figs. 20.32 and 20.33). Human nerves have more abundant connective tissue than rodent nerves. Other PNS cell types commonly include mast cells (the granules of which are especially prominent on toluidine blue-stained sections) and endothelial cells lining capillaries within the nerve core.

Other Considerations

Conventions for Neuroanatomic Terminology

Correct terminology is essential in naming neuroanatomic structures. This is particularly important in the CNS because it is based on body posture as mentioned above. As noted at the beginning of the chapter, because the orientation of the CNS in space differs between rodents, as well as the angle present in humans but not rodents, the dorsal and ventral surfaces of the horizontal mouse or rat brain are comparable to the superior and inferior poles, respectively, of a vertical human brain. However, in some cases, the same names apply to equivalent structures in rodent and human, such as rostral and caudal for the front and back poles of the brain. The use of eponyms (i.e., the name of the individual who first described a feature) as an official name has been discouraged in favor of the formal designations, as set forth in the *Nomina Anatomica Medica* and *Nomina Anatomica Veterinaria*, as this consensus nomenclature can be compared more easily across species.

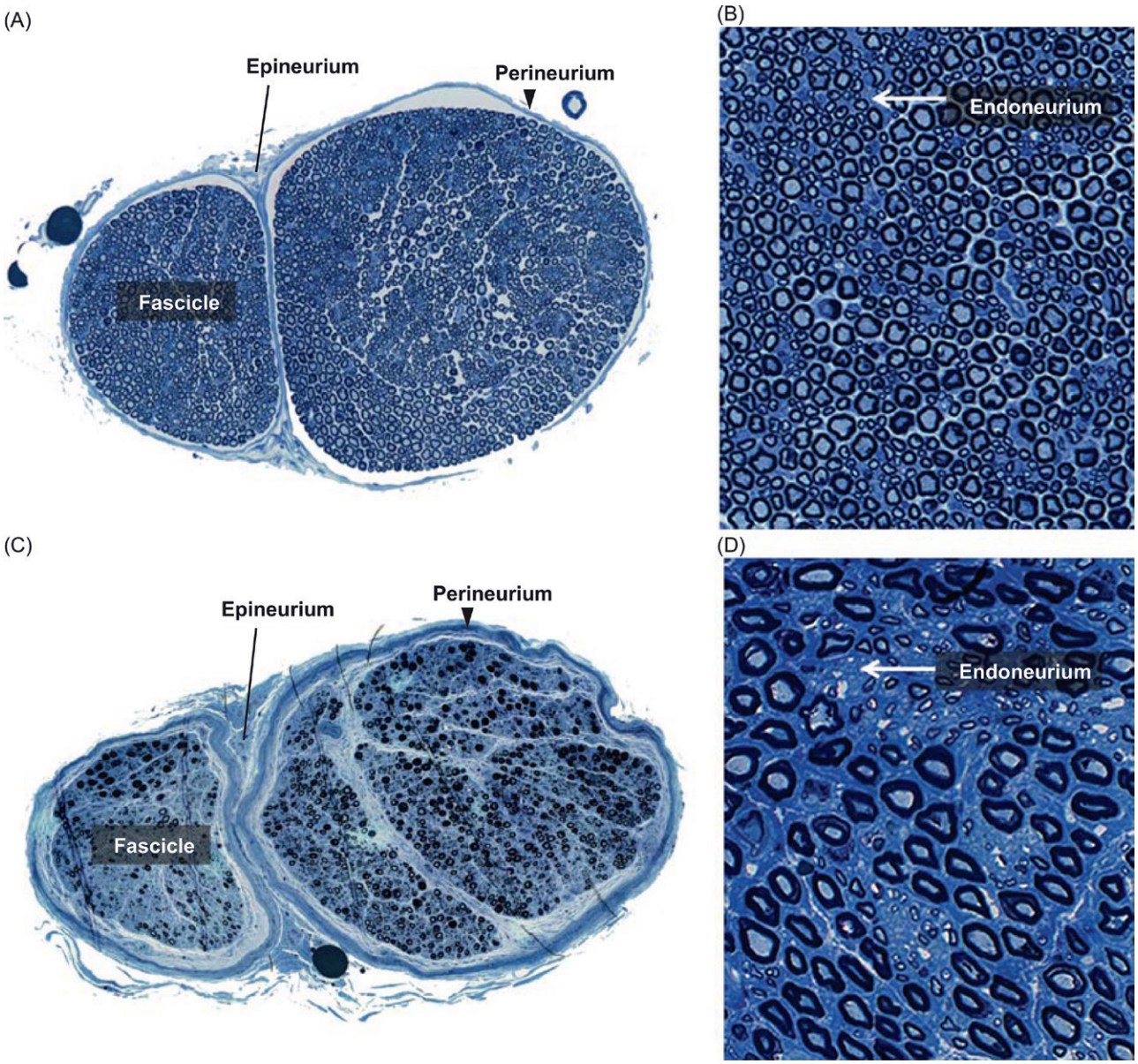

FIGURE 20.32 Peripheral nerve trunks. Rodent (mouse) (A and B) and human (C and D). The subgross images (mouse, A; human, C) are shown at different magnifications to facilitate the anatomical comparison, whereas the microscopic images (mouse, B; human, D) are rendered at the same magnification to demonstrate the size differences among axons of these species. Axons (nerve "fibers") are evident as pale blue, elliptical structures surrounded by variable amounts of myelin (dark blue). Myelinated axons have larger diameters and thicker myelin sheaths, whereas unmyelinated axons are of much smaller caliber and have very thin myelin sheaths. Axons are bundled into fascicles, and fascicles into nerve trunks, with connective tissue between axons (endoneurium), around fascicles (perineurium), and around the entire nerve (epineurium). Human nerves have larger fibers, thicker myelin, and more abundant connective tissue than their rodent counterparts. Toluidine blue stain.

SPECIAL METHODS IN NEUROHISTOLOGIC PREPARATION

Proper sampling, processing, and sectioning are critical for effective and efficient microscopic assessment of neural tissues.

For the best morphologic preservation, the CNS and PNS should be fixed by intravascular perfusion rather than immersion. While immersion fixation of the brain often is adequate for routine screening and superficial analyses, common artifacts of immersion fixation include perivascular retraction spaces and cleft formation in white matter and

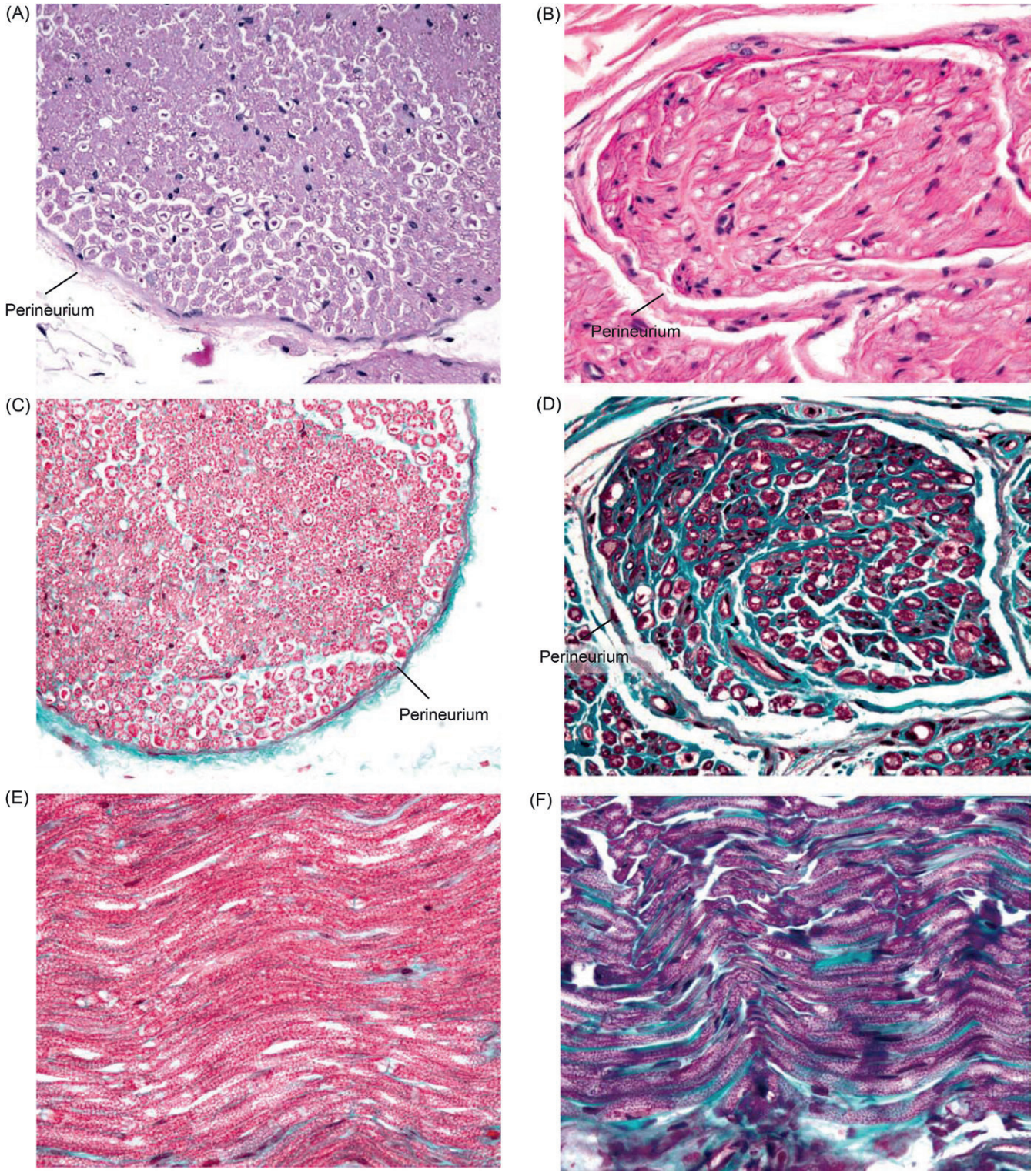

FIGURE 20.33 Peripheral nerve. Rodent (mouse) (A, C, and E) and human (B, D, and F) showing the typical appearance of paraffin-embedded tissue stained with H&E (mouse, A; human B) or Gomori trichrome (mouse, C and E; human, D and F). Gomori stains myelin purple, whereas trichrome provides a blue color to connective tissue (e.g., the perineurium surrounding nerve fascicles), giving myelinated axons in cross section a "peppermint candy" appearance.

Need-to-know

- Peripheral nerves of humans have more abundant connective tissue than do rodent peripheral nerves.

contracted basophilic "dark neurons" (Fig. 20.18). The latter change, which may be misinterpreted as evidence of neuronal degeneration by inexperienced morphologists, frequently occurs in large-sized neurons in the deep layers of the cerebral cortex (especially in rodents), the pyramidal layer of the hippocampus, and Purkinje cells of the cerebellum. Intravascular perfusion provides the most rapid entry of the fixative into the dense neural tissues, although improper perfusion may also result in artifacts such as enlarged perivascular spaces in the event of elevated perfusion pressures. For specific details on the appropriate sampling, preparation, and processing of CNS and PNS specimens, see Further Reading.

Numerous histological stains are available for evaluating CNS and PNS tissues. H&E permits a global assessment of basic architecture; cresyl violet (CV) is a Nissl stain for evaluating neuronal cell body numbers and features (Fig. 20.8); Luxol fast blue (LFB) and Marchi's stains bind myelin and thus white matter (Fig. 20.7); Bielschowsky's or Bodian's silver stains emphasize axons; and Fluoro Jade dyes reveal degenerating neurons. Cell type-specific markers (as discussed above) may be used to demonstrate subcellular structures or neurochemicals in specific cell populations. In general, the initial analysis for possible neural lesions should be done with simple, inexpensive, conventional methods such as H&E, CV, and/or LFB.

For optimal PNS examination, several other special techniques may be necessary. Nerve sections often are stained with toluidine blue (Fig. 20.32), which provides good contrast between the axoplasm (axonal cytoplasm) and the myelin sheath. Postfixation in osmium tetroxide (OsO_4) is used to more fully preserve the fine architecture of lipid-rich myelin; the very dark color associated with OsO_4 treatment limits evaluation of osmicated nerves to cross sections (i.e., where adjacent nerve fibers do not overlap with one another). The use of plastic as an embedding medium for nerves permits acquisition of thinner sections (approximately 2 µm for soft plastic and 1 µm or less for hard plastic) relative to those that can be obtained with paraffin (4–8 µm), which improves the resolution of subcellular structures.

ACKNOWLEDGMENTS

We thank the following individuals for providing illustrations: Sara Samuelson, S. S. Illustrations (sarasamuelson.com); Dr. Robert Garman, University of Pittsburgh; Dr. Noor Kabani, McGill University; and Dr. Robert Switzer III of Neuroscience Associates. We also thank Kerrie Allen, Brian Johnson, Meilany Wijaya, Mike Hobbs, Randy Small, Christiane Ullness, Susan Rozelle, Kim Howard, and Chiyen Miller for expert technical assistance. Finally, we thank Dr. Denny Liggitt, Dr. Piper Treuting, and Dr. Thomas Montine for encouragement.

FURTHER READING AND RELEVANT WEBSITES

Adams JH, Duchen LW: *Greenfield's neuropathology*, ed 5, Oxford, 1992, Oxford University Press.

Allen Institute for Brain Science: http://www.brain-map.org.

Atlas of Laboratory Mouse Histology: http://ctrgenpath.net/static/atlas/mousehistology.

Bolon B, Butt M, editors: *Fundamental neuropathology for pathologists and toxicologists: principles and techniques*, New York, 2011, Wiley.

Bolon B, Garman R, Jensen K, et al: A "best practices" approach to neuropathologic assessment in developmental neurotoxicity testing—for today. *Toxicol Pathol* 34:296–313, 2006.

Bolon B, Butt MT, Garman RH, et al: Nervous system. In Haschek WM, Rousseaux CG, Wallig MA, editors: *Haschek and Rousseaux's handbook of toxicologic pathology* (ed 3), San Diego, CA, 2013, Academic Press (Elsevier), pp 2005–2093.

Bolon B, Garman RH, Pardo ID, et al: STP position paper: recommended practices for sampling and processing the nervous system (brain, spinal cord, nerve, and eye) during nonclinical general toxicity studies. *Toxicol Pathol* 41:1028–1048, 2013.

Butler AB, Hoods W: *Comparative vertebrate neuroanatomy: evolution and adaptation*, ed 2, Hoboken, NJ, 2005, John Wiley & Sons.

Cooper JR, Bloom FE: *The biochemical basis of neuropharmacology*, ed 8, New York, 2003, Oxford University Press.

de LaHunta A, Glass E: *Veterinary neuroanatomy and clinical neurology*, ed 4, Philadelphia, PA, 2014, Saunders.

Dorr A, Sled JG, Kabani N: Three-dimensional cerebral vasculature of the CBA mouse brain: a magnetic resonance imaging and micro computed tomography study. *Neuroimage* 35(4):1409–1423, 2007.

Duvernoy HM, Risold PY: The circumventricular organs: an atlas of comparative anatomy and vascularization. *Brain Res Rev* 56(1):119–147, 2007.

e-Mouse Atlas Project: http://www.emouseatlas.org/emap/ema/home.html.

Espinosa-Medina I, Saha O, Boismoreau F, et al: The sacral autonomic outflow is sympathetic. *Science* 354(6314): 893–897, 2016.

Fix AS, Garman RH: Practical aspects of neuropathology: a technical guide for working with the nervous system. *Toxicol Pathol* 28:122–131, 2000.

Fliegauf M, Benzing T, Omran H: When cilia go bad: cilia defects and ciliopathies. *Nat Rev Mol Cell Biol* 8(11):880–893, 2007.

Franklin KBJ, Paxinos G: *The mouse brain in stereotaxic coordinates*, ed 3, San Diego, CA, 2007, Academic Press.

Garman RH: Artifacts in routinely immersion fixed nervous tissue. *Toxicol Pathol* 18:149–153, 1990.

Garman RH: Histology of the central nervous system. *Toxicol Pathol* 39(1):22–35, 2011.

Hof PR, Young PR, Bloom FE, et al: *Comparative cytoarchitectonic atlas of the C57BL/6 and 129/Sv mouse brains*, New York, 2000, Elsevier.

Jacobowitz D, Abbott L: *Chemoarchitectonic atlas of the developing mouse brain*, Boca Raton, FL, 1998, CRC Press.

Jordan WH, Hall DG, Hyten MJ, et al: Practical neuropathology of the rat and other species. In Bolon B, Butt M, editors: *Fundamental neuropathology for pathologists and toxicologists: principles and techniques*, New York, 2011, Wiley.

Jortner BS: Preparation and analysis of the peripheral nervous system. *Toxicol Pathol* 39(1):66–72, 2011.

Junqueira LC, Carneiro J: *Basic histology*, ed 4, Los Altos, CA, 1983, Lange.

Kandel ER, Schwartz JH: *Principles of neural science*, ed 5, New York, 2012, McGraw-Hill.

Kaufman M: *Atlas of mouse development*, San Diego, CA, 1992, Academic Press.

Love S, Louis DN, Ellison DW: *Greenfield's neuropathology*, ed 8, London, 2008, Hodder Arnold.

Ma Y, Smith D, Hof PR, et al: *In vivo* 3D digital atlas database of the adult C57BL/6J mouse brain by magnetic resonance microscopy. *Front Neuroanat* 2:1, 2008.

Mai JK, Paxinos G: The human nervous system, San Diego, 2012, CA, Academic Press (Elsevier).

Maronpot RR, Pathology of the mouse: reference and atlas, 1999, Cache River Press; Vienna, IL

Michigan State University Brain Biodiversity Bank: *Brain biodiversity bank atlases*. https://www.msu.edu/user/brains/brains/index.html.

National High Magnetic Field Laboratory (NHMFL). *MRM NeAt (neurological atlas) mouse brain database*: http://brainatlas.mbi.ufl.edu.

Nestor SL: Techniques in neuropathology. In Bancroft JD, Gamble M, editors: *Theory and practice of histological techniques* (ed 6), New York, 2008, Elsevier.

Neurogenetics at UT Health Science Center: http://www.nervenet.org, including *The Mouse Brain Library* (http://www.mbl.org) and *Mouse Brain Atlases* (http://www.mbl.org/atlas/atlas.php).

Pardo ID, Garman RH, Weber K, et al: Technical guide for nervous system sampling of the cynomolgus monkey for general toxicity studies. *Toxicol Pathol* 40(4):624–636, 2012.

Paxinos G: *The rat nervous system*, San Diego, 2004, Academic Press.

Paxinos G and Watson C, The rat brain in stereotaxic coordinates, ed 7, 2014, Academic Press (Elsevier); San Diego, CA.

Peters A, Palay SL, Webster HD: *The fine structure of the nervous system: neurons and their supporting cells*, ed 3, New York, 1991, Oxford University Press.

Pronichev IV, Lenkov DN: Functional mapping of the motor cortex of the white mouse by a microstimulation method. *Neurosci Behav Physiol* 28(1):80–85, 1998.

Saver JL: Time is brain—quantified. *Stroke* 37:263–266, 2006.

Sidman RL, Kosaras B, Misra B, et al.: *High resolution mouse brain atlas: 2d atlas*: http://www.hms.harvard.edu/research/brain/atlas.html. *3D Visualization*: http://www.hms.harvard.edu/research/brain/3D_atlas_vDemo.html.

Siegel GJ, Agranoff BW, Albers RW, et al: *Basic neurochemistry: molecular, cellular, and medical aspects*, ed 5, New York, 1994, Raven Press.

Summers BA, Cummings JF, de Lahunta A: *Veterinary neuropathology*, St. Louis, MO, 1995, Mosby.

Suttie AW, Leininger JR, Bradley AE: *Boorman's pathology of the rat: reference and atlas*, ed 2, New York, 2017, Academic Press.

Toronto Centre for Phenogenomics, Mouse Imaging Centre: http://www.mouseimaging.ca/technologies/mouse_atlas/index.html.

Vanderhaeghen P, Lu Q, Prakash N, et al: A mapping label required for normal scale of body representation in the cortex. *Nat Neurosci* 3(4):358–365, 2000.

Ward JM, Mahler JF, Maronpot RR, et al: *Pathology of genetically engineered mice*, Ames, IA, 2000, Iowa State University Press.

Watson C, Paxinos G, Puelles L: *The mouse nervous system*, San Diego, 2012, CA, Academic Press (Elsevier).

Watson C, Paxinos G, Kayalioglu G: *The spinal cord: a Christopher and Dana Reeve foundation text and atlas*, New York, 2008, Academic Press.

Williams PL, Warwick R: *Gray's anatomy*, ed 36, Philadelphia, PA, 1980, Saunders.

SPECIAL SENSES: EYE 21

CAROLINE J. ZEISS
Yale University School of Medicine, New Haven, CT, United States

DANIEL C. TU
Oregon Health & Sciences University, Casey Eye Institute, Portland, OR, United States

ISABELLA PHAN
Kaiser Permanente, San Francisco, CA, United States

RACHEL WONG AND PIPER M. TREUTING
University of Washington School of Medicine, Seattle, WA, United States

Introduction

The mammalian eye is similar between rodents and humans, with most gross and histological differences due to relative sizing.

Fixation of the eye and the retina in particular can be challenging due to poor penetration of fixatives through the sclera. In addition, routine formalin fixation can impart numerous artifacts, including separation of the retinal pigment epithelium (RPE) from the outer segment of the retina. Davidson's fixative [ethyl alcohol (33%), 37–39% formalin (22%), glacial acetic acid (11.5%), and water (33%)] provides excellent preservation of the retina but is not commonly used by most investigators. Therefore, except where noted, the mouse tissues in this chapter were fixed with 10% neutral buffered formalin. Refer to the Further Reading section for additional methods regarding eye dissection and histological techniques.

The Eye

Gross Anatomy

The terms eye and eyeball are commonly used interchangeably and here are considered the portion contain within the orbit excluding the appendages (i.e., eyelids, optic nerve, muscles, glands). The orbit of all three species contains the optic globe, the optic nerve, extraocular muscles, and the intraorbital lacrimal gland, as well as blood, lymphatics, and nerves. The eyeball is protected by the conjunctiva and eyelid, and associated with retroobrital glands within loose fibroadipose connective tissue.

The rodent orbit is composed of eight bones: maxilla, lacrimal, zygomatic, frontal, temporal, sphenoid, ethmoid, and palatine. This differs from humans: the temporal bone serves as the caudal wall in rodents, whereas in humans the sphenoid is the principal bone of the caudal wall. The external

Comparative Anatomy and Histology. DOI: http://dx.doi.org/10.1016/B978-0-12-802900-8.00021-X
© 2018 Elsevier Inc. All rights reserved.

bony orbit is oval, with the space projecting in a roughly pyramidal manner to a depth of approximately 5 mm.

The average adult mouse eye is approximately 4 mm in diameter, the rat eye is approximately 6 mm, and the human eye measures 23.5–25 mm in diameter. In all three species, the eye has three layers. The outer layer consists anteriorly of the cornea and posteriorly of the sclera. The middle and inner layers are the uvea and retina, respectively. The space within these layers can be subdivided into three chambers: the anterior (between the iris and cornea; contains aqueous humor), posterior (bound anteriorly by the iris and posteriorly by the lens and anterior vitreous face; contains aqueous humor), and vitreous (between the posterior chamber and retina; contains vitreous humor) (Figs. 21.1 and 21.2).

The Harderian gland in rodents is located behind the eye deep within the orbit and is variably colored due to melanocytes and porphyrin pigment (Fig. 21.3). The Harderian duct opens at the base of the nictitating membrane (sometimes referred to as the "third eyelid"). Humans lack a Harderian gland and a nictitating membrane, but they do possess a fold of conjunctiva at the medial canthus.

Cornea and Sclera

GROSS ANATOMY

In all three species, the outer layer of the eye (sometimes referred to as the fibrous tunic) is composed of the cornea and sclera. The transition zone between the cornea and the sclera is known as the limbus. The cornea is a transparent tissue that contributes to the structural integrity and optical properties. The sclera is the tough opaque outer layer of the eye that provides it with protection and structural integrity. The sclera transitions anteriorly (at the limbus) into cornea and posteriorly into the optic nerve dural sheath (Fig. 21.4). There are a number of emissarial channels that pierce the sclera, serving as conduits for nerves and vasculature. Episcleral nerve loops may be visible in all three species as pigmented spots on the anterior sclera. The extraocular muscles insert into the sclera (Fig. 21.4B). In rodents, the posterior sclera is thickest and the anterior sclera is very thin, such that the underlying uvea may be visible. The sclera ranges from 0.3 to 1.0 mm thick in humans; the posterior pole is the thickest area, and the area behind the rectus muscle insertions is the thinnest (Table 21.1).

HISTOLOGY

The rodent and human cornea are made up of five layers (from anterior to posterior): epithelium, Bowman's layer, stroma, Descemet's membrane, and endothelium (Fig. 21.5). The epithelium is thickest centrally in all three species and composed of nonkeratinizing stratified squamous cells with up to 12 layers in rodents and up to 7 layers in humans. The corneal stem cells that repopulate the epithelial layer are found at the limbus, the transition zone between the cornea and sclera. The epithelium rests on a basement membrane. Posterior to the epithelial basement membrane is Bowman's layer. Bowman's layer is not a true basement membrane but is a condensation of stroma made up of acellular type I collagen. If Bowman's layer has been violated, it will not regenerate. In rodents, Bowman's layer is difficult to see by light microscopy but is readily seen by electron microscopy. In humans, Bowman's layer is easily visualized and is 8–14 µm thick; posterior to Bowman's layer is the corneal stroma, which makes up the bulk of the cornea. Stroma contains collagen fibrils, collagen-producing keratocytes, and glycosaminoglycans, predominantly keratan sulfate. The collagen fibers are arranged in a regular orientation and spacing that confers optical clarity.

Histologically, the corneal stroma often shows regular lamellar clefting, which is an artifact of

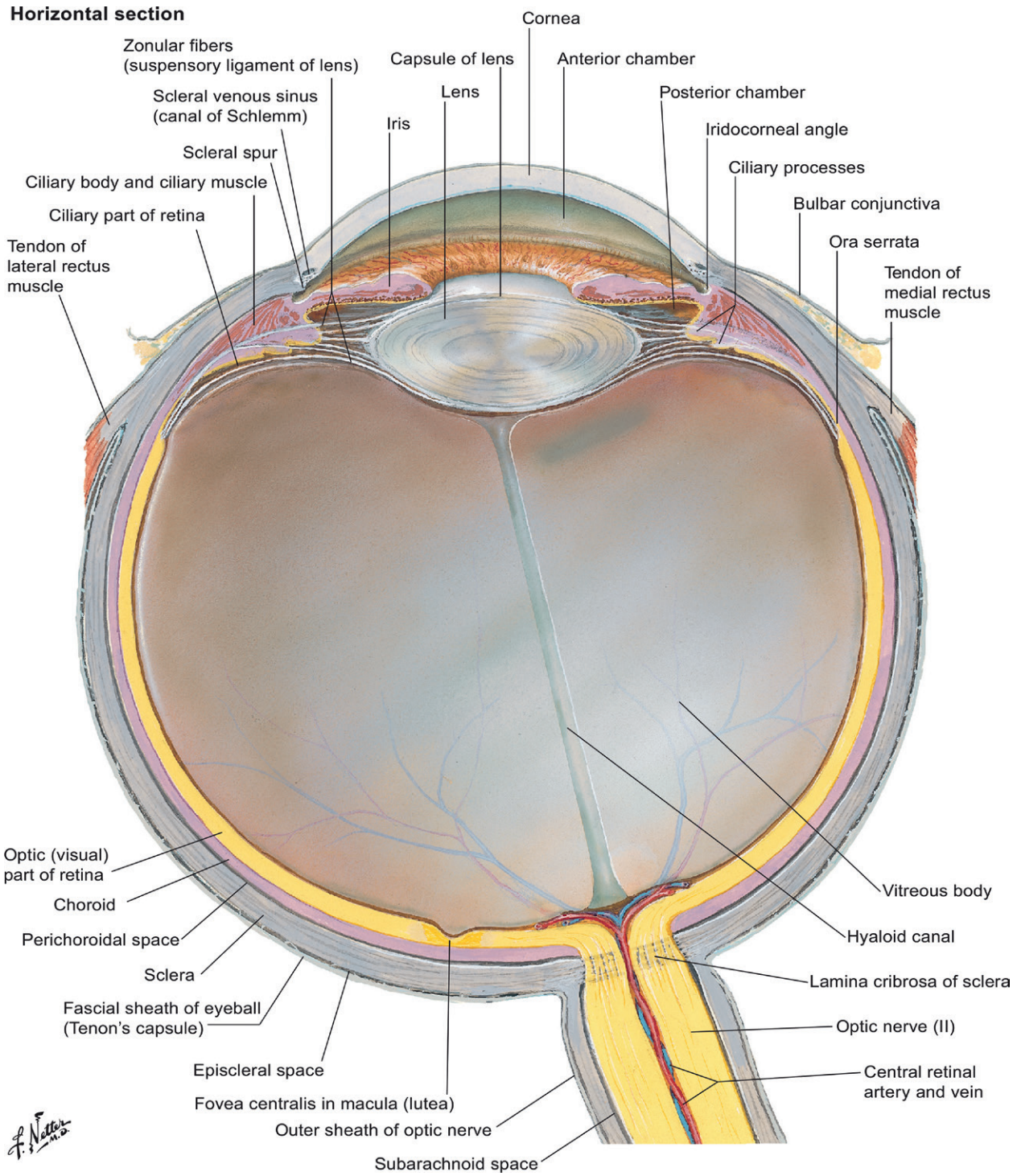

FIGURE 21.1 Horizontal section of human eyeball. The basic structure of the eye is similar between humans and rodents. The outer layer provides structural integrity and consists of the cornea anteriorly and the sclera posteriorly. The transition zone between cornea and sclera is termed the limbus. The eyeball consists of three main layers (from external to internal): cornea and sclera, uvea, and retina. The interior space within the eye is subdivided into three compartments: the anterior chamber, the posterior chamber, and the vitreous cavity. The anterior chamber and posterior chamber are filled with aqueous humor. The vitreous is filled with vitreous gel.

Need-to-know

- The rodent eye lacks a macular and a fovea centralis.
- The rat has a poorly developed lamina cribosa, whereas the mouse has none.

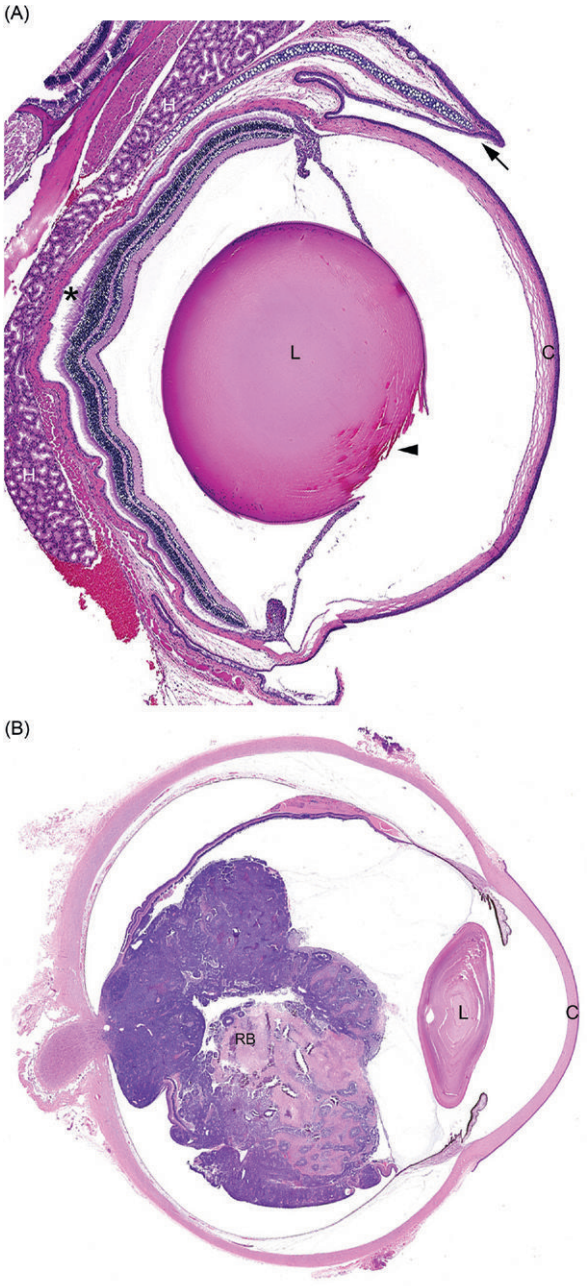

FIGURE 21.2 Eyeball. (A) Rodent (mouse). Eyeball *in situ*. In this coronal section of decalcified mouse head, the eye is maintained *in situ*. Note the large, round lens (L) that fills the majority of the vitreous chamber. The Harderian gland (H) is located deep in the posterior orbit. Artifactual shredding of the lens (arrowhead) and separation of the retina (asterisk) are common in this type of preparation. The nictitating membrane (arrow) is located on the dorsal aspect of the optic globe. The eyelids and optic nerve are not present in this section. Cornea (C) is indicated. (B) Juvenile human eyeball with retinoblastoma (RB), horizontal section. Note the flattened and relatively smaller lens (L) of the human. Cornea (C) is indicated.

Need-to-know

- The human eye has a relatively smaller lens.
- Formalin fixation imparts numerous artifacts to the eye, including retinal separation from the pigmented epithelium and lens fiber shredding.

processing. The posterior-most layers of the cornea are Descemet's membrane, followed by a thin flattened layer of corneal endothelium. Descemet's membrane is the basement membrane of the corneal endothelium. It contains type IV collagen and thereby stains positive with periodic acid–Schiff (PAS). Descemet's membrane is arranged in two layers: an anterior banded zone is laid down *in utero* and a posterior nonbanded zone is added throughout life. The termination of Descemet's membrane in the peripheral cornea is thickened (termed Schwalbe's line) in humans and in some mouse strains. The corneal endothelium is a monolayer of cells that actively transport water from the corneal stroma to the anterior chamber, thereby maintaining the cornea's optical clarity.

The rodent and human sclera both have three layers. The episclera is the outermost layer of fibrovascular tissue. Scleral stroma is the middle layer, composed primarily of densely packed type I collagen fibers with a random arrangement that accounts for the opaque white color. The lamina fusca is the thin innermost layer of collagen fibers connecting the scleral stroma to the uvea.

Uvea

Gross Anatomy

In all three species, the pigmented middle layer of the eye is the uvea, which consists of three components: the iris, ciliary body, and choroid. The iris is a ring of tissue with a central opening forming the pupil; it separates the anterior and posterior chambers. The outer edge of the iris, known as the iris root, inserts into the ciliary body. The ciliary body is a band of tissue located between the iris and sclera. In all three species, the ciliary body is divided into two parts: a folded anterior portion (pars plicata) and a flatter posterior (pars plana); these regions are evident histologically in rodents. The pars plana of the ciliary body is continuous with the choroid, the most posterior

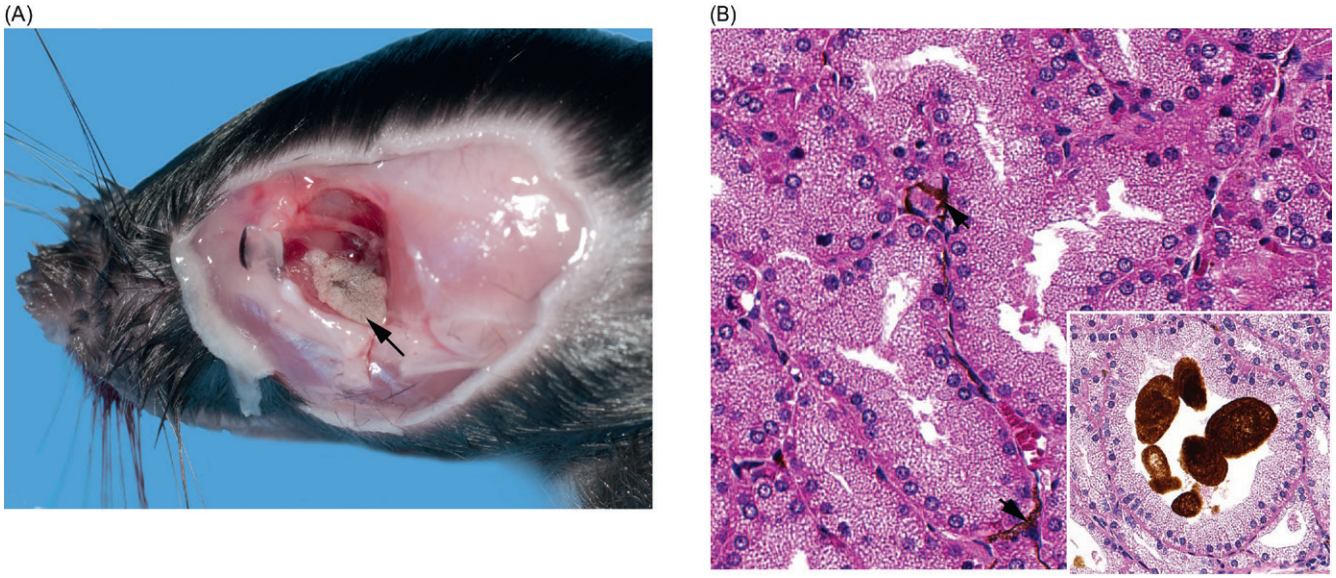

FIGURE 21.3 Rodent (mouse) Harderian gland. (A) Gross dissection of the rodent (mouse) orbit with the eye and extraocular muscles removed to expose the retrobulbar Harderian gland (arrow). This structure is unique to rodents, located behind the eye deep within the orbit with the ductal opening at the base of nictitating membrane. This large lobular gland has variable brown coloration due to melanocytes and porphyrin pigment. (B) Harderian gland, mouse. Histologically, the gland is a branched tubuloalveolar gland lacking distinct ducts. Acini are lined by a single layer of columnar epithelium. The cytoplasm has numerous droplets containing the secretory products, which are lipids and porphyrin. Porphyrin can accumulate within the acinar lumens as a dark-staining laminated material (inset). Note the mild melanosis (black arrows).

Need-to-know

- Humans do not have a Harderian gland.
- Trauma to the gland from retroorbital sinus phlebotomy can occur.
- Female rodents in certain strains have increased porphyrin production.

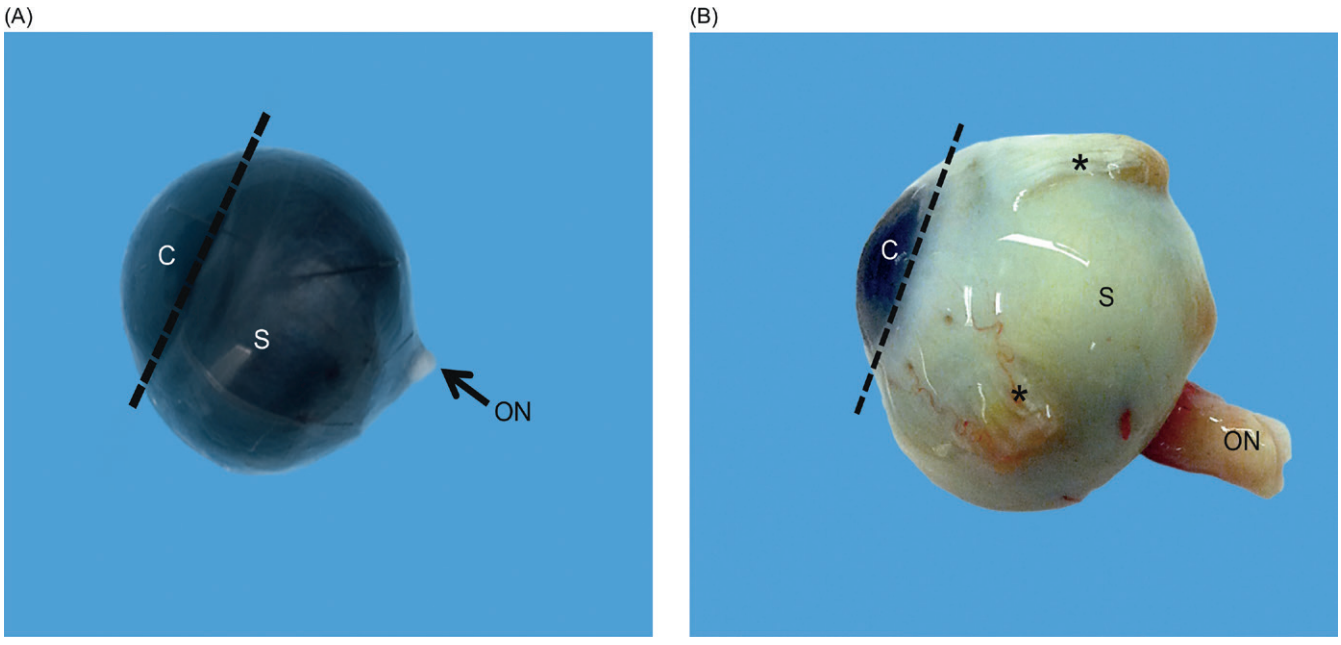

FIGURE 21.4 Enucleated eyeball. (A) Rodent (mouse). The sclera (S; limbus marked by dashed line) is so thin that the choroid is visible through it, making the eyeball appear dark in pigmented strains. Cornea (C) and optic nerve (ON) are indicated. (B) Human. The sclera (S; limbus marked by dashed line) is thick and white. Note the insertions of ocular muscles (asterisks). Cornea (C) and optic nerve (ON) are indicated.

Need-to-know

- In contrast to all other rodent orbital muscles that insert on the anterior sclera, the inferior oblique muscle inserts on the posterior sclera, lateral to the optic nerve. This insertion can serve as a histological landmark in enucleated sections.

TABLE 21.1 Eye

Feature	Rodent	Human
	Gross	
Orbital bones	Mouse: 8 bones Rat: 7 bones	Similar to rat
Extraocular muscles	7 (four recti, two oblique, one retractor bulbi)	6 (four recti, two oblique)
Harderian gland	Large retrobulbar gland, variably pigmented	Absent
Lacrimal glands	Mouse: Two glands (intra- and exorbital); no accessory glands Rat: Two glands (exorbital and infraorbital)	Two lobes (palpebral and orbital); accessory glands—Krause and Wolfring
Nictitating membrane	Mouse: Present Rat: Rudimentary	Plica semilunaris, a fold of conjunctiva at the medial canthus, thought to be a vestige of nictitating membrane
Conjunctiva	Tarsal, forniceal, bulbar; no caruncle present at medial canthus	Tarsal, forniceal, bulbar; caruncle present at medial canthus
Cornea	Transparent anterior portion of the optic globe	Similar to rodent
Sclera	Tough outer sheath of optic globe; thickest posteriorly	Similar to rodent
Lens	Huge volume (proportion) compared with human	9–10 × 3–6 mm (35 vs 5 mm^3 vitreous volume)
Pupil	Round	Similar to rodent
Retina	Mouse: Vasculature radial Rat: Radial inner retinal vasculature	Vasculature with arcades
Optic nerve	Mouse: Centrally located on optic globe; leaves orbit inferocaudal position Rat: Centrally located; emerges through superior and inferior scleral openings	Nasally located on optic globe
	Histologic	
Cornea	Five layers; Bowman's layer indistinct; thinner stroma (proportionately); stroma is bulk of mass	Five layers; Bowman's layer prominent
Sclera	Relatively thin; poorly developed lamina cribrosa; Mouse: Choroid often seen through sclera anteriorly; Rat: Choroid not apparent through sclera	Thinnest behind rectus insertions
Lens	Avascular; posterior capsule is thinnest; epithelium originates at equator	Similar to rodent
Iris	Pupillary border of the iris often in contact with anterior lens capsule; iridial layers same as humans but indistinct	Iridial layers: Anterior border layer, stroma, muscular layer, posterior pigmented epithelium
Ciliary body	Mouse: Posterior ciliary processes attach directly to the sclera; anterior ciliary processes blend with iris; Rat: No published data	Directly attached to the sclera; clear separation of iris
Iridiocorneal angle	Mouse: Iris processes often present; Rat: Similar trabecular outflow pathway anatomy to mouse	Absent
Retina	Lack fovea; dichromatic vision	Fovea; trichromatic vision
Retinal pigmented epithelium	Present	Similar to rodent
Choroid	Thin pigmented vascular network consisting of three layers (from inner to outer): choriocapillaris, stroma, lamina fusca	Proportionately thicker than in rodents
	Cellular	
Iris clump cells	Mouse: Contain phagocytized melanosomes that are round and located at root and pupillary margin; numbers vary by strain; Rat: No published data	Absent
Dendritic melanocytes	In albino rodents, melanosomes lack melanin. Mouse: Contain numerous melanosomes; determine iris color Rat: Smooth muscle cells of pupillary constrictor may contain melanin	Albino humans have variable pigmentation depending on type and subtype of albinism
Iridial fibrocytes	No published data	Present
Rods	95% of photoreceptors	Similar to rodent
Cones	Two types	Three types; highest density at the macula
Orbital muscles	Skeletal	Similar to rodent

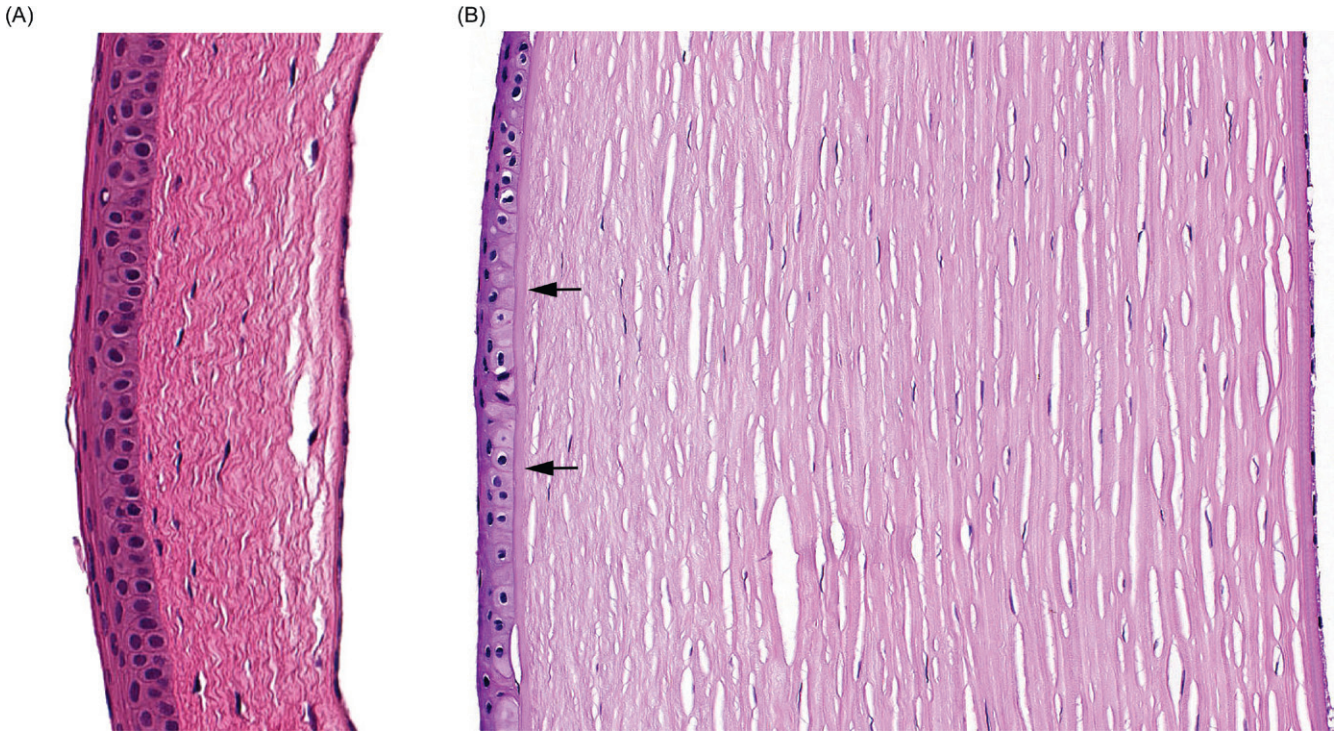

FIGURE 21.5 Cornea. (A) Rodent (mouse) cornea. The mouse corneal epithelium comprises four to seven layers of noncornified stratified squamous cells. In all three species, the epithelium rests on a basement membrane. Caudal (posterior) to the epithelial basement membrane is Bowman's layer, which is indistinct in rodents. (B) Human cornea. Posterior to the epithelial basement membrane is Bowman's layer (arrow), which is prominent and 8–14 µm. In all species, the bulk of the cornea is the stromal layer and is lined by Descemet's membrane anteriorly and the internal surface is lined by flat endothelium. In both panels, the corneal stromal clefts are artifacts produced during processing.

Need-to-know

- Bowman's layer is indistinct in rodents.
- Corneal stroma often shows regular lamellar clefting, which is an artifact of processing.
- Rodents have more layers of epithelial cells than humans.

component of the uvea. The choroid extends from termination of the pars plana at the ora serrata to the optic nerve.

HISTOLOGY

Iris

The iris consists of five layers (from anterior to posterior): anterior border layer, stroma, muscular layer, and anterior and posterior pigment epithelial layers (Figs. 21.6 and 21.7). The anterior border layer is not a separate layer within the stroma but is a condensation of iris stroma. Iris stroma contains vasculature, nerves, melanocytes, macrophages, and fibrocytes (not reported in rodents). In rodents, the iris stroma appears empty on routine sections or is obscured by heavy pigment (Fig. 21.6), but contains components of the extracellular matrix and collagen. Iris color is derived from the pigmentation and melanin content of melanosomes within stromal melanocytes. Albino rodents and humans both have a normal number of melanocytes. Albino rodents have a normal number of melanosomes, whereas albino humans may have a normal or decreased number of melanosomes. Albino mice carrying the *c/c* allele have decreased melanin within their melanosomes resulting from deficient tyrosinase activity. Variable pigmentation and melanosome morphology of uvea and RPE, depending on the type and subtype of albinism

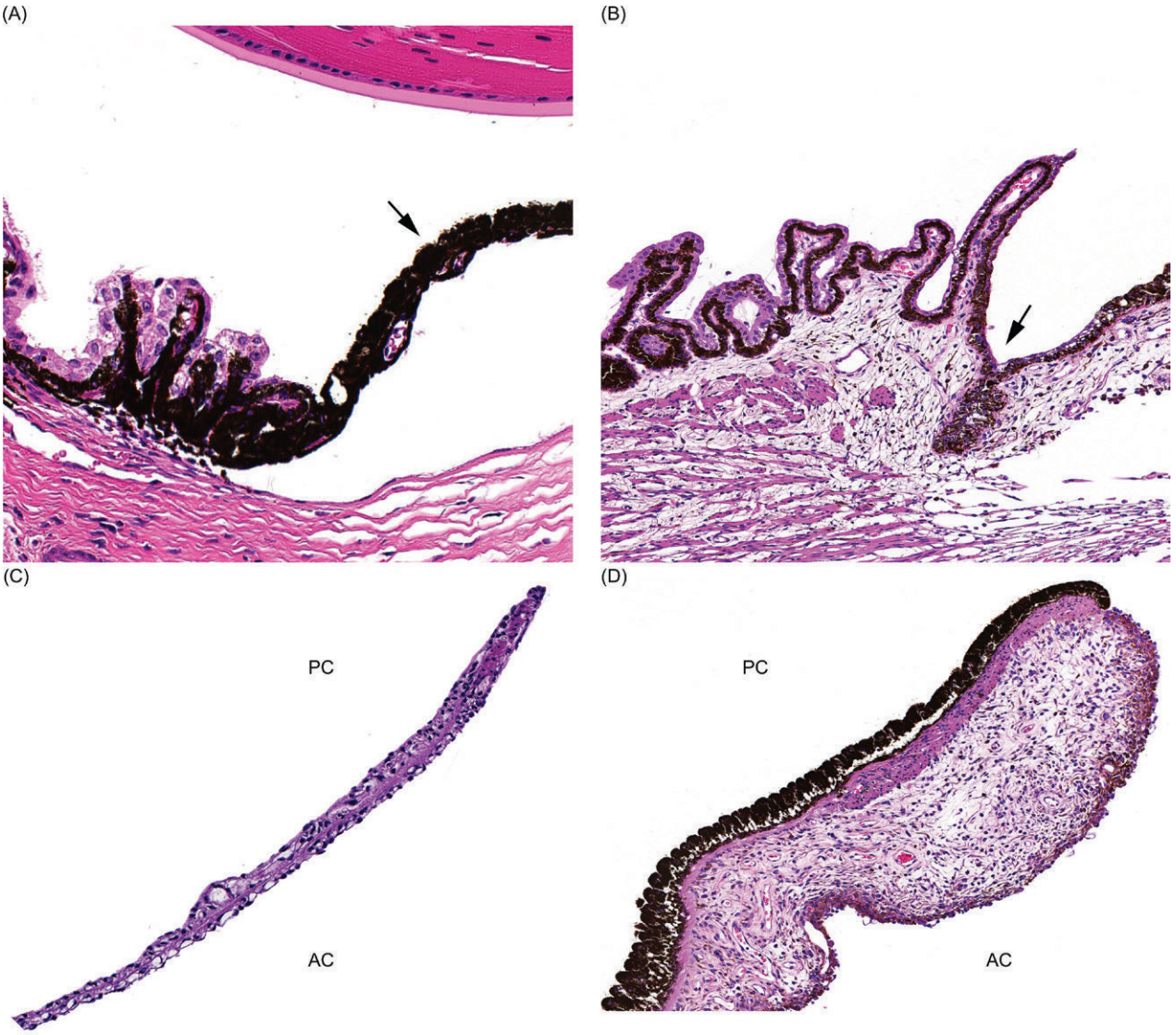

FIGURE 21.6 Ciliary body and iris. (A) Rodent (mouse) ciliary body and iris (arrow) from a pigmented strain. Note the small cylindrical shape and the seamless merging of the peripheral iris with the anterior ciliary body process. Rodents lack the ability to accommodate; this is visible histologically in their small, cylindrical ciliary bodies, which lack circular muscle fibers. (B) Human. The human ciliary body is triangular and consists of a double layer of epithelium overlying stroma and three muscle groups within the ciliary body: circular (innermost), radial, and longitudinal (outermost). Note the clear separation between the posterior iris and ciliary body (arrow). (C) Rodent (mouse) iris from a nonpigmented strain. Contrast this with the iris shown in Fig. 21.6A The anterior chamber (AC) and posterior chamber (PC) are indicated. (D) Human iris with abundant stroma and clearly visible smooth muscle layer at the posterior aspect of the iris, beneath the pigmented epithelium. The anterior chamber (AC) and posterior chamber (PC) are indicated.

Need-to-know

- The anterior rodent ciliary body merges with the iris.
- Rodents cannot accommodate due to lack of circular muscle fibers; it is evidenced histologically in small ciliary bodies.
- Rodents have thin iris stroma that maybe obscured in pigmented strains by iris clump cells and dendritic melanocytes.

(Figs. 21.6 and 21.7), are seen in humans with ocular albinism, and in mouse models for these syndromes. The pupillary border of the iris is often in contact with the anterior lens capsule (see below); however, aqueous humor is still able to flow in the potential space. The muscular layer includes a circular sphincter muscle near the pupil margin that can constrict and thereby limit

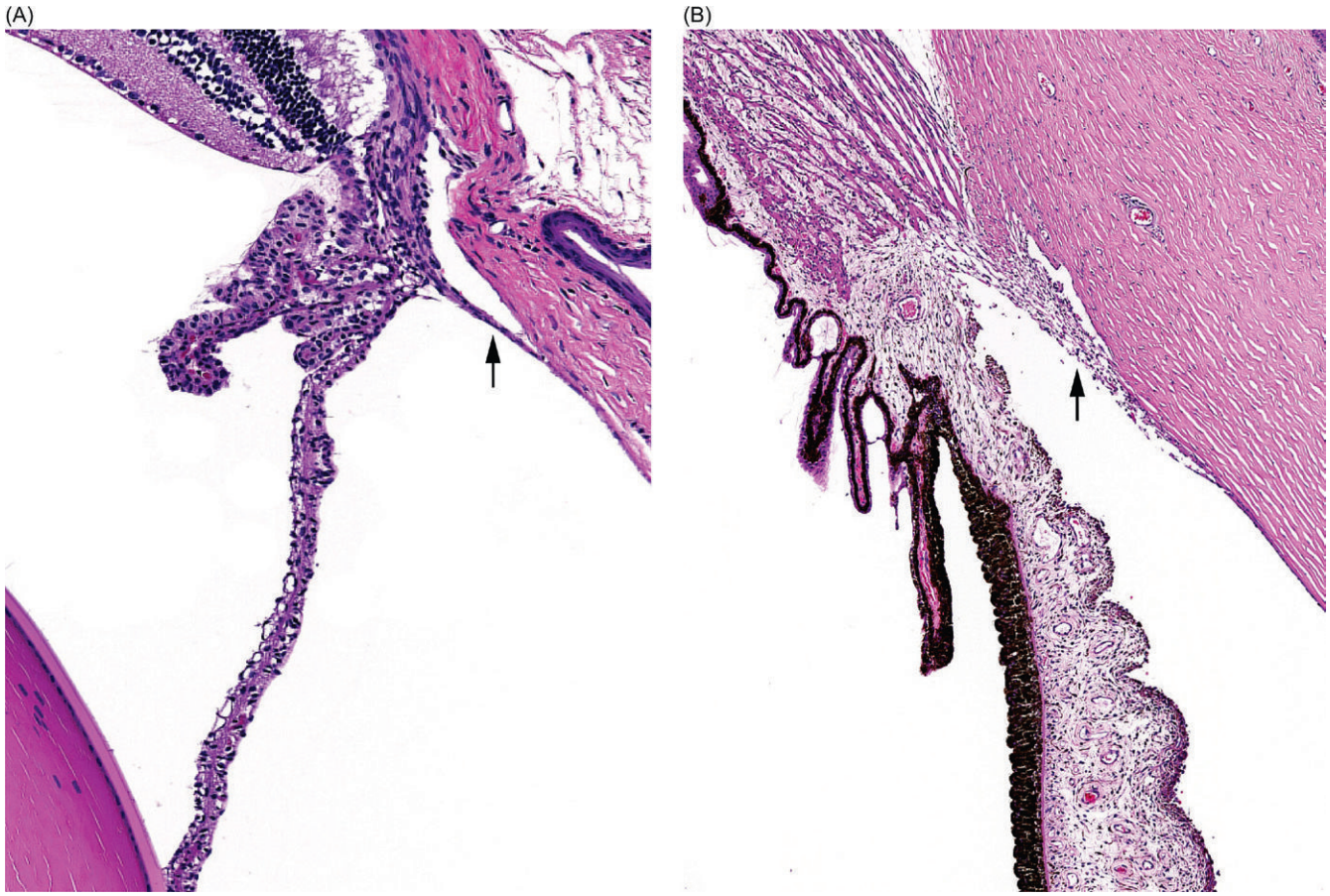

FIGURE 21.7 Iridiocorneal angle. (A) Rodent (mouse) from a nonpigmented strain. Iris processes (arrow) can occasionally be seen extending from the anterior iris to the peripheral thickening of Descemet's membrane (Schwalbe's line). Schlemm's canal is indistinct in this section. (B) Human. Note Schlemm's canal (arrow) and the absence of iris processes.

Need-to-know

- In rodents the iris may be in contact with the anterior lens capsule.

the amount of light allowed through the pupil. In addition, the muscular layer contains radial dilator muscles that can expand the pupillary aperture. Immediately posterior to the thin layer of dilator muscles are the anterior and posterior pigment epithelial layers arranged in an apex-to-apex configuration. In rodent eyes, the peripheral iris merges seamlessly with the ciliary body such that ciliary processes can be visible on the posterior aspect of the iris (Fig. 21.7). In humans, the iris and ciliary body are more clearly defined distinct structures.

Iridocorneal Angle and Aqueous Humor Drainage

The base of the iris attaches to the peripheral cornea and sclera at the iridocorneal angle (Figs. 21.6–21.8), the site of aqueous humor drainage. The iridocorneal angle's anterior border is Schwalbe's line at the trabecular meshwork (TM), which contains numerous trabecular beams composed of cores of collagen surrounded by flat endothelium. Rodents have fewer trabecular beams than humans; however, theirs are more tightly packed in the posterior meshwork. In rodents, numerous iris processes may be present, extending from the iris root to Schwalbe's line. These iris processes are only infrequently seen in humans. Aqueous humor leaves the anterior chamber via two routes. Drainage via the iridocorneal angle is known as the conventional, or trabecular route. Fluid filters through the TM into Schlemm's canal. This circular canal

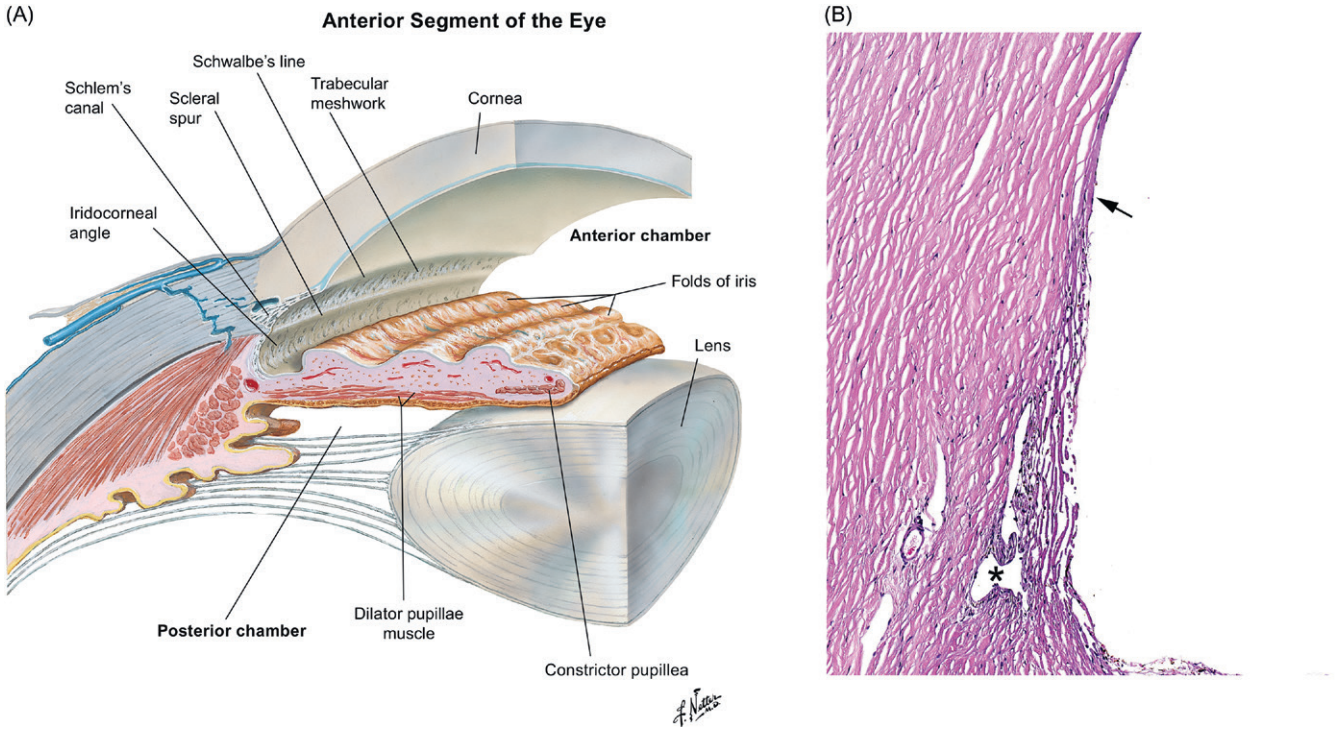

FIGURE 21.8 Human iridocorneal angle. (A) Schlemm's canal is visible close to the corneoscleral junction. (B) High magnification view of Schlemm's canal (asterisk) and peripheral thickening of Descemet's membrane (Schwalbe's line; arrow).

just outside the TM is lined by endothelial cells and in turn empties into collector channels and venous outflow vessels within the uvea, sclera, and episclera. In the unconventional (or uveosclera) pathway, aqueous humor drains via the uveal meshwork and anterior face of the ciliary muscle, between muscle bundles, through the suprachoroidal space, and out through the sclera.

This unconventional pathway is thought to play a greater role in rodents than in primates. The intraocular pressure (IOP) is a balance of production and drainage of aqueous humor. Mouse IOP ranges from 10 to 15 mm Hg and is affected by strain, anesthesia (decreased), and in C57BL/6J mice, advancing age (increased). Rats have slightly higher IOP up to 18 mm Hg; humans have pressures up to 21 mm Hg. In rodents, there is no scleral spur—the protrusion of the sclera into the anterior chamber; instead, smooth muscle bundles mark the posterior aspect of the canal.

Ciliary Body

The ciliary body in cross section is cylindrical in rodents and triangular in humans, consisting of a double-layered epithelium overlying stroma and muscle (Figs. 21.6 and 21.7). The double layer of epithelial cells includes an outer (facing the ciliary body stroma) pigmented and inner (facing the vitreous) nonpigmented epithelium contiguous with the RPE and retina, respectively. Zonules arise from the nonpigmented epithelium and insert onto the equatorial lens. The nonpigmented epithelium is also the source of aqueous humor. The stroma of the pars plicata is vascular, whereas the pars plana is relatively avascular. There are three muscle groups within the ciliary body (from inner to outer): circular, radial, and longitudinal muscle fibers. These muscles help to control the tension on zonular fibers extending from the ciliary processes to the crystalline lens, thereby facilitating the focusing of the lens to near objects (accommodation).

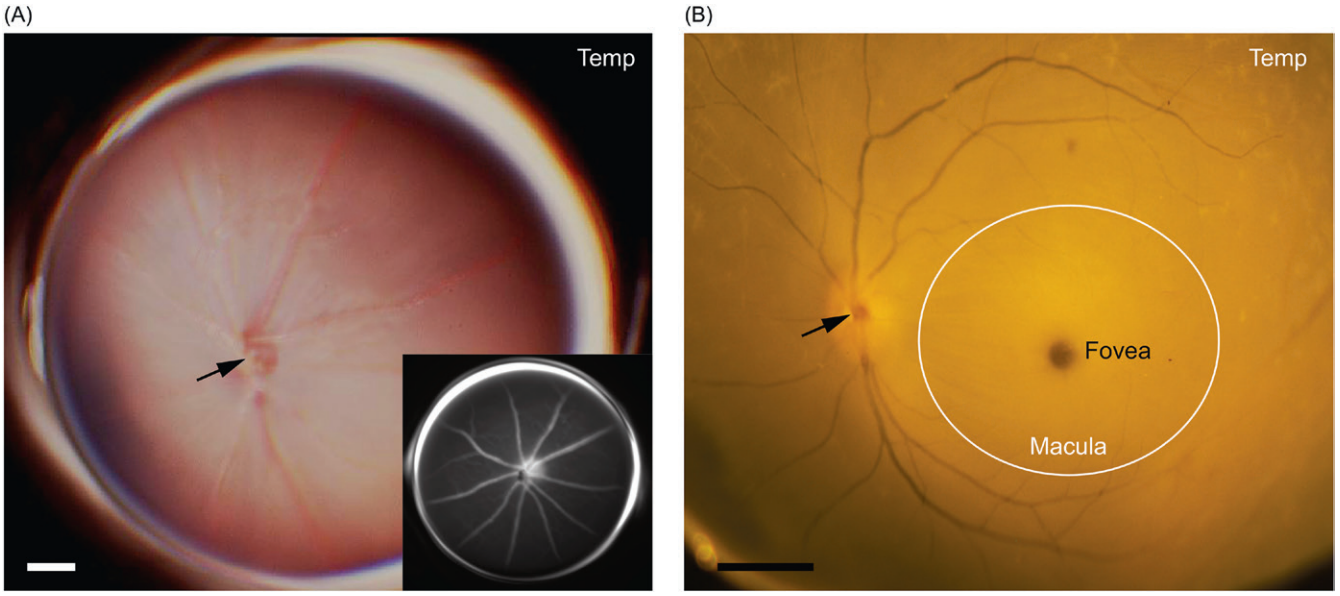

FIGURE 21.9 Fundus morphology. (A) Rodent (mouse). No macula is present, and retinal vasculature is evenly distributed in radial fashion around the optic disk (arrow). Inset illustrates retinal venous drainage using fluorescein angiography. Bar = 50 µm; temporal aspect is indicated (Temp). (B) Primate (rhesus macaque). The posterior segment (Bouin's fixative). Retinal vessels emanate from the optic nerve head (arrow) and extend in an arc-like fashion on the temporal side. The macula (indicated by a white circle) is located temporally to the optic nerve and has at its center the cone-rich avascular fovea, which appears dark because of the underlying choroid visible in the foveal pit. Bar = 1 mm; temporal aspect is indicated (Temp).

Rodents lack the ability to accommodate due to lack of circular fibers; this is evidenced histologically in small ciliary bodies. The longitudinal muscle fibers connect to the scleral spur (anterior to the ciliary body), providing one of the main attachments of the uvea to the sclera.

Choroid

The choroid is a thin, pigmented vascular network consisting of three layers (from inner to outer): choriocapillaris, stroma, and lamina fusca. The choriocapillaris provides nutrients to the RPE and the outer third of the retina. The choroidal stroma is proportionally thinner in rodents than in humans, and it contains dendritic melanocytes, fibroblasts, and mast cells. The choroidal vasculature is supplied by the long and short posterior ciliary arteries and the anterior ciliary arteries; drainage occurs via the vortex vessels. The vortex vessels and optic nerve provide additional points of attachment between uvea and sclera. The lamina fusca serves as a thin weblike attachment between the choroid and sclera.

Retina

Gross Anatomy

The inner layer of the eye is the retina, a complex tissue with multiple layers of cells responsible for absorption of light and transmission of this signal to the brain and includes the neurosensory retina (neuronal layers) and the RPE. The retina has a dual vascular supply that is similar between the three species (Fig. 21.9). The central retinal artery—a branch of the ophthalmic artery—and its branches supply the anterior two-thirds of the neurosensory retina. The outer one-third is supplied by the choriocapillaris (described above). In rodents, there are usually four to six retinal arterioles, but this is highly variable. In humans, the central retinal artery exits the optic nerve and branches into four arterial arcades near the

anterior surface of the retina. The venous drainage follows a similar vascular pattern.

HISTOLOGY

Neuorsensory Retina

There are five types of neurons in the neurosensory retina: photoreceptors, bipolar cells, ganglion cells, horizontal cells, and amacrine cells. These neurons are arranged in layers from inner (vitreous side) to outer as follows: internal limiting membrane, nerve fiber layer, ganglion cell layer, inner plexiform layer, inner nuclear layer, outer plexiform layer, outer nuclear layer, external limiting membrane, and photoreceptor layer (Figs. 21.10–21.13). External to the neurosensory retina is the RPE (see next), which is separated from the choroid by Bruch's membrane. Bruch's membrane is a trilaminar structure composed of a central collagenous and elastic matrix bounded by the basement membranes of the RPE and the choriocapillaris. Bruch's membrane is less prominent in rodents than in humans, but can be easily visualized in rodents with PAS stain.

The internal limiting membrane is a PAS-positive basement membrane formed by the footplates of glial cells that span the normal retina and whose cell bodies lie within the inner nuclear layer (Müller cells). The nerve fiber layer is a collection of unmyelinated ganglion cell axons. In rodents, this layer thickens toward the optic nerve and can be indistinct peripherally. These axons become myelinated as they exit the eyeball through the lamina cribrosa, a fenestrated portion of the sclera which is nonexistent in mice and poorly developed in rats. The average human has 1–1.2 million ganglion cell axons; rodents have approximately one-tenth of this number, but this is highly variable between inbred strains. The most striking difference between rodent and human retina is that human retina utilizes a specialized area called the macula, which is responsible for high acuity central vision. The macula is defined histologically as the region of the human retina with more than one cell layer of

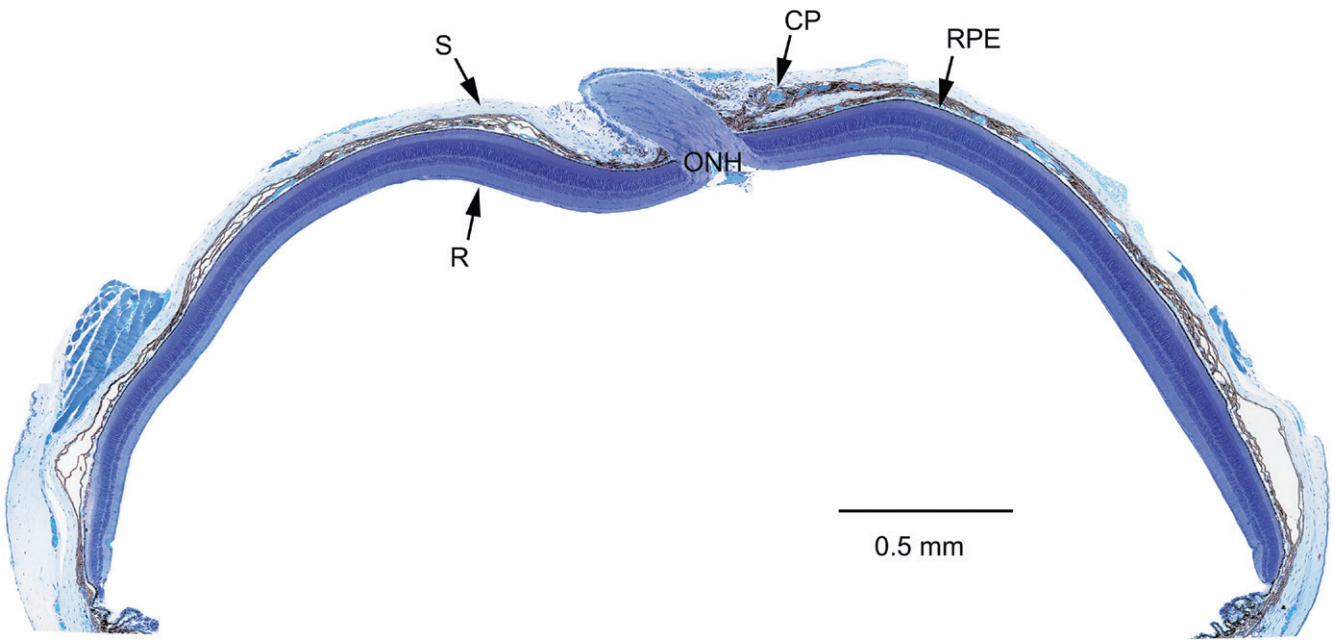

FIGURE 21.10 Posterior rodent (mouse) eye. In this cross section stained with Richardson's stain, the optic nerve head (ONH), RPE, choroidal plexus (CP), and sclera (S) are clearly visible. Unlike the human retina, the rodent retina does not show any regional specialization, such as a fovea; however, the nerve fiber and ganglion cell layers become thin peripherally. Source: Dan Possin.

ganglion cell bodies within the ganglion cell layer and is located within the temporal retinal vascular arcades. A depression at the center of the macula marks the location of the fovea; in addition to the macula, rodents also lack a fovea. At the center of the human fovea, the retina is avascular and consists primarily of photoreceptors (Figs. 21.9 and 21.13). In rodents and in the human nonmacular peripheral ganglia cell layer, there is one layer of cell bodies. The highest density of ganglion cells in rodents is temporal to the optic nerve with decreasing density toward the dorsal and peripheral retina. The inner plexiform layer consists of synapses between bipolar cells, ganglion cells, and amacrine cells. The inner nuclear layer contains the nuclei of bipolar, Müller, horizontal, and amacrine cells and is usually 6–9 layers thick. The overall human retinal thickness is variable depending on its relationship to the fovea. The retinal layers up to the inner third of the inner nuclear layer are nourished by the retinal arteries, whereas the outer retinal layers, beginning at the outer two-thirds of the inner nuclear layer, are nourished by the choroidal vessels. The outer plexiform layer constitutes synaptic processes between the horizontal and bipolar cells. In the macula, the outer plexiform layer is thick, and the axons are oriented obliquely. This region of the outer plexiform layer is known as Henle's layer. The outer nuclear layer contains photoreceptor (cone and rod) nuclei and cell bodies. Rods account for approximately 95% of photoreceptors in all three species, and are the cell type responsible for thickness of the outer nuclear layer. In rodents, this layer is 10–12 cells thick. Cone nuclei are arranged as a single layer beneath the external limiting membrane. Rod nuclei are slightly smaller than cone nuclei, and have more tightly condensed (heterochromatic) chromatin.

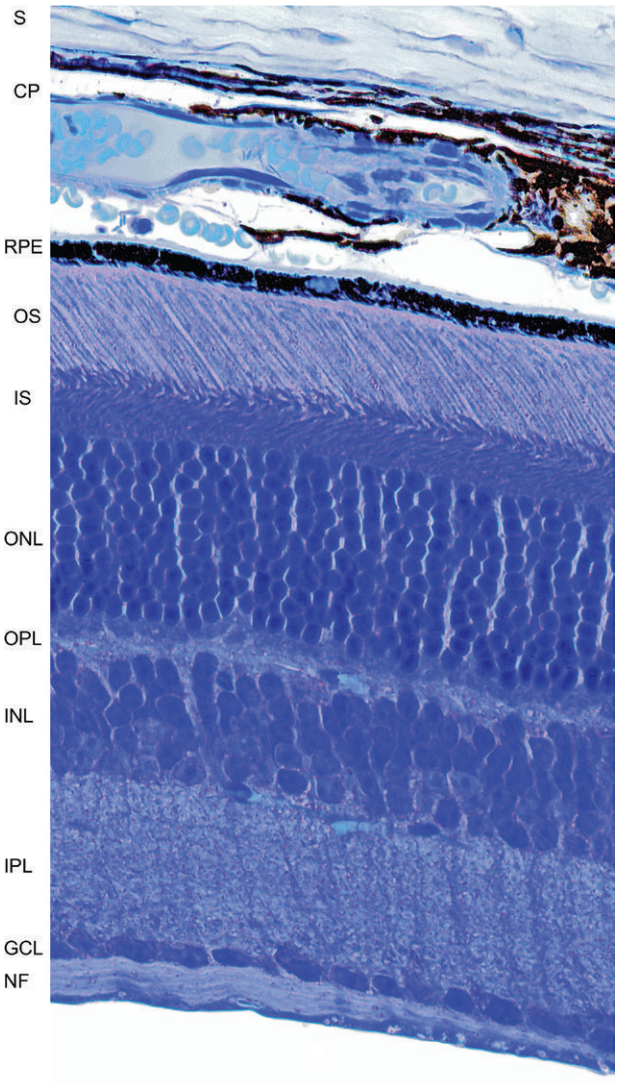

FIGURE 21.11 Cross section of a rodent (mouse) retina. In this cross section stained with Richardson's stain showing three cellular layers and two synaptic layers of the retina. The cellular layers are the nerve fiber layer (NF), ganglion cell layer (GCL), inner nucleus layer (INL), and outer nuclear layer (ONL). Synaptic layers are the inner plexiform layer (IPL) and outer plexiform layer (OPL). Sclera (S), RPE, choroid plexus (CP), and photoreceptor inner (IS) and outer (OS) segments are indicated. Source: Dan Possin.

Need-to-know

- The outer nuclear layer is usually twice as thick as the inner one in rodents.

Humans and Old World primates of both sexes are trichromatic and have three types of cones, which are each specialized to detect short, medium, or long wavelengths of light, whereas rodents have only two types of cones (harboring short and medium wavelength pigments). The external limiting membrane is not a true basement membrane, but is formed by tight junctions between apical processes of Müller cells and photoreceptor cells. It serves as an anatomical landmark that separates photoreceptor nuclei and cell bodies from the photoreceptor inner and outer segments. These

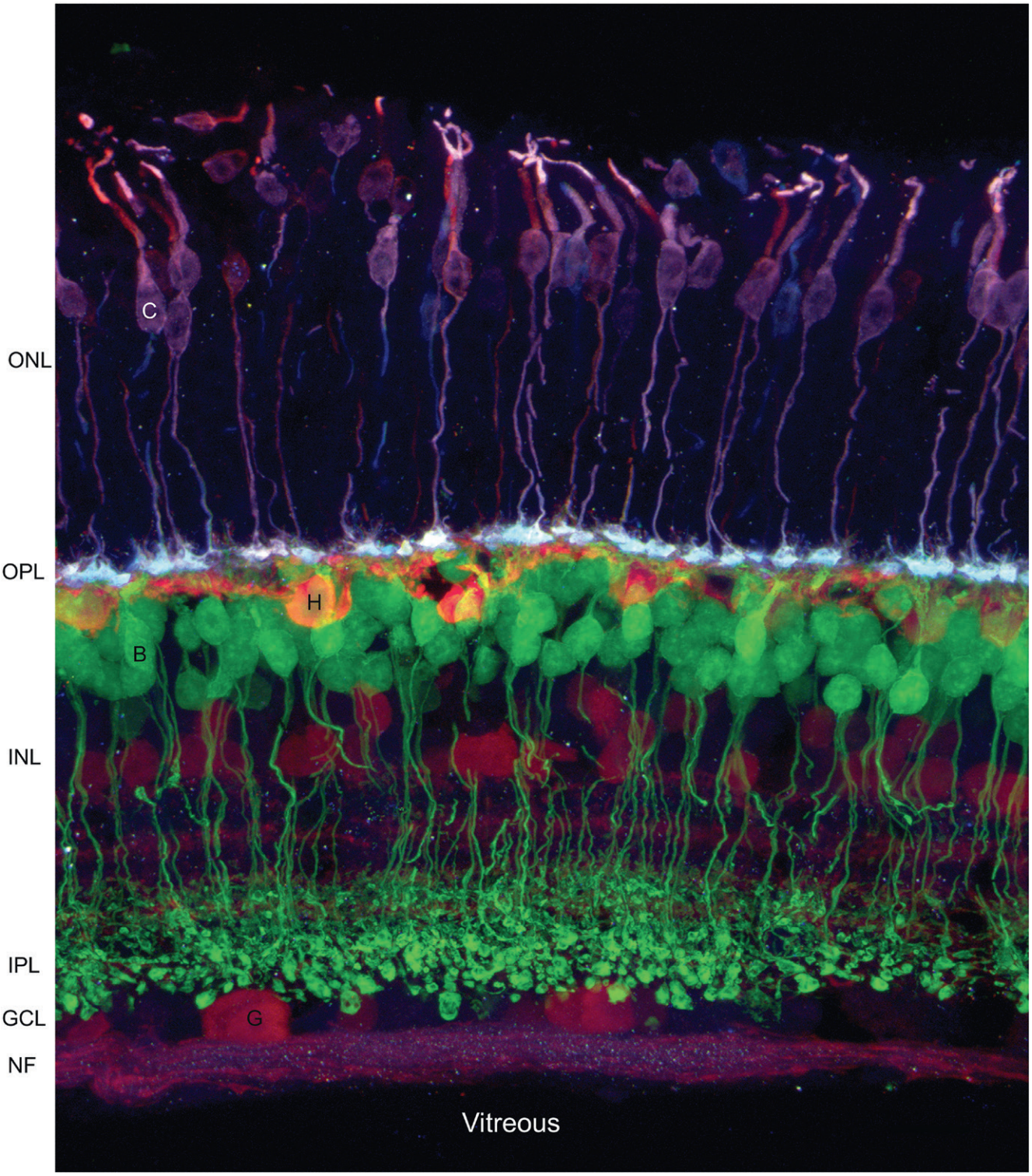

FIGURE 21.12 Rodent (mouse) retina. The major cell types of the mouse retina can be visualized by a combination of transgenic cell-labeling methods and immunostaining procedures. Shown here is a vibratome section (60 µm) of paraformaldehyde-fixed retina from a transgenic mouse with metabotropic glutamate receptor 6 promoter driven expression of green fluorescent protein. Cone photoreceptors (C) are immunoreactive for cone arrestin; horizontal cells (H), a subset of amacrine cells, and ganglion cells (G) are immunoreactive for calbindin. One subtype of retinal bipolar cell (B) is labeled. The retinal layers (see Fig. 21.11 legend) are indicated. Reproduced from Morgan et al.: *Nat Neurosci* 9(1):85–92, 2006.

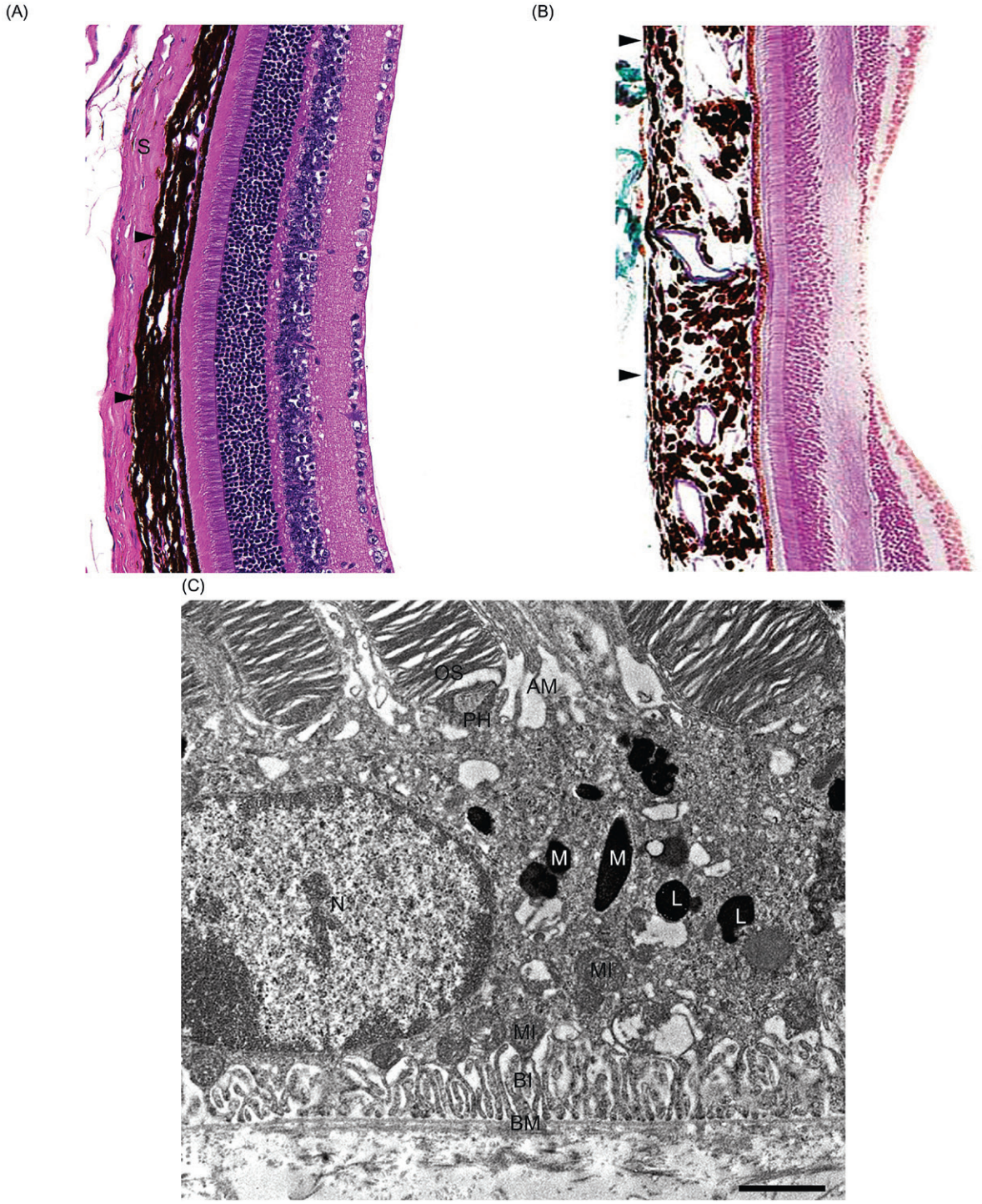

FIGURE 21.13 Retina. (A) Rodent (mouse). Note the lack of fovea and the relatively thin, heavily pigmented choroid (arrowheads) adjacent to the posterior sclera (S). (B) Human. The macula center marks the location of the fovea, which is the region corresponding to highest visual acuity in humans. At the foveolar (foveal center), the retina is avascular and consists primarily of photoreceptors. The thick choroid is well vascularized with prominent stroma (arrowhead). (C) Mouse. Ultrastructure of the RPE and adjacent structures. Apical microvilli (AM) enclose the distal tips of the photoreceptor outer segments (OS). Outer-segment disks break off and are phagocytosed (PH) by the RPE cell. Phagosome content is degraded and accumulates in lipofuscin granules (L). Melanosomes (M) occupy the apical two-thirds to one-half of the cell. The basal aspect of the RPE cell rests on Bruch's membrane (BM) and elaborates membranous folds known as basal infoldings (BI). Mitochondria (MI) are located in the basal third of the cell, and a large nucleus (N) occupies the majority of its width. Transmission electron micrograph.

Need-to-know

- The macula is the center of visual acuity in humans and is lacking in rodents.
- Albino rodents and humans with Hermansky–Pudlak syndrome do not have pigmented melanosomes.

photoreceptor segments have differential staining: inner are broader (more so in cones than in rods) and present a higher packing density (Fig. 21.11) and more eosinophilic appearance than the thin outer segments on HE-stained sections (Fig. 21.13). These segments are composed of stacks of membranous structures (disks) harboring the phototransduction machinery. New outer-segment disks are continuously formed at the cilium (visible ultrastructurally) at the same rate that old disks are shed from the tip of the outer segment and phagocytosed by the RPE (Fig. 21.13C).

Retinal Pigment Epithelium

The RPE is composed of a monolayer of pigmented epithelial cells that lies outside the neurosensory retina and is attached to the underlying choroid. It extends from the optic disk to the ora serrata, where it is contiguous with the pigmented epithelium of the ciliary body. The apical aspect of RPE cells abuts the photoreceptor outer segments, whereas the RPE basement membrane forms the inner lamella of Bruch's membrane (Fig. 21.13). RPE cells have intercellular junctional complexes (zonulae occludentes) that make up the outer blood–retina barrier. Numerous round pigment granules (melanosomes) are visible within the RPE cytoplasm, particularly in pigmented individuals. Albino rodents have unpigmented melanosomes. In albino humans, there is a variable amount of pigmentation, depending on the subtype of oculocutaneous or ocular albinism. At the human fovea, RPE cells are tall and thin with numerous melanosomes. In the periphery, the RPE cells are shorter, broader, and less pigmented. The RPE has numerous functions: it phagocytoses photoreceptor outer segments, regenerates photoactive 11-cis retinal, forms the outer blood–retina barrier, absorbs light, elaborates the interphotoreceptor matrix, transports ions and nutrients, and actively transports water out of the subretinal space to maintain adhesion of the neurosensory retina.

Vitreous Chamber and Lens

GROSS ANATOMY

Within the three layers of the eye described above lie the vitreous chamber and lens. The vitreous chamber is relatively smaller in rodents and mainly occupied by the large lens (Figs. 21.2 and 21.14). The remaining space is filled with vitreous, a gel composed of water (99%), collagen (types II and IX), glycosaminglycans, glycoproteins, and soluble proteins. Because of the large lens, the volume of vitreous in rodents is proportionately less than that in humans.

The structure of the lens is similar among the three species; however, the round rodent lens is proportionately larger than the biconvex human, occupying nearly 75% of the eye (Figs. 21.2A and 21.14A). In adult humans, the biconvex lens is approximately 9 or 10 mm in diameter and approximately 3.5 mm in anterior–posterior depth (Figs. 21.2B and 21.14B). The lens of all three species is avascular and aneural, and it is surrounded by a lens capsule that is twice as thick anteriorly as posteriorly (Fig. 21.14). The lens is suspended by zonular fibers extending from the ciliary body processes to the mid-equatorial lens capsule. Because lens fibers are continuously produced, the lens increases in size throughout life. As new lens fibers are laid down on top of old, the central lens (nucleus) contains the oldest fibers produced *in utero*, whereas the peripheral lens (cortex) has the newer lens fibers.

HISTOLOGY

The vitreous chamber appears empty as a result of its high water content. The vitreous chamber's exterior surface, known as the anterior hyaloid face, is behind the lens, whereas the posterior hyaloid face lies just anterior to the retina. The vitreous is firmly attached at the vitreous base located at the ora serrata. Additional firm

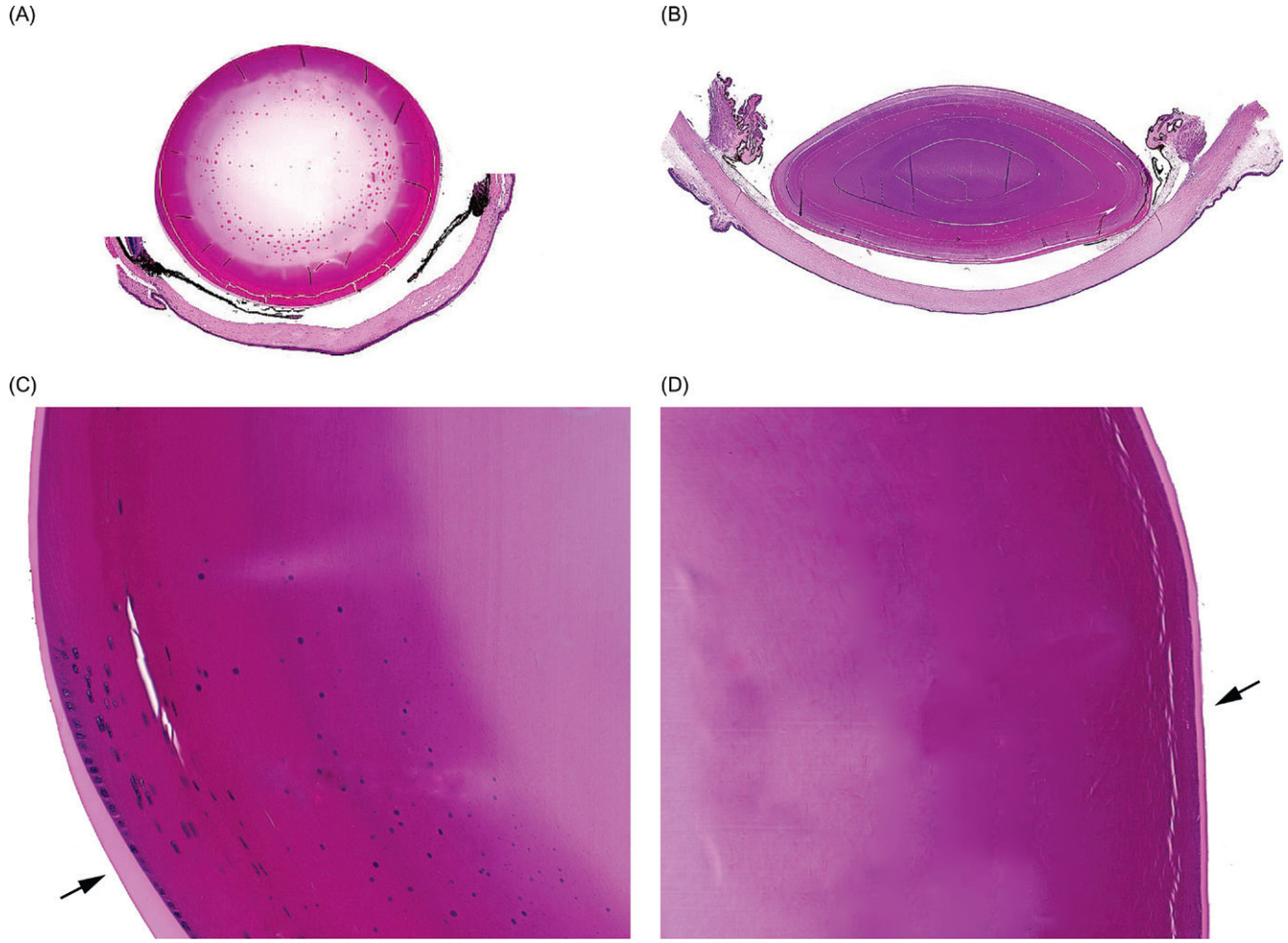

FIGURE 21.14 Lens. (A) Rodent (mouse). The lens is relatively large and round. (B) Human. The lens is flattened and occupies less volume than the rodent lens. (C) Rodent (mouse) lens equator. The capsule is thickest anteriorly (arrow) where the lens epithelial nuclei bend inward. The histological appearance of the lens is similar to that of the human lens. The clefting present in the lens is a fixation artifact. (D) Posterior rodent (mouse) lens. The posterior capsule is thinner (arrow), and normally no nuclei are present.

Need-to-know

- Rodents have a relatively large, round lens.

attachments exist at the optic nerve head, overlying retinal vessels, and near the human fovea.

The lens epithelium is a monolayer of cuboidal cells located just below the anterior and equatorial lens capsule where the cells are columnar. The lens epithelial cells located at the lens equator continue to divide and produce lens fibers throughout life, with mitotic figures sometimes present. Epithelial cells are not present posterior to the lens equator under normal conditions. The central lens fibers, which are the oldest lens fibers, lack nuclei and have few intracellular organelles.

Optic Nerve

Gross Anatomy

The optic nerve (cranial nerve II) is the convergence of retinal ganglion cell axons that has extracranial and intracranial sections. The extracranial can be divided into intraocular and intraorbital sections. The rodent extracranial optic nerve is divided into the optic nerve head, the lamina cribosa region, and unmyelinated and myelinated regions (Fig. 21.15). Posterior to the sclera, the optic nerve becomes myelinated in all

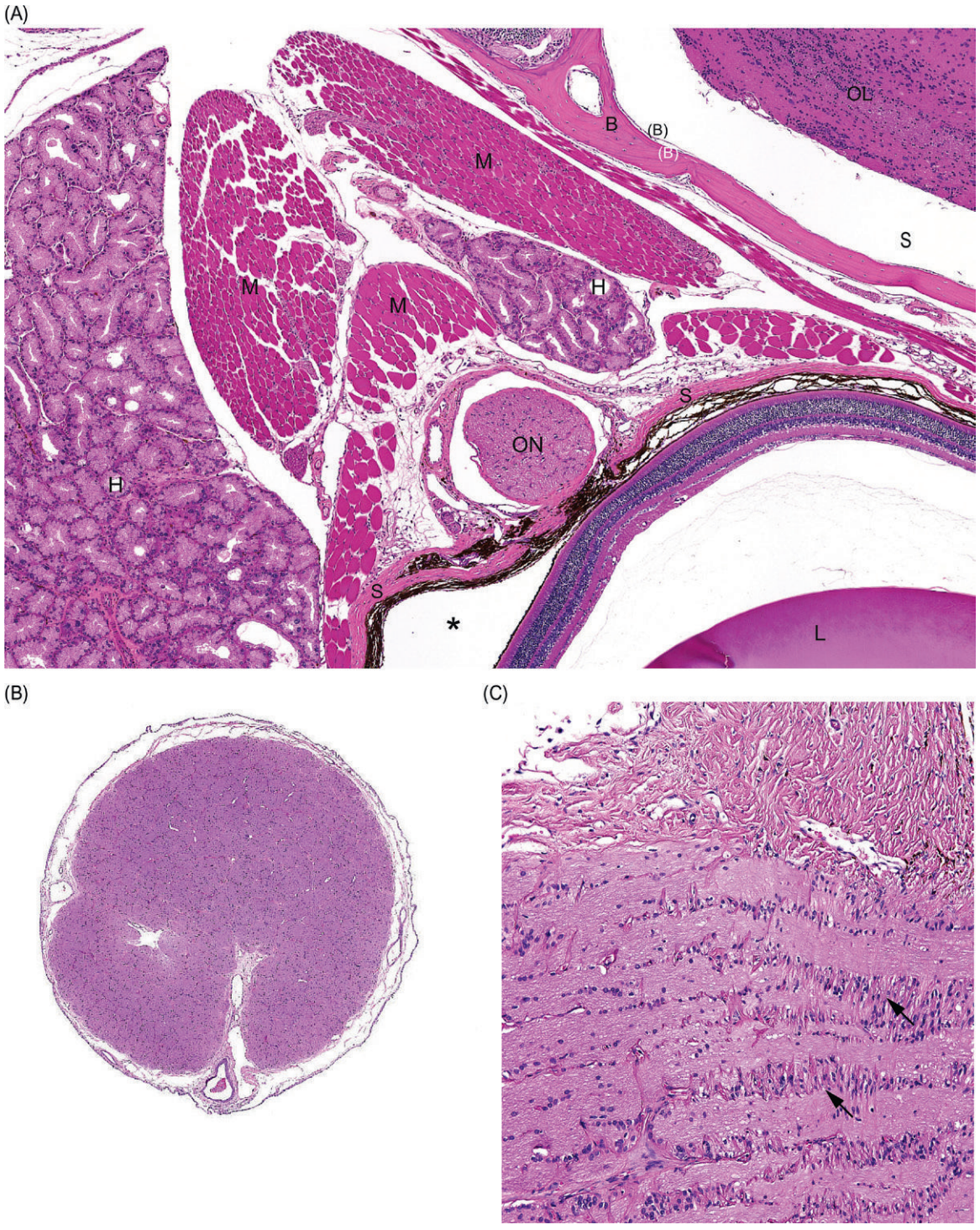

FIGURE 21.15 Optic nerve. (A) Rodent (mouse) posterior orbit. The orbital muscles (M) are surrounded by the Harderian gland (H). The extraorbital muscles are typical skeletal muscle (M) and attach to the sclera (S). The Harderian gland (H) is indicated. Note the retina is artifactually detached from the retinal pigmented epithelium (asterisk). Optic nerve (ON), lens (L), olfactory lobes (OL), and bone (B) are indicated. (B) Human. The optic nerve in all three species is invested by meninges. Branches of the central retinal artery and vein at their entry point to the optic nerve are visible. (C) Human lamina cribosa. The lamina cribosa is a fenestrated collection of horizontal connective tissue plates (arrows) with pores that transmit the optic nerve axons (A).

Need-to-know

- The optic nerve in rodents has10-fold fewer axons than that of humans.
- Axon number varies greatly between inbred strains.
- The lamina cribosa is not well developed in the rat and is not observable in the mouse.

three species, which increases its diameter. The optic nerve intraorbital segment extends from the eyeball to the orbit and becomes enveloped in meninges consisting of three layers: dura mater (outer), arachnoid (center), and pia mater (inner). The intraorbital optic nerve in all three species is surrounded by connective tissue, fat, and the rectus muscles. In rodents, the Harderian gland also covers the optic nerve.

HISTOLOGY

Intraocular Optic Nerve

In the rodent optic nerve, the number of ganglion cell axons is highly strain dependent; in mice ranging from 32,000 to 87,000 cells. In rats, there is less variability (approximately 72,000–113,000). In humans, the optic nerve consists of the 1–1.2 million axons that originate in the ganglion cell layer. Axons terminate in the lateral geniculate nucleus of the thalamus in all three species. The portion of the optic nerve visible ophthalmoscopically is termed the optic disk. In all three species, a normal optic disk has a temporally displaced depression termed the optic cup.

The central retinal artery and vein traverse through the center of the cup. As ganglion cell axons enter the optic disk, they are divided into fascicles by intervening astrocytic glial cells. When the optic nerve sustains physiologic damage, supporting glial cells may be lost; this may manifest as an enlargement of the optic cup. Immediately posterior to the optic nerve head is the lamina cribrosa region (Fig. 21.15C), where in humans and less so in rats, a collection of connective tissue plates composed of collagen, elastin, laminin, and fibronectin, with pores that transmit the optic nerve axons fenestrates the sclera. There is no lamina cribosa in mice.

Intraorbital Optic Nerve

In all three species, posterior to the lamina cribrosa region, the optic nerve becomes myelinated by oligodendrocytes.

Extraocular Muscles

GROSS ANATOMY

The six extraocular muscles (four rectus and two oblique) are located in the retrobulbar space and attach to the sclera and control the movement of the eyeball. Although the six extraocular muscles are generally similar between the three species; in rodents, an additional retractor bulbi muscle surrounds the optic nerve and is internal to the four rectus muscles. In rodents, the Harderian gland surrounds the extraocular muscles (Fig. 21.15A). The inferior oblique may be used for orientation of the eyeball in histological sections of enucleated eyes as it inserts on the posterior sclera. Details on the insertions and innervations of the mouse extraocular muscles may be found in Smith et al. (see Further Reading).

HISTOLOGY

The extraocular muscles of both rodents and humans are similar histologically to other skeletal muscles (Fig. 21.15A), yet functionally, biochemically, and structurally distinct, with a number of muscle fiber types. See Further Reading for details on the unique function and ultrastructure of extraocular muscles.

Conjunctiva

GROSS ANATOMY

The eyeball is protected from the external environment by the conjunctiva and eyelids. The conjunctiva is a ring of mucus membrane that lines the posterior lids and anterior eye. The palpebral conjunctiva begins at the lid margin and lines the posterior aspect of the eyelids. It then reflects back on itself to form the dorsal (superior) and ventral (inferior) fornices. The conjunctiva drapes over the anterior surface of the eye as bulbar conjunctiva and inserts at the limbus. In rodents, the dorsal fold of conjunctiva is supported by a cartilaginous plate to form the nictitating membrane (also called the third

eyelid). This membrane is composed of a thin core of cartilage covered by loose connective tissue and conjunctiva, is located between the upper lid and the eyeball at the medial canthus of the rodent eye. It is very small, challenging to grossly observe, and only occasionally seen in histological sections (Fig. 21.16).

In humans, the conjunctiva at the medial canthus forms a small fold termed the plica semilunaris. Rodents lack a caruncle which, in humans, is a fleshy knob of tissue covered by conjunctival epithelium and located just medial to the plica semilunaris. It contains adnexal structures including hair follicles, sebaceous glands, and accessory lacrimal glands.

HISTOLOGY

Normal rodent and human conjunctiva consists of stratified nonkeratinizing squamous epithelium with goblet cells (Fig. 21.16). Goblet cells produce mucins that contribute to the tear film. They can be visualized with PAS, mucicarmine, and alcian blue. Goblet cells are most abundant in the fornices and overlying the nictitating membrane in rodents and human plica semilunaris; they are sparse or absent at the limbus. Beneath the conjunctival epithelium lies the substantia propria, which contains vasculature, nerves, mast cells, lymphocytes, and plasma cells. The substantia propria of the conjunctiva also contains lymphoid tissue and lymphatic vessels. Although the cornea is alymphatic under normal conditions, limbal lymphatics can develop and regress in response to inflammatory stimuli. Normal human conjunctiva is not pigmented, but pigmented mouse strains may have collections of pigment-laden macrophages in the conjunctiva, particularly in the conjunctiva overlying the nictitating membrane.

EYELIDS

GROSS ANATOMY

The eyelid in all three species is often divided into two leaflets known as the anterior and posterior lamellae. The anterior lamella consists of skin and concentric skeletal muscle that functions in eyelid closure (orbicularis oculi). The posterior lamella consists of the tarsal plate (see below, histology) and palpebral conjunctiva. Eyelid skin is the thinnest skin on the human body. At the eyelid margin, the eyelashes (cilia) project through the skin anteriorly. In humans, a "gray line" can be visualized at the lid margin posterior to the cilia that represents the muscle of Riolan, an extension of the orbicularis oculi. This structure is not seen in rodents. Posteriorly, rodents and humans have meibomian gland orifices, which are openings of sebaceous glands embedded within the tarsal plate. In rodents, the mucocutaneous junction occurs anterior to the meibomian gland orifices, so these glands open onto conjunctiva. In humans, the skin transitions from keratinized stratified squamous epithelium to nonkeratinized conjunctiva at the mucocutaneous junction, posterior to the meibomian glands. The medial aspects of both superior and inferior lids contain the lacrimal puncta, which are a conduit for tear drainage.

HISTOLOGY

In all three species, the eyelids consist of four layers (from outer to inner): skin, skeletal muscle, tarsus, and palpebral conjunctiva. The external eyelid is covered by a thin keratinizing (cornified) stratified squamous epithelium (Fig. 21.17). Deep to the epidermis and dermis of the anterior eyelid are the skeletal muscle fibers of the orbicularis oculi. Deep to the orbicularis lies the levator palpebrae superioris, a muscle that inserts onto the superior anterior margin of the tarsus to elevate the eyelid. Posterior to these skeletal muscles is a dense plate-like collection of fibrous connective tissue known as the tarsal plate (Fig. 21.17). Within the tarsal plate are multiple sebaceous glands called meibomian glands that empty secretions at the lid margin to contribute a lipid layer to the tear film. The meibomian glands are more numerous in the upper lid than in the lower lid (Fig. 21.18). Additional

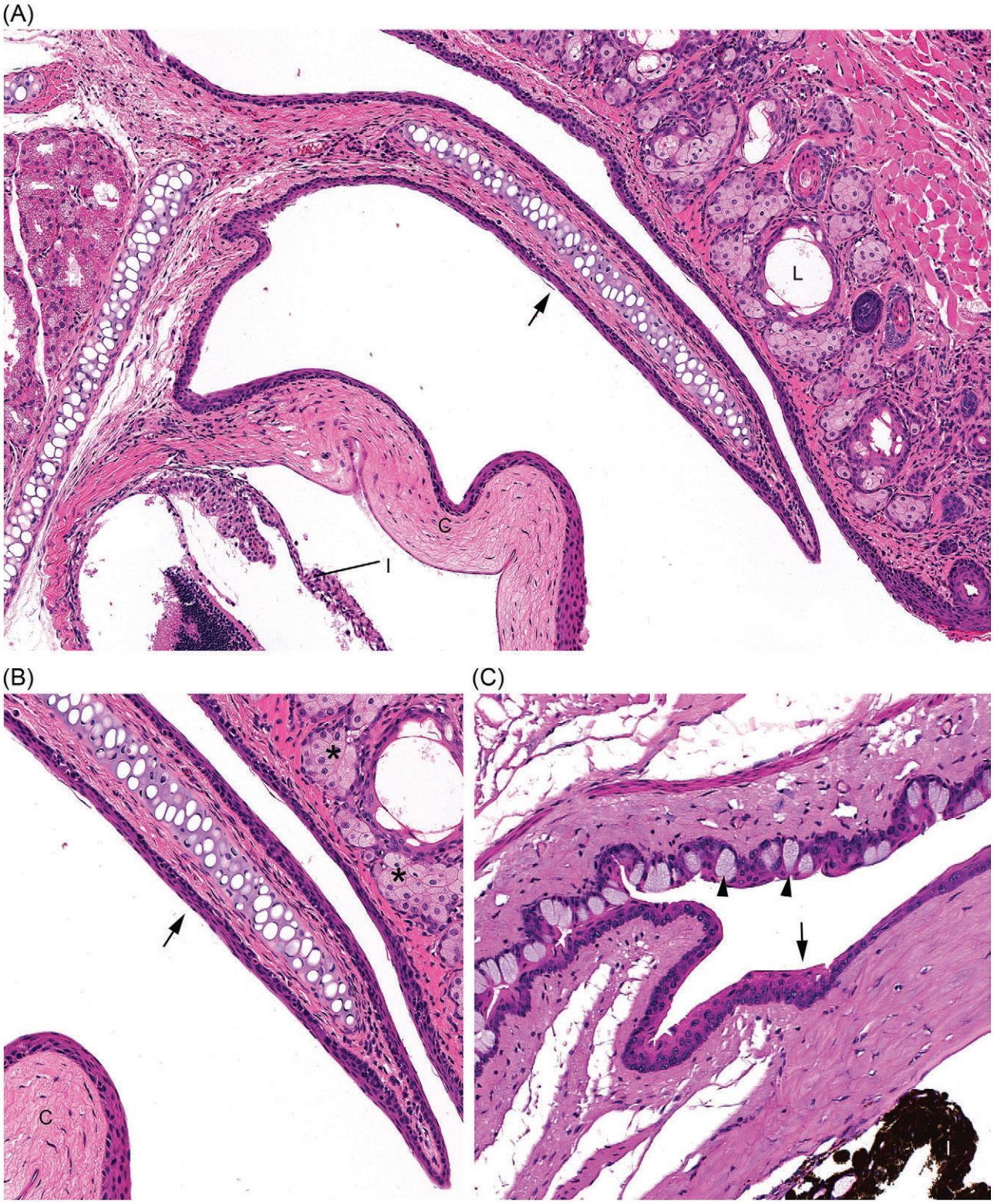

FIGURE 21.16 Rodent (mouse) eye features. (A) The nictitating membrane (arrow) is very small, composed of a thin core of cartilage covered by loose connective tissue, and occasionally seen in histological sections. Note the eyelid with sebaceous (meibomian) glands adjacent to the membrane (L). The cornea (C) is artifactually folded. Note that this is tissue from an albino mouse; the iris (I) is nonpigmented. (B) Rodent (mouse) nictitating membrane (arrow) and sebaceous glands of the palpebra (meibomian, asterisks). Cornea (C) is indicated. (C) Rodent (mouse) conjunctiva. The conjunctiva is similar between the three species. The conjunctiva is a stratified epithelium, noted for abundant goblet cells (arrowheads) which are large and pale-staining. Note the lack of goblet cells at the limbus (arrow). Tissue from a pigmented mouse, note the dark iris (white I).

Need-to-know

- Humans have a medial fold of conjunctiva called the plica semilunar is that is thought to be a vestigial nictitating membrane.
- The conjunctiva is similar among the species.

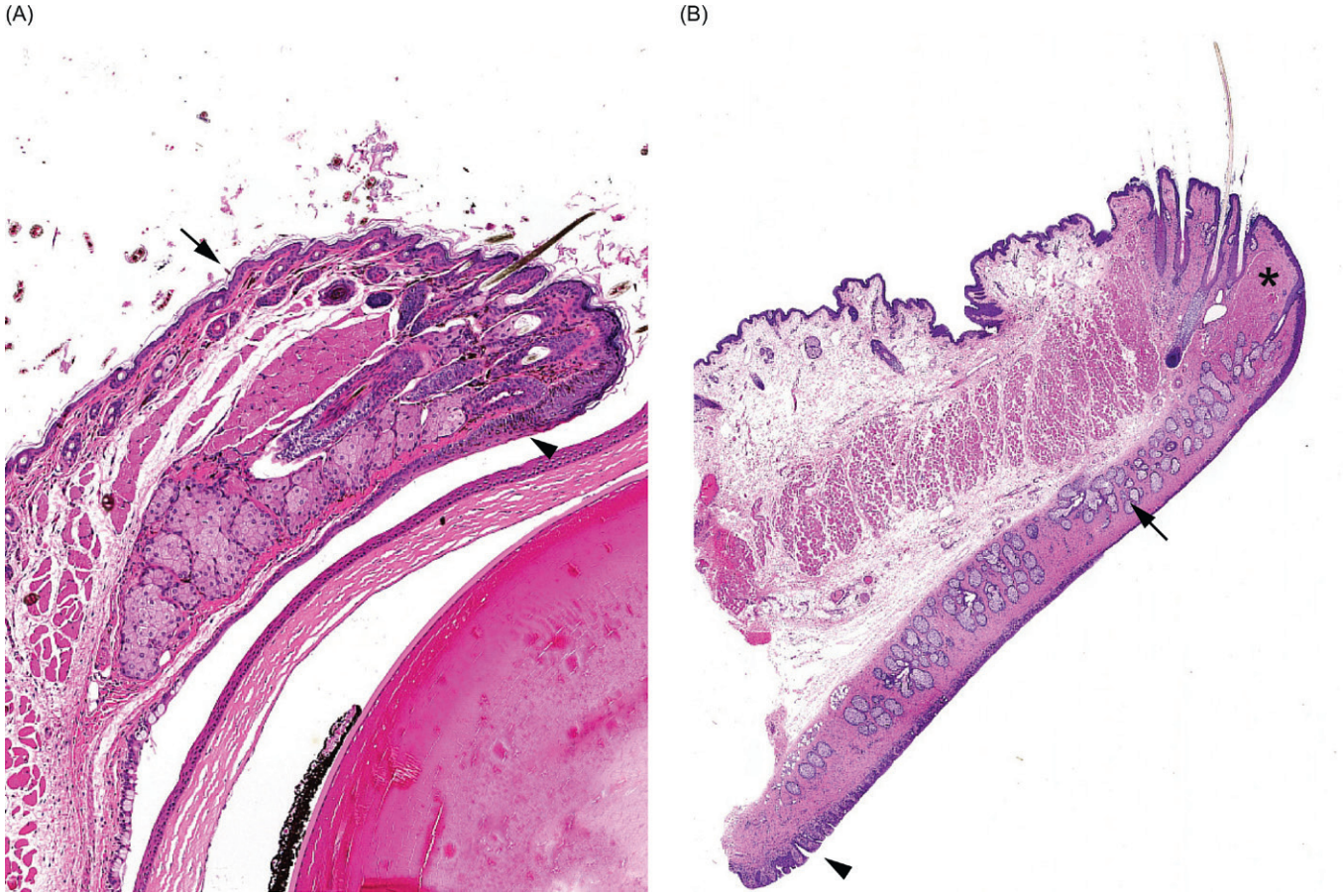

FIGURE 21.17 Eyelid. (A) Rodent (mouse). In all three species, the external eyelid is covered by a thin cornified stratified squamous epithelium (arrow) that transitions to the noncornified palpebral mucosa at the mucocutaneous junction (arrowhead) located anterior to the sebaceous glands. Tissue from a mouse. (B) Human. Note the prominent tarsal plate (arrow) with embedded sebaceous glands. The gray line, the muscle of Riolan (asterisk), is absent in rodents. The mucocutaneous junction (arrowhead) is indicated.

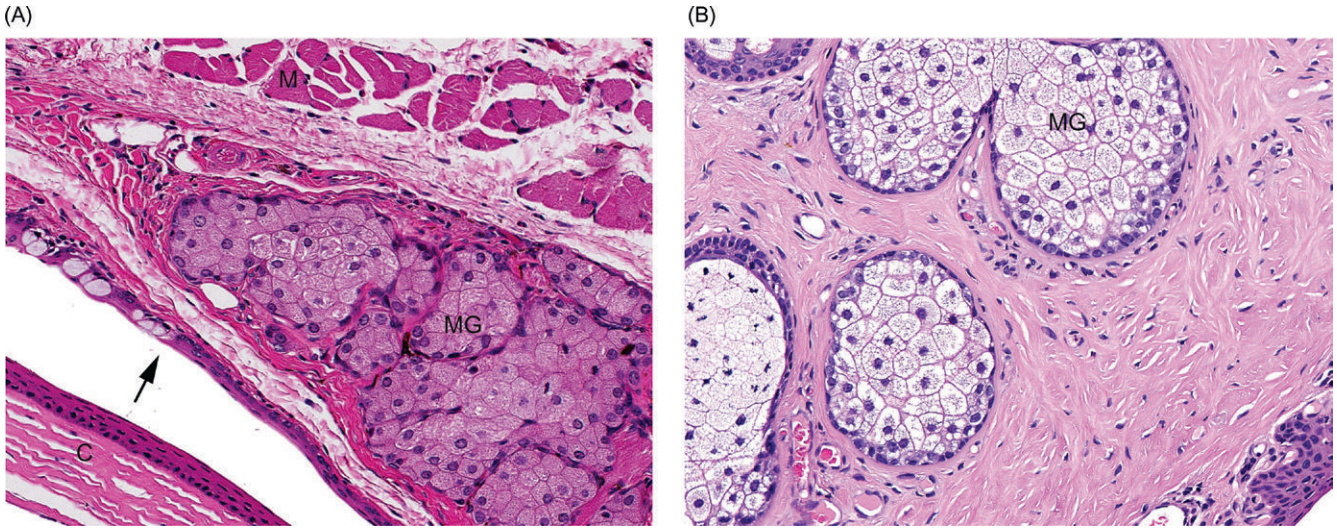

FIGURE 21.18 Meibomian glands. (A) Rodent (mouse). Meibomian glands (MG) are embedded within a dense connective tissue. Note the transition from palpebral noncornified epithelium to the conjunctiva with numerous goblet cells (arrow). Cornea (C) and palpebral muscles (M) are indicated. (B) Human. Notice that—as with other human tissues—the connective tissue stroma is much more prominent than in rodents.

Need-to-know

- In rodents the mucocutaneous junction occurs anterior to the Meibomian gland orifices, which open onto conjunctiva.

sebaceous glands of Zeis exist more anteriorly; these connect to the cilia at the eyelid margin. Rodents have meibomian and glands of Zeis; they lack eccrine sweat and lacrimal glands seen within the palpebral of humans. Deep to the tarsal plates is the palpebral conjunctiva. As described above, the conjunctival epithelium has goblet cells that provide the mucin layer to the tear film.

Lacrimal Gland and Drainage System

GROSS ANATOMY

The lacrimal glands are eccrine glands responsible for the bulk of aqueous tear production. Rodents have two paired lacrimal glands. The smaller is the intraorbital gland, located superficially at the lateral canthus, where both the lacrimal ducts open, as well as the Harderian gland. The larger rodent exorbital lacrimal gland is located at the anteroventral base of the ear adjacent to the parotid salivary gland and is often seen in histological sections of salivary glands (see Chapter 8: Salivary Glands). In humans, the lacrimal gland is located at the superotemporal aspect of the orbit and consists of two contiguous lobes: a larger and more superficially located orbital lobe and a smaller palpebral lobe. The lacrimal gland ducts from the larger orbital lobe pass through and join with ducts from the palpebral lobe prior to emptying into the superior fornix. In all three species, the tears flow across the ocular surface and drain via punctal openings at the medial lid margin. The fluid within the nasolacrimal sac passes down the nasolacrimal duct before emptying into the inferior meatus of the nose in all three species. The tear film is composed of three primary components: lipid, aqueous, and mucin components produced by meibomian glands, lacrimal glands, and goblet cells, respectively. Rodents and humans have similar meibomian lipidomes.

HISTOLOGY

The lacrimal gland consists of acinar cells and myoepithelial cells (Fig. 21.19). The cuboidal acinar cells are arranged in lobules that line the lumen of the gland, whereas the myoepithelial cells contain flattened nuclei and surround the acinar cells and the ducts. Human acinar cells have a characteristic basophilic granular cytoplasm. Rodent acinar cells have basophilic basilar cytoplasm with pale-staining apical regions and moderate nuclear pleomorphism that may increase with age. The rodent, especially the rat, exorbital lacrimal gland tends to have nuclear atypia.

The lacrimal drainage systems are similar in all three species and are located inferonasal to the optic globe. The lacrimal puncta and canaliculi are lined by noncornified stratified squamous epithelium. The substantia propria consists of both collagenous and elastic tissue. The lacrimal sac is lined by pseudostratified columnar epithelium with goblet cells and occasional cilia. The lacrimal sac wall is highly vascularized

The Developing Eye

Mammalian ocular development requires orchestrated interaction between three embryonic tissue sources—neural ectoderm, surface ectoderm, and periocular mesenchyme (including neural crest-derived tissue). Rodents are frequent animal models of human eye development. Ocular development is similar across mice, rats, and humans; however, the main difference is that rodents experience a relatively greater period of neonatal ocular development, while humans are born with more developed eyes. Similar morphologic milestones can be observed across human and rodent development, with the human eye having reached a comparably more advanced stage of development at birth. In humans, eyelid closure is complete by week 8, and eyelids reopen by week 28. Retinal lamination is complete by week 30, with formed inner and out photoreceptor segments at birth. Foveal cone

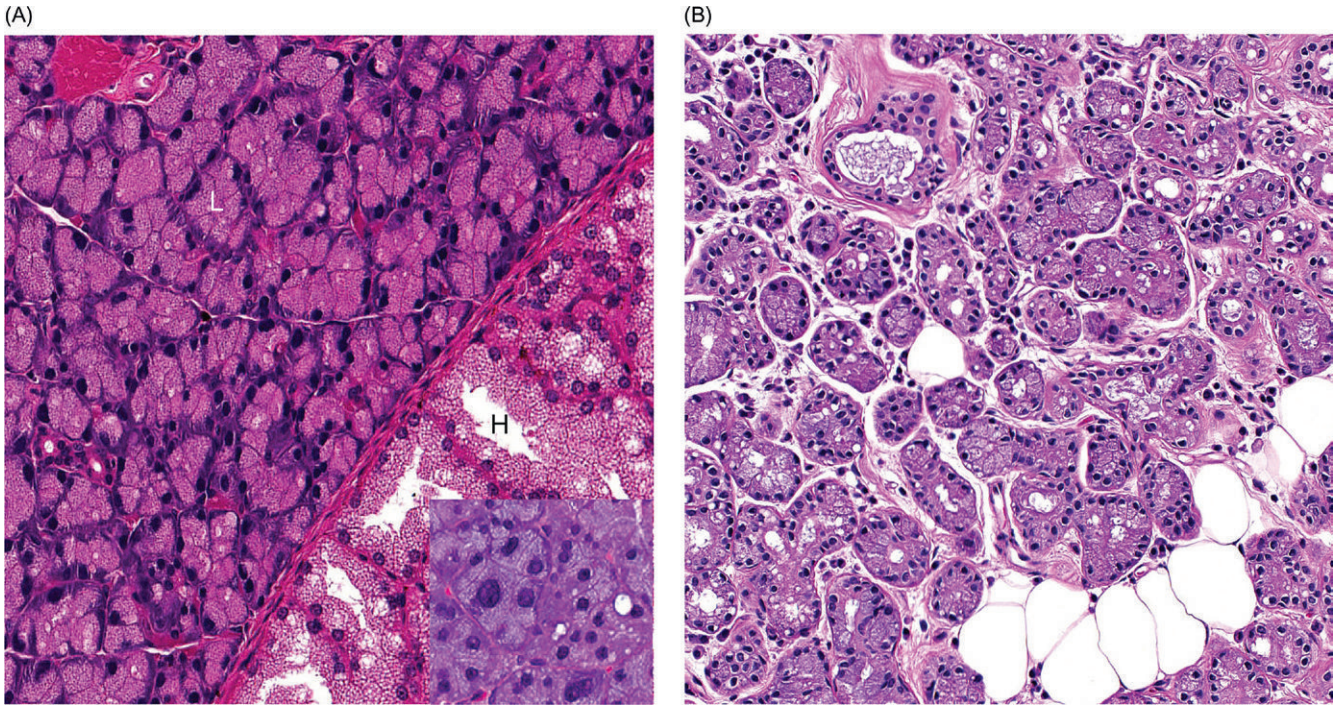

FIGURE 21.19 Lacrimal gland. (A) Rodent (mouse) intraorbital lacrimal gland (L) and Harderian glands (H). Rodents have an additional exorbital lacrimal gland that is adjacent to the salivary glands. Inset shows marked atypia karyo- and cytomegaly in a rat exorbital lacrimal gland. (B) Human lacrimal gland is an eccrine gland. The cuboidal acinar cells are arranged in lobules and have a characteristic basophilic granular cytoplasm. The clear areas are adipose tissue. Inset source: Suttie et al.: *Boorman's pathology of the rat: reference and atlas*, ed 2, New York, 2017, Academic Press. Used by permission from Elsevier.

Need-to-know

- Rodents have two lacrimal glands: intra- and exorbital.

development continues through childhood. The kinetics of ocular development is mostly described for mice. In mice (Fig. 21.20), the first visible sign of eye field development is the formation of bilateral indentations (optic pits) in the prospective forebrain at embryonic (E) days 7–8. This is followed by bilateral evagination of the walls of the diencephalon toward the overlying ectoderm to form the optic vesicle (E8–9.5). On contact with the overlying ectoderm, invagination of the optic vesicle begins, until the inner layer apposes its external layer to form the optic cup (E10–11). The inner layer is fated to become the neurosensory retina, and the outer layer the RPE. An additional invagination occurs in the ventral aspect of the optic vesicle to generate the optic or choroidal fissure, which provides a conduit for retinal axons (fated to become the optic nerve) and the hyaloid artery (the precursor to the retinal artery). The lens placode invaginates from the overlying ectoderm and pinches off to form the lens vesicle (E10–11). Primary and secondary lens fibers develop within the lens placode, and the hyaloid vasculature grows through the optic fissure to invest the posterior lens (beginning at E11.5). Development of different retinal cell types occurs in two waves: ganglion cells, horizontal cells, cone photoreceptors, and a subset of amacrine cells develop during the first wave of retinogenesis (E11–E18). At birth, retinal cell layers comprise a layer of ganglion cells and a thick outer neuroblastic layer. Further lamination of the retina to form distinct outer and inner nuclear layers occurs postnatally (second wave of retinogenesis P0–P7) with development of rod photoreceptors, bipolar interneurons, and Muller glial cells. The eyelids begin to grow at E15.5, fuse by E17.5, and

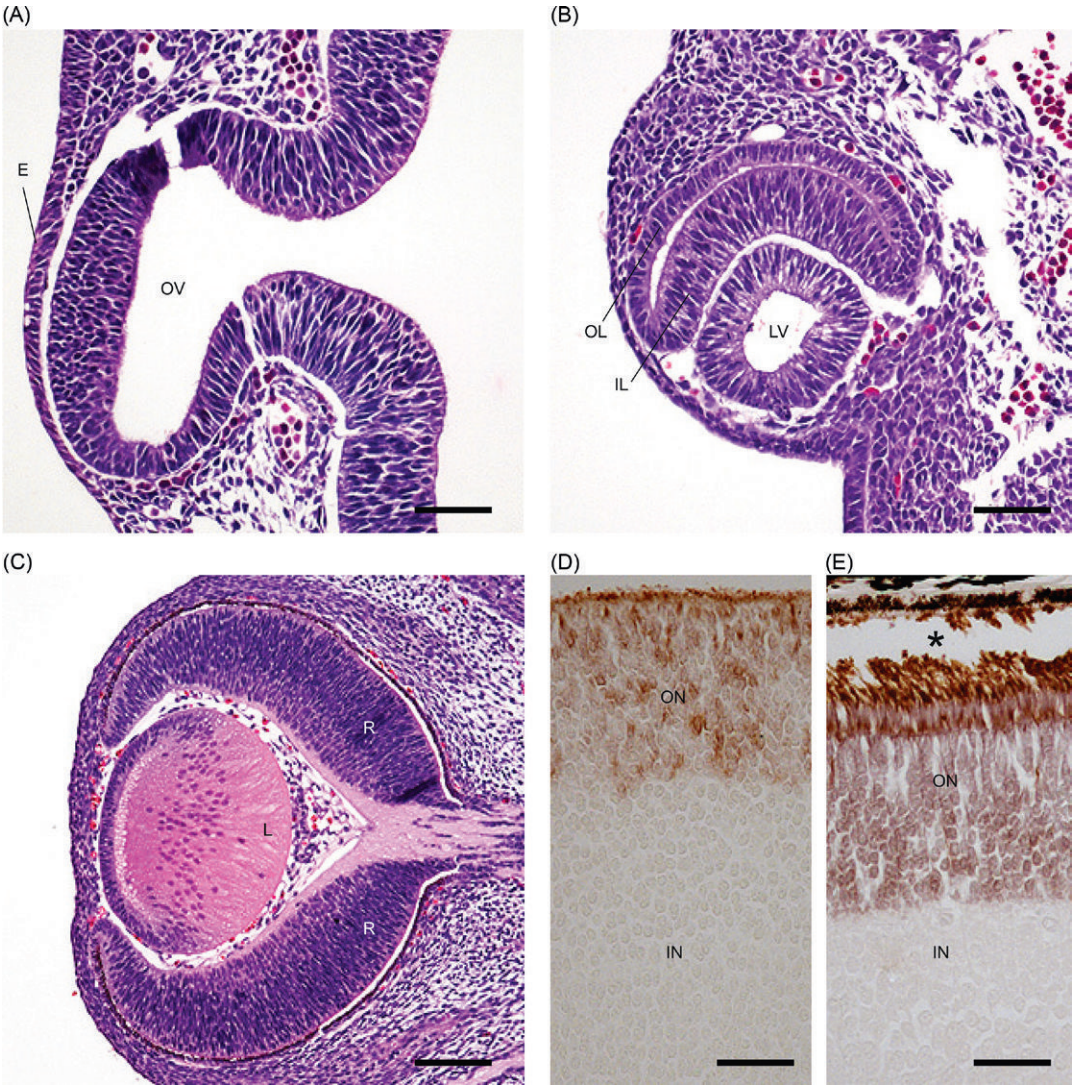

FIGURE 21.20 Ocular development in the rodent (mouse). (A) Bilateral evagination of the optic vesicle (OV) toward the overlying ectoderm (E) begins by E7. (B) On contact with the overlying ectoderm, invagination of the optic vesicle begins until the inner layer apposes its external layer. The inner layer is fated to become the neural retina, and the outer layer the RPE. The lens placode invaginates from the overlying ectoderm and pinches off to form the lens vesicle (LV). (C) Primary and secondary lens fibers develop within the lens placode, and the hyaloid vasculature grows through the optic fissure to invest the posterior lens (L). Inner and outer retinal (R) layers are indistinguishable. (D, E) Visual pigment expression. Rhodopsin expression is first evident at postnatal (PN) day 5 (D), coincident with differentiation of outer (ON) and inner (IN) nuclear layers. At this stage, cell bodies have formed, but inner and outer segments are vestigial. By PN 13, the retina nears full development, and rhodopsin immunoreactivity is evident in fully formed inner and outer segments (the outer segments are artifactually fragmented; asterisk). Bar = 50 μm (A–C); 20 μm (D, E). Hematoxylin and eosin (A–C), rhodopsin immunostaining (D, E).

Need-to-know

- Similar developmental milestones occur in humans and rodents; however, much of the postnatal development seen in rodents has already occurred *in utero* in humans.

reopen by PN 10. This process is essential for normal development of the cornea, as well as ocular adnexal tissues. The periocular mesenchyme is of both neural crest and mesoderm origin and gives rise to stroma of the iris and cornea, corneal endothelium, TM, Schlemm's canal, ciliary body, extraocular muscles, sclera, and ocular blood vessels.

FURTHER READING

Albrecht May C: Comparative anatomy of the optic nerve head and inner retina in non-primate animal models used for glaucoma research. *Open Ophthalmol J* 2:94–101, 2008.

American Academy of Opthalmology *Basic and clinical science course, Section 2: Fundamentals and principles of ophthalmology*, San Francisco, CA, 2009, American Academy of Opthalmology.

American Academy of Opthalmology *Basic and clinical science course, Section 4: Ophthalmic pathology and intraocular tumors*, San Francisco, CA, 2009, American Academy of Opthalmology.

American Academy of Opthalmology *Basic and clinical science course, Section 7: Orbit, eyelids, and lacrimal system*, San Francisco, CA, 2009, American Academy of Opthalmology.

Bisaria KK, Bisaria SD: The third eyelid in the albino rats (a histological study). *Indian J Ophthalmol* 26(2):25–28, 1978. PubMed PMID: 721238.

Chalupa LM, Williams RW: *Eye, retina, and visual system of the mouse*, Cambridge, MA, 2008, MIT Press.

Choi WJ, Zhi Z, Wang RK: In vivo OCT microangiography of rodent iris. *Opt Lett* 39(8):2455–2458, 2014.

Frame NJ, Burkat CN: Identifying an appropriate animal model for the nasolacrimal drainage system. *Ophthal Plast Reconstr Surg* 25(5):354–358, 2009.

Gillum W: Mechanisms of accommodation in vertebrates. *Ophthalmic Semin* 1(3):253–286, 1976.

Heavner W, Pevny L: Eye development and retinogenesis. *Cold Spring Harb Perspect Biol* 4(12), 2012.

Johansson JO: The lamina cribrosa in the eyes of rats, hamsters, gerbils and guinea pigs. *Acta Anat (Basel)* 128(1):55–62, 1987.

Maronpot RR, Boorman GA, Gaul BW: *Pathology of the mouse: reference and atlas*, Vienna, IL, 1999, Cache River Press.

May CA, Lütjen-Drecoll E: Morphology of the murine optic nerve. *Invest Ophthalmol Vis Sci* 43(7):2206–2212, 2002.

McMenamin PG, al-Shakarchi MJ: The effect of various levels of intraocular pressure on the rat aqueous outflow system. *J Anat* 162:67–82, 1989.

Meng ID, Barton ST, Mecum NE, et al: Corneal sensitivity following lacrimal gland excision in the rat. *Invest Ophthalmol Vis Sci* 56(5):3347–3354, 2015.

Pachter BR, Davidowitz J, Breinin GM: Morphological fiber types of retractor bulbi muscle in mouse and rat. *Invest Ophthalmol* 15(8):654–657, 1976.

Pazos M, Yang H, Gardiner SK, et al: Rat optic nerve head anatomy within 3D histomorphometric reconstructions of normal control eyes. *Exp Eye Res* 139:1–12, 2015.

Reichard M, Hovakimyan M, Wree A, et al: Comparative in vivo confocal microscopical study of the cornea anatomy of different laboratory animals. *Curr Eye Res* 35(12):1072–1080, 2010.

Remtulla S, Hallett PE: A schematic eye for the mouse, and comparisons with the rat. *Vision Res* 25(1):21–31, 1985.

Santaolalla-Montoya F, Martinez-Ibargüen A, Sánchez-Fernández JM, et al: Principles of cranial base ossification in humans and rats. *Acta Otolaryngol* 132(4):349–354, 2012.

Smith RS, John SWM, Nishina PM, editors: *Systematic evaluation of the mouse eye: anatomy, pathology, and biomethods*, Boca Raton, FL, 2001, CRC Press.

Spencer RF, Porter JD: Biological organization of the extraocular muscles. *Prog Brain Res* 151:43–80, 2006.

Stanka P, Bargsten G, Sahlmann B: On the formation and degradation of melanosomes in smooth muscle cells: electron microscopic investigation on the M. sphincter pupillae of the rat. *Pigment Cell Res* 1(5):358–360, 1988.

Suttie AW, Leininger JR, Bradley AE: *Boorman's pathology of the rat*, ed 2, San Diego, CA, 2017, Academic Press.

Wang W-H, Cameron Millar J, Pang I-H, et al: Noninvasive measurement of rodent intraocular pressure with a rebound tonometer. *Invest Ophthalmol Vis Sci* 46(12):4617–4621, 2005.

Wobmann PR, Fine BS: The clump cells of Koganei. A light and electron microscopic study. *Am J Ophthalmol* 73(1):90–101, 1972.

Yücel YH: Discovery of lymphatics in the human eye and implications. *Can J Ophthalmol* 45(2):115–117, 2010.

Yu Wai Man CY, Chinnery PF, Griffiths PG: Extraocular muscles have fundamentally distinct properties that make them selectively vulnerable to certain disorders. *Neuromuscul Disord* 15(1):17–23, 2005.

Zhi Z, Cepurna WO, Johnson EC, et al: Impact of intraocular pressure on changes of blood flow in the retina, choroid, and optic nerve head in rats investigated by optical microangiography. *Biomed Opt Express* 3(9):2220–2233, 2012. Epub 2012 Aug 24.

SPECIAL SENSES: EAR 22

PIPER M. TREUTING AND SUZANNE M. DINTZIS
University of Washington School of Medicine, Seattle, WA, United States

RANI SELLERS
Pfizer Drug Safety Research and Development, New York, NY, United States

Introduction

The ear of mice, rats, and humans detects sound and maintains balance. In mammals, this "stato-acoustic" system is traditionally divided into three structural units: the external, middle, and inner ear (Table 22.1; Figs. 22.1 and 22.2). The external and middle ear are designed to receive, transmit, and amplify sound. The membranous portion of the inner ear houses the sensory receptors for both hearing and balance. Sensory receptors in all three species have similar histologic design with some minor variations.

External Ear

GROSS ANATOMY

The external ear is composed of the pinna (also known as the auricle) and the external acoustic meatus (external ear canal) (Figs. 22.1 and 22.2) and is designed to funnel sounds to the tympanic membrane, which separates the external and middle ear. The rodent pinna is relatively thin and less folded compared to that of humans but is otherwise similarly structured. In mice, the pinna is located on the lateral aspect of the head and is roughly cone-shaped, with few folds on the conchal surface (Fig. 22.1A), and has a greater surface area relative to body size than rats. Hairs cover both sides of the pinna, with shorter, less dense hairs found on the conchal surface and proximal to the external acoustic meatus. The human pinna has complex cartilage folds with fewer hairs than rodents (Fig. 22.1B). Rodents have a unique gland, Zymbal's gland, located subcutaneously at the base of the ear (Fig. 22.3). Zymbal's gland is grossly visible in rats but not mice. Rat Zymbal's gland is 3–5 mm in diameter, comprises 3–4 lobes, and is located anteroventrally to the base of the ear (Fig. 22.3A). It has been noted that beneath Zymbal's gland in rats are two smaller sebaceous glands, which some include as part of Zymbal's gland. The external acoustic (or auditory) meatus (EAM) in mice is approximately 6.25 mm and has a slight rostral curve to its canal as it approaches the tympanic membrane. In rats, the EAM is approximately 1–1.5 cm long. In humans, the EAM is S-shaped and approximately 2.5 cm long.

HISTOLOGY

The pinna in all three species is covered by cornified skin and hair, sebaceous glands, supporting elastic cartilage, thin connective tissue containing blood and lymph vessels, and nerves.

Comparative Anatomy and Histology. DOI: http://dx.doi.org/10.1016/B978-0-12-802900-8.00022-1
© 2018 Elsevier Inc. All rights reserved.

TABLE 22.1 The Ear

Feature	Rodent	Human
	Gross	
Pinnae/auricle	Relatively smooth inner conchal surface; few surface folds; on lateral aspect of head. Rat ears are smaller relative to body size than mouse ears.	Complicated conchal surface
External acoustic (auditory) meatus	Mouse: Approximately 6.25 mm; slight rostral curve to canal; Rat: Approximately 1–1.5 cm	Approximately 2.5 cm; S-shaped
Zymbal's gland	At base of auricular cartilage; Mouse: not grossly visible; Rat: Grossly visible	Not present
Middle ear/tympanic cavity	Bulla expansion of the temporal bone; sutures are fibrous; epitympanum, mesotympanum, hypotympanum divisions	Within space in petrous temporal bone
Tympanic membrane	Mouse: Elliptical; ~1–1.13 mm diameter; surface area ~3–4 mm^2; two portions—left larger pars tensa, right smaller pars flaccida; Rat: ~1.87–2 mm diameter; ~11 mm^2 surface area with similar pars tensa and pars flaccida	Diameter ~9 mm; surface area ~64 mm^2; outer surface concave
Inner ear	Petrous part of temporal bone	Similar to rodent
Ossicular system	Microtype (restricted mobility)	Freely mobile (synovial joints)
Malleus	Orbicular apophysis on head and gonial bony fusion between transverse process of malleus to tympanic ring contribute to microtype system. Superior ligament aids suspension. Rat: Malleus long process that bends sharply at the manubrium	Attached to wall of middle ear by ligament
Incus	Synchondrosis with malleus; posterior ligament aids suspension	Attached to wall of middle ear by ligament
Stapes	Diarthrosis with incus	Similar to rodent
Mastoid cells (a network of intercommunicating air cells composed of trabecular bone)	Mouse: not present Rat: Present	Present
Cochlea	Mouse: 2.5 bony spirals around modiolus; Rat: 2.5 spirals around modiolus, ~11 mm in length	2.75 bony spirals, 30–35 mm in length
Auditory (Eustachian) tube	Connects middle ear to nasopharynx	Similar to rodent
	Histologic	
Auricle	Haired epidermis; sebaceous glands; supporting elastic cartilage; well-vascularized	Fewer hairs; otherwise similar to rodent
External acoustic (auditory) meatus	Few hairs; sebaceous and ceruminous glands	Similar to rodent
Middle ear/tympanic cavity	Ciliated and secretory mucosa; squamous to cuboidal over epitympanum	Similar to rodent
Tympanic membrane	Three layers: outer epithelium continuous with external meatus, middle lamina propria, inner respiratory epithelium	Similar to rodent
Pars tensa	Lamina propria has abundant collagen, microcapillaries, trigeminal nerve endings	Lower four-fifths of tympanic membrane, organized core of connective tissue
Pars flaccida	Lamina propria has more elastin; otherwise similar to pars tensa	Upper one-fifth of tympanic membrane; lacks a middle fibrous layer
Cochlea		
Scala vestibule	Perilymph-filled	Similar to rodent
Scala tympani	Perilymph-filled	Similar to rodent
Scala media = cochlear duct	Endolymph-filled	Similar to rodent
Reisner's (vestibular) membrane	Surfaces lined by simple squamous epithelium; fibrous substantia propria anchored at the annulus fibrosis continuous with periosteum of tympanic sulcus; separates s. media from s. vestibuli	Similar to rodent
Organ of Corti		
Sensory hair cells	Inner single row; outer three or more layers; detects sound	Similar to rodent
Vestibular system	Three semicircle canals	Similar to rodent
Utrical	Sensory cells in macule	Similar to rodent
Saccule	Sensory cells in macule	Similar to rodent
Crista ampullaris	Sensory hair cells and supportive cells; detects equilibrium	Similar to rodent
Auditory canal (Eustachian tube)	Ciliated pseudostratified epithelium	Similar to rodent

(Continued)

TABLE 22.1 The Ear (Contined)

Feature	Rodent	Human
	Cellular	
Crista ampullaris		
Type I sensory hair cells	Neuroepithelial hair cells; flask-shaped; 40–80 stereocilia	Similar to rodent
Type II sensory hair cells	Neuroepithelial hair cells; cylindrical; 40–80 stereocilia	Similar to rodent
Supporting cells of ampulla	Tall columnar; synthesize matrix	Similar to rodent
Membrane	Cupula	Similar to rodent
Macula utriculi and saccule		
Type I sensory hair cells	Similar to cristae	Similar to rodent
Type II sensory hair cells	Similar to cristae	Similar to rodent
Supporting cells	Similar to cristae	Similar to rodent
Membrane	Statoconial/otolithic membrane; statoconia/otoliths ($CaCO_3$ crystals) and supporting gelatinous matrix	Similar to rodent
Organ of Corti		
Type I sensory hair cells	Neuroepithelial hair cells; flask-shaped; 40–80 stereocilia	Similar to rodent
Type II sensory hair cells	Neuroepithelial hair cells; cylindrical; 40–80 stereocilia	Similar to rodent
Supporting cells	Support cells: border cells, inner and outer pillar cells, inner and outer phalangeal (Deiter's) cells, outer limiting (Hensen) cells, external supporting (Claudius) cells	Similar to rodent
Membrane	Tectorial membrane; gelatinous structure overlying hair cells attaches to the spiral limbus	Similar to rodent

The external acoustic meatus in rodents and humans is lined by similar cornified epidermis transitioning to the tympanic membrane at the middle ear (Fig. 22.2). Zymbal's gland is a modified sebaceous gland and secretes directly into the auditory canal (Fig. 22.3B and C), also known as the Eustachian tube. In humans, waxy cerumen is produced by modified apocrine (ceruminous) glands, which secrete either directly onto the skin surface or into the sebaceous glands of the external meatus (Fig. 22.3D).

Middle Ear

Gross Anatomy

The middle ear resides within the tympanic cavity, also known as the bulla, an air-filled expansion of the petrous portion of the temporal bone (Fig. 22.2). The middle ear houses the three ossicles; the small bones that transmit vibration of sound (see below). In humans, a network of intercommunicating spaces composed of trabecular bone, termed mastoid air cells, lie within the temporal bone underlying the middle ear epithelium. While rats have mastoid air cells, mice do not. The middle ear is separated from the external ear by the tympanic membrane, which converts sound waves into mechanical vibrations through the ossicles. The tympanic membrane is divided into the pars tensa and pars flaccida. Its surface area in mice is approximately 3–4 mm^2, ~11 mm^2 in the adult rat, and ~64 mm^2 in humans. In rodents, the pars tensa makes up the bulk of the tympanic membrane.

The three ossicles (Fig. 22.4) are the malleus, which is directly attached to the tympanic membrane; the incus, and the stapes, which transmit vibrations from the tympanic membrane to the oval window of the cochlea. Rodents have a "microtype" ossicle system whereas humans have a "freely mobile" ossicle system in which all three ossicles articulate with one another through synovial joints (diarthrosis), allowing relatively free motion between bones. The rodent microtype ossicle system involves relatively restricted movement between the ossicles provided by the orbicular apophysis (a bony nodule) near the base of the manubrium (the elongated portion of the malleus attached to the tympanic membrane). Unlike in humans, the rat malleus long process bends at the manubrium at a near 90° angle. In all three species, the manubrium of the malleus attaches to the tympanic membrane and the stapes base. Interestingly, rats have a gap in the tympanic

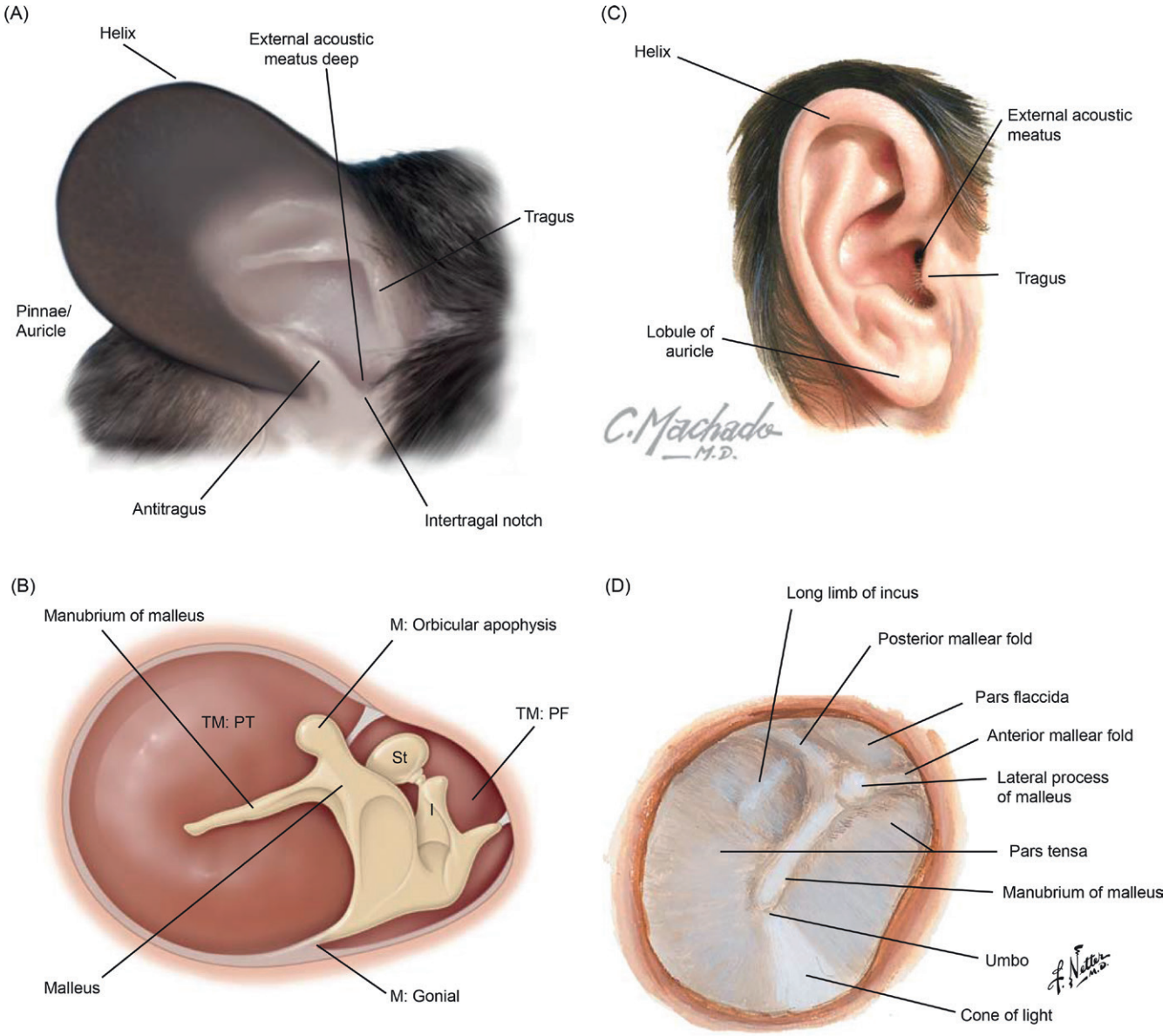

FIGURE 22.1 Regional anatomy of the external ear and tympanic membrane. (A, B) Rodent (mouse) ear and tympanic membrane (TM). Rodent ears are located laterally on the head. (A) The auricular cartilage has less prominent folds than human auricular cartilage. (B) The ossicles of the middle ear, incus (I), stapes (St), and malleus (M), form a microtype ossicle system. Note that the malleus has a prominent protuberance, the orbicular apophysis, which is in close association with the TM. The two parts of the TM, pars flaccida (TM:PF) and pars tensa (TM:PT), are indicated. The ossicles are suspended by attachments to the tympanic ring by the malleus gonial and superior ligaments and the posterior ligament of the incus. Note that in this artist's rendition the ossicles are accentuated. (C, D) Human ear and tympanic membrane. Sources of A and C, and D © Elsevier, Inc., www.netterimages.com. Source B: Modified after J.F. Willott (ed.): *Auditory Psychobiology of the Mouse*, Charles C. Thomas, Publisher, pp 131–168. © Elsevier, Inc., www.netterimages.com.

Need-to-know

- In rodents the articulation between the malleus and incus is a cartilaginous synchondrosis, whereas in humans, the ossicular articulations are diarthrotic.
- Rodents have a microtype ossicular system, which gives them better high-frequency hearing than humans.

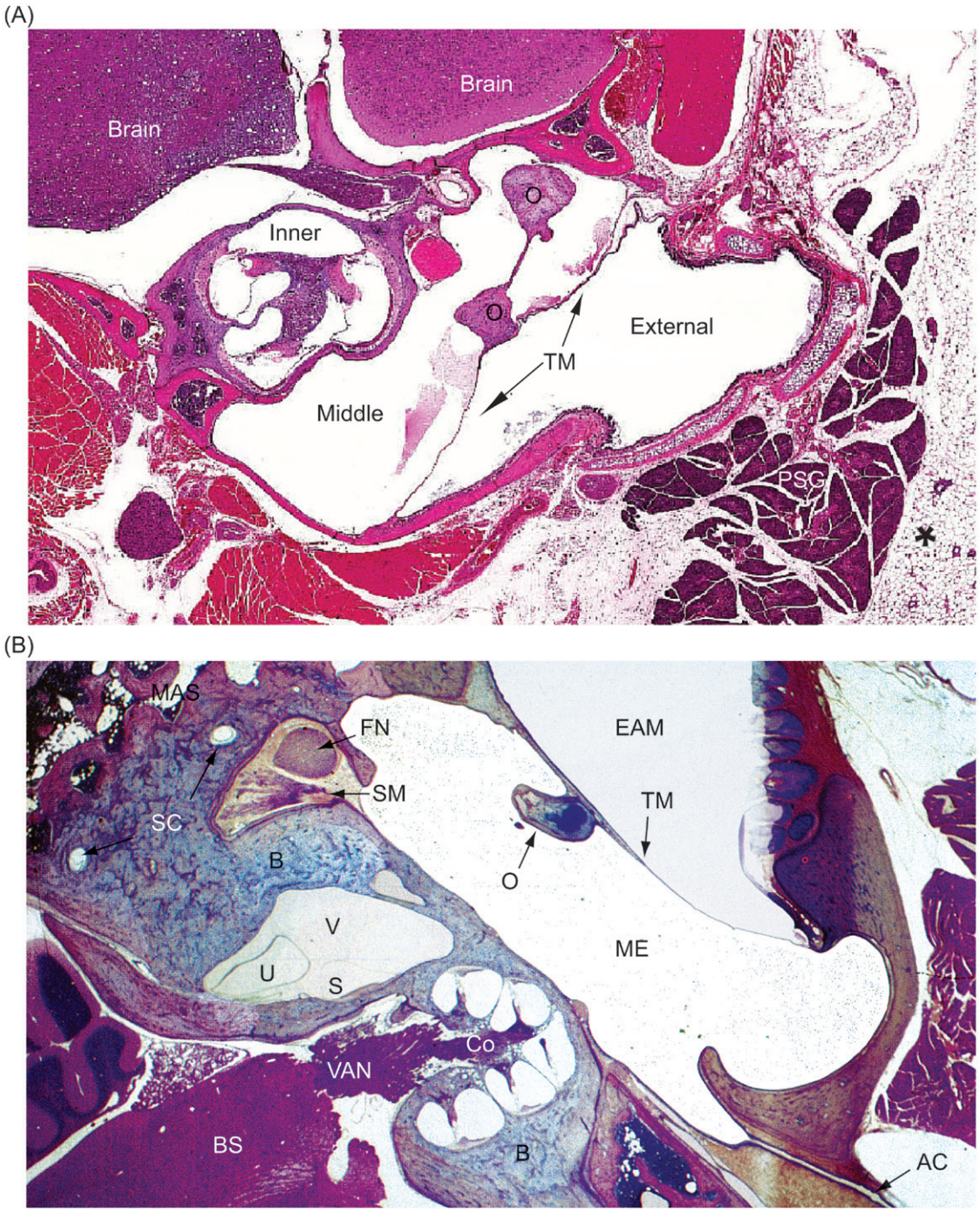

FIGURE 22.2 Subgross regional anatomy of the ear. (A) Rodent (mouse) skull and ear. The middle ear is contained within the bulla, an expansion of the temporal bone. The ear is divided into external, middle, and inner parts. The tympanic membrane (TM) can be identified dividing the eternal from the middle ear. Parotid salivary gland (PSG) and mammary fat pad (asterisk) are indicated. (B) Human ear. This micrograph shows a horizontal section through the external, middle, and inner ear of humans. The middle and inner ear lies within the temporal bone (B). The tympanic membrane (TM) can be seen stretched between the tympanic plate of the temporal bone anteriorly and the lateral part of the petrous temporal bone posteriorly, dividing the external acoustic meatus (EAM) from the cavity of the middle ear (ME). Part of one of the ossicles (O), the handle of the malleus, can be seen attached to the inner aspect of the tympanic membrane. From the anterior aspect of the middle ear chamber, the auditory canal (Eustachian tube; AC) passes forward toward the nasopharynx; in the mastoid part of the temporal bone there are numerous irregular mastoid airspaces (MAS). Near the center of the field is the vestibule of the inner ear (V) containing two delicate membranous structures, the utricle (U) and saccule (S) more anteriorly. Two of the semicircular canals (SC) can be identified deep in the posterior part of the petrous temporal bone. Immediately posterior to the middle ear cavity, the facial nerve (FN) is seen in transverse section as it passes inferiorly; just medial to it lies the stapedius muscle (SM). Anterior to the vestibule, the conical spiral of the cochlea (Co) has been cut in longitudinal section through its central bony axis. From the base of the cochlea, the vestibulo-auditory nerve (VAN) passes toward the brain stem (BS), behind which the cerebellum is easily recognizable. Source: Reprinted from Young et al: *Wheater's functional histology*, ed 5, 2006, with permission from Elsevier.

Need-to-know

- Glands located at or near the base of the ear in rodents include Zymbal's gland and the parotid salivary gland.
- In female rodents the mammary fat pad occasionally may be seen.

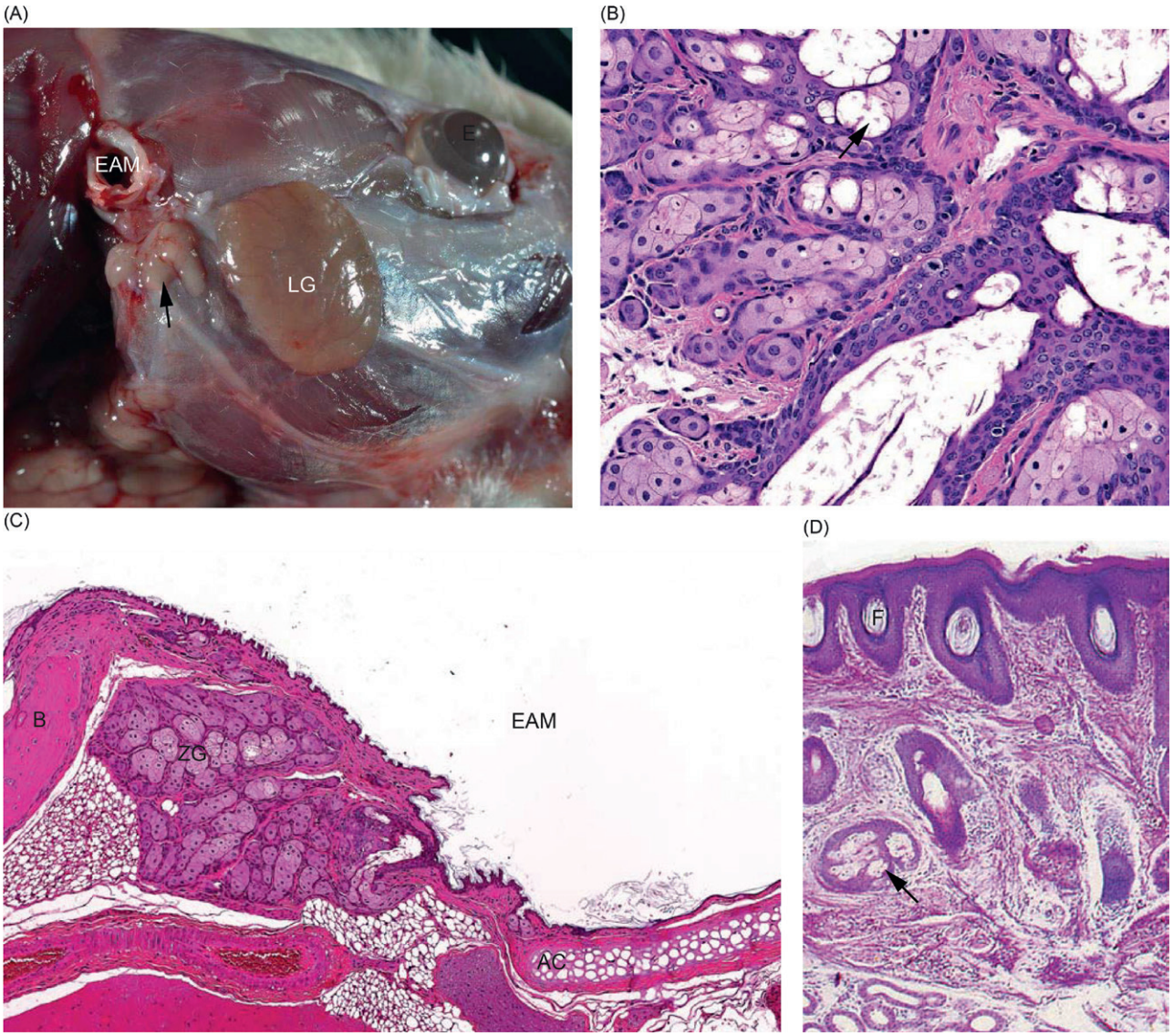

FIGURE 22.3 Zymbal's gland and the external acoustic meatus. (A) Rat regional anatomy. The skin and external pinna have been removed to expose the external acoustic meatus (EAM) and Zymbal's gland (arrow), which surrounds the base of the opening. The large exorbital lacrimal gland (LG) is noted. Photo courtesy of Dr. Krista La Perle. (B) Zymbal's gland in rat. The sebaceous acini secrete into the external meatus via keratinized squamous intralobular and excretory ducts. Enlargement and degeneration of the cells near intralobular ducts (arrow) are normal. (C) Rodent (rat) EAM. The ducts of Zymbal's gland (ZG) empty into the EAM. Auricular cartilage (AC) and bone (B) are indicated. (D) Human EAM. Ceruminous glands (arrow) and hair follicles (F) are indicated. Source: Reprinted from Young et al: *Wheater's functional histology*, ed 5, 2006, with permission from Elsevier.

Need-to-know

- Zymbal's gland is more prominent in rats than in mice.
- Humans do not have a Zymbal's gland.

membrane between the malleus and incus, such that the middle ear is not completely isolated from the external environment. In mice, the malleus and incus are firmly joined by cartilaginous synarthrosis (Fig. 22.4C) and in rat the incus and malleus are formed an articulation and are readily separated. In mice, only the incus-stapes articulation is a true diarthrosis (Fig. 22.4D). The malleus gonial and superior ligament and the posterior ligament of the incus suspend rodent ossicles. Likewise in humans, the malleus and incus are attached to the wall of the middle ear cavity

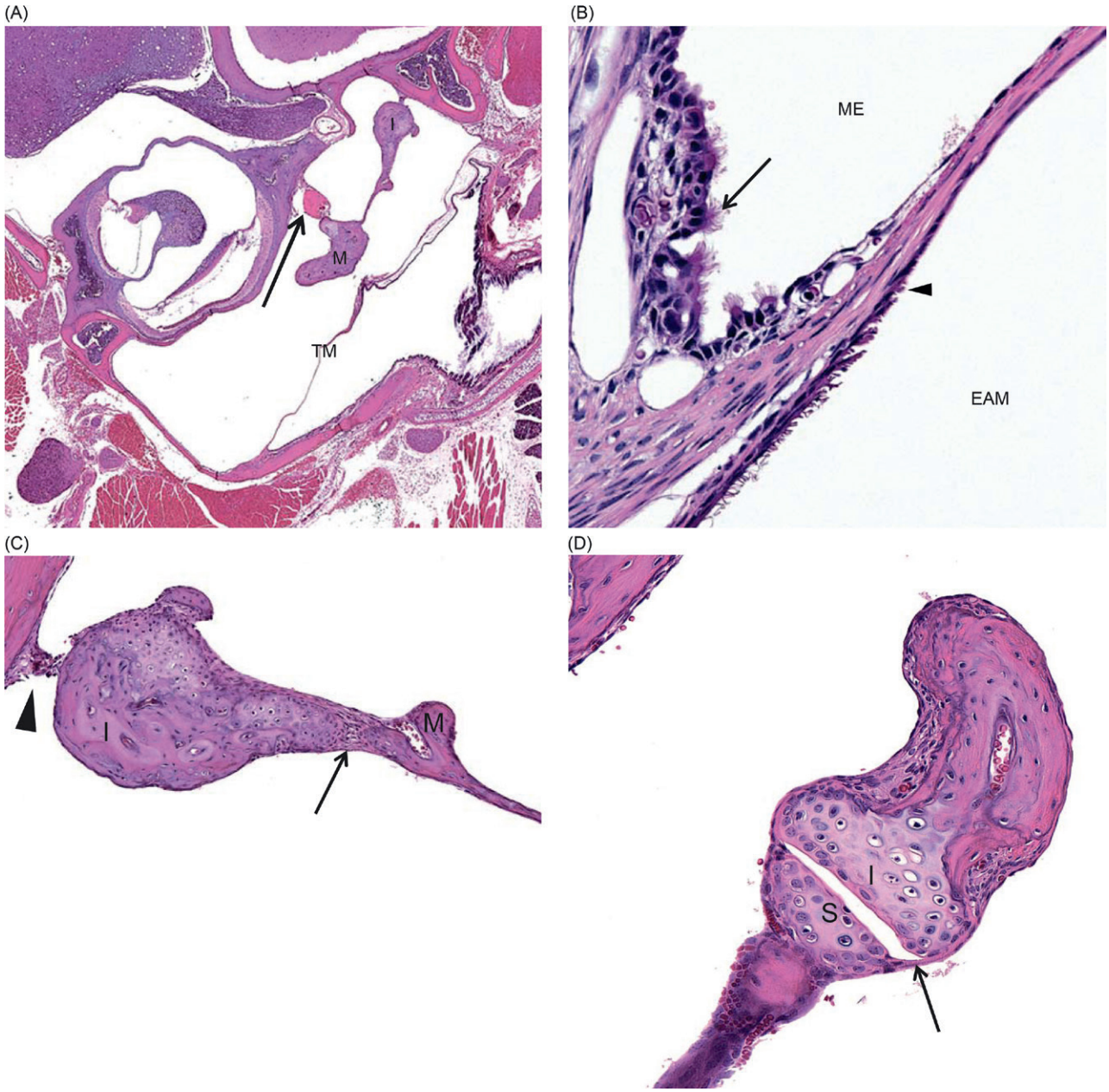

FIGURE 22.4 Rodent (mouse) ear. (A) The tympanic membrane (TM), ossicles (malleus; M), suspensory ligaments, and middle ear muscles (tensor tympani; arrow) are responsible for conducting sound waves. (B) Tympanic membrane. The three layers are indistinct. The external layer is lined by thin squamous epithelium that is continuous with that of the external acoustic meatus (EAM; note exfoliating keratin layers which can resemble cilia; arrowhead) and is supported by a lamina propria. The inner layer is lined by modified respiratory epithelium (arrow indicates ciliated cells) that line the middle ear (ME). (C) Ossicles. The malleus and incus articulate with a synchondrosis (arrow). Malleus (M) and posterior incal ligament (arrowhead) are indicated. (D) Incus (I) and stapes (S). The incudostapedial joint in mice is a true diarthrosis (arrow).

Need-to-know

- The rodent malleus has distinctive morphology, including the orbicular apophysis, near the base of the manubrium of the malleus.
- In humans the ossicle articulations are diarthrotic.
- In rodents the articulation between the malleus and incus is a cartilaginous synchondrosis.
- There is a gap in the tympanic membrane of rats, which allows communication between the external meatus and the middle ear.

by ligaments. In rodents and humans, two skeletal muscles, the tensor tympani and tensor stapedius, contract to adjust membrane tension and to dampen excessive vibration. The tensor tympani muscle inserts into the tympanic membrane and malleus handle, and the tensor stapedius inserts into the stapes bone. In rodents, the stapedial artery courses through the crura of the stapes. The auditory canal (Eustachian tube) connects the middle ear to the pharynx and has both cartilaginous and bony portions; it serves to equilibrate pressure within the middle ear (Fig. 22.5).

HISTOLOGY

In rodents and humans, the tympanic membrane has three layers: thin squamous epithelium, collagenous fibers, and respiratory epithelium. In mice, these are challenging to distinguish on routine histology (Fig. 22.4). The external layer of the tympanic membrane is lined by thin squamous epithelium that is continuous with that of the external ear and is supported by a lamina propria. The central layer is composed of collagenous fibers. The internal tympanic membrane is lined by respiratory epithelium that cover the middle

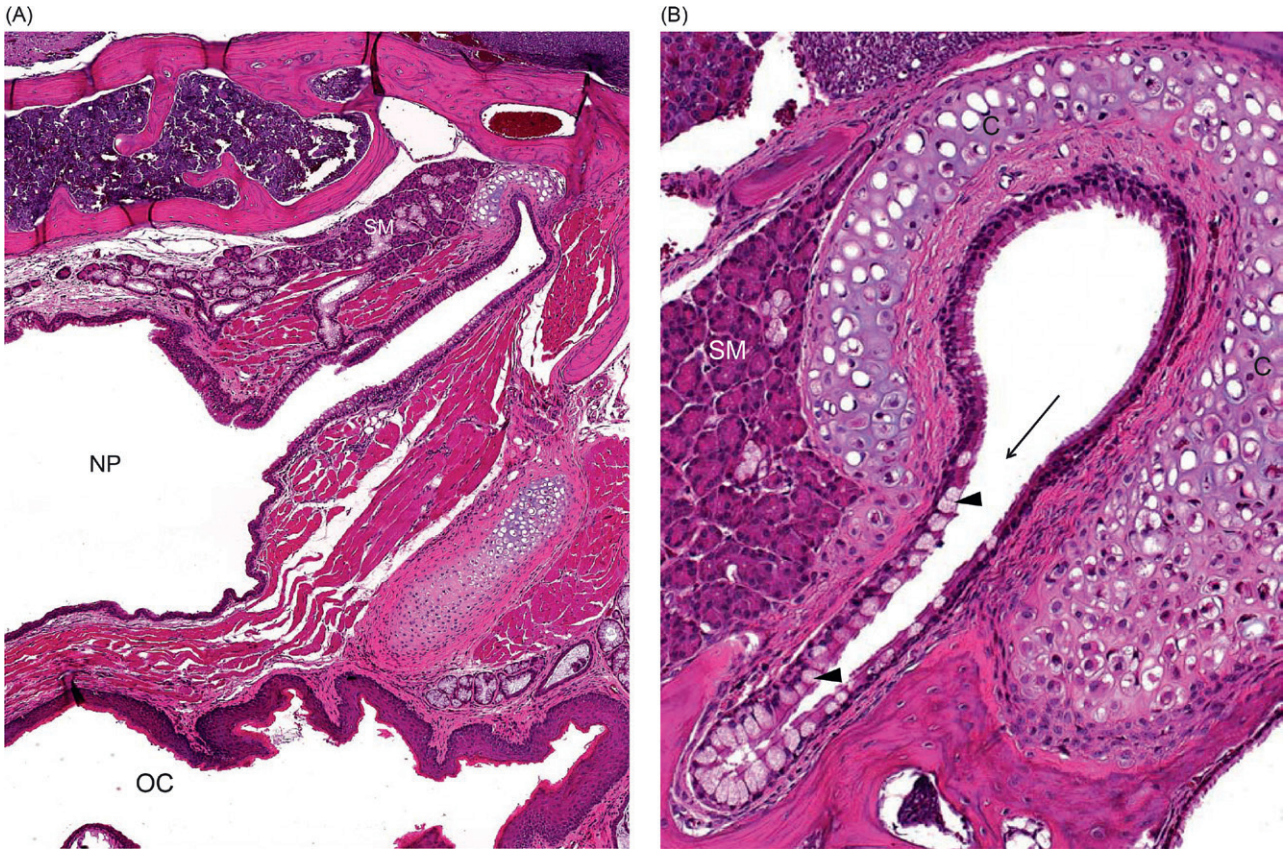

FIGURE 22.5 Rodent (mouse) auditory canal (Eustachian tube). (A) Meatus into the nasopharynx (NP). Seromucinous gland (SM) and oral cavity (OC) are indicated. (B) High power magnification view of auditory tube. Note the increase in goblet cells (arrowheads) as the tube nears the nasopharyngeal region. In contrast, the epithelium lining the tympanic portion (within the cartilaginous canal (C)) is devoid of goblet cells. The arrow points in the direction of the nasopharynx. Seromucinous gland (SM) is indicated.

Need-to-know

- In rodents, as opposed to humans, the auditory canal (Eustachian tube) lacks substantial cartilaginous support throughout its length and has minimal lymphoid tissue associated with it.

ear cavity. This epithelial layer has ciliated cells and a few secretory mucous cells (Fig. 22.4B) and extends to the auditory canal. In contrast, the inner mucous layer of the tympanic membrane in humans is a modified respiratory epithelium consisting of a single layer of cuboidal cells lacking cilia and goblet cells.

The auditory canal is composed of bony and cartilaginous sections and is lined by ciliated pseudostratified epithelium with goblet cells (Fig. 22.5) as well as nonsecretory/nonciliated cells and basal cells. Also present are serous and mucous glands, which are more prominent near the nasal cavity. The cilia beat toward the nasopharynx. At the opening of the auditory canal in humans, there are aggregates of lymphoid nodules known as the tubal tonsil. In contrast, rodents have aggregates of nasopharyngeal lymphoid tissues (Chapter 6: Nose, Sinus, Pharynx, and Larynx) considered to be equivalent to Waldeyer's ring; however, they lack tonsils.

Inner Ear

Gross Anatomy

The inner ear is contained in the temporal bone within the bony (also called osseous) labyrinth, lined by the membranous labyrinth (Figs. 22.2 and 22.6). It comprises the vestibule, semicircular canals, and cochlea. The vestibule and semicircular canals contain the sensory receptors that are essential for equilibrium (Fig. 22.7), whereas the cochlea contains the hair cells that are essential for hearing.

Histology

Labryinths and Fluid

Within the inner ear, the epithelial-lined sacs and ducts of the membranous labyrinth communicate with each other and contain endolymph, which is produced by the cells of the stria vascularis, the pseudostratified and well-vascularized epithelia that line the lateral cochlear wall (Figs. 22.8 and 22.9). External to the membranous labyrinth is a perimembranous space, which separates the membranous labyrinth from the surrounding bony labyrinth and is filled with sodium-rich fluid called perilymph (Figs. 22.6 and 22.9). In rodents and humans, the perimembranous space is in diffusional continuity with cerebrospinal fluid (CSF). In rodents, perilymph is produced locally within the cochlea and is dependent on blood flow and CSF influx through the cochlear aqueduct, which is not patent in humans. In humans, this diffusional continuity is thought to be through spaces associated with the auditory nerve, although the exact means of perilymph production in humans is still controversial. Perilymph closely resembles extracellular fluid, whereas endolymph is more similar to intracellular fluid.

Vestibule and Semicircular Canals

The vestibule sits between and connects the cochlea and semicircular canals and helps to maintain equilibrium (Figs. 22.6 and 22.9). Within the vestibule are two regions lined by the membranous labyrinth; the utricle, which is closer to the semicircular canals, and the saccule, which is closer to the cochlea. Three semicircular canals, which lie at right angles to each other in three planes, arise from the posterior vestibule. There are five sensory receptor regions associated with the vestibular system in both rodents and humans: one in the utricle, one in the saccule, and one for each of the three semicircular canals. The balance receptors, known as the cristae ampullaris and maculae, are located within the vestibular membranous labyrinth (Figs. 22.6 and 22.7). The maculae are located in the utricle and saccule and detect linear acceleration and deceleration, with the utricle maculae sensing horizontal movement

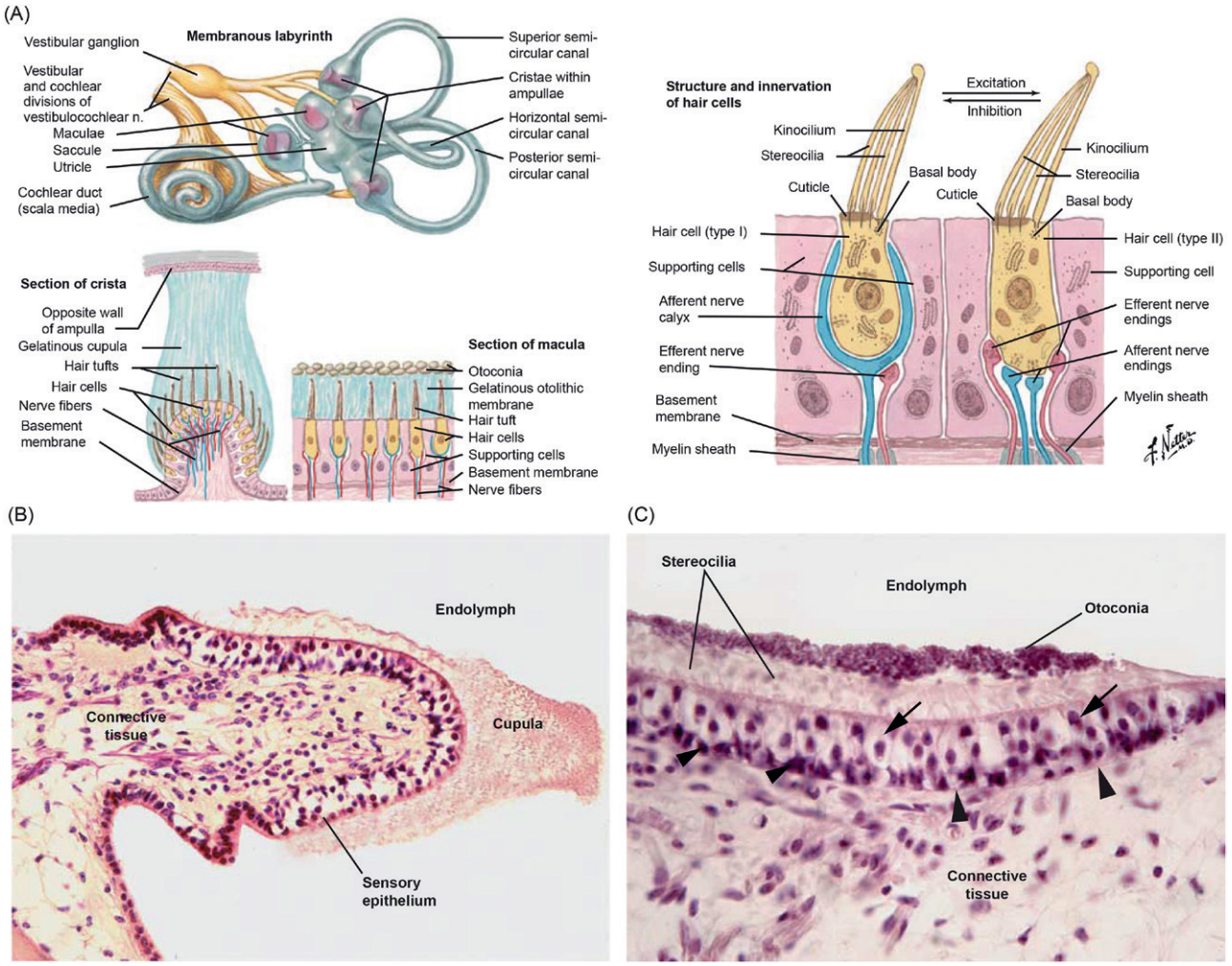

FIGURE 22.6 Human membranous labyrinth. (A) Structure and innervation of hair cells. (B) The crista ampullaris. A cone-shaped cupula forms a cap over the crest of sensory epithelium, which consists of hair cells and supporting cells. Apical stereocilia of hair cells normally insert into the cupula, but are not well preserved because of preparation artifacts. The loose connective tissue contains nerve fibers, which are dendrites of the vestibular part of cranial nerve VIII. (C) The macula comprises apical hair cells (arrows) and basal supporting cells (small arrowheads). They rest on an ill-defined basement membrane (large arrowheads) and underlying connective tissue. Each hair cell has many apical projections—multiple stereocilia and one kinocilium. These surface specializations insert into the overlying otolithic membrane, which contains calcium carbonate-rich otoconia. Source: Reprinted from Ovalle and Nahirney: *Netter's essential histology*, 2008, with permission from © Elsevier, www.netterimages.com.

and the saccule detecting vertical movement. The cristae ampullaris are located at the base of each of the semicircular canals and detect angular acceleration and deceleration (Fig. 22.7). The sensory epithelium of the cristae ampullaris appears as a prominent crest overlying cone-shaped connective tissue; the extracellular membrane of the crista ampullaris is a cone-shaped cupula surrounded by endolymph (Figs. 22.6 and 22.7).

In the maculae, the receptors rest low on an ill-defined basement membrane and have calcium carbonate concretions (otoconia) that stain light blue to pink and are roughly spherical masses overlying the gelatinous otolithic membrane (Fig. 22.7). The hair cells of the maculae and cristae are also divided ultrastructurally into types I and II. These cells are innervated by the vestibular branch of the eighth cranial nerve.

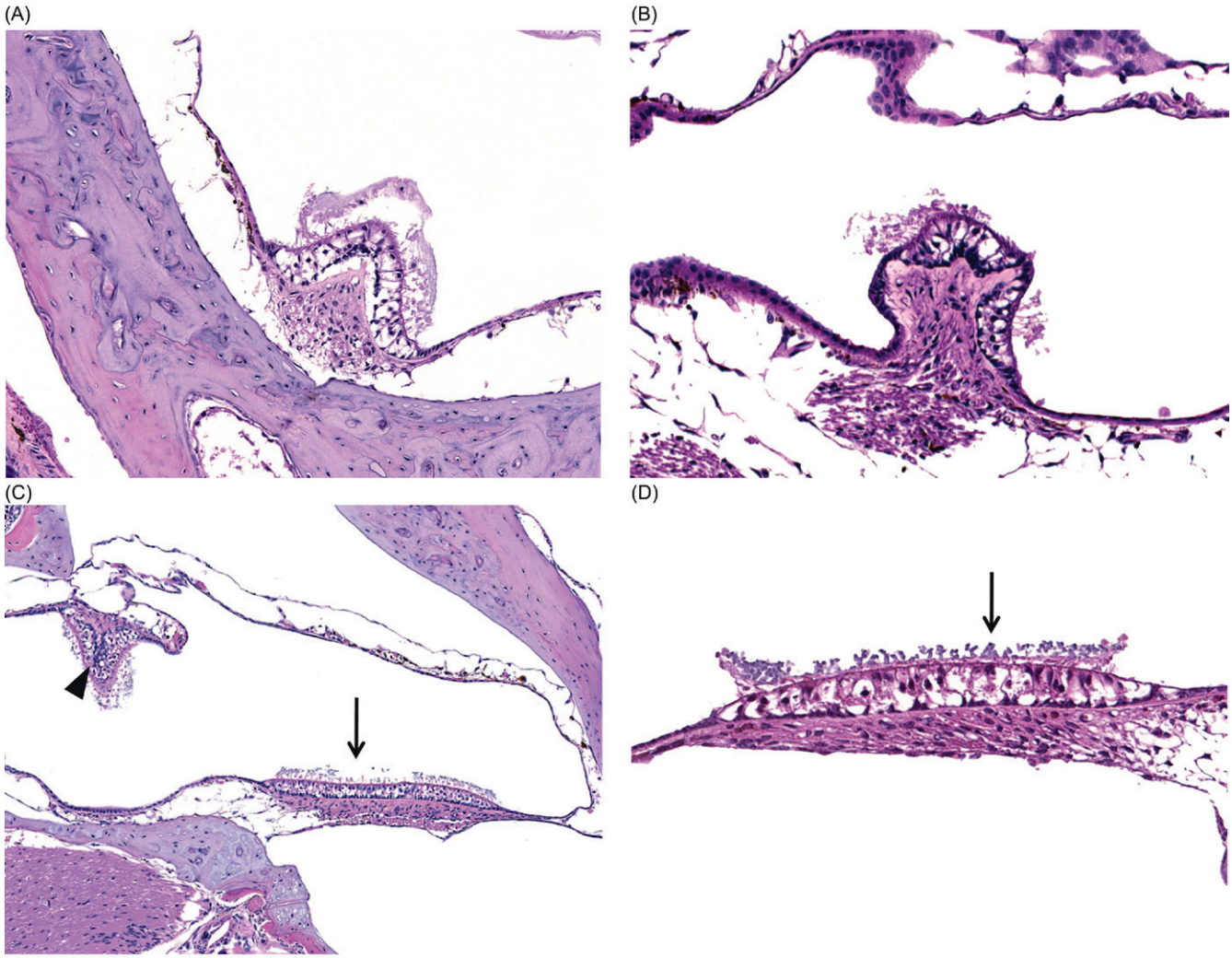

FIGURE 22.7 Rodent (mouse) sensory receptors. (A) Crista ampullaris. The distinctive crest of sensory epithelium overlying cone-shaped connective tissue detects angular acceleration and deceleration. (B) Crista ampullaris. The appearance of the receptors may vary with sectional plane and fixation. (C) Macula (arrow) and crista ampulla (arrowhead). Note the distinct shapes of the two receptors. The sensory macular epithelium is low and rests on an ill-defined basement membrane. The macula detects linear acceleration and deceleration. (D) Macula. Note the otoconia, the light blue granular calcium carbonate concretions (arrow).

Need-to-know

- The sensory receptors are similarly structured in mice, rats, and humans.

Cochlea

The cochlea serves as the component of the inner ear dedicated to hearing. In mice, the cochlea makes 2.5 turns around the central modiolus bone and is approximately 5 or 6 mm long; in rats, it makes 2.5 turns and is approximately 11 mm long; in humans, it makes 2.75 turns and is approximately 30–35 mm long. In rodents and humans, the cochlea is divided into three compartments: the scala vestibule, the cochlear duct, and the scala tympani. Arising from the anterior vestibule is the cochlear duct, also known as the scala media. The cochlear duct is triangular in shape (Fig. 22.8), contains endolymph and the organ of Corti (the receptor for hearing, see below) (Figs. 22.8–22.10). The cochlear

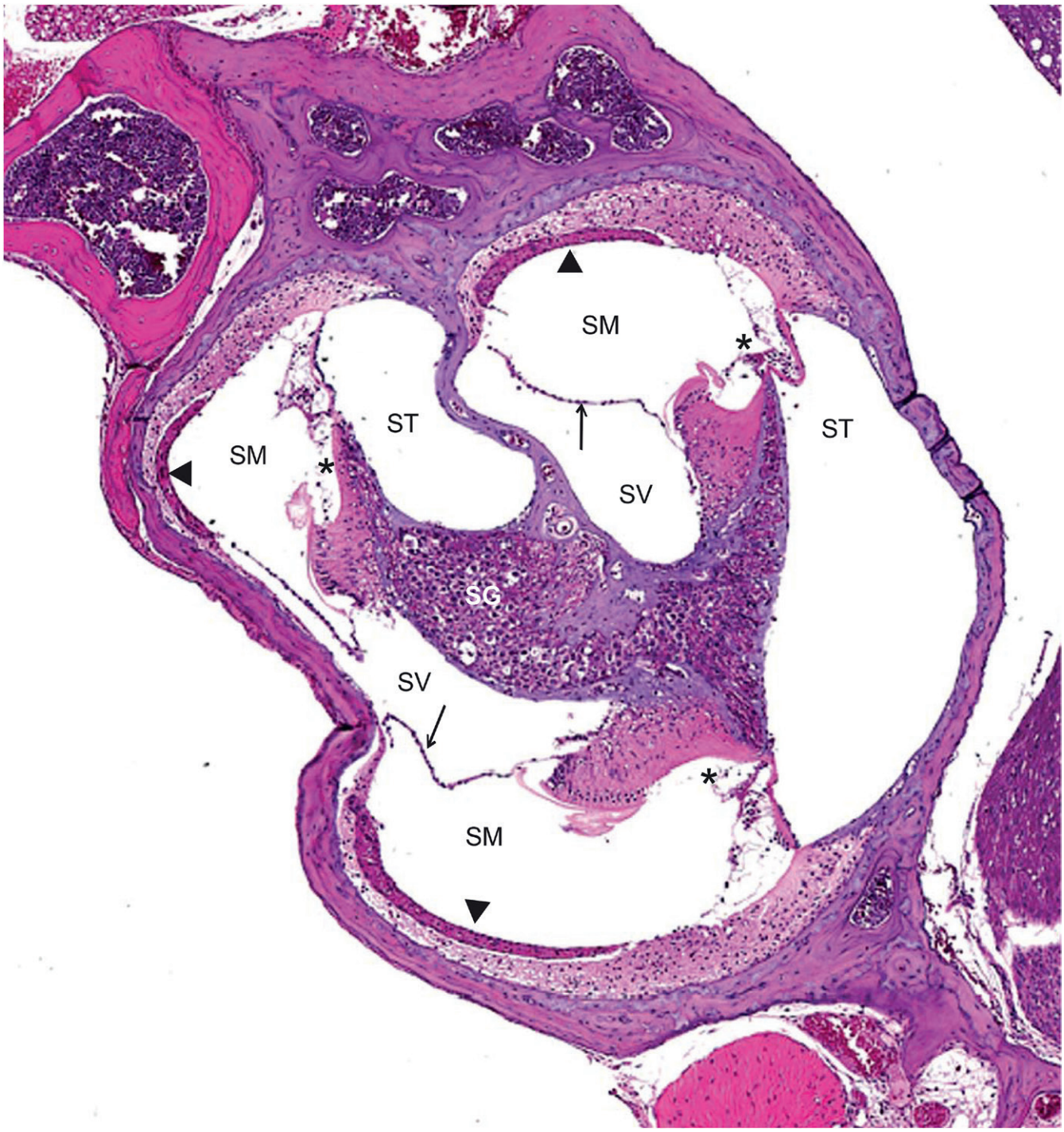

FIGURE 22.8 Rodent (mouse) cochlea. Three cross sections of the organ of Corti (asterisks) are present in this section. Note the spiral ganglia (SG) located within the modiolus. The mouse cochlea completes 2.5 turns. Endolymph is found within the cochlear duct [scala media (SM)]. This duct is bounded by Reissner's (vestibular) membrane (arrows) above, basilar membrane below, and the stria vascularis (arrowhead) laterally. Endolymph is produced by the cells of the stria vascularis, the pseudostratified and well-vascularized epithelia that line the lateral aspect of the cochlear ducts. Scala vestibuli (SV) and scala tympani (ST) are indicated.

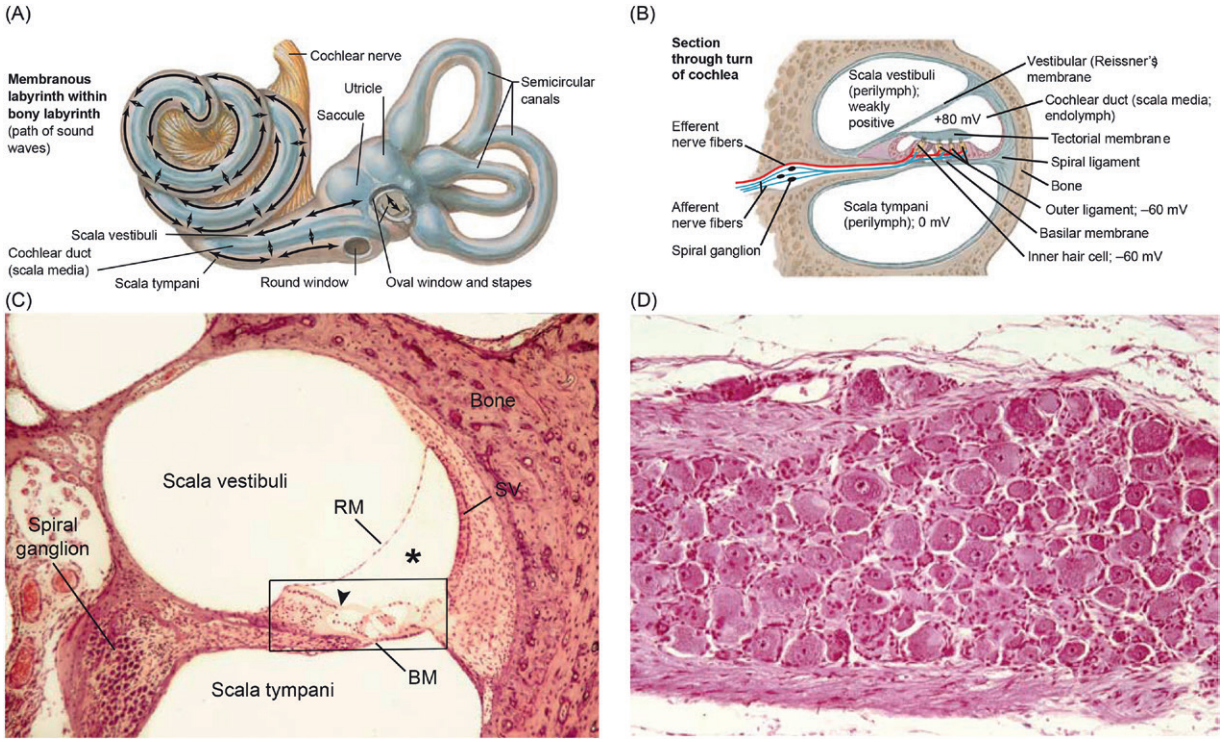

FIGURE 22.9 Human cochlea. (A) Membranous labyrinth within the bony labyrinth. (B) Section through the turn of the cochlea. (C, D) The spiral ganglion. Located in the modiolus of the bony labyrinth, it contains cell bodies of bipolar neurons of the auditory nerve. Dendrites of these neurons emanate from the organ of Corti (boxed region), where they synapse with cochlear hair cells. Bipolar neuron axons enter the brain stem to end in the cochlear nuclei of the medulla. (B) One turn of the cochlea in the inner ear showing the organ of Corti. Cochlear hair cells and supporting cells sit on the basilar membrane (BM). Tips of hair cell stereocilia insert in the tectorial membrane (arrowhead). Stria vascularis (SV) produces endolymph of the cochlear duct (asterisk). Scalae tympani and vestibuli contain perilymph. Reissner's membrane (RM) separates the cochlear duct from scala vestibuli. (D) Spiral ganglion. Afferent nerve fibers in the base of the organ have cell bodies in the spiral ganglion where their proximal axons form the auditory part of cranial nerve VIII. Source: Reprinted from Ovalle and Nahirney: *Netter's essential histology*, 2008, with permission from © Elsevier, www.netterimages.com.

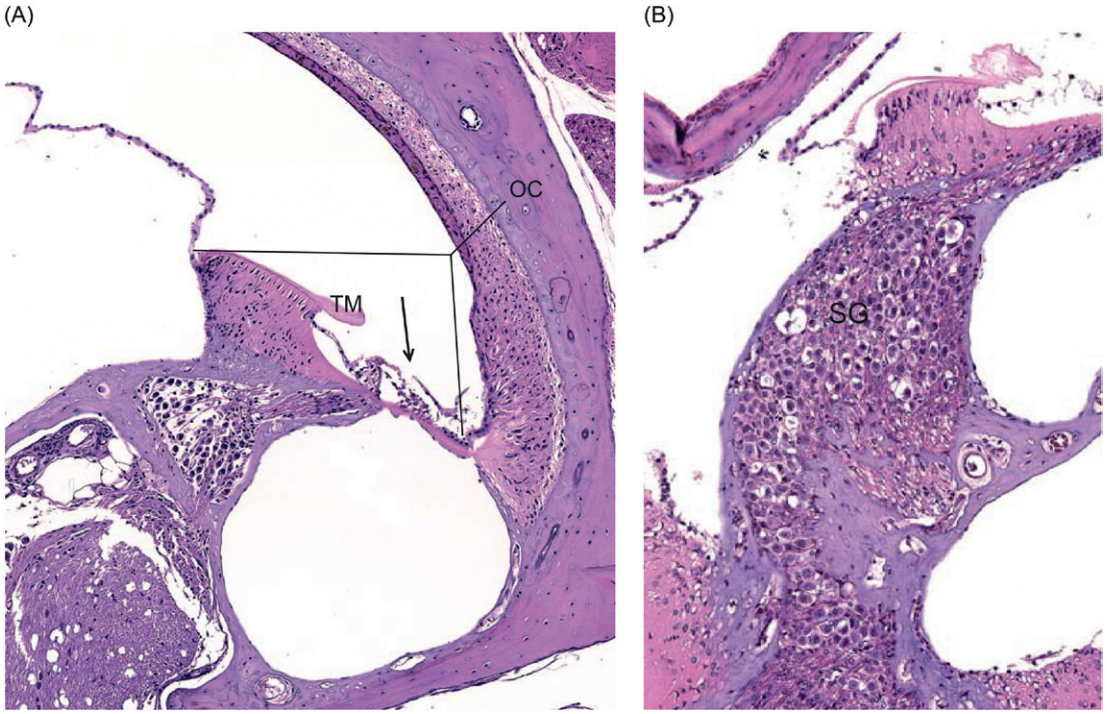

FIGURE 22.10 Rodent (mouse) inner ear. (A) Organ of Corti (OC). The tectorial membrane (TM) is well-preserved, whereas the hair cells (arrow) are less so in this routinely processed tissue. (B) Spiral ganglia (SG). High power magnification view of the spiral ganglia located within the modiolus bone.

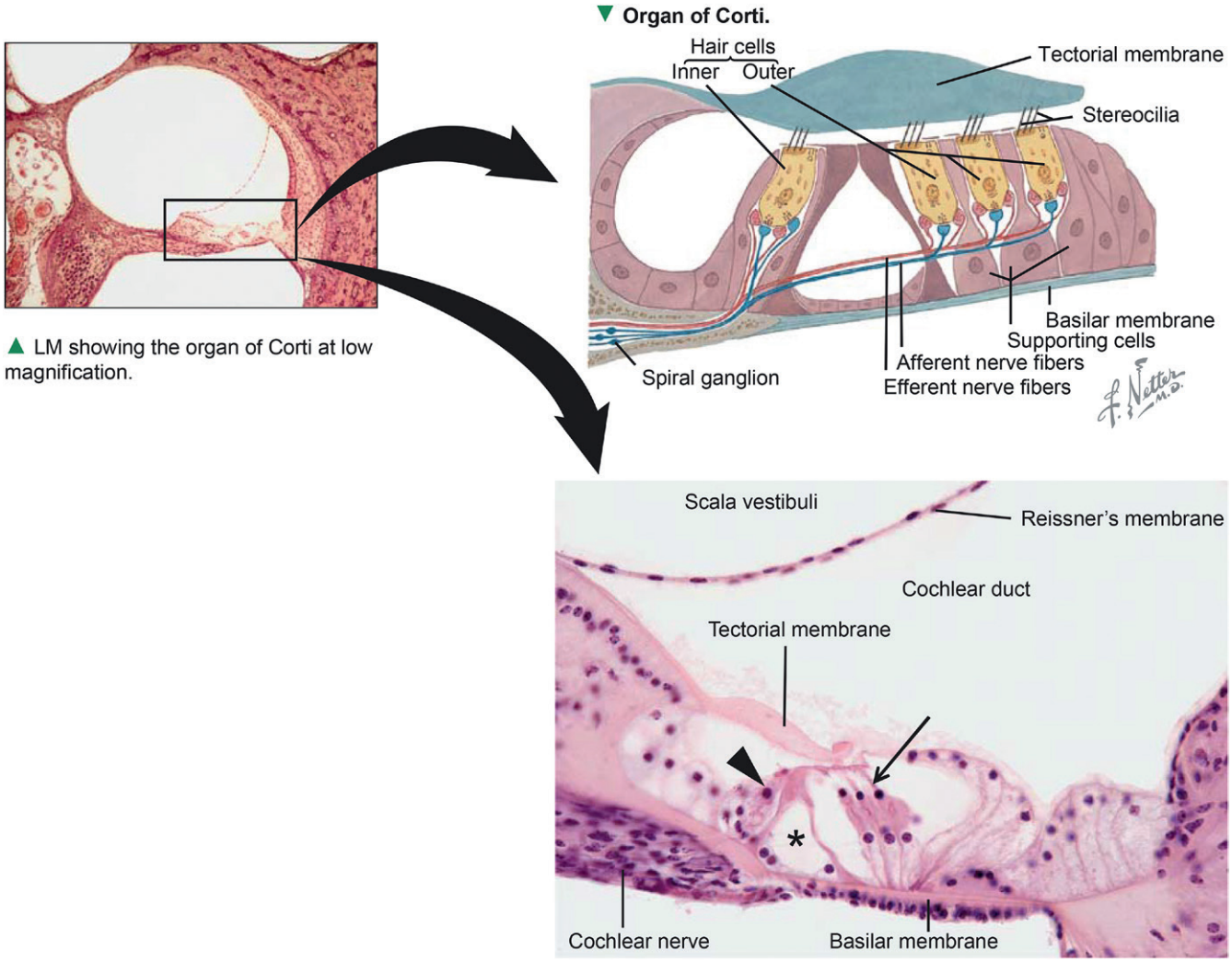

FIGURE 22.11 Human organ of Corti. The organ of Corti at high magnification. On the sides of the inner tunnel (asterisk), three rows of outer hair cells (arrow) and a row of inner hair cells (arrowhead) rest on the basilar membrane. Apical stereocilia of outer hair cells protrude into the tectorial membrane. A thin, slanting Reissner's (vestibular) membrane separates perilymph in the scala vestibuli from endolymph in the cochlear duct. Dendrites of the cochlear nerve travel from the organ of Corti toward the spiral ganglion, which houses cell bodies of these bipolar neurons. Source: © Elsevier, Inc., www.netterimages.com.

duct is bounded by Reissner's membrane above, the basilar membrane below, and the lateral cochlear wall on the sides (Figs. 22.8 and 22.9). Reissner's membrane, also called the vestibular membrane, is a thin epithelial bilayer. The cochlea is further divided into two additional spaces, the scala vestibuli and the scala tympani, which are separated from the cochlear duct by Reissner's membrane (Fig. 22.11), contain perilymph, and connect with each other at the apical helicotrema. There are two membrane-covered openings that connect the inner and middle ear, the round and the oval windows. The round window is an opening which sits at the base of the scala tympani in the medial wall middle ear of the cochlea and is covered by the secondary tympanic membrane. The oval window is a membrane-covered opening in the scala vestibuli along the inner wall of the middle ear at the head of the cochlea, which is encircled by the stapes foot plate. The oval window allows for transmission of movement from the stapes to the fluid-filled cochlea; the round window moves in the opposite direction as the oval, allowing for fluid movement in the cochlea and detection by the inner hair cells of the organ of Corti.

The organ of Corti is the receptor for hearing and is comprised of sensory inner and outer hair cells flanked by support cells. The cells rest on the basilar membrane (Figs. 22.8 and 22.9), which separates the endolymph-containing cochlear duct from the perilymph-containing scala tympani along the spirals of the cochlea. The hair cells are covered by the tectorial membrane, a gelatinous extracellular membrane (Figs. 22.9–22.11) that is produced by the supporting cells and covers the apical stereocilia of the outer hair cells (Fig. 22.11). It responds to changes in fluid pressure in the tympanic and vestibular canals generated by movement of the perilymph.
The inner and outer hair cells of the cochlea are separated by the inner tunnel (Fig. 22.11). The typically rounded inner hair cells lie in a single row along the basilar membrane and are completely surrounded by supporting cells. The cylindrical outer hair cells lie in three to five rows along the basilar membrane and are surrounded on their apical and basal surface by supporting cells. Efferent and afferent nerve endings at each hair cell's base transmit impulses to the bipolar neurons of the spiral ganglion (Figs. 22.8–22.10). These impulses are subsequently transmitted to the auditory cortex via the auditory branch of the eighth cranial nerve.

FURTHER READING

Albiin N, Hellström S, Salén B, Stenfors LE, Söderberg O, et al: The anatomy of the Eustachian tube in the rat: a macro- and microscopical study. *Anatom Rec* 207:513–521, 1983.

Albuquerque AA, Rossato M, Oliveira JA, Hyppolito MA, et al: Understanding the anatomy of ears from Guinea pigs and rats and its use in basic otologic research. *Braz J Otorhinolaryngol* 75(1):43–49, 2009.

Argyle EC, Mason MJ: Middle ear structures of Octondon degus (Rodentia: Octodontidae), in comparison with those of subterranean caviomorphs. *J Mammol* 89(6):1447–1455, 2008.

Iurato C, Bredberg G, Bock G: *Functional histopathology of the human audio-vestibular organ. Eurodata Hearing Project*, Brussels, 1982, Commission of the European Communities.

Johnsson LG, Hawkins JE: A direct approach to cochlear anatomy and pathology in man. *Arch Otolaryngol Head Neck Surg* 85:599–613, 1967.

Lavender D, Taraskin SN, Mason MJ, et al: Mass distribution and rotational inertia of "microtype" and "freely mobile" middle ear ossicles in rodents. *Hearing Res* 282:97–107, 2011.

Swan EE, Mescher MJ, Sewell WF, Tao SL, Borenstein JT, et al: Inner ear drug delivery for auditory applications. *Adv Drug Deliv Rev* 60(15):1583–1599, 2008.

Li P, Gao K, Ding D, Salvi R, et al: Characteristic anatomical structures of rat temporal bone. *J Otol* 10:118–124, 2015.

Maronpot R, editor: *Pathology of the mouse: reference and atlas*, Vienna, IL, 1999, Cache River Press.

Mey KH, Sørensen MS, Homøe P, et al: Histomorphometric estimation of air cell development in experimental otitis media. *Laryngoscope* 116(10):1820–1823, 2006.

Michaels L: *Ear, nose and throat histopathology*, London, 1987, Springer-Verlag.

Michaels L: *Atlas of ear, nose and throat histopathology*, Lancaster, 1990, MTP Press.

Michaels L: The ear. In Sternberg SS, editor: *Histology for pathologists* (ed 2), Philadelphia, PA, 1997, Lippincott–Raven, pp 337–366.

Rudmann D, Cardiff R, Chouinard L, Goodman D, Küttler K, Marxfeld H, et al: Proliferative and nonproliferative lesions of the rat and mouse mammary, Zymbal's, prepucial and clitoral glands. *Tox Pathol* 40:7S–39S, 2012.

Schuknecht HF: *Pathology of the ear*, ed 2, Philadelphia, PA, 1993, Lea & Febiger.

Sosa GA, Roux ME: Development of T lymphocytes in the nasal-associated lymphoid tissue (NALT) from growing Wistar Rats. *Clin Develop Immunol* 11(1):29–34, 2004.

Suttie AW, Leininger JR, Bradley AE: *Boorman's pathology of the rat: reference and atlas*, ed 2, New York, 2017, Academic Press.

Willott JF: *Handbook of mouse auditory research: from behavior to molecular biology*, Boca Raton, FL, 2001, CRC Press.

Young B, Lowe JS, Stevens AS, et al: *Wheater's functional histology: a text and colour atlas*, ed 5, Philadelphia, PA, 2006, Churchill Livingstone.

Zimmer WM, Rosin DF, Saunders JC, et al: Middle ear development VI: structural maturation of the rat conducting apparatus. *Anat Rec* 234:475–484, 1999.

This page intentionally left blank

MAMMARY GLAND 23

ROBERT D. CARDIFF
University of California at Davis, Davis, CA, United States

SONALI JINDAL
Oregon Health & Sciences University, Portland, OR, United States

PIPER M. TREUTING
University of Washington School of Medicine, Seattle, WA, United States

JAMES J. GOING
University of Glasgow, Glasgow, Scotland, United Kingdom

BARRY GUSTERSON
University of Glasgow, Glasgow, Scotland, United Kingdom

HENRY J. THOMPSON
Colorado State University, Fort Collins, CO, United States

Introduction

The mammary glands of all mammals are structurally and functionally designed to produce milk for offspring. Rodent mammary glands are encased within the mammary fat pad. The human mammary glands are within the breasts, which are complex and unique anatomic structures. All mammary glands are relatively simple branching tubular organs with typically one to two layers of epithelial cells. The mammary gland is a dynamic organ that is constantly responding to the hormonal milieu and local epigenetic changes. Major changes such as puberty, pregnancy, lactation, and senescence are accompanied by well-chronicled changes in glandular structure and function. However, these changes are not uniform, resulting in morphological heterogeneity that is frequently observed within a single gland. We have tried to provide the reader with an "idealized" version of typical morphology found at any one developmental or physiological phase while underscoring that considerable variability exits.

Mammary Gland

GROSS ANATOMY

Mice have five and rats have six pairs of bilaterally symmetrical mammary glands, located along the ventral milk line between the neck and perianal area (Fig. 23.1). Male rodents do not have nipples, as these regress during embryonic development. The mammary glands segregate

Comparative Anatomy and Histology. DOI: http://dx.doi.org/10.1016/B978-0-12-802900-8.00023-3
© 2018 Elsevier Inc. All rights reserved.

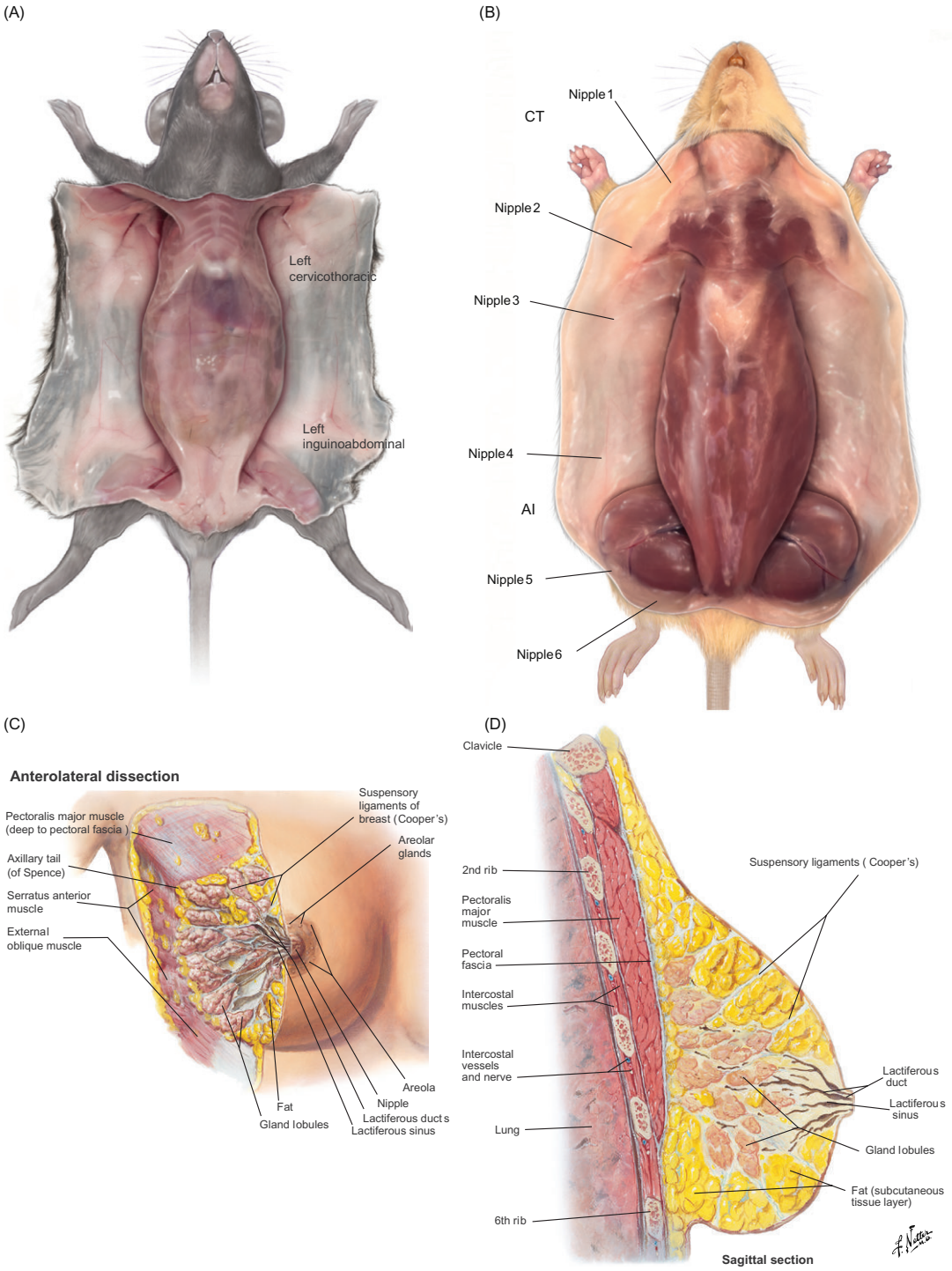

FIGURE 23.1 Regional and gross anatomy of mammary glands. (A) Rodent (mouse) mammary glands are aligned along the milk lines bilaterally. Each gland terminates into a single collecting duct that releases milk through a single nipple. (B) Approximate location of the six nipples in the rat. Three glands are located in the cervicothoracic (CT) region and three in the abdominal-inguinal (AI) region. (C) In humans, the single pair of mammary glands are located predominantly over the pectoralis major muscle of the anterior chest. The tail of the human mammary gland extends into the axilla. (D) Human cross-sectional mammary anatomy. The human mammary gland contains 11–48 collecting ducts draining the lobes (labeled "gland lobules" here) of parenchymal tissue that are embedded in variably dense fibrous and adipose tissue. Each lobe connects with one of several major lactiferous ducts that expand to lactiferous sinuses at the base of the nipple. Connective tissue suspensory ligaments known as Cooper's ligaments connect the skin of the mammary gland with the deep fascia. The rodent mammary glands do not have comparable structures. Source: © Elsevier, Inc., www.netterimages.com.

Need-to-know

- The mouse has 10 and the rat 12 mammary glands; humans have 2.
- Male rodents lack nipples.
- The structural separation of lobes in human mammary gland allows for surgical segmental resectioning (lumpectomy) without sacrificing the integrity of the remaining lobes.

TABLE 23.1 Mammary Gland

Feature	Rodent		Human
	Mouse	Rat	
Gross			
Number of mammary glands	10 (five pairs); adult male lacks mammary tissue	12 (six pairs)	2 (one pair)
Nipples	Present only in female	Similar to mouse	Present in both male and female
Organization of major lactiferous ducts	Single lactiferous duct/sinus that forms 5–10 secondary ducts that further branch	Similar to mouse	10 or more lactiferous ducts in the nipple that branch to form a segmentally branched ductal system
Separate lobes	Absent; single complex branching system	Similar to mouse	Present; 15–20 separate lobes feed into separate major lactiferous ducts
Histologic			
Mature functional glandular unit	Lobuloalveolar (LA) unit	TDLU	Similar to rat
Development of functional glandular unit	Mature only in pregnancy	Similar to mouse	Similar to rodent
Premature mammary gland	No LA unit; ducts have blunt ends until develop TEBs in pregnancy	Forms TDLU	Mature by age 20 years, predominantly TDLU Types 1 and 2
Mature mammary gland	Only adipose tissue with scanty connective tissue surrounding quiescent ducts	Similar to mouse	Variably dense amounts of surrounding collagenous connective tissue as well as adipose tissue surrounding TDLUs
Lactating mammary gland	Well-developed acini (acini) with intraluminal milk and nuclear atypia	Similar to mouse	Similar to rodent

into cervical-thoracic (containing three glands on each side in mice and rats) and abdominal-inguinal regions (containing two glands on each side in mice and three glands in rats). Interspersed within the cervical-thoracic mammary glands in rodents is a band of muscle (the pectoralis), which is not present in the abdominal-inguinal mammary glands. Male mice retain only vestigal mammary glandular tissue. In contrast, male rats have prominent glandular structures, which are morphologically distinguishable from those of female rats (sexually dimorphic) and are less extensively branched. Female rodent mammary fat pads, when fully developed, are extensive, wrapping from the ventrum to the intrascapular region cranially, and from the lateral flanks to the perineal region, caudally. In female rodents, there is a single lactiferous duct per mammary gland, which drains milk into the nipple. In humans, there are two bilaterally symmetrical mammary glands, termed breasts, which are situated within the superficial facia of the anterior thoracic wall above the pectoralis major, extending upwards into the axilla (Table 23.1, and Fig. 23.1). Supernumerary nipples and glands in humans are rarely present anywhere along the milk line. In males, the mammary glandular tissue is rudimentary. In female humans, many ducts extend in a segmentally branching, radial pattern from the nipple to form 11–48 separate lobes composed of glandular tissue embedded in fibrocollagenous stroma (Fig. 23.1). These lobes are separated from each other by variable amounts of adipose tissue, and each lobe is drained by its own lactiferous duct leading to the nipple. Humans have multiple lactiferous ducts leading to the nipple (Fig. 23.2C), whereas rodents have a single duct (Fig. 23.3). Fibrous thickenings of connective tissue interdigitate between these parenchymal structures, connecting the deep fascia with the dermis of the overlying skin to form suspensory ligaments called Cooper's ligaments. These ligaments provide support, as well as mobility, to the human mammary gland. Rodents do not have comparable ligaments.

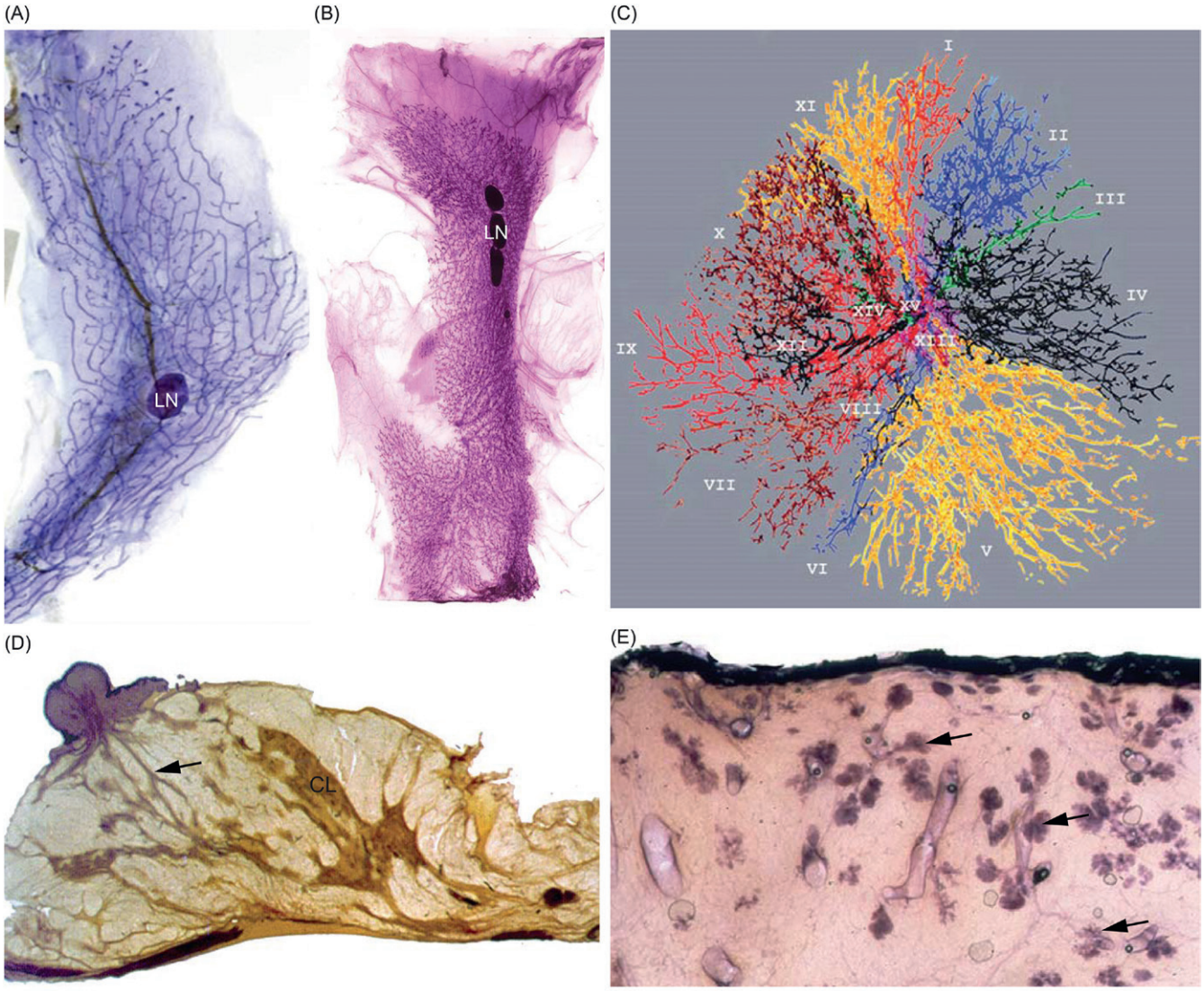

FIGURE 23.2 Subgross anatomy of mammary gland. (A) Mammary gland from an FVB/N mouse shows the branching ductal trees of mouse number 4 (inguinal) mammary gland stained with hematoxylin. A lymph node (LN) is indicated. (B) Rat abdominal-inguinal mammary glands number 4, 5, and 6 stained with carmine red. A lymph node (LN) is indicated. (C) A comparable representation of the human mammary glands requires a 3D computer assisted multiple 2 mm reconstruction using images of 2mm thick subgross slides. This image shows the en face pattern with 28 overlapping tree-like branches that compose this *Human Mammary Forest.* (D) Whole mount of a sagittally sectioned human mammary gland shows the branching ductal system (arrow) that terminates at the nipple, as well as the relative proportions of surrounding fibroadipose tissue. Cooper's suspensory ligaments (CL) are also visualized. (E) High magnification of a human subgross illustrating the ductal structure in a young nulliparous female. This view reveals the organization of the collecting ducts and TDLUs (arrows). Source of C: Moffat and Going: Three-dimensional anatomy of complete duct systems in human breast: pathological and developmental implications, *J Clin Pathol* **49**(1):48–52, 1996. Sources of D and E: Images from the collection of Drs Wellings and Jensen (Wellings, Jensen, et al: An atlas of subgross pathology of the human breast with special reference to possible precancerous lesions, *J Natl Cancer Inst* 55:213–273, 1975; Cardiff, Wagner, et al: Mammary cancer in humans and mice. A tutorial for comparative pathology. The CDROM. *J Mammary Gland Biol Neoplasia* 5:243–244, 2000).

SUBGROSS ANATOMY AND HISTOLOGY

Terminal Duct Lobular Unit (TDLU)

The mammary gland has a compound tubuloalveolar morphology, comprised of branching tubular ducts which terminate in secretory glandular acini (or alveoli) (Fig. 23.2). Acini is the preferred term for mice and humans, where as in rats, alveoli is more commonly used. In all three species, these terms are interchangeable and herein we use acini. Lobules are composed of groups of acini. There

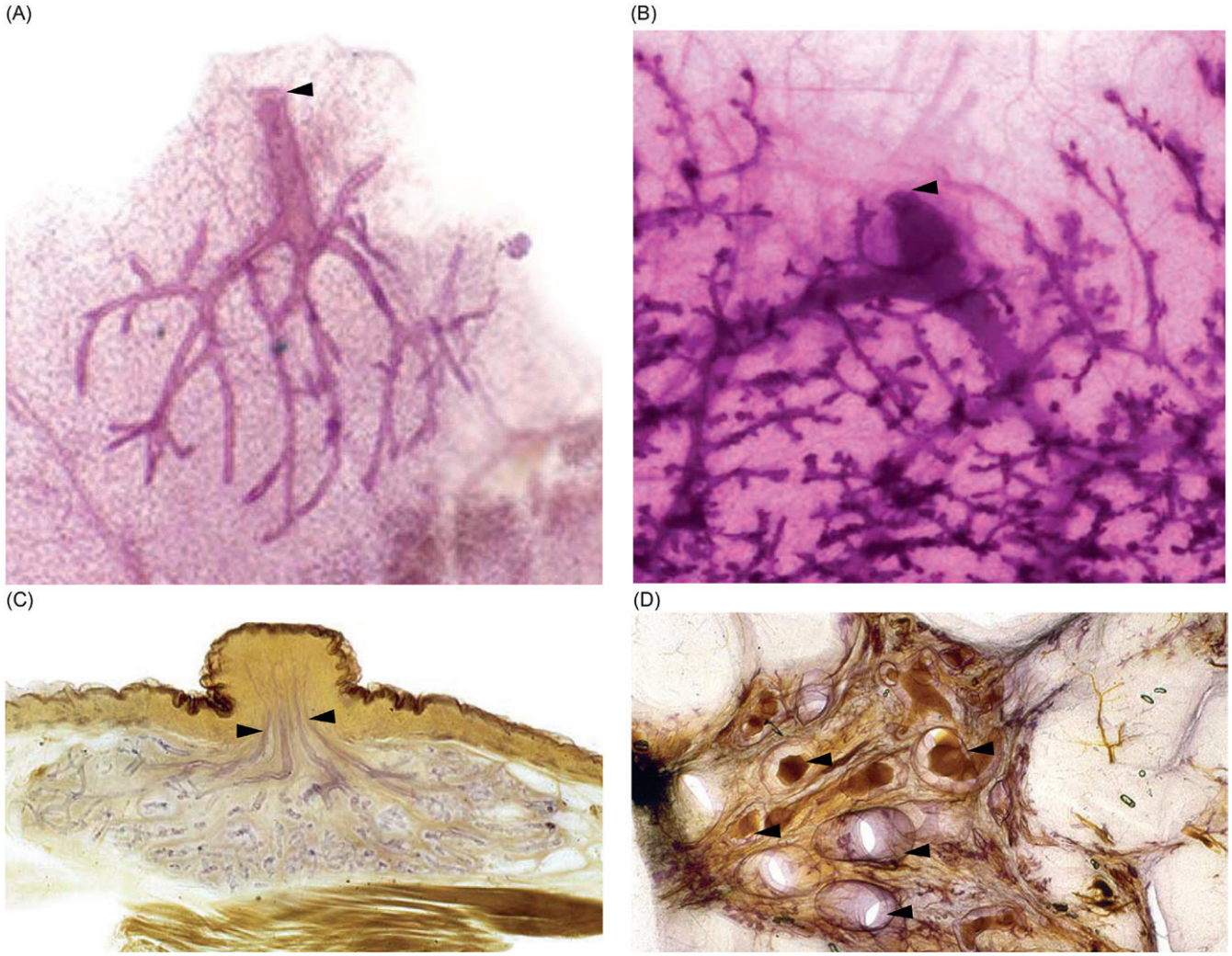

FIGURE 23.3 Subgross anatomy of the lactiferous duct and nipple. (A) Each mouse (whole mount) mammary gland has a single major lactiferous duct (arrowhead). In the nulliparous mouse pictured, the terminal ducts are blunted without a lobuloalveolar unit. (B) Whole mount of rat stained with Carmine Red with emphasis on the lactiferous duct (arrowhead) and primary branching. The lactiferous duct divides into two large secondary ducts that then subdivides to fill the mammary fat pad. The rodent has multiple glands but each nipple has only one lactiferous duct and outlet. (C) Human fetal tissue showing lactiferous ducts (arrowheads). (D) Cross section through a mature human nipple showing 5 of the 15 lactiferous ducts (arrowheads). Note that five of the ducts are plugged with debris. Source: Images from the collection of Drs Wellings and Jensen (Wellings, Jensen, et al: An atlas of subgross pathology of the human breast with special reference to possible precancerous lesions. *J Natl Cancer Inst* 55:213–273, 1975; Cardiff, Wagner, et al: Mammary cancer in humans and mice. A tutorial for comparative pathology. The CDROM. *J Mammary Gland Biol Neoplasia* 5:243–244, 2000).

are multiple lobules within the larger lobe. In all three species, the basic milk producing unit of the mammary gland is the terminal duct lobular unit (TDLU). A TDLU is composed of a lobule associated intralobular and extralobular terminal ducts. TDLUs (Figs. 23.4 and 23.5) are readily visualized at the subgross level (Fig. 23.4), which can most easily be assessed using a traditional preparation known as the whole mount (Figs. 23.2 and 23.3). The combination of whole mount and routine histology provides the full spectrum of mammary morphology and is presented together in the following sections. Methods for preparation of whole mount mammary fat pads are listed in the Further Reading section.

TDLUs drain into the intralobular and then extralobular terminal ducts, to collecting ducts, and then ultimately to the lactiferous duct(s) out through the ostia (outlets) of the nipples.

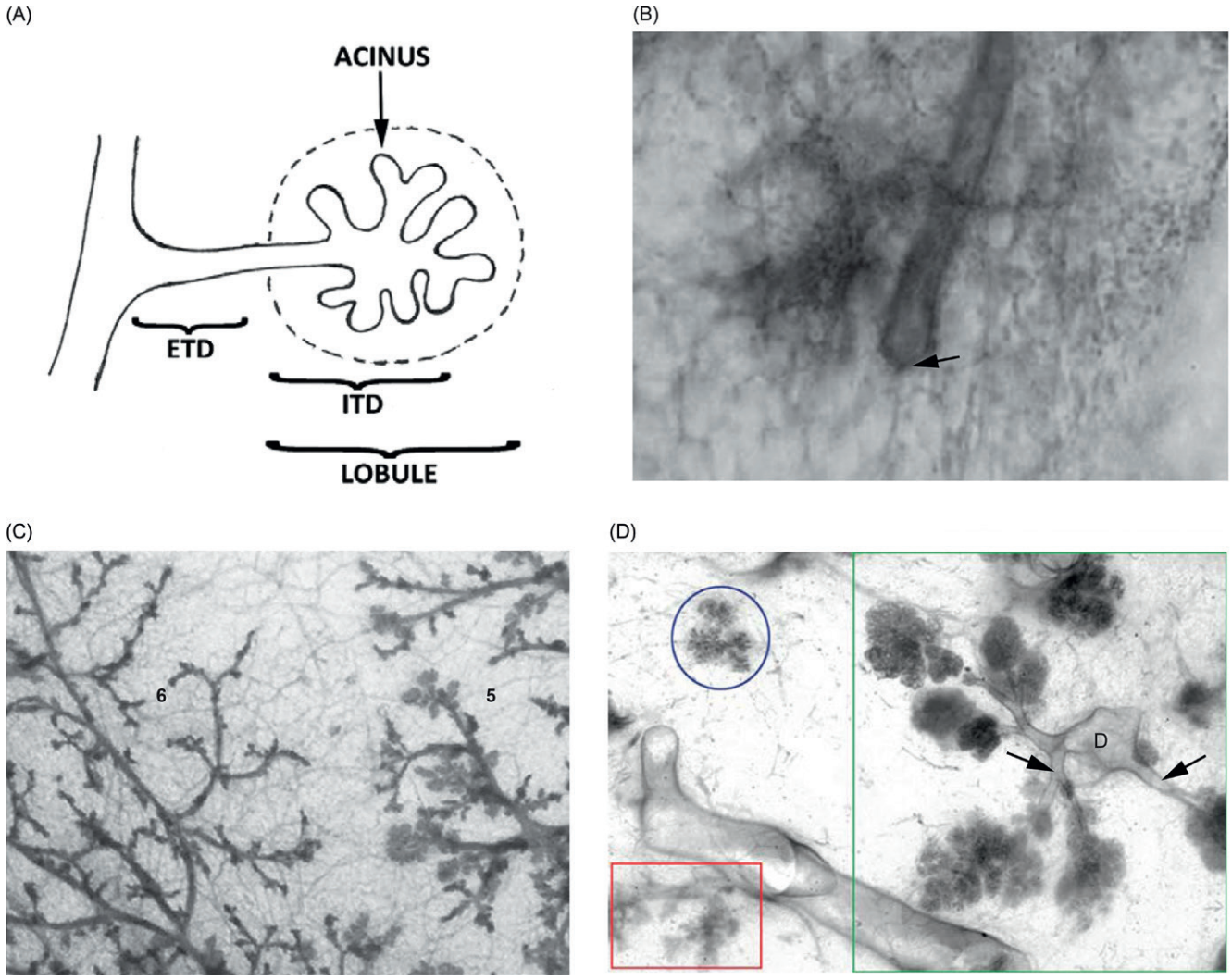

FIGURE 23.4 Subgross anatomy of the TDLU. TDLUs are the functional mammary gland units that reflect the hormone status of the female. (A) Diagram of a TLDU. The TDLU consists of an extralobular terminal duct (ETD) and an intralobular terminal duct (ITD), which is the axial core of the lobule connecting to the acinus. Multiple acini are found within the lobule. (B) In mice, the ducts in a quiescent gland end in a blunt duct (arrow). (C) In rats, the ducts terminate in a TDLU. Note that the number 5 gland on the right has well-developed TDLUs while the number 6 gland has poorly developed ones. (D) In humans, a single field has Type 1 (red box), Type 2 (blue circle), and Type 3 (green box) TDLUs. *D*, duct; *arrows*, extralobular collecting ductules. Source: Wellings, Jensen, et al: An atlas of subgross pathology of the human breast with special reference to possible precancerous lesions. *J Natl Cancer Inst* 55:213–273, 1975; Cardiff, Wagner, et al: Mammary cancer in humans and mice. A tutorial for comparative pathology. The CDROM. *J Mammary Gland Biol Neoplasia* 5:243–244, 2000.

Need-to-know

- Lobules, composed of multiple acini, are the ultimate milk-producing functional units.
- Milk is expulsed through intra- and extralobular terminal ducts into collecting ducts and through lactiferous ducts to the nipple.
- In the resting mammary gland the lobule is referred to as the terminal ductal lobular unit (TDLU).
- TDLUs are heterogeneous even within a single mammary gland.

The TDLU is embedded in a loose, intralobular connective tissue matrix that is distinct from the surrounding dense, interlobular connective tissue (Fig. 23.5). The importance of the TDLU in disease is underscored by the fact that most human breast cancer is now recognized to originate there. Cancers of the rodent mammary gland also originate from abnormal TDLUs. Therefore, an understanding of the structure, function, and diseases of the mammary gland begins with an understanding of the TDLU's organizational and histologic complexity.

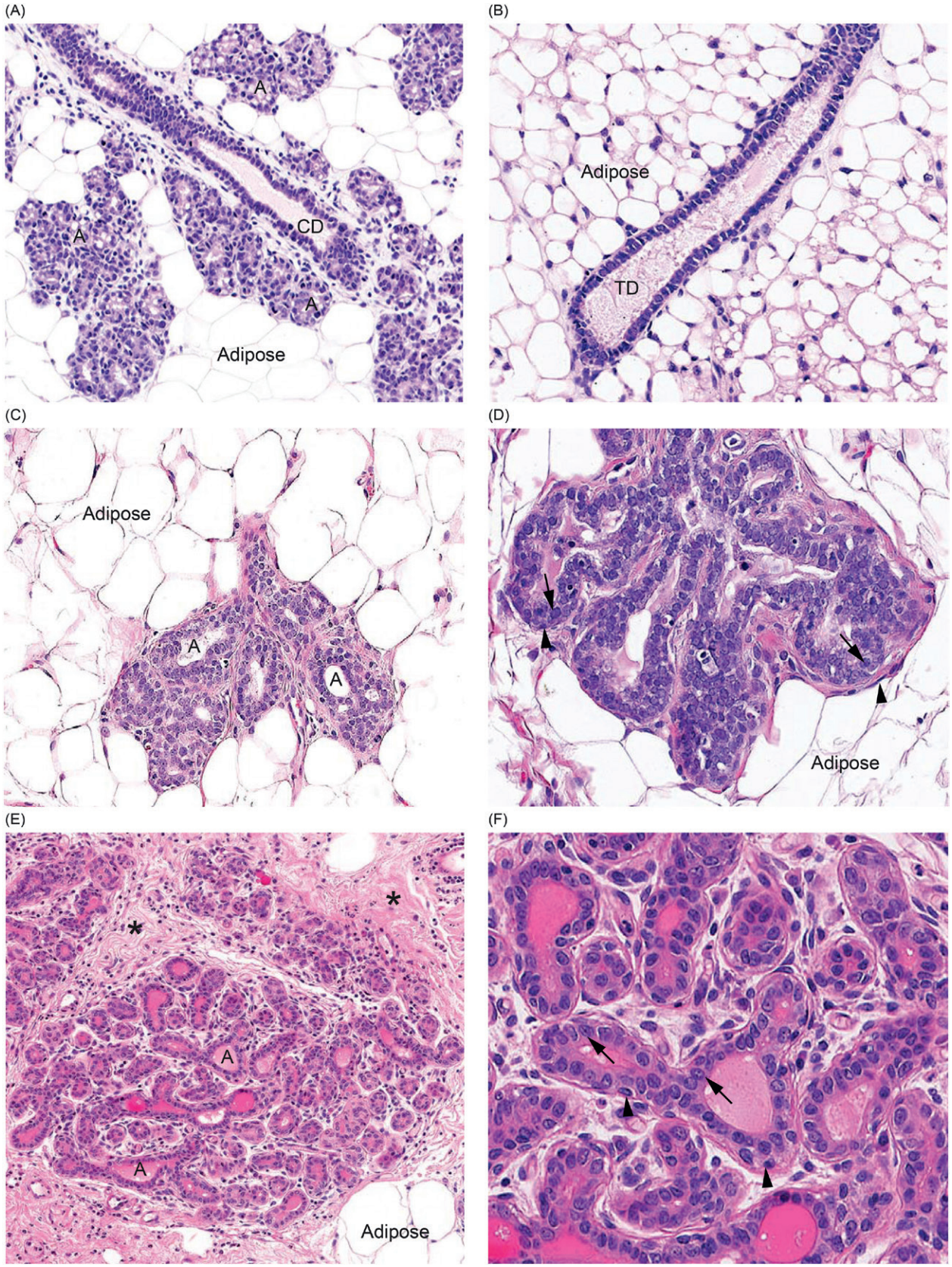

FIGURE 23.5 The TDLU across species. (A, B) Mouse. (C, D) Rat. (E, F) Human. (A) Mouse. With pregnancy, there is TDLU development with numerous acini (A) budding from the collecting duct (CD) in this mid-prelactation mammary gland. The mouse does not retain lobules postpartum and nulliparous mice do not have TDLUs (see B). (B) Mouse resting gland (postpartum or nulliparous). The terminal ends become inactive blunt terminal ducts (TD) without alveolar development set in mature adipose tissue. Rat (C, D) and human (E, F) mammary glands retain their lobules after pregnancy. Acini (A) are indicated. The TDLU is composed of intralobular ducts and two distinctive cell types: basal myoepithelial cells (arrowheads, D and F) and luminal cells (arrows, D and F). Note the abundant interlobular stroma (asterisks) in human tissue relative to rodent.

The TDLU appears in mice in response to pregnancy but in rats and human females upon sexual maturity. In mice, the mammary tree in a nonlactating female terminates in a blind ductule (Fig. 23.4). Lobuloalveolar development to a TDLU appears only during pregnancy and does not normally persist in most strains following weaning and involution. The heterogeneity in rat and human TDLUs in any given mammary gland is striking (Figs. 23.6 and 23.7). The human TDLU has been classified according to area occupied by lobules, number of acini per lobule, secretory morphology, and cellularity (Fig. 23.7). Lobules are classified as Types 1–4 depending on stage of morphological differentiation with Type 1 being the least mature with up to 11 alveolar buds surrounding a terminal duct. Types 2 and 3 represent increasing differentiation, lobular area, and number of acini (also termed dutcules). Type 4 lobules are terminally differentiated, milk producing units found in the lactating mammary gland. The relative proportion of each TDLU type will vary according to age and parity. In like manner, the rat TDLUs are also variable within any one gland with a full range of TDLU appearing in varying proportions.

In female rodents and humans, the mammary gland acini are lined by one to two layers of cuboidal epithelial cells, which are the functional secretory cell during lactation. These epithelial cells vary in numbers of mitochondria, ribosomes, lipid droplets, and secretory vacuoles and are classified morphologically as clear, dark, and intermediate cells. The appearance of the mammary gland changes in accordance with the estrous cycle. During proestrous and estrous in rodents, there is epithelial cell proliferation at the outer edges of the gland, which regresses during metestrous and diestrous (descriptions of these changes are included later in this chapter). Male rat mammary glands have a lobuloalveolar morphology (as compared to the tubuloalveolar morphology in females) and have prominent glandular tissue with indistinct lumens (Table 23.2; Fig. 23.6). The acini are lined by large cells, which have ample foamy cytoplasm. While the acini have indistinct lumina in male rats, they may contain scant proteinaceous secretions. As with the acini, mammary gland ducts are typically lined by one or two layers of cuboidal epithelium in females (Fig. 23.5). However, ductal epithelial cells can range in shape from tall columnar in the major ducts to cuboidal in the smaller terminal ducts. In male rats, the larger ducts are lined by vacuolated epithelial cells, but smaller ducts can be lined by doubled layers of low cuboidal epithelial cells. Immunohistochemical stains can be used to distinguish the different cell types within the lobules and ducts (Fig. 23.8). Although the intralobular luminal cells appear to be histologically uniform, their population is actually quite diverse. For example, not all of them express the estrogen receptor or progesterone receptor. In all three species, the basic histologic structure is one with mammary ducts and lobules that contain two primary cell types: basal myoepithelial and luminal epithelial (Fig. 23.5). A basement membrane surrounds these epithelial components. The myoepithelial cells form a basal layer of stellate cells with pale-to-clear cytoplasm (Fig. 23.5). The myoepithelial cells associated with the mammary gland contain actin, which has contractile properties and responds to oxytocin (Fig. 23.8) and helps to move secretions toward the ducts. In all three species, myoepithelial cells can be challenging to identify without the aid of special stains.

In most fixed, stained histologic sections, a slight separation of the loose (intralobular) connective tissue matrix and the surrounding denser (interlobular) connective tissue creates an artifactual space around the TDLU. The loose intralobular stroma includes cellular elements including fibroblasts, microvasculature, and occasional inflammatory cells. Each element has important functions that are not always apparent

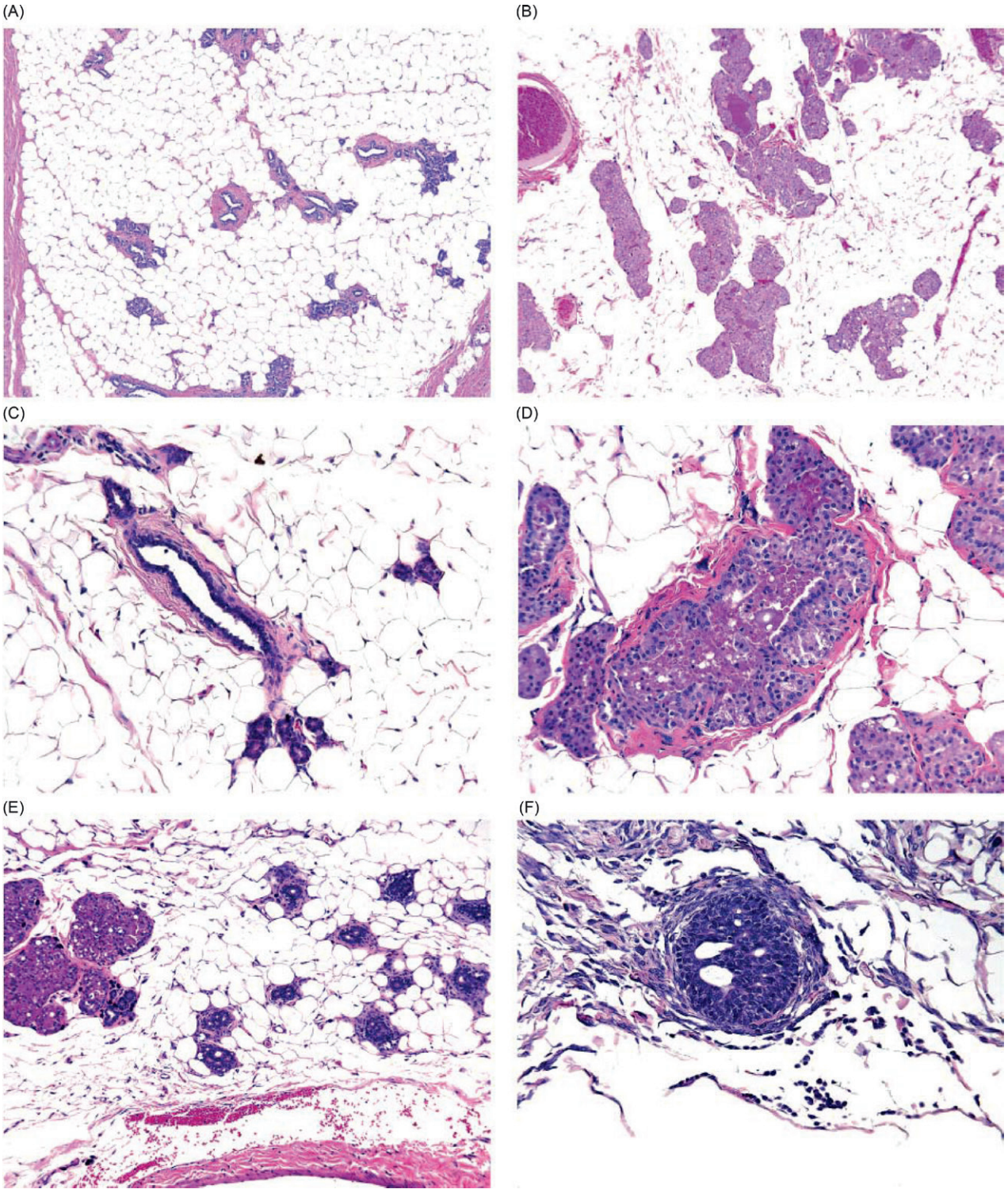

FIGURE 23.6 Mammary gland from sexually mature male and female rats. (A, B) The mammary gland from the female rat (A) is characterized by a predominance of ducts and fewer acini compared to the male (B), which is mostly lobules of acini. (C, D) Intralobular ducts in females (C) are lined by one layer of cuboidal epithelial cells with sparse cytoplasm, in contrast to ducts in males (D) that have a stratified epithelium and epithelial cells with abundant, vacuolated cytoplasm. (E) Occasionally, ducts and tubules with morphologic characteristics similar to those observed in female rats are observed in male rats subadjacent to normal male lobuloalveolar morphology and should not be diagnosed as feminization. (F) TEBs are structures observed commonly in sections of mammary gland from young rats and should not be confused with foci of hyperplasia. Magnification ×25 for A and B, ×200 for C, D, and F, and ×100 for E. Source: Lucas et al: The rat mammary gland: morphologic changes as an indicator of systemic hormonal perturbations induced by xenobiotics. *Toxicol Pathol* 35(2):199–207, 2007. Review. Reprinted by Permission of SAGE Publications, Inc.

Need-to-know

- In the rat, there are morphologic differences between female and male mammary glands.

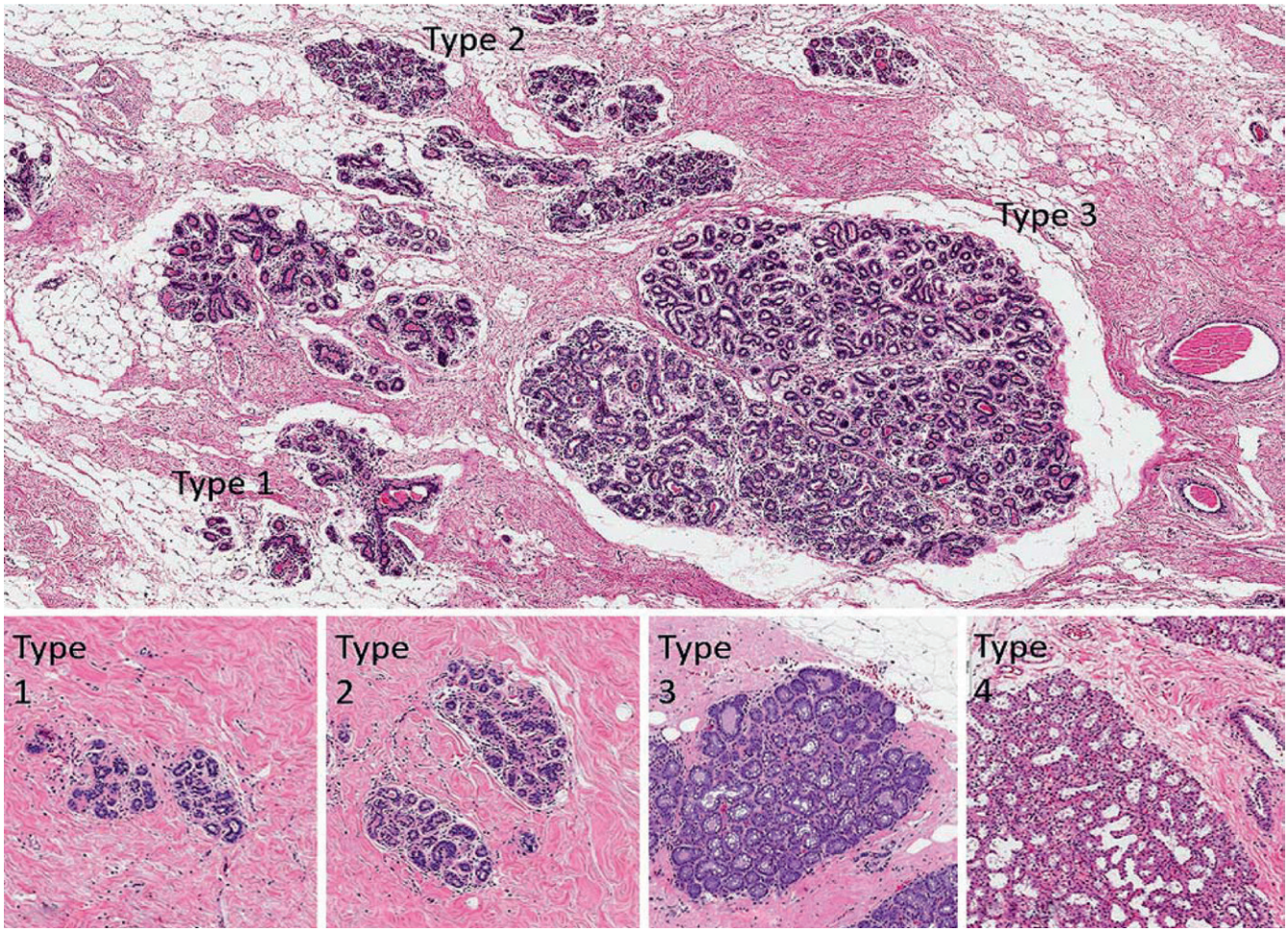

FIGURE 23.7 Heterogeneity of human TDLUs. The mature human mammary gland is composed of a variety of lobules. The top low-magnification image shows a variety of lobular sizes and configurations that can be classified into different types according to area occupied by lobules, number of acini per lobule, and number of nuclei per lobule. Representative lobular types 1–4 are shown.

TABLE 23.2 Histologic Differences in Mammary Glands of Sexually Mature Rats.

Overall Structure	Female Rat	Male Rat
	Duct	
Name	Tubuloalveolar	Lobuloalveolar
Number	High	Low
Epithelium	Simple cuboidal	Pseudostratified or stratified cuboidal or short columnar
Epithelial cytoplasm	Scant, basophilic, nonvacuolated	Abundant, eosinophilic, vacuolated
Epithelial apoptosis	Rare	Frequent
Luminal space	Prominent	Not usually evident
	Acinus	
Number	Low, centered on ductules	High, contiguous lobules
Epithelium	Simple cuboidal	Pseudostratified or stratified cuboidal or short columnar
Epithelial cytoplasm	Scant, basophilic, nonvacuolated	Abundant, eosinophilic, vacuolated
Epithelial apoptosis	Rare	Frequent
Luminal space	Prominent	Not usually evident

Adapted from: Lucas et al: The rat mammary gland: morphologic changes as an indicator of systemic hormonal perturbations induced by xenobiotics. *Toxicol Pathol* 35(2):199–207, 2007. Review. Reprinted by Permission of SAGE Publications, Inc.

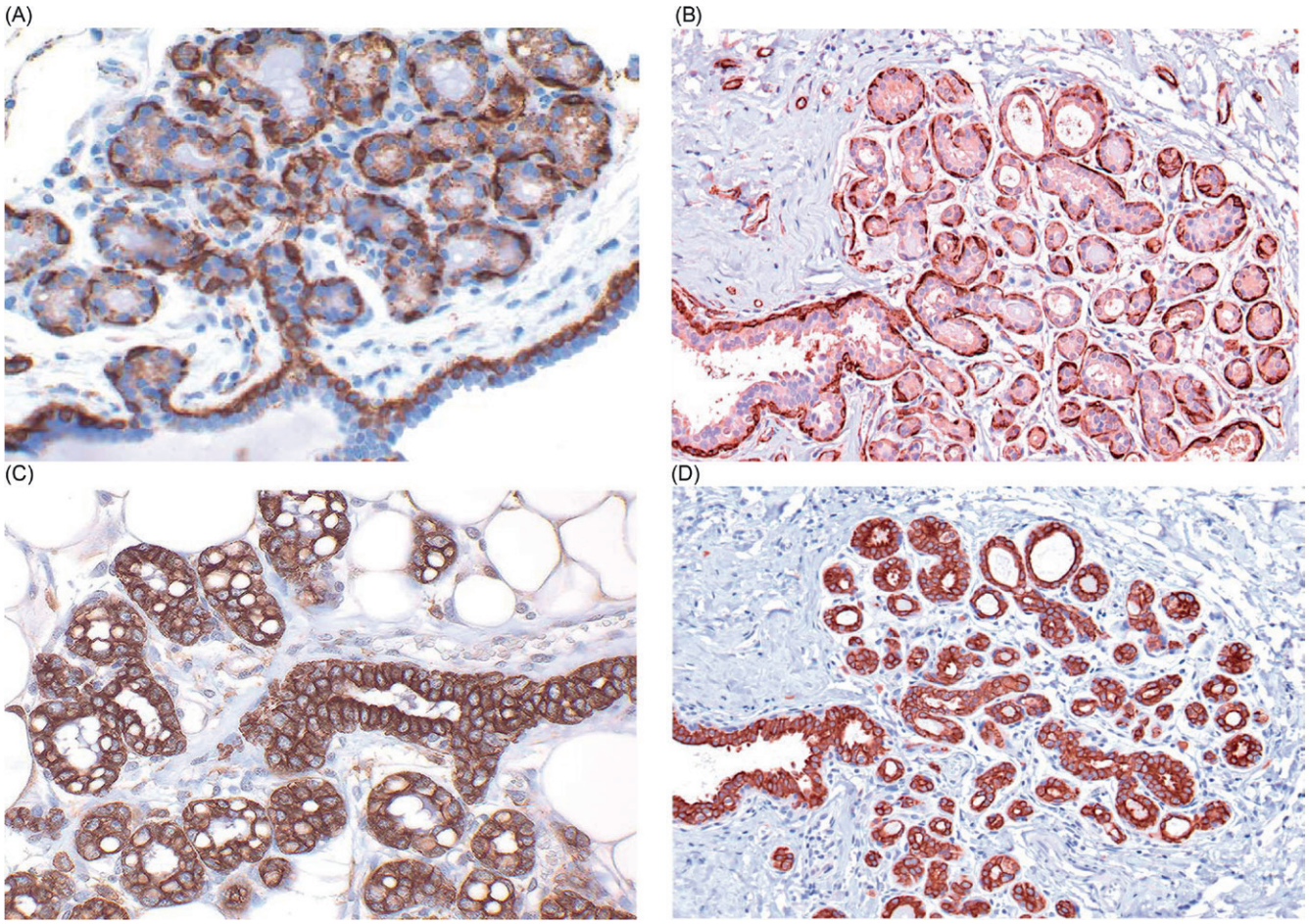

FIGURE 23.8 Basal and luminal cell immunohistochemical markers in mouse and human mammary gland. Immunohistochemistry highlights the basal and luminal cell populations in these low-magnification images of a mouse prelactating lobular-acinar unit (A, C) and a human TDLU (B, D). (A, B) Smooth muscle actin expression of the basal myoepithelial cell population. (C, D) Cytokeratin 8/18 labeling of luminal epithelial cells.

Need-to-know

- In all three species, there are two major epithelial cell types in the mammary gland: basal myoepithelial cells and luminal epithelial cells.

upon microscopic inspection, such as plasma cell production of milk IgA.

Lactiferous Duct

The mammary gland is a tree-like ductal system that leads to the nipple. Each rodent mammary gland contains 5–10 secondary collecting ducts, which drain into a single lactiferous duct or sinus (Figs. 23.3 and 23.9). The secondary collecting ducts are present in the deeper mammary fat pad and develop in a more linear pattern than in humans (Figs. 23.2 and 23.3).

In contrast, the human has multiple ductal trees radially arrayed to form a complex overlapping "forest" of trees (Fig. 23.2C). The ducts drain through a single shared nipple. However, in contrast to the rodents, the each nipple has multiple outlets or ostia ($n = 10–20$). The number of ostia, however, does not equal the number of lobes or lactiferous ducts because the ducts tend to coalesce above the sinuses to share ostia. Furthermore, lactating mothers generally have even fewer (ave = 8) functional ostia expressing milk (Figs. 23.2, 23.3, and 23.9). The complex organization of the human breast and its

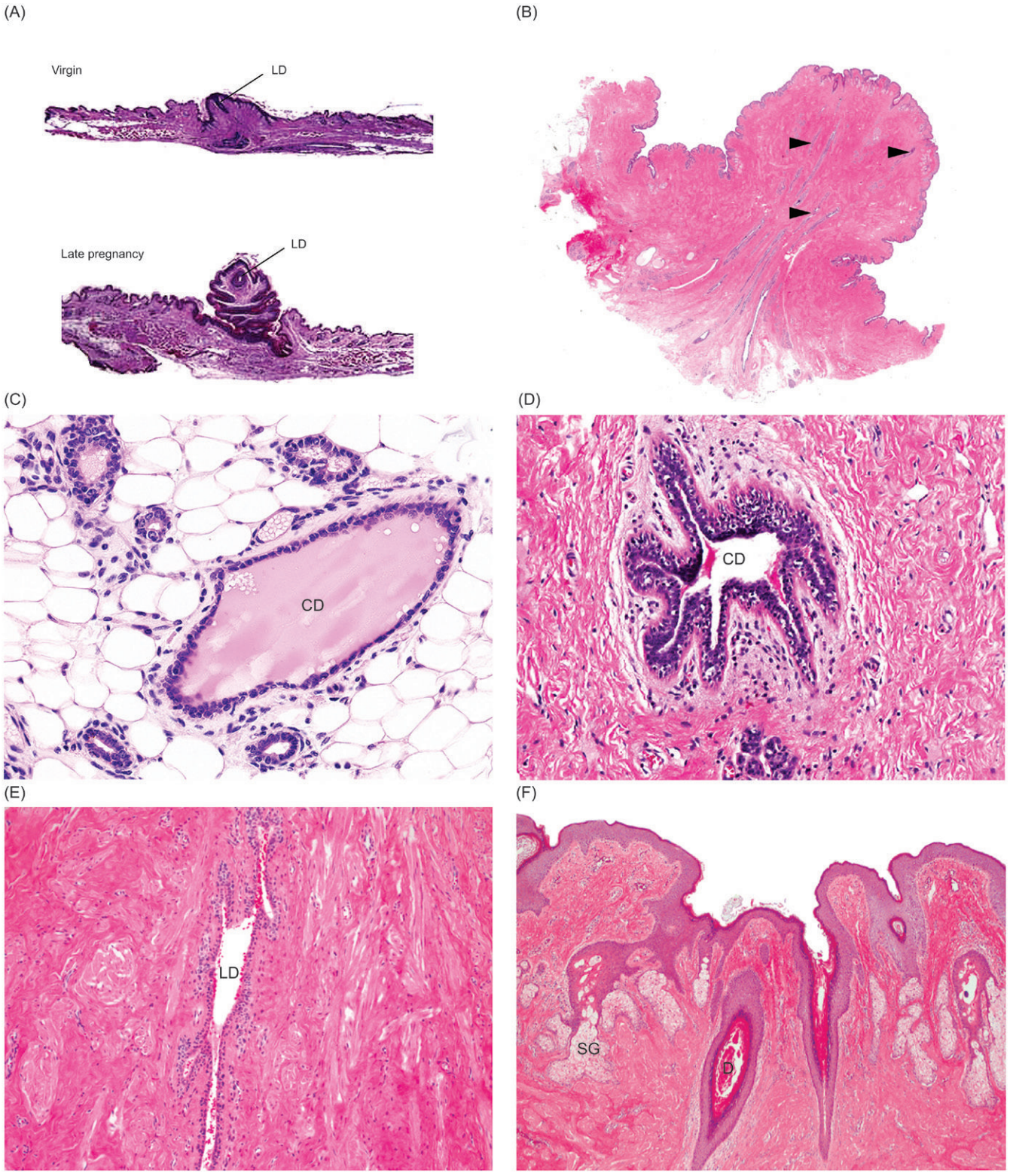

FIGURE 23.9 The nipple and collecting ducts. (A) The mouse nipple becomes prominent during pregnancy. Note the single lactiferous duct (LD). (B) The human nipple in cross section contains multiple major lactiferous ducts (arrowheads). (C) Mouse collecting duct (CD). (D) Human collecting duct. (E) Human lactiferous duct. Smooth muscle bundles are arranged around the lactiferous ducts to aid in ejection of milk. (F) Human areola. The surface of the nipple is covered with stratified squamous epithelium, which plugs the openings of some of the nonlactating ducts (D). Sebaceous glands (SG) are also found in the skin of nipple and areola. Source of A: Wu et al: Expansion of specialized epidermis induced by hormonal state and mechanical strain. *Mech Dev* 136:73–86, 2015, with permission from Elsevier.

Need-to-know

- A single rodent mammary gland empties into one lactiferous duct, whereas the human nipple has multiple major lactiferous ducts.

mammary forest should be considered by clinicians when evaluating, interpreting, and treating breast diseases.

Histologic differences also exist in the lactiferous duct of female and male rats (Table 23.2, Fig. 23.6) with females having more prominent lumina that are lined by a single layer of low cuboidal epithelium. In contrast, the infrequent male ducts have indistinct lumina and are lined by vacuolated pseudostratified epithelial cells. Male mice do not have lactiferous ducts. Similar to the rest of the glandular tissue, the lactiferous duct is lined by myoepithelial cells. The rodent ductal systems are primarily surrounded by adipose tissue, with scanty fibrous connective tissue (Fig. 23.9).

Human lactiferous ducts are lined by tall columnar epithelium and myoepithelial cells. They course through the nipple to the surface (Fig. 23.9). Within each lobe, secondary collecting ducts branches from TDLU drain into lactiferous ducts. In contrast to the rodent, the branching terminal duct lobular system of human mammary gland is supported by relatively abundant fibrovascular tissue admixed with adipose tissue (Fig. 23.9). Although these supporting components are a constant finding in humans, there is striking variability in their relative densities.

There are histologic differences in the collecting ducts of female and male rats (Table 23.2, Fig. 23.6) with females having more prominent lumina that are lined by a single layer of low cuboidal epithelium. In contrast, the infrequent male ducts have indistinct lumina and are lined by pseudostratified or stratified epithelium. Male mice do not have collecting ducts.

Human lactiferous ducts course through the nipple to the surface (Fig. 23.9). Within each lobe, the main collecting duct forms secondary branches called extralobular terminal ducts; these branch further into the TDLU.

Nipple

In all species, the surface of the nipple–areolar complex is covered by keratinizing squamous epithelium (Fig. 23.9). Sebaceous glands are also found in association with the epithelium in this area (Fig. 23.9). Hair follicles can be found in the areola and skin of the mammary gland. The nipple contains bands of smooth muscle that run parallel to the major lactiferous ducts as well as circumferentially toward the base (Fig. 23.9). The smooth muscle acts as erectile tissue and is involved in eliminating milk from the nipple. Recall that the human nipple has numerous ostia (Fig. 23.3D) while rodent nipple has only a single outlet (Figs. 23.3A and B and 23.9A). Male rodents lack nipples.

Mammary Gland Natural History and Reproductive Cycles

EARLY DEVELOPMENT

The rodent mammary gland is often used to model human mammary natural history, including changes from early development to puberty, through reproduction and senescence (Fig. 23.10). Shortly after birth, the rodent mammary gland can be seen extending from the mammary bud with primary and secondary branches (Fig. 23.11). At this early stage, 90% of the mammary fat pad contains no epithelial cells. The mammary gland continues to extend into and fill the mammary fat pad until shortly before puberty. In the rat, the ducts and side branches terminate in early TDLU, which can be observed as early as 2 weeks after birth.

The early phase of development entails extension into the rodent mammary fat pad; the key feature is emergence of the terminal end bud (TEB)

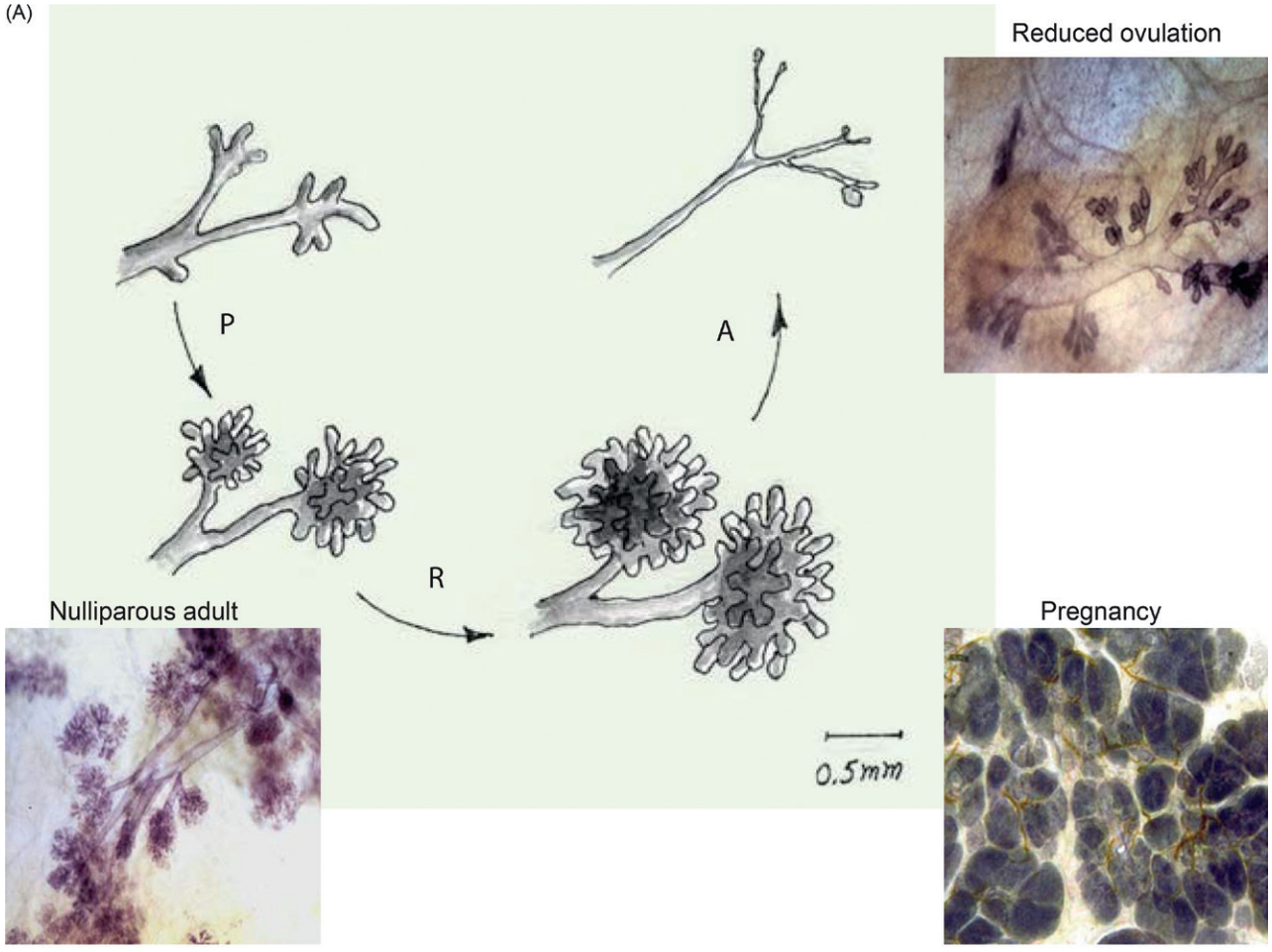

FIGURE 23.10 The natural history of the mammary gland. (A) Diagram illustrating the natural history of a normal human mammary lobule which progresses from prepubertal (P) through reproduction (R) to atrophy (A). (B) Stages of normal rat mammary gland (MG) development. *TEB*, terminal end bud. Source of A: Human whole mount images from the collection of Drs Wellings and Jensen (Wellings, Jensen, et al: An atlas of subgross pathology of the human breast with special reference to possible precancerous lesions. *J Natl Cancer Inst* 55: 213–273, 1975; Cardiff, Wagner, et al: Mammary cancer in humans and mice. A tutorial for comparative pathology. The CDROM. *J Mammary Gland Biol Neoplasia* 5:243–244, 2000). Source of B: Adapted from Enoch et al. (Mammary gland development as a sensitive end point after acute prenatal exposure to an atrazine metabolite mixture in female Long-Evans rats. *Environ Health Perspect* 115(4):541–547, 2007) and Rudel et al. (Environmental exposures and mammary gland development: state of the science, public health implications, and research recommendations. *Environ Health Perspect* 119(8):1053–1061, 2011), with permission from *Environmental Health Perspectives*. http://ehp.niehs.nih.gov/1002864/. Bars = 2 mm.

Need-to-know

- The natural history of the mammary gland is similar between all three species.

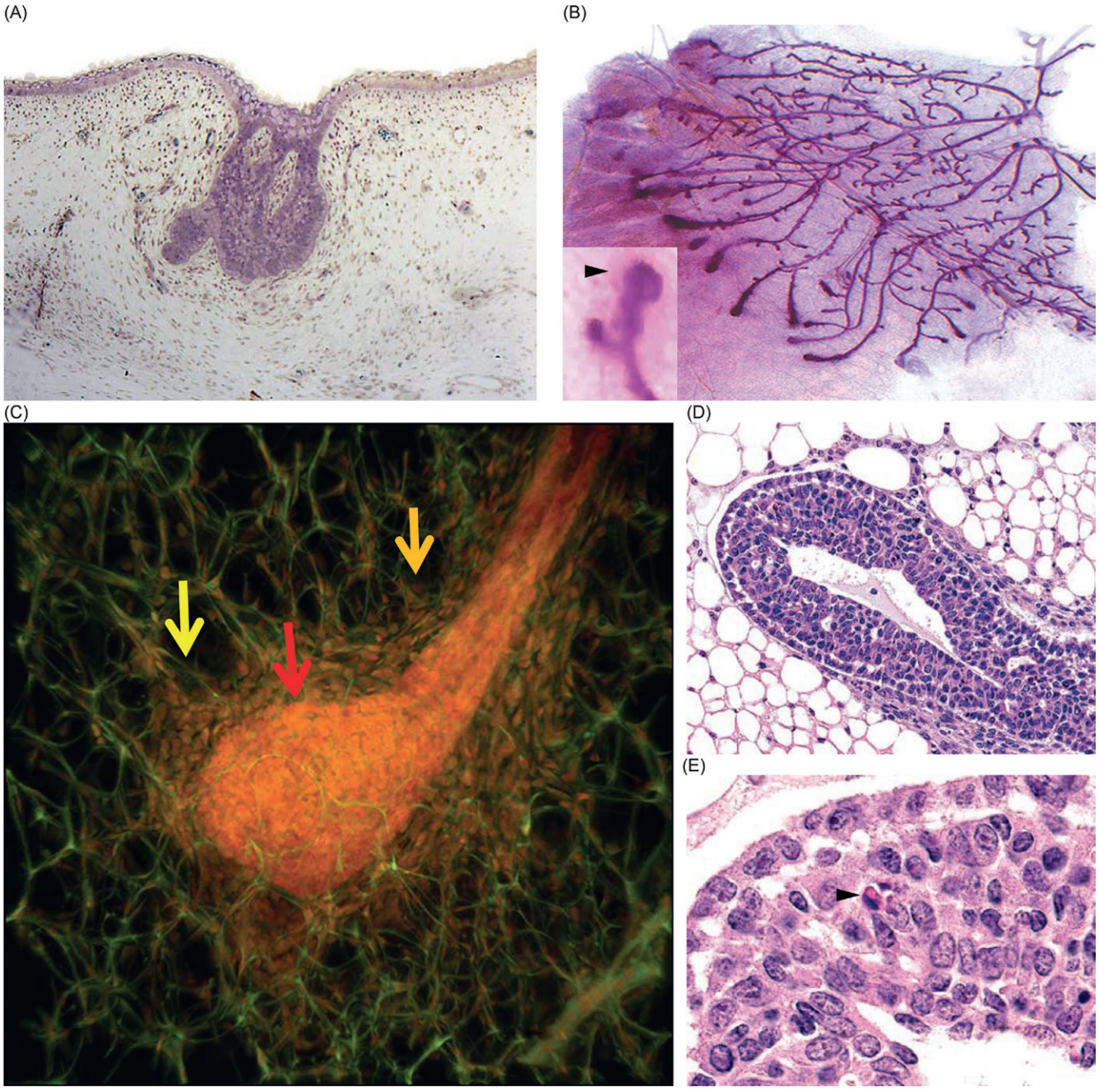

FIGURE 23.11 Mammary gland development. (A) Human mammary bud whole mount. The natural history of the mammary gland begins with development of the mammary bud *in utero*. (B) Early in life, the rodent (rat) mammary bud extends via extension of TEBs into the fat pad. Inset: Rat TEB with fuzzy halo (arrowhead), which contains inflammatory cells. (C) Rodent (mouse) TEB. The TEB is rich with interactions with the surrounding stroma, which is essential for the extension of the TEB through the mammary fat pad. Laser scanning-based tissue autofluorescence/fluorescence imaging (LS-TAFI) provides 3D images with artificial colorization of nuclei (orange) and blood vessels (green). Note the small round cells around the neck and the leading edge of the head and the collar of small cells around the neck (orange arrow), the body of the TEB (red arrow) and the small cells forming an "escort" for the TEB (yellow arrow). Scale bar = 50 µm. (D) Mouse TEB. Note the peripheral rim of cap cells and the central body of core cells. (E) Mouse TEB at high magnification demonstrates apoptosis (arrowhead) in the core cell population. Source of C: Hidetoshi Mori.

Need-to-know

- The TEB is the growing end of the mammary tree.
- The TEB has a body and a cap cell layer and is supported by an infiltrate composed of macrophages, mast cells, and eosinophils that escort the growing end.
- The TEB has a rich blood supply.

(Fig. 23.11). The TEB is the growing end of the mammary tree; it is also found in prelactating mammary glands, where it involves side branching and production of additional milk-producing lobules. The TEB forms as a club-like structure at the end of a duct (Fig. 23.11). It is composed of a central body surrounded by a single layer of pluripotent epithelial "cap" cells (Fig. 23.11). The undifferentiated body cells hollow out to form the epithelium of the nascent duct and the "neck" of the TEB, and the cap cells merge with the myoepithelial cells of the duct.

Significantly, the TEB is surrounded by host inflammatory cells that are difficult to appreciate in microscopic sections, but appear as "fuzzy halos" in whole mount preparations (Inset, Fig. 23.11). Three-dimensional imaging using laser scanning-based tissue autofluorescence/fluorescence provides a more complete picture of TEB histology (Fig. 23.11). The interaction between these host elements and the epithelium is critical to mammary development. The human TEB has not been described in detail.

OVARIAN (ESTROUS AND MENSTRUAL) CYCLE

The mammary gland of all three species responds to the surges in hormones associated with ovulation and luetinization (Fig. 23.12) with increased mitotic activity. In general, this increased mitotic activity can be detected during estrus in rodents and during the luteal phase in humans (Fig. 23.12). In all three species, in the absence of fertilization, the TDLU epithelium undergoes atrophy with autophagy. However, given the heterogeneity in each mammary gland, these changes are extremely difficult to detect, evaluate, and interpret on a single microscopic slide.

Ovarian cycle changes tend to occur in a regional pattern in rodents. For example, when viewed in whole mounts, lobule expansion during estrous is more readily observed close to the nipple, while the peripheral mammary ducts may appear thicker than diestrus ducts, which tend to appear smaller in whole mounts (Fig. 23.12), as do proestrous ducts. Four distinct phases have been described during the human menstrual cycle based on the number of cell layers in the acini, degree of vacuolation of the myoepithelial cells, amount of stromal edema, immune cell infiltration, rate of mitosis, and amount of apoptosis or autophagy.

PREGNANCY AND LACTATION

During rodent pregnancy, a series of gross and histologic changes occur in the mammary glands that are similar to those seen during human pregnancy (Fig. 23.13). Rodent gestational and lactational changes are generally divided into early (Day 7), mid (Day 14), and late (Days 18–20) prelactation; lactation (Fig. 23.13); and involution. During pregnancy, the epithelial cells proliferate, alveolar differentiation occurs, and external nipple and areolar development is observed (Fig. 23.13). The mammary gland stroma becomes increasingly cellular, and there is a relative decrease in adipose tissue (Fig. 23.13). Later, alveolar epithelium becomes presecretory and begins to produce milk components (protein, fat, and lactose) (Fig. 23.13). In human pregnancy and lactation, there is a 10-fold increase in epithelial content, which expands from an average of 5% in nulliparous to 52% in lactating tissue.

In all three species, pregnancy is associated with mammary gland enlargement and cell proliferation as the TDLU grows and acini develop and mature. Toward the end of pregnancy and during lactation, cell proliferation slows and further mammary gland enlargement results from alveolar hypertrophy. In all three species, with the onset of lactation, luminal alveolar cells produce large fat vacuoles and Golgi vesicles containing lactose, protein, and water (Fig. 23.14). These

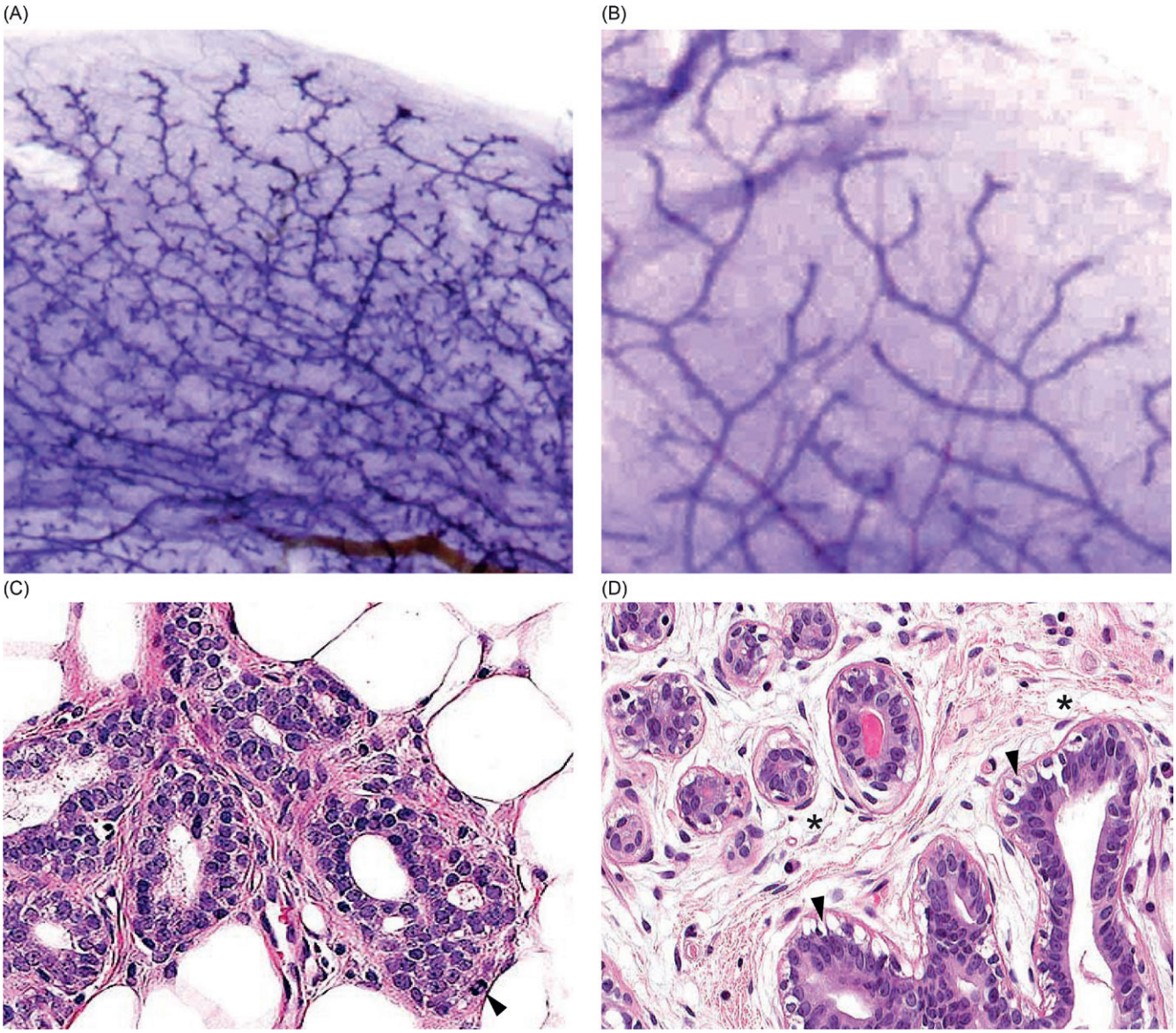

FIGURE 23.12 Mammary gland during the ovarian cycle. (A, B) Whole mounts comparing mouse estrus (A) and diestrus (B). Note that during estrus the mammary ducts are thicker, more abundant, and have multiple side buds. During diestrus, the glands regress to a simple branching structure with slender ducts with few side buds. (C) Rat estrus. Note mitotic figure (arrowhead). (D) Human secretory (luteal) phase. Acini have extensive myoepithelial cell vacuolization (arrowhead) and increased immune cells with stromal edema (asterisks).

Need-to-know

- Mammary epithelium proliferates during the estrus phase (rodent) or secretory (luteal) phase (human).
- In all species the mammary luminal epithelium undergoes atrophy and apoptosis during the interphases.
- The human cytoplasm of myoepithelium becomes prominent and clear, and the stroma becomes edematous, at the peak of the luteal phase.

contents are released by apocrine secretion. Milk is expressed from the acini to the collecting ducts and out the nipple during nursing, resulting in depleted acini (Fig. 23.14).

POSTPARTUM INVOLUTION

Cessation of lactation causes postpartum involution with return of epithelial cells to a nonsecretory state and decreased numbers and

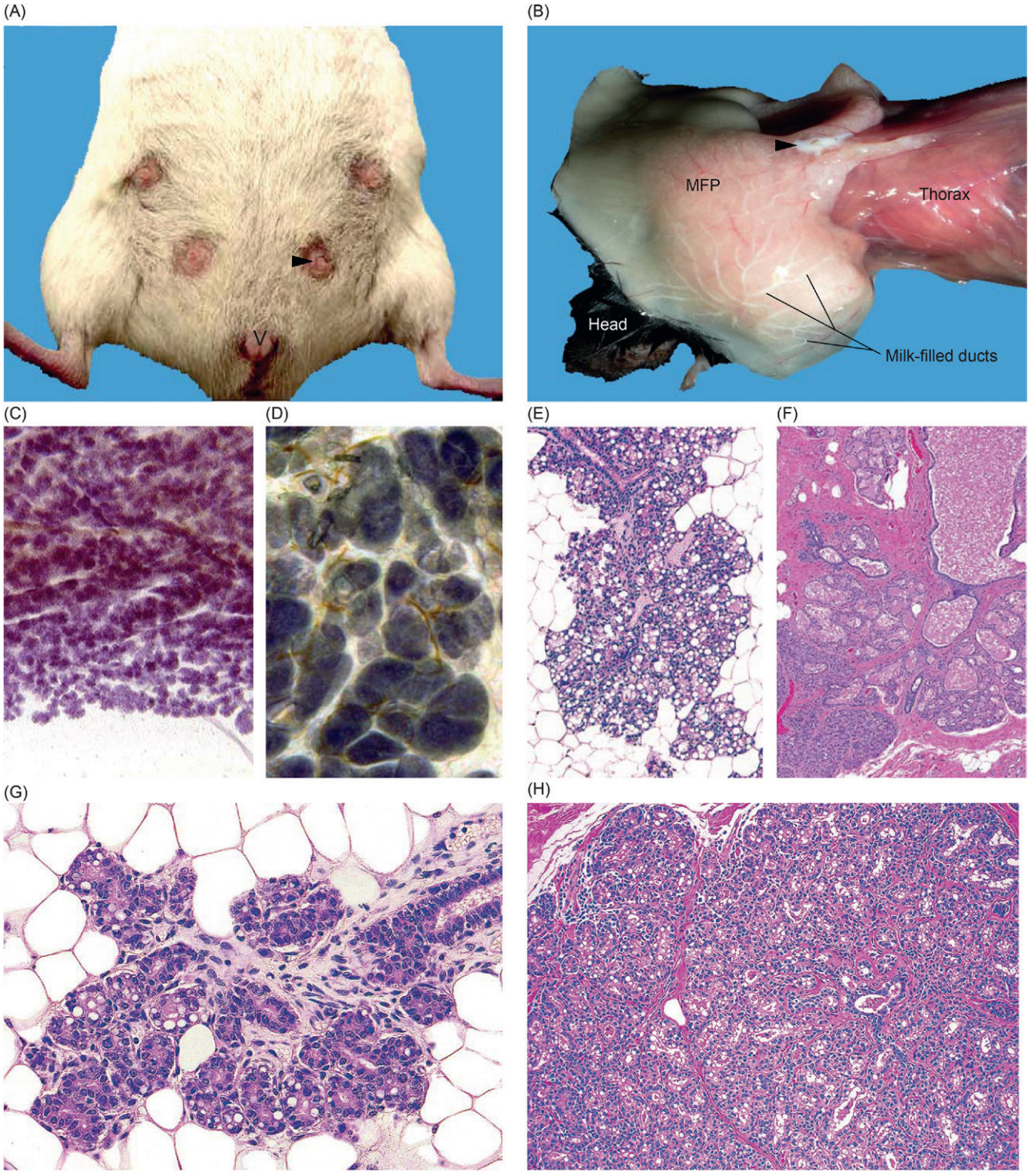

FIGURE 23.13 Pregnancy and lactation. (A) During pregnancy, the rodent (mouse) nipples (arrowhead) and areola develop and protrude. The vulva (V) is indicated. (B) The rodent lactating mammary fat pad (MFP) is extensive. In this mouse necropsy dissection, the pelt was degloved and reflected over the head, and the subcutaneous MFP removed with the skin. Milk-filled ducts are visible as white branching lines. Incidental transection of a duct at necropsy results in expression of milk (arrowhead). Thorax and head are indicated for orientation. (C, D) Subgross anatomy (C, mouse; D, human) of milk-laden lobules with preservation of lobular architecture. (E, F) Lactating mouse (E) and human (F) mammary gland. Milk is produced by acini, filling and distending the TDLU. (G, H) High magnification of pregnant mouse (G) and human (H) mammary epithelium. The acinar units are fully developed and quite similar in appearance between the three species. Source of A: Wu et al: Expansion of specialized epidermis induced by hormonal state and mechanical strain. *Mech Dev* 136:73–86, 2015, with permission from Elsevier.

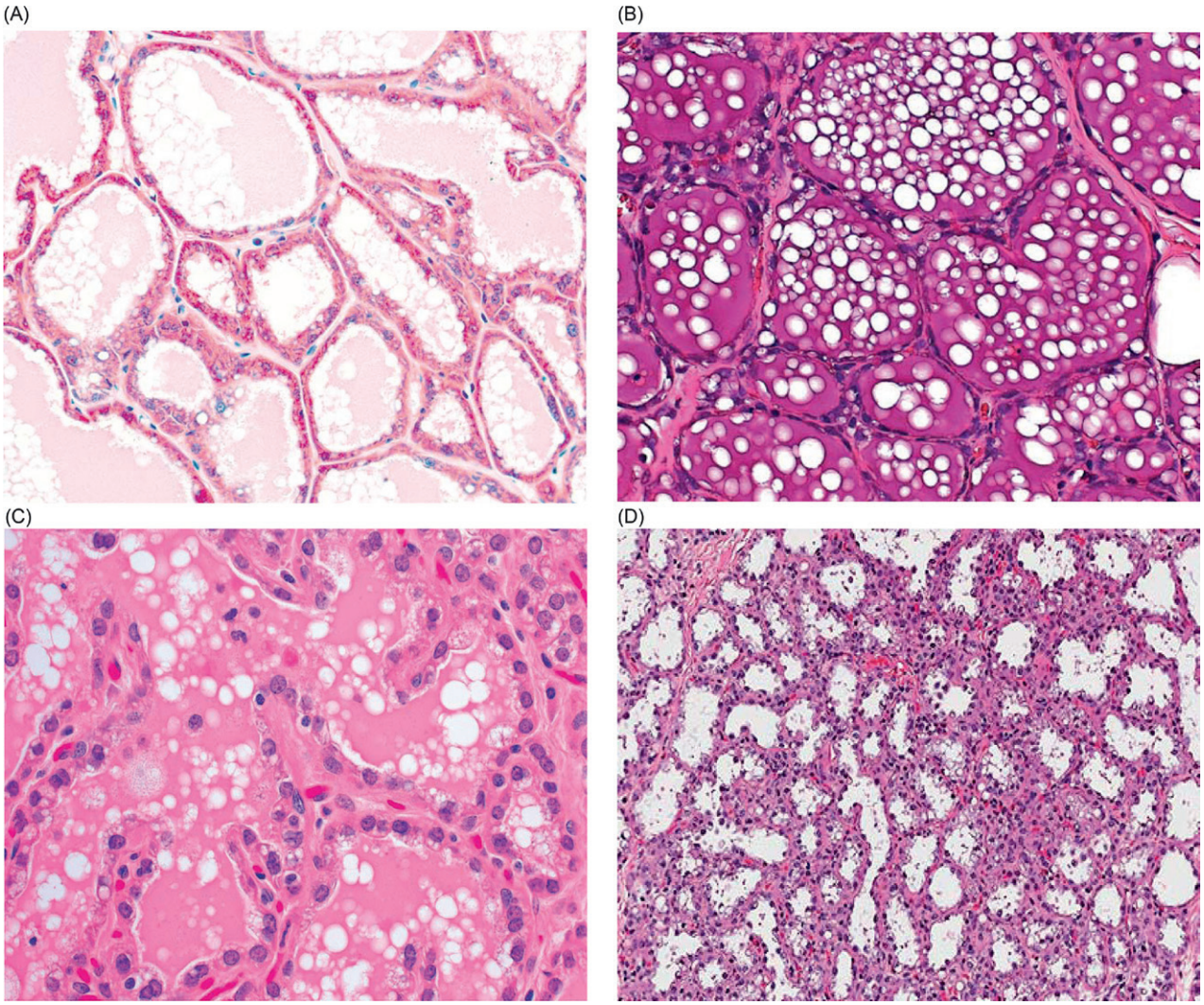

FIGURE 23.14 Lactation. (A) Mouse. (B) Rat. (C) Human. Note the high volume of fat globules in the rat mammary gland. Images show secretory morphology comprised of acini with distended lumen that are filled with secreted milk and lined with flattened epithelial cells. (D) Human. Postnursing without milk secretions in the acini.

Need-to-know

- The morphology of lactation is similar in all three species.

size of glandular units, with many regions of the gland returning to a prepregnancy morphology. As noted above, TDLUs persist in rats and humans, but not mice.

Postpartum involution in rodents begins immediately after weaning. It is a very rapid process, which is usually complete in 7–10 days (Fig. 23.15). The first 3 days involve extensive epithelial cell apoptosis or autophagy with loss of acini. Epithelial cell loss is accompanied by immune cell infiltrates consistent with acute, proliferative, and resolution phases of wound healing, as well as extracellular matrix remodeling. In human postpartum involution, the epithelial content returns to an average of 7%, which is comparable to the prepregnant nulliparous state. However, the epithelial content in breast can vary between 3% and 13%, thus suggesting epithelial heterogeneity in breast tissue. Lobular subtype analysis suggests a similar pattern with loss of secretory lactating lobules following weaning, and return of the lobular composition to that of the prepregnant nulliparous state.

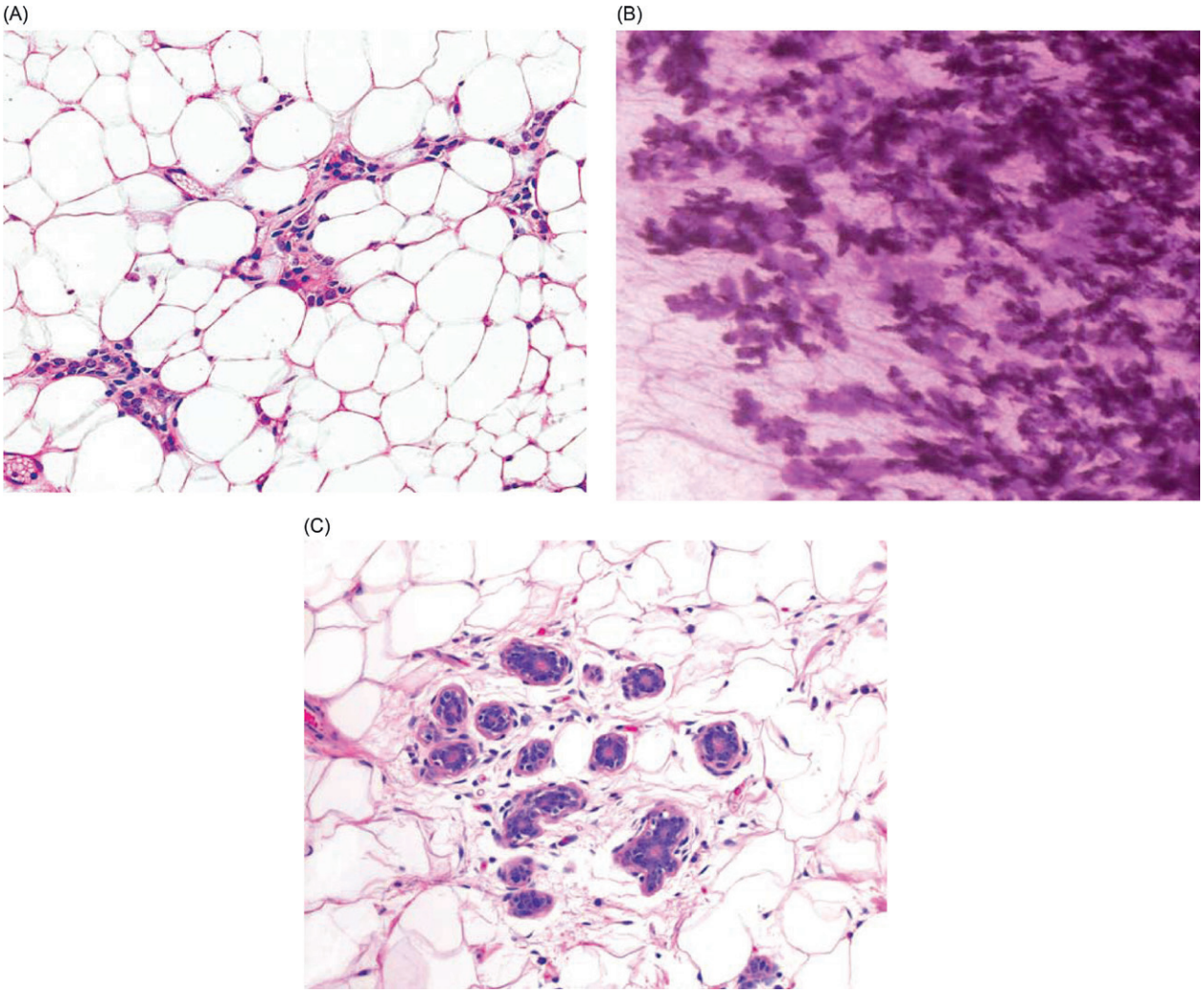

FIGURE 23.15 Mammary gland involution. (A) Mouse. In the postpartum setting, the mouse mammary gland undergoes drastic involution, with a similar histologic appearance to the menopausal human mammary gland (see panel C). This image shows the spiculated "chicken wire" pattern of a regressed mammary gland in a multiparous mouse. (B) Rat. Whole mount. The mammary gland 3 weeks postweaning shows atrophy of the TDLU. (C) Human. The human mammary gland does not undergo significant involution until menopause. At that point the TDLUs become smaller, and the supporting stroma more adipose-rich, with relative depletion of fibrocollagenous stroma.

Need-to-know

- Postpartum involution takes less than a week in rodents.
- The TDLU persists in rats and humans.

SENESCENCE

Rodents do not undergo the equivalent of menopause. In most laboratory colonies, females are retired from breeding when their litter size diminishes, but they continue to cycle and remain fertile; rarely, they may become anovulatory. When the mammary glands of retired breeders are examined, they are generally atrophied but otherwise not remarkable (Fig. 23.16) and thus not considered senescent. However, artificial senescence of the mammary gland can be achieved in rodents by ovariectomy, which experimentally mimics the anovulatory stage of the postmenopausal human female and induces a remarkable atrophy of the TDLU (Fig. 23.16).

In humans, during perimenopause, or following surgically or chemically induced menopause, the mammary gland atrophies to senescence, resulting in decreases in the secretory glandular component and an alteration in the relative proportion of

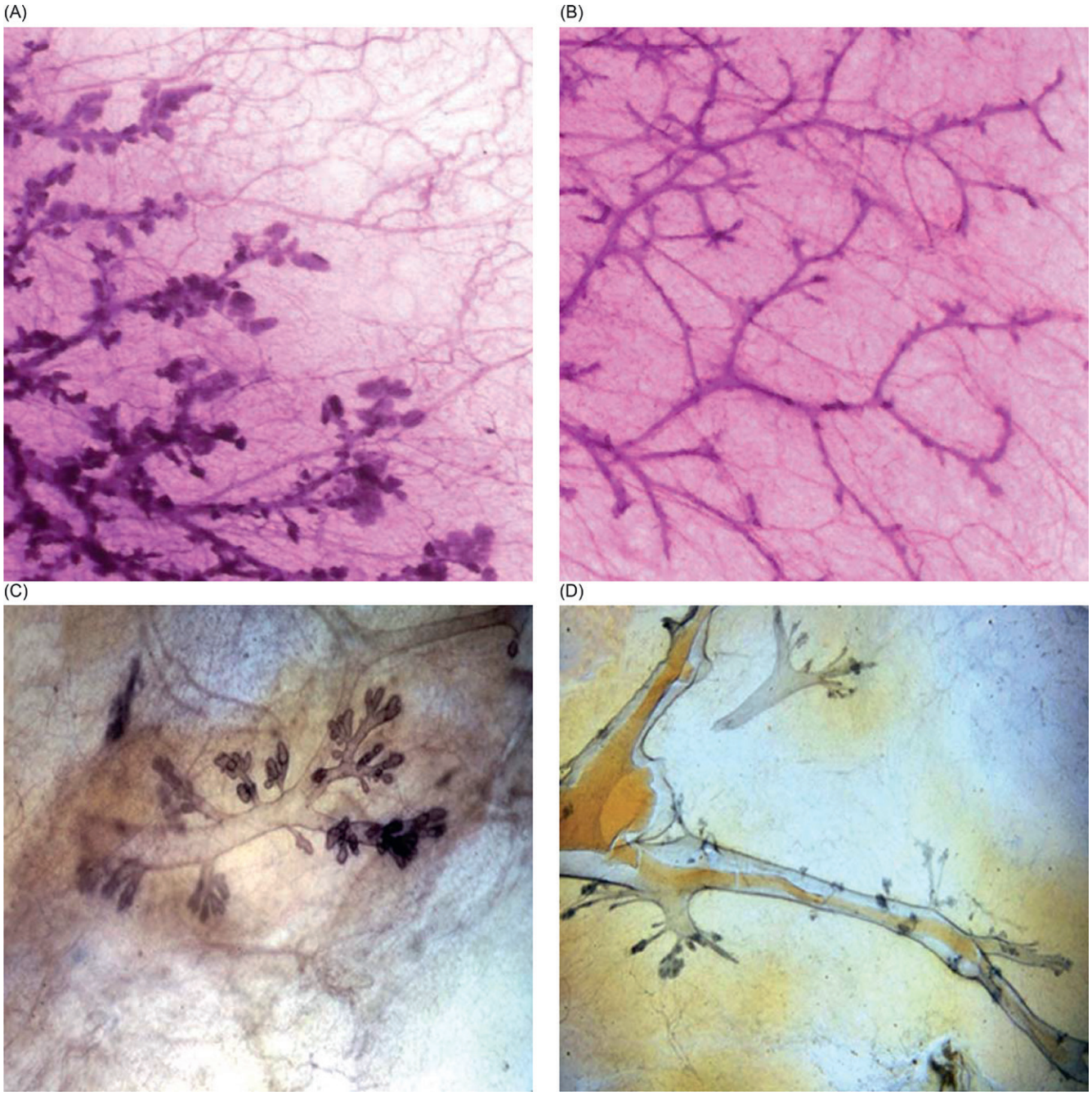

FIGURE 23.16 Mammary gland senescence. Rat (A, B) and human (C, D) whole mounts. (A) TDLU pattern in a 146-day-old nulliparous rat mammary gland. Note the prominent lobular development. (B) TDLU pattern in a 128-day-old ovariectomized rat. Note the atrophy of the lobular structure. (C) Human at menopause. With loss of ovarian function, the mammary gland undergoes loss of TDLU. (D) Human at senescence. The TDLUs have virtually disappeared. Source: Human images from the collection of Drs Wellings and Jensen (Wellings, Jensen, et al: An atlas of subgross pathology of the human breast with special reference to possible precancerous lesions. *J Natl Cancer Inst* 55:213–273, 1975; Cardiff, Wagner, et al: Mammary cancer in humans and mice. A tutorial for comparative pathology. The CDROM. *J Mammary Gland Biol Neoplasia* 5:243–244, 2000).

Need-to-know

- The number and type of TDLUs change with hormone status and age.
- The TDLU is ovarian hormone dependent.

each TDLU type (Figs. 23.10 and 23.16). Atrophy continues through menopause to senescence with further glandular involution and replacement of the secretory glandular component with adipose and connective tissue, both of which also diminish over time.

FURTHER READING

Monographs

Green EL, editor. *Biology of the laboratory mouse, by the staff of the Jackson Laboratory*, ed 2, New York, 1966, McGraw-Hill, xii, 706 p. illus.

Haagensen DC: *Diseases of the breast*, ed 3, Philadelphia, PA, 1986, Saunders.

McCarty KS, Nath M: Breast. In Sternberg SS, editor: *Histology for pathologists*, Philadelphia, PA, 1997, Lippincott-Raven, pp 71–82.

Osborne MP: Breast anatomy and development. In Harris JR, Lippman ME, Morrow M, editors: *Diseases of the breast* (ed 3), Philadelphia, PA, 2004, Lippincott Williams & Wilkins, pp 3–13.

Page DL, Anderson TJ: Anatomy. In Page DL, Anderson TJ, editors: *Histopathology of the breast*, Edinburgh, 1987, Churchill Livingstone, pp 4–10.

Rosen P: Anatomy and physiologic morphology. In Rosen P, editor: *Rosen's breast pathology* (ed 3), Philadelphia, PA, 2009, Lippincott Williams & Wilkins, pp 1–15.

Russo J, Russo IH: *Techniques and methodological approaches in breast cancer research*, New York, 2014, Springer.

Schnitt SJ, Millis RR, Hanby AM, et al: The breast. In Mills SE, editor: *Diagnostic surgical pathology* (ed 4), Philadelphia, PA, 2004, Lippincott Williams& Wilkins, pp 323–395.

Tavassoli FA: Normal development and anomalies. In Tavassoli FA, editor: *Pathology of the breast* (ed 2), Stamford, CT, 1999, Appleton & Lange, pp 1–25.

Scientific Papers

Anbazhagan R, Osin PP, Bartkova J, et al: The development of epithelial phenotypes in the human fetal and infant breast. *J Pathol* 184(2):197–206, 1998.

Ball SM: The development of the terminal end bud in the prepubertal-pubertal mouse mammary gland. *Anat Rec* 250(4):459–464, 1998.

Cardiff RD, Wagner U, Hennighausen L: Mammary cancer in humans and mice: a tutorial for comparative pathology. The CD-ROM. *J Mammary Gland Biol Neoplasia* 5(2): 243–244, 2000.

Cardiff RD, Wagner U, Hennighausen L: Mammary cancer in humans and mice: a tutorial for comparative pathology. *Vet Pathol* 38(4):357–358, 2001.

Cardiff RD, Wellings SR: The comparative pathology of human and mouse mammary glands. *J Mammary Gland Biol Neoplasia* 4(1):105–122, 1999.

de Assis S, Warri A, Cruz MI, et al: Changes in mammary gland morphology and breast cancer risk in rats. *J Vis Exp* 44:e2260, 2010.

Dontu G, Ince TA: Of mice and women: a comparative tissue biology perspective of breast stem cells and differentiation. *J Mammary Gland Biol Neoplasia* 20(1–2):51–62, 2015.

Enoch RR, Stanko JP, Greiner SN, et al: Mammary gland development as a sensitive end point after acute prenatal exposure to an atrazine metabolite mixture in female Long-Evans rats. *Environ Health Perspect* 115(4):541–547, 2007.

Going JJ, Moffat DF: Escaping from Flatland: clinical and biological aspects of human mammary duct anatomy in three dimensions. *J Pathol* 203(1):538–544, 2004.

Going JJ, Mohun TJ: Human breast duct anatomy, the 'sick lobe' hypothesis and intraductal approaches to breast cancer. *Breast Cancer Res Treat* 97(3):285–291, 2006.

Goldhar AS, Vonderhaar BK, Trott JF, et al: Prolactin-induced expression of vascular endothelial growth factor via Egr-1. *Mol Cell Endocrinol* 232(1-2):9–19, 2005.

Gusterson BA, Stein T: Human breast development. *Semin Cell Dev Biol* 23(5):567–573, 2012.

Hens JR, Wysolmerski JJ: Key stages of mammary gland development: molecular mechanisms involved in the formation of the embryonic mammary gland. *Breast Cancer Res* 7(5):220–224, 2005.

Hinck L, Silberstein GB: Key stages in mammary gland development: the mammary end bud as a motile organ. *Breast Cancer Res* 7(6):245–251, 2005.

Jindal S, Gao D, Bell P, et al: Postpartum breast involution reveals regression of secretory lobules mediated by tissue-remodeling. *Breast Cancer Res* 16(2):R31, 2014.

Love SM, Barsky SH: Anatomy of the nipple and breast ducts revisited. *Cancer* 101(9):1947–1957, 2004.

Lucas JN, Rudmann DG, Credille KM, et al: The rat mammary gland: morphologic changes as an indicator of systemic hormonal perturbations induced by xenobiotics. *Toxicol Pathol* 35(2):199–207, 2007.

Moffat DF, Going JJ: Three dimensional anatomy of complete duct systems in human breast: pathological and developmental implications. *J Clin Pathol* 49(1):48–52, 1996.

Mori H, Borowsky AD, Bhat R, et al: Laser scanning-based tissue autofluorescence/fluorescence imaging (LS-TAFI), a new technique for analysis of microanatomy in whole-mount tissues. *Am J Pathol* 180(6):2249–2256, 2012.

Nandi S: Endocrine control of mammary gland development and function in the C3H/He Crgl mouse. *J Natl Cancer Inst* 21(6):1039–1063, 1958.

Nandi S, Bern HA: The hormones responsible for lactogenesis in BALB/cCrgl mice. *Gen Comp Endocrinol* 1:195–210, 1961.

Osin PP, Anbazhagan R, Bartkova J, et al: Breast development gives insights into breast disease. *Histopathology* 33(3):275–283, 1998.

Pensa S, Lloyd-Lewis B, Sargeant TJ, et al: Signal transducer and activator of transcription 3 and the phosphatidylinositol 3-kinase regulatory subunits p55α and p50α regulate autophagy in vivo. *FEBS J* 281(20):4557–4567, 2014.

Ramakrishnan R, Khan SA, Badve S: Morphological changes in breast tissue with menstrual cycle. *Mod Pathol* 15(12):1348–1356, 2002.

Richert MM, Schwertfeger KL, Ryder JW, et al: An atlas of mouse mammary gland development. *J Mammary Gland Biol Neoplasia* 5(2):227–241, 2000.

Rudel RA, Fenton SE, Ackerman JM, et al: Environmental exposures and mammary gland development: state of the science, public health implications, and research recommendations. *Environ Health Perspect* 119(8):1053–1061, 2011.

Rudmann D, Cardiff R, Chouinard L, et al: Proliferative and nonproliferative lesions of the rat and mouse mammary, Zymbal's, preputial, and clitoral glands. *Toxicol Pathol* 40(6 Suppl):7S–39S, 2012.

Rusby JE, Brachtel EF, Othus M, et al: Development and validation of a model predictive of occult nipple involvement in women undergoing mastectomy. *Br J Surg* 95(11):1356–1361, 2008.

Russo J, Hu YF, Silva ID, et al: Cancer risk related to mammary gland structure and development. *Microsc Res Tech* 52(2):204–223, 2001.

Sternlicht MD: Key stages in mammary gland development: the cues that regulate ductal branching morphogenesis. *Breast Cancer Res* 8(1):201, 2006.

Suttie AW, Leininger JR, Bradley AE: *Boorman's pathology of the rat: reference and atlas*, ed 2, New York, 2017, Academic Press.

Wellings SR, Jensen HM: On the origin and progression of ductal carcinoma in the human breast. *J Natl Cancer Inst* 50(5):1111–1118, 1973.

Wellings SR, Jensen HM, Marcum RG: An atlas of subgross pathology of the human breast with special reference to possible precancerous lesions. *J Natl Cancer Inst* 55(2):231–273, 1975.

Williams JM, Daniel CW: Mammary ductal elongation: differentiation of myoepithelium and basal lamina during branching morphogenesis. *Dev Biol* 97(2):274–290, 1983.

Wu HJ, Easwaran T, Offutt CD, et al: Expansion of specialized epidermis induced by hormonal state and mechanical strain. *Mech Dev* 136:73–86, 2015.

This page intentionally left blank

SKIN AND ADNEXA 24

JOHN P. SUNDBERG
The Jackson Laboratory, Bar Harbor, ME, United States

CARMEN J. BOOTH
Yale University School of Medicine, New Haven, CT, United States

LILLIAN B. NANNEY
Vanderbilt University Medical Center, Nashville, TN, United States

PHILIP FLECKMAN
University of Washington School of Medicine, Seattle, WA, United States

LLOYD E. KING JR.
Vanderbilt University Medical Center, Nashville, TN, United States

Introduction

The skin is the largest organ of the body based on surface area, although the muscles and bones have more mass. One of its primary functions is as a barrier against desiccation and the hostilities of microbial invaders from the outside world. The skin is one of the largest components of the immune system, is a key component of the nervous and endocrine systems, and provides vitamins in response to sunlight (Table 24.1). This complex organ comprises a variety of adnexal structures: (1) pilosebaceous units, (2) modified sebaceous glands, (3) eccrine and apocrine sweat glands, and (4) nails. The mammary glands, an example of a modified apocrine sweat gland, are sometimes considered cutaneous adnexa because they form from epidermal precursors that invaginate downward during prenatal development. They are covered in Chapter 23: Mammary Gland.

Dermatopathology of mice, rats, and humans is well covered in other textbooks and review articles as are the molecular events involved in development and maintenance of these structures. Likewise, optimal methods to collect and process these tissues are described in detail elsewhere. Several cutaneous structures are unique to rodents that are not found in humans, notably the preputial and clitoral glands, as well as the tail. Conversely, humans, but not rodents, have apocrine sweat glands.

An obvious difference in the structure of humans and other mammals is the relative looseness of the skin based on the structure of the dermis. Another obvious difference is humans do not have the same relative distribution or amount of hair or a hair cycle as seen in rodents and other hairy mammals. Furthermore, nails, while basically in sagittal sections, are identical but smaller in rodents than humans. On a broad scale, the skin

Comparative Anatomy and Histology. DOI: http://dx.doi.org/10.1016/B978-0-12-802900-8.00024-5
© 2018 Elsevier Inc. All rights reserved.

and adnexa of these three mammalian species are essentially identical except for size. Similarities and differences among these species are summarized in Table 24.2. Regardless of differences, the skin and adnexa are critical to how mammalian skin controls the epidermal barrier for protection.

Skin

The skin provides the highly visible covering for the entire body. Its borders are marked by well-defined transition zones where cornified stratified squamous epithelia change to noncornified squamous epithelia at the mucocutaneous junctions found in the eye, mouth, nose, anus, and external genitalia (see descriptions and illustrations below). However, the basic structure of the skin itself is relatively similar throughout the body, with some regional exceptions. Rodent tail skin has relatively sparse hair follicles. Rodents have specialized sebaceous glands in the genital region, the preputial and clitoral glands, which do not occur in humans. Lastly, rodent muzzle skin and the skin just above the feet have vibrissae, a somatosensory organ also not found in humans. Vibrissae, known as whiskers, are specialized tactile sensing hairs found in most mammals including all primates except humans. Human male facial hair, which is often incorrectly called whiskers, is a form of terminal hair. Sexually dichotomous terminal hair type is not found in rodents although vibrissae are commonly mistaken as the homolog of human beard hair. The nonhair-bearing, thickened

TABLE 24.1 Functions of the Skin

Barrier: Physical, percutaneous absorption, chemical
Endocrine: Vitamin D
Immunological: Innate (antimicrobial peptides, cytokines) and acquired
Mechanical: Stretch and compression
Repair injury or damage
Sensory and autonomic
Sociosexual communication
Temperature regulation
Ultraviolet radiation protection

TABLE 24.2 Skin and Adnexa

Feature	Rodent	Human
Epidermal thickness of body (thin) skin	Mouse: 10–15 μm Rat: 25–35 μm	50–100 μm
Epidermal thickness of thick skin	Variable	300–400 μm on palms of hands, soles of feet
Tail	Mouse: 70–80 μm Rat: 80–110 μm	
Foot pad	Mouse: 150–400 μm Rat: 350–450 μm	
Muzzle	Mouse: 20–30 μm Rat: 30–35 μm	
Eyelid	Mouse: 50–60 μm Rat: 35–40 μm	
Hair types: Body	Guard, Auschene, Zigzag, Awl	Vellus, terminal
Hair types: Other	Cilia (eyelashes) Facial/muzzle (vibrissae) Perianal Distal limbs (vibrissae) Tail hair Ear hair	Cilia (eyelashes) Eyebrows Pubic Facial (beard, mustache) Axillary
Emergence of hair	Mouse: 5 days postpartum Rat: 4 days postpartum	19–21 weeks' gestation
Hair cycle	Mouse: Wave pattern with zones in adults Rat: Wave pattern	Mosaic pattern
Tail and tail hairs	Present	Absent
Sebaceous glands	Present	Present
Modified Sebaceous glands	Meibomian Zymbal Clitoral/preputial Perianal gland	Meibomian glands
Eccrine sweat glands	Foot pads	Entire body including soles and palms
Apocrine sweat glands	Mammary glands	Axilla, genito-anal region, ceruminous glands, ciliary, and mammary glands
Nails	Digits	Digits

epidermis on human palms and soles is likewise markedly thickened in comparable rodent regions; both have eccrine sweat glands in this location. In contrast to human exacerbated rete ridges and pegs in the palms, soles, and digits (finger- and toe-prints), rodents have relatively smooth plantar and palmar surfaces on their footpads. The human axilla, with its apocrine sweat glands, represents a unique combination of apocrine and eccrine sweat glands that has no apparent equivalent in rodents. Both the tail and muzzle skin in rodents has a thicker epidermis than the trunk; however, unlike palms, soles, and rodent foot pads, they are hair-bearing.

The skin consists of a series of distinct tissue types: (1) epidermis (epithelial cells), (2) dermis (collagen, fibroblasts, mast cells, nerves, blood vessels), (3) hypodermis (white adipose tissue), (4) panniculus carnosus muscle (in rodents), and (5) adventitia (subcutaneous tissue). Each is a complex structure in and of itself, as described and illustrated below.

HISTOLOGY

Epidermis

The epidermis consists of a composite wall of stratified squamous epithelial cells arranged in four histologic strata (layers): basale, spinous, granulosum, and corneum. These strata exhibit various characteristics based on degree of differentiation (Figs. 24.1 and 24.2). The first layer (stratum basale, or basal layer) consists of cuboidal to slightly rectangular cells. The most immature of these cells, more specifically called keratinocytes, are attached to the dermis by hemi-desmosomes that hook into collagen bundles at the basement membrane. A few of the keratinocytes in this proliferative layer provide a population of stem cells that divide to produce transient amplifying cells. Cells in this layer that are destined for terminal differentiation eventually dissolve their hemi-desmosomal connections at the dermal–epidermal junction and exit the basal layer by moving upward toward the epidermal surface. As cells differentiate, they begin to flatten out in the plane of the epidermis. These cells are tightly attached to each other by desmosomes. These intercellular adhesion structures maintain attachments during dehydration of skin for histologic preparation, resulting in cellular shrinkage that leaves a slight separation of the cells but the presence of small, dark, structures between the cells. Such structures were described historically as spines. The second layer (stratum spinosum or spinous layer) is named for these spines. As keratinocytes continue to undergo terminal differentiation, they undergo remarkable changes in protein expression. Fig. 24.2A illustrates the presence of keratin 14 in the basal layer while other keratins such as 1 and 10 become characteristic features in the outer more differentiated strata (Fig. 24.2B and C). Identical expression patterns are found in rat skin (Fig. 24.3; keratin 10 (A), keratin 14 (B)). Other proteins are prominently featured as cells differentiate. Small, basophilic granules begin to accumulate throughout cytoplasm of the upper layers of keratinocytes. These amorphous structures are known as keratohyalin granules and consist of filaggrin and loricrin proteins (Fig. 24.2D and F). In humans, the stratum spinosum comprises multiple layers of keratinocytes; however, in the rodent epidermis the stratum spinosum is typically one cell layer deep in its extent in truncal skin. Epidermal cells become further elongated as they approach the surface of the skin. The third layer (stratum granulosum or granular cell layer) is named for the abundance of highly visible dark blue granules observed in hematoxylin and eosin-stained paraffin sections (Fig. 24.2G–J). The most external cells of the stratum granulosum secrete the contents of lamellar bodies that form the complex lipid (hydrophobic) barrier that retains the body's moisture and is usually successful in keeping out microbial invaders. Cells external to this layer enter the final stages of terminal differentiation. The fourth layer (stratum corneum or cornified

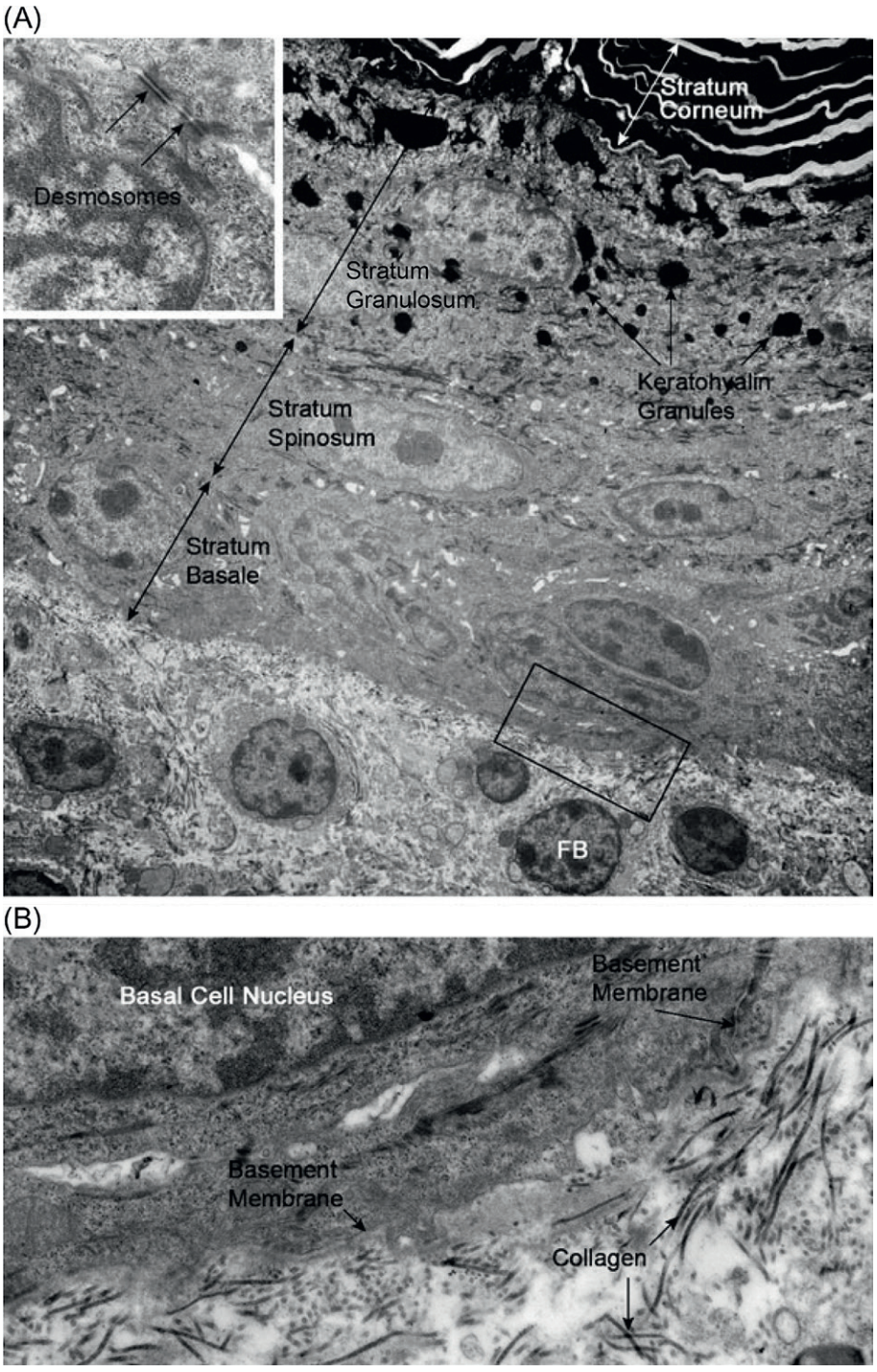

FIGURE 24.1 Basic ultrastructural features of the skin. The mouse, rat, and human skin are fundamentally similar. As the mouse skin is the thinnest of the three, it is presented here to demonstrate all the layers. (A) As shown in this transmission electron micrograph, the epidermis is layered from the basement membrane toward the surface by the stratum basale, stratum spinosum (cells held together by desmosomes, square inset), stratum granulosum, and the stratum corneum. A fibroblast (FB) is indicated. (B) Represents the area enclosed in the rectangular box in A. Below the basement membrane are a mixture of collagen bundles and fibroblasts (seen in A), as well as nerves and blood vessels (not evident in this figure).

Need-to-know

- Mouse, rat, and human skin are fundamentally similar.
- The basement membrane separates the epidermis and dermis.
- Basal keratinocytes proliferate and move upward.
- Superficial, differentiated keratinocytes flatten and lose nuclei.
- Keratohyalin granules contain filaggrin and loricrin.

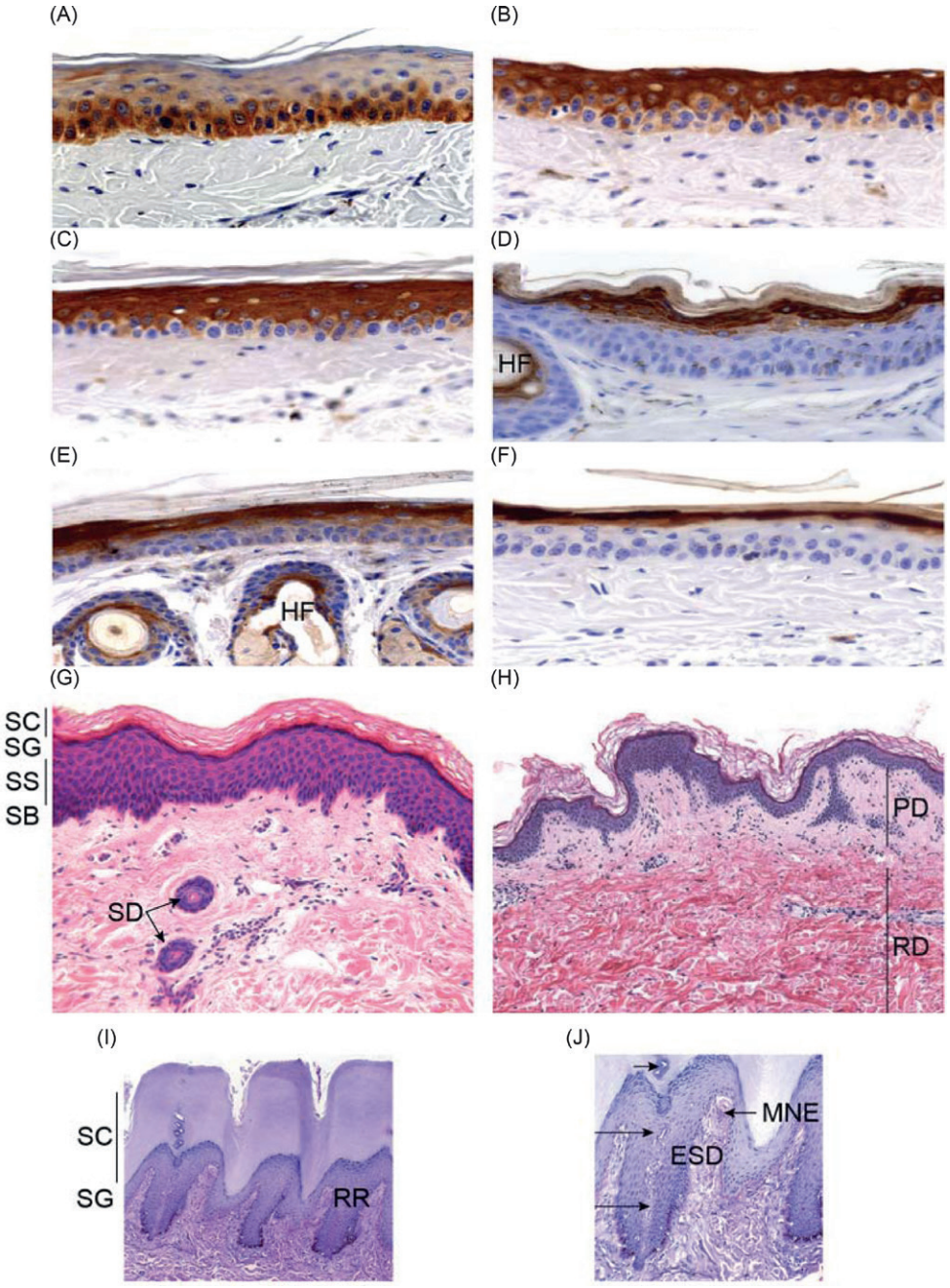

FIGURE 24.2 Epidermal and dermal features of rodent and human skin. (A–F) Immunostaining of thickened mouse tail epidermis showing the specialized protein distributions for (A) keratin 5, (B) keratin 1, (C) keratin 10, (D) filaggrin, (E) involucrin, and (F) loricrin, as keratinocytes move from proliferative stages to highly differentiated cells. (G, H) Examples of human thin epidermis reveal a few more cells in some strata than in rodents and slight rete ridge development. Note the paler papillary dermis (PD) and darker reticular dermis (RD) in H. (I, J) Thickened human epidermis of the palmar region. Note the increased number of cells in each upper stratum in I. An epidermal sweat duct (ESD) coiling through the epidermis to reach the surface and Meissner's corpuscle (MNE), a sensory nerve ending mediating fine touch on the fingertip (arrows), are shown in J. Rete ridge formation is more pronounced here than in thin epidermis (G, H). *SB*, stratum basale; *SS*, stratum spinosum; *SG*, stratum granulosum; *SC*, stratum corneum; *SD*, eccrine sweat gland duct; *PD*, papillary dermis; *RD*, reticular dermis; *RR*, rete ridges; *ESD*, epidermal sweat duct; *MNE*, Meissner's nerve ending; *HF*, hair follicle.

Need-to-know

- Types of keratin change with differentiation and in different structures.
- In all three species, a thickened epidermis compensates for lack of hair.
- Rodent footpads are similar to human palms and soles.
- Deeper dermal collagen is thicker and provides structural integrity in humans.
- The dermis has regional differences and changes with age in humans.

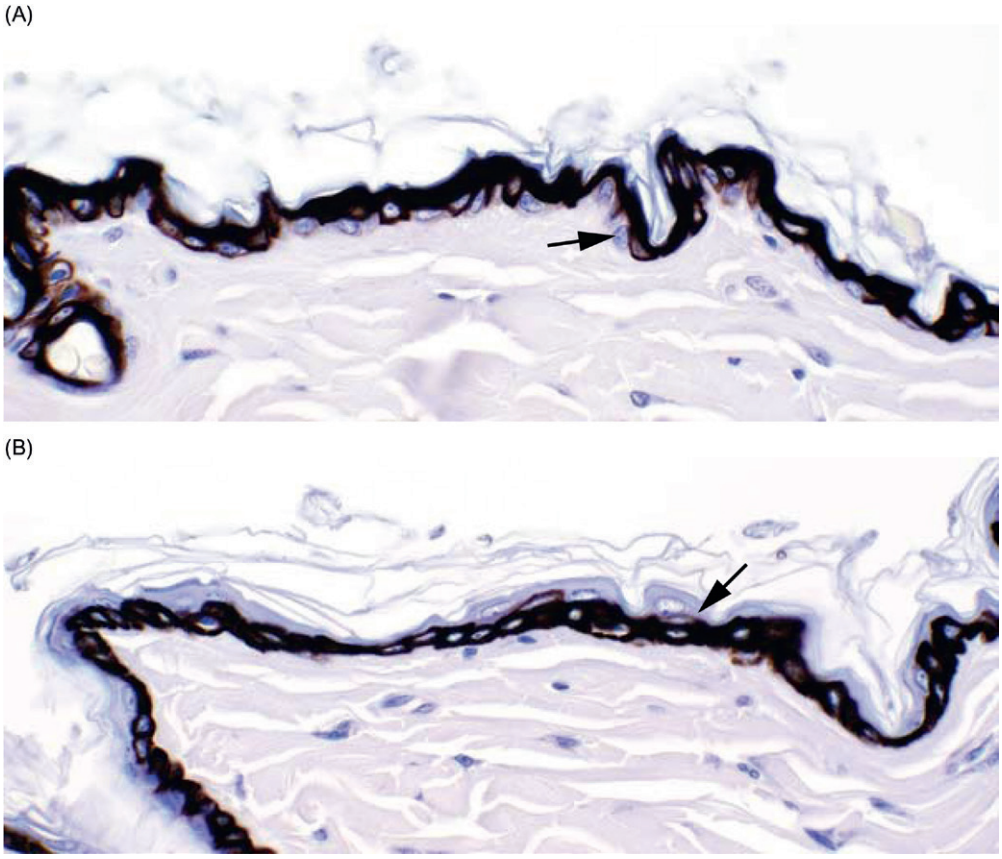

FIGURE 24.3 Keratin expression in rodent epidermis. (A) Dorsal rat epidermis is thin and expresses keratin 1 (KRT1) in the suprabasal epidermis (arrow). (B) Basal cells express keratin 14 (KRT14) (arrow). In this case, mouse-specific anti-keratin antibodies cross react with rat skin keratin with a similar pattern of expression. This is not the case for all mouse-specific anti-keratin antibodies.

Need-to-know

- Antibodies directed against rodent keratins may cross react.
- The epidermis is similar between rats and mice.

layer) contains cells that are flattened, completely filled with a coalescence of filaggrin and keratin intermediate filaments, and simultaneously exhibit a total loss of all their cytoplasmic organelles including the nucleus. In combination with the lipid material in the extracellular space, this most external layer creates a physical barrier to the outside world. A fifth strata, the stratum lucidum, may occur in nonhairy regions of the skin of some species including humans, particularly human palms and soles. This light staining layer contains eleidin, an intermediate form of keratin.

The epidermis on the vast proportion of the rodent's body is relatively thick at the time of birth but as the hair coat begins to grow it quickly thins out by 2 weeks of age at which point its thickness remains constant throughout life. The epidermis on the muzzle is thicker than the trunk, presumably since this is a relatively higher frictional area. The epidermis covering the ears is similar to the trunk but slightly thicker. The epidermis on the tail is significantly thicker (Fig. 24.2A). At the gross and histologic levels, the mouse tail appears to have scale-like structures due to the emergence and regular distribution of very large and thick hair shafts. The foot pads of mice, similar to the plantar and palmar surfaces in humans (Fig. 24.2I and J) contain epidermal sweat glands and Meissner's nerve ending, a sensory nerve ending mediating

fine touch on the fingertip. These are anatomically similar to the skin of the body in their arrangement into strata, but the numbers of cells in each layer are expanded making these regions very thick compared to the truncal skin (Fig. 24.2B and G). The foot pads are the only anatomic region that contains eccrine sweat glands in rodents. As such, the acrosyringium, the keratinized, stratified efferent duct from these glands, coils and twists its way through the thick epidermis in the mouse foot pad (see under Eccrine sweat glands). This structure is identical in human plantar and palmar skin (Fig. 24.2I and J).

While keratinocytes represent more than 95% of the epidermal cell population, other minor cell types are present. In human interfollicular epidermis, melanocytes are interspersed among the keratinocytes at a ratio of approximately 1:30 (Fig. 24.4A). As soon as they produce melanin pigment, the subcellular organelles containing this protective protein are exported and phagocytized by keratinocytes. Thus melanocytes possess a clear cytoplasm in hematoxylin and eosin preparations that is devoid of pigment, as well as keratin filaments, and can best be illustrated by special immunostaining procedures (Fig. 24.4A). While pigmented mice appear to have pigmented skin, it is usually patchy, ranging from pink to various shades of gray. This reflects the fact that in most strains of mice there is no interfollicular epidermal pigmentation. Pigment seen grossly is a reflection of the stage of the hair cycle (see below) as pigment is usually only produced in the deeply positioned hair bulb in the mid to late anagen stage (growing stage). Albino (white) rat strains have the same Arg299His missense mutation in the Tyrosinase gene as some of the commonly used albino mouse strains, although 138 allelic mutations in *Tyr* are listed in Mouse Genome Informatics (October 29, 2015) for the mouse. Rodents and humans with albinism have melanocytes and melanosomes but lack tyrosinase, an enzyme which is needed to produce melanin.

Other epidermal cell types include Merkel and Langerhans cells. Specialized epidermal thickenings in the rat epidermis, known as touch domes, are relatively common and contain Merkel cells, which are specialized mechanoreceptors. These touch domes surround large tylotrich follicles. Touch domes are not features of mouse or human skin although Merkel cells are present in the basal layer of the epidermis in all three species. Dendritic cells, which include epidermal dendritic cells and Langerhans cells, are involved with antigen presentation. A variety of markers can be used to identify these cells, which are not obvious in tissue sections, but can be inferred by their dendritic cell morphology, suprabasal location, and clear cytoplasm from a lack of keratin filaments. At the ultrastructural level, Langerhans cells have rod- or racket-shaped cytoplasmic organelles known as Birbeck granules.

Dermis

The dermis is a region of dense irregular collagenous connective tissue. It is the major region that gives the skin its toughness and provides structural protection for underlying skeletal (striated) muscles and organs. There are very few anatomic differences other than thickness between the dermal composition of rodents and humans. The dermis is located immediately below the epidermis (Fig. 24.2). In many regions of human skin, prominent downward extensions of the epidermis, known as rete ridges, interdigitate with corresponding upward extensions of the papillary dermis, providing an architectural mechanism to increase the surface area, which maintains a tight attachment between the dermis and epidermis (Fig. 24.2I and J). Undulations at the dermal epidermal junction are modest in thin skin, where there is little frictional stress (truncal skin) (Fig. 24.2G and H) but serve as a distinguishing feature in areas where there is heightened friction (digits, palms, and soles in humans and foot pads in rodents), creating what

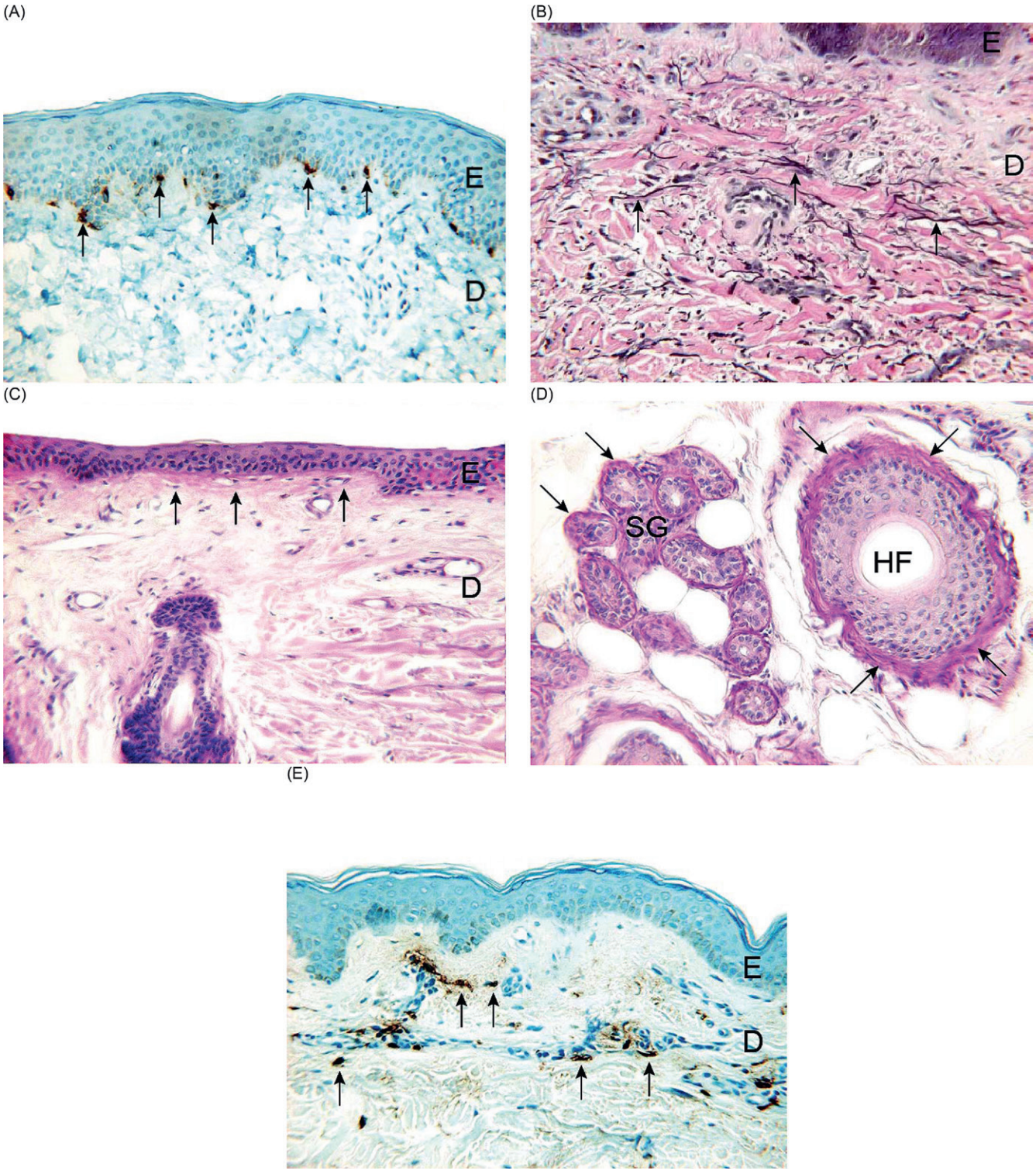

FIGURE 24.4 Specialized staining of human skin structures and cells. (A) Immunostaining with MLANA (melan-A, formerly called MART 1) antisera shows the frequency and distribution of melanocytes (brown) in human epidermis (arrows). (B) Elastin fibers of various sizes and distribution in the dermis are visible (black) with Verhoff-van Giesin staining (arrows). (C, D) Staining with Periodic-Acid-Schiff (PAS) reagents shows the bright pink basement membrane at the dermal–epidermal junction (C), around a hair follicle (HF) in cross section (D), and around an eccrine sweat gland (SG) (D). (E) Immunostaining for tryptase shows the number and distribution of mast cells in human dermis (arrows). *D*, dermis; *E*, epidermis.

Need-to-know

- Melanocytes are normally restricted to hair follicles in rodents.
- Epidermal melanin protects human skin from UV damage.
- Elastic fibers provide flexibility.
- PAS stains collagen type IV around follicles, glands, and the dermal-epidermal junction.
- Mast cell granules contain tryptase.

we know as (in the digits) fingerprints (Fig. 24.2I and J). In rodents, truncal skin does not display prominent rete ridges, although this is a common misinterpretation in wound healing studies. Rodent foot pads have an undulating dermal–epidermal junctional morphology (see Eccrine sweat glands below). Presumably, the hair present protects against frictional stresses and obviates the need for elaborate rete ridge morphology. This is supported by the observation that the mouse truncal epidermis is moderately to markedly thickened in mice with mutations that cause alopecia. However, in rodent foot pads, where the epidermis is markedly thicker than truncal, ear, or muzzle skin, there *is* rete ridge formation.

The dermis in rodents and humans contains an abundance of Types I and III collagen, as well as elastic fibers (Fig. 24.4B). Fibroblast cells are primarily responsible for production of extracellular matrix molecules, which include additional proteoglycans, glycoproteins, and minor collagens. These molecules are best observed by special staining preparations. Both the epidermal and dermal cells are responsible for construction of the basement membrane, which marks the abutment of epidermal structures against the dermis at the dermal–epidermal junction (Fig. 24.4C) and surrounding the keratinocytes of the hair follicles and eccrine sweat glands and ducts (Fig. 24.4D). Interspersed throughout the dermis are resident macrophages, as well as occasional T lymphocytes and dendritic cells. Mast cells, with metachromatic (purple by toluidine blue) granules (Fig. 24.5C), are scattered throughout the dermis and show high similarity between rodents and humans. They contain many bioactive molecules that allow for their immunodetection (Fig. 24.4E). In the thin skin of human truncal regions, there is a visible histologic difference between the upper and lower dermis when stained with hematoxylin and eosin (Fig. 24.2H). The upper papillary dermis contains small collagen fibrils and has a higher cellular composition, a feature that is presumed to allow for better diffusion of nutrients for the epidermis. By contrast, the lower dermis contains larger collagen bundles, a circumstance that affords more structural stability to protect underlying organs. The dermal region usually does not change its thickness in rodents as they age or as the skin goes through the hair cycle. However, in humans, the dermis shows definitive regional differences and thins with age. For example, eyelid skin has a relatively loose density of extracellular matrix components, while dorsal (back) skin and skin over other extensor surfaces show a denser and thicker arrangement.

Other notable features that differ between human and rodent dermis are the patterns of vascularization and the density of hair. The human dermis is highly vascularized with both a rich papillary network and a deep dermal network. This system is an essential component of the thermoregulatory network that allows the human body to dissipate heat through flushing and progressive shut down to conserve heat in response to hypothermia. Rodent dermis is poorly vascularized in comparison to human dermis. In rodents, the predominant capillary networks are associated with the hair bulbs.

Nerves are found throughout both the epidermis and dermis. Dermal nerves innervate the arrector pili muscle in the adnexa (see below) and can be studied using fluorescence-labeled reporter genes. Ubiquitin carboxy-terminal hydrolase L1 (formerly called PGP 9.5) has been used to label the nerves that form a plexus around the bulge in hair follicles. In humans, nerves reach the eccrine sweat secretory segments and are responsible for sweating that is associated with autonomic stimulation.

Hypodermis

Below the dermis is a layer of white adipose tissue (white fat) known as the hypodermis. Adipocytes in white fat are large, round cells filled with a single large vacuole of fat with

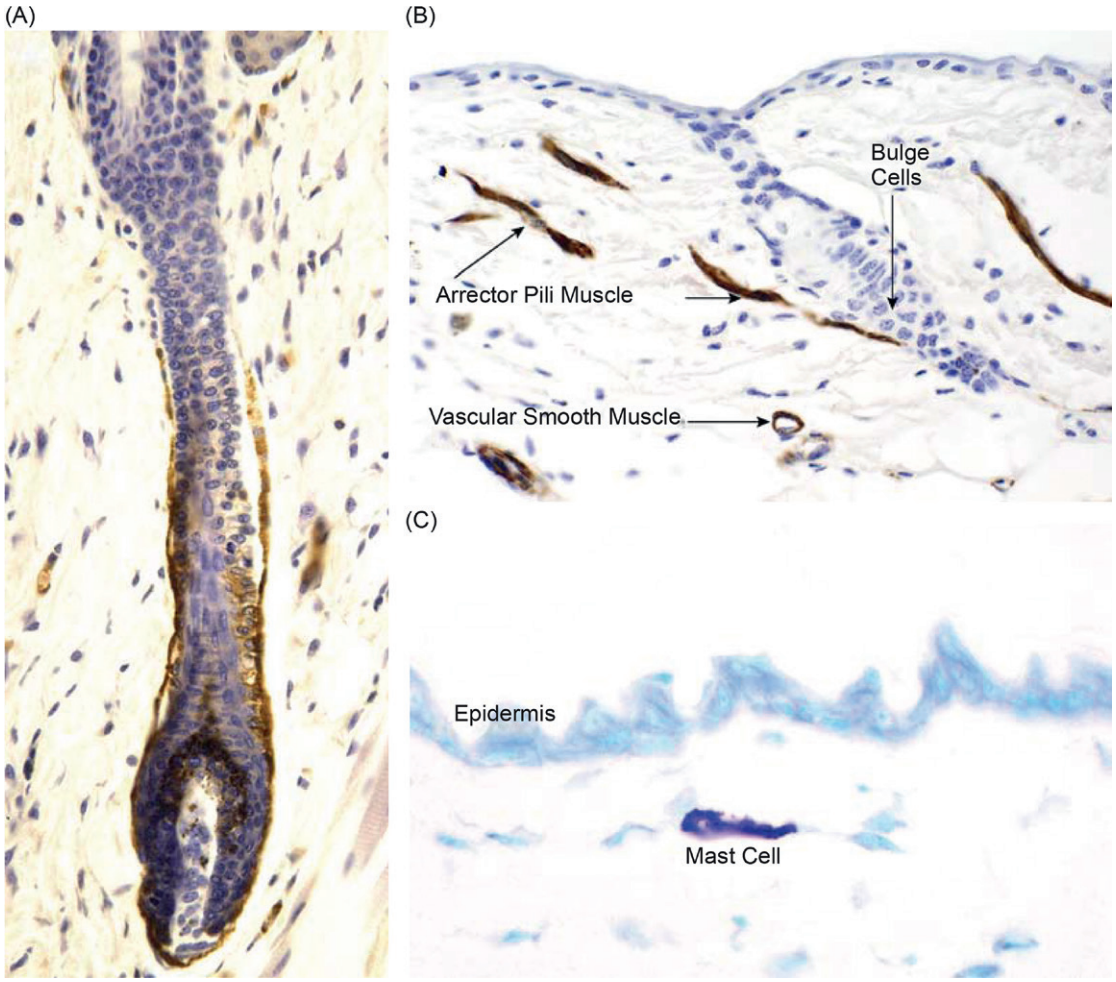

FIGURE 24.5 Smooth muscle actin and mast cells in rodent skin. Mouse. (A) Smooth muscle actin is present in the outer root sheath cells (brown) and retracts the dermal papilla up to the bulge region at the end of the hair cycle. (B) Smooth muscle (brown) is also present in the walls of small vessels and the arrector pili muscle. (C) Mast cells have metachromatic granules (purple) that contrast with the light blue toluidine blue epidermal stain.

Need-to-know

- Smooth muscle is present in multiple sites in mammalian skin.
- The arrector pili smooth muscle attaches to the follicle in the bulge region.
- At the end of the hair cycle, smooth muscle actin surrounding the follicle retracts the hair bulb up to the bulge region.
- Vascular smooth muscle and mast cells are present to control vessel responses.
- Human dermis has high vascularity.

a flattened, eccentrically placed nucleus (Fig. 24.6A). In humans, this region is also known as the superficial fascial layer (Fig. 24.7A). It is characterized as a loose type of connective tissue that conducts the major neurovascular bundles and lymphatics that supply and drain the skin. The thickness of this layer exhibits tremendous regional variability in humans, with males having prominent deposition patterns around the girth regions and females in the hip and thigh regions.

Hypodermal thickness is very much an indicator of the nutritional status of the organism. The hypodermis is slightly different in rodents. These animals have brown fat (BAT) that is commonly found in the dorsal interscapular region. Brown adipocytes are rounder and smaller than white fat and contain numerous small, clear, fat filled

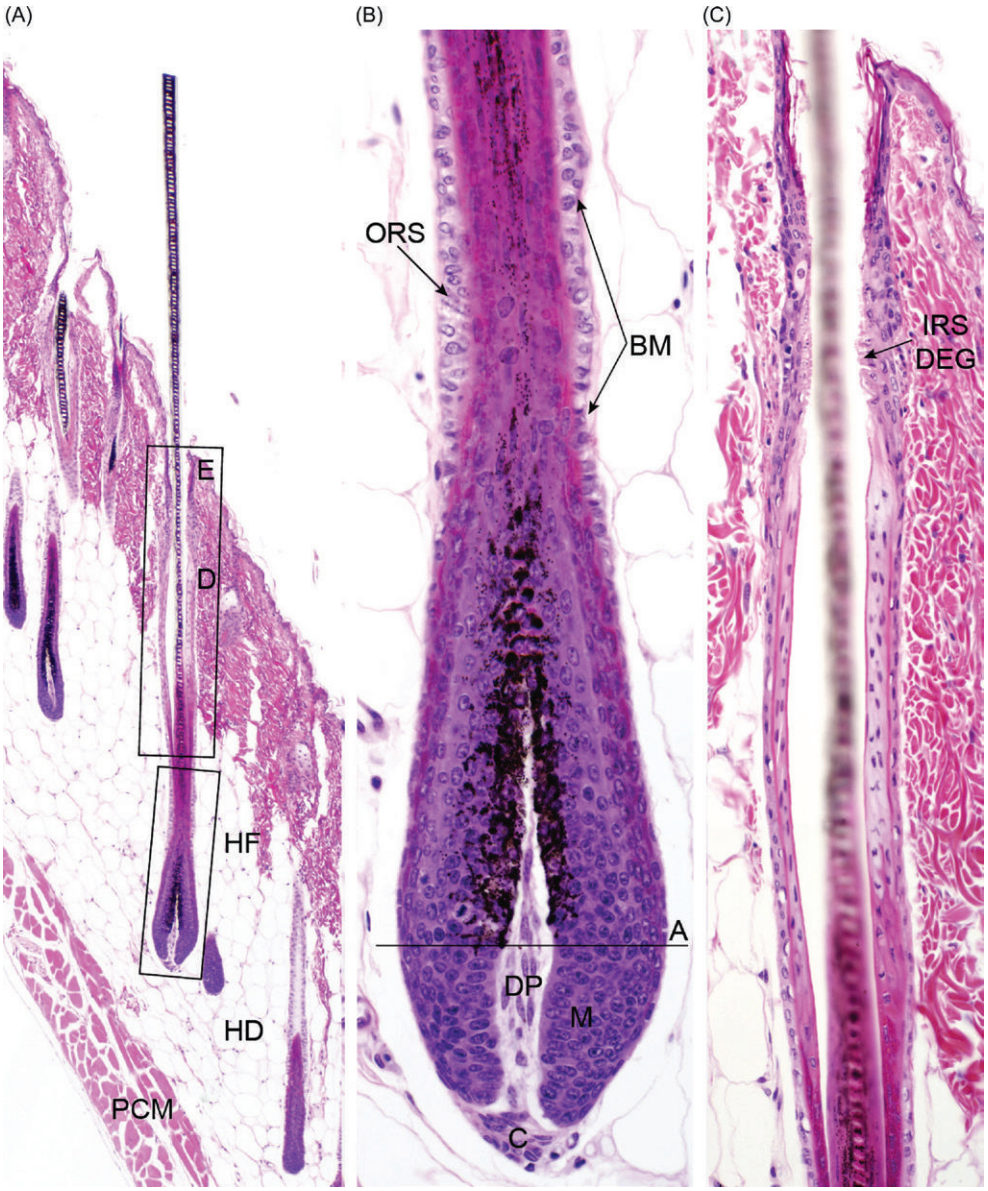

FIGURE 24.6 Rodent skin with anagen stage hair follicle. (A) Mouse epidermis (E), dermis (D), hair follicle (both boxed areas), hypodermis (HD), and panniculus carnosus muscle (PCM) demonstrate the basic layering of the skin. (B, C) The anagen hair follicle is enlarged to illustrate dermal papilla cap cells (C), dermal papilla (DP), matrix (M), Auber's line (A, line transecting the midbulb region), outer root sheath (ORS), inner root sheath (IRS), basement membrane (BM), and region of degeneration of the inner root sheath (IRS DEG).

Need-to-know

- Hypodermal thickness indicates nutritional status.
- Rodents have brown fat cells that can convert to white fat cells if needed.
- Hair cycle and seasonal changes alter rodent hypodermal thickness.
- Panniculus carnosus muscle is skeletal (striated) muscle in rodents.
- Anagen hair follicles have specialized layers of keratinocytes that produce hair.
- Hair bulbs contain vessels and nerves and interact with follicular cells.

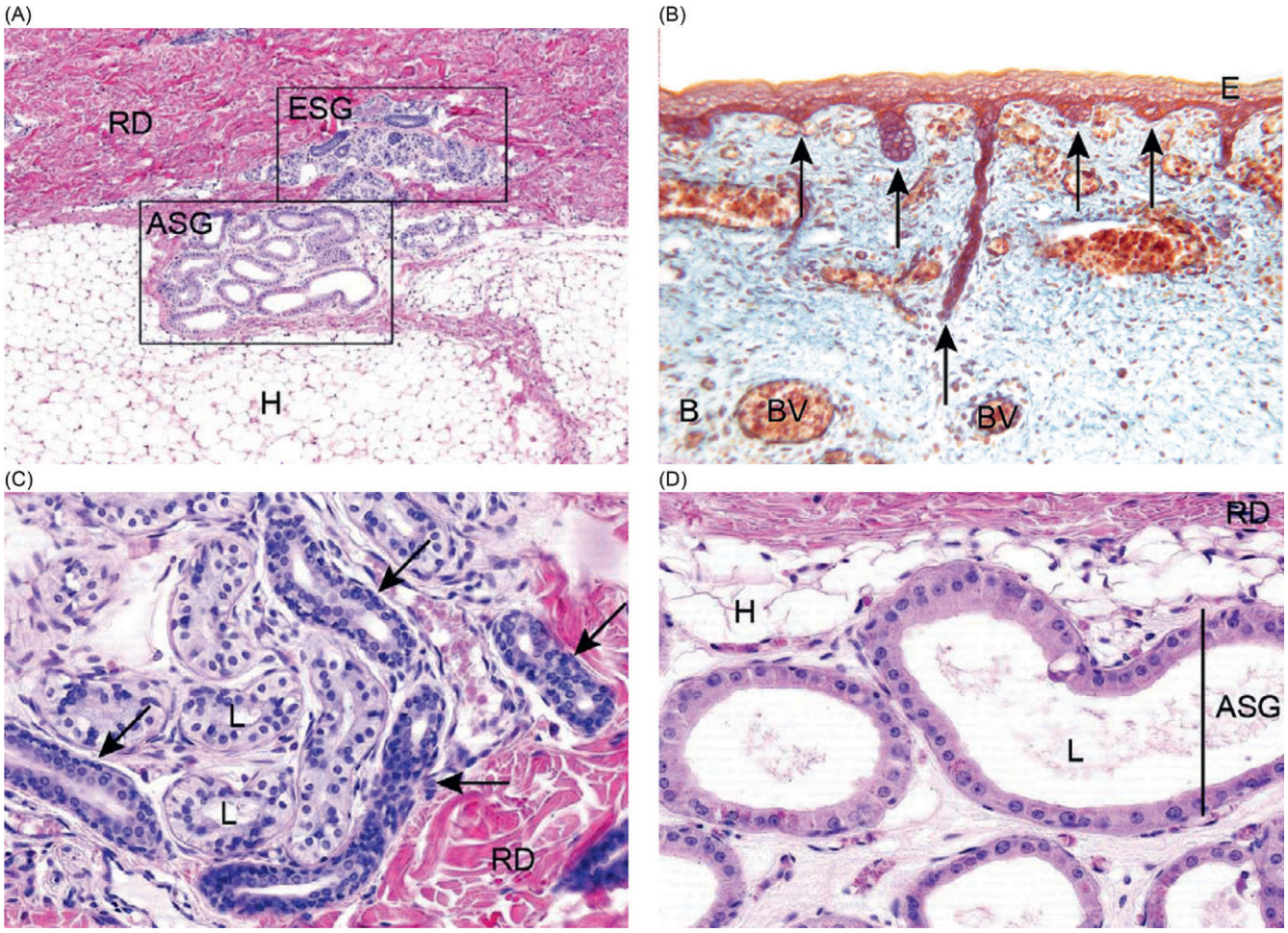

FIGURE 24.7 Human eccrine and apocrine sweat glands. (A) An orientation view of the lower reticular dermis (RD) and upper hypodermis (H) with both eccrine sweat glands (ESG) and apocrine sweat glands (ASG) from axillary skin. (B) The downward growth of nascent eccrine sweat ducts (arrows) from the surface epithelium (E) during prenatal development. Masson's Trichrome performed with aniline blue. Cells in the dermis remain mesenchymal without obvious differentiation at this stage. Blood vessels (BV) are present. (C) Coiled tubular secretory segments, as well as the darker stained double-cuboidal epithelia of the dermal sweat ducts (arrows). Note that the acinar arrangement of cells in the secretory segment surrounds a narrow lumen (L). (D) Cuboidal epithelium keratinocytes of the apocrine sweat gland (ASG) within the hypodermal fat (H) surrounding a lumen (L) contains some characteristic debris below the reticular dermis (RD).

Need-to-know

- Rodents do not have axillary apocrine sweat glands, and eccrine glands are restricted to the foot pads.
- In all three species, eccrine sweat gland ducts open directly to the epidermal surface.
- Ducts of human apocrine sweat glands predominantly open into the hair follicle.
- Sweat gland secretions are important in thermoregulation in humans, but not rodents.
- Mammary glands are modified apocrine glands present in all three species.

vacuoles. These cells can convert to white fat, so transitions can be found where BAT pads are changing to white fat, particularly in adults. For additional information on BAT, see Chapter 5, Skeletal System. The thickness of the hypodermal fat layer changes dramatically in size as the hair follicles move through their growth cycles and as the seasons change. These changes will be described and illustrated below.

Panniculus Carnosus Muscle

In contrast to the arrector pili muscle (Fig. 24.5A), the paniculus carnosus muscle (Fig. 24.6A)

is skeletal and marks what most consider the boundary between the dermal layers and the underlying adventia and muscle found in many species including rodents. This is a relatively thin layer that remains constant in thickness throughout the life of the rodent, although its thickness may appear to vary based on orientation of the histologic sections (i.e., if sections are oblique, the muscle will appear to be much thicker than normal). Innervation can be studied using fluorescence-labeled reporter genes. The panniculus carnosus is much less prevalent in humans. Although the platysma muscle of the neck has well-defined features of the panniculus carnosus, the panniculus carnosus is ill-defined everywhere else.

Adventitia

The adventitia beneath the panniculus carnosus muscle is a loose, irregular, collagenous connective tissue whose components include fibroblasts, nerves, and blood vessels. It connects the skin to the underlying skeletal muscle but also allows for flexibility and mobility of the skin. In humans, the downward tethers of collagen (cutis reticularis) can be rather stout in some regions (i.e., palms, soles, gluteal region, and thighs). When these regions accumulate excessive numbers of adipocytes, this can result in a dimpled appearance, known as cellulite. In rodents, these collagen tethers are exceedingly loose, the primary distinction that classifies them as loose skinned.

Adnexa

Adnexa is a term used to include (1) pilosebaceous units, (2) modified sebaceous glands, (3) eccrine and apocrine sweat glands, and (4) nails. Each of these are integrated into the skin as a whole, but are usually considered as independent organs because their anatomy, development, and molecular regulation is highly specialized and relatively independent of the epidermis and dermis.

HISTOLOGY

Pilosebaceous Unit

This unit comprises the hair follicle, its associated sebaceous gland(s), and the arrector pili muscle (Figs. 24.6 and 24.8). The general anatomic features are the same regardless of hair type, location, or species. The pilosebaceous unit constantly cycles throughout life, as described below.

Hair Follicle

The large, fully developed hair follicle found in late anagen stage is classically used to illustrate the hair follicle in mammals (Figs. 24.6, 24.8–24.13). The hair follicle is divided into the infundibulum (between the surface epidermis and the entrance of the sebaceous gland duct), the isthmus (between the arrector pili muscle insertion and the sebaceous gland duct), the lower follicle (between the arrector pili muscle insertion and the bulb), and the hair root or bulb region (the lowest portion of the follicle). The commonly used terms proximal and distal may be confusing because proximal can imply either the region closest to structural development (skin) or hair shaft production (bulb). As such, it is best to avoid these terms when describing the hair follicle.

The hair follicle is essentially a series of keratinocyte layers (Fig. 24.9) that undergo a unique series of stages in differentiation as these cells move upward from the bulb to the surface of the skin. This differentiation process is associated with a complex expression pattern of keratins and keratin-associated proteins in various layers, which differ from the keratins produced at the surface of the interfollicular epidermis. The bulb region is the most complex. There, an invagination of specialized fibroblasts and a capillary tuft of endothelial cells form the dermal papilla, which extends from the peribulbar dermal sheath cup cells into the bulb region. These fibroblasts are contiguous with the dermal sheath surrounding

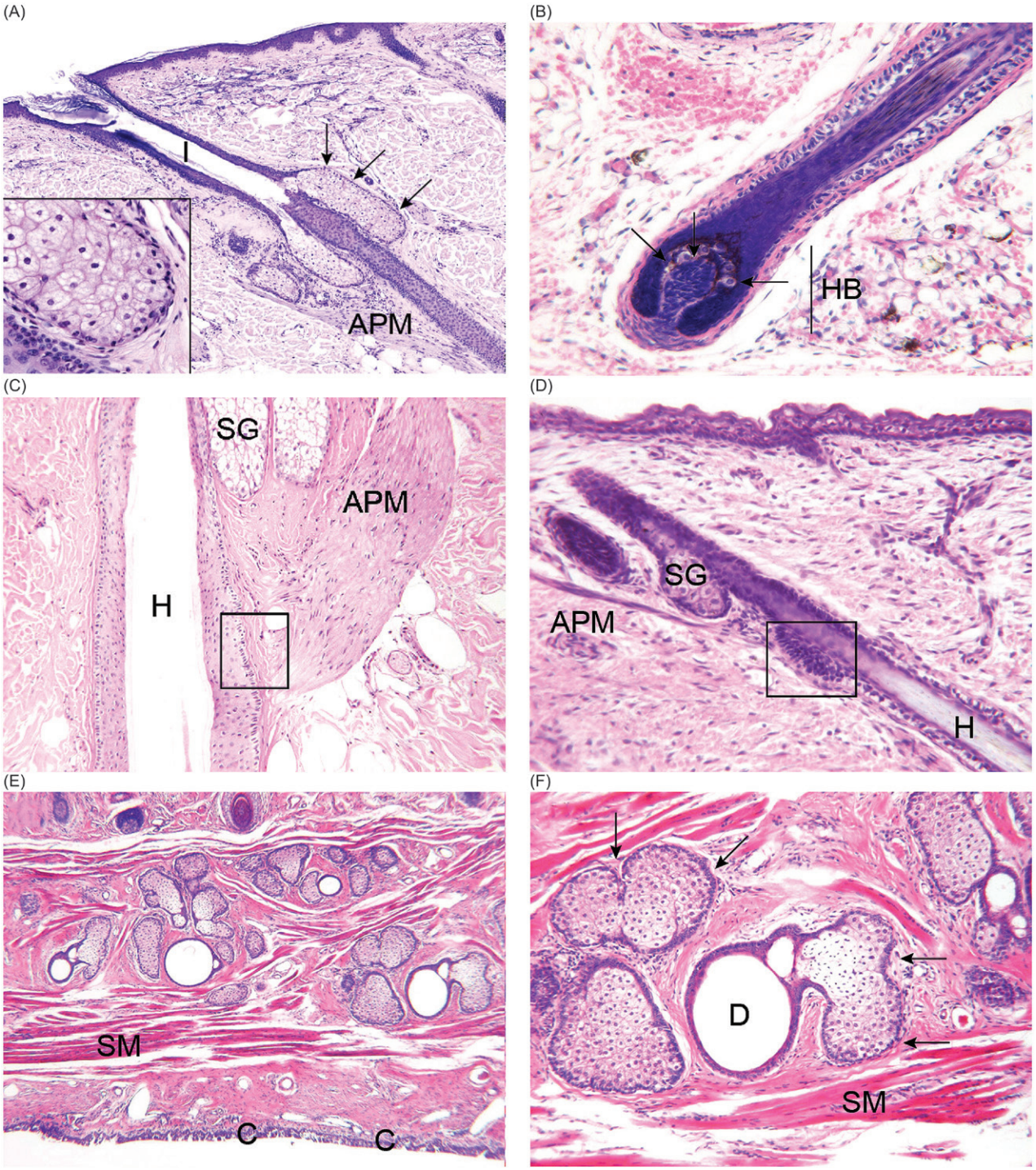

FIGURE 24.8 Human hair follicle structure. (A) The pilosebaceous unit from human skin with sebaceous glands surrounding the upper portion of the hair shaft (infundibulum, I) and an intersecting arrector pili muscle (APM). Inset depicts sebocytes, both proliferating at the periphery and more differentiated in the center with progressively more lipid. (B) The human hair bulb region (HB) in anagen stage with deeply pigmented hair matrix cells and dispersed clear cells (melanocytes indicated by arrows) surrounding the tuft of cells in the dermal papilla. (C) The bulge region (boxed area) below the sebaceous gland (SG) that contains the stem cells. The hair shaft (H) is in the center of the hair follicle. The arrector pili muscle (APM) is in close proximity to the hair follicle at this point. (D) The very prominent bulge region (boxed area) in the hair follicle during fetal development when stem cells are evident (*SG*, sebaceous gland; *HS*, hair shaft). (E, F) Meibomian glands (F, arrows) shown are emptying their contents into ducts (D). Conjunctival epithelium (C) and smooth muscle (SM) are indicated.

Need-to-know

- Holocrine secretions by sebaceous glands discharge into the hair follicle infundibulum.
- The arrector pili muscle attaches near the stem cell niche below the sebaceous gland.
- The rodent stem cell niche is best seen in telogen but difficult to see in human hair.
- Anagen hair bulbs have melanocytes above the dermal papilla.
- The rodent and human eyelid (meibomian) gland and auditory sebaceous gland are similar.

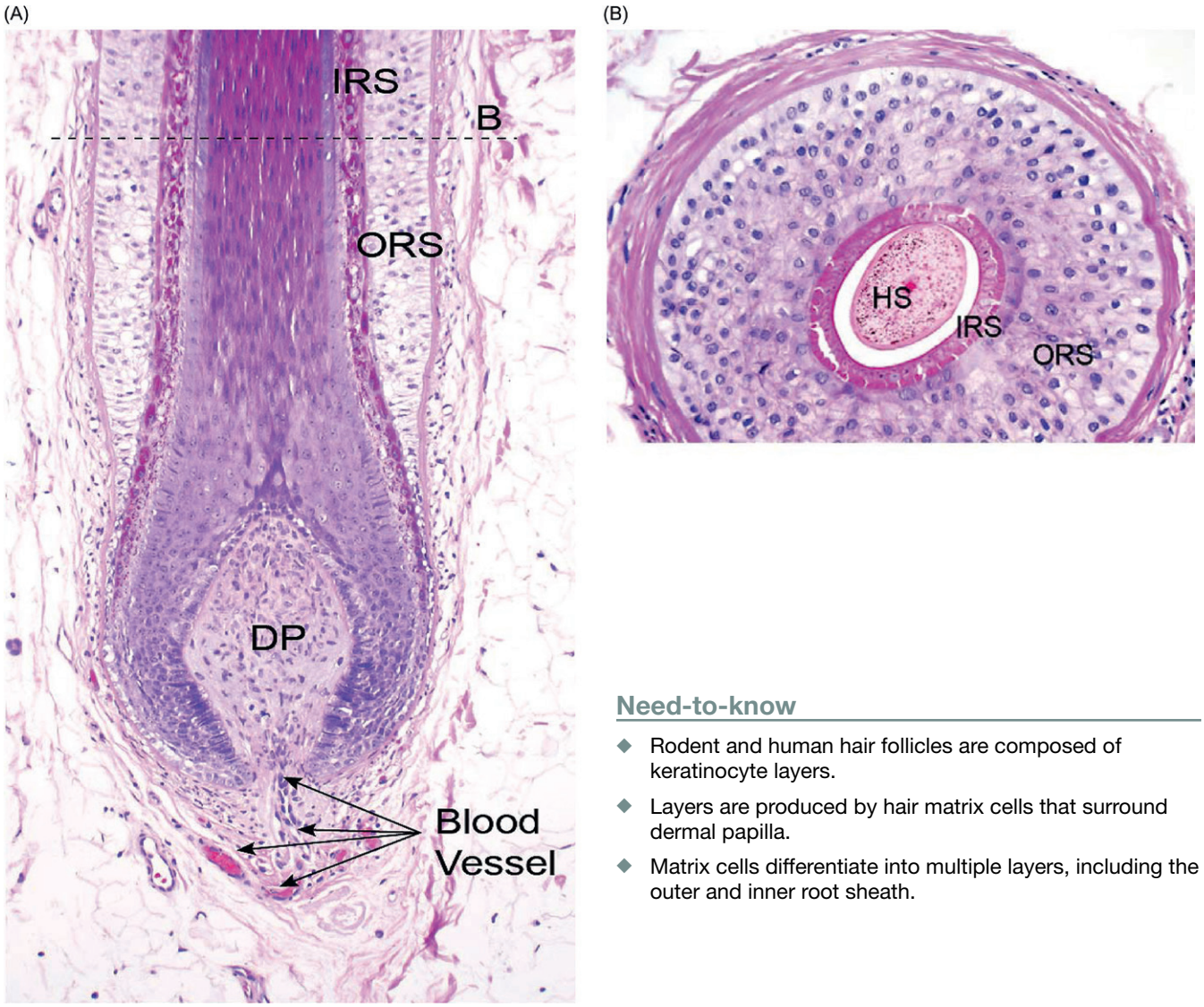

Need-to-know

- Rodent and human hair follicles are composed of keratinocyte layers.
- Layers are produced by hair matrix cells that surround dermal papilla.
- Matrix cells differentiate into multiple layers, including the outer and inner root sheath.

FIGURE 24.9 Late anagen human hair. (A) A vertical section of a human hair follicle in late anagen is the standard way to illustrate this structure. Dotted line indicates the level of the hair follicle cut in cross section and shown in (B). (B) The concentric layers of the hair follicle and hair shaft. *DP*, dermal papilla; *IRS*, inner root sheath; *ORS*, outer root sheath; *HS*, hair shaft.

the hair follicle. Melanocytes may be present and interspersed among the hair matrix cells of the hair bulb of pigmented hair (Fig. 24.6B and 24.9). The epidermal keratinocyte layers surrounding the dermal papilla form the hair matrix cells. They consist of a transient amplifying cell population that differentiates into the outer root sheath, the companion layer (biochemically part of the inner root sheath), the two inner root sheath layers (Henle's layer, more correctly called pale epithelial layer, on the outside and Huxley's layer, more correctly called the granular layer, on the inside), the hair shaft cuticle, cortex, and medulla. The hair shaft (edges pointing up) and inner root sheath (edges pointing down) cuticles interdigitate to help anchor the hair shaft in the follicle.

Arrector Pili Muscle

The arrector pili muscle in rodents and humans is smooth muscle that inserts into the connective tissue of the dermis below the epidermis. It angles down to the hair follicle, inserting in multiple

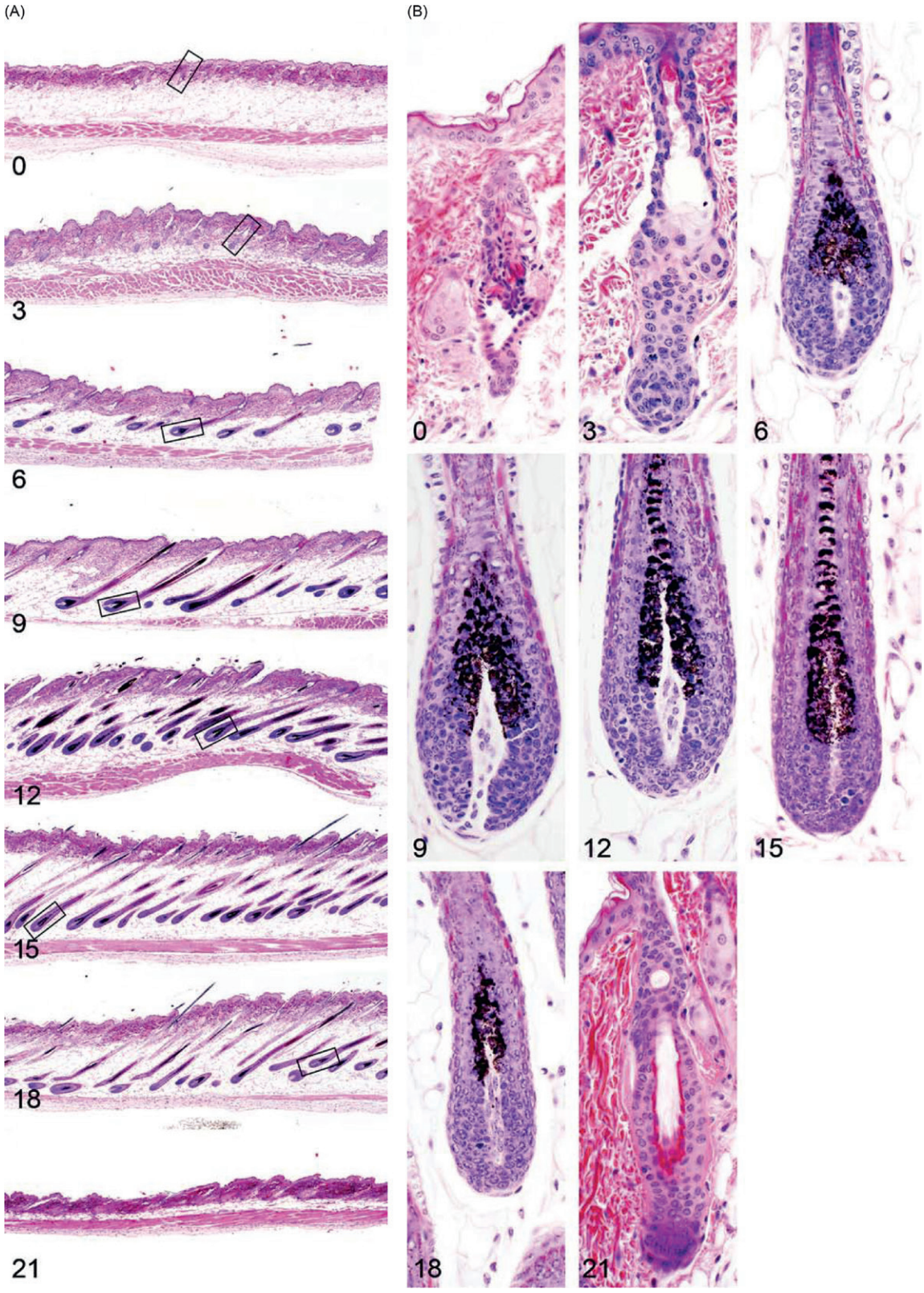

FIGURE 24.10 Hair cycle in a C57BL/6J mouse induced by wax stripping. (A) Low magnification orientation view, numbers indicate days poststripping. (B) High magnification of indicated days. Damaged telogen hair follicles seen immediately after hair shaft removal by wax stripping on Day 1. They rapidly enter early anagen and are in mid anagen by Day 3, with pigment production by Day 6. Anagen persists for 2 weeks until Day 18, when follicles enter catagen (seen on Day 21), eventually returning to telogen. Pigment production persists only from mid to late anagen. Interfollicular epidermal pigmentation is not normally seen in the mouse. Numbers in the lower left corner indicate days postwax stripping.

Need-to- know

- In rodents, all hair follicles in a given area cycle in a wave growth pattern.
- In humans, the individual follicles cycle in a mosaic growth pattern.
- Rodent hair follicles persist in telogen until the next wave starts.
- Human hair follicles persist in anagen for months to years.

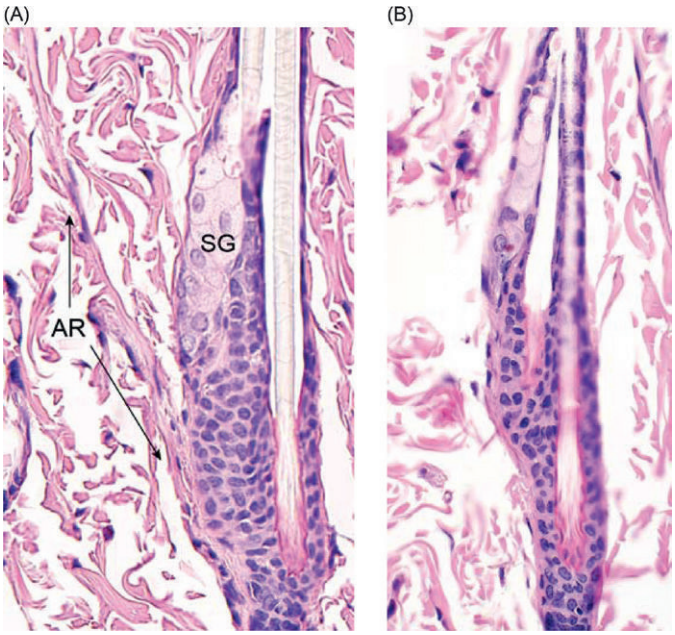

FIGURE 24.11 Rodent telogen follicles. A common misconception is that a new anagen hair pushes out the old telogen (club) hair. Rather, the old hair is pushed to the side, as shown in this pair of images of rat telogen follicles at different orientations. (A, B) Rat teleogen follicle with a sebaceous gland (SG). The bulge below the sebaceous gland is where the arrector pili (AR) muscle attaches.

Need-to-know

- Hair follicles are essentially the same regardless of species.
- New hair shafts push old ones to the side, not out.

sites below the sebaceous gland in the region of hair follicle stem cells known as the bulge region (Figs. 24.5B and 24.8C and D). During autonomic stimulation, the arrector pili muscle moves the hair follicle, which raises the hair shaft above the skin. While essentially the same in humans, human fetal specimens are more similar with a stem cell bulge region and connected arrector pili muscle, while in adults the arrector pili muscle is close to but not actually connected to the follicle (Fig. 24.8A, C, and D). Hair follicle stem cells within the bulge region are found immediately below the sebaceous gland. In rodents, these structures are best visualized during telogen (resting phase) below the club hair (described below). They appear as a group of cells protruding from the side of the follicle with characteristic nuclei with undulating membranes. These cells can be seen at all hair cycle stages, but because they do not completely surround the follicle, the bulge is only seen when sectioned appropriately.

Sebaceous Glands

The sebaceous glands exhibit a holocrine form of secretion. These alveolar structures are lined by transient amplifying cells, historically called reserve cells, which differentiate into sebocytes (Fig. 24.8A, E, and F). Sebocytes are polyhedral with numerous small, clear, lipid-filled cytoplasmic vacuoles. As sebocytes mature, they rupture and are excreted in toto. Their lipids and detritus initially fill the infundibulum and spread across the skin surface, contributing to the hydrophobic barrier. Mutant mice with sebaceous gland abnormalities have provided evidence that this process is critical to maintaining epidermal hydration of the epidermis. In addition, enzymes are released that help degrade the inner root sheath, another functional barrier, allowing the hair shaft to emerge to the skin surface.

Hair Cycle

The hair cycles of the rodent trunk and human scalp are quite different. Rodents have a relatively short first hair cycle, more correctly called the completion of embryogenesis. Their hair cycle has a wave-like pattern at birth (hair emerges at around 5 days of age) and to various degrees throughout life. The first true adult hair cycle, beginning at 2–3 weeks of age depending on strain, as well as subsequent cycles, displays a prolonged period of telogen. As rodents age, this wave-like cycle transitions to a more regional cycling domain pattern. By contrast, humans exhibit a wave-like growth pattern *in utero* (hair emerges at around 24 weeks gestation) that changes to a mosaic growth pattern. As adults, human scalp—and in males, facial hair follicles—remain in anagen for long periods of time (1–7 years in general, with females often having much longer cycles than males).

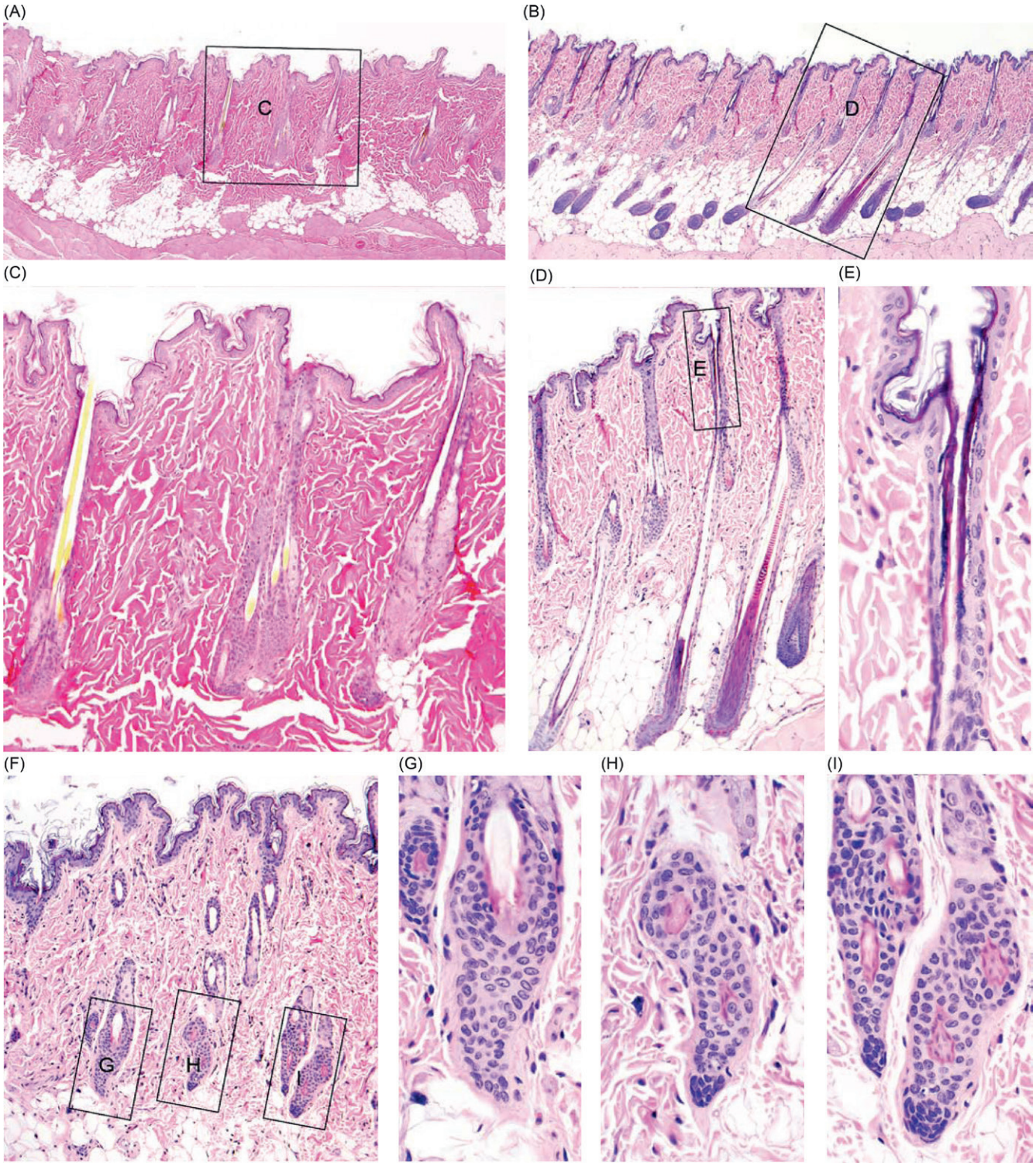

FIGURE 24.12 Truncal skin hair cycle. The rat truncal hair follicle cycle is similar among the three species. The major stages are illustrated here in rat: telogen (A, C); mature growing stage, late anagen (B, D, E); and catagen (F–I).

Need-to-know

- Rodent follicles cycle in waves rather than in a mosaic pattern as seen in humans.

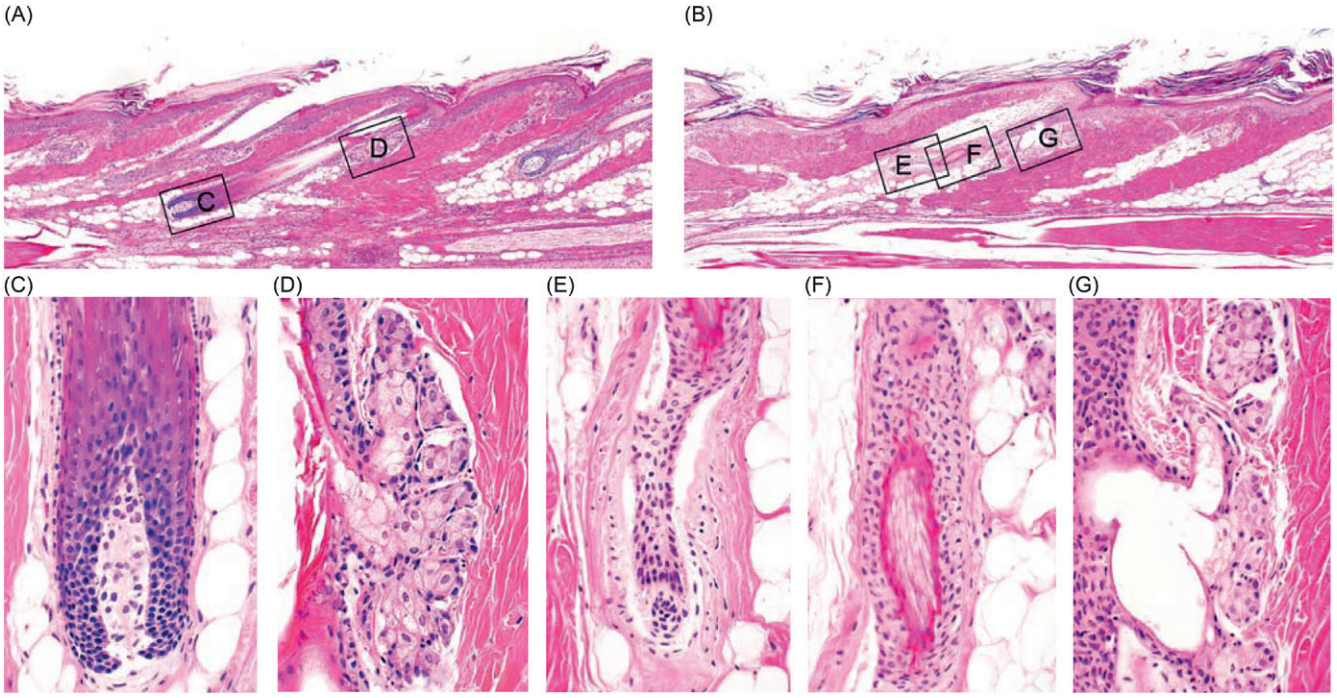

FIGURE 24.13 Rodent tail hair cycle. Rodent tails have specialized hair follicles and shafts that are similar between species. Tail hair follicles cycle in a manner similar to other hair follicle types. Late anagen with its accompanying sebaceous gland (A, C, D) and catagen (B, E–G) are shown.

A common and serious misinterpretation is to assume that the cycling hair follicle looks like a late-stage anagen follicle at all stages of the hair cycle. This issue can be best illustrated in a reproducible manner by mildly traumatic removal of hair from a mouse by wax stripping (Fig. 24.10), similar to the depilation method commonly used by humans. Similar changes in follicle morphology can be seen in unmanipulated samples, as illustrated for truncal (Fig. 24.12) and tail (Fig. 24.13) skin in the rat. With the traumatic removal of telogen hair (Fig. 24.10, time 0), the hair cycle enters anagen. The onset of anagen in wax-stripped skin is associated with increased epidermal thickness, a sequella to the mild trauma. This observation has given rise to the mistaken idea that the epidermis thickens during anagen, but this is not the case in unmanipulated skin samples.

A variety of scoring systems have been developed to subdivide this growth phase into at least six parts, with some subparts, in both mice and humans (Table 24.3); it has not yet been applied to rats. Mid to late anagen is associated with the production of pigment. Unlike humans, mice rarely have interfollicular epidermal pigmentation; thus, apparent skin color in mice with pigmented hair is entirely dependent upon the growth phase of the hair cycle. Mouse and rat hair follicles remain in the anagen stage a relatively short time to produce hair of a defined length based on the hair follicle

TABLE 24.3 Stages of the Mouse Hair Cycle

Anagen	Catagen	Telogen	Exogen
I	I	One stage, although more complicated based on hypodermal fat thickness	Not defined anatomically
II	II		
III a, b, c	III		
IV	IV		
V	V		
VI	VI		
	VII		
	VIII		

From Muller-Rover, et al. A comprehensive guide for the accurate classification of murine hair follicles in distinct hair cycle stages. *J Invest Dermatol* 117:3, 2001; Milner, et al. Exogen, shedding phase of the hair growth cycle: characterization of a mouse model. *J Invest Dermatol* 119:639–644, 2002.

type. At the end of anagen, the region below the sebaceous gland undergoes massive apoptosis, thereby entering catagen (transition phase). Catagen has been divided into at least eight stages (Table 24.3). After 2–4 days, the remaining dermal papilla, with some surrounding keratinocytes, retracts upward to the level of the sebaceous gland by actin filaments that surround the hair follicle (Fig. 24.4A) to form a small structure that can remain in telogen for various lengths of time. The hair shaft (called a club hair) is retained at this stage but is eventually shed during exogen, and a new hair follicle develops. When the new hair follicle is initiated, it forces the club hair to the side and grows down into the hypodermal fat layer to produce the new hair shaft. A common misconception is that the new anagen hair follicle and shaft push the old club hair out. As shown in Fig. 24.11, the hair shaft remains, such that multiple hair shafts can be seen exiting follicular openings known as follicular ostea when viewed with a dissecting or scanning electron microscope.

One common phenotyping mistake is to compare catagen or telogen hair follicles from alopecia mutants with control anagen hair follicles. It is also worth noting that hypodermal fat layer thickness varies dramatically during the hair cycle, from very thick in late anagen, when a lot of protein is synthesized to produce the hair shaft, to almost nonexistent in late telogen, when the follicle is resting and not producing the hair shaft (Fig. 24.10). Finally, when comparing mutant and control mice, it is critical that skin be compared during the same stage of the hair cycle. Differences in hair follicle growth in mice of the same age may be the result of mismatched hair cycles and not the inherent hair follicle structure.

In humans, individual hair follicles cycle in the same manner as rodents, but human hair does not cycle in synchronous waves in an anatomic pattern. Human hair follicles persist in anagen whereas mouse hair follicles persist in telogen until the next wave occurs or is induced by trauma. Human scalp follicles may continue in anagen for many months to years. There are broad differences in human hair cycle duration at different anatomic sites such that eyelash regrowth is approximately 2 months, while scalp hair can be from 3 to 4 months to more than 6 years.

Hair Types

Rodents have a multitude of hair types based on the subtleties of anatomic location, while human's hair is classified by major structural features into only two types. Rodents have a variety of hair types on their bodies, including large guard hairs, which stand above the rest and act as somatosensory organs; auchene and awl hairs; which are intermediate in size and shape; and zigzag hairs; which are very thin underhairs that provide insulation. Human hair is classified by structure into vellus and terminal, with the largest terminal hairs found on the head. However, transcriptome studies of whole skin biospies from both mice and humans indicate that different anatomic sites are so distinct they may as well be different organs. Rodents have specialized hair types that includes hairs on both the inside and outside of the ear, eyelashes, vibrissae, and perianal hairs. With the exception of vibrissae, which are somatosensory organs surrounded by a blood-filled sinus (Fig. 24.14), the basic anatomic structure of hair follicles in rodents and humans is the same.

Modified Sebaceous Glands

Meibomian, Zymbal, clitoral/preputial, and perianal glands are modified sebaceous glands found in rodents; only two of which (meibomian and Zymbal) are similar to those found in humans. Meibomian glands are found in the eyelid and Zymbal glands are found outside the external ear canal. The clitoral/preputial glands are located anterior to the external genitalia, and the anal/perianal glands are part of specialized hair follicles in the anal region. The modified sebaceous glands are similar to the sebaceous

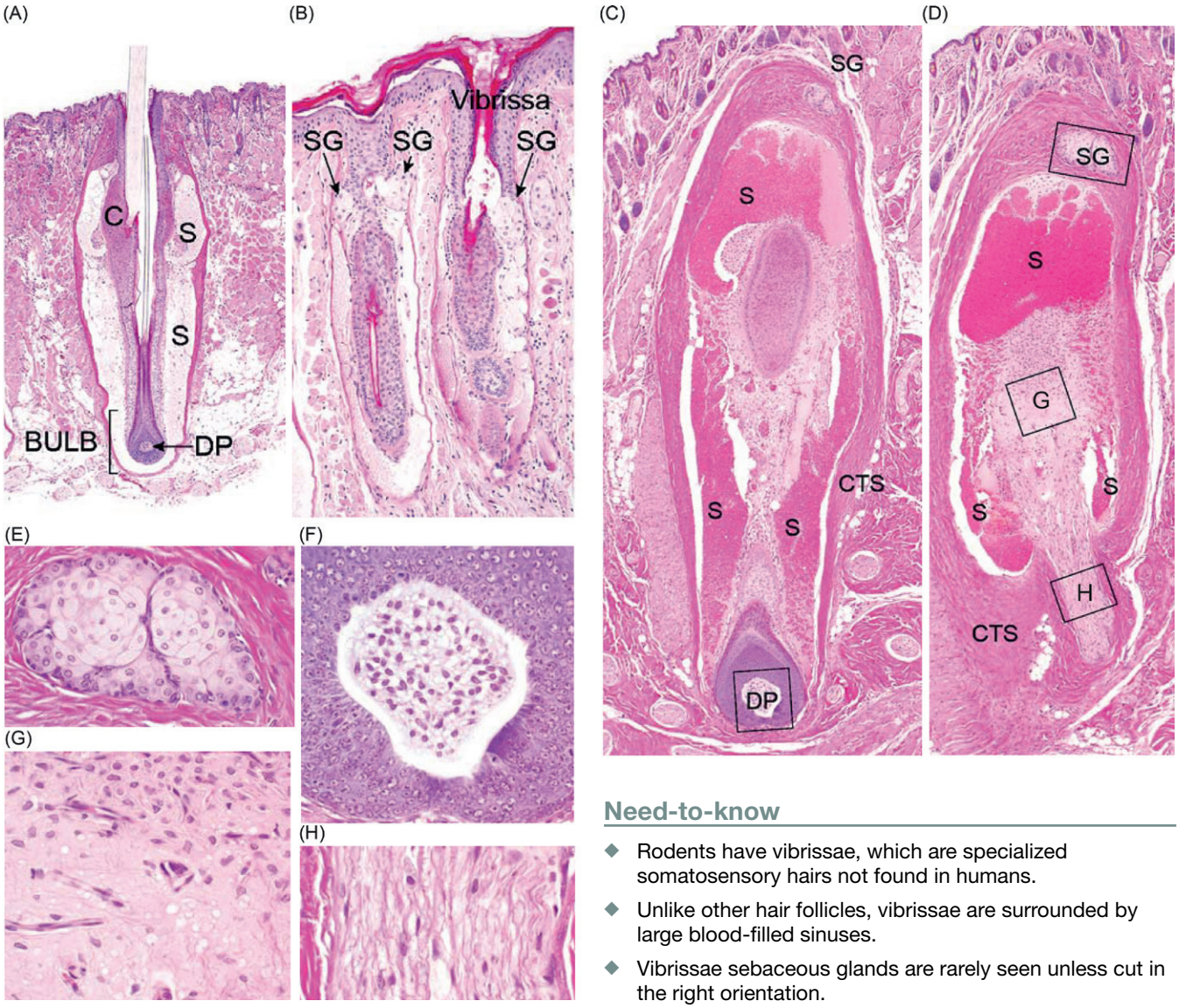

Need-to-know

- Rodents have vibrissae, which are specialized somatosensory hairs not found in humans.
- Unlike other hair follicles, vibrissae are surrounded by large blood-filled sinuses.
- Vibrissae sebaceous glands are rarely seen unless cut in the right orientation.

FIGURE 24.14 Rodent vibrissae hair follicles. Rodents have specialized somatosensory hairs located on the face and around the feet. These hairs have long, thick hair shafts that are produced by very large follicles. These follicles are similar to other hair follicles except that they are surrounded by a large blood-filled sinus. (A) A late anagen vibrissa hair follicle from a mouse with the club hair (C) from the previous cycle pushed to the side. These follicles have a bulb (BULB) and dermal papilla (DP), as well as two sinuses (S). (B) Orientation demonstrating the full length of mouse anagen vibrissae rarely reveals their sebaceous glands, which are shown in these two vibrissae in catagen. (C–H) Rat vibrissae are anatomically similar to those found in mice and in similar locations, only they are much larger. The connective tissue sheath (A, CTS) surrounds the blood-filled sinuses (S). The bulb, dermal papilla (DP, higher magnification in F), and sebaceous gland (SG, higher magnification in E) are shown in C. The large nerve attaches to a reticular network at the upper third of the follicle (boxed areas G, H, enlarged in lower panels).

glands of the pilosebaceous unit in that they are all holocrine glands. However, they are much larger, have specialized functions, and three have their own ducts. When abnormalities of any sebaceous glands are found during phenotyping mutant mice, it is important to evaluate all of these glands as each is known or may be under its own genetic control.

Meibomian Glands

Meibomian glands are located at the rim of the eyelids in humans (Fig. 24.8E and F), mice (Fig. 24.15A and C), and rats (Fig. 24.15B, D, and E) and are quite large. Each gland is lobulated, with each lobule anatomically similar to the sebaceous gland of the pilosebaceous unit (Fig. 24.8E and F). Stratified squamous epithelia line ducts that arborize

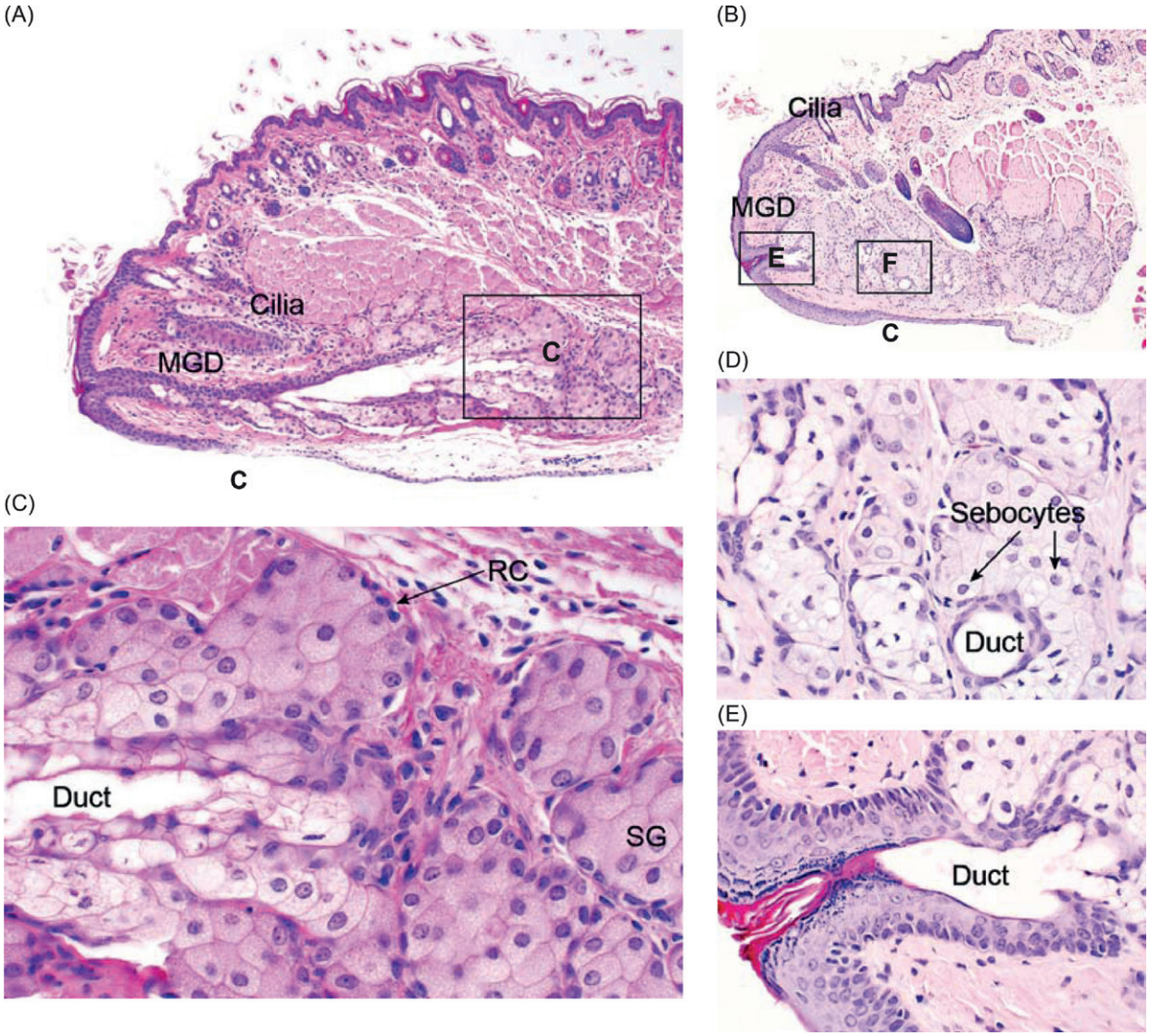

FIGURE 24.15 Rodent eyelid and meibomian gland. The cornified stratified squamous epithelium of the skin changes to a mucous membrane (C) at the eyelid mucocutaneous junction. The rodent (A, C, mouse; B, D, E, rat) meibomain gland duct (MGD) empties into the conjunctiva near the mucocutaneous junction. It is not connected to the eyelashes (cilia). The meibomian gland is a large, specialized sebaceous gland that is similar in structure to the glands of the pilosebaceous unit. Its duct contains extruded sebocytes. *SG*, sebaceous gland lobules; *RC*, reserve cells.

Need-to-know

- Eyelid skin in all three species changes form stratified squamous to mucous membrane epithelium (conjunctiva)
- The meibomian gland is a modified lobulated sebaceous gland at the rim of the eyelid.
- Meibomian gland lipid secretions provide a barrier to prevent dessication of the cornea.
- Meibomian glands are not connected to the eyelashes (cilia).

to form a solitary duct that exits via a slit-like structure in the conjunctiva (Fig. 24.15). Meibomian glands secrete lipids that act as a barrier to dehydration of the cornea. These glands may be missing or malformed in some mutant mouse models, as well as in homologous human diseases.

Zymbal Glands

Zymbal glands are auditory sebaceous glands that are anatomically similar to other modified sebaceous glands. They are located beneath the stratified squamous epithelium lining the external ear canal near the tympanic membrane,

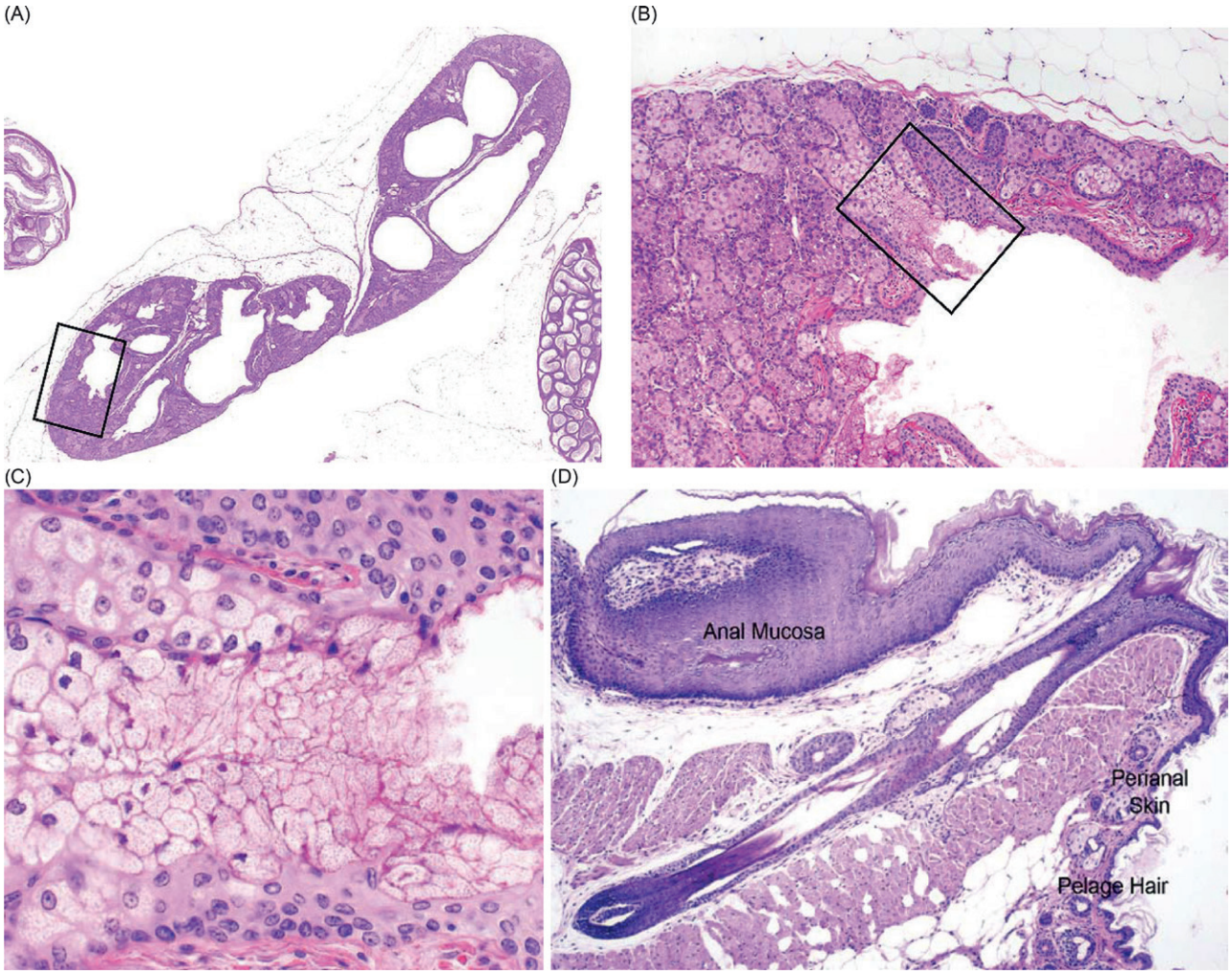

FIGURE 24.16 Preputial gland in rodents. Male and female rodents have large, lobulated modified sebaceous glands located near the penis (A, mouse preputial gland) or clitoris (clitoral gland). These holocrine glands both have ducts and are similar to other sebaceous glands. Boxed areas are progressively enlarged (B, C). (D) Perianal hair follicle and its associated sebaceous gland. The mouse perianal hair follicle is anatomically similar to other mouse hair follicles except that it is much larger, as shown here. As it produces a long hair, the follicle remains in anagen much longer than the pelage hairs, which are all in telogen in this figure. The sebaceous glands are similar to those in other hair follicles, except that they are proportionally bigger relative to the size of the follicle. The hair shaft exits at the mucocutaneous junction.

Need-to-know

- Rodents have clitoral (female), preputial (male), and perianal modified sebaceous glands with holocrine secretions.
- Human do not have these glands.
- These glands are under different molecular regulation than other sebaceous or modified sebaceous glands making them inappropriate for biochemical modelling relative to humans.
- Perianal hair follicle and its gland are larger than other mouse follicles and remain in anagen longer than follicles at other body sites.

as well as anterioventral to the base of the external ear canal. These large, multilobulated glands are often overlooked, but can be observed in rodents when sectioning decalcified skulls. For figures, see Chapter 22, Special Senses: Ear.

Clitoral/Preputial Glands

These glands are commonly referred to only as preputial glands because of a typographic error in a classic mouse gross anatomy text; however, they are also found in clitoral glands in rodents (Fig. 24.16A–C). There are no equivalent

glands in humans, and as a result, they are occasionally misdiagnosed as sebaceous gland tumors or teratomas by researchers more familiar with human than rodent anatomy. Clitoral/preputial gland structure is similar to the other modified sebaceous glands, but they are under different molecular regulation as they do not develop in *Hoxd13*^{spdh} null mice while the other glands are present. Little is known about their function and, unlike other sebaceous glands, they undergo progressive atrophy of the glandular portion with marked ductal ectasia as rodents age.

Perianal Glands

The rodent perianal gland is part of the anal or perianal hair, similar to other pilosebaceous units. As shown in Fig. 24.16D, specialized large hair follicles form a network around the anus. The perianal glands empty into these follicles. They may function as scent glands, as a variety of glands found in this region in many wild and domestic species have this function.

Sweat Glands

There are two types of sweat glands: eccrine and apocrine. Their function and distribution show marked differences between rodents and humans. Rodents sweat only through eccrine sweat glands found in the footpad and do not rely on this for cooling. Humans sweat through both types of glands. Cooling comes primarily from the eccrine type, which have a body-wise distribution. The apocrine type is deeply positioned within the dermis and hypodermis of the axillary skin (Fig. 24.2G, I, and J). Modified apocrine sweat glands include ceruminous, mammary, and human ciliary glands each of which produces secretions other than sweat.

Eccrine Sweat Glands

In humans, the production of sweat is critical to evaporative heat loss. For this reason, the eccrine sweat glands are widely considered one of the most important epidermally derived structures. Indeed, when these glands are no longer functional, humans can quickly become hyperthermic and develop heat stroke. Eccrine sweat glands in rodents are found only on the footpads and, when mature, closely resemble human eccrine sweat glands (Fig. 24.17).

The eccrine sweat gland anlagen are first evident at 16.5 days postconception in mouse embryos as small accumulations of cells in the mesenchymal tissue beneath the developing epidermis, resembling hair follicle placodes. These keratinocytes subsequently extend into the dermis, where significant cell organization, ductal development, and evidence of the acrosyringium are evident by 6–7 days of age in mice. By 3 weeks of age, these structures are fully mature, adult glands. In humans, eccrine sweat gland anlagen first appear as disorganized accumulations of mesenchymal cells that aggregate beneath the epidermis at about 94 days estimated gestational age (EGA). By 115 days EGA, human eccrine sweat gland anlagen appear in increasing numbers with readily apparent but still poorly organized ducts. Once keratinocytes have fully differentiated in this location, the coiled tubular secretory segments contain a mixture of mucus- and serous-secreting cells that give rise to coiled dermal ductal segments lined with double-cuboidal epithelium (Fig. 24.2G, I, and J). The epidermal ductal segment that winds its way to the surface, where it empties its eccrine sweat contents (Figs. 24.2I and 24.17C and D).

Apocrine Sweat Glands

Apocrine sweat glands are not found in rodents. In humans, they are predominantly restricted to the human axillae and anogenital region. Apocrine sweat glands are tubular, coiled secretory glands lined by simple cuboidal epithelium that surround a larger lumen than eccrine sweat glands. Within the basal region, they contain myoepithelial cells with contractile properties that assist in the movement of secretory products upward and outward. Apocrine sweat gland ducts have the same histologic features as

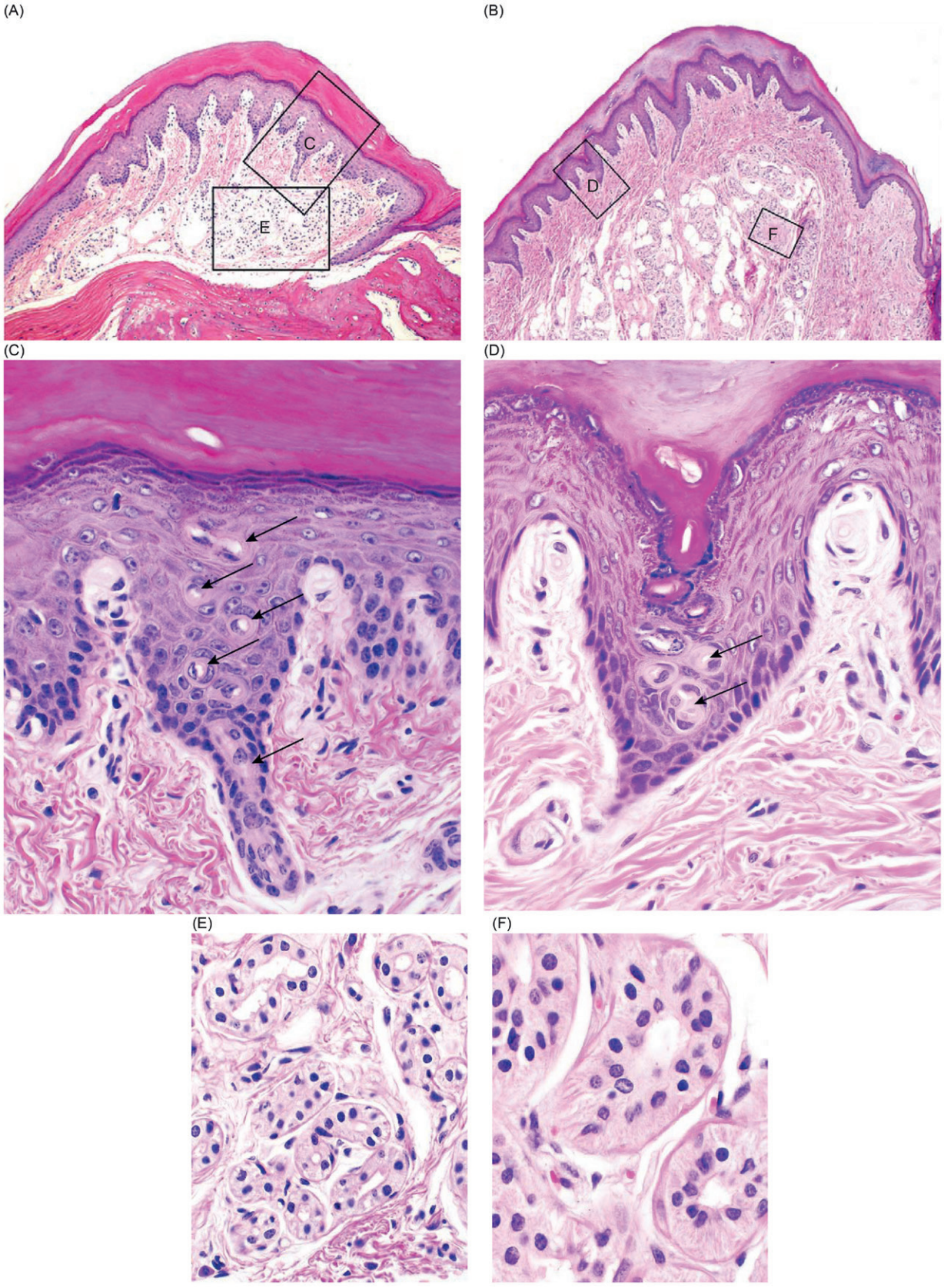

FIGURE 24.17 Rodent foot pad and eccrine sweat glands. Mouse (A, C, E) and rat (B, D, F) adult foot pads are markedly cornified with a thick epidermis with what appear to be rete ridges, where the acrosyringia (intraepidermal spiral ducts of the eccrine sweat glands) are located. The coiled acini of the eccrine sweat gland are enlarged (E and F) and empty their contents via the tortuously coiled acrosyringia (C and D, arrows). Note the acini are lined by cuboidal epithelium surrounding a central lumen (E and F).

Need-to-know

- Rodent foot pads have a thick epidermis and eccrine glands similar to human palms and soles.
- The eccrine duct (acrosyringeum) extends from the gland to exit through the thick epidermis.
- These structures are anatomically similar in all three species.

do the ducts of eccrine sweat glands. However, the intraepidermal portion of the apocrine sweat gland is straight and not coiled as is the eccrine duct (acrosyringium). Their decapitation secretions are thought to be propelled through the lumen by myoepithelial cells around the periphery of the secretory segment. Secretions and cellular detritus move most commonly through the apocrine duct into the pilosebaceous follicle in the infundibulum, but can be found opening directly onto the epidermal surface close to the hair follicle ostia.

Modified apocrine sweat glands also vary between rodents and humans. Ceruminous glands are found within the human, but not rodent, external ear canal and are responsible for wax secretion. Ciliary glands (also called the glands of Moll) are found at the margins of the eyelids, produce secretions that lubricate the eyeball, and have ducts that open into the follicles of the eyelashes in humans but not in rodents. Finally, mammary glands are considered apocrine sweat glands that and secrete milk. Due to the large size of rodent litters, enormous volumes of milk must be produced. As such, lactating rodents have mammary glands that extend over most of their bodies, including the back and leg regions. Raised areas, sometimes misinterpreted as hyperplasia or papillomas, are in fact the teats. See Chapter 23, Mammary Gland.

The Nail

The nails of mice and rats are anatomically similar to each other but quite different from human (Fig. 24.18). The rodent nail extends as a semicircular, laterally flattened, circumferential plate over the distal digit. The rodent nail plate (onycholemmal), the translucent and hard portion of the nail, encircles the distal digit on three sides: the dorsal surface and both sides of the distal digit, leaving only the volar surface of the digit exposed. The nail plate both supports the underlying dorsal surface of the distal phalangeal pad and is used as a sharp extension of the phalanx for climbing, scratching, and digging for food. It is surrounded by and invaginates into the eponychium (proximal nail fold) at its base, similar to humans. The eponychium extends laterally to cover the matrix, which continues to form the nail plate on the sides of the digit. The rodent cuticle grows out with the nail plate, attached to the dorsal and lateral surfaces of the plate. It is usually only seen by retracting the skin backwards, because it is hidden under the eponychium and hair that cover the digits on their dorsal aspect. The lunula is seen as a pale area at the origin of the visible nail that extends distal to the eponychium and shows a pointed shape. It can be seen in all nails and can occupy up to one-third of the visible nail. In a tangential view, the white color of the lunula is even more accentuated and opaque. One blood vessel at each side of the nail matrix in the surrounding nail bed, the skin beneath the nail plate, can be readily seen through the very transparent nail plate. The nail bed itself has a pink color that reflects the underlying dermal vasculature, which is also noticeable in histologic sections.

The rodent nail is thickest in the dorsal ridge (center) area and thins out laterally. The granular layer within the ventral (under) surface of the eponychium is lost prior to reflection of the tissue, similar to what is seen in the human. The germinal epithelium of the nail matrix is thick, but abruptly thins at the juncture with the nail bed. The keratogenous zone of the nail matrix stands out through its more eosinophilic color than lower layers of the nail matrix. The nail bed epithelium is thin, composed of 2–3 cell layers, and forms short papillae that are connected through collagen fibers to dermal structures and the distal phalanx bone. The granular layer reappears at the site of

detachment of the nail plate from the nail bed. At this point, volar epithelium is present, which differs from foot pad epithelium by decreased thickness and relatively rare occurrence of dermal papillae and which ends at the distal groove. The area between the nail bed and the distal groove is analogous to the human hyponychium (described below) although it differs in its extension because the distal groove in rodents is much farther from the site of detachment of the nail plate. The nail plate tip continues to arc around as it extends over the tip of the digit.

The human nail unit comprises the nail bed and the hyponychium, the thickened layer of dermis beneath the free end of the nail. The human nail plate extends as a relatively flat, slightly curved, plate-like structure covering the dorsal surface of the distal digit and extending over its free edge. Thus, the nail plate acts as protection from trauma, as a pressure plate to amplify fine touch perception in underlying structures, and as an extension of the distal digit. It is surrounded by and invaginates into the eponychium at its base and the lateral nail folds on either side. The human cuticle, which is the stratum corneum of the tip and undersurface of the eponychium, attaches to and seals the eponychium to the dorsal surface of the nail plate. The presence of the lunula varies between individuals and digits, depending upon the length of the matrix and how far the eponychium invaginates proximally; individual digits may or may not have a detectable lunula. The nail bed is the red-pink area beneath the nail plate and begins where the nail matrix (or lunula) ends. Because the nail bed epithelium lacks pigmentation, the pink color observed reflects blood in the vessels below, a fortuitous circumstance when medical professionals need to quickly assess oxygenation status. An accentuated band of hyperemia in the distal nail bed marks the onychodermal band; the color change (from the white of the lunula to the red/pink of the nail bed) marks change in the underlying vasculature. The hyponychium, where volar epidermis begins and the under surface of the nail plate separates from the nail bed, begins at the distal edge of the onychodermal band and extends to the distal groove. The free edge of the nail plate is seen as a white band around the margin of the plate; the color change reflects light that is refracted in the air beneath the unattached plate, rather than reflected from blood beneath the nail bed epithelium.

Human nail unit histology is shown in Fig. 24.19. The eponychium reflects at its tip and proceeds proximally and ventrally 5–8 mm before reflecting distally. The stratum corneum attached to the dorsal surface of the nail plate from the distal tip of the eponychium and ventral surface of the eponychium can be seen attached to the dorsal surface of the nail plate as the cuticle. Just before the distal reflection of the eponychium, the granular layer disappears; this marks the beginning of the nail matrix and the onset of nail plate (onycholemmal) cornification. The thick, germinative matrix abruptly thins to a few cells at the juncture of the nail matrix and bed. The characteristic histology of the nail bed is seen in transverse section, revealing the regular pattern of nail bed epithelium interdigitating with papillary dermis. This regular pattern extends longitudinally (proximal-distal) the length of the nail bed, producing a pattern resembling tongue-in-groove lumber. The nail bed ends at the hyponychium with the reappearance of the granular layer, cornification, and the separation of the under surface of the nail plate from the nail bed. The distal groove is seen as an invagination of the epidermis and dermis just distal to the hyponychium and inferior to the free edge of the nail plate; it represents the distal aspect of the primary nail field, an area that denotes the forming nail unit in the embryo. The dermis of the nail unit is thin, and no subcutis is present between the dermis and bone of the distal phalanx.

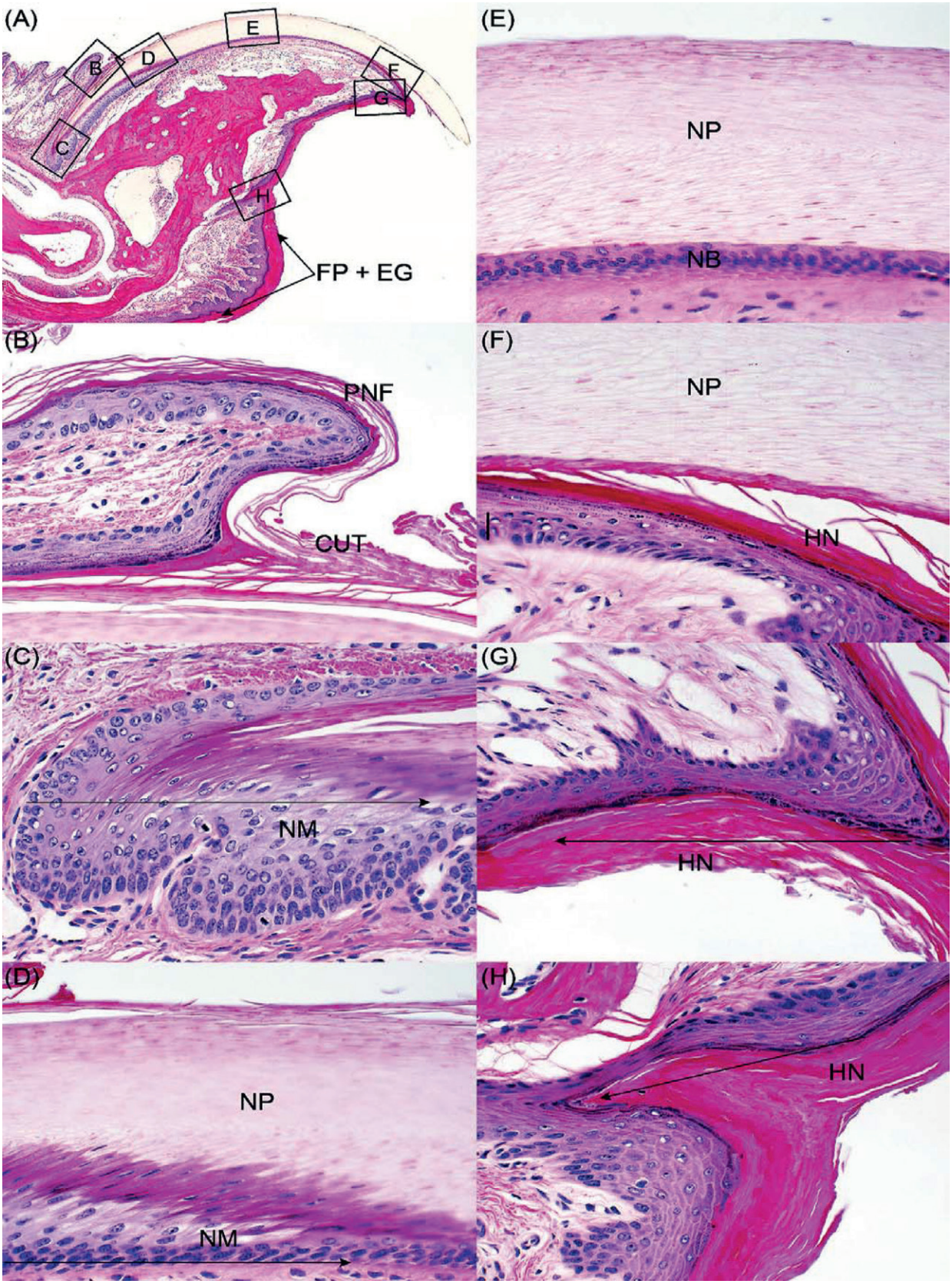

FIGURE 24.18 Rodent nail unit. (A) A sagital section of the distal digit from an adult mouse nail unit. The rodent nail unit is much smaller than the human embryonic digit (Fig. 24.19), making the layers appear larger. The foot pad and eccrine sweat glands are shown in detail in Fig. 24.17. Labeled boxes are shown at higher magnification in B–H. (B) Eponychium (PNF) and cuticle (CUT). The eponychium is artifactually displaced from the underlying nail plate. (C, D) Nail matrix region (NM) as it extends below the nail plate (NP). Nail matrix region limits are indicated by an arrow in both panels. (E) Nail plate (NP) and nail bed (NB). (F) Nail bed end and hyponychium (HN) beginning. Note the formation of a stratum granulosum and stratum corneum. This cornification process results in the separation of the nail plate and nail bed. (G, H) The hyponychium reflects toward the footpad where there is a long region of heavily cornified stratified squamous epithelium without eccrine sweat glands. Its limits are defined as the area between where the nail plate lifts off the nail bed and the stratum granulosum begins and the distal groove (arrow).

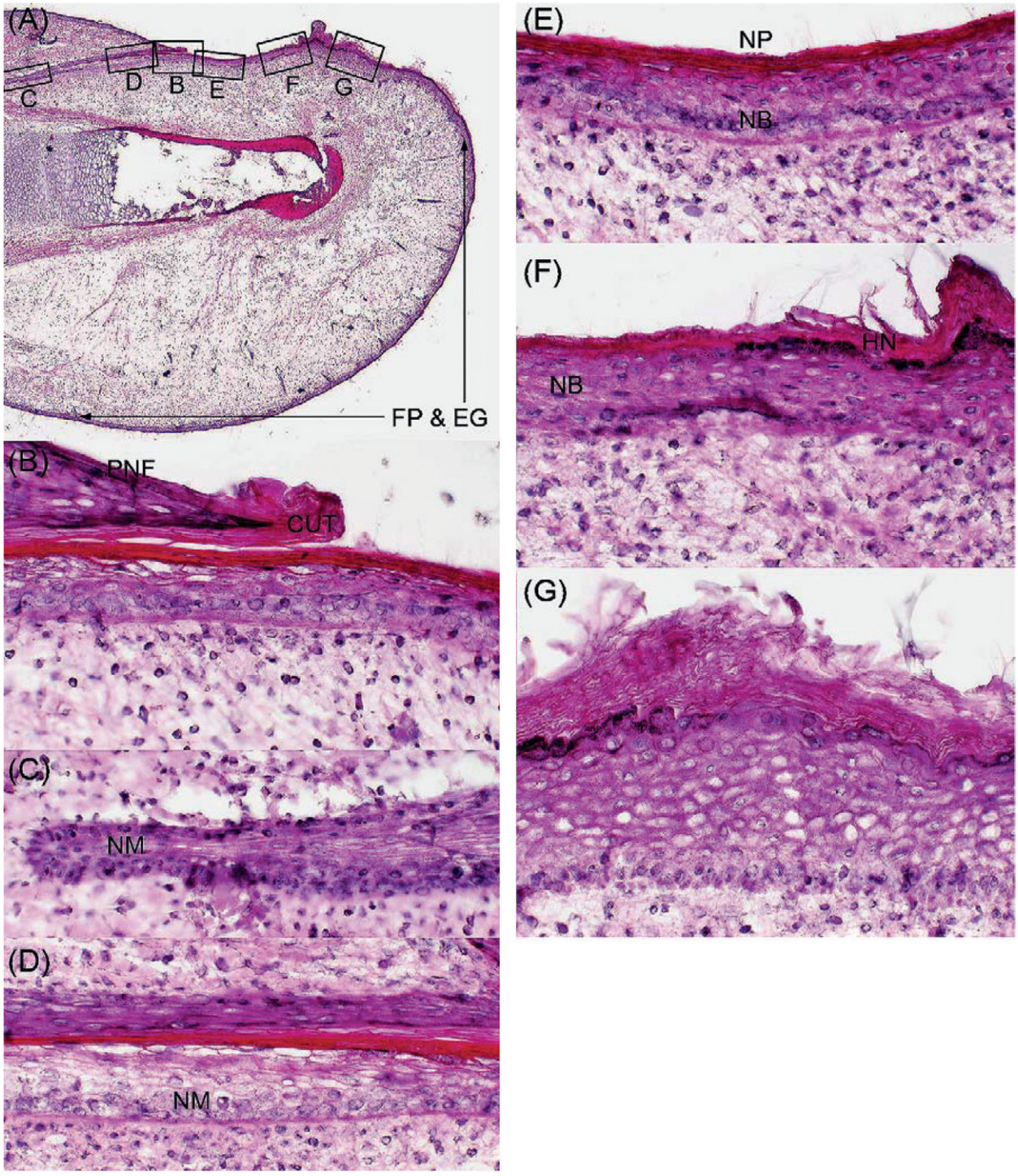

FIGURE 24.19 Human nail unit. (A) Saggital section of the distal digit from a 124-day-old human embryo. The nail unit is at the top and the palmar surface or foot pad equivalent (FP) containing the eccrine sweat glands (EG) extends from the left to the lower surface as indicated. Labeled boxes are shown at higher magnification in B–G. (B) Eponychium (PNF) and cuticle (C). (C) Apical nail matrix region (NM). (D) Mid region of the nail matrix. (E) Location of nail plate (NP) formation when the embryo matures. The nail plate covers the nail bed (NB). (F) Nail bed end and hyponychium (HN) beginning. Note the formation of a stratum granulosum and stratum corneum. This cornification process results in the separation of the nail plate and nail bed. (G) This region marks the transition from hyponychium to distal groove, which can be seen at the extreme right of the plate.

Need-to-know

- The rodent and human nail units are essentially identical but differ in size and shape.
- Human nails form as a gradually curved plate with a rounded distal margin, whereas rodent nails sharply curl laterally, forming an open tubular structure that comes to a distal point.

FURTHER READING

Al-Nuaimi Y, Baier G, Watson REB, et al: The cycling hair follicle as an ideal systems biology research model. *Exp Dermatol* 19(8):707–713, 2010.

Barnhill RL: *Dermatology*, New York, 2010, McGraw-Hill Medical.

Bolognia JL, Jorizzo JL, Rapini RP: *Dermatology*, ed 2, Spain, 2008, Mosley Elsevier.

Burns T, Breathnach S, Cox N, et al: *Rook's textbook of dermatology*, ed 8, New York, 2010, Wiley-Blackwell.

Calhoun ML, Stinson AW: Integument. In Dellmann HD, Brown EM, editors: *Textbook of veterinary histology*, Philadelphia, PA, 1981, Lea & Febiger, pp 378–411.

Carroll J, McElwee KJ, King LE, et al: Gene array profiling and immunomodulation studies define a cell mediated immune response underlying the pathogenesis of alopecia areata in a mouse model and humans. *J Invest Dermatol* 119:392–402, 2002.

Chase HB: Growth of the hair. *Physiol Rev* 34:113–126, 1954.

Chase HB: The physiology and histochemistry of hair growth. *J Soc Cosmetic Chem* 6:9–14, 1955.

Chase HB, Eaton GJ: The growth of hair follicles in waves. *Ann NY Acad Sci* 83:365–368, 1959.

Chase HB, Montagna W, Malone JD: Changes in the skin in relation to the hair growth cycle. *Anat Rec* 116:75–82, 1953.

Chuong CM, Nickloff BJ, Elias PM, et al: What is the "true" function of skin? *Exp Dermatol* 11(2):159–187, 2002.

Cotsarelis G, Sun T-T, Lavker RM: Label-retaining cells reside in the bulge of pilosebaceous unit: implications for follicular stem cells, hair cycle and skin carcinogenesis. *Cell* 61:1329–1337, 1990.

Detlefsen JA: A new mutation in the house mouse. *Am Naturalist* 55:469–473, 1921.

Diegel KL, Danilenko DM, Wojcinski ZW: Integument. In Haschek WM, Rousseaux CG, Wallig MA, editors: *Haschek and Rousseaux's handbook of toxicologic pathology* (ed 3), San Diego, CA, 2013, Academic Press, pp 2219–2275.

Dry FW: The coat of the mouse (*Mus musculus*). *J Genetics* 16:287–340, 1926.

Elenitsas R, Johnson BL, Murphy GF, et al: *Lever's histopathology of the skin*, Philadelphia, PA, 2009, Lippincott, Williams and Wilkins.

Elias PM, Franz TJ, Juin-Chen T, et al: Skin barrier and percutaneous drug delivery. In Bolognia J, Jorizzo JL, Rapini RP, editors: *Dermatology* (ed 2), Philadelphia, PA, 2008, Mosley Elsevier.

English KB, Munger BL: Normal development of the skin and subcutis of the albino rat. In Mohr U, Dungworth DL, Capen CC, editors: *Pathobiology of the aging rat*, Washington, DC, 1994, ILSI Press, pp 363–389.

English KB, Harper S, Stayner N, et al: Localization of nerve growth factor (NGF) and low-affinity NGF receptors in touch domes and quantification of NGF mRNA in keratinocytes of adult rats. *J Comp Neurol* 344:470–480, 1994.

Fleckman P, Jaeger K, Silva KA, et al: Comparative anatomy of mouse and human nail units. *Anat Rec* 296(3):521–532, 2013.

Fluhr JW, Mao-Qiang M, Brown BE, et al: Glycerol regulates stratum corneum hydration in sebaceous gland deficient (asebia mice). *J Invest Dermatol* 120(5):728–737, 2003.

Fu L, Pelicano H, Liu J, et al: Erratum. *Cell* 111:1055, 2002.

Fu L, Pelicano H, Liu J, et al: The circadian gene Period2 plays an important role in tumor suppression and DNA damage response in vivo. *Cell* 111:41–50, 2002.

Goldsmith LA: My organ is bigger than your organ. *Arch Dermatol* 126:301–302, 1990.

Haldane JBS, Sprunt AD, Haldane NM: Reduplication in mice. *J Genet* 5:133–135, 1915.

Haschek WM, Rousseaux CG, Wallig MA: *Haschek and Rousseaux's handbook of toxicologic pathology*, ed 3, San Diego, CA, 2013, Academic Press.

Hesse M, Zimek A, Weber K, et al: Comprehensive analysis of keratin gene clusters in humans and rodents. *Eur J Cell Biol* 83(1):19–26, 2004.

Hosoi J, Murphy GF, Egan CL, et al: Regulation of Langerhans cell function by nerves containing calcitonin gene-related peptide. *Nature* 363(6425):159–163, 1993.

Ishii Y, Tsutsui S, Doi K, et al: Hair follicles of young Wistar strain hairless rats: a histological study. *J Anat* 191(Pt 1): 99–106, 1997.

Johnson KR, Sweet HO, Donahue LR, et al: A new spontaneous mouse mutation of *Hoxd13* with a polyalanine expansion and phenotype similar to human synpolydactyly. *Hum Mol Genetics* 7:1033–1038, 1998.

Kuramoto T, Nakanishi S, Ochiai M, et al: Origins of albino and hooded rats: implications from molecular genetic analysis across modern laboratory rat strains. *PLoS One* 7(8):e43059, 2012.

Madison KC: Barrier function of the skin: "la raison d'être" of the epidermis. *J Invest Dermatol* 121(2):231–241, 2003.

Maronpot RR, Boorman GA, Gaul BW: *Pathology of the mouse. Reference and atlas*, Vienna, IL, 1999, Cache River Press.

McElwee KJ, Kissling S, Wenzel E, et al: Cultured peribulbar dermal sheath cells can induce hair follicle development and contribute to the dermal sheath and dermal papilla. *J Invest Dermatol* 121(6):1267–1275, 2003.

Mecklenburg L, Kusewitt D, Kolly C, et al: Proliferative and non-proliferative lesions of the rat and mouse integument. *J Toxicol Path* 26(3 Suppl):27S–57S, 2013.

Mohr U, Dungworth DL, Capen CC: *Pathobiology of the aging rat*, Washington, DC, 1992, ILSI Press.

Mohr U, Dungworth DL, Capen CC: *Pathobiology of the aging rat*, Washington, DC, 1994, ILSI Press.

Mohr U, Dungworth DL, Capen CC, et al: *Pathobiology of the aging mouse*, Washington, DC, 1996, ILSI Press.

Moll R, Divo M, Langbein L: The human keratins: biology and pathology. *Histochem Cell Biol* 129(6):705–733, 2008.

Morioka K: Hair follicle. *Differentiation under the electron microscope. An atlas*, Tokyo, 2005, Springer-Verlag.

Nakamura Y, Fukami K, Yu H, et al: Phospholipase Cdelta1 is required for skin stem cell lineage commitment. *EMBO J* 22(12):2981–2991, 2003.

Paus R, Peker S, Sundberg JP: Biology of hair and nails. In Jorizzo JL, Rapini RP, editors: *Dermatology* (ed 2), Bolognia, 2008, Mosby Elsevier, pp 965–986.

Perrin C, Langbein L, Schweizer J: Expression of hair keratins in the adult nail unit: an immunohistochemical analysis of the onychogenesis in the eponychium, matrix and nail bed. *Br J Dermatol* 151(2):362–371, 2004.

Plikus MV, Chuong CM: Complex hair cycle domain patterns and regenerative hair waves in living rodents. *J Invest Dermatol* 128(5):1071–1080, 2008.

Plikus MV, Sundberg JP, Chuong C-M: Mouse skin ectodermal organs. In Fox JG, Davisson MT, Quimby FW, Barthold SW, Newcomer CE, Smith AL, editors: *The mouse in biomedical research* (ed 2), Amsterdam, 2007, Elsevier, pp 691–730.

Popesko P, Rajtov V, Hork J: *A color atlas of anatomy of small laboratory animals*, London, 1992, Wolfe Publishing, Ltd.

Presland RB, Boggess D, Lewis SP, et al: Loss of normal profilaggrin and filaggrin in flaky tail (ft/ft mice): an animal model for the filaggrin-deficient skin disease ichthyosis vulgaris. *J Invest Dermatol* 115:1072–1081, 2000.

Priestley GC: Histological studies of the skin follicle types of the rat with special reference to the structure of the Huxley layer. *J Anat* 101(Pt 3):491–504, 1967.

Relyea MJ, Miller J, Boggess D, et al: Necropsy methods for laboratory mice: biological characterization of a new mutation. In Sundberg JP, Boggess D, editors: *Systematic approach to evaluation of mouse mutations*, Boca Raton, FL, 2000, CRC Press, pp 57–90.

Rosbash M, Takahashi JS: Circadian rhythms: the cancer connection. *Nature* 420(6914):373–374, 2002.

Schweizer J, Bowden PE, Coulombe PA, et al: New consensus nomenclature for mammalian keratins. *J Cell Biol* 174(2):169–174, 2006.

Seely JC, Boorman GA: Mammary gland and specialized sebaceous glands (Zymbal, preputial, clitoral, anal). In Maronpot RR, Boorman GA, Gaul BW, editors: *Pathology of the mouse. Reference and atlas*, Vienna, IL, 1999, Cache River Press, pp 613–635.

Seymour R, Ichiki T, Mikaelian I, et al: Necropsy methods. In Hedrich HJ, editor: *Laboratory mouse*, London, 2004, Academic Press, pp 495–516.

Smith RS, John SWM, Nashina PM, et al: *Systematic evaluation of the mouse eye. anatomy, pathology, and biomethods*, Boca Raton, FL, 2002, CRC Press.

Sperling LC: Hair anatomy for the clinician. *J Am Acad Dermatol* 25:1–17, 1991.

Stinson AW, Calhoun ML: Epithelium. In Dellmann H-D, Brown EM, editors: *Textbook of veterinary histology*, Philadelphia, PA, 1981, Lea & Febiger, pp 20–37.

Sundberg JP: *Handbook of mouse mutations with skin and hair abnormalities. Animal models and biomedical tools*, Boca Raton, FL, 1994, CRC Press, Inc.

Sundberg JP, Hogan ME: Hair types and subtypes in the laboratory mouse. In Sundberg JP, editor: *Handbook of mouse mutations with skin and hair abnormalities: animal models and biomedical tools*, Boca Raton, FL, 1994, CRC Press, pp 57–68.

Sundberg JP, King LE: Skin and its appendages: normal anatomy and pathology of spontaneous, transgenic and targeted mouse mutations. In Ward JM, Mahler JF, Maronpot RR, Sundberg JP, editors: *Pathology of genetically engineered mice*, Ames, IA, 2000, Iowa State University Press, pp 181–213.

Sundberg JP, Silva KA: What color is the skin of a mouse? *Vet Pathol* 49(1):142–145, 2012.

Sundberg JP, Boggess D, Sundberg BA, et al: Epidermal dendritic cell populations in the flaky skin mutant mouse. *Immunol Invest* 22:389–401, 1993.

Sundberg JP, Rourk M, Boggess D, et al: Angora mouse mutation: altered hair cycle, follicular dystrophy, phenotypic maintenance of skin grafts, and changes in keratin expression. *Vet Pathol* 34:171–179, 1997.

Sundberg JP, Boggess D, Sundberg BA, et al: Asebia-2J (*Scd1*$^{ab\text{-}2}$): a new allele and a model for scarring alopecia. *Am J Pathol* 156(6):2067–2075, 2000.

Sundberg JP, Peters EM, Paus R: Analysis of hair follicles in mutant laboratory mice. *J Investig Dermatol Symp Proc* 10(3):264–270, 2005.

Sundberg JP, Stearns TM, Joh J, et al: Immune status, strain background, and anatomic site of innoculation affect mouse papillomavirus (MmuPV1) induction of exophytic papillomas or endophytic trichoblastomas. *PLos One* 9(12):e113582, 2014.

Suttie AW, Leininger JR, Bradley AE: *Boorman's pathology of the rat: reference and atlas*, ed 2, New York, 2017, Academic Press.

Takeo M, Chou WC, Sun Q, et al: *Wnt* activation in nail epithelium couples nail growth to digit regeneration. *Nature* 499(7457):228–232, 2013.

Taylor DK, Bubier JA, Silva KA, et al: Development, structure, and keratin expression in mouse eccrine sweat glands. *Vet Pathol* 49(1):146–154, 2012.

Tosti A, Cameli N, Piraccini BM, et al: Characterization of nail matrix melanocytes with anti-PEP1, anti-PEP8, TMH-1, and HMB-45 antibodies. *J Am Acad Dermatol* 31(2 Pt 1): 193–196, 1994.

VanHorn RN: Vibrissae structure in the rhesus monkey. *Folia Primatol* 13(4):241–285, 1970.

Wacnik PW, Baker CM, Herron MJ, et al: Tumor-induced mechanical hyperalgesia involves CGRP receptors and altered innervation and vascularization of DsRed2 fluorescent hindpaw tumors. *Pain* 115(1–2):95–106, 2005.

Ward JM, Mahler J, Maronpot R, et al: *Pathology of genetically engineered mice*, Ames, IA, 2000, Iowa State University Press.

Webb CM, Cameron EM, Sundberg JP: Fluorescence-labeled reporter gene in transgenic mice provides a useful tool for investigating cutaneous innervation. *Vet Pathol* 49(4):727–730, 2012.

Weedon D: *Weedon's skin pathology: expert consult*, New York, 2010, Elsevier.

Whiting DA: The value of horizontal sections of scalp biopsies. *J Cut Aging Cosmetic Dermatol* 1:165–173, 1990.

Whiting DA: *The structure of the human hair follicle. Light microscopy of vertical and horizontal sections of scalp biopsies*, Fairfield, NJ, 2004, Canfield Publishing.

Whiting DA, Hosden FL: *Color atlas of differential diagnosis of hair loss*, Cedar Grove, NJ, 1996, Canfield Publishing.

Zaias N: Embryology of the human nail. *Arch Dermatol* 87: 77–93, 1963.

Zaias N: *The nail in health and disease. Anatomy and physiology*, ed 2, Norwalk, CT, 1990, Appleton & Lange.

INDEX

Note: Page numbers followed by "*f*" and "*t*" refer to figures and tables, respectively.

A

Abdominal anatomy
  lower gastrointestinal tract
    human, 220*t*
    rodent, 220*t*
  upper gastrointestinal tract
    human, 195*f*
    rodent, 194*f*
Abdominal cavity, 32–39, 32*f*, 34*f*
Accessory olfactory organs in rodents, 103–104
Acetic zinc formalin (AZF), 366–369
Acinar cells, 142, 243–246
Acini, 243–246, 245*f*, 490–491
Adenohypophysis, 262
Adipose tissue, 169, 307
Adnexa, 512*t*, 523–540. *See also* Skin
  nail, 536–537
  pilosebaceous unit, 523–530
  sebaceous glands, 530–534
  sweat glands, 534–536
Adrenal cortex, 258–261
Adrenal glands, 256–262, 263*f*, 264*f*, 266*f*, 277
Adrenal medulla, 261–262, 266*f*
Adrenals, 39
Adrenocorticotropic hormone (ACTH), 256–258
Adult mouse eye, 446
Adventitia, 523
Alcohols, 25
Aldehydes, 24
Alpha cells, 241, 246–247
Alveolus, 157
Amacrine cells, retina, 456–457
Ameloblasts, 131–133
Amelogenesis, 131–133, 131*f*
Ammon's horn of hippocampus, 412, 428
Ampulla, 312–314, 344
Ampullary glands, 354–355, 354*f*
Anatomic organization, 433–434
Annulus, 178
ANS. *See* Autonomic nervous system (ANS)
Anterior lamellae, 464
Antidiuretic hormone (ADH), 267–268
Antigen retrieval, 58
Antrum, stomach, 194, 197*f*
Aorta, 42, 165*f*, 182–183, 185*f*
Aortic sinus, 182–183
Apex, 167–169
Apical foramina, 126–131
Apocrine sweat glands, 534–536
Appendix, 216–220, 218*f*
Aqueous humor drainage, 453–454
Archicortex, 419–421
Area postrema (AP), 418
Arrector pili muscle, 525–527
Articular cartilage, 83–85
Astrocytes, 425
Atretic follicles, 307
Atrial walls, 171
Atrioventricular (AV) node, 181
Atrioventricular valves, 178
Auditory brain stem response (ABR), 15
Auditory canal, 478*f*, 479
Auditory tube, 89
Auerbach's plexus, 193–194
Auricle, 471
Automated cell counting, 371
Autonomic nerves, 439
Autonomic nervous system (ANS), 412, 438
Axons, 440

B

Baculum, 295
Bartholin's gland, 321
Basal cells, 102, 148–150, 353–354
Basal ganglia, 411–412, 420*f*, 427–428
Basal layer, 513–516
Basal myoepithelial cells, 494
Basal nuclei. See Basal ganglia
Basal plate, 324, 330–332
Base of heart, 167–169
Basophilic granulosa cells, 307
Basophils, 262–264, 374*f*, 375
Beta cells, 241, 246–247
Biconvex lens, 460
Bicuspid. *See* Mitral valve
Bile canaliculi, 238
Bile duct, 201–202, 233, 238
Bile ductules, 229–230, 233–235, 238
Birbeck granules, 517
Bladder, 291, 299*f*
  urinary, 291–301
Blood, 181–182
  flow models, pancreas, 247–249
  vessels, 307
Blood–brain barrier (BBB), 339, 418, 433
Body weight (BW), 230–233

Bone, 73–82. *See also* Skeletal system
  development and maturation, 71–73
  marrow, 82, 365–370, 368*f*
    collection and processing, 366–369
    examination, 369
  remodeling, 67
  samples decalcification, 26–27
Bowman's capsule, 282, 283*f*, 287*f*
Bowman's glands, 96*f*, 102–103
Bowman's layer, 446, 451*f*
Brachiocephalic trunk (Bct), 165*f*
Brain, 406*f*, 408*f*, 409*f*, 410*f*, 411*f*
  anatomy, 405–424
    endocrine brain, 417–418
    internal landmarks, 406–417
    surface features, 405–406, 407*f*
  BBB, 433
  CVOs, 419*f*
  functional specialization, 419–424
  functional zones, 422*f*
  gray matter, 425*f*
  histology
    cell types, 424–427
    region-specific, 427–432
  regions, 420*f*
  stem, 412–414, 432
  structures, 432–433
  vascular supply, 415–417
  white matter, 426*f*
Breasts, 487–489
Bronchi to terminal bronchioles, 151–156, 152*f*
  BALT, 155–156
  bronchi, 152–154, 153*f*, 154*f*, 155*f*
  bronchioles, 154–155
Bronchopulmonary segments, 151
Bronchus-associated lymphoid tissue (BALT), 155–156
Brown adipose tissue (BAT), 85–87
Bruch's membrane, 456
Brünner's glands (BG), 206–208, 206*f*
Bulbourethral glands, 355, 356*f*
Bulla, 473
Bundle of His (BoH), 181, 182*f*

C

C57BL/6 mice, 5
Calcitonin immunohistochemical staining, 254, 259*f*
Calcitriol, 275
Cancellous bone, 73–74, 73*f*
Cancers of rodent mammary gland, 491–492
Capillaries, 186
Capillary network, 157
Capsularis, 324
Cardiac interstitium, 172–175
Cardiac skeleton, 178
Cardiac valves, 178–181, 179*f*, 180*f*
Cardiac veins (CV), 170*f*, 184
Cardiomyocytes, 159, 163, 172–175
Cardiovascular systems, 163
  cardiac valves, 178–181
  conduction system, 181, 182*f*
  great vessels and coronary vasculature, 181–187
  heart, 164*t*, 165*f*, 166*f*, 167–178, 167*f*, 168*f*, 170*f*, 172*f*
  incidental findings in rodents, 187
Caudate lobe, 233
C cells, 253–254
Cecum, 213–216, 216*f*, 217*f*, 221*f*
Cell rests, 432
Cellularity, 365, 369
Cellulite, 523
Cementum, 133
Central conduction system axis, 181
Central fibrous body, 181
Central isthmus beneath, 230–233
Central nervous system (CNS), 403, 424
Central vascular medulla, 307
Centrilobular
  hepatocytes, 237
  regions, 233–235, 237*f*
Cerebellum, 412, 428–429, 431*f*
Cerebral cortex, 411, 427, 428*f*
Cerebrospinal fluid (CSF), 414, 479
Cervix, 319*f*, 320–321, 320*f*
Chemoreceptors, 270
Chief cells, 256
Chordae tendineae, 178
Chorioallantoic plate, 323–324
Chorionic leave trophoblasts, 332
Choroid, 455
Choroid plexus (CP), 414
  epithelium, 426
Chromaffin cells. *See* Polygonal pheochromocytes
Chromophils, 264–267
Chromophobes, 264–267
Ciliary body, 448–451, 452*f*, 454–455
Ciliary glands, 536
Circumventricular organs (CVOs), 418, 418*f*, 419*f*
Cirrhosis, 229–230
Classical liver lobules, 233
Clearing, tissue processing, 47
Clitoral fossa, 320–321
Clitoral glands, 533–534
Clitoris, 320–321, 325*f*
Club hair, 529–530
Coagulating gland. *See* Dorsocranial/cranial prostate
Cochlea, 481–485, 482*f*, 483*f*
  cochlear aqueduct, 479
  cochlear duct, 481–484
Colliculus seminalis, 354, 361*f*
Colon, 220–228, 222*f*
  anorectal junction, 226*f*, 227*f*
Comparative neuroanatomy, considerations for, 440–443
Conduction system, 181, 182*f*
Conjunctiva, 463–464
Cooper's ligaments, 487–489
Cornea, 446–448, 451*f*
  corneal endothelium, 446–448
  corneal stroma, 446–448
Cornified layer, 513–516
Cornu Ammonis (CA), 412
Coronary arteries, 169–170, 182–183
Coronary branches, 183–184
Coronary vasculature, 181–187, 185*f*, 186*f*, 187*f*, 188*f*

Corpora albicans, 307
Corpus luteum, 307, 312*f*
Cortex, 286*f*, 307
  lymph node, 387–390
  sexual dimorphism, 293*f*
Cortical bone, 80*f*, 81–82, 81*f*
Cortical interstitial cells, 289–291
Cortical labyrinths, 284–289
Cortical tubules, 292*f*
Corticosteroid production. *See* Zona fasciculata
Cranial nerve II. *See* Optic nerve
Cranial nerves, 439
Cresyl violet (CV), 443
Cristae ampullaris, 479–480
"Cross-linking" fixatives, 23
Crux of heart, 183–184
Cuboidal epithelium, 341
Cutback zone, metaphysis, 79

D

Decidua basalis, 321, 333*f*
Decidualized stromal cells, 315–316
Dehydration, tissue processing, 47
Dendritic cells, 517
Dental formula, 121–125
Dentin, 126–131
Dermal nerves, 519
Dermis, 517–519
Descemet's membrane, 446–448
Diaphysis, 79–82
Diarthrosis, 473–478
Diastema, 121–125
Dichotomous branching, 151
Diencephalon, 412, 428
Digital imaging approach, 61–62, 62*f*
Directional anatomy terminology in mouse and human, 5*t*
Dorsal lingual mucosa, 119
Dorsal root ganglion (DRG), 435, 439
Dorsocranial/cranial prostate, 348
Dorsolateral lobe, 348
Drainage system, 467
Ductal ectasia, 357
Ductal epithelial cells, 246
Ductular system, 142
Ductus deferens. *See* Vas deferens
Duodenum, 201–202, 208*f*

E

Ear, 472*t*–473*t*
  ampulla, 312–314, 344
  auditory tube, 89
  external ear, 471–473, 474*f*
  inner ear, 479–485, 483*f*
  of mice, rats, and humans, 471
  middle ear, 473–479
  rodent, 477*f*
  subgross regional anatomy, 475*f*
Eccrine sweat glands, 534, 535*f*
Ectopic cervical thymus, 380
Ectopic parathyroid glands, 255
Ectopic thyroid tissue, 251–253
Efferent ducts, 341–342, 343*f*
Elastic arteries, 159, 185
Elastic fibers, 150, 185–186
Electrocardiography (ECG), 15
Embedding, 49
  artifacts, 49*t*
Embryonal endothelium, 330
Enamel matrix proteins, 131–133
Endocardium, 175–178
Endocrine brain, 417–418
Endocrine gland, 241–243
Endocrine system, 251, 252*t*
  adrenal gland, 256–262
  paraganglia, 270–272, 271*f*
  parathyroid gland, 255–256
  pineal gland, 268–270
  pituitary gland, 262–268
  thyroid gland, 251–255
Endolymph, 479
Endometrium, 315–316, 317*f*
Enterocytes, 208–209
Enzyme-linked immunosorbent assay (ELISA), 56
Eosinophils, 372, 374*f*
Ependyma, 426
Epicardial adipose tissue, 176–177
Epicardium, 175–178
Epidermis, 513–517
Epididymis, 342–343, 344*f*, 345*f*
Epiglottis, 115–117
Epiphysis, 75–76
Episclera, 448
Epithelium, 142, 342
Erythrocytes, 372
Erythroid cells, 369
Esophagus, 191–194, 192*t*, 198*f*–199*f*, 199*f*
Estrous and menstrual cycles. *See* Ovarian cycles
Estrus cycle, 303, 318*f*, 323*f*
Ethylenediamine tetraacetic acid (EDTA), 26, 366
Eustachian tube, 471–473
Exocrine gland, 241–243
Exorbital lacrimal gland, 135, 142
External acoustic meatus (EAM), 471, 476*f*
External ear, 471–473, 474*f*
External elastic lamina (EEL), 184–186
External epithelium, 115
Extramedullary hematopoiesis (EMH), 365, 393–397
Extraocular muscles, 463
Extrapulmonary bronchi, 147
Eye, 450*t*
  conjunctiva, 463–464
  cornea and sclera, 446–448
  development, 467–469
  drainage system, 467
  extraocular muscles, 463
  eyelids, 463–464, 466*f*
  fixation, 445
  gross anatomy, 445–446
  lacrimal gland, 467, 468*f*
  lens, 460–461, 461*f*
  ocular development, 469*f*
  optic nerve, 461–463, 462*f*

Eye (*Continued*)
retina, 455–460, 457*f*, 458*f*, 459*f*
uvea, 448–455
vitreous chamber, 460–461
Eyeball, 448*f*, 449*f*, 463–464
Eyelids, 463–464, 466*f*

F

Facial nerve, 142
Female genital system, 303
Female reproductive system
clitoris, 320–321
female reproductive tract, 304*t*
gestation and placentation, 305*t*
ovary, 303–310
placenta, 321–334
sexual maturity and ovulation, 304*t*
vagina, 320–321
Femur, 67–68, 75–76
cortex, 79
Fibroblast cells, 519
Fibroelastic framework, 161
Fibroelastic tissue, 150–151
Fibrous pericardium, 169, 177–178
Field of view (FOV), 53–54
Fischer 344 (F344), 91
Fixation, 24–25
frozen tissue, 27
osmolarity, 26
pH, 26
size, 25
temperature, 25
time, 25–26
tissue, 25–26
volume ratio, 25
Follicle, ovary, 253
Follicle-stimulating hormone (FSH), 262–264
Follicular cells, 253
Follicular ostea, 529–530
Foot pads, 516–517
Fordyce granules, 119
Fordyce spots, 115, 119
Formalin fixed paraffin embedded (FFPE) tissues, 56, 365
Frozen tissue, 27
Fundic mucosa, 195–196, 201*f*
Fundic-type mucosa, 196

G

Gallbladder, 229–230, 230*t*, 238, 239*f*
Gamma cells, 246–247
Ganglia, 435–440
Gastrointestinal (GI), 28
MALT, 398–399
tract, 34–37, 36*f*, 191, 229–230, 251
Genetically engineered mice (GEM), 1–2, 5, 9
Genetically engineered rats (GM rats), 9
Germinal epithelium, 307
Glands of Moll. *See* Ciliary glands
Glial cells
modified, 267–268
processes, 433
Glisson's capsule, 233
Globose basal cells (GBCs), 102
Glomerular basement membrane (GBM), 282, 291*f*
Glomeruli, 282, 287*f*, 288*f*, 290*f*
Glycoprotein thyroglobulin, 253
Goblet cells, 152
Granular cell layer, 513–516
Granular convoluted duct, 142
Granular layer, 523–525
Great vessels, 181–187, 185*f*, 186*f*, 187*f*, 188*f*
Greater omentum, 194
Growth hormone (GH), 262–264
Growth plate, 76–77, 77*f*
Gut-associated lymphoid tissue (GALT), 202, 207*f*, 209–211, 228, 397–398

H

Hair cycle, 526*f*, 527–530
rodent tail hair cycle, 529*f*
stages of mouse hair cycle, 529*t*
truncal skin hair cycle, 528*f*
Hair follicles, 499, 523–525, 524*f*, 529–530
Hair types, 530
Hard palate, 115–116, 119–120, 126*f*
Harderian gland, 446, 448*f*, 449*f*, 460, 468*f*
Hassall's corpuscles (HCs), 378–379
Head, 42–44
Heart, 42, 43*f*, 44*f*, 165*f*, 166*f*, 167–178, 167*f*, 168*f*, 170*f*, 172*f*
endocardium, epicardium and pericardial sac, 175–178, 177*f*
myocardium, 172–175, 174*f*, 175*f*, 176*f*
size considerations, 170–171, 173*f*
Helicobacter species, 10
Hematopoietic and lymphoid tissues, 365
bone marrow, 365–370, 367*f*
comparison of reference ranges, 371*t*
lymph nodes, 381–390, 382*f*, 383*t*, 384*f*, 385*f*, 387*f*
MALT, 397–399
maturational sequence of hematopoietic cells, 366*f*
milky spots, 400
peripheral blood, 370–375
spleen, 390–397, 391*t*, 392*f*, 394*f*
thymus, 375–381, 376*t*, 377*f*, 380*f*
Hematopoietic stem cells (HSCs), 365
Hematoxylin and eosin (H&E), 5–6, 23, 366, 425, 429*f*
Henle's layer, 456–457, 523–525
Hepatic lobular architecture, 233, 234*f*
"Hepatic stem" cells, 238
Hepatobiliary system. *See also* Endocrine system; Urinary system
gallbladder, 238
liver, 230–238
Hepatocellular enzymatic function, 233–235
Hepatocytes plates, 233
High endothelial venules (HEVs), 385
Hippocampus, 412
Ammon's horn of, 412, 428
organization, 430*f*
Histochemical stains, 185
Horizontal basal cells (HBCs), 102
Hormones erythropoietin, 275

Howship's lacuna, 72–73
Human nail unit, 537, 539*f*
Hyaline droplets, 285–289
Hydropic degeneration, 229–230
Hyperkeratosis, 357
Hypodermis, 519–522
Hypophysis. *See* Pituitary gland
Hypothalamus, 262–264, 412

I
Ileocecal junction, 216
Ileum, 191, 209*f*
Image analysis technique, 64
  reproducibility, 64–65
Immunoglobulin A, 98–101
Immunohistochemistry (IHC), 56–61, 237–238, 256, 397
  antibody controls for, 60
  antibody specificity validation, 56–58
  detection, 388*f*
  labeling, 396*f*
  protocol optimization, 58–60, 59*f*, 59*t*
  reproducibility, 64–65
  tissue controls for, 60–61
  tissue processing, 56
Incisors, 121–125, 131–133
Incus, 473–478, 474*f*
Induced BALT (iBALT), 398
Inferior parathyroid glands, 255
Infiltration, tissue processing, 48
Insulo-acinar portal system, 247–249
Intercalated disks, 172
Intercalated ducts, 135–139, 142–143
Intermolar eminence, 117
Internal carotid arteries (ICs), 415–417
Internal elastic lamina (IEL), 184–186
International Harmonization of Nomenclature and Diagnostic Criteria (INHAND), 16–19
International Knockout Mouse Consortium (IKMC), 9–10
International Mouse Phenotyping Consortium (IMPC), 9–10
Interstitial fluid (ISF), 414
Interstitium, 172–175
Interventricular septum (IVS), 167*f*
Intervertebral discs, 83, 83*f*
Intralobular intercalated ducts, 135–139
Intraocular optic nerve, 463
Intraocular pressure (IOP), 454
Intraorbital optic nerve, 463
Iodinated thyroglobulin, 253
Iridocorneal angle, 453–454, 453*f*
Iris, 448–454, 452*f*
Islets of Langerhans, 61, 241, 246
Isthmus, 251, 310–312

J
Jejunum, 209*f*
Joints, 83–85
  adipose tissues, 86*f*
  articular cartilage, 83–85
  knee joint, 84*f*
  meniscus, 85
Juxtaglomerular apparatus (JGA), 285–289, 289*f*

K
Karnovsky's fixative, 24
Keratin
  expression in rodent epidermis, 516*f*
  layer, 119
Keratinocytes, 513–517
Keratins, 513–516
Kidneys, 39, 40*f*, 280*f*, 284*f*, 285*f*
  anatomy, 278*f*, 279*f*
  cortical labyrinths, 284–289
  glomeruli, 282
  gross anatomy, 275–280
  histology, 282–291
  medulla, 289–291, 295*f*
  nephron, 282, 283*f*
  papilla, 289–291, 296*f*
  urinary system, 276*t*–277*t*
Küpffer cells, 237–238

L
Labia majora, 320–321
Labryinths, 479
Lacrimal gland, 467, 468*f*
Lactation, 502–503, 504*f*, 505*f*
Lactiferous ducts, 497–499
Lamellar clefting, 446–448
Lamina densa, 282
Lamina fusca, 448
Lamina propria (LP), 117–119, 150
Lamina rara externa, 282
Lamina rara interna, 282
Langerhans cells, 517
Large intestine (LI), 36*f*, 209–211, 213
  human, 217*f*
  rodent, 216*f*
Laryngeal cartilages, 251
Larynx, 105–112, 106*t*
  epiglottis, 110*f*
  MALT in nasopharynx, 107*f*
  pharyngeal submucosa, 108*f*
  rodent larynx, 111*f*
  rodent tissues for microscopic examination, 106
  vocal processes, 111*f*
Lateral nasal gland (LNG), 98
Lens, 460–461, 461*f*
Leptomeninges, 432–433
Lesser omentum, 194
Leukocytes, 372–375
Leydig cells, 340
Lieberkühn, crypts of, 202–206, 223
Limbic system, 412
Limbus, 446
Linea alba, 119
Lingual frenum, 117
Lingula, 151
Lipofuscin, 172, 175*f*, 237
  granules, 261
Lips, 115, 117–119, 117*f*
Littre glands, 297–298

Liver, 33–34, 35*f*, 230*t*
anatomy, 230–233, 231*f*, 232*f*
histology, 233–238
Lobes, 335
Lobules, 233–235, 235*f*, 243, 244*f*
Lower gastrointestinal tract, 213, 220*t*
human, 215*f*
rodent, 214*f*
Luminal secretory cells, 353–354
Lungs, 41–42, 42*f*, 251
anatomy, 151
circulatory system, 159, 160*f*, 161*t*
Luteinizing hormone (LH), 262–264
Luxol fast blue (LFB), 443
Lymph nodes (LN), 32, 137*f*, 381–390, 382*f*, 383*t*, 384*f*, 385*f*, 387*f*
Lymphatic vessels, 161
Lymphocytes, 150, 228, 370, 373*f*, 375
Lymphoepithelium (LE), 104
Lymphoid aggregate, 370
Lymphoid cells, 155
Lymphopoiesis, 370

M

Macula, 456–457, 479–480
Male reproductive system, 335, 338*f*
ampullary glands, 354–355
bulbourethral glands, 355
efferent ducts, 341–342, 343*f*
epididymis, 342–343
male reproductive tract, 336*t*–337*t*
penis, 360–362, 362*f*
preputial glands, 355–357, 357*f*
prostate gland, 348–354
seminal vesicles, 346–348
testes, 336–341, 339*f*
urethra, 357–360, 359*f*
vas deferens, 343–346, 346*f*
Male urogenital mating protuberance (MUMP), 360
Malleus, 473–478
Mallory–Heidenhain stain, 285–289
Mammary fat pad (MFP), 487, 499, 504*f*
female rodent, 487–489
Mammary glands, 31–32, 32*f*, 487, 489*t*, 511
development, 501*f*
gross anatomy, 487–489, 488*f*
involution, 506*f*
natural history and reproductive cycles, 499–508, 500*f*
during ovarian cycle, 503*f*
senescence, 507*f*
from sexually mature male and female rats, 495*f*
subgross anatomy and histology, 490–499, 490*f*, 491*f*
Mandibular gland. *See* Submandibular (SM) gland
Margo plicatus, 191–192
Mast cells, 117–119, 385
Median eminence (ME), 418
Medulla, 289–291, 295*f*
Megakaryoblasts, 370
Megakaryocytes, 370
Meibomian glands, 464–467, 466*f*, 530–532, 532*f*
Melanosomes, 460
Meninges, 432–433
Meniscus, 85
Menstrual cycle, 303
Menstrual endometrium, 315–316
Mercuric chloride, 25
Merkel cells, 517
Mesometria, 315
Mesothelial cells (MC), 170*f*
Mesothelium, 307
Mesotubarium, 310
Metaphysis, 77–79
Microfold cells (M cells), 209–211
Microglia, 426
Microscopy, 53–56
contrast, 54–56
functions, 55*f*
magnification, 53–54
resolution, 54
Middle ear, 473–479
Midzonal regions, 233–235, 236*f*
Milky spots, 400
Mitral valve, 178
Modified sebaceous glands, 530–534
Monocytes, 369–370, 373*f*, 375
Mouse Disease Clinics (MODICs), 15
Mouse Genome Informatics (MGI), 9–10
Mouse Phenome Database (MPD), 9–10
Mucocutaneous junction, 117–119
Mucosa-associated lymphoid tissues (MALT), 108, 365, 397–399, 398*f*, 399*f*
Mucoserous labial glands, 117–119
Mucous cells, 142
granules, 135
Mucus-producing cells, 150
Muscular arteries, 185–186, 186*f*
Muscularis propria, 191
Mus musculus, 1–3, 3*t*
Myelin basic protein (MBP), 425–426
Myeloid cells, 369–370
Myelopoiesis, 369–370
Myocardium, 172–175
Myoepithelial cells, 135

N

Nail, 536–537
Nasal blood vessels, 105
Nasal cavity
accessory olfactory organs in rodents, 103–104
nasal blood vessels, 105
nasal passage, 93*f*
nasal SE, 94, 95*f*, 96*f*, 98*f*
nasal trigeminal nerves, 104–105
olfactory epithelium, 101–103
rodent nasal tissues, 92–94
Nasal epithelium, 94–103. *See also* Olfactory epithelium
respiratory, 97–101
squamous, 94
transitional, 94–97
Nasal-associated lymphoid tissue (NALT), 104, 397–398
National Institutes of Health (NIH), 1–2
National Toxicology Program (NTP), 16–19
Natural killer (NK) cells, 370, 375

Necropsy, 23, 27–28
bone samples decalcification, 26–27
external examination, 29
first incision, 30–32
frozen tissue, 27
internal examination, 32–45
materials, 28
tissue fixation, 25–26
Neocortex, 419–421
Nephron, 275, 282, 283*f*
Nerves, 435–440, 519
fiber layer, 456–457
Nervous system, 403
brain, 405–433, 406*f*, 408*f*, 409*f*, 410*f*, 411*f*
circumventricular organs, 418*f*
considerations for comparative neuroanatomy, 440–443
CVOs in rodent brain, 419*f*
human surface arteries, 417*f*
nerves and ganglia, 435–440
rodent surface arteries, 416*f*
spinal cord, 433–435, 436*f*, 438*f*
ventricular systems, 415*f*
Neuroanatomic terminology, 440
Neurohistological preparation, methods in, 441–443
Neurohypophysis, 262
Neurons, 424–425, 434, 456
Neurosensory retina, 456–460
Neutrophils, 372, 373*f*
Nipple, 498*f*, 499
Nomia Anatomica Veterinaria (NAV), 1
Nonciliated cells, 148–150
Nonneoplastic Lesion Atlas (NNLA), 16–19
Nonpigmented epithelium, 454–455
Nose. *See* Nasal cavity

O

Odontoblasts, 126–131
Odorant receptors (ORs), 101
Olfactory epithelium (OE), 90, 101–103. *See also* Nasal epithelium
basal cells, 102
OSN, 101–102
sustentacular cells, 102
Olfactory marker protein (OMP), 101
Olfactory sensory neurons (OSN), 101–102, 107*f*
Oligodendrocytes, 425–426
Oncocytes, 142
Optic nerve, 461–463, 462*f*
Oral cancers, 115–116
Oral cavity, 115–121, 116*t*
functions, 115
hard palate, 115–116, 119–120, 126*f*
head coronal section, 120*f*
longitudinal section of lip, 122*f*
mucosa, 119
muzzle and lips, 117*f*
regional anatomy, 118*f*
rodent tongue, 123*f*, 124*f*, 125*f*
sebaceous gland, 123*f*
soft palate, 115–116, 119
Oral mucosa, 115–116, 119
Orange-Fuschin-Green (OFG), 262–264
Organ of Corti, 484*f*, 485
Osseous, 479
Ossicles, 473–478
Osteoblasts, 67, 72
Osteoclasts, 67, 72–73
Osteocytes, 72
Ovarian cycles, 502, 503*f*
Ovary
anatomy, 303–307, 305*f*, 306*f*
histology, 307–310
human, 309*f*, 311*f*
rodent, 308*f*, 310*f*
Oviduct, 310–315, 313*f*, 314*f*
Oxidizing agents, 25
Oxyphil cells, 256
Oxyphilic cells, 256

P

Paleocortex, 419–421
Pancreas, 33, 34*f*, 243*t*
anatomy, 241–243, 242*f*
histology, 243–249
Pancreatic duct, 241, 246
Paneth cells (PC), 202–208, 205*f*, 209*f*, 223
Panniculus carnosus muscle, 522–523
Papilla, 291, 294*f*, 296*f*
Parafollicular cells. *See* C cells
Paraformaldehyde, 23
Paraganglia, 270–272, 272*f*
Parathyroid gland, 255, 260*f*, 261*f*
Parathyroid hormone (PTH), 254
Paraurethral glands, 297–298
Parietal epithelial cells, 282
Parietal pericardium, 169
Parotid acini, 142–143
Parotid glands, 135–139, 141*f*, 142–143, 143*f*
Pars distalis, 262
Pars intermedia, 262
Pars nervosa, 262
Pars tuberalis, 262
PAS-positive basement membrane, 456–457
Pasteurella pneumotropica, 355
Pathologic evaluations, 16
Pencil fibers, 427–428
Penis, 362*f*
anatomy, 360
histology, 360
Perianal glands, 534
Periarteriolar sheaths of lymphocytes (PALS), 397
Pericardial sac, 169, 175–178
Pericytes, 186
Perimembranous space, 479
Perimysium, 172–175
Periodic acid–Schiff (PAS), 282, 339–340, 446–448
Peripheral blood, 370–375
cell counting, 371
collection, 371
erythrocytes, 372
leukocytes, 372–375
platelets, 375
smear, 372

Peripheral nerve, 442*f*
  trunks, 441*f*
Peripheral nervous system (PNS), 403, 438–443
Peripheral zone, 348
Peroxisome proliferator-activated receptor-α (PPAR-α), 229–230
Peyer's patches (PP), 397
Pharynx, 105–112, 106*t*
  MALT in nasopharynx, 107*f*
  pharyngeal submucosa, 108*f*
  rodent tissues for microscopic examination, 106
Phenotyping, 9–10
  animals, 10–15
  pathologic evaluations, 16
  reporting, 16–19
  strategies, 10
  tests, equipment, procedures, and analyses, 15
Picric acid, 25
Pilosebaceous unit, 523–530
Pineal gland, 268–270, 271*f*, 418
Pinealocytes, 269–270
Pituitary gland, 262–268, 267*f*, 269*f*, 417–418
Placenta, 329*f*, 330*f*
  anatomy, 321–324
  histology, 324–332
  human, 328*f*
  rodent, 327*f*
Platelets, 374*f*, 375
Pleura, 159–162, 161*f*
Plicae, 201
Polygonal pheochromocytes, 261–262
Polymerase chain reaction (PCR), 101
Polymorphonuclear neutrophilic granulocytes. *See* Neutrophils
Pores of Kohn, 156–157
Portal regions, 233, 234*f*, 236*f*
Portal triads, 233–235
Posterior lamellae, 464
Postpartum involution, 503–505
Pregnancy, 502–503, 504*f*
Preputial glands, 355–357, 357*f*, 358*f*, 533–534, 533*f*
Proerythroblast, 369
Promegakaryocytes, 370
Prostate gland, 348–354, 349*f*, 350*f*, 351*f*, 352*f*–353*f*
Proximal airways, 152
Proximal convoluted tubules (PCT), 284–285, 288*f*
Pulmonary artery, 181–182
Pulmonary capillaries, 159
Pulmonary system, 159
Pulmonary vessels, 161
Pyloric mucosa, 195–196, 202*f*
Pylorus, 203*f*
Pyramidal lobe, 251–253
Pyramidal mucous cells, 144
Pyramidal neurons, 424–425

Q

Quantitative microscopy, 62–64
  image analysis technique, 64
  stereology, 63–64, 64*t*

R

Rat genome database (RGD), 9
Rattus fuscipes, 340
Rattus norvegicus, 1–3, 3*t*
Rectum, 213, 220–221, 223
Reissner's membrane, 481–484
Renal papilla, 280
Renal pelvis, 280, 280*f*
Renal vasculature diagram, 281*f*
Reproductive cycles, 499–508, 500*f*
Reserve cells, 527
Respiratory bronchioles (RB), 156*f*
Respiratory epithelium (RE), 94, 97–101, 99*f*, 100*f*
Respiratory system, 147, 149*t*
  bronchi to terminal bronchioles, 151–156
  lung, 151
    circulatory system, 159
  pleura, 159–162
  regional anatomy of lungs, 148*f*
  respiratory zone, 156–159
  trachea, 147–151
Respiratory zone, 156–159, 156*f*, 157*f*, 158*f*
Rete ridges, 517–519
Rete testis, 341, 342*f*
Reticulocytes, 369
Retina, 457*f*, 458*f*, 459*f*
  anatomy, 455–456
  histology, 456–460
Retinal pigment epithelium (RPE), 445, 456, 460
Retinoblastoma (RB), 448*f*
Rod nuclei, 456–457
Rugae, 320–321

S

Saccule, 479–480
Salivary glands, 135, 136*t*, 137*t*
  anatomy, 142
  histology, 142–143
Satellite cells, 439
Scala media. *See* Cochlea: cochlear duct
Scattered ganglion cells. *See* Polygonal pheochromocytes
Schwann cells, 439
Sclera, 446–448
Scleral stroma, 448
Sebaceous glands, 527
Secretions, 135–139, 346
Sectioning, 49
Segmental bronchi, 152
Segmented filamentous bacteria (SFB), 225–227
Semicircular canals, 479–480
Semilunar valves, 178
Seminal vesicles, 346–348, 347*f*
Seminiferous tubules, 339–341, 341*f*
Septal artery, 183
Septal branches, 184
Septal organ of Grüneberg (SOG), 103–104
Septal organ of Masera (SOM), 103
Serous glands, 119
Sertoli cells, 339
Sexual dimorphism, 142, 285–289
Signal-to-background (SBR) ratio, 54
Signal-to-noise (SNR) ratio, 54
Sinoatrial node (SA), 181
Sinus. *See* Nasal cavity
Sinusoidal capillaries, 247–249

Skeletal system, 44–45. *See also* Joints; Bone
bone development and maturation, 71–73
bone marrow, 82
diaphysis, 79–82
epiphysis, 75–76
gross anatomy, 68–69, 68*f*, 70*f*
growth plate, 76–77, 77*f*
metaphysis, 77–79, 78*f*
soft tissues, 85–87
spine, 82–83
undecalcified bone, 71*f*
Skin, 511–523, 512*t*. *See also* Adnexa
adventitia, 523
dermis, 517–519
epidermis, 513–517
eyelid, 464
functions, 512*t*
hypodermis, 519–522
panniculus carnosus muscle, 522–523
ultrastructural features, 514*f*
Small intestine, 196*t*, 201–211, 204*f*
Smooth endoplasmic reticulum (SER), 97
Soft palate, 115–116, 119
Soft tissues, 85–87
Solitary chemoreceptive cells (SCCs), 104–105
Specific pathogen free (SPF), 148–150
Sperm, 343
Spermatogonia, 339–340
Sphenoid, 445–446
Spinal cord, 433–435, 436*f*, 437*f*, 438*f*
functional specialization of, 434
spinal nerves, 439
Spine, 82–83
Spinous layer, 513–516
Spleen, 33, 34*f*, 391*t*, 392*f*, 394*f*
anatomy, 391
histology, 391–397
Spleen, 395*f*
Spongiosa, 179
Sprague-Dawley (SD) rat, 5
Squamous endocervical epithelium, 317–318
Squamous epithelium (SE), 90, 94
nasal, 94, 95*f*, 96*f*, 98*f*
Staining, 49–51
routine, 49
special, 49, 50*t*
Staphylococcus aureus, 355
Statoacoustic system, 471
Stem cells, 208
Steno's gland. *See* Lateral nasal gland (LNG)
Stereology, 63–64, 64*t*
Steroid hormone synthesis, 261
Stomach, 193*t*. *See also* Necropsy
anatomy, 194–195
histology, 195–200
Stratum basale, 513–516
Stratum corneum, 513–516
Stratum granulosum, 513–516
Stratum spinosum, 513–516
Striated ducts, 135–139, 141*f*
Stromal cells, 315–316
Subchondral plate, 75–76
Subcommissural organ (SCO), 418
Subendocardium, 175–176
Subfornical organ (SFO), 418
Sublingual (SL) gland, 137*f*, 140*f*, 143–144, 144*f*
Sublingual gland, 143–144, 144*f*
Submandibular (SM) gland, 135, 136*t*, 137*f*, 138*f*, 139–142, 140*f*
Submaxillary gland. *See* Submandibular (SM) gland
Submucosal glands, 150
Superficial fascial layer, 519–522
Superficial lymphatic network, 161
Superior parathyroid glands, 255
Suprarenal glands. *See* Adrenal glands
Sustentacular cells, 102
Sweat glands, 534–536
Syncytiotrophoblast, 332

T

Tarsal plate, 464–467
Taste buds, 119–120, 125*f*
T cells, 237–238, 238*f*
Teeth, 116*t*, 121–133
Terminal Duct Lobular Unit (TDLU), 490–497, 492*f*, 493*f*, 496*f*
Terminal end bud (TEB), 499–502
Terminologia Anatomica (TA), 1
Tertiary lymphoid tissues, 365
Testes, 336–341, 339*f*, 340*f*
Tetraiodothyronine (T4), 253
"Third eyelid", 446, 463–464
Thoracic cavity, 39–42
Thoracic organs removal en bloc, 41, 41*f*
Thymocytes, 376–378
Thymus, 42, 375–381, 376*t*, 377*f*, 380*f*
Thyroid gland, 251–255, 255*f*, 257*f*, 259*f*
Thyroid-stimulating hormone (TSH), 253
Thyromeres, 251–253
Thyrotropin-releasing hormone (TRH), 253
Tissue processing, 47–49
clearing, 47
dehydration, 47
infiltration, 48
Tongue, 115–117, 119
Touch domes, 517
Trabecular meshwork (TM), 453–454
Trachea, 147–151, 150*f*
Transition zone, 348
Transitional epithelium (TE), 94–97
Triiodothyronine (T3), 253
Tri-lineage hematopoiesis, 369
Trophoblasts, 332, 332*f*
Truncal skin, 517–519
Tubal tonsil, 479
Tunica media, 184–185
Tunica vaginalis, 336–338
Tympanic membrane, 471, 473, 474*f*, 478–479

U

Ubiquitin carboxy-terminal hydrolase L1, 519
Umbrella cells, 296
Upper GI tract, 197*f*
duodenum, 208*f*

Upper GI tract (*Continued*)
esophagus, 191–194, 192*t*
fundic mucosa, 201*f*
gastric squamocolumnar junction, 200*f*
gut-associated lymphoid tissue (GALT), 207*f*
human regional abdominal anatomy, 195*f*
ileum, 209*f*
jejunum, 209*f*
methods, 211
rodent regional abdominal anatomy, 194*f*
small intestine, 201–211, 204*f*
stomach, 194–201
Ureters, 291–301, 298*f*
Urethra, 291–301, 300*f*, 321, 357–360, 359*f*
Urinary system, 276*t*–277*t*, 282. *See also* Endocrine system; Hepatobiliary system
kidney, 275–291
ureters, 291–301
urethra, 291–301
urinary bladder, 291–301
Urogenital system, 37–39, 37*f*
female, 38–39, 39*f*
male, 37–38, 38*f*
Urothelium, 296, 297*f*
Uterine tube. *See* Oviduct
Uterus, 303, 316*f*
anatomy, 315
histology, 315–320
Utricle, 479–480
Uvea
anatomy, 448–451
histology, 451–455

V

Vagina, 303, 320–321
Vaginal mucosa, 321, 324*f*
Vaginal vault, 321
Vas deferens, 343–346, 346*f*
Vascular organ of lamina terminalis (OVLT), 418
Vasculature, 181–182
Veins, 186, 187*f*
Venous plexus, 251–253
Ventral lobes, 353
Ventricular system, 414, 415*f*
Ventricular vein, 183
Vermillion, 115, 117–119
Vertebrae, 83
Vertebral arteries (VAs), 415–417
Vesicular glands. *See* Seminal vesicles
Vestibular membrane. *See* Reissner's membrane
Vestibular system, 479–480
Vestibule, 479–480
Vibrissae, 512–513
Villi, 201
small intestine, 205*f*
Villous chorion, 321
Visceral epithelial cells, 282
Visceral pericardium, 177–178
Visceral peritoneum, 211
Visceral pleura, 160
Vitreous chamber, 460–461
Vomeronasal organ (VNO), 93–94, 103
Vulval vestibule, 320–321

W

Waldeyer's ring, 104, 108
Wear-and-tear pigment. *See* Lipofuscin
Whiskers, 512–513
White adipose tissue (WAT), 85–87
Wilson's pencils. *See* Pencil fibers

X

X-zone, 258

Y

Yolk sac, 323–324

Z

Z-line, 191–193
Zona fasciculata, 258
Zona glomerulosa, 258
Zona pellucid, 307
Zymbal's gland, 471, 476*f*, 532–533

COMPARATIVE ANATOMY AND HISTOLOGY

A MOUSE, RAT, AND HUMAN ATLAS

EDITED BY

PIPER M. TREUTING, DVM, MS, Diplomate, ACVP
Associate Professor, Chief of Comparative Pathology, Department of Comparative Medicine
Adjunct Associate Professor, Department of Pathology, University of Washington School of Medicine, Seattle, WA, United States

SUZANNE M. DINTZIS, MD, PhD
Associate Professor, Department of Anatomic Pathology, University of Washington School of Medicine, Seattle, WA, United States

KATHLEEN S. MONTINE, PhD, ELS
Senior Principal Research Scientist, Department of Pathology, University of Washington School of Medicine, Seattle, WA, United States

Praise for the First Edition:

"…Chapters are clearly written and organized for easy access to important comparative features of mouse and human anatomy. As an additional bonus, brief 'Need-to-Know' snippets of take-away summary points are provided throughout each chapter…I highly recommend this book."—*R.R. Maronpot, CVM. MS, MPH. Chief of Laboratory of Experimental Pathology, NIEHS, NIH (Retired). Maronpot Consulting LLC, Raleigh, NC, United States*

"…we now have a comparative anatomy and histology book that will be an indispensable reference source for laboratory animal veterinarians and biomedical researchers…the reader will benefit from a healthy sprinkling of physiology that is found throughout the book…it has my strongest recommendation as a 'got to have it' book."
—*Laboratory Animal Practitioner, March 2014*

"This volume is an excellent resource with illustrative histological and anatomical figures, comprehensive and comparative descriptions, and recommended references. It will be especially useful to investigations using mice as models of human disease as well as to medical and veterinary pathologists."
—*Anticancer Research, Volume 33, Issue no. 5, May 2013*

"…The scope and completeness of this work makes an exhaustive review of every chapter or feature beyond the scope of any one reviewer, but the editors have done a yeoman's job in striving for both completeness and consistent presentation…. This is a book that many scientists from a wide range of disciplines will want to have on their shelves or computers long into the future."
—*Lab Animal, August 2012, Volume 41, No.8, Page 223*

Comparative Anatomy and Histology: A Mouse, Rat, and Human Atlas, Second Edition is aimed at the new rodent investigators as well as medical and veterinary pathologists who need to expand their knowledge base into comparative anatomy and histology. It guides the reader through normal mouse and rat anatomy and histology using direct comparison to the human. The side-by-side comparison of mouse, rat, and human tissues highlights the unique biology of the rodents, which has great impact on the validation of rodent models of human disease.

New to this edition:

- Offers the only comprehensive source for comparing mouse, rat, and human anatomy and histology
- Over 1500 full-color images
- Includes Netter human anatomy images along with Netter-style mouse and rat images

ExpertConsult.com

Enhanced eBooks for medical professionals

Compatible with PC, Mac®, most mobile devices, and eReaders, Expert Consult allows you to browse, search, and interact with this title – online and offline. Redeem your PIN at expertconsult.com today!

- Straightforward navigation and search across all Elsevier titles
- Seamless, real-time integration between devices
- Adjustable text size and brightness
- Notes and highlights sharing with other users through social media
- Interactive content

Look for instructions on how to redeem your PIN on the inside front cover!

ELSEVIER

ACADEMIC PRESS
An imprint of Elsevier
elsevier.com/books-and-journals

ISBN 978-0-12-802900-8